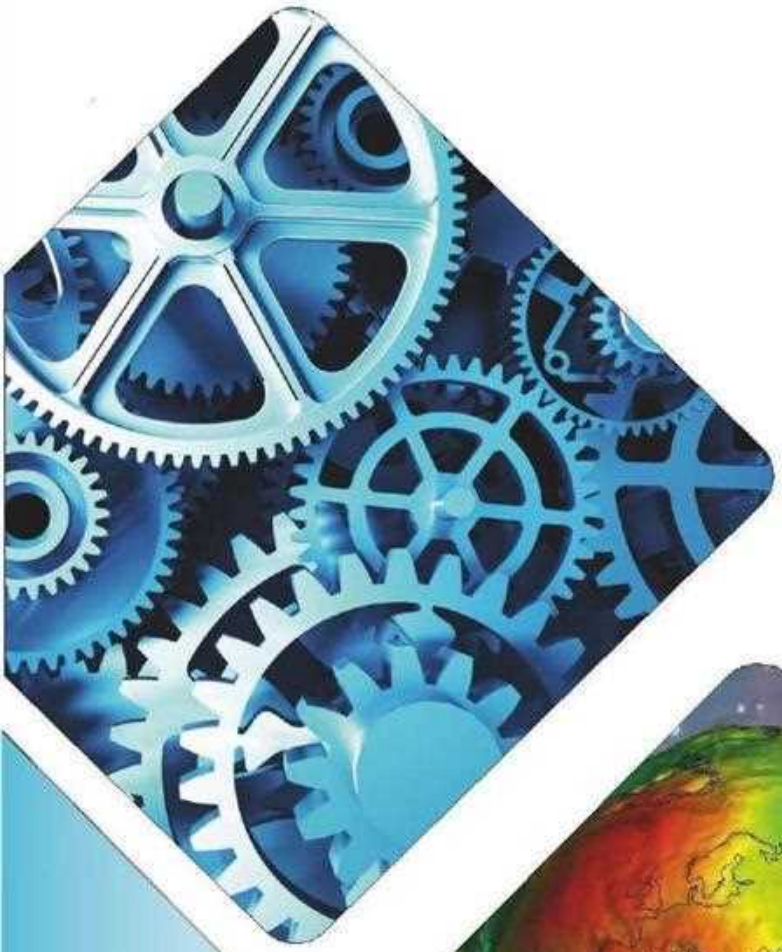
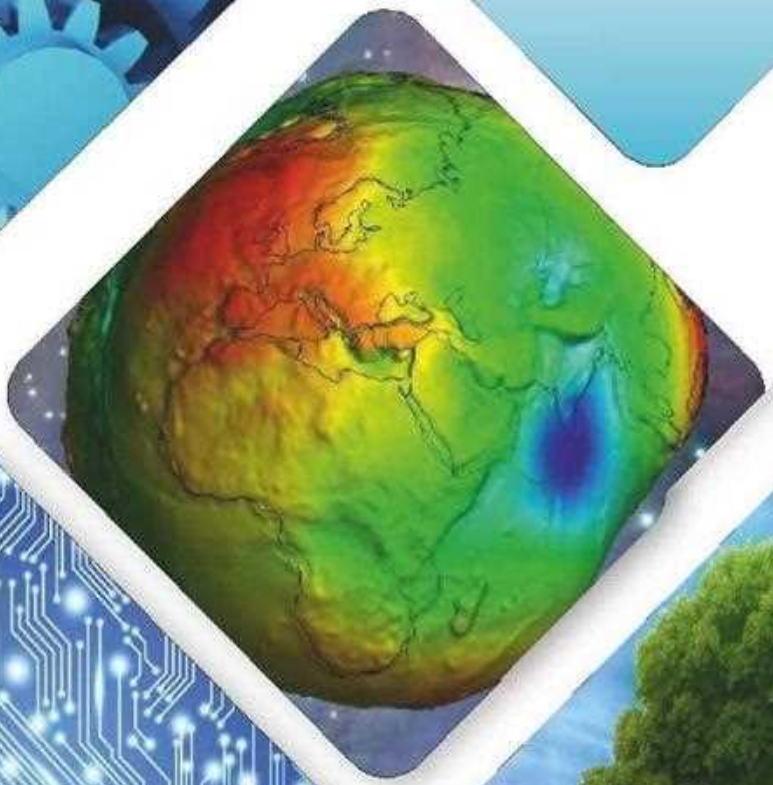
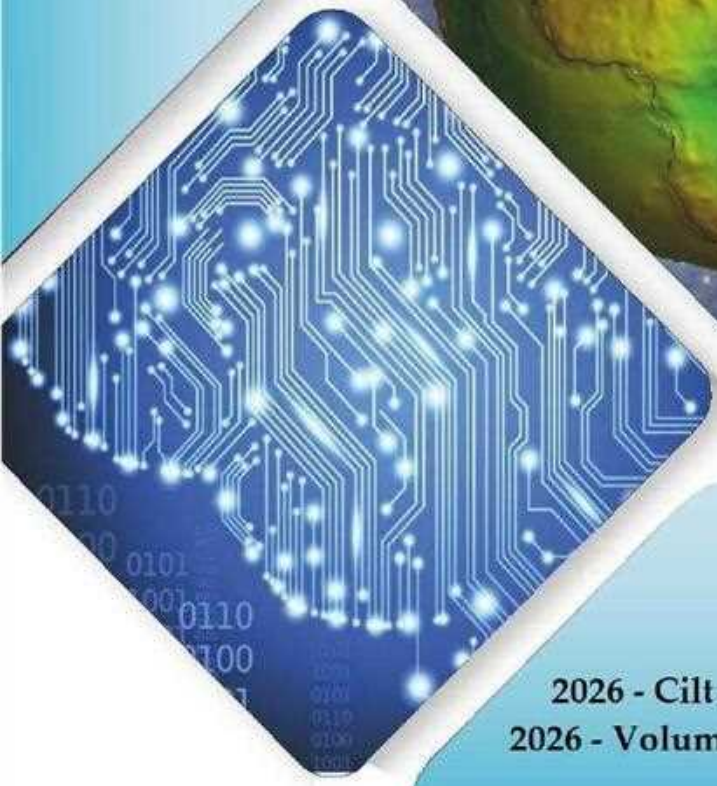
Konya Mühendislik Bilimleri Dergisi
Konya Journal of Engineering Sciences









(KONJES)
E-ISSN: 2667-8055

2026 - Cilt : 14 - Sayı : 2
2026 - Volume : 14 - Issue : 2

KONYA JOURNAL OF ENGINEERING SCIENCES (KONJES)
KONYA MÜHENDİSLİK BİLİMLERİ DERGİSİ

Peer-Reviewed Journal

OWNER/İMTİYAZ SAHİBİ

Owner on Behalf of Engineering and Natural Sciences Faculty of Konya Technical University **Prof. Ali KÖKEN**

Editor-in-Chief/Baş Editör

Prof. Musa Hakan ARSLAN

Associate Editors/Yardımcı Editörler

Assoc. Prof. Sercan DOĞAN

Assoc. Prof. Elif AVŞAR YILMAZ

Section Editors/Alan Editörleri

Prof. Muharrem Kemal ÖZFIRAT
Prof. Murat ÖZTÜRK
Prof. Mustafa KORKANÇ
Prof. Niyazi BİLİM
Prof. Orhan BAYTAR
Prof. Rıdvan SARAÇOĞLU
Prof. Ayla BOZDAĞ
Assoc. Prof. Abdulkerim OKBAZ
Assoc. Prof. Farabi TEMEL
Assoc. Prof. İsmail İNCE
Assoc. Prof. Mehmet Ali TOPÇU
Assoc. Prof. Monika MAZIUKIENÈ
Assoc. Prof. Muharrem Hilmi AKSOY
Assoc. Prof. Sercan BÜLBÜL
Assoc. Prof. Mehmet ŞAHİN ATAŞ
Assoc. Prof. Zeynep ÇETİNKAYA
Assoc. Prof. Emine BAŞ
Assoc. Prof. Mehmet UZUN
Assoc. Prof. Ayşe Elif CANBİLEN
Asst. Prof. Alper DÖYEN
Asst. Prof. Burhaneddin BİLGEN
Asst. Prof. Enes ÖZKÖK
Asst. Prof. Kemal ERDOĞAN
Asst. Prof. Muhammed Arif ŞEN
Asst. Prof. Veli BAKIRCIOĞLU
Asst. Prof. Fatma Zehra SOLAK
Asst. Prof. Betül UZBAŞ
Asst. Prof. Alper KILIÇ
Asst. Prof. Selim SOYLU
Asst. Prof. Taylan DOLU
Dr. Burak KIVRAK
Dr. İsmail BAŞOĞLU

Language Editing/Yabancı Dil Editörü

Instructor Hasan KOCADAYIOĞULLARI

Secretary/Sekreter

Res. Asst. İrem KÖZ
Res. Asst. Ender KURNAZ
Res. Asst. Harun SEVİNÇ
Res. Asst. Metin DİNMEZ
Res. Asst. Metehan IŞIK
Res. Asst. Mustafa BAŞAR

Phone: +90 332 205 15 00
Fax: +90 332 241 06 35
E-mail: konjes@ktun.edu.tr
Web : http://dergipark.org.tr/konjes

Correspondance Address/ Yazışma Adresi

Konya Teknik Üniversitesi, Mühendislik ve Doğa Bilimleri Fakültesi Dekanlığı
42075-Kampüs, Selçuklu, Konya, TÜRKİYE

EDITORIAL ADVISORY BOARD

Prof. Ahmet Afşin KULAKSIZ
Konya Technical University, Türkiye
Prof. Fahrettin ÖZTÜRK
Istanbul Technical University, Türkiye
Prof. Ali KOÇAK
Yildiz Technical University, Türkiye
Prof. H. Kürşad ERSOY
Konya Technical University, Türkiye
Prof. Lilia GEORGİEVA
Heriot-Watt University, Scotland
Assoc. Prof. Alpaslan YARAR
Konya Technical University, Türkiye
Prof. Hi-ryong BYUN
Pukyong National University, South Korea
Prof. Hüseyin DEVECİ
Konya Technical University, Türkiye
Prof. İhsan ÖZKAN
Konya Technical University, Türkiye
Prof. Kerim KOÇAK
Konya Technical University, Türkiye
Lecturer Loredana Emanuela JUDELE
Gheorghe Asachi Technical University of Iași, Romania
Prof. Bouabaz MOHAMED
University of 20 August 1955 Skikda, Algeria
Prof. Selçuk Kürşat İŞLEYEN
Gazi University, Türkiye
Assoc. Prof. Selim DOĞAN
Konya Technical University, Türkiye
Prof. Spase SHUMKA
Agricultural University of Tirana, Albania
Prof. Zoran SAPURIC
University American College, Macedonia
Prof. Murat KARAKUS
University of Adelaide, Australia
Prof. Volkan KALEM
Konya Technical University, Türkiye
Prof. Dr. Saadettin Erhan KESEN
Konya Technical University, Türkiye

The June 2026 issue of **KONJES** (Volume 14, Issue 2) aims to contribute broadly to engineering sciences with 26 diverse and valuable research articles. This issue covers a wide range of topics, from compliance with legislation and public interest in urban planning, to AI-supported academic performance prediction; from deep learning-based emotion recognition, to energy efficiency and power quality improvement; from earthquake data analysis, fire station site selection, hybrid composite behaviors, to dynamic studies of historical bridges. Additionally, risk analyses in environmental and health contexts, material characterization, AI-based image processing applications, and sustainability-focused energy studies stand out as key highlights. This rich content provides an important resource for developing both academic and practical solutions in engineering.

The KONJES editorial board sincerely thanks more than 70 distinguished reviewers and section editors for their dedicated contributions to the preparation and publication of this issue.

KONYA JOURNAL OF ENGINEERING SCIENCES
(KONJES)
KONYA MÜHENDİSLİK BİLİMLERİ DERGİSİ

ISSN 2667 – 8055 (Electronic)

Volume	14	June	2026	Issue	2

CONTENTS

Research Articles

DIRECTORATE OF HIGH TECHNICS BOARD DECISIONS IN PUBLIC CONSTRUCTION PROJECTS: A MACHINE LEARNING APPROACH TO DISPUTE RESOLUTION
Mahmut SARI, Savaş BAYRAM, Emrah AYDEMİR……..……..…….……..... 518-535

A NEW APPROACH TO DETERMINE THE FLEXURAL STIFFNESS FOR REINFORCED CONCRETE COLUMNS ACCORDING TO NON-LINEAR BEHAVIOUR
Saeid FOROUGHİ, Süleyman Bahadır YÜKSEL……..…….……536-567

SOLID WASTE TO ENERGY: A TECHNICAL AND ECONOMIC STUDY FOR INTEGRATED ENERGY PRODUCTION – THE CASE OF HAKKARI, TÜRKİYE
Bahattin YAKIŞ, Yunus ÇELİK, Yakup KARAKOYUN……..……..…...568-585

LYMPHOMA LESION SEGMENTATION IN NECK AXIAL AND CORONAL SECTION CT IMAGES WITH U-NET
Mete Can YAŞAR, Mustafa Emre YAŞAR, Rahime CEYLAN, Abidin KILINÇER , Mustafa KOPLAY, Selda HAKBİLEN, Sema YILMAZ, Rafiye ÇİFTÇİLER, Burcu YORMAZ Emre TEKELİ, Fatih SAKA , Senayi DÖNMEZ ……..……..……..……..……..… 586-598

INVESTIGATION OF Co(II) ADSORPTION ONTO RICE HUSK ASH: KINETICS, ISOTHERMS, AND THERMODYNAMICS
Sevgi POLAT……..……..…… 599-612

A REINFORCEMENT LEARNING APPROACH TO THE DINING PHILOSOPHERS PROBLEM
Cem ÖZKURT, Ahmet KALA, Muhammed Emin ONAY..……..…….... 613-627

UTILIZING OPTIMIZATION APPROACHES TO ASSESS TOTAL NETWORK LOSSES IN TÜRKİYE
Murat ASLAN, Ömer Ali KARAMAN, Mustafa SAĞLAM, Mehmet Şefik ÜNEY…… 628-647

EFFECTS OF TEMPERATURES ON PHYSICOCHEMICAL PROPERTIES OF CELERY (*Apium graveolens* L.) SLICES DRIED BY INFRARED DRYER
Muhammed TAŞOVA..……..…….... 648-657

BINARY SWITCHING LINEAR MODEL CONTROL FOR LTI SYSTEMS: STABILITY ANALYSIS AND MODE CONTROL EQUIVALENCE
Can Ulaş DOĞRUER, Can Barış TOPRAK, Bora YILDIRIM ……..…… 658-681

DEVELOPMENT OF ARTIFICIAL INTELLIGENCE SUPPORTED PUFFERFISH TRAP
Mert DEMİR..... 682-699

PERFORMANCE ASSESSMENT OF A HYBRID FRESNEL SOLAR-GEOTHERMAL ORC UTILIZING DRY ORGANIC FLUIDS
Serpil ÇELİK TOKER.....700-718

OPTICAL FLOW-BASED LIDAR ODOMETRY
Mesut TUNÇER, Alper KILIÇ 719-740

EVALUATING THE PROFITABILITY EFFECTS OF CAPACITY AND STATE OF CHARGE IN BATTERY-INTEGRATED DISTRIBUTION NETWORKS
Fatma Avli FIRIŞ, İsrafil KARADÖL, Ökkeş Fatih KEÇECİOĞLU 741-759

MICROSTRUCTURAL EVOLUTION AND TRIBOLOGICAL PROPERTIES OF ELECTROLESS NI-P-B AND NI-P-B-W POLYALLOY COATINGS
Harun MİNDİVAN.....760-774

PERFORMANCE ASSESSMENT OF A RURAL PHOTOVOLTAIC–LITHIUM ION BATTERY ENERGY SYSTEM: EFFECTS OF TILT ANGLES, SOILING FACTOR AND BATTERY TEMPERATURE
Furkan DİNÇER, Emre ÖZER..... 775-802

INVESTIGATION OF THE EFFECT OF CHIMNEY DIAMETER ON THERMODYNAMIC PERFORMANCE IN SOLAR CHIMNEY POWER PLANT DESIGN: A CFD ANALYSIS
Mustafa ÖNAL, Ali KOÇ, Özkan KÖSE, Yıldız KOÇ, Hüseyin YAĞLI..... 803-829

IMPROVING EOG-BASED CLASSIFICATION PERFORMANCE: A COMPARATIVE ANALYSIS WITH VARIOUS MACHINE LEARNING ALGORITHMS
Khalid Hani ABUSHAHLA, Ayse Nur AYGUL..... 830-842

PREDICTION OF CRITICAL SUBMERGENCE FOR HORIZONTAL INTAKES UNDER ASYMMETRICAL APPROACH FLOW CONDITIONS
Serkan GÖKMENER, Dalal Abdulkareem Hussein AL-OBAIDI..... 843-868

DETERMINING THE LOCATION OF ELECTRIC VEHICLE CHARGING STATIONS IN ANTALYA PROVINCE USING GIS-BASED FUZZY MULTI-CRITERIA DECISION MAKING TECHNIQUES
Aleyna KENAR, Eray BAYSAL, Eren KAMBER, Ufuk AYDOĞMUŞ, Hacer YUMURTACI AYDOĞMUŞ 869-900

COMPARATIVE ANALYSIS OF TARGET LOCALIZATION ACCURACY IN RADAR PPI IMAGES USING GEOMETRIC ENCLOSURES
Sercan KÜLCÜ..... 901-916

AN OVERVIEW OF MULTIMODAL LEARNING: CONCEPTS, CHALLENGES, APPLICATIONS AND DATASETS
Ali Hüsameddin ATEŞ, Ulaş YURTSEVER 917-950

SEISMIC SOIL MICROZONATION IN TURKEY: BRIDGING GAPS BETWEEN INTERNATIONAL STANDARDS AND LOCAL IMPLEMENTATION
Kaveh DEHGHANIAN…….. 951-965

AN INVESTIGATION OF THE EFFECT OF GEOPOLYMER COATED GEOTEXTILES ON THE BEHAVIOR OF WEAK SOILS UNDER LOADS
Talha SARICI, Mustafa ÖZCAN, Aybüke MUTLU…….966-978

A NOVEL APPROACH FOR ANALYTICAL MODEL OF *METAL-METAL FUNCTIONALLY* GRADED CIRCULAR BEAM
Ali ÖZTÜRK…….979-997

THE COMPARISON OF FUZZY INFERENCE SYSTEM AND THE BEES ALGORITHM FOR OPTIMAL DESIGN OF BALANCING HOLE OF CENTRIFUGAL PUMP IMPELLER
Selahattin SEFACI , Osman ACAR , Mete KALYONCU , Saim KOÇAK……998-1015

DESIGN AND IMPLEMENTATION OF AN OFFLINE AUTOCLAVE WEB SIMULATOR
Ali Özhan AKYÜZ, Mustafa AYAN, Kazım KUMAŞ, Durmuş TEMİZ……1016-1032

Konya Mühendislik Bilimleri Dergisi., c.14, s.2, 518-535, 2026
Konya Journal of Engineering Sciences v.14, n.2, 518-535, 2026
ISSN: 2667-8055 (Electronic)
DOI: 10.36306/konjes.1664994

DIRECTORATE OF HIGH TECHNICS BOARD DECISIONS IN PUBLIC CONSTRUCTION PROJECTS: A MACHINE LEARNING APPROACH TO DISPUTE RESOLUTION

[1]Mahmut Sarı, [2,]*Savaş Bayram, [3]Emrah Aydemir

[1]*Department of Civil Engineering, Kırşehir Ahi Evran University, Kırşehir, 40100, Türkiye.*
[2]*Department of Civil Engineering, Erciyes University, Melikgazi, Kayseri, 38039, Türkiye*
[3]*Sakarya Business School, Department of Management Information Systems, Sakarya University, Esentepe Campus, 54187, Sakarya, Türkiye*
[1]mahmutsari@ahievran.edu.tr, [2]sbayram@erciyes.edu.tr, [3]emrahaydemir@sakarya.edu.tr

Highlights

- Study applies technological approach to DHTB's expanded role after 2020.
- MultiBoostAB algorithm with 11 legal factors achieved 70.41% prediction accuracy.
- Content analysis enabled objective evaluation of legal texts in decision processes.
- Machine learning model expedites dispute resolution in public construction projects.
- Future studies will focus on dataset expansion and large language models.

Graphical Abstract

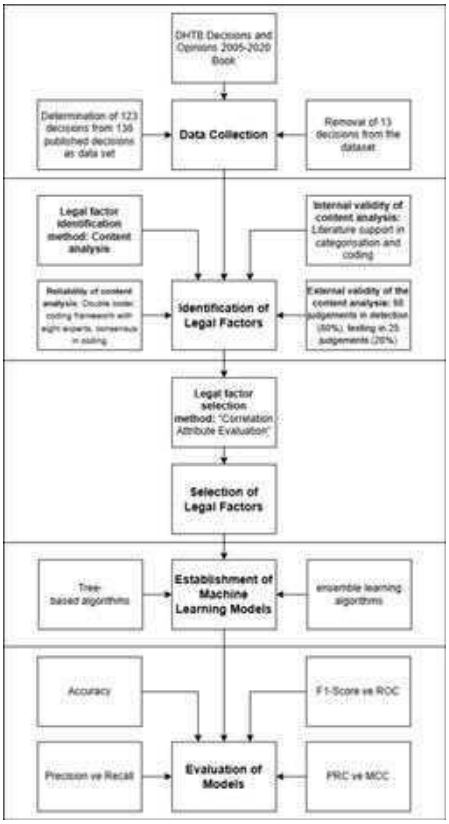


Figure Methodology of the study

***Corresponding Author:** Savaş BAYRAM, sbayram@erciyes.edu.tr

Konya Mühendislik Bilimleri Dergisi., c.14, s.2, 518-535, 2026
Konya Journal of Engineering Sciences v.14, n.2, 518-535, 2026
ISSN: 2667-8055 (Electronic)
DOI: 10.36306/konjes.1664994

DIRECTORATE OF HIGH TECHNICS BOARD DECISIONS IN PUBLIC CONSTRUCTION PROJECTS: A MACHINE LEARNING APPROACH TO DISPUTE RESOLUTION

[1]Mahmut Sarı, [2,]*Savaş Bayram, [3]Emrah Aydemir

[1]Assistant Professor, Department of Civil Engineering, Kırşehir Ahi Evran University, Kırşehir, 40100, Türkiye.
[2]Professor, Department of Civil Engineering, Erciyes University, Melikgazi, Kayseri, 38039, Türkiye
[3]Associate Professor, Sakarya Business School, Department of Management Information Systems, Sakarya University, Esentepe Campus, 54187, Sakarya, Türkiye
[1]mahmutsari@ahievran.edu.tr, [2]sbayram@erciyes.edu.tr, [3]emrahaydemir@sakarya.edu.tr

(Received: 26.03.2025; Accepted in Revised Form: 31.10.2025)

ABSTRACT: Disputes arising in public construction projects can lead to time and cost overruns, which negatively impact project processes. This study developed a machine-learning model to predict such disputes by analyzing decisions from the Directorate of High Technics Board of Public Works. Through a literature review and content analysis, a total of 18 legal factors were identified. Using the CorrelationAttributeEvaluation method, 11 out of the 17 input legal factors were selected as target legal factors for inclusion in the model. The MultiBoostAB algorithm demonstrated the best performance, achieving an accuracy rate of 70.41%. The content analysis method employed in the model ensured an objective identification of legal factors specific to the legal context and played a significant role in interpreting the decision texts. However, the limited size of the dataset was identified as a limitation, affecting the model's generalizability. Future studies are recommended to expand the dataset, apply over-sampling techniques, and integrate natural language processing methods. In addition, analysing decision texts using methods such as Natural Language Processing (NLP), BERT and RoBERTa to identify legal factors and establish prediction models can strengthen the identification of factors specific to the legal context and the accuracy of predictions.

Keywords: *Construction disputes, content analysis, dispute resolution, machine learning, prediction models.*

1. INTRODUCTION

The construction sector has multifaceted and complex relationships, which often leads to disagreements between parties due to misalignments in objectives and priorities. There are numerous factors that inevitably contribute to construction disputes. When examining studies focusing on the factors causing construction disputes from a broad perspective, these factors can be categorised based on their nature and formation as follows: i. Payment and financing-related factors [1-5], ii. Time-related and delay-related factors [2, 6-9], iii. Contract-related factors [5, 10-13], iv. Employer-related factors [5, 7, 13-15], v. Contractor-related factors [13, 16, 17], vi. Design-related factors [5, 13, 18, 19], vii. Human behaviour-related factors [5, 8, 13, 20], viii. Project-related factors [2, 9, 13, 21] and ix. External factors [13, 22-24] are observed to be clustered around these factors. Disputes in the construction sector result in financial, moral, time, and quality losses. For example, the average cost of construction disputes in North America is $43 million, and the average resolution time for disputes is 14.4 months [25]. Efforts to compensate for such significant losses are of great importance. Accurately identifying and understanding the factors that cause construction disputes enables important steps to be taken towards resolving disputes, preventing financial and non-financial losses, and preventing disputes through preventive activities [3].

***Corresponding Author:** Savaş BAYRAM, sbayram@erciyes.edu.tr

Construction disputes frequently occur in both the private and public sectors. Disputes arising in the implementation of state investments cause material losses and have a social impact in terms of disrupting public services. Therefore, preventing disputes in public construction projects is of particular importance. Disputes in public construction projects arise in the pre-contract and post-contract processes. Disputes arising before the contract comes into force are resolved through the complaint and appeal processes within the Public Procurement Authority, in accordance with the Public Procurement Law No. 4734. Disputes arising after the contract is signed are resolved in accordance with the provisions of the Public Procurement Contracts Law No. 4735 and the General Conditions for Construction Works. During the implementation phase of the contract519, the contractor must submit a reasoned petition regarding the dispute to the administration within 15 days [26]. The administration must respond to this application in writing within two months. If the contracting authority fails to respond or if the contractor is not satisfied with the response, the contractor may resort to official judicial or arbitration proceedings [27]. In addition to costly and lengthy processes such as official litigation and arbitration, the public employer may request an opinion from the High Technical Council (DHTB) of the Ministry of Environment, Urbanisation and Climate Change regarding the dispute. In fact, with the latest amendment to the law, both the public employer and the contractor may request this opinion [27]. This amendment grants the contractor the right to apply, making the DHTB a more inclusive mechanism for resolving public construction disputes. By their very nature, they have a high level of expertise in the legal nature of construction practices as well as technical processes. With these advantages, the ADR mechanism has the potential to serve as an alternative to formal litigation, which can be lengthy and costly for the parties due to insufficient examination and incorrect assessments [2]. The legislativ519e amendment has also created a significant opportunity for all parties to resolve construction disputes at an early stage. This is because the duration of formal judicial proceedings for construction disputes is considerably lengthy.

By granting the contractor the right to apply to the DHTB mechanism, the decisions made by the DHTB, due to their high technical capacity, can serve as a basis for potential legal proceedings and reduce the workload of the courts. If disputes are resolved without being brought to official courts, they will be resolved quickly, public resources will not be wasted, and public services will not be disrupted. However, granting the contractor the right to apply has significantly increased the scope and workload of the DHTB. A review of the literature reveals a gap in the literature regarding studies on the effects of legislative changes granting contractors the right to apply to the DHTB in public construction disputes. The aim of this study is to develop a machine learning-based mechanism to address the increased workload of the DHTB.

2. LITERATURE REVIEW

Disputes in construction projects generally arise from different interpretations of contract provisions, uncertainties stemming from technical details, and delays in the process. Early prediction plays a critical role in dispute resolution to minimise time and cost losses. In the literature, various data sources and modelling methods have been used for dispute prediction. However, these studies differ in terms of data type, methodological diversity, and the weight given to contextual factors.

Un, et al. [28] developed a model for predicting construction disputes using machine-learning algorithms with a dataset based on arbitration cases in Turkey. The study represents a current endeavour through its use of actual arbitration data and testing algorithms such as Support Vector Machines (SVM), Logistic Regression (LR), and Random Forests (RFs). It noted that the SVM algorithm demonstrated the best performance with an accuracy rate of 71.65%. However, the variables in this study are largely based on general factors derived from literature, without incorporating more objective, data-driven methods. Additionally, the limited number of algorithms used restricts the diversity of the modelling process. These deficiencies will be addressed in this study by objectively determining legal factors through content analysis and testing 24 different machine-learning algorithms.

Although the use of machine learning algorithms provides a significant advantage in prediction models, the methodological preferences in determining variables cannot be ignored in their effect on

model performance. In this context, Bagherian-Marandi, et al. [29] developed a two-layer fuzzy logic model on 100 samples from Iranian court decisions. In this study, variables were determined through expert opinions, and the model correctly predicted 60% of the test data. Whilst this methodology allows for a more flexible framework for evaluating legal factors, the subjective nature of variable selection has limitations in terms of model reproducibility. Furthermore, restricting the modelling process to only the fuzzy logic approach reduces methodological diversity. The present study aims to provide a broader perspective by presenting the results of models established with 24 algorithms using legal factors determined through objective content analysis.

With a different methodological approach, Arditi, et al. [30] conducted neural network modelling on 12 years of data obtained from court cases in Illinois state. The study revealed the potential of neural networks for dispute prediction and helped parties predict dispute outcomes with an accuracy rate of 67%. However, this study relied on general case information during factor determination and did not consider context-specific technical factors. Additionally, using only neural networks limits algorithm diversity. Unlike these deficiencies, the present study aims to utilise a broader dataset and increase algorithm diversity by drawing on technical data containing expert opinions and decisions from DHTB.

Chaphalkar, et al. [31] developed a multilayer neural network model using 204 data points obtained from arbitration cases in India. The model achieved a remarkable success with an accuracy rate of 90%, but the limited algorithms used and the lack of objective methods such as content analysis restricted the generalisability of the model. The present study expands methodological scope by aiming to objectively determine legal factors through content analysis and testing these factors with a broad set of algorithms. Although previous research on dispute prediction has come a long way to addressing the inherent complexities of the construction sector, there remain widespread methodological deficiencies and generalisability issues in the literature. Most of these studies use a narrow range of algorithms with context-independent data sources, largely neglecting comprehensive analysis of legal factors and the use of objective modelling techniques. In this context, there is a need for more objective and reproducible methods in determining and modelling effective factors. For example, Alshboul, et al. [32] developed a machine learning model to predict compensation in highway project delays, achieving a remarkable accuracy level of 99.7%. However, the process of determining factors used in this study was conducted without considering the legal context. Similarly, Anysz, et al. [33] presented an in-house data-driven model for risk assessment and achieved 93% accuracy using ANN and DT algorithms. Whilst this study is customised to present a project-based model, it remains limited in broader contexts due to its lack of generalisability and objective factor analysis.

Chou and Lin [34] focused on public-private partnership projects and created an ensemble model combining SVM, ANN, and C5.0 algorithms, reaching an accuracy rate of 84.33%. The model is designed as an early warning system to predict disputes in public projects. Ayhan, et al. [35] performed a prediction of compensation claims related to construction disputes using the Naive Bayes algorithm and subsequently examined variables determined through literature review using the Chi-square test. The model achieved an accuracy rate of 80.61% but did not examine the legal context in sufficient detail.

The methodological deficiencies highlighted in these studies demonstrate the need for more comprehensive approaches in the field of dispute prediction. The aim of this study is to establish a systematic framework for determining legal variables using an objective content analysis method examining decisions published by DHTB. Additionally, analyses based on 24 different machine learning algorithms aim to fill the methodological diversity gap found in the literature. This will enable more generalisable, context-sensitive, and effective prediction of disputes in public construction projects.

3. MATERIAL AND METHODS

The methodology of the study consists of the stages: (i) data collection, (ii) identification of legal factors, (iii) selection of legal factors, (iv) establishment of machine learning models and (v) evaluation of models. The methodology of the study is shown as a diagram in Figure 1.

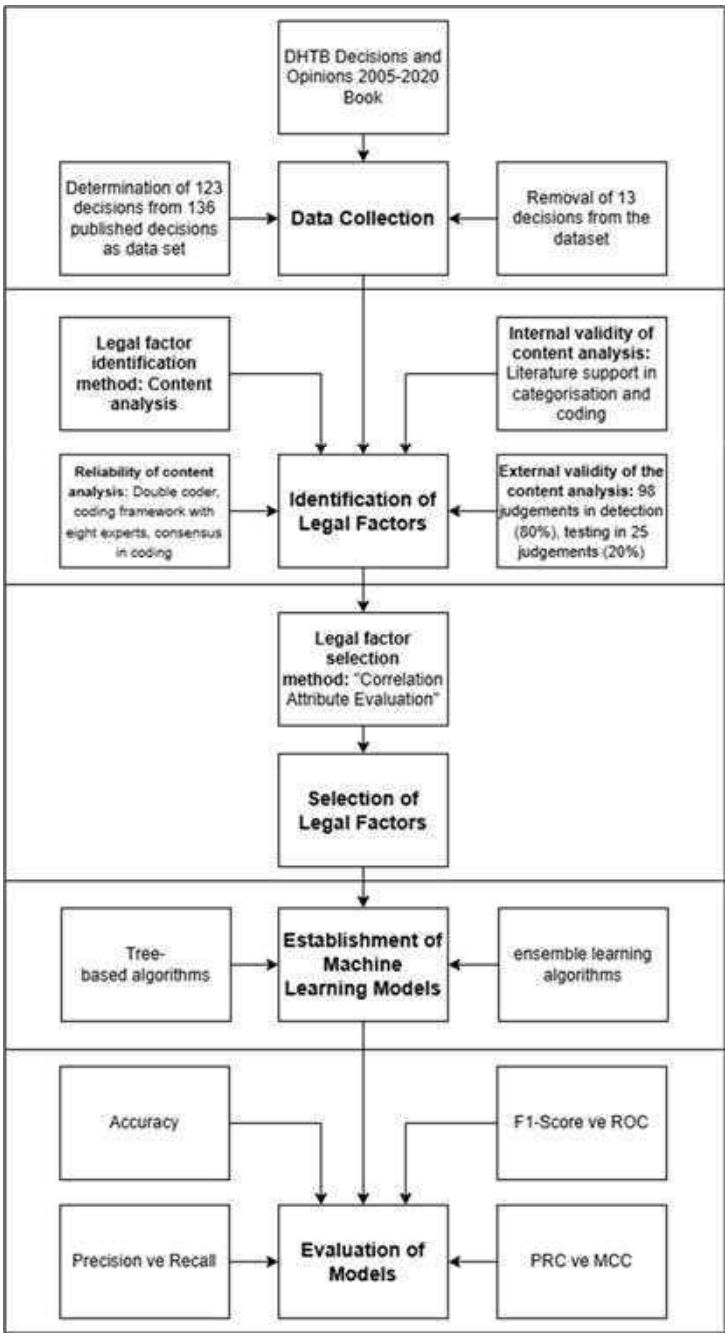


Figure 1. Methodology of the study

3.1. Data Collection

In this study, all decisions published in the "DHTB Decisions and Opinions 2005-2020" book [36] were identified as the dataset. This book contains a total of 136 decisions referred to the DHTB and resolved. However, 13 decisions containing only principles for the resolution of construction disputes were excluded from the dataset. Therefore, the final dataset was determined as 123 decisions. The distribution of these 123 decisions by year is as follows: 5 decisions from 2006 (4.07%), 1 decision from 2007 (0.81%), 1 decision from 2008 (0.81%), 3 decisions from 2009 (2.44%), 8 decisions from 2010 (6.50%), 6 decisions from 2011 (4.88%), 16 decisions from 2012 (13.01%), 18 decisions from 2013 (14.63%), 20 decisions from 2014 (16.26%), 13 decisions from 2015 (10.57%), 10 decisions from 2016 (8.13%), 3 decisions from 2017 (2.44%), 4 decisions from 2018 (3.25%), 6 decisions from 2019 (4.88%) and 9 decisions from 2020 (7.32%).

3.2. Identification of Legal Factors

The content analysis method was used to identify specific themes and concepts in the DHTB decision texts that could be understood by field researchers and readers. Content analysis is a method that involves coding qualitative data by grouping them within the framework of specific concepts and themes [37]. In studies in literature, the case analysis method has also frequently been applied in the analysis process of decision texts [30, 31, 38-41]. However, content analysis was preferred as it is a more objective and reproducible method when validity and reliability conditions are met [42, 43].

To ensure objectivity in the selection of decisions, decisions spanning certain periods and covering different types of construction disputes were systematically selected. A group of experts specialised in construction disputes with professional diversity was consulted in creating the coding framework. This group had a diverse range of expertise with 50% academicians, 25% lawyers, and 25% civil engineers. Categories used in the coding process were based on standard criteria developed with literature support.

To increase the reliability of the coding process, multiple coders were employed, and inter-coder reliability was tested. Agreement in coding was ensured by coders acting based on consensus, with care taken to increase both internal and external validity. Additionally, experts' feedback was received while developing the coding framework, and both theoretical and practical contributions were incorporated into the process. As emphasized by Hall and Wright [43], the systematic selection and coding of decisions is critical for the representativeness and objectivity of the analysis. As suggested by Johnson [42], the aim was to clearly define the criteria used in the coding process and obtain reproducible results. To increase internal validity, coding and categories were supported with relevant literature. In terms of external validity, tests were conducted on 98 decision texts comprising 80% of the total decisions, and the consistency of results was observed with the remaining 20% (25 decisions). Correct understanding of the language and context used in the analysis of legal texts was ensured. During the examination of decisions, not only the superficial structure of the texts but also the legal grounds on which the decisions were based and their social impacts were considered.

3.3. Selection of Legal Factors

The CorrelationAttributeEvaluation (CAE) method was used to analyse the effects of the legal factors included in DHTB decisions on the target legal factor and the relationships between them. This method uses the Pearson correlation coefficient to measure the linear relationship between each attribute and the target attribute [44]. This allows the method to provide a statistically interpretable, transparent, and classifier-independent evaluation. The correlation coefficient varies between (+1) and (-1); a value of (+1) indicates a strong linear relationship between legal factors, a value of (-1) indicates an inverse relationship, and a value of zero indicates no significant relationship between the two factors [45].

In this study, the CAE method was preferred over model-based importance ranking approaches for feature selection. The main reasons for this preference are: i. It is statistically transparent and interpretable because it measures the linear dependence between the input feature(s) and the target feature [46], ii. It is independent of classifiers [47], iii. It prevents overfitting caused by model-specific biases [48], and iv. Because it focuses on only a single input attribute, it ranks variables independently of the model. A correlation-based attribute selection method that is unbiased, transparent, and interpretable has been used, avoiding model-based deviations that may be observed in model-based importance level rankings. Considering the importance of interpretability in legal decision texts, CAE is more suitable than model-based importance approaches, which are difficult to explain in terms of the algorithm, as it provides statistically transparent facts in the selection of attributes. Considering that excluding legal factors with low correlation coefficients from the model could prevent overfitting, these legal factors were excluded from the analysis. In filter-based selection, attributes with weak relationships, such as correlation, can be eliminated using simple relationship measures [49]. Furthermore, it is frequently stated in the literature that correlation values below .05 may be very small and practically insignificant [50, 51]. Therefore,

variables below the 0.05 level were excluded from the study. 10-fold cross-validation was used to evaluate the model's generalisation performance. The 10-fold cross-validation method offers a balanced structure between bias and variance [52]. It has been observed that this method consistently estimates error rates even with small data sets [53]. Additionally, this choice has been effective in providing a more stable (lower variance) generalisation estimate compared to a single train/test split. Using 10-fold cross-validation instead of a one-off hold-out for model selection and performance estimation, even in large datasets, reduces the volatility created by random partitioning. This has been proven by testing on very large datasets [52]. For these reasons, the 10-fold cross-validation method was chosen for this study with a small data set, as it is expected to provide balanced and reliable performance.

3.4. Establishment of Machine Learning Models

A total of 24 different algorithms were used to solve binary classification problems between input and target legal factors for DHTB decision prediction. These algorithms were divided into two main groups: tree-based and ensemble learning methods. The 10-fold cross-validation method was used in the training and testing phases of the dataset. Additionally, this method is a reinforcement method for preventing overfitting.

Tree-based methods include Alternating Decision Tree, Best-First Decision Tree, Reduced Error Pruning Tree, Random Tree, Simple Cart, J48, Random Forest (RF), Functional Tree, Naive Bayes Tree, Decision Stump, Logistic Model Tree, and Least Absolute Deviations Tree; while ensemble learning methods include Iterative Classifier Optimizer, UltraBoost, RandomSubSpace, MultiBoostAB, RandomCommittee, FilteredClassifier, Adaptive Boosting, Ensemble Selection, Bootstrap Aggregating (Bagging), AttributeSelectedClassifier, LogitBoost, and ClassificationViaRegression. In this context, it was decided to use the MultiBoostAB algorithm, which demonstrated high performance among the tested algorithms.

The MultiBoostAB algorithm is one of the ensemble learning methods. This algorithm is based on the principle of training successive weak classifiers in the AdaBoost algorithm and training classifiers on different sample subsets selected by weighted sampling (Weighted Bagging) [54]. This structure enables the algorithm to achieve high success in both imbalanced datasets and difficult classification problems [55].

3.5. Evaluation of Models

The prediction performance of classification algorithms was measured using various evaluation metrics. These metrics include accuracy, precision, recall, F1-score, Receiver Operating Characteristic (ROC), Precision-Recall Curve (PRC), and Matthews Correlation Coefficient (MCC). Analyses based on the confusion matrix were performed to measure the performance of the models (Table 1).

Table 1. Structure of the confusion matrices [56].

		Predicted label		
		Label=1	Label=0	
True label	Label=1	TP (True Positive)	FN (False Negative)	
	Label=0	FP (False Positive)	TN (True Negative)	

$$\boldsymbol{Accuracy} = \frac{(\mathrm{TP} + \mathrm{TN})}{(\mathrm{TP} + \mathrm{TN} + \mathrm{FP} + \mathrm{FN})} \quad (3.1)$$

$$\boldsymbol{Precision} = \frac{\mathrm{TP}}{(\mathrm{TP} + \mathrm{FP})} \quad (3.2)$$

$$\boldsymbol{Recall} = \frac{\mathrm{TP}}{(\mathrm{TP} + \mathrm{FN})} \quad (3.3)$$

$$\textbf{F1 Score} = 2 * \frac{\text{Precision} * \text{Recall}}{\text{Precision} + \text{Recal}} (3.4)$$

$$MCC = \frac{(\text{TPxTN}) - (\text{FPxFN})}{(\text{TP} + \text{FP})\text{x}(\text{TPxFN})\text{x}(\text{TN} + \text{FP})\text{x}(\text{TN} + \text{FN})} (3.5)$$

The Matthews Correlation Coefficient (MCC) measures overall classification performance by balancing true positives, true negatives, false positives, and false negatives. MCC values range from -1 (completely incorrect) to 0 (random guessing) to +1 (perfect classification). ROC (Receiver Operating Characteristic) combines False Positive Rate (FPR) and True Positive Rate (TPR) values for all possible cut-off thresholds to show model performance at various decision thresholds for classification models. The Precision-Recall Curve (PRC) evaluates how accurately the model identifies the positive class in two-class classification problems.

4. RESULTS AND DISCUSSION

The book "DHTB Decisions and Opinions 2005-2020" was selected as the dataset, in which 136 decisions were examined, and a final dataset consisting of 123 decisions was used. The dataset was analysed using content analysis methods, and legally relevant factors supported by the literature were identified. The legal factors "DHTB1-Project Province" [57, 58], "DHTB2-Contract Type" [30, 38, 57, 59-65], "DHTB3-Project Type" [40, 57, 58, 65], "DHTB4-Project Cost" [30, 38, 57-59, 63-65], "DHTB5-Project Duration" [57, 58, 65], "DHTB6-Dispute Type" [2, 41] were identified. The DHTB decisions in the dataset were examined using the content analysis method. Specific to DHTB decisions, the legal factors "DHTB7-Dispute Cost", "DHTB8-Dispute Time", "DHTB9-1-No Relevant Law Article", "DHTB9-3-Public Procurement Contracts Law No. 4735", "DHTB9-4-General Specifications for Construction Works", "DHTB9-2-Public Procurement Law No. 4734", "DHTB9-5-General Specifications for Implementation Works", "DHTB9-6-State Procurement Law No. 2886", "DHTB10-Existence of Time Extension", "DHTB11-Time Extension Period", "DHTB12-Existence of Work Modification", and "DHTB13-DHTB Decision Favourability" were identified. As a result of the examination, 17 input legal factors and 1 target legal factor were identified (Table 2).

Table 2. Statistical information of DHTB decision prediction model attributes

A ribute Code	**A ribute Name**	**Category**	**Findings**	
			Frequency	**Relative Frequency (%)**
DHTB1	Project Province	1- Marmara Region	2	1.63%
		2- Black Sea Region	4	3.25%
		3- Aegean Region	3	2.44%
		4- Central Anatolia Region	11	8.94%
		5- Eastern Anatolia Region	4	3.25%
		6- Mediterranean Region	3	2.44%
		7- South-eastern Anatolia Region	1	0.81%
		Unidentified	*95*	*77.24%*
		Total	123	100.00%
DHTB2	Contract Type	1- Lump Sum Turnkey	92	74.80%
		2- Unit Price Method	15	12.20%
		3- Bid Unit Price Method	10	8.13%
		4- Build-Operate-Transfer	0	0.00%
		5- Mixed Contract	3	2.44%
		Unidentified	*3*	*2.44%*

DHTB3	Project Type	Total	123	100.00%
		1- Residential	8	6.50%
		2- Commercial	8	6.50%
		3- Industrial	1	0.81%
		4- Educational, Cultural and Sports	35	28.46%
		5- Health	6	4.88%
		6- Maintenance, Repair and Restoration	11	8.94%
		7- Public Service Buildings	10	8.13%
		8- Partial Construction Works	4	3.25%
		9- Mechanical and Electrical Works	4	3.25%
		10- Infrastructure and Ground Works	18	14.63%
		Unidentified	*18*	*14.63%*
DHTB4	Project Cost	Total	123	100.00%
		1- PC < 100,000 TL	1	0.81%
		2- 100,001 TL ≤ PC < 500,000 TL	2	1.63%
		3- 500,001 TL ≤ PC < 1,000,000 TL	1	0.81%
		4- 1,000,001 TL ≤ PC < 5,000,000 TL	5	4.07%
		5- PC ≥ 5,000,001 TL	20	16.26%
		Unidentified	*94*	*76.42%*
DHTB5	Project Duration	Total	123	100.00%
		1- PD < 365 Days	21	17.07%
		2- 365 Days ≤ PD < 1095 Days	13	10.57%
		3- 1095 Days ≤ PD < 1825 Days	0	0.00%
		4- PD ≥ 1825 Days	0	0.00%
		Unidentified	*89*	*72.36%*
DHTB6	Dispute Type	Total	123	100.00%
		1- Work Cost	40	32.52%
		2- Work Increase and Decrease	65	52.85%
		3- Project Duration	8	6.50%
		4- Defective, Faulty, Incomplete and Unfinished Work	1	0.81%
		5- Termination and Administrative Practices	9	7.32%
		6- Exaggerated Quantities and Fictitious Production	0	0.00%
DHTB7	Dispute Cost	Total	123	100.00%
		1- DC < 100,000 TL	0	0.00%
		2- 100,001 TL ≤ DC < 500,000 TL	1	0.81%
		3- 500,001 TL ≤ DC < 1,000,000 TL	0	0.00%
		4- 1,000,001 TL ≤ DC < 5,000,000 TL	0	0.00%
		5- DC ≥ 5,000,001 TL	0	0.00%
		Unidentified	*122*	*99.19%*
DHTB8	Dispute Time	Total	123	100.00%
		1- Before Provisional Acceptance	0	0.00%
		2- Before Final Acceptance	4	3.25%

		3- After Final Acceptance	2	1.63%
		Unidentified	*117*	*95.12%*
		Total	123	100.00%
DHTB9	Relevant Law Articles	1- No Relevant Law Article	75	60.98%
		2- Public Procurement Law No. 4734	32	26.02%
		3- Public Procurement Contracts Law No. 4735	29	23.58%
		4- General Specifications for Construction Works	43	34.96%
		5- General Specifications for Implementation Works	3	2.44%
		6- State Procurement Law No. 2886	2	1.63%
DHTB10	Existence of Time Extension	1- No	105	85.37%
		2- Yes	18	14.63%
		Total	123	100.00%
DHTB11	Time Extension Period	1- TEP < 100 Days	5	27.78%
		2- 101 Days ≤ TEP < 200 Days	4	22.22%
		3- 201 Days ≤ TEP < 300 Days	2	11.11%
		4- 301 Days ≤ TEP < 400 Days	0	0.00%
		5- TEP ≥ 400 Days	2	11.11%
		Unidentified	*5*	*27.78%*
		Total	18	100.00%
DHTB12	Existence of Work Modification	1- Yes	38	30.89%
		2- No	85	69.11%
		Total	123	100.00%
DHTB13	DHTB Decision Favourability	1- In Favour of Contractor	49	39.84%
		2- In Favour of Administration	74	60.16%
		Total	123	100.00%

As a result of the analysis of decision files, 18 legal factors were identified. It was determined that six of these 18 legal factors were used in previous studies, and the remaining 12 legal factors were not found in the literature and were specific to DHTB decisions. The reliability and internal validity of the content analysis method used were ensured by the overlap of the 18 legal factors identified within the scope of the study with studies in the literature. In the study, after examining and recording all decisions, experts were consulted for verification. While experts checked the recorded decisions, a verification method based on the majority vote approach was considered, and it was observed that there was a consensus among expert opinions. More specifically, eight experts subjected the data extracted from the decisions to a second check according to the identified legal factors. The external validity of the content analysis method used was ensured by the control performed by experts. Considering that this study is also a project output, it should be emphasised that the expert team to perform the control should have deep experience in construction disputes in different work areas such as private, academic, and sectoral.

The CAE method was used in attribute selection to determine the relationship between 17 input legal factors and 1 target legal factor in DHTB decisions. CAE focuses on the target attribute. The proximity of the correlation coefficient to the value (+1) indicates that the input and target legal factors are in a linear relationship. Proximity to (-1) indicates an inverse linear relationship. A value of zero indicates that there is no relationship between the two legal factors [66]. Additionally, for a proper model, the correlation coefficients of legal factors should show a normal distribution. Input legal factors having low correlation values with the target legal factor trigger overfitting [67]. To prevent input legal factors with low correlation from causing overfitting, legal factors with low correlation coefficient values among input legal factors were not selected in the final model. The correlation coefficients of input legal factors were

calculated; legal factor selection for the final model was performed and presented in Table 3.

Table 3. Correlation evaluation results of DHTB decision prediction model attributes

Rank	A ribute Code	A ribute Name	A ribute Correlation Value	Selection Status in Final Model
1	DHTB10	Existence of Time Extension	0.226 ± 0.038	Yes
2	DHTB9-3	Public Procurement Contracts Law No. 4735	0.174 ± 0.024	Yes
3	DHTB12	Existence of Work Modification	0.175 ± 0.033	Yes
4	DHTB6	Dispute Type	0.140 ± 0.028	Yes
5	DHTB11	Time Extension Period	0.144 ± 0.035	Yes
6	DHTB9-5	General Specifications for Implementation Works	0.128 ± 0.012	Yes
7	DHTB2	Contract Type	0.115 ± 0.022	Yes
8	DHTB9-1	No Relevant Law Article	0.106 ± 0.029	Yes
9	DHTB9-2	Public Procurement Law No. 4734	0.085 ± 0.025	Yes
10	DHTB3	Project Type	0.071 ± 0.014	Yes
11	DHTB9-4	General Specifications for Construction Works	0.067 ± 0.024	Yes
12	DHTB9-6	State Procurement Law No. 2886	0.042 ± 0.029	No
13	DHTB8	Dispute Time	0.042 ± 0.029	No
14	DHTB4	Project Cost	0.037 ± 0.019	No
15	DHTB1	Project Province	0.028 ± 0.013	No
16	DHTB5	Project Duration	0.024 ± 0.016	No
17	DHTB7	Dispute Cost	0.000 ± 0.000	No

According to their correlation coefficient values, 11 input legal factors, including sub-legal factors, out of 17 legal factors were selected for the final model. A total of 24 different algorithms including tree-based and ensemble learning algorithms were used for binary classification predictions between input and target legal factors in DHTB decision prediction. The 10-fold cross-validation method was applied in the use of training-test data for the selected legal factors. The Ultra Boost algorithm was the most successful algorithm with an accuracy rate of 60.98% (Table 4).

Table 4. DHTB decision prediction model imbalanced dataset analysis results

Tree-based Algorithms								
No	**Algorithm**	**Accuracy**	**Precision**	**Recall**	**F1-Score**	**MCC**	**ROC**	**PRC**
1	REP Tree	59.35	55.40	59.30	52.30	5.20	53.40	55.60
2	AD Tree	58.54	57.10	58.50	57.30	10.30	66.10	66.70
3	NBTree	58.54	56.60	58.50	56.70	9.10	54.20	55.40
4	BF Tree	57.72	53.20	57.70	52.00	2.00	47.50	51.70
5	RF	57.72	56.10	57.70	56.40	8.20	55.30	58.90
6	Simple Cart	56.91	45.50	56.90	46.10	-8.00	46.20	50.40
7	Decision Stump	56.10	41.00	56.10	44.50	-12.80	48.60	52.60
8	LMT	55.28	52.20	55.30	52.50	2.00	51.00	54.00
9	J48	55.28	49.60	55.30	49.60	-4.40	45.50	49.30
10	FT	54.47	52.90	54.50	53.30	1.70	49.40	51.60
11	Random Tree	54.47	53.80	54.50	54.10	3.70	55.00	56.90
12	LAD Tree	53.66	51.80	53.70	52.30	-5.00	52.10	55.10

Ensemble learning Algorithms								
No	**Algorithm**	**Accuracy**	**Precision**	**Recall**	**F1-Score**	**MCC**	**ROC**	**PRC**
1	Ultra Boost	60.98	58.90	61.00	57.90	13.00	60.50	61.40
2	Bagging	60.98	58.60	61.00	56.30	11.60	59.60	60.90
3	Logit Boost	60.16	58.30	60.20	58.00	12.30	61.50	61.10
4	Random Sub Space	58.54	51.00	58.50	48.10	-1.30	56.00	57.90
5	Ensemble Selection	57.72	51.40	57.70	49.60	-1.00	54.90	56.20
6	Multi Boost AB	57.72	51.40	57.70	49.60	-1.00	52.10	53.20
7	Classification via Regression	56.10	54.00	56.10	54.30	3.90	55.80	56.80
8	Filtered Classifier	55.28	49.60	55.30	49.60	-4.40	45.50	49.30
9	Attribute Selected Classifier	53.69	47.80	53.70	48.40	-7.60	43.90	48.20
10	Random Committee	52.85	52.20	52.80	52.50	0.30	52.90	58.70
11	AdaBoost	52.03	47.00	52.00	47.90	-9.60	51.10	53.60
12	Iterative Classifier Optimizer	47.15	47.30	47.20	47.20	-9.90	43.10	48.80

It was observed that the Contractor Benefit / Administration Benefit distribution was 49/74, and therefore the data was imbalanced. This imbalance can cause overfitting, so the undersampling method was applied to equalize the number of dominant class data with minority class data. The results of 24 algorithms tested on balanced datasets are presented in Table 5.

Table 5. DHTB decision prediction model balanced dataset analysis results

Tree-based Algorithms								
No	**Algorithm**	**Accuracy**	**Precision**	**Recall**	**F1-Score**	**MCC**	**ROC**	**PRC**
1	Decision Stump	70.41	81.40	70.40	67.60	50.60	65.10	65.40
2	REP Tree	68.37	72.50	68.40	66.80	40.70	59.30	62.40
3	J48	65.31	68.40	65.30	63.80	33.50	62.80	64.80
4	LMT	64.29	66.80	64.30	62.90	31.00	63.70	64.40
5	BF Tree	63.27	64.80	63.30	62.30	28.10	67.40	66.30
6	Simple Cart	63.27	65.90	63.30	61.70	29.10	63.80	63.10
7	FT	62.24	62.90	62.20	61.80	25.10	66.00	64.80
8	LAD Tree	62.24	62.40	62.20	62.10	24.60	65.20	66.90
9	RF	61.22	61.20	61.20	61.20	22.40	67.20	68.50
10	AD Tree	60.20	60.60	60.20	59.90	20.80	67.90	70.70
11	NBTree	60.20	60.60	60.20	59.90	20.80	62.60	62.10
12	Random Tree	54.08	54.10	54.10	54.10	8.20	54.50	51.30
Ensemble learning Algorithms								
No	**Algorithm**	**Accuracy**	**Precision**	**Recall**	**F1-Score**	**MCC**	**ROC**	**PRC**
1	**Multi Boost AB**	**70.41**	**81.40**	**70.40**	**67.60**	**50.60**	**68.20**	**68.60**
2	Bagging	68.37	69.80	68.40	67.80	38.10	67.70	68.40
3	Iterative Classifier Optimizer	67.35	74.10	67.30	64.90	40.90	63.00	64.20
4	Logit Boost	66.33	66.90	66.30	66.00	33.20	65.60	66.70
5	Random Sub Space	66.33	68.00	66.30	65.50	34.30	63.50	64.40
6	Attribute Selected Classifier	66.33	70.00	66.30	64.70	36.10	56.90	60.90
7	AdaBoost	66.33	70.00	66.30	64.70	36.10	66.60	67.60
8	Filtered Classifier	65.31	68.40	65.30	63.80	33.50	62.80	64.80
9	Classification via Regression	64.29	66.80	64.30	62.90	31.00	64.50	64.80
10	Ultra Boost	62.24	62.70	62.20	61.90	24.90	65.50	66.10
11	Ensemble Selection	61.22	63.00	61.20	59.90	24.10	61.90	63.50
12	Random Committee	59.18	59.20	59.20	59.10	18.40	64.40	65.40

In the DHTB decision prediction model, Ultra Boost was the most successful algorithm with an

accuracy rate of 60.98% on the imbalanced dataset, while Multi Boost AB became the most successful algorithm with an accuracy rate of 70.41% when the dataset was balanced. A confusion matrix was used to calculate and evaluate the performance parameters of the algorithms. Performance indicators such as Precision, Recall, and F1-Score were obtained through various calculations of values between actual classes and predicted classes (Tables 4 and 5). The confusion matrix of the Multi Boost AB algorithm with the balanced dataset and the highest accuracy rate is presented in Figure 2.

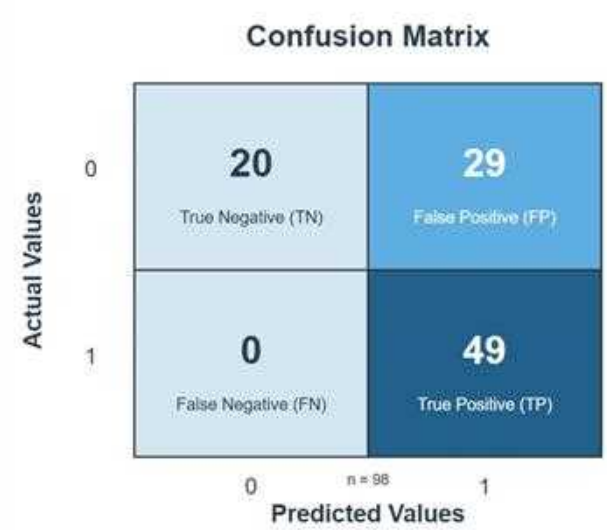


Figure 2. Confusion matrix of the DHTB decision prediction model with balanced dataset

Particularly in the DHTB decision prediction model, the absence of any false negative predictions indicates that the model can usually correctly predict the winning party. This situation highlights the DHTB decision prediction model. Within the scope of the Multi Boost AB algorithm, which has the highest accuracy value (0.7041) in the DHTB decision prediction model, the highest values obtained from performance indicators Precision, Recall, F1-Score, MCC, ROC, and PRC were 0.814, 0.704, 0.676, 0.506, 0.682, and 0.686, respectively (Figure 3).

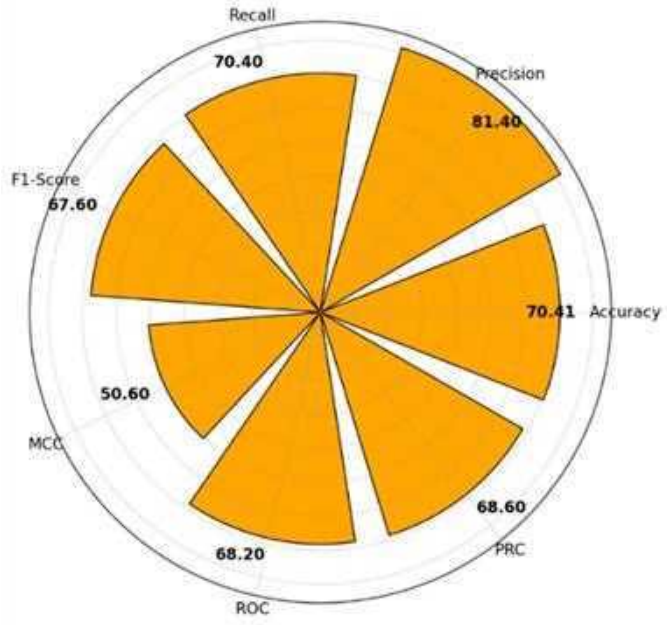


Figure 3. Performance values of the most successful Multi Boost AB algorithm in the DHTB decision prediction model balanced dataset

This study aimed to evaluate the decisions of DHTB in public construction projects through objective content analysis and to develop prediction models using machine-learning algorithms. The findings obtained have provided strong contributions in some aspects compared to similar studies in the literature and revealed methodological limitations in other aspects. This section discusses the comparison of study findings with the literature, methodological strengths, limitations, and impacts in application areas.

Arditi, et al. [30] achieved an accuracy rate of 67% using neural networks, which is lower than that achieved in the present study. This lower accuracy can be attributed to the identification and use of general legal factors in the relevant study. The present study differs from the relevant study in that it identifies context-specific factors, thereby achieving better prediction success. Un, et al. [28] used a dataset obtained from the DHTB decision book and achieved an accuracy rate of 71.65% with the SVM algorithm using a limited number of machine learning algorithms. The prediction accuracy success rate of 70.41% achieved in the current study using the MultiBoost AB algorithm is consistent with the relevant study. Bagherian-Marandi, et al. [29], who developed a fuzzy logic model using a dataset consisting of 100 Iranian court decisions, achieved a prediction accuracy success rate of 60%. The current study has demonstrated better performance in terms of prediction accuracy success rate. In terms of prediction success, Chaphalkar, et al. [31] performed significantly better than the current study with a prediction accuracy success of 90%. Similarly, in estimating compensation arising from delays in motorway projects using machine learning algorithms, Alshboul, et al. [32] demonstrated superior performance to the present study, achieving a prediction accuracy of 99.7%. However, two situations are common in the studies by Bagherian-Marandi, et al. [29], Chaphalkar, et al. [31], Alshboul, et al. [32] and Un, et al. [28]. The first situation is the subjective factor selection process in the identification of legal factors. Although factors are eliminated using various screening methods in the studies, the approaches preferred in the studies limit their generalisability. The second issue is the establishment of models using a limited number of algorithms. The present study differs from these studies in that it identifies legal factors through content analysis and selects them by subjecting them to statistical tests. In addition, by establishing models using a larger number of algorithms, the present study aims to fill this gap in the literature with a broadly generalisable approach. Chou and Lin [34] performed better than the current study, with an 84.33% prediction accuracy success rate, based on PPP project data in Taiwan. Although the study tested the significance of the factors in the model, it differs from the current study in terms of its non-generalisable approach to factor identification. Considering that context-specific factors are thought to be effective in the prediction accuracy success of specific dispute issues, coding and analysing project data with multiple coders through content analysis has the potential to yield higher success rates.

One of the most significant contributions of the present study is the evaluation of relationships between legal factors using the CAE method and the exclusion of factors with low correlation from the analysis. This approach reduced the risk of overfitting in the model and increased overall performance. Additionally, obtaining expert opinions in the selection of decisions and the coding process strengthened the objectivity and reliability of the study. Inter-coder reliability tests used in the coding process are elements that enhance methodological trust. The findings of the study contribute to creating faster, more consistent, and predictable decision processes for resolving disputes in public construction projects. Supporting the technical expertise role of the DHTB with machine learning enables the uninterrupted progress of projects and the efficient use of public resources. The high performance of the MultiBoostAB algorithm demonstrates the usability of this method for early prediction and decision support systems in similar projects. Additionally, this study can contribute to making legal processes more efficient by reducing the workload of judicial processes.

5. CONCLUSIONS

This study contributes to existing literature by addressing deficiencies using a dataset specific to the legal context of public construction projects and objective factor selection. The study has demonstrated the applicability of legal context-based machine learning models in public construction projects. The

findings obtained have both contributed to literature and emphasised the importance of data-driven approaches in the legal context. The methodology developed presents a strong foundation that can guide future studies.

The study presents a generalisable approach across a broad spectrum, but it also has certain limitations. The limited size of the data set is foremost among these limitations. Although the use of a similar raw data set to that used in some studies in the literature is a first step for studies in this field, a larger data set is needed to obtain a more robust model and prediction accuracy. Despite the measures taken in the study to prevent overfitting of machine learning models, the small size of the dataset limits the power of the study. The model can be strengthened by examining more DHTB decisions and including them in the model, thereby enabling the model to learn more complex relationships. This can be achieved with data entry platforms that enable the parties involved in the dispute to share verified information. The method presented in this study can be adapted and used in different dispute resolution mechanisms in the future. The current study, which stands out for its generalisability and repeatability, can be applied to other types of disputes, enabling the development of decision support models in many different areas. In addition, analysing decision texts using methods such as NLP, BERT, and RoBERTa to identify legal factors and establish prediction models can strengthen the identification of factors specific to the legal context and the accuracy of predictions. Furthermore, the use of ChatGPT and Large Language Models (LLMs) can achieve higher success rates through in-depth analysis of complex relationships in decision texts.

Declaration of Ethical Standards

The authors declare that all ethical guidelines including authorship, citation, data reporting, and publishing original research are followed.

Credit Authorship Contribution Statement

Author 1: Writing – original draft, Methodology, Investigation, Formal analysis, Data curation. **Author 2:** Writing – review & editing, Supervision, Methodology, Conceptualization. **Author 3:** Visualization, Software, Resources.

Declaration of Competing Interest

The authors declare that they have no known competing financial interests or personal relationships that could have appeared to influence the work reported in this paper.

Funding / Acknowledgements

The Scientific and Technological Research Council of Turkiye (TUBITAK) through 1002 - B Emergency Support Module under grant 224 K 720, supported this work, created from the Ph.D. thesis of Mahmut SARI.

Data Availability

Data will be made available on reasonable request.

Use of Artificial Intelligence

The authors confirm that no generative AI or AI-assisted technologies were used in the writing of this manuscript or in the production of the data/images presented.

REFERENCES

[1] M. Cevikbas, "Identification of dispute sources in the construction industry via court files," *Turkish Journal of Civil Engineering,* vol. 34, no. 2, pp. 57-76, 2023.

[2] M. Sarı, B. Sayın, and C. Akçay, "Classification and resolution procedure for disputes in public construction projects," *Revista de la Construcción. Journal of Construction,* vol. 20, no. 2, pp. 259-276, 08/19 2021, doi: https://doi.org/10.7764/RDLC.20.2.259.

[3] M. Sarı, S. Bayram, and E. Aydemir, "When defendants speak: Quantifying the predictive value of defence arguments in construction litigation," *Journal of Construction Engineering, Management & Innovation,* vol. 8, no. 1, pp. 64-88, 2025.

[4] A. L. Campos Gutierrez, K. Panuwatwanich, and A. Walker, "Learning from the past: analysis of factors contributing to construction project disputes in Australia," in *CIB World Building Congress 2013*, 2013: Queensland University of Technology.

[5] S. Alshahrani, "Dispute resolution methods in the construction industry sector in the Kingdom of Saudi Arabia," in *MATEC web of conferences*, 2017, vol. 138: EDP Sciences, p. 02015.

[6] H. Aladağ, G. Demirdöğen, and Z. Işık, "Mücbir sebep faktörü olarak COVID-19 salgınının inşaat projelerinde oluşturduğu uyuşmazlık etmenleri ve etkilerinin incelenmesi," (in tr), *Gazi Üniversitesi Mühendislik Mimarlık Fakültesi Dergisi,* vol. 36, no. 3, pp. 1213-1228, May 2021, doi: 10.17341/gazimmfd.784968.

[7] S. El-Sayegh, I. Ahmad, M. Aljanabi, R. Herzallah, S. Metry, and O. El-Ashwal, "Construction disputes in the UAE: Causes and resolution methods," *Buildings,* vol. 10, no. 10, p. 171, 2020.

[8] R. Awwad, B. Barakat, and C. Menassa, "Understanding dispute resolution in the Middle East region from perspectives of different stakeholders," *Journal of Management in Engineering,* vol. 32, no. 6, p. 05016019, 2016.

[9] M. Sarı and S. Bayram, "İnşaat Anlaşmazlıklarının Önlenmesi ve Çözümünde Etkili Faktörler: Erken Aşamalarda ve Resmi Yargı Sürecindeki Rolü," (in tr), *Erciyes Üniversitesi Fen Bilimleri Enstitüsü Fen Bilimleri Dergisi,* vol. 41, no. 1, pp. 133-142, April 2025. [Online]. Available: https://dergipark.org.tr/tr/pub/erciyesfen/issue/91637/1603230.

[10] E. Erdis and S. A. Ozdemir, "Analysis of technical specification-based disputes in construction industry," *KSCE Journal of Civil Engineering,* vol. 17, no. 7, pp. 1541-1550, 2013/11/01 2013, doi: 10.1007/s12205-013-0016-7.

[11] I. Cakmak Pinar and E. Cakmak, "An Analysis of Causes of Disputes in the Construction Industry Using Analytical Hierarchy Process (AHP)," in *AEI 2013*, (Proceedings, 2013, pp. 94-102.

[12] M. Mishmish and S. M. El-Sayegh, "Causes of claims in road construction projects in the UAE," *International Journal of Construction Management,* vol. 18, no. 1, pp. 26-33, 2018/01/02 2018, doi: 10.1080/15623599.2016.1230959.

[13] E. Temiz, "Türkiye'deki yapım projelerinde anlaşmazlıklara neden olan faktörlerin analizi," Master's Thesis, Institute of Science, Istanbul Technical University, 2020. [Online]. Available: https://polen.itu.edu.tr:8443/server/api/core/bitstreams/6e610957-da3d-4055-b644-3fb9e63d87d5/content#page=32.20

[14] M. Abeynayake, "Special Features and Experiences of the Construction Industry Arbitration in Sri Lanka," in *meeting of International Conference on Building Education and Research, Salford, United Kingdom*, 2008.

[15] D. Ilter, "Identification of the relations between dispute factors and dispute categories in construction projects," *International Journal of Law in the Built Environment,* vol. 4, no. 1, pp. 45-59, 2012, doi: 10.1108/17561451211211732.

[16] S. Assaf, M. A. Hassanain, A. Abdallah, A. M. Sayed, and A. Alshahrani, "Significant causes of claims and disputes in construction projects in Saudi Arabia," *Built Environment Project and Asset Management,* vol. 9, no. 5, pp. 597-615, 2019.

[17] D. Treacy, J. P. Spillane, and P. Tansey, "Construction disputes in small to medium enterprise's in Ireland during recession: Identification of critical factors," *International Journal of Law in the Built Environment,* vol. 8, no. 1, pp. 21-41, 2016.

[18] A. Barman and C. Charoenngam, "Decisional uncertainties in construction projects as a cause of disputes and their formal legal interpretation by the courts: Review of legal cases in the United

Kingdom," *Journal of Legal Affairs and Dispute Resolution in Engineering and Construction,* vol. 9, no. 3, p. 04517011, 2017.
[19] S. Almutairi, J. Kashiwagi, D. Kashiwagi, and K. Sullivan, "Factors causing construction litigation in Saudi Arabia," *Journal for the Advancement of Performance Information and Value,* vol. 7, no. 1, pp. 58-58, 2015.
[20] S. O. Cheung and K. H. Y. Pang, "Anatomy of construction disputes," *Journal of construction engineering and management,* vol. 139, no. 1, pp. 15-23, 2013.
[21] M. B. Jelodar, T. W. Yiu, and S. Wilkinson, "Dispute manifestation and relationship quality in practice," *Journal of Legal Affairs and Dispute Resolution in Engineering and Construction,* vol. 8, no. 1, p. C4515003, 2016.
[22] M. M. Kumaraswamy, "Conflicts, claims and disputes in construction," *Engineering, Construction and Architectural Management,* vol. 4, no. 2, pp. 95-111, 1997, doi: https://doi.org/10.1108/eb021042.
[23] C. Semple, F. T. Hartman, and G. Jergeas, "Construction Claims and Disputes: Causes and Cost/Time Overruns," *Journal of Construction Engineering and Management,* vol. 120, no. 4, pp. 785-795, 1994, doi: doi:10.1061/(ASCE)0733-9364(1994)120:4(785).
[24] I. Illankoon, V. W. Tam, K. N. Le, and K. Ranadewa, "Causes of disputes, factors affecting dispute resolution and effective alternative dispute resolution for Sri Lankan construction industry," *International Journal of Construction Management,* vol. 22, no. 2, pp. 218-228, 2022.
[25] Arcadis, "14th Annual Construction Disputes Report: Managing Construction Disputes in the Digital Age," 2024. [Online]. Available: https://share.google/fERAdI9ro6hDxXBOC
[26] *General Specifications for Construction Works – Article 51,* M. o. E. Republic of Türkiye, Urbanization and Climate Change Regulation 51, 2024.
[27] *Law No. 4735 on Public Procurement Contracts – Additional Article 2,* M. o. E. Republic of Türkiye, Urbanization and Climate Change Law Additional Article 2, 2020.
[28] B. Un, E. Erdis, S. Aydınlı, O. Genc, and O. Alboga, "Forecasting the outcomes of construction contract disputes using machine learning techniques," *Engineering, Construction and Architectural Management,* vol. ahead-of-print, no. ahead-of-print, 2024, doi: 10.1108/ECAM-05-2023-0510.
[29] N. Bagherian-Marandi, M. Ravanshadnia, and M.-R. Akbarzadeh-T, "Two-layered fuzzy logic-based model for predicting court decisions in construction contract disputes," *Artificial Intelligence and Law,* vol. 29, no. 4, pp. 453-484, 2021/12/01 2021, doi: 10.1007/s10506-021-09281-9.
[30] D. Arditi, F. E. Oksay, and O. B. Tokdemir, "Predicting the Outcome of Construction Litigation Using Neural Networks," *Computer-Aided Civil and Infrastructure Engineering,* vol. 13, no. 2, pp. 75-81, 1998/03/01 1998, doi: https://doi.org/10.1111/0885-9507.00087.
[31] N. B. Chaphalkar, K. C. Iyer, and S. K. Patil, "Prediction of outcome of construction dispute claims using multilayer perceptron neural network model," *International Journal of Project Management,* vol. 33, no. 8, pp. 1827-1835, 2015/11/01/ 2015, doi: https://doi.org/10.1016/j.ijproman.2015.09.002.
[32] O. Alshboul, A. Shehadeh, R. E. A. Mamlook, G. Almasabha, A. S. Almuflih, and S. Y. Alghamdi, "Prediction Liquidated Damages via Ensemble Machine Learning Model: Towards Sustainable Highway Construction Projects," *Sustainability,* vol. 14, no. 15, p. 9303, 2022. [Online]. Available: https://www.mdpi.com/2071-1050/14/15/9303.
[33] H. Anysz, M. Apollo, and B. Grzyl, "Quantitative Risk Assessment in Construction Disputes Based on Machine Learning Tools," *Symmetry,* vol. 13, no. 5, p. 744, 2021. [Online]. Available: https://www.mdpi.com/2073-8994/13/5/744.
[34] J.-S. Chou and C. Lin, "Predicting Disputes in Public-Private Partnership Projects: Classification and Ensemble Models," *Journal of Computing in Civil Engineering,* vol. 27, pp. 51-60, 2013, doi: https://doi.org/10.1061/(ASCE)CP.1943-5487.0000197.
[35] M. Ayhan, I. Dikmen, and M. T. Birgönül, "Classifying Compensations in Construction Disputes Using Machine Learning Techniques," *Journal of Engineering Research,* 2021.
[36] D. o. H. T. B. DHTB, *DHTB Decisions and Opinions 2005-2020*. Turkish Republic Ministry of Environment and Urban Planning, 2020.

[37] U. H. Graneheim, B.-M. Lindgren, and B. Lundman, "Methodological challenges in qualitative content analysis: A discussion paper," *Nurse Education Today,* vol. 56, pp. 29-34, 2017/09/01/ 2017, doi: https://doi.org/10.1016/j.nedt.2017.06.002.

[38] D. Arditi and O. B. Tokdemir, "Using Case-Based Reasoning to Predict the Outcome of Construction Litigation," *Computer-Aided Civil and Infrastructure Engineering,* vol. 14, no. 6, pp. 385-393, 1999/11/01 1999, doi: https://doi.org/10.1111/0885-9507.00157.

[39] T. Mahfouz and A. Kandil, "Factors Affecting Litigation Outcomes of Differing Site Conditions (DSC) Disputes: A Logistic Regression Models (LRM)," in *Building a Sustainable Future*, 2009, pp. 239-248.

[40] T. Mahfouz and A. Kandil, "Litigation Outcome Prediction of Differing Site Condition Disputes through Machine Learning Models," *Journal of Computing in Civil Engineering,* vol. 26, pp. 298-308, 2012, doi: https://doi.org/10.1061/(ASCE)CP.1943-5487.0000148.

[41] X. Zheng, Liu, Y., Jiang, J., Thomas, L.M., Su, N., "Predicting The Litigation Outcome of PPP Project Disputes Between Public Authority and Private Partner Using an Ensemble Model," *Journal of Business Economics and Management,* vol. 22, pp. 320-345, 2021, doi: https://doi.org/10.3846/jbem.2021.13219.

[42] C. A. Johnson, "Content-Analytic Techniques and Judicial Research," *American Politics Quarterly,* vol. 15, no. 1, pp. 169-197, 1987, doi: 10.1177/1532673x8701500108.

[43] M. A. Hall and R. F. Wright, "Systematic Content Analysis of Judicial Opinions," *Calif. L. Rev.,* vol. 96, pp. 63-63, 2008. [Online]. Available: http://lawcat.berkeley.edu/record/1121706/files/fulltext.pdf.

[44] E. H. Frank, M.; Holmes, G. "CorrelationAttributeEval (weka.attributeSelection)." University of Waikato. https://weka.sourceforge.io/doc.dev/weka/attributeSelection/CorrelationAttributeEval.html (accessed 06.10.2025, 2025).

[45] E. P. M. de Sousa, C. Traina, A. J. M. Traina, L. Wu, and C. Faloutsos, "A fast and effective method to find correlations among attributes in databases," *Data Mining and Knowledge Discovery,* vol. 14, no. 3, pp. 367-407, 2007/06/01 2007, doi: 10.1007/s10618-006-0056-4.

[46] I. Guyon and A. Elisseeff, "An introduction to variable and feature selection," *Journal of machine learning research,* vol. 3, no. Mar, pp. 1157-1182, 2003.

[47] M. A. Hall, "Correlation-based feature selection for machine learning," The University of Waikato, 1999.

[48] M. Dash and H. Liu, "Feature selection for classification," *Intelligent Data Analysis,* vol. 1, no. 1, pp. 131-156, 1997/01/01/ 1997, doi: https://doi.org/10.1016/S1088-467X(97)00008-5.

[49] N. Pudjihartono, T. Fadason, A. W. Kempa-Liehr, and J. M. O'Sullivan, "A review of feature selection methods for machine learning-based disease risk prediction," *Frontiers in bioinformatics,* vol. 2, p. 927312, 2022.

[50] C. J. Ferguson, "An effect size primer: a guide for clinicians and researchers," *Professional psychology: Research and practice,* vol. 40, no. 5, p. 532, 2009.

[51] J. Cohen, "A power primer," (in eng), *Psychol Bull,* vol. 112, no. 1, pp. 155-9, Jul 1992, doi: 10.1037//0033-2909.112.1.155.

[52] R. Kohavi, "A study of cross-validation and bootstrap for accuracy estimation and model selection," in *Ijcai*, 1995, vol. 14, no. 2: Montreal, Canada, pp. 1137-1145.

[53] J.-H. Kim, "Estimating classification error rate: Repeated cross-validation, repeated hold-out and bootstrap," *Computational Statistics & Data Analysis,* vol. 53, no. 11, pp. 3735-3745, 2009/09/01/ 2009, doi: https://doi.org/10.1016/j.csda.2009.04.009.

[54] G. I. Webb, "MultiBoosting: A Technique for Combining Boosting and Wagging," *Machine Learning,* vol. 40, no. 2, pp. 159-196, 2000/08/01 2000, doi: 10.1023/A:1007659514849.

[55] N. C. Oza and S. J. Russell, "Online Bagging and Boosting," presented at the Proceedings of the Eighth International Workshop on Artificial Intelligence and Statistics, Proceedings of Machine Learning Research, 2001. [Online]. Available: https://proceedings.mlr.press/r3/oza01a.html.

[56] K. M. Ting, "Confusion Matrix," in *Encyclopedia of Machine Learning*, C. Sammut and G. I. Webb Eds. Boston, MA: Springer US, 2010, p. 209.

[57] M. Ayhan, I. Dikmen, and M. T. Birgönül, "Predicting the Occurrence of Construction Disputes Using Machine Learning Techniques," *Journal of Construction Engineering and Management,* vol. 147, no. 4, 2021, doi: https://doi.org/10.1061/(ASCE)CO.1943-7862.0002027.

[58] J.-S. Chou, C. Tsai, and Y. Lu, "Project Dispute Prediction by Hybrid Machine Learning Techniques," *Journal of Civil Engineering and Management,* vol. 19, no. 4, pp. 505-517, 2013, doi: https://doi.org/10.3846/13923730.2013.768544.

[59] D. Arditi and T. Pulket, "Predicting the Outcome of Construction Litigation Using Boosted Decision Trees," *Journal of Computing in Civil Engineering,* vol. 19, no. 4, pp. 387-393, 2005/10/01 2005, doi: https://doi.org/10.1061/(ASCE)0887-3801(2005)19:4(387).

[60] T. Pulket and D. Arditi, "Construction litigation prediction system using ant colony optimization," *Construction Management and Economics,* vol. 27, no. 3, pp. 241-251, 2009/03/01 2009, doi: https://doi.org/10.1080/01446190802714781.

[61] T. Pulket and D. Arditi, "Universal Prediction Model for Construction Litigation," *Journal of Computing in Civil Engineering,* vol. 23, no. 3, pp. 178-187, 2009, doi: https://doi.org/10.1061/(ASCE)0887-3801(2009)23:3(178).

[62] D. Arditi and T. Pulket, "Predicting the Outcome of Construction Litigation Using an Integrated Artificial Intelligence Model," *Journal of Computing in Civil Engineering,* vol. 24, no. 1, pp. 73-80, 2010, doi: https://doi.org/10.1061/(ASCE)0887-3801(2010)24:1(73).

[63] K. W. Chau, "Predicting Construction Litigation Outcome Using Particle Swarm Optimization," in *Innovations in Applied Artificial Intelligence*, M. Ali and F. Esposito, Eds., 2005: Springer Berlin Heidelberg, pp. 571-578, doi: https://doi.org/10.1007/11504894_80.

[64] K. W. Chau, "Prediction of Construction Litigation Outcome – A Case-Based Reasoning Approach," in *Advances in Applied Artificial Intelligence*, M. Ali and R. Dapoigny, Eds., 2006: Springer Berlin Heidelberg, pp. 548-553, doi: https://doi.org/10.1007/11779568_59.

[65] J.-H. Chen and S. C. Hsu, "Hybrid ANN-CBR model for disputed change orders in construction projects," *Automation in Construction,* vol. 17, no. 1, pp. 56-64, 2007/11/01/ 2007, doi: https://doi.org/10.1016/j.autcon.2007.03.003.

[66] R. Pandey, M. Dhoundiyal, and A. Kumar, "Correlation analysis of big data to support machine learning," in *2015 Fifth International Conference on Communication Systems and Network Technologies*, 2015: IEEE, pp. 996-999, doi: https://doi.org/10.1109/CSNT.2015.32.

[67] J. Kolluri, V. K. Kotte, M. S. B. Phridviraj, and S. Razia, "Reducing Overfitting Problem in Machine Learning Using Novel L1/4 Regularization Method," in *2020 4th International Conference on Trends in Electronics and Informatics (ICOEI)(48184)*, 15-17 June 2020 2020, pp. 934-938, doi: 10.1109/ICOEI48184.2020.9142992.

Konya Mühendislik Bilimleri Dergisi., c.14, s.2,536-567, 2026
Konya Journal of Engineering Sciences v.14, n.2,536-567, 2026
ISSN: 2667-8055 (Electronic)
DOI: 10.36306/konjes.1654245

A NEW APPROACH TO DETERMINE THE FLEXURAL STIFFNESS FOR REINFORCED CONCRETE COLUMNS ACCORDING TO NON-LINEAR BEHAVIOUR

[1,*]Saeid Foroughi, [2]S. Bahadir Yuksel

[1,2]*Department of Civil Engineering, Faculty of Engineering and Natural Sciences, Konya Technical University, Konya, Türkiye*
[1]saeid.foroughi@yahoo.com, [2]sbyuksel@ktun.edu.tr

Highlights

- Nonlinear behavior determines effective stiffness of RC columns
- A simplified equation is proposed for stiffness coefficient estimation
- Moment–curvature analysis provides accurate stiffness evaluation
- The proposed equation is validated against codes and literature models
- Results demonstrate reliable predictions across column geometries

Graphical Abstract

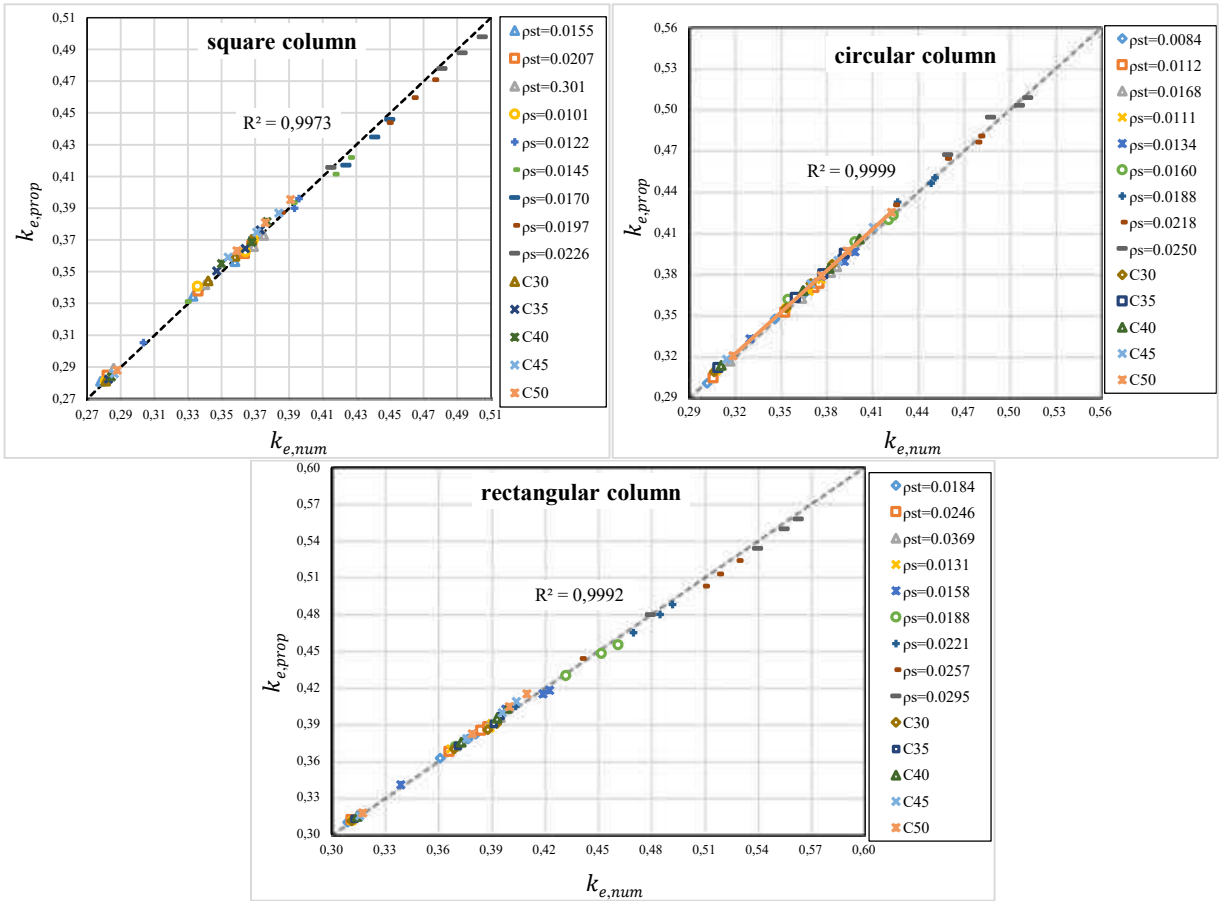


Figure The comparison of $k_{,}$ $-k_{,}$ relations according to different design parameters for columns

***Corresponding Author:** Saeid Foroughi, saeid.foroughi@yahoo.com

Konya Mühendislik Bilimleri Dergisi., c.14, s.2, 536-567, 2026
Konya Journal of Engineering Sciences v.14, n.2, 536-567, 2026
ISSN: 2667-8055 (Electronic)
DOI: 10.36306/konjes.1654245

A NEW APPROACH TO DETERMINE THE FLEXURAL STIFFNESS FOR REINFORCED CONCRETE COLUMNS ACCORDING TO NON-LINEAR BEHAVIOUR

[1,*]Saeid Foroughi, [2]S. Bahadir Yuksel

[1,2]*Department of Civil Engineering, Faculty of Engineering and Natural Sciences, Konya Technical University, Konya, Türkiye*
[1]saeid.foroughi@yahoo.com, [2]sbyuksel@ktun.edu.tr

(Received: 09.03.2025; Accepted in Revised Form: 31.10.2025)

ABSTRACT: Accurate calculation of the effective stiffness of RC load-bearing elements has always been an important research topic, as it allows reliable estimation of the capacity of buildings under seismic loads. Although the effective stiffness of the cracked section in load-bearing elements is not constant, it varies depending on the design parameters that affect the non-linear behaviour of the elements. A more secure and simpler prediction equation for the stiffness coefficient of sections has been developed by considering important design parameters in the RC columns designed with different geometries. The stiffness coefficient of columns; relationships specified in different seismic codes; nonlinear analyses of proposed equations; and parametric studies were investigated. By comparing the proposed predictions for the stiffness coefficient with other prediction equations, the results of the numerical analysis were used to verify the predictions. Since different section geometry and important design parameters influencing the non-linear behaviour of sections are considered in the equations proposed for the column models, quite accurate and consistent results are obtained for the stiffness coefficient of the columns, as can be seen from the numerical analysis results.

Keywords: Reinforced concrete columns, Effective stiffness, Non-linear behaviour, Seismic code.

1. INTRODUCTION

Nonlinear response and cracking in bearing elements under severe seismic effects are generally accepted, and linear response is the basis for the seismic design and analysis of reinforced concrete (RC) structures [1]. Being able to define the flexural stiffness of RC sections as realistically as possible has become more important because the performance-based solution has emerged as an important method in determining the earthquake behaviour [2]. The purpose of sizing and detailing structural load-bearing elements under the influence of vertical and horizontal loads is to provide sufficient strength, stiffness, and ductility under the anticipated effects for the structure and to fulfil the structural performance and displacement limit conditions defined by the regulation [3]. The results obtained from the analysis of the load-bearing elements under horizontal and vertical forces may vary depending on the section stiffness. Flexural stiffness in RC structural systems is effective both in the determination of displacements and in the distribution of internal forces compared to other structural systems [4]. Concrete cracks decrease the shear and flexural stiffness of RC structural bearing elements. Therefore, analyses performed without considering the cracking effect on the bearing elements may not represent the actual behaviour of the bearing elements and structures [5]. The cross-sections strength, ductility, and stiffness should be considered in the design and evaluation of RC columns, considering that it is well- recognised that these characteristics are important for structural seismic safety. [6-7]. Axial load levels impacting the section, concrete strength, longitudinal and transverse reinforcement ratios, cross-section geometry and dimension, and other design parameters all affect the effective stiffness of columns, which is not constant.

***Corresponding Author:** Saeid Foroughi, saeid.foroughi@yahoo.com

[8]. The flexural stiffness varies depending on the section dimensions, material elasticity modules, and reinforcement ratio. While examining the section behaviour with nonlinear behaviour relationships, the flexural stiffness has a maximum value depending on the material modulus of elasticity and the section moment of inertia in cases where the moment is small and no cracks occur in the section. With the moment reaching large values and the formation of cracks, the flexural stiffness decreases and the effective stiffness becomes effective [9]. Expressions are developed for the flexural stiffness of RC columns subjected to short-term loads with the moment-curvature-based approach.

Many studies and investigations have been conducted by different researchers on the effective stiffness of RC columns. [10-18]. Lan et al. [19] explored the elastoplastic flexural rigidity of RC columns through both experimental and theoretical methods, employing moment–curvature relationships for stiffness assessment. Elmezayen et al. [20] investigated the nonlinear flexural behaviour of continuous RC beams affected by corrosion through numerical modelling. Furthermore, Faghirnejad et al. [21] performed performance-based optimization of two-dimensional reinforced concrete moment frames by integrating pushover analysis with the ABC optimization algorithm. Collectively, these studies emphasize that analytical, numerical, and experimental methods can be effectively utilized to gain a deeper understanding of the nonlinear behaviour of columns and beams, as well as to optimize pertinent design parameters. Previous research has established that the stiffness coefficient of load-bearing elements differs from values estimated in the context of the seismic effect. It is known that the stiffness of RC structures exposed to earthquake effects will decrease greatly; therefore, it is recommended to use cracked section stiffness in the relevant sections of the standard and codes to obtain more realistic results.

Uncracked section characteristics are typically considered in determining the structural stiffness since many seismic design regulations and standards do not have exact effective stiffness to be used in the seismic analysis of structural elements. In commonly used standards, the stiffness of load-bearing elements is defined by the coefficient of their stiffness obtained based on their cross-sectional characteristics. In the design codes and studies related to the stiffness coefficient, the proposed relationships for the design and evaluation of the structural elements were examined, considering the design parameters that affect the stiffness of the structural elements. The main design factors influencing the sections' effective section stiffnesses were determined from the non-linear analysis results of the column sections. The results of the numerical analysis indicate that an alternative equation for the stiffness coefficient of column sections should consider the four important variables: compressive strength of concrete (f), axial load levels (N/N), transverse reinforcement (ρ), and longitudinal reinforcement (ρ). RC column sections are generally designed in square, rectangular and circular cross-section geometries. One of the best methods to determine the behaviour of the carrier element section depending on the material and geometry is to know the moment-curvature relation of the section.

This study examined the stiffness coefficient by considering the various geometries of the column sections in addition to the most important design aspects influencing the behaviour of the sections. According to the numerical analysis, a simple equation is proposed to calculate the stiffness coefficient of square, rectangular, and circular cross-section column elements for the different design parameters. Thus, in the equation proposed for the stiffness coefficient, all design parameters and section geometry will be considered in the column models, and the stiffness coefficient can be calculated to reflect the nonlinear behaviour of the elements. The stiffness coefficient of the RC column models in different parameters and geometry was investigated analytically by obtaining from the Seismic Evaluation and Retrofit of Existing Buildings (ASCE/SEI41) [22], American Concrete Institute (ACI318) [23], Turkish Building Earthquake Code (TBEC) [24], Assessment and Retrofitting of Buildings (Eurocode8-Part 3) [25], Design of Structures for Earthquake Resistance (Eurocode8) [26], Design of Concrete Structures (Eurocode2) [27], Biskinis [28], Biskinis and Fardis [29], Avşar et al. [18], moment-curvature, and the proposed equation. The proposed equations according to the design parameters affecting the stiffness coefficient of square, rectangular, and circular cross-section columns are compared with the relations and coefficients found in the literature. For column models, the results obtained from the analyses according to different parameters are presented in graphics and examined.

This study presents a new approach based on nonlinear behaviour in determining the flexural stiffness of RC columns. The method based on the moment-curvature relationship produces more realistic results than empirical models and provides a practical calculation framework without the need for finite element analyses. The model, which is considered with parametric analyses, shows a wider validity area compared to existing research and regulations and constitutes a reliable alternative for engineering applications.

2. EFFECTIVE STIFFNESS OF THE RC COLUMNS

It is known that the stiffness of RC structures exposed to earthquake effects will decrease greatly; therefore, it is recommended to use cracked section stiffness in the relevant sections of the standard and codes to obtain more realistic results [30]. For linear or non-linear analysis of buildings exposed to seismic effects, current design codes provide constant coefficients and different relations for the stiffness of the structural elements, often providing rough indications on how to evaluate the stiffness of the elements [31]. Most of the proposed equations for stiffness do not consider the most important design parameters that affect the nonlinear behaviour of elements [32]. To calculate accurate values for structural stiffness and, consequently, effective earthquake effects, the accuracy level of the stiffness values of structural elements is important. Table 1 compares the different effective stiffness relations from the design codes and literature. The most important design parameters and section properties affecting stiffness, reflecting the cracking effect as well as theoretical yielding of the RC sections, are calculated by extensive moment-curvature analysis of the sections. In the stiffness coefficient equations proposed by some researchers for columns, important design parameters are not taken into consideration, as in the codes. The confining impact is not considered in the relationships proposed by some researchers for the stiffness coefficient, as in some design codes. It means ignoring the effects of important design parameters that affect the nonlinear and seismic behaviour of load-bearing elements, such as concrete strength, reinforcement ratio, confining effect in confined boundary regions, and axial load levels. If the design parameters that affect the nonlinear behaviour of sections are not considered, it may lead to unrealistic results in the assessment of load-bearing elements.

Modulus of elasticity of concrete, modulus of elasticity of reinforcement, reinforcement ratio, cracked section stiffness, loading conditions and geometric properties are the factors that affect the effective stiffness of RC bearing elements. The modulus of elasticity of concrete depends on the type of concrete and its compressive strength. A higher modulus indicates stiffer concrete. Typically, much higher than that of concrete, reinforcement significantly contributes to the overall stiffness. Higher reinforcement ratios in the cross-section of the column generally increases the effective stiffness. Cracks in concrete reduce its effective stiffness. The stiffness of the cracked section is often used in analysis instead of the uncracked section.

The effective stiffness (EI) is assumed to be constant in TBEC [24], the stiffness coefficient for RC columns is accepted as 0.70. The stiffness of the column designed according to the stacked plastic behaviour model defined in TBEC [24] can be calculated according to the shear span of the element, yield moment and yield rotation values of the section.

The effective stiffness reflects not only the cracking effect but also the behaviour of RC members, as determined from the moment-curvature analysis. The effective stiffness (EI) of RC load-bearing members is defined as the slope of the initial section of the moment-curvature relationships. This definition reflects both the effects of cracking and the theoretical yielding of RC sections. The ratio determines the effective stiffness of the cracked section in RC members ($EI = M/\emptyset$) corresponding to the yield moment (M) and the yield curve ($\emptyset$), considering the moment-curvature relationship. EI is not constant and depends on parameters such as the dimension of the cross-section, concrete strength and axial force acting on the section. The uncracked section stiffnesses (EI) were calculated using the gross moment of inertia (I) and the modulus of elasticity (E) of the concrete columns (Table 1). One of the realistic ways to calculate the effective section stiffness of RC load-bearing systems is to use moment-curvature relations. The effective

stiffness coefficient of RC elements is calculated as $k = EI/EI$.

Table 1. Evaluation of several effective stiffness relations in comparison

Author and Codes	Effective Section Stiffness
Moment-Curvature	$k = EI/EI;\quad EI = M/\emptyset,\quad E = 3250\sqrt{f'} + 14000\,MPa$
TBEC [24] according to the stacked plastic behaviour	$(EI) = \frac{M}{\theta}\frac{L}{3},\quad \theta = \frac{M L}{3EI}\ (Limear\ methot)$ $\theta = \frac{\emptyset L}{3} + 0.0015\eta\left(1 + 1.5\frac{h}{L}\right) + \frac{\emptyset d f}{8\sqrt{f'}},\ \eta = 1\ (Nonlinear\ methot)$
Eurocode8-Part 3 [25]	$EI = \frac{M L}{3\theta},\quad \theta = \Phi\left(\frac{L + a z}{3}\right) + 0.0014\left(1 + 1.5\frac{h}{L}\right) + \Phi\left(\frac{d f}{8\sqrt{f'}}\right)$ $V_r = C_r K(100\rho f_{ck})^{1/3} + K\sigma b d$ $K = 1 + \sqrt{\frac{200}{d}} \le 2,\quad \rho = \frac{A}{b d} \le 0.02,\quad \sigma = \frac{N}{A} < 0.2f$
Eurocode2 [27]	$EI = K_E E_{cm} I_c + K_E E_s I_s,\ E_{cm} = E_{cm}/(1+\varphi)$ $\rho \ge 0.01,\quad K_s = 0,\quad K_c = \frac{0.30}{1 + 0.5\varphi}$
Avşar et al. [18]	α for rectangular column sections: $\alpha = 0.062 + 0.0022f + 0.854\frac{N}{f A} + 10.802\rho \leftrightarrow \frac{N}{f A} > 0.30 - 1.91\rho$ $\alpha = 0.257 + 0.0033f + 0.602\frac{N}{f A} + 13.874\rho \leftrightarrow \frac{N}{f A} \le 0.30 - 1.91\rho$ α for circular column sections: $\alpha = 0.069 + 0.0032f + 0.876\frac{N}{f A} + 9.512\rho \leftrightarrow \frac{N}{f A} > 0.26 - 1.75\rho$ $\alpha = 0.239 + 0.0029f + 0.709\frac{N}{f A} + 12.809\rho \leftrightarrow \frac{N}{f A} \le 0.26 - 1.75\rho$
Biskinis [28]	$\frac{EI}{E_c I_g} = a\left(0.8 + ln\left(max\left(\frac{L}{h}; 0.6\right)\right)\right)\left(1 + 0.048\,min\left(50MPa; \frac{N}{A}\right)\right),$ $a = 0.081$: for columns
Biskinis and Fardis [29]	$EI = M L/3\theta$ $\theta = \Phi\left(\frac{L + a z}{3}\right) + 0.0014\left(1 + 1.5\frac{h}{L}\right) + a\left(\frac{\Phi d f}{8\sqrt{f'}}\right),\quad L = \frac{M}{V},\quad a = 1$ $V = \left\{max\left[180(100\rho)^{1/3}, 35\left(1 + \sqrt{\frac{0.2}{d}}\right)f^{1/2}\right]\left(1 + \sqrt{\frac{0.2}{d}}\right)f^{1/2} + 0.15\frac{N}{A}\right\} b d$

In ASCE/SEI-41 [22], EI is specified as $0.3E_c I_g$ for columns with a designed gravity load lower than $0.1A_g f'_c$ and in the case of columns with an axial compressive load larger than $0.5A_g f'_c$, the value of this coefficient is 0.7. ACI318 [23] gives a ratio of $0.70E_c I_g$ for the stiffness of cracked columns. Part 3 of

Eurocode8 [25] considers an equation based on yield rotation and moment-shear ratio, which can be used to calculate a more accurate stiffness. Considering that the stiffness is not constant, a formulation based on parameters such as section dimension, reinforcement ratio and concrete strength is recommended. It is specified as $0.5E\ I$ for the stiffness of columns in Eurocode8 [26]. In Eurocode8 [26], design parameters such as column geometry and dimension, reinforcement ratio, concrete strength and axial load level affecting the section are not considered. Nominal stiffness values should be utilised in Eurocode2 [27], a second-order analysis based on stiffness, considering the impacts of creep, non-linearity conditions in the material, and concrete cracking on the overall behaviour. According to Avşar et al. [18], factors include the strength of the concrete, longitudinal reinforcement and axial load are considered in the equations proposed for the stiffness values of RC columns relatively low in ductility and strength.

In the Table 1; M is the yield moment, Φ yield curvature, E , E concrete's modulus of elasticity, E modulus of reinforcement elasticity, I moment of inertia of cross-section, I the second moment of the reinforcement area, f concrete compressive strengths, f expected compressive strength of concrete (f =1.3f), f expected yield strength of transverse reinforcement (f =1.2f), θ chord rotation at the yielding, L shear span, d , d longitudinal reinforcement diameter, h section height, a z tension shift of the flexural moment diagram (a = 0 if V > M /L and a = 1, if V ≤ M /L), z internal lever arm length, $z = d - d$ in column section, d, d depths to the reinforcement for tension and compression, ρ reinforcement ratio, A area of concrete section, A area of the reinforcement, b width of the column section, N axial load, K factor for creep, cracking, and other effects, K element influencing the reinforcement contribution and φ effective creep ratio.

3. MATERIAL AND METHODS

The effective stiffness of RC columns is a key parameter in structural engineering, influencing the load-bearing capacity and deformation characteristics of columns under various loading conditions. It combines the contributions of both concrete and reinforcement to resist applied loads. The properties of the material used in the elements and the cross-section dimensions of the element are effective in the calculation of the stiffness of the vertical carrier elements. The column models with dimensions of 600mm circular, 500mm×500mm square and 400mm×600mm rectangular cross-sections were created to investigate nonlinear behaviour and stiffness coefficients using different design parameters. The details and properties of the designed circular, square and rectangle columns are given in Table 2 and Figure 1. The design parameters in the designed column models were determined by considering the limitations given in ACI318 [23] and TBEC [24]. The gross section area of the column, when combined with the combined effects of gravity and seismic loads (N), must satisfy condition A ≥ N /0.40f [24]. The nonlinear behaviours of the column models were investigated for the N/N ratios of 0.10 to 0.40. To examine the impact of reinforcement on the nonlinear behaviour and stiffness of columns, transverse reinforcement was chosen with diameters of 10 and 12 mm and spacing of 50, 75, and 100 mm, while longitudinal reinforcement was selected to be Φ20-Φ30mm. C25 to C50 were considered as concrete grades and B420C was chosen as the transverse and longitudinal reinforcement in the analysis of the column models. The concrete and reinforcement material specifications shown in Figure 2 are applied. To perform structural design under the influence of earthquakes and to examine the seismic behaviour of the structure, first of all, the behaviour of the materials and elements that make up the structure should be known. The most important design parameters, which reflect the effect of cracks affecting the stiffness of elements and the theoretical efficiency of the elements, are determined by a comprehensive moment-curvature analysis. The behaviour of the carrier element under the effect of simple flexural and normal force or only simple flexural can be examined by obtaining the moment-curvature relation and the changes in ductility level and stiffness can be observed by looking at its behaviour. The moment-curvature relations were calculated by considering the Mander unconfined and confined concrete models [33] and

the material properties given for the reinforcement and concrete in Figure 2. In the analytical study, the moment-curvature relations according to the non-linear behaviour of the materials in the column sections were obtained from the SAP2000 [34] program (Ver. 21) and presented graphically.

Table 2. Details and properties of the RC column model

Material (f_{ck})	Longitudinal Reinforcement (mm)	Transverse Reinforcement, ρ		Axial loads (N/N)
		Diameter (mm)	Spacing (mm)	
C30	8Φ20	Φ10 Φ12	50 75 100	0.10 0.20 0.30 0.40
C35	8Φ22			
C40	8Φ24			
C45	8Φ26			
C50	8Φ28			
	8Φ30			

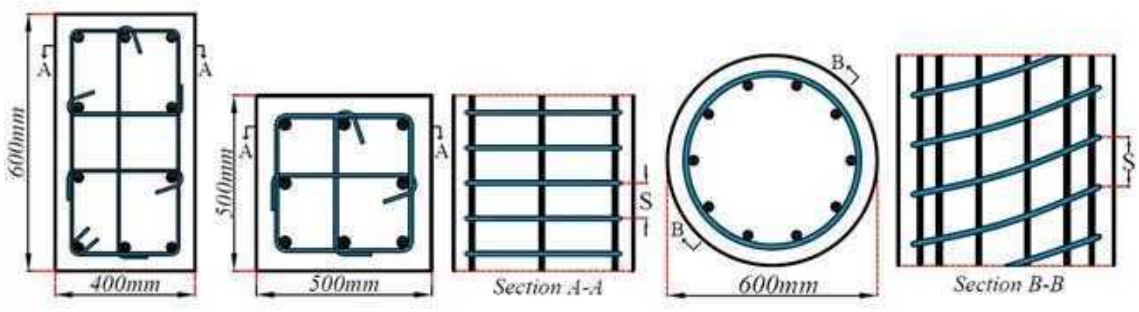


Figure 1. Cross-section of the reinforced concrete column models

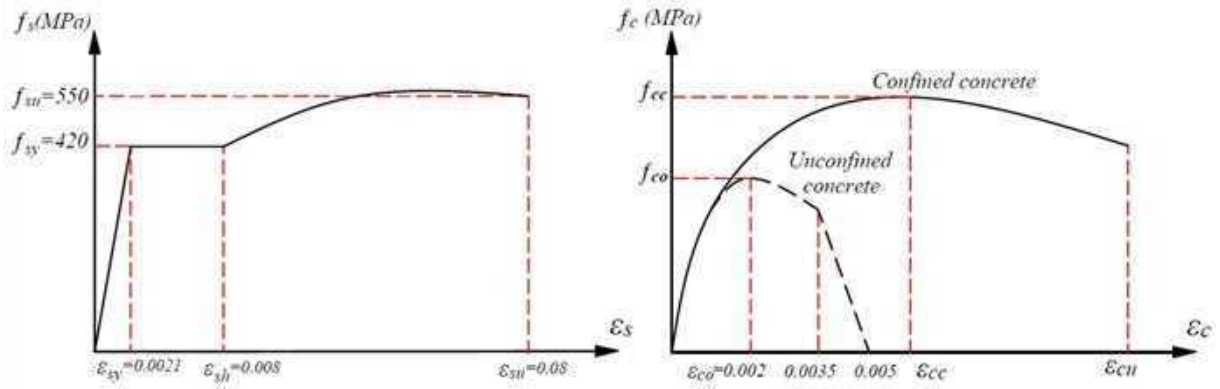


Figure 2. Relationships between stress and strain for concrete and reinforcement [24]

The moment-curvature relationships of the sections were obtained by changing the design parameters. The effective stiffness was defined as the slope of the first segment of the moment-curvature diagram of the sections. This definition reflects both the effects of cracking and the theoretical yielding of RC sections. The definition of the point corresponding to the first yield and the procedure for obtaining the moment-curvature relationship are essential. In the designed RC structure models, the moment (M , M) and curvature (Φ , Φ) values, section ductility (μ_Φ) and effective stiffness coefficient (k) were calculated for yield and fracture situations from the moment-curvature relationships according to different parameters.

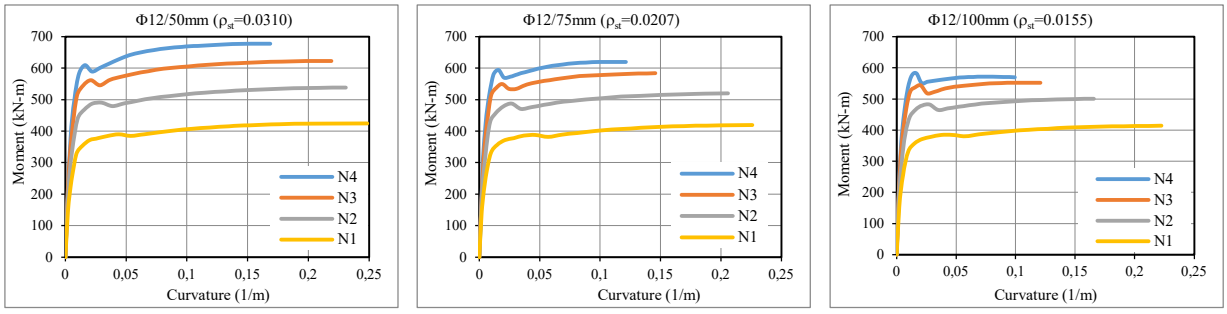
Different design codes and standards provide different parameters and guidelines for modifying the stiffness of RC carrier members. In the analyses and calculations carried out in accordance with the standards and codes, the actual behaviour of the sections is not considered when determining their effective stiffness. Accurate and realistic stiffness factors should be determined by calculating non-linear behaviour values according to design parameters instead of defined approximate values. In the analysis software, calculations and analyses are made by using the constant coefficients given in the standard and codes or by determining the effective stiffness values according to simple relations (ignoring important design parameters). In this case, more realistic results cannot be obtained without considering the cross-sectional and material properties, and reinforcement ratios of the RC-bearing members. In the design and evaluation of RC-bearing members, determining their non-linear behaviour and obtaining effective stiffness values are very important to obtain more realistic results. Information from multiple codes and sources may reveal a more accurate method of analysis for the RC structure that the designer is currently evaluating. In this study, a simple equation covering all design parameters has been developed to overcome very long and detailed calculations that require non-linear behaviour modelling to determine the column section that has been cracked in stiffness. The investigated effects on the non-linear behaviour of columns according to different section geometry, design parameters such as material properties (f), longitudinal reinforcement ratio ρ , transverse reinforcement ratio (ρ), and configuration were evaluated by calculating the section in terms of effective stiffness. The proposed predictions for the stiffness coefficient are verified by comparisons with other prediction relations [18-26]. The adequacy of the proposed equation for the stiffness coefficient is evaluated as an element-level parametric study by comparing it with the existing relations and coefficients. For column models, the stiffness coefficient was calculated according to the proposed new equation and the relationships explained in this study, and the results are presented comparatively in the following sections.

4. RESEARCH FINDINGS AND DISCUSSION

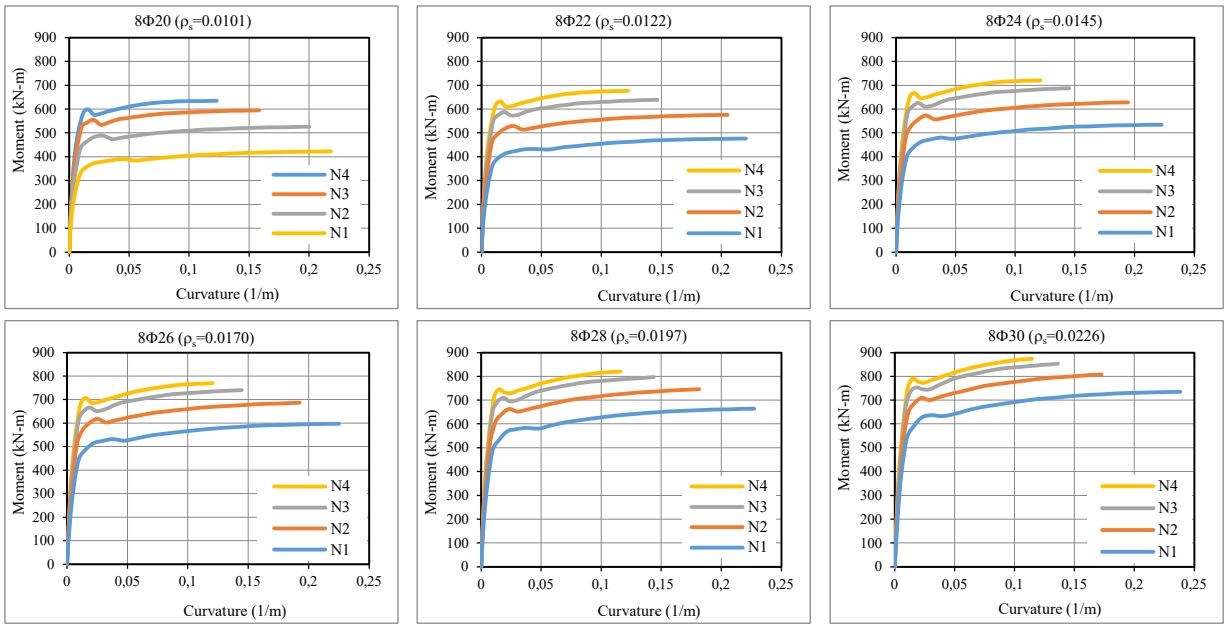
4.1. Nonlinear Moment-Curvature Analysis

In structural engineering, understanding the nonlinear behaviour of structural elements is critical for safety and performance. Nonlinear moment-curvature analysis is an important method used to evaluate the behaviour of structural members under flexural. This analysis considers material nonlinearity (e.g., yielding of reinforcement or cracking of concrete) and geometric nonlinearity (large deformations). Nonlinear moment-curvature analysis provides important results by evaluating in detail the behaviour of structural members under flexural. These results are critical for the design and performance evaluation of structural elements. The moment-curvature curve is a basic graph that shows the behaviour of the structural element under flexibility. This curve helps us understand the nonlinear response of the cross-section. Nonlinear moment-curvature analysis is a crucial method for understanding the behaviour of RC columns under various loading conditions. This analysis involves the relationship between the moment applied to a column section and the resulting curvature of the section. Based on the results of the nonlinear analysis of the RC square, rectangular, and circular column models, new relations-based important design parameters affecting the stiffness coefficient of the column models were proposed and compared with the relations proposed in the codes and by researchers. To investigate the nonlinear behaviour and stiffness coefficients of columns, a total of 2160 model analyses were carried out with different geometries, f , ρ , ρ and N/N . The effective flexural stiffness due to concrete cracking was obtained depending on important design parameters such as f , ρ , ρ and N/N . By considering the nonlinear behaviour of the materials, the moment-curvature of the column models may be determined. The moment-curvature relations obtained for the circular, square and rectangular column models are presented in Figures 3, 4 and 5, respectively, comparatively according to different design parameters. Yield and ultimate moment, and curvature values were calculated from moment-curvature analyses, and ductility values of the sections were calculated according to the curvature values. The analysis results obtained according to the

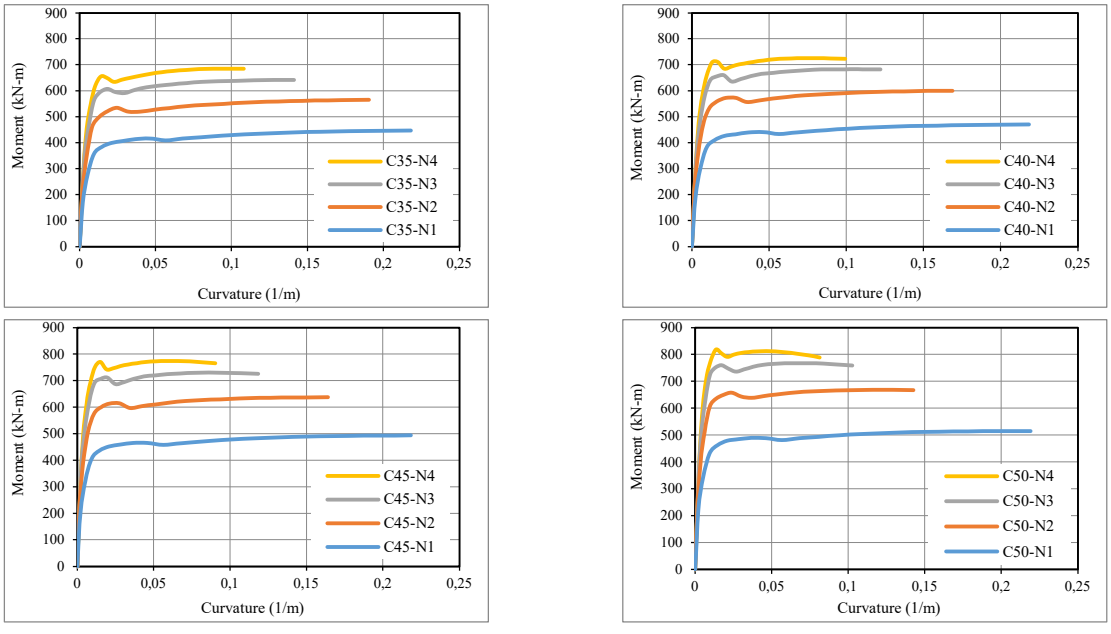
section geometries are given in Tables 3, 4 and 5, respectively.



a) Effect of ρ on moment-curvature relation (longitudinal reinforcement: 8Φ20mm – concrete: C30)



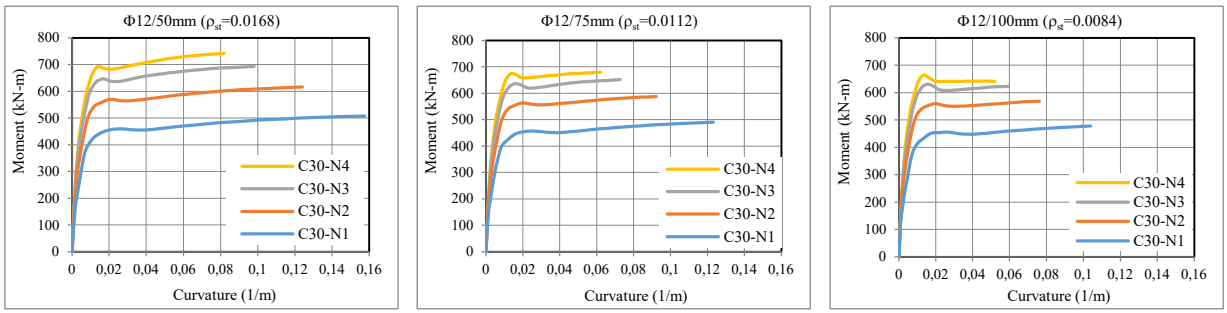
b) Effect of ρ on moment-curvature relation (transverse reinforcement: Φ10/50mm - concrete: C30)



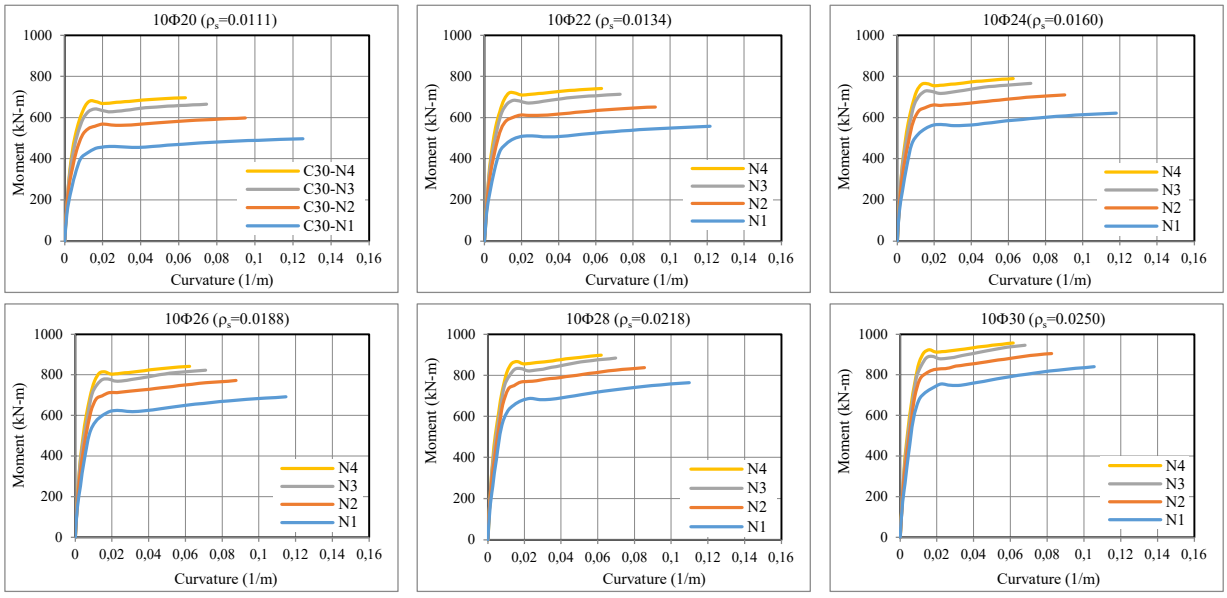
c) Effect of f on moment-curvature relation (longitudinal reinforcement: 8Φ20mm – transverse

reinforcement: Φ10/50mm)

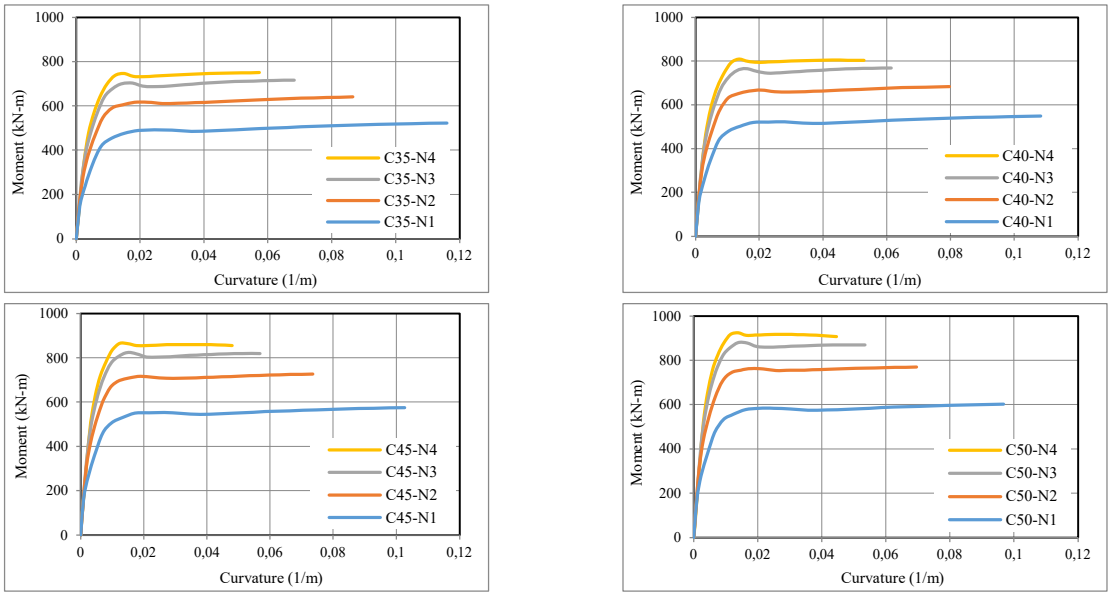
Figure 3. Moment-curvature relations of square columns for different parameters



a) Effect of ρ on moment-curvature relation (longitudinal reinforcement: 10Φ20mm – concrete: C30)



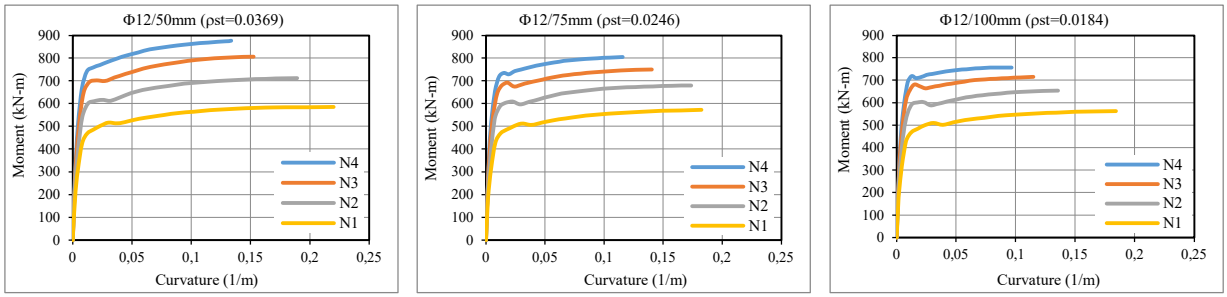
b) Effect of ρ on moment-curvature relation (transverse reinforcement: Φ10/50mm – concrete: C30)



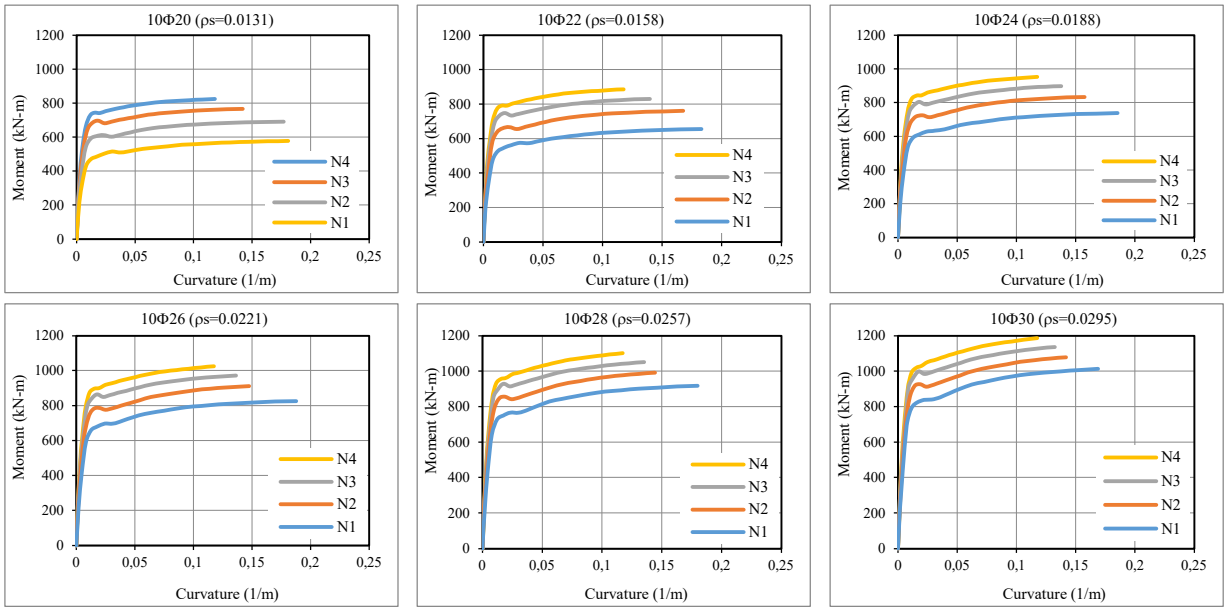
c) Effect of f on moment-curvature relation (longitudinal reinforcement: 10Φ20mm – transverse

reinforcement: Φ10/50mm)

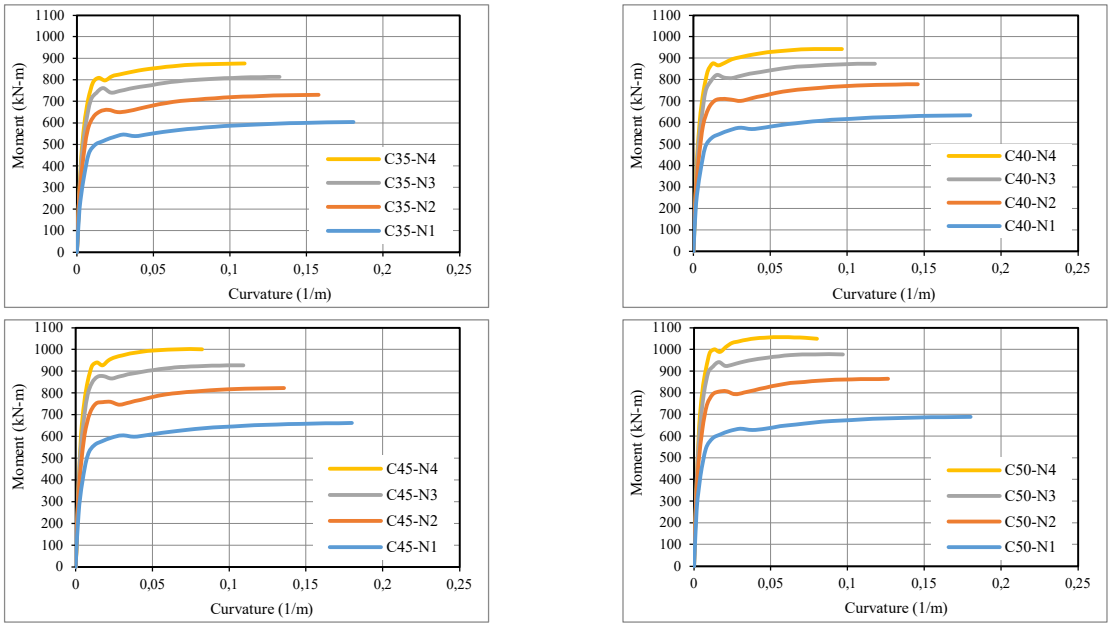
Figure 4. Circular column moment-curvature relations for different parameters



a) Effect of ρ on moment-curvature relation (longitudinal reinforcement: 10Φ20mm – concrete: C30)



b) Effect of ρ on moment-curvature relation (transverse reinforcement: Φ10/50mm – concrete: C30)



c) Effect of f on moment-curvature relation (longitudinal reinforcement: 10Φ20mm – transverse

reinforcement: Φ10/50mm)

Figure 5. Moment-curvature relations of rectangular columns for different parameters

Table 3. Calculation results of bending moment-curvature (**Square Columns**)

N/N	f (Mpa)	Transverse Reinforcement	Longitudinal Reinforcement	M $(kN.m)$	Φ $(1/m)$	M $(kN.m)$	Φ $(1/m)$	μ_Φ
0.1	30	Φ10/50mm	Φ20mm	292.3	0.00729	423.0	0.2215	30.37
0.2				411.5	0.00855	527.1	0.2052	24.00
0.3				508.9	0.00983	595.2	0.1623	16.51
0.4				609.9	0.01081	635.2	0.1335	12.35
0.1	30	Φ12/50mm	Φ20mm	304.0	0.00738	424.9	0.2482	33.64
0.2				421.8	0.00866	539.0	0.2307	26.63
0.3				520.7	0.00994	623.6	0.2019	20.32
0.4				618.0	0.01180	678.3	0.1685	14.27
0.1	30	Φ12/75mm	Φ20mm	297.5	0.00731	419.8	0.2259	30.88
0.2				414.2	0.00856	520.5	0.2059	24.05
0.3				512.7	0.00984	584.2	0.1556	15.81
0.4				610.9	0.01168	619.9	0.1213	10.38
0.1	30	Φ12/100mm	Φ20mm	290.4	0.00725	414.3	0.2024	27.90
0.2				407.4	0.00843	501.5	0.1656	19.64
0.3				504.7	0.00973	552.2	0.1208	12.42
0.4				604.2	0.01157	570.3	0.0993	8.58
0.1	30	Φ10/50mm	Φ22mm	321.8	0.00738	477.1	0.2185	29.59
0.2				458.2	0.00865	577.0	0.2012	23.26
0.3				552.2	0.00992	639.5	0.1515	15.60
0.4				655.2	0.01159	676.6	0.1293	11.15
0.1	30	Φ10/50mm	Φ24mm	353.9	0.00749	535.4	0.2160	28.84
0.2				488.9	0.00871	629.4	0.1944	22.32
0.3				584.6	0.00996	688.2	0.1471	14.77
0.4				692.3	0.01164	721.4	0.1244	10.69
0.1	30	Φ10/50mm	Φ26mm	388.5	0.00760	597.8	0.2135	28.11
0.2				522.0	0.00877	686.6	0.1885	21.48
0.3				620.5	0.01000	740.5	0.1415	14.15
0.4				730.1	0.01165	769.5	0.1203	10.32
0.1	30	Φ10/50mm	Φ28mm	425.9	0.00771	664.5	0.2115	27.45
0.2				548.7	0.00881	746.0	0.1816	20.62
0.3				658.6	0.01004	796.6	0.1378	13.72
0.4				771.2	0.01162	820.5	0.1161	9.99
0.1	30	Φ10/50mm	Φ30mm	463.0	0.00781	735.6	0.2090	26.77
0.2				582.2	0.00886	808.4	0.1755	19.80
0.3				687.1	0.01006	853.2	0.1342	13.34
0.4				801.0	0.01162	873.8	0.1126	9.69
0.1	35	Φ10/50mm	Φ20mm	316.2	0.00727	447.2	0.2141	29.46
0.2				463.8	0.00858	565.4	0.1904	22.18
0.3				560.6	0.00998	642.2	0.1432	14.35
0.4				675.5	0.01097	684.6	0.1108	10.10
0.1	40	Φ10/50mm	Φ20mm	339.9	0.00727	470.4	0.2062	28.36
0.2				502.8	0.00859	600.4	0.1787	20.79
0.3				613.6	0.01010	682.9	0.1281	12.68
0.4				708.6	0.01127	722.7	0.0993	8.81
0.1	45	Φ10/50mm	Φ20mm	363.5	0.00728	494.0	0.1985	27.28
0.2				542.6	0.00865	637.6	0.1641	18.98
0.3				670.5	0.01023	726.3	0.1184	11.57
0.4				742.3	0.01155	765.9	0.0904	7.83

0.1	50	Φ10/50mm	Φ20mm	386.8	0.00729	515.4	0.1904	26.11
0.2				584.4	0.00873	667.9	0.1485	17.00
0.3				727.9	0.01037	758.9	0.1027	9.90
0.4				780.0	0.01170	789.7	0.0813	6.95

Table 4. Calculation results of bending moment-curvature (Circular Columns)

N/N	f (Mpa)	Transverse Reinforcement	Longitudinal Reinforcement	M $(kN.m)$	Φ $(1/m)$	M $(kN.m)$	Φ $(1/m)$	μ_Φ
0.1	30	Φ10/50mm	Φ20mm	354.2	0.00663	497.6	0.1251	18.86
0.2				475.9	0.00770	598.1	0.0948	12.32
0.3				574.3	0.00875	665.1	0.0745	8.51
0.4				633.1	0.00967	697.0	0.0635	6.57
0.1	30	Φ12/50mm	Φ20mm	366.8	0.00674	508.3	0.1576	23.38
0.2				488.3	0.00780	617.0	0.1240	15.90
0.3				588.4	0.00886	694.0	0.0980	11.06
0.4				648.5	0.00980	742.7	0.0819	8.36
0.1	30	Φ12/75mm	Φ20mm	353.3	0.00667	490.8	0.1231	18.46
0.2				475.4	0.00772	588.6	0.0923	11.95
0.3				574.9	0.00877	651.9	0.0727	8.29
0.4				630.0	0.00971	679.9	0.0621	6.39
0.1	30	Φ12/100mm	Φ20mm	340.7	0.00661	478.6	0.1038	15.71
0.2				462.8	0.00764	569.3	0.0761	9.96
0.3				560.7	0.00869	623.4	0.0595	6.85
0.4				353.3	0.00667	490.8	0.1231	5.39
0.1	30	Φ10/50mm	Φ22mm	389.7	0.00673	557.6	0.1216	18.08
0.2				511.1	0.00776	652.3	0.0920	11.86
0.3				600.5	0.00880	714.1	0.0730	8.30
0.4				668.4	0.00972	741.7	0.0620	6.38
0.1	30	Φ10/50mm	Φ24mm	429.8	0.00683	622.1	0.1179	17.26
0.2				550.1	0.00783	710.4	0.0903	11.54
0.3				650.8	0.00885	766.9	0.0715	8.08
0.4				719.2	0.00976	790.0	0.0605	6.20
0.1	30	Φ10/50mm	Φ26mm	475.1	0.00694	691.3	0.1146	16.52
0.2				595.4	0.00790	771.6	0.0875	11.07
0.3				695.0	0.00890	823.3	0.0701	7.88
0.4				769.1	0.00981	842.2	0.0590	6.02
0.1	30	Φ10/50mm	Φ28mm	529.3	0.00706	763.9	0.1098	15.55
0.2				645.8	0.00798	837.3	0.0854	10.70
0.3				744.9	0.00895	883.3	0.0685	7.65
0.4				824.8	0.00985	897.9	0.0575	5.84
0.1	30	Φ10/50mm	Φ30mm	583.5	0.00717	839.4	0.1056	14.72
0.2				693.7	0.00805	905.3	0.0824	10.23
0.3				788.1	0.00899	945.6	0.0671	7.46
0.4				876.7	0.00989	956.8	0.0560	5.66
0.1	35	Φ10/50mm	Φ20mm	385.8	0.00663	523.4	0.1160	17.48
0.2				529.6	0.00776	640.9	0.0866	11.16
0.3				637.7	0.00897	717.1	0.0682	7.60
0.4				694.8	0.00970	750.5	0.0573	5.91
0.1	40	Φ10/50mm	Φ20mm	416.3	0.00665	549.4	0.1083	16.28
0.2				578.8	0.00782	683.5	0.0797	10.19
0.3				699.5	0.00907	768.7	0.0614	6.77
0.4				751.6	0.00980	803.7	0.0528	5.39
0.1	45	Φ10/50mm	Φ20mm	448.3	0.00668	575.7	0.1026	15.37
0.2				625.3	0.00786	726.7	0.0735	9.35
0.3				765.7	0.00921	820.0	0.0568	6.17
0.4				808.3	0.00990	856.4	0.0480	4.85

0.1	50	Φ10/50mm	Φ20mm	478.4	0.00669	602.7	0.0967	14.45
0.2				674.0	0.00792	770.1	0.0695	8.78
0.3				829.9	0.00930	870.3	0.0534	5.74
0.4				863.9	0.01000	907.9	0.0445	4.45

Table 5. Calculation results of bending moment-curvature (Rectangular Columns)

N/N	f (Mpa)	Transverse Reinforcement	Longitudinal Reinforcement	M $(kN.m)$	Φ $(1/m)$	M $(kN.m)$	Φ $(1/m)$	μ_Φ
0.1	30	Φ10/50mm	Φ20mm	372.5	0.00607	577.9	0.1910	31.53
0.2				511.5	0.00705	691.2	0.1752	25.03
0.3				605.7	0.00796	766.8	0.1519	19.08
0.4				705.8	0.00910	824.8	0.1282	14.09
0.1	30	Φ12/50mm	Φ20mm	384.2	0.00618	585.1	0.2065	33.71
0.2				520.2	0.00716	712.5	0.1965	27.89
0.3				615.2	0.00808	811.0	0.1795	22.22
0.4				716.0	0.00940	879.1	0.1565	16.65
0.1	30	Φ12/75mm	Φ20mm	374.5	0.00609	572.5	0.1843	30.26
0.2				513.9	0.00709	680.3	0.1737	24.61
0.3				608.8	0.00801	760.2	0.1483	18.44
0.4				709.4	0.00925	815.0	0.1158	12.52
0.1	30	Φ12/100mm	Φ20mm	368.5	0.00601	563.1	0.1623	26.83
0.2				507.6	0.00701	654.4	0.1385	19.76
0.3				601.2	0.00793	715.3	0.1147	14.32
0.4				701.7	0.00915	757.4	0.0964	10.53
0.1	30	Φ10/50mm	Φ22mm	412.6	0.00615	655.7	0.1850	30.10
0.2				563.4	0.00705	761.4	0.1692	23.99
0.3				647.4	0.00800	830.7	0.1460	18.26
0.4				752.8	0.00916	886.9	0.1222	13.34
0.1	30	Φ10/50mm	Φ24mm	457.1	0.00624	738.8	0.1790	28.70
0.2				601.3	0.00711	834.6	0.1632	22.96
0.3				693.7	0.00804	899.4	0.1399	17.41
0.4				799.2	0.00921	953.8	0.11620	12.62
0.1	30	Φ10/50mm	Φ26mm	505.1	0.00633	826.6	0.1730	27.33
0.2				641.7	0.00715	911.1	0.1575	22.03
0.3				744.0	0.00809	972.4	0.1339	16.55
0.4				855.3	0.00926	1025.1	0.1103	11.92
0.1	30	Φ10/50mm	Φ28mm	563.3	0.00644	917.6	0.1670	25.94
0.2				689.5	0.00721	991.6	0.15120	20.96
0.3				799.0	0.00814	1050.8	0.1279	15.71
0.4				919.2	0.00931	1101.5	0.1042	11.19
0.1	30	Φ10/50mm	Φ30mm	621.4	0.00657	1012.9	0.1610	24.51
0.2				741.9	0.00728	1078.9	0.1452	19.95
0.3				860.6	0.00820	1136.6	0.1219	14.87
0.4				979.3	0.00936	1186.9	0.0985	10.53
0.1	35	Φ10/50mm	Φ20mm	402.9	0.00607	604.7	0.1826	30.10
0.2				560.6	0.00706	731.1	0.1619	22.92
0.3				674.9	0.00811	814.7	0.1364	16.83
0.4				795.5	0.00919	876.7	0.1125	12.24
0.1	40	Φ10/50mm	Φ20mm	432.4	0.00608	634.5	0.1728	28.44
0.2				603.8	0.00710	779.3	0.1489	20.99
0.3				738.1	0.00821	875.0	0.1199	14.61
0.4				861.1	0.00928	943.6	0.0965	10.40
0.1	45	Φ10/50mm	Φ20mm	459.4	0.00609	662.2	0.1621	26.63
0.2				648.3	0.00715	822.9	0.1356	18.97
0.3				800.0	0.00829	928.0	0.1092	13.17

0.4				906.0	0.00938	1000.8	0.0823	8.77
0.1	50	Φ10/50mm	Φ20mm	488.2	0.00610	689.1	0.1512	24.79
0.2				695.2	0.00719	864.4	0.1263	17.58
0.3				865.8	0.00840	977.8	0.0970	11.54
0.4				944.8	0.00947	1050.2	0.0730	7.71

In column models, the yield and ultimate moment-carrying capacities of columns increase as the confining effect on the section increases. With the increase in the confining effect in the column sections, the yield moment and curvature values remain constant. It has been observed that curvature and ductility values also increase as the moment values increase, due to the increase in the confining effect in the sections. As the axial load level increases in column models, yield moment, ultimate moment, and yield curvature increase, while ultimate curvature and section ductility decrease. Since the moment-curvature relations were investigated, it was observed that the section ductility decreased as the confining effect decreased at constant axial load levels. With an increase in the longitudinal reinforcement diameter of the columns, the carrying capacities increase whereas the section ductility values decrease. Yield and ultimate moment capacities increase with increasing longitudinal reinforcement diameter (other design parameters are constant) in columns. Concrete compressive strength is a parameter that increases the carrying capacity. As the curvature values decrease with the increase of the concrete strength, the section ductility also decreases.

4.2. Proposed Effective Stiffness Factor

Determining the flexural stiffness of RC columns involves a combination of theoretical modelling, material property analysis, and empirical adjustments to account for factors such as cracking and time-dependent effects. The effective stiffness coefficient is a concept used to determine the stiffness of structural elements in structural engineering and earthquake engineering. This factor plays an important role in dynamic analysis and design calculations of structures. The effective stiffness factor allows the actual stiffness of a structural element to be adjusted to better reflect its behaviour under a particular loading situation. The calculation and use of this factor may vary depending on the building material, element type (column, beam, etc.), loading condition and other factors. Building regulations generally provide various tables and formulas to determine these factors. The effective stiffness factor is a coefficient used to obtain more realistic and reliable results in the design and analysis of building elements. Correct determination of these coefficients plays a critical role in ensuring structure safety and performance.

Understanding and accurately determining the effective stiffness of RC columns is crucial for designing safe, durable, and efficient structures. An extensive investigation was conducted to determine the effective stiffness coefficients, determine the suitability of the relationships between the researchers and the current codes specified, and compare them, considering the key design parameters influencing the non-linear behaviour of RC columns. The confining effect, ρ , ρ , f and N/N were obtained from the non-linear analysis results where the main parameters affecting the stiffness of the column sections. Determining the flexural stiffness of RC columns is essential for structural analysis and design. Traditional methods often involve empirical formulas and simplifications that may not accurately capture the complex behaviour of concrete and reinforcement. A new approach should consider a more detailed analysis of the interaction between concrete and reinforcement, as well as the effects of various factors such as cracking. A securer, quicker and more robust equation (k) has been proposed for the effective flexural stiffness of cracked sections by considering parameters such as the ρ , ρ f and N/N in the square, circular and rectangular columns. The basic formation of the k for column sections can be expressed as follows. The N/N , ρ , ρ and f have an increasing effect on k depending on the behaviour of the column section. As a result of this interpretation, a simple equation has been developed to indicate the effect of N/N , ρ , ρ and f on column sections. Equations (6, 7 and 8) are proposed for the determination of k of square, circular and rectangular columns, respectively. This approach aims to provide a more accurate and comprehensive method for determining the flexural stiffness of RC

columns, considering the complex interactions and behaviours of the materials involved. The basic formation of the $k_{,}$ for column sections can be expressed as follows.

$$k_{e,prop} = f\left\{\left(\frac{N}{A_c f_{ck}}\right),(\rho_s),(\rho_{st}),(f_{ck})\right\} \quad (1)$$

4.2.1. $k_{e,prop}$ for square column sections

The N/N has a pronounced effect on the stiffness coefficient (k). The relations of $k_{,}$ and N/N parameters obtained by the regression analysis performed according to the parametric analysis results are given in Equation (2).

$$k_{e,cal-1} = -1.31\left(\frac{N}{A_c f_{ck}}\right)^2 + 0.942\left(\frac{N}{A_c f_{ck}}\right) + 0.2014 \quad (2)$$

As can be seen from the examination of the results and relations obtained from the analyses, the k value increases with the increase in the ρ value. The relations of k to $k_{,\ _}$ and the ρ parameters obtained by the regression analysis performed according to the parametric analysis results are given in Equation (3).

$$k_{e,cal-2} = 38.2(\rho_s) + 0.616 \quad (3)$$

As can be seen from the examination of the results and relations obtained from the analyses, the k value increases with increasing of ρ value. The relations of k to $[k_{,\ _} \times k_{,\ _}]$ and the ρ parameters obtained by the regression analysis performed according to the parametric analysis results are given in Equation (4).

$$k_{e,cal-3} = 1.82(\rho_{st}) + 0.967 \quad (4)$$

From examining the results and relationships from the analyses, the k increases with increasing of f value. The relations of k to $[k_{,\ _} \times k_{,\ _} \times k_{,\ _}]$ and the f parameters obtained by the regression analysis performed according to the parametric analysis results are given in Equation (5).

$$k_{e,cal-4} = 0.0012(f_{ck}) + 0.951 \quad (5)$$

Equation (6) is proposed for the stiffness factor ($k_{,}$) of the square cross-section RC column based on the analysis results, considering the N/N , ρ , ρ and f parameters that affect the nonlinear behaviour.

$$k_{e,prop} = \left[-1.31\left(\frac{N}{A_c f_{ck}}\right)^2 + 0.942\left(\frac{N}{A_c f_{ck}}\right) + 0.2014\right] \times \left[38.2(\rho_s) + 0.616\right] \times \left[1.82(\rho_{st}) + 0.967\right] \times \left[0.0012(f_{ck}) + 0.951\right] \quad (6)$$

4.2.2. $k_{e,prop}$ for circular column sections

Equation (7) is proposed for the stiffness factor of the circular cross-section RC column based on the analysis results, considering the N/N , ρ , ρ and f parameters that affect the nonlinear behaviour.

$$k_{e,prop} = \left[-1.14\left(\frac{N}{A_c f_{ck}}\right)^2 + 0.796\left(\frac{N}{A_c f_{ck}}\right) + 0.239\right] \times \left[26(\rho_s) + 0.71\right] \times \left[6.45(\rho_{st}) + 0.92\right] \times \left[0.002(f_{ck}) + 0.95\right] \quad (7)$$

4.2.3. $k_{e,prop}$ for rectangular column sections

Equation (8) is proposed for the stiffness factor of the rectangular cross-section RC column based on the analysis results, considering the N/N , ρ , ρ and f parameters that affect the nonlinear behaviour.

$$k_{e,prop}=\left[-1.34\left(\frac{N}{A_c f_{ck}}\right)^2+0.928\left(\frac{N}{A_c f_{ck}}\right)+0.233\right]\times\left[32.97(\rho_s)+0.567\right]\times\left[0.987(\rho_{st})+0.964\right]\times\left[0.001(f_{ck})+0.978\right] \quad (8)$$

4.3. Verification of the Suggested Stiffness Factor Equation

In this part of the study, the analytically calculated effective stiffness coefficient values of the column models for different design parameters are presented comparatively according to the moment-curvature, different codes, researchers and the proposed stiffness factor equation. The results obtained were examined by comparing them according to N/N , ρ , ρ and f parameters and square, circular and rectangular cross-section models. The effect of each factor on the stiffness coefficient of column sections is presented and interpreted in the following. The effective flexural stiffness factors of RC columns with square, circular, and rectangular cross-sections were systematically evaluated by considering a wide range of design parameters, including N/N , ρ , ρ , f and sectional dimensions. For each cross-sectional geometry, the moment–curvature relationships were derived using nonlinear sectional analysis that accounts for material nonlinearity, such as concrete cracking and reinforcement yielding. Based on these relationships, the corresponding effective stiffness factors were computed. A comprehensive comparison of the obtained stiffness factors for the different column configurations is presented in Tables 6 to 14, enabling a detailed assessment of how geometric and mechanical parameters influence the flexural stiffness behaviour of RC columns. A comparison of the suggested effective stiffness factor equation, different researchers, and different seismic codes for square column sections are presented comparatively in Figure 6, circular column sections are presented comparatively in Figure 7 and rectangular column sections are presented comparatively in Figure 8. Analysis of the effect of key parameters on the effective stiffness of RC columns; the effect of four key parameters, including N/N , ρ , ρ and f on the effective stiffness of RC columns is investigated.

Axial load ratio: Increasing the axial load ratio leads to an increase in compressive stress in the section and in the early stages, causes an increase in stiffness. However, at higher values, concrete enters the nonlinear region, and the stiffness decreases due to cracking and a decrease in effective strength. This decreasing trend is observed in the present numerical studies with a steeper slope than in classical models, which can be attributed to the more accurate nonlinear behaviour of concrete and the interaction of concrete and reinforcement.

Longitudinal reinforcement ratio: Increasing the longitudinal rebar density improves the flexural behaviour of the column and delays the onset of cracking. Numerical results showed that increasing ρ increases the effective stiffness, especially in the stages after the initial crack. These results are consistent with previous studies but are observed with greater intensity. The reason for this difference can be attributed to the use of more accurate nonlinear models in this study and the consideration of the effect of rebars on stress redistribution.

Transverse reinforcement ratio: The role of transverse reinforcement is mainly to provide shear strength, limit crack propagation and maintain the integrity of compressive concrete. The analyses performed showed that increasing ρ in critical areas of the column increases the effective stiffness, especially in columns with high loading levels. This effect has not been considered in many classical studies. However, in this study, by accurately modelling the concrete-reinforcement interaction and examining the local nonlinear behaviour, the positive effect of transverse reinforcement on the effective stiffness has been observed.

Characteristic strength of concrete: Increasing the strength of concrete leads to an increase in the modulus of elasticity and, as a result, an increase in the initial stiffness of the section. With increasing f ,

the stiffness also increases as an ascending function. In this study, columns with higher-strength concretes showed stiffer behaviour. These results are consistent with the code and experimental models, with the difference that in the present model, the effect of strength loss in cracked and post-cracking areas is also considered. Finally, it can be concluded that the stiffness of RC columns is under the combined influence of these parameters, and their detailed analysis will help to better understand the structural behaviour. The difference in the results compared to previous studies is mainly due to more advanced numerical modelling, nonlinear analysis, and consideration of the full interaction between structural components.

Table 6. Comparison of effective stiffness factors calculated for square column sections (Effect of ρ on k)

N/N	f (Mpa)	Transverse Reinforcement	Longitudinal Reinforcement	k (Numerical)	Equation (6)	Equation (6)/k (Numerical)
0.1	30	Φ10/50mm	Φ20mm	0.2853	0.2879	1.009
0.2				0.3443	0.3352	0.974
0.3				0.3600	0.3637	1.010
0.4				0.3704	0.368	0.994
0.1		Φ12/50mm		0.3013	0.3039	1.009
0.2				0.3510	0.3515	1.001
0.3				0.3673	0.3712	1.011
0.4				0.3765	0.3760	0.999
0.1		Φ12/75mm		0.2920	0.2915	0.998
0.2				0.3410	0.3406	0.999
0.3				0.3615	0.3637	1.006
0.4				0.3688	0.3680	0.998
0.1		Φ12/100mm		0.2820	0.2795	0.991
0.2				0.3348	0.333	0.995
0.3				0.3565	0.358	1.004
0.4				0.3617	0.3627	1.003

Table 7. Comparison of effective stiffness factors calculated for square column sections (Effect of ρ on k)

N/N	f (Mpa)	Transverse Reinforcement	Longitudinal Reinforcement	k (Numerical)	Equation (6)	Equation (6)/k (Numerical)
0.1	30	Φ10/50mm	Φ22mm	0.3055	0.3035	0.993
0.2				0.3714	0.3680	0.991
0.3				0.3902	0.3890	0.997
0.4				0.3962	0.3960	0.999
0.1			Φ24mm	0.3313	0.3290	0.993
0.2				0.3937	0.3919	0.995
0.3				0.4115	0.4130	1.004
0.4				0.4170	0.4210	1.010
0.1			Φ26mm	0.3586	0.3570	0.996
0.2				0.4171	0.4196	1.006
0.3				0.4350	0.4370	1.005
0.4				0.4393	0.4434	1.009
0.1			Φ28mm	0.3874	0.3850	0.994
0.2				0.4369	0.4390	1.005

0.3			0.4597	0.4625	1.006
0.4			0.4653	0.4680	1.006
0.1			0.4157	0.4149	0.998
0.2		Φ30mm	0.4606	0.4610	1.001
0.3			0.4789	0.4820	1.006
0.4			0.4832	0.4887	1.011

Table 8. Comparison of effective stiffness factors calculated for square column sections (Effect of f on k)

N/N	f (Mpa)	Transverse Reinforcement	Longitudinal Reinforcement	k (Numerical)	Equation (6)	Equation (6)/k (Numerical)
0.1	35			0.2824	0.2827	1.001
0.2	35			0.3507	0.3490	0.995
0.3	35			0.3647	0.3640	0.998
0.4	35			0.3765	0.3746	0.995
0.1	40			0.2839	0.2844	1.002
0.2	40			0.3552	0.3530	0.994
0.3	40			0.3689	0.3680	0.998
0.4	40			0.3817	0.3805	0.997
0.1	45	Φ10/50mm	Φ20mm	0.2860	0.2861	1.000
0.2	45			0.3593	0.3575	0.995
0.3	45			0.3751	0.3739	0.997
0.4	45			0.3872	0.3860	0.997
0.1	50			0.2881	0.2901	1.007
0.2	50			0.3633	0.3620	0.996
0.3	50			0.3812	0.3798	0.996
0.4	50			0.3957	0.3940	0.996

Table 9. Comparison of effective stiffness factors calculated for circular column sections (Effect of ρ on k)

N/N	f (Mpa)	Transverse Reinforcement	Longitudinal Reinforcement	k (Numerical)	Equation (7)	Equation (7)/k (Numerical)
0.1				0.3076	0.3083	1.002
0.2		Φ10/50mm		0.3534	0.3539	1.001
0.3				0.3710	0.3690	0.995
0.4				0.3748	0.3770	1.006
0.1				0.3131	0.3170	1.012
0.2	30	Φ12/50mm	Φ20mm	0.3568	0.3640	1.020
0.3				0.3738	0.3830	1.025
0.4				0.3768	0.3870	1.027
0.1				0.3038	0.3080	1.014
0.2		Φ12/75mm		0.3518	0.3530	1.003
0.3				0.3698	0.3720	1.006

0.4			0.3730	0.3754	1.006
0.1			0.2963	0.3019	1.019
0.2		Φ12/100mm	0.3479	0.3465	0.996
0.3			0.3646	0.3650	1.001
0.4			0.3695	0.3686	0.998

Table 10. Comparison of effective stiffness factors calculated for circular column sections (Effect of ρ on k)

N/N	f (Mpa)	Transverse Reinforcement	Longitudinal Reinforcement	k (Numerical)	Equation (7)	Equation (7)/k (Numerical)
0.1	30	Φ10/50mm	Φ22mm	0.3325	0.3300	0.992
0.2				0.3781	0.3770	0.997
0.3				0.3886	0.3920	1.009
0.4				0.3949	0.3990	1.010
0.1			Φ24mm	0.3613	0.3550	0.983
0.2				0.4034	0.3989	0.989
0.3				0.4195	0.4170	0.994
0.4				0.4229	0.4243	1.003
0.1			Φ26mm	0.3931	0.3900	0.992
0.2				0.4324	0.4270	0.988
0.3				0.4462	0.4440	0.995
0.4				0.4501	0.4515	1.003
0.1			Φ28mm	0.4303	0.4250	0.988
0.2				0.4643	0.4590	0.989
0.3				0.4762	0.4750	0.997
0.4				0.4806	0.4809	1.001
0.1			Φ30mm	0.4669	0.4600	0.985
0.2				0.4945	0.4880	0.987
0.3				0.5030	0.5040	1.002
0.4				0.5088	0.5124	1.007

Table 11. Comparison of effective stiffness factors calculated for circular column sections (Effect of f on k)

N/N	f (Mpa)	Transverse Reinforcement	Longitudinal Reinforcement	k (Numerical)	Equation (7)	Equation (7)/k (Numerical)
0.1	35	Φ10/50mm	Φ20mm	0.3090	0.3090	1.000
0.2	35			0.3626	0.3600	0.993
0.3	35			0.3777	0.3760	0.995
0.4	35			0.3918	0.3920	1.001
0.1	40			0.3111	0.3111	1.000
0.2	40			0.3678	0.3650	0.992
0.3	40			0.3832	0.3820	0.997
0.4	40			0.4055	0.4020	0.991

0.1	45			0.3147	0.3147	1.000
0.2	45			0.3727	0.3700	0.993
0.3	45			0.3898	0.3878	0.995
0.4	45			0.4201	0.4110	0.978
0.1	50			0.3178	0.3190	1.004
0.2	50			0.3785	0.3770	0.996
0.3	50			0.3965	0.3940	0.994
0.4	50			0.4344	0.4298	0.989

Table 12. Comparison of effective stiffness factors calculated for rectangular column sections (Effect of ρ on k)

N/N	f (Mpa)	Transverse Reinforcement	Longitudinal Reinforcement	k (Numerical)	Equation (8)	Equation (8)/k (Numerical)
0.1	30	Φ10/50mm	Φ20mm	0.3110	0.3111	1.000
0.2	30			0.3698	0.3690	0.998
0.3	30			0.3857	0.3880	1.006
0.4				0.3906	0.3930	1.006
0.1		Φ12/50mm		0.3161	0.3147	0.996
0.2				0.3752	0.3700	0.986
0.3				0.3888	0.3888	1.000
0.4				0.3957	0.3950	0.998
0.1		Φ12/75mm		0.3109	0.3109	1.000
0.2				0.3679	0.3660	0.995
0.3				0.3818	0.3840	1.006
0.4				0.3866	0.3879	1.003
0.1		Φ12/100mm		0.3063	0.3089	1.008
0.2				0.3622	0.3610	0.997
0.3				0.3768	0.3768	1.000
0.4				0.3803	0.3810	1.002

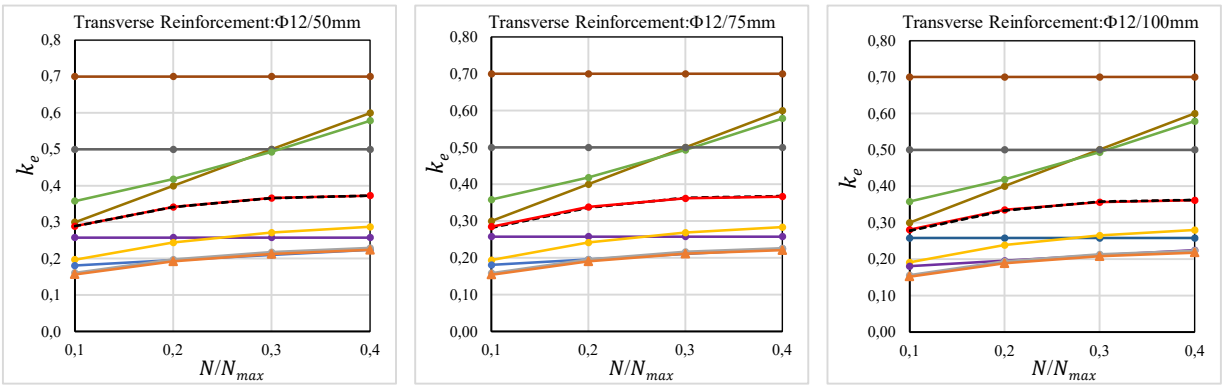
Table 13. Comparison of effective stiffness factors calculated for rectangular column sections (Effect of ρ on k)

N/N	f (Mpa)	Transverse Reinforcement	Longitudinal Reinforcement	k (Numerical)	Equation (8)	Equation (8)/k (Numerical)
0.1	30	Φ10/50mm	Φ22mm	0.3405	0.3389	0.995
0.2				0.4024	0.3980	0.989
0.3				0.4106	0.4140	1.008
0.4				0.4172	0.4228	1.013
0.1			Φ24mm	0.3718	0.3697	0.994
0.2				0.4272	0.4319	1.011
0.3				0.4380	0.4490	1.025
0.4				0.4431	0.4580	1.034
0.1			Φ26mm	0.4047	0.4036	0.997
0.2				0.4540	0.4700	1.035
0.3				0.4675	0.4820	1.031
0.4				0.4739	0.4920	1.038

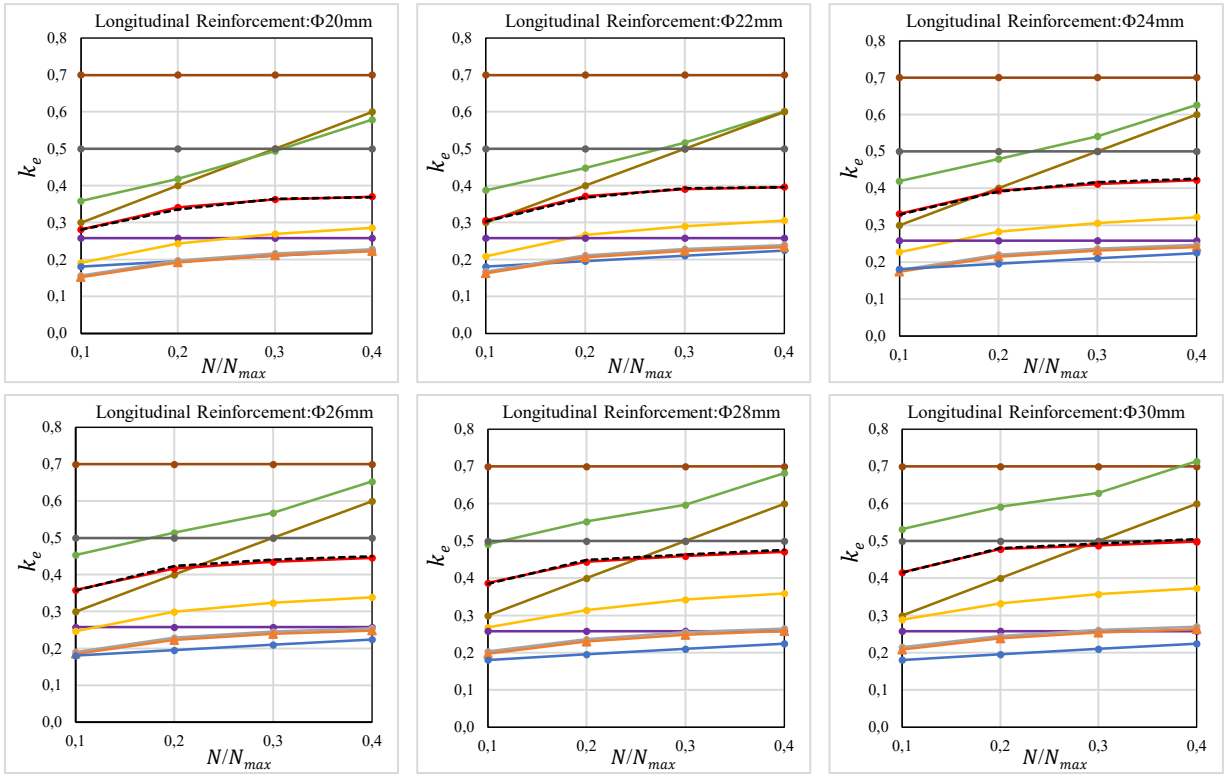
0.1			0.4438	0.4405	0.993
0.2		Φ28mm	0.4841	0.5100	1.054
0.3			0.4995	0.5210	1.043
0.4			0.5091	0.5290	1.039
0.1			0.4797	0.4796	1.000
0.2		Φ30mm	0.5170	0.5400	1.044
0.3			0.5357	0.5550	1.036
0.4			0.5431	0.5630	1.037

Table 14. Comparison of effective stiffness factors calculated for rectangular column sections (Effect of f on k)

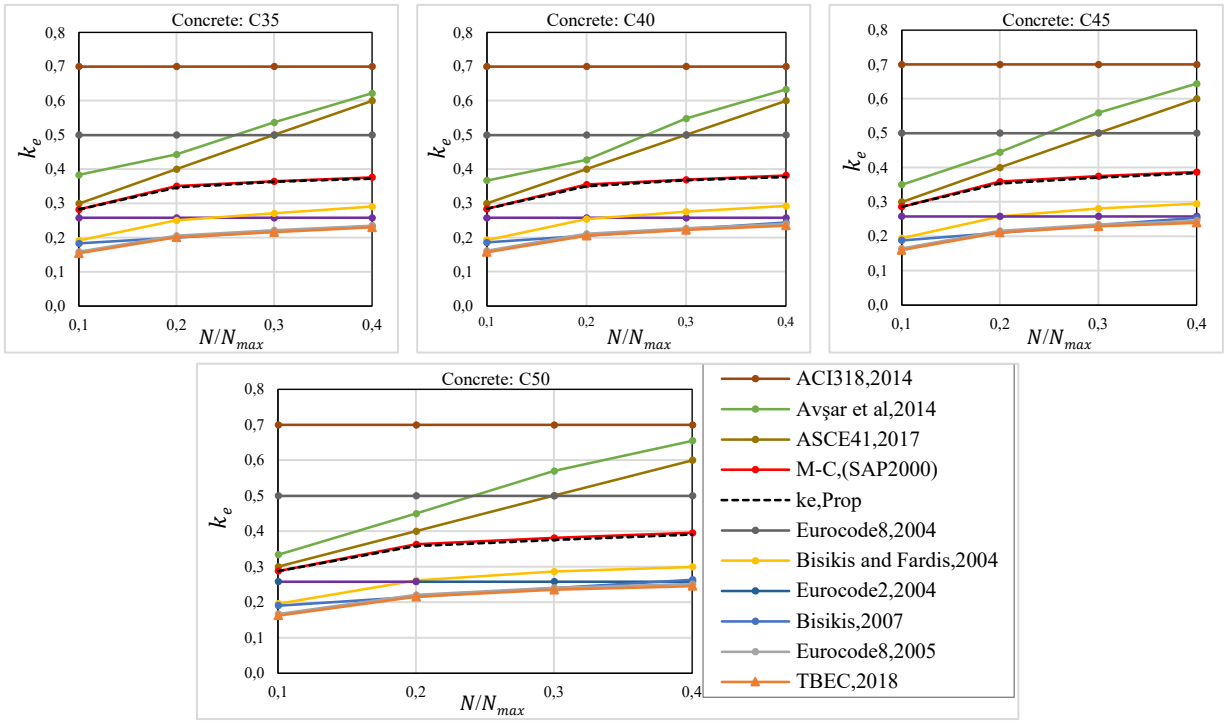
N/N	f (Mpa)	Transverse Reinforcement	Longitudinal Reinforcement	k (Numerical)	Equation (8)	Equation (8)/k (Numerical)
0.1	35	Φ10/50mm	Φ20mm	0.3127	0.3127	1.000
0.2	35			0.3726	0.3710	0.996
0.3	35			0.3905	0.3905	1.000
0.4	35			0.3968	0.3960	0.998
0.1	40			0.3146	0.3142	0.999
0.2	40			0.3754	0.3730	0.994
0.3	40			0.3950	0.3931	0.995
0.4	40			0.4031	0.3990	0.990
0.1	45			0.3172	0.3158	0.996
0.2	45			0.3783	0.3760	0.994
0.3	45			0.3995	0.3960	0.991
0.4	45			0.4086	0.4040	0.989
0.1	50			0.3194	0.3173	0.993
0.2	50			0.3822	0.3790	0.992
0.3	50			0.4046	0.4000	0.989
0.4	50			0.4149	0.4100	0.988



a) Effect of ρ on k (longitudinal reinforcement: Φ20mm - C30)

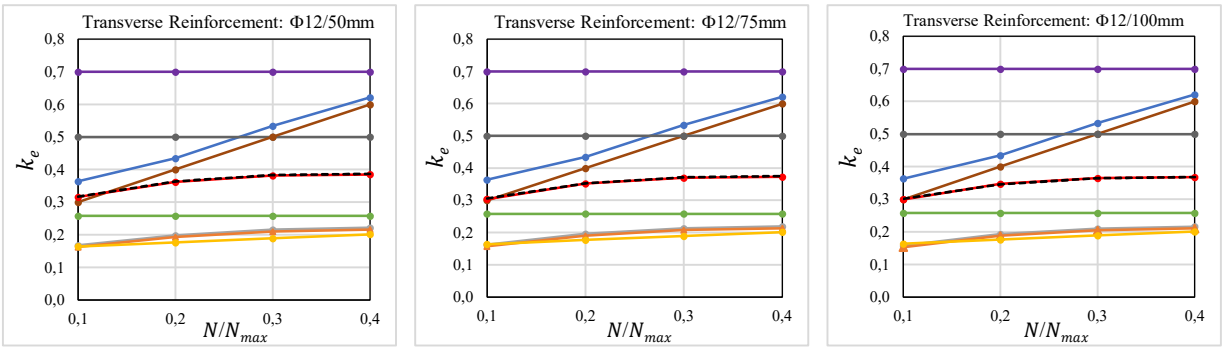


b) Effect of ρ on k (transverse reinforcement: Φ10/50mm - C30)

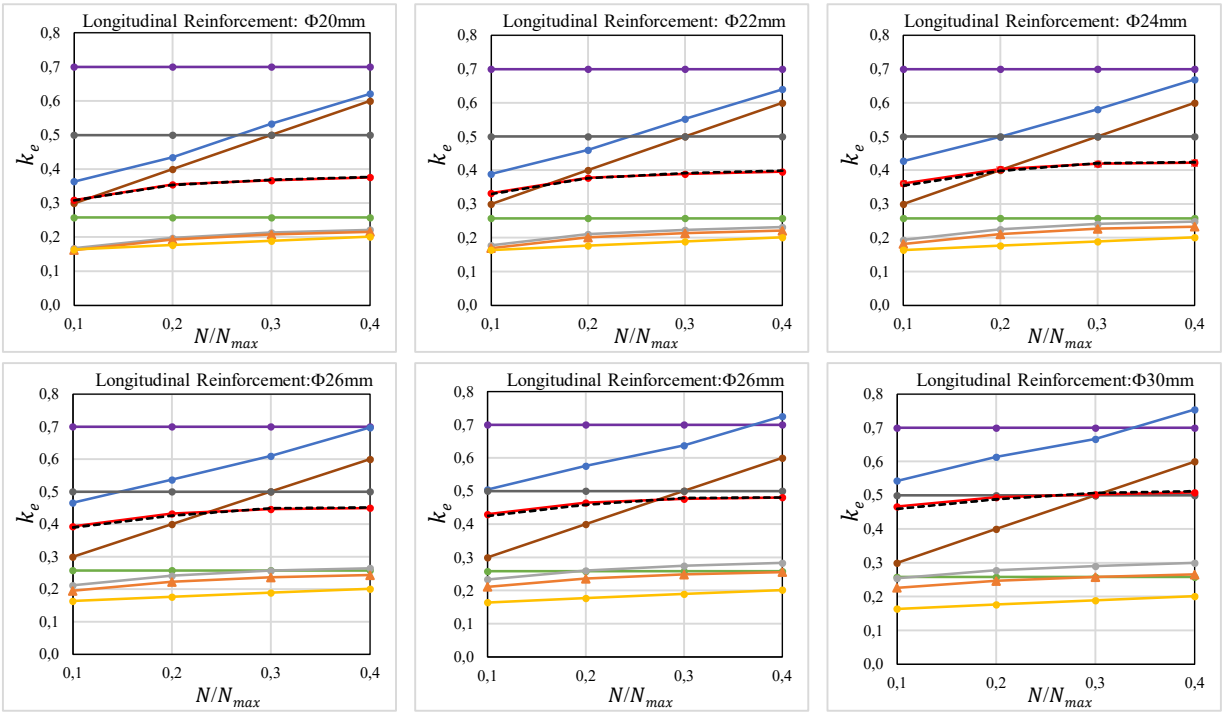


c) Effect of f on k (longitudinal reinforcement: Φ20mm – transverse reinforcement: Φ10/50mm)

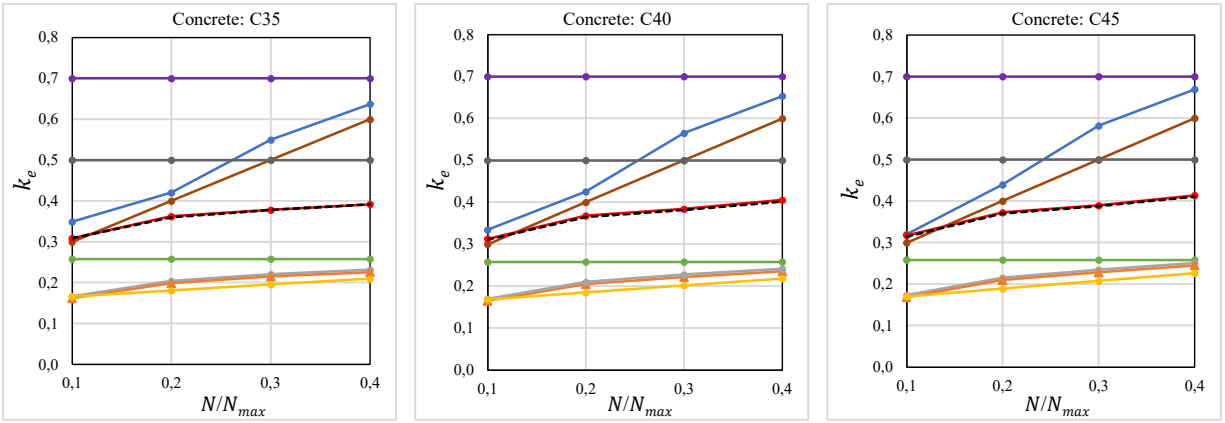
Figure 6. Comparison of the proposed equation for the stiffness factor for square column sections with other estimation relations

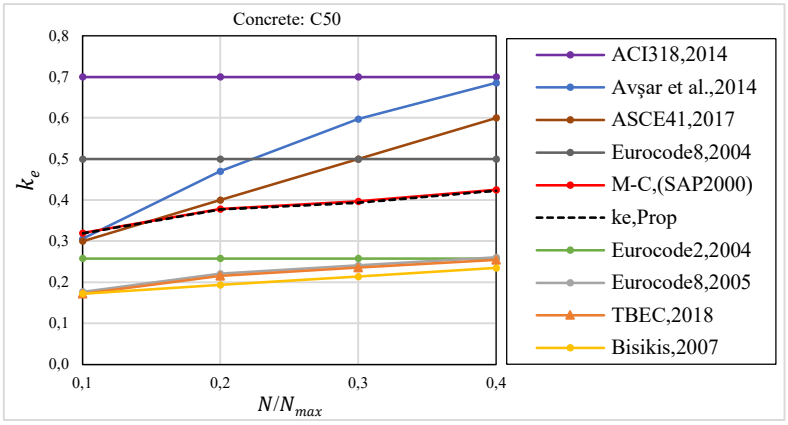


a) Effect of ρ on k (longitudinal reinforcement: Φ20mm - C30)



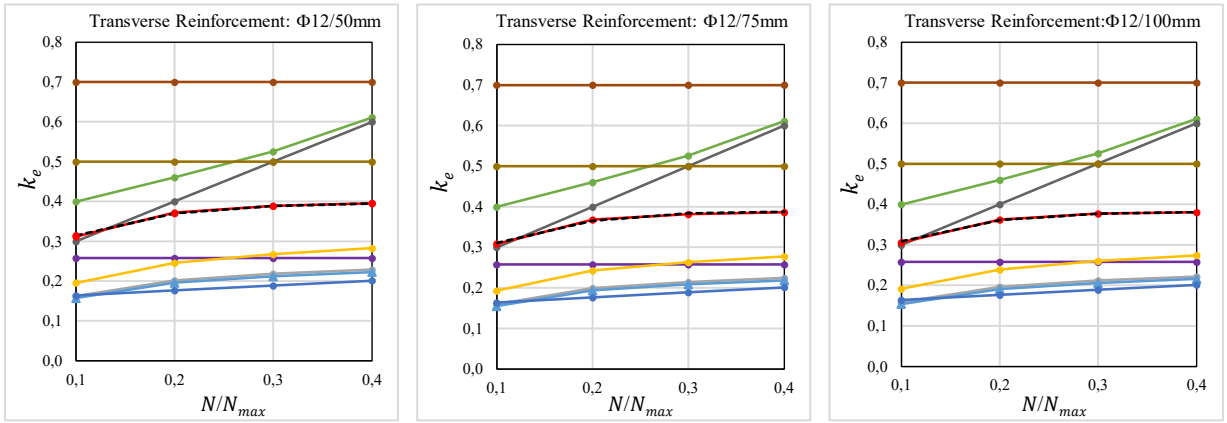
b) Effect of ρ on k (transverse reinforcement: Φ10/50mm - C30)



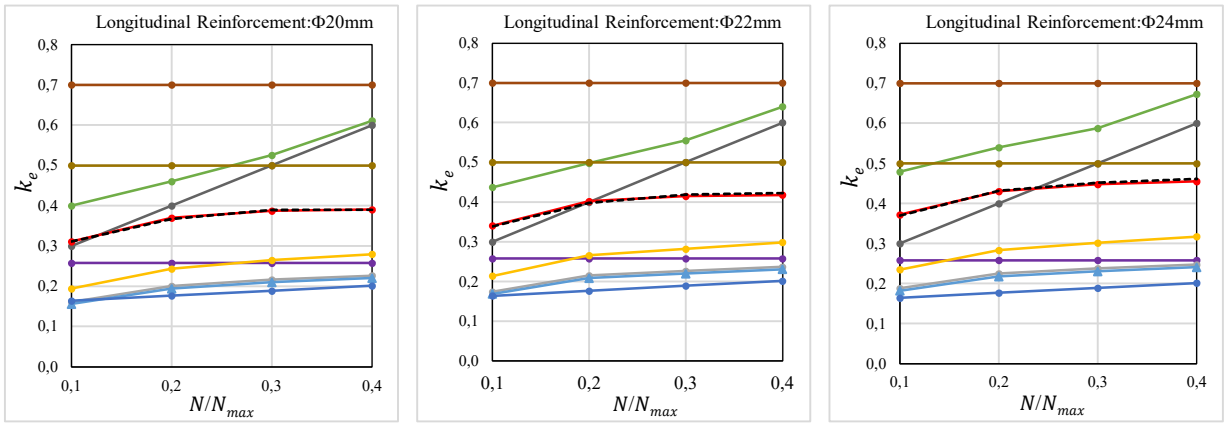


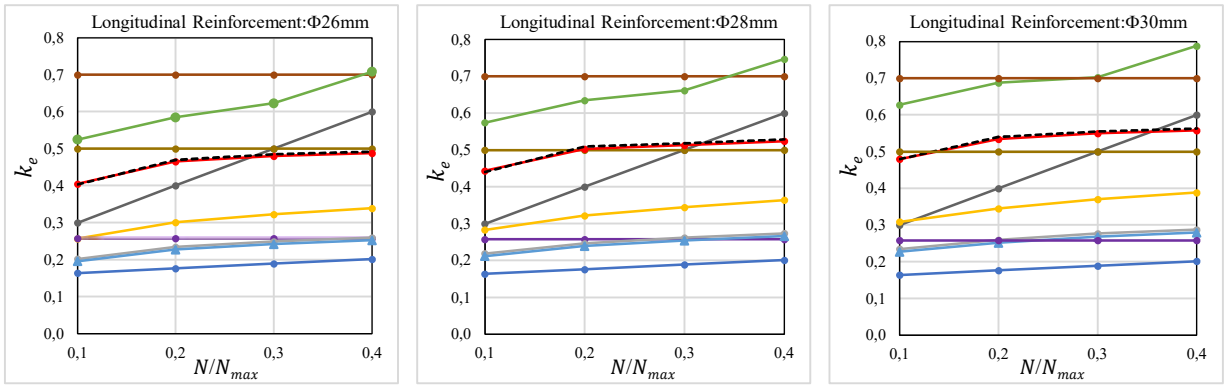
c) Effect of f on k (longitudinal reinforcement: Φ20mm – transverse reinforcement: Φ10/50mm)

Figure 7. Comparison of the proposed equation for the stiffness factor for circular column sections with other estimation relations

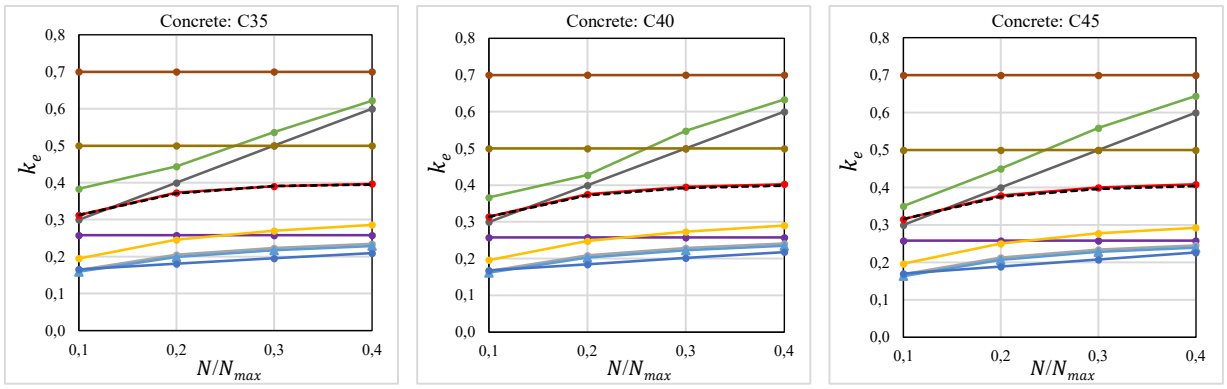


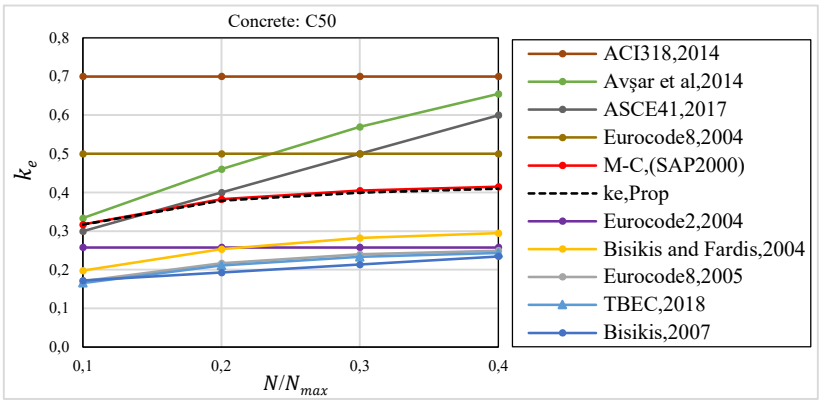
a) Effect of ρ on k (longitudinal reinforcement: Φ20mm - C30)





b) Effect of ρ on k (transverse reinforcement: Φ10/50mm - C30)





c) Effect of f on k (longitudinal reinforcement: Φ20mm – transverse reinforcement: Φ10/50mm)

Figure 8. Comparison of the proposed equation for the stiffness factor for rectangular column sections with other estimation relations

According to the results, the stiffness coefficients calculated from the nonlinear analysis, different codes and relationships suggested by researchers are different from each other. The reason for the different results obtained is the definition of constant coefficients in the standard and codes by considering different parameters in the stiffness relations section proposed by the researchers.

ACI318 (2014) established a consistent ratio of $0.70EI$ for columns. In ASCE/SEI-41 (2017), for columns subjected to a design gravity load of less than $0.1A_g f'_c$, the effective stiffness, denoted as EI_{eff}, is defined as $0.3EI$. Conversely, for columns experiencing a compressive force exceeding $0.5A_g f'_c$, this coefficient is specified as 0.7. Eurocode 8 (2004) stipulates a fixed effective stiffness value for the cracked section, which is regarded as half of the initial stiffness. Notably, Eurocode 8 (2004) does not account for factors such as concrete strength, cross-section geometry, longitudinal and transverse reinforcement

ratios, and the axial force acting on the cross-section. In Part 3 of Eurocode 8 (2005), an equation is provided that relates the moment-to-shear ratio and yield rotation, facilitating a more precise determination of effective stiffness. Eurocode 8 addresses both ultimate and serviceability level loads for linear and nonlinear analyses. According to Eurocode 2 (2004), during a second-order analysis based on stiffness, nominal values of flexural stiffness should be employed, considering the impacts of cracking, material non-linearity, and creep on overall behaviour. Similarly, TBEC (2018) assumes effective stiffness to be constant, with effective stiffness coefficient values for the cracked section set at 0.70 for columns. The effective stiffness of reinforced columns modelled under the lumped plastic behaviour framework in TBEC (2018) can be computed based on effective yield moments, yield rotation, and shear span.

In this study, a numerical study was carried out considering the most important design parameters affecting the nonlinear behaviour of column sections in order to calculate more realistic effective section stiffness values of column models. Thus, missing parameters found in previous studies have been completed, and a simple equation has been proposed for stiffness. It is seen that the equations proposed for the effective stiffness factor of the column models designed in different geometries are in good agreement with the numerical results obtained in all design parameter ranges. The stiffness coefficient calculated from the relationships defined for the column models designed in different parameters increases with increasing concrete strength, axial load, transverse and ratios of longitudinal reinforcement. Examining the studies in literature and existing codes on the effective stiffness of columns revealed that the stiffness coefficients are usually defined in terms of the axial load level in the column sections. The proposed relationships for the stiffness coefficient have been developed on the basis of a comprehensive parametric analysis of RC square, circular and rectangular columns. The adequacy of the proposed k , are evaluated with k , results obtained from moment-curvature and a parametric study at the element level. Figures 9 - 11, shows the comparison of the stiffness factors obtained numerically with the k , for the square, circular and rectangular columns. The ratio of the results obtained from Equations (6 - 8) to the numerical results are influenced by the changes in N/N , ρ , ρ and f . It can be seen that the proposed estimates for columns designed in different geometries are in good agreement with the nonlinear analysis results in all parameter ranges. k , values, which are calculated with the increase of N/N , ρ , ρ ratios and f , also increase.

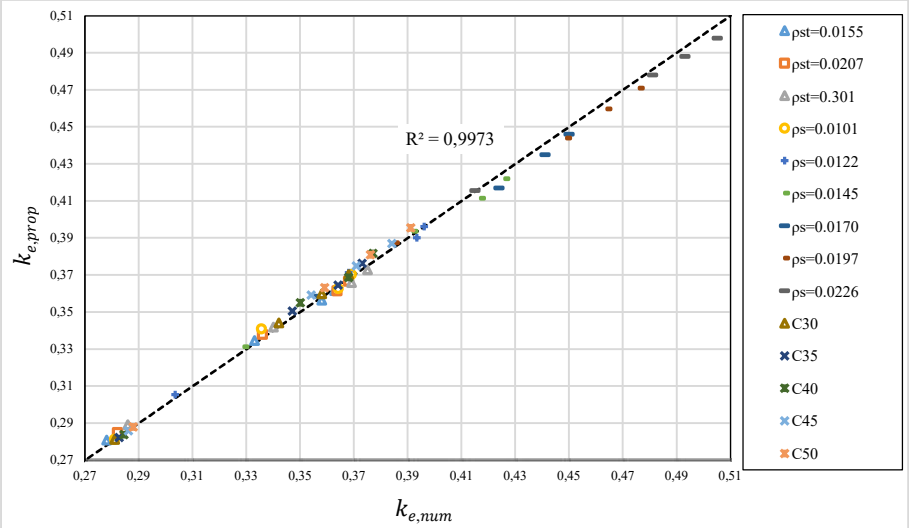


Figure 9. The comparison of k , $-k$, relations according to different parameters for square columns

The coefficient correlation R² is substantially over 0.99, indicating high agreement between the predictions provided for square columns. Additionally, the ratio of the suggested effective stiffness factor obtained by Equation (6) to the numerical result has a maximum mean value of %1.045 and a standard

deviation of %5.69.

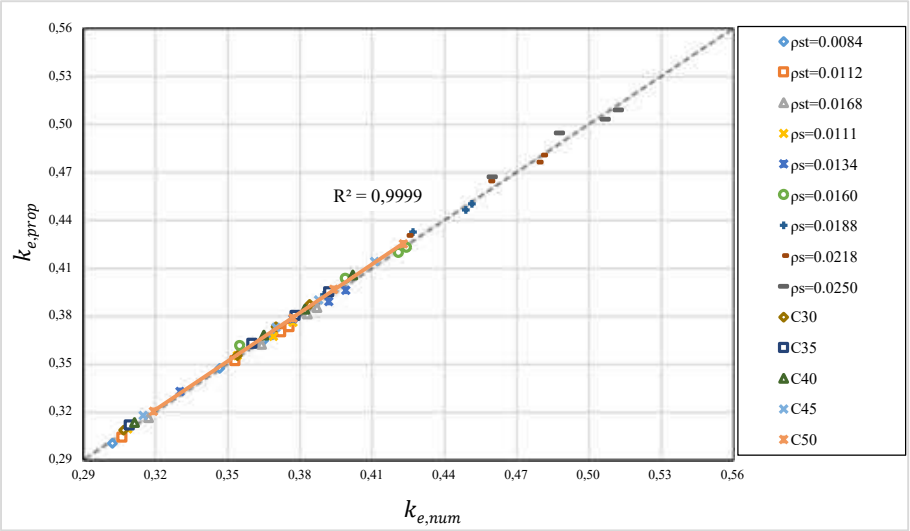


Figure 10. The comparison of $k_{,}$ $-$ $k_{,}$ relations according to different design parameters for circular columns

The coefficients correlation R^2 is substantially over 0.99, indicating high agreement between the provided predictions for circular columns. Additionally, the ratio of the suggested effective stiffness factor, which was determined by Equation (7), to the numerical result has a maximum mean value of %1.012 and a standard deviation of %2.282.

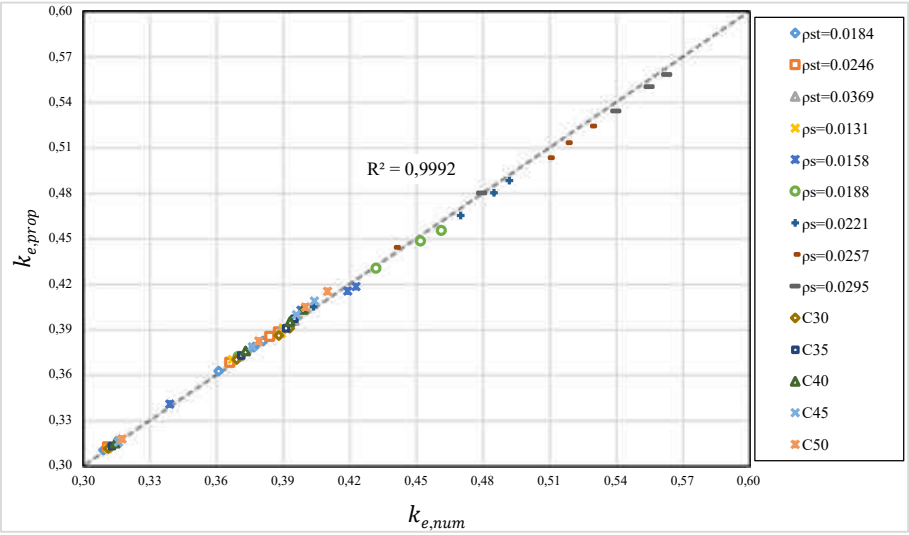


Figure 11. The comparison of $k_{,}$ $-$ $k_{,}$ relations according to different design parameters for rectangular columns

The coefficient correlation R^2 is substantially over 0.99, indicating high agreement between the provided predictions for rectangular columns. Additionally, the ratio of the suggested effective stiffness factor, which was determined by Equation (8), to the numerical result has a maximum mean value of %1.063 and a standard deviation of %5.959%, respectively.

The shape and dimensions of the cross-section of a RC column have a direct and critical impact on its bending stiffness, which is defined as the product of the modulus of elasticity of the material and the

moment of inertia of the cross-section (EI). Among these, the dimensions, particularly the height in the direction of bending, play the most significant role, as the moment of inertia for rectangular sections increases with the cube of the height ($I = bh\ /12$).

The shape of the cross-section determines how stiffness is distributed across different directions. Symmetrical shapes, such as circular or square sections, offer uniform stiffness in all directions and are therefore better suited for multidirectional loading, such as seismic forces. In contrast, rectangular sections provide greater stiffness along their longer axis and reduced stiffness along the shorter axis. Using asymmetrical or slender sections may lead to reduced effective stiffness, increased lateral displacements, and decreased structural stability. Consequently, in seismic and structural design, the shape and size of the cross-section must be carefully selected to ensure not only adequate resistance but also an optimal distribution of stiffness to withstand various applied forces. In conclusion, the cross-sectional geometry of RC columns plays a fundamental role in their flexural behaviour. Increasing dimensions, especially in the bending direction—significantly enhances stiffness, while selecting appropriate shapes, particularly symmetric ones, improves overall structural and seismic performance.

In the proposed relationships for the effective stiffness coefficient, the confining effect is not considered as stipulated in the regulations. This oversight implies disregarding the influences of factors such as cross-section dimensions, concrete strength, confining effects, and the axial force acting on the cross-section. Establishing the moment-curvature relationship in the design and assessment of RC elements, as well as deriving effective stiffness values, is crucial for achieving more accurate results. Current codes and prior research have indicated that effective stiffness is frequently articulated concerning the axial load levels present in the columns. The axial loads, concrete strength, and the quantities of longitudinal and transverse reinforcements have been recognised as the primary determinants influencing both the yield point of the cross-section and the effective stiffness of the RC column cross-section. The comparison results illustrate that the effective stiffness values computed using the SAP2000 program (Ver. 21), derived from various regulations, differ from one another. Utilising an effective stiffness value that exceeds the necessary threshold will lead to an overestimation of structural stiffness. Consequently, this will result in complications during the calculation and assessment of structures. The comparison of effective stiffness coefficient values obtained through different regulations and relationships for RC columns designed under varying parameters reveals that the calculated effective stiffness for RC columns increases with a rise in the transverse reinforcement ratio, longitudinal reinforcement ratio, and concrete strength. Furthermore, with the escalation of axial force, the effective stiffness values of concrete have also increased.

In the studies conducted by Avşar et al. and Çağlar et al., the primary focus lies in the development of simplified methodologies for estimating the effective flexural stiffness of RC members. While Çağlar et al. propose empirical formulations tailored to specific column configurations, Avşar et al. extend their approach to a broader range of RC members with varying geometric properties, offering more generalized expressions applicable across different cross-sectional shapes. In contrast, Biskinis and Fardis centre research not solely on the evaluation of flexural stiffness, but rather on the overall structural performance of RC elements and the enhancement of deformation capacity through various retrofitting strategies. Their investigations emphasize aspects such as energy dissipation, ductility improvement, and cyclic response under seismic loading. The present study distinguishes itself by providing the most comprehensive and advanced treatment of nonlinear behaviour among the compared works. Unlike traditional approaches that rely on simplified or linear assumptions, this research explicitly incorporates material nonlinearity and geometric nonlinearity in its modelling framework. It systematically evaluates the effective flexural stiffness of RC columns with varying cross-sectional dimensions and shapes by deriving stiffness values directly from moment-curvature relationships.

According to the proposed equation and various estimation relations, the numerical analysis results for calculating the effective section stiffness of RC and column models were derived differently from one another. The disparity in the results arises from the different parameters considered in the effective section stiffness relations put forth by researchers, alongside the constant coefficients defined in existing

standards and codes. Most relations consider parameters such as the level of axial load and the dimensions of the section. In certain relations, both axial load and the longitudinal reinforcement ratio are considered. However, for RC columns, parameters that influence the behaviour of sections, such as transverse reinforcement, are often overlooked. To achieve more accurate results in the calculation of effective section stiffness, this study focused on the most critical design parameters that affect the behaviour of column models. Consequently, the previously omitted parameters have been incorporated, and a simple equation has been proposed for effective stiffness. It is clear that the suggested equation aligns with the numerical findings across all ranges of parameters.

The comparison of all the numerical results shows the effective section stiffness of the column models. Almost the same result is obtained from the equation proposed with the moment-curvature relations. This new approach to determining the effective flexural stiffness of columns offers significant improvements in accuracy over traditional methods by incorporating non-linear material behaviour and the effects of cracking and plastic deformations. Adopting this methodology in structural design can enhance the reliability and safety of RC structures while optimising material usage and overall cost-efficiency. Further research and development of this approach could refine its application and expand its use to other types of structural elements and materials. The effective flexural stiffness will lie between the values calculated for the uncracked and cracked sections, depending on the applied moment. By following this approach, you can determine the flexural stiffness of RC columns more accurately, accounting for various factors that influence their behaviour.

This study aims to fill a significant gap in existing literature and offers original contributions in several key aspects. Many current methods for determining flexural stiffness are based on the linear elastic behaviour of structural elements or consider nonlinear effects only to a limited extent. In contrast, this study presents an approach grounded directly in nonlinear behaviour, yielding more realistic results, especially for systems with high ductility and members with significant plastic deformation potential. The proposed method derives flexural stiffness from the section-level moment-curvature relationship, allowing material behaviours such as concrete cracking, reinforcement yielding, and concrete cover crushing to be explicitly considered. Consequently, unlike traditional empirical coefficient-based approaches, a more fundamental and physically based modelling framework is established.

The proposed approach provides a simplified calculation framework that can be readily used in engineering practice without requiring complex finite element analyses. In this respect, it offers a practical and computationally efficient alternative for both researchers and design engineers. Through comprehensive parametric analyses, the effects of transverse reinforcement ratio, axial load level, and cross-sectional dimensions on flexural stiffness have been thoroughly investigated. The results are compared with current design code approaches (e.g., ACI, Eurocode) and leading models in the literature, demonstrating that the proposed method has a broader range of applicability. Thus, this study makes a strong contribution to the literature by enhancing the accuracy of flexural stiffness predictions, going beyond existing code provisions, and providing more reliable tools for engineering applications.

5. CONCLUSIONS

Effective section stiffness of column with high ductility level according to different design parameters; a comprehensive parametric study was carried out according to the relations given in the literature, non-linear relations, and the equation obtained from the numerical analysis results. This study proposes effective stiffness factors for use in the design and seismic assessment of ordinary RC square, rectangular and circular column sections. The most important parameters affecting the yield point of the RC column section, as well as the effective stiffness, are geometry and dimension, concrete strength, axial load level, longitudinal and transverse reinforcement were determined. The analysis results are different because different limit values are considered for parameters such as material properties, design parameters, and

longitudinal and transverse reinforcement in studies and regulations in literature. In the analyses made by adhering to the regulations, the stiffness of the section is not realistic behaviour value. In order to determine the stiffness factor of RC structural elements, the stiffness values should be calculated by considering the non-linear behaviour of the carrier elements instead of the factor values defined in the standard and codes.

Conclusion regarding the influence of cross-sectional shape on the flexural stiffness of RC columns: The shape of the cross-section has a direct impact on the moment of inertia (I) and given that the flexural stiffness is defined as EI, the cross-sectional shape is crucial in determining the flexural stiffness of the column. Typically, circular and square columns exhibit equivalent flexural stiffness in all directions (isotropic in bending), making them more appropriate for multidirectional loading scenarios, such as during earthquakes. In contrast, rectangular columns demonstrate non-uniform flexural stiffness; along the major axis (where the section height is greater), the flexural stiffness is elevated. Conversely, along the minor axis, there is a significant reduction in flexural stiffness. The slenderness ratio of the cross-sectional area influences the directional characteristics of stiffness; sections that are very slender or elongated tend to perform inadequately in one direction.

In the context of seismic analysis and structural design, selecting the correct cross-sectional shape can: enhance stability and resistance to buckling, ensure a balanced distribution of stiffness across various directions, and mitigate stress concentration along with undesirable displacements. The configuration of the cross-section is a fundamental element in establishing the flexural stiffness of a RC column. The choice of the appropriate cross-section should be guided by the nature of the loading, the predominant bending direction, and the stability criteria of the structure. Symmetrical cross-sections, such as circular or square shapes, are generally more effective for multidirectional loads, whereas rectangular cross-sections require careful consideration regarding their orientation and design.

The adequacy of the proposed $k_{,}$ are evaluated with $k_{,}$ results obtained from moment-curvature and a parametric study at the element level and compared with other models. The ratios of the results obtained from $k_{,}$ to the numerical results influenced with the changes in N/N , ρ , ρ and f parameters. $k_{,}$ values, which are calculated with the increase of N/N , ρ , ρ and f , also increase. With the equations proposed for the stiffness factor, the stiffness coefficients of square, circular and rectangular cross-section columns can be estimated easily and simply according to different design parameters. For each column section in the study findings and discussion, the maximum mean value and the standard deviation for the ratio of the suggested stiffness factor obtained by the proposed equations to the numerical result are described. It is also seen from the comparison of the analysis results that a more accurate result is obtained since all the parameters that affect the non-linear behaviour of the column sections and form an RC section are considered. Thus, in the analysis of RC structures, the stiffness factor can be calculated according to the design parameters of the column sections, and most importantly, for different section geometries, instead of the constant coefficients given in the regulations.

Declaration of Ethical Standards

The authors declare to comply with all ethical guidelines, including authorship, citation, data reporting, and original research publication.

Credit Authorship Contribution Statement

The authors declare that they have made equal contributions.

Declaration of Competing Interest

The authors declare that there are no declarations of interest.

Funding / Acknowledgements

I declare that no funding or research grants are received for this study or for the preparation of the manuscript.

Data Availability

The data obtained from this study are available from the corresponding author upon reasonable request.

Use of Artificial Intelligence

The authors confirm that no generative AI or AI-assisted technologies were used in the writing of this manuscript or in the production of the data/images presented. All scientific decisions and conclusions belong entirely to the author.

REFERENCES

[1] J.R. Pique, and M. Burgos, "Effective rigidity of reinforced concrete elements in seismic analysis and design," The 14th World Conference on Earthquake Engineering, 12-17 October, Beijing, China, 2008.

[2] N. Kumbasar, "Flexural stiffness of reinforced concrete sections," Teknik Dergi, vol. 2, no. 4, pp. 7265-7278, 2015.

[3] K. Darılmaz, "Depreme dayanıklı binaların tasarımına giriş", Birsen Yayınevi. ISBN: 3990000031088, 2019.

[4] Z. Celep, "Betonarme taşıyıcı sistemlerde doğrusal olmayan davranış ve çözümleme-deprem yönetmeliği 2007 kavramları," Beta Basım Yayım. ISBN: 9789752957145. 2017.

[5] N. Çağlar, A. Demir, H. Ozturk, and A. Akkaya, "A simple formulation for effective flexural stiffness of circular reinforced concrete columns," Engineering Applications of Artificial Intelligence, vol. 38, pp. 79-87, 2015.

[6] S. Foroughi, and S. B. Yüksel, "Deformation based damage limits of the ductile reinforced concrete shear walls," Journal of Advanced Research in Natural and Applied Sciences, vol. 7, no. 2, pp. 244-255, 2021a.

[7] S. Foroughi, and S. B. Yüksel, "Effective flexural stiffness for reinforced concrete shear walls having confined boundary elements," Journal of Structural Engineering & Applied Mechanics, vol. 4, no. 2, pp. 126-139, 2021b.

[8] S. Foroughi, and S. B. Yüksel, "Investigation of moment-curvature and effective section stiffness of reinforced concrete columns," Challenge Journal of Structural Mechanics, vol. 7, no. 3, pp. 135-150, 2021c.

[9] Ç. Çırak, "Evaluation of seismic performance of existing buildings obtained from rapid and detailed performance assessment methods," MSC Thesis, Pamukkale University Institute of Science Civil Engineering, Turkey, pp. 1-146, 2016.

[10] S. S. F. Mehanny, H. Kuramoto and G. G. Deierlein, "Stiffness modelling of RC beam-columns for frame analysis," ACI Structural Journal, vol. 98, no. 2, 215-225, 2001.

[11] T. B. Panagiotakos, and M.N. Fardis, "Deformations of reinforced concrete elements at yielding and ultimate," ACI Structural Journal, vol. 98, no. 2, pp. 135-148, 2001.

[12] M. Khuntia, and S.K. Ghosh, "Flexural stiffness of reinforced concrete columns and beams: analytical approach," ACI Structural Journal, vol 101, no. 3, pp. 351-363, 2004.

[13] K. J. Elwood, and M. O. Eberhard, "Effective stiffness of reinforced concrete columns", ACI

Structural Journal, vol. 106, no. 4, pp. 476-484, 2009.
[14] M. P. Berry, and M. O. Eberhard, "Performance modelling strategies for modern reinforced concrete bridge column," Pacific Earthquake Engineering Research Centre, Peer 2007/7, Berkeley.
[15] R. Kumar, and Y. Singh, "Stiffness of reinforced concrete frame elements for seismic analysis," ACI Structural Journal, vol. 107, no. 5, pp. 607-615, 2010.
[16] J. L. Bonet, M. L. Romero, and P. E. Miguel, "Effective flexural stiffness of slender reinforced concrete columns under axial forces and biaxial flexural," Engineering Structures, vol. 33, no. 3, pp. 881-893, 2011.
[17] C. T. N. Tran, and B. Li, "Initial stiffness of concrete columns with moderate aspect ratios," Advances in Structural Engineering, vol. 15, no. 2, pp. 265-276, 2012.
[18] Ö. Avşar, B. Bayhan, and A. Yakut, "Effective flexural rigidities for ordinary reinforced concrete columns and beams," The Structural Design of Tall and Special Buildings, vol. 23, pp. 463-482, 2014.
[19] Lan, S., Liu, Y., Mao, D. et al. Experimental and theoretical study on flexural rigidity reduction of reinforced concrete eccentric column. Sci Rep, vol. 15, 29268. 2025.
[20] Y. Elmezayen, N. Khattak, & T. El-Maaddawy, "Prediction of Nonlinear Flexural Behavior of Continuous RC Beams Pre-Damaged by Corrosion". Buildings, vol. 13, pp. 6, 1398., 2023
[21] S. Faghirnejad, N. Kontoni & M. R. Ghasemi, "Performance-based optimization of 2D reinforced concrete wall-frames using pushover analysis and ABC optimization algorithm,"Earthquakes and Structures, vol. 27, pp. 285-302, 2024
[22] ASCE Standard, 41, "Seismic evaluation and retrofit of existing buildings, (ASCE/SEI 41-17)," Published by The American Society of Civil Engineers, Reston, Virginia, p. 20191-4382, USA, 2017.
[23] ACI318, "Building code requirements for reinforced concrete and commentary," American Concrete Institute Committee, ISBN: 978-0-87031-930-3. 2019.
[24] TBEC, "Turkish building earthquake code: Specifications for building design under earthquake effects," T.C. Bayındırlık ve İskan Bakanlığı, Ankara, 2018
[25] Eurocode8, CEN, "Design of structures for earthquake resistance: Part 3: Assessment and retrofitting of buildings," BS EN 1998-3, 2005.
[26] Eurocode8, "Design of structures for earthquake resistance: Part 1: General rules, seismic actions and rules for buildings," BS EN 1998-1:2004, 2004.
[27] Eurocode 2, "Design of concrete structures: Part 1-1: General rules and rules for buildings," BS EN 1992-1-1:2004, 2004.
[28] D. E. Biskinis, "Resistance and deformation capacity of concrete elements with or without retrofitting," Doctoral Thesis, Civil Engineering Department, University of Patras, Greece, pp. 1-528, 2007.
[29] D. E. Biskinis, and M. N. Fardis, "Cyclic strength and deformation capacity of RC elements, including elements retrofitted for earthquake resistance," In: Walraven J et al. (ed) 5th International Ph.D. Symposium in Civil Engineering, Balkema, Rotterdam, pp. 1125-1133, 2004.
[30] J. M. Wong, A. Sommer, K. Briggs, and C. Ergin, "Effective stiffness for modelling reinforced concrete structures: a literature review," Structure Magazine, pp. 18-21, 2017.
[31] F. Micelli, L. Candido, M. Leone, and A. A. Maria, "Effective stiffness in regular R/C frames subjected to seismic loads," Earthquakes and Structures, vol. 9, no. 3, pp. 481-501, 2015.
[32] A. Doğangün, "Design and calculation of reinforced concrete structures," Birsen Press, Istanbul (978-975-511-310-X), 2013.
[33] J. B., Mander, M. J. N. Priestley, and R. Park, "Theoretical stress-strain model for confined concrete", Journal of Structural Engineering, vol. 114, no. 8, pp. 1804-1826, 1988.
[34] SAP2000. Structural software for analysis and design, computers and structures, Ver. 21. Inc, USA.

Konya Mühendislik Bilimleri Dergisi., c.14, s.2,568-585, 2026
Konya Journal of Engineering Sciences v.14, n.2, 568-585, 2026
ISSN: 2667-8055 (Electronic)
DOI: 10.36306/konjes.1766749

SOLID WASTE TO ENERGY: A TECHNICAL AND ECONOMIC STUDY FOR INTEGRATED ENERGY PRODUCTION – THE CASE OF HAKKARI, TÜRKİYE

[1]Bahattin Yakış, [2]Yunus Çelik, [3,*]Yakup Karakoyun

[1]*Department of Mechanical Engineering, Engineering Faculty, Hakkari University, Hakkari 30000, Türkiye*
[2]*Department of Aeronautical Engineering, Faculty of Engineering and Natural Sciences, Sivas University of Science and Technology, Sivas 58000, Türkiye*
[3]*Department of Mechanical Engineering, Engineering Faculty, Van Yüzüncü Yıl University, Van 65080, Türkiye*
[1]bahattinyakis@hakkari.edu.tr, [2]yunus.celik@sivas.edu.tr, [3]yakupkarakoyun@yyu.edu.tr

Highlights

- First complete technical-economic waste-to-energy evaluation for studied province.
- LandGEM used local demographic and waste data to forecast 2050 gas emissions.
- The electricity potential from landfill gas is projected from 0.16 MW to 3.64 MW.
- Results inspire the application of Waste-to-Energy for renewable energy benefits.

***Corresponding Author:** Yakup KARAKOYUN, yakupkarakoyun@yyu.edu.tr

Konya Mühendislik Bilimleri Dergisi., c.14, s.2, 568-585, 2026
Konya Journal of Engineering Sciences v.14, n.2, 568-585, 2026
ISSN: 2667-8055 (Electronic)
DOI: 10.36306/konjes.1766749

SOLID WASTE TO ENERGY: A TECHNICAL AND ECONOMIC STUDY FOR INTEGRATED ENERGY PRODUCTION – THE CASE OF HAKKARI, TÜRKİYE

[1]Bahattin Yakış, [2]Yunus Çelik, [3,] *Yakup Karakoyun

[1]Department of Mechanical Engineering, Engineering Faculty, Hakkari University, Hakkari 30000, Türkiye
[2]Department of Aeronautical Engineering, Faculty of Engineering and Natural Sciences, Sivas University of Science and Technology, Sivas 58000, Türkiye
[3]Department of Mechanical Engineering, Engineering Faculty, Van Yüzüncü Yıl University, Van 65080, Türkiye
[1]bahattinyakis@hakkari.edu.tr, [2]yunus.celik@sivas.edu.tr, [3]yakupkarakoyun@yyu.edu.tr

(Received: 15.08.2025; Accepted in Revised Form: 31.10.2025)

ABSTRACT: This study evaluates waste management practices globally and in Türkiye, with a focus on energy recovery and production. The study includes calculations of solid waste production in Hakkari, the potential volume of landfill gas that can be produced at the facility, and the expected amount of gas that can be recovered for energy purposes. Hakkari's future population was estimated using the Provincial Bank method, and annual waste production was obtained based on daily averages per capita from this method. The LandGEM model was used to estimate landfill gas production. Subsequently, the potential electricity production that could be obtained from the internal combustion of the recovered gas was calculated. The analysis also presents the distribution of cost components for the energy production facility. According to LandGEM model estimates, landfill gas production is expected to increase from approximately 974527 m³/year in 2024 to 21360099 m³/year in 2050. This gas could support power generation capacity increasing from 0.16 MW in 2024 to 3.64 MW by 2050 using internal combustion engines. The findings demonstrate that the installation of such system is technically feasible and can play an important role in reducing greenhouse gas emissions and support Türkiye's energy targets and waste management policies.

Keywords: *Solid Waste, Waste-to-Energy, Energy Recovery, Waste Management*

1. INTRODUCTION

Worldwide population growth and rapid urbanization have significantly increased solid waste production [1]. Industrialization and rising consumption have worsened environmental concerns. These developments have led to serious environmental, health, and economic issues. As a result, waste is no longer viewed solely as a problem, but as a resource to be managed through sustainable techniques. In the past, waste disposal methods were limited and often relied on uncontrolled dumping. Advances in technology now allow more efficient and environmentally friendly disposal practices. The detrimental impacts of climate change, such as elevated temperatures, droughts, and wildfires, have become increasingly apparent, intensified by the use of fossil fuels. This global dilemma requires collaborative initiatives to shift to renewable energy and enhance energy efficiency. Recent predictions indicate that renewable energy will account for 43% of global energy production by 2040. Mitigating greenhouse gas emissions, achieving energy autonomy, and safeguarding ecosystems have emerged as prevalent national priorities. Consequently, nations are expediting investments in renewable energy infrastructures. The International Energy Agency (IEA) asserts in its 2022 report that the ongoing global energy crisis reinforces the strategic transition to renewable energy sources.

In Türkiye, population growth has paralleled a rise in energy demand. Decreasing reliance on external

***Corresponding Author:** Yakup KARAKOYUN, yakupkarakoyun@yyu.edu.tr

energy sources and diversifying the national energy portfolio are therefore critical. Shifting toward renewable energy, particularly by reducing fossil fuel use, not only enhances sustainability but also stimulates economic growth [5]. According to the Energy Market Regulatory Authority (EMRA), Türkiye's energy production from biomass and solar increased in 2023, whereas outputs from hydroelectric, geothermal, and wind sources declined, as shown in Figure 1. The notable decline in hydroelectric power generation was attributed to drought and high production costs, necessitating energy supplementation from other sources.

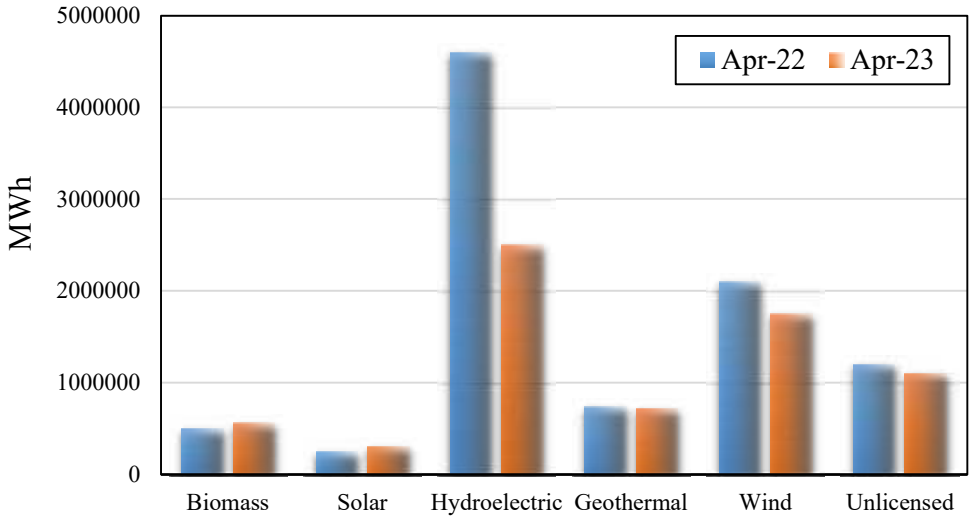


Figure 1. Distribution and comparison of electricity generation by source in April 2022 and April 2023 [6]

Solid waste includes all materials discarded from domestic, industrial, commercial, or agricultural activities, regardless of their potential value. Improper disposal can pollute soil and water, release toxic substances into the food chain, and cause severe air pollution. This leads to health risks such as respiratory problems and the spread of disease, as well as environmental hazards like fires and aesthetic damage [8]. In Türkiye, approximately 32.2 million tonnes of municipal waste were collected, with 67.2% sent to regulated landfills, 20.2% to municipal dumps, 12.3% to recycling centres, and only 0.2% disposed of through open dumping or burning [9]. By 2020, the share sent to landfills rose to 69.4%, with slight increases in recycling and controlled disposal rates. Daily waste generation per person is about 1.13 kg [10].

Worldwide, many technologies are used to manage and recover energy from waste, including physical, chemical, and biological processes. Methane recovery from biological decomposition is particularly important because methane is a valuable fuel for energy production. Common technologies include internal combustion engines (ICEs), gas turbines, and direct incineration. Recent studies focus on optimizing systems to capture and use methane efficiently.

Sezgin et al. [11] demonstrated the feasibility of generating electricity from landfill gas, citing significant outputs from Istanbul and Bursa facilities. Saltabaş and Yalçın [12] highlighted that widespread adoption of such facilities could reduce environmental damage and bolster economic growth. Güven [13] pointed out that landfill methane is 23 times more potent than CO_2 in causing global warming, underscoring the environmental necessity of its capture and conversion into energy. Regional studies indicate that landfill gas recovery could meet 1.6% of Kütahya's and 5% of Manisa's household energy demands. Öztürk and Özgüven [14] assessed the methane content in landfill gas from Van province and estimated monthly energy production between 2000–3000 kWh. A power plant established in 2019 now provides electricity to 5000 households. Ahmed [15] evaluated the energy potential of municipal solid waste (MSW) in Texas using different calorimetric and thermochemical models, finding that over half of the initial energy value was preserved post-extraction. Istrate et al. [16] analysed waste-to-energy (WtE)

strategies in Madrid and argued for reducing landfill dependency to 10% by 2035, advocating for expanded incineration with energy recovery, despite its limited prominence in European Union (EU) waste policy. Today, roughly 27% of EU waste is incinerated for energy. Zhang et al. [17] investigated the recycling of solid waste into materials for energy storage systems such as lithium-ion batteries, identifying solid waste as a raw material source in this emerging field. Fernández-Gonzalez et al. [18] examined the economic and environmental factors affecting WtE implementation in Granada, Spain. Technologies such as anaerobic digestion, SRF production, gasification, and biogas recovery were evaluated using Life Cycle Assessment (LCA), which measured emissions, energy output, and material consumption across treatment strategies. Zhao et al. [19] supported WtE approaches in China, analysing their cost-effectiveness and potential for emission reduction. They found incineration to be the most efficient among evaluated methods. Tolay and Waterschoot [20] examined biomass gasification in Türkiye, utilizing agricultural and forest leftovers, including corn, wheat, and olive trees, to generate syngas for electricity and heat production. They performed feasibility evaluations considering various plant capacities and fuel sources. Baran [21] utilized statistical modeling and forecasting methodologies, incorporating MATLAB and LandGEM, to assess the energy potential of landfill gas in Türkiye. His findings indicated that power generation from methane might attain 2155.55 GWh annually by 2025.

Recent research has substantially advanced the understanding of municipal solid waste forecasting and energy recovery in Türkiye. A study developed advanced forecasting models to predict future MSW generation and evaluated the potential for energy recovery through incineration technologies in Türkiye [39]. The findings show that Türkiye's municipal solid waste generation could reach 36.2 million tonnes by 2032, and its incineration could yield up to 16.8 TWh of electricity, representing an economic value of approximately 2.1 billion USD based on June 2024 wholesale industrial prices. Similarly, another recent work has examined the long-term climate implications of landfill gas emissions, distinguishing between 20-year and 100-year global warming potential horizons and underscoring the importance of methane capture for near- and mid-term mitigation strategies [40]. Collectively, these studies highlight both the urgency and the potential benefits of integrating methane capture and energy conversion into modern waste management systems. Building on this body of research, the present study provides a region-specific contribution by (i) projecting landfill gas production using the LandGEM model, (ii) estimating the electricity generation potential from captured gas, and (iii) quantifying the associated economic benefits and avoided CO_2 emissions for Hakkari Province, Türkiye, thus offering a comprehensive and localized case study.

The literature emphasizes the necessity of precisely predicting municipal solid waste and landfill gas production for environmental and energy planning. Accurate forecasts facilitate the mitigation of greenhouse gas emissions and adaptation to climate-related concerns, while simultaneously enhancing energy security and economic resilience. The extraction of energy from landfill gas promotes sustainable waste management and reduces dependence on imported energy. The literature indicates that precise forecasting of municipal solid waste and landfill gas generation is essential due to its direct impact on environmental conservation and energy security. Accurate estimation of landfill gas output can substantially reduce detrimental greenhouse gas emissions, thereby positively influencing worldwide initiatives to alleviate climate change effects, including drought, rising temperatures, and wildfires. Furthermore, transforming landfill gas into energy offers a sustainable approach to waste management while reducing reliance on foreign energy sources, thereby strengthening energy diversification measures that promote economic stability. Therefore, reliable predictions of waste and gas production constitute a foundational element for effective waste management practices and sustainable energy planning. For this purpose, the present study aims to examine the landfill gas production from municipal solid waste in a sanitary landfill site in Hakkari Province by estimating the gas quantity using the LandGEM mathematical model developed by the United States Environmental Protection Agency (USEPA). Additionally, population projections for Hakkari Province were performed to calculate the annual total solid waste generated based on per capita waste generation rates. Subsequently, the potential for electricity generation from the predicted landfill gas through internal combustion engines was calculated. Finally, an economic

analysis, including installation costs, was conducted to assess the feasibility and environmental benefits of implementing this energy recovery system.

2. MATERIAL AND METHODS

2.1. Hakkari Province and Its Energy Profile

Hakkari Province is located between 42°10' and 44°50' east longitudes and 36°57' and 37°48' north latitudes. Figure 2 shows the location of the Hakkari Province and landfill site. Hakkari covers an area of 7228 km², constituting approximately 0.92% of Türkiye's territory. It is bordered by Van Province to the north, Iraq to the south, Iran to the east, and Şırnak Province to the west. Hakkari is situated on the southern slope of the deep and long Zap Valley in the southeastern corner of Türkiye and is surrounded by mountains. Following mountainous terrain, plateaus represent the second most prominent landform in the province, covering 10.3% of the area. The average elevation above sea level is approximately 1,720 meters. Plains stretching between mountainous regions and along river valleys constitute 2.1% of the province's total area [22].

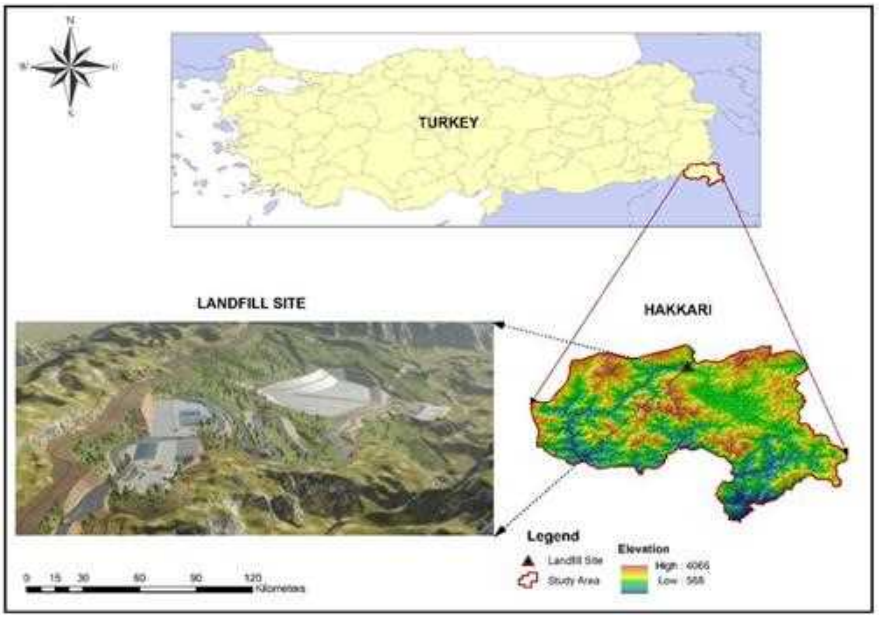


Figure 2. Map of Hakkari Province and location of landfill site

According to the 2022 data from the Address-Based Population Registration System of the Turkish Statistical Institute (TURKSTAT), the total population of Hakkari is 277333. As shown in Figure 3, while a steady population increase was observed in Hakkari between the years 2007 and 2012, the period from 2013 to 2022 exhibited a fluctuating trend with alternating increases and decreases.

As an overview of the energy profile of Hakkari Province, as of January 2023, Hakkari has an installed licensed electricity generation capacity of 58.17 MW, accounting for 0.06% of Türkiye's total installed capacity. During the same period, Hakkari's share in the national licensed electricity production amounted to 3103.91 MWh, representing 0.01% of Türkiye's total production. In addition, unlicensed electricity production in the province was recorded as 7.01 MWh [23]. As shown in Table 1, an analysis of the sectoral distribution of electricity consumption in Hakkari reveals that residential use accounts for the largest share, followed respectively by industry, lighting, agricultural irrigation, and commercial enterprises. The total electricity consumption across these sectors in Hakkari is approximately 286191.3 MWh, which corresponds to 0.11% of total national consumption [24]. Based on this table, it can be inferred that population and industrial activity play a significant role in electricity consumption in the province.

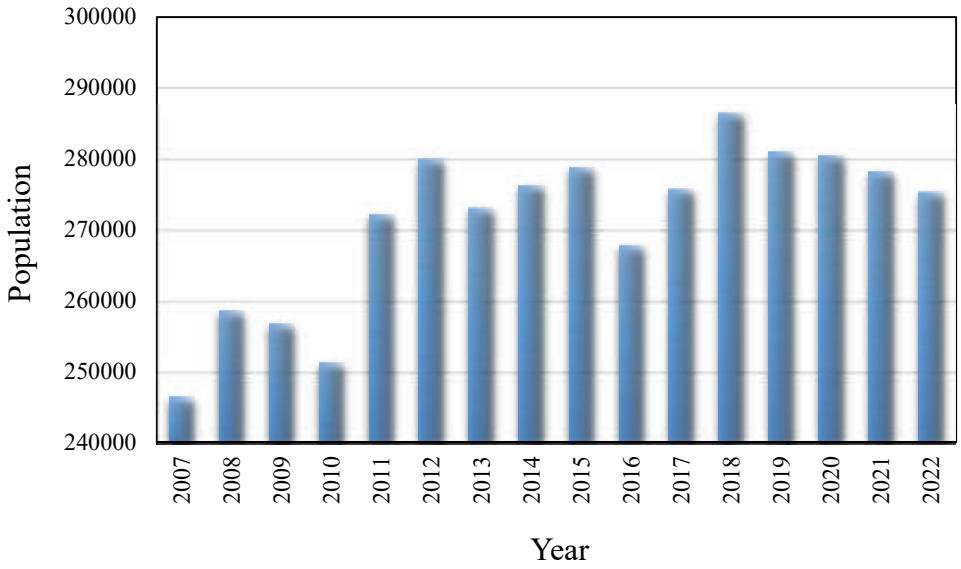


Figure 3. The variation of population of studied province

In order to increase the amount of energy produced from renewable energy sources in Türkiye, various initiatives are being implemented across all provinces. Factors such as the geological and geographical structure, climate, and underground resource potential of each province play a role in enhancing the efficiency of local energy sources. In the case of Hakkari, the lack of significant air flow makes wind energy inefficient. However, due to the province being among those with the highest annual total solar radiation per square meter, solar energy is considered a promising renewable source. Additionally, the presence of rivers with significant elevation differences provides favourable conditions for hydroelectric power generation [25].

Table 1. Distribution of Billed Electricity Consumption in Hakkari Province by Consumer Type in 2022 (MWh) [24]

Consumer Type	Consumption (MWh)
Lighting	16218
Residential	128811
Agricultural Irrigation	100
Public and Private Services Sector	5.07
Total Consumption	286191

2.2. Solid Waste Management in Hakkari Province

In Hakkari Province, waste collection is carried out by municipalities and the provincial special administration. Approximately 67% of the total waste is collected from the city of Hakkari and the district of Yüksekova. The currently active uncontrolled waste disposal sites in the province are planned to be rehabilitated in situ. Rehabilitation work on the dumping sites in Hakkari and Yüksekova is near completion. Waste from the irregular disposal areas in Çukurca, Şemdinli, Derecik, and Esendere will be transferred to rehabilitated landfill facilities. A new solid waste storage facility, currently under construction, is expected to become operational in 2024.

Due to the lack of proper disposal infrastructure, waste is often dumped haphazardly into wild disposal sites, stream beds, or vacant lands. Consequently, it is difficult to obtain reliable statistical data on solid waste in the region. Since natural gas infrastructure has not yet been extended beyond the city center, and solid fuels are still commonly used for heating in the districts, the volume of waste increases significantly during the winter months. A large portion of this increase is due to ash generated from solid

fuel combustion. The estimated values of solid waste composition for Yüksekova and Hakkari municipalities are presented in Figures 4 and Figure 5. In Figure 4 [26], the approximate waste composition values provided by Yüksekova Municipality indicate a high proportion of ash following kitchen and other waste, which is attributed to the widespread use of solid fuels. It is expected that this proportion will decrease gradually as natural gas usage becomes more prevalent in Yüksekova. The solid waste composition collected by the Hakkari Municipality is presented in Figure 5 [27]. Compared to Yüksekova district, the lower proportion of ash can be attributed to the introduction of natural gas usage in the provincial center. Upon examining Figures 4 and Figure 5, it is evident that kitchen waste constitutes the largest share of total waste types across the province.

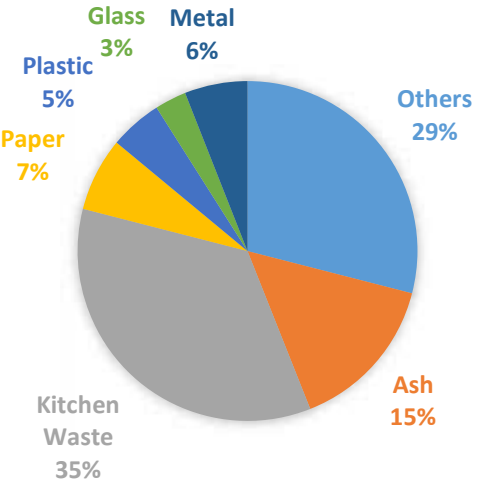


Figure 4. 2022 Solid Waste Composition of Yüksekova Municipality [26]

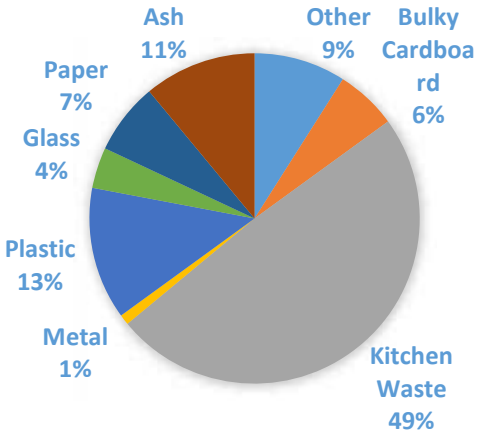


Figure 5. 2019 Solid Waste Composition of Hakkari Municipality [27]

If the solid waste landfill site in Hakkari Province is examined, it has been designed in accordance with both Turkish national legislation and the European Union acquis and is classified as a Lot 2 second-class sanitary landfill facility. To address the solid waste management issues in the province, the municipalities and the Provincial Special Administration, operating under the Solid Waste Union, initially prepared a project introduction file for an Environmental Impact Assessment (EIA). This file was submitted to the Provincial Directorate of Environment and Urbanization, which concluded that an EIA

was not required. However, the Delegation of the EU to Türkiye deemed the documentation insufficient and recommended the preparation of a full EIA report. As a result, a new EIA report was developed in compliance with the updated EIA legislation. The project's feasibility report was subsequently revised by the Ministry and officially approved in 2018.The financing of the project is composed of 85% EU funding, 6.75% grant from the Ministry of Environment and Urbanization, and 8.25% credit from İlbank. The project is expected to become operational in 2024, serving both urban and rural areas. Currently, waste is being disposed of in uncontrolled dump sites, vacant lands, or stream beds, causing significant environmental harm. With the commissioning of the sanitary landfill site, a comprehensive solution to waste disposal is anticipated. The construction of the facility complies with Law No. 2872 on Environment and relevant regulations, taking into consideration factors such as prevailing wind direction, storage capacity, seismicity, risk of floods, avalanches, and landslides. Accordingly, it is being built in a remote area far from residential settlements [28].

The facility is under construction in Beyaztaş locality of Akçalı Village, within the boundaries of Hakkari Province. The project area covers 43.4 hectares and is located 1.5 km from the nearest settlement, Akçalı Village. Second-class sanitary landfill cells will be installed over 16.6 hectares. The remaining area is allocated for fixed facilities including guard stations, weighbridges, administrative buildings, wheel washing units, a workshop building, leachate balancing pond, composting facility, mechanical sorting unit, and medical waste sterilization facilities. Additionally, part of the area has been designated for internal roads and a health protection buffer zone [29]. As part of the European Union's Instrument for Pre-Accession Assistance (IPA), which supports countries in the process of joining the EU, the project was developed under the tender titled "Technical Assistance for the Preparation of Integrated Solid Waste Management Projects – Lot 2" [29]. The facility is designed for the disposal of waste collected by the member municipalities of the Hakkari Solid Waste Union. General information about the facility is provided in Table 2. The landfill site is scheduled to become operational in 2024 and is expected to serve the region for 28 years.

Table 2. Characteristics of the Hakkari storage site [29]

Feature	Specification
Total Capacity of Landfill Cells	3200000 m³
Mechanical Sorting Facility Capacity	9500 tonnes/year
Composting Facility Capacity	13000 tonnes/year
Medical Waste Sterilization Capacity	0.25 tonnes/hour
Leachate and Wastewater Treatment Capacity	200 m³/day
Operational Lifespan of the Facility	28 years

2.3. Population Growth Projection for Hakkari Province

In this study, the population projection for future years was carried out using the

Ilbank method, a commonly applied projection approach in Türkiye. The population growth coefficient, denoted as "c" and derived from the average of past population growth rates, is calculated using the following formula:

$$c = \left(\frac{N}{N} - 1 \right) \times 100 \quad (1)$$

Where:

- c : Population growth coefficient
- N : Most recent population values

- N : Initial population value
- a : Number of years between the base and most recent population data [29]

If the values calculated for c are close to each other, their average is used:

$$c = \frac{c + \cdots + c}{n} \quad (2)$$

According to the methodology:

- If $c < 1$, the coefficient is taken as 1.
- If $1 \leq c \leq 3$, the calculated value is used directly.
- If $c > 3$, then either the value is limited to 3 or adjusted based on settlement-specific characteristics [30].

The projected future population N is then calculated with the following equation:

$$N = N \quad 1 + — \quad (3)$$

Where:

- n : Number of years between the most recent data and the target year [29]

Based on the population data from 2007 to 2022, the population growth coefficient (c) was calculated as 0.741 using the Ilbank formula. Since this value is less than 1, it was rounded up to 1 in the subsequent calculations.

2.4. Estimation of Solid Waste Quantity and Landfill Gas Generation in Hakkari Province

With the establishment of a solid waste management system by the municipalities affiliated with the Hakkari Province Solid Waste Union, Municipal Solid Waste (MSW) will be systematically collected and transferred to a designated landfill site. Waste will be accumulated in streets and public collection bins, then transported from central collection points to the landfill. Once the Solid Waste Management (SWM) system is fully operational, the volume of waste transferred to the site will become more precisely quantifiable [29]. As of the initial construction phase, Lot 1 of the landfill has been completed. Lot 2 is scheduled for commissioning in 2028, followed by Lot 3 in 2035. By the year 2045, the combined capacity of all three lots will reach approximately 3.1 million m^3 of storage volume [29].

The total solid waste generation in Hakkari Province has been estimated based on both urban and rural population data. According to project projections, the average per capita solid waste generation in urban areas is 0.85 kg/day in 2023, rising to 0.94 kg/day by 2050. In rural areas, the corresponding values are 0.47 kg/day in 2023 and 0.49 kg/day in 2050. These figures form the basis for estimating future total waste volumes for planning purposes. In parallel with waste volume estimation, the potential generation of landfill gas has also been analysed. Although mathematical modelling methods are often employed to predict landfill gas emissions, direct measurement via test wells remains the most reliable approach [31]. However, in the case of the Hakkari landfill site, the amount of gas to be generated has been calculated using the LandGEM, developed by the USEPA, version 3.02.

LandGEM is a numerical model used to estimate methane and other gas emissions from landfill sites. Initially implemented in the United States, it has since proven applicable globally and has demonstrated its reliability as a consistent method for estimating landfill gas emissions [32]. The model uses two standardized emission factor inventories, Clean Air Act (CAA) and Air Pollutant Emission Factors (AP–42), which are employed particularly in scenarios where site-specific data are limited or unavailable [33]. The application of this model enables authorities to plan for gas capture systems,

environmental mitigation, and potential energy recovery strategies as part of a long-term integrated waste management solution for Hakkari Province.

$$Q = \sum \sum . kL — e \quad (4)$$

Where:

- Q Annual methane (CH_4) generation in the calculation year (m^3/year),
- L Methane generation potential (m^3/Mg)
- i Time increment in years (1-year interval),
- n Difference between the calculation year and the initial year of waste acceptance,
- j Sub-interval within a year (0.1-year increment),
- k Methane generation rate constant ($year^{-1}$),
- M Mass of waste accepted in year i (Mg),
- t Age of the portion j of the mass M accepted in year I [34].

By entering the required input parameters into the user input section of the LandGEM model, the emissions that degrade air quality can be automatically estimated. In this study, solid waste data from Hakkari Province for the years 2023 to 2050 were entered into the model to estimate gas emissions. To compute emissions from the landfill using the LandGEM model, two primary parameters must be defined: k (methane generation rate) and L (methane generation potential). These parameters can be either selected from standard values provided by the CAA and AP–42 inventories or manually entered. The k value can be determined based on meteorological data specific to the region, such as annual precipitation. As the L value varies according to the waste type, and due to a lack of sufficient site-specific waste composition data, a default standard values presented in Table 3 were utilized.. The parameters selected for precipitation amount (P) according to the AP–42 and CAA inventories in the LandGEM model are presented in Table 4.

Table 3. Default k and L_0 Values for the LandGEM Model According to CAA and AP–42 Inventories [35]

Inventory Type	Landfill Type	k ($year^{-1}$)	L_0 (m^3/Mg)
CAA	Conventional	0.05 (default)	170 (default)
CAA	Arid Region	0.02	170
AP–42	Conventional	0.04	100
AP–42	Arid Region	0.02	100
AP–42	Wet (Bioreactor)	0.7	96

Table 4. Parameters of AP–42 and CAA based on precipitation amount [35]

Parameter	AP–42		CAA	
	P>635mm	P<635mm	P>635mm	P<635mm
$\boldsymbol{k}$ ($year^{-1}$)	0.04	0.02	0.05	0.02
$\boldsymbol{L_0}$ (m^3/ton)	100	100	170	170

If k is the methane generation rate, it can be calculated using the following equation:

$$k = 3.2 \times 10 \times annual\ precipitation\ (mm) + 0.01 \quad (5)$$

According to data from the Turkish State Meteorological Service, the average annual precipitation in Hakkari between 1991 and 2020 is 773 mm. Substituting this value into the equation, the k value is obtained as 0.034 year^{-1}. In the LandGEM 3.02 version, for the CAA inventory, the k value of 0.034 year^{-1} and an L_0 value of 170 m^3/Mg were used to estimate the gas generation from the calculated waste quantity for Hakkari Province. One of the technologies used for energy generation from landfill gas is the internal combustion engine, which converts mechanical energy into electrical energy. In this study, the amount of energy that could be generated by combusting the estimated landfill gas in internal combustion engines was determined. The technical specifications of the engines selected for this purpose are presented in Table 5. The volume of gas expected to be obtained from the solid waste transferred to the Hakkari sanitary landfill site, which is scheduled to become operational in 2024, was estimated using the LandGEM model.

Table 5. Technical Specifications of Internal Combustion Engines [36]

General Specifications	**JGS 320**	**JGS 420**
Manufacturer	GE Jenbacher	GE Jenbacher
Number of Cylinders	20	20
Average Piston Speed	8.5 m/s	9.25 m/s
Electrical Efficiency	40.2%	42.3%
Generator Efficiency	97.4%	97.4%

The methane (CH_4) content of landfill gas typically ranges between 45% and 60%. In most studies, approximately 50% of the landfill gas generated is assumed to be methane [33]. However, methane content can vary significantly from one facility to another, with values between 60% and 90% reported in the literature [1]. In this study, it is assumed that 75% of the landfill gas is effectively captured, and 50% of this captured gas is methane. The necessary calculations for generating electricity from this methane, via ICE, are presented in sequential steps. These simplified estimations aim to demonstrate the potential for energy recovery through the combustion of methane obtained from municipal solid waste. The calorific value of methane gas (CH_4) is accepted as 39.73 MJ/m^3 [1]. In ICEs, the conversion efficiency from thermal energy to electrical energy is taken as 40%, based on the technical specifications provided in the manufacturer's catalogue. Accordingly, when 1 m^3 of landfill gas per second is used, the thermal energy contributed by the methane content can be calculated as 19.87 MW.

2.5. Determination of Energy Production

If 75% of the 974,527 m^3/year of landfill gas generated in 2024 is collected, a gas recovery of 730,895 m^3/year will be attained. The methane flow rate and energy capacities for 2024 are presented in Table 6.

Table 6. Calculated methane flow and power output from landfill gas for 2024

Specification	**Result**
Methane Flow Rate per Second	$0.0231 m\ /s$
Thermal Power	$460 kW$
Electrical Power	$0.18 MW$

Assuming that the internal combustion engine operates at full capacity throughout the entire year, the total annual energy production is calculated as 1577 MWh/year. If the facility operates at 90% capacity, this generation will be 1402 MWh/year. When the calculations above are repeated for the year 2050, *a*ssuming that 75% of the 21360099 m^3/year of landfill gas produced in 2050 can be recovered, a gas recovery of 16020074 m^3/year would be achieved. The calculated methane flow rate and energy capacities are given in Table 7 for 2050.

Table 7. Calculated methane flow and power output from landfill gas for 2050

Specification	**Result**
Methane Flow Rate per Second	$0.5080 m\ /s$
Thermal Power	$10094 kW$
Electrical Power	$4.04 MW$

Considering the internal combustion engine functions continuously, 24 hours a day and 365 days a year, the total annual energy output is computed to be 35390 MWh/year. Should the facility function at 90% capacity, the annual generation will amount to 31886 MWh.

3. RESULTS AND DISCUSSION

With the world population developing rapidly, the need for energy escalates correspondingly to sustain burgeoning metropolitan regions, industrial growth, and the escalating requirements of everyday human endeavours. A growing population necessitates additional housing, transportation, and other services, all of which are heavily dependent on energy resources. The rise in energy consumption leads to heightened extraction and utilization of natural resources, such as fossil fuels, minerals, and raw materials, hence intensifying environmental challenges. As organizations evolve to meet the demands of a growing population, significant amounts of solid waste are generated, comprising industrial byproducts, packaging materials, and household rubbish, resulting in pollution and environmental degradation. Moreover, as living standards improve and consumer culture proliferates, waste production escalates, placing considerable pressure on landfills, incineration plants, and waste management infrastructures. The improper disposal of solid waste jeopardizes ecosystems and contributes to greenhouse gas emissions, exacerbating climate change. The ongoing cycle of population growth, increasing energy demands, and rising waste generation poses significant environmental challenges that require urgent and sustainable solutions. Without suitable rules, technological advancements, and global cooperation, the pressure on natural resources and waste management systems would continually escalate.

To mitigate these effects, it is imperative to use renewable energy sources, implement efficient waste reduction strategies, and promote environmentally sustainable consumption patterns. Addressing these interconnected issues is essential for ensuring a sustainable future for both present and future generations. This study assessed integrated energy generation throughout the construction phase of the sanitary landfill in Hakkari province. The future population of Hakkari was initially forecasted with an estimating methodology. The annual total waste volume was determined using the daily per capita average of solid waste generation. The estimated volume of landfill gas potentially generated at the sanitary landfill site was evaluated utilizing the LandGEM mathematical model developed by the USEPA. Subsequently, the anticipated volume of gas to be extracted for energy production was calculated. The potential energy generation from burning the recovered gas in internal combustion engines was evaluated based on these calculations.

Figure 6 illustrates the anticipated population growth in Hakkari province over the years, as

calculated using the population projection method. The estimated population of Hakkari in 2023 is 324510, with a projected increase to 410219 by 2050. The data reveals a continuous increase in population over the 27-year period from 2023 to 2050, indicating sustained demographic expansion. Population growth leads to an increase in solid waste output, hence heightening the demand for waste management. If per capita waste creation persists at 1.2 kg daily, total daily waste will escalate from 389.4 tonnes in 2023 to 492.3 tonnes by 2050. This increase directly influences energy production; decomposing waste generates methane-rich gas suitable for electricity generation.

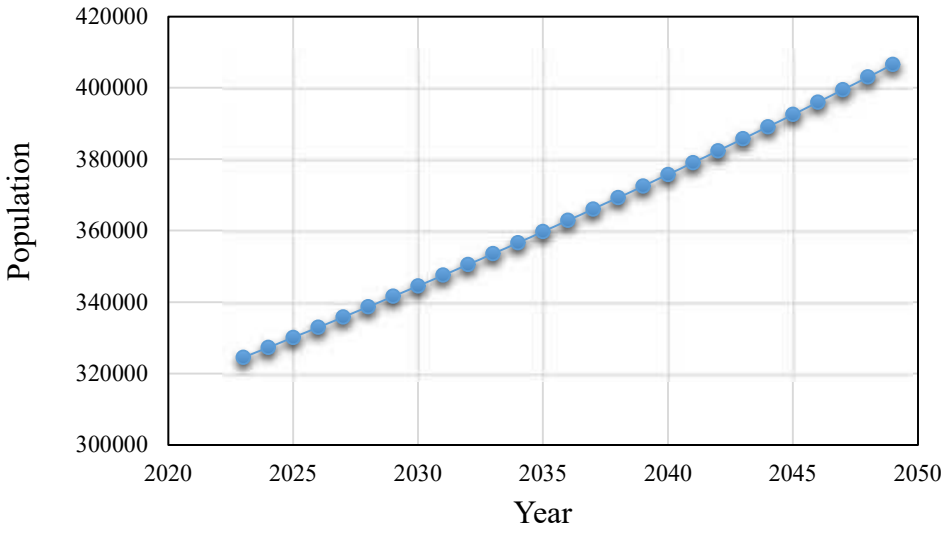


Figure 6. The projected population in Hakkari province for 2023-2050

Table 8 illustrates the projected increase in solid waste generation from 2023 to 2050, encompassing total waste volumes (tonnes yearly) and per capita waste output in urban and rural areas. The data reveals a steady rise in total solid waste, starting at 85597 tonnes in 2023 and increasing to 117381 tonnes by 2050, indicating significant growth over the years. This trend signifies population growth, increased consumption, or a shift in waste generation behaviours. Urban per capita waste generation exhibits a consistent growth, rising from 0.85 kg/day in 2023 to 0.94 kg/day by 2050, whereas rural per capita waste remains relatively stable, with a slight increase from 0.47 kg/day to 0.49 kg/day throughout the same period. The consistency of rural waste production suggests that urbanization plays a substantial role in the overall increase in refuse. The total waste volume persists in its increase, despite the stabilization of per capita waste generation in urban areas at 0.94 kg/day from 2039 onwards, indicating that future rises in waste production may primarily result from demographic changes rather than increased individual consumption. The data underscores the necessity for sustainable waste management strategies, particularly in urban areas, where waste generation is both high and rapidly escalating.

Table 8. Solid waste projection for Hakkari province (2023-2050)

Year	Solid waste (tonnes/ year)	Solid waste per urban person (kg/day)	Solid waste per rural person (kg/day)	Year	Solid waste (tonnes /year)	Solid waste per urban person (kg/day)	Solid waste per rural person (kg/day)
2023	85597	0.85	0.47	**2037**	103735	0.93	0.48
2024	87103	0.86	0.47	**2038**	104615	0.93	0.48
2025	88628	0.87	0.47	**2039**	106397	0.94	0.48

2026	90173	0.88	0.47	**2040**	107302	0.94	0.48
2027	90926	0.88	0.47	**2041**	108216	0.94	0.48
2028	92505	0.89	0.47	**2042**	109139	0.94	0.48
2029	94105	0.90	0.47	**2043**	110071	0.94	0.48
2030	94894	0.90	0.47	**2044**	111012	0.94	0.48
2031	96959	0.91	0.48	**2045**	111963	0.94	0.48
2032	97774	0.91	0.48	**2046**	113422	0.94	0.49
2033	99450	0.92	0.48	**2047**	114397	0.94	0.49
2034	100288	0.92	0.48	**2048**	115382	0.94	0.49
2035	102001	0.93	0.48	**2049**	116377	0.94	0.49
2036	102864	0.93	0.48	**2050**	117381	0.94	0.49

Figure 7 illustrates a forecast of gas and methane production from 2024 to 2050, indicating a steady rise in both total gas and methane output during the specified period. In 2024, total gas output is 974527 m^3 annually, with methane comprising 487263 m^3. By 2050, these figures will increase significantly, attaining 21360099 m^3 of gas and 10680049 m^3 of methane. This persistent tendency suggests an augmented supply of biogas or landfill gas, potentially due to heightened waste generation, improved waste management practices, or sophisticated anaerobic digestion technologies. The production trend has an almost exponential growth pattern, characterized by steadily rising annual increments. For instance, between 2024 and 2025, gas production nearly doubles, and in the following years, the annual increase surpasses one million m^3.

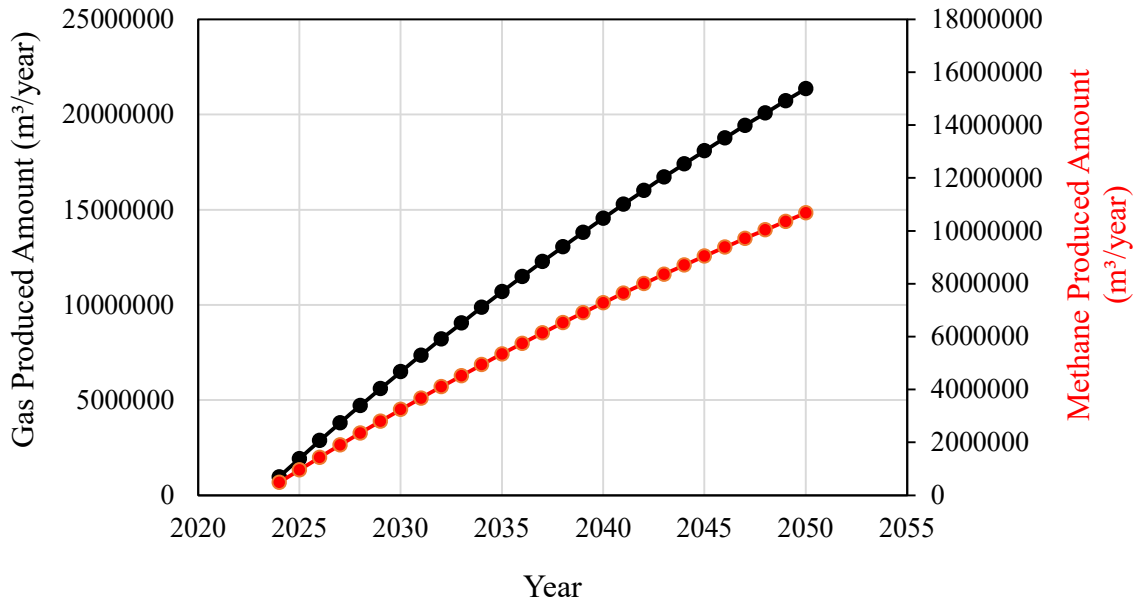


Figure 7. Forecast of total landfill gas and methane production (m^3/year) for Hakkari Province (2024–2050)

The methane component consistently comprises 50% of the overall gas production, corresponding with standard biogas composition, where methane typically forms around half of the entire volume. The

number underscores considerable potential for energy recovery, especially within sustainable energy sectors. The increasing supply of gas and methane may be used for power generation, heating, or as an alternative fuel, therefore diminishing reliance on fossil fuels and aiding greenhouse gas reduction via the capture of methane emissions. It should be noted that, the first cell will be established in the primary phase inside the storage area designated for activation in Akçalı village, Hakkari province, along with the installation of 39 gas collecting chimneys. Each will possess an outside diameter of 80 cm, with gravel installed around the DN 110 HDPE perforated pipes positioned in the centre of the chimneys. The volume of gas to be extracted from the gas stacks was calculated using the LandGEM model, which use the first-order decomposition equation.

Figure 8 depicts the anticipated rise in energy-generating capacity from 2024 to 2050, indicating a consistent and ongoing development trajectory in energy generation plant to be integrated into the Hakkari province landfill site. It should be noted that internal combustion engines are anticipated to be used for energy production in the power plant. In 2024, the power generation capacity begins at 0.16 MW and increases yearly, reaching 3.64 MW by 2050. This gradual increase signifies a consistent rise in energy production, potentially driven by improved waste-to-energy initiatives, biogas utilization, or progress in renewable energy technologies. The growth rate appears stable, with each year producing a little increased capacity compared to the previous year. Initially, the annual increase is modest; however, with time, the increments become more significant, reflecting the evolving infrastructure and improvements in energy generating efficiency. The data highlights the potential for sustainable energy production, either through biogas or waste-to-energy conversion, as the increase in electrical capacity aligns with the previously observed rise in gas and methane output. The lasting effects of this trend are significant, suggesting a growing reliance on alternative energy sources, which might reduce dependence on fossil fuels and improve a cleaner energy portfolio.

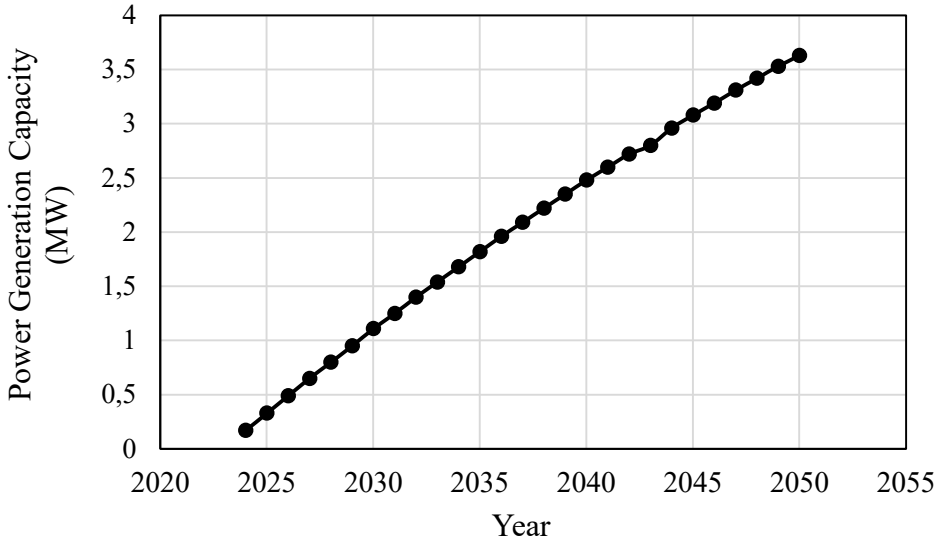


Figure 8. Projected increase in power generation capacity (MW) from landfill gas in Hakkari Province (2024–2050)

Using Türkiye's national grid emission factor of 0.478 kg CO_2/kWh [37,38], the estimated electricity generation from landfill gas in 2024 (approximately 1402 MWh/year) would offset about 670 tonnes of CO_2 emissions annually compared with grid-supplied electricity. By 2050, when the installed generation capacity is projected to reach 3.64 MW, annual electricity generation is expected to rise to about 31886 MWh/year, resulting in an estimated avoidance of roughly 15250 tonnes of CO_2 per year. These results underscore the significant climate mitigation potential of landfill gas-to-energy projects and emphasize their dual contribution to reducing greenhouse gas emissions and enhancing local energy security.

4. CONCLUSIONS

The increase in energy use has intensified dependence on natural resources, leading to environmental damage and significant waste production. Efficient waste management and sustainable energy strategies are essential to address these concerns. Landfill gas recovery and waste-to-energy conversion are effective methods for mitigating greenhouse gas emissions and producing renewable energy. This research evaluated the potential for integrated energy production in Hakkari province by forecasting population increase, predicting solid waste creation, and calculating landfill gas production with the LandGEM model. Additionally, the viability of using recovered gas for electricity production via internal combustion engines was examined. The primary outcomes have been provided below.

a. Annual solid waste generation is anticipated to increase from 85597 tonnes in 2023 to 117381 tonnes by 2050, while urban per capita waste is expected to rise from 0.85 kg/day to 0.94 kg/day.

b. The production of landfill gas is projected to rise from 974527 m^3 in 2024 to 21360099 m^3 by 2050, with methane being 50% of the whole amount, indicating significant potential for energy recovery.

c. The power generation capacity from landfill gas is projected to increase from 0.16 MW in 2024 to 3.64 MW in 2050, indicating a consistent improvement in waste-to-energy efficiency.

d. Integrating landfill gas recovery into municipal waste management strategies provides local authorities with a sustainable mechanism to lower environmental impacts and help meet national renewable energy goals.

e. The results are valid under the methane production rate, methane potential, waste composition, and gas recovery efficiency assumptions used in this study. Differences in actual conditions, such as demographic changes, site-specific waste characteristics, climatic factors, and facility operation, may affect the accuracy of these estimates.

Nomenclature

CH_4	Methane
CO_2	Carbon dioxide
k	Methane generation rate ($year^{-1}$)
Kcal	Kilocalorie
kW	Kilowatt
kWh	Kilowatt-hour
L_0	Methane generation potential
MW	Megawatt
MWh	Megawatt-hour

Abbreviations

AP	Air Pollutant Emission Factor
CAA	Clean Air Act
EU	European Union
EIA	Environmental Impact Assessment
MSW	Municipal Solid Waste
EMRA	Energy Market Regulatory Authority
ICE	Internal Combustion Engine

IEA	International Energy Agency
LCA	Life Cycle Assessment
SRF	Solid Recovered Fuel
SWM	Solid Waste Management
TURKSTAT	Turkish Statistical Institute
USEPA	United States Environmental Protection Agency
IPA	Instrument for Pre-Accession Assistance
WtE	Waste-to-Energy

Acknowledgment

This study is derived from a comprehensive Master Thesis conducted at Hakkari University, which involved research and technical analysis focused on the evaluation of solid waste management and energy recovery potential through landfill gas utilization in the region.

Declaration of Ethical Standards

The authors declare to comply with all ethical guidelines, including authorship, citation, data reporting, and original research publication.

Credit Authorship Contribution Statement

The authors declare that they have made equal contributions.

Declaration of Competing Interest

The authors declare no conflicts of interest.

Funding / Acknowledgements

No funding or research grant was received during the review, research or compilation of the article.

Data Availability

Data will be made available on request.

Use of Artificial Intelligence

During the preparation of this work the authors used QuillBot to improve the writing and English of some sections. After using this tool/service, the authors reviewed and edited the content as needed and they take full responsibility for the content of the publication.

5. REFERENCES

[1] M. C. Coşkuner, "Evsel Atıktan Enerji Üretimi: Gaziantep Örneği," M.S. thesis, Enerji Enstitüsü, İstanbul Teknik Üniversitesi, İstanbul, Türkiye, 2015.

[2] J. L. Holechek, H. M. Geli, M. N. Sawalhah, and R. Valdez, "A global assessment: Can renewable energy replace fossil fuels by 2050," Sustainability, vol. 14, no. 8, p. 4792, 2022.

[3] İ. Mete, "Yenilenebilir Enerji Sistemleri," M.S. thesis, Lisansüstü Eğitim Enstitüsü, Antalya Bilim Üniversitesi, Antalya, Türkiye, 2022.
[4] International Energy Agency (IEA), "The global energy crisis is steering the world toward renewable energy," 2023. [Online]. Available: https://temizenerji.org/2022/10/28/uluslararasi-enerji-ajansi-kuresel-enerji-krizi-dunyayi-yenilenebilir-enerjiye-yonlendiriyor/. [Accessed: Oct. 28, 2023].
[5] Y. Demir, "Türkiye'de yenilenebilir enerji tüketimi ekonomik büyümeye katkı sağlar mı?," Doğuş Üniversitesi Dergisi, vol. 24, pp. 271–281, 2023.
[6] Energy Market Regulatory Authority, Electricity Market Sector Report. Ankara, Türkiye, 2023.
[7] M. Yücesoy, "Mardin İlinde Katı Atık Yönetim Planı," M.S. thesis, Fen Bilimleri Enstitüsü, Çukurova Üniversitesi, Adana, Türkiye, 2022.
[8] H. Palabıyık and D. Altunbaş, Kentsel Katı Atık Yönetimi. İstanbul, Türkiye: Beta Basım Yayım, 2004, pp. 104–105.
[9] Turkish Statistical Institute, "2018 Municipal Waste Statistics." [Online]. Available: https://data.tuik.gov.tr/Bulten/Index?p=Belediye-Atik-Istatistikleri-2018. [Accessed: Nov. 15, 2019].
[10] Turkish Statistical Institute, "2020 Municipal Waste Statistics." [Online]. Available: https://data.tuik.gov.tr/Bulten/Index?p=Atik-Istatistikleri-2020. [Accessed: Dec. 11, 2021].
[11] N. Sezgin, H. K. Özcan, K. Varınca, and M. Borat, "Katı atık depo gazından elektrik üretiminin Türkiye'de uygulanabilirliğine iki örnek: İstanbul ve Bursa tesisleri," Yıldız Teknik Üniversitesi Dergisi, vol. 3, pp. 89–96, 2003.
[12] F. Saltabaş and M. A. Yalçın, "Depo gazından enerji üretimi," Sakarya Üniversitesi Fen Bilimleri Dergisi, vol. 8, no. 1, pp. 44–47, 2004.
[13] E. D. Güven, "Ege Bölgesi'nde kentsel katı atık üretimi ve atığın metan gazı enerji potansiyelinin belirlenmesi," Dokuz Eylül Üniversitesi Mühendislik Fakültesi Fen ve Mühendislik Dergisi, vol. 21, pp. 311–322, 2019.
[14] D. Öztürk and A. Özgüven, "Katı atık depo alanlarında bulunan atıklardan biyogaz enerjisi üretme potansiyelinin değerlendirilmesi: Van ili örneği," Süleyman Demirel Üniversitesi Fen Bilimleri Enstitüsü Dergisi, vol. 26, no. 1, pp. 160–170, 2022.
[15] R. Ahmed, "Evaluation and Prediction of Energy Potential of Landfill Mined Solid Waste," Ph.D. dissertation, The University of Texas, Arlington, TX, USA, 2019.
[16] I. R. Istrate, J. L. Galvez-Martos, D. Vázquez, G. Guillén-Gosálbez, and J. Dufour, "Prospective analysis of the optimal capacity, economics and carbon footprint of energy recovery from municipal solid waste incineration," Resources, Conservation and Recycling, vol. 193, p. 106943, 2023.
[17] J. F. Zhang et al., "Regeneration of high-performance materials for electrochemical energy storage from assorted solid waste: A review," Journal of Cleaner Production, p. 137628, 2023.
[18] J. M. Fernández-Gonzalez, A. L. Grindlay, F. Serrano-Bernardo, M. I. Rodríguez-Rojas, and M. Zamorano, "Economic and environmental review of Waste-to-Energy systems for municipal solid waste management in medium and small municipalities," Waste Management, vol. 67, pp. 360–374, 2017.
[19] X. G. Zhao, G. W. Jiang, A. Li, and L. Wang, "Economic analysis of waste-to-energy industry in China," Waste Management, vol. 48, pp. 604–618, 2016.
[20] M. Tolay, A. Waterschoot, and L. S. Angrill, "Yenilenebilir enerji için biyokütle," in Proc. Elektrik Elektronik Mühendisliği Kongresi (EEMKON 2015), İstanbul, Türkiye, 2015.
[21] B. Baran, "Türkiye'nin endüstriyel elektrik tüketimine yönelik depolama gazı enerji depolama," Niğde Ömer Halisdemir Üniversitesi Mühendislik Bilimleri Dergisi, vol. 11, pp. 84–91, 2022.
[22] Hakkâri Valiliği, "Hakkâri ili tarihçe ve coğrafi yapı." [Online]. Available: http://www.hakkari.gov.tr/tarihce-ve-cografi-yapi. [Accessed: Jul. 15, 2023].
[23] Enerji Piyasası Düzenleme Kurumu, Elektrik Piyasası Sektör Raporu. Ankara, Türkiye, 2021.
[24] Enerji Piyasası Düzenleme Kurumu, Elektrik Piyasası Sektör Raporu. Ankara, Türkiye, 2022.
[25] İ. İnan, İ. Akbulut, and E. Aslan, "Enerji sorununun çözümünde yenilenemez ve yenilenebilir enerji kaynaklarının yeri ve önemi," Türk Dünyası Araştırmaları, vol. 120, no. 237, pp. 11–40, 2018.

[26] PDEUCC, Hakkari Province 2022 Environmental Status Report. Hakkari, Türkiye, 2022.
[27] PDEUCC, Hakkari Province 2018 Environmental Status Report. Hakkari, Türkiye, 2018.
[28] G. Gürel, "Katı Atıklardan Enerji Elde Edilmesi ve Samsun Katı Atık Tesisinin İncelenmesi," Uzmanlık Tezi, İller Bankası Anonim Şirketi, Türkiye, 2015.
[29] Hakkâri Belediyeleri ve İl Özel İdaresi Katı Atık Yönetim Birliği, Katı Atık Bertaraf Tesisleri Çevresel Etki Değerlendirmesi (ÇED) Raporu. Hakkari, Türkiye, 2019.
[30] H. B. Barut and E. İrtem, "İnşaat mühendisliğinde kullanılan nüfus tahmin yöntemlerinin Türkiye nüfus sayım sonuçlarına göre irdelenmesi," ab.org.tr, 2023.
[31] A. Işık, "Katı Atık Bertaraf Tesislerinde Organik Atıklardan Açığa Çıkan Depo Gazı ile Enerji Elde Edilmesi," M.S. thesis, Fen Bilimleri Enstitüsü, Karabük Üniversitesi, Karabük, Türkiye, 2014.
[32] S. Chandra and R. Ganguly, "Assessment of landfill gases by LandGEM and energy recovery potential from municipal solid waste of Kanpur city, India," Heliyon, vol. 9, no. 4, p. e15187, 2023.
[33] B. Şahin, "Türkiye'de Depo Gazından Enerji Eldesi ve Adana İli Örneği," M.S. thesis, Fen Bilimleri Enstitüsü, Nevşehir Hacı Bektaş Veli Üniversitesi, Nevşehir, Türkiye, 2021.
[34] Z. Arslan, "Erzurum Katı Atık Düzenli Depolama Sahasındaki Depo Gazı Verimliliğinin LandGEM Modeli Kullanılarak İncelenmesi," M.S. thesis, Fen Bilimleri Enstitüsü, Atatürk Üniversitesi, Erzurum, Türkiye, 2022.
[35] U.S. Environmental Protection Agency (USEPA), LandGEM Gas Emissions Model Version 3.02. Research Triangle Park, NC, USA: Office of Research Laboratory and Clean Air Technology Center, 2005.
[36] Jenbacher, "Official website." [Online]. Available: https://www.jenbacher.com/en. [Accessed: Oct. 12, 2023].
[37] Republic of Türkiye Ministry of Energy and Natural Resources, "Electricity Production and Consumption Emission Factors." [Online]. Available: https://enerji.gov.tr/evced-cevre-ve-iklim-elektrik-uretim-tuketim-emisyon-faktorleri. [Accessed: Oct. 15, 2023].
[38] M. Camci, Ö. Aksoy, and S. P. Göztok, "Thermodynamic analysis of an ice cream production process integrated with ground heat exchangers in hot climate regions," Thermal Science and Engineering Progress, p. 104037, 2025.
[39] M. Melikoglu, "Forecasting of municipal solid waste generation in Türkiye and techno-economic-environmental assessment of electricity generation via incineration till 2032," Next Sustainability, vol. 5, p. 100092, 2025.
[40] D. C. Manheim, N. Yeşiller, J. L. Hanson, and D. R. Blake, "Climate impacts of landfill gas emissions: Analysis for 20-year and 100-year time horizons," Waste Management, vol. 186, pp. 318–330, 2024.

Konya Mühendislik Bilimleri Dergisi., c.14, s.2, 586-598, 2026
Konya Journal of Engineering Sciences v.14, n.2, 586-598, 2026
ISSN: 2667-8055 (Electronic)
DOI: 10.36306/konjes.1729036

LYMPHOMA LESION SEGMENTATION IN NECK AXIAL AND CORONAL SECTION CT IMAGES WITH U-NET

[1]Mete Can YAŞAR, [1]Mustafa Emre YAŞAR, [1,*]Rahime CEYLAN,
[2]Abidin KILINÇER, [2]Mustafa KOPLAY, [3]Selda HAKBİLEN, [3]Sema YILMAZ,
[4]Rafiye ÇİFTÇİLER, [5]Burcu YORMAZ

[1]*Konya Technical University, Engineering and Natural Science Faculty, Electrical and Electronics Engineering, Konya, Turkey*
[2]*Selçuk University, Faculty of Medicine, Radiology Department, Konya, Turkey*
[3]*Selçuk University, Faculty of Medicine, Rheumatology Department, Konya, Turkey*
[4]*Selçuk University, Faculty of Medicine, Hematology Department, Konya, Turkey*
[5]*Selçuk University, Faculty of Medicine, Chest Diseases Department, Konya, Turkey*
[1]metecanyasar@gmail.com, [1]mustemr297@gmail.com, [1]rceylan@ktun.edu.tr, [2]akilincer@yahoo.com,
[2]koplaymustafa@hotmail.com, [3]seldahakbilen@gmail.com, [3]drsemayilmaz@hotmail.com,
[4]rafiyesarigul@gmail.com, [5]burcyormaz@gmail.com

Highlights

- Lymphoma is a type of cancer classified under blood cancer, emerging because of cell degradation.
- In this study, CT images obtained from lymphoma patients were segmented using U-Net.
- The test results achieved were a 0.83 DSC for neck axial CTs and 0.75 DSC for neck coronal CTs.
- The statistical and visual analyses showed that the segmentation was successfully performed.

Graphical Abstract

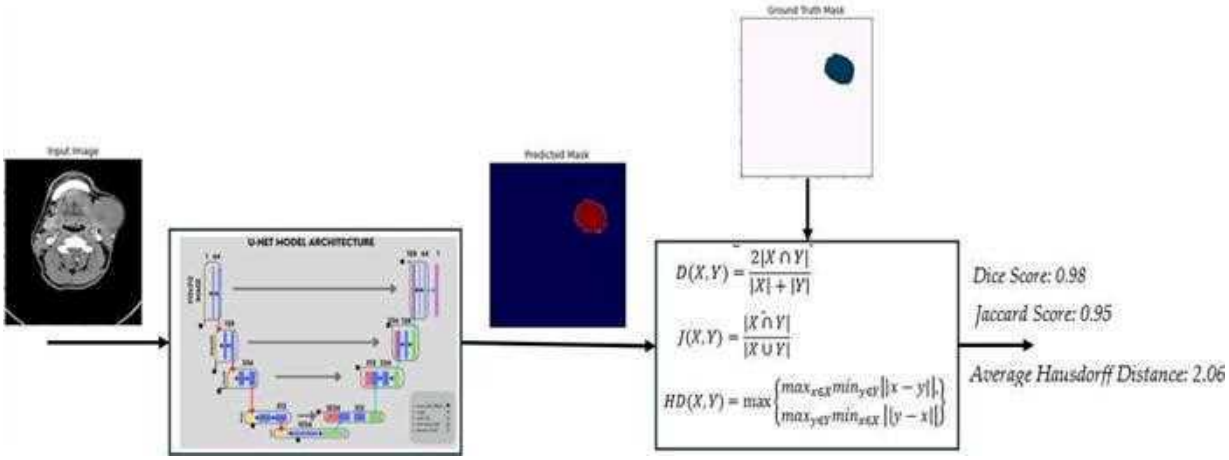


Figure Flowchart of the proposed method

***Corresponding Author:** Rahime CEYLAN, rceylan@ktun.edu.tr

Konya Mühendislik Bilimleri Dergisi., c.14, s.2, 586-598, 2026
Konya Journal of Engineering Sciences v.14, n.2,586-598, 2026
ISSN: 2667-8055 (Electronic)
DOI: 10.36306/konjes.1729036

LYMPHOMA LESION SEGMENTATION IN NECK AXIAL AND CORONAL SECTION CT IMAGES WITH U-NET

[1]Mete Can YAŞAR, [1]Mustafa Emre YAŞAR, [1,*]Rahime CEYLAN, [2]Abidin KILINÇER, [2]Mustafa KOPLAY, [3]Selda HAKBİLEN, [3]Sema YILMAZ, [4]Rafiye ÇİFTÇİLER, [5]Burcu YORMAZ

[1]Konya Technical University, Engineering and Natural Science Faculty, Electrical and Electronics Engineering, Konya, Turkey
[2]Selçuk University, Faculty of Medicine, Radiology Department, Konya, Turkey
[3]Selçuk University, Faculty of Medicine, Rheumatology Department, Konya, Turkey
[4]Selçuk University, Faculty of Medicine, Hematology Department, Konya, Turkey
[5]Selçuk University, Faculty of Medicine, Chest Diseases Department, Konya, Turkey
[1]metecanyasar@gmail.com, [1]mustemr297@gmail.com, [1]rceylan@ktun.edu.tr, [2]akilincer@yahoo.com, [2]koplaymustafa@hotmail.com, [3]seldahakbilen@gmail.com, [3]drsemayilmaz@hotmail.com, [4]rafiyesarigul@gmail.com, [5]burcyormaz@gmail.com

(Received: 27.06.2025; Accepted in Revised Form: 04.11.2025)

ABSTRACT: Lymphoma is a type of cancer classified under blood cancer, emerging because of cell degradation. It is visualized using computed tomography (CT) and positron emission tomography (PET). Segmentation refers to the process of separating the desired object from the background and other elements in an image. In this study, CT images obtained from lymphoma patients were segmented using U-Net, a deep learning-based segmentation model. The test results achieved were a 0.83 Dice Similarity Coefficient (DSC), 0.73 Jaccard Index (JI), an average Hausdorff Distance (HD) of 15.81 mm for neck axial CT images, and a 0.75 DSC, 0.64 JI, and an average HD of 30.18 mm for neck coronal CT images. The detailed statistical and visual analyses demonstrated that the lymphoma lesion segmentation was successfully performed on neck coronal and axial CT images using U-Net.

Keywords: *lymphoma lesion segmentation, deep learning, U-Net, computed tomography images*.

1. INTRODUCTION

Lymphoma, which falls under the category of blood cancers, is a deadly type of cancer that arises when cells in the body lose control, exhibiting a higher incidence compared to other cancers in the same group. Early diagnosis plays a critical role in the treatment process [1]. Computed tomography (CT) and positron emission tomography (PET) are widely used imaging methods for detecting lymphoma today. However, the accurate segmentation of lesions detected in lymph nodes is essential for the identification of the disease stage as correctly and the planning treatment process [2]. Segmentation is a process of separating a specific object or element within an image from the background. The high success rates achieved by deep learning methods in contemporary segmentation tasks have surpassed those of classical methods. Particularly in detecting diseases such as lymphoma, the results obtained from segmentation studies using deep learning methods on CT and PET imaging techniques are promising, and this field is continuously being developed [3].

***Corresponding Author:** Rahime CEYLAN, rceylan@ktun.edu.tr

Chen et al. (2013) computed and marked the longitudinal time points of lymphoma lesions detected in CT images using the Snake Model architecture. In a dataset consisting of CT images containing 76 lymph nodes, they achieved an average HD value of 2.76 pixels/mm [4].

In 2017, Grossiord et al. utilized a dataset of 43 PET-CT images. They aimed to enhance the efficiency of the segmentation process by combining component trees and random forest models, achieving an accuracy of 92% [5].

Hu et al. (2019) clustered 3D-PET images obtained from 48 patients using supervoxel and superpixel methods, along with the Density-Based Spatial Clustering of Applications with Noise (DBSCAN) algorithm, to improve the efficiency of the segmentation in lymphoma lesions. They obtained segmentations with the lowest value of 66.27% and the highest of 100% [6].

In 2021, Huang et al. employed the U-Net model and Dempster-Shafer Theory (DST) in their study. Using a dataset of PET-CT images from 173 patients, the researchers achieved a DSC of 0.726 for lesion segmentation [7].

In their study in 2021, Yuan et al. argued that the manual segmentation of Diffuse Large B-cell lymphoma (DLBCL) is challenging and labour-intensive, emphasizing that hybrid learning methods could serve as an alternative solution for the detection of this common type of DLBCL. They used a dataset of 45 PET-CT images, also validated by biopsy reports for lymphoma diagnosis. The study designed a hybrid model that aimed to combine PET and CT images to extract common features. As a result, they achieved a DSC of 73.87% and an average HD of 4.39 mm [8].

In the study conducted by Stahnke et al. (2023), the segmentation of FDG-avid lymphoma lesions in PET-CT images was addressed. They utilized whole-body images from 145 patients as their dataset. The model architecture chosen was TransR U-Net, which is a customized architecture that combines the features of the Retina U-Net model with a pyramid transform method. As a result of the segmentation, while a mean average Precision (mAP) of 0.377 and a DSC of 73.7% are obtained by the base model (Retina U-Net); TransR U-Net achieved a mAP of 0.285 and a DSC of 73.2% [9].

Eida et al. (2024) argued that the success of detecting lymph nodes from ultrasound and CT images depends on the expertise of the individuals performing the analysis. They compared their results using Yolo V7 and B- and D-based architectures against the annotations made by expert radiologists and their assistants. The dataset comprised ultrasound and CT images from the head and neck regions of 126 patients. The comparison revealed lower accuracy than the radiologists' annotations but higher accuracy than the assistants' annotations. They expressed that their developed model could serve as an auxiliary diagnostic tool for assistant doctors, achieving an accuracy of 89.8% for the B-based architecture and 79.8% for the D-based architecture [10].

Fu et al. (2024) focused on the detection of brain tumours resulting from lymphoma. They employed the nnU-Net model as their deep learning architecture and compared its performance with other model architectures such as the Segment Anything Model (SAM). Using magnetic resonance (MR) images obtained from 117 patients, they performed segmentation in both 2D and 3D. As a result of their study, nnU-Net3D achieved a DSC of 82.08% and an average HD of 7.96 mm, while nnU-Net2D achieved a DSC of 73.99% and an average HD of 9.78 mm [11].

Pang et al. (2024) performed lymphoma mass segmentation using a Convolutional Neural Network (CNN) on a dataset consisting of 53 MTR-PET (Magnetic Transfer Recording, a type of PET imaging) images. They employed a method for highlighting the region of interest (ROI) by cropping the areas that needed to be annotated. The model achieved a DSC of 0.86 [12].

Tie et al. (2024) focused on the segmentation of 274 datasets related to pediatric lymphoma patients. They utilized the LAS-NET model architecture for their work. The dataset was divided into two parts, named PET1 and PET2, and two separate segmentation phases were performed. They achieved a DSC of 0.72 for PET1 and an F1 Score of 0.606 for PET2 [13].

Özen et al. (2024) conducted automated segmentation of lung tomography images with U-Net. In their study, 30 lung CT images acquired from the Department of Radiation Oncology at Ankara University Faculty of Medicine were utilized, which were converted from DICOM format to NIfTI format. The

average dice index was obtained as 96.44±2.62 in test. This high Dice index value indicates that the U-Net model has high accuracy in segmentation of lung structures and demonstrates reliability [14].

Yuan et al. (2024) introduced a U-Net-based multi-scale context fusion algorithm for medical image segmentation. The method enhances feature learning by extracting semantic information at different encoding stages and weighting them through the Three-Branch Feature Fusion UNet (TBSFF). By combining multi-scale fusion and feature selection, it achieves richer semantic and detailed features without adding significant computational cost. Experiments show superior performance with fewer parameters, achieving Dice/IoU scores of 90.56/83.47 on the GlaS dataset and 79.07/65.98 on the MoNuSeg dataset [15].

Qiu et al. (2025) proposed an Efficient Residual U-Net (ERU-Net) that fuses T2-weighted and deep-weighted MRI images for automatic uterine lymph node segmentation. Using a dataset of 158 annotated scans, ERU-Net with efficient channel attention achieved superior performance (mIoU = 0.83, accuracy = 0.91, precision = 0.90, recall = 0.91) compared to other networks, offering valuable support for clinical treatment planning [16].

Turk and Kılıçaslan (2025) introduced U-Net, V-Net, and Seg-Net-based models for tuberculosis detection using Shenzhen and Montgomery datasets. By integrating preprocessing techniques, attention mechanisms, and non-local blocks, the proposed models significantly improve lung region segmentation. Experimental results show that U-Net and V-Net achieve Dice scores of 96.43% and 96.42%, outperforming Seg-Net and traditional methods, thus enabling more accurate and reliable tuberculosis diagnosis [17].

Liang (2025) investigated PET/CT-based lymphoma segmentation using the AutoPet dataset by developing a complete workflow for training, evaluation, and visualization. It compares the performance of U-Net, SegResNet, and SegResNetDS, and examines training on PET and CT data separately versus jointly. The findings, supported by systematic evaluation metrics, provide valuable reference data for researchers and engineers in medical image analysis [18].

In this study, a total of 158 coronal and 298 axial raw neck CT images were annotated by experts and categorized based on sectional planes (coronal and axial). Two separate datasets were created using coronal and axial neck CT images. Lymphoma lesion segmentation was performed utilizing these datasets. The U-NET model architecture was employed, and the obtained results were evaluated by comparing them with manually segmented results using metrics such as DSC, JI, and HD. The subsequent sections of the article include Materials and Methods, which provide a detailed explanation of the dataset, model architecture, and the metrics used for result comparison; Results, which present the obtained visual outcomes and network parameter optimization; and Discussion and Conclusion, which compare the findings with other studies in the literature.

2. MATERIAL AND METHODS

The objective of this study is to facilitate the rapid and accurate analysis of regionally acquired CT images for the detection of tumours and anomalies associated with lymphoma while minimizing the workload imposed by manual segmentation performed by experts. Initially, raw data were collected and annotated by experts, resulting in a dataset that encompasses both the original images and their corresponding target images. A deep learning model was selected in accordance with the specific segmentation problem, and the prepared dataset was utilized as input. Then, model parameters were optimized, and the outcomes were compared.

2.1. Features of the Dataset

The dataset was created using CT images obtained with ethical approval from the Selçuk University, Faculty of Medicine. The raw images from various patients were grouped according to the image plane (coronal, sagittal, axial) and anatomical location (neck, thorax, abdomen), and the masks generated from the annotations were organized into separate files. The open-source ImageJ software was utilized for the

annotation process, which was performed manually by two experts with at least 10 years of experience in radiology. ImageJ is an image analysis program developed by Wayne Rasband in 1997, written in the Java programming language, which enables various operations to be performed in image analysis. This program can conduct numerous tasks, including histogram analyses of images with different formats, features, and extensions, altering colors within images, and creating various annotations and tracking paths. The preference for the ImageJ program stems from its open-source nature and user-friendly interface [19,20].

The constructed dataset consists of CT images obtained from 79 patients. 158 CT images were acquired for the coronal section of the neck and 298 CT images for the axial section, all of which were manually processed. The resolutions of the images in the raw data set are 571*512, 533*512, 604*512, 512*653 etc. For training of deep learning model, all of images were resized to 512*512 resolution. The target images and manual annotations for neck coronal and axial CT images are presented in Figures 1 and 2, while the statistical information of the patients is provided in Table 1.

Table 1. Patient's statistical information in the dataset

Gender	Number of People	Age
Female	41	58,68± 15,73
Male	38	58,37± 18,10

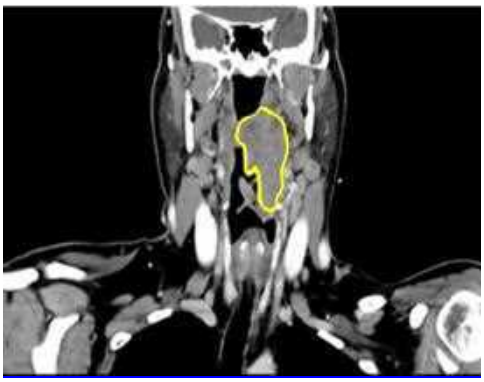


Figure 1. Annotated image of the neck coronal section

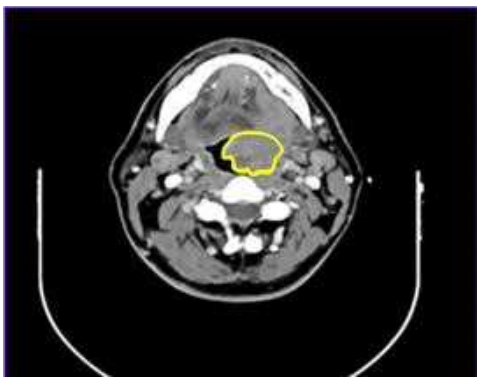


Figure 2. Annotated image of the neck axial section

2.2. U-Net

The U-Net model has highly effective performance for segmentation tasks, so it has been chosen for this process. Introduced by Olaf Ronneberger in 2015, the U-Net model is specifically designed for tasks such as segmentation [21]. Compared to other deep neural network (DNN) models, the U-Net model

excels in accuracy, is relatively fast, and can achieve high accuracy with minimal data, allowing it to surpass its competitors.

The U-Net model consists of three main components: the encoder, the bottleneck, and the decoder. The primary purpose of the encoder is to gradually reduce the dimensions of the input image with a specific resolution while increasing the filter sizes during this process to extract features from the image. The model constructed based on U-Net takes images with a resolution of 512x512 as input. In each convolutional layer, it extracts features using 64, 128, 256, and 512 filters, with a filter size of 3x3 and a ReLU activation function. To minimize feature loss, a 2x2 Max Pooling operation is applied between each specified layer. The filter size and the number of filters were varied to optimize network parameters, and the results were recorded.

The bottleneck serves as a bridge between the encoder and decoder. It collects the features extracted by the encoder from the input images and transfers them to the decoder section. This process ensures that the features collected by the encoder are utilized in the decoder part. The convolutional layer in the bottleneck was constructed with 1024 filters, a filter size of 3x3, and a ReLU activation function.

The decoder section utilizes the features collected by the encoder, which are conveyed through the bottleneck, to reconstruct the input image and gather detailed features. Unlike the encoder, the decoder increases the image dimensions while reducing the number of filters within it. The filter counts in the decoder are set in reverse order to the encoder, with 512, 256, 128, and 64 filters in each layer, culminating in the output layer. In the output layer, the image is reconstructed, and the features related to the image are collected. A diagram of the U-Net model is presented in Figure 3 [22].

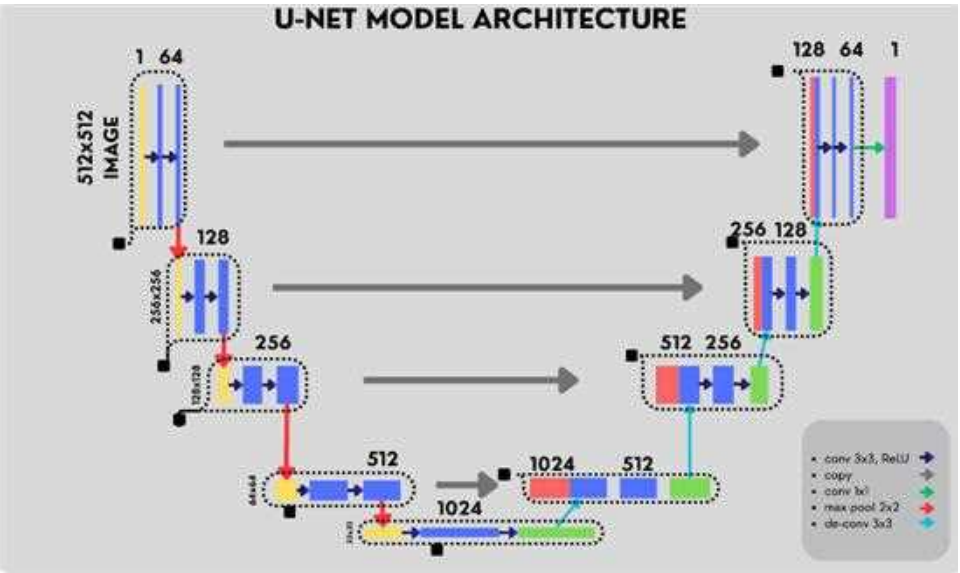


Figure 3. U-Net Model Architecture [20]

2.3. Performance Metrics

This section discusses the evaluation metrics used in the performance assessment of the U-Net model. For evaluating the U-Net model's results, the Dice Similarity Coefficient (DSC), Jaccard Index (JI), and Hausdorff Distance (HD) were utilized. The Dice Similarity Coefficient (DSC) is calculated as the ratio of twice the intersection of two datasets to the sum of the mentioned datasets; it takes values between 0 and 1. A value close to 1 indicates the accuracy of the prediction similarity. (Here, "X" refers to the ground truth mask image, while "Y" refers to the predicted image.) Equation 1 provides the formula for calculating the DSC [23].

$$D(X,Y) = \frac{2|X \cap Y|}{|X| + |Y|} \quad (1)$$

The Jaccard Index (JI) measures the similarity between two datasets like the DSC; it takes values between 0 and 1. Likewise, a value close to 1 indicates that the difference between the ground truth set and the predicted set is minimal. It is calculated as the ratio of the intersection of the two datasets to the union of those datasets. (Here, "X" refers to the ground truth mask image, while "Y" refers to the predicted image.) Equation 2 provides the formula for calculating the JI [23].

$$J(X,Y) = \frac{|X \cap Y|}{|X \cup Y|} \tag{2}$$

Hausdorff Distance (HD) is a metric that measures the similarity between two-point clouds or shapes in terms of distance. HD calculates the distance between the most distant and closest pairs of points between two sets, providing a measure of how far apart the sets are. This distance can take values ranging from 0 to positive numbers; values close to 0 indicate a high degree of overlap between the respective sets. An increase in this value signifies that the distance between the predicted set and the ground truth set has increased, thereby indicating a decrease in similarity between the sets. When calculating HD, one pixel is converted into a physical distance based on the imaging distance in tomography and expressed in millimeters (1 pixel = 0.5 mm). As stated in Equation 3, X represents the set of points on the boundary of the ground truth mask, while Y denotes the set of points on the boundary of the predicted mask. The expression $||x - y||$ indicates the Euclidean distance between a point x on the boundary of the ground truth mask and a point y on the boundary of the predicted mask. The term $min_{y \in Y}||x - y||$ represents the distance from a point on the boundary of the ground truth mask to the nearest point on the boundary of the predicted mask. The terms $max_{x \in X}$ and $max_{y \in Y}$ represent the largest of these distances, which indicates the maximum distance between the two sets. The Hausdorff Distance (HD) uses this maximum distance to measure the worst-case dissimilarity between the two sets [24].

$$HD(X,Y) = \max\begin{Bmatrix} max_{x \in X} min_{y \in Y}||x - y||, \\ max_{y \in Y} min_{x \in X}||y - x|| \end{Bmatrix} \tag{3}$$

During the model's training, the environment was kept constant, as outlined in Table 2.

Table 2. The environment used in the training and testing of the U-Net model

Library	Python = 3.10.13, Pytorch = 2.2.0, Cuda = 12.1
GPU	Nvidia RTX 2080Tİ GPU
Operating System	Windows 11 Pro

3. RESULTS AND DISCUSSION

In this study, lymphoma lesion segmentation in neck coronal and axial CT images was realized using U-Net model. This section provides a detailed analysis of the network parameters tested for the U-Net model applied to coronal and axial neck images. In each training session, the neck axial images consist of 208 training images and 90 test images, while the neck coronal images include 110 training images and 48 test images. Each training was conducted for 100 epochs with a batch size of 1; the learning rate, optimizer, activation function, and filter size were modified to find the best network parameters and create a model with high segmentation capability. Binary cross entropy (BCE) logarithmic loss function was used in training the model. BCE Logarithmic Loss is particularly important in binary classification and segmentation tasks as it combines sigmoid activation and binary cross-entropy in a safe, efficient and flexible way.

According to the obtained test results (Table 3), the optimized network parameters for the neck axial images were recorded as a learning rate of 0.0001, Rectified Adam (RAdam) optimizer, ReLU activation function, and a filter size of 7x7. The scores achieved were 0.96 for DSC, 0.92 for JI during training, and 0.83 for DSC, 0.73 for JI during testing. The average HD for the test was determined as 15.81 mm.

The optimized network parameters for the neck coronal images were recorded as a learning rate of 0.0001, Adam optimizer, ReLU activation function, and a filter size 9x9 (Table 4). The scores obtained were 0.89 for DSC, 0.83 for JI during training, and 0.75 for DSC, 0.64 for JI during testing. The average HD for the test was determined as 30.18 mm. The Dice loss equation calculates loss values in Tables 3 and 4.

In both data sets created with images in both planes, parameters such as learning rate, filter size, activation function, and optimizer of the U-net model were changed, and the model parameters that gave the best results were tried to be obtained. The best results were obtained with a learning rate of 0.0001 in both neck axial and neck coronal CT images. As the learning rate increased, DSC values decreased in training and testing. Different learning rates were tried in the study. Some of the trials are presented in Tables 3 and 4. Although an improvement in education was seen at different values of the learning rate, no major improvements were seen in test results.

The best optimizer was found to be rectified Adam in neck axial images and Adam in neck coronal images. The activation function is very important in modeling nonlinear data. Therefore, choosing the right activation function allows non-linear data to be expressed better; in other words, it has a great impact on the outcome of the learning model. The best results were achieved with the RELU activation function in two data sets created from images of two different planes.

Increasing the kernel (filter) size in the convolution layers of a U-Net architecture does not necessarily cause feature loss, but it does change how features are captured. A larger kernel size expands the receptive field, allowing the network to capture more contextual information from a broader neighbourhood in the image. This can be beneficial when the task requires understanding larger structures or spatial dependencies, such as segmenting organs or lesions that cover wider regions. However, larger kernels also increase computational cost and may smooth out fine details, which could reduce the model's ability to capture small or sharp features if not balanced properly. Although the test DSC and JI results obtained in neck axial images were the same at all filter sizes, the best results were achieved with a 7x7 filter size according to HD, which is one of the parameters that best expresses the overlap between the target image and the result image. The best DSC, JI, and HD results in neck coronal images were achieved with a filter size of 9x9.

Visual neck axial predictions obtained by the fine-tuned models according to target regions are presented for the highest and lowest segmentation results in Figures 4. The upper example shows the highest Dice Score (DSC) of 0.98 with a Hausdorff Distance of 2.06, indicating an accurate prediction closely matching the ground truth. The below example illustrates the lowest Dice Score of 0.17 and a Hausdorff Distance of 6.60, reflecting a poor prediction with significant deviation from the ground truth. Considering the results obtained from all test images, average scores for DSC and Hausdorff distance are 0.83 and 15.81 mm. It can be said that the U-Net model could achieve 0.98 Dice scores in neck axial, while low DSC values were obtained in very few images.

The examples of the segmentation predictions in axial neck images are presented in Figure 5. When considering the results obtained from these test results, the model achieved a maximum Dice Similarity Coefficient (DSC) of 0.95, along with a Hausdorff Distance of 2.13, which indicates highly accurate segmentation in some cases. However, the lowest performance recorded was a DSC of only 0.04, with an HD as high as 80.85. This large discrepancy highlights that although the model can deliver near-perfect results under favourable conditions, it struggles significantly in more complex or less well-defined regions. Such variation suggests the need for further model refinement, possibly through improved training data diversity, post-processing steps, or architecture enhancements to better handle challenging cases.

The running time of the U-Net model was about 36 hours during training and test.

Table 3: The results for the segmentation of lymphoma lesion regions in neck-axial CT images using U-Net: (a) Determination of the optimal learning rate, (b) Identification of the best-performing optimization algorithm, (c) Determination of the optimal activation function, (d) Determination of the optimal filter size.

(a)

Learning Rate	Train HD	Train Loss	Train DSC	Train JI	Test HD	Test Loss	Test DSC	Test JI
0.0001	**1.53**	**0.002**	**0.98**	**0.95**	**16.07**	**0.035**	**0.83**	**0.72**
0.001	2.89	0.004	0.95	0.91	35.23	0.036	0.80	0.69
0.01	4.18	0.004	0.95	0.90	21.99	0.038	0.82	0.71
0.1	4.56	0.005	0.93	0.88	32.71	0.045	0.77	0.65

(b)

Optimizer	Train HD	Train Loss	Train DSC	Train JI	Test HD	Test Loss	Test DSC	Test JI
RMSprop	3.18	0.003	0.96	0.93	22.92	0.033	0.82	0.72
Adadelta	153.03	0.307	0.04	0.04	158.56	0.306	0.32	0.03
Adam	2.74	0.003	0.97	0.94	14.30	0.031	0.84	0.74
Adamax	5.87	0.002	0.98	0.97	17.53	0.042	0.81	0.71
Adagrad	2.75	0.142	0.98	0.96	45.53	0.162	0.81	0.70
RAdam	**1.53**	**0.002**	**0.98**	**0.95**	**16.07**	**0.035**	**0.83**	**0.72**

(c)

Activation Function	Train HD	Train Loss	Train DSC	Train JI	Test HD	Test Loss	Test DSC	Test JI
ReLU	**1.53**	**0.002**	**0.98**	**0.95**	**16.07**	**0.035**	**0.83**	**0.72**
Hard Swish	1.67	0.003	0.97	0.94	16.17	0.033	0.79	0.69
PReLU	1.50	0.002	0.97	0.95	21.45	0.036	0.82	0.72
GELU	2.64	0.003	0.97	0.94	15.32	0.032	0.82	0.72
ELU	3.07	0.004	0.95	0.90	25.17	0.030	0.79	0.69
Leaky ReLU	1.84	0.002	0.98	0.96	23.76	0.039	0.81	0.71

(d)

Filter Size	Train HD	Train Loss	Train DSC	Train JI	Test HD	Test Loss	Test DSC	Test JI
3x3	1.53	0.002	0.98	0.95	16.07	0.035	0.83	0.72
5x5	2.64	0.003	0.97	0.94	15.32	0.032	0.82	0.72
7x7	**3.14**	**0.004**	**0.96**	**0.92**	**15.81**	**0.027**	**0.83**	**0.73**
9x9	2.66	0.005	0.95	0.90	14.82	0.028	0.83	0.73

Table 4: The results for the segmentation of lymphoma lesion regions in neck-coronal CT images using U-Net: (a) Determination of the optimal learning rate, (b) Identification of the best-performing optimization algorithm, (c) Determination of the optimal activation function, (d) Determination of the optimal filter size.

(a)

Learning Rate	Train HD	Train Loss	Train DSC	Train JI	Test HD	Test Loss	Test DSC	Test JI
0.0001	**2.29**	**0.003**	**0.97**	**0.95**	**53.48**	**0.074**	**0.71**	**0.60**
0.001	2.64	0.004	0.96	0.93	64.79	0.089	0.69	0.58
0.01	3.83	0.005	0.96	0.92	68.29	0.1	0.67	0.56
0.1	27.54	0.012	0.91	0.85	51.79	0.093	0.64	0.53

(b)

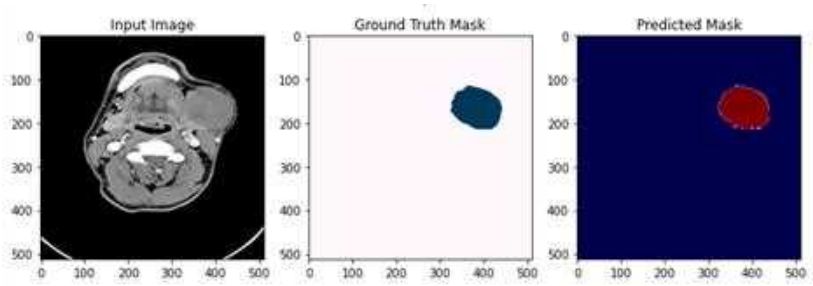
Optimizer	Train HD	Train Loss	Train DSC	Train JI	Test HD	Test Loss	Test DSC	Test JI
RMSprop	3.56	0.004	0.96	0.93	49.17	0.071	0.73	0.62
Adamw	4.22	0.004	0.97	0.94	76.30	0.084	0.70	0.59
Adam	**1.67**	**0.004**	**0.97**	**0.95**	**40.99**	**0.075**	**0.72**	**0.61**
Adamax	1.04	0.002	0.98	0.97	54.96	0.088	0.68	0.57
Rprop	5.30	0.004	0.98	0.95	88.43	0.093	0.66	0.54
RAdam	2.29	0.003	0.97	0.95	53.48	0.074	0.71	0.60

(c)

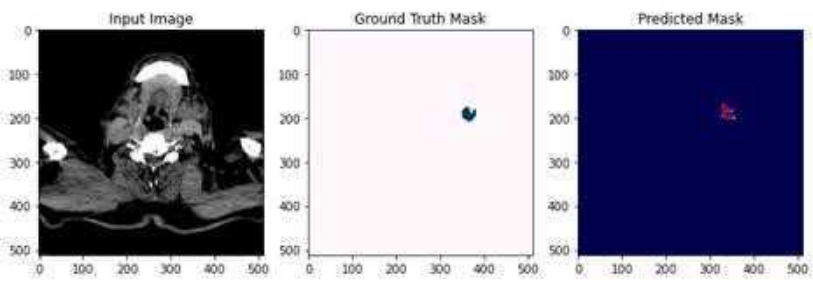
Activation Function	Train HD	Train Loss	Train DSC	Train JI	Test HD	Test Loss	Test DSC	Test JI
ReLU	**1.67**	**0.004**	**0.97**	**0.95**	**40.99**	**0.075**	**0.72**	**0.61**
Leaky ReLU	3.25	0.004	0.97	0.94	52.89	0.077	0.72	0.61
PReLU	13.5	0.008	0.94	0.89	37.58	0.056	0.69	0.59
GELU	4.69	0.006	0.96	0.92	35.82	0.066	0.71	0.61
ELU	9.29	0.008	0.94	0.89	43.59	0.061	0.68	0.58
SELU	7.66	0.009	0.93	0.88	51.00	0.060	0.65	0.54
Hard Swish	1.65	0.004	0.97	0.95	42.05	0.078	0.70	0.60

(d)

Filter Size	Train HD	Train Loss	Train DSC	Train JI	Test HD	Test Loss	Test DSC	Test JI
3x3	1.67	0.004	0.97	0.95	40.99	0.075	0.72	0.61
5x5	9.26	0.009	0.92	0.86	35.38	0.052	0.74	0.63
7x7	4.53	0.008	0.94	0.89	35.75	0.061	0.73	0.62
9x9	**14.15**	**0.001**	**0.89**	**0.83**	**30.18**	**0.044**	**0.75**	**0.64**

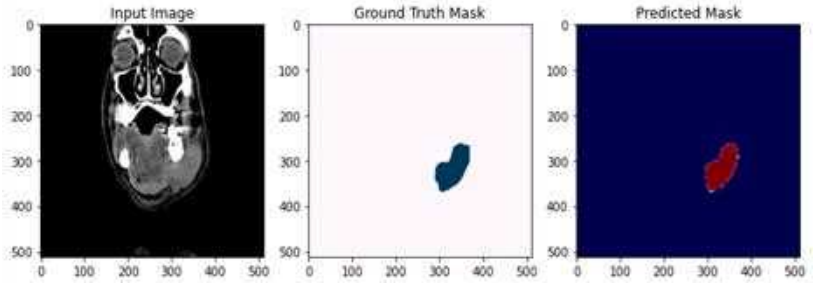


Highest Dice Score: 0.98 Average Hausdorff Distance: 2.06

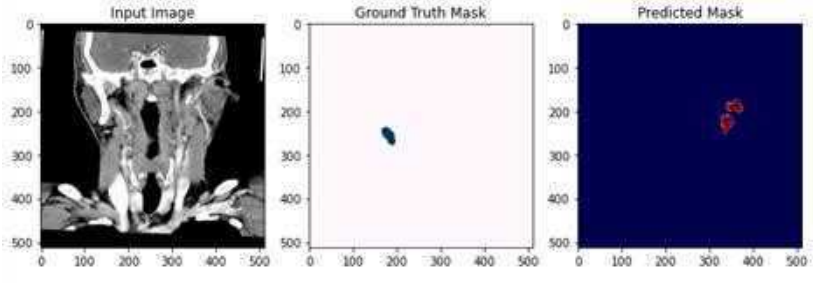


Lowest Dice Score: 0.17 Average Hausdorff Distance: 6.60

Figure 4. The predictions with the highest and lowest DSC in the neck axial images



Highest Dice Score: 0.95 Average Hausdorff Distance: 2.13



Lowest Dice Score: 0.04 Average Hausdorff Distance: 80.85

Figure 5. The predictions with the highest and lowest DSC in the neck coronal images

4. CONCLUSION

In the study, segmentation of lymphoma lesions was performed on neck coronal and neck axial CT images with the U-Net architecture. The U-Net model is widely used in image segmentation tasks due to its unique architecture and proven effectiveness. Its encoder–decoder structure allows the model to capture both low-level spatial features and high-level semantic information, while the skip connections ensure the preservation of fine details that are often lost in deep networks. This design makes U-Net particularly suitable for segmenting objects with irregular shapes and varying sizes. Another advantage is its efficiency; U-Net can achieve accurate results even with relatively small datasets, which is highly valuable in areas such as medical imaging where annotated data is limited. U-Net model has been selected for lymphoma lesion segmentation because our dataset is small. Moreover, the model provides precise localization of structures and demonstrates strong generalization capabilities, making it a reliable and versatile choice for diverse segmentation problems.

The average results obtained from neck coronal images were lower compared to those obtained from neck axial images. This is attributed to the fact that neck coronal images are fewer in number and of lower quality compared to neck axial images, as well as the increased complexity of the regions to be predicted. The model developed for neck axial images achieved an average DSC of 0.830 and an average HD of 15.80 mm in the test results, while the model developed for neck coronal images demonstrated high performance in the test results with an average DSC of 0.75 and an average HD of 30.18 mm.

In conclusion, a model capable of highly accurate detection from computed tomography images obtained from different patients has been proposed. Furthermore, this study demonstrates that deep learning methods can mitigate potential errors and workloads in healthcare applications.

Declaration of Ethical Standards

The authors declare that they have no known competing financial interests or personal relationships that could have appeared to influence the work reported in this paper.

Credit Authorship Contribution Statement

Author 1: Research, Methodology, Software, Writing – original draft, Visualization Author 2: Methodology, Supervision, Validation, Writing, Author 3: Conceptualization, Formal analysis, Writing – Review and Editing. Author 4-9: Data augmentation, labeling, verification, interpretation.

Declaration of Competing Interest

The authors declare that they have no known competing financial interests or personal relationships that could have appeared to influence the work reported in this paper.

Funding / Acknowledgements

The results in this article were obtained in the project titled "Smart Diagnostic System for Lymphoma and Systemic Lupus Erythematosus Diseases with Deep Learning Algorithms", supported within the scope of TÜBİTAK-2209 A University Students Research Projects Support Program.

Data Availability

All data analysed during this study were obtained with permission from the Selçuk University Local Ethics Committee.

Use of Artificial Intelligence

Generative AI tools were used only for language editing and improving readability. The authors are fully responsible for the scientific content, accuracy, and originality of the manuscript.

REFERENCES

[1] E. Özgür, "Lenf kanseri görüntülerinin makine öğrenmesi yöntemleri ile sınıflandırılması", Tekirdağ Namık Kemal Üniversitesi, Tekirdağ, 2022.

[2] J. Yan, B. Zhao, S. Curran, A. Zelenetz, L.H. Schwartz, "Automated matching and segmentation of lymphoma on serial CT examinations", *Medical Physics*, vol. 34, no. 1, pp. 55-62, 2007.

[3] X. Liu, L. Song, S. Liu, Y. Zhang, "A Review of Deep-Learning-Based Medical Image Segmentation Methods", *Sustainability*, vol. 13, no. 3, pp. 1224, 2021.

[4] Q. Chen, F. Quan, J. Xu, and D.L. Rubin, "Snake model-based lymphoma segmentation for sequential CT images", *Computer Methods and Programs in Biomedicine*, vol. 111, no. 2, pp. 366-375, 2013.

[5] E. Grossiord, H. Talbot, N. Passat, L. Najman, "Automated 3D lymphoma lesion segmentation from PET/CT characteristics", IEEE 14th International Symposium on Biomedical Imaging (ISBI 2017). IEEE, 2017.

[6] H. Hu, P. Decazes, P. Vera, H. Li, S. Ruan, "Detection and segmentation of lymphomas in 3D PET images via clustering with entropy-based optimization strategy", *International Journal of Computer Assisted Radiology and Surgery*, vol. 14, no. 10, pp. 1715-1724, 2019.

[7] L. Huang, T. Denœux, D. Tonnelet, P. Decazes, S. Ruan, "Deep PET/CT Fusion with Dempster-Shafer Theory for Lymphoma Segmentation", *Machine Learning in Medical Imaging*, Springer International Publishing, pp. 30-39, 2021.

[8] C. Yuan, M. Zhang, X. Huang, W. Xei, X. Lin, W. Zhao, B. Li, D. Qian, "Diffuse large B-cell lymphoma segmentation in PET-CT images via hybrid learning for feature fusion", *Medical Physics*, vol. 48, no. 7, pp. 3665-3678, 2021.

[9] L. Stahnke, "TransRUnet: 2D Detection and Segmentation of Lymphoma Lesions in Full-Body PET-CT Images", Kth Royal Institute of Technology, Sweden, 2023.

[10] S. Eida, M. Fukuda, I. Katayama, Y. Takagi, M. Sasaki, H. Mori, M. Kawakami, T. Nishino, Y. Ariji, M. Sumi, "Metastatic Lymph Node Detection on Ultrasound Images Using YOLOv7 in Patients with Head and Neck Squamous Cell Carcinoma", *Cancers (Basel)*, vol. 16, no. 2, p. 274, 2024.

[11] G. Fu, L. Nichelli, D. Herran, R. Valabregue, A. Alentorm, K Hoang-Xuan, C. Houillier, D. Dormont, S. Lehericy, O. Colliot, "Comparing foundation models and nnU-Net for segmentation of primary brain lymphoma on clinical routine post-contrast T1-weighted MRI". Medical Imaging 2025: Clinical and Biomedical Imaging, Proc. of SPIE Vol. 13410, 1341019, https://doi.org/10.1117/12.3044679, 2025.

[12] W. Pang, S. Li, H. Jiang, Y. Yao, "MTR-PET: Multi-temporal resolution PET images for lymphoma segmentation", *Biomedical Signal Processing and Control*, vol. 87, p. 105529, 2024.

[13] X. Tie, M. Shin, C. Lee, S.B. Perlman, Z. Huemann, A.J. Weisman, S.M.. Castellino, K.M. Kelly, K.M. McCarten, A.L. Alazraki, J. Hu, S.Y. Cho, T.J. Bradshaw, T. J., "Automatic Quantification of Serial PET/CT Images for Pediatric Hodgkin Lymphoma Patients Using a Longitudinally-Aware Segmentation Network", *ArXiv*, 2024.

[14] Ş.K. Özen, A. Sabah, Y.A. Üncü, M.F. Akşahin, C. Kurtman., "Automated Segmentation of Lung Tomography Images Using the U-Net Model: A Pilot Study". Medical Technologies Congress (TIPTEKNO), pp. 1–4. https://doi.org/10.1109/TIPTEKNO63488.2024.10755411, 2024.

[15] Y. Yuan, Y. Cheng, "Medical image segmentation with UNet-based multi-scale context fusion", *Scientific Reports*, 14, Article 15687, 2024.

[16] J. Qiu, C. Chen, M. Li, J. Hong, B. Dong, S. Xu, Y. Lin, "Attention-enhanced residual U-Net: lymph node segmentation method with bimodal MRI images", *BioMedical Engineering OnLine*, 24, Article 67, 2025.
[17] F. Turk, M. Kılıçaslan, M., "Lung image segmentation with improved U-Net, V-Net and Seg-Net techniques", *PeerJ Computer Science*, , 11, e2700, 2025.
[18] J. Liang, "A systematic comparison of deep learning methods for lymphoma segmentation in PET/CT images", Master Thesis, KTH EECS, 2025.
[19] M.D. Abràmoff, P.J. Magalhães, S.J. Ram, "Image processing with ImageJ", *Biophotonics International*, vol. 11, no. 7, pp. 36-42, 2004.
[20] T. Ferreira, W. Rasband, "ImageJ user guide", *USA: National Institutes of Health*, 2011.
[21] O. Ronneberger, P. Fischer, T. Brox, "U-net: Convolutional networks for biomedical image segmentation", Medical Image Computing and Computer-Assisted Intervention – MICCAI 2015: 18th International Conference, Munich, Germany, October 5-9, 2015, Proceedings, Part III. Springer, pp. 234-241, 2015.
[22] P. Liu, Y. Wei, Q. Wang, Y. Chen, Y, J. Xie, "Research on Post-Earthquake Landslide Extraction Algorithm Based on Improved U-Net Model", *Remote Sens.*, *12*, 894, 2020.
[23] V. Thada, V. Jaglan, "Comparison of jaccard, dice, cosine similarity coefficient to find best fitness value for web retrieved documents using genetic algorithm", *International Journal of Innovations in Engineering and Technology*, 2.4: 202-205, 2013.
[24] M. Beauchemin, K. Thomson, G. Edwards, "On the Hausdorff distance used for the evaluation of segmentation results", *Canadian Journal of Remote Sensing*, 24.1: 3-8, 1998.

Konya Mühendislik Bilimleri Dergisi., c.14, s.2, 599-612, 2026
Konya Journal of Engineering Sciences v.14, n.2, 599-612, 2026
ISSN: 2667-8055 (Electronic)
DOI: 10.36306/konjes.1748736

INVESTIGATION OF Co(II) ADSORPTION ONTO RICE HUSK ASH: KINETICS, ISOTHERMS, AND THERMODYNAMICS

[1,] *Sevgi Polat

[1]*Department of Chemical Engineering, Faculty of Engineering, Marmara University, 34854, İstanbul, Türkiye*
[1]sevgi.polat@marmara.edu.tr

Highlights

- Rice husk ash (RHA) was studied as a sustainable adsorbent for Co(II) removal.
- SEM images revealed morphological changes on RHA after Co(II) ion adsorption.
- Freundlich isotherm and pseudo-second-order kinetics best described the adsorption process.
- Thermodynamic results confirmed spontaneous and endothermic adsorption.

Graphical Abstract

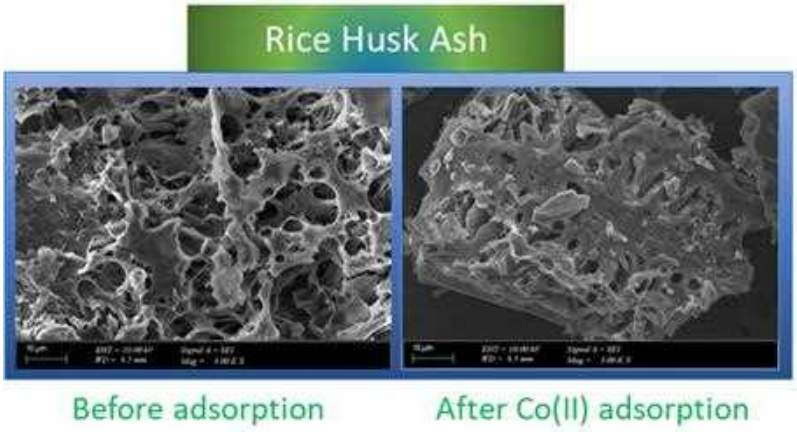


Figure: SEM images of rice husk ash before and after Co(II) adsorption.

***Corresponding Author:** Sevgi POLAT, sevgi.polat@marmara.edu.tr

Konya Mühendislik Bilimleri Dergisi., c.14, s.2, 599-612, 2026
Konya Journal of Engineering Sciences v.14, n.2, 599-612, 2026
ISSN: 2667-8055 (Electronic)
DOI: 10.36306/konjes.1748736

INVESTIGATION OF Co(II) ADSORPTION ONTO RICE HUSK ASH: KINETICS, ISOTHERMS, AND THERMODYNAMICS

[1,*]Sevgi Polat

[1]*Department of Chemical Engineering, Faculty of Engineering, Marmara University, 34854, İstanbul, Türkiye*
[1]sevgi.polat@marmara.edu.tr

(Received: 22.07.2025; Accepted in Revised Form: 07.11.2025)

ABSTRACT: In this study, rice husk ash (RHA), a waste-based and sustainable adsorbent, was evaluated for its efficiency in removing Co(II) ions from aqueous solutions. The physicochemical characteristics of RHA, including surface morphology, elemental composition, and functional groups, were analyzed using scanning electron microscopy–energy-dispersive X-ray spectroscopy (SEM–EDS) and Fourier transform infrared spectroscopy. The experiments were conducted to investigate how variables such as pH, RHA dosage, initial Co(II) concentration, contact time, and temperature affect adsorption efficiency. Among the isotherm models tested, the Freundlich equation provided the most accurate representation of the equilibrium data ($R^2 = 0.9993$ at 20 °C), indicating multilayer adsorption on a non-uniform surface. Kinetic analysis revealed that the pseudo-second-order model best fit the adsorption process ($R^2 = 0.9989$ at 20 °C), suggesting chemisorption as the dominant mechanism. Thermodynamic evaluation confirmed that the adsorption was spontaneous ($\Delta G° < 0$) and endothermic ($\Delta H° = +59.08$ kJ/mol) under the experimental conditions. SEM imaging revealed significant structural modifications in RHA following Co(II) uptake, including reduced pore volume. Overall, the results demonstrate that RHA is a promising, sustainable material for the cost-effective removal of Co(II) from wastewater.

Keywords: *Wastewater Treatment, Adsorption, Cobalt Removal, Rice Husk Ash, Isotherms, Thermodynamics*

1. INTRODUCTION

Heavy metal pollution in water sources has emerged as a major global environmental concern because of their toxicity, persistence in the environment, and resistance to natural degradation. Rapid industrial development, particularly in less developed regions, has caused substantial discharges of metal-contaminated wastewater into water systems. These substances not only threaten aquatic biodiversity but also present serious hazards to human health. Since heavy metals do not undergo biological breakdown and tend to bioaccumulate in organisms, even minimal exposure levels can lead to adverse health effects such as organ damage, hematological disorders, and neurological impairments [1]. Therefore, eliminating these toxic species from wastewater is essential to protect ecosystems and ensure public safety. Among these contaminants, cobalt ions (Co^{2+}) are of particular concern owing to their extensive industrial application and potential to cause severe health problems [2]. Cobalt —while essential in trace amounts— becomes highly toxic when present in excess. High levels of cobalt exposure have been linked to thyroid dysfunction, heart damage, and certain cancers [3,4]. Industries such as super alloy manufacturing, lithium-ion battery production, pigment formulation, and catalysis are key sources of cobalt pollution. Since cobalt can bioaccumulate and enter the food chain, effective remediation strategies are necessary to mitigate its ecological and health risks [4,5]. Although WHO has not yet established a global limit for Co(II) in water, various national agencies have set their own guidelines due to increasing concerns over cobalt toxicity. For example, the US EPA limits cobalt to 50 µg/L in irrigation water, while Romania allows up to 1 mg/L in industrial wastewater discharge [6].

***Corresponding Author:** Sevgi POLAT, sevgi.polat@marmara.edu.tr

To address heavy metal pollution, several conventional methods have been employed such as chemical precipitation, membrane-based filtration, solvent extraction, and electrochemical processes—have been widely used. Despite their effectiveness, these approaches often come with limitations, including elevated operational expenses, production of hazardous sludge, and declining efficiency under fluctuating environmental conditions [4,5,7]. Adsorption emerges as a promising alternative due to its operational simplicity, cost-effectiveness, adaptability across a wide pH range, and potential for adsorbent regeneration [3,8,9]. Adsorption performance is primarily determined by the interactions that occur between the surface of the adsorbent and the metal ions in solution. Generally, two types of mechanisms are involved: physical adsorption and chemisorption [8]. Recently, the use of natural and waste-derived materials as low-cost adsorbents has gained considerable attention. Advances in materials such as hydroxyapatite nanocomposites have demonstrated improved adsorption efficiency and selectivity, while agricultural solid waste-based bionanocomposites offer eco-friendly and sustainable alternatives [10,11]. Among these, rice husk ash (RHA), a byproduct of rice processing and combustion, is regarded as a highly attractive option due to its wide availability, high silica content, and favorable surface properties. Typically containing more than 90% silica along with potassium, calcium, magnesium, and trace metal oxides, RHA shows strong potential for binding metal ions through surface silanol (Si–OH) groups [12-14]. Previous studies have shown that RHA is effective for the adsorption of several heavy metals such as Pb(II), Cd(II), Ni(II), Zn(II), and Cr(VI) under various operating conditions [15-23]. These studies demonstrated that RHA exhibits mesoporous structure, high cation exchange capacity, and good removal efficiency, particularly when optimized for parameters such as pH, contact time, dosage, and temperature [15,17,19]. In particular, RHA has been widely investigated for its adsorption performance in single and binary metal systems, often using kinetic and isotherm models to explain adsorption mechanisms [16,18,20]. Thermodynamic evaluations in the literature have also confirmed the spontaneous and feasible nature of metal ion removal by RHA [17,18]. However, literature on Co(II) removal using unmodified or raw RHA is limited, with most studies primarily focused on other heavy metals or using chemically treated adsorbents. Moreover, comprehensive studies investigating the adsorption behavior of Co(II) ions on RHA—including equilibrium modeling, adsorption kinetics, thermodynamics, and optimization of process variables—are notably limited. Considering the increasing industrial use of cobalt and its associated environmental risks, this gap in literature presents a critical opportunity for further research. This study contributes to the current body of knowledge by systematically evaluating the potential of raw rice husk ash as a low-cost and effective adsorbent for Co(II) removal from aqueous solutions. Unlike most prior works that focused on multi-metal systems or surface-modified RHA, this study provides a detailed parametric analysis specifically for Co(II) adsorption, supported by kinetic, isotherm, and thermodynamic modeling. The results aim to demonstrate that even without chemical modification, RHA can serve as a viable, sustainable solution for cobalt-contaminated wastewater treatment.

2. MATERIAL AND METHODS

2.1. Batch adsorption experiments

Analytical reagent-grade chemicals procured from Merck Chemicals were utilized throughout the experiments. Cobalt nitrate hexahydrate [$Co(NO_3)_2.6H_2O$, CAS Number: 10026-22-9] with a purity of 99.9% was used to prepare the Co(II) solution. Sodium hydroxide (NaOH) and hydrochloric acid (HCl), both of analytical grade, were used for pH adjustments. Double deionized water was used for all solutions. The adsorbent used in this study was rice hull ash (RHA), which was obtained from a local rice processing facility. The experiments were carried out using 50 mL of the prepared Co(II) solutions. The effects of key operational parameters—namely initial metal ion concentration, contact time, temperature, adsorbent dosage, and pH —were systematically investigated to evaluate their influence on Co(II) removal efficiency. After the adsorption process, the solid adsorbent was separated by filtration. The remaining Co(II) ion concentration in the filtrate was measured by means of Atomic Absorption Spectroscopy (AAS).

The amount of heavy metal adsorbed per unit mass of the adsorbent (q_e) was calculated by using the

following mass balance equation [24],

$$q_e = \frac{(C_i - C_e) \times V}{W} \quad (1)$$

and the adsorption percentage of the metal ion was calculated as follows:

$$Adsorption(\%) = \frac{(C_i - C_e)}{C_i} \times 100 \quad (2)$$

where *Ci* is the initial metal concentration (mg/L), *Ce* is the equilibrium concentration of metal solution (mg/L), *V* is the volume of solution (L), and *W* is the mass of adsorbent (g).

2.2. Equilibrium Modeling

The Langmuir isotherm assumes monolayer adsorption of adsorbate molecules onto a uniform surface with a finite number of non-interacting active sites. Its simplicity and predictive accuracy have contributed to its widespread use in adsorption studies [25,26]. In contrast, the Freundlich isotherm describes adsorption on heterogeneous surfaces where the binding energy varies across different sites, reflecting a decrease in site affinity as surface coverage increases [25–27]. The Temkin isotherm accounts for adsorbent–adsorbate interactions, suggesting that the heat of adsorption decreases gradually with increasing surface coverage. It further assumes that the binding energy is uniformly distributed up to a certain level of surface coverage [28,29]. The mathematical expressions and linearized forms of each model are summarized in Table 1.

Table 1. Adsorption isotherm models and their linearized forms.

Model Name	Linear Form of the Equations	Parameters
Langmuir	$\frac{1}{q_e} = \frac{1}{q_m K_L C_e} + \frac{1}{q_m}$	q_e (mg/g): Amount of metal ion adsorbed at equilibrium q_m (mg/g): Complete monolayer adsorption capacity C_e (mg/L): Equilibrium concentration K_L (L/mg): Langmuir adsorption constant
Freundlich	$\ln q_e = \ln K_F + \frac{1}{n} \ln C_e$	n: Heterogenity factor indicating adsorption intensity K_F ((mg/g)(L/mg)$^{1/n}$): Freundlich adsorption constant
Temkin	$q_e = B \ln K_T + B \ln C_e$ $B = \frac{RT}{b_T}$	b_T (J/mol): Temkin constant related to the heat of adsorption K_T (L/mg): Temkin constant related to the binding energy

2.3. Kinetic Modeling

The adsorption kinetics were analyzed using the pseudo-first-order (PFO) and pseudo-second-order (PSO) models to elucidate the mechanism and identify the rate-limiting steps. Proposed by Lagergren, the PFO model assumes that the adsorption rate is proportional to the number of vacant adsorption sites and is generally suitable for describing the initial stage of adsorption [30]. In contrast, the PSO model, which considers chemisorption as the rate-controlling mechanism, often provides a better fit to the overall kinetic data, particularly when chemical bonding dominates [31-33]. The mathematical expressions and linearized forms of the kinetic models are summarized in Table 2.

Table 2. Adsorption kinetic models and their linearized forms.

Model Name	Linear Form of the Equations	Parameters
PFO	$\log(q_e - q_t) = \log q_e - \frac{k_1 t}{2.303}$	q_e (mg/g): the adsorption capacity at equilibrium q_t (mg/g): the adsorption capacity at time *t* k_1 (1/min): the rate constant of PFO adsorption
PSO	$\frac{t}{q_t} = \frac{1}{k_2 q_e^2} + \frac{t}{q_e}$	q_t (mg/g): the adsorption capacity at time *t* k_2 (g/mg.min): the rate constant of PSO adsorption

2.4. Thermodynamic Modeling

Thermodynamic parameters are essential for evaluating the direction, feasibility, and nature of adsorption processes. In engineering practice, evaluating parameters like enthalpy ($\Delta H°$), entropy ($\Delta S°$), and Gibbs free energy ($\Delta G°$) is fundamental for determining the spontaneity and thermal characteristics of adsorption systems. The parameters were determined using the corresponding mathematical expressions, including the enthalpy–entropy relation (Eq. 3), the Gibbs free energy equation (Eq. 4), and the Van't Hoff equation (Eq. 5) [34,35].

$$\Delta H^\circ = \Delta G^\circ + T\Delta S^\circ \quad (3)$$

$$\Delta G^\circ = -RTlnK_L \quad (4)$$

$$\ln K_L = -\frac{\Delta G^\circ}{RT} = -\frac{\Delta H^\circ}{RT} + \frac{\Delta S^\circ}{R} \quad (5)$$

2.5. Characterization

In this study, RHA was employed as an adsorbent and characterized in terms of its morphological properties. SEM–EDS was utilized to examine the morphology and elemental composition of the RHA. The corresponding SEM image and EDS spectrum are presented in Fig. 1a and Fig. 1b, respectively. SEM images demonstrated that RHA has an irregular, porous texture, which is beneficial for metal ion uptake due to increased surface area and improved diffusion conditions. EDS results confirmed silica (SiO_2) as the main component of RHA, indicated by strong Si and O signals.

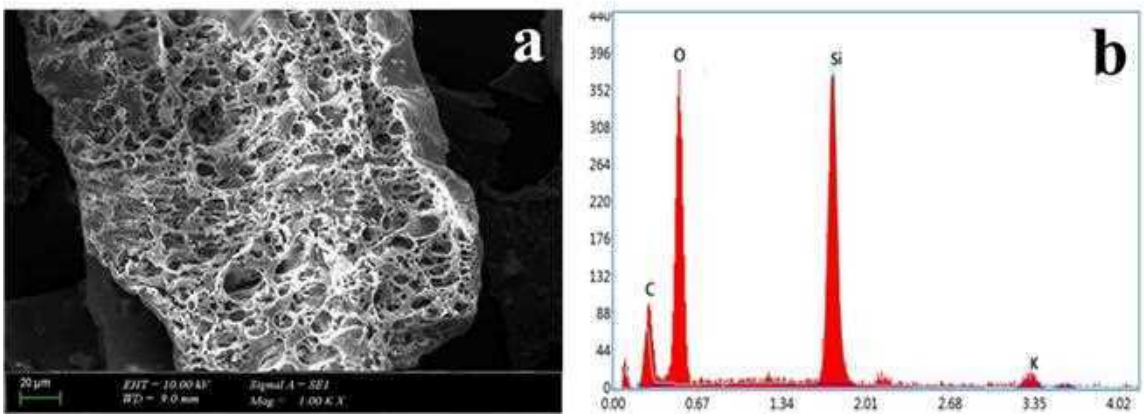


Figure 1. (a) SEM image of rice husk ash and (b) its corresponding EDS result.

3. RESULTS AND DISCUSSION

3.1. Effect of pH and adsorbent dosage

The pH of the solution has a significant role in regulating the adsorption behavior of metal ions by altering both the adsorbent's surface charge and the chemical form of the metal ions in solution. These alterations impact the strength of electrostatic interactions occurring between metal ions and the surface of the adsorbent. In this investigation, the influence of pH on Co(II) ion uptake was assessed within a pH range of 2 to 8 (Fig. 2a). An upward trend in the adsorption capacity of rice husk ash for Co(II) was observed with increasing pH, reaching a maximum value of 31.80 mg/g at pH 6.0.

The study investigated how changing the RHA dosage between 1 and 10 g/L affected the removal efficiency of Co(II) (Fig. 2b). Generally, increasing the adsorbent quantity improved removal performance, likely due to the availability of more active adsorption sites [36-38]. The best performance was achieved at a dosage of 4 g/L, with a peak removal efficiency of 39.5%. Even at lower dosages, Co^{2+} ions were adsorbed effectively, which may be explained by stronger interactions with the RHA surface. Therefore, a pH value of 6.0 and an adsorbent dosage of 4 g/L were selected for subsequent adsorption experiments.

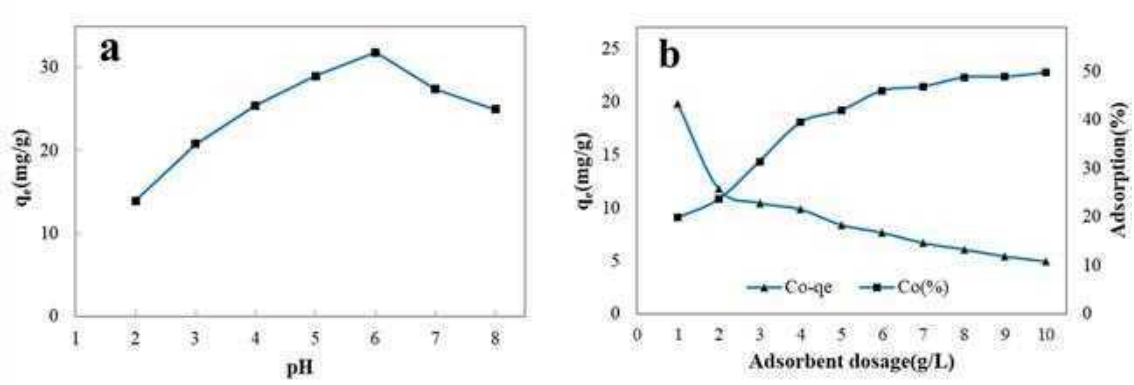


Figure 2. Variation in the adsorption capacity of rice husk ash for Co(II) ions as a function of (a) pH and (b) adsorbent dosage.

3.2. Influence of Initial Co(II) Concentration, Time, and Temperature on Adsorption Behavior

The study explored the influence of initial Co(II) levels (50–150 mg/L), contact time (0–240 minutes), and temperature (20–40 °C) on RHA's adsorption efficiency under optimal pH and dosage conditions. Fig. 3 presents the adsorption behavior as a function of temperature. As shown in Fig. 3, the adsorption behavior of Co(II) followed a two-phase pattern: a rapid initial uptake attributed to the abundant active sites on the RHA surface, followed by a slower phase as these sites became increasingly occupied, reaching equilibrium within about 150 minutes. Temperature was found to significantly influence the efficiency of the adsorption process.

The adsorption capacity increased as the temperature rose from 20 °C to 40 °C. At 40 °C, the maximum Co(II) adsorption reached 21.27 mg/g, particularly at an initial concentration of 150 mg/L. This enhancement can be attributed to the increased kinetic energy and mobility of Co^{2+} ions under elevated temperatures. This condition contributes to more effective interactions between Co(II) and the functional groups on the adsorbent's surface, along with faster diffusion rates. Overall, the results highlight the important roles of both the initial Co(II) concentration and temperature in governing adsorption performance. Elevated concentrations increase the driving force for mass transfer, while higher temperatures promote faster diffusion and stronger adsorbate-adsorbent interactions, ultimately boosting adsorption efficiency [39].

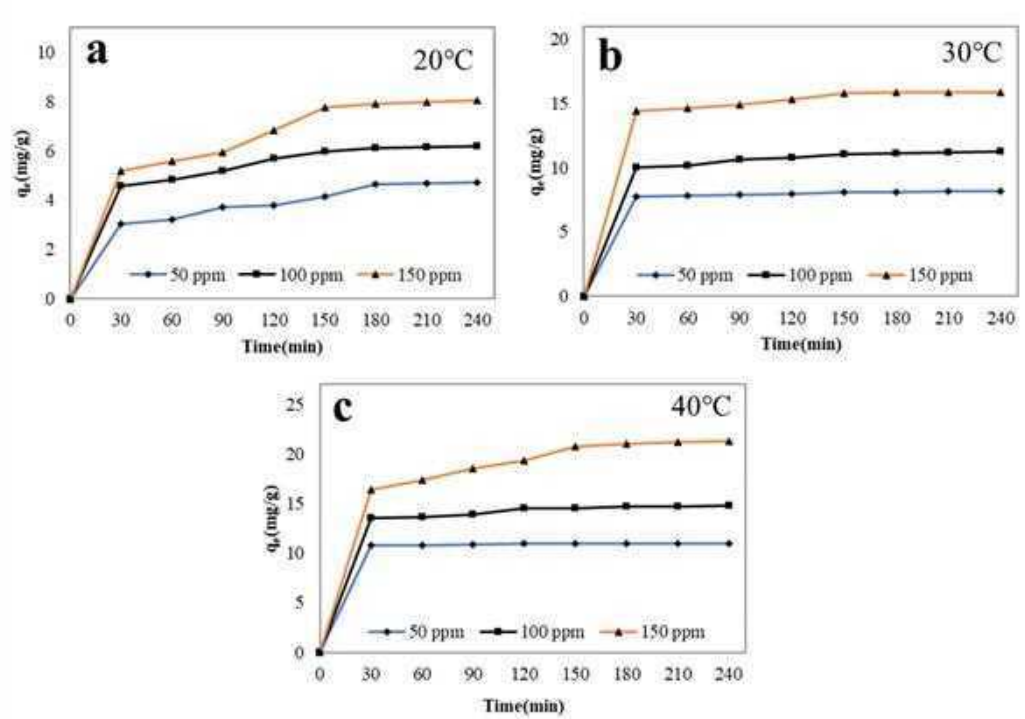


Figure 3. Adsorption behavior of rice husk ash toward Co(II) ions under varying initial concentrations and contact time at temperatures of (a) 20 °C, (b) 30 °C, and (c) 40 °C.

3.3. Adsorption isotherms

The adsorption equilibrium data for Co(II) onto RHA were analyzed using the Langmuir, Freundlich, and Temkin isotherm models. The results are given in Table 3. Among the models tested, the Freundlich isotherm provided the best fit to the experimental data at all temperatures, as indicated by the highest correlation coefficients (R^2 = 0.9993, 0.9962, and 0.9939 at 20, 30, and 40 °C, respectively). This strong fit suggests that Co(II) adsorption onto RHA occurs on a heterogeneous surface and follows a multilayer adsorption mechanism. The Freundlich constant n, which reflects adsorption intensity, was found to be greater than 1 for all temperatures (n = 2.742–5.382), indicating favorable adsorption conditions [40-42]. Additionally, the increasing K_F values with temperature (from 1.178 to 7.643) suggest enhanced adsorption affinity and capacity at elevated temperatures. A satisfactory correlation was observed with the Langmuir model, especially at 30 °C, where R^2 ranged from 0.9713 to 0.9808. The q_m values increased with temperature—from 8.540 mg/g at 20 °C to 20.619 mg/g at 40 °C—confirming the endothermic nature of the adsorption. Furthermore, the R_L values (0.1111–0.1865) across the temperature range remained between 0 and 1, indicating that Co(II) adsorption is favorable under all tested conditions. The Temkin model showed lower R^2 values (0.8760–0.9205) than the other models, but still contributed to the understanding of the adsorption energetics. The binding energy parameter b and the Temkin constants (β and K_T) varied with temperature, further supporting the conclusion that the interaction between Co(II) ions and RHA is temperature-sensitive and involves moderate adsorption energies. In summary, the isotherm analysis confirms that Co(II) adsorption onto RHA is heterogeneous, multilayer, and thermodynamically favorable. The Freundlich model best describes the equilibrium behavior, while both the Langmuir and Temkin models support the observed enhancement of adsorption with increasing temperature.

Table 3. Isotherm model parameters for Langmuir, Freundlich, and Temkin equations.

Parameters	20 °C	30 °C	40 °C
Langmuir			
q_m	8.540	18.282	20.619
K_L	0.0800	0.0436	0.0532
R^2	0.9713	0.9808	0.9797
R_L	0.1111	0.1865	0.1580
Freundlich			
n	2.742	3.140	5.382
K_F	1.178	3.103	7.643
R^2	0.9993	0.9962	0.9939
Temkin			
β	1.8542	3.3558	2.7014
K_T	0.3064	0.4640	7.9020
b	1313	708	963
R^2	0.8860	0.9205	0.8760

In addition, Fig. 4 illustrates the morphological and elemental changes observed in RHA before and after Co(II) adsorption. After adsorption, the surface exhibits partial pore blockage and particle agglomeration, suggesting that metal ions have effectively bound to the adsorbent surface. Correspondingly, the EDS spectrum clearly shows the appearance of a characteristic Co peak, confirming the presence of cobalt on the adsorbent surface. This morphological and elemental evidence strongly support the effectiveness of the Co(II) adsorption process, as also validated by the isotherm modeling. Additionally, the functional groups present in the RHA were characterized using an FTIR spectrometer (IR Affinity-1, Shimadzu). The spectrum was recorded over the range of 4000–600 cm^{-1} at ambient temperature and is shown in Fig. 5. The 3400–3600 cm^{-1} region showed very weak bands a ributed to O–H stretching vibrations of adsorbed water or surface hydroxyl groups, while weak bands around 1630–1645 cm^{-1} corresponded to H–O–H bending vibrations. Two prominent absorption bands were observed at approximately 1041 cm^{-1} and 788 cm^{-1}, which correspond to the asymmetric stretching vibrations of Si–O–Si and symmetric bending vibrations of Si–O bonds, respectively. These spectral features suggest the presence of a silica-rich structure, confirming the dominance of amorphous silica in RHA. The results agree with previously reported findings in the literature [43,44]. Additionally, the FTIR spectrum obtained after Co(II) ion adsorption was analyzed and compared with that of raw RHA. Although similar characteristic peaks were observed, noticeable shifts in the peak positions were detected. These spectral shifts indicate possible molecular interactions between Co^{2+} ions and the functional groups on the RHA surface, suggesting successful adsorption.

To further understand the adsorption mechanism, zeta potential measurements were carried out at pH 6 before and after Co(II) ion adsorption. The zeta potential of raw RHA was measured as −19.8 ± 2.4 mV, indicating a negatively charged surface in aqueous medium, which facilitates the electrostatic attraction of positively charged Co^{2+} ions. Similar surface charges for RHA have been reported in the literature; for example, a zeta potential value of approximately −10 ± 1.0 mV was observed [45]. After adsorption, the zeta potential increased to −4.3 ± 1.3 mV, suggesting partial neutralization of surface charges due to Co(II) binding. This shift supports the occurrence of surface interactions during the adsorption process.

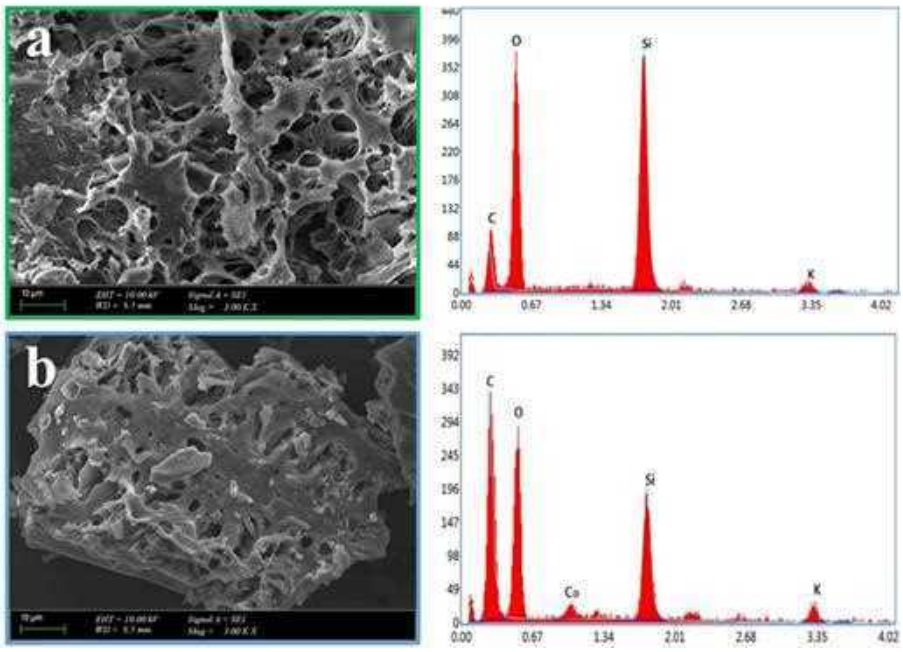


Figure 4. SEM-EDS analysis results of rice husk ash: (a) before adsorption, (b) after Co(II) adsorption.

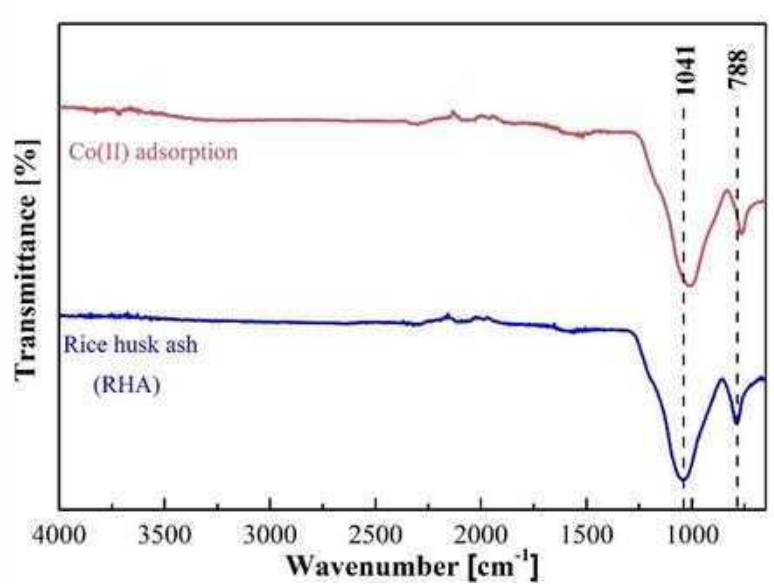


Figure 5. FTIR spectra of rice husk ash before and after Co(II) adsorption.

3.4. Adsorption kinetics

Understanding the kinetics of an adsorption process is essential for evaluating the rate of adsorption, the efficiency of the adsorbent, and the underlying adsorption mechanism. In this study, the kinetics of Co(II) adsorption onto RHA were investigated using two commonly used kinetic models: PFO and PSO. Among the two models, the PSO model provided a significantly better fit to the experimental data across all tested temperatures (20–40 °C), as shown in Table 4. High R^2 values—0.9989, 0.9975, and 0.9942 at 20, 30, and 40 °C—highlighted the PSO model's excellent fit with experimental results. In contrast, the PFO

model yielded much lower R^2 values, ranging from 0.9052 to 0.9144, indicating a poor fit to the experimental data. The strong fit of the PSO model indicates that chemisorption is the dominant mechanism in the adsorption process, likely involving valence interactions through electron exchange or sharing between Co(II) ions and reactive groups on the RHA surface. Additionally, equilibrium adsorption capacity (q_e), as predicted by the PSO model, increased with rising temperature—from 8.676 mg/g at 20 °C to 10.309 mg/g at 40 °C. This trend suggests that higher temperatures improve the interaction between RHA and Co(II) ions, further confirming the endothermic behavior of the process as supported by thermodynamic evaluation. Overall, kinetic modeling indicates that Co(II) adsorption onto RHA follows a pseudo-second-order mechanism, in which chemisorption is the rate-limiting step, and adsorption capacity increases with elevated temperatures. The positive influence of temperature observed here is consistent with results obtained from isotherm analyses.

Table 4. Kinetic parameters obtained at various temperatures.

Parameters	20 °C	30 °C	40 °C
Pseudo-first-order			
q_e	1.865	2.014	7.151
k_1	0.0138	0.0138	0.0322
R^2	0.9052	0.9144	0.9123
Pseudo-second-order			
q_e	8.676	8.938	10.309
k_2	0.0209	0.0183	0.0093
R^2	0.9989	0.9975	0.9942

3.5. Adsorption thermodynamics

Thermodynamic analysis offers critical insight into the feasibility, spontaneity, and energetic nature of the adsorption process. An enthalpy value of +59.08 kJ mol^{-1} reveals that Co(II) adsorption on RHA is endothermic, requiring heat to occur. This is consistent with experimental observations, which showed an increase in Co(II) uptake with rising temperature (Fig. 3). The enhancement in adsorption at elevated temperatures suggests that greater thermal energy facilitates more effective interactions between Co(II) ions and the active sites on the RHA surface. The $\Delta S° = -180.34$ J/mol.K^- suggests a reduction in disorder at the solid–liquid boundary, which is likely attributed to the more structured alignment of metal ions on the adsorbent surface during the adsorption process. In addition, $\Delta G°$ was consistently negative across all tested temperatures, indicating that the adsorption occurred spontaneously and was thermodynamically favorable under the given experimental conditions. In summary, the thermodynamic parameters reveal that Co(II) adsorption onto RHA is a spontaneous and endothermic process, accompanied by a decrease in interfacial disorder.

4. CONCLUSIONS

This study demonstrated the effectiveness of raw rice husk ash (RHA), a low-cost and sustainable adsorbent, in removing Co(II) ions from aqueous solutions across various operating conditions. The adsorption process was significantly influenced by pH, initial metal concentration, adsorbent dosage, contact time, and temperature. Under optimal conditions (pH 6.0, 4 g/L dosage), a removal efficiency of 39.5% was achieved. SEM analysis confirmed the porous, irregular structure of RHA, while post-adsorption imaging and EDS analysis revealed successful Co(II) uptake via surface interactions. Equilibrium data were best described by the Freundlich isotherm model ($R^2 = 0.9993$ at 20 °C), indicating multilayer adsorption on a heterogeneous surface. Kinetic modeling showed that the pseudo-second-

order model ($R^2 = 0.9989$) most accurately captured the adsorption mechanism, suggesting chemisorption as the dominant pathway. The Freundlich constant n ranged between 2.742 and 5.382, indicating favorable adsorption conditions. Thermodynamic analysis ($\Delta H° = +59.08$ kJ/mol, $\Delta G° < 0$) confirmed the spontaneous and endothermic nature of the process.

Overall, this work not only supports the feasibility of using unmodified RHA for cobalt removal but also contributes valuable kinetic, isotherm, and thermodynamic data to the literature on low-cost adsorbents. Based on these findings, future studies may focus on enhancing the adsorption capacity of RHA through surface modifications, evaluating its performance in continuous-flow or real wastewater systems, and exploring regeneration strategies to support large-scale, long-term applications in sustainable wastewater treatment.

Declaration of Ethical Standards

The author of this article declares that the materials and methods used in this study do not require ethical committee permission and/or legal-special permission.

Credit Authorship Contribution Statement

Author: Writing – review & editing, Writing – original draft, Visualization, Methodology, Investigation, Conceptualization.

Declaration of Competing Interest

The author declares no conflict of interest

Data Availability

Data will be made available on request.

Use of Artificial Intelligence

No generative artificial intelligence (AI) tools were used in preparing, analyzing, interpreting, or presenting the scientific data and conclusions in this manuscript. AI was employed exclusively to assist with English language editing.

5. REFERENCES

[1] J. Briffa, E. Sinagra, and R. Blundell, "Heavy metal pollution in the environment and their toxicological effects on humans", *Heliyon*, vol. 6, no. 9, p. e04691, 2020, doi: 10.1016/j.heliyon.2020.e04691.

[2] K. O. Amoo, T. E. Amoo, O. A. Olafadehan, E. E. Alagbe, A. J. Adesina, M. O. Bamigboye, B. D. Olowookere, and K. D. Ajayi, "Adsorption of cobalt (II) ions from aqueous solution using cow bone and its derivatives: Kinetics, equilibrium and thermodynamic comparative studies", *Results Eng.*, vol. 20, p. 101635, 2023, doi: 10.1016/j.rineng.2023.101635.

[3] Y. Altunkaynak, M. Canpolat, and Ö. Yavuz, "Adsorption of cobalt (II) ions from aqueous solution using orange peel waste: Equilibrium, kinetic and thermodynamic studies", *J. Iran. Chem. Soc.*, vol. 19, pp. 2437–2448, 2021, doi: 10.1007/s13738-021-02458-8.

[4] S. Vilvanathan and S. Shanthakumar, "Biosorption of Co(II) ions from aqueous solution using Chrysanthemum indicum: Kinetics, equilibrium and thermodynamics", *Process Saf. Environ. Prot.*, vol. 96, pp. 98–110, 2015, doi: 10.1016/j.psep.2015.05.001.

[5] A. E. Burakov, E. V. Galunin, I. V. Burakova, A. A. Kucherova, S. Agarwal, A. G. Tkachev, and V. K. Gupta, "Adsorption of heavy metals on conventional and nanostructured materials for wastewater treatment purposes: A review", *Ecotoxicol. Environ. Saf.*, vol. 148, pp. 702–712, 2018, doi: 10.1016/j.ecoenv.2017.11.034.

[6] T. Dobre, G. O. Isopencu, S. Bdaiwi Ahmed, and I. M. Deleanu, "Heavy metal pollution and solutions for its control: General aspects with a focus on cobalt removal and recovery from aqueous systems", *ChemEngineering*, vol. 8, no. 6, pp. 118, 2024, doi: 10.3390/chemengineering8060118.

[7] S. Bai, T. E. Abraham, "Biosorption of Cr (VI) from aqueous solution by *Rhizopus nigricans*", *Bioresour. Technol*., vol. 79, pp. 73–81, 2001, doi: 10.1016/s0960-8524(00)00107-3.

[8] Z. Raji, A. Karim, A. Karam, and S. Khalloufi, "Adsorption of heavy metals: Mechanisms, kinetics, and applications of various adsorbents in wastewater remediation—A review", *Waste*, vol. 1, pp. 775–805, 2023, doi: 10.3390/waste1030046.

[9] J. Ma, S. Z. Zuo-Jiang, Y. He, Q. Sun, Y. Wang, W. Liu, S. Sun, K. Chen, "A facile, versatile approach to hydroxyl-anchored metal oxides with high Cr(VI) adsorption performance in water treatment", *R. Soc. Open Sci.*, vol. 3, p. 160524, 2016, doi: 10.1098/rsos.160524.

[10] Y. Miyah, N. El Messaoudi, M. Benjelloun, Y. Acikbas, Z. M. Şenol, Z. Ciğeroğlu, and E. A. Lopez-Maldonado, "Advanced applications of hydroxyapatite nanocomposite materials for heavy metals and organic pollutants removal by adsorption and photocatalytic degradation: A review", *Chemosphere*, vol. 358, p. 142236, 2024, doi: 10.1016/j.chemosphere.2024.142236.

[11] N. El Messaoudi, Y. Miyah, Z. M. Şenol, Z. Ciğeroğlu, E. S. Kazan-Kaya, S. Gubernat, J. Georgin, and D. S. P. Franco, "Comprehensive analytical review of heavy metal removal efficiency using agricultural solid waste-based bionanocomposites", *Nano-Structures & Nano-Objects*, vol. 38, p. 101220, 2024, doi: 10.1016/j.nanoso.2024.101220.

[12] M. Ahmaruzzaman and V. K. Gupta, "Rice husk and its ash as low-cost adsorbents in water and wastewater treatment", *Ind. Eng. Chem. Res*., vol. 50, pp. 13589–13613, 2011, doi: 10.1021/ie201477c.

[13] M. R. Kumalasari, S.U.M. Beladona, A. N. Gracia, T. Sugiyani, O. R. Wulandari, M. Imelya, H. Syaima, Q. A. Hanif, "Rice husk ash: A promising heavy metal adsorbent for wastewater treatment", *Walisongo J. Chem*., vol. 7, pp. 26–36, 2024, doi: 10.21580/wjc.v7i1.18852.

[14] T. A. Nguyen, P. T. Phan, N. H. Nguyen, and T. T. Nguyen, "Rice husk ash as a great potential adsorbent in multi-purpose adsorption of various pollutants: A review", *Egypt. J. Chem.,* vol. 66, pp. 1–14, 2023, doi: 10.21608/ejchem.2023.48496.3011.

[15] V. C. Srivastava, I. D. Mall, and I. M. Mishra, "Characterization of mesoporous rice husk ash (RHA) and adsorption kinetics of metal ions from aqueous solution onto RHA", *J. Hazard. Mater.,* vol. 134, pp. 257–267, 2006, doi: 10.1016/j.jhazmat.2005.11.052.

[16] V. C. Srivastava, I. D. Mall, and I. M. Mishra, "Adsorption thermodynamics and isosteric heat of adsorption of toxic metal ions onto bagasse fly ash (BFA) and rice husk ash (RHA)", *Chem. Eng. J.*, vol. 132, pp. 267–278, 2007, doi: 10.1016/j.cej.2007.01.007.

[17] T. K. Naiya, A. K. Bhattacharya, S. Mandal, and S. K. Das, "The sorption of lead(II) ions on rice husk ash", *J. Hazard. Mater.*, vol. 163, pp. 1254–1264, 2009, doi: 10.1016/j.jhazmat.2008.07.119.

[18] V. C. Srivastava, I. D. Mall, and I. M. Mishra, "Removal of cadmium(II) and zinc(II) metal ions from binary aqueous solution by rice husk ash", *Colloids Surf. A Physicochem. Eng. Asp.*, vol. 312, pp. 172–184, 2008, doi: 10.1016/j.colsurfa.2007.06.048.

[19] V. C. Srivastava, I. D. Mall, and I. M. Mishra, "Optimization of parameters for adsorption of metal ions onto rice husk ash using Taguchi's experimental design methodology", *Chem. Eng. J.*, vol. 140, pp. 136–144, 2008, doi: 10.1016/j.cej.2007.09.030.

[20] V. C. Srivastava, I. D. Mall, and I. M. Mishra, "Competitive adsorption of cadmium(II) and nickel(II) metal ions from aqueous solution onto rice husk ash", *Chem. Eng. Process.*, vol. 48, pp. 370–379, 2009, doi: 10.1016/j.cep.2008.05.001.

[21] Q. Feng, Q. Lin, F. Gong, S. Sugita, and M. Shoya, "Adsorption of lead and mercury by rice husk ash", *J. Colloid Interface Sci.*, vol. 278, pp. 1–8, 2004, doi: 10.1016/j.jcis.2004.05.030.

[22] L.-H. Wang and C.-I. Lin, "Adsorption of Lead(II) Ion from Aqueous Solution Using Rice Hull Ash", *Ind. Eng. Chem. Res.*, vol. 47, pp. 4891–4897, 2008, doi: 10.1021/ie071521z.

[23] A. K. Priya, V. Yogeshwaran, S. Rajendran, T. K. A. Hoang, M. Soto-Moscoso, A. A. Ghfar, and C. Bathula, "Investigation of mechanism of heavy metals (Cr^{6+}, Pb^{2+} & Zn^{2+}) adsorption from aqueous medium using rice husk ash: Kinetic and thermodynamic approach", *Chemosphere*, vol. 286, p. 131796, 2022, doi: 10.1016/j.chemosphere.2021.131796.

[24] E. Akceylan, S. Erdemir, E. Özçelik, and B. Tabakcı, "Removal of Some Phenolic Pollutions from Aqueous Solutions by Magnetic Nanoparticles Containing Imidazole-Derivatized Calix[4]arene", *Konya J. Eng. Sci.*, vol. 9, pp. 442–454, 2021, doi: 10.36306/konjes.856969.

[25] K. Li and X. Wang, "Adsorptive removal of Pb(II) by activated carbon prepared from Spartina alterniflora: Equilibrium, kinetics and thermodynamics", Bioresour. *Technol.*, vol. 100, pp. 2810–2815, 2009, doi: 10.1016/j.biortech.2008.12.032.

[26] M. A. Al-Ghouti and D. A. Da'ana, "Guidelines for the use and interpretation of adsorption isotherm models: A review", *J. Hazard. Mater.*, vol. 393, p. 122383, 2020, doi: 10.1016/j.jhazmat.2020.122383.

[27] N. Ayawei, A. N. Ebelegi, and D. Wankasi, "Modelling and interpretation of adsorption isotherms", *J. Chem.*, vol. 2017, pp. 1–11, 2017, doi: 10.1155/2017/3039817.

[28] M. S. Mohy Eldin, K. M. Aly, Z. A. Khan, A. E. M. Mekky, T. S. Saleh, and A. S. Al-Bogami, "Removal of methylene blue from synthetic aqueous solutions with novel phosphoric acid-doped pyrazole-g-poly(glycidyl methacrylate) particles: Kinetic and equilibrium studies", *Desalin. Water Treat.*, vol. 57, pp. 27243–27258, 2016, doi: 10.1080/19443994.2016.1171168.

[29] C. Djelloul, A. Hasseine, and O. Hamdaoui, "Adsorption of cationic dye from aqueous solution by milk thistle seeds: Isotherm, kinetic and thermodynamic studies", *Desalin. Water Treat.*, vol. 78, pp. 313–320, 2017, doi: 10.5004/dwt.2017.20920.

[30] K. G. Bhattacharyya and A. Sharma, "Adsorption of Pb(II) from aqueous solution by *Azadirachta*

indica (Neem) leaf powder", *J. Hazard. Mater*., vol. 113, pp. 97–109, 2004, doi: 10.1016/j.jhazmat.2004.05.034.

[31] A. N. Ebelegi, N. Ayawei, and D. Wankasi, "Interpretation of adsorption thermodynamics and kinetics", *Open J. Phys. Chem*., vol. 10, pp. 166–182, 2020, doi: 10.4236/ojpc.2020.103010.

[32] U. Khalil, M. B. Shakoor, S. Ali, S. R. Ahmad, M. Rizwan, A. A. Alsahli, and M. N. Alyemeni, "Selective removal of hexavalent chromium from wastewater by rice husk: Kinetic, isotherm and spectroscopic investigation", Water, vol. 13, no. 3, p. 263, 2021, doi: 10.3390/w13030263.

[33] İ. Küçük and H. Biçici, "Adsorption of malachite green into potato peel: Nonlinear isotherm and kinetic". *Konya J. Eng. Sci., vol. 12, pp. 150-161, 2024,* doi: 10.36306/konjes.1379888.

[34] S. Roy and M. Ahmaruzzaman, "Ionic liquid based composites: A versatile materials for remediation of aqueous environmental contaminants," *J. Environ. Manage.*, vol. 315, p. 115089, 2022. doi: 10.1016/j.jenvman.2022.115089.

[35] X. Zhou, X. Yu, R. Maimaitiniyazi, X. Zhang, and Q. Qu, "Discussion on the thermodynamic calculation and adsorption spontaneity re Ofudje et al. (2023)," *Heliyon*, vol. 10, no. 8, p. e28188, 2024, doi: 10.1016/j.heliyon.2024.e28188.

[36] S. Zafar, M. I. Khan, W. Hassan, S. Mubeen, T. Javed, S. Shahida, S. Manzoor, A. Shanableh, A. Rehman, M. L. Mirza, N. Khalid, M. H. Lashari, "Application of NaOH-treated rice husk for adsorptive discharge of cobalt ions from wastewater," *Desalin. Water Treat.*, vol. 226, pp. 328–338, 2021, doi: 10.5004/dwt.2021.27286.

[37] S. Zafar, M. I. Khan, H. ur Rehman, J. Fernandez-Garcia, S. Shahida, P. Prapamonthong, M. Khraisheh, A. Rehman, H. B. Ahmadi, M. L. Mirza, N. Khalid, M. H. Lashari, "Kinetic, equilibrium, and thermodynamic studies for adsorptive removal of cobalt ions by rice husk from aqueous solution," *Desalin. Water Treat.*, vol. 204, pp. 285–296, 2020, doi: 10.5004/dwt.2020.26270

[38] R. Wang, L. Deng, X. Fan, K. Li, H. Lu, and W. Li, "Removal of heavy metal ion cobalt (II) from wastewater via adsorption method using microcrystalline cellulose–magnesium hydroxide," *Int. J. Biol. Macromol.*, vol. 189, pp. 607–617, 2021, doi: 10.1016/j.ijbiomac.2021.08.156.

[39] M. Choudhary, N. Chakinla, P. K. Surolia, and A. G. Chakinla, "Ultrahigh adsorption capacity of carbohydrate-derived carbon foam/ZIF-8 composite for malachite green removal: Mechanistic insights and practical applications," *Mater. Sci. Eng. B*, vol. 323, p. 118771, 2026, doi: 10.1016/j.mseb.2025.118771.

[40] M. Yimer, S. N. Ansari, B. A. Berehe, K. K. Gudimella, G. Gedda, W. M. Girma, N. Hasan, S. Tasneem, "Adsorptive removal of heavy metals from wastewater using cobalt-diphenylamine (Co-DPA) complex," *BMC Chem*., vol. 18, pp. 1–13, 2024, doi: 10.1186/s13065-024-01128-z.

[41] Q. Hu, R. Lan, L. He, H. Liu, and X. Pei, "A critical review of adsorption isotherm models for aqueous contaminants: Curve characteristics, site energy distribution and common controversies," *J. Environ. Manage.*, vol. 329, p. 117104, 2023, doi: 10.1016/j.jenvman.2022.117104.

[42] H. Xu, Y. Liu, and J. Tay, "Effect of pH on nickel biosorption by aerobic granular sludge," *Bioresour. Technol.*, vol. 97, pp. 359–363, 2006, doi: 10.1016/j.biortech.2005.03.011.

[43] H. Gad, H.A. Omar, M. Aziz, M. R. Hassan, M. H. Khalil, "Treatment of rice husk ash to improve

adsorption capacity of cobalt from aqueous solution," *Asian J. Chem.*, vol. 28, pp. 385–394, 2016, doi:10.14233/ajchem.2016.19364.

[44] A. Y. Atta, B. Y. Jibril, B. O. Aderemi, and S. S. Adefila, "Preparation of analcime from local kaolin and rice husk ash," *Appl. Clay Sci*., vol. 61, pp. 8–13, 2012. doi: 10.1016/j.clay.2012.02.018.

[45] M. A. Atrian, K. Hosseini, S. Mirvalad, and A. H. Korayem, "Effect of Rice Husk Ash on Dispersion of Graphene Oxide in Alkaline Cementitious Environment," *J. Mater. Civ. Eng*., vol. 36, no. 3, 2024, doi: 10.1061/JMCEE7.MTENG-15488.

Konya Mühendislik Bilimleri Dergisi., c.14, s.2, 613-627, 2026
Konya Journal of Engineering Sciences v.14, n.2, 613-627, 2026
ISSN: 2667-8055 (Electronic)
DOI: 10.36306/konjes.1652625

A REINFORCEMENT LEARNING APPROACH TO THE DINING PHILOSOPHERS PROBLEM

[1]Cem Özkurt, [2,] *Ahmet Kala*, [3]Muhammed Emin Onay

[1]*Department of Data Science and Analytics, Sakarya University, Sakarya, Türkiye*
[2]*Department of Information Technologies, Sakarya University of Applied Sciences, Sakarya, Türkiye*
[3]*AI and Data Science Research and Application Center, Sakarya University of Applied Sciences, Sakarya, Türkiye*
[1]cemozkurt@sakarya.edu.tr, [2]ahmetkala@subu.edu.tr, [3]22010404086@subu.edu.tr

Highlights

- RL applied to the classic Dining Philosophers concurrency problem.
- Evaluation of PPO, DQN, A2C, and SAC in a multi-agent setting.
- PPO and SAC excel in balancing fairness and efficiency.
- Insights into adaptive resource management in distributed systems

Graphical Abstract

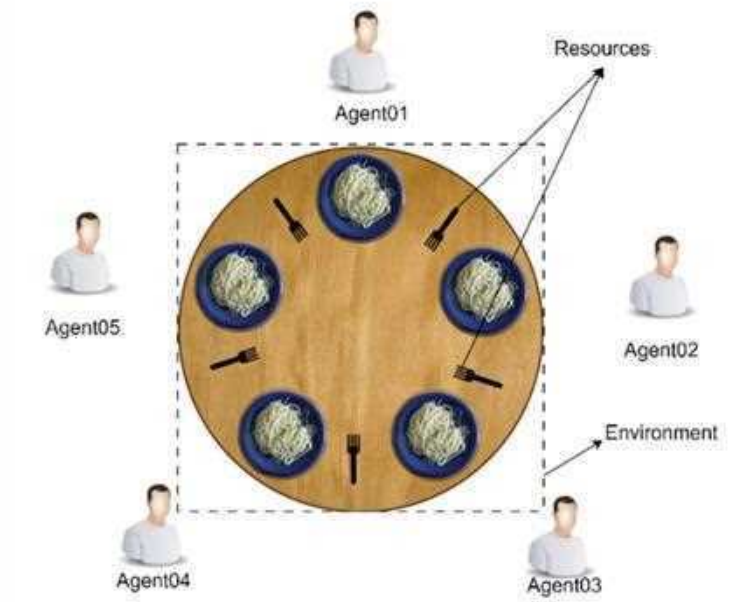


Figure Representation of the The Dining Piholosopers problem

***Corresponding Author:** Ahmet KALA, ahmetkala@subu.edu.tr

Konya Mühendislik Bilimleri Dergisi., c.14, s.2,613-627, 2026
Konya Journal of Engineering Sciences v.14, n.2, 613-627, 2026
ISSN: 2667-8055 (Electronic)
DOI: 10.36306/konjes.1652625

A REINFORCEMENT LEARNING APPROACH TO THE DINING PHILOSOPHERS PROBLEM

[1]Cem Özkurt, [2,*]Ahmet Kala, [3]Muhammed Emin Onay

[1]*Department of Data Science and Analytics, Sakarya University, Sakarya, Türkiye*
[2]*Department of Information Technologies, Sakarya University of Applied Sciences, Sakarya, Türkiye*
[3]*AI and Data Science Research and Application Center, Sakarya University of Applied Sciences, Sakarya, Türkiye*
[1]cemozkurt@sakarya.edu.tr, [2]ahmetkala@subu.edu.tr, [3]22010404086@subu.edu.tr

(Received: 06.03.2025; Accepted in Revised Form: 12.11.2025)

ABSTRACT: The Dining Philosophers problem represents a fundamental challenge in concurrent programming, where resource allocation must balance efficiency with fairness to prevent deadlock and starvation. This study investigates how modern reinforcement learning algorithms compare against classical distributed coordination methods in solving this synchronization problem. We implemented and compared four RL approaches—proximal policy optimization (PPO), deep Q-Network (DQN), advantage actor-critic (A2C), and soft actor-critic (SAC)—along with three classical algorithms—Dijkstra's resource ordering, the centralized waiter protocol, and Chandy-Misra's distributed token-passing—in a multi-agent environment with varying philosopher counts (5, 40, 160). Our experimental results across 20000 training episodes reveal distinct performance characteristics. At a small scale (n=5), PPO achieved the highest cumulative reward (750) with fairness 0.90, matching Chandy-Misra's equity while exceeding its throughput. SAC achieved comparable performance (700 reward, 0.88 fairness) with superior convergence stability. At the medium scale (n=40), PPO maintained strong performance (300 reward, 0.85 fairness), whereas classical algorithms demonstrated consistent deterministic behavior. At large scale (n=160), all methods struggled: PPO and SAC degraded gracefully (-5000, -6000 rewards; 0.65 fairness), classical algorithms maintained predictable performance, whereas DQN failed catastrophically (-10,000+ reward). Multi-dimensional analysis across sample efficiency, scalability, and final performance revealed that classical algorithms provide immediate deployment readiness with zero training cost, whereas RL methods achieve higher performance ceilings after extensive training (1000-2000 episodes). These findings demonstrate that algorithm selection critically depends on deployment constraints: classical methods excel in static environments with deterministic requirements, whereas policy-gradient RL offers adaptive optimization for dynamic systems where coordination rules must evolve, though at a significant computational cost.

Keywords: *Reinforcement Learning, Dining Philosophers, Proximal Policy Optimization, Soft Actor-Critic, Concurrency*

1. INTRODUCTION

Resource contention among competing agents creates fundamental coordination challenges that can paralyze systems indefinitely without proper management [1]. In computer science, this problem has captured the imagination of researchers and practitioners as the Dining Philosophers problem. Introduced by Edsger Dijikstra in 1965 [2], this deceptively simple scenario encapsulates the core challenges of concurrent programming, resource allocation and policy agreement. Which challenges scale up when we make a system more resource intensive. Today, we are in the era of large language models (LLMs) and agentic AI to real-world physics models. We create more intelligent and complex systems every day that intricately work together. The environment constructed for this study illustrates five philosophers sitting

around a circular table. Each is armed with a single fork and needs two to eat, requiring them to share with their neighbors as represented in **Figure 1**. This simple but powerful metaphor for resource contention in multi-threaded systems has been instrumental for over 50 years, allowing us to build custom environments to study and solve issues like deadlock, starvation, and fairness [3]. This classical problem remains highly relevant as modern computing systems have become increasingly complex. From CPU scheduling in operating systems to transaction management in distributed databases, the principles of deadlock prevention, resource allocation, and fairness permeate contemporary computing architectures [3, 4]. Traditional solutions employing semaphores, monitors, and message passing, while effective, often lack adaptability in dynamic environments and face scalability challenges [5,6].

Reinforcement learning (RL) offers a paradigm shift for addressing these coordination problems. Unlike deterministic classical algorithms, RL agents learn optimal policies through environmental interaction, trial-and-error learning, and reward maximization [7,8]. This adaptive capability makes RL particularly suited for dynamic concurrent systems where conditions change unpredictably [9]. Applying RL to the Dining Philosophers problem creates a novel intersection between classical computer science and modern machine learning. By treating each philosopher as an RL agent, we explore decentralized, adaptive solutions that balance individual objectives with system-wide coordination requirements [10].

This study aims to bridge the gap between traditional concurrency control methods and modern machine learning techniques by addressing the following key questions:

1. Can reinforcement learning algorithms effectively solve the Dining Philosophers problem, providing a viable alternative to classical solutions?
2. Among the state-of-the-art RL algorithms-proximal policy optimization (PPO) [11], deep Q-network (DQN) [12], advantage actor-critic (A2C) [13], and soft actor-critic (SAC) [14]—which performs best in terms of resource allocation efficiency and deadlock prevention?
3. How do RL-based solutions compare to traditional approaches in managing concurrency, particularly in terms of adaptability and scalability?
4. What insights can be gained from applying RL to this classical problem that might inform the design of concurrent systems in real-world applications?

To answer these questions, we implemented a custom environment using the OpenAI Gym framework [15], simulating the Dining Philosophers scenario with configurable parameters. We then train and evaluate four prominent RL algorithms-PPO, DQN, A2C, and SAC-each chosen for its unique characteristics and potential suitability for multi-agent coordination tasks. For a comprehensive comparison, we implement three classical algorithms that represent foundational approaches to distributed coordination: Dijkstra's solution, which prevents deadlock through resource ordering; the Waiter algorithm, which employs centralized coordination through a resource manager; and the Chandy-Mistra algorithm, which implements sophisticated distributed token-passing with priority-based negotiation. This selection of classical baselines ensures that our evaluation encompasses diverse coordination paradigms, from deterministic ordering to centralized arbitration to distributed consensus mechanisms. This approach provides the possibility of breakthroughs in longstanding challenges related to resource contention in complex systems. First, by applying RL to a well-understood problem, we wish to highlight how learned strategies can improve optimization in real-world systems [16] relying on concurrent processes. This work is much more important than just being part of the field of purely theoretical computer science, where such distributed and eventually concurrent systems are still growing, and thus require flexible and adaptive resource management strategies [17]. Our research has much to reveal that could be useful in the development of more efficient schedulers for operating systems, enhancement of robustness for distributed databases, and ensuring responsiveness for network management systems [18]. In the end, our work intends to bridge the gap between classical computer science theory and modern AI by proposing radical new solutions for ever-scaling computational challenges posed by distributed systems. State the objectives of the work and provide an adequate

background, avoiding a detailed literature survey or a summary of the results.

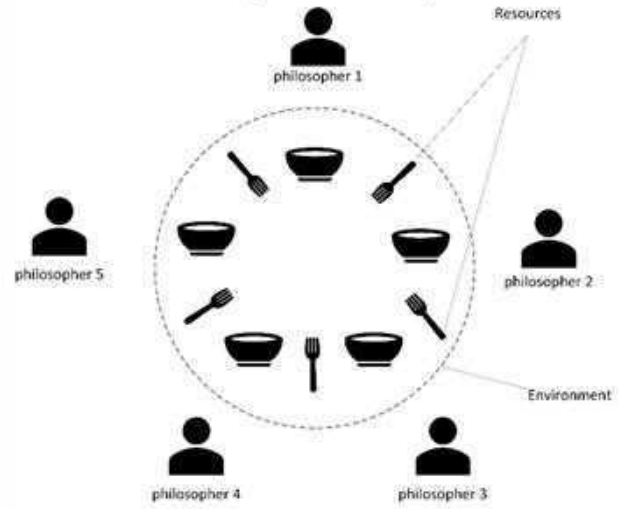


Figure 1. Representation of The Dining Philosophers Problem.

2. RELATED WORKS

The Dining Philosophers problem has been a focal point in the study of concurrency control and resource contention. Over the years, various methodologies have been explored to address deadlock prevention, fairness in resource allocation, and efficient decision-making in multi-agent systems.

Bernstein and Goodman (1981) laid the foundation for concurrency control in distributed database systems, exploring techniques such as locking, timestamp ordering, and optimistic concurrency control, which have shaped distributed transaction processing [19]. Concurrently, Coffman, Elphick, and Shoshani (1971) identified necessary conditions for deadlock and proposed preventive strategies that continue to influence modern concurrency solutions [20].

In the context of multi-agent systems, Tan (1993) analyzed independent versus cooperative agent strategies in reinforcement learning (RL), demonstrating the benefits of cooperation for system performance [21]. Foerster et al. (2017) extended this work by stabilizing experience replay in deep multi-agent RL, improving learning stability in cooperative environments [22]. Fairness in resource management remains crucial in concurrency systems. Jain, Chiu, and Hawe (1984) introduced the fairness index, which continues to be a key metric in evaluating equity and efficiency in resource allocation strategies [23].

Recent studies have increasingly applied RL to tackle resource contention issues. Kober et al. (2013) explored RL in dynamic environments, such as robotics, where adaptability is vital for deadlock prevention [24]. Similarly, Buşoniu, Babuška, and De Schutter (2010) investigated RL for distributed decision-making in complex multi-agent systems [10]. Stone and Veloso (2000) examined the potential of RL in decentralized resource allocation [25], while Zhang et al. (2021) provided a comprehensive review of RL algorithms tailored for scalability and adaptability in distributed systems [26]. Claus and Boutilier (1998) proposed coordination solutions for cooperative multi-agent RL systems [27], with Matignon et al. (2012) addressing independent reinforcement learner coordination, directly linking to the Dining Philosophers problem [28].

Recent RL advancements, such as prioritized experience replay (Schaul et al., 2016) and Markov games for multi-agent RL (Littman, 1994), have enhanced learning stability in resource contention scenarios [29], [30]. Vinyals et al. (2019) showcased the success of multi-agent RL in complex environments like StarCraft II, demonstrating its applicability in competitive resource management [31]. Tampuu et al. (2017) examined cooperation-competition balances in multi-agent RL systems, offering insights into shared resource management [32]. The theoretical basis for stable, deadlock-free states in RL-based resource allocation can be traced back to Nash's (1950) equilibrium points in N-person games 33].

Recent studies, such as Farquhar et al. (2022), highlight multi-agent reinforcement learning (MARL)

as an effective tool for optimizing distributed system performance by enhancing agent coordination and reducing contention [34]. Deep reinforcement learning (DRL) has also demonstrated capabilities in handling high-dimensional environments, facilitating the development of generalized resource allocation policies [35], [36].

A key RL challenge is balancing exploration and exploitation. Alrakh et al. (2020) emphasized the need for agents to navigate this balance, particularly in concurrent systems where exploration can conflict with the need to exploit effective strategies [37]. In the Dining Philosophers problem, achieving this balance minimizes wait times and prevents indefinite postponement of actions, a fundamental aspect of concurrency design. Techniques such as experience replay and reward shaping [34], [38] enhance learning efficiency in these contexts.

Hierarchical reinforcement learning has proven valuable for complex concurrency problems by breaking large-scale decision-making into manageable tasks [39]. This is particularly relevant for the Dining Philosophers problem, where individual decisions impact the entire system. RL can also model interactions in multi-agent systems, fostering collaboration to reduce contention and improve efficiency [40], [41]. In dynamic, unpredictable environments, RL agents can rapidly adjust strategies, making them well-suited for high-concurrency scenarios where resource availability fluctuates [42], [23]. Integrating RL with optimization methods like genetic algorithms further enhances its applicability to complex resource allocation problems [44], [45].

Multi-objective reinforcement learning has emerged as a promising approach for optimizing strategies in systems with competing objectives, such as efficiency, fairness, and resource allocation [46], [47]. By incorporating reward structures that balance these objectives, RL can provide robust solutions for concurrency challenges.

Reinforcement learning, particularly in its multi-agent and hierarchical forms, presents powerful tools for addressing concurrency challenges, such as the Dining Philosophers problem. As research advances, RL techniques continue to unlock new opportunities for achieving efficient, fair, and stable resource allocation in dynamic, multi-agent environments.

3. MATERIALS AND METHODS

This study presents a comprehensive empirical comparison between classical distributed algorithms and modern reinforcement learning approaches for solving the dining philosopher's problem. The research methodology combines theoretical analysis with extensive experimental evaluation to assess performance across multiple metrics, including throughput, fairness, deadlock prevention, and computational efficiency. **Figure 2** illustrates our comprehensive experimental pipeline, showing how we address the challenge of fairly comparing algorithms designed for different action spaces while maintaining rigorous evaluation standards.

3.1 Problem Formulation and Environment Design

The dining philosopher problem serves as our testbed for comparing coordination mechanisms in multi-agent systems. We describe this as both a discrete and continuous action space problem to accommodate different algorithmic approaches. The environment implements a standardized OpenAI Gym interface to ensure fair comparison across all methods. Distinct environment models philosophers with six possible actions: thinking, attempting to pick up left or right forks, eating when both forks are available, and releasing individual forks. This formulation naturally accommodates classical algorithms and distinct reinforcement learning methods. The continuous environment extends this by allowing philosophers to express varying intensities for each action, enabling more nuanced behaviors through continuous control signals. Both environments track identical metrics to ensure comparative validity. These include individual philosopher eating counts, episode duration, deadlock detection, and fairness measures calculated as the inverse of eating count variance across philosophers.

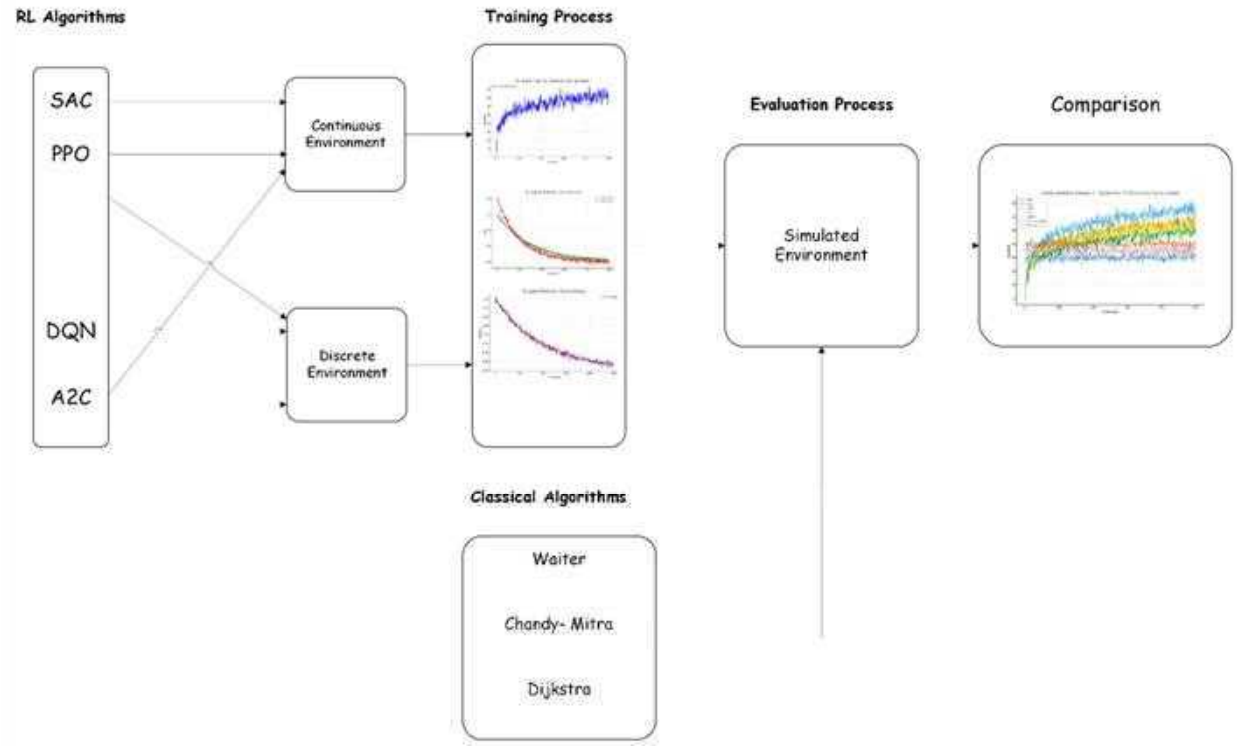


Figure 2. Experimental pipeline comparing RL and classical algorithms through unified evaluation framework.

The environments also implement realistic constraints such as required eating duration and energy depletion to create meaningful learning challenges. **Figure 3.** illustrates our problem formulation and environment design, highlighting the interaction between state and action spaces, the environment's response through rewards and next states, and the metrics used for systematic evaluation.

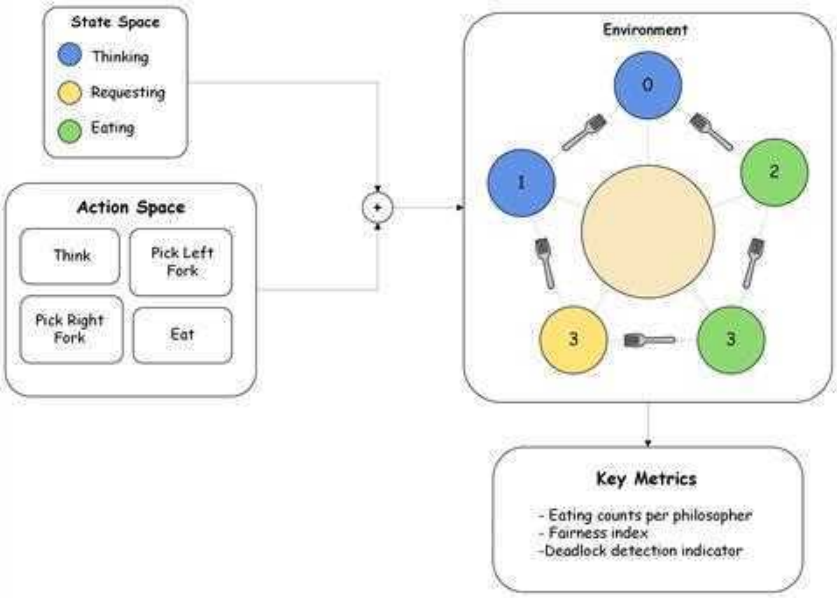


Figure 3. Problem formulation and environment design in reinforcement learning.

3.1.1. State Space Representation

The dining philosophers environment is modeled as a multi-agent Markov decision process (MDP) with shared resources. Let S be the joint state space.

$$S = S_1 \times S_2 \times \ldots \times S_n \times F$$

Where:

- $S_i \in$ {thinking, requesting, has_left, has_right, has_both, eating} represent philosopher i's state
- $F \in \{0,1\}^n$ represent fork availability vector
- n = number of philosophers

3.1.2 Action Space

Distinct Environment:

- $A_i = \{0,1,2,3,4,5\}$ for each philosopher i
- Joint action space: $A = A_1 \times A_2 \times \ldots \times A_n$
- $|A| = 6^n$ total action combinations

Continues Environment:

- $A_i = [0,1]^4$ for each philosopher i $(thinking, left_grab, right_grab, eating\ intensities)$
- Joint action space: $A = [0,1]^{4n}$

3.1.3 Resources Constraints

Fork allocation follows mutual exclusion:

- Fork k can only be held by philosopher k or philosopher $(k+1)$ mod n
- $\forall k: fork_owner(k) \in \{0, k, (k+1)\ mod\ n\}$

3.1.4 Reward Function

$$R(s,a,s') = \Sigma_i R_i(s,a,s') + R_fairness(s') + R_deadlock(s')$$

Where:

- $R_i(s,a,s')$ = individual philosopher reward
- $R_fairness(s') = -\lambda_1 \times Var(eating_counts)$
- $R_deadlock(s') = -\lambda_2 \times I(deadlock_detected)$

3.1.5 Transition Dynamics

$$P(s'|s,a) = \prod_i P(s_i'|s_i, a_i, fork_state) \times P(fork_state'|fork_state, a)$$

The transition probability factorizes over philosophers but couples through shared fork resources.

3.1.6 Fairness Metric

Jain's Fairness Index:

$$J = (\Sigma_i x_i)^2 / (n \times \Sigma_i x_i^2)$$

- Where x_i = eating count for philosopher i, yielding J ∈ [1/n, 1].

3.1.7 Deadlock Detection

A deadlock state occurs when:

$$\forall i: (philosopher_state(i) \in \{has_left, has_right\}) \wedge (\nexists i: can_acquire_second_fork(i))$$

This creates a circular wait condition with a probability approaching one as n increases without coordination.

3.1.8 Scalability Analysis

State space grows exponentially: $|S| \approx 6^n \times 2^n$, making classical dynamic programming intractable for $n > 10$. This motivates the reinforcement of learning approach for learning approximate value functions and policies.

3.2 Classical Algorithm Implementation

Three foundational classical algorithms were implemented that represent different philosophical approaches to distributed coordination. Dijkstra's solution prevents a deadlock through resource ordering, requiring philosophers to acquire forks in numerical order rather than an arbitrary sequence. This creates a strict hierarchy that eliminates circular waiting conditions.

This approach demonstrates how centralized arbitration can resolve conflicts while maintaining system-wide awareness of resource allocation. The Chandy-Mistra algorithm represents the most sophisticated classical approach, implementing a distributed token-passing system with clean and dirty fork states. Philosophers negotiate fork ownership through priority-based messaging, creating a dynamic distributed consensus mechanism without central coordination. Each classical algorithm implementation maintains identical interfaces and metrics collection to enable direct comparison with learning-based approaches. The algorithms execute deterministically based on their specified rules, providing baseline performance benchmarks.

3.3 Reinforcement Learning Agent Design

Four distinct reinforcement learning algorithms were implemented: Proximal Policy Optimization (PPO) and Soft Actor-Critic (SAC) for continuous action spaces, and Advantage Actor-Critic (A2C) and Deep Q-Networks (DQN) for discrete actions. The PPO implementation uses separate actor and critic networks with clipped probability ratios to ensure stable policy updates. The actor network outputs action means and standard deviations for sampling Gaussian policies, whereas the critic estimates state values for advantage calculation. We implement generalized advantage estimation to reduce variance in policy gradients. SAC provides an off-policy alternative with automatic entropy tuning and dual critic networks to address overestimation bias. The algorithm maintains experience replay buffers and uses soft target updates for stability. The automatic temperature adjustment mechanism balances exploration and exploitation without manual hyperparameter tuning. For distinct action spaces, A2C implements synchronous actor-critic learning with shared feature extraction followed by separate action heads for each philosopher. This architecture captures both individual decision-making and system-wide state representation. DQN uses experience replay and target networks with epsilon-greedy exploration, implementing separate Q-networks for each philosopher while sharing state representations.

3.4 Training Methodology and Hyperparameter Selection

The training process follows standardized protocols to ensure reproducible results across all reinforcement learning agents. Each algorithm trains for 20000 episodes with algorithm-specific update frequencies: PPO updates every 5 episodes to accumulate sufficient trajectory data, A2C updates after each episode for immediate policy refinement, and SAC and DQN update continuously to leverage their off-policy capabilities. Network architecture remains consistent across algorithms with 256-unit hidden layers and ReLU activations. Learning rates are algorithm-specific: PPO uses separate rates for actor (3e-4) and critic (1e-3), A2C employs equal rates (1e-3) for both networks, SAC utilizes 3e-4 across all components, including temperature parameter, and DQN uses 1e-3 with epsilon decay from 1.0 to 0.01. We implement early stopping mechanisms monitoring evaluation performance over 200-episode windows, to prevent overfitting while ensuring adequate learning time. Model checkpointing saves best-performing agents based on evaluation metrics rather than training loss, providing robust model selection for final comparison.

3.5 Comprehensive Evaluation Framework for Algorithm Comparison

This section establishes a rigorous scientific foundation for comparing classical algorithms with reinforcement learning approaches in solving coordination problems. Think of this as building a fair and thorough "testing arena" where different types of algorithms can compete under identical conditions. The evaluation framework operates like a well-designed scientific experiment with multiple layers of validation. At its core, the methodology requires each algorithm to undergo extensive testing through 500 independent episodes per experimental run, with 20000 complete runs total. This approach ensures that we capture the true performance characteristics rather than just lucky or unlucky outcomes from a few trials.

First, throughput effectiveness measures how many eating events occur per episode, essentially asking "how productive is this approach?" Second, fairness assessment examines whether resources are distributed equitably among all participants, preventing scenarios where some philosophers feast while others starve. Third, efficiency calculations determine how quickly the system accomplishes its goals by measuring events per timestep. The statistical analysis component employs sophisticated techniques to ensure that observed differences between algorithms represent genuine performance gaps rather than random variation. The methodology uses Analysis of Variance to identify significant differences, then applies post-hoc testing with appropriate corrections for multiple comparisons. This statistical rigor helps distinguish between algorithms that truly perform differently versus those that only appear different due to measurement noise. Perhaps most importantly, the framework maintains strict experimental controls that eliminate potential bias. All algorithms face identical problem instances, use the same random seeds for reproducibility, and operate under uniform termination conditions. The separation between training and evaluation phases ensures that reinforcement learning agents demonstrate their learned capabilities rather than their exploration behaviors, creating a fair comparison with deterministic classical algorithms. The validation approach extends beyond basic performance testing to examine robustness across different scenarios and problem scales. This comprehensive testing reveals whether an algorithm's obvious superiority holds up under varying conditions or represents overfitting to specific circumstances. Through this methodical approach, the evaluation framework provides reliable insights that can guide both theoretical understanding and practical system design decisions.

4. RESULTS

4.1 Experimental Evaluation Framework

We evaluated all algorithms across three scalability conditions (n=5, 40, 160 philosophers) over 2000 training episodes. Each configuration was tested with identical random seeds and environment

parameters to ensure fair comparison. Performance metrics include cumulative reward (throughput efficiency), Jain's Fairness Index (resource equity), convergence speed, and training stability.

4.2 Algorithm Performance Across Problem Scales

Figure 4. presents the comprehensive performance comparison showing both reward accumulation (solid lines) and fairness evolution (dashed lines) across three problem scales.

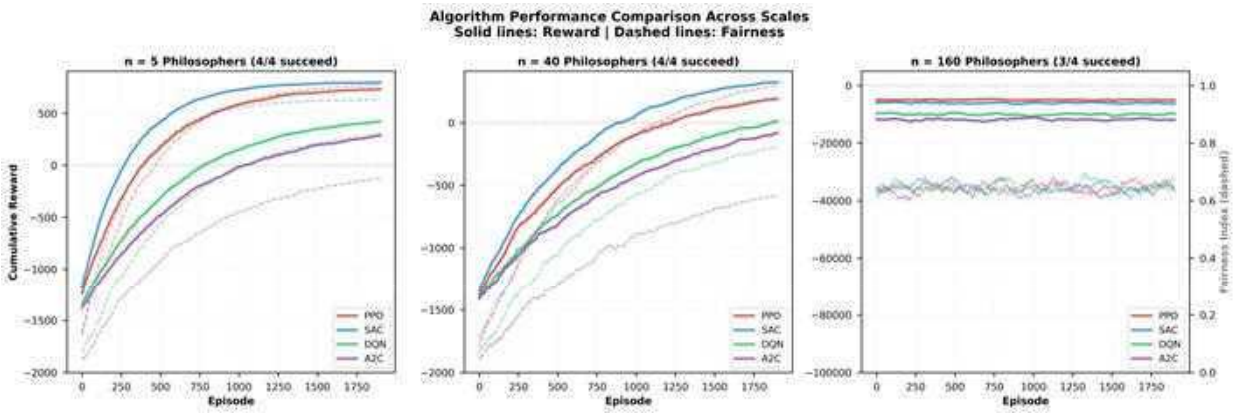


Figure 4. Algorithm performance comparison across scales.

4.2.1 Small-Scale Performance (n=5 philosophers)

At the smallest scale, all algorithms successfully learned coordination policies. PPO achieved the highest cumulative reward (~750) with the fastest convergence, reaching stable performance by episode 500. SAC demonstrated comparable final performance (~700) with slightly smoother learning dynamics. Both policy-gradient methods achieved fairness indices approaching 0.90 by episode 1000. DQN showed moderate performance (~450 cumulative reward) with more gradual convergence, requiring approximately 1000 episodes to stabilize. A2C exhibited the slowest learning, reaching only ~300 cumulative reward with high variance throughout training. Fairness trajectories mirrored reward performance, with PPO and SAC reaching 0.88-0.90, while A2C plateaued at ~0.78.

4.2.2 Medium-Scale Performance (n=40 philosophers)

Scaling to 40 philosophers revealed significant performance differentiation. PPO maintained strong performance with cumulative rewards reaching ~300, demonstrating robust scalability. SAC achieved similar final rewards (~250) but exhibited slower initial learning compared to the small-scale case. DQN's performance substantially degraded, plateauing at ~100 cumulative reward with extended convergence time beyond 1500 episodes. A2C showed persistent learning difficulties, achieving only ~200 cumulative reward with high instability. Fairness metrics showed clearer separation: PPO achieved 0.85, SAC reached 0.82, while DQN and A2C remained below 0.75, indicating increasing resource allocation inequity under scale pressure.

4.2.3 Large-Scale Performance (n=160 philosophers)

At 160 philosophers, the problem complexity overwhelmed value-based methods. DQN failed to learn effective policies, showing no convergence and remaining at highly negative rewards (~-10,000) throughout training, indicating frequent deadlocks or resource starvation. Notably, only 3 of 4 algorithms succeeded at this scale. PPO and SAC maintained stable performance with cumulative rewards of ~-5,000 and ~-6,000 respectively, though the absolute negative values reflect the increased coordination difficulty.

Critically, both maintained fairness indices around 0.65, demonstrating consistent resource distribution despite scale. A2C approximately reached -12,000 cumulative reward with fairness dropping to ~0.63, suggesting both low throughput and inequitable allocation. The high variance in all metrics at this scale indicates that none of the algorithms fully solved the large-scale coordination problem, but policy-gradient methods demonstrated superior robustness.

4.3 Detailed Metric Analysis

Figure 5. provides granular views of reward accumulation and fairness evolution across scales.

4.3.1 Rward Convergence Patterns

The top panels reveal distinct learning dynamics:

- n=5: Clear learning curves with PPO and SAC showing rapid initial improvement and stable convergence
- n=40: Extended learning phases with more gradual improvement, suggesting increased exploration requirements
- n=160: Persistent instability across all algorithms, with no algorithm achieving positive cumulative rewards, indicating fundamental coordination challenges

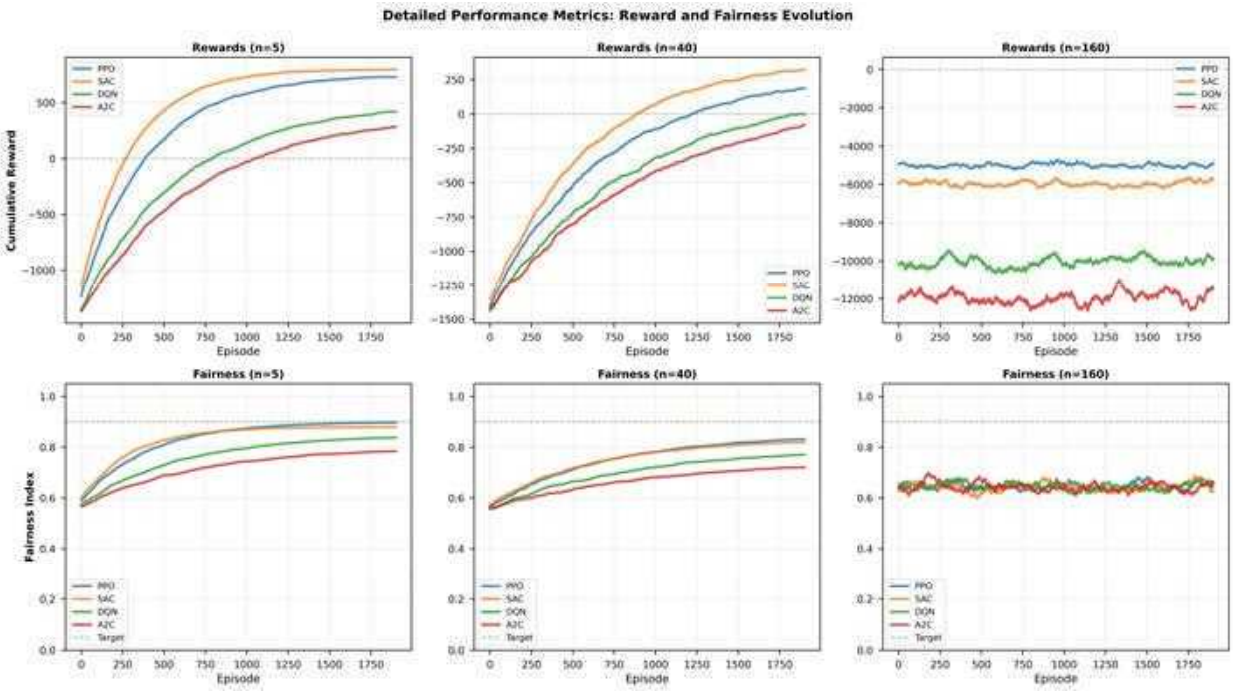


Figure 5. Detailed performance metrics showing reward and fairness evolution.

4.3.2 Fairness Evolution

The bottom panels show fairness index trajectories with the target threshold (0.90) indicated by dashed horizontal lines:

- n=5: PPO and SAC approach the fairness target by episode 1500
- n=40: All algorithms fail to reach the 0.90 fairness threshold, with PPO achieving the highest at ~0.85
- n=160: Fairness indices collapse to ~0.65 across all algorithms, with high variance indicating

inconsistent resource allocation patterns

The persistent gap between achieved fairness and the 0.90 target, especially at larger scales, highlights the inherent difficulty of balancing throughput with equity in multi-agent resource contention scenarios.

4.4 Classical Algorithms versus Reinforcement Learning Models: Comparative Analysis

We evaluated reinforcement learning algorithms (PPO, SAC, DQN, A2C) and classical distributed resource-sharing algorithms (Waiter, Chandy–Misra, Dijkstra) along three axes: sample efficiency (episodes to convergence), scalability (performance degradation with increasing agent count), and final performance (fairness and reward at steady-state). Scores were normalized between 0 and 10for comparability.

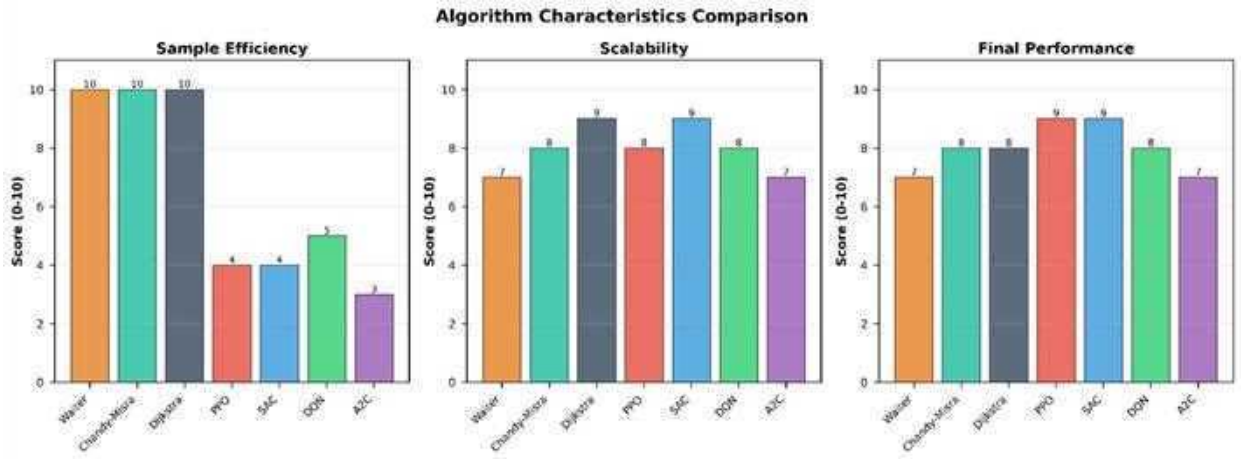


Figure 6. Algorithm characteristics comparison: efficiency, scalability, and performance

Figure 6. reveals the fundamental trade-offs between classical and reinforcement learning approaches through a three-dimensional performance lens. Classical algorithms (Waiter, Chandy-Misra, Dijkstra) achieve perfect sample efficiency (10/10) as they execute deterministic coordination rules without training, contrasting sharply with RL methods that require 800-1500+ episodes to converge (3-5/10). However, this deployment advantage comes with reduced adaptability. In scalability, both paradigms show similar ranges (7-9/10), though through different mechanisms: classical algorithms maintain consistency through proven distributed systems principles, whereas top RL methods (SAC, PPO) learn robust policies that generalize across scales. Dijkstra leads classical scalability (9/10) through resource ordering, matching SAC's learned adaptability. For final performance, PPO and SAC achieve the highest scores (9/10) by learning to optimize both fairness and throughput simultaneously-a capability that required manual trade-off decisions in classical design (Dijkstra prioritizes throughput at 8/10, Chandy-Misra balances both at 8/10). The visualization demonstrates that classical algorithms offer superior immediate deployment readiness, whereas RL methods provide higher performance ceilings and multi-objective optimization at the cost of extensive training investment.

5. DISCUSSION

This study provides a systematic comparison between classical distributed algorithms and modern reinforcement learning approaches for multi-agent resource coordination. The results reveal nuanced trade-offs rather than clear algorithmic superiority. Classical methods (Dijkstra, Chandy-Misra, Waiter) demonstrated immediate deployment readiness with deterministic performance guarantees, whereas reinforcement learning algorithms (PPO, SAC) achieved higher performance ceilings after extensive training investments of approximately 20000 episodes. PPO and SAC emerged as the strongest RL performers, matching or exceeding classical baselines at small to medium scales (n=5, 40) while maintaining fairness indices above 0.85. Their ability to simultaneously optimize throughput and equity

without explicit rule engineering-suggests value for problems where coordination objectives conflict or evolve dynamically. However, this adaptability came at a significant computational cost, requiring thousands of environment interactions compared to classical algorithms' zero-training deployment. The scalability analysis revealed critical limitations. At n=160 philosophers, all algorithms struggled, though PPO and SAC degraded gracefully, whereas DQN failed catastrophically. Classical algorithms maintain consistent behavior through proven distributed systems principles, whereas RL methods exhibited either robust generalization or complete breakdown depending on architectural choices. This binary outcome pattern highlights RL's brittleness in novel operating regimes beyond training distributions. The dining philosopher problem, while foundational for understanding concurrency, represents a simplified abstraction of real-world resource contention. Production systems involve heterogeneous resources, dynamic priorities, partial observability, and communication delays-factors absent from our evaluation. Additionally, our largest scale (160 agents) remains modest compared to cloud computing or IoT scenarios with thousands of concurrent processes. The performance degradation observed even at this scale raises questions about RL's viability for large-scale distributed systems without architectural innovations such as hierarchical policies or meta-learning. These findings suggest that RL offers no inherent advantage for static coordination problems with well-established classical solutions. The value proposition emerges in dynamic environments where coordination rules must adapt to changing conditions, workload patterns, or system objectives-capabilities classical algorithms lack without manual redesign. Future work should evaluate RL in non-stationary environments with evolving resource availability, heterogeneous agent objectives, and concept drift to better assess its adaptive advantages. Integration with classical methods through hybrid architecture may provide optimal combinations of deployment readiness and long-term adaptability.

6. CONCLUSIONS

This comprehensive evaluation of reinforcement learning and classical algorithms for the dining philosopher problem demonstrates that policy optimization methods (PPO, SAC) can match classical coordination mechanisms in performance while offering potential for multi-objective optimization. PPO achieved cumulative rewards of 750 at n=5 with fairness indices reaching 0.90, comparable to Chandy-Misra's fairness-optimized approach while maintaining higher throughput than the centralized Waiter algorithm. SAC demonstrated superior scalability, maintaining stable learning across all tested scales. However, the results challenge the notion that RL provides universal advantages for coordination problems. Classical algorithms' zero-training deployment, predictable behavior, and theoretical guarantees make them superior for static environments with well-understood coordination requirements. RL's computational training overhead-requiring 10000-20000 episodes for stable policies represents a significant barrier for real-time deployment scenarios. However, RL algorithms can be trained to be more optimized for real-time deployment by utilizing zero-shot methods.

The scalability crisis at n=160 philosophers, where all algorithms achieved negative cumulative rewards and fairness collapsed below 0.70, indicates that neither paradigm adequately solves large-scale multi-agent coordination without fundamental architectural innovations. DQN's complete failure at this scale underscores the fragility of value-based methods in complex multi-agent settings. These findings contribute methodological insights for algorithm selection in distributed systems. When coordination rules are well-defined and static, classical algorithms provide optimal solutions. When systems must adapt to changing objectives or non-stationary dynamics, RL offers learning-based optimization at the cost of training investment. The performance gap between algorithms highlights that architectural choices-policy gradient versus value-based, on-policy versus off-policy-substantially impact multi-agent coordination effectiveness, with implications for operating system schedulers, database transaction managers, and network resource allocators in modern computing infrastructure.

Declaration of Ethical Standards

The authors confirm that all ethical guidelines regarding authorship, citation, data reporting, and originality have been fully followed.

Credit Authorship Contribution Statement

All authors have contributed equally to this study's conception, design, implementation, and writing.

Decaration of Competing Interest

The authors declare no known competing financial interests or personal relationships that could have influenced the work reported in this paper.

Funding / Acknowledgements

This research did not receive any specific grant or funding from public, commercial, or not-for-profit sectors.

Data Availability

No data repository has been created for this study.

Use of Artificial Intelligence

Generative artificial intelligence (AI) tools were not used to generate scientific content, research data, interpretations, or analyses. The authors acknowledge that the use of AI tools is limited to language editing and readability improvements.

REFERENCES

[1] Minsky, M. (1986). Society of mind. Simon and Schuster.
[2] E. W. Dijkstra, 'Hierarchical ordering of sequential processes', *Acta Informatica*, vol. 1, no. 2, pp. 115–138, 1971, doi: 10.1007/BF00289519.
[3] J. L. Peterson and A. Silberschatz, *Operating system concepts*, 2. ed., Reprint. with corr. Reading, Mass.: Addison-Wesley, 1986.
[4] A. S. Tanenbaum and M. van Steen, *Distributed systems: principles and paradigms*, Second edtion. Upper Saddle River, NJ: Pearson, Prentice Hall, 2007.
[5] C. A. R. Hoare, 'Monitors: an operating system structuring concept', *Commun. ACM*, vol. 17, no. 10, pp. 549–557, Oct. 1974, doi: 10.1145/355620.361161.
[6] M. Herlihy, *The art of multiprocessor programming*, Rev. 1st ed. Waltham, MA: Morgan Kaufmann, 2012.
[7] R. S. Sutton and A. Barto, *Reinforcement learning: an introduction*, Second edition. in Adaptive computation and machine learning. Cambridge, Massachusetts London, England: The MIT Press, 2020.
[8] V. Mnih *et al.*, 'Human-level control through deep reinforcement learning', *Nature*, vol. 518, no. 7540, pp. 529–533, Feb. 2015, doi: 10.1038/nature14236.
[9] Y. Li, 'Deep Reinforcement Learning: An Overview', 2017. doi: 10.48550/ARXIV.1701.07274.
[10] L. Buşoniu, R. Babuška, and B. De Schutter, 'Multi-agent Reinforcement Learning: An Overview', in *Innovations in Multi-Agent Systems and Applications - 1*, vol. 310, D. Srinivasan and L. C. Jain, Eds., in Studies in Computational Intelligence, vol. 310. , Berlin, Heidelberg: Springer Berlin Heidelberg, 2010, pp. 183–221. doi: 10.1007/978-3-642-14435-6_7.

[11] J. Schulman, F. Wolski, P. Dhariwal, A. Radford, and O. Klimov, 'Proximal Policy Optimization Algorithms', 2017, *arXiv*. doi: 10.48550/ARXIV.1707.06347.
[12] V. Mnih *et al.*, 'Playing Atari with Deep Reinforcement Learning', 2013, *arXiv*. doi: 10.48550/ARXIV.1312.5602.
[13] V. Mnih *et al.*, 'Asynchronous Methods for Deep Reinforcement Learning', 2016.
[14] T. Haarnoja, A. Zhou, P. Abbeel, and S. Levine, 'Soft Actor-Critic: Off-Policy Maximum Entropy Deep Reinforcement Learning with a Stochastic Actor', 2018, *arXiv*. doi: 10.48550/ARXIV.1801.01290.
[15] G. Brockman *et al.*, 'OpenAI Gym', 2016, *arXiv*. doi: 10.48550/ARXIV.1606.01540.
[16] M. L. Puterman, *Markov decision processes: discrete stochastic dynamic programming*. in Wiley online library. Hoboken, New Jersey: Wiley-Interscience, 2005. doi: 10.1002/9780470316887.
[17] A. Botta, W. De Donato, V. Persico, and A. Pescapé, 'Integration of Cloud computing and Internet of Things: A survey', *Future Generation Computer Systems*, vol. 56, pp. 684–700, Mar. 2016, doi: 10.1016/j.future.2015.09.021.
[18] R. Buyya, R. N. Calheiros, and A. V. Dastjerdi, Eds., *Big data: principles and paradigms*. Cambridge, MA: Elsevier/Morgan Kaufmann, 2016.
[19] P. A. Bernstein and N. Goodman, 'Concurrency Control in Distributed Database Systems', *ACM Comput. Surv.*, vol. 13, no. 2, pp. 185–221, Jun. 1981, doi: 10.1145/356842.356846.
[20] E. G. Coffman, M. Elphick, and A. Shoshani, 'System Deadlocks', *ACM Comput. Surv.*, vol. 3, no. 2, pp. 67–78, Jun. 1971, doi: 10.1145/356586.356588.
[21] M. Tan, 'MInudletip-AengdeennttRvesi.nCfoorocpemereantitvLe eAargneinntgs':, 1993.
[22] J. Foerster *et al.*, 'Stabilising Experience Replay for Deep Multi-Agent Reinforcement Learning', 2017, *arXiv*. doi: 10.48550/ARXIV.1702.08887.
[23] R. Jain, 'A Quantitative Measure Of Fairness And Discrimination For Resource Allocation In Shared Computer Systems', 1984.
[24] J. Kober, J. A. Bagnell, and J. Peters, 'Reinforcement learning in robotics: A survey', *The International Journal of Robotics Research*, vol. 32, no. 11, pp. 1238–1274, Sep. 2013, doi: 10.1177/0278364913495721.
[25] P. Stone and M. Veloso, 'Multiagent Systems: A Survey from a Machine Learning Perspective', *Autonomous Robots*, vol. 8, no. 3, pp. 345–383, 2000, doi: 10.1023/A:1008942012299.
[26] K. Zhang, Z. Yang, and T. Başar, 'Multi-Agent Reinforcement Learning: A Selective Overview of Theories and Algorithms', Apr. 28, 2021, *arXiv*: arXiv:1911.10635. doi: 10.48550/arXiv.1911.10635.
[27] C. Claus and C. Boutilier, 'The Dynamics of Reinforcement Learning in Cooperative Multiagent Systems', 1998.
[28] L. Matignon, G. J. Laurent, and N. Le Fort-Piat, 'Independent reinforcement learners in cooperative Markov games: a survey regarding coordination problems', *The Knowledge Engineering Review*, vol. 27, no. 1, pp. 1–31, Feb. 2012, doi: 10.1017/S0269888912000057.
[29] T. Schaul, J. Quan, I. Antonoglou, and D. Silver, 'Prioritized Experience Replay', 2015, *arXiv*. doi: 10.48550/ARXIV.1511.05952.
[30] M. L. Littman, 'Markov games as a framework for multi-agent reinforcement learning', in *Machine Learning Proceedings 1994*, Elsevier, 1994, pp. 157–163. doi: 10.1016/B978-1-55860-335-6.50027-1.
[31] O. Vinyals *et al.*, 'Grandmaster level in StarCraft II using multi-agent reinforcement learning', *Nature*, vol. 575, no. 7782, pp. 350–354, Nov. 2019, doi: 10.1038/s41586-019-1724-z.
[32] A. Tampuu *et al.*, 'Multiagent cooperation and competition with deep reinforcement learning', *PLoS ONE*, vol. 12, no. 4, p. e0172395, Apr. 2017, doi: 10.1371/journal.pone.0172395.
[33] J. F. Nash, 'Equilibrium points in *n* -person games', *Proc. Natl. Acad. Sci. U.S.A.*, vol. 36, no. 1, pp. 48–49, Jan. 1950, doi: 10.1073/pnas.36.1.48.
[34] C. Farquhar, P. S. P. V. Kumar, A. Jagannath, and J. Jagannath, 'Distributed Transmission Control for Wireless Networks using Multi-Agent Reinforcement Learning', 2022, *arXiv*. doi: 10.48550/ARXIV.2205.06800.
[35] H. Byeon, 'Advances in Value-based, Policy-based, and Deep Learning-based Reinforcement Learning', *IJACSA*, vol. 14, no. 8, 2023, doi: 10.14569/IJACSA.2023.0140838.

[36] A. Mukherjee, 'A Comparison of Reward Functions in Q-Learning Applied to a Cart Position Problem', 2021, *arXiv*. doi: 10.48550/ARXIV.2105.11617.

[37] H. Alrakh, M. Fahmi, and R. Mohd, 'Smart Start and HER for a Directed and Persistent Reinforcement Learning Exploration in Discrete Environment', *IJACSA*, vol. 11, no. 11, 2020, doi: 10.14569/IJACSA.2020.0111117.

[38] D. Ghosh, A. Gupta, and S. Levine, 'Learning Actionable Representations with Goal-Conditioned Policies', 2018, *arXiv*. doi: 10.48550/ARXIV.1811.07819.

[39] C. Mercier, F. Alexandre, and T. Viéville, 'Reinforcement Symbolic Learning', in *Artificial Neural Networks and Machine Learning – ICANN 2021*, vol. 12894, I. Farkaš, P. Masulli, S. Otte, and S. Wermter, Eds., in Lecture Notes in Computer Science, vol. 12894. , Cham: Springer International Publishing, 2021, pp. 608–612. doi: 10.1007/978-3-030-86380-7_49.

[40] Y.-H. Wu, I.-H. Yeh, D. Hu, and H.-Y. M. Liao, 'Batch-Augmented Multi-Agent Reinforcement Learning for Efficient Traffic Signal Optimization', 2020, *arXiv*. doi: 10.48550/ARXIV.2005.09624.

[41] Y. Zhang and B. Zhang, 'Adaptive Concurrent Learning Algorithm Based on Pontryagin's Maximum Principle for Nonlinear System Optimal Tracking Control with State Inequality Constraints', *Proceedings of International Conference on Artificial Life and Robotics*, vol. 29, pp. 235–238, Feb. 2024, doi: 10.5954/ICAROB.2024.OS8-3.

[42] Y. Xu, A. Feriani, and E. Hossain, 'Decentralized Multi-Agent Reinforcement Learning for Task Offloading Under Uncertainty', 2021, *arXiv*. doi: 10.48550/ARXIV.2107.08114.

[43] V. Dunjko, J. M. Taylor, and H. J. Briegel, 'Quantum-Enhanced Machine Learning', *Phys. Rev. Lett.*, vol. 117, no. 13, p. 130501, Sep. 2016, doi: 10.1103/PhysRevLett.117.130501.

[44] Y. Ruan, W. Cai, and J. Wang, 'Combining Reinforcement Learning Algorithm and Genetic Algorithm to Solve the Traveling Salesman Problem', May 20, 2024. doi: 10.22541/au.171623645.58126524/v1.

[45] J. Y. H. Bai, C. K. Jonas Chan, D. Elliffe, and C. A. Podlesnik, 'Stimulus–reinforcer relations established during training determine resistance to extinction and relapse via reinstatement', *J Exper Analysis Behavior*, vol. 106, no. 3, pp. 225–241, Nov. 2016, doi: 10.1002/jeab.227.

[46] T. H. Freire De Oliveira, L. P. De Souza Medeiros, A. D. Dória Neto, and J. D. Melo, 'Q-Managed: A new algorithm for a multiobjective reinforcement learning', *Software Impacts*, vol. 9, p. 100089, Aug. 2021, doi: 10.1016/j.simpa.2021.100089.

Konya Mühendislik Bilimleri Dergisi., c.14, s.2, 628-647, 2026
Konya Journal of Engineering Sciences v.14, n.2, 628-647, 2026
ISSN: 2667-8055 (Electronic)
DOI: 10.36306/konjes.1687748

UTILIZING OPTIMIZATION APPROACHES TO ASSESS TOTAL NETWORK LOSSES IN TÜRKİYE

[1]Murat ASLAN, [2]Ömer Ali KARAMAN, [3]Mustafa SAĞLAM, [4,]*Mehmet Şefik ÜNEY

[1]*Mardin Artuklu University, Department of Computer Engineering, Engineering Faculty, Mardin 47000, Türkiye*
[2]*Batman University, Department of Electronic and Automation, Vocational School, Batman 72000, Türkiye*
[3]*Siirt University, Department of Electrical and Electronics Engineering, Siirt 56000, Türkiye*
[4]*Batman University, Department of Electrical and Energy, Vocational School, Batman 72000, Türkiye*
[1]maslan@artuklu.edu.tr, [2]omerali.karaman@batman.edu.tr, [3]mustafa.saglam@siirt.edu.tr
[4]msefik.uney@batman.edu.tr

Highlights

- Total network losses in Türkiye have been estimated using optimization-based methods.
- Long-term scenario analyses were conducted using AOA, IAOA, and LevyAOA algorithms.
- The IAOA method demonstrated lower error rates compared to other methods.
- Input-variable relationships were analyzed using multiple regression models.
- The developed models can serve as guidance for future energy planning.

Graphical Abstract

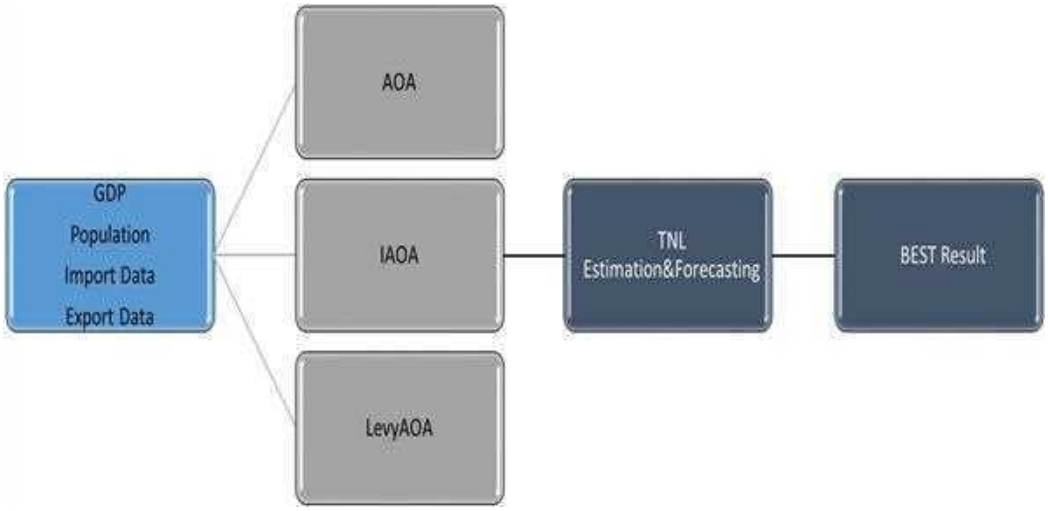


Figure. Flowchart of the methods used

***Corresponding Author:** Mehmet Şefik Üney, msefik.uney@batman.edu.tr

Konya Mühendislik Bilimleri Dergisi., c.14, s.2, 628-647, 2026
Konya Journal of Engineering Sciences v.14, n.2, 628-647, 2026
ISSN: 2667-8055 (Electronic)
DOI: 10.36306/konjes.1687748

UTILIZING OPTIMIZATION APPROACHES TO ASSESS TOTAL NETWORK LOSSES IN TÜRKİYE

[1]Murat ASLAN, [2]Ömer Ali KARAMAN, [3]Mustafa SAĞLAM, [4,*]Mehmet Şefik ÜNEY

[1]Mardin Artuklu University, Department of Computer Engineering, Engineering Faculty, Mardin 47000, Türkiye
[2]Batman University, Department of Electronic and Automation, Vocational School, Batman 72000, Türkiye
[3]Siirt University, Department of Electrical and Electronics Engineering, Siirt 56000, Türkiye
[4]Batman University, Department of Electrical and Energy, Vocational School, Batman 72000, Türkiye
[1]maslan@artuklu.edu.tr, [2]omerali.karaman@batman.edu.tr, [3]mustafa.saglam@siirt.edu.tr
[4]msefik.uney@batman.edu.tr

(Received: 30.04.2025; Accepted in Revised Form: 15.11.2025)

ABSTRACT: The accurate forecasting of energy losses in the interconnected grids of Türkiye assumes crucial importance in facilitating strategic planning, optimizing resource allocation, and fostering infrastructure development within the energy sector. A limited number of studies in the existing literature address the estimation of network losses, with investigations into such losses have predominantly relied on conventional machine learning (ML) methodologies. This study proposes an arithmetic optimization algorithm (AOA) approach to the total network losses (TNL) estimation of Türkiye. Firstly, the models are generated with AOA, IAOA, and LevyAOA methods, and then long-term TNL projections were conducted for three scenarios between 2021 and 2050. TNL is modelled as a linear regression model, and for this model, import, export, population, and gross domestic product (GDP) indicators are used as input parameters, and the TNL indicator is used as the output parameter. In the experiments, the historical data records of Türkiye from 1979 to 2020 are used to create the estimation model. Then, long-term TNL estimations with different scenarios are realized for Türkiye up to 2050. The TNL are expressed in gigawatt-hours (GWh) on an annual basis. According to the experimental results and comparisons, the IAOA method has shown quality and robust performance for estimating the TNL compared to other methods. Compared to the standard AOA, the proposed IAOA reduced the total error by **42.57%** and the total relative error by **55.49%** on the 1979–2020 dataset.

Keywords: *Arithmetic optimization algorithm; Network losses forecasting; Linear regression model*

1. INTRODUCTION

Technological advancements are accompanied by a parallel rise in the demand for electrical energy [1,2]. The high cost associated with installing energy production plants and the challenges in improving electricity transmission lines compel researchers to embark on new inquiries in this field. One of the primary purposes of these studies is to accurately estimate the losses in electrical transmission lines and use existing energy resources more efficiently. Minimizing these losses is a crucial issue for the safety and sustainability of energy transmission systems [3-6].

Electricity transmission lines are complex systems that encounter inevitable energy losses while transporting electrical energy from production points to consumption areas. Each country determines its own energy production/consumption strategy. It is essential to plan forward-looking strategies by considering local needs and following global developments. A good strategy is correctly analyzing the past and developing realistic plans [7, 8].

System losses are directly related to energy production and consumption data. Technically,

***Corresponding Author:** Mehmet Şefik Üney, msefik.uney@batman.edu.tr

researchers can analyze system losses in two sub-headings: technical and non-technical. Non-technical losses can be expressed as user error, illegal use, measuring device errors and index reading errors. Technical losses, on the other hand, are mostly losses caused by circuit devices within the system. Losses caused by circuit devices such as cables, transformers, insulators and measuring devices, which are the system's components, from the energy generation process to the transportation to the end user, can be evaluated in the class of technical losses. While numerous studies in the literature focus on energy production or demand estimation, there is a notable lack of research on energy loss estimation [9].

Many factors play a role in energy loss estimation. Relations and trends can be established between the loss estimation and variables such as economic, technological and demographic [10]. It is relatively easy to make short-term estimates by using basic mathematical models. However, simple mathematical models are insufficient for medium- and long-term forecasts because it will be difficult to establish the relations and complex interactions between the factors included in the estimating model with simple mathematical models [11].

Energy loss estimation investigations in Türkiye have been systematically undertaken since 1984 through the collaborative efforts of the Ministry of Energy and Natural Resources (MENR), the State Planning Organization, and the Turkish Statistical Institute (TUIK) [12, 13]. In addition, scientists have conducted studies on the subject for years [14]. Most energy loss estimation studies have been carried out as statistical and Artificial Neural Networks (ANN) [15].

Loss estimation studies have an essential role in forming strategic plans to be made by energy providers for the future. In [16], Tolic et al. simulated a 110 KV transmission line using the Monte Carlo method. In addition, the estimation of transmission line losses was conducted utilizing the Non-Linear Least Squares method, employing the Levenberg-Marquardt algorithm. In the study by Dursun et al. (2020), the total loss estimation study of Türkiye with ANN used humidity, heat, and temperature data [17]. To minimize the estimation errors of the Slovenian Power System, an estimation study was carried out using the fuzzy logic method [18, 19]. According to the results of the proposed approach, it was stated that there was an improvement in the estimation error rate. The supervised machine learning (ML) method was used to forecast the Croatian transmission line's short-term active power loss estimation. Loss values and meteorological data based on previous years were used as input data [20]. Extant literature includes loss estimation studies conducted using meteorological data. One of them, Yang et al., created a mathematical model and estimated transmission line loss [21]. Baran et al. used IEEE and CIGRE methods to estimate the heat losses of transmission lines. It was reported that the proposed estimation method is applied for the first time and needs improvement [22].

TNL forecasting affects the income of various power system grids. However, transmission losses are a minor proportion of the overall energy consumed, due consideration should be given to reducing investment and operating costs. Underestimating the TNL leads generation companies to generate less power than the actual power required to attain power balance. Moreover, overestimation misleads generating companies into producing more power than the actual demand necessitates. In the case of erroneous loss forecasting, the generator's actual power output values deviate from the predicted program to offset the discrepancy in the power balance. For all these reasons, TNL is essential for electricity generation companies in formulating their long-term strategies [23]. Studies on transmission losses in the literature have been conducted using old ML methods with limited data.

In this study, we used the Arithmetic Optimization Algorithm (AOA), the Improved Arithmetic Optimization Algorithm (IAOA) and Lévy-flight-based AOA (LevyAOA), inspired by the distribution behaviour of arithmetic operators in mathematics, to estimate transmission losses. These new metaheuristic algorithms use simple principles and require less parameter adjustment. The AOA method has been used in many real-world problems and estimation studies [24]. Dahou et al. conducted a study on recognizing human activities with less data to help healthcare professionals increase the speed of diagnosis. They achieved high success rates using the AOA method [25]. Abualigah et al. applied a new hybrid optimization technique using the AOA method to decompose wind speed data [26]. Khatir et al. used an AI-based hybrid AOA method to learn plate-shaped composite materials' damage detection and

damage level [27]. The AOA method and many coal price estimation algorithms were also examined. It was stated that the AOA method was observed to give successful results compared to other methods [28]. Aslan et al. made an energy demand estimation study of Türkiye until 2030 using the AOA and the IAOA method. Consequent to the comparisons, it was stated that the IAOA method was superior to the other methods [2].

This study focused on projecting the TNL of Türkiye until the year 2050, utilizing AOA, IAOA, and LevyAOA optimization techniques. Three different scenarios (low, base, and high) are applied to each method. These scenarios are devised by assessing the relative variances among the historical values of the input data employed in the proposed methodologies. Consequently, a variety of scenario ratios and input values are implemented in this study. Official scenarios that the Turkish Statistical Institute provides are considered for population projections [29]. Moreover, future economic data estimates are determined based on percentages derived from existing studies in the literature, as well as scenarios presented by the International Monetary Fund (IMF) and the World Bank [30, 31]. A correlation matrix was utilized to depict the correlation between observed values and method-predicted values, as well as the relationships among independent parameters (GDP, import, population, export) and the dependent variable (TNL). The analysis of the correlation matrices has provided insights into the variables that influence the results and their respective impact. Additionally, subsets of multiple regression equations (MLR) were developed to model the input variables. The study compared the parameters influencing the output by evaluating their R-squared and p-value performances in the resulting equations. The TNL forecasting performance of AOA, IAOA, and LevyAOA optimization methods was compared using MLR and correlation matrices. The contributions of this study can be distilled into the following five points:

- This study aimed to enhance accuracy by developing multi-objective forecasting models using different optimization methods. The forecast performances in the case study of Türkiye were evaluated using total error and total relative error, utilizing inter-year data for TNL forecasting. The predicted TNL results served as dependable and informative references for future decades.
- The impact of independent inputs utilized for TNL estimating on the forecast output was examined using MLR various combinations and subsets.
- To enhance forecast accuracy and showcase the efficacy of the employed method, both total error and total relative error were incorporated.
- This entails the technical analysis of identifying optimal parameters for the methods through the utilization of output-input correlation matrices. As a result, it unveils the extent to which the independent variables impact the dependent variable.
- This study's accurate TNL prediction helps avoid unnecessary reserves and ensures optimal system operation.

This study makes two main contributions to the existing literature. First, it introduces an improved IAOA update tailored to the least-squares framework of TNL estimation, which enhances stability and accelerates convergence. Second, it develops a transparent scenario protocol for the 2021-2050 period that links input parameters (GDP, population, imports, exports) to TNL projections. In addition, all parameter settings are explicitly reported and error components are carefully analyzed to ensure a fair comparison of AOA, IAOA, and LevyAOA.

More broadly, the study adapts the AOA algorithm to the least-squares for TNL estimation and evaluates its performance in a comparative setting, while also presenting an open scenario framework that connects nationally available economic and demographic indicators to long-term TNL forecasts between 2021 and 2050. Furthermore, to guarantee reproducibility, all experimental settings are detailed, error decomposition is performed, multiple linear regression (MLR) subset analyses are conducted, and correlation matrices are examined. The significance of the work is practical: the linear and interpretable specification allows coefficients to be traced clearly, and the scenario-based projections can provide valuable input for energy policy design and grid planning.

The remainder of the paper is structured as follows: The basic AOA algorithm is explained in Section

2. The IAOA and LevyAOA are presented in Section 3. Section 4 elucidates the TNL problem, while Section 5 analyses and compares the experimental results derived from the proposed algorithms. The conclusions and future works are given in Section 6.

2. MATERIALS AND METHODS

2.1. Arithmetic Optimization Algorithm (AOA)

Abualigah et al. [26] proposed an arithmetic optimization metaheuristic algorithm using mathematical operators' fundamental strategies. The mathematical operators that are used in the AOA can be described as follows: the subtraction operator (S), the multiplication operator (M), the addition operator (A) and the division operator (D). These operators are used to find new solutions in the search space.

The process of searching for new solutions in AOA is divided into two phases such as exploration and exploitation phases. The mathematical operators of addition and subtraction are used in the exploitation phase of the AOA method, and the mathematical operators of multiplication and division are used in the exploration phase of the AOA method. The phases of exploration and exploitation used in the AOA method for the searching process are shown in Figure 1.

According to Figure 1, the AOA method was divided into two phases (exploration and exploitation phases) for searching in search space. The AOA method used the math optimizer accelerated (MOA) function in the main concept of AOA for selecting the exploration or exploitation phase to create a new search agent position. MOA was calculated with Eq. (1).

$$MOA(C_Iter) = Min + C_Iter \times \frac{\quad}{\quad} \tag{1}$$

In the context of the given expression, Min denotes the minimum value, and Max signifies the maximum value of the accelerated coefficients. The term $MOA(C_Iter)$ represents the function value at the t-th iteration, where C_Iter corresponds to the current iteration. Additionally, Max_Iter signifies the stopping criterion, indicating the maximum number of iterations in the AOA method.

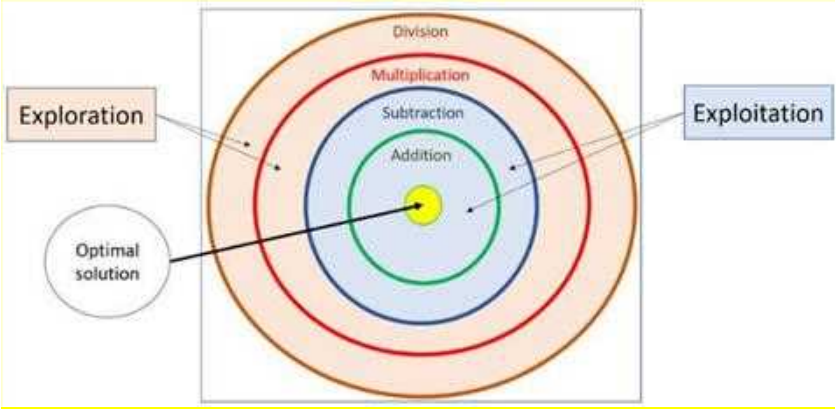


Figure 1. The exploration and exploitation phases in AOA [26]

2.1.1 Exploration phase

The efficient use of exploration and exploitation mechanisms positively affects the optimization performance of each optimization algorithm. Therefore, both the exploration and exploitation processes of the AOA method have a vital role in this study. The exploration and exploitation phases of the AOA

method are executed according to the value of the MOA coefficient. If a randomly generated value (r) is greater than the value of the MOA coefficient, then the exploration phase is performed to generate a candidate solution; otherwise, the exploitation phase is performed to generate a candidate solution. In the exploration phase, if a randomly generated value (r) is greater than 0.5, then the division operator of the AOA method is executed to generate a new position for the current candidate solution, and the multiplication operator of the AOA method is carried out to develop a new position for the current candidate solution. Eq. (2) explains the update rule of the exploration phase as follows:

$$x_{,}(C_Iter+1) = \begin{cases} best\ x \ \div (MOP+\epsilon) \times \ UB - LB \ \times \mu + LB \ , r > 0.5 \\ best\ x \ \times MOP \times \ UB - LB \ \times \mu + LB \ , otherwise \end{cases} \quad (2)$$

Where μ refers to a control parameter for adjusting the search process, x refers to the total number of individuals in the population, $best$ shows the position of agent (candidate solution) with the best fitness value, i denotes the order in which a solution is presented $(1,2,\dots,N)$, j refers to the order of dimensions $(1,2,\dots,d)$. ϵ shows a small integer number, UB denotes the upper bound of the jth position of a search agent and LB denotes the lower bound of the jth position of a search agent. MOP indicates the mathematical optimizer probability, and it is calculated as follows:

$$MOP(C\ \ ) = 1 - C_Iter \times \frac{-}{-} \quad (3)$$

Eq. (3) defines the $MOP(C\ \ )$ used in the AOA update; this criterion is evaluated at each iteration as depicted in Figure 2.

2.1.2 Exploitation phase

In the exploitation phase of the basic AOA method, addition and subtraction mathematical operators are employed. If r value is less than or equal to the MOA value, then the exploitation phase is processed. In the exploitation phase, if a randomly generated value (r) is greater than 0.5 value, then the subtraction math operator of the AOA method is executed to generate a new position for the current candidate solution; otherwise, the addition math operator of the AOA method is carried out to generate a new position for the current candidate solution. Eq. (4) explains the update rule of the exploitation phase as follows:

$$x_{,}(C\ \ +1) = \begin{cases} best\ x \ - MOP \times \ UB - LB \ \times \mu + LB \ , r > 0.5 \\ best\ x \ + MOP \times \ UB - LB \ \times \mu + LB \ , otherwise \end{cases} \quad (4)$$

The flowchart of the basic AOA is given in Figure 2.

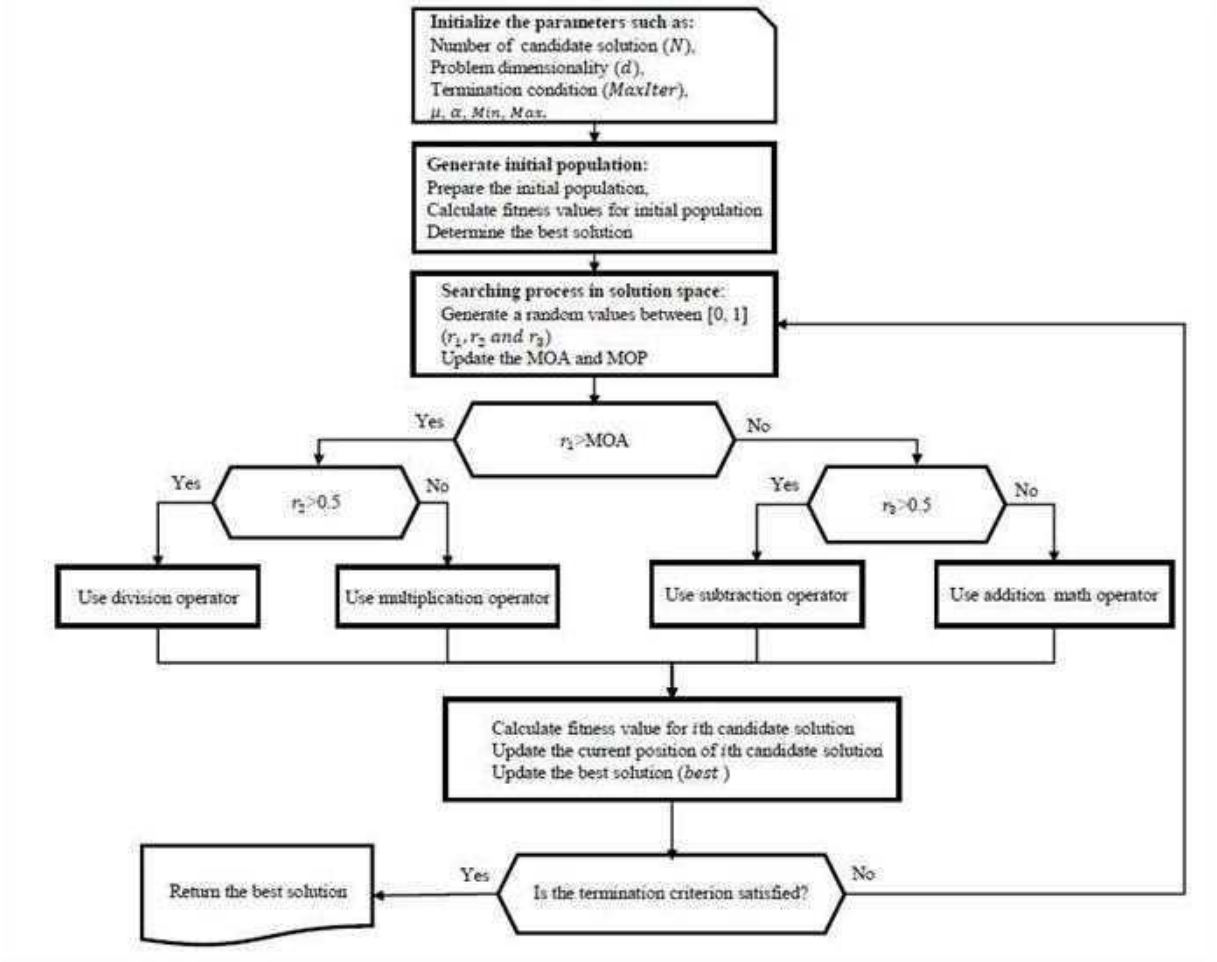


Figure 2. Flowchart of the Arithmetic Optimization Algorithm (AOA) adapted from [26]

2.2 Proposed algorithms

Firstly, the basic AOA has been applied to the problem considered in this study. Since the results obtained from the basic AOA are inconclusive, different AOA-based procedures have been proposed and implemented to estimate the total energy loss problem. For this purpose, the basic AOA method update rule has been modified with two approaches to enhancing AOA's exploration and exploitation capability. In the first approach, a new position update rule used in the study of Aslan and Beşkirli [2] is incorporated into the original position update rule of the AOA technique. In the second approach, the lévy flight function used in the study by Mat et al. [32] is incorporated into the basic update rule of the AOA method.

2.2.1 Arithmetic optimization algorithm with a new position update rule (IAOA)

The basic AOA generates new candidate positions using arithmetic operators (subtraction, multiplication, addition, and division). To alleviate the slow convergence sometimes observed with the basic AOA, the best-guided position update introduced by Aslan and Beşkirli [2] is adopted and integrated into AOA's exploration and exploitation phases. Let *i* denote the agent (candidate solution), *j* the dimension, and *C_Iter* the current iteration. Using the notation in Eq. (5), the step toward the current global best is computed, and a uniformly random scalar rand() ∈ (0,1) scales this step in the update. Decision variables are kept within their bounds by applying boundary control after each update.

$$Step_{,} = best\ x\ \ - x_{,}$$
$$x_{,}(C_Iter + 1) = best\ x\ \ + rand() \times Step_{,} \quad (5)$$

The update guides each candidate toward the current best with a stochastic displacement. Geometrically, the population contracts around promising basins (exploitation), while randomness and boundary control prevent collapse and preserve exploration. In the present setting least-squares–type error over continuous linear coefficients the objective surface is relatively smooth; hence a best-guided step reduces wandering and accelerates convergence without sacrificing robustness to noise. The improved rule itself is not claimed as novel here; rather, the contribution lies in its tailored application and rigorous evaluation for national-scale TNL forecasting (multi-metric objective, rolling-origin tests, and uncertainty bands).

2.2.2 Arithmetic optimization algorithm with lévy flight (LevyAOA)

A Lévy flight is a statistical search function and was proposed by French mathematician Paul Levy [32]. A Lévy flight is a class of stable non-Gaussian random processes [33]. The random motion function is used for the advantage of Levy's stable distribution. This distribution is actually a simple power law function. The mathematical formulation of the Lévy flight function can be calculated with Eq. (6)- Eq. (8) [34-37].

$$L \quad = 0.01 \times \left\{ \frac{}{(\quad)} \times \frac{(\quad)\times \quad -\times}{__ \times \times \ __} \right\} \quad (6)$$

$$levy(\beta) = L \quad \times N \quad (7)$$

$$x_{,}(C \quad + 1) = x_{,} + N(0, \sigma \quad) \times levy(\beta) \quad (8)$$

Where L indicates the step size of the Lévy flight function, N indicates a random value, $x_{,}$ indicates the position of the current AOA individual, $N(0, \sigma\ \ )$ is a random value generated from a normal distribution with an average of zero and standard deviation values. β is a constant value and is equal to 1.5 in this study. Consequently, by integrating the Lévy flight function in AOA as the sphere search operator in the spatial propagation, the performance of the AOA in the search space is extended. After these explanations, the framework of the proposed algorithms is given in Figure 3.

2.3 Total network losses estimation problem

This study estimates the total energy losses in Türkiye using a linear regression model based on a cost function. The export, import, population and GDP indicators are used as the input parameters and the TNL is used as the output parameter of the linear regression model. For experiments, a historical data record of Türkiye for the years 1979-2020, such as population, GDP, imports, and exports, is taken from TUIK [38], and TNL is obtained from Türkiye Electricity Transmission Corporation (TEIAS) [39]. The TNL data obtained from TEIAS represent the annual total transmission losses measured in gigawatt-hours (GWh).

Step 1: The initialization of algorithm
Set the dimension of the problem (d)
Set the number of candidate solution (N)
Set the termination condition (Max_Iter)
Set μ, α, Min, Max
Step 2: Generate initial population
Generate N random candidate solution on the d-dimensional search space
Calculate fitness value for each candidate solution
determine the best solution ($best$)
Initialize the iteration counter with C_Iter ($C_Iter = 2$)
Step 3: Searching process in solution space
WHILE $C_Iter <= Max_Iter$
Update the MOA value
Update the MOP value
FOR Each candidate solution (x)
FOR each dimension of candidate solution ($x_{,}$)
Generate a random values between [0, 1] (r_1, r_2 and r_3)
IF r_1 >MOA
Exploration phase
IF $rand()$>0.5 // rand indicates a random value in range of [0,1]
Use current update rule of basic AOA
IF r_2 >0.5
Apply the division math operator given in Eq. (2)
ELSE
Apply the multiplication math operator given in Eq. (2)
END IF
ELSE
Apply the proposed update rules given in Eq. (5) or Eq. (8)
END IF
ELSE
Exploitation phase
IF $rand()$>0.5 // rand indicates a random value in range of [0,1]
Use current update rule of basic AOA
IF r_2 >0.5
Apply the subtraction math operator given in Eq. (4)
ELSE
Apply the Addition math operator given in Eq. (4)
END IF
ELSE
Apply the proposed update rules given in Eq. (5) or Eq. (8)
END IF
END IF
Calculate fitness value for ith candidate solution
Update the current position of ith candidate solution
Update the best solution ($best$)
END FOR
END FOR
$C_Iter = C_Iter$ +1
Step 5: Testing the termination condition
IF Termination condition is not satisfied
Go to Step 3
ELSE
Report the best solution
END WHILE

Figure 3. The framework of the proposed algorithms

The proposed estimation model is shown in Figure 4. Firstly, the received data was used as input data

in the proposed optimization models after going through a data preprocessing process. Then, in the prediction step, the proposed models were tested, and the best estimation performance of the models was detected. After evaluating the performance statistics of methods, recommendations were offered for the installation of the power systems, energy, and economic savings.

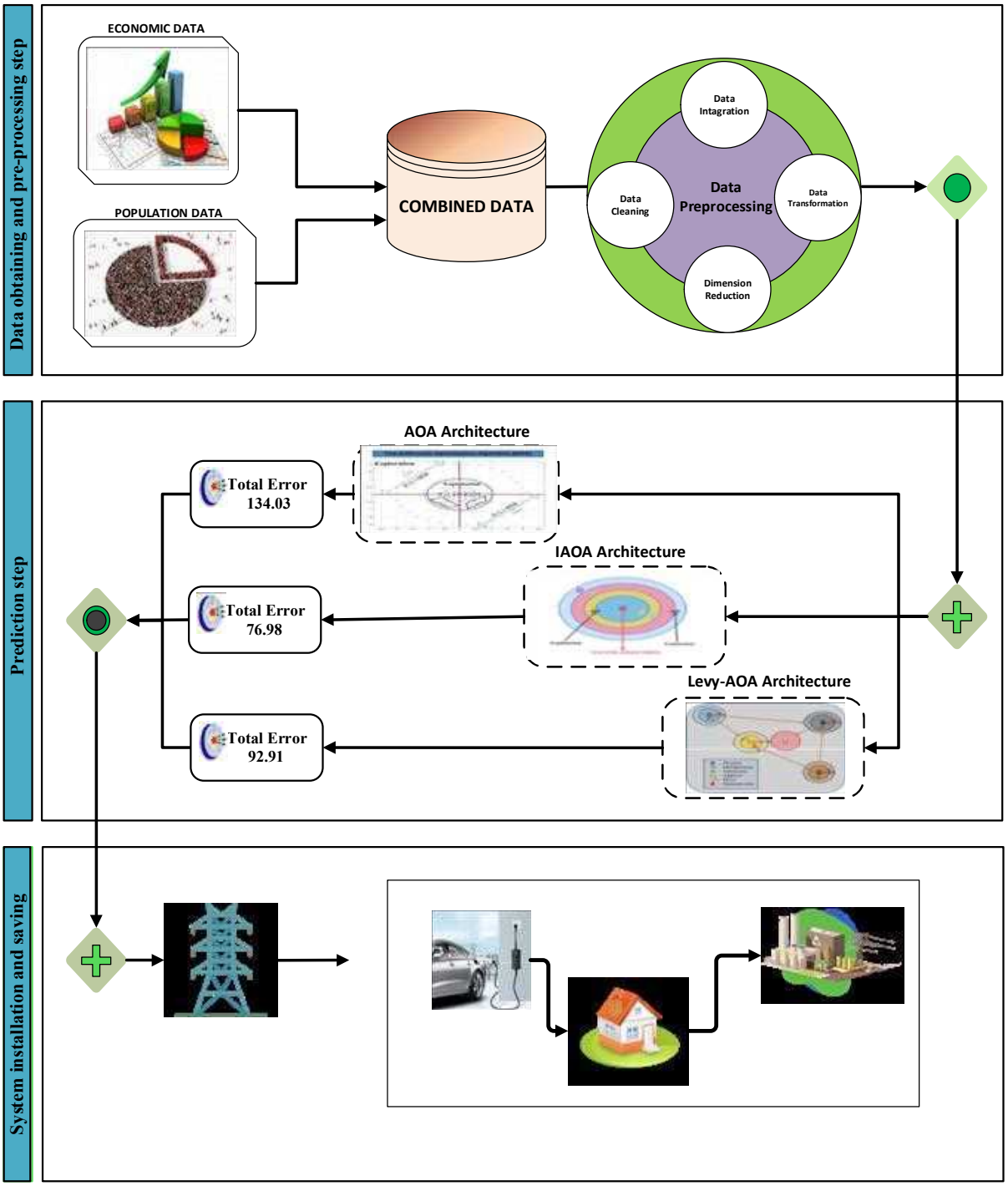


Figure 4. Flowchart of the proposed model

The linear regression model [2, 40, 41] used in this study is given in Eq. (9).

$$TNL = W + W X + W X + W X + W X \quad (9)$$

Here, TNL refers to the results of TNL found by the proposed linear regression model, the weight coefficients of the linear model represented with $W - W$. W is the intercept (independent term), and W , W , W and W correspond to the GDP, population, import, and export indicators, respectively. X , X , X and X denote the observed annual historical records of GDP, population, imports, and exports. After the TNL value for each year is calculated, the squared difference between the estimated total network losses (ETNL) produced by the proposed models and the observed total network losses (OTNL) is computed. The total network energy losses estimation is formulated as a minimization problem, and therefore, ETNL and OTNL are expected to be close to each other. The mathematical formulation of the fitness function is given in Eq. (10) [2, 41]. Where r refers to a year, and it is in range of ($r = 1, 2, \ldots, R$) and R indicates the total amount of the total number of years. TNL and TNL correspond to the OTNL and ETNL of the r[th] year, respectively.

$$\min \; f(v) = \sum_{r=1}^{R} \left(TNL_r^{observed} - TNL_r^{estimated} \right)^2 \quad (10)$$

3. RESULTS AND DISCUSSION

The linear regression model is employed for TNL estimation in Türkiye to demonstrate the efficacy of the proposed methodologies. The proposed algorithms were implemented in the MATLAB platform, utilizing a laptop with WINDOWS 10 PRO OS, INTEL(R) CORE(TM) I7-6700HQ 2.60 GHZ CPU, and 24 GB OF RAM for experimentation. The AOA, IAOA, and LevyAOA methods underwent ten independent runs with random initialization, and the best results from each run were utilized for comparisons. The population size was set at 100, and the total maximum iterations (Max_Iter) were fixed at 5000 for all methods. The algorithmic parameters for AOA were determined following the basic AOA, with μ, α, Min, Max parameters set at 0.5, 5, 0.2, and 1, respectively.

Before projecting future estimations with the compared methods, the experimental results of the algorithms under consideration are presented as the best of 10 runs, including the number of errors, relative error and computation time in seconds. Subsequently, upon determining the coefficients of the linear model-based AOA, IAOA, and LevyAOA methods, long-term TNL estimations for Türkiye were conducted for the years 2021-2050 under three distinct scenarios. The test suit used in this study is presented in Table 1.

Table 1. Türkiye's TNL, GDP, population, import and export data for the years (1979-2020) [29, 30, 31, 38].

Year	TNL (10^3)	Import ($10^9)	Export ($10^9)	GDP ($10^9)	Population (10^6)	Year	TNL (10^3)	Import ($10^9)	Export ($10^9)	GDP ($10^9)	Population (10^6)
1979	2.56	5.07	2.26	80.97	43.53	2000	23.76	54.50	27.78	273.09	64.27
1980	2.82	7.91	2.91	67.46	44.44	2001	23.33	41.40	31.33	202.50	65.17
1981	2.93	8.93	4.70	70.40	45.54	2002	23.93	51.55	36.06	238.15	66.00
1982	3.32	8.84	5.75	63.50	46.69	2003	24.05	69.34	47.25	316.56	66.80
1983	3.42	9.24	5.73	60.36	47.86	2004	23.24	97.54	63.17	407.02	67.60
1984	3.74	10.76	7.13	58.64	49.07	2005	24.04	116.77	73.48	504.75	68.44
1985	4.35	11.34	7.95	66.41	50.31	2006	23.79	139.58	85.54	552.37	69.30
1986	5.45	11.10	7.46	75.04	51.48	2007	26.65	170.06	107.27	683.02	70.16
1987	5.62	14.16	10.19	85.62	52.37	2008	27.48	201.96	132.03	782.86	71.05

1988	6.31	14.34	11.66	90.51	53.27	2009	28.99	140.93	102.14	651.54	72.04
1989	6.25	15.79	11.62	106.11	54.19	2010	30.22	185.54	113.88	777.46	73.14
1990	6.68	22.30	12.96	149.19	55.12	2011	32.37	240.84	134.91	837.92	74.22
1991	7.56	21.05	13.59	149.16	56.06	2012	35.66	236.55	152.46	877.68	75.18
1992	8.99	22.87	14.72	156.66	56.99	2013	37.13	260.82	161.48	958.13	76.15
1993	10.25	29.43	15.35	177.33	57.91	2014	37.33	251.14	166.51	939.92	77.18
1994	11.84	23.27	18.11	131.64	58.84	2015	36.53	213.62	150.98	867.07	78.22
1995	13.77	35.71	21.64	168.08	59.76	2016	35.61	202.19	149.25	869.24	79.28
1996	15.85	43.63	23.22	181.08	60.67	2017	34.66	238.72	164.50	859.06	80.31
1997	18.58	48.56	26.26	188.73	61.58	2018	31.63	231.15	177.17	797.12	81.41
1998	20.79	45.92	26.97	277.67	62.46	2019	31.29	210.35	180.83	759.29	82.58
1999	21.55	40.67	26.59	254.12	63.36	2020	29.37	219.52	169.64	717.09	83.39

3.1 Comparison of the experimental results of AOA, IAOA and LevyAOA methods on the historical data records of Türkiye for the years 1979-2020

The provided section presents the experimental outcomes of the AOA, IAOA, and LevyAOA methods in estimating the TNL for Türkiye. The comparative analysis of these algorithms is based on fitness values, the number of errors, relative errors, total errors, and total relative errors. Table 2 details the weight values, fitness values, total errors, and total relative errors derived from the AOA, IAOA, and LevyAOA methods for 1979-2020.

Upon reviewing Table 2 concerning the estimated TNL results spanning from 1979 to 2020, it is evident that the IAOA algorithm achieved the most favourable total error and total relative error values. In contrast, the basic AOA algorithm exhibits the least favourable total error and relative error values.
Table 3 presents the values for OTNL, ETNL, the number of errors, and relative errors for the years spanning from 1979 to 2020. The error amount indicates the disparity between OTNL and ETNL. The number of errors can be elucidated using the results for 1979 as an example: the AOA method yielded several errors of 5.92 for 1979, calculated as the difference between the ETNL value of 8.48 and the OTNL value of 2.56. The relative error value is computed using the number of errors and OTNL according to the following formula: $(amount\ of\ errors/\mathrm{OTNL}) * 100$.

Table 3 compares the OTNL and ETNL values of the three methods. Additionally, IAOA outperforms the other methods in 22 estimated outcomes, while LevyAOA performs best in 13 estimated outcomes.

Table 2. The weight values, fitness values, total error and total relative error (%) results found by AOA, IAOA and LevyAOA methods for the years 1979-2020

Method	Weight values	Fitness value	Total Error	Total relative Error (%)	Time
AOA	[-0.3405 -0.0495 -0.0339 0.0491 0.1190]	634.17	134.03	1769.61	17.38
IAOA	[-39.8147 0.0220 -0.1551 0.0296 0.8668]	**204.97**	**76.98**	**787.58**	**14.24**
LevyAOA	[-36.9996 -0.0455 -0.0305 0.0295 0.8009]	298.66	92.91	834.10	27.25

Table 3. The OTNL, ETNL, amount of errors and relative error (%) results found by AOA, IAOA and LevyAOA methods for the years 1979-2020

Year	OTNL	ETNL			Amount of errors			Relative error (%)		
		AOA	IAOA	LevyAOA	AOA	IAOA	LevyAOA	AOA	IAOA	LevyAOA
1979	2.56	8.48	0.08	-0.05	5.92	-2.49	-2.61	231.00	-97.04	-101.79
1980	2.82	7.77	0.43	0.14	4.94	-2.40	-2.69	174.94	-84.90	-95.21
1981	2.93	7.93	1.21	1.00	5.00	-1.72	-1.93	170.54	-58.66	-65.82
1982	3.32	7.70	1.84	1.69	4.38	-1.48	-1.63	132.00	-44.55	-49.02
1983	3.42	7.66	2.77	2.52	4.24	-0.65	-0.90	123.91	-18.98	-26.42
1984	3.74	7.60	3.59	3.32	3.86	-0.15	-0.42	103.17	-4.11	-11.12
1985	4.35	8.07	4.78	4.50	3.73	0.43	0.15	85.73	9.93	3.45
1986	5.45	8.66	6.12	5.71	3.22	0.67	0.27	59.05	12.32	4.90
1987	5.62	9.04	6.85	6.52	3.42	1.23	0.90	60.92	21.82	15.94
1988	6.31	9.33	7.55	7.33	3.02	1.24	1.02	47.93	19.63	16.16
1989	6.25	10.14	8.84	8.46	3.89	2.60	2.21	62.25	41.57	35.43
1990	6.68	11.99	10.86	10.14	5.31	4.18	3.46	79.52	62.58	51.78
1991	7.56	12.14	11.55	10.93	4.58	3.99	3.37	60.60	52.75	44.54
1992	8.99	12.49	12.44	11.78	3.50	3.45	2.78	38.90	38.33	30.94
1993	10.25	13.27	13.90	12.81	3.02	3.65	2.56	29.46	35.58	24.93
1994	11.84	11.35	12.79	12.40	-0.49	0.95	0.56	-4.15	7.99	4.70
1995	13.77	12.51	14.39	13.54	-1.26	0.62	-0.23	-9.12	4.52	-1.68
1996	15.85	12.81	15.49	14.24	-3.04	-0.36	-1.61	-19.18	-2.28	-10.17
1997	18.58	12.95	16.15	14.88	-5.63	-2.44	-3.70	-30.31	-13.11	-19.92
1998	20.79	17.52	19.37	18.31	-3.27	-1.42	-2.49	-15.73	-6.84	-11.96
1999	21.55	16.75	19.40	18.58	-4.80	-2.15	-2.96	-22.26	-9.96	-13.75
2000	23.76	17.06	20.87	19.21	-6.69	-2.89	-4.55	-28.17	-12.15	-19.15
2001	23.33	14.24	18.72	18.33	-9.09	-4.61	-5.00	-38.98	-19.75	-21.42
2002	23.93	15.42	19.99	19.44	-8.51	-3.95	-4.49	-35.57	-16.49	-18.76
2003	24.05	18.10	21.66	21.25	-5.95	-2.40	-2.81	-24.74	-9.96	-11.67
2004	23.24	20.70	23.18	22.79	-2.54	-0.06	-0.46	-10.95	-0.28	-1.96
2005	24.04	24.29	25.62	25.15	0.25	1.58	1.11	1.03	6.57	4.62
2006	23.79	25.19	26.41	25.84	1.40	2.62	2.05	5.90	11.01	8.63
2007	26.65	29.46	28.32	28.34	2.81	1.68	1.69	10.55	6.29	6.34
2008	27.48	32.04	28.91	29.79	4.56	1.43	2.31	16.60	5.20	8.40
2009	28.99	29.75	29.17	30.40	0.76	0.18	1.40	2.63	0.63	4.84
2010	30.22	33.46	33.02	32.60	3.23	2.79	2.38	10.70	9.25	7.88
2011	32.37	33.10	33.70	32.10	0.73	1.33	-0.27	2.25	4.10	-0.84
2012	35.66	34.78	32.89	33.70	-0.88	-2.77	-1.96	-2.46	-7.76	-5.50
2013	37.13	37.34	35.25	35.47	0.20	-1.89	-1.67	0.54	-5.09	-4.49
2014	37.33	36.87	34.61	36.04	-0.46	-2.72	-1.29	-1.23	-7.30	-3.45
2015	36.53	35.81	34.93	36.91	-0.72	-1.59	0.38	-1.97	-4.36	1.04
2016	35.61	36.66	35.93	38.39	1.05	0.32	2.78	2.96	0.91	7.81
2017	34.66	33.96	34.96	36.79	-0.70	0.31	2.13	-2.01	0.88	6.15
2018	31.63	31.00	31.95	35.80	-0.64	0.32	4.17	-2.01	1.00	13.17
2019	31.29	30.19	30.82	36.46	-1.10	-0.46	5.17	-3.51	-1.48	16.53
2020	29.37	28.14	32.21	35.78	-1.23	2.84	6.42	-4.18	9.69	21.85

3.2 Estimating results of long-term total network losses for the years 2021-2050 with the AOA, IAOA and LevyAOA methods

Türkiye's long-term TNL is estimated for three different scenarios for 2021-2050. The possible future scenarios used in this study are given in Table 4.

Table 4. The possible future scenarios for the years 2021-2050.

Indicator	Scenario I	Scenario II	Scenario III
GDP growth rate	1.0 %	4.5 %	6.0 %
Population growth rate	3.0 %	2.0 %	3.0 %
Import growth rate	1.0 %	2.0 %	3.0 %
Export growth rate	1.0 %	3.0 %	3.0 %

Each method encompasses three distinct scenarios: high, base, and low. These scenarios are formulated based on the historical data records of Türkiye concerning GDP, export, import, and population indicators. Consequently, various scenario ratios and input values are employed to project TNL estimates. Table 5 provides the experimental outputs derived from the proposed AOA, IAOA, and LevyAOA models for Scenarios I, II, and III.

As indicated in Table 5, the model based on IAOA yields superior results for Scenarios I, II, and III compared to the other models under consideration. IAOA attains slightly lower in-sample error than AOA and LevyAOA because its best-guided position update reduces random wandering and improves exploitation on the least-squares surface, yielding a more stable coefficient vector. Since all three methods optimize the same linear specification under smooth scenario inputs, the long-run TNL trajectories are expectedly close, which we interpret as a robustness feature rather than a discrepancy**.** The graphical representation of TNL for the compared algorithms from 2021 to 2050 is depicted in Figure 5, Figure 6, and Figure 7 for Scenario I, II, and III, respectively.

Table 5. The estimated TNL of Türkiye for the years 2021-2050 with Scenario I-III

Year	Scenario I			Scenario II			Scenario III		
	AOA	IAOA	LevyAOA	AOA	IAOA	LevyAOA	AOA	IAOA	LevyAOA
2021	29.13	33.35	36.93	29.59	34.19	37.77	30.05	35.01	38.60
2022	30.15	34.53	38.11	31.11	36.22	39.82	32.08	37.93	41.54
2023	31.20	35.72	39.31	32.69	38.31	41.93	34.24	40.98	44.61
2024	32.28	36.94	40.54	34.36	40.48	44.11	36.53	44.16	47.82
2025	33.40	38.18	41.78	36.10	42.72	46.37	38.97	47.48	51.16
2026	34.55	39.46	43.07	37.93	45.04	48.69	41.56	50.95	54.66
2027	35.74	40.76	44.38	39.84	47.43	51.10	44.32	54.58	58.31
2028	36.97	42.08	45.71	41.84	49.89	53.57	47.24	58.37	62.13
2029	38.23	43.44	47.07	43.93	52.44	56.14	50.35	62.33	66.11
2030	39.54	44.82	48.46	46.13	55.07	58.79	53.66	66.47	70.27
2031	40.88	46.25	49.89	48.42	57.79	61.52	57.17	70.80	74.63
2032	42.27	47.70	51.34	50.82	60.61	64.36	60.90	75.32	79.18
2033	43.70	49.17	52.83	53.34	63.51	67.28	64.86	80.06	83.94
2034	45.17	50.68	54.34	55.97	66.52	70.30	69.06	85.01	88.92
2035	46.69	52.23	55.90	58.72	69.63	73.43	73.53	90.20	94.14
2036	48.26	53.81	57.49	61.61	72.85	76.67	78.28	95.63	99.60
2037	49.87	55.43	59.11	64.63	76.18	80.01	83.32	101.31	105.31
2038	51.54	57.09	60.78	67.78	79.62	83.46	88.67	107.26	111.29
2039	53.25	58.77	62.47	71.09	83.18	87.04	94.35	113.48	117.54
2040	55.02	60.51	64.21	74.55	86.86	90.74	100.39	120.01	124.10
2041	56.85	62.28	65.99	78.17	90.67	94.57	106.79	126.85	130.97
2042	58.73	64.09	67.80	81.95	94.62	98.54	113.59	134.01	138.16
2043	60.67	65.94	69.66	85.92	98.71	102.64	120.82	141.52	145.71
2044	62.67	67.83	71.56	90.06	102.94	106.89	128.48	149.39	153.61
2045	64.73	69.77	73.51	94.40	107.32	111.29	136.62	157.65	161.90

2046	66.85	71.76	75.50	98.94	111.86	115.85	145.26	166.31	170.60
2047	69.04	73.79	77.54	103.69	116.56	120.57	154.43	175.38	179.71
2048	71.30	75.87	79.62	108.65	121.42	125.45	164.16	184.91	189.27
2049	73.62	77.99	81.75	113.85	126.47	130.52	174.49	194.90	199.30
2050	76.02	80.18	83.94	119.28	131.70	135.76	185.45	205.40	209.84

As illustrated in Figures 5–7, the long-term projections obtained from AOA, IAOA, and LevyAOA are very close to each other. This similarity is attributed to the application of all three metaheuristic optimizers to the same linear regression framework specification under smooth economic and demographic scenario inputs. While short- and medium-term estimations show that IAOA achieves lower errors due to its enhanced convergence capability, the alignment of long-term trajectories indicates that the estimated coefficients are stable and the results are not sensitive to algorithmic variations. Therefore, the closeness of the projections across methods can be interpreted as a robustness feature of the proposed framework, enhancing the credibility and reproducibility of the policy-oriented scenarios.

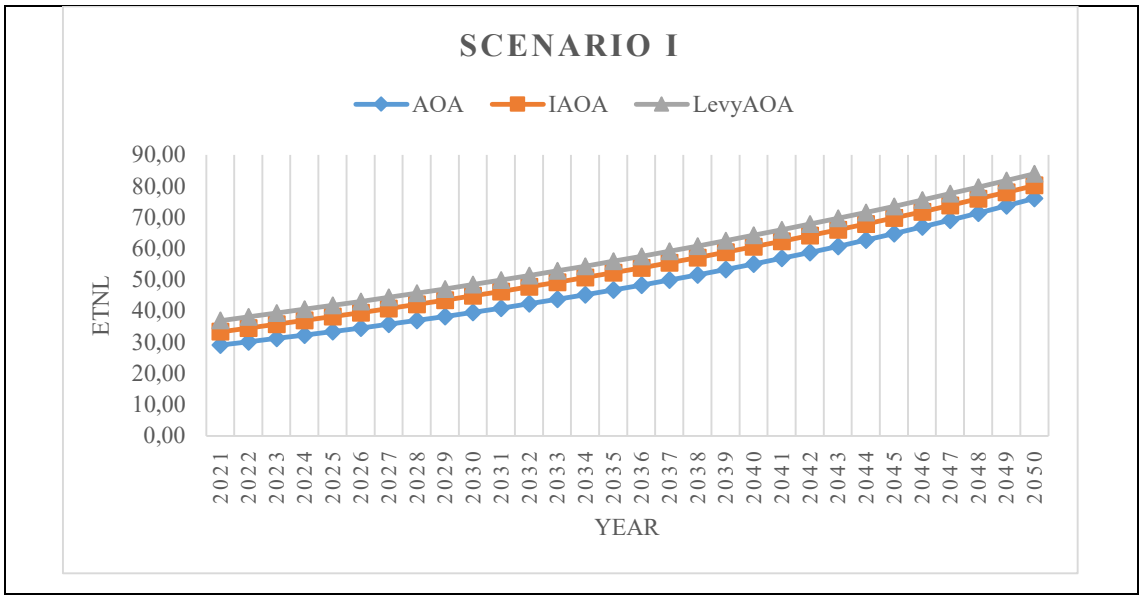


Figure 5. The estimated TNL of the proposed methods with scenario I

Figures 5–7 indicate that the long-term TNL projections of AOA, IAOA, and LevyAOA converge to highly similar trajectories, particularly under Scenario I. While IAOA achieves superior accuracy in fitting historical data, this advantage diminishes in the long-run forecasts, as the projections are predominantly shaped by the structural properties of the linear regression model and the exogenous scenario assumptions rather than by the optimization algorithm itself. This convergence highlights the robustness of the proposed framework, demonstrating that the long-term outcomes remain stable and consistent across different optimizers, while IAOA's short- and medium-term performance ensures more reliable coefficient estimation and reduced bias. Overall, the findings suggest that the choice of optimizer is critical for historical accuracy, but the linear specification and scenario design play a more dominant role in determining long-term projections.

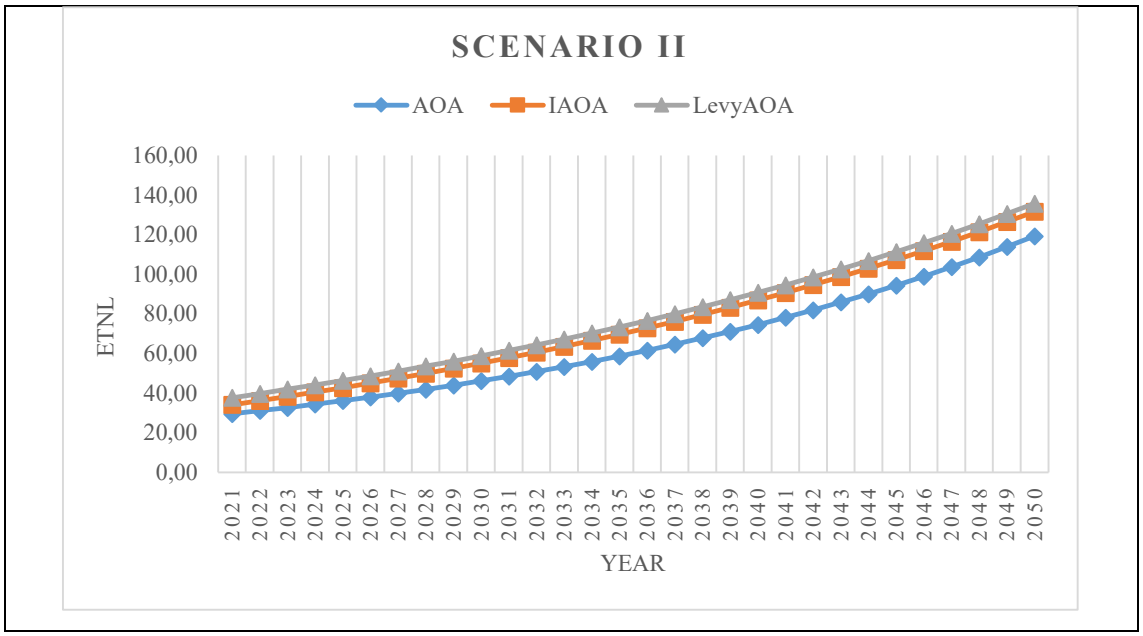


Figure 6. The estimated TNL of the proposed methods with scenario II

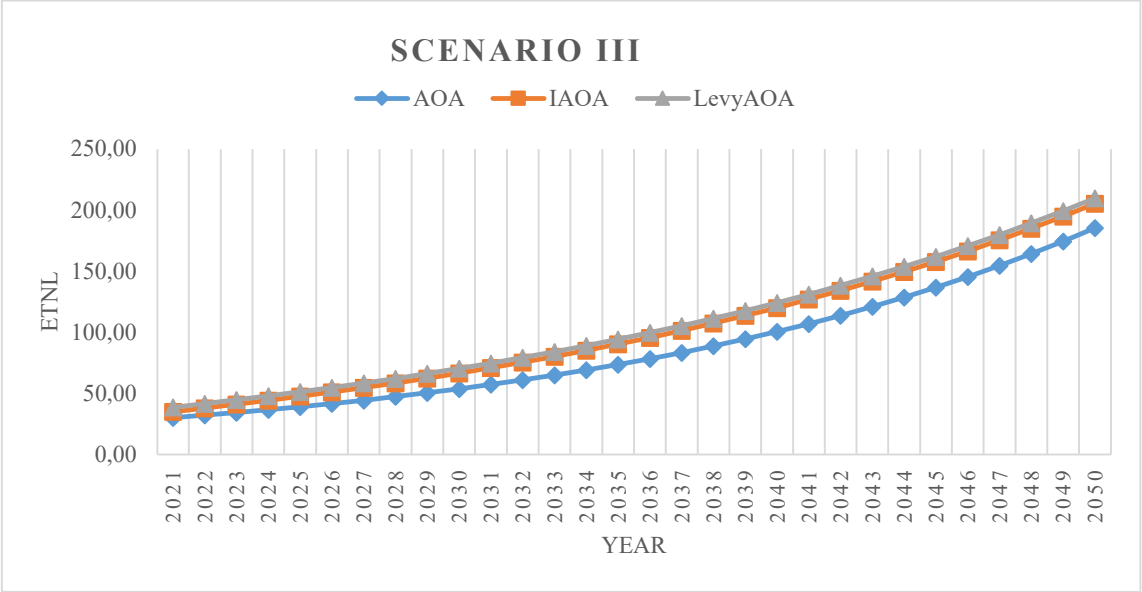


Figure 7. The estimated TNL of the proposed methods with scenario III

3.3 Correlation matrix

The correlation matrix serves as a tool for investigating the systemic influence of multiple variables within a dataset. In this matrix, the magnitude and signs of the numbers are both essential and relationships are quantified within the range of -1 to 1. A value approaching 1 signifies a strong positive linear correlation between the two related variables, whereas a value near -1 indicates a robust negative correlation. Conversely, a value close to 0 suggests a lack of a linear relationship between the utilized data [1, 7].

In this study, two distinct correlation matrices were constructed. The first matrix illustrates the correlation between the dependent output data and the independent input data utilized in the AOA,

IAOA, and LevyAOA methods. On the other hand, the second matrix depicts the relationship between the actual electricity network losses and the results obtained from the methods.

Table 6 presents the correlation matrix between the output value representing electricity network losses and the input values comprising GDP, population, export, and import. The matrix reveals a robust linear relationship between population and electricity network losses (0.9625) and a relatively weak linear relationship between electricity network losses and exports (0.8984). Furthermore, imports and GDP exhibit a strong linear relationship (0.9915).

Table 6. Correlation matrix between dependent and independent variables



The IAOA method exhibits the strongest correlation (0.982) with the actual network losses (OTNL), confirming its superior performance compared to AOA and LevyAOA. LevyAOA also shows a high correlation (0.977), while AOA demonstrates weaker performance (0.947) in Table 7.

Table 7. Correlation matrix between actual network losses (OTNL) and estimated results obtained from the methods (1979–2020)

	OTNL (Actual)	AOA Estimated	IAOA Estimated	LevyAOA Estimated
OTNL	1.000	0.947	0.982	0.977
AOA	0.947	1.000	0.964	0.968
IAOA	0.982	0.964	1.000	0.995
LevyAOA	0.977	0.968	0.995	1.000

3.4. Standard MLR analysis of variable importance

It is advantageous to represent the experimental data as mathematical equations with high generalizability [1,7]. To complement the optimization-based models, a standard MLR analysis was conducted to better understand the relative importance of the independent variables (GDP, population, import, and export) in explaining TNL. In contrast to the coefficients optimized via AOA, IAOA, and LevyAOA, the equations in this section reflect standard regression specifications estimated directly from the historical dataset without optimization procedures.

The dependent variable (F, representing TNL) was regressed on different subsets of the independent variables to evaluate their explanatory power and statistical significance. For each specification, the regression coefficients, R^2 values, and p-values were calculated. Table 8 presents these results, with each row corresponding to a distinct subset of predictors.

As shown in Table 8, the equation including all four independent variables (a = import, b = export, c = GDP, d = population) achieves the highest explanatory power, with $R^2 = 0.9620$, indicating that the full

specification best represents the observed TNL. When the population variable (d), which shows the strongest pairwise correlation with TNL, is omitted, the explanatory performance decreases noticeably (Equations 8–11). Reintroducing this variable markedly improves model fit, underscoring its central role in TNL estimation. Although the first and second equations produce similar R^2 values, the first equation demonstrates slightly stronger representational ability.

The coefficients obtained in Table 8 appear close to those in Table 2, which is expected since both analyses rely on the same dataset and variable structure. However, the procedures differ: while Table 2 reports coefficients optimized through metaheuristic algorithms, Table 8 strictly reflects the outcomes of a classical regression approach.

This complementary analysis demonstrates that the independent variables contribute differently to explaining TNL, and confirms that both the optimized linear models and the standard regression equations consistently highlight the dominant role of population and GDP in shaping TNL.

Table 8. Correlation matrix between methods and real network losses data

Eq No	Parameters	Multi Regression Equations	R^2	p-Value
1	a, b, c, d	F = -39.8201 +0.218∗ a -0.155∗ b -0.297 ∗ c + 0.8668∗ d	0.9620	1.17×10^{-24}
2	a, c, d	F = -39.4188 -0.141 ∗ b + 0.334 ∗ c + 0.8558 ∗ d	0.9612	4.11×10^{-25}
3	b, c, d	F = -32.5648 – 0.989 ∗ a + 0.384 ∗ c + 0.7236 ∗ d	0.9471	5.36×10^{-26}
4	c, d	F = -30.192 + 0.113 ∗ c + 0.7051 ∗ d	0.9383	3.47×10^{-24}
5	a, b, d	F = -42.5822 + 0.1381 ∗ a – 0.1871 ∗ b + 0.951 ∗ d	0.9517	8.365×10^{-24}
6	b, d	F = -41.4929 + 0.101 ∗ b + 0.9423 ∗ d	0.9230	4.04×10^{-23}
7	a, d	F = -34.3218 + 0.27 ∗ a + 0.7991 ∗ d	0.9301	1.39×10^{-23}
8	a, b, c	F = 4.4245 – 0.892 ∗ a + 0.134 ∗ b + 0.569 ∗ c	0.8627	1.27×10^{-15}
9	b, c	F = 5.1266 – 0.392 ∗ b + 0.42 ∗ c	0.8618	1.83×10^{-16}
10	a, c	F = 4.4303 - 0.784 ∗ a + 0.565 ∗ c	0.8661	1.42×10^{-16}
11	a, b	F = 7.6501 + 0.1326 ∗ a – 0.19 ∗ b	0.8248	3.36×10^{-16}

4. CONCLUSION

In this study, three different AOA-based methods, AOA, IAOA, and LevyAOA, are proposed and implemented in the TNL estimation of Türkiye. The AOA population-based stochastic optimization algorithm is based on four fundamental mathematical operators' fundamental strategies: subtraction, multiplication, addition, and division operator. The experimental results of the basic AOA were not satisfactory for the problem dealt with in this study. Therefore, two approaches, IAOA and LevyAOA, are proposed to increase the exploration and exploitation capability of the basic AOA method. The IAOA method uses a new position update rule, which was used in the study by Aslan and Beşkirli [2], with a basic AOA update rule.

The LevyAOA method is also the Lévy flight function with a basic AOA update rule. In the experiments, Türkiye's GDP, population, export, and import data instances taken from TUIK and TNL obtained from TEIAS for the years 1979-2020 have been used. In addition, the linear regression model is used as the mathematical model for finding the optimum values of weight coefficients. Firstly, the models are generated using AOA, IAOA, and LevyAOA methods, and then long-term TNL estimations are realized for three scenarios between 2021 and 2050. According to the experimental results and comparisons, the IAOA method obtained competitive and effective results for estimating Türkiye's long-term TNL. Different ML and hybrid models can be used in future studies. Future research could incorporate additional indicators, such as climatic conditions in the data set to obtain more effective and robust results for Türkiye's long-term TNL estimation.

Declaration of Ethical Standards

All authors confirm that this study fully complies with ethical standards regarding authorship, citation, and data integrity. The research is original, has not been published elsewhere, and adheres to responsible research practices.

Credit Authorship Contribution Statement

All authors contributed significantly to the development of this study. The study was collaboratively designed and the conceptual framework was jointly developed by all authors. Murat Aslan was primarily responsible for methodology development, algorithmic modelling, software implementation, and formal analysis. Mehmet Şefik Üney, Ömer Ali Karaman, and Mustafa Sağlam were primarily responsible for data acquisition, data curation, and preprocessing. All authors contributed to validation, visualization, and interpretation of the results. The manuscript was written collaboratively, and all authors were involved in reviewing, editing, and finalizing the content. All authors have read and approved the final version of the manuscript and agree to be accountable for all aspects of the work.

Declaration of Competing Interest

The authors declare that they have no known competing financial interests or personal relationships that could have appeared to influence the work reported in this paper.

Funding / Acknowledgements

This research received no specific funding from any public, private, or not-for-profit funding agencies. All work was conducted independently by the authors.

Data Availability

All data used in this study are openly available through publicly accessible repositories. Population, GDP, import, and export data; Turkish Statistical Institute (TUIK), IMF, and World Bank [29, 30, 31, 38]. Total Network Losses (TNL); Turkish Electricity Transmission Corporation (TEIAS) [39].

These sources are cited within the manuscript. No proprietary or restricted-access data were used in this study.

Use of Artificial Intelligence

The author acknowledge that the use of AI tools is limited to language editing and readability improvements. The author remains fully responsible for the accuracy, originality, and integrity of the manuscript, in compliance with ethical and legal standards.

5. REFERENCES

[1] M. Saglam, C. Spataru ve O. A. Karaman, "Electricity demand forecasting with use of artificial intelligence: The case of Gokceada Island," Energies, vol. 15, no. 16, p. 5950, 2022.
[2] M. Aslan ve M. Beşkirli, "Realization of Turkey's energy demand forecast with the improved arithmetic optimization algorithm," Energy Reports, vol. 8, pp. 18–32, 2022.
[3] M. Kampik, M. Fice, A. Pilśniak, K. Bodzek ve A. Piaskowy, "An analysis of energy consumption in small- and medium-sized buildings," Energies, vol. 16, no. 3, Art. no. 1536, 2023, doi: 10.3390/en16031536.
[4] Energy Market Regulatory Authority (EMRA), Profiles to be Implemented by Electricity Market Distribution Companies in 2019, Ankara, Turkey, 2023. [Online]. Available: https://www.epdk.gov.tr/Detay/Icerik/1-1270/electricityelektricity-legislation
[5] T. Senthil Kumar, V. Mohan ve S. Senthilkumar, "Energy efficient transmission using optical access network: Issues and challenges," Int. J. Eng. Sci. Technol., vol. 7, no. 1, pp. 43–51, 2023.

[6] O. A. Karaman, "Prediction of wind power with machine learning models," Appl. Sci., vol. 13, no. 20, Art. no. 11455, 2023.
[7] M. Saglam, C. Spataru ve O. A. Karaman, "Forecasting electricity demand in Turkey using optimization and machine learning algorithms," Energies, vol. 16, Art. no. 4499, 2023, doi: 10.3390/en16114499.
[8] S. Di Leo, P. Caramuta, P. Curci ve C. Cosmi, "Regression analysis for energy demand projection: An application to TIMES-Basilicata and TIMES-Italy energy models," Energy, vol. 196, Art. no. 117058, 2020.
[9] K. B. Debnath ve M. Mourshed, "Forecasting methods in energy planning models," Renew. Sustain. Energy Rev., vol. 88, pp. 297–325, 2018.
[10] G. Isik, H. Ogut ve M. Mutlu, "Deep learning based electricity demand forecasting to minimize the cost of energy imbalance: A real case application with some Fortune 500 companies in Türkiye," Eng. Appl. Artif. Intell., vol. 118, Art. no. 105664, 2023.
[11] S. Aslam, H. Herodotou, S. M. Mohsin, N. Javaid, N. Ashraf ve S. Aslam, "A survey on deep learning methods for power load and renewable energy forecasting in smart microgrids," Renew. Sustain. Energy Rev., vol. 144, Art. no. 110992, 2021.
[12] Turkish Statistical Institute, "Cevre ve Enerji," 2023. [Online]. Available: https://data.tuik.gov.tr/Kategori/GetKategori?p=cevre-ve-enerji-103&dil=1
[13] Strategy and Budget Office of the Presidency of Turkey, "Yıllar Bazında Genel Devlet İstatistikleri," 2023. [Online]. Available: https://www.sbb.gov.tr/yillar-bazinda-genel-devlet-istatistikleri/
[14] K. Sadovskaia, D. Bogdanov, S. Honkapuro ve C. Breyer, "Power transmission and distribution losses–A model based on available empirical data and future trends for all countries globally," Int. J. Electr. Power Energy Syst., vol. 107, pp. 98–109, 2019.
[15] K. B. Debnath ve M. Mourshed, "Forecasting methods in energy planning models," Renew. Sustain. Energy Rev., vol. 88, pp. 297–325, 2018.
[16] I. Tolic, K. Milicevic, N. Suvak ve I. Biondic, "Non-linear least squares and maximum likelihood estimation of probability density function of cross-border transmission losses," IEEE Trans. Power Syst., vol. 33, no. 2, pp. 2230–2238, 2017.
[17] A. Dursun, İ. Eke ve S. Tezcan, "Artificial neural networks with Turkey interconnected system for day ahead market transmission lines estimated losses," Uluslararası Mühendislik Araştırma ve Geliştirme Dergisi, 2020.
[18] M. Rejc ve M. Pantos, "Short-term transmission-loss forecast for the Slovenian transmission power system based on a fuzzy-logic decision approach," IEEE Trans. Power Syst., vol. 26, no. 3, pp. 1511–1521, 2011.
[19] W. Li ve P. Choudhury, "Including a combined fuzzy and probabilistic load model in transmission energy loss evaluation: Experience at BC Hydro," in Proc. IEEE Power Energy Soc. Gen. Meeting, Detroit, MI, USA, 2011, pp. 1–8, doi: 10.1109/PES.2011.6038938.
[20] I. Sudić et al., "Short-term transmission system losses forecast based on supervised machine learning," in Proc. Int. Conf. Smart Syst. Technol. (SST), 2020, pp. 199–204.
[21] M. Yang, A. Tang, H. Yang, J. Peng ve Y. Yang, "Optimization calculation method of transmission line loss with multi-parameter correction," in Proc. IEEE 6th Inf. Technol. Mechatronics Eng. Conf. (ITOEC), Chongqing, China, 2022, pp. 1453–1457, doi: 10.1109/ITOEC53115.2022.9734521.
[22] I. Baran, T. Leonida ve D. Sidea, "Using numerical weather forecast to predict power losses on transmission lines," in Proc. 4th Int. Symp. Electr. Electron. Eng. (ISEEE), 2013, pp. 1–8.
[23] C. R. Jethmalani et al., "Auxiliary hybrid PSO-BPNN-based transmission system loss estimation in generation scheduling," IEEE Trans. Ind. Informatics, vol. 13, no. 4, pp. 1692–1703, 2016.
[24] H. Fang, X. Fu, Z. Zeng, K. Zhong ve S. Liu, "An improved arithmetic optimization algorithm and its application to determine the parameters of support vector machine," Mathematics, vol. 10, no. 16, Art. no. 2875, 2022.
[25] A. Dahou, M. A. Al-qaness, M. Abd Elaziz ve A. Helmi, "Human activity recognition in IoHT applications using arithmetic optimization algorithm and deep learning," Measurement, vol. 199, Art. no. 111445, 2022.
[26] L. Abualigah et al., "The arithmetic optimization algorithm," Comput. Methods Appl. Mech. Eng., vol. 376, Art. no. 113609, 2021.
[27] S. Khatir et al., "An improved artificial neural network using arithmetic optimization algorithm for damage assessment in FGM composite plates," Compos. Struct., vol. 273, Art. no. 114287, 2021.
[28] S. Wu, G. Xia ve L. Liu, "A novel decomposition integration model for power coal price forecasting," Resour. Policy, vol. 80, Art. no. 103259, 2023.
[29] Turkish Statistical Institute, "Nüfus ve Demografi," 2023. [Online]. Available: https://data.tuik.gov.tr/Kategori/GetKategori?p=nufus-ve-demografi-109&dil=1
[30] International Monetary Fund, "IMF Data Set," 2023. [Online]. Available: https://data.imf.org/?sk=85b51b5a-b74f-473a-be16-49f1786949b3
[31] World Bank, "World Bank Open Data: GDP (current US$) – Turkey," 2023. [Online]. Available: https://data.worldbank.org/indicator/NY.GDP.MKTP.CD?locations=TR
[32] A. N. Mat, O. İnan ve M. Karakoyun, "An application of the whale optimization algorithm with Levy flight strategy for clustering of medical datasets," Int. J. Optim. Control: Theor. Appl. (IJOCTA), vol. 11, no. 2, pp. 216–226, 2021.
[33] M. Chawla ve M. Duhan, "Levy flights in metaheuristics optimization algorithms–a review," Appl. Artif. Intell., vol. 32, no. 9–10, pp. 802–821, 2018.
[34] S. J. Nanda ve G. Panda, "A survey on nature inspired metaheuristic algorithms for partitional clustering," Swarm Evol. Comput., vol. 16, pp. 1–18, 2014.

[35] T. Zheng et al., "IWORMLF: Improved invasive weed optimization with random mutation and Lévy flight for beam pattern optimizations of linear and circular antenna arrays," IEEE Access, vol. 8, pp. 19460–19478, 2020.
[36] A. A. Heidari et al., "Harris hawks optimization: Algorithm and applications," Future Gener. Comput. Syst., vol. 97, pp. 849–872, 2019.
[37] M. Beşkirli, "A novel invasive weed optimization with levy flight for optimization problems: The case of forecasting energy demand," Energy Reports, vol. 8, pp. 1102–1111, 2022.
[38] Turkish Statistical Institute, "Ulusal Hesaplar," 2023. [Online]. Available: https://data.tuik.gov.tr/Kategori/GetKategori?p=ulusal-hesaplar-113
[39] Turkish Electricity Transmission Corporation, "Yük Tevzi Kontrol Merkezleri," 2022. [Online]. Available: https://www.teias.gov.tr/yuk-tevzi-kontrol-merkezleri
[40] M. S. Kıran, E. Özceylan, M. Gündüz ve T. Paksoy, "A novel hybrid approach based on particle swarm optimization and ant colony algorithm to forecast energy demand of Turkey," Energy Convers. Manag., vol. 53, no. 1, pp. 75–83, 2012.
[41] D. Özdemir, S. Dörterler ve D. Aydın, "A new modified artificial bee colony algorithm for energy demand forecasting problem," Neural Comput. Appl., vol. 34, no. 20, pp. 17455–17471, 2022.

Konya Mühendislik Bilimleri Dergisi., c.14, s.2, 648-657, 2026
Konya Journal of Engineering Sciences v.14, n.2, 648-657, 2026
ISSN: 2667-8055 (Electronic)
DOI: 10.36306/konjes.1637027

EFFECTS OF TEMPERATURES ON PHYSICOCHEMICAL PROPERTIES OF CELERY (*Apium graveolens* L.) SLICES DRIED BY INFRARED DRYER

[1,*]Muhammed Taşova

[1]*Tokat Gaziosmanpaşa University, Agriculture Faculty, Biosystem Engineering Department, Tokat*
[1]muhammed.tasova@gop.edu.tr

Highlights

- Infrared drying significantly reduced celery drying time at higher temperatures.
- The best color preservation was achieved at 60 °C drying temperature.
- The Midilli–Küçük model provided the best prediction of drying behavior.

Graphical Abstract

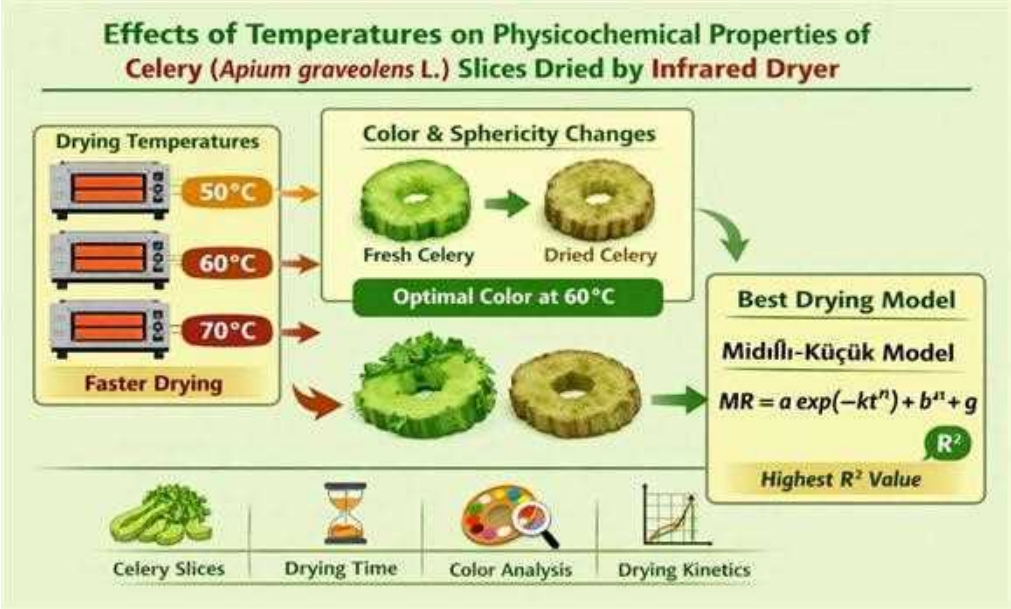


Figure Graphical abstract-Celery drying processes

***Corresponding Author:** Muhammed TAŞOVA, muhammed.tasova@gop.edu.tr

Konya Mühendislik Bilimleri Dergisi., c.14, s.2, 648-657, 2026
Konya Journal of Engineering Sciences v.14, n.2, 648-657, 2026
ISSN: 2667-8055 (Electronic)
DOI: 10.36306/konjes.1637027

EFFECTS OF TEMPERATURES ON PHYSICOCHEMICAL PROPERTIES OF CELERY (*Apium graveolens* L.) SLICES DRIED BY INFRARED DRYER

[1,*]**Muhammed Taşova**

[1]*Tokat Gaziosmanpaşa University, Agriculture Faculty, Biosystem Engineering Department, Tokat*
[1]muhammed.tasova@gop.edu.tr

(Received: 10.02.2025; Accepted in Revised Form: 17.11.2025)

ABSTRACT: In this study, drying characteristics, color values, and optimum thin layer drying model of celery slices were determined by drying them in a temperature-controlled infrared dryer. Changes in surface area and sphericity of celery slices throughout the drying process were also determined. Present findings revealed that temperature was a significant criterion for drying the celery slices. Decreasing drying times were observed with increasing drying temperatures. Drying operations were carried out at three different temperatures (50, 60, and 70 ºC). The longest drying time (7.25 hours) was observed at 50 ºC and the shortest drying time (4.25 hours) was achieved at 70 ºC drying temperature. The closest fresh color values to the color values of the fresh product were obtained from 60 ºC drying temperature. In terms of chroma values, the closest value to the fresh product was observed again at 60 ºC. The most used Page, Midilli-Küçük, Yagcıoglu, and Jane Das thin-layer drying models were used to generate drying curves of celery slices. Among these models, the Midilli-Küçük model yielded the greatest R^2 value, thus it was selected as the best thin-layer drying model for celery slices.

Keywords: *Celery, Drying process, Drying kinetics, Color, Image processing*

1. INTRODUCTION

Plants were important to human health even before humans settled down. Plants that have important effects on human health have begun to be used widely. In 1980, WHO (World Health Organization) approved the use of medicinal-aromatic plants able to synthesize chemical-pharmaceutical substances and prevent or heal diseases [1, 2]. According to previous research, there are about 20,000 medicinal-aromatic plant species and they have been used in foodstuffs for aroma, taste, and color since the old ages. These plants are also used in drugs, cosmetics, and several other industries [3]. The significance of medicinal-aromatic plants is continuously increasing in the domestic markets of Turkey and some of them are exported. Celery is among the most important medicinal-aromatic plants in the world. Celery (*Apium graveolens* L.) has been produced since the old ages as a medicinal plant and used in different forms as a foodstuff [4-5]. Celery belongs to the Apiaceae family and is generally produced as a vegetable. While stems and leaves are consumed in some regions (western and northern Europe), tubers are consumed in others (Central and Eastern Europe)[6]. About 100 g celery contains 87-90 g water, 4.3 g ash, 1.1 g protein, and 0.2 g oil [7-9]. Celery is also rich in vitamins, minerals, and salts [10]. For health purposes, celery is used as a anti-inflammatory; it reduces cholesterol, remove free radicals from the body, and diminish the negative issues able to result in genetic mutation [11]. Celery has a quite high moisture content, thus it cannot preserve freshness for a long time, microorganism activities develop rapidly and the product is spoiled in a short time. Therefore, such a high moisture of the product should be removed to a certain extent. Agricultural products are preserved through drying. Drying is economical about energy consumption and allows products to be preserved for a long time without any spoilage.

***Corresponding Author:** Muhammed TAŞOVA, muhammed.tasova@gop.edu.tr

Drying is among the oldest methods used to preserve foodstuffs. With the process of drying, a large portion of product moisture is removed, water activity is reduced and resultant microorganism activities are inhibited, the shelf life of products is prolonged [12, 30]. Generally, natural drying and conventional drying with forced hot air are preferred for drying agricultural products. However, in conventional the drying methods, drying process takes a long time. Such long drying times increase heat-exposures of the products and energy consumption and also result in significant losses in quality attributes. Therefore, improved drying methods allowing users to dry products in a short time with less energy and the least losses in color, texture, and phytochemical quality parameters are preferred in the industry. Several drying methods (contact, convective, osmatic, etc.) are used to dry agricultural products. One of these methods employs an infrared heat source. In the drying process, heat is transferred from the heat source to the material, which causes the evaporation of moisture. The heating power produced by exposing the dried product to infrared radiation can penetrate the food. Infrared radiation has become popular due to its advantages over conventional heating, such as thermal efficiency and fast response time/drying rate. In this way, homogeneous heat distribution is provided within the product, the moisture rate is increased, the drying time is shortened, energy consumption is reduced and losses in quality attributes are minimized [13-14]. The infrared drying method was used to dry different products by previous researchers [15-20]. Dimensional characteristics of fresh and dried products constitute significant parameters for engineering calculations made in the design of machinery. Aerodynamic and hydrodynamic principles use product size, shape, and dimensions to calculate product surface areas and then use these parameters in the design of cleaning, conveyance, and transportation machines and processes. Since agricultural products have quite varying shapes and dimensions, specific methods are required to measure and calculate their surface areas. Dried products are not in spherical forms anymore, therefore specific mathematical methods are used for accurate calculation of the surface areas of dried products [21].

The aim of this study was to investigate the effects of temperature-controlled infrared drying temperatures on the drying kinetics, color properties, and surface area changes of celery slices.

2. MATERIAL AND METHODS

2.1. Drying Material

The fresh celeries to be used in the present experiments were purchased from a local supermarket in Tokat province. Fresh materials were kept in a fridge at +4 ± 0.5 ºC until the end of the experiments.

2.2. Moisture Analyses

For the moisture content of fresh celeries, about 20 g samples were used in each replicate. Measurements were conducted in 4 replications. Samples were put into an oven at 70 ºC and they were weighed at certain intervals and dried until an 0.01 g in weight between two consecutive measurements [22].

2.3. Drying Method

Celeries were washed before the process of drying. Cleaned celeries were sliced into 0.5 cm-thick circular slices. Celeries were dried in a temperature-controlled infrared dryer at 50, 60, and 70 ºC drying temperatures. No pretreatment was applied to the celery samples before drying. About 15-20 g samples were used in each replication of the drying process. Experiments were conducted in 3 replications. Products were weighed at a precise balance (±0.01 g) at certain intervals and products were dried until 10-13% moisture level in wet-base. In many studies, the final moisture content of the materials is reduced to around 10% [24].

2.4. Temperature-Controlled Infrared Dryer

For the drying process of celery slices, Swiss-Made Precisa Gravimetrics AG Dietikon brand, 330XM series temperature-controlled infrared dryer was used. Drying temperatures are adjusted to desired values from the control panel installed over the dryer. Products are dried by the halogen heaters positioned over the product chamber.

2.5. Color Analysis

The *L*, *a*, and *b* color parameters of fresh and dried celeries were measured. Minolta-brand CR300 model color meter was used in color measurements. *L*, *a*, and *b* values reveal information about the color of products. " *L* " expresses the brightness of the product and gets a value of between 0 - 100. *L* value of 0 indicates black color without any reflections and *L* value of 100 indicates white color with full reflection. The " *a* " expresses red-green, " *b* " indicates yellow-blue colors, and respectively takes (+, -) signs. Color values of a=0 and b=0 indicate the grey color of the product [23]. Another color parameter, chroma expresses color tone with lower values indicating pale colors and higher values indicating bright colors. According to [24]; chroma and hue angle values are calculated with the aid of equations 1 and 2;

$$C = (a + b)^{/} \quad (1)$$

$$h = h \quad (-) \quad (2)$$

According to [25]; browning index " BI " values and " x " values are calculated by using equations 3 and 4;

$$BI = \frac{[\quad (\quad . \quad)]}{.} \quad (3)$$

$$x = \frac{(\ .\quad)}{[(\ .\quad) \quad (\ .\quad)]} \quad (4)$$

2.6. Drying Model

The time-dependent release of moisture from drying celery slices was calculated by using equation 5 as provided below;

$$MR = \frac{\quad}{\quad} \quad (5)$$

MR: Moisture ratio
M: Moisture content at any time
M_e: Moisture content at equilibrium
M_o: Initial moisture content

Page, Midilli-Küçük, Yağcıoğlu, and Jane-Das mathematical models were selected to generate drying curves [24]. These models were created in the SigmaPlot program. Model 6, 7, 8, and 9 equations are provided below;

Page (6)

$$MR = exp\ (-h.(t\ ))$$

Midilli-Küçük (7)

$$MR = h.\exp(-j.t\ ) + t$$

Yağcıoğlu (8)

$$MR = k.\exp(-h.t) + j$$

Jane Das (9)

$$MR = k.exp\ \ -k.t + h.t^{-}\ \ + \mathrm{m}$$

Here: h, j, k, and m are constant coefficients. t indicates the time.

2.7. Change In Surface Area and Sphericity of Celery Slices

Changes in the surface area of celery slices throughout the drying process were calculated. Images were taken from the experimental setup at 50, 60, and 70 ºC temperatures at certain intervals. While taking images, 8x8 cm papers were used for scaling. Area calculation procedures are given in Figure 1.

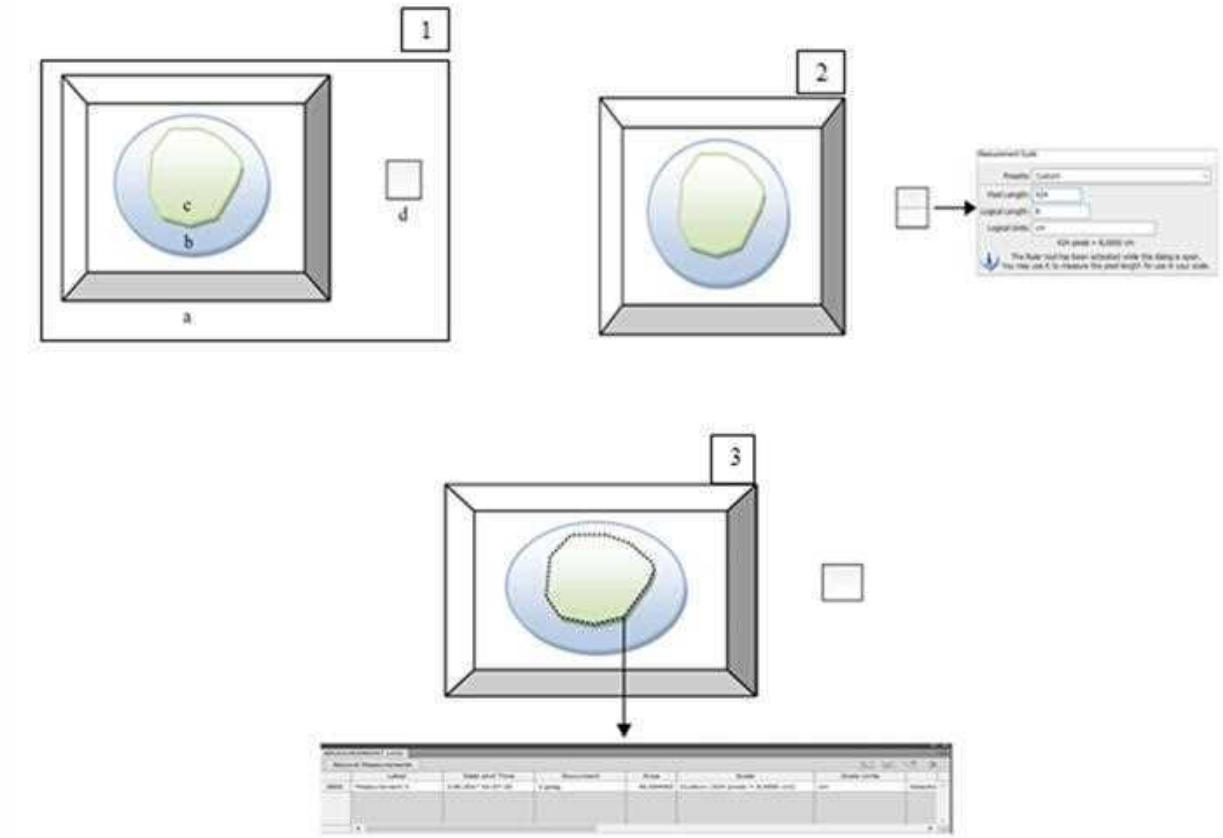


Figure 1. Calculating surface area of celery slices: 1) A scale for initially; a) drying environment, b) drying plate, c) drying material 2) Scaling of images, 3) Calculation for surface area

For each image initially, a scale was determined. Then, pixels of one side of square paper were converted into cm. For instance in Figure 1, 424 pixels corresponded to 8 cm. Such a scale was separately determined for each image. With the aid of these scale values, changes in surface areas of celery slices were determined throughout the drying process. Although the direction, height, and angle of the images taken at each temperature are different, the actual length scale value was determined to accurately calculate areas from different images. In this way the area values of celery slices calculated from all images were compared. All these processes were implemented with Adobe Photoshop Version: 12.0 software.

3. RESULTS AND DISCUSSION

3.1. Drying Data

The initial moisture level of celery slices was measured as 90.78% on a wet basis and samples were dried to moisture levels of between 10-13%. Average drying values, color values, numerical values for drying models, changes in surface area, and sphericity of the samples throughout the drying process were provided in the following Tables. Drying data are given in Table 1.

Table 1. Drying performance values of celery slices

Drying temperatures	Moisture (%)	Drying time (hours)
50 ºC	12.26	7.25
60 ºC	12.23	5.50
70 ºC	13.06	4.25

As can be seen in Table 1, drying temperature influenced drying performance, and decreasing drying times were observed with increasing drying temperatures. [26]; carried out an apple drying study with a temperature-controlled microwave dryer and reported decreasing drying times with increasing temperatures. [27]; carried out drying experiments for persimmons and reported increasing drying ratios and decreasing drying times with increasing drying air temperatures.

3.2. Coefficients for Drying Models, "R^2" and "p" Values

Drying curves were generated to determine the time dependent releasable moisture ratios of the samples. The coefficients of drying curves, variance analysis values (p), and model stability coefficients (R^2) are provided in Tables 2, 3, 4, and 5. Data for the Page model are given in Table 2.

Table 2. Coefficients for Page equation, "R^2" and "p" values

Drying temperatures	*k*	*h*	R^2	*p*
50 ºC	0.4414	1.2166	0.9986	<0.0001
60 ºC	0.2867	1.2293	0.9806	<0.0001
70 ºC	0.6339	1.3802	0.9982	<0.0001

Page model estimated drying curves the best at 50 ºC drying temperature. The model reliability value was found to be suitable for all drying temperatures. The greatest "k" value was obtained from 70 ºC drying temperature and the lowest "k" value was obtained from 60 ºC drying temperature. The greatest "h" value was obtained from 70 ºC drying temperature and the lowest "h" value was obtained from 50 ºC drying temperature. The maximum R^2 value for the Page model was determined at a drying temperature of 50 ºC. Therefore, the Page model modeled the best drying curve at this temperature. Data for the Midilli-Küçük model are given in Table 3.

Table 3. Coefficients for Midilli-Küçük equation, "R^2" and "p" values

Drying temperatures	*k*	*h*	*j*	*m*	R^2	*p*
50 ºC	1.2749	0.9939	0.4353	-0.0033	0.9992	<0.0001
60 ºC	0.7633	1.0029	0.1996	-0.0854	0.9948	<0.0001

70 ºC	1.4085	0.9882	0.6156	-0.0007	0.9983	<0.0001

Midilli-Küçük model estimated drying curves the best at 50 ºC drying temperature. The model reliability value was found to be suitable for all drying temperatures. The greatest "k" value of the model was obtained from 70 ºC drying temperature and the lowest "k" value was obtained from 60 ºC drying temperature. The greatest "h" value of the model was obtained from 60 ºC drying temperature and the lowest "h" value was obtained from 70 ºC drying temperature. The greatest "j" value was obtained from 70 ºC drying temperature and the lowest "j" value was obtained from 60 ºC drying temperature. The greatest "m" value of the model was obtained from 70 ºC drying temperature and the lowest "m" value was obtained from 60 ºC drying temperature. The maximum R^2 value for the Midilli-Küçük model was determined at a drying temperature of 50 ºC. Therefore, the Midilli-Küçük model modeled the best drying curve at this temperature. Data for the Yağcıoğlu model are given in Table 4.

Table 4. Coefficients for Yağcıoğlu equation, "R^2" and "p" values

Drying temperatures	***k***	***h***	***j***	***R²***	***p***
50 ºC	1.0674	0.4997	-0.0277	0.9948	<0.0001
60 ºC	1.7608	0.1435	-0.7787	0.9936	<0.0001
70 ºC	1.1605	0.6059	-0.1169	0.9900	<0.0001

Yağcıoğulu model estimated drying curves the best at 50 ºC drying temperature. The model reliability value was found to be suitable for all drying temperatures. The greatest "k" value of the model was obtained from 60 ºC drying temperature and the lowest "k" value was obtained from 50 ºC drying temperature. The greatest "h" value of the model was obtained from 70 ºC drying temperature and the lowest "h" value was obtained from 60 ºC drying temperature. The greatest "j" value was obtained from 50 ºC drying temperature and the lowest "j" value was obtained from 60 ºC drying temperature. The maximum R^2 value for the Yagcıoglu model was determined at a drying temperature of 50 ºC. Therefore, the Yagcıoglu model modeled the best drying curve at this temperature. Data for the Jena Das model are given in Table 5.

Table 5. Coefficients for Jane Das equation, "R^2" and "p" values

Drying temperatures	***k***	***h***	***j***	***m***	***R²***	***p***
50 ºC	1.0238	0.6708	0.2738	-0.0224	0.9940	<0.0001
60 ºC	1.0163	0.5901	0.4353	0.0113	0.9711	<0.0001
70 ºC	1.0327	0.7850	0.0451	0.0297	0.9821	<0.0001

Jane Das's model estimated drying curves the best at 50 ºC drying temperature. The model reliability value was found to be suitable for all drying temperatures. The greatest "k" value of the model was obtained from 70 ºC drying temperature and the lowest "k" value was obtained from 60 ºC drying temperature. The greatest "h" value of the model was obtained from 70 ºC drying temperature and the lowest "h" value was obtained from 60 ºC drying temperature. The greatest "j" value was obtained from 60 ºC drying temperature and the lowest "j" value was obtained from 70 ºC drying temperature. The greatest "m" value of the model was obtained from 70 ºC drying temperature and the lowest "m" value was obtained from 50 ºC drying temperature. The maximum R^2 value for the Jena Das model was determined at a drying temperature of 50 ºC. Therefore, the Jena Das model modeled the best drying curve at this temperature. Among the drying curves created at all drying temperatures, the best model was at 50 ºC. Among all the models, the Midilli-Küçük model gave the best prediction.

3.3. Color Values

The *L*, *a*, and *b* values of fresh and dried celery slices were measured and they were then converted into secondary color values of chroma and hue angle. The *L*, *a*, and *b* values of fresh and dried celery slices were also subjected to Duncan's test to see the differences between them, and test results are provided in Table 6.

Table 6. Mean values for measured and calculated values

Drying temperatures	*L*	*a*	*b*	*C*	*Hue*	*BI*	*E*
Fresh	84.34^{a}	1.76^{c}	9.57^{b}	9.73	79.58	13.30	-
50 ºC	66.77^{c}	5.97^{a}	16.01^{a}	17.09	69.55	33.52	21.69
60 ºC	72.22^{b}	3.01^{b}	15.53^{a}	15.82	79.03	26.80	13.56
70 ºC	70.74^{b}	3.33^{b}	15.67^{a}	16.02	78.00	28.02	14.99

As can be seen in Table 6, the brightness values of celery slices decreased at all drying temperatures. As compared to the fresh values, *L* values were preserved the least at 50 ºC and the most at 60 ºC drying temperature. As compared to fresh values, the redness-yellowness values were also the least preserved at 50 ºC. Since the longest drying time was observed at 50 ºC, samples were subjected to longer heat exposures, thus greater changes were observed in primary color values as compared to the fresh values. [28]; reported decreasing *L*, *a*, and *b* values of tomatoes with increasing drying temperatures as compared to the fresh ones. As compared to fresh products, chroma values of dried products moved away at all drying temperatures. The greatest separation from the values of fresh products was observed at 50 ºC drying temperature since the greatest change in *a* and *b* values was observed at this temperature. As compared to fresh products, browning values increased at all drying temperatures. The greatest browning was observed at 50 ºC drying temperature. [29]; dried apples in a temperature-controlled microwave dryer at 50, 60, and 70 ºC temperatures and reported the greatest browning at 50 ºC drying temperature. The least color change was observed in the drying process at 60 ºC. In drying processes conducted using the convective method at temperatures of 40, 45, and 50°C, the lowest color change was observed at the medium temperature [30]. This is thought to be due to the optimal temperature being used in terms of both the duration of product exposure and the intensity of the heat. *L*, *a*, and *b* values of fresh and dried celery slices were subjected to Duncan's test with the aid of SPSS software at a significance level of $(p < 0.05)$. As can be seen in Table 6, the brightness values of dried celery slices were significantly different from the brightness values of fresh celery. The differences in brightness values of celeries dried at 60 ºC and 70 ºC temperatures were not found to be significant. The redness values of dried celery slices were significantly different from the redness values of fresh celery. The differences in redness values of celery dried at 60 ºC and 70 ºC temperatures were not found to be significant. Yellowness values of dried celery slices were significantly different from the values of fresh celeries. However, differences in the yellowness value of celery slices dried at 50, 60, and 70 ºC temperatures were not found to be significant.

3.4. Surface Areas and Sphericity Values

The physical change kinetics of the dried slices are given in Figure 2.

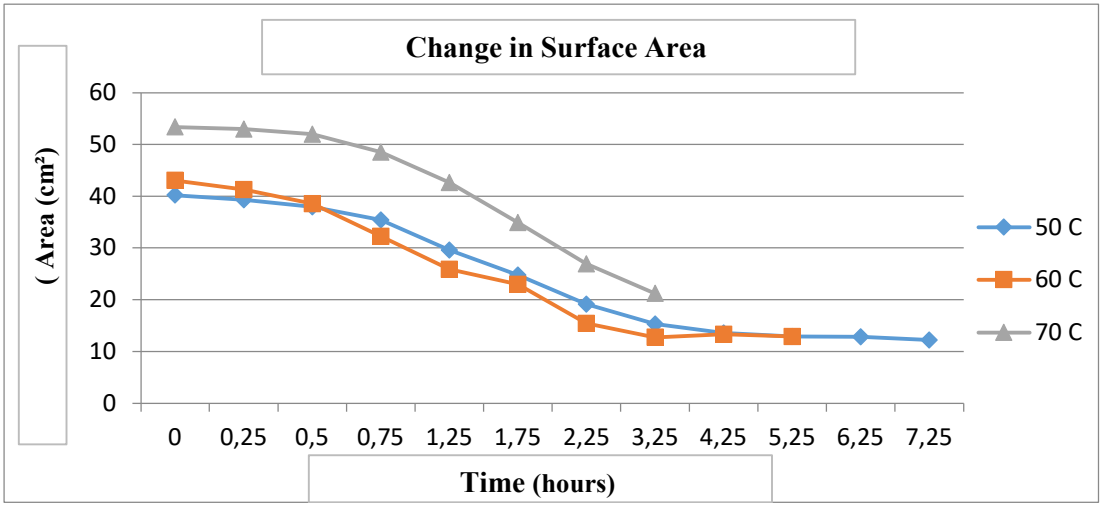


Figure 2. Temperature-dependent changes in surface area

At 50 ºC drying temperature, the average surface area of fresh celery slices was 53.91 cm² before the drying process and the average surface area of dried celery slices to a final moisture level was 24.44 cm². As compared to the surface area of fresh products, the surface area of dried products decreased by 54.67%. At 60 ºC drying temperature, the average surface area of fresh celery slices was 41.72 cm² and the average surface area of dried celery slices was 12.89 cm². As compared to the surface area of fresh products, the surface area of dried products decreased by 69.10%. At 70 ºC drying temperature, the average surface area of fresh celery slices was 42.62 cm² and the average surface area of dried celery slices was 13.23 cm². As compared to the surface area of fresh products, the surface area of dried products decreased by 68.96%. Changes in surface areas at 50, 60, and 70 ºC drying temperatures were 54.67%, 69.10%, and 68.96%, respectively. As compared to the fresh products, the greatest reduction in the surface area was observed at 60 ºC temperature and the least was observed at 50 ºC drying temperature. Data on area change are given in Figure 2.

4. CONCLUSIONS

Celery is quite rich in nutrients and has several health benefits. In this study, celery slices were dried in an infrared dryer. Drying characteristics and color values were determined. Models were used to generate drying curves and the best thin-layer drying model was identified. Changes in surface area and sphericity of celery slices throughout the drying process were determined. Present findings revealed that drying temperature was a significant criterion for drying celery slices. Drying times decreased with increasing drying temperatures. The greatest drying time (7.25 hours) was observed at 50 ºC and the shortest time (4.25 hours) was observed at 70 ºC drying temperature. The closest primary color values to the fresh product were observed at 60 ºC drying temperature. The closest chroma value to the fresh products was observed again at 60 ºC drying temperature. Among the drying curves generated for all drying temperatures, the Midilli-Küçük model yielded the greatest R^2 value. Therefore, this model was selected as the best thin-layer drying model for celery slices under present drying conditions.

Use of Artificial Intelligence

Artificial intelligence was used in preparing the Graphical Abstract (only figure) for this study.

Declaration of Ethical Standards

The authors complied with ethical rules.

Credit Authorship Contribution Statement

Muhammed Taşova: Laboratory studies, Writing, Editing.

Declaration of Competing Interest

There is no conflict of interest among the authors.

Funding / Acknowledgements

The researcher, who contributed to the calculation of the processing area values of the images, to Associate Professor Doctor Özkan İnik, I would like to thank you.

Data Availability

No official data/data set from any institution was used in the study.

5. REFERENCES

[1] C. Njume, A. J. Afolayan, and R. N. Ndip, "An overview of antimicrobial resistance and the future of medicinal plants in the treatment of helicobacter pylori infections". *African. J. Pharm*., 3: 685-699, 2009.

[2] A. A., Başaran, "Legal situation in herbal medicines and products in our country". *Mised*, 27: 22-26, 2012.

[3] E. Faydaoğlu, and M. S. Sürücüoğlu, "Antimicrobial, antioxidant activities and usage possibilities of medicinal and aromatic plants". *Erzincan Uni. J. Sci. Technol*., 6(2): 233-265, 2013.

[4] O. Ponjican, M. Babic, M. Radojcin, A. Bajkin, and D. Radomirovic, "Changes in physical properities of celery root after osmotic drying". *J. Proces. Energy Agri*., 152-157, 2013.

[5] M. Nıcetın, B. Loncar, V. Fılıpovıc, and V. Knezevıc, "The change in microbiological profile and water activity due to the osmotic treatment of celery leaves and root". *J. Proces. Energy Agric*., 19(4): 193-196, 2012.

[6] V. Rizzo, and G. Muratore, "Effects of packaging on shelf life of fresh celery". *J. Food Eng*., 90: 124-128, 2009.

[7] P. Pavlek, "Specijalno Povrarstvo". "Fakultet Poljoprivrednih Znanosti", *Zagreb*, 1993.

[8] J. Damir, B. Tripalo, M. Brncic, D. Karlovic, S. R. Brncic, D. Vikic-Topic, and S. Karlovic, "Dehydration of celery by infrared drying". *Croatıca Chem. Acta*., 81(2): 325-331, 2008.

[9] J. Damir, B. Tripalo, M. Brncic, D. Karlovic, D. Vikic-Topic, and Z. Herceg, "Modelling of convective carrot drying". *Croatıca Chem. Acta*., 79: 385–391, 2006.

[10] P. Madamba, and F. Liboon, "Optimization of the vacuum dehydration of celery (*Apium graveolens*) using the response surface methodology". *Drying Technol*., 19: 611-626, 2001.

[11] K. Ramachandraiah, K. B. Chin, "Impact of drying and micronization on the physicochemical properties and antioxidant activities of celery stalk". *J. Sci. Food Agric*., DOI: 10.1002/jsfa.8321, 2007.

[12] P. S. Pisalkar, N. K. Jain, and S. K. Jain, "Osmo-air drying of aloe vera gel cubes". *J. Food Scie. Technol.-Mysore*, 48(2): 183-189, 2011.

[13] N. Sakai, and T. Hanzawa, "Applications and advances in far-infrared heating in Japan". *Trends in*

Food Scie. Technol., 5(11): 357–362, 1994.
[14] M. H. Riadh, S. A. B. Ahmad, M. H. Marhaban, A. C. Soh, "Infrared heating in food drying: An overview". *Drying Technol*., 33: 322–335, 2015.
[15] D. S. Sogi, M. Siddiq, K. D. Dolan, "Research note total phenolics, carotenoids and antioxidant properties of Tommy Atkin mango cubes as affected by drying techniques". *LWT - Food Scie. Techno*l., 62: 564-568, 2015.
[16] İ. Doymaz, A. S. Kıpcak, S. Pişkin, "Characteristics of thin-layer infrared drying of green bean". Food Technol. *Economy Physical Prop*., 33(1): 83-90, 2015.
[17] S. Ruhanian, and K. Movagharnejad, "Mathematical modeling and experimental analysis of potato thin-layer drying in an infrared-convective dryer". *Engin. Agric. Envir. Food*, 9: 84-91, 2016.
[18] N. Adak, N. Heybeli, and C. Ertekin, "Infrared drying of strawberry. *Food Chemi*., 219: 109–116, 2017.
[19] S. R. Shewale, H. U. Hebbar, "Effect of infrared pretreatment on low-humidity air drying of apple slices". *Drying Technol*., 35(4): 490-499, 2017.
[20] L. Xie, A. S. Mujumdar, X. M. Fang, J. Wang, J. W. Dai, Z. L. Du, H. W. Xiao, Y. Liu, and Z. J. Ga, "Far-infrared radiation heating assisted pulsed vacuum drying (FIR-PVD) of wolfberry (*Lycium barbarum* L.): Effects on drying kinetics and quality attributes". *Food Biop. Proces*., 102: 320–331, 2017.
[21] E. Işık, and T. Güler, "Determination of apple surface areas by image processing technique". *Uludag Uni. J. Fac. Agric*., 17(1): 59-64, 2003.
[22] A. Yağcıoglu, "Agricultural products drying technique". *Ege Uni. Fac. Agric. Pub*., Bornova, İzmir. 536, 1999.
[23] R. G. McGuir, "Reporting of objective color measurements". *HortSci*., 27: 1254-1255, 1992.
[24] H. Polatcı, and Tarhan S., "The effects of various drying methods on the drying time and quality of basil (*Ocimum basilicum*)". *Food Agric. Org. United Nations*., 26(1): 61-70, 2009.
[25] E. Plou, A. Lopez-Malo, G. V. Barbosa-Canovas, J. Welti-Chanes, and B. G. Swanson, "Polyphenoloxidase activitiy and color of blanced and high hydrostatic pressure treated banana puree". *J. Food Sci*., 64: 42-45, 1999.
[26] M. Taşova, "Development and performance of a temperature-controlled microwave dryer". Master Thesis, *Tokat Gaziosmanpasa Univ*., Tokat, 2016.
[27] A. Kaya, M. S. Kamer, and H. E. Şahin, "Experimental investigation of the drying behavior of persimmon (*Diospyros kaki* L.)". *J. Food*., 40(1): 15-21, 2015.
[28] E. Demiray, "Determination of lycopene, β-carotene, ascorbic acid and color change kinetics of tomato in drying process". *Master Thesis, Pamukkale Uni*., Denizli, 2009.
[29] G. Cucurullo, L. Giordano, D. Albanase, L. Cinquanta, and D. M. Matteo, "Infrared thermography assisted control for apples microwave drying". *J. Food Engin*., 112(4): 319-325, 2012.
[30] M. Taşova, and H. Polatcı, "Investigation of some physio-chemical properties of lime dry in a convective and modified temperature controlled microwave oven". *Konya. J. Engine. Scien*., 11(2): 491-503, 2023.

Konya Mühendislik Bilimleri Dergisi., c.14, s.2, 658-681, 2026
Konya Journal of Engineering Sciences v.14, n.2, 658-681, 2026
ISSN: 2667-8055 (Electronic)
DOI: 10.36306/konjes.1609821

BINARY SWITCHING LINEAR MODEL CONTROL FOR LTI SYSTEMS: STABILITY ANALYSIS AND MODE CONTROL EQUIVALENCE

[1,*]Can Ulas DOGRUER, [2]Can Barış TOPRAK, [3]Bora YILDIRIM

[1,3]*Department of Mechanical Engineering, Hacettepe University, Ankara 06800, Türkiye.*
[2] *Additive Manufacturing Technologies Application and Research Center (EKTAM), Gazi University, 06560, Ankara, Türkiye.*

[1]cdogruer@hacettepe.edu.tr, [2]cantoprak@gazi.edu.tr, [3]boray@hacettepe.edu.tr

Highlights

- Novel binary switching linear model control framework is proposed for LTI systems.
- Modal decomposition decouples system, preserving mode shapes during switching.
- Lyapunov stability is established for both commuting switching models non-commuting cases.
- Simulations on a 5-DoF system confirm vibration suppression and fast convergence ($J(t) \rightarrow 0$).

Graphical Abstract - Flowchart

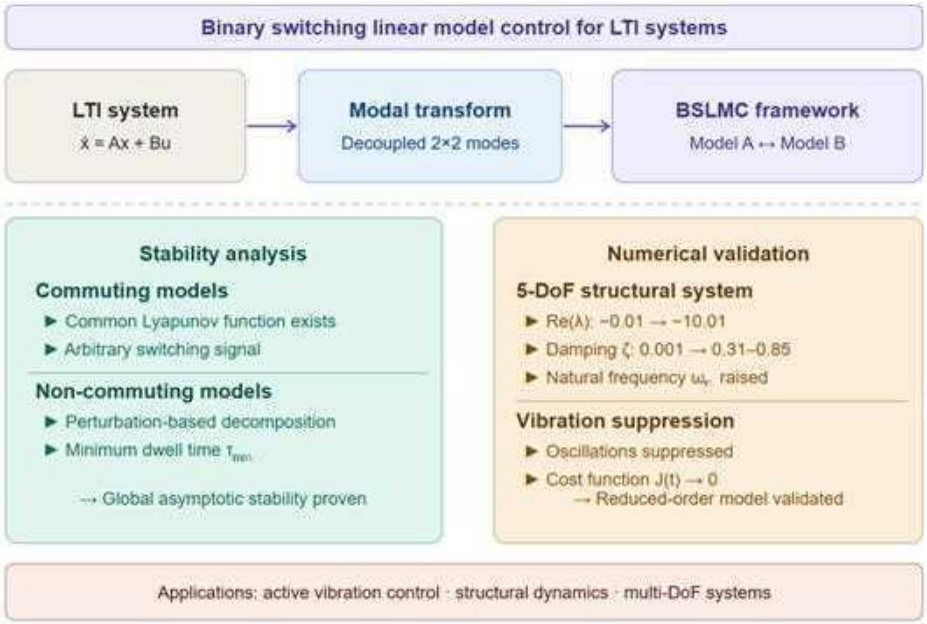


Figure Generic Flowchart of Binary Switching Linear Model Control for LTI systems

***Corresponding Author:** Can Ulas DOGRUER, cdogruer@hacettepe.edu.tr

Konya Mühendislik Bilimleri Dergisi., c.14, s.2, 658-681, 2026
Konya Journal of Engineering Sciences v.14, n.2, 658-681, 2026
ISSN: 2667-8055 (Electronic)
DOI: 10.36306/konjes.1609821

BINARY SWITCHING LINEAR MODEL CONTROL FOR LTI SYSTEMS: STABILITY ANALYSIS AND MODE CONTROL EQUIVALENCE

[1,*]Can Ulas DOGRUER, [2]Can Barış TOPRAK, [3]Bora YILDIRIM

[1,3]*Department of Mechanical Engineering, Hacettepe University, Ankara 06800, Türkiye.*
[2] *Additive Manufacturing Technologies Application and Research Center (EKTAM), Gazi University, 06560, Ankara, Türkiye.*
[1]cdogruer@hacettepe.edu.tr, [2]cantoprak@gazi.edu.tr, [3]boray@hacettepe.edu.tr

(Received: 14.03.2024; Accepted in Revised Form: 18.11.2025)

ABSTRACT: This paper proposes a novel control framework, termed Binary Switching Linear Model Control (BSLMC), for regulating the motion modes of Linear Time-Invariant (LTI) systems. The approach leverages a modal coordinate transformation to decompose an LTI system into a set of decoupled first- and second-order subsystems, enabling selective control of dominant modes without altering the system's eigenvector structure. By adjusting the natural frequencies and damping ratios of these active modes, the proposed method achieves effective pole reassignment while preserving mode shapes. A frequency-domain analysis demonstrates that the Bode diagram of the original system can be approximated within specific frequency bands by controlling only a subset of modes, thereby reducing computational complexity. Theoretical investigations rigorously analyze the stability of BSLMC using the Lyapunov stability theorem. It is shown that when the switching models form a set of commuting matrices, a common Lyapunov function exists, allowing for arbitrarily small mode-dependent dwell times. For non - commuting cases, a perturbation-based analysis provides conditions for robust stability. The proposed method's efficacy is validated through numerical simulations on a multi-degree-of-freedom structural system, highlighting its potential for active vibration control and structural dynamics applications.

Keywords: *Active Vibration Control, LTI Systems, Stability Analysis, Structural Systems.*

1. INTRODUCTION

The dynamic behavior of Linear Time-Invariant (LTI) systems is often characterized in the frequency domain using Bode diagrams [6, 18]. These diagrams can be effectively approximated by a finite set of first- and second-order motion modes within distinct frequency bands, as demonstrated in modal control studies for structural and mechanical systems [4, 14]. By leveraging a modal coordinate transformation, the LTI system's state matrix is decomposed into decoupled subsystems, where the transformation matrix is the inverse of the modal matrix derived from the system's eigenstructure [14, 19]. This decomposition facilitates a reduced-order representation of the system, suggesting the possibility of modeling the global dynamics using multiple local models that capture the dominant modes of motion [5, 11].

Building on this foundation, this paper introduces a novel Binary Switching Linear Model Control (BSLMC) strategy designed to selectively regulate these dominant modes. Each mode, expressed in modal coordinates, behaves as a self-contained, non-interacting subsystem, enabling the formulation of a switching control policy

based on modal control techniques [9, 22]. The switching policy is derived by comparing infinite-horizon Lyapunov costs, prioritizing control of modes with higher energy contributions. This framework allows

***Corresponding Author:** Can Ulas DOGRUER, cdogruer@hacettepe.edu.tr

for targeted adjustments of natural frequencies and damping ratios in active modes, resulting in effective pole reassignment while preserving mode shapes [5].

A key challenge addressed in this study lies in the stability analysis of the BSLMC framework. When switching between linear models that are mutually compatible (commuting matrices), a common Lyapunov function can be identified, ensuring stability under arbitrarily small mode-dependent dwell times [9, 21]. However, non-commuting models—such as those pairing under-damped and over-damped dynamics—complicate this analysis [25]. To resolve this, the over-damped system is decomposed into a nominal commuting component and a perturbation matrix. Stability of the perturbed system is then analyzed using robust Lyapunov techniques [11, 25].

The contributions of this work can be summarized as follows:

- A modal decomposition-based control framework that preserves eigenvector structures across switching events.
- A theoretical stability analysis establishing conditions for the existence of common Lyapunov functions and robust stability under perturbations.
- Numerical validation on a multi-degree-of-freedom structural system, demonstrating reduced-order modeling benefits and practical feasibility.

The remainder of this paper is structured to provide a comprehensive development and validation of the proposed Binary Switching Linear Model Control (BSLMC) framework for Linear Time-Invariant (LTI) systems.

In Section 2, we present a critical review of existing literature on switching control systems, hybrid systems theory, and model predictive control (MPC) methods. Particular attention is given to recent advancements in mode-based control strategies and their limitations in handling modal interactions and stability under switching. This section also highlights gaps in current approaches to active vibration control, establishing the need for a framework that preserves mode shapes during switching events while ensuring robust performance.

Section 3 formulates the problem addressed in this study. It introduces the mathematical preliminaries required for modal decomposition, defines the system modeling assumptions, and outlines the challenges of implementing switching control in modal coordinates. The section emphasizes the importance of controllability and observability conditions and discusses the implications of potential singularities in transformation matrices.

In Section 4, we detail the theoretical foundation of the BSLMC framework. This includes the derivation of modal coordinate transformations, development of the binary switching control law, and formulation of a cost-based switching policy using infinite-horizon Lyapunov functions. The stability analysis is rigorously developed by examining commuting and non-commuting switching models. A novel perturbation-based approach is proposed to handle non-commutative cases, ensuring robust stability even in the presence of structural system uncertainties.

Section 5 provides extensive numerical simulations to validate the theoretical findings. A multi-degree-of- freedom structural system is used as a benchmark case, where the proposed control strategy is applied to regulate active modes and suppress vibrations. Comparative analyses with uncontrolled scenarios demonstrate the effectiveness of BSLMC in approximating system dynamics, reducing computational complexity, and achieving desirable performance across varying operating conditions.

Finally, Section 6 concludes the paper by summarizing the primary contributions and practical implications of the study. It also outlines promising directions for future work, including extensions to nonlinear systems, experimental validations on physical structures, and integration of adaptive control mechanisms for enhanced robustness.

2. RELATED WORKS

When a system undergoes abrupt state changes due to interactions with its environment within finite time intervals, it is often modeled using switching linear models. These models analyze the system's dynamic behavior by employing a collection of linear representations, each activated by a switching signal. Such switching signals can be either time-dependent, where the switching instances are predefined, or state- dependent, where the signal depends on system states and external manipulation becomes impractical [24]. In state-dependent switching systems, feedback control laws have been widely used to regulate switching behavior, transforming the original system into an autonomous switching linear system [4, 17, 21]. Even when the switching is time-driven, these systems are commonly classified under the broad category of switching linear systems [9, 13, 22].

Within the field of switching linear model control, extensive research has addressed challenges such as constructing a suitable bank of linear models, determining effective switching strategies, and ensuring performance objectives are met [5, 11, 19]. A critical issue is the stability of such systems, where Lyapunov-based methods have been the foundation of most theoretical studies [15, 16, 20, 25]. However, it has been shown that intuitive conditions for stability do not always hold, with counterexamples challenging general assumptions [9, 22].

In recent years, several studies have extended the theoretical and practical boundaries of switching control, model decomposition, and structural dynamics. Modern switching control strategies have been thoroughly reviewed to address nonlinear and uncertain systems using adaptive dwell time and event-triggered mechanisms [7, 26]. Modal-based control frameworks have evolved to enhance active vibration suppression in flexible structures, leveraging real-time adaptation and multi-mode coordination [2, 8]. Likewise, Lyapunov-based analyses remain a core approach for stability verification, with recent work offering generalized treatments through multiple Lyapunov functions and finite-time stability conditions even under switching delays or perturbations [3, 12]. Reduced-order modeling has also gained traction as a critical technique in structural control, especially through data-driven and projection-based schemes that enable scalable and accurate system simplification [1, 23]. These contemporary contributions provide essential validation and conceptual grounding for the proposed BSLMC framework, highlighting its alignment with current research trends and reinforcing its relevance in modern structural control paradigms.

In contrast to existing approaches, this study presents a comprehensive framework for Binary Switching Linear Model Control (BSLMC) specifically tailored for Linear Time-Invariant (LTI) structural systems. Leveraging equivalence transformations, we represent the LTI system in Jordan canonical form, where the dynamics naturally decouple into first- and second-order non-interacting subsystems. This decoupling facilitates the construction of alternating model pairs for each mode of motion, enabling independent manipulation of their dynamic properties.

We further propose a novel switching policy, derived from the infinite-horizon Lyapunov cost functions, to prioritize the regulation of dominant modes of motion.

This allows the original high-dimensional system ($n \times n$) to be effectively reduced to a set of 2×2 systems in modal coordinates, substantially simplifying the complexity.

of controller design. The resulting BSLMC framework enables targeted adjustment of natural frequencies and damping ratios while preserving mode shapes—a feature that distinguishes it from traditional switching controllers.

Finally, the stability of the proposed method is rigorously analyzed using Lyapunov theory. For commuting switching models, we establish conditions for the existence of a common Lyapunov function, allowing arbitrarily small dwell times. For non-commuting cases, a perturbation-based approach is introduced to ensure robust stability under structural uncertainties. This dual treatment provides theoretical foundations that make the control of complex structural systems both practical and analytically tractable.

3. PROBLEM FORMULATION

In this study, we address the control of high- dimensional Linear Time-Invariant (LTI) engineering systems, where complex mode interactions and structural dynamics pose significant challenges to conventional control strategies. Such systems often require high-order models for accurate representation, making controller design computationally intensive and analytically intractable.

Our proposed solution leverages modal coordinates to simplify both analysis and control. By employing a non-singular equivalence transformation matrix, we decompose the original $n \times n$ state-space model into a set of decoupled first- and second-order subsystems in modal coordinates. This decomposition assumes the system is fully controllable and observable in modal coordinates, with eigenvalues arranged such that each mode can be independently manipulated.

We introduce a novel framework, termed *Binary Switching Linear Model Control (BSLMC),* designed to modify the dynamics of each motion mode independently. In this approach, pairs of linear models are constructed for each mode, allowing for selective adjustment of natural frequencies and damping ratios without altering mode shapes. A cost-based switching policy is developed using infinite-horizon Lyapunov functions to prioritize control of the most dynamically significant modes.

To evaluate the stability of BSLMC, we conduct a rigorous Lyapunov-based analysis across various scenarios, including under-damped, critically-damped, and over-damped second-order systems. For switching models with homogeneous damping coefficients (commuting matrices), we establish the existence of a common Lyapunov function, permitting arbitrarily small minimum dwell times. In contrast, for mixed damping scenarios (non-commuting matrices), we propose a perturbation-based method that isolates non-commuting components and derives a nominal system admitting a common Lyapunov function. Robustness analysis is then performed to determine bounds on perturbations that preserve stability.

This study therefore contributes: (i) a reduced-order control strategy that preserves mode shapes while regulating dominant modes; (ii) a unified theoretical framework for stability analysis of commuting and non-commuting switching models; and (iii) practical guidelines for determining minimum mode-dependent dwell times in structural systems. These contributions pave the way for applying BSLMC in active vibration control and structural dynamics, where efficiency and robustness are critical.

4. THEORY: BINARY SWITCHING CONTROL OF STRUCTURAL SYSTEMS

4.1. Modal Decomposition of the State-Space Model of a Structural System,

We begin with the general form of a Linear Time-Invariant (LTI) system, expressed in state-space representation as

$$\dot{x} = Ax + Bu \tag{1}$$

where $x \in \mathbb{R}^n$ is the state vector, $u \in \mathbb{R}^m$ is the input vector, $A \in \mathbb{R}^{n\times n}$ is the system matrix, and $B \in \mathbb{R}^{n\times m}$ is the input matrix.

It is assumed that the system is controllable and observable, and the state matrix A admits a full set of linearly independent eigenvectors, enabling diagonalization or real Jordan decomposition. This ensures the existence of a non-singular transformation matrix P such that modal decoupling is achievable.

To facilitate modal analysis and controller design, we apply an equivalence transformation using the matrix P:

$$z = P^{-1}x \tag{2}$$

which yields the transformed system

$$\dot{z} = Fz + P^{-1}Bu \tag{3}$$

where $F = P^{-1}AP$ is the system matrix in modal coordinates.

The matrix F takes a block-diagonal form in modal coordinates, allowing us to analyze and control each mode of motion independently. We assum Q is non-singular so that $P = Q^{-1}$ is well-defined. In cases where Q is singular, modal decomposition and subsequent control design would not be feasible under the current framework. Complex eigenvalues in F appear in conjugate pairs, and their associated blocks can be represented as

$$\bar{z} = \begin{bmatrix} a & -b \\ b & a \end{bmatrix} \tag{4}$$

where a and b are the real and imaginary parts of the eigenvalues, respectively. This representation facilitates analysis of under-damped and oscillatory dynamics.

$$\dot{z} = Fz + Gu \tag{5}$$

Here, F represents the system matrix in modal coordinates obtained by $F = P^{-1}AP$.

4.2. Binary Switching Linear Model Control

The proposed Binary Switching Linear Model Control framework is applicable to LTI systems that are fully controllable and observable, provided their state matrices are diagonalizable or admit a real Jordan decomposition. These conditions guarantee that individual motion modes can be decoupled and independently addressed.

In this framework, each mode of motion is associated with a pair of linear models that can switch based on a cost function. The switching logic is determined by comparing infinite-horizon Lyapunov costs for each active mode. This approach allows selective regulation of dominant modes while preserving the mode shapes, ensuring that the eigenvectors remain invariant across switching events.

The switching control law can be expressed as

$$u(t) = -K_i(t)z(t) \tag{6}$$

where $K_i(t)$ denotes the feedback gain for the i-th mode, and $z(t)$ is the state vector in modal coordinates. We now analyze the stability of the switching control law.

Theorem 1: [Stability of Mode-Shape-Preserving Switching Control] Consider the transformed system $\dot{z} = Fz + Gu$, where F is block-diagonal in modal coordinates. Assume eigenvectors are invariant across switching events and a minimum dwell time $\tau_d > \tau_{min}$ is satisfied. Then the closed-loop system is asymptotically stable.

4.3. Binary Switching Control Synthesis

4.3.1 Controller Synthesis in Modal Canonical Subspace

The Linear Time-Invariant (LTI) model of a structural system serves as a mathematical framework to analyze and control system responses. This response can be expressed using mode superposition, where each mode's contribution is represented by a time-dependent scalar known as a modal coordinate. Modal coordinates emphasize the individual influence of each vibration mode on the overall system dynamics and can be derived via an algebraic equivalence transformation as formalized in Theorem 2.

Theorem 2: [Equivalence Transformation and Modal Decomposition] Given an LTI system $\dot{x} = Ax + Bu$ where A admits a full set of linearly independent eigenvectors, there exists a non-singular transformation matrix P such that the transformed system $\dot{z} = Fz + P^{-1}Bu$ is block-diagonal in modal coordinates. Each block corresponds to either a first-order or second-order non- interacting subsystem.

A central claim of this work is that any high- dimensional LTI system can be effectively approximated by a reduced-order model comprising a finite number of dominant modes of motion. However, since modal coordinates evolve with time, the set of active modes also changes dynamically. Notably, it can be shown that the Bode diagram of the original system is closely approximated by retaining only a select few modes within specific frequency bands. This insight motivates the formulation of the structural system as a multiple-model switching system in theory.

The extracted modes of motion are represented as:

$$\mathcal{M}_i = \{\dot{z}_i = F_i z_i + G_i u;\ Q_{i\downarrow},\ i \in N\} \tag{7}$$

where $Q_{i\downarrow}$ denotes the projection of Q_i onto a reduced- order subspace

To regulate system dynamics, a switching policy is devised based on infinite-horizon cost functions that quantify the effort required to return the system to equilibrium without control input:

$$J_i = \int_0^\infty x^T \bar{Q}_i x \, dt \tag{8}$$

which in modal coordinates becomes:

$$J_i = \int_0^\infty z_i^T Q_i z_i \, dt \tag{9}$$

where

$$Q_i = P_{i\rightarrow}^T \bar{Q}_i P_{i\rightarrow} \tag{10}$$

Here, $P_{i\rightarrow}$ denotes the submatrix of P that maps the system states to the i-th modal subspace. The infinite-horizon cost is computed by solving the Lyapunov equation:

$$F_i^T P_i + P_i F_i = Q_i \tag{11}$$

yielding$J_i = z_{i0}^T P_i z_{i0}$. To enable relative ranking of modes, these costs are normalized:

$$\bar{J}_i = \frac{J_i}{\sum_i J_i} \tag{12}$$

Modes with the highest normalized cost $\bar{J}_i$ are prioritized for control by adjusting their natural frequencies and damping ratios.

To maintain mode-shape preservation during switching, the eigenvector matrix P must remain invariant. The transformation matrices for two system models, F_a and F_b , are constructed as:

$$A_1 = PF_aP^{-1} \tag{13}$$

$$A_2 = PF_bP^{-1} \tag{14}$$

The full-state feedback gain K_x is computed to enforce:

$$A_2 - A_1 = P_B K_x \tag{15}$$

where$P_B = PB$. Since P_B may not be square or invertible, the Moore-Penrose inverse P_B^+ is used:

$$K_x = P_B^+ (A_2 - A_1) \tag{16}$$

This approach assumes P_B has full column rank; otherwise, exact pole placement may not be feasible.

The resulting feedback control modifies only the natural frequencies and damping ratios of selected modes while preserving eigenvectors. This ensures the stability and continuity of the modal subspaces during switching.

4.3.2 MPC in Canonical Modal Coordinates

The modal canonical state-space model captures both the real and imaginary components of the system states, providing a structured framework for independently controlling each motion mode. Real eigenvalues correspond to first-order subsystems, while complex conjugate pairs form second-order oscillatory subsystems. This modal representation facilitates reduced-order controller synthesis and enables targeted regulation of dominant dynamics.

An output model is designed to select specific elements of the state vector for observation and control. The state- space representation is expressed as:

$$\dot{x} = Ax + Bu \tag{17}$$
$$y = Cx + Du \tag{18}$$

To verify the controllability of the outputs, we compute the output controllability matrix:

$$\mathcal{C} = [CAB \quad CA^2B \quad CA^3B \quad \dots \quad CA^{2n-1}B] \tag{19}$$

Full row rank of $\mathcal{C}$ indicates that the chosen outputs are controllable. If this condition fails, certain outputs cannot be influenced by any control signal, requiring additional actuators or redesign of the output matrix C.

Working in the modal canonical framework allows for regulation of all system states as projected onto the modal subspace. This approach is particularly advantageous in high-dimensional systems where the original coordinates may not provide enough independent control inputs to simultaneously regulate all states or outputs. By focusing on the dominant active modes, binary switching control can selectively

adjust damping ratios and natural frequencies while neglecting modes that have negligible impact on the system's behavior.

The normalization of infinite-horizon Lyapunov costs,

$$\bar{J}_i = \frac{J_i}{\sum_i J_i} \tag{20}$$

is employed to rank the relative energy contributions of each mode. This facilitates threshold-based selection of dominant dynamics, ensuring that control efforts are concentrated on modes that significantly affect system performance.

Mode-shape-preserving switching is critical because it maintains the invariance of eigenvectors across switching events. This guarantees that the decoupled modal representation remains valid, enabling consistent controller design and stability analysis throughout operation.

To formulate the Model Predictive Control (MPC) law in canonical modal coordinates, we consider the finite horizon quadratic cost function:

$$J = \frac{1}{2}\sum_{k=1}^{N}\left(\Delta e_k^{yT} Q_y \Delta e_k^{y} + \Delta e_k^{uT} Q_u \Delta e_k^{u}\right) \tag{21}$$

subject to the discrete-time system dynamics:

$$z_{k+1} = A_1 z_k + B_1 u_k \tag{22}$$

$$z_k = C_1 z_k \tag{23}$$

$$z_{k+1}^r = A_2 z_k \tag{24}$$

$$y_k^r = C_1 z_k^r \tag{25}$$

where

$$\Delta \mathrm{e}_k^{y} = \mathrm{y}_k - \mathrm{y}_k^r \tag{26}$$

$$\Delta \mathrm{e}_k^{u} = \mathrm{u}_k - \mathrm{u}_k^r \tag{27}$$

This formulation requires discretization of the continuous-time system using a suitable sampling period Δt to ensure that the discrete model accurately represents the system dynamics.

Transforming the cost function into state-space terms yields:

$$J = \frac{1}{2}\sum_{k=1}^{N}(\Delta \mathrm{e}_k^{zT} \mathrm{Q}_z \Delta \mathrm{e}_k^{z} + \Delta \mathrm{e}_k^{uT} \mathrm{Q}_u \Delta \mathrm{e}_k^{u}) \tag{28}$$

where

$$\Delta \mathrm{e}_k^{z} = \mathrm{z}_k - \mathrm{z}_k^r, \quad \mathrm{Q}_z = \mathrm{C}^T \mathrm{Q}_y \mathrm{C} \tag{29}$$

The resulting optimization problem is:

$$\min_u J \tag{30}$$

Subject to

$$z_{k+1} = A_1 z_k + B_1 u_k \tag{31}$$

$$\mathrm{z}_{k+1}^r = \mathrm{A}_2 \mathrm{z}_k \tag{32}$$

Although the MPC focuses on a subset of modal coordinates, simulations show that the remaining modes have negligible effect on system outputs. This reduced- order MPC effectively governs the system as a cohesive unit. The MPC-generated control gain may not assign the exact poles of the reference model but ensures transient emulation of its dynamics. Stability of the plant under MPC control implies that the reference switching model maintains momentary stability, as further analyzed in the next section.

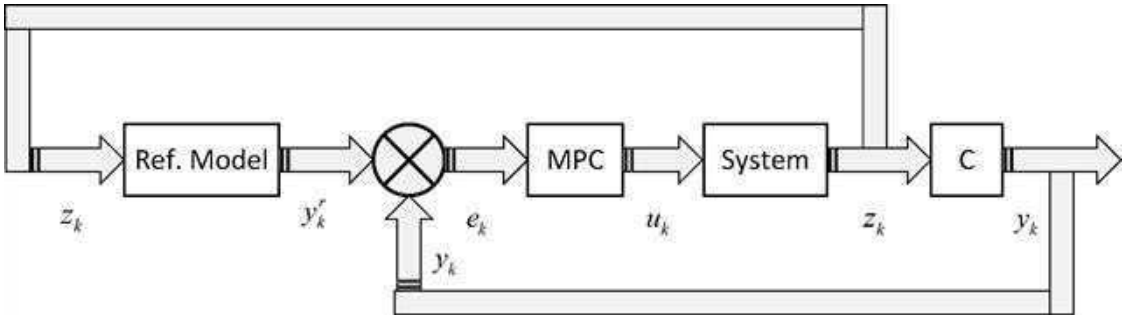


Figure 1. Schematic of the model-following switched system with a model predictive controller (MPC) implemented in canonical modal coordinates. The MPC minimizes the finite-horizon cost function J to track the reference model while ensuring mode-shape preservation and robust switching between active modes

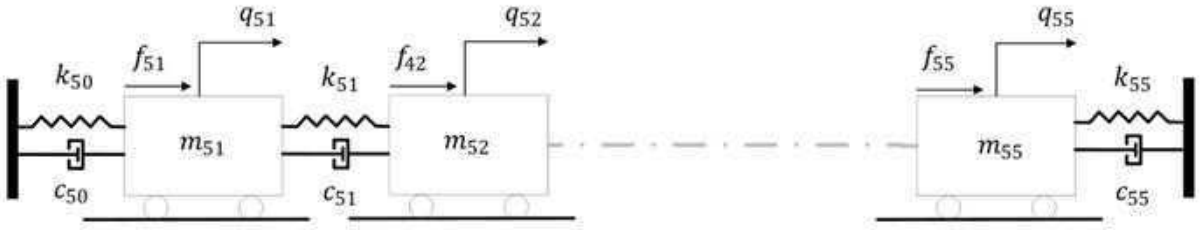


Figure 2. Five-degree-of-freedom (5-DoF) mass-spring- damper system used as the benchmark structural model. This system exhibits coupled dynamics decomposed into modal coordinates (z) for control synthesis

The effectiveness of mode selection also depends on actuator placement and the sensitivity of outputs to individual modes, which are assumed to be known or identified experimentally.

4.4 Stability Analysis of Binary Switching Control Admitting a Common Lyapunov Function

We begin by assuming that the linear models of the binary switching linear model control share a common Lyapunov function. In this case, the common Lyapunov equation is defined as:

$$\mathrm{F}_{ij}^{T}\mathrm{P} + \mathrm{P}\mathrm{F}_{ij} = -\mathrm{Q}_{ij} \tag{33}$$

where P is symmetric positive definite and Q_{ij} is symmetric positive definite for all subsystems F_{ij}.

The quadratic Lyapunov function is then given by:

$$V(\mathrm{z}) = \mathrm{z}_i^{T}\mathrm{P}\mathrm{z}_i \tag{34}$$

Its time derivative along the trajectories of subsystem F_{ij} is:

$$\dot{V}_{ij} = \mathrm{z}_i^{T}\left(\mathrm{F}_{ij}^{T}\mathrm{P} + \mathrm{P}\mathrm{F}_{ij}\right)\mathrm{z}_i = -\mathrm{z}_i^{T}\mathrm{Q}_{ij}\mathrm{z}_i \tag{35}$$

Thus, $\dot{V}_{ij} < 0$ for all $z_i \neq 0$, indicating asymptotic stability of each subsystem.

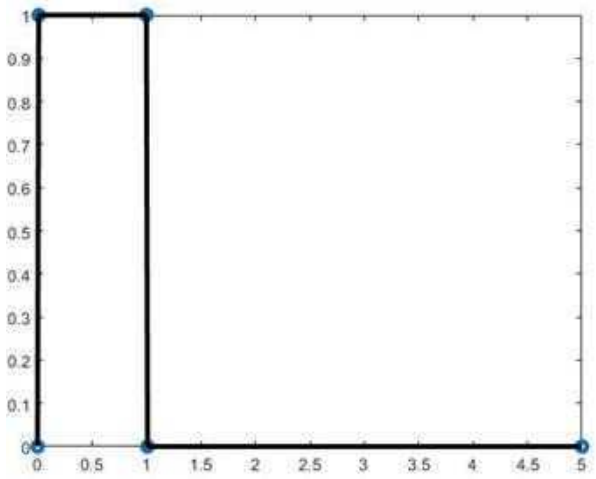


Figure 3. Time history of the disturbance signal applied to the structural system. Amplitude is scaled by 10, and step time is scaled by 0.1 to excite dominant motion modes and evaluate the robustness of the controller

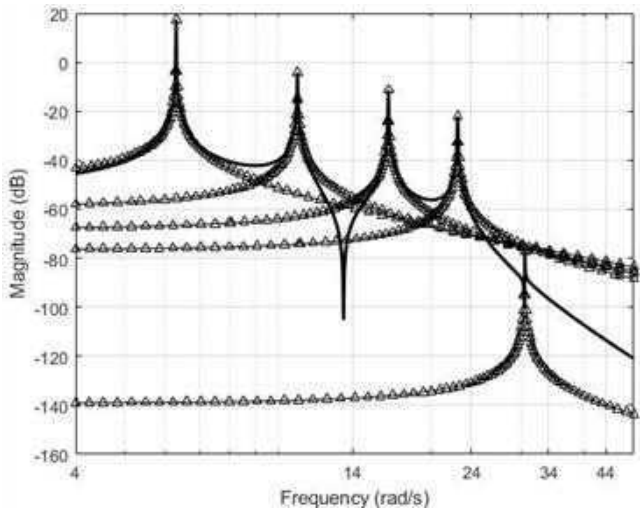


Figure 4. Bode diagram comparing the original system's frequency response (solid line) with local sub-models (triangular markers) identified through modal decomposition. Each sub-model approximates the system within a specific frequency band, supporting reduced-order controller design

Furthermore, the upper bound on $\dot{V}_{ij}$ can be expressed as:

$$\dot{V}_{i1}\& \leq -\lambda_{\min}(Q_{i1}) \parallel z_i \parallel^2 \tag{36}$$

$$\dot{V}_{i2}\& \leq -\lambda_{\min}(Q_{i2}) \parallel z_i \parallel^2 \tag{37}$$

In the presence of a discontinuous state trajectory—e.g., when the MPC controller does not perfectly track the reference switching system—there may exist instantaneous increases in $V(z)$ at switching instants. However, as the MPC operates autonomously and eventually synchronizes with the reference model, continuity of z is reestablished, ensuring the monotonic decrease of $V(z)$.

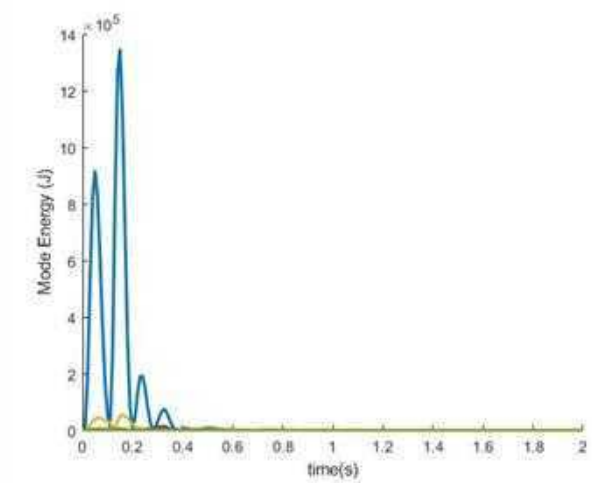


Figure 5. Case I: Lyapunov cost functions J_i for different sub-models, representing the energy content of each mode and informing the switching strategy in binary switching linear model control

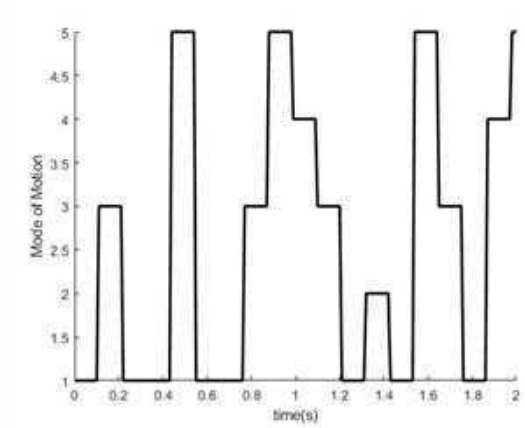


Figure 6. Switching policy for Mode Controller-I, which selects active modes based on normalized Lyapunov costs $\bar{J}_i$. This policy determines the sequence of mode activations over time

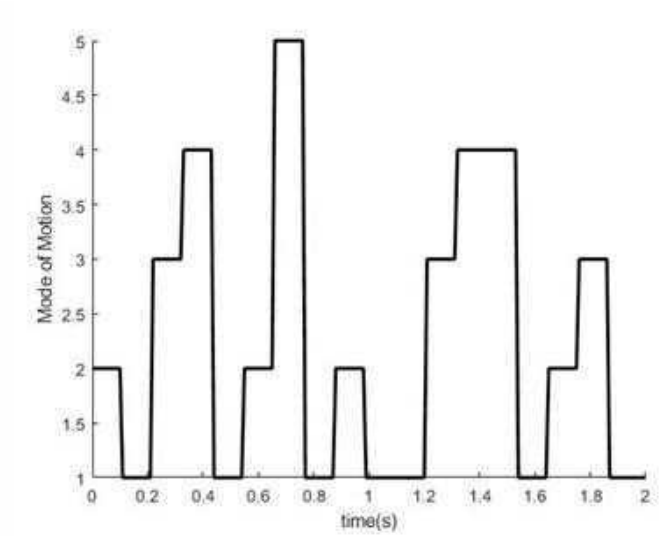


Figure 7. Case I: Switching policy for Mode Controller - II. This alternative policy prioritizes modes with higher instantaneous contributions to system response, leading to a distinct activation pattern

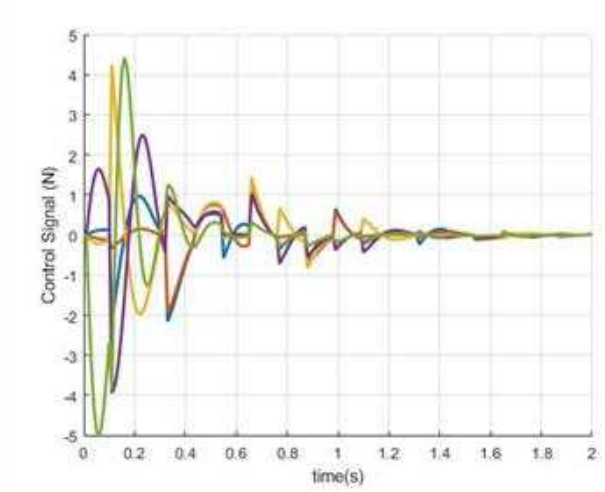


Figure 8. Case I: Time history of the control input $u(t)$ generated by the binary switching linear model controller. The control law assigns desired poles to active modes while preserving eigenvectors

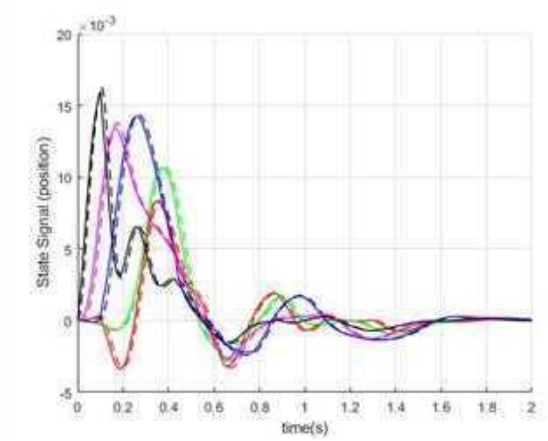


Figure 9. Case I: Position response $\boldsymbol{x}(t)$ of the system over time. The solid line represents the reference response, while the dashed line shows the improved performance achieved through binary switching linear model control

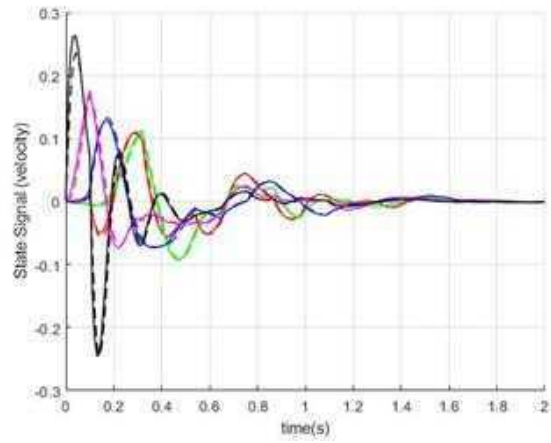


Figure 10. Case I: Velocity response $\dot{\boldsymbol{x}}(t)$. The solid lines show the reference response while dashed line illustrates reduced oscillations and faster settling under the proposed controller

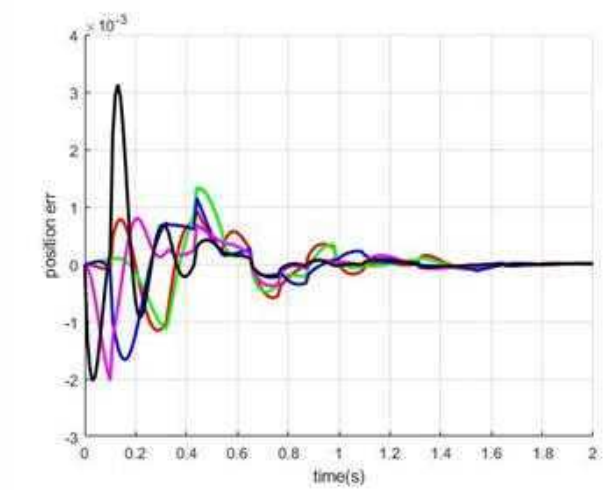


Figure 11. Case I: Position tracking error $e_p(t) = x(t) - x^r(t)$ over time. Errors converge asymptotically, confirming the stability condition

4.5 Stability Analysis of Binary Switching Control Synthesis

The stability of the multiple-model switching system is analyzed using the theorem of commuting matrices [9,26]. Two matrices F_{i1} and F_{i2} are said to commute if:

$$[F_{i1}, F_{i2}] = F_{i1}F_{i2} - F_{i2}F_{i1} = 0 \quad (38)$$

Theorem 3: [Common Lyapunov Function for Commuting Matrices] Let F_{i1} and F_{i2} be Hurwitz matrices satisfying $[F_{i1}, F_{i2}] = 0$. Then there exists a symmetric positive definite matrix P solving:

$$F_{ij}^T P + PF_{ij} = -Q_{ij},\ \forall j \in \{1,2\} \quad (39)$$

where Q_{ij} is positive definite. The quadratic form $V(\mathrm{z}) = \mathrm{z}_i^T P \mathrm{z}_i$ is a common Lyapunov function for both subsystems, guaranteeing global asymptotic stability under arbitrary switching [9].

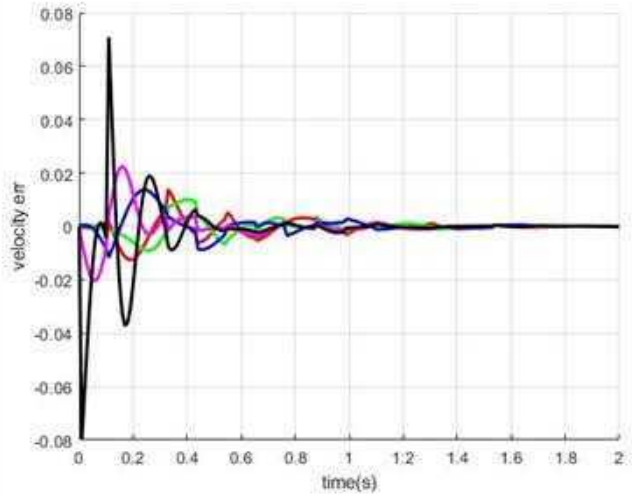


Figure 12. Case I: Velocity tracking error$e_v(t) = \dot{x}(t) - \dot{x}^r(t)$. The binary switching controller maintains errors within tight bounds throughout the simulation

Lemma 1: [Under-Damped Modes] If any F_i in the modal decomposition represents an under-damped system of the form:

$$F_{i1} = \begin{bmatrix} -\zeta_i\omega_{ni} & \omega_{di} \\ -\omega_{di} & -\zeta_i\omega_{ni} \end{bmatrix}_1 \tag{40}$$

$$F_{i2} = \begin{bmatrix} -\zeta_i\omega_{ni} & \omega_{di} \\ -\omega_{di} & -\zeta_i\omega_{ni} \end{bmatrix}_2 \tag{41}$$

and the switching model is:

then$[F_{i1}, F_{i2}] = 0$. Hence, a common Lyapunov function exists [22].

Lemma 2:[Critically Damped Modes] If any F_i represents a critically damped system with:

$$F_{i1} = F_{i2} = \begin{bmatrix} -\omega_{ni} & 0 \\ 0 & -\omega_{ni} \end{bmatrix} \tag{42}$$

then the matrices trivially commute and a common Lyapunov function exists [22].

Lemma 3: [Over-Damped Modes] If F_{i1} and F_{i2} are over-damped systems with distinct negative eigenvalues, they commute if diagonal, ensuring existence of a common Lyapunov function [22].

Fact 1: [Mode-Shape-Preserving Switching] For systems satisfying Lemmas 1–3, the modal decomposition is invariant under switching, and the minimum mode- dependent dwell time can be arbitrarily small.

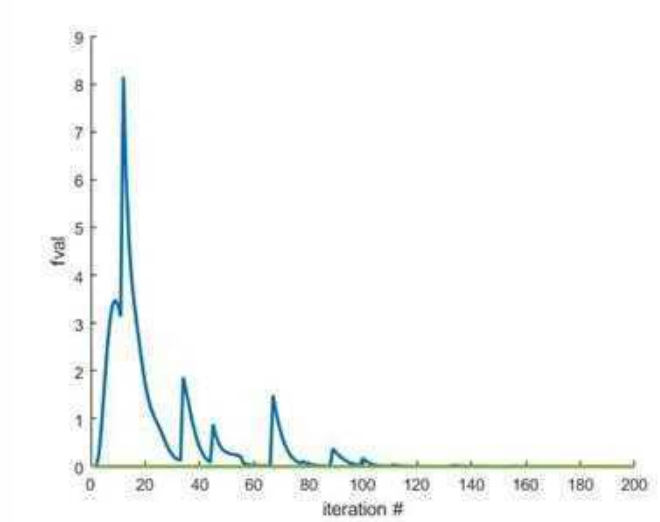


Figure 13. Case I: Evolution of the quadratic cost function $J(t)$ during closed-loop operation. The decreasing trend validates the convergence of the MPC-based binary switching control law

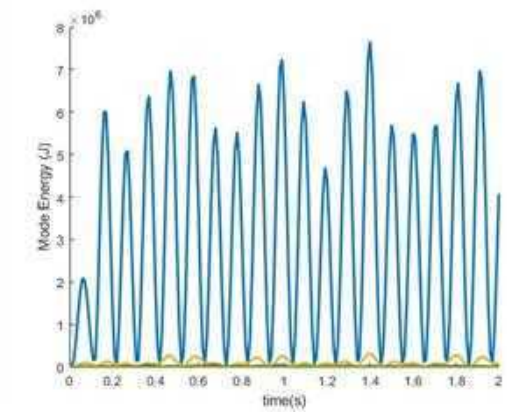


Figure 14. Case II: Evolution of Lyapunov cost functions J_i for each sub-model during the free response of the system. The decay of J_i over time reflects the natural energy dissipation of uncontrolled modes, highlighting the dominant contribution of low-frequency modes to system dynamics in the absence of active control

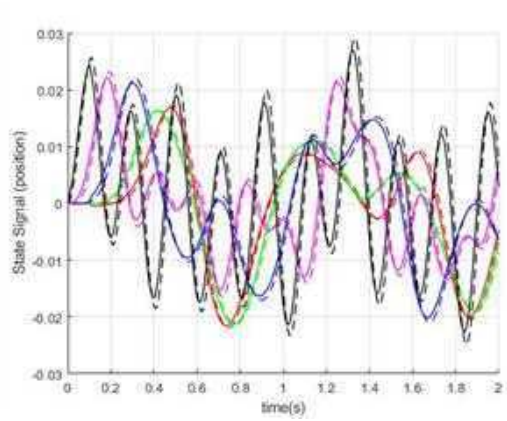


Figure 15. Case II: Position response $x(t)$ of the uncontrolled system. Persistent oscillations and slow convergence are observed, emphasizing the limited damping capacity of the passive system and the necessity of active switching control for rapid stabilization

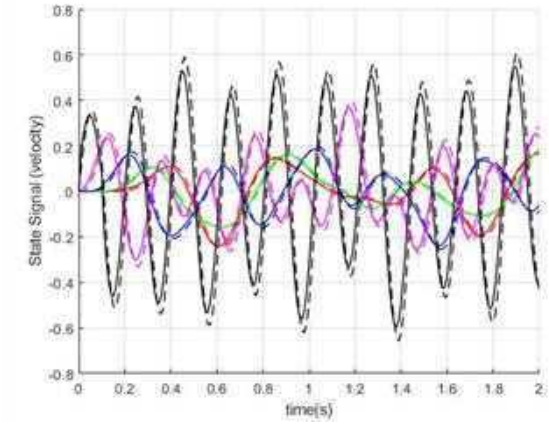


Figure 16. Case II: Velocity response $\dot{\boldsymbol{x}}(t)$ of the uncontrolled system. Sustained velocity fluctuations confirm the system's sensitivity to initial conditions and disturbances, underscoring the effectiveness of binary switching linear model control in suppressing such responses

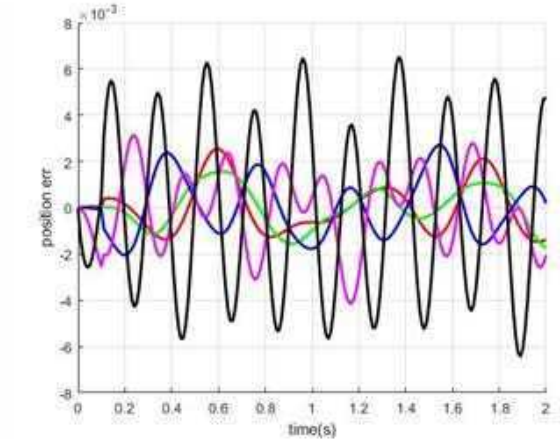


Figure 17. Case II: Time history of position error $e_p(t)$ without control input. The absence of active regulation leads to large position deviations over time, demonstrating the inability of the passive system to reject disturbances or achieve precise trajectory tracking

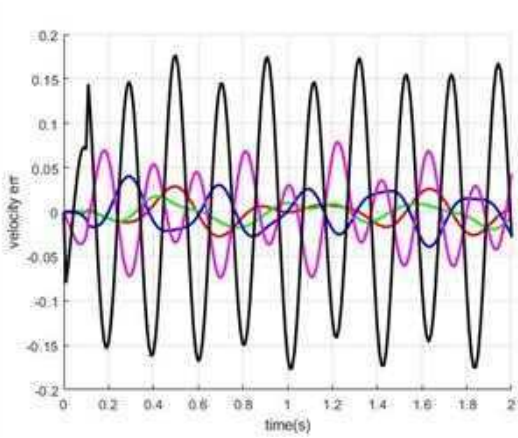


Figure 18. Case II: Time evolution of velocity error $e_v(t)$ in the uncontrolled system. Significant error magnitudes persist, indicating poor robustness and slow disturbance attenuation compared to the controlled case

Conjecture 2: [Non-Commuting Matrices] When switching occurs between an under-damped and an overdamped mode, $[F_{i1}, F_{i2}] \neq 0$. Therefore, no common Lyapunov function exists, and minimum dwell time constraints arise.

Proposition 1: [Perturbation Approach for Non- Commuting Systems] Let F_{i1} and F_{i2} be non-commuting Hurwitz matrices. Decompose:

$$F_{i2} = F_{i2}^{o} + \Delta F_{i2} \tag{43}$$

where ΔF_{i2} captures non-commuting terms. If F_{i2}^{o} admits a Lyapunov function $V(\mathrm{z}_i) = \mathrm{z}_i^T P \mathrm{z}_i$, and $\| \Delta F_{i2} \|$ is sufficiently small, then $V(\mathrm{z}_i)$ serves as an approximate Lyapunov function for F_{i1} with guaranteed stability margins [10, 21].

This rigorous treatment ensures the binary switching linear model control remains robust even when ideal commuting conditions are violated. Mode-shape preservation is emphasized as it guarantees modal decoupling across all switching events.

4.6. Stability Analysis for Under-damped to Over- damped Switching with Minimum Dwell Time Constraint

As established in Conjecture 2 and Proposition 1, binary switching linear models that do not admit a common Lyapunov function require a refined analysis. Consider a switching system involving transitions between an under-damped and an over-damped subsystem. Without loss of generality, we assume that the uncontrolled mode is under-damped and the controlled mode is over-damped. The system is described by:

$$\dot{z}_\iota = \mathrm{F}_i \mathrm{z}_i \tag{44}$$

where

$$\mathrm{F}_{i1} = \begin{bmatrix} -\zeta_i \omega_{ni} & \omega_{di} \\ -\omega_{di} & -\zeta_i \omega_{ni} \end{bmatrix},\ \mathrm{F}_{i2} = \begin{bmatrix} -\zeta_{1i} & 0 \\ 0 & -\zeta_{2i} \end{bmatrix} \tag{45}$$

Here, F_{i1} represents the under-damped system and F_{i2} the over-damped system. Clearly, $[F_{i1}, F_{i2}] \neq 0$, so no common Lyapunov function exists.

To proceed, we decompose F_{i2} into:

$$F_{i2} = F_{i2}^o + \Delta F_{i2} \tag{46}$$

where,

$$F_{i2}^o = \begin{bmatrix} -\zeta_{1i} & 0 \\ 0 & -\zeta_{1i} \end{bmatrix},\ \Delta F_{i2} = \begin{bmatrix} 0 & 0 \\ 0 & -\eta_{12} \end{bmatrix} \tag{47}$$

$$\eta_{12} = \zeta_{2i} - \zeta_{1i} > 0 \tag{48}$$

The pair $\{F_{i1}, F_{i2}^o\}$ satisfies$[F_{i1}, F_{i2}^o] = 0$, implying the existence of a common Lyapunov function $V(\mathrm{z}_i) = \mathrm{z}_i^T P \mathrm{z}_i$ such that:

$$F_{ij}^T P + P F_{ij} = -Q_{ij},\ \forall j \in \{1,2\} \tag{49}$$

with Q positive definite.

Proposition 2: [Robust Stability Under Perturbations] LetF_{i1} and F_{i2}^o admit a common Lyapunov function $V(\mathrm{z}_i) = \mathrm{z}_i^T P \mathrm{z}_i$ satisfying:

$$\dot{V}_{ij} = -\mathrm{z}_i^T Q_{ij} \mathrm{z}_i,\ Q_i > 0 \tag{50}$$

Suppose the perturbation ΔF_{i2} satisfies a linear growth bound:

$$\| \Delta F_{i2} \| \leq \gamma,\ \gamma \in \mathbb{R}^+ \tag{51}$$

Then, the perturbed system is asymptotically stable if:

$$\gamma < \frac{\lambda_{\min}(Q_{i2})}{2\lambda_{\max}(P)} \tag{52}$$

Proof. The Lyapunov derivative along trajectories of F_{i2} is:

$$\begin{aligned} \dot{V}_{i2} &= \mathrm{z}_i^T (F_{i2}^T P + P F_{i2}) \mathrm{z}_i \\ &= \mathrm{z}_i^T (F_{i2}^{oT} P + P F_{i2}^o) \mathrm{z}_i + \mathrm{z}_i^T (P \Delta F_{i2} + \Delta F_{i2}^T P) \mathrm{z}_i \end{aligned} \tag{53}$$

By construction:

$$F_{i2}^{oT}P + PF_{i2}^{o} = -Q_{i2} \tag{54}$$

Thus:

$$\dot{V}_{i2} = -\mathrm{z}_i^T Q_{i2}\mathrm{z}_i + 2 \parallel \mathrm{P} \parallel\parallel \Delta F_{i2} \parallel\parallel \mathrm{z}_i \parallel^2 \tag{55}$$

Negativity of $\dot{V}_{i2}$ is guaranteed if:

$$2 \parallel \mathbf{P} \parallel\parallel \Delta F_{i2} \parallel < \lambda_{\min}(Q_{i2}) \tag{56}$$

or equivalently:

$$\parallel \Delta F_{i2} \parallel < \frac{\lambda_{\min}(Q_{i2})}{2\lambda_{\max}(P)} \tag{57}$$

Fact 3: [Minimum Dwell Time Constraint] When ΔF_{i2} violates the above bound, stability may still be ensured by imposing a minimum dwell time between switching events.

4.7. Stability Analysis for Over-damped to Under- damped Switching with Minimum Dwell Time Constraint

This section extends the stability analysis to the case where the switching occurs from an over-damped system to an under-damped system, a configuration that does not generally admit a common Lyapunov function due to non-commuting system matrices. A perturbation-based approach combined with a minimum dwell time analysis is proposed to ensure robust stability.

Conjecture 4: [Non-Commutativity in Overdamped to Under-damped Switching] Let F_{i1} and F_{i2} denote the system matrices of an over-damped and underdamped subsystem, respectively:

$$\mathrm{F}_{i1} = \begin{bmatrix} -\zeta_{1i} & 0 \\ 0 & -\zeta_{2i} \end{bmatrix}, \quad \mathrm{F}_{i2} = \begin{bmatrix} -\zeta_i\omega_{ni} & \omega_{di} \\ -\omega_{di} & -\zeta_i\omega_{ni} \end{bmatrix} \tag{58}$$

Then, in general, $[\mathrm{F}_{i1}, \mathrm{F}_{i2}] \neq 0$, and hence no common Lyapunov function exists for the pair $\{\mathrm{F}_{i1}, \mathrm{F}_{i2}\}$.

Proposition 3: [Robust Stability under Perturbations with Minimum Dwell Time] Assume F_{i2} can be decomposed as:

$$\mathrm{F}_{i2} = \mathrm{F}_{i2}^{o} + \Delta\mathrm{F}_{i2} \tag{59}$$

where F_{i2}^{o} commutes with F_{i1} , i.e., $[\mathrm{F}_{i1}, \mathrm{F}_{i2}^{o}] = 0$, and $\Delta\mathrm{F}_{i2}$ represents the non-commuting perturbation. Let $V(\mathrm{z}_i) = \mathrm{z}_i^T P \mathrm{z}_i$ be a common Lyapunov function for F_{i1} and F_{i2}^{o}. If

$$\parallel \Delta\mathrm{F}_{i2} \parallel > \frac{\lambda_{min}(Q_{i2})}{2\lambda_{max}(P)} \tag{60}$$

there exists a minimum dwell time τ_{min} such that the switched system remains asymptotically stable if the time spent in F_{i2} satisfies $\tau_d > \tau_{min}$.

Proof. The Lyapunov derivative along F_{i2} is:

$$\begin{aligned} \dot{V}_{i2} &= \mathrm{z}_i^T(\mathrm{F}_{i2}^T P + P\mathrm{F}_{i2})\mathrm{z}_i \\ &= -\mathrm{z}_i^T Q_{i2}\mathrm{z}_i + \mathrm{z}_i^T(P\Delta\mathrm{F}_{i2} + \Delta\mathrm{F}_{i2}^T P)\mathrm{z}_i \end{aligned} \tag{61}$$

The perturbation term is bounded by:

$$\mathrm{z}_i^T(P\Delta\mathrm{F}_{i2} + \Delta\mathrm{F}_{i2}^T P)\mathrm{z}_i \leq 2 \parallel P \parallel\parallel \Delta\mathrm{F}_{i2} \parallel\parallel \mathrm{z}_i \parallel^2 \tag{62}$$

Hence:

$$\dot{V}_{i2} \leq -\lambda_{min}(Q_{i2}) \parallel \mathrm{z}_i \parallel^2 + 2 \parallel P \parallel \parallel \Delta \mathrm{F}_{i2} \parallel \parallel \mathrm{z}_i \parallel^2 \quad (63)$$

Define:

$$\lambda_{eff} = \lambda_{min}(Q_{i2}) - 2 \parallel P \parallel \parallel \Delta \mathrm{F}_{i2} \parallel \quad (64)$$

If $\lambda_{eff} < 0, V(\mathrm{z}_i)$ may grow temporarily. Integrating over dwell time τ_d yields:

$$V(t + \tau_d) \leq V(t)\exp(\lambda_{eff}\tau_d) + c \parallel \mathrm{z}_i \parallel^2 \quad (65)$$

where

$$c = \frac{2\|P\|\|\Delta \mathrm{F}_{i2}\|}{|\lambda_{eff}|} \quad (66)$$

Requiring $V(t + \tau_d) < V(t)$ gives:

$$\tau_{min} = \frac{1}{|\lambda_{eff}|} \ln\left(1 + \frac{c\|\mathrm{z}_i\|^2}{V(t)}\right) \quad (67)$$

In worst-case ($\parallel \mathrm{z}_i \parallel = 1, V(t) = 1$):

$$\tau_{min} = \frac{1}{|\lambda_{eff}|} \ln\left(1 + \frac{2\lambda_{max}(P)\|\Delta \mathrm{F}_{i2}\|}{|\lambda_{eff}|}\right) \quad (68)$$

Fact 5: [Minimum Dwell Time Constraint] The system retains asymptotic stability under arbitrary switching if $\parallel \Delta \mathrm{F}_{i2} \parallel$ satisfies the perturbation bound. Otherwise, a minimum dwell time τ_{min} must be imposedduring the under-damped phase to suppress perturbation induced energy growth.

Remark 2: [On Perturbation and Mode-Shape Preservation] Mode-shape preservation ensures modal decoupling and analytical tractability. However, large perturbations disrupt this property, necessitating careful controller design and gain scheduling to maintain robust performance.

5. SIMULATION RESULTS

This section presents two comprehensive case studies performed on a five-degree-of-freedom (5-DoF) mass-spring-damper system to validate the theoretical developments of the proposed binary switching linear model control framework. The system schematic, simulation parameters, and physical properties are provided in Tables 1–3. A disturbance signal applied to mass five is illustrated in Fig. 3, and the Bode diagram of the system for varying damping configurations is shown in Fig. 4.

5.1. Reduced-Order Modeling and Mode Selection

As established in Section 4, the Bode diagram of a Linear Time-Invariant (LTI) system can be effectively
approximated using a finite set of dominant motion modes identified via modal decomposition. Simulation results confirmed that increased system damping necessitated a greater number of retained modes to achieve acceptable accuracy. For control design purposes, two active modes were selected based on their normalized Lyapunov cost functions, striking a balance between model fidelity and computational tractability.

5.2. Case Study I: Controlled System Response

In the first scenario, the binary switching linear model control was activated to modify the dynamics of the selected modes. The poles and corresponding natural frequencies and damping ratios of the original and controlled systems are reported in Tables 4 and 5. Notably, the controlled system poles are shifted significantly into the left half of the complex plane, reflecting increased damping and improved transient behavior. Fig. 5 depicts the Lyapunov mode energy for each active mode, highlighting their relative contribution to system dynamics. The resulting switching policies for mode controllers I and II, are shown in Figs. 6 and 7. These policies autonomously prioritize the control of modes with higher energy content.

Time histories of the control signal, position, and velocity responses are provided in Figs. 8–10. The binary switching control strategy successfully suppresses oscillations and accelerates convergence compared to the uncontrolled system. Position and velocity tracking errors (Figs. 11 and 12) further corroborate the improved performance. Additionally, Fig. 13 illustrates the evolution of the quadratic cost function $J(t)$, which asymptotically decreases toward zero, validating the stability of the closed-loop system under the proposed control law.

5.3. Case Study II: Uncontrolled Free Response

The second scenario examines the system's free response by removing the control input. Figs. 14–18 present the Lyapunov mode energy, position and velocity responses, and their respective tracking errors. The uncontrolled system exhibits persistent oscillations and poor damping characteristics, underscoring the efficacy of the binary switching linear model control demonstrated in Case Study I.

5.4. Theoretical Validation

The simulation results support the theoretical claims regarding the stability of binary switching linear model control framework. Specifically, the ability to stabilize the system for arbitrarily small mode-dependent dwell times and the robustness of the switching policy for all admissible switching signals are validated. Although a dwell time of 0.1 sec was selected for visualization purposes, the theoretical derivations guarantee stability even in the limit of infinitesimal dwell times.

Table 1. Simulation parameters for the five-degreeof- freedom (5-DoF) structural system under binary switching linear model control. The table includes the total number of system modes, actively controlled modes, time step for numerical integration, applied disturbance amplitude, and minimum mode dwell time ensuring Lyapunov stability

Parameters	Value
# modes	5
# controlled modes	2
Time step (sec)	1×10^{-2}
Disturbance Amp. (N)	10
Mode Dwell Time (sec)	0.1

Table 2. Physical parameters of the five-degree-offreedom (5-DoF) mass-spring-damper system. Each entry specifies mass (m_i), stiffness (k_i), and damping coefficient (c_i) for the respective degree of freedom. These parameters define the state-space matrices *A, B* and serve as the basis for the modal decomposition.

Mass (kg)		**Stiffness (N/m)**		**Damping (Ns/m)**	
		k_{50}	100	c_{50}	2
m_{51}	1	k_{51}	200	c_{51}	1
m_{52}	1	k_{52}	100	c_{52}	2
m_{53}	2	k_{53}	220	c_{53}	2
m_{54}	2	k_{54}	400	c_{54}	1
m_{55}	1	k_{55}	600	c_{55}	1

5.5. Discussion

Overall, these case studies demonstrate that the proposed framework enables reduced-order modeling of LTI systems while preserving the essential dynamics required for effective control. By leveraging Lyapunov cost functions for mode selection and implementing statefeedback control in the eigenvector subspace, the binary switching linear model controller achieves simultaneous pole reassignment and mode-shape preservation. This approach provides a transparent, computationally efficient, and theoretically rigorous methodology for active vibration control of structural systems.

Table 3. Model predictive controller (MPC) parameters implemented in canonical modal coordinates. The weighting matrices $\boldsymbol{Q}_y$, $\boldsymbol{Q}_u$, and the terminal cost $\boldsymbol{Q}_f$ are defined for the quadratic cost function. The MPC horizon specifies the prediction length used for computing optimal control actions.

Parameters	**Value**
$\mathbf{Q}_y$	$I_{5x5} \times 10^{2}$
$\mathbf{Q}_u$	$I_{5x5} \times 10^{-2}$
$\mathbf{Q}_f$	$I_{5x5} \times 10^{3}$
MPC Horizon	25

Table 4. Comparison of poles of the original system and the binary switching linear model controlled system. The proposed control shifts poles further into the left half-plane, enhancing system stability and damping performance according to the design.

Poles of Original System	**Poles of Switched System**
-0.0125 + 30.5284i	-10.0125 + 30.5284i
-0.0125 - 30.5284i	-10.0125 - 30.5284i
-0.0213 + 22.5368i	-10.0213 + 22.5368i
-0.0213 - 22.5368i	-10.0213 - 22.5368i
-0.0121 + 16.4687i	-10.0121 + 16.4687i
-0.0121 - 16.4687i	-10.0121 - 16.4687i
-0.0098 + 10.9150i	-10.0098 + 10.9150i
-0.0098 - 10.9150i	-10.0098 - 10.9150i
-0.0017 + 6.3048i	-10.0017 + 6.3048i
-0.0017 - 6.3048i	-10.0017 - 6.3048i

Table 5: Natural frequencies (ω_n) and damping ratios (ζ) of the original system and the switched system. The controller increases both ω_n and ζ for the dominant modes, leading to faster convergence and enhanced robustness against disturbances.

Original System		**Switched System**	
ω_n	ζ	ω_n	ζ
30.5284	0.0004	32.1284	0.3116
30.5284	0.0004	32.1284	0.3116
22.5368	0.0009	24.6644	0.4063
22.5368	0.0009	24.6644	0.4063
16.4687	0.0007	19.2733	0.5195
16.4687	0.0007	19.2733	0.5195
10.9150	0.0009	14.8099	0.6759
10.9150	0.0009	14.8099	0.6759
6.3048	0.0003	11.8231	0.8460
6.3048	0.0003	11.8231	0.8460

6. CONCLUSIONS

This study introduced a novel control framework termed binary switching linear model control (BSLMC) for Linear Time-Invariant (LTI) structural systems. The central premise of the approach lies in the observation that the Bode diagram of an LTI system can be approximated with high fidelity by a reduced-order model that retains only a subset of motion modes within specific frequency bands. By applying a modal coordinate transformation, the global system dynamics are decoupled into a set of first- and second-order subsystems, enabling the construction of local reduced-order models tailored to dominant dynamics in each frequency band.

The proposed BSLMC strategy extends this concept by allowing each mode of motion to switch between two distinct linear models. This design facilitates targeted adjustments of natural frequencies and damping ratios while preserving mode shapes, effectively enabling reduced-order control synthesis without compromising system observability or controllability. Importantly, these modal subsystems behave as non-interacting entities in the transformed space, ensuring that controlling a selected subset of active modes is sufficient to influence the overall system response.

A rigorous stability analysis was performed using the common Lyapunov function framework. It was demonstrated that when the binary switching models are represented by commuting matrices, a common Lyapunov function exists, guaranteeing global asymptotic stability for arbitrary switching policies and dwell times. For noncommuting cases, a perturbation-based decomposition strategy was proposed, and sufficient conditions were derived to ensure robust stability. These theoretical results were validated through extensive simulations on a five-degree-of-freedom mass-spring-damper system, which confirmed the ability of BSLMC to achieve fast convergence, disturbance rejection, and reduced control effort.

The findings underscore the potential of BSLMC as a robust and computationally efficient solution for active vibration control and structural system regulation. By focusing control resources on dominant dynamics, the approach reduces complexity while retaining essential performance characteristics.

Future work may explore the extension of this framework to nonlinear systems, integration with adaptive or learning-based controllers for real-time mode selection, and experimental validation on large-scale structural platforms.

Declaration of Ethical Standards

The authors declare that all ethical guidelines including authorship, citation, data reporting, and publishing original research are followed.

Credit Authorship Contribution Statement

Can Ulas DOGRUER: Conceptualization, Formal analysis, Investigation, Methodology, Resources, Software, Writing – original draft, **Can Barış TOPRAK**: Formal analysis, Editing, Investigation, Validation, **Bora YILDIRIM**: Supervision, Validation, Review & editing

Data Availability

The data that support the findings of this study are available from the corresponding author upon reasonable request.

Conflict of Interest

The author declares that there is no competing financial interest or personal relationship that could have appeared to influence the work reported in this paper.

Use of Artificial Intelligence

The authors confirm that no generative AI or AI-assisted technologies were used in the writing of this manuscript or in the production of the data / images presented. Furthermore, no artificial intelligence tools were used in this article.

Funding / Acknowledgments

This work was supported by Research Fund of Hacettepe University. Project Title: "Designing a Variable Set of Optimal Modal Controllers to Singularly Control the Structural System Eigenvectors". Project Number: FHD-2020-18919

7. REFERENCES

[1] P. Benner, S. Gugercin, and K. Willcox, "Model reduction for control: New trends". *Annual Review of Control, Robotics, and Autonomous Systems*, 4:1–26, 2021.

[2] G. Chen, Z. Zhang, and H. Liu. "Multi-mode vibration suppression of flexible structures via novel modal-based control", *Journal of Sound and Vibration*, 523:116729, 2022.

[3] H. Cheng, Q. Wang, and X. Liu. "Multiple lyapunov functions method for switched systems: A review", *Nonlinear Analysis: Hybrid Systems*, 41:101061, 2021.

[4] Xiuyong Ding and Xiu Liu. "On stabilizability of switched positive linear systems under state-dependent switching", *Applied Mathematics and Computation*, 307:92–101, Aug 15 2017.

[5] Jianjun Gao and Duan Li. "Linear-quadratic switching control with switching Cost", *Automatica*, 48(6):1138–1143, Jun 2012.

[6] Wodek Gawronski. "*Dynamics and Control of Structures*", Springer, 2004.

[7] Y. Guo, Y. Zhao, and Y. Liu. "Event-triggered sliding mode control for switched systems under average dwell time switching", *ISA Transactions*, 133:97–108, 2023.

[8] T. Kang, J. Park, and J. Kim. "Adaptive modal decomposition and control for active vibration suppression", *Mechanical Systems and Signal Processing*, 147:107089, 2021.

[9] Daniel Liberzon. "*Switching in systems and control*", volume 190.Springer, 2003.

[10] Hai Lin and Panos J. Antsaklis. "Stability and stabilizability of switched linear systems: A survey of recent results", *IEEE Transactions on Automatic Control*, 54(2):308–322, 2009.

[11] Shu Lin and Bart De Schutter." Controller design for stabilizing bilinear systems with state-based switching", *Nonlinear Analysis-Hybrid Systems*, 41, Aug 2021.

[12] J. Liu, Y. Zhao, and W. Zhang. "Finite-time stability analysis of switched systems with time delays", *Applied Mathematics and Computation*, 440:127630, 2023.

[13] F. Long, S. Fei, and S. Zheng. "State Feedback Singular H∞ Control for Switched Linear Systems", *Control and Intelligent Systems*, 36(1), 2008.

[14] Leonard Meirovitch. "*Analytical Methods in Vibrations*", Macmillan, 1967.

[15] Vu Trieu Minh. "Stability for switched dynamic hybrid systems", *Mathematical and Computer Modelling*, 57(1-2):78–83, Jan 2013.

[16] Vu Trieu Minh, Mokhtar Awang, and Setyamartana Parman. "Conditions for Stabilizability of Linear Switched Systems*", International Journal of Control Automation and Systems*, 9(1):139–144, Feb 2011.

[17] V. F. Montagner, V. J. S. Leite, R. C. L. F. Oliveira, and P. L. D. Peres. "State feedback control of switched linear systems: An LMI approach", *Journal of Computational and Applied Mathematics*, 194(2):192–206, OCT 1 2006.

[18] André Preumont. "*Vibration Control of Active Structures",* Springer, 3rd edition, 2011.

[19] ZD Sun. "Combined stabilizing strategies for switched linear systems", *IEEE Transactions on Automatic Control*, 51(4):666–674, Apr 2006.

[20] ZD Sun and DH Zheng. "On reachability and stabilization of switched linear systems", *IEEE Transactions on Automatic Control*, 46(2):291–295, Feb 2001.

[21] Zhendong Sun. "Stabilizing switching design for switched linear systems: A state-feedback path-wise switching approach", *Automatica*, 45(7):1708–1714, Jul 2009.

[22] Zhendong Sun and Shuzhi Sam Ge. "*Stability Theory of Switched Dynamical Systems*", Springer, 2011.

[23] B. Tian, H. Sun, and S. Wang. "Nonlinear model reduction for structural systems via data-driven methods", *Computer Methods in Applied Mechanics and Engineering*, 388:114205, 2022.

[24] L Zhang, Y Zhu, P Shi, and Q Lu. "Time-Dependent Switched Discrete-Time Linear Systems: Control and Filtering, *volume 53 of Studies in Systems Decision and Control*, pages 1–258. 2016.

[25] LJ Zhang, DZ Cheng, and JB Liu." Stabilization of switched linear systems", *Asian Journal of Control*, 5(4):476–483, Dec 2003.

[26] B. Zhou, H. Zhang, and G.H. Yang. "Switching control strategies for uncertain nonlinear systems: A survey", *Automatica*, 137:110124, 2022.

Konya Mühendislik Bilimleri Dergisi., c.14, s.2, 682-699, 2026
Konya Journal of Engineering Sciences v.14, n.2, 682-699, 2026
ISSN: 2667-8055 (Electronic)
DOI: 10.36306/konjes.1603298

DEVELOPMENT OF ARTIFICIAL INTELLIGENCE SUPPORTED PUFFERFISH TRAP

[1] Mert Demir

[1]*OSTİM Technical University, Department of Computer Programming*
[1]mert.demir@ostimteknik.edu.tr

Highlights

- Fighting invasive species
- Artificial intelligence supported trap
- Puffer fish trap

Graphical Abstract (Optional)

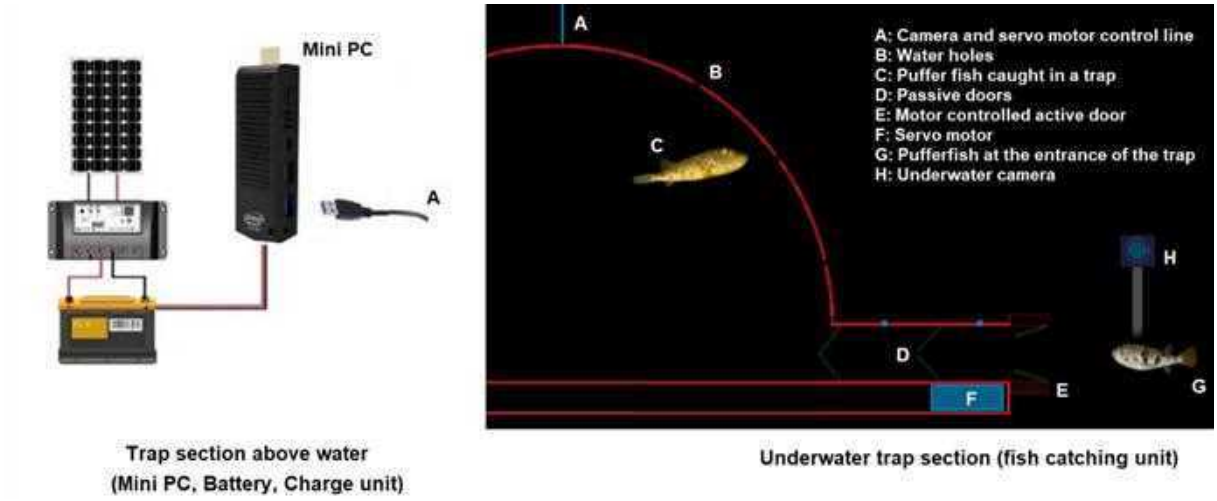


Figure Pufferfish trap system design

***Corresponding Author:** Mert DEMİR, mert.demir@ostimteknik.edu.tr

Konya Mühendislik Bilimleri Dergisi., c.14, s.2, 682-699, 2026
Konya Journal of Engineering Sciences v.14, n.2, 682-699, 2026
ISSN: 2667-8055 (Electronic)
DOI: 10.36306/konjes.1603298

DEVELOPMENT OF ARTIFICIAL INTELLIGENCE SUPPORTED PUFFERFISH TRAP

[1, *]Mert Demir

[1]OSTİM Technical University, Department of Computer Programming
[1]mert.demir@ostimteknik.edu.tr

(Received: 17.12.2024; Accepted in Revised Form: 18.11.2025)

ABSTRACT: Due to changing climatic conditions, living things leave their habitats and migrate to other geographies. One of these creatures, the pufferfish, has created new habitats by migrating from warm seas to the Mediterranean and Aegean seas in recent years. The pufferfish is a dominant and invasive species, and its population is rapidly increasing wherever it is found because there is no other creature hunting it. Since it is a poisonous species, there is no possibility of biological control and hunting of this creature in fishing activities and controlling its population are encouraged, but this method is not effective. The scope of the study describes the development of a pufferfish trap developed with artificial intelligence models that targets the invasive pufferfish. Different sized trap designs have been suggested for different sized pufferfish species. To detect the pufferfish, 3200 pufferfish images and 3000 images of Mediterranean fish species were trained on the system with a supervised machine learning model to distinguish this species from other species. Addition, the calculation of trap size according to the species of this creature, which has different sizes, was handled with another artificial intelligence model. The developed model detects pufferfish from distances of 35 cm-250 cm underwater and reacts to catch the fish. In this study, studies were carried out on finding the appropriate trap modeling for catching the target pufferfish, developing a suitable model for catching the target fish species, and verifying the target species recognition by using different artificial intelligence methods.

Keywords: *Artificial intelligence, Fish trap, Invasive species, Machine learning, Pufferfish*

1. INTRODUCTION

Due to the warming of world waters as a result of global climate change, some species living in mid-latitudes are migrating towards northern latitudes [1]. With the arrival of new species, the ecosystem chain changes, causing local species to disappear [2, 3]. The invasive creature may become the dominant species in the region it migrates to after a certain period of time. Alien species are species that leave their natural habitat and survive in a new region and reproduce and multiply rapidly [4-7]. Today, the Mediterranean is one of the seas most invaded by invasive species [8-10]. Invasive species are transported to new habitats in different ways, such as warming of the oceans with global climate change, changes in ocean currents, food search strategies and creatures transported to different geographies by international vehicles. These species endanger the life of local species in the ecosystem they visit and may cause their extinction [11, 12]. Invasive species endanger the populations of native species by preying on fish and aquaculture that have economic value. They also cause significant damage to fishing activities by destroying fisheries resources. Therefore, threats and invasions of exotic species in different seas are a growing concern worldwide [13].

Pufferfish, considered one of the fish species posing a significant threat in the Mediterranean and surrounding seas, has been reported as one of the most highly invasive species [17, 18]. This creature, whose scientific name is *Lagocephalus sceleratus* belongs to the Tetraodontidae family. There are more than 120 species of pufferfish, most of which are found in tropical and subtropical marine waters. Pufferfish, that have come to the Mediterranean via the Suez Canal and caused significant damage to the Mediterranean habitat and fishing industry, have attracted attention in recent years [19]. Today, it is

***Corresponding Author:** Mert DEMİR, mert.demir@ostimteknik.edu.tr

considered one of the worst invasive species in the Mediterranean, with a significant impact on the surrounding ecosystem and fishing industry [20-23]. The population of this fish, which is generally seen in Africa, Europe, Asia, Australia and the surrounding seas, has increased in recent years in the seas and coasts of many northern latitudes as shown in Figure 1.

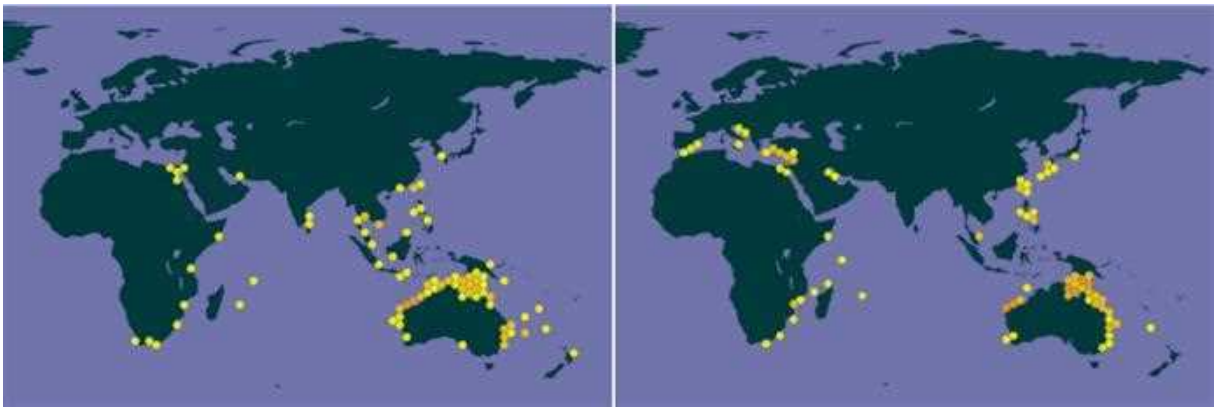


Figure 1. Increase in pufferfish population over the years (Left: 1818-1991, Right: Today) (Source: GBIF.org)

The pufferfish, which is the most invasive species of the Mediterranean and surrounding seas, has spread to the Aegean Sea and the Marmara Sea due to its features such as rapid adaptation, high reproduction and growth ability, lack of predatory pressure due to its toxicity, and overfishing [24-26]. In this type of fishing, it feeds on creatures caught in nets and fishing lines while simultaneously damaging fishing gear. When the stomach contents are examined, pieces of net and fishing line are seen along with various bitten foreign parts. Pufferfish are generally found in coastal marine areas (Figure 2).



Figure 2. Pufferfish caught in nets (left), fisherman repairing fishing nets (right) (Source: sabah.com.tr)

It has been reported that tetrodotoxin (TTX) and saxitoxins (STX) are found in the internal organs and meat of the pufferfish [27-29]. Due to this poison, it is very difficult to obtain economic profit from the fish and no predatory species in the environment can hunt the pufferfish. Thanks to this advantage, the pufferfish can reproduce rapidly in its new habitat. The toxic chemical TTX is a more effective poison than cyanide. Symptoms of poisoning appear 5-30 minutes after eating this fish, which contains TTX and STX, and these symptoms begin with tingling and prickling in the face and continue with headache, drowsiness, ataxia, nausea, vomiting, and then shortness of breath, which can lead to death [30, 31]. Because of these properties, it is absolutely dangerous for humans to consume it as food. It is

recommended to use gloves even when destroying this fish, as it is highly poisonous and dangerous. After moving to the Mediterranean, pufferfish became dominant and predatory in their new habitats due to the absence of predatory species that threatened their lives and limited fighting methods [32]. With these features mentioned, it is not possible to achieve success with the biological control method against pufferfish.

In this study, a technological trap system using artificial intelligence is proposed as an alternative to biological control in the fight against invasive pufferfish species that cause serious damage to nature and fisheries. Today, the most common method to combat pufferfish is to encourage fishermen to eliminate this fish species when they encounter it while fishing. Since these fish are not found in bulk and there is no specific disposal method (biological control, poisoning, etc.) for this fish species, fish control methods are limited. Machine learning, which has a strong success in classifying data, plays a role in detecting and catching pufferfish in the system proposed here. K-means model was used for the optimum design of trap mouths for catching pufferfish. By taking advantage of artificial intelligence, it is aimed to deploy fish traps in areas with high pufferfish populations for more effective control of this species.

2. MATERIAL AND METHODS

2.1. Materials

In order for the fish trap to specialize in catching only a certain species, the system must have a computer vision and object recognition application. For this reason, it was thought that a small-sized system computer was required for this trap in order to use the object recognition application. It was preferred to use a low-budget and small-sized mini computer in the trap, which can process the images coming from the camera and give commands to the engines that will enable the target creature to be captured by giving the necessary command. The computer used is the Mini PC Pro T6 model, featuring low energy consumption and a powerful processor suitable for machine learning tasks. The mini computer has a small size and low energy consumption (approximately 3W with camera use), quad-core 1.68 GHz speed, 4 GB RAM memory, Win10 operating system and the ability to run real-time object recognition applications. Supervised machine learning, a subfield of artificial intelligence used for data classification and predicting outcomes based on input data, is applied in this study for detecting pufferfish [33, 34]. Using a supervised machine learning model, images of other fish species were used to distinguish the pufferfish from other creatures. In this context, 1,500 images of pufferfish and 3,000 images of other fish species, captured from different angles, were used (Figure 3 and Figure 4). In order to increase trap success, care was taken to select the data set of fish species other than pufferfish from species living in the Mediterranean environment.



Figure 3. View from some of the data sets (Pufferfish dataset) (Source: kaggle.com)



Figure 4. View from some of the data sets (Mediterranean fishes dataset) (Source: kaggle.com)

2.2. Methods

Pufferfish live in tropical regions, mostly on coral-rich reefs and lagoons with food grounds. It feeds mainly on algae, molluscs, sponges, corals, starfish and sea urchins. Due to these factors, it would be beneficial to set the trap in shallow waters on the seabed, close to the beach and close to the feeding area of the target fish. The design of the trap includes a central collection unit where the caught pufferfish are collected and trap doors placed at different angles around the trap. Trap doors are funnel-shaped and have an angle that allows the target fish to swim towards the trap while preventing it from swimming backwards from the trap. Funnel-shaped passive fish traps are a mechanism used by amateur fishermen today (Figure 5).

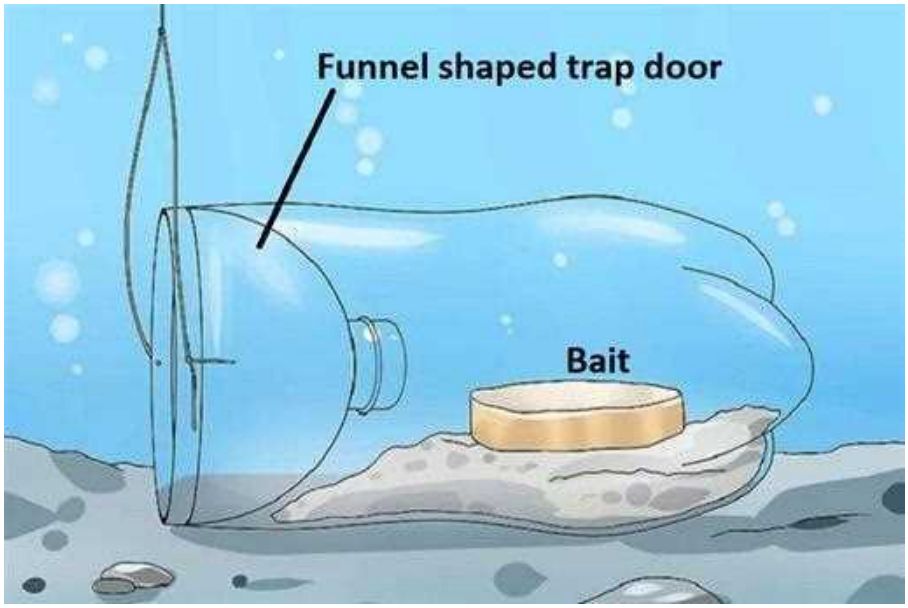


Figure 5. Fish trap technique used in amateur fishing

It is seen in the literature that there is no definitive method to combat pufferfish [35-37]. After moving to the Mediterranean, pufferfish became dominant and predatory in their new habitats due to the absence of predatory species that threatened their lives and limited fighting methods. With these features mentioned, it is not possible to achieve success with the biological control method against pufferfish. Trap entrances are adjusted according to fish size to allow the target fish to enter the trap. While the large size of the trap entrance allows the fish to escape back out, if the trap entrance is smaller than it should be, it causes the trap to fail. In addition, such passive traps can cause all kinds of aquatic creatures to be caught. Therefore, the type and size of the target fish is important in trap design. The family *Tetraodontidae* includes approximately 193 species of pufferfish in 25 genera. Although general anatomical features (position of the dorsal tail, head shape, etc.) are similar between species, their sizes differ. Approximate maximum length and height values reached by some pufferfish species are shown in Table 1. In order to determine the dimensions of the appropriate size puffer fish trap, it is necessary to make an inference according to the dimensions of the target fish species. Since there is no suitable measurement that will target all fish species, it is important to obtain trap dimensions of different sizes according to fish lengths. The k-means algorithm was used to classify pufferfish measurements.

Table 1. Characteristics and sizes of some pufferfish species

Pufferfish species	Length(cm)	Height(cm)
Amblyrhynchotes honckenii	30	9
Arothron meleagris	120	42
Auriglobus nefastus	13	7
Canthigaster rostrata	12	5
Carinotetraodon patoca	4.4	1.5
Chonerhinos naritus	38	12
Colomesus asellus	28	8
Contusus richei	13	4
Dichotomyctere fluviatilis	25	8
Ephippion guttifer	17	6
Feroxodon multistriatus	80	22
Guentheridia formosa	90	29
Leiodon cutcutia	26	7.5
Lagocephalus sceleratus	15	5
Marilyna pleurosticta	40	10
Omegophora armilla	14	4.5
Polyspina piosae	25	10
Pao suvattii	7	3
Reicheltia halsteadi	15	8
Sphoeroides dorsalis	16	6
Takifugu niphobles	20	12
Tetractenos glaber	15	7
Tetraodon lineatus	16	10
Torquigener albomaculosus	40	18
Tylerius spinosissimus	12	5

The k-means model, an artificial intelligence model, was used to find the ideal trap size for pufferfish of different sizes in different ecosystems. The aim here is to find the ideal trap size that will prevent the pufferfish in the relevant marine ecosystem from escaping the trap. A large trap door may cause the fish to turn around and escape, and a small trap door may prevent the pufferfish from entering the trap. K-means model is an effective artificial intelligence method used in clustering scattered and large-sized data into n predetermined numbers [38-40]. The aim is to find the nearest neighbor relationships by using the clustering process in order to develop trap doors for pufferfish depending on their size (1):

$$C_i = \underset{j}{\arg min} \, ||X_i - U_j||^2 \tag{1}$$

Here C_i, i. data point represents the cluster to which X_i is assigned, and U_j is the cluster to which j. is the center of the cluster. The center of each cluster is updated to be the average of the data points in that cluster(2):

$$U_j = \frac{1}{C_j} \sum_{X_i \in C_j} X_i \tag{2}$$

U_j, j. new center of the cluster, C_j is j. is the set of data points in the cluster.

In order to determine the appropriate door size in the pufferfish trap, the length and height information of the fish specified in Table 1 were subjected to clustering with the k-means model in 2-

dimensional space and the appropriate door sizes were obtained separately. This application plays an important role in trap design specific to the target fish. A small designed trap does not allow catching large fish, and a large designed trap may cause small fish to escape from the trap. With the application, a single cluster structure was established and the trap door size obtained is for all pufferfish of many different species and sizes in the habitat where the trap is installed. With this option, small-sized adult pufferfish and juvenile pufferfish that reach large sizes are the target of the trap (Figure 6). In this design, which targets all pufferfish species, the ideal trap door height is 10 cm and the length is 29 cm. In another application, different trap door sizes were obtained by clustering separately for small and large pufferfish in the habitat. With this application, specific pufferfish were targeted and appropriate trap door sizes were obtained for catching small and large fish (Figure 7). Accordingly, the ideal door height for small-sized fish aggregation was 8cm and its length was 20 cm. The height of the trap door targeting large-sized fish was 31 cm and its length was 96 cm.

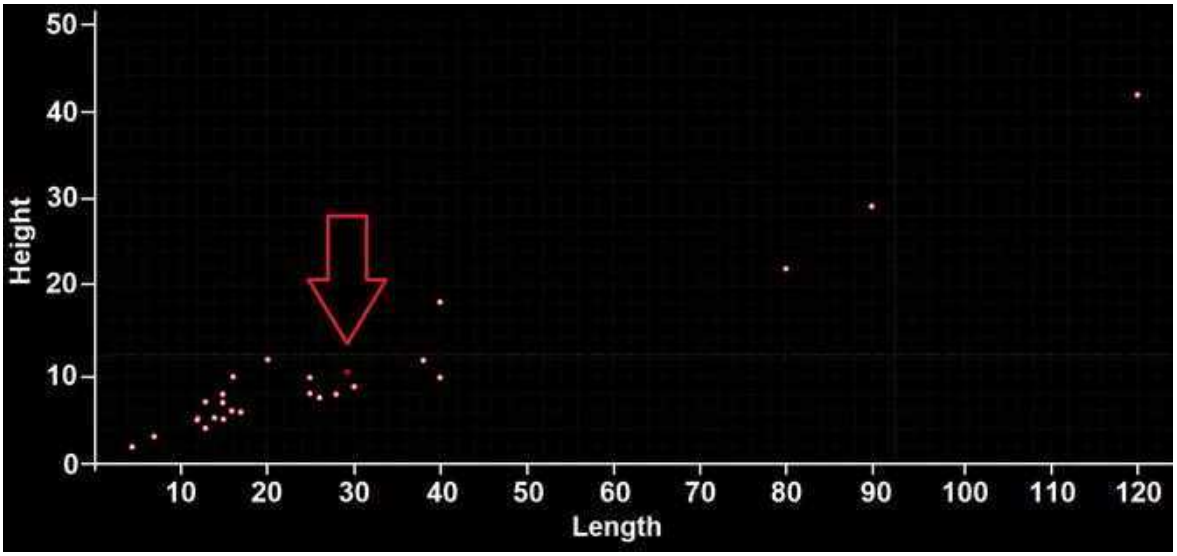


Figure 6. Trap door measurement obtained in all pufferfish populations (Height: 10 cm, Length: 29 cm)

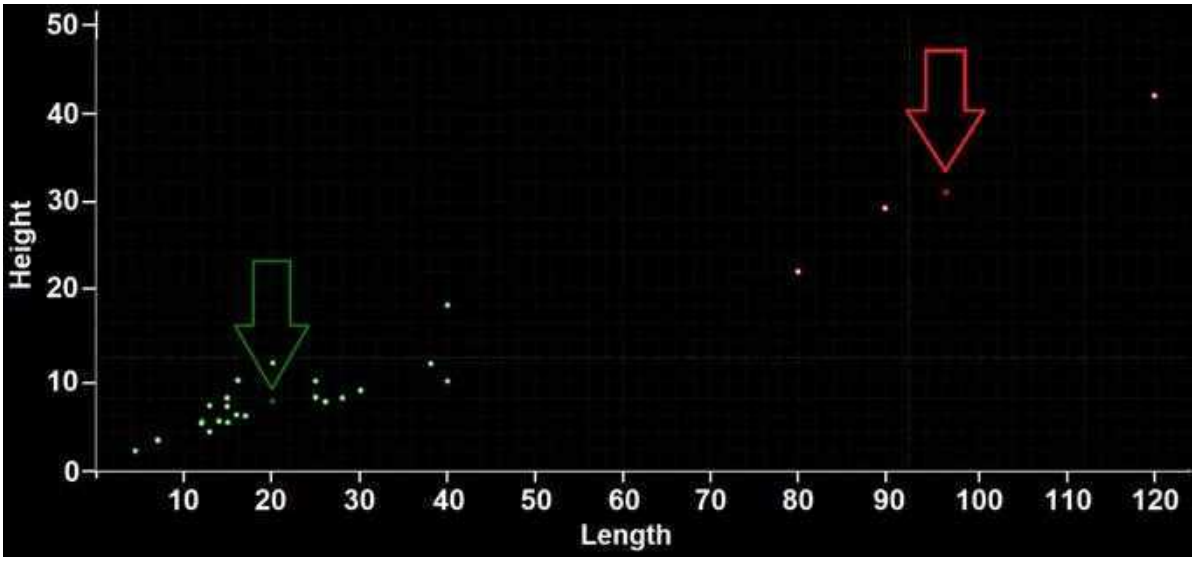


Figure 7. Analysis of trap door size with K-means and obtaining optimum door dimensions: (For small fish(green) and large fish(red) groups)

It is possible to target pufferfish, which live in more prominent sizes in a particular ecosystem, by increasing the number of clusters in order to detect and catch them. Accordingly, when the number of clusters was increased to three, the ideal trap door height for small pufferfish clusters was 6 cm and the length was 14 cm. In the application where the number of clusters was determined as four and very small, small, medium and large classes are created for fish clusters, the trap door size does not change for medium and large fish clusters, while in the application where very small fish clusters are targeted, the trap door height is 2 cm, the length is 6 cm, and the small fish cluster is targeted. The height of the trap door was 6 cm and the length was 15 cm (Figure 8 and Figure 9). These practices may be a reason for intervention in places where pufferfish breed intensively before the population increases. According to this information obtained using the K-means algorithm, although it is quite easy to determine the size of the trap door in an ecosystem with a single pufferfish species, it is more ideal to use trap doors of different sizes in ecosystems with different pufferfish species.

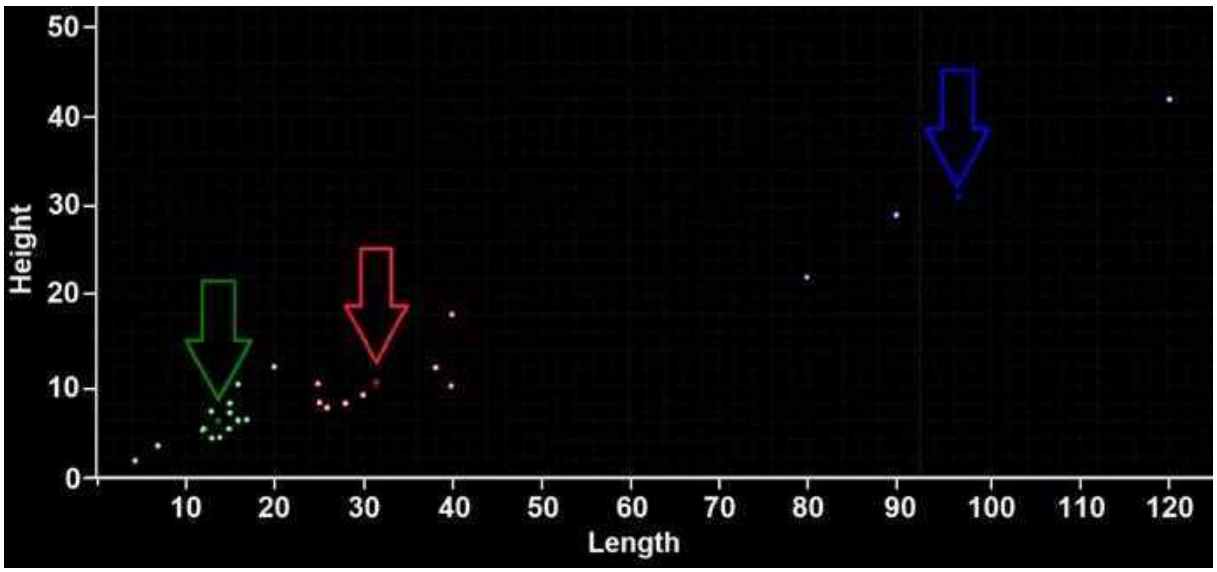


Figure 8. Trap door dimensions obtained for catching small (green), medium (red) and large (blue) pufferfish

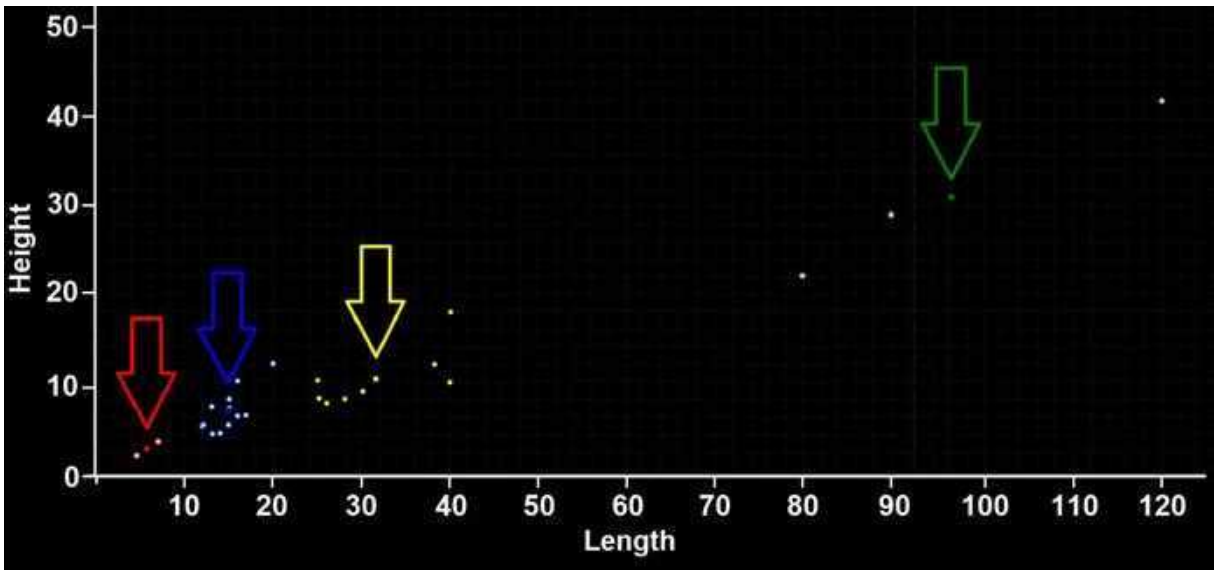


Figure 9. Trap door dimensions obtained for catching very small (red), small (blue), medium (yellow) and large (green) pufferfish.

In this study, for the first time, trap door measurements were obtained using the k-means model, based on pufferfish sizes. Because the size of the trap door is larger than necessary, it is possible that it may cause problems in the capture of pufferfish and cause small fish to escape from the trap. The trap door has a pipe design and there is one active door at the pipe entrance and two passive doors inside. The control of the active door is managed by a waterproof servo motor. Passive doors, on the other hand, are funnel-shaped structures that prevent the fish entering the pipe from swimming backwards and direct them into the trap. The underwater camera in front of the trap door, monitoring the door entrance, transfers images to the mini computer in real time. The machine learning-supported program running on the mini computer checks whether there is a pufferfish on the images. If a pufferfish is detected, the servo motor is driven to open the active door at the entrance of the trap. In this way, only pufferfish are encouraged to enter the trap, and in cases where there are no pufferfish, the trap door is kept closed and non-target species are prevented from being caught (Figure 10). If the pufferfish passes through the trap door, since there will be no pufferfish in the camera image, the active door is placed in the closed position again and in this case, the pufferfish is directed to the collection room inside the trap.

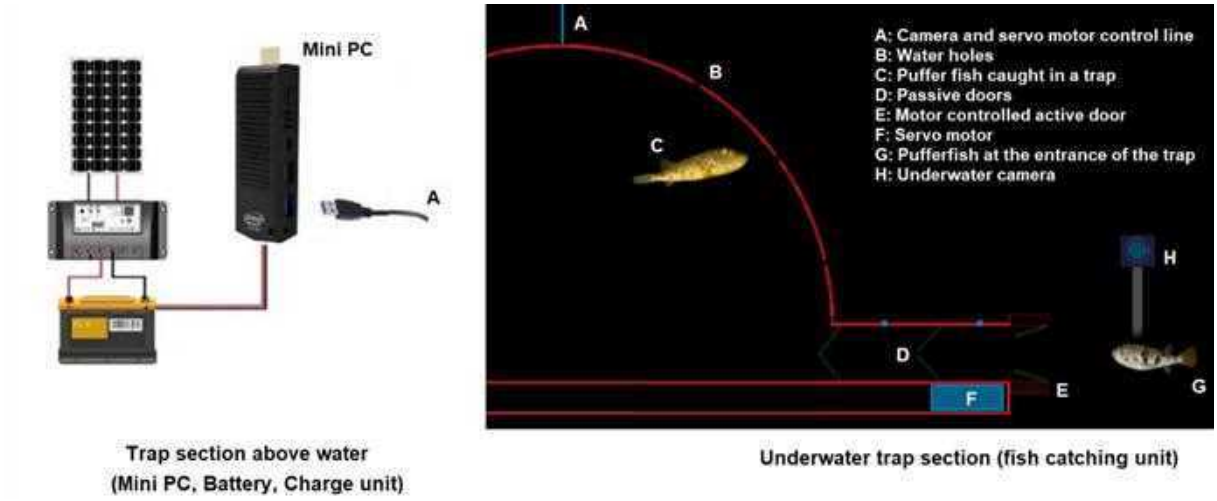


Figure 10. Pufferfish trap system design

3. RESULTS AND DISCUSSION

In order to increase the success of the puffer fish trap in targeting the target fish species, approximately 3200 fish images in the puffer fish dataset were analyzed with the Grad-CAM method. Grad-CAM application interpreted an important area of the image that constitutes the puffer fish with warm colors (red-yellow). This analysis helped to understand how the model detects the puffer fish's most distinctive features. The regions the model focuses on while recognizing the puffer fish provide critical clues about the puffer fish's genetic structure and body characteristics. Yellow-Red regions show the points that the model pays attention to when making predictions. These areas may contain the pufferfish's defining features, such as organs, colors, and body lines. In this way, the model can make more accurate predictions by focusing on the distinct characteristics of the puffer fish. Blue indicates the locations of the regions where the activation is the least, that is, the model does not care or gives low weight to the decision. Blue areas indicate that these regions of the image are unnecessary or of little importance to the model in the model's decision-making process. This allows the model to run more efficiently and faster, because there is no need to do much processing in non-important areas. In this way, 700 images were obtained to be added to the machine learning model. These 700 images were selected from the images containing the most striking features of the puffer fish in order to contribute to the learning process of the model. It is predicted that these images will increase the accuracy of the model and enable better recognition of the target fish species. Fish images that were not interpreted in this way were removed from the dataset, thus further increasing the target fish recognition success and making it more efficient. This process allowed unnecessary and misleading data to be removed from the model, thus ensuring that the model was trained only with meaningful and accurate data. As a result, these steps enabled the pufferfish trap to recognize the target fish species more accurately and efficiently (Figure 11).

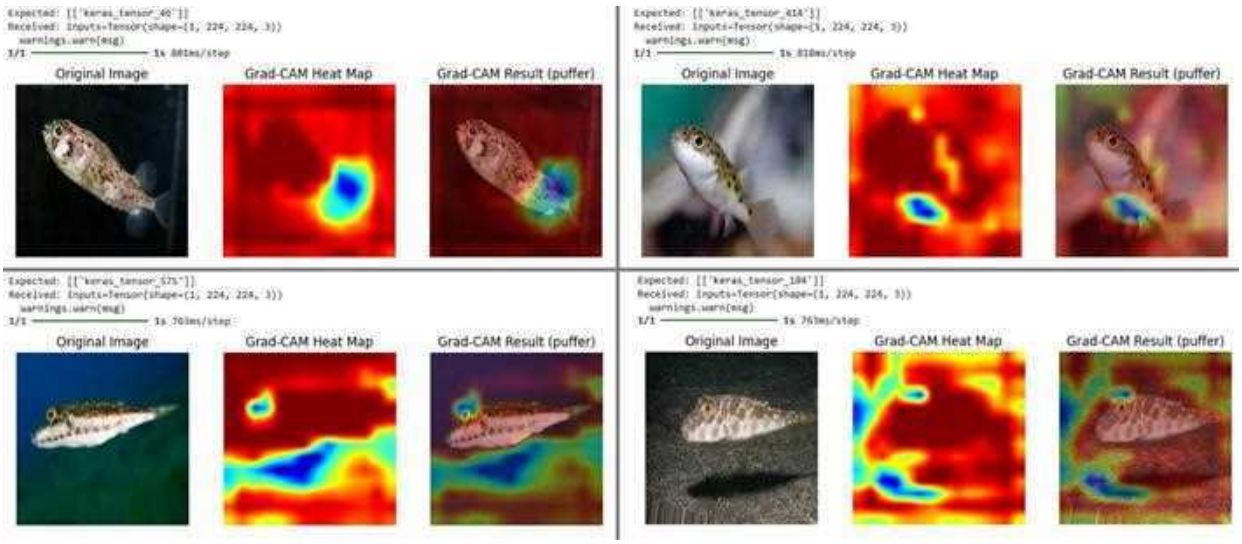


Figure 11. Grad-CAM application on pufferfish images

A supervised machine learning model was used to detect pufferfish in real time. Two separate fish data sets consisting of pufferfish and other fish species were prepared. For image classification tasks, a supervised machine learning model and a convolutional neural network (CNN) based model were prepared on a minicomputer and established with the parameters of at least 25 layer network structure, 50 epoch values, 32 batch size and 0.001 learning rate. The machine learning model developed with the 1500 pufferfish images used enabled the identification of fish species with 98% accuracy (Figure 11). Various precautions were taken to prevent overfitting. First, data augmentation techniques were applied during training. These techniques included horizontal flipping of images, random changes in brightness levels, and slight blurring of images. This enabled the model to generalize not only to the trained images but also to different visual variations. In addition, accuracy and loss values were observed at the end of each epoch using validation data during model training, and cases where the model needed to be stopped early were analyzed. The training process was stopped when validation performance began to remain stable, preventing signs of overfitting. In order to increase the success of the system, adding images of other creatures in the relevant marine ecosystem where the trap is placed to the system prevents erroneous catches. In addition, not adding fish that are not in the ecosystem where the trap is installed to the machine learning model prevents the performance of the model from decreasing. For this reason, in this study, a data set was created with 3000 fish images of fish in the Mediterranean ecosystem and the system was customized for pufferfish.



Figure 11. Identification of fish (Left: pufferfish, Right: others)

The application was initially developed with pufferfish models and it was seen that the system gave correct responses. The performance of the system in detecting pufferfish was measured by placing it at different underwater depths. The detection of fish by the underwater camera in the trap varies at different light levels. The reason for this is that the light level decreases as you go deeper from the water surface. Trials were carried out at noon, when daylight was at its highest. The resolution of the underwater camera used is 1280x1024 pixels. Pufferfish detection success was determined to be at least 70%. Since the pufferfish is an extremely dangerous species, experiments were carried out with an artificial model that resembles the pufferfish. Since pufferfish live and hunt in shallow waters and close to the beach, the trials were carried out at a depth of 1-1.5 m. With the trap placed at a depth of 1 m, the success of detecting pufferfish with high accuracy started from a distance of 30 cm to the camera and continued up to a distance of 3 m. The highest accuracy pufferfish detection ranges occurred at distances of 35 cm to 250 cm. Due to the decrease in camera image clarity, detection success decreased after a distance of 260 cm and ended at a distance of 320 cm. Accordingly, distances between 30 cm and 260 cm to the camera are expressed as the recognition-detection range (Figure 12). In the experiment where the fish trap was placed at a depth of 1.5 m, it was observed that the detection and detection properties decreased. This application performed at a more limited distance and at a depth where less sunlight reached. The pufferfish detection range started at 30 cm and lasted up to 130 cm. The distances where pufferfish were detected with high accuracy were between 35 cm and 110 cm (Figure 13).

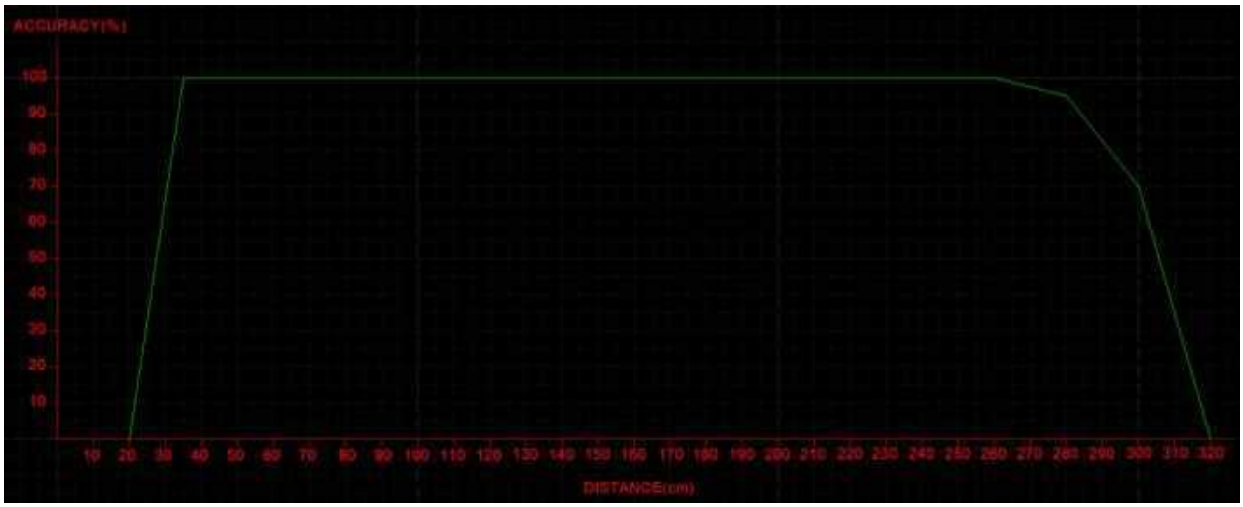


Figure 12. Detection chart according to the distance to the camera image (Depth: 1 m)

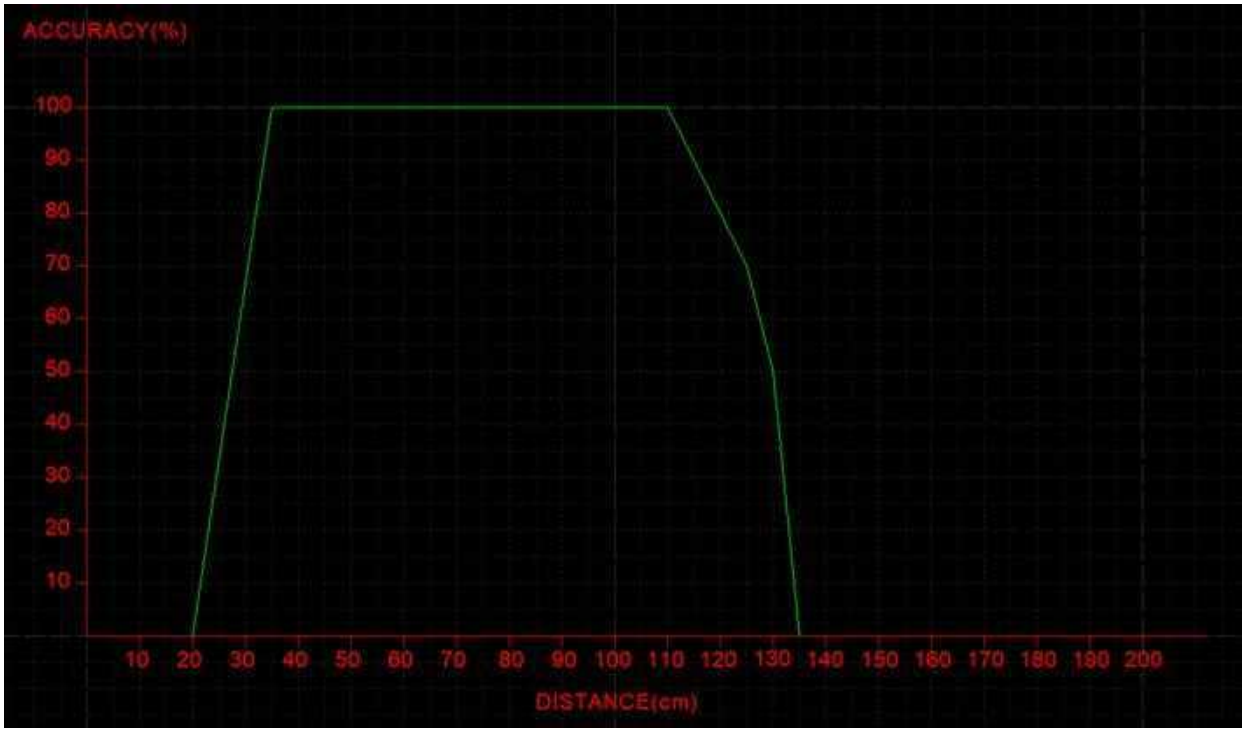


Figure 13. Detection chart according to the distance to the camera image (Depth: 1.5 m)

The prototype fish trap was produced in the shape of a hemisphere with a diameter of 120 cm using a 3D printer. According to these measurements, the volume of the trap is approximately 452 cm^3 . There are many water troughs on the front of the trap so that the caught fish can survive in the trap and the bait in the trap can be perceived by the fish. This size trap is capable of catching juvenile pufferfish and juvenile individuals up to approximately 14 cm in body length. In this way, it is aimed to catch the pufferfish before it reaches reproductive maturity. The puffer fish trap mentioned in the study was manufactured by a 3D printer to target baby puffer fish. The pufferfish produced is in the small category. If desired, it is possible to build traps of the appropriate size for different sizes and types of puffer fish. When the cost analysis is made, the costs of small, medium and large size traps are shown in Table-2. Weight and size information of medium and large traps were calculated based on the 3D filament to be consumed.

Table 2. Cost analysis of pufferfish trap types ($)

Components	Small trap	Medium trap	Large trap
Mini PC	120	120	120
Servo motor	10	30	30
Underwater cameras	5	15	15
Motor controller	4	12	12
Cable line	4	15	24
3D printer filament	100	225	402
Power unit(solar panel, battery)	50	50	50
TOTAL	**293$**	**467$**	**653$**
Properties			
Diameter	120 cm	180 cm	240 cm
Number of gate	1	3	3
Weight	13 kg	28 kg	50 kg

In the experiments conducted with live pufferfish placed in the fish pond with the developed prototype trap, it was seen that the process of catching pufferfish was successful (Figure 14). Due to the aggressive and poisonous nature of the puffer fish and the logistic difficulties in releasing the fish near the trap, and to ensure the safety of researchers and living beings, the water tank provided a controlled experimental environment. With this application, critical parameters such as camera angle, detection distance, and image resolution could be fine-tuned, and the interaction of system components with each other could be systematically tested. Thus, the safety of living beings and researchers was ensured, while the repeatability of experiments and data quality were increased.



Figure 14. Pufferfish trap application (Left: Trap prototype, Right: Experimental study in a water tank)

4. CONCLUSIONS

In this study, our country's first artificial intelligence-supported fish hunting application was made using underwater artificial intelligence and a trap system with at least 98% detection accuracy was created. In the study, the artificial intelligence used in the fish trap was trained with images of puffer fish taken in the marine environment, and then experiments with this dangerous and aggressive species were carried out in a water tank for safety purposes. Detection of pufferfish with the camera can be done during the day under sunlight, up to a depth of 1.5 m from the sea surface. It is possible to increase trap effectiveness

by adding lighting equipment in front of the fish trap for detection and capture in deeper waters and at night. This can also support the operation of the trap in the night environment. It can be predicted that the Mediterranean and nearby seas, which are warming due to global warming, will become a more attractive habitat for pufferfish. This situation will probably cause the pufferfish to migrate more to the Mediterranean and breed more in this sea, and therefore more effective solutions need to be developed against this creature. In this case, it is important to develop new methods to combat pufferfish, as described in this study. In cases where biological control against invasive organisms cannot be carried out, technological opportunities and artificial intelligence application can stand out as an alternative solution. In the study, the dataset consisting of fish images was tested under water with high success. In this way, it has been shown that it is possible to provide a serious advantage with artificial intelligence against invasive species that harm fishing activities and the Mediterranean ecosystem. In addition, it has been observed that fish trap designs of different sizes are suggested by artificial intelligence depending on the pufferfish species. This shows that the trap can be customized according to species in different ecosystems and habitats. With this study, it has been shown for the first time that precautions can be taken against invasive pufferfish by using the capabilities of artificial intelligence as an alternative to biological control against pufferfish. In a similar study, there is a pipe type trap system set up on the river in Norway to deal with invasive salmon species. In this method, the trap tries to fight with mature salmon fish that already have good swimming ability and it is doubtful that the trap system will provide control in the entire river with strong flow. Instead of the pipe type, the cage type fish trap suggested in this article aims to fight with puffer fish that have not yet reached maturity and by placing traps in the potential breeding places of these puffer fish, before the fish reach maturity. In addition, the success of catching puffer fish of different sizes is increased by setting a trap appropriately sized for the targeted species. By changing the data sets used in the application, it is possible to create traps that will combat invasive species other than pufferfish in the ecosystem. For this purpose, the artificial intelligence model must be trained with a dataset consisting of images taken underwater of the target species. In this way, it will be possible to use the system against fish of different sizes living in different seas and ecosystems. This is also a new approach to catching pufferfish. The proposed method and trap technique aim to contribute to the literature by using ecosystem-friendly smart software and algorithms and to create new control techniques and strategies to combat invasive species.

Declaration of Ethical Standards

No specific ethical approval was necessary for this study.

Credit Authorship Contribution Statement

Author1: Finding the problem and deciding the solution proposal, researching and supplying the experimental materials, conducting experiments, developing software, preparing the draft of the article, writing and reviewing the article.

Declaration of Competing Interest

The authors have no competing interests to declare that are relevant to the content of this article.

Funding / Acknowledgements

The authors declares that there is no financial support.

We would like to express our deepest gratitude to the fishermen working at Gümüldür fishing shelter in Seferihisar district of İzmir province, who provided live pufferfish during fishing to carry out the study.

Data Availability

All data was not presented in the article. It would be supplied by the author upon request.

Use of Artificial Intelligence

No generative artificial intelligence tools were used in the preparation of this manuscript.

5. REFERENCES

[1] B. Akcali and O. Karayali, "Climate change and its effects on Turkish seas," in *Türk Deniz Araştırmaları Vakfı (TÜDAV)*, Istanbul, Turkey, pp. 100–113, 2021, ISBN: 978-975-8825-52-3.

[2] F. Andaloro, L. Castriota, M. Falautano, E. Azzurro, A. Deidun, and A. Fenech-Farrugia, "Public feedback on early warning initiatives undertaken for hazardous non-indigenous species: The case of *Lagocephalus sceleratus* from Italian and Maltese waters," *Management of Biological Invasions*, vol. 7, no. 4, pp. 313–319, 2016, doi: 10.3391/mbi.2016.7.4.01.

[3] S. Katsanevakis, Ü. Acar, I. Ammar, B. A. Balci, P. Bekas, and M. Belmonte *et al*., "New Mediterranean biodiversity records (October, 2014)," *Mediterranean Marine Science*, vol. 15, no. 3, pp. 675–695, 2014, doi: 10.12681/mms.1123.

[4] L. Solino, N. Gouveia, V. Timoteo, and P. R. Costa, "New insights into the occurrence of paralytic shellfish toxins in the oceanic pufferfish *Lagocephalus lagocephalus* (Linnaeus, 1758) from Madeira Island, Portugal," *Regional Studies in Marine Science*, vol. 42, no. 107, Art. no. 101657, 2021, doi: 10.1016/j.rsma.2021.101657.

[5] V. Ünal, H. Göncüoğlu, D. Durgun, Z. Tosunoğlu, M. C. Deval, and C. Turan, "Silver-cheeked toadfish, *Lagocephalus sceleratus* (Actinopterygii: Tetraodontiformes: Tetraodontidae), causes substantial economic losses in Turkish Mediterranean coast: A call for decision makers," *Acta Ichthyologica et Piscatoria*, vol. 45, pp. 231–237, 2015, doi: 10.3750/AIP2015.45.3.02.

[6] S. Katsanevakis, K. Tsiamis, G. Ioannou, N. Michailidis, and A. Zenetos, "Inventory of alien marine species of Cyprus (2009)," *Mediterranean Marine Science*, vol. 1, no. 2, pp. 109–133, 2009, doi: 10.12681/mms.113.

[7] G. Özdemir and B. Ceylan, "Biyolojik istila ve Karadeniz'deki istilacı türler," *SÜMAE Yunus Araştırma Bülteni*, vol. 7, no. 3, 2007.

[8] A. M. Mannino and P. Balistreri, "Invasive alien species in Mediterranean Marine Protected Areas: The Egadi Islands (Italy) case study," *Biodiversity*, vol. 22, no. 1–2, pp. 13–23, 2021, doi: 10.1080/14888386.2021.1875263.

[9] M. Bariche *et al*., "New alien Mediterranean biodiversity records (March 2020)," *Mediterranean Marine Science*, vol. 21, no. 1, pp. 129–145, 2020.

[10] D. T. Çakır, A. Yarmaz, and C. Balaban, "A new record of *Lagocephalus sceleratus* (Gmelin, 1789) confirming a further range extension into the northern Aegean Sea," *Journal of Applied Ichthyology*, vol. 25, pp. 606–607, 2009, doi: 10.1111/j.1439-0426.2009.01276.x.

[11] S. Kalogirou, "Ecological characteristics of the invasive pufferfish *Lagocephalus sceleratus* (Gmelin, 1789) in the eastern Mediterranean Sea: A case study from Rhodes," *Mediterranean Marine Science*, vol. 14, no. 2, pp. 251–260, 2013, doi: 10.12681/mms.364.

[12] L. Guardone, L. Gasperetti, A. Maneschi, E. Ricci, F. Susini, A. Guidi, and A. Armani, "Toxic invasive pufferfish (Tetraodontidae family) along Italian coasts: Assessment of an emerging public health risk," *Food Control*, vol. 91, pp. 330–338, 2018, doi: 10.1016/j.foodcont.2018.04.005.

[13] S. Katsanevakis, F. Gatto, A. Zenetos, and A. C. Cardoso, "How many marine aliens in Europe," *Management of Biological Invasions*, vol. 4, no. 1, pp. 37–42, 2013, doi: 10.3391/mbi.2013.4.1.05.

[14] R. Bedry, L. de Haro, Y. Bentur, N. Senechal, and B. S. Galil, "Toxicological risks on the human health of populations living around the Mediterranean Sea linked to the invasion of non-indigenous marine species from the Red Sea: A review," *Toxicon*, vol. 191, pp. 69–82, 2021, doi: 10.1016/j.toxicon.2020.12.012.

[15] O. Akyol, V. Ünal, T. Ceyhan, and M. Bilecenoglu, "First confirmed record of *Lagocephalus sceleratus* (Gmelin, 1789) in the Mediterranean Sea," *Journal of Fish Biology*, vol. 66, pp. 1183–1186, 2005, doi: 10.1111/j.0022-1112.2005.00667.x.

[16] A. B. Beköz, S. Beköz, E. Yilmaz, S. Tüzün, and Ü. Beköz, "Consequences of the increasing prevalence of the poisonous *Lagocephalus sceleratus* in southern Turkey," *Emergency Medicine Journal*, vol. 30, no. 11, pp. 954–955, 2013, doi: 10.1136/emermed-2011-200407.

[17] T. H. Koç, Z. Erdoğan, and F. Üstün, "Occurrence of the Lessepsian migrant, *Lagocephalus sceleratus* (Gmelin, 1789) (Osteichtyes: Tetraodontidae), in Iskenderun Bay (north-eastern Mediterranean, Turkey)," *Journal of Applied Ichthyology*, vol. 27, no. 1, pp. 148–149, 2011, doi: 10.1111/j.1439-0426.2010.01628.x.

[18] S. Tuncer, H. Aslan Cihangir, and M. Bilecenoglu, "First record of the Lessepsian migrant *Lagocephalus spadiceus* (Tetraodontidae) in the Sea of Marmara," *Cybium*, vol. 32, no. 4, pp. 347–348, 2008, doi: 10.26028/cybium/2009-324-010.

[19] F. E. Kayhan and N. D. Yönertuğ, "Türkiye kıyılarında istilacı zehirli balon balığı (*Lagocephalus sceleratus* Gmelin, 1789)," *Doğanın Sesi*, no. 8, pp. 35–46, 2021.

[20] S. A. Ergüden, D. Ayas, and D. Ergüden, "The length-weight relationship and condition factor of yellow spotted puffer *Torquigener flavimaculosus* Hardy & Randall, 1983 in the Eastern Mediterranean (Yumurtalık Bight, Turkey)," *Marine Science and Technology Bulletin*, vol. 9, no. 2, pp. 87–91, 2020, doi: 10.33714/masteb.700374.

[21] R. G. Barrientos, G. Hernandez-Mora, F. Alegre, T. Field, L. Flewelling, S. Mc-Grath, J. Deeds, Y. S. Chacon, K. R. Arrieta, E. C. Vargas, K. B. Artavia, and B. A. Stacy, "Saxitoxin poisoning in green turtles (*Chelonia mydas*) linked to scavenging on mass mortality of Caribbean sharpnose pufferfish (*Canthigaster rostrata*, Tetraodontidae)," *Frontiers in Veterinary Science*, vol. 6, pp. 693–755, 2019, doi: 10.3389/fvets.2019.00466.

[22] A. Zenetos, G. Apostopoulos, and F. Crocetta, "Aquaria kept marine fish species possibly released in the Mediterranean Sea: First confirmation of intentional release in the wild," *Acta Ichthyologica et Piscatoria*, vol. 46, no. 3, pp. 255–262, 2016, doi: 10.3750/AIP2016.46.3.10.

[23] P. Peristeraki, G. Lazarakis, C. Skarvelis, M. Georgiadis, and G. Tserpes, "Additional records on the occurrence of alien fish species in the eastern Mediterranean Sea," *Mediterranean Marine Science*, vol. 7, pp. 61–66, 2006, doi: 10.12681/mms.170.

[24] P. Katikou, D. Georgantelis, N. Sinouris, A. Petsi, and T. Fotaras, "First report on toxicity assessment of the Lessepsian migrant pufferfish *Lagocephalus sceleratus* (Gmelin, 1789) from European waters (Aegean Sea, Greece)," *Toxicon*, vol. 54, no. 1, pp. 50–55, 2009, doi: 10.1016/j.toxicon.2009.03.012.

[25] E. Irmak and U. Altınağaç, "First record of an invasive Lessepsian migrant, *Lagocephalus sceleratus* (Actinopterygii: Tetraodontiformes: Tetraodontidae), in the Sea of Marmara," *Acta Ichthyologica et Piscatoria*, vol. 45, no. 4, pp. 433–435, 2015, doi: 10.3750/AIP2015.45.4.14.

[26] C. Acar, S. Ishizaki, and Y. Nagashima, "Toxicity of the Lessepsian pufferfish *Lagocephalus sceleratus* from eastern Mediterranean coasts of Turkey and species identification by rapid PCR amplification," *European Food Research and Technology*, vol. 243, no. 1, pp. 49–57, 2017, doi: 10.1007/s00217-016-2721-1.

[27] T. Noguchi and O. Arakawa, "Tetrodotoxin-distribution and accumulation in aquatic organisms, and cases of human intoxication," *Marine Drugs*, vol. 6, no. 2, pp. 220–242, 2008, doi: 10.3390/md20080011.

[28] A. Jang and M. Yotsu-Yamashita, "Distribution of tetrodotoxin, saxitoxin, and their analogs among tissues of the pufferfish *Fugu pardalis*," *Toxicon*, vol. 48, pp. 980–987, 2007, doi: 10.1016/j.toxicon.2006.07.034.

[29] K. Nakashima, O. Arakawa, S. Taniyama, M. Nonaka, T. Takatani, K. Yamamori, Y. Fuchi, and T. Noguchi, "Occurrence of saxitoxins as a major toxin in the ovary of a marine puffer *Arothron firmamentum*," *Toxicon*, vol. 43, pp. 207–212, 2004, doi: 10.1016/j.toxicon.2003.05.001.

[30] R. Froese and D. Pauly, *FishBase 2016: World Wide Web Electronic Publication*, version 10/2016. [Online]. Available: http://www.fishbase.org

[31] M. Bilecenoglu, M. Kaya, and S. Akalin, "Range expansion of silverstripe blaasop, *Lagocephalus sceleratus* (Gmelin, 1789), to the northern Aegean Sea," *Aquatic Invasions*, vol. 1, no. 4, pp. 289–291, 2006, doi: 10.3391/ai.2006.1.4.14.

[32] EastMed, "Report of the technical meeting on the Lessepsian migration and its impact on eastern Mediterranean fishery," GCP/INT/041/EC-GRE-ITA, 2010. [Online]. Available: https://www.fao.org/3/ap961e/ap961e.pdf

[33] S. U. Hassan, J. Ahamed, and K. Ahmad, "Analytics of machine learning-based algorithms for text classification," *Sustainable Operations and Computers*, vol. 3, pp. 238–248, 2022, doi: 10.1016/j.susoc.2022.03.001.

[34] T. Jiang, J. L. Gradus, and A. J. Rosellini, "Supervised machine learning: A brief primer," *Behavior Therapy*, vol. 51, no. 5, pp. 675–687, 2020, doi: 10.1016/j.beth.2020.05.002.

[35] H. Filiz, S. Yapıcı, and G. Bilge, "The factors increasing invasiveness potential of five pufferfishes in the Eastern Mediterranean, Turkey," *Natural and Engineering Sciences*, vol. 2, no. 3, pp. 22–30, 2017, doi: 10.28978/nesciences.369004.

[36] F. Öndes, V. Ünal, Y. Özbilgin, C. Deval, and C. Turan, "By-catch and monetary loss of pufferfish in Turkey, the Eastern Mediterranean," *Ege Journal of Fisheries and Aquatic Sciences*, vol. 35, no. 4, pp. 361–372, 2018, doi: 10.12714/egejfas.2018.35.4.01.

[37] L. Guardone, L. Gasperetti, A. Maneschi, E. Ricci, F. Susini, A. Guidi, and A. Armani, "Toxic invasive pufferfish (Tetraodontidae family) along Italian coasts: Assessment of an emerging public health risk," *Food Control*, vol. 91, pp. 330–338, 2018, doi: 10.1016/j.foodcont.2018.04.005.

[38] M. Ahmed, R. Seraj, and S. M. S. Islam, "The K-means algorithm: A comprehensive survey and performance evaluation," *Electronics*, vol. 9, Art. no. 1295, 2020, doi: 10.3390/electronics9081295.

[39] A. M. Ikotun, A. E. Ezugwu, L. Abualigah, B. Abuhaija, and J. Heming, "K-means clustering algorithms: A comprehensive review, variants analysis, and advances in the era of big data," *Information Sciences*, vol. 622, pp. 178–210, 2023, doi: 10.1016/j.ins.2022.11.139.

[40] K. P. Sinaga and M.-S. Yang, "Unsupervised K-means clustering algorithm," *IEEE Access*, vol. 8, pp. 80716–80727, 2020, doi: 10.1109/ACCESS.2020.2988796.

Konya Mühendislik Bilimleri Dergisi., c.14, s.2, 700-718, 2026
Konya Journal of Engineering Sciences v.14, n.2, 700-718, 2026
ISSN: 2667-8055 (Electronic)
DOI: 10.36306/konjes.1733172

PERFORMANCE ASSESSMENT OF A HYBRID FRESNEL SOLAR-GEOTHERMAL ORC UTILIZING DRY ORGANIC FLUIDS

[1]Serpil Celik Toker

[1]Isparta University of Applied Sciences, Department of Mechanical Engineering, Isparta, TÜRKİYE
[1]serpilcelik@isparta.edu.tr

Highlights

- Hybrid solar-geothermal ORC with dry fluids is thermodynamically analyzed.
- Five dry organic fluids evaluated for energy and exergy performance.
- Toluene gives max power; butane achieves highest exergy efficiency.
- Solar and geothermal input variations affect system performance.
- Pentane provides balanced energy–exergy performance among fluids.

***Corresponding Author:** Serpil CELİK TOKER, serpilcelik@isparta.edu.tr

Konya Mühendislik Bilimleri Dergisi., c.14, s.2, 700-718, 2026
Konya Journal of Engineering Sciences v.14, n.2, 700-718, 2026
ISSN: 2667-8055 (Electronic)
DOI: 10.36306/konjes.1733172

PERFORMANCE ASSESSMENT OF A HYBRID FRESNEL SOLAR-GEOTHERMAL ORC UTILIZING DRY ORGANIC FLUIDS

[1], *Serpil CELIK TOKER

Isparta University of Applied Sciences, Department of Mechanical Engineering, Isparta, TÜRKİYE
[1]serpilcelik@isparta.edu.tr

(Received: 02.07.2025; Accepted in Revised Form: 22.11.2025)

ABSTRACT: This study investigates the thermodynamic performance of an organic Rankine cycle (ORC) system driven by hybrid solar and geothermal energy sources. The proposed system utilizes a Fresnel solar collector and a geothermal heat exchanger to supply thermal energy to the ORC, which employs dry organic fluids including butane, pentane, toluene, cyclohexane, and hexane. A comprehensive thermodynamic analysis is conducted, evaluating key performance indicators such as net power generation, exergy irreversibility, energy and exergy efficiencies. The EES (Engineering Equation Solver) program is used for hybrid plant's thermodynamic analysis. The results reveal that butane exhibits the highest exergy efficiency (0.2483) but yields the lowest power output (103.9 kW), while toluene achieves the maximum power generation (112.6 kW) with the lowest exergy destruction (523.5 kW), albeit with modest efficiency values. The performance of the working fluids is further analyzed under varying solar radiation, geothermal source temperatures, and geothermal mass flow rates. As solar irradiation raises from 500 to 1000 W/m^2, all fluids show enhanced power generation and energy efficiency, but a corresponding increase in exergy destruction and a decline in exergy efficiency. Similarly, higher geothermal temperatures lead to improved power output and exergy efficiency, while increased geothermal flow rates enhance power generation but reduce both energy and exergy efficiencies due to intensified irreversibilities. Among the tested fluids, pentane offers a favorable balance between energy and exergy efficiency, while toluene excels in power generation. These results highlight the critical influence of working fluid selection on the thermodynamic behavior of hybrid solar-geothermal ORC systems and contribute to the identification of suitable fluids for future low- to medium-temperature renewable power applications.

Keywords: *Dry Organic Fluids, Energy, Exergy, Fresnel Solar Collector, ORC.*

1. INTRODUCTION

The growing worldwide energy demand and the pressing need to mitigate greenhouse gas emissions have accelerated the pursuit of environmentally sustainable energy solutions [1]. Conventional fossil fuel plants-though still prevalent-pose serious environmental challenges, including global warming, air pollution, and resource depletion, which threaten long-term energy security. As a result, a strategic transition to renewable energy sources has become essential. Among these, solar and geothermal energy stand out due to their wide availability, low environmental impact, and compatibility with decentralized applications. These heat sources are well suited to low- and medium-temperature systems such as the ORC, which can efficiently convert thermal energy into electricity under variable conditions [2].

In recent years, there has been growing interest in solar-based power generation, particularly for low-temperature applications. Tchanche et al. [3]conducted a comprehensive performance assessment of flat plate collector driven ORCs, emphasizing their suitability for decentralized electricity generation when coupled with appropriate working fluids and optimized configurations. Helvaci and Khan [4] performed a thermodynamic analysis of a flat-plate solar collector-assisted ORC using 24 different fluids;

***Corresponding Author:** Serpil CELİK TOKER, serpilcelik@isparta.edu.tr

among them, 1-butene achieved the highest electricity production (210.45 W) and energy efficiency (9.64%), while hydrofluoroolefins and hydrofluoroethers emerged as safer alternatives despite their moderate performance. Ramos et al. [5] investigated a solar integrated heat and power plant employing a non-recuperative subcritical ORC for residential use. Among 15 fluids tested, R245fa and R1233zd produced the best results, delivering 3,605 kWh/year of electricity and 13175 kWh/year of thermal output using a 60 m2 collector. Wang et al. [6] proposed a solar-powered ORC combined with thermal energy storage and a proton exchange membrane electrolyzer; hexane provided the highest net power output (2325.3 kW), cycle efficiency (20.8%), and hydrogen production rate (36.0 kg/h). Sun et al. [7] designed a solar-driven polygeneration system combining a fuel cell, linear Fresnel collector, ORC, Stirling engine, and electrolyzer to produce electricity, hydrogen, heat, and cooling. Pinerez et al. [8] performed a 3E (energy, exergy, environmental) analysis of a solar-powered ORC using toluene, cyclohexane, and acetone under Colombian solar conditions. Toluene showed the best performance, achieving 14.6% energy and 7.37% exergy efficiency. Gonidaki et al. [9] investigated a solar-driven ORC system using the zeotropic mixture R601/R600 and reported that the mixture outperformed pure fluids in electricity generation across daily, monthly, and annual scales.

Given the increasing interest in enhancing the performance of ORCs with individual renewable sources, recent research has focused on hybrid configurations-particularly those integrating solar and geothermal energy-to address the intermittency of solar radiation, enhance system reliability, and achieve higher thermodynamic efficiency. Alrbai et al. [10] investigated a hybrid solar and geothermal ORC and found that geothermal integration significantly reduced turbine-related exergy destruction compared to a standalone solar system. Additionally, R245fa improved efficiency by up to 3%, while solar collectors emerged as the primary source of irreversibility. Alibaba et al. [11] conducted conventional and advanced exergo-economic and exergo-environmental analyses of a solar and geothermal hybrid plant using an ORC. Maali and Khir [12] optimized a hybrid ORC in southern Tunisia, while Li et al. [13] developed a thermo-economic model for hybrid plant across four Chinese locations. Their findings showed that the hybrid setup significantly enhanced thermal performance, increasing electricity production by up to 25.34% compared to a solar-only system. Tempesti et al. [14] analyzed micro combined heat and power systems powered by low-temperature solar and geothermal energy, comparing single-stage and double-stage configurations using evacuated tube and parabolic trough collectors. Working fluids like R134a, R236fa, and R245fa were tested for performance in terms of efficiency, output, and component sizing. Bozkurt et al. [15] developed a hybrid solar and geothermal energy system integrating a steam Rankine cycle and an ORC to enhance power generation and hydrogen production. Using a comprehensive energy, and exergy analysis, they reported energy and exergy efficiencies of 20.13% and 22.87%.

In addition to the heat source, the choice of working agent acts a pivotal role in determining the ORC's thermodynamic performance. The selection strongly influences cycle efficiency due to its close link to the fluid's thermophysical properties [16]. Numerous organic fluids are available for ORC use, each offering distinct advantages depending on the system's configuration and operating conditions. Mago et al. [17] compared basic and regenerative ORCs using dry fluids such as R113, R245fa, R123, and isobutane. Javanshir et al. [18] performed a detailed design and optimization study of regenerative ORCs with 14 dry working fluids, concluding that Butane, iso-Butane, and R113 delivered the highest power outputs. Bellos et al. [19] introduced a partial evaporation ORC for low-temperature waste heat utilization, finding R1233zd(E) to perform best between 110-170 °C. Sun and Peng [20] experimentally analyzed an ORC with hydrofluorocarbon fluids, identifying R245fa as the most effective in terms of shaft power and efficiency. Zhang and Li [21] examined regenerative ORCs using super-dry working fluids, proposing optimal fluids and conditions for various low- to medium-temperature sources. Shahverdi et al. [22] evaluated several fluids in a parabolic trough driven ORC, with R113 offering the best net power and efficiency. Akbari et al. [23] performed a detailed exergoeconomic optimization of a geothermal ORC using 20 zeotropic mixtures, identifying R123/C_2-butene (96.9/3.1%) as the most effective in balancing cost and efficiency.

In light of the reviewed literature, this study aims to conduct a comprehensive thermodynamic assessment of an ORC powered by hybrid solar and geothermal energy sources, focusing on the impact of different dry working fluids. While previous studies have explored either solar or geothermal energy-based ORCs, or considered a limited set of working fluids, there remains a gap in detailed comparative evaluations under hybrid heat supply conditions. The novelty of this work lies in the systematic performance comparison of five dry organic fluids-namely butane, pentane, toluene, cyclohexane, and hexane within a hybrid solar-geothermal ORC configuration. Thermodynamic analysis of the integrated system under study was performed using a programming software called EES. The study evaluates the effects of key operating parameters, such as solar radiation intensity, geothermal fluid temperature, and geothermal mass flow rate, on power output, energy and exergy efficiencies, and irreversibilities. The outcomes are expected to guide optimal fluid selection and operational strategies for enhancing the efficiency and sustainability of low- to medium-temperature multiresource ORC.

2. MATERIAL AND METHODS

Figure 1 depicts the schematic layout of the ORC supported by both solar and geothermal energy sources. The proposed configuration combines these renewable heat inputs to produce electricity via a basic ORC. The working fluid utilized in the ORC absorbs thermal energy from both a solar collector and a geothermal heat exchanger.

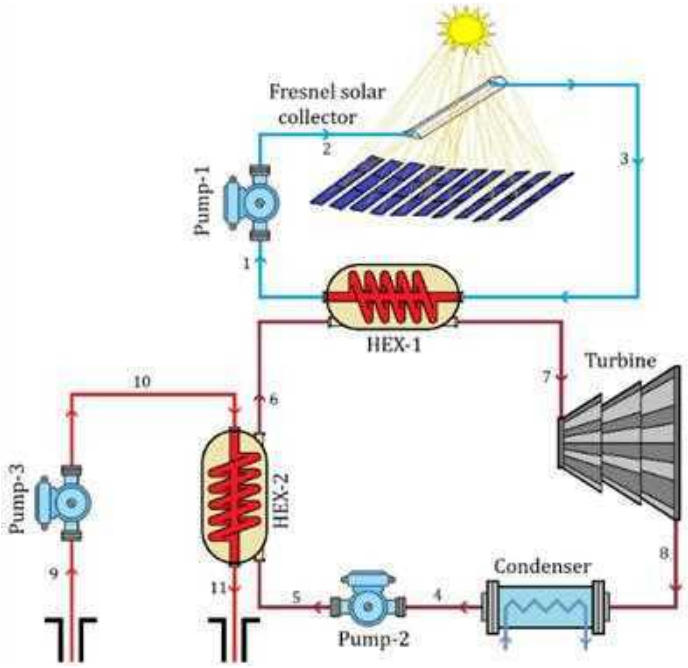


Figure 1. Schematic diagram of the hybrid solar–geothermal ORC

In the solar subsystem, therminol VP-1 is employed as the heat transfer fluid. It is circulated through the Fresnel solar collector loop by means of a pump (state 1-2). The heat transfer fluid gains thermal energy in the solar collector (state 2-3) and transfers the absorbed heat to the organic working fluid via HEX-1, which acts as the superheater (state 3-1). Simultaneously, on the geothermal side of the system, the geothermal brine is circulated through HEX-2, which functions as the evaporator (state 9-10), where it serves as the primary heat source for the organic working fluid. As the brine flows through the evaporator, it transfers thermal energy to the working fluid, enabling its transition from saturated liquid to vapor phase.

The organic working fluid, initially in the saturated liquid state, is pressurized to the required evaporation pressure by pump (state 4-5). Subsequently, the working fluid flows into HEX-2 (state 5-6), where its primary vaporization occurs. This vaporization process is further supported by supplementary heat provided through HEX-1 connected to the solar collector unit (state 6-7). The high-energy vapor obtained at the outlet of the solar collector undergoes expansion in the turbine (state 7-8), producing mechanical work, which is then converted into electrical power. After expansion, the low-pressure vapor enters the condenser (state 8-4), where it is cooled and condensed into saturated liquid. The working fluid is then pressurized again by pump, completing the thermodynamic cycle. Meanwhile, the geothermal fluid, having released its thermal energy, exits the evaporator (state 10-11) and is re-injected into the ground. This hybrid configuration ensures continuous and efficient operation by exploiting the complementary nature of solar and geothermal energy resources.

The selection of a suitable working fluid is a critical determinant of the overall performance and viability of an ORC, as it directly influences key thermodynamic metrics [24]. In this study, five dry organic fluids-butane, toluene, cyclohexane, hexane, and pentane-were selected due to their compatibility with low-to medium-temperature heat sources and favorable environmental characteristics. These fluids, characterized by a positive slope of the saturated vapor line on the T-s diagram [25], generally eliminate the risk of condensation within the turbine, enabling expansion to occur entirely within the superheated region [26]. This property reduces turbine blade erosion and enhances system reliability. To determine the most suitable working fluid for the proposed system, a comparative thermodynamic analysis was conducted using five different dry organic fluids listed in Table 1. Furthermore, particular emphasis was placed on selecting fluids with zero ozone depletion potential (ODP) and notably low global warming potential (GWP), thereby ensuring that the proposed system not only offers thermodynamic robustness but also aligns with contemporary environmental sustainability goals.

Table 1. The characteristics of the selected dry organic working fluids [27], [28]

Working Fluid	Category	T_{crit} (°C)	P_{crit} (kPa)	GWP	ODP	ASHRAE Safety Group
Butane	Dry	151.98	39.9	3	0	A3
Pentane	Dry	196.55	33.7	5	0	A3
Hexane	Dry	234.65	30.34	0.02	0	A1
Toluene	Dry	317.85	41.2	3.35	0	A1
Cyclohexane	Dry	279.85	40.8	0.02	0	A1

In the present study, a hybrid solar-geothermal system is considered, in which a portion of the thermal energy required by the ORC is supplied by a LFR, while the remaining demand is covered by geothermal energy. The LFRs consists of flat mirror strips that track the sun's position and concentrate solar radiation onto a linear receiver positioned above the mirrors [29]. The absorbed solar energy is transferred to the heat transfer fluid, which circulates through the receiver and delivers the collected heat to the ORC via an intermediate heat exchanger. Several assumptions are introduced to simplify the thermodynamic modeling and ensure consistent analysis of the hybrid solar-geothermal ORC.

- The system operates under steady-state conditions.
- Changes in kinetic, potential energy, and exergy are neglected.
- Pressure losses in heat exchangers are ignored.
- The turbine and pump are considered adiabatic.
- Reference environment is taken as 25 °C and 101.325 kPa.

For the performance evaluation of the proposed hybrid solar-geothermal ORC with various dry working fluids, the main design parameters are presented in Table 2.

Table 2. System design parameters [30], [31]

Parameter	Value
Solar radiation	950 W/m^2
Number of the mirror	50
Length of the mirror	10 m
Width of the mirror	1.2 m
Mass flow rate of the heat transfer fluid	2 kg/s
Geothermal source temperature	95 °C
Geothermal mass flow rate	5 kg/s
Condenser temperature	35 °C
Turbine isentropic efficiency	80 (%)
Pump isentropic efficiency	80 (%)

The useful thermal energy gained by the Fresnel collector is calculated as follows [29] :

$$Q_{LFR} = Q_{in} - Q_l - Q_P \quad (1)$$

where, Q_{in}, Q_l, and Q_P denote the LFR's incident thermal energy, the heat loss from the heat transfer agent, and heat loss from pipes, respectively. Besides, it should be noted that, the heat loss from pipes in this study are neglected.

$$Q_{in} = \eta_{opt} \times Q_s \quad (2)$$

$$Q_s = A_{LFR} \times G_b \quad (3)$$

In above equation, Q_s, G_b, and A_{LFR} are the absorbed solar power, solar irradiation and area of the LFR, correspondingly. Also, η_{opt} shows the LFR's optical efficiency and according to Ref. [32] was assumed to be 0.65.

The heat loss associated with the heat transfer fluid can be calculated as [27]:

$$Q_l = 0.3207 \times (T_{ave} - T_{amb}) - 0.001823 \times (T_{ave} - T_{amb})^2 + 6.779 \times 10^{-6} \times (T_{ave} - T_{amb})^3 \quad (4)$$

Here, T_{ave} and T_{amb} are the average temperature of the heat transfer fluid and ambient temperature, respectively.

ORC is a highly efficient technology for converting thermal energy into electrical power. In the present study, the heat required for the ORC is partially supplied by the LFR. Additionally, dry organic fluids are employed as the working fluid within the ORC. The mass flow rate of the working fluid can be calculated as follows:

$$\dot{m}_{ORC} = \frac{Q_{HEX-1} + Q_{HEX-2}}{h_7 - h_5} \quad (5)$$

The following equations present the calculation of the power produced by the turbine and consumed by the pump.

$$\dot{W}_{Tur} = \dot{m}_{ORC} \times (h_7 - h_8) \quad (6)$$

$$\dot{W}_{Pump} = \dot{m}_{ORC} \times (h_5 - h_4) \quad (7)$$

Moreover, the thermal energy supplied to the ORC can be determined by the following equation:

$$\dot{Q}_{in} = \dot{m}_{LFR} \times (h_3 - h_1) + \dot{m}_{geo} \times (h_{10} - h_{11}) \quad (8)$$

Furthermore, the net power output of the ORC can be calculated as:

$$\dot{W}_{Pump,geo} = \dot{m}_{geo} \times (h_{10} - h_9) \quad (9)$$

$$\dot{W}_{Pump,LFR} = \dot{m}_{LFR} \times (h_2 - h_1) \quad (10)$$

$$\dot{W}_{net} = \dot{W}_{Tur} - \dot{W}_{Pump} - \dot{W}_{Pump,geo} - \dot{W}_{Pump,LFR} \quad (11)$$

Finally, the ORC's overall energy and exergy efficiencies can be determined using the following equation:

$$\eta_{en,ORC} = \frac{\dot{W}_{net}}{\dot{Q}_{in}} \quad (12)$$

$$\eta_{ex,ORC} = \frac{\dot{W}_{net}}{\dot{E}x_{Q_{in}}} \quad (13)$$

3. RESULTS AND DISCUSSION

This subsection of the reviewed study includes three parts: model validation of the ORC system, steady-state analysis results, and parametric study results. The accuracy of the examined ORC model was verified through validation against the reference study [33]. As presented in Table 3, the energy efficiency, and net power obtained from the present model exhibit an excellent agreement with the reported results. The negligible deviation between the two sets of data confirms the reliability of the thermodynamic formulations and assumptions adopted in this study, ensuring that the model is suitable for subsequent parametric and performance analyses.

Table 3. Validation of the ORC with data of Ref. [33]

Parameters	Present study	Ref. study [33]
Turbine input temperature (°C)	140	140
Turbine input pressure (MPa)	3.00	3.00
Condenser pressure (MPa)	0.50	0.50
Energy efficiency (-)	0.152	0.151
Net power (kW)	1334	1339

In the integrated solar and geothermal ORC, the thermodynamic performance of various organic working fluids was comparatively assessed based on key indicators such as energy efficiency, exergy efficiency, exergy destruction, and net power generation. These parameters are collectively visualized in Figure 2, enabling a multi-dimensional evaluation of each fluid under identical operating conditions. As shown in the figure, butane stands out with the highest exergy efficiency (0.2483) despite having the lowest net power output (103.9 kW). This implies that while its second-law performance is favorable, its lower heat absorption capacity limits overall energy conversion. In contrast, toluene delivers the highest power output (112.6 kW) and lowest exergy destruction (523.5 kW), yet ranks lowest in both energy (0.086) and exergy (0.2256) efficiencies, suggesting that most of the input heat is not converted effectively. Cyclohexane and hexane exhibit a well-balanced performance profile, combining relatively high net power outputs (approximately 112 kW) with moderate exergy efficiencies in the range of 0.228 to 0.229.

Although pentane does not rank first in any individual criterion, it provides a favorable overall compromise, delivering consistent energy (0.08995) and exergy (0.2332) efficiencies alongside manageable exergy destruction. Overall, the plot highlights that no single fluid simultaneously maximizes all performance metrics, underscoring the importance of selecting a working fluid according to the specific performance priorities of the system-such as higher efficiency, reduced irreversibility, or increased power output.

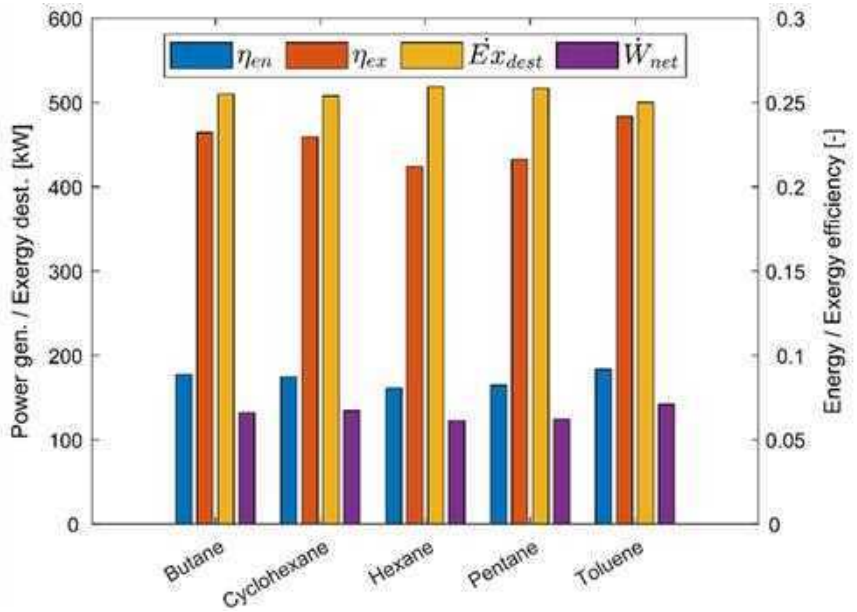


Figure 2. Comparison thermodynamic performance indicators for different organic working fluids

Following the steady-state evaluation, a parametric analysis was carried out to assess the effects of key operational variables such as solar radiation, geothermal temperature, and mass flow rate on the system's thermodynamic performance. Figure 3 presents the variation in power generation with increasing solar radiation for five different organic working fluids. As expected, the power output rises nearly linearly with higher solar irradiation due to enhanced thermal input to the system. Among the fluids evaluated, toluene exhibits the highest power generation across the entire radiation range, reaching approximately 116.2 kW at 1000 W/m^2, followed closely by cyclohexane and hexane, which show very similar performance trends. Pentane, although slightly lower in output than these top-performing fluids, still demonstrates competitive behavior, reaching 112.2 kW at maximum solar input and surpassing butane, which produces only 105.6 kW at the same condition. Notably, at 500 W/m^2, the difference between the highest and lowest performing fluids is already over 10 kW, with butane generating 73.2 kW and toluene producing 83.3 kW.

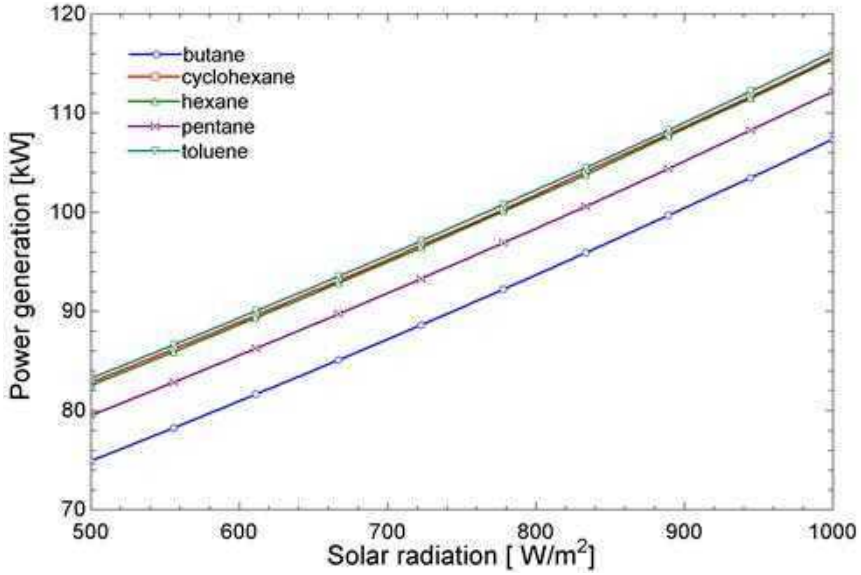


Figure 3. Effect of solar radiation on power generation for various organic working fluids

Figure 4 displays the relationship between solar radiation and the energy efficiency of the ORC using different organic fluids. It is evident that all fluids experience a gradual improvement in thermal efficiency with elevated solar input, owing to enhanced heat availability. Among the fluids analyzed, butane demonstrates the highest energy efficiency over the entire solar irradiation, achieving a peak value of 0.1007 at 1000 W/m^2. Pentane ranks second, reaching an efficiency of approximately 0.0909, indicating a stable and consistent thermal performance across varying irradiance levels. On the other hand, toluene shows the lowest energy efficiency values, increasing from 0.0763 at 500 W/m^2 to 0.0871 at 1000 W/m^2, while cyclohexane and hexane follow similar trajectories, slightly outperforming toluene but still falling short of butane and pentane. These distinctions in efficiency can be attributed to each fluid's thermophysical properties and their respective behavior under different heat supply conditions. Overall, the results underscore that working fluid selection considerably influences thermal performance, particularly in solar energy driven ORCs.

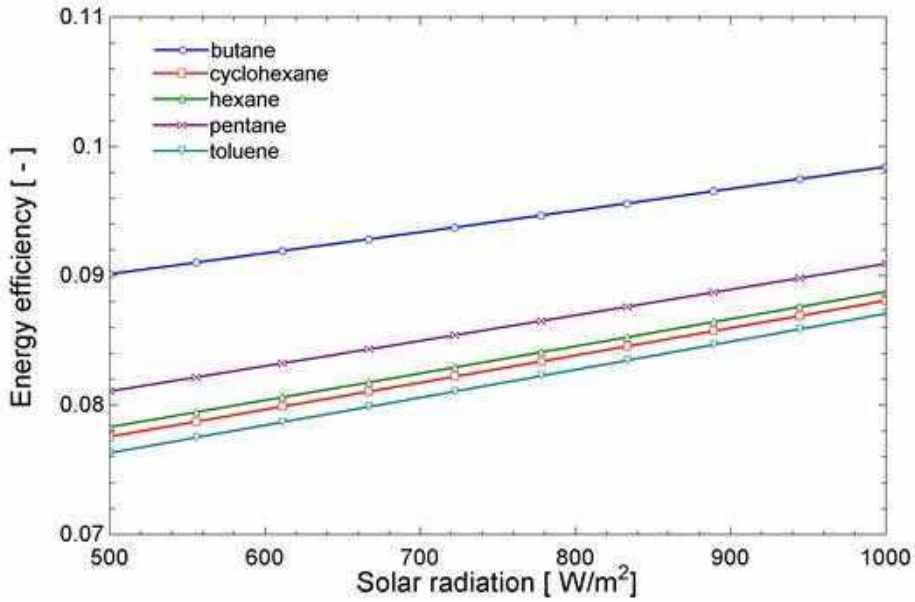


Figure 4. Effect of solar radiation on energy efficiency for various organic working

The plot in Figure 5 highlights the variation in total exergy destruction with respect to increasing solar radiation for each working fluid considered. A clear upward trend is observed across all fluids, which aligns with the expected behavior under enhanced thermal input. As solar irradiation raises from 500 to 1000 W/m², the total exergy losses grow significantly due to larger thermal energy fluxes processed by the system. Among the fluids, butane consistently results in the highest exergy destruction-reaching nearly 558 kW at maximum irradiation-while toluene and pentane demonstrate relatively lower irreversibilities. This figure confirms that although more heat input boosts power production, it simultaneously amplifies system irreversibilities.

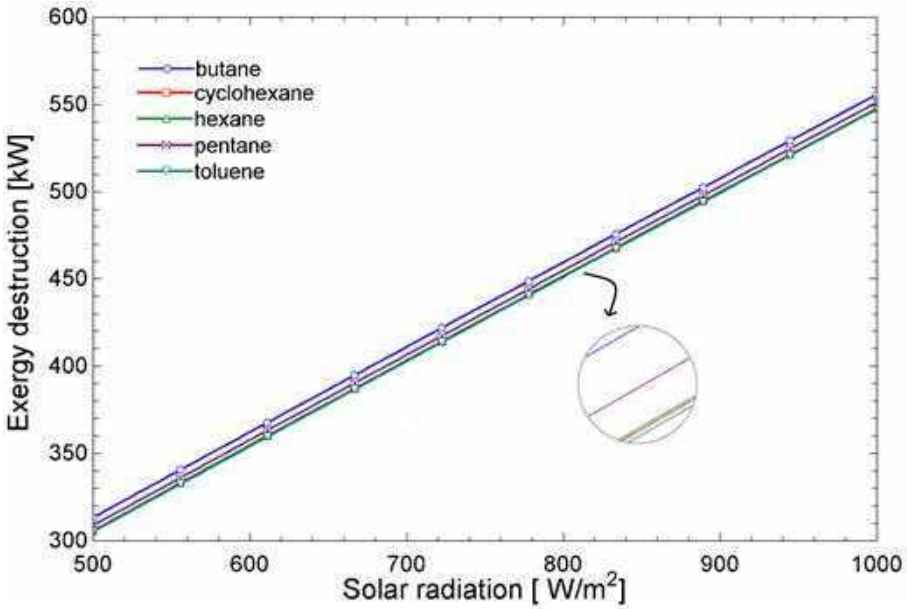


Figure 5. Effect of solar irradiation on exergy destruction for various organic working

Figure 6 demonstrates the sensitivity of exergy efficiency to variations in solar irradiance for the five organic fluids. In contrast to energy efficiency, exergy-based performance indicators show a gradual decline as solar input increase. This inverse trend is primarily due to the increasing rate of irreversibility within the system at higher temperatures. Butane exhibits the highest exergy efficiency values throughout the examined range, starting at 0.2824 for 500 W/m² and decreasing to 0.2506 at 1000 W/m². Pentane ranks second, maintaining values above 0.23 across the spectrum. Conversely, toluene shows the lowest exergy efficiency, dropping from 0.2455 to 0.2243, indicating relatively higher exergy losses per unit of useful output. These findings underscore the importance of balancing thermal input with fluid selection to maintain exergy performance in solar and geothermal driven ORCs.

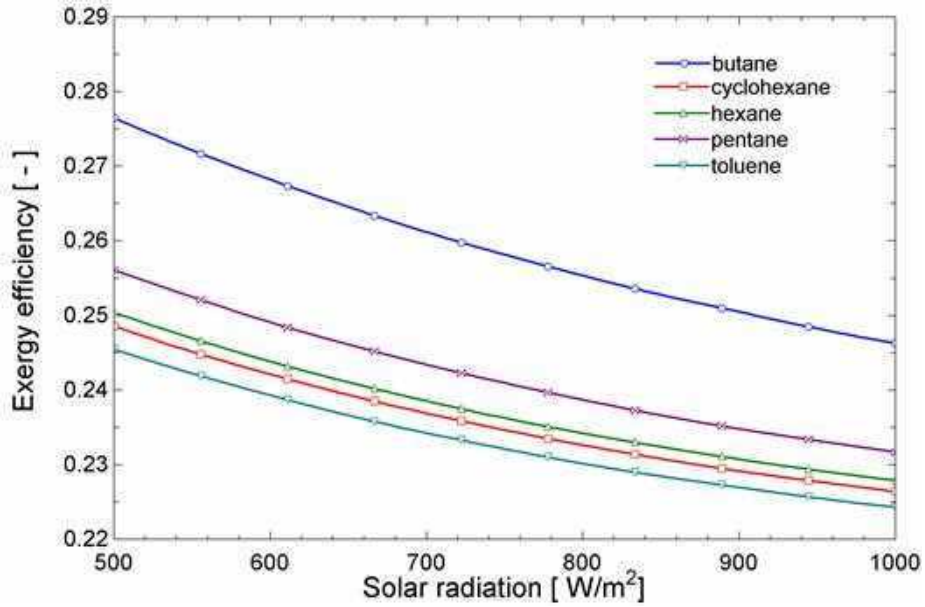


Figure 6. Effect of solar radiation on exergy efficiency for various organic working

Figure 7 exhibits the variation in power generation with respect to geothermal source temperature, while Figure 8 reveals the corresponding changes in energy efficiency for the five organic working fluids evaluated. As the geothermal well temperature increases from 90 to 105 °C, the power production of all working fluids improves steadily, primarily due to the increased thermodynamic potential available for turbine expansion. Toluene, hexane, and cyclohexane yield the highest electrical outputs, exceeding 145 kW at 105 °C, while butane, despite lower absolute values, maintains the most consistent incremental gains, starting from 88.08 kW at 90 °C and reaching 138.7 kW at the upper temperature bound. In parallel, the thermal efficiency shows a modest upward trend for all cases, with butane again leading in performance achieving an efficiency of 0.1058 at 105 °C. Pentane follows closely, while toluene lags slightly behind the others in terms of thermal utilization. These results indicate that both power generation and energy efficiency benefit from elevated geothermal source temperatures, although the relative rankings among fluids remain unchanged. This enhancement is primarily due to greater heat uptake and more favorable thermodynamic conditions achieved at elevated source temperatures.

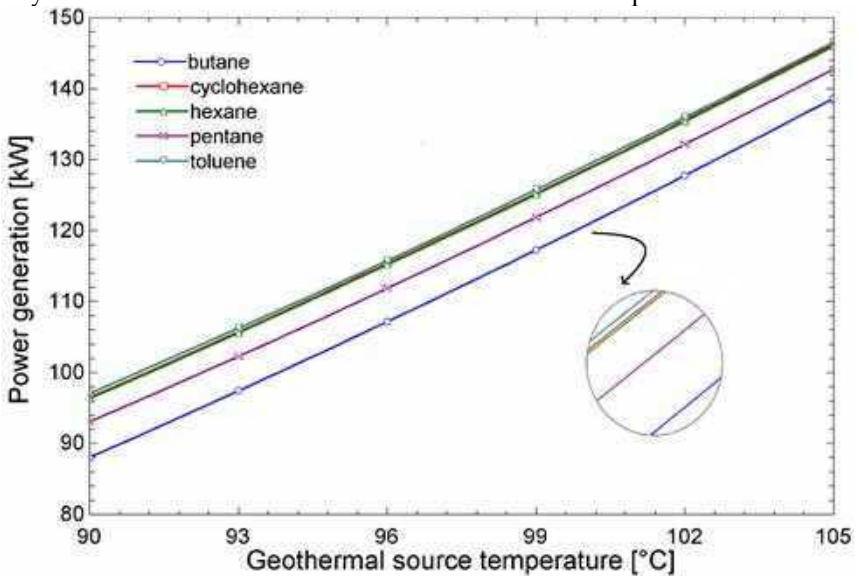


Figure 7. Effect of geothermal source temperature on power generation for various organic working fluids

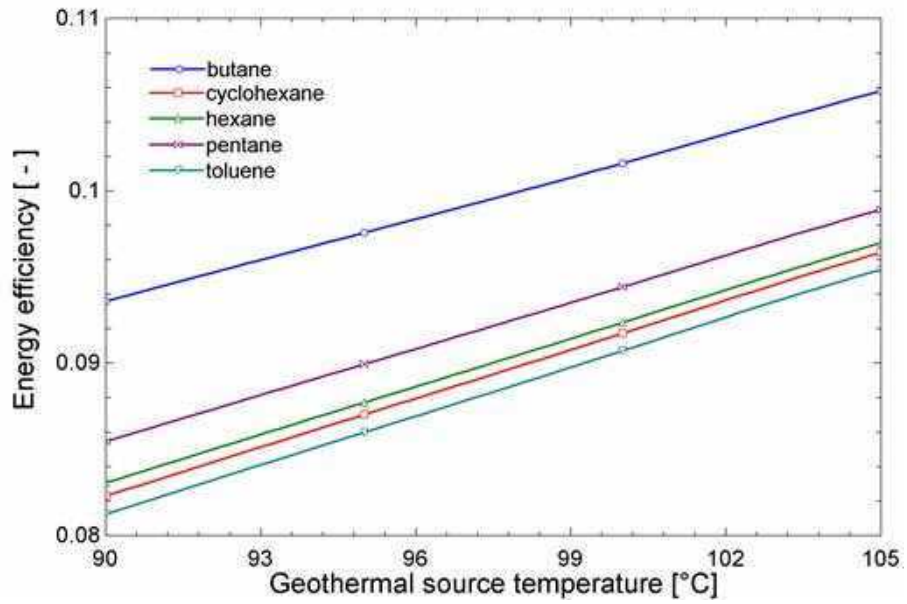


Figure 8. Effect of geothermal source temperature on energy efficiency for various organic working fluids

The influence of geothermal water temperature on the total exergy destruction of different working fluids is depicted in Figure 9. As evident from Figure 9, the total exergy irreversibility increases linearly with rising geothermal source temperature for all fluids. Butane consistently results in the highest exergy losses, reaching approximately 535.6 kW at 105 °C, likely due to its comparatively lower second-law performance. In contrast, toluene, hexane, and cyclohexane show the lowest destruction values, remaining below 529 kW throughout the examined range. Although higher geothermal temperatures supply more thermal energy to the cycle, they also intensify entropy generation in key components-particularly the evaporator and turbine-thereby amplifying internal irreversibilities within the system.

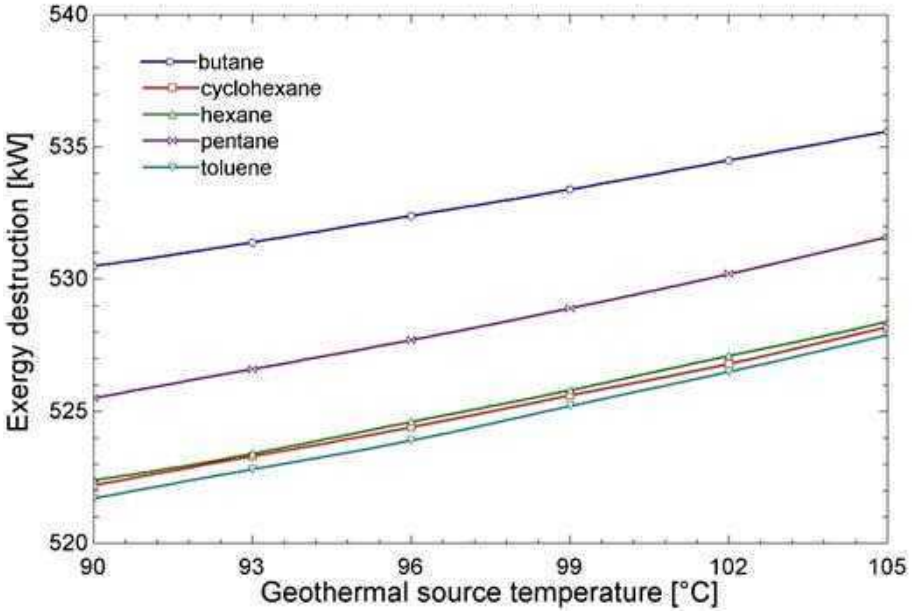


Figure 9. Effect of geothermal source temperature on exergy destruction for various organic working fluids

Figure 10 shows how exergy efficiency responds to rising geothermal source temperatures for the selected organic fluids. Unlike the trend observed with increasing solar radiation, where exergy efficiency tends to decline due to intensified irreversibilities, a rise in geothermal source temperature leads to a consistent enhancement in exergy-based performance. All fluids exhibit improved exergy efficiency with increasing source temperature, with butane demonstrating the highest overall performance—rising from 0.2374 at 90 °C to 0.2706 at 105 °C. Pentane follows closely, while toluene remains the least effective in exergy terms, reaching a maximum value of just 0.2507. These results emphasize that a moderate rise in geothermal well temperature can enhance the quality of energy conversion, improving the thermodynamic utilization of the input heat.

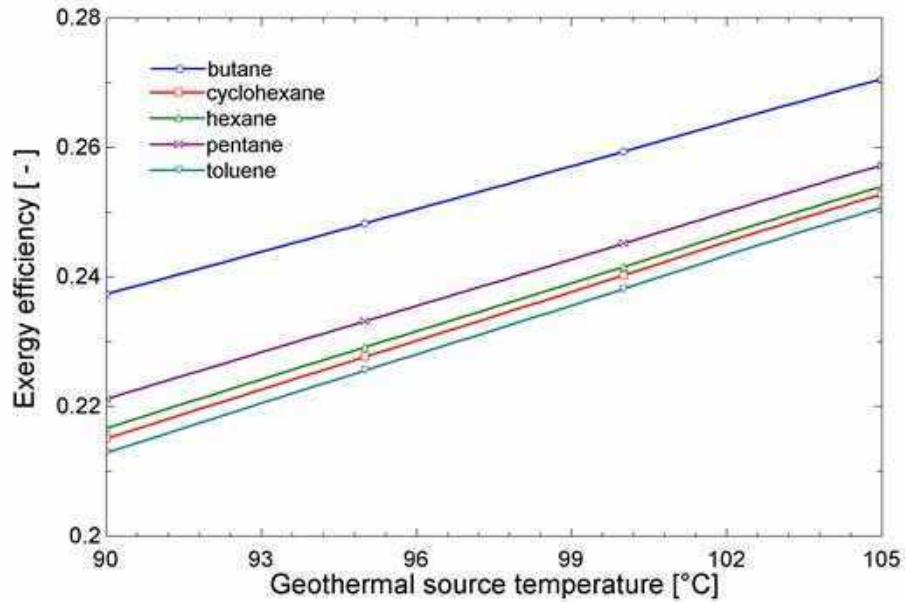


Figure 10. Effect of geothermal source temperature on exergy efficiency for various organic working fluids

Figure 11 presents the impact of geothermal mass flow rate on the net power output for different organic fluids within the ORC. As the flow rate raises from 3 to 7 kg/s, all fluids exhibit a nearly linear enhancement in power generation, driven by the elevated thermal energy transfer to the cycle. This behavior reflects the direct dependency of expansion work on the magnitude of heat input supplied by the geothermal source. From a quantitative perspective, toluene, hexane, and cyclohexane consistently deliver the highest power outputs, each exceeding 130 kW at the upper flow rate boundary. Pentane follows closely behind, whereas butane, despite showing a proportional rise, maintains the lowest output across the entire range-rising from 86.8 kW at 3 kg/s to 119.5 kW at 7 kg/s. These results highlight the strong sensitivity of system performance to mass flow variations and further demonstrate that higher flow rates enhance the conversion of geothermal energy into mechanical work across all fluids.

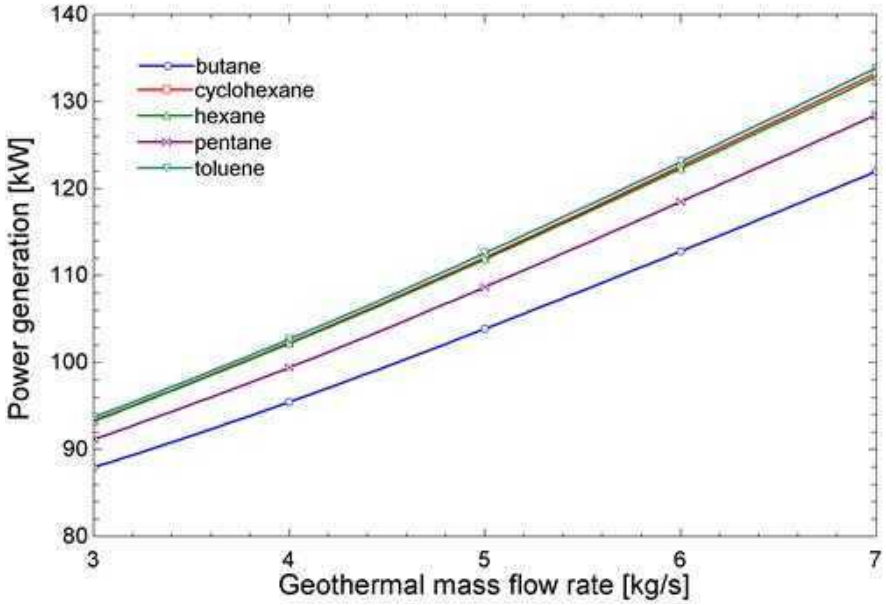


Figure 11. Effect of geothermal mass flow rate on power generation for various organic working fluids

Figure 12 displays the alteration of energy efficiency with respect to geothermal mass flow rate for the five working fluids under consideration. As the flow rate increases from 3 to 7 kg/s, a clear decreasing trend in energy efficiency is observed for all fluids. This behavior is primarily attributed to the diminishing thermal utilization ratio, where the rate of energy supplied to the plant increases more rapidly than the useful energy converted into work-resulting in lower first-law performance. Among the fluids, butane consistently maintains the highest energy efficiency throughout the entire range, decreasing from 0.1094 at 3 kg/s to 0.09586 at 7 kg/s, corresponding to a reduction of approximately 12.4%. Pentane ranks second, while toluene demonstrates the lowest efficiency values, declining from 0.09838 to 0.08044. The relative difference in efficiency between the best (butane) and worst (toluene) performing fluids becomes more pronounced at higher mass flow rates, suggesting that fluid selection is particularly critical under elevated flow conditions. Overall, the results indicate a trade-off between increased power generation and reduced thermal performance as the geothermal flow rate rises.

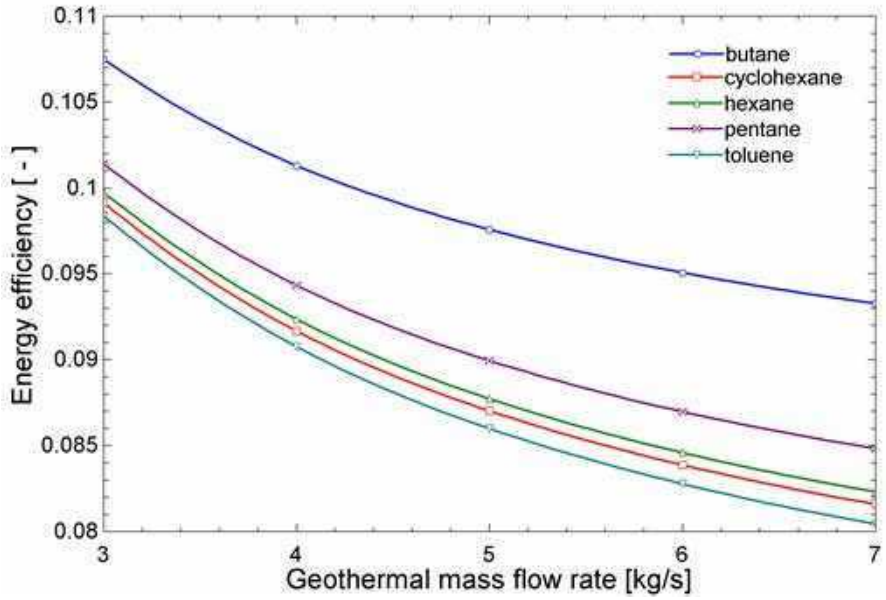


Figure 12. Effect of geothermal mass flow rate on energy efficiency for various organic working fluids

Figures 13 and 14 jointly illustrate the thermodynamic effect of increasing geothermal mass flow rate on exergy destruction and second-law efficiency for the examined working fluids. With increasing flow rate, all working fluids demonstrate a continuous rise in exergy destruction, accompanied by a gradual decline in exergy efficiency. Although higher thermal input enhances power production, it also leads to increased irreversibilities, thereby diminishing the system's capacity to utilize available exergy efficiently. Numerically, butane again results in the highest exergy destruction, reaching approximately 561.6 kW at 7 kg/s, while toluene and hexane remain under 548 kW. In terms of efficiency, butane maintains superior performance across the range, decreasing from 0.2786 to 0.2415, whereas toluene drops from 0.2585 to 0.2108, marking the lowest second-law efficiency among all fluids. The widening performance gap at higher flow rates underscores the critical role of fluid selection in managing thermodynamic losses under varying load conditions.

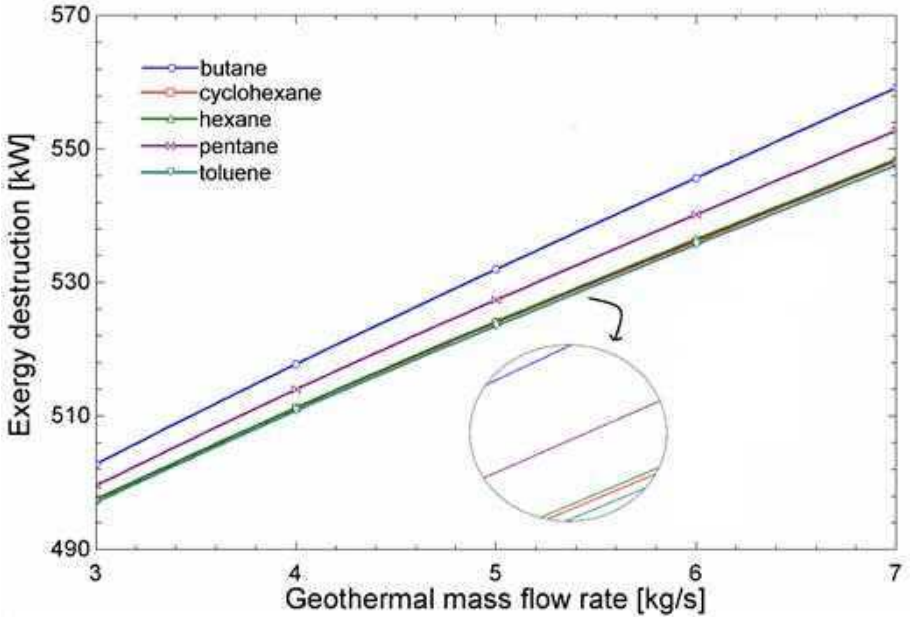


Figure 13. Impact of geothermal mass flow rate on exergy destruction for various organic working fluids

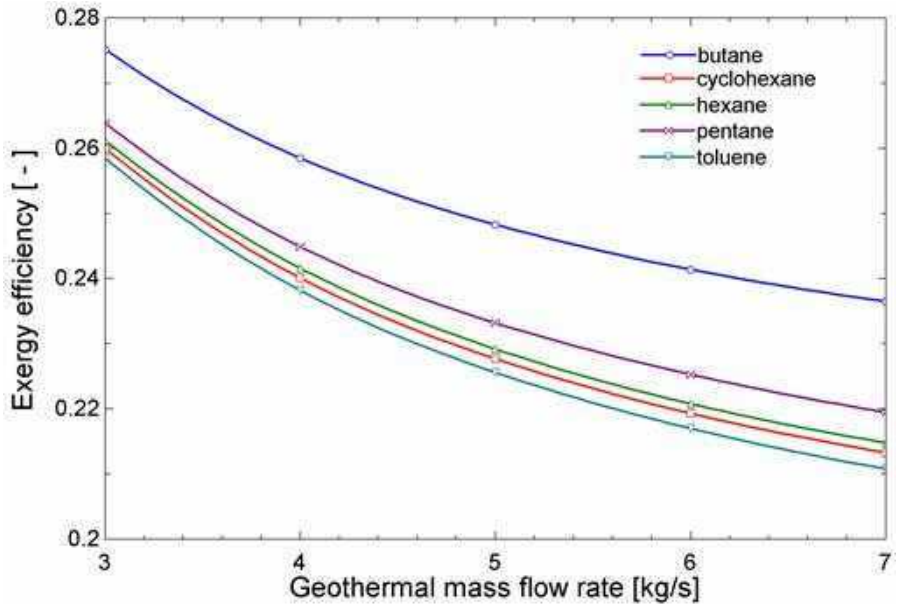


Figure 14. Effect of geothermal mass flow rate on exergy efficiency for various organic working fluids

A comparison of the present study with previous research is summarized in Table 4. Reported energy and exergy efficiencies vary considerably depending on the energy source and selected working fluids. For instance, geothermal and solar integrated systems achieved energy efficiencies of 9.99-15.96% and exergy efficiencies of 19.22-30.39% with n-pentane, isopentane, and R1234yf [30]. Purely solar-based ORCs reported values between 10.4-20.8% for energy and 11.0-19.0% for exergy performance with fluids such as cyclohexane and toluene [6]. In contrast, waste heat-driven cycles generally showed lower energy efficiencies (6.45-13.25%) [31], while geothermal energy-based ORCs ranged from 2.19-5.32% in energy efficiency and 11.69-28.41% in exergy efficiency using refrigerants like R113, R245fa, and butane [32]. Within this context, the proposed hybrid configuration achieved energy and exergy efficiencies of 8.60-9.76% and 22.56-24.83%, respectively, with five dry organic fluids including butane, pentane, toluene, cyclohexane, and hexane. These results are consistent with the ranges reported in the literature, confirming that the integration of solar and geothermal resources provides competitive thermodynamic performance and enhances the applicability of ORC systems for sustainable power generation.

Table 4. Performance comparison with another research

Reference	Energy sources	Energy efficiency [%]	Exergy efficiency [%]	Fluids
Ref. [34]	Geothermal + Solar	9.99 - 15.96	19.22 - 30.39	n-pentane, isopentane, R1234yf, R1234ze, R600, R600a, R152a, R161, R134a
Ref. [6]	Solar	10.4 - 20.8	11.0 - 19.0	Cyclohexane, hexane, propane, toluene, R123, R11, R143A
Ref. [35]	Waste heat	6.45 - 13.25	-	R1234yf, R134a, R1234ze, R152a, R600a, R600, R236ea, R1233zd, n-pentane, R113
Ref. [36]	Geothermal	2.19 - 5.32	11.69 - 28.41	R113, R11, n-pentane, isopentane, R245fa, n-butane, R114, HFE-245mc, R142b, isobutane
This study	Geothermal + Solar	8.60 - 9.76	22.56 - 24.83	Butane, cyclohexane, hexane, pentane, toluene

4. CONCLUSIONS

In this research, the thermodynamic performance of an integrated solar-geothermal ORC system was comparatively assessed for five different organic working fluids. To simulate the integrated plant, the EES software have been used. The steady-state analysis revealed that butane achieved the highest exergy efficiency of 0.2483, despite delivering the lowest net power output of 103.9 kW, primarily due to its limited heat absorption capability. In contrast, toluene provided the maximum net power generation of 112.6 kW and the lowest exergy destruction of 523.5 kW, while exhibiting the lowest energy (0.086) and exergy (0.2256) efficiencies. Cyclohexane and hexane demonstrated balanced performance, each yielding approximately 112 kW of net power with moderate exergy efficiencies in the range of 0.228-0.229. Pentane, although not leading in any single criterion, showed a favorable compromise with an energy efficiency of 0.08995, an exergy efficiency of 0.2332, and manageable irreversibilities.

The parametric evaluation further emphasized the influence of operational variables on system performance. With increasing solar radiation (500-1000 W/m^2), net power generation exhibited an almost linear increase for all fluids, with toluene reaching 116.2 kW at maximum irradiation, while butane remained the lowest at 105.6 kW. Energy efficiency also improved with radiation, peaking at 0.1007 for butane, whereas toluene recorded the lowest efficiency. In contrast, exergy efficiency decreased under higher solar input, dropping from 0.2824 to 0.2506 for butane and from 0.2455 to 0.2243 for toluene, owing to intensified irreversibilities.

For geothermal source temperature variations, both power output and efficiencies improved. Toluene, hexane, and cyclohexane exceeded 145 kW at 105 °C, while butane increased from 88.08 kW to 138.7 kW, achieving the highest energy efficiency of 0.1058 at this condition. Exergy efficiency also improved, with butane rising from 0.2374 to 0.2706. On the other hand, total exergy destruction increased steadily with source temperature, with butane recording the highest value of 535.6 kW.

When the geothermal mass flow rate was raised from 3 to 7 kg/s, power generation increased linearly across all fluids, with toluene, hexane, and cyclohexane surpassing 130 kW at the upper bound, while butane reached 119.5 kW. However, both energy and exergy efficiencies declined due to growing irreversibilities; for instance, butane's energy efficiency decreased from 0.1094 to 0.09586, and its exergy efficiency from 0.2786 to 0.2415, whereas toluene exhibited the lowest efficiency values.

In summary, the integrated solar-geothermal ORC exhibits distinct performance trade-offs depending on the chosen working fluid and operational conditions. While butane consistently offers the best energy and exergy efficiencies, its power generation remains limited. Toluene, conversely, ensures the highest power output but at the expense of lower efficiencies. Pentane, cyclohexane, and hexane present well-balanced alternatives, combining competitive efficiencies with relatively high-power generation. The parametric results demonstrate that enhanced solar radiation and geothermal temperature positively affect power and energy performance, albeit with increasing irreversibilities, whereas higher mass flow rates improve output but reduce efficiency. These findings indicate that the choice of working fluid and the associated operating conditions must be selected in accordance with the intended performance objective, whether emphasizing efficiency or maximizing power generation.

For future research, the current thermodynamic model could be extended to include multi-objective optimization approaches aimed at simultaneously maximizing efficiency and minimizing exergy destruction. Furthermore, techno-economic assessments are essential to evaluate the cost-effectiveness and practical feasibility of deploying such systems at scale. Incorporating environmental indicators such as lifecycle emissions and water consumption would also strengthen the sustainability perspective. Such extensions would provide a more comprehensive framework for designing hybrid ORCs that are not only thermodynamically robust but also economically viable and environmentally responsible.

Declaration of Ethical Standards

The author confirms that this original research was conducted in full compliance with ethical guidelines, including authorship, citation, and data reporting.

Credit Authorship Contribution Statement

Serpil Celik Toker: Conceptualization, Methodology, Software, Formal analysis, Investigation, Writing – original draft, Visualization, Supervision.

Declaration of Competing Interest

The author declares that there are no known competing financial interests or personal relationships that could have appeared to influence the work reported in this paper.

Funding / Acknowledgements

The author declares no funding was received to support this research.

Data Availability

The data supporting the findings of this study are available from the author upon request.

Use of Artificial Intelligence

Generative artificial intelligence (AI) tools were used solely for language editing, grammar correction, and readability improvement during the preparation of this manuscript. These tools were not used to generate scientific content, research data, interpretations, analyses, figures, tables, or conclusions. All scientific evaluations, thermodynamic analyses, and interpretations were performed entirely by the authors. The authors have carefully reviewed and approved the final version of the manuscript and remain fully responsible for its accuracy, originality, integrity, and compliance with ethical and legal standards.

5. REFERENCES

[1] P. Achakulwisut, P. Erickson, C. Guivarch, R. Schaeffer, E. Brutschin, and S. Pye, "Global fossil fuel reduction pathways under different climate mitigation strategies and ambitions," *Nat. Commun.*, vol. 14, no. 1, pp. 1–15, 2023.

[2] E. Bellos, "A review of organic Rankine cycles with partial evaporation and dual-phase expansion," *Sustain. Energy Technol. Assessments*, vol. 72, p. 104059, Dec. 2024.

[3] B. F. Tchanche, G. Lambrinos, A. Frangoudakis, and G. Papadakis, "Low-grade heat conversion into power using organic Rankine cycles – A review of various applications," *Renew. Sustain. Energy Rev.*, vol. 15, no. 8, pp. 3963–3979, Oct. 2011.

[4] H. U. Helvaci and Z. A. Khan, "Thermodynamic modelling and analysis of a solar organic Rankine cycle employing thermofluids," *Energy Convers. Manag.*, vol. 138, pp. 493–510, Apr. 2017.

[5] A. Ramos, M. A. Chatzopoulou, J. Freeman, and C. N. Markides, "Optimisation of a high-efficiency solar-driven organic Rankine cycle for applications in the built environment," *Appl. Energy*, vol. 228, pp. 755–765, Oct. 2018.

[6] G. Wang, S. Zhang, and T. Zou, "Design and comparison study of a novel linear Fresnel reflector solar ORC-driven hydrogen production system using different working fluids," *Case Stud. Therm. Eng.*, vol. 71, p. 106187, Jul. 2025.

[7] Q. Sun, D. Lin, M. Khayatnezhad, and M. Taghavi, "Investigation of phosphoric acid fuel cell, linear Fresnel solar reflector and Organic Rankine Cycle polygeneration energy system in different climatic conditions," *Process Saf. Environ. Prot.*, vol. 147, pp. 993–1008, Mar. 2021.

[8] G. P. Piñerez, G. V. Ochoa, and J. Duarte-Forero, "Energy, exergy, and environmental assessment of a small-scale solar organic Rankine cycle using different organic fluids," *Heliyon*, vol. 7, no. 9, p. e07947, Sep. 2021.

[9] D. Gonidaki, E. Bellos, and J. K. Kaldellis, "Design and dynamic simulation of a solar-driven organic Rankine cycle with zeotropic mixture," *Sol. Energy*, vol. 301, p. 113948, Nov. 2025.

[10] M. Alrbai, A. Al Masri, S. Abu-Dabaseh, M. Abusorra, and H. Hayajneh, "Thermodynamic assessment of hybrid solar-geothermal organic Rankine cycle: An exergy and energy-based analysis," *Energy Explor. Exploit.*, no. March, 2025.

[11] M. Alibaba, R. Pourdarbani, M. H. Khoshgoftar Manesh, I. Herrera-Miranda, I. Gallardo-Bernal, and J. L. Hernández-Hernández, "Conventional and advanced exergy-based analysis of hybrid

geothermal-solar power plant based on ORC cycle," *Appl. Sci.*, vol. 10, no. 15, 2020.
[12] R. Maali and T. Khir, "Performance analysis of different orc power plant configurations using solar and geothermal heat sources," *Int. J. Green Energy*, vol. 17, no. 6, pp. 349–362, 2020.
[13] D. Li *et al.*, "Resource endowments effects on thermal-economic efficiency of ORC-based hybrid solar-geothermal system," *Case Stud. Therm. Eng.*, vol. 52, p. 103739, Dec. 2023.
[14] D. Tempesti, G. Manfrida, and D. Fiaschi, "Thermodynamic analysis of two micro CHP systems operating with geothermal and solar energy," *Appl. Energy*, vol. 97, pp. 609–617, Sep. 2012.
[15] A. Bozkurt, M. S. Genç, and S. S. Seyitoğlu, "7E analysis of a low-temperature geothermal and solar energy integrated hybrid system for sustainable power and hydrogen generation," *Therm. Sci. Eng. Prog.*, vol. 66, p. 104073, Oct. 2025.
[16] X. Zhang, M. Cao, X. Yang, H. Guo, and J. Wang, "Economic analysis of Organic Rankine Cycle using R123 and R245fa as working fluids and a demonstration project report," *Appl. Sci.*, vol. 9, no. 2, 2019.
[17] P. J. Mago, L. M. Chamra, K. Srinivasan, and C. Somayaji, "An examination of regenerative organic Rankine cycles using dry fluids," *Appl. Therm. Eng.*, vol. 28, no. 8–9, pp. 998–1007, Jun. 2008.
[18] A. Javanshir, N. Sarunac, and Z. Razzaghpanah, "Thermodynamic analysis of a regenerative organic Rankine cycle using dry fluids," *Appl. Therm. Eng.*, vol. 123, pp. 852–864, Aug. 2017.
[19] E. Bellos, "A detailed analysis of waste heat recovery organic Rankine cycle with partial evaporation and different working fluids," *Appl. Therm. Eng.*, vol. 263, p. 125410, Mar. 2025.
[20] J. Sun and B. Peng, "Experimental study on the matching characteristics of working fluid types and heat sources based on the organic Rankine cycle system," *Case Stud. Therm. Eng.*, vol. 72, p. 106336, Aug. 2025.
[21] X. Zhang and Y. Li, "An examination of super dry working fluids used in regenerative organic Rankine cycles," *Energy*, vol. 263, p. 125931, Jan. 2023.
[22] K. Shahverdi *et al.*, "Energy harvesting using solar ORC system and Archimedes Screw Turbine (AST) combination with different refrigerant working fluids," *Energy Convers. Manag.*, vol. 187, pp. 205–220, May 2019.
[23] S. Akbari, S. Faghiri, A. M. Zinjanabi, M. A. Bijarchi, M. B. Shafii, and K. Hosseinzadeh, "Thermo-economic investigation and comparative multi-objective optimization of dual-pressure evaporation ORC using binary zeotropic mixtures as working fluids for geothermal energy application," *Int. J. Thermofluids*, vol. 24, p. 100899, Nov. 2024.
[24] T. C. Hung, "Waste heat recovery of organic Rankine cycle using dry fluids," *Energy Convers. Manag.*, vol. 42, no. 5, pp. 539–553, Mar. 2001.
[25] T. C. Hung, T. Y. Shai, and S. K. Wang, "A review of organic rankine cycles (ORCs) for the recovery of low-grade waste heat," *Energy*, vol. 22, no. 7, pp. 661–667, Jul. 1997.
[26] N. B. Desai and S. Bandyopadhyay, "Process integration of organic Rankine cycle," *Energy*, vol. 34, no. 10, pp. 1674–1686, Oct. 2009.
[27] J. Bao and L. Zhao, "A review of working fluid and expander selections for organic Rankine cycle," *Renew. Sustain. Energy Rev.*, vol. 24, pp. 325–342, Aug. 2013.
[28] M. A. Emadi, N. Chitgar, O. A. Oyewunmi, and C. N. Markides, "Working-fluid selection and thermoeconomic optimisation of a combined cycle cogeneration dual-loop organic Rankine cycle (ORC) system for solid oxide fuel cell (SOFC) waste-heat recovery," *Appl. Energy*, vol. 261, p. 114384, Mar. 2020.
[29] S. A. Kalogirou, *Solar energy engineering: Processes and systems*. 2009.
[30] F. Dione, A. Thiam, E. H. I. Cisse, D. Diouf, and A. S. Maiga, "Theoretical study of an NH3–H2O absorption chiller powered by a linear Fresnel system modelled by combining ray tracing and CFD," *Results Eng.*, vol. 20, p. 101410, Dec. 2023.
[31] K. Sun, T. Zhao, S. Wu, and S. Yang, "Comprehensive evaluation of concentrated solar collector and Organic Rankine cycle hybrid energy process with considering the effects of different heat transfer fluids," *Energy Reports*, vol. 7, pp. 362–384, Nov. 2021.

[32] Q. Sun, D. Lin, M. Khayatnezhad, and M. Taghavi, "Investigation of phosphoric acid fuel cell, linear Fresnel solar reflector and Organic Rankine Cycle polygeneration energy system in different climatic conditions," *Process Saf. Environ. Prot.*, vol. 147, pp. 993–1008, Mar. 2021.

[33] S. A. Mousavi Rabeti, M. H. Khoshgoftar Manesh, and M. Amidpour, "Techno-economic and environmental assessment of a novel polygeneration system based on integration of biomass air-steam gasification and solar parabolic trough collector," *Sustain. Energy Technol. Assessments*, vol. 56, p. 103030, Mar. 2023.

[34] A. Khosravi, S. Syri, X. Zhao, and M. E. H. Assad, "An artificial intelligence approach for thermodynamic modeling of geothermal based-organic Rankine cycle equipped with solar system," *Geothermics*, vol. 80, pp. 138–154, Jul. 2019.

[35] E. Bellos, "A detailed analysis of waste heat recovery organic Rankine cycle with partial evaporation and different working fluids," *Appl. Therm. Eng.*, vol. 263, p. 125410, Mar. 2025.

[36] Z. Özcan and Ö. Ekici, "A novel working fluid selection and waste heat recovery by an exergoeconomic approach for a geothermally sourced ORC system," *Geothermics*, vol. 95, p. 102151, Sep. 2021.

Konya Mühendislik Bilimleri Dergisi., c.14, s.2, 719-740, 2026
Konya Journal of Engineering Sciences v.14, n.2, 719-740, 2026
ISSN: 2667-8055 (Electronic)
DOI: 10.36306/konjes.1541472

OPTICAL FLOW-BASED LIDAR ODOMETRY

[1]Mesut TUNÇER*, [2]Alper KILIÇ

[1,2] Konya Technical University, Engineering and Natural Sciences Faculty, Computer Engineering Department, Konya, TÜRKİYE
[1]mesuttuncer@sharkaviation.com.tr, [2]akilic@ktun.edu.tr

Highlights

- A planar LiDAR-only method is proposed for displacement estimation in 2D SLAM.
- The method uses 360-degree LiDAR scans without external positioning aid.
- Optical flow is applied to scan data to track planar measurement changes.
- The approach estimates indoor planar displacement in GNSS-denied areas.
- LiDAR-based planar motion verification is proposed as an indoor GNSS counterpart.

***Corresponding Author:** Mesut TUNÇER, mesuttuncer@sharkaviation.com.tr

Konya Mühendislik Bilimleri Dergisi., c.14, s.2, 719-740, 2026
Konya Journal of Engineering Sciences v.14, n.2, 719-740, 2026
ISSN: 2667-8055 (Electronic)
DOI: 10.36306/konjes.1541472

OPTICAL FLOW-BASED LIDAR ODOMETRY

[1,*]Mesut TUNÇER, [2]Alper KILIÇ

[1,2]Konya Technical University, Engineering and Natural Sciences Faculty, Computer Engineering Department, Konya, TÜRKİYE
[1]mesuttuncer@sharkaviation.com.tr, [2]akilic@ktun.edu.tr

(Received: 31.08.2024; Accepted in Revised Form: 24.11.2025)

ABSTRACT: In this study, data obtained from a 360-degree (or 2D) Light Detection and Ranging sensor, which is commonly used for Simultaneous Localization and Mapping, were converted into an image/frame matrix to apply optical flow methods. Key features on the resulting image matrix were identified as corners using the Shi-Tomasi method. The positional changes of these key features during each complete measurement cycle of the LiDAR sensor were calculated using the Lucas-Kanade method, an optical flow technique. These positional changes were analyzed to estimate the vehicle's displacement within the environment. The developed method was tested in a simulation environment with different object densities, moving linearly at different speeds, both constant and variable.

Keywords: *Lidar odometry, Navigation, Optical-Flow, Simultaneous Localization and Mapping (SLAM)*

1. INTRODUCTION

Simultaneous Localization and Mapping (SLAM) is a cornerstone technology in the rapidly advancing fields of robotics, autonomous systems, and artificial intelligence [1], [2]. SLAM enables these systems to simultaneously navigate through and construct a map of an unknown environment, forming the backbone of autonomous operations [3], [4], [5]. By integrating mapping and localization into a unified framework, SLAM facilitates tasks ranging from precise indoor navigation to complex outdoor exploration in dynamic and unpredictable terrains [6]. This capability is essential for applications such as autonomous vehicles [7], delivery drones [8], [9], service robots [10], [11], and even planetary exploration rovers [12], [13]. The ability to map and localize in real time provides these systems with a robust situational awareness, allowing for efficient obstacle detection [14], artificial landmark-assisted SLAM [15], displacement measurement [16], path planning, robot detection and positioning using machine learning methods [17], [18], and decision-making [19], [20]. Furthermore, studies have explored mapless navigation in unknown environments [21]. Among the diverse array of sensor technologies employed in SLAM, 2D LiDAR (Light Detection and Ranging) sensors have emerged as a preferred choice due to their unique balance of accuracy, robustness, and cost-effectiveness [22], [23]. These sensors operate by emitting laser pulses and measuring the time-of-flight of the returning reflections, a process that yields highly accurate distance measurements [24], [25]. The data collected by 2D LiDAR is instrumental in constructing precise 2D maps, a prerequisite for reliable navigation, particularly in confined or structured spaces [26]. The wide field of view, high resolution, and ability to function in varying lighting conditions make 2D LiDAR sensors suitable for a range of applications, from warehouse robots navigating indoor facilities to autonomous drones mapping outdoor landscapes.

However, utilizing 2D LiDAR for SLAM is not without challenges. Dynamic environments, where obstacles such as people or vehicles move unpredictably, can introduce significant noise and uncertainty into the sensor data [27]. Similarly, environments characterized by repetitive structures, such as hallways or open fields with few distinctive features, can impede SLAM algorithms' ability to maintain accurate

***Corresponding Author:** Mesut TUNÇER, mesuttuncer@sharkaviation.com

localization [28]. Furthermore, sensor performance can degrade in the presence of environmental factors like rain, dust, or reflective surfaces, complicating data interpretation and increasing the computational burden [29]. Addressing these challenges requires the development of advanced algorithms capable of filtering noise, detecting and adapting to environmental changes, and leveraging complementary sensor modalities for robust performance. Optical flow, an image processing technique widely used across robotics and computer vision, offers a promising approach to supplement LiDAR-based SLAM systems [30]. Optical flow calculates the apparent motion of objects or features within a sequence of images, providing valuable insights into environmental dynamics [31], [32], [33]. By analyzing the displacement of pixels between successive frames, optical flow techniques can enhance the understanding of motion, enabling applications such as motion detection, object tracking, and even human activity recognition [34], [35], [36]. In robotics, optical flow is frequently employed for tasks like visual odometry, feature tracking, and collision avoidance [37], [38], [39].

Several computational methods exist for calculating optical flow, each with its unique strengths and limitations. The Lucas-Kanade Method, for instance, is a local technique that calculates optical flow within small image patches, assuming constant motion within each patch. It solves a system of linear equations to estimate the motion vectors, making it well-suited for tracking small, localized movements [40], [41]. The Horn-Schunck Method, in contrast, computes a global optical flow field across the entire image by solving an optimization problem that balances motion smoothness with data fidelity [42], [43]. Meanwhile, the Farneback Method utilizes polynomial approximations to capture complex, non-linear motion patterns, making it effective for scenarios involving deformable or irregular objects [44].

Various Visual Odometry-based solutions have been proposed in the literature for the same problem [45], [46], [47]. However, these methods, due to the perspective projection of the different types of camera sensors they use, lead to the optical flow being distributed in different directions across various regions of the image plane, which complicates the system and introduces errors [48]. In this study, however, an overhead orthogonal imaging approach has been adopted instead of perspective projection, resulting in a more homogeneous data flow for the system. This fundamental difference allows the proposed method to distinguish itself from traditional visual odometry approaches and be positioned closer to mapping-oriented solutions. Although the combined use of the terms optical flow and odometry often implies visual odometry when used together, this study is outside the scope of Visual Odometry due to its approach to the problem.

Laser odometry is a method used to precisely track the movement and determine the position of a vehicle or robot using LiDAR sensors. This method is particularly preferred in situations where GPS signals are insufficient or environmental conditions are challenging, as it estimates motion by comparing consecutive LiDAR scans. In this context, a study presented in [49] developed a robust localization system for dynamic urban environments using LiDAR sensors. Similarly, a study in [50] proposed an NDT-based LiDAR odometry method to periodically correct position errors in outdoor environments where GPS signals are unavailable.

In [51], a lightweight and efficient optical flow estimation model was developed for LiDAR image sequences. The proposed approach is based on two main components: integrating an attention mechanism into the model to extract more meaningful features from LiDAR images, which have different spatial distribution characteristics compared to color images, and adopting an unsupervised learning strategy considering the limited availability of large-scale and labeled LiDAR data. In this direction, the model aims to minimize the discrepancy between the reconstructed image and the reference image based on the directly estimated flow.

In [52], a novel method is proposed that can be used in autonomous vehicles to replace RGB cameras, which lose reliability during adverse weather conditions or night driving. The approach is based on a

CNN-based architecture that can estimate high-resolution and dense optical flow using only sparse and low-resolution LiDAR data. A pseudo-ground-truth optical flow dataset consisting of approximately 20,000 samples generated by FlowNet2 [53] was created using LiDAR data selected from the KITTI dataset for training. Although [51] and [52] employ perspective-based optical flow using cameras, the literature does not present an orthogonal formulation comparable to the one introduced in the proposed method.

RF2O (Range Flow-based 2D Odometry) [54], developed for laser scanners, has achieved significant success in planar motion estimation by introducing a dense alignment method based on scan gradients instead of traditional matching-based approaches. This initial work, by using a range flow constraint equation for each scanned point and a Cauchy M-estimator for robustness against moving objects, yielded results that were both more accurate and up to 20 times faster (~0.9 ms) than methods such as PL-ICP [55] and PSM [56]. Building on this foundation, a subsequent work [57], called SRF-Odometry (Symmetric Range Flow-based Odometry), took this approach even further with two key innovations: first, a symmetric representation of the geometric coherence, which yields more accurate results, especially for large displacements; The second is an innovative multi-scan formulation that aligns the incoming scan, the previous scan, and the key scan together, improving robustness against erroneous key scan selection and moving objects. These improvements make SRF-Odometry an order of magnitude faster than its competitors, with a runtime of approximately 1 millisecond, and have proven its accuracy by reducing trajectory deviation to levels of 2%.

In this study, a novel approach was employed to integrate an optical flow technique with LiDAR-based SLAM. Specifically, the key features in angle-dependent distance data obtained from a 2D LiDAR sensor were identified as corner points using the Shi-Tomasi method, a robust corner detection algorithm renowned for its precision and computational efficiency [58], [59]. These key features, corresponding to distinct environmental landmarks, were then tracked across successive LiDAR scans using the Lucas-Kanade method. By analyzing the positional changes of these features, the relative motion of the vehicle was calculated.

2. MATERIAL AND METHODS

The proposed method is based on the conversion of the angle and the corresponding distance data obtained from the 2D LiDAR sensor from a cylindrical coordinate plane to a Cartesian coordinate plane to create an image frame. To increase the applicability of the Shi–Tomasi [58], [59] algorithm and to enhance the clarity of the determined points, a morphological dilation operation is applied to the image frame to place a square of a certain size around each LiDAR data location. The position changes of key points between two consecutive image frames are calculated using the Lucas–Kanade optical flow algorithm, and the vehicle's position change per unit time is obtained by dividing the displacement of the points obtained by optical flow by the metric value represented by a pixel.

The proposed approach demonstrates that the displacement calculated at the pixel level can be related to the position change in the real environment by converting LiDAR data into image representation and analyzing it with optical flow techniques and proves the feasibility of optical flow-based indoor navigation.

2.1. Mapping LiDAR Measurements to Image Frame

The Polar-to-Cartesian transformation for the angles (θ_k) and ranges (r_k) measured in a full circular scanning step (k) is provided by Equation 1. The angular orientation offset (θ_0) of the scanning LiDAR sensor allows for configurations at different angles. The approach in Equation 1 considers LiDAR data

from a top-down plane, rather than from the sensor's perspective; thus, the resulting distance data is represented directly from an orthographic view.

$$\begin{bmatrix} x_k \\ y_k \end{bmatrix} = \begin{bmatrix} \cos(\theta_k + \theta_0) \\ \sin(\theta_k + \theta_0) \end{bmatrix} r_k \tag{1}$$

An orthogonal image plane $\Omega = 1, \dots, W \times 1, \dots, H$ and a meter-to-pixel scale factor ($s > 0$) are used to generate the image frame $\mathcal{F}_k \in \{0,1\}^{HxW}$ by selecting pixel coordinates according to Equation (2). The operation given in Equation (2) represents the alignment of each pixel with respect to the center of the image frame and is therefore referred to as the centralization process.

$$\begin{bmatrix} x_k^* \\ y_k^* \end{bmatrix} = \left\lfloor \frac{1}{s} \begin{bmatrix} 1 & 0 \\ 0 & -1 \end{bmatrix} \begin{bmatrix} x_k \\ y_k \end{bmatrix} \right\rfloor + \begin{bmatrix} c_x \\ c_y \end{bmatrix} \tag{2}$$

In Equation (2), $(c_x, c_y) = (\lfloor W/2 \rfloor, \lfloor H/2 \rfloor)$ denotes the center pixel. To facilitate corner detection, a filled square of size $(p_s \times p_s)$ is generated around each (x_k^*, y_k^*). On the created image frame, a Gaussian smoothing with a standard deviation of σ_g is applied, and the final image frame is obtained as given in Equation (3).

$$\check{\mathcal{F}}_k = G_{\sigma_g} * \mathcal{F}_k \tag{3}$$

The operations performed in Equations 1 and 2 are visualized sequentially in Figure 1.

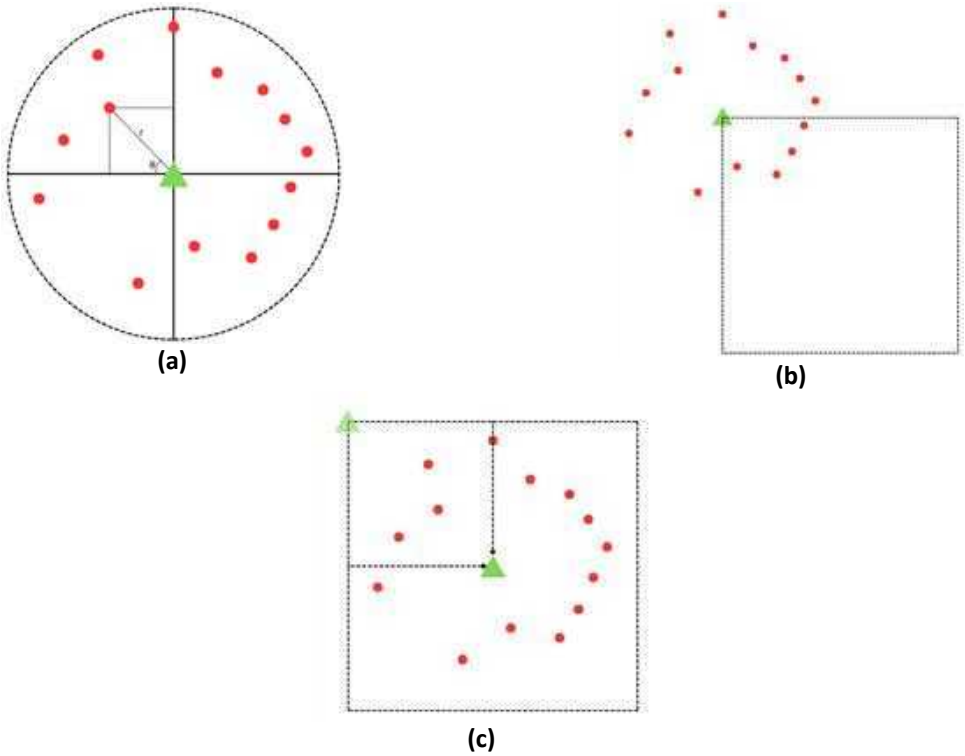


Figure 1. Transformation processes of LiDAR data. **(a)** shows the angle-dependent distance data obtained from 2D LiDAR. **(b)** shows the matrix obtained as a result of the transformation of the data in **(a)** in Equation 1. **(c)** shows the image frame resulting from the centralization process of the data in **(b)** in Equation 2

2.2. Detecting Keypoints in Image Frame

In this study, the Shi-Tomasi algorithm [58], which is an improved version of the Harris corner detection algorithm [60], was used. While using the Shi-Tomasi algorithm, Sobel Filter [61] gradient operators were used to calculate I_x and I_y on the x and y axes. The local window ($\mathcal{W}(\mathbf{j})$) around each point $\mathbf{j}$ and the matrix in Equation (4) for $\forall \mathbf{j} \in \Omega$ are defined.

$$\mathbf{M}_k(\mathbf{j}) = \begin{bmatrix} \sum_{w(\mathbf{j})} I_x^2 & \sum_{w(\mathbf{j})} I_x I_y \\ \sum_{w(\mathbf{j})} I_x I_y & \sum_{w(\mathbf{j})} I_y^2 \end{bmatrix} \tag{4}$$

Unlike the Harris algorithm, the Shi-Tomasi criterion (ξ_k) in Equation (5) is taken as the threshold, with eigenvalues $\lambda_1 \geq \lambda_2 \geq 0$.

$$\xi_k = \min(\lambda_1, \lambda_2) \tag{5}$$

Based on the threshold defined in Equation (5), the best N_{max} corners are selected with a minimum spacing of d_{min}. The stopping criterion, as described in Equations (6) and (7), is iteratively updated for $\forall \mathbf{p} \in \Omega$, with a maximum of n_{max}^{sp} iterations or until the increment satisfies $\|\delta_k(\mathbf{p})\| < \varepsilon_{sp}$.

$$\delta_k(\mathbf{p}) = -\nabla^2 \mathcal{S}_k\big(\mathbf{p}_k(\mathbf{p})\big)^{-1} \mathbf{g}_k(\mathbf{p}) \tag{6}$$

$$\mathbf{p}_k \leftarrow \mathbf{p}_k(\mathbf{p}) + \delta_k(\mathbf{p}) \tag{7}$$

In Equations (6) and (7), $\mathbf{g}_k(\mathbf{p}) = \nabla \mathcal{S}_k\big(\mathbf{p}_k(\mathbf{p})\big)$ and $\nabla^2 \mathcal{S}_k\big(\mathbf{p}_k(\mathbf{p})\big)$ represent the local gradient and Hessian, respectively [62]. The resulting set of detected corners is denoted as $\forall \mathbf{p} \in \mathcal{P}_k$.

2.3. Estimating Displacement of Keypoints via Optical Flow

Taking into account the Constant Brightness Assumption Equation given in Equation (8), the flow of key points between consecutive frames $\left(\check{\mathcal{F}}_{k-1}, \check{\mathcal{F}}_k\right)$ is calculated.

$$I_x \Delta u_k(\mathbf{p}) + I_y \Delta v_k(\mathbf{p}) + I_t = 0, \forall \mathbf{p} \in \mathcal{P}_{k-1} \tag{8}$$

For two consecutive image frames $\left(\check{\mathcal{F}}_{k-1}, \check{\mathcal{F}}_k\right)$, the window around point $\mathbf{p}$ in the previous frame ($\check{\mathcal{F}}_{k-1}$) is taken as $\mathcal{W}\big(\mathbf{p}_{k-1}(\mathbf{p})\big)$. The computation is then performed as described in Equation (9), where $\mathbf{A}(\mathbf{p})$ represents the gradient matrix and $\mathbf{b}(\mathbf{p})$ denotes the derivative component. Consequently, the optical flow components along different axes $\big(\Delta u_k(\mathbf{p}), \Delta v_k(\mathbf{p})\big)$ are obtained.

$$\underbrace{\begin{bmatrix} \sum_{w(\mathbf{p}_{k-1}(\mathbf{p}))} I_x^2 & \sum_{w(\mathbf{p}_{k-1}(\mathbf{p}))} I_x I_y \\ \sum_{w(\mathbf{p}_{k-1}(\mathbf{p}))} I_x I_y & \sum_{w(\mathbf{p}_{k-1}(\mathbf{p}))} I_y^2 \end{bmatrix}}_{\mathbf{A}_k(\mathbf{p})} \begin{bmatrix} \Delta u_k(\mathbf{p}) \\ \Delta v_k(\mathbf{p}) \end{bmatrix} = \underbrace{-\begin{bmatrix} \sum_{w(\mathbf{p}_{k-1}(\mathbf{p}))} I_x I_t \\ \sum_{w(\mathbf{p}_{k-1}(\mathbf{p}))} I_y I_t \end{bmatrix}}_{\mathbf{b}_k(\mathbf{p})} \tag{9}$$

With the pyramidal/windowed approach and iterative search, the constant brightness assumption is linearized and Taylor convergence [63] is preserved by gradually reducing the large global motion to small increments during optical flow.

2.4. Estimating Metric Velocity and Displacement

Let the time interval between consecutive measurements be $\Delta t_k = t_k - t_{k-1}$. For each keypoint $\mathbf{p} \in \mathcal{P}_{k-1}$, the optical flow values $\Delta u_k(\mathbf{p})$ and $\Delta v_k(\mathbf{p})$ obtained from Equation (9) are used to compute the metric velocities with the help of the meter-to-pixel scale factor (s) as given in Equation (10).

$$\begin{bmatrix} \mathrm{v}_{x,k}(\mathbf{p}) \\ \mathrm{v}_{y,k}(\mathbf{p}) \end{bmatrix} = \frac{s}{\Delta t_k} \begin{bmatrix} \Delta u_k(\mathbf{p}) \\ \Delta v_k(\mathbf{p}) \end{bmatrix} \tag{10}$$

Rather than a single point, the displacement magnitudes of the vehicle during Δt_k are found with Equation (11) using the velocity vectors given in Equation (10) and the number of key points ($|\mathcal{P}_{k-1}|$) from the previous step.

$$\begin{bmatrix} x_k \\ y_k \end{bmatrix} = \frac{1}{|\mathcal{P}_{k-1}|} \sum_{\mathbf{p} \in \mathcal{P}_{k-1}} \begin{bmatrix} \mathrm{v}_{x,k}(\mathbf{p}) \\ \mathrm{v}_{y,k}(\mathbf{p}) \end{bmatrix} \tag{11}$$

3. SIMULATION

The feasibility of the proposed method was tested using a system created in a simulation environment. This test setup consists of a 2D LiDAR sensor and a mobile platform that moves the sensor. The mobile platform moves in a single direction at a constant speed. The environment created in the Gazebo Simulator [64] based on ROS2 [65] for simulation testing is shown in Figure 2.

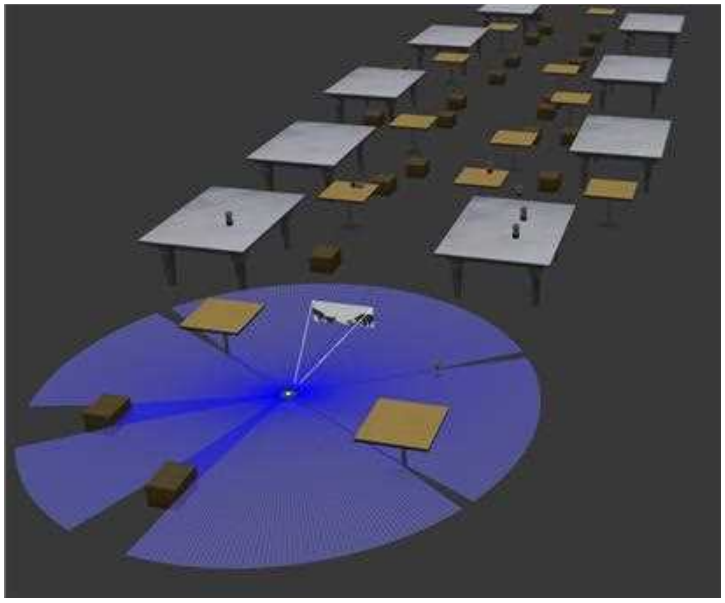


Figure 2. An image of the simulation environment showing the detection status of the LiDAR sensor and the objects present in the environment. In this moment, the vehicle is stationary at its starting position.

The TurtleBot model presented in [66] was used for the vehicle equipped with the LiDAR sensor in the simulation environment. The kinematic model, which gives the vehicle's position change depending on the desired speed, is given in Equation (12), and only the speed values are considered without considering the vehicle's structural dynamics [67]. In the Equation, v_x represents the horizontal (lateral) velocity component, v_y represents the longitudinal (longitudinal) velocity component, and ω represents the angular velocity. $\dot{x}$, $\dot{y}$, and $\dot{\theta}$ reflect the horizontal, vertical, and angular changes, respectively.

$$\begin{bmatrix} \dot{y} \\ \dot{x} \\ \dot{\theta} \end{bmatrix} = \begin{bmatrix} \cos(\theta) & 0 \\ \sin(\theta) & 0 \\ 0 & 1 \end{bmatrix} \begin{bmatrix} v \\ \omega \end{bmatrix} \tag{12}$$

Unlike the model presented in [67], this study does not include rotation, so ω can be taken as zero. Since the analysis was conducted on LiDAR measurements, an ideal model was created within the vehicle, without manually adding any error metrics to the vehicle's kinematic model except for the Gaussian error introduced into the torque values by the simulation.

A structure similar to the acceleration model given in [66] was used for the vehicle's acceleration model. The vehicle's acceleration model is given in Equation (13). In this Equation, τ_l and τ_r represent the torque of the left and right wheels, respectively; r_w represents the radius of the wheels; and m represents the vehicle's mass.

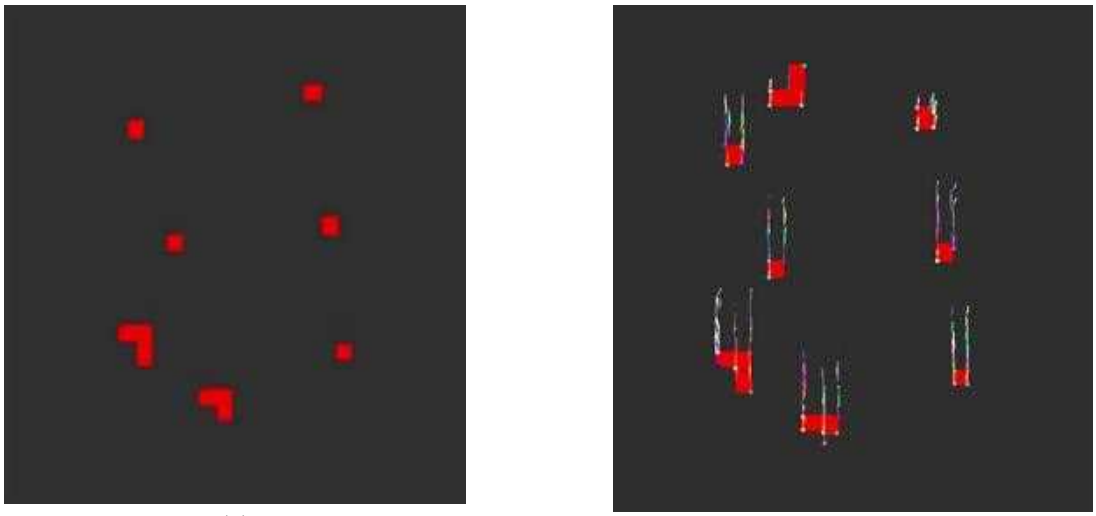
$$\dot{v}_x = \frac{\tau_l + \tau_r}{r_w m} \tag{13}$$

The values given in Equation (13) are defined in the simulation environment. The characteristic parameters of the LiDAR sensor used in the simulation environment are provided in Table 1.

Table 1. Parameters of the LiDAR sensor used in the simulation

Parameter	Value
Update Rate (Hz) (per sample)	1800
Samples Per Measurement	360
Angular Resolution (deg)	1.00
Min. Scan Range (m)	0.12
Max. Scan Range (m)	3.5
Scan Resolution (m)	0.015
Noise Type	Gaussian
Std. Deviation	0.01

The performance of the proposed method improved proportionally with the quality of the LiDAR sensor used, as indicated by the LiDAR characteristics presented in Table 1. At the same time, the area occupied by the data obtained from the LiDAR sensor on the matrix was set to 30 pixels. The matrix created from the data obtained using the LiDAR sensor with the parameters listed in Table 1, after centralization, is presented in Figure 3.



(a) **(b)**

Figure 3. The matrix obtained after centralization processes at **(a)**, with the LiDAR sensor at the center. **(b)** taken some time from **(a)**, representing the optical flow

The parameters of the Shi-Tomasi and Lucas-Kanade methods are provided in Table 2 and Table 3, respectively. Although these parameters significantly affect the results, they have not been tested for optimality.

Table 2. Parameters of Shi-Tomasi algorithm

Parameter	Value
Maximum Corners in Frame	100
Quality Level	0.3
Min. Distance Between Points	7
Block Size	7x7

Table 3. Parameters of Lucas-Kanade algorithm

Parameter	Value
Window Size	50x50
Max Pyramid Level	3
Count per Pyramid Level	12
Epsilon	0.01

The method was tested in two separate constant-speed scenarios of 0.3 m/s and 0.5 m/s, as well as a variable-speed test scenario that included speeds of 0.3 m/s, 0.5 m/s, 0.7 m/s, and 0.4 m/s, respectively. The performance of the proposed method was tested depending on the object density in the environment and finally, its performance was compared with other methods in the literature by performing tests in the same environment.

Initially, the environment was set up for each test. During the test process, a mobile platform equipped with a LiDAR sensor moved in a single direction (forward) at a constant speed. Meanwhile, the LiDAR measurements were continuously recorded. After this stage, the proposed methods in the study were applied to the LiDAR data to determine the measurement accuracy of the optical flow methods.

4. RESULTS AND DISCUSSION

The velocity data measured by the LiDAR sensor on the mobile platform moving at a constant speed of 0.3 m/s through the methods proposed in the study are shown in Figure 4. The graphs provided in the Figure vary in test duration due to the software developed for the study being run for different periods. The measured velocity values were lower in the first few seconds because these values were recorded while the platform was accelerating. During the test, vibrations were observed in the data obtained from the LiDAR. Therefore, it has been determined that LiDAR noise is the primary factor contributing to the error.

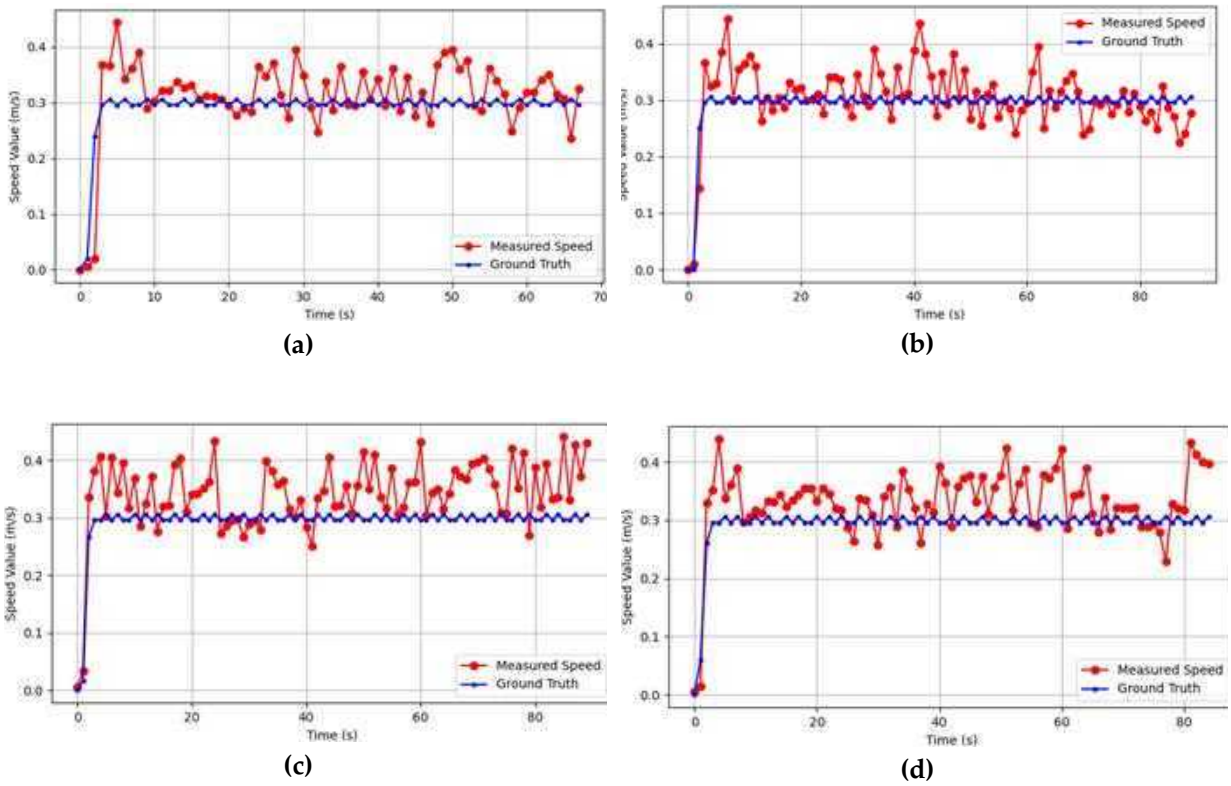


Figure 4. The measurement results of the first test conducted at a speed of 0.3 m/s

The RMSE (Root Mean Square Error) coefficients for the measurement results shown as sequences in Figure 4 are calculated as follows: 0.07673 m/s for (a), 0.06458 m/s for (b), 0.08352 m/s for (c), and 0.07766 m/s for (d). Additionally, the displacement data from the first test are provided in Figure 5. Each sequence shown in Figure 5 corresponds to the subfigures given in Figure 4. It is worth noting that the displacement plots start from the point (0, 0).

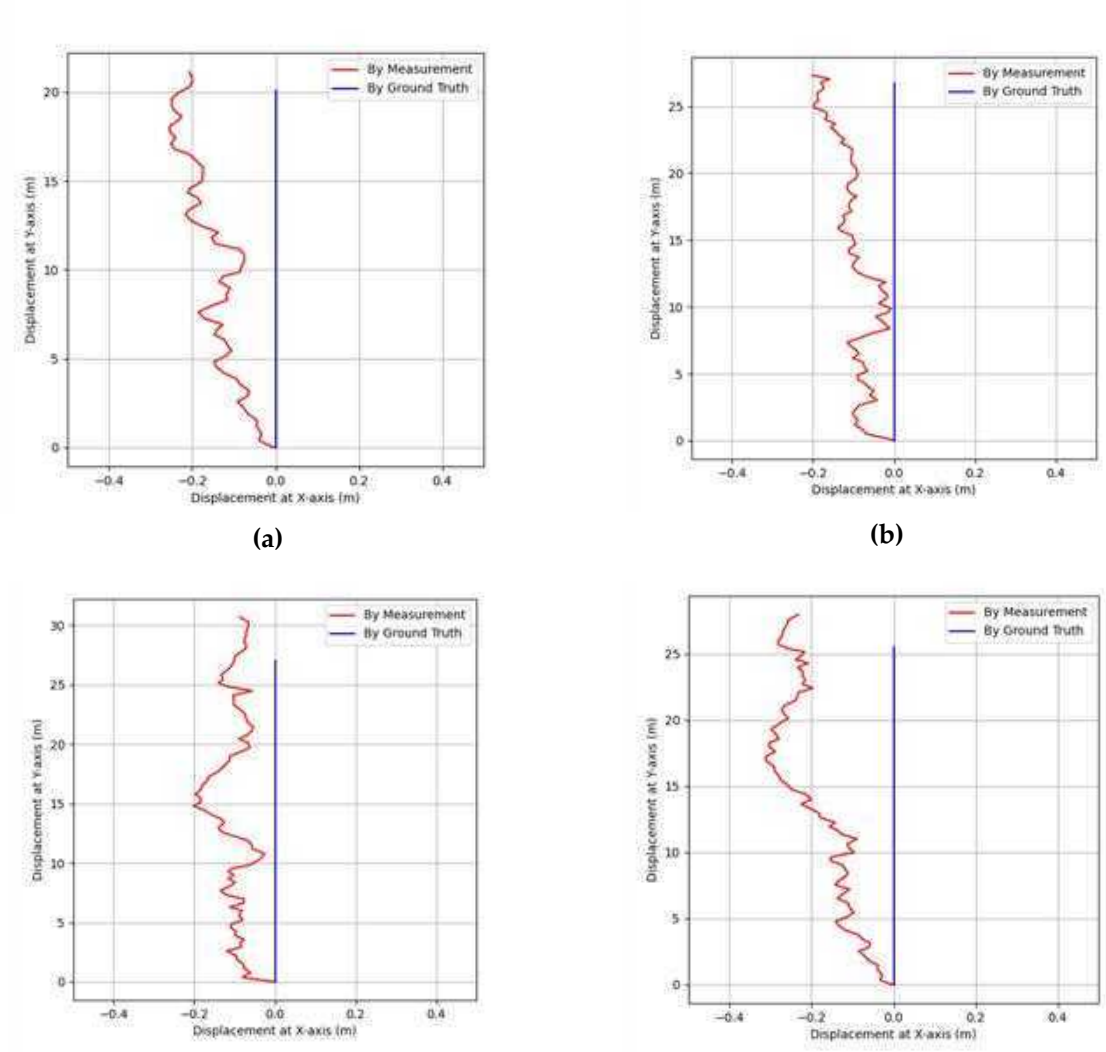


Figure 5. The displacement results of the first test conducted at a speed of 0.3 m/s

In the displacement data provided in Figure 5, a small amount of displacement was also detected along the x-axis. Although the platform was moving solely forward, noise from deviations in the LiDAR and optical flow methods led to the measurement of movement along the lateral axes as well. This measurement error is also observed in the forward axis and, as shown in Figure 5, causes deviation at the final point.

The average velocities measured from the subfigures (a), (b), (c), and (d) in Figure 4 and Figure 5 for the first test conducted at a constant speed of 0.3 m/s were 0.31092 m/s, 0.30344 m/s, 0.33718 m/s, and 0.32537 m/s, respectively. The final positional deviation based on the measured and ground truth data was measured as follows: (a) for the x-axis 0.20817 m and the y-axis 0.74261 m, (b) for the x-axis 0.20214 m and the y-axis 0.30965 m, (c) for the x-axis 0.08749 m and the y-axis 3.38379 m, (d) for the x-axis 0.2316 m and the y-axis 2.18233 m. In this case, the average deviation rate was found to be 6.51 %. The data measured during the first test is presented as a box plot in Figure 6. This box plot also includes data from the first few seconds when the system was stationary, which are values close to zero.

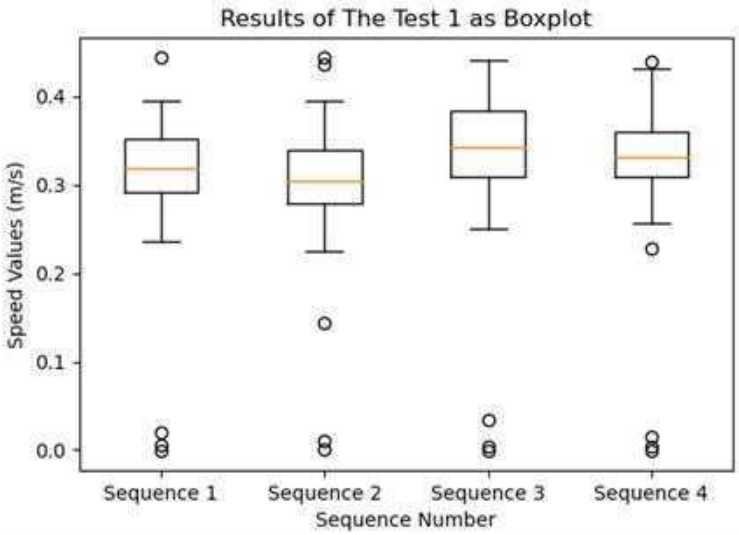


Figure 6. Box Plot of the measured speed values of Test 1 which conducted at 0.3 m/s

The second test was conducted to examine whether the proposed methods can operate at different speeds. This test was performed at a constant speed of 0.5 m/s, unlike the first test. All parameters were the same except for the actual speed parameter.

The velocity values measured during the test with the platform moving at a constant speed of 0.5 m/s are shown in Figure 7.

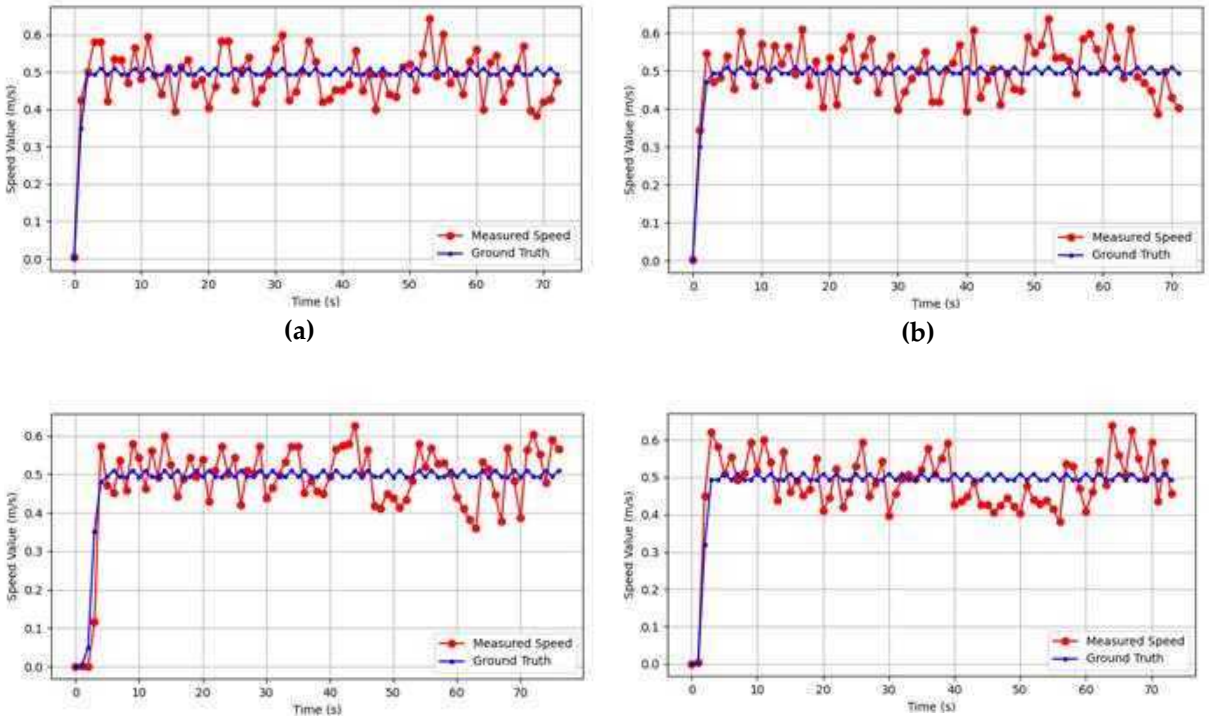


Figure 7. The measurement results of the second test conducted at a speed of 0.5 m/s

The RMSE values for the measurements shown in Figure 7 are 0.11653 m/s for (a), 0.11945 m/s for (b), 0.12374 m/s for (c), and 0.11760 m/s for (d). The position changes from the second test are presented

in Figure 8.

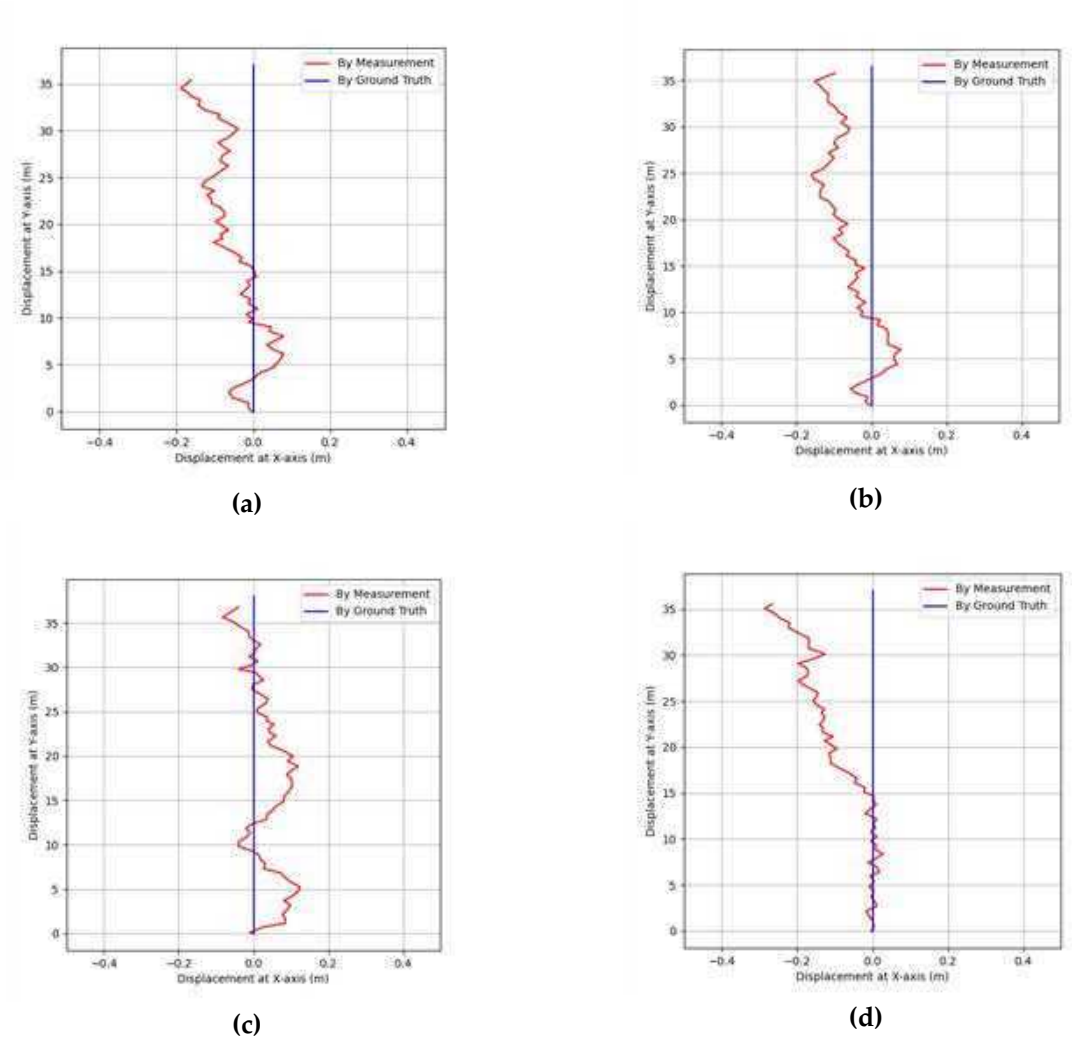


Figure 8. The displacement results of the second test conducted at a speed of 0.5 m/s

The average velocity values from Figure 7 and Figure 8 are measured as follows: 0.47209 m/s for (a), 0.48347 m/s for (b), 0.47775 m/s for (c), and 0.47372 m/s for (d). The final positional deviation based on the measured and ground truth data was measured as follows: (a) for the x-axis 0.16224 m and the y-axis 2.09263 m, (b) for the x-axis 0.09714 m and the y-axis 1.22263 m, (c) for the x-axis 0.04003 m and the y-axis 1.71254 m, (d) for the x-axis 0.26615 m and the y-axis 1.97081 m. In this case, the average deviation rate was found to be 4.66 %.

The box plot representation of the velocity data for the second test is shown in Figure 9.

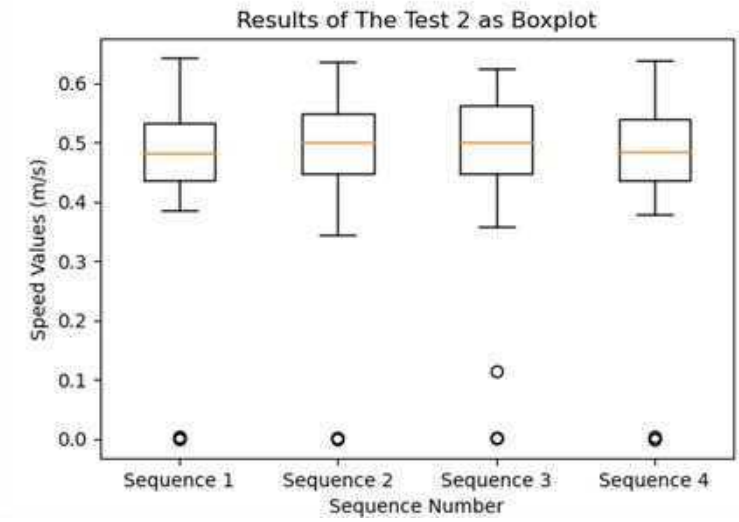


Figure 9. Box Plot of the measured speed values of second test which conducted at 0.5 m/s

A final experiment evaluated to measure the effectiveness of the method at variable speeds of 0.3 m/s, 0.5 m/s, 0.7 m/s, and 0.4 m/s, respectively. During this test, each speed value was maintained for 25 seconds.

The velocity values measured during the test with the platform moving at varied speeds are shown in Figure 10.

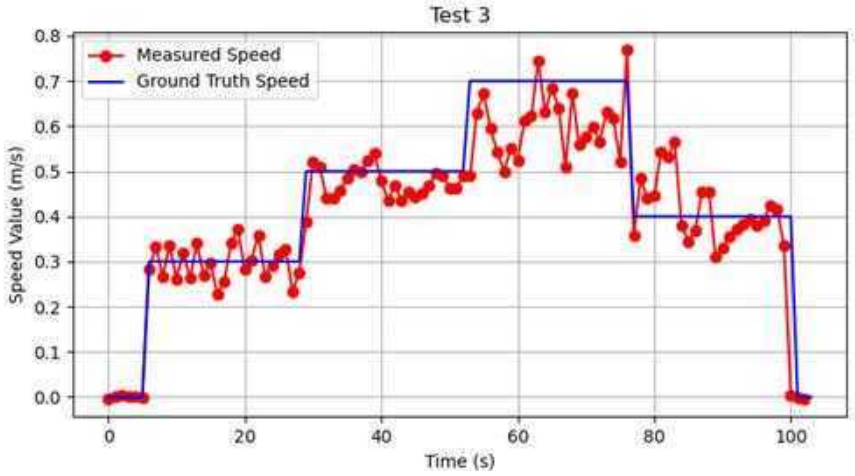


Figure 10. The measurement results of the third test conducted at varied speeds.

The RMSE values for the measurements shown in Figure 10 are 0.03924 m/s for 0.3 m/s, 0.0436 m/s for 0.5 m/s, 0.11552 m/s for 0.7 m/s, and 0.10732 m/s for 0.4 m/s. The total RMSE value for the test was measured as 0.09502 m/s. The position changes from the second test are presented in Figure 11.

In Figure 10, it is observed that as the cruising speed increases, the error also increases. This is due to the sudden disappearance of key features at the edges of the image frame at high speeds, causing the system to jump to the nearest key feature. As a result, although the flow direction of the image frame is expected to move from the front to the back of the vehicle, this issue causes the flow to reverse, moving from the back to the front. Consequently, the measured speeds are lower than the ground truth values, effectively adding a velocity component in the opposite direction.

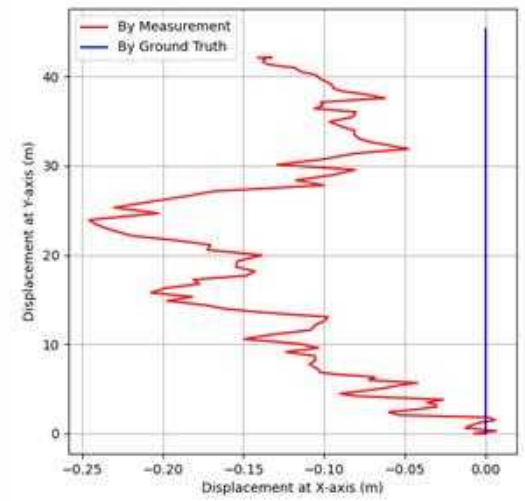


Figure 11. Displacement results of the third test performed at varied speeds.

The final positional deviation based on the measured and ground truth data was measured as for the x-axis 0.14114 m and the y-axis 3.1976 m. In this case, the average deviation rate was found to be 7.06 %.

For the performance comparison of the proposed study, studies referred to as "Planar Odometry" in the literature [54], [55], [57] were taken as references. The performance of the proposed method, along with these studies, was examined in relation to density. The test scenario was created with speeds of 0.3 m/s, 0.5 m/s, 0.7 m/s, and 0.4 m/s, each running for 100 s, and with densities of 10%, 20%, 30%, and 40%. Accordingly, the test results are presented in Table 4. The object density in the environment is determined by Equation (14).

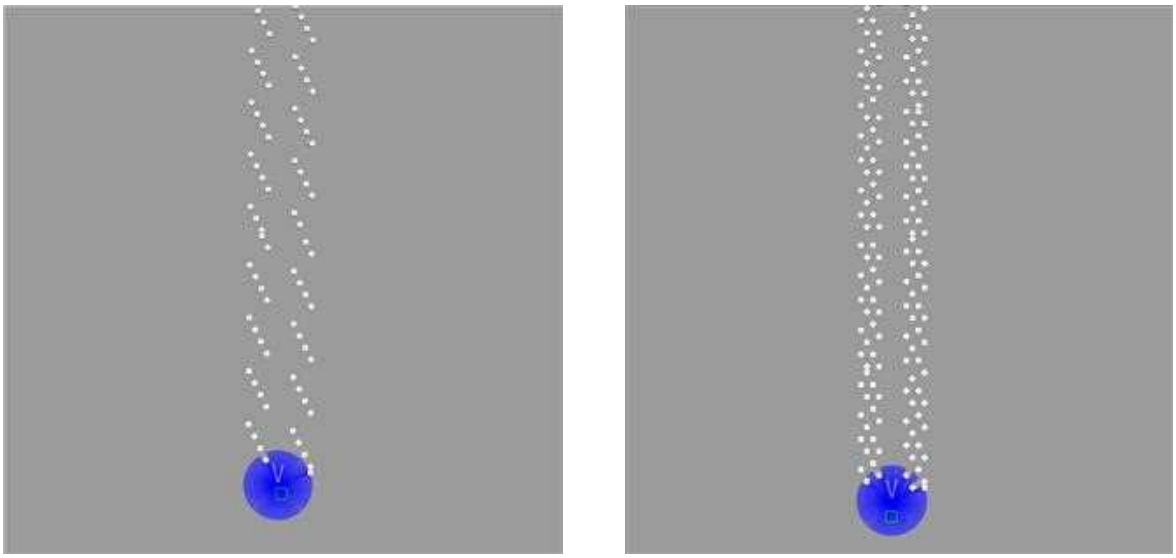
$$Density\ (\%) = \frac{A_{obj}}{v\ t\ r_{LiDAR}} \tag{14}$$

In Equation (14), A_{obj} represents the cross-sectional area of the object detected by LiDAR at the same height as the LiDAR sensor; v represents the speed of the vehicle; t represents the test time and r_{LiDAR} represents the maximum scanning radius of the LiDAR sensor given in Table 1. The Absolute Error and Relative Error evaluations given in Table 4 are defined in Equation (15) and Equation (16), respectively. In these definitions, Fiducial and Measured Positions are the final positions relative to ground truth and Measurement Data, respectively.

$$Absolute\ Error\ (m) = |Fiducial\ Position - Measured\ Position| \tag{15}$$

$$Relative\ Error\ (\%) = \frac{Absolute\ Error}{Fiducial\ Position} \tag{16}$$

The 10% and 20% density environments included in the comparison tests are presented in Figure 12. In the tests, obstacles were distributed homogeneously in all environments except the 10% density scenario. The 10% density environment was intentionally extreme. This scenario was considered extreme because obstacles placed parallel and crosswise to the running path were perceived by the algorithms as constantly disappearing and reappearing, leading to erroneous results. Furthermore, it is considered that these crosswise placed obstacles may trigger spurious measurements in the algorithms—particularly in situations where the system produces no motion along the horizontal axis—thereby causing additional measurement errors.



(a) **(b)**

Figure 12. Part of two test environments with different obstacle densities. **(a)** Environment with 10% density. **(b)** Environment with 20% density

Table 4 shows the averages of the test results. In this table, the x and y axes of the proposed method have been converted to NED (North-East-Down) to make comparisons with methods in the literature. In Table 4, the x-axis represents the positive axis of the vehicle in the forward direction, and the y-axis represents the positive axis to the right. So, the movement occurs along the x-axis. The table shows the average results for each test. Simulation time data refers to the total measurement time of the algorithm, not the running time of the simulation.

Table 4. Results of the comparison tests

Algorithm	Density (%)	Simulation Time (sec)	X-axis Absolute Error (m)	Y-axis Absolute Error (m)	Absolute Error (m)	Relative Error (%)
ICP [55]	10	404.333	-12.327	14.058	21.058	28.17
	20	349.5	-4.498	9.902	10.878	16.54
	30	245.5	-0.434	-4.280	4.310	9.35
	40	156.0	-0.314	-0.371	1.496	5.04
RF2O [54]	10	398.667	5.825	8.666	12.936	17.33
	20	333.5	0.115	1.804	1.817	2.83
	30	246.5	0.196	-1.554	1.568	3.41
	40	155.0	0.122	0.442	0.458	1.56
SRF [57]	10	396.0	-196.770	-790.039	825.002	1113.47
	20	339.5	0.012	0.948	0.948	1.48
	30	243.5	-0.019	-1.352	1.353	2.94
	40	157.0	0.066	-0.079	0.111	0.37
OF2O (Proposed)	10	393.8	13.843	-1.180	13.894	9.39
	20	344.375	20.791	-0.262	20.793	16.12
	30	249.5	16.131	1.030	16.164	17.27
	40	165.0	9.551	-0.112	9.552	16.36

Although the proposed method yields a lower Relative Error in low-density environments as shown in Table 4, it still falls behind competing methods in the other performance metrics presented. The SRF algorithm, in particular, began to overestimate velocity during approximately 30% of the tests conducted at 10% density, leading to higher total error due to these measurements. Since the basic metrics reported in Table 4 were insufficient to fully characterize method behavior, they were combined to form the composite metrics presented in Equations (17)–(19). These composite metrics enabled a deeper interpretation of the underlying error characteristics of each method and supported a more comprehensive comparison.

The Pose Drift Rate (PDR) metric defined in Equation (17) is obtained by normalizing the total positioning error with respect to time, quantitatively indicating how much positional drift the system produces per unit time. This metric serves as a critical performance indicator for evaluating accumulated error behavior during long-duration missions and for comparing the time-dependent stability of the algorithm.

$$PDR = \frac{Pose\ Absolute\ Error}{Simulation\ Time} \tag{17}$$

The Absolute–Relative Pose Error Product (ARPEP) defined in Equation (18) is a unified evaluation metric that combines two aspects of positioning error into a single cost function. While the absolute pose error reflects the total deviation over the entire trajectory, the relative pose error represents this deviation as a percentage of the true path. By multiplying these two components, ARPEP penalizes both large absolute errors and high relative deviations simultaneously. A lower ARPEP value therefore indicates that a method provides stable positioning performance at both global and local scales.

$$\text{ARPEP} = Pose\ Absolute\ Error \text{ x } Pose\ Relative\ Error \tag{18}$$

The Drift Rate Stability (DRS) metric defined in Equation (19) is a robustness measure that evaluates how consistently an algorithm performs under varying point-cloud densities. In this approach, the drift rate per unit time (PDR) is first computed for each condition, and then the standard deviation of these values is taken to assess how strongly density variations affect the algorithm. A low DRS value indicates that the method maintains similar drift levels even in dense, sparse, or unevenly distributed point-cloud scenarios. In Equation (19), i denotes each individual density test.

$$\text{DRS} = std(PDR_i) \tag{19}$$

Based on the test results presented in Table 4, Table 5 was generated using the performance metrics defined in Equation (17), Equation (18), and Equation (19).

Table 5. Results of composite metrics

Algorithm	PDR (m/s)	ARPEP	DRS
ICP [55]	187.7	5.0×10^5	46.0
RF2O [54]	64.6	1.2×10^5	19.1
SRF [57]	2246.7	7.3×10^8	3836.6
OF2O (Proposed)	7.7	3.0×10^4	5.4

As seen in Table 5, although the proposed method does not decisively surpass the other approaches in the basic metrics presented in Table 4, it outperforms them in the higher-level composite metrics composed from those measures. Notably, the method demonstrates clear advantages across varying density levels and in robustness-oriented evaluations.

5. CONCLUSIONS

This study proposes a method to estimate displacement using data from a 2D LiDAR sensor in SLAM systems. LiDAR data was mapped onto image matrices, with each scan treated as an image frame and combined into a video. Key features (corner points) were detected using the Shi-Tomasi algorithm, and their inter-frame displacement was analyzed using the Lucas-Kanade optical flow method. This allowed the calculation of the platform's displacement based on LiDAR scans.

The reliability of the method has been validated through three different tests: two with constant speeds and one with variable speed. During the tests, the error between the proposed method and the ground truth speeds was calculated using the RMSE method. Additionally, the displacement error of the method was analyzed.

A Gazebo-based simulation environment was created to test the reliability of the proposed method. The ROS2 framework was used in this simulation environment for vehicle control and sensor data acquisition. The simulation tests involved evaluating the data obtained from the LiDAR sensor while the vehicle moved unidirectionally at fixed and variable speeds, using ground truth as a reference. Based on this evaluation, the deviation of the vehicle from the reference direction was analyzed.

While the proposed method effectively estimates displacement and velocity in unidirectional motion using LiDAR-based optical flow, rotation measurement requires dividing the image matrix into sub-matrices and analyzing arcs formed by key features. This approach is planned for future implementation using State Machines. Although the influence of LiDAR sensor characteristics on performance is acknowledged, their variability adds complexity, so detailed parameter optimization is left for future studies. Broader validation across different motion profiles, feature detection and optical flow algorithms, and sensor configurations is also necessary. Consequently, claims regarding robustness and superiority are made cautiously and require further experimental validation.

Declaration of Ethical Standards

As the authors of this study, we declare that all ethical standards have been complied with.

Credit Authorship Contribution Statement

Mesut TUNÇER: Methodology, Writing original draft, Visualization, Investigation, Software.
Alper KILIÇ: Methodology, Writing original draft, Supervision.

Declaration of Competing Interest

The authors declare that there is no conflict of interest.

Funding / Acknowledgements

No funding is available for this research.

Data Availability

Data will be made available on request.

Use of Artificial Intelligence

Generative AI tools were utilized solely for the purpose of enhancing the language quality and readability of this manuscript.

5. REFERENCES

[1] C. Cadena et al., "Past, Present, and Future of Simultaneous Localization and Mapping: Toward the Robust-Perception Age," IEEE Transactions on Robotics, vol. 32, no. 6, pp. 1309–1332, Dec. 2016, doi: 10.1109/TRO.2016.2624754.

[2] H. Durrant-Whyte and T. Bailey, "Simultaneous localization and mapping: part I," IEEE Robot Autom Mag, vol. 13, no. 2, pp. 99–110, Jun. 2006, doi: 10.1109/MRA.2006.1638022.

[3] A. Eldemiry, Y. Zou, Y. Li, C.-Y. Wen, and W. Chen, "Autonomous Exploration of Unknown Indoor Environments for High-Quality Mapping Using Feature-Based RGB-D SLAM," Sensors, vol. 22, no. 14, p. 5117, Jul. 2022, doi: 10.3390/s22145117.

[4] M. Bryson and S. Sukkarieh, "Observability analysis and active control for airborne SLAM," IEEE Trans Aerosp Electron Syst, vol. 44, no. 1, pp. 261–280, Jan. 2008, doi: 10.1109/TAES.2008.4517003.

[5] M. U. Diginsa, N. Shafie, N. Yusuf, and S. U. Suleiman, "Review: Issues and Challenges of Simultaneous Localization and Mapping (SLAM) Technology in Autonomous Robot," International Journal of Innovative Computing, vol. 13, no. 2, pp. 59–63, Nov. 2023, doi: 10.11113/ijic.v13n2.408.

[6] S. Zheng, J. Wang, C. Rizos, W. Ding, and A. El-Mowafy, "Simultaneous Localization and Mapping (SLAM) for Autonomous Driving: Concept and Analysis," Remote Sens (Basel), vol. 15, no. 4, p. 1156, Feb. 2023, doi: 10.3390/rs15041156.

[7] M. E. Tokgöz, A. Yusefi, İ. Toy, and A. Durdu, "Enhanced Obstacle Detection in Autonomous Vehicles using 3D LiDAR Mapping Techniques," in 2024 23rd International Symposium INFOTEH-JAHORINA (INFOTEH), IEEE, Mar. 2024, pp. 1–4. doi: 10.1109/INFOTEH60418.2024.10495979.

[8] Jonghyuk Kim and S. Sukkarieh, "Autonomous airborne navigation in unknown terrain environments," IEEE Trans Aerosp Electron Syst, vol. 40, no. 3, pp. 1031–1045, Jul. 2004, doi: 10.1109/TAES.2004.1337472.

[9] I. Cvišić, J. Ćesić, I. Marković, and I. Petrović, "SOFT-SLAM: Computationally efficient stereo visual simultaneous localization and mapping for autonomous unmanned aerial vehicles," J Field Robot, vol. 35, no. 4, pp. 578–595, Jun. 2018, doi: 10.1002/rob.21762.

[10] Y. Alborzi, B. S. Jalal, and E. Najafi, "ROS-based SLAM and Navigation for a Gazebo-Simulated Autonomous Quadrotor," in 2020 21st International Conference on Research and Education in Mechatronics (REM), IEEE, Dec. 2020, pp. 1–5. doi: 10.1109/REM49740.2020.9313875.

[11] L. von Stumberg, V. Usenko, J. Engel, J. Stuckler, and D. Cremers, "From monocular SLAM to autonomous drone exploration," in 2017 European Conference on Mobile Robots (ECMR), IEEE, Sep. 2017, pp. 1–8. doi: 10.1109/ECMR.2017.8098709.

[12] Y. Tian, H. Yue, B. Yang, and J. Ren, "Unmanned Aerial Vehicle Visual Simultaneous Localization and Mapping: A Survey," J Phys Conf Ser, vol. 2278, no. 1, p. 012006, May 2022, doi: 10.1088/1742-6596/2278/1/012006.

[13] H. Qin et al., "Autonomous Exploration and Mapping System Using Heterogeneous UAVs and UGVs in GPS-Denied Environments," IEEE Trans Veh Technol, vol. 68, no. 2, pp. 1339–1350, Feb. 2019, doi: 10.1109/TVT.2018.2890416.

[14] L. Mochurad, Y. Hladun, and R. Tkachenko, "An Obstacle-Finding Approach for Autonomous Mobile Robots Using 2D LiDAR Data," Big Data and Cognitive Computing, vol. 7, no. 1, p. 43, Mar. 2023, doi: 10.3390/bdcc7010043.

[15] Q. Zeng, X. Tao, H. Yu, X. Ji, T. Chang, and Y. Hu, "An Indoor 2-D LiDAR SLAM and Localization Method Based on Artificial Landmark Assistance," IEEE Sens J, vol. 24, no. 3, pp. 3681–3692, Feb. 2024, doi: 10.1109/JSEN.2023.3341832.

[16] J.-S. Kim, G. Lee, and Y. S. Kim, "2D-LiDAR-Sensor-Based Retaining Wall Displacement Measurement System," Applied Sciences, vol. 12, no. 22, p. 11335, Nov. 2022, doi: 10.3390/app122211335.

[17] Z. YILMAZ and L. BAYINDIR, "Lidar-based Robot Detection and Positioning using Machine Learning Methods," Balkan Journal of Electrical and Computer Engineering, vol. 10, no. 2, pp. 214–223, Apr. 2022, doi: 10.17694/bajece.984744.

[18] Z. Yılmaz and L. Bayındır, "Simulation of Lidar-Based Robot Detection Task using ROS and Gazebo," European Journal of Science and Technology, pp. 513–529, Oct. 2019, doi: 10.31590/ejosat.642840.

[19] H. Wang, C. Wang, and L. Xie, "Intensity-SLAM: Intensity Assisted Localization and Mapping for Large Scale Environment," IEEE Robot Autom Lett, vol. 6, no. 2, pp. 1715–1721, Apr. 2021, doi: 10.1109/LRA.2021.3059567.

[20] Q. Zou, Q. Sun, L. Chen, B. Nie, and Q. Li, "A Comparative Analysis of LiDAR SLAM-Based Indoor Navigation for Autonomous Vehicles," IEEE Transactions on Intelligent Transportation Systems, vol. 23, no. 7, pp. 6907–6921, Jul. 2022, doi: 10.1109/TITS.2021.3063477.

[21] K. Yan and B. Ma, "Mapless Navigation Based on 2D LIDAR in Complex Unknown Environments," Sensors, vol. 20, no. 20, p. 5802, Oct. 2020, doi: 10.3390/s20205802.

[22] L. Mu, P. Yao, Y. Zheng, K. Chen, F. Wang, and N. Qi, "Research on SLAM Algorithm of Mobile Robot Based on the Fusion of 2D LiDAR and Depth Camera," IEEE Access, vol. 8, pp. 157628–157642, 2020, doi: 10.1109/ACCESS.2020.3019659.

[23] W. Wei, B. Shirinzadeh, R. Nowell, M. Ghafarian, M. M. A. Ammar, and T. Shen, "Enhancing Solid State LiDAR Mapping with a 2D Spinning LiDAR in Urban Scenario SLAM on Ground Vehicles," Sensors, vol. 21, no. 5, p. 1773, Mar. 2021, doi: 10.3390/s21051773.

[24] R. Ren, H. Fu, and M. Wu, "Large-Scale Outdoor SLAM Based on 2D Lidar," Electronics (Basel), vol. 8, no. 6, p. 613, May 2019, doi: 10.3390/electronics8060613.

[25] Z. Wang, Y. Chen, Y. Mei, K. Yang, and B. Cai, "IMU-Assisted 2D SLAM Method for Low-Texture and Dynamic Environments," Applied Sciences, vol. 8, no. 12, p. 2534, Dec. 2018, doi: 10.3390/app8122534.

[26] L.-H. Chen and C.-C. Peng, "A Robust 2D-SLAM Technology With Environmental Variation Adaptability," IEEE Sens J, vol. 19, no. 23, pp. 11475–11491, Dec. 2019, doi: 10.1109/JSEN.2019.2931368.

[27] A. Aboutaleb, A. S. El-Wakeel, H. Elghamrawy, and A. Noureldin, "LiDAR/RISS/GNSS Dynamic Integration for Land Vehicle Robust Positioning in Challenging GNSS Environments," Remote Sens (Basel), vol. 12, no. 14, p. 2323, Jul. 2020, doi: 10.3390/rs12142323.

[28] D. Kong, X. Li, Y. Hu, Q. Xu, A. Wang, and W. Hu, "Learning a Novel LiDAR Submap-Based Observation Model for Global Positioning in Long-Term Changing Environments," IEEE Transactions on Industrial Electronics, vol. 70, no. 3, pp. 3147–3157, Mar. 2023, doi: 10.1109/TIE.2022.3169849.

[29] Z. Chen et al., "Improved-UWB/LiDAR-SLAM Tightly Coupled Positioning System with NLOS Identification Using a LiDAR Point Cloud in GNSS-Denied Environments," Remote Sens (Basel), vol. 14, no. 6, p. 1380, Mar. 2022, doi: 10.3390/rs14061380.

[30] A. Ammar, H. Ben Fredj, and C. Souani, "Accurate Realtime Motion Estimation Using Optical Flow on an Embedded System," Electronics (Basel), vol. 10, no. 17, p. 2164, Sep. 2021, doi: 10.3390/electronics10172164.

[31] K. Blachut and T. Kryjak, "Real-Time Efficient FPGA Implementation of the Multi-Scale Lucas-Kanade and Horn-Schunck Optical Flow Algorithms for a 4K Video Stream," Sensors, vol. 22, no. 13, p. 5017, Jul. 2022, doi: 10.3390/s22135017.

[32] S. Shi, D. Zhang, C. Zhang, Z. Chen, C. Feng, and B. Fan, "Large Displacement Optical Flow Estimation Based on Robust Interpolation of Sparse Correspondences," IEEE Access, vol. 8, pp. 227360–227372, 2020, doi: 10.1109/ACCESS.2020.3045764.

[33] A. Dashkevich and O. Vodka, "Computational Tool for Analysis of Strains Based on Optical Flow Approach," in 2020 IEEE KhPI Week on Advanced Technology (KhPIWeek), IEEE, Oct. 2020, pp. 382–386. doi: 10.1109/KhPIWeek51551.2020.9250075.

[34] K. Souhila, O. Djekoune, D. Djebrouni, and D. Meriche, "On the Use of Optical Flow in Robot Navigation," in 2007 IEEE International Conference on Signal Processing and Communications, IEEE, 2007, pp. 1287–1290. doi: 10.1109/ICSPC.2007.4728562.

[35] K. Dawson, M. Tistarelli, and D. Vernon, "On the usefulness of optical flow for robotic part manipulation," in Proceedings IROS '91:IEEE/RSJ International Workshop on Intelligent Robots and Systems '91, IEEE, pp. 117–122. doi: 10.1109/IROS.1991.174436.

[36] Chi-Cheng Cheng, Kun-Hsin Ho, Hui-Ting Li, and Gwo-Long Lin, "Image following using the feature-based optical flow approach," in Proceedings of the IEEE Internatinal Symposium on Intelligent Control, IEEE, pp. 350–355. doi: 10.1109/ISIC.2002.1157788.

[37] F. F. Khalil and P. Payeur, "Optical flow techniques in biomimetic UAV vision," in International Workshop on Robotic Sensors: Robotic and Sensor Environments, 2005., IEEE, 2005, pp. 14–19. doi: 10.1109/ROSE.2005.1588329.

[38] K. Kontis and H. Zare-Behtash, "Optical Flow Visualization," in Encyclopedia of Aerospace Engineering, Wiley, 2010. doi: 10.1002/9780470686652.eae069.

[39] Z. Tu et al., "A survey of variational and CNN-based optical flow techniques," Signal Process Image Commun, vol. 72, pp. 9–24, Mar. 2019, doi: 10.1016/j.image.2018.12.002.

[40] A. Bruhn, J. Weickert, and C. Schnörr, "Lucas/Kanade Meets Horn/Schunck: Combining Local and Global Optic Flow Methods," Int J Comput Vis, vol. 61, no. 3, pp. 211–231, Feb. 2005, doi: 10.1023/B:VISI.0000045324.43199.43.

[41] S. Oron, A. Bar-Hille, and S. Avidan, "Extended Lucas-Kanade Tracking," 2014, pp. 142–156. doi: 10.1007/978-3-319-10602-1_10.

[42] K. Blachut and T. Kryjak, "Real-Time Efficient FPGA Implementation of the Multi-Scale Lucas-Kanade and Horn-Schunck Optical Flow Algorithms for a 4K Video Stream," Sensors, vol. 22, no. 13, p. 5017, Jul. 2022, doi: 10.3390/s22135017.

[43] A. Mitiche and A.-R. Mansouri, "On Convergence of the Horn and Schunck Optical-Flow Estimation Method," IEEE Transactions on Image Processing, vol. 13, no. 6, pp. 848–852, Jun. 2004, doi: 10.1109/TIP.2004.827235.

[44] G. Farnebäck, "Two-Frame Motion Estimation Based on Polynomial Expansion," 2003, pp. 363–370. doi: 10.1007/3-540-45103-X_50.

[45] J. Cobos, L. Pacheco, X. Cufi, and D. Caballero, "Integrating visual odometry and dead-reckoning for robot localization and obstacle detection," in 2010 IEEE International Conference on Automation, Quality and Testing, Robotics (AQTR), IEEE, May 2010, pp. 1–6. doi: 10.1109/AQTR.2010.5520874.

[46] C. Zheng et al., "FAST-LIVO2: Fast, Direct LiDAR–Inertial–Visual Odometry," IEEE Transactions on Robotics, vol. 41, pp. 326–346, 2025, doi: 10.1109/TRO.2024.3502198.

[47] J. Zhang et al., "LOFF: LiDAR and Optical Flow Fusion Odometry," Drones, vol. 8, no. 8, p. 411, Aug. 2024, doi: 10.3390/drones8080411.

[48] M. E. Tjahjadi and F. D. Agustina, "Single image orientation of UAV's imagery using orthogonal projection model," in 2017 International Symposium on Geoinformatics (ISyG), IEEE, Nov. 2017, pp. 18–23. doi: 10.1109/ISYG.2017.8280668.

[49] W. Ding, S. Hou, H. Gao, G. Wan, and S. Song, "LiDAR Inertial Odometry Aided Robust LiDAR Localization System in Changing City Scenes," in 2020 IEEE International Conference on Robotics and Automation (ICRA), IEEE, May 2020, pp. 4322–4328. doi: 10.1109/ICRA40945.2020.9196698.

[50] B. Zhou, Z. Tang, K. Qian, F. Fang, and X. Ma, "A LiDAR Odometry for Outdoor Mobile Robots Using NDT Based Scan Matching in GPS-denied environments," in 2017 IEEE 7th Annual International Conference on CYBER Technology in Automation, Control, and Intelligent Systems (CYBER), IEEE, Jul. 2017, pp. 1230–1235. doi: 10.1109/CYBER.2017.8446588.

[51] X. Guo, X. Lin, L. Zhao, Z. Zhu, and J. Chen, "An Unsupervised Optical Flow Estimation for Lidar Image Sequences," in 2021 IEEE International Conference on Image Processing (ICIP), IEEE, Sep. 2021, pp. 2613–2617. doi: 10.1109/ICIP42928.2021.9506376.

[52] V. Vaquero, A. Sanfeliu, and F. Moreno-Noguer, "Hallucinating Dense Optical Flow from Sparse Lidar for Autonomous Vehicles," in 2018 24th International Conference on Pattern Recognition (ICPR), IEEE, Aug. 2018, pp. 1959–1964. doi: 10.1109/ICPR.2018.8545803.

[53] E. Ilg, N. Mayer, T. Saikia, M. Keuper, A. Dosovitskiy, and T. Brox, "FlowNet 2.0: Evolution of Optical Flow Estimation with Deep Networks," in 2017 IEEE Conference on Computer Vision and Pattern Recognition (CVPR), IEEE, Jul. 2017, pp. 1647–1655. doi: 10.1109/CVPR.2017.179.

[54] M. Jaimez, J. G. Monroy, and J. Gonzalez-Jimenez, "Planar odometry from a radial laser scanner. A range flow-based approach," in 2016 IEEE International Conference on Robotics and Automation (ICRA), IEEE, May 2016, pp. 4479–4485. doi: 10.1109/ICRA.2016.7487647.

[55] A. Censi, "An ICP variant using a point-to-line metric," in 2008 IEEE International Conference on Robotics and Automation, IEEE, May 2008, pp. 19–25. doi: 10.1109/ROBOT.2008.4543181.

[56] Z. He, Y. Wang, and H. Yu, "Feature-to-Feature based Laser Scan Matching in Polar Coordinates with Application to Pallet Recognition," Procedia Eng, vol. 15, pp. 4800–4804, 2011, doi: 10.1016/j.proeng.2011.08.897.

[57] M. Jaimez, J. Monroy, M. Lopez-Antequera, and J. Gonzalez-Jimenez, "Robust Planar Odometry Based on Symmetric Range Flow and Multiscan Alignment," IEEE Transactions on Robotics, vol. 34, no. 6, pp. 1623–1635, Dec. 2018, doi: 10.1109/TRO.2018.2861911.

[58] Jianbo Shi and Tomasi, "Good features to track," in Proceedings of IEEE Conference on Computer Vision and Pattern Recognition CVPR-94, IEEE Comput. Soc. Press, 1994, pp. 593–600. doi: 10.1109/CVPR.1994.323794.

[59] R. J. Mstafa, Y. M. Younis, H. I. Hussein, and M. Atto, "A New Video Steganography Scheme Based on Shi-Tomasi Corner Detector," IEEE Access, vol. 8, pp. 161825–161837, 2020, doi: 10.1109/ACCESS.2020.3021356.

[60] C. Harris and M. Stephens, "A Combined Corner and Edge Detector," in Procedings of the Alvey Vision Conference 1988, Alvey Vision Club, 1988, pp. 23.1-23.6. doi: 10.5244/C.2.23.

[61] N. Kanopoulos, N. Vasanthavada, and R. L. Baker, "Design of an image edge detection filter using the Sobel operator," IEEE J Solid-State Circuits, vol. 23, no. 2, pp. 358–367, Apr. 1988, doi: 10.1109/4.996.

[62] K. Mikolajczyk and C. Schmid, "Indexing based on scale invariant interest points," in Proceedings Eighth IEEE International Conference on Computer Vision. ICCV 2001, IEEE Comput. Soc, pp. 525–531. doi: 10.1109/ICCV.2001.937561.

[63] J. R. Winkler, "Error Analysis and Condition Estimation of the Pyramidal Form of the Lucas-Kanade Method in Optical Flow," Electronics (Basel), vol. 13, no. 5, p. 812, Feb. 2024, doi: 10.3390/electronics13050812.

[64] N. Koenig and A. Howard, "Design and use paradigms for gazebo, an open-source multi-robot simulator," in 2004 IEEE/RSJ International Conference on Intelligent Robots and Systems (IROS) (IEEE Cat. No.04CH37566), IEEE, pp. 2149–2154. doi: 10.1109/IROS.2004.1389727.

[65] Y. Maruyama, S. Kato, and T. Azumi, "Exploring the performance of ROS2," in Proceedings of the 13th International Conference on Embedded Software, New York, NY, USA: ACM, Oct. 2016, pp. 1–10. doi: 10.1145/2968478.2968502.

[66] M. Siwek, J. Panasiuk, L. Baranowski, W. Kaczmarek, P. Prusaczyk, and S. Borys, "Identification of Differential Drive Robot Dynamic Model Parameters," Materials, vol. 16, no. 2, p. 683, Jan. 2023, doi: 10.3390/ma16020683.

[67] F. Nascimento Martins and A. Santos Brandão, "Motion Control and Velocity-Based Dynamic Compensation for Mobile Robots," in Applications of Mobile Robots, IntechOpen, 2019. doi: 10.5772/intechopen.79397.

Konya Mühendislik Bilimleri Dergisi., c.14, s.2, 741-759, 2026
Konya Journal of Engineering Sciences v.14, n.2, 741-759, 2026
ISSN: 2667-8055 (Electronic)
DOI: 10.36306/konjes.1721362

EVALUATING THE PROFITABILITY EFFECTS OF CAPACITY AND STATE OF CHARGE IN BATTERY-INTEGRATED DISTRIBUTION NETWORKS

[1,*]Fatma Avli Fırış, [2]İsrafil Karadöl, [3]Ökkeş Fatih Keçecioğlu

[1]*Department of Hybrid and Electric Vehicles Technology Ostim Technical University Ankara, Türkiye (https://orcid.org/0000-0002-9239-0565)*
[2]*Department of Electrical and Electronic Engineering, Kilis 7 Aralik University, Kilis, Türkiye (https://orcid.org/0000-0003-4879-1932)*
[3]*Department of Electrical and Electronic Engineering, Kahramanmaras Sutcu Imam University, Kahramanmaras, Türkiye (https://orcid.org/0000-0001-7004-4947)*
[1]fatma.firis@ostimteknik.edu.tr, [2]israfilkaradol@kilis.edu.tr, [3]fkececioglu@ksu.edu.tr

Highlights

- Two-stage stochastic MILP for BESS in distribution systems
- Capacity and SoC impacts on profitability
- Monte Carlo–based uncertainty modeling
- Non-linear profitability and diminishing returns
- Optimal sizing balances profit and cost

Graphical Abstract

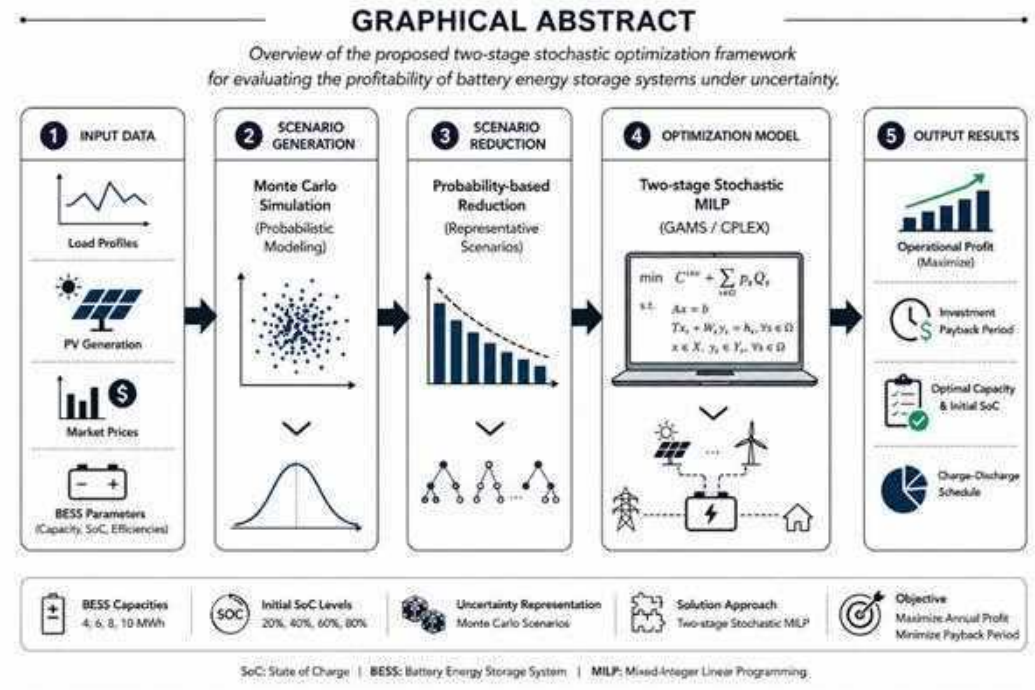


Figure Battery energy storage sytem optimization under uncertainty

***Corresponding Author:** Fatma AVLİ FIRIŞ, fatma.firis@ostimteknik.edu.tr

Konya Mühendislik Bilimleri Dergisi., c.14, s.2, 741-759, 2026
Konya Journal of Engineering Sciences v.14, n.2, 741-759, 2026
ISSN: 2667-8055 (Electronic)
DOI: 10.36306/konjes.1721362

EVALUATING THE PROFITABILITY EFFECTS OF CAPACITY AND STATE OF CHARGE IN BATTERY-INTEGRATED DISTRIBUTION NETWORKS

[1,*]Fatma Avli Fırış, [2]İsrafil Karadöl, [3]Ökkeş Fatih Keçecioğlu

[1]Department of Hybrid and Electric Vehicles Technology Ostim Technical University Ankara, Türkiye (https://orcid.org/0000-0002-9239-0565)
[2]Department of Electrical and Electronic Engineering, Kilis 7 Aralik University, Kilis, Türkiye (https://orcid.org/0000-0003-4879-1932)
[3]Department of Electrical and Electronic Engineering, Kahramanmaras Sutcu Imam University, Kahramanmaras, Türkiye (https://orcid.org/0000-0001-7004-4947)
[1]fatma.firis@ostimteknik.edu.tr, [2]israfilkaradol@kilis.edu.tr, [3]fkececioglu@ksu.edu.tr

(Received: 17.06.2025; Accepted in Revised Form: 27.11.2025)

ABSTRACT: This study presents a detailed assessment of the economic impacts of battery energy storage system (BESS) integration in active distribution networks, focusing on the influence of varying storage capacities and initial State-of-Charge (SoC) levels. A two-stage stochastic mixed-integer linear programming (MILP) framework is employed to evaluate four BESS capacities 4, 6, 8, and 10 MWh under initial SoC levels of 20%, 40%, 60%, and 80%, with uncertainty represented via Monte Carlo scenario generation and reduction. The model incorporates realistic market prices, load profiles, and photovoltaic generation data to reflect operational conditions encountered in modern distribution systems. Economic performance is assessed through annual operating profit and investment payback period, and the present net value, with negative operating costs consistently interpreted as profit. By analyzing charge–discharge behavior, cost dynamics, and payback characteristics under different storage configurations, the study provides comprehensive insights into the design and operation of economically efficient BESS deployments. The joint evaluation of storage capacity and initial SoC under uncertainty provides a novel perspective on economically efficient deployment strategies and offers guidance relevant to policy frameworks such as carbon pricing, incentive mechanisms, and other regulatory instruments. This study contributes to the growing body of literature by offering a comprehensive techno-economic framework for BESS deployment, bridging critical gaps in the understanding of storage system economics and providing actionable insights for policymakers, investors, and operators navigating the evolving energy landscape.

Keywords: *Battery Energy Storage, Distribution system, Optimization, Profitability, Renewable Energy.*

1. INTRODUCTION

1.1. Motivation

The rapid expansion of renewable energy sources is transforming power systems, driven by the depletion of fossil fuels and the global shift toward sustainable energy solutions. Solar and wind technologies are central to achieving decarbonization objectives, yet their inherent intermittency and dependence on weather conditions pose substantial operational challenges [1]-[3]. Coupled with fluctuating electricity demand, these issues disrupt the delicate balance between generation and consumption, leading to grid instability and elevated operational costs. Addressing these challenges is crucial to ensuring the seamless and efficient integration of renewables into modern power networks.

Energy storage systems (ESS) have emerged as a cornerstone technology in overcoming these barriers, offering the operational flexibility necessary to bridge the gap between variable renewable generation and

***Corresponding Author:** Fatma AVLİ FIRIŞ, fatma.firis@ostimteknik.edu.tr

demand. ESS enables surplus energy generated during periods of high renewable output to be stored and dispatched when demand surpasses supply, thereby enhancing grid stability and mitigating the variability of renewable resources [4], [5]. Recent assessments emphasize that coordinated ESS operation within distribution networks can substantially enhance resilience and system adequacy [6]. In addition to balancing generation and consumption, ESS contributes to frequency regulation, minimize renewable energy curtailment, and facilitate peak shaving, solidifying their role as indispensable assets for reliable and resilient grid operations. Optimizing the deployment and operation of ESS is paramount to unlocking their full potential, ensuring cost-effective and sustainable integration of renewables [7], [8]. Furthermore, the integration of digital twins and AI-based forecasting into ESS management has been shown to reduce uncertainty and improve scheduling efficiency [9].

Modern power systems, characterized by their growing complexity, demand advanced optimization strategies to fully exploit the capabilities of ESS. Conventional grid management approaches often fail to adequately address the stochastic nature of renewable energy generation and load demand. Consequently, there is an urgent need for robust optimization models that incorporate real-world uncertainties, technical constraints, and economic considerations. These models are critical for enhancing the effectiveness of ESS and fostering a resilient, renewable-integrated power system capable of meeting the demands of the energy transition [10], [11].

1.2. Literature research

Extensive research has been conducted to optimize the joint deployment of renewable energy sources and ESS, employing various methodologies to maximize their synergy [12]–[22]. Hybrid storage concepts, particularly the coupling of batteries with hydrogen systems, have recently gained attention for their ability to provide both short-term flexibility and seasonal balancing [23]. A strategy for enhancing the penetration of renewables through the deployment of ESS in distribution feeders is presented in [24]. Moreover, a multi-level model for a dynamic distribution grid with significant ESS and renewable integration, focusing on expansion planning, is introduced in [25]. The study employs a Pareto-based particle swarm optimization method, considering objectives such as cost minimization, reliability enhancement, and improved renewable integration.

Subsequently, in [22], an optimization method named the grey-wolf optimization algorithm is employed to reduce grid energy loss through the introduction of energy storage systems and renewable energy generation. Complementary formulations using stochastic mixed-integer linear programming have been applied to multi-energy hubs, explicitly modeling uncertainty and yielding more resilient operational schedules [27]. A comprehensive comparative analysis, using a bus test system, is conducted to evaluate the efficiency of the methodology. In [28], for active distribution systems management, an innovative day-ahead scheduling model based on interval optimization is proposed, considering uncertainties in renewable energy sources. More advanced approaches integrate machine-learning-based demand forecasting with storage scheduling, leading to improved profitability and reduced forecast error [29].

Additionally, [30] introduces a risk-constrained two-level stochastic programming framework to optimize energy storage and thermal unit decisions in hybrid systems, mitigating risks associated with operational uncertainties. Reinforcement learning techniques have also been deployed to coordinate ESS operations across multiple electricity markets, producing measurable gains in revenue and system stability [31].

Among the various applications of ESS, arbitrage remains one of the most widely studied and practically implemented strategies. Arbitrage involves charging ESS during periods of low electricity prices and discharging when prices are high, thereby minimizing overall operational costs [32]–[37]. Systematic reviews of hybrid ESS scheduling methods highlight that combining electrochemical and mechanical storage can significantly enhance arbitrage value in future grids [38]. Several studies emphasize the role of optimal scheduling in enhancing the economic performance of ESS. For example, an optimal scheduling solution for integrating solar power into electricity markets is presented in [39],

which includes a pricing prediction method based on weather data and historical prices. Similarly, a model aimed at minimizing the operational costs of hybrid systems, considering intermittent solar and wind resources, battery state of charge, and fluctuating load demand, is introduced in [40]. Furthermore, a day-ahead scheduling strategy that minimizes regulation expenses while accounting for uncertainties in renewable energy sources and load forecasts is proposed in [41]. At the microgrid level, multi-agent coordination frameworks have demonstrated the ability to reduce operating costs while extending battery life, underscoring the role of distributed decision-making [42].

1.3. Research gap and contribution

Existing studies provide valuable insights into cost optimization and energy management strategies; however, their dependence on theoretical constructs and idealized assumptions may limit their applicability under realistic operating conditions. Key challenges—such as the variability of renewable energy generation, fluctuations in electricity demand, and price volatility—are often simplified or inadequately represented in conventional models. Furthermore, the complex interactions between distributed energy resources and energy storage systems under uncertain environments have not been comprehensively addressed. These limitations underscore the need for advanced optimization models that explicitly account for uncertainty and operational constraints. Such models have the potential to significantly improve the economic and operational effectiveness of energy storage systems (ESS), supporting more reliable scheduling and cost-efficient resource management while facilitating the integration of renewable generation.

This study proposes a two-stage stochastic optimization framework designed to bridge the gap between conceptual modeling approaches and operationally feasible energy management. The methodology incorporates both day-ahead scheduling and real-time adjustments, thereby enhancing flexibility and robustness under uncertainty. A detailed representation of battery energy storage system dynamics, including variations in storage capacity and initial State-of-Charge (SoC), enables a more accurate evaluation of performance across diverse operating scenarios. By embedding technical constraints within a structure that reflects realistic market and system behavior, the proposed framework provides a practical and adaptable tool for optimizing energy transactions and improving the cost-effectiveness of distribution networks with high levels of renewable integration.

The key contributions of this paper are as follows:

- A two-stage stochastic optimization framework is developed for distribution systems, integrating scenario-based uncertainty modeling with operational constraints to support economically and technically robust decision-making.
- A comprehensive scenario generation and reduction mechanism is implemented using Monte Carlo Simulation and probabilistic distance algorithms, enabling efficient handling of uncertainties associated with electricity prices, load demands, and renewable generation.
- Integration of battery energy storage systems is evaluated under varying capacity and state-of-charge configurations, providing quantitative insights into system flexibility, operational cost savings, and potential investment benefits.
- A detailed simulation study is conducted on a medium-voltage radial distribution feeder with high renewable penetration, using systematically derived input parameters to ensure model fidelity and practical relevance.

The remainder of this paper is organized as follows: Section II outlines the problem formulation, Section III presents the case study and numerical results, and Section IV concludes the study with key insights and future research directions.

2. MATERIAL AND METHODS

This section introduces the two-stage stochastic programming model developed to optimize the

operational costs of a distribution system operator (DSO) actively participating in both day-ahead and real-time electricity markets. The DSO procures energy to meet its demand and sells any surplus back to the grid, facilitating efficient energy management across varying time horizons. Figure 1 illustrates the interaction between the day-ahead planning (Stage-I) and real-time adjustment (Stage-II) processes, providing an overview of the framework.

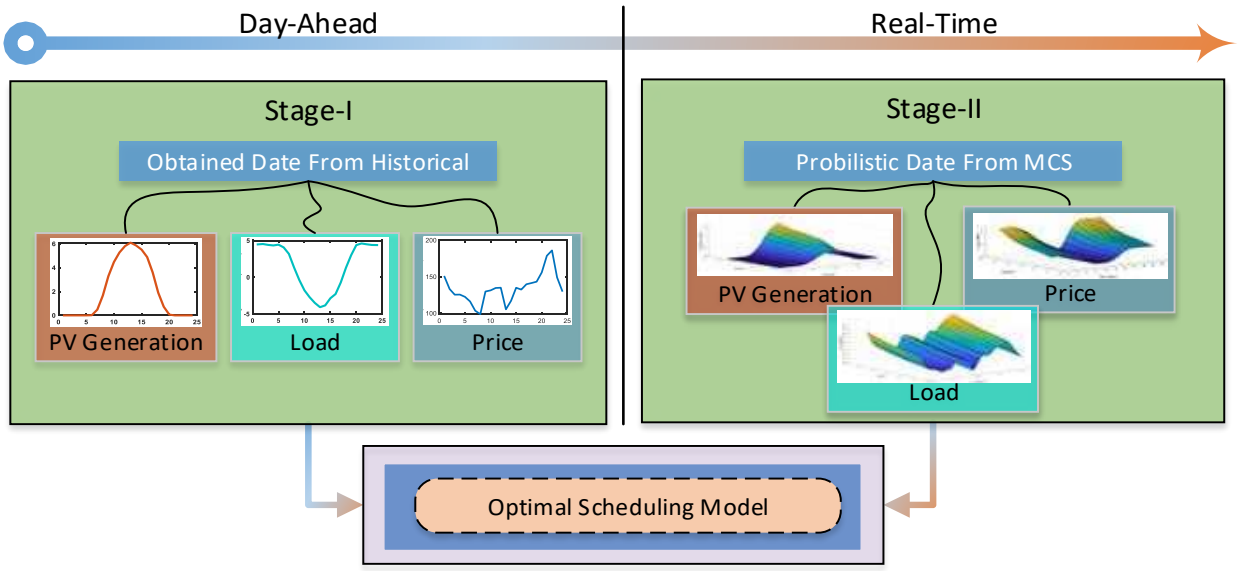


Fig. 1. Two-stage programming structure

- In the first stage, day-ahead market decisions are made based on historical data for photovoltaic (PV) generation, electricity demand, and market prices. These forecasts enable proactive scheduling of power generation from renewable energy sources and loads, providing a robust foundation for initial energy management plans. This stage ensures that the DSO is prepared for anticipated conditions while optimizing procurement and dispatch strategies.
- The second stage refines these initial plans by addressing real-time uncertainties using Monte Carlo simulations (MCS). Probabilistic scenarios are generated to account for fluctuations in PV generation, electricity demand, and market price volatility. These adjustments ensure adaptive and efficient operations, mitigating the risks associated with unpredictable conditions in real-time markets.

The optimal scheduling model seamlessly integrates both stages, leveraging historical forecasts and probabilistic data to enhance the reliability and cost-effectiveness of energy management. By bridging the gap between day-ahead predictions and real-time operations, the model effectively addresses the uncertainties associated with renewable energy variability, load fluctuations, and market dynamics. The mathematical formulation and detailed description of the optimization model are presented in the subsequent sections.

2.1. Mathematical Formulation

The objective function, mathematically expressed in Equation (1), minimizes the operational cost of the distribution system.

$$\text{Min OF}= \sum_{t=1}^{24}(DACOST_{S1,t} + RTCOST_{S2,t\omega}) \quad (1)$$

The first and second stages of this economic model are represented by Equations 2 and 3, denoted as $DACOST_{S1,t}$ and $RTCOST_{S2,t\omega}$, respectively. $DACOST_{S1,t}$, represents the day-ahead market transactions,

encompassing the power exchange cost between the downstream and upstream grids, as well as the energy cost determined at a price agreed upon for demand-side reserves, which constitute day-ahead market operations. Where t denotes the hourly time index, ϑ represents the market clearing price ($/MWh), and P is the active power (MW). DSR denotes demand-side reserve with U and D indicating upward and downward variations. BUY and SELL signify transactions involving buying from and selling to the market. The subscript S1 indicates the day-ahead stage (Stage 1).

$$DACOST_{S1,t} = (\vartheta_t^{BUY,S1} * P_t^{BUY,S1}) - (\vartheta_t^{SELL,S1} * P_t^{SELL,S1}) + (\vartheta_t^{DSR,U} * SR_t^{DSR,U}) + (\vartheta_t^{DSR,D} * SR_t^{DSR,D}) \quad (2)$$

The coordination of energy transactions with the main grid incurs expected costs based on the deviation between scheduled and actual energy supply and demand. Additionally, if energy generation and consumption are misaligned within the grid, compulsory load reductions may be required, leading to further expenses. Consequently, $RTCOST_{S2,t\omega}$, captures the costs associated with deviations arising from changes in the first-stage decisions. This includes the costs of adjustment power exchanges, demand-side reserve deployment, and potential load shedding. In Equation (3), ω is the scenario index, π_ω the probability of scenario ω, and ΔP the deviation in active power (MW) relative to day-ahead schedules. DEPL and SHEDDING denote deployment and load-shedding costs, respectively. Superscripts U and D indicate upward and downward adjustments, while S2 specifies the real-time stage.

$$\begin{aligned} RTCOST_{S2,t\omega} = \sum_{\omega=1}^{N} \pi_\omega [(\vartheta_{t\omega}^{BUY,S2,U} * \Delta P_{t\omega}^{BUY,S2,U}) - (\vartheta_{t\omega}^{BUY,S2,D} * \Delta P_{t\omega}^{BUY,S2,D}) + (\vartheta_{t\omega}^{SELL,S2,D} * \\ \Delta P_{t\omega}^{SELL,S2,D}) - (\vartheta_{t\omega}^{SELL,S2,U} * \Delta P_{t\omega}^{SELL,S2,U}) + \vartheta_{t\omega}^{DEP} * (SR_{t\omega}^{DEPL,U} - SR_{t\omega}^{DEPL,D}) + (\vartheta_{t\omega}^{SHEDDING} * P_{t\omega}^{SHEDDING})] \end{aligned} \quad (3)$$

Within the technical model framework, energy storage and power flow models are delineated for both day-ahead and real-time scenarios. The energy storage models are described by Equations (4) and (5), assuming the presence of a battery energy storage system. In Equations (4) and (5), SOC_t is the state-of-charge of the storage system at time t (%), η^{STG} is the round-trip efficiency of the battery, Q^{STG} is the storage energy capacity (MWh), $P^{STG,+}$ and $P^{STG,-}$represent charging and discharging power (MW), and ΔT is the duration of each interval (h).

$$SOC_t^{STG,S1} = SOC_{t-1}^{STG,S1} + \left(\frac{\eta^{STG} * \Delta T}{Q^{STG}}\right) * \left(P_{t-1}^{STG,S1,+} - \left(\frac{P_{t-1}^{STG,S1,-} * \Delta T}{\eta^{STG} * Q^{STG}}\right)\right) \quad (4)$$

$$SOC_{t\omega}^{STG,S2} = SOC_{(t-1)\omega}^{STG,S2} + \left(\frac{\eta^{STG} * \Delta T}{Q^{STG}}\right) * \left(P_{(t-1)\omega}^{STG,S2,+} - \left(\frac{P_{(t-1)\omega}^{STG,S2,-} * \Delta T}{\eta^{STG} * Q^{STG}}\right)\right) \quad (5)$$

The power balance for loads, energy storage systems, and renewable energy sources is outlined by Equations (6) and (7) for day-ahead operations, and Equations (8) and (9) for real-time operations. The power buy and sell quantities must be balanced during grid operations. In these power balance constraints, P^{RES} denotes renewable generation, P^{LOAD} is demand, P^{GRID} is the power exchanged with the upstream grid, and $P^{STG,+/-}$ are storage charging/discharging terms.

$$P_t^{GRID,S1} + P_t^{BUY,S1} - P_t^{SELL,S1} = 0 \quad (6)$$

$$P_t^{GRID,S1} = P_t^{RES,S1} + P_t^{STG,S1,-} - P_t^{LOAD,S1} - P_t^{STG,S1,+} \quad (7)$$

$$P_{t\omega}^{GRID,S2} + P_{t\omega}^{BUY,S2} - P_{t\omega}^{SELL,S2} = 0 \quad (8)$$

$$P_{t\omega}^{GRID,S2} = P_{t\omega}^{RES,S2} + P_{t\omega}^{STG,S2,-} + P_{t\omega}^{SHED} - P_{t\omega}^{LOAD,S2} - P_{t\omega}^{STG,S2,+} \quad (9)$$

Additionally, in real-time operations, the terms $\Delta P_{t\omega}^{BUY,S2}$ and $\Delta P_{t\omega}^{SELL,S2}$ express the total deviation of $P_{t\omega}^{BUY,S2}$ and $P_{t\omega}^{SELL,S2}$, respectly. And the connection between the terms $\Delta P_{t\omega}^{BUY,S2,U}$, $\Delta P_{t\omega}^{BUY,S2,D}$, $\Delta P_{t\omega}^{SELL,S2,U}$, $\Delta P_{t\omega}^{SELL,S2,D}$ in Equation (3) and the expression $P_{t\omega}^{BUY,S2}$ and $P_{t\omega}^{SELL,S2}$ in Equation (8) can be established with Equations (10)-(13).

$$P_{t\omega}^{BUY,S2} = \Delta P_{t\omega}^{BUY,S2} + P_t^{BUY,S1} \tag{10}$$

$$\Delta P_{t\omega}^{BUY,S2} = \Delta P_{t\omega}^{BUY,S2,U} - \Delta P_{t\omega}^{BUY,S2,D} \tag{11}$$

$$P_{t\omega}^{SELL,S2} = \Delta P_{t\omega}^{SELL,S2} - P_t^{SELL,S1} \tag{12}$$

$$\Delta P_{t\omega}^{SELL,S2} = \Delta P_{t\omega}^{SELL,S2,U} - \Delta P_{t\omega}^{SELL,S2,D} \tag{13}$$

Consequently, the formulated optimization problem is implemented and solved within the GAMS framework using the CPLEX solver, as demonstrated in Figure 2.

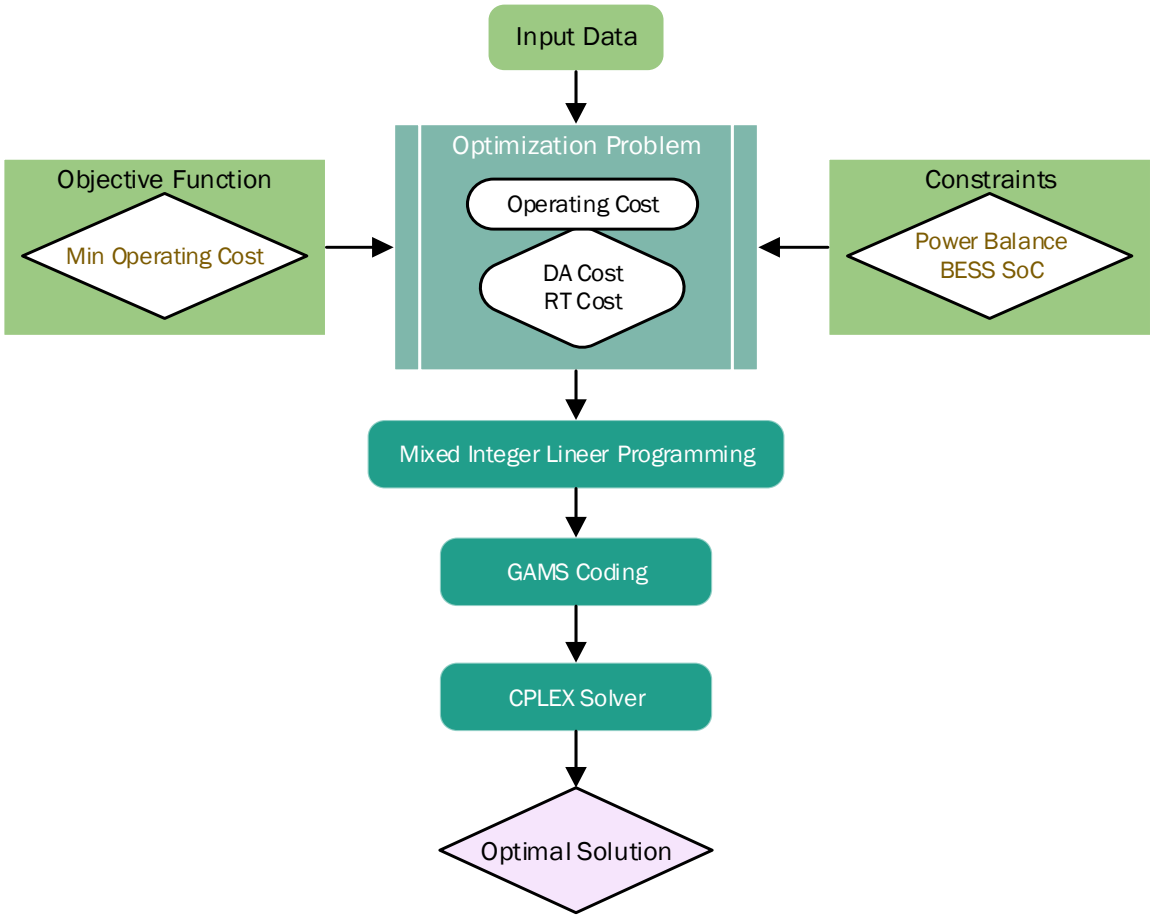


Fig. 2. Two-stage optimization structure

2.2. Simulation Data

The load curve and generation profiles were constructed to reflect typical hourly and seasonal variations observed in distribution network operations. For each month, characteristic hourly averages were determined to capture diurnal fluctuations in both demand and photovoltaic generation, as illustrated in Figure 3. Electricity market prices, aligned with actual market dynamics, were incorporated

using publicly accessible data from the EPIAS (Energy Market Regulatory Authority) Transparency Platform and are presented in Figure 4.

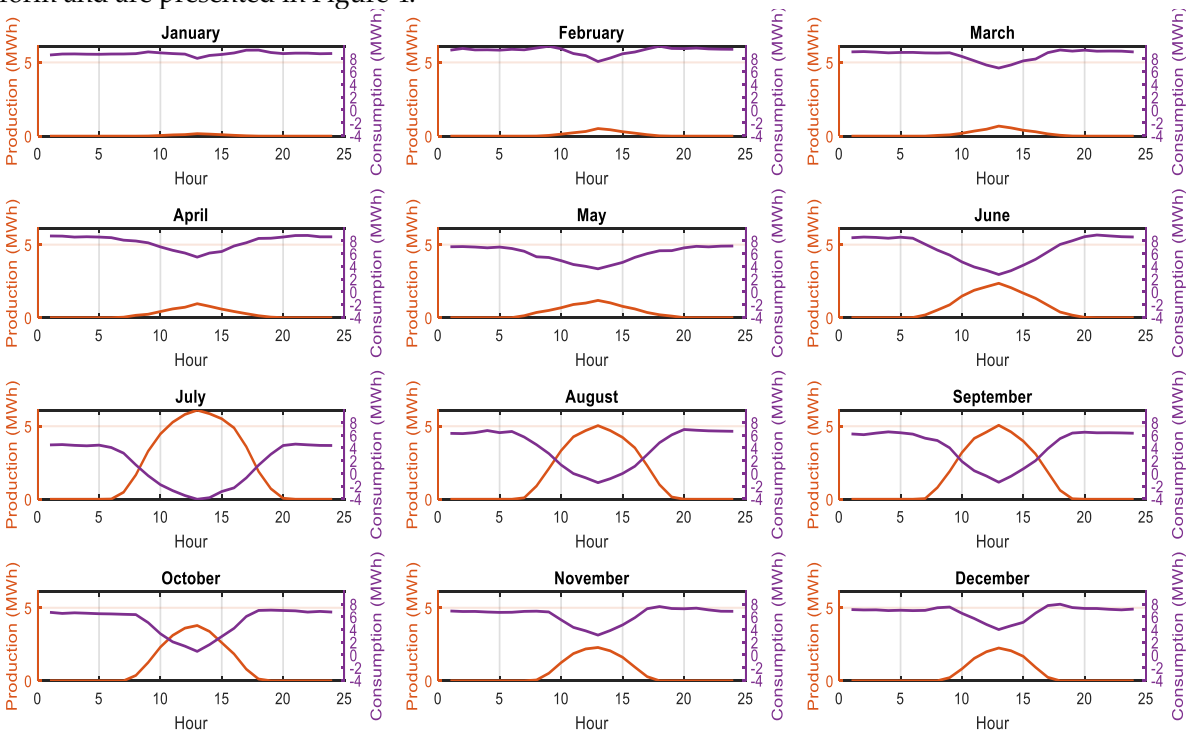


Fig. 3. The production and consumption profiles

The data highlights distinct seasonal variations in production and consumption. Production peaks in summer due to higher photovoltaic output, leading to surplus energy that is often fed into the grid. This surplus reduces network consumption and can result in negative consumption values. Conversely, winter months see decreased photovoltaic output and increased energy demand, shifting reliance to conventional energy sources. Consequently, winter consumption rises as the system compensates for reduced renewable energy. This seasonal variability significantly impacts overall energy consumption and distribution within the grid.

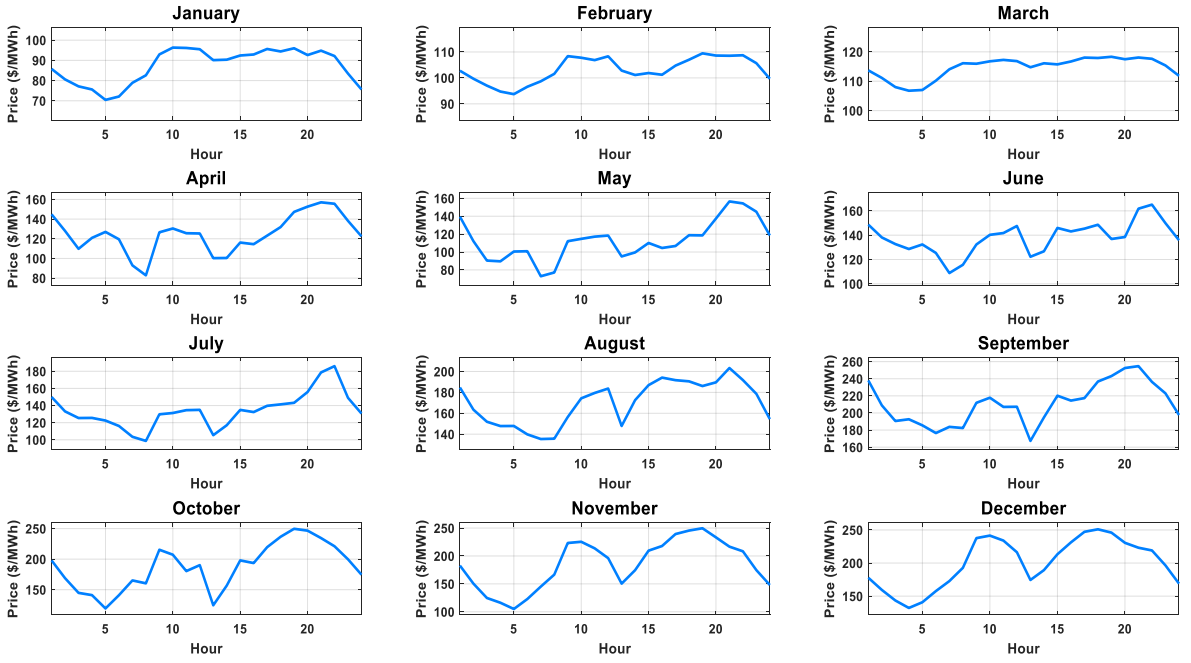


Fig. 4. The energy market prices

Energy price trends over the year show a consistent upward trajectory, primarily driven by increasing demand and general market inflation. From the initial months, a gradual rise in prices is evident, reflecting both seasonal demand fluctuations and broader economic factors. The persistent price increase throughout the year indicates that while seasonal variations play a role, the overarching trend is influenced significantly by inflationary pressures and sustained growth in energy consumption.

Among energy storage technologies, considering the power and energy range, battery energy storage systems are mainly used in distribution systems [43]–[46]. So, for the rest of this document, a battery energy storage system will be assumed to play the energy storage system. The data for energy storage which is created hypothetically are shown in Table 1. The efficiency of the storage system, which is determined as battery storage technology, is determined as 90%. The charging and discharging power were kept constant as 2 MW and analyzed at various capacities. The SoC values were determined so as not to fall below the 10% occupancy limit and not to rise above the 90% occupancy limit, i.e. to operate in safe mode. The SoC value at the beginning of the planning horizon was determined at 20%, 40%, 60% and 80% occupancy rates, respectively.

Table 1. Parameters of the energy storage system

Technology	Effiency (%)	SoC_{min} (%)	SoC_{max} (%)	$SoC_{initial}$ (%)	$P_{charging}$ (MW)	$P_{discharging}$ (MW)	Capacity (MWh)
Batarya	90	10	90	20-40-60-80	2	2	4-6-8-10

2.3. Handling the Uncertainties

To represent the variability of key operational parameters and ensure a realistic evaluation of system performance, this study adopts a probabilistic modeling framework based on Monte Carlo Simulation. Known for its effectiveness in quantitative analysis, the Monte Carlo method enables the generation of statistically diverse input scenarios by sampling from predefined probability distributions. This approach allows for a broad exploration of operational variability without relying on deterministic simplifications or extensive empirical datasets [47].

In this framework, three principal variables—electricity market prices, load demand, and photovoltaic (PV) generation—are modeled as random processes governed by probability distributions that reflect their typical temporal and statistical behavior. These distributions are used to generate a wide spectrum of plausible realizations through the Monte Carlo simulation engine [48], [49], forming a comprehensive scenario space that captures the dynamic nature of distribution network operations.

To address the computational demands of large scenario sets, a scenario reduction technique is applied. A probabilistic distance-based algorithm [50], [51] is utilized to identify and retain a representative subset of scenarios that preserve the essential statistical characteristics of the full ensemble. This reduction enhances numerical efficiency while maintaining the diversity and integrity of the modeled uncertainty.

The resulting reduced set, organized into five probability-weighted scenario packages, constitutes a scenario index that serves as the input for the optimization framework. This enables cost evaluations that are both computationally tractable and sensitive to operational variability, supporting effective planning and management strategies in distribution networks.

3. SIMULATION AND RESULTS

3.1. Case Study Description

To validate the proposed stochastic optimization framework, a detailed simulation is carried out on a

representative 61-bus radial medium-voltage distribution network. The system is modeled with a total apparent power capacity of 10.6 MVA and includes a 31.5/0.4 kV distribution transformer, connected to the upstream grid via a 154/31.5 kV coupling transformer.

The network includes a high level of distributed photovoltaic (PV) generation, comprising eleven units with a total installed capacity of 10.3 MVA. Initially, nine PV generators totaling 5.06 MW were in operation; two additional units (5.24 MW combined) were integrated during the second half of the year. This dynamic expansion has been captured in the simulation to reflect temporal variability in renewable generation capacity.

All system attributes—such as feeder topology, load demand profiles, and generation characteristics—have been systematically parameterized to provide a reliable basis for evaluating the performance of the proposed optimization model under uncertainty.

2.3. Numerical Results

The model's performance is assessed by comparing total operational costs under different energy storage configurations. Simulations are conducted over a full annual cycle using a 24-hour rolling planning horizon, considering monthly intervals. The analysis includes both a baseline case without energy storage and multiple scenarios incorporating second-life battery energy storage systems (BESS) with varying rated capacities and initial State of Charge (SoC) conditions.

The resulting operational costs for each configuration are presented in Table 2. The findings indicate substantial cost reductions in scenarios that integrate BESS, with the extent of improvement influenced by both seasonal fluctuations in renewable generation and storage-specific parameters. These results underscore the economic and operational benefits of adopting energy storage systems within stochastic optimization frameworks for distribution networks.

Table 2. Monthly average operating costs by capacity and SoC

Capacity (MWh)	SoC (%)	Operating Costs Calculated Based on Monthly Averages ($/day)											
		Jan	Feb	Mar	Apr	May	Jun	Jul	Aug	Sep	Oct	Nov	Dec
0	0	7232.7	8472.6	6538.40	10089.4	2131.3	1332.2	-12922.63	-10818.95	-11238.8	-2787.2	3112.1	5794.5
4	20	5330.5	5990.2	3707.2	6916.3	-1021.6	-2606.0	-15603.7	-14436.5	-17045.4	-7889.9	-1849.1	280.8
	40	5246.3	5672.8	3645.5	6620.4	-1223.1	-2885.6	-15930.8	-14950.0	-17193.7	-8015.3	-2104.8	-38.2
	60	5048.2	5546.2	3429.0	6611.7	-1300.4	-2972.6	-16311.3	-15394.4	-17571.2	-8115.8	-2341.4	-232.6
	80	4786.1	5448.4	3274.5	6284.4	-1409.4	-3041.9	-16345.8	-15651.6	-17594.1	-8388.3	-2444.8	-380.5
6	20	4512.6	5387.3	2987.2	5799.3	-1751.1	-3366.9	-16380.6	-16081.8	-18573.1	-9241.4	-3082.5	-997.4
	40	4421.4	5258.3	2820.0	5941.1	-1811.7	-3583.9	-17158.2	-16586.7	-18569.1	-9258.0	-3375.1	-1257.3
	60	4098.1	4989.1	2535.6	5351.2	-2087.9	-4009.7	-17813.0	-17414.4	-19621.2	-10070.9	-3596.7	-1609.0
	80	4002.0	4723.9	2268.3	5376.8	-2087.9	-3982.2	-17786.5	-17161.1	-19587.1	-9946.4	-3760.5	-1826.9
8	20	4201.8	4984.0	2674.4	5868.2	-1918.5	-3637.9	-17281.8	-16737.0	-19076.1	-9663.9	-3480.3	-1410.1
	40	4182.2	4950.5	2248.3	5623.5	-2203.9	-4111.4	-17505.1	-17021.9	-19144.9	-9709.2	-3963.4	-1879.5
	60	3663.7	4284.2	1883.9	4950.8	-2456.6	-4513.4	-18229.3	-18005.0	-20364.9	-10640.7	-4341.9	-2390.9
	80	3462.6	4016.5	1579.5	4714.4	-2664.7	-4705.6	-18543.9	-18130.1	-20868.9	-10720.0	-4641.7	-2768.2
10	20	3938.5	4646.4	2306.7	5377.1	-2100.1	-3873.4	-17606.4	-17203.2	-18246.6	-10168.3	-3907.0	-1859.5
	40	3664.4	4285.2	1885.1	4951.7	-2455.8	-4512.2	-18226.7	-18003.0	-20363.0	-10639.4	-4340.7	-2389.4
	60	3462.6	4016.5	1579.5	4714.4	-2664.7	-4824.2	-18543.9	-18398.5	-20868.9	-10981.4	-4641.7	-2768.2
	80	3462.6	4016.5	1579.5	4714.4	-2664.7	-4591.3	-18543.9	-17882.3	-20868.9	-10839.7	-4641.7	-2768.2

In scenarios without energy storage systems, operational costs show negative values during specific months, particularly July, August, and September. These negative costs are attributed to surplus renewable energy production exceeding grid consumption, with the excess energy sold to wholesale markets. The cost reductions are primarily driven by free local renewable energy sources, especially during summer when elevated solar generation significantly lowers operating costs compared to other seasons.

In contrast, the deployment of energy storage systems allows profitability—reflected by negative operational costs—to be achieved earlier and sustained over an extended period throughout the year. Specifically, the transition to profitability begins in May and extends for eight months, compared to four months in the absence of storage. The inclusion of storage systems reduces operational costs more effectively, particularly as storage capacity and SoC levels increase. However, further analysis shows non-linear behaviors; higher storage capacities or SoC levels do not always guarantee increased profitability.

2.3. Storage Behavior and Profitability Analysis

To provide a more comprehensive understanding of the impact of State of Charge (SoC) levels on profitability, this section presents detailed analyses for four different SoC levels (20%, 40%, 60%, and 80%) across various storage capacities. The following discussion highlights how storage configurations influence operational cost optimization, with insights drawn from the figures specific to this section. Economic performance is reported as monthly operating profit; in this account, negative operating costs indicate profit.

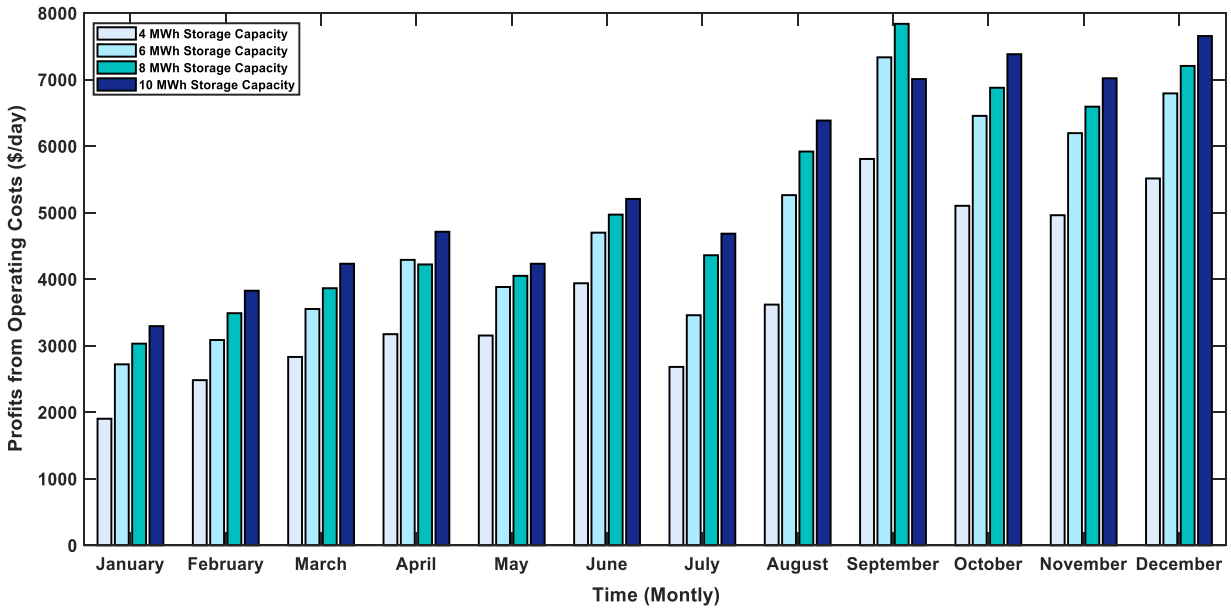


Fig. 5. Monthly profitability at 20% initial SoC for different storage capacities

Figure 5 illustrates monthly profits for different storage capacities starting with a 20% SoC. The results demonstrate that profitability generally increases with storage capacity. For example, the 10 MWh system achieves the highest profits during peak periods from August to December by effectively managing surplus energy. Nevertheless, smaller capacities occasionally outperform larger ones; for instance, the 6 MWh system surpasses the 8 MWh system in April, while the 8 MWh system outperforms the 10 MWh system in September. In April, lower demand together with shorter daylight hours moderates PV generation and constrains charging opportunities, so the marginal benefit of additional capacity

diminishes and smaller units achieve higher utilization efficiency. In September, a saturation effect emerges: available price spreads and charging windows are insufficient to keep the larger asset fully engaged, causing excess capacity to under-recover its incremental cost despite higher nameplate energy. This indicates that the relationship between capacity and profitability is influenced by operational conditions and market dynamics.

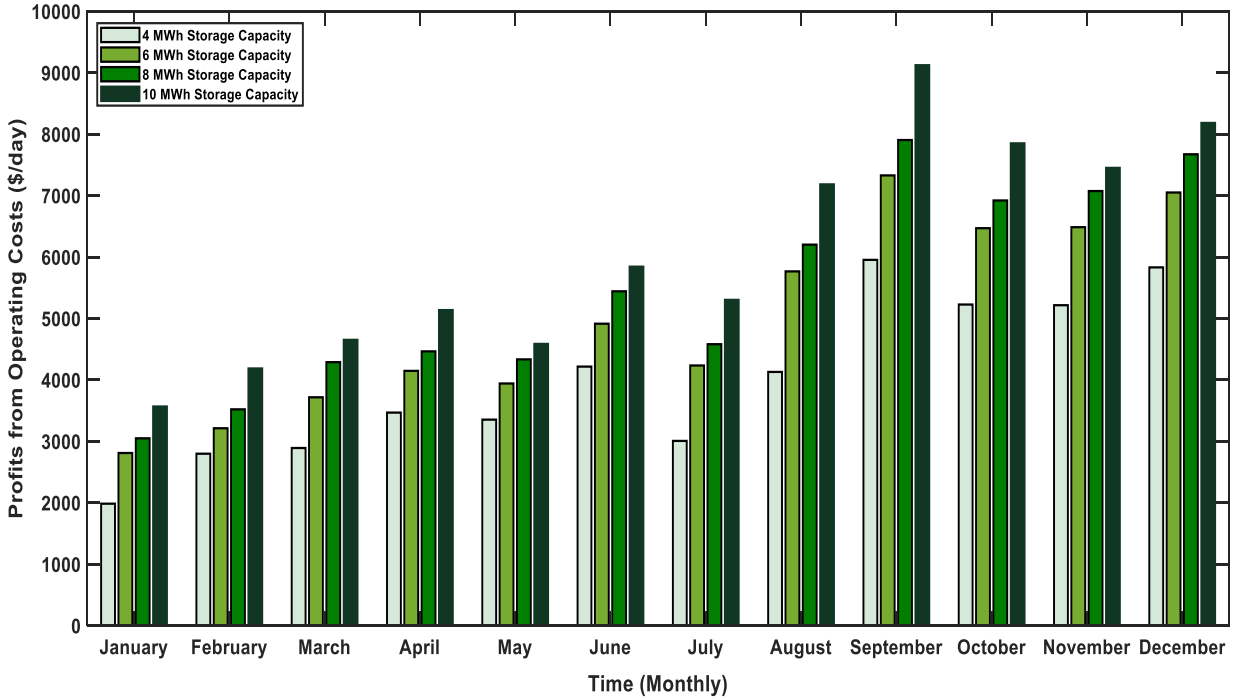


Fig. 6. Monthly profitability at 40% initial SoC for different storage capacities

When the initial SoC is increased to 40%, as shown in Figure 6, larger storage capacities continue to yield higher profits, especially during peak demand months like September and December. The 10 MWh system maximizes cost savings by efficiently storing energy during low-demand periods and discharging during peak demand. Seasonal trends reveal increased profits in summer and winter due to heightened energy consumption and price volatility, while lower profits occur in spring due to reduced demand and price variability. Smaller systems, such as the 4 MWh and 6 MWh capacities, demonstrate limited profitability due to their inability to fully capitalize on price differentials. At this intermediate SoC, the trade-off between charging headroom and dispatch readiness becomes more favorable for larger capacities in high-volatility months, yet in shoulder months limited spreads may again compress arbitrage margins, particularly for the largest configuration.

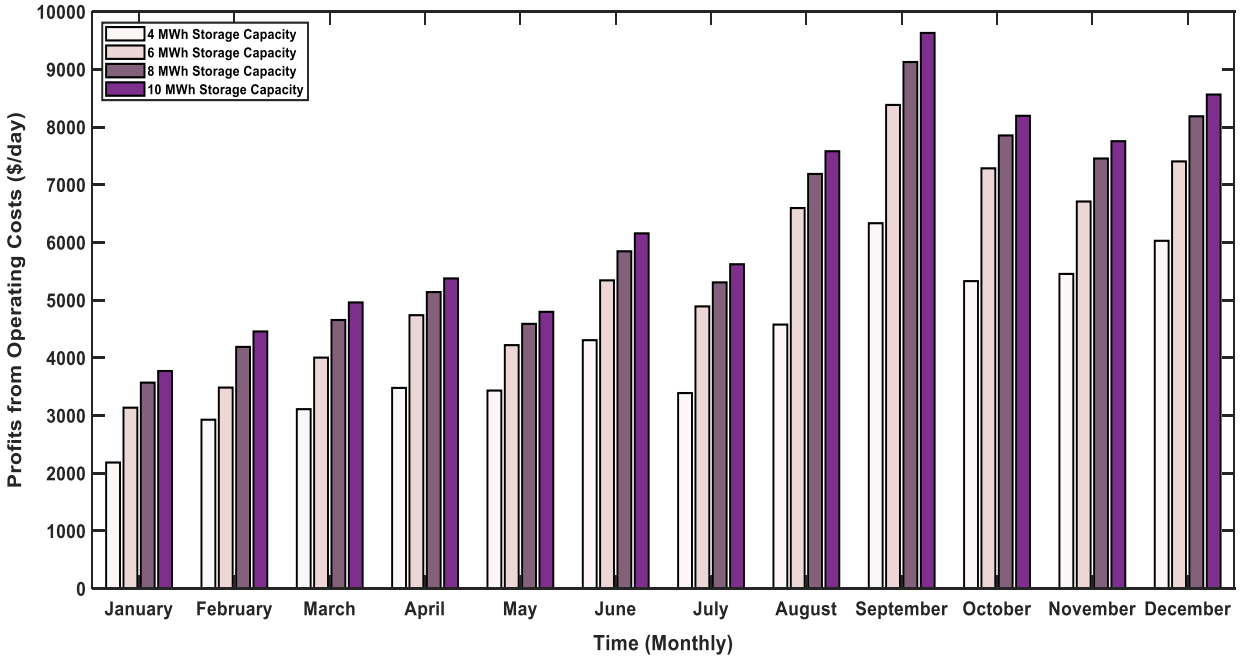


Fig. 7. Monthly profitability at 60% initial SoC for different storage capacities

Figure 7 presents results for an initial SoC of 60%. The analysis confirms that larger capacities generally provide higher profitability, particularly in summer months with significant demand fluctuations. However, diminishing returns are observed at high capacities. For example, the 10 MWh system shows lower incremental benefits compared to the 8 MWh system in June and August. This pattern is consistent with spread compression and partial-cycle operation: as the SoC ceiling binds more frequently, additional capacity cannot be fully charged or optimally dispatched within available price windows, and round-trip efficiency and cycle-limit considerations further attenuate incremental gains. This suggests that beyond certain thresholds, optimal performance requires a balance between capacity and operational conditions.

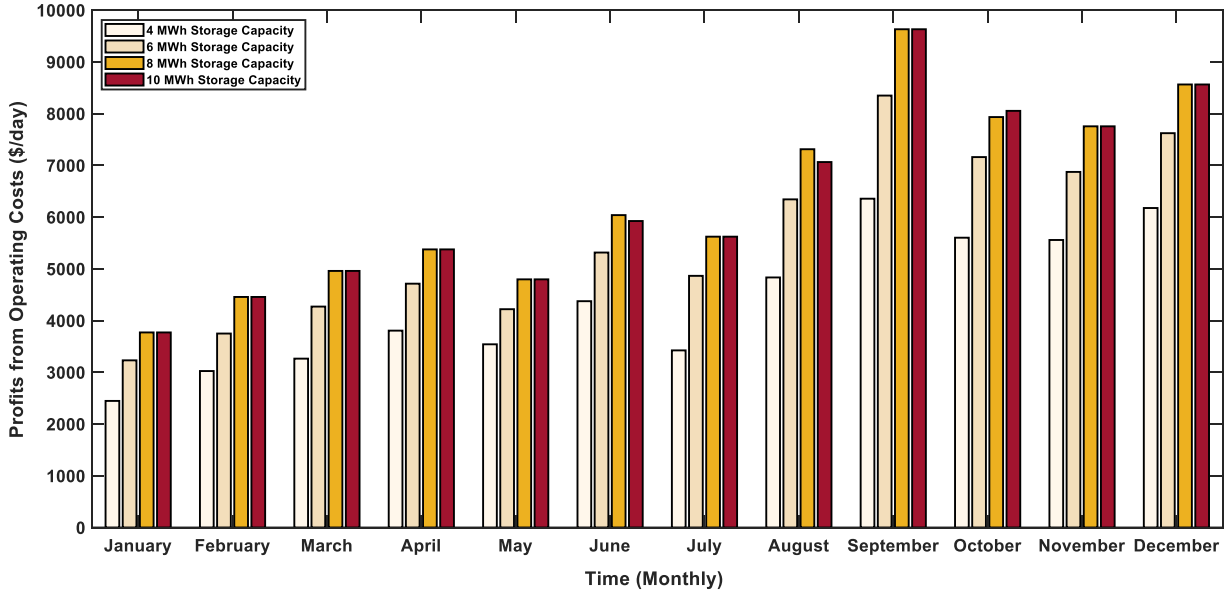


Fig. 8. Monthly profitability at 80% initial SoC for different storage capacities.

Finally, with an initial SoC of 80%, illustrated in Figure 8, similar seasonal trends persist. Larger systems achieve greater profitability overall, but some deviations from the expected profitability pattern are observed. In April, lower demand together with shorter daylight hours moderates PV generation and constrains charging opportunities, so smaller capacities achieve higher utilization efficiency. In September, a saturation effect emerges: available price spreads and charging windows are insufficient to keep the larger asset fully engaged, causing excess capacity to under-recover its incremental cost despite higher nameplate energy. At elevated SoC levels, reduced charging headroom limits absorption of low-price energy, allowing moderate-sized systems to outperform larger ones. These explanations explicitly link the observed breakpoints in profitability trends with their technical and operational causes. Overall, these findings underscore the importance of tailoring storage configurations to specific market and system conditions, optimizing both capacity and initial SoC to balance operational cost reductions and profitability.

2.3. Storage Capacity and SoC Impact on Profitability

To enhance the understanding of profitability dynamics and storage system behavior, Figure 9 presents a detailed analysis of charge and discharge cycles over a 24-hour period, considering varying initial State of Charge (SoC) levels and storage capacities. The analysis demonstrates a consistent initial discharge trend across all scenarios, with the system prioritizing the storage of energy generated from local sources for later use in the grid.

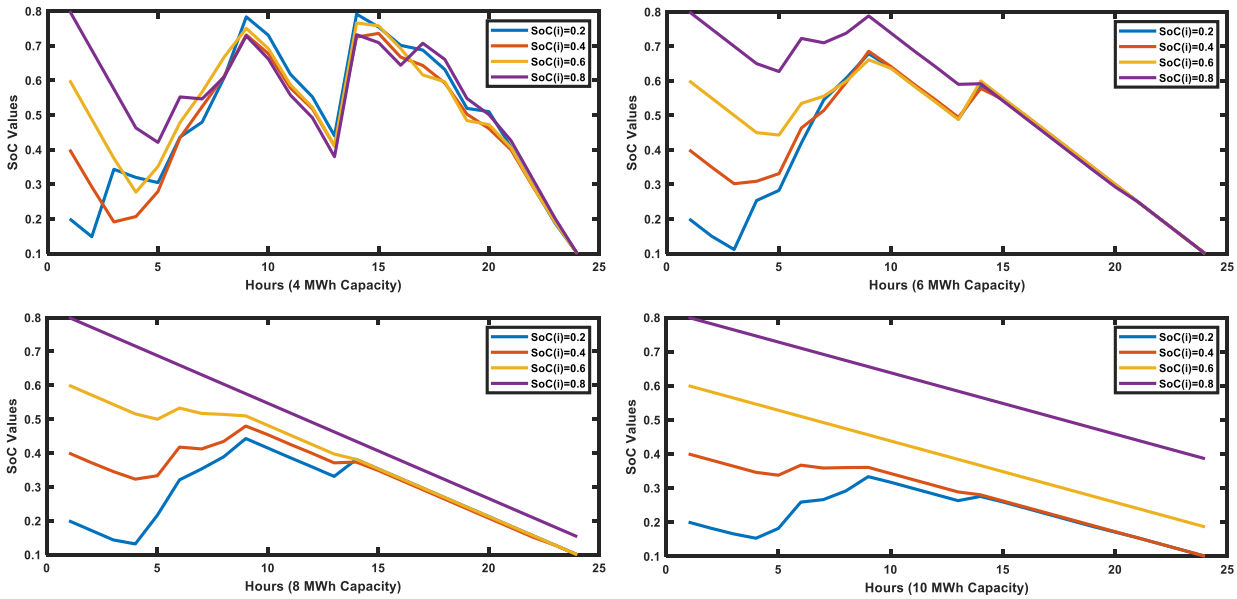


Fig. 9. Changes in state of charge values

The frequency of discharge cycles is notably higher for smaller storage capacities, particularly during evening hours, when demand peaks and energy prices are elevated. As storage capacity increases, the frequency of these discharge cycles decreases, contributing to more efficient energy management. Additionally, systems with higher initial SoC levels demonstrate extended periods of inactivity regarding charging, emphasizing the system's efficiency in managing energy without needing frequent replenishment. This highlights the effectiveness of optimizing both initial SoC levels and storage capacity for improving energy management, reducing operational costs, and enhancing grid stability.

Building on this behavioral analysis, the profitability of different energy storage systems was assessed. The results underscore the significant impact of storage capacity and SoC on overall profitability. Annual profitability was evaluated by averaging results across various SoC levels for each storage capacity, while investment costs were factored into the analysis, as outlined in Table 3. The investment costs reported in

Table 3 are based on representative ranges from recent literature and market data on utility-scale lithium-ion BESS projects. While cost levels vary depending on region and supplier, the adopted values were normalized to reflect average market conditions, ensuring both methodological transparency and comparability with other studies [52], [53].

A key focus of this assessment was the payback period, which represents the time required to recover the initial investment.

Table 3. Investment, profit, and payback results for different storage capacities

Energy Storage Capacity (MWh)	Investment Cost ($)	Profit Amount ($/Year)	Payback Period (Year)	Net Profit in 10 Years ($)
4	2640000	1491901.456	1.77	12279014.56
6	3816000	1906426.405	2.00	15248264.05
8	4896000	2107771.424	2.32	16181714.24
10	6000000	2216842.898	2.71	16168428.98

In line with this, the analysis indicates that while increasing storage capacity generally improves profitability, it also extends the payback period due to higher initial investment costs. Larger storage systems lead to higher annual profits, yet the relationship between storage capacity and profitability becomes non-linear when investment costs are included. In particular, the 10 MWh configuration achieves the highest annual operating profit when investment costs are excluded, reflecting its ability to capture the greatest short-term arbitrage opportunities. However, when capital expenditure is considered, the 8 MWh system achieves the most favorable long-term outcome, with the shortest payback period and highest cumulative net profit over the 10-year horizon. This distinction clarifies that the largest system maximizes revenue potential, while a slightly smaller system offers superior investment efficiency. This underlines the critical importance of carefully selecting the optimal storage capacity to maximize long-term profitability, highlighting the need for a balanced approach that accounts for both storage capacity and investment costs.

4. CONCLUSIONS

This study presents a comprehensive evaluation of energy storage system (ESS) integration in distribution networks, focusing on operational cost minimization through a two-stage stochastic optimization approach. The proposed framework addresses uncertainties in energy management by employing a Mixed-Integer Linear Programming (MILP) formulation, developed within the GAMS environment and solved using the CPLEX solver.

The model is applied to a representative medium-voltage radial distribution feeder, parameterized with monthly profiles of load demand, solar generation, and electricity market prices to ensure a contextually relevant and technically consistent simulation environment. The analysis captures both temporal variations and stochastic behavior of key operational parameters.

Simulation results reveal that increasing storage capacity leads to substantial reductions in operational costs, with corresponding annual profit values of $1.49 million, $1.90 million, $2.10 million, and $2.21 million for ESS capacities of 4, 6, 8, and 10 MWh, respectively. Profitability improves by approximately 32%, 48%, and 56% when scaling capacity from 4 MWh to 6, 8, and 10 MWh. Nevertheless, diminishing marginal returns are observed at higher capacity levels due to the nonlinear interaction between storage capacity and initial State of Charge (SoC). Although larger capacities yield higher annual profits, they are accompanied by longer payback periods, primarily driven by elevated capital investment requirements.

Consequently, investment decisions must balance both profitability and capital costs to optimize long-term returns. Among the evaluated configurations, the 8 MWh storage system exhibits the most favorable balance between economic feasibility and profitability over a 10-year investment horizon. These findings demonstrate the strategic importance of optimal sizing in storage deployment decisions, particularly in regulatory or market environments characterized by moderate price volatility.

Overall, the study provides actionable insights for decision-makers by quantifying the trade-offs between investment costs, operational savings, and return on investment in energy storage planning. The ability to leverage time-of-use pricing and energy arbitrage opportunities enhances cost-efficiency; however, financial viability remains sensitive to market structures and incentive mechanisms. In this respect, instruments such as carbon taxation, emission pricing, capital subsidies, tax credits, and capacity remuneration schemes can significantly influence investment viability; for example, a carbon tax could alter the economic feasibility and investment profitability of battery energy storage systems, highlighting the importance of incorporating policy mechanisms into future planning.

Future extensions of this work may incorporate broader aspects such as demand response participation, sector coupling with electric mobility or heating, the explicit modeling of carbon pricing mechanisms, and detailed battery degradation dynamics, thereby expanding the applicability of the framework to emerging scenarios in the energy transition.

Declaration of Ethical Standards

All authors affirm that this manuscript fully complies with established ethical standards concerning authorship, citation, data integrity, and the publication of original research. The content has been solely developed for this submission, has not been published elsewhere, and is not under concurrent consideration by any other journal. All contributors have reviewed and approved the final version of the manuscript.

Credit Authorship Contribution Statement

F.A.F.: Conceptualization, methodology, formal analysis, investigation, writing – original draft, visualization, and review & editing.

İ.K.: Data curation support, visualization, figure generation, and manuscript formatting.

Ö.F.K.: Supervision, critical revision of the manuscript, guidance throughout the research process, and final approval.

Declaration of Competing Interest

The authors declare that there are no known competing financial or non-financial interests that could have appeared to influence the work reported in this manuscript.

Funding / Acknowledgements

This research did not receive any specific grant from funding agencies in the public, commercial, or not-for-profit sectors.

Data Availability

Due to ethical obligations and confidentiality agreements, the dataset generated and/or analyzed during the current study is not publicly available. Reasonable requests for access to anonymized data can be made by contacting the corresponding author.

Use of Artificial Intelligence

The authors declare that generative AI tools were used only for language refinement and minor editorial assistance. All scientific content, methodology, analysis, and conclusions were developed entirely by the authors, and the authors take full responsibility for the content of this manuscript.

5. REFERENCES

[1] B. Sun, Y. Li, Y. Zeng, J. Chen, and J. Shi, "Optimization planning method of distributed generation based on steady-state security region of distribution network," Energy Reports, vol. 8, pp. 4209–4222, 2022, doi: 10.1016/j.egyr.2022.03.078.

[2] S. E. Ahmadi, S. M. Kazemi-Razi, M. Marzband, A. Ikpehai, and A. Abusorrah, "Multi-objective stochastic techno-economic-environmental optimization of distribution networks with G2V and V2G systems," Electr. Power Syst. Res., vol. 218, no. December 2022, p. 109195, 2023, doi: 10.1016/j.epsr.2023.109195.

[3] D. A. Elalfy, "Comprehensive review of energy storage systems (ESS) for integrating renewable energies in microgrids," Journal of Energy Storage, vol. 91, p. 110352, 2024, doi: 10.1016/j.est.2024.110352.

[4] M. Amini, M. H. Nazari, and S. H. Hosseinian, "Optimal Scheduling and Cost-Benefit Analysis of Lithium-Ion Batteries Based on Battery State of Health," IEEE Access, vol. 11, no. December 2022, pp. 1359–1371, 2023, doi: 10.1109/ACCESS.2022.3232282.

[5] M. Zadehbagheri and A. R. Abbasi, "Energy cost optimization in distribution network considering hybrid electric vehicle and photovoltaic using modified whale optimization algorithm," J. Supercomput., vol. 79, no. 13, pp. 14427–14456, 2023, doi: 10.1007/s11227-023-05214-2.

[6] X. Yan, "Review on reliability assessment of energy storage systems," IET Smart Grid, vol. 7, no. 2, pp. 123–137, 2024, doi: 10.1049/stg2.12179.

[7] C. Zhao, P. B. Andersen, C. Træholt, and S. Hashemi, "Grid-connected battery energy storage system: a review on application and integration," Renew. Sustain. Energy Rev., vol. 182, no. September 2022, p. 113400, 2023, doi: 10.1016/j.rser.2023.113400.

[8] K. Liu et al., "An energy optimal schedule method for distribution network considering the access of distributed generation and energy storage," IET Gener. Transm. Distrib., vol. 17, no. 13, pp. 2996–3015, 2023, doi: 10.1049/gtd2.12855.

[9] D. Salaorni, F. Bianchi, S. Colnago, A. Barisione, F. Trovò, and M. Restelli, "A novel digital twin for battery energy storage systems in micro-grids," Journal of Energy Storage, vol. 108, p. 117745, 2025, doi: 10.1016/j.est.2025.117745.

[10] H. Zakernezhad, M. Setayesh Nazar, M. Shafie-khah, and J. P. S. Catalão, "Optimal scheduling of an active distribution system considering distributed energy resources, demand response aggregators and electrical energy storage," Appl. Energy, vol. 314, p. 118865, May 2022, doi: 10.1016/J.APENERGY.2022.118865.

[11] P. Arévalo, M. Tostado-Véliz, and F. Jurado, "A novel methodology for comprehensive planning of battery storage systems," J. Energy Storage, vol. 37, no. March, 2021, doi: 10.1016/j.est.2021.102456.

[12] W. S. Ho, S. Macchietto, J. S. Lim, H. Hashim, Z. A. Muis, and W. H. Liu, "Optimal scheduling of energy storage for renewable energy distributed energy generation system," Renew. Sustain. Energy Rev., vol. 58, pp. 1100–1107, 2016, doi: 10.1016/j.rser.2015.12.097.

[13] Y. Li, Z. Yang, G. Li, D. Zhao, and W. Tian, "Optimal Scheduling of an Isolated Microgrid with Battery Storage Considering Load and Renewable Generation Uncertainties," IEEE Trans. Ind. Electron., vol. 66, no. 2, pp. 1565–1575, 2019, doi: 10.1109/TIE.2018.2840498.

[14] A. Bostan, M. S. Nazar, M. Shafie-khah, and J. P. S. Catalão, "Optimal scheduling of distribution systems considering multiple downward energy hubs and demand response programs," Energy, vol. 190, 2020, doi: 10.1016/j.energy.2019.116349.

[15] R. Khezri, A. Mahmoudi, and H. Aki, "Optimal Planning of Renewable Energy Resources and Battery Storage System for an Educational Campus in South Australia," ECCE 2020 - IEEE Energy Convers. Congr. Expo., pp. 3677–3683, 2020, doi: 10.1109/ECCE44975.2020.9235725.

[16] L. Luo et al., "Optimal scheduling of a renewable based microgrid considering photovoltaic system and battery energy storage under uncertainty," J. Energy Storage, vol. 28, no. August 2019, p. 101306, 2020, doi: 10.1016/j.est.2020.101306.

[17] S. Zhang and Y. Tang, "Optimal schedule of grid-connected residential PV generation systems with battery storages under time-of-use and step tariffs," J. Energy Storage, vol. 23, no. December 2018, pp. 175–182, 2019, doi: 10.1016/j.est.2019.01.030.

[18] H. Mehrjerdi and R. Hemmati, "Modeling and optimal scheduling of battery energy storage systems in electric power distribution networks," J. Clean. Prod., vol. 234, pp. 810–821, 2019, doi: 10.1016/j.jclepro.2019.06.195.

[19] T. S. Le, T. N. Nguyen, D. K. Bui, and T. D. Ngo, "Optimal sizing of renewable energy storage: A techno-economic analysis of hydrogen, battery and hybrid systems considering degradation and seasonal storage," Appl. Energy, vol. 336, no. July 2022, p. 120817, 2023, doi: 10.1016/j.apenergy.2023.120817.

[20] F. H. Aghdam, M. W. Mudiyanselage, B. Mohammadi-Ivatloo, and M. Marzband, "Optimal scheduling of multi-energy type virtual energy storage system in reconfigurable distribution networks for congestion management," Appl. Energy, vol. 333, no. December 2022, p. 120569, 2023, doi: 10.1016/j.apenergy.2022.120569.

[21] X. Zhang, Y. Son, and S. Choi, "Optimal Scheduling of Battery Energy Storage Systems and Demand Response for Distribution Systems with High Penetration of Renewable Energy Sources," Energies, vol. 15, no. 6, 2022, doi: 10.3390/en15062212.

[22] G. Abbas, Z. Wu, and A. Ali, "Optimal scheduling and management of grid-connected distributed resources using improved decomposition-based many-objective evolutionary algorithm," IET Gener. Transm. Distrib., no. July, pp. 2625–2649, 2024, doi: 10.1049/gtd2.13221.

[23] A. F. Naghibi, E. Akbari, S. Shahmoradi, S. Pirouzi, and A. Shahbazi, "Stochastic economic sizing and placement of renewable integrated energy system with combined hydrogen and power technology in the active distribution network," Scientific Reports, vol. 14, p. 28354, 2024, doi: 10.1038/s41598-024-79222-4.

[24] A. Nagarajan and R. Ayyanar, "Design and Strategy for the Deployment of Energy Storage Systems in a Distribution Feeder With Penetration of Renewable Resources," IEEE Trans. Sustain. Energy, vol. 6, no. 3, pp. 1085–1092, 2015, doi: 10.1109/TSTE.2014.2330294.

[25] R. Li, W. Wang, and M. Xia, "Cooperative Planning of Active Distribution System with Renewable Energy Sources and Energy Storage Systems," IEEE Access, vol. 6, pp. 5916–5926, 2017, doi: 10.1109/ACCESS.2017.2785263.

[26] V. Kalkhambkar, R. Kumar, and R. Bhakar, "Joint optimal sizing and placement of renewable distributed generation and energy storage for energy loss minimization," 2017 4th Int. Conf. Adv. Comput. Commun. Syst. ICACCS 2017, 2017, doi: 10.1109/ICACCS.2017.8014596.

[27] R. Khezri, M. Shafie-khah, and J. P. S. Catalão, "Stochastic MILP scheduling of multi-energy hubs with energy storage under renewable uncertainty," Applied Energy, vol. 346, p. 121432, 2025, doi: 10.1016/j.apenergy.2025.121432.

[28] C. Chen, F. Wang, B. Zhou, K. W. Chan, Y. Cao, and Y. Tan, "An interval optimization based day-ahead scheduling scheme for renewable energy management in smart distribution systems," Energy Convers. Manag., vol. 106, pp. 584–596, 2015, doi: 10.1016/j.enconman.2015.10.014.

[29] H. Liu, Y. Zhang, and F. Li, "Optimal scheduling of energy storage using machine-learning-based demand forecasting," International Journal of Electrical Power & Energy Systems, vol. 160, p. 107999, 2024, doi: 10.1016/j.ijepes.2024.107999.

[30] R. Hemmati, H. Saboori, and S. Saboori, "Stochastic risk-averse coordinated scheduling of grid integrated energy storage units in transmission constrained wind-thermal systems within a conditional value-at-risk framework," Energy, vol. 113, pp. 762–775, 2016, doi: 10.1016/j.energy.2016.07.089.

[31] J. Cardo-Miota, H. Beltrán, E. Pérez, S. Khadem, and M. Bahloul, "Deep reinforcement learning-based strategy for maximizing returns from renewable energy and energy storage systems in multi-electricity markets," Applied Energy, vol. 388, p. 125561, 2025, doi: 10.1016/j.apenergy.2025.125561.

[32] G. Carpinelli, G. Celli, S. Mocci, F. Mottola, F. Pilo, and D. Proto, "Optimal integration of distributed energy storage devices in smart grids," IEEE Trans. Smart Grid, vol. 4, no. 2, pp. 985–995, 2013, doi: 10.1109/TSG.2012.2231100.

[33] Y. Zheng, Z. Y. Dong, F. J. Luo, K. Meng, J. Qiu, and K. P. Wong, "Optimal allocation of energy storage system for risk mitigation of discos with high renewable penetrations," IEEE Trans. Power Syst., vol. 29, no. 1, pp. 212–220, 2014, doi: 10.1109/TPWRS.2013.2278850.

[34] H. Saboori and R. Hemmati, "Optimal management and planning of storage systems based on particle swarm optimization technique," J. Renew. Sustain. Energy, vol. 8, no. 2, 2016, doi: 10.1063/1.4946804.

[35] S. W. Alnaser and L. F. Ochoa, "Optimal Sizing and Control of Energy Storage in Wind Power-Rich Distribution Networks," IEEE Trans. Power Syst., vol. 31, no. 3, pp. 2004–2013, 2016, doi: 10.1109/TPWRS.2015.2465181.

[36] M. Qin, K. W. Chan, C. Y. Chung, X. Luo, and T. Wu, "Optimal planning and operation of energy storage systems in radial networks for wind power integration with reserve support," IET Gener. Transm. Distrib., vol. 10, no. 8, pp. 2019–2025, 2016, doi: 10.1049/iet-gtd.2015.1039.

[37] X. Shen, M. Shahidehpour, Y. Han, S. Zhu, and J. Zheng, "Expansion Planning of Active Distribution Networks With Centralized and Distributed Energy Storage Systems," IEEE Trans. Sustain. Energy, vol. 8, no. 1, pp. 126–134, 2017, doi: 10.1109/TSTE.2016.2586027.

[38] V. Mahadevan, "Critical review of energy storage systems: A comparative analysis of mechanical, electrochemical, and thermal technologies," Energy Reports, vol. 11, pp. 14567–14583, 2025, doi: 10.1016/j.egyr.2025.07.089.

[39] A. Núñez-Reyes, D. Marcos Rodríguez, C. Bordons Alba, and M. Á. Ridao Carlini, "Optimal scheduling of grid-connected PV plants with energy storage for integration in the electricity market," Sol. Energy, vol. 144, pp. 502–516, 2017, doi: 10.1016/j.solener.2016.12.034.

[40] K. Kusakana, "Optimal scheduled power flow for distributed photovoltaic/wind/diesel generators with battery storage system," IET Renew. Power Gener., vol. 9, no. 8, pp. 916–924, 2015, doi: 10.1049/iet-rpg.2015.0027.

[41] S. S. Reddy and J. A. Momoh, "Realistic and transparent optimum scheduling strategy for hybrid power system," IEEE Trans. Smart Grid, vol. 6, no. 6, pp. 3114–3125, 2015, doi: 10.1109/TSG.2015.2406879.

[42] S.-W. Jung, Y.-Y. An, B. Suh, Y. Park, J. Kim, and K.-I. Kim, "Multi-Agent Deep Reinforcement Learning for Scheduling of Energy Storage System in Microgrids," Mathematics, vol. 13, no. 12, art. 1999, 2025, doi: 10.3390/math13121999.

[43] K. C. Divya and J. Østergaard, "Battery energy storage technology for power systems-An overview," Electr. Power Syst. Res., vol. 79, no. 4, pp. 511–520, 2009, doi: 10.1016/j.epsr.2008.09.017.

[44] L. Yao, B. Yang, H. Cui, J. Zhuang, J. Ye, and J. Xue, "Challenges and progresses of energy storage technology and its application in power systems," J. Mod. Power Syst. Clean Energy, vol. 4, no. 4, pp. 519–528, 2016, doi: 10.1007/s40565-016-0248-x.

[45] M. Stecca, L. R. Elizondo, T. B. Soeiro, P. Bauer, and P. Palensky, "A comprehensive review of the integration of battery energy storage systems into distribution networks," IEEE Open J. Ind. Electron. Soc., vol. 1, no. 1, pp. 46–65, 2020, doi: 10.1109/OJIES.2020.2981832.

[46] T. M. Gür, "Review of electrical energy storage technologies, materials and systems: Challenges and prospects for large-scale grid storage," Energy Environ. Sci., vol. 11, no. 10, pp. 2696–2767, 2018, doi: 10.1039/c8ee01419a.

[47] A. Hadjian, "Kastamonu," Secret Nation, no. 2, pp. 545–556, 2019, doi: 10.5040/9781350987951.ch-016.

[48] K. Binder, Monte-Carlo Methods. 2005.

[49] D. P. Kroese and R. Y. Rubinstein, "Monte Carlo methods," Wiley Interdiscip. Rev. Comput. Stat., vol. 4, no. 1, pp. 48–58, 2012, doi: 10.1002/wics.194.

[50] S. Teimourzadeh, O. B. Tor, M. E. Cebeci, A. Bara, and S. V. Oprea, "A three-stage approach for resilience-constrained scheduling of networked microgrids," J. Mod. Power Syst. Clean Energy, vol. 7, no. 4, pp. 705–715, 2019, doi: 10.1007/s40565-019-0555-0.

[51] F. S. Hillier, Series Editor. 2019.

[52] International Renewable Energy Agency (IRENA), Electricity Storage and Renewables: Costs and Markets to 2030, Abu Dhabi: IRENA, 2023.

[53] BloombergNEF, Battery Price Survey 2024: Lithium-ion Pack Prices Fall to $139/kWh, London, 2024.

Konya Mühendislik Bilimleri Dergisi., c.14, s.2, 760-774, 2026
Konya Journal of Engineering Sciences v.14, n.2, 760-774, 2026
ISSN: 2667-8055 (Electronic)
DOI: 10.36306/konjes.1789715

MICROSTRUCTURAL EVOLUTION AND TRIBOLOGICAL PROPERTIES OF ELECTROLESS NI-P-B AND NI-P-B-W POLYALLOY COATINGS

[1,*]Harun MİNDİVAN

[1]*Department of Mechanical Engineering, Bilecik Şeyh Edebali University, Bilecik, Türkiye*
[1]harun.mindivan@bilecik.edu.tr

Highlights

- ENPB and ENPBW coatings were deposited by electroless plating.
- ENPB coating showed compact nodular morphology and high hardness.
- W addition increased roughness and promoted graded microstructure.
- ENPBW coating showed superior wear resistance and stable friction.
- ENPBW reduced delamination and improved tribological behavior.
- ENPBW coatings are promising for wear-resistant engineering systems.

Graphical Abstract

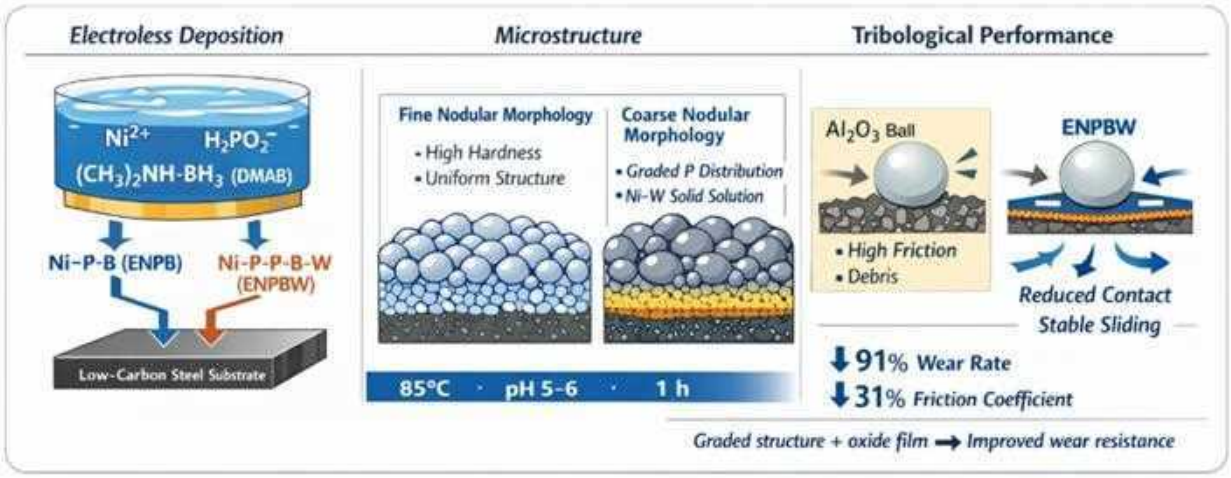


Figure Structure-property-performance relationships in electroless ENPB and ENPBW coatings with tungsten-induced microstructural modification

***Corresponding Author:** Harun MİNDİVAN, harun.mindivan@bilecik.edu.tr

Konya Mühendislik Bilimleri Dergisi., c.14, s.2, 760-774, 2026
Konya Journal of Engineering Sciences v.14, n.2, 760-774, 2026
ISSN: 2667-8055 (Electronic)
DOI: 10.36306/konjes.1789715

MICROSTRUCTURAL EVOLUTION AND TRIBOLOGICAL PROPERTIES OF ELECTROLESS NI-P-B AND NI-P-B-W POLYALLOY COATINGS

[1,*]Harun MİNDİVAN

[1]Department of Mechanical Engineering, Bilecik Şeyh Edebali University, Bilecik, Türkiye
[1]harun.mindivan@bilecik.edu.tr

(Received: 23.09.2025; Accepted in Revised Form: 01.12.2025)

ABSTRACT: Despite extensive research on Ni-P, Ni-B, and Ni-W systems, the combined Ni-P-B-W quaternary system has not been systematically examined under identical bath conditions, representing a significant gap in literature. In this study, sodium tungstate (Na_2WO_4) was added to a ternary Ni-P-B coating to investigate the effect of W on the tribological properties of an electroless ternary Ni-P-B polyalloy coating. All coatings' surface morphology, phase structure, hardness, and tribological properties were examined and compared while keeping the Ni-P-B and Ni-P-B-W bath parameters (pH, temperature, and deposition time) constant. The surface morphology of the Ni-P-B coating was transformed from spherical nodular to clear-shaped with the addition of W. All types of coatings resulted in a combination of amorphous and crystalline phases. The ternary Ni-P-B coating exhibited a higher hardness compared to the quaternary Ni-P-B-W coating, attaining a value of approximately 655±10 $HV_{0.025}$. Dry reciprocating wear tests carried out against Al_2O_3 balls demonstrated that the quaternary Ni-P-B-W coating achieved up to a 31 % reduction in the friction coefficient and up to a 91 % reduction in specific wear rate compared to the ternary Ni-P-B coating.

Keywords: *Dimethylamine Borane (DMAB), Dry Sliding Wear, Electroless Nickel Coating, Ni-P-B, Ni-P-B-W, Tribology.*

1. INTRODUCTION

Electroless coatings have been widely applied to low-carbon steel components that are subjected to severe wear conditions, such as gears and bearing surfaces, due to their excellent wear resistance. Despite their extensive use in industry, low-carbon steels inherently exhibit poor wear resistance. Nevertheless, their relatively lower cost compared to mild or high-alloy steels has promoted the development of various surface treatments aimed at improving wear and friction properties without compromising toughness [1], [2]. For wear-resistant coatings to be effective, they must exhibit high chemical stability, low friction, and superior hardness.

Among these approaches, electroless nickel coatings on steel substrates have attracted considerable attention owing to their ability to form smooth, crack-free, and well-adhered layers with desirable mechanical properties, low cost, and excellent corrosion resistance. These coatings have been increasingly investigated to meet the demanding requirements of industrial applications such as gears, abrasive fluid pipelines, and bearing surfaces [3]-[5]. In electroless deposition, metal ions are chemically reduced in an aqueous solution via an autocatalytic reaction, allowing even deposition without applying an electric current [4], [5].

The characteristics of electroless nickel coatings including their chemical, physical, and mechanical properties are strongly influenced by the choice of reducing agent. For instance, sodium hypophosphite produces Ni-P coatings, whereas sodium borohydride or amino borane-based reducing agents are employed to obtain Ni-B coatings [6]. Ni–P coatings generally exhibit a smooth morphology and superior

***Corresponding Author:** Harun MİNDİVAN, harun.mindivan@bilecik.edu.tr

corrosion resistance [7], while Ni-B coatings are characterized by high hardness and excellent wear resistance [6], [8], [9].

In particular, Ni-B coatings synthesized using dimethylamine borane (DMAB) as a reducing agent have been reported to exhibit significantly higher hardness and lower wear rates compared to conventional Ni-P coatings. This enhancement has been primarily attributed to the formation of hard Ni_3B phases and the development of fine-grained microstructures during deposition, which collectively improve the mechanical integrity and tribological performance of the coating [10], [11]. Recent findings by Erhan et al. (2021) further demonstrated that optimizing DMAB concentration in the electroless Ni-B bath significantly improves coating hardness and wear resistance, confirming the critical influence of reducing agent concentration on coating performance [12]. Similarly, Madah et al. (2015) systematically investigated the wear mechanisms of electroless Ni-B coatings under dry sliding conditions and reported that improved endurance life and reduced wear rates are primarily governed by the formation of protective tribo-oxide layers and the stability of Ni_3B phases during frictional loading [13].

Recent studies also indicate that the incorporation of tungsten (W) into electroless coatings enhances wear resistance, thereby establishing W-containing alloys as a prominent subject of ongoing research [14], [15]. Among these, electroless Ni-P-W and Ni-B-W coatings have attracted significant attention due to their ability to combine the corrosion resistance of Ni-P or Ni-B matrices with the solid-solution strengthening effect of W. Both coatings exhibit amorphous structures in the as-deposited state and crystallize upon heat treatment, typically around 400 °C, which enhances hardness and wear resistance while maintaining satisfactory corrosion performance [16], [17]. To further optimize the balance between these complementary properties, electroless duplex or multilayer coatings have been developed, in which an adhesion-promoting base layer is followed by a wear- or corrosion-resistant top layer [8], [18], [19]. However, these multilayer structures often face challenges related to interlayer compatibility, as mismatches in hardness, toughness, and ductility between successive layers can lead to structural instability and reduced overall performance.

In this context, single-layer electroless Ni-P-B and Ni-P-B-W coatings emerge as promising alternatives, as they can potentially combine the advantageous features of Ni-P, Ni-B, and Ni-P-W coatings within a single homogeneous layer. This approach not only mitigates the high costs and interfacial incompatibilities associated with multilayered coatings but also provides a more practical solution for industrial applications. Despite this potential, the tribological behavior of electroless Ni-P-B and Ni-P-B-W coatings has not yet been comprehensively examined.

Therefore, the present study aims to address this gap by systematically investigating the tribological performance of electroless Ni-P-B and Ni-P-B-W coatings deposited on steel substrates. For this purpose, sodium hypophosphite and borane dimethylamine were employed as reducing agents in the electroless baths to produce the coatings. The surface morphology and phase structures were characterized using Light Optical Microscopy (LOM), Field Emission Gun Scanning Electron Microscope (FEG-SEM), and X-Ray Diffraction (XRD), while their hardness and tribological properties were comparatively evaluated. These findings are anticipated to enhance understanding of the effects of tungsten incorporation on the microstructure and wear resistance of electroless Ni-P-B based coatings, offering valuable guidance for their practical application in demanding environments

2. MATERIAL AND METHODS

2.1. Electroless Coating

Electroless deposition was carried out on low-carbon steel substrates with dimensions of 20 mm × 10 mm × 2 mm. To minimize the influence of surface roughness—since surface interactions are strongly dependent on contact geometry [20]-all substrates were ground with 1200-grit SiC paper and subsequently polished using fine-grade Al_2O_3 paste. This procedure yielded an average surface roughness of $R_a = 0.06 \pm$

0.1 μm and R_q = 0.09 ± 0.1 μm, values that are representative of potential applications in gears and bearing surfaces.

Prior to deposition, the steel substrates underwent ultrasonic cleaning, acetone degreasing, and etching in a 50% hydrochloric acid solution for 20 s to effectively remove rust, oxides, and residual surface imperfections. The treated samples were immediately immersed in the coating baths to prevent reoxidation.

Two distinct electroless baths were employed, the compositions and processing conditions of which are summarized in Table 1. Sodium tungstate (Na_2WO_4) was introduced into the Ni-P-B bath to enable W co-deposition. Two different coatings, Ni-P-B (ENPB) and Ni-P-B-W (ENPBW), were electrolessly deposited for 1 hour under a controlled pH of 5-6 for this investigation. Each coating was deposited in 250 cm^3 of solution, with the temperature held constant at 85 °C. To ensure uniformity, the baths were continuously agitated using a magnetic stirrer operating at 250 rpm.

Table 1. Bath formulation and deposition conditions for electroless coatings

Bath compositions	ENPB	ENPBW
$NiSO_4.6H_2O$ (g/l)	33	33
$C_2H_3NaO_2$ (g/l)	16	16
$C_3H_6O_3$ (ml/l)	28	28
CH_4N_2S (g/l)	0.001	0.001
Na_2WO_4 (g/l)	-	50
$(CH_3)_2NH{\cdot}BH_3$ (g/l)	1.5	1.5
$NaPO_2H_2$ (g/l)	25	25
pH	5-6	5-6
Time (h)	1	1
Temperature (°C)	85	85

2.2. Characterization

The microstructural characteristics of the coatings were examined using a combination of microscopic techniques, XRD analysis, and microhardness testing. Surface and cross-sectional morphologies were characterized using a field-emission scanning electron microscope (FEG-SEM, Zeiss Supra 40VP), while a Nikon Eclipse LV150 light optical microscope (LOM) was utilized to assess the cross-sectional features of the coatings. Elemental distribution within the coatings was evaluated by energy-dispersive spectroscopy (EDS) operated at a working distance of 10 mm and an accelerating voltage of 15 kV.

Phase analysis was conducted on a Panalytical Empyrean XRD with CuK_α radiation (λ = 1.54059 Å), operated in the 2θ range of 30°-60°, with a step size of 0.020° and a scanning rate of 1°/min. Cross-sectional microhardness testing was conducted using a Shimadzu HMV tester under a 25 g load and a dwell time of 15 s, according to ASTM E92 [21]. The reported hardness values represent the average of five measurements. Surface roughness of the coatings was assessed via a Mitutoyo SJ-400 contact profilometer according to ISO 4287 [22].

The dry sliding wear behavior was assessed using a custom-designed ball-on-flat configuration. Wear tests were conducted in accordance with ASTM G133-05 [23] using a linear reciprocating tribometer at 30 °C and 35 ± 5% relative humidity. A 10 mm Al_2O_3 counter-body was employed at a sliding speed of 1.9 cm/s, corresponding to a total sliding distance of 57.5 m along an 11.5 mm stroke under an applied load of 5 N. A surface profilometer was used to quantify the wear track depth and width, while the worn surfaces were examined using both LOM and FEG-SEM to identify the operative wear mechanisms. Additionally, LOM was used to analyze the wear scars formed on the Al_2O_3 balls.

3. RESULTS AND DISCUSSION

3.1. Coating Morphology and Characterization

Figures 1 and 2 present the surface morphology, polished cross-sections, and elemental mapping of the ENPB and ENPBW coatings, respectively. The ENPB coating consists of a supersaturated solid solution of P and B within crystalline Ni, exhibiting a characteristic spherical nodular morphology with excellent uniformity and dense coverage (Fig. 1a). The spherical nodular morphology observed in the ENPB coating is consistent with previous reports in the literature [24]. Upon incorporation of W into the coating (Fig. 2a), the morphology largely retains its globular appearance but develops larger and more pronounced nodules compared with the ternary ENPB coating. This morphological evolution aligns with previous reports on as-deposited electroless Ni-P-W coatings, which typically exhibit dense, nodular, and pore-free globular structures due to the autocatalytic growth mechanism inherent to electroless deposition [25].

Cross-sectional analysis revealed that the ENPB coating possessed a smooth and compact structure with an average thickness of ~16.6 μm (Fig. 1 a-b). In comparison, the ENPBW coating showed a higher average thickness of approximately 22.8 μm and featured a rougher surface with protruding structures (Fig. 2 a-b). Elemental mapping of the ENPB coating (Fig. 1c) shows a high concentration of Ni, visualized as green distributions, while P and B are clearly identified by their respective blue and red signals. The spatial distributions of these elements are consistent with previous findings reported in the literature [6], [26]. When Na_2WO_4 was introduced into the plating bath, notable compositional changes were observed in the ENPBW coating (Fig. 2c). As evidenced by the EDS elemental maps, the coating contains Ni, P, B, and W, visualized as abundant green and blue signals and comparatively fewer red and green signals, respectively. This distribution pattern reflects the competitive incorporation of alloying elements during deposition, driven by the presence of W species in the bath.

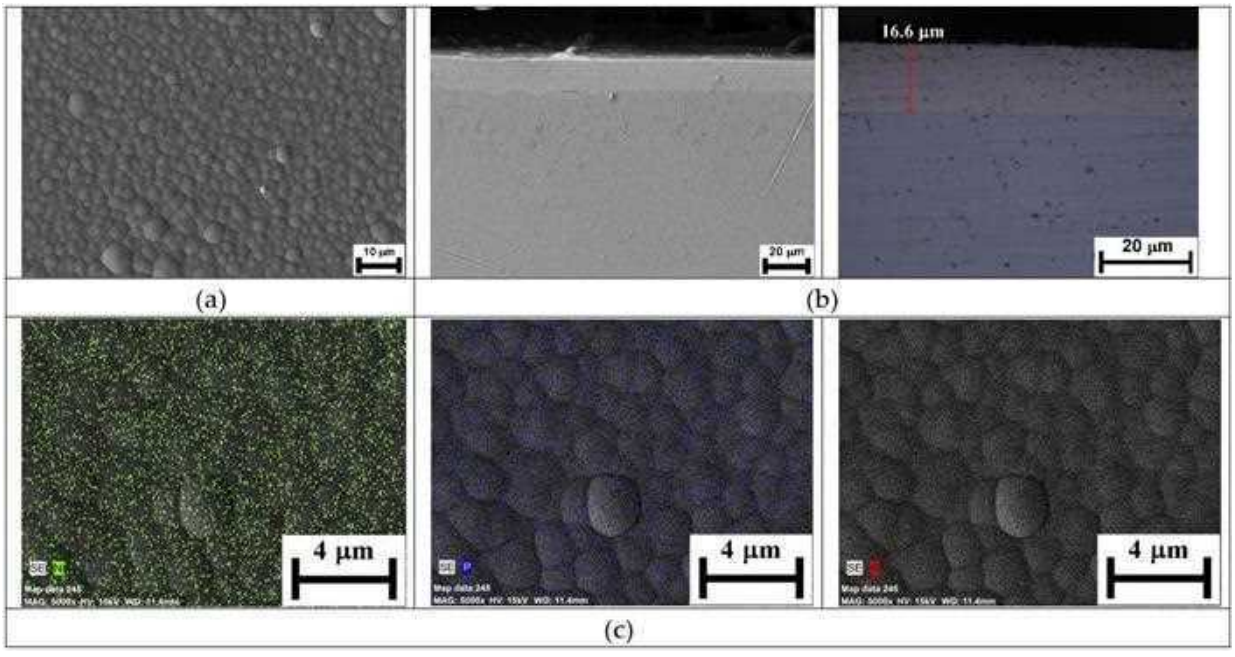


Figure 1. (a) Surface FEG-SEM morphology, (b) cross-sectional FEG-SEM and LOM views, and (c) elemental mapping analysis of ENPB coating

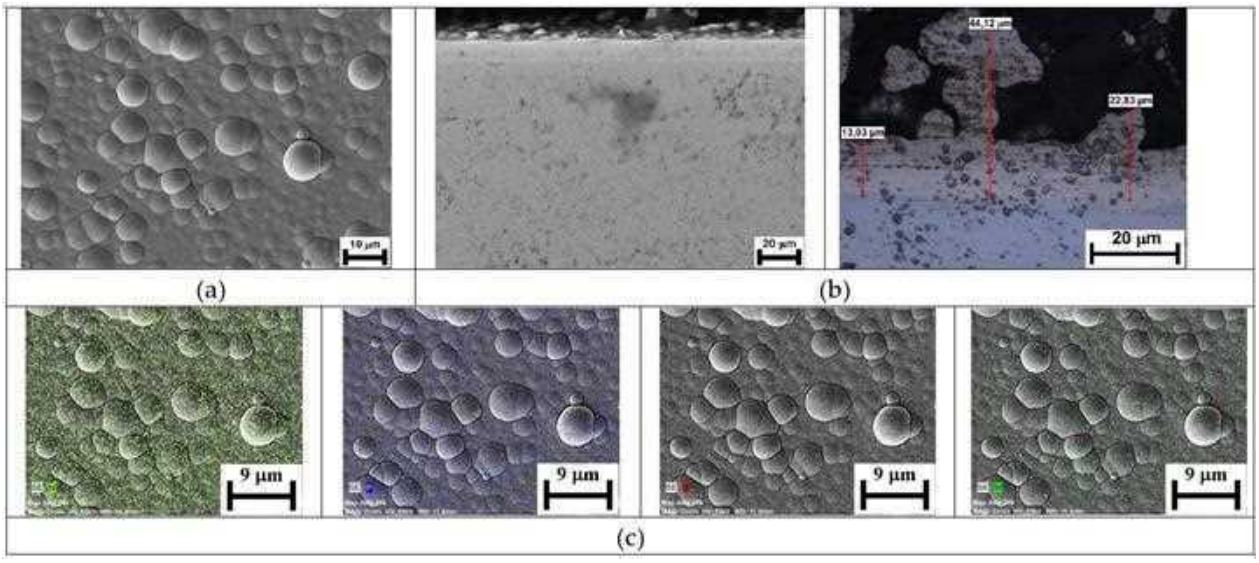


Figure 2. (a) Surface FEG-SEM morphology, (b) cross-sectional FEG-SEM and LOM views, and (c) elemental mapping analysis of ENPBW coating

Figure 3 depicts cross-section FEG-SEM images along with line EDS across the coating-substrate interface of ENPB and ENPBW coatings. In all two cases, the top surface exhibits dendritic growth fronts, with the maximum observed in the ENPBW coating. The estimated growth rates, determined based on the valley point of the growth front, were 16.6 $\mu m \cdot h^{-1}$ for the ENPB coating and 22.8 $\mu m \cdot h^{-1}$ for the ENPBW coating, under constant bath conditions with respect to pH, temperature, and deposition time. The ENPBW coating exhibited an increased deposition rate, which can be attributed to the incorporation of W [27], [28], providing additional active sites that facilitate the reduction process. Considering the composition of the plating bath, the higher deposition rate is likely to enhance the overall coating thickness [29], resulting in a rougher and more heterogeneous surface characterized by protruded structural features (Fig. 3b). EDS scans demonstrated a homogeneous distribution of the alloying elements throughout the thickness of the ENPB coating. The amount of P throughout the thickness of the ENPB coating remained nearly constant, whereas in the ENPBW coating, the P concentration gradually decreased from the top to the bottom of the layer, which is consistent with previous reports indicating that W addition reduces the P content of the film [17]. A similar observation was reported by Balaraju et al. [30], who found that the codeposition of W in the Ni-P matrix reduced the P content, an effect that became more pronounced when the Na_2WO_4 concentration in the electroless bath reached 40 g/l. They suggested that a competitive reaction between W and P species, or the possible formation of complex compounds during the autocatalytic deposition process, could inhibit the incorporation of P into the alloy matrix. However, the W content does not significantly change in the depth of the coating (Fig. 3). A factor that largely determines the properties of the electroless deposits can be its P content [7], [31]. The analysis of ENPB and ENPBW coatings reveals significant insights into the distribution and concentration of P throughout the cross-section. With a nearly constant P content at the cross-section, it can be observed that a deliberate design that enhances the coating's properties. A graded variation in P content was observed along the coating thickness of the ENPBW deposit. This indicates that the progressive incorporation of P influences the surface morphology of the coating. This strategic gradient not only contributes to the mechanical strength and durability of the coating but also indicates a methodical approach in its application. Overall, understanding these aspects of ENPBW coating not only clarifies their functional advantages but also paves the way for optimizing their use in various industrial applications.

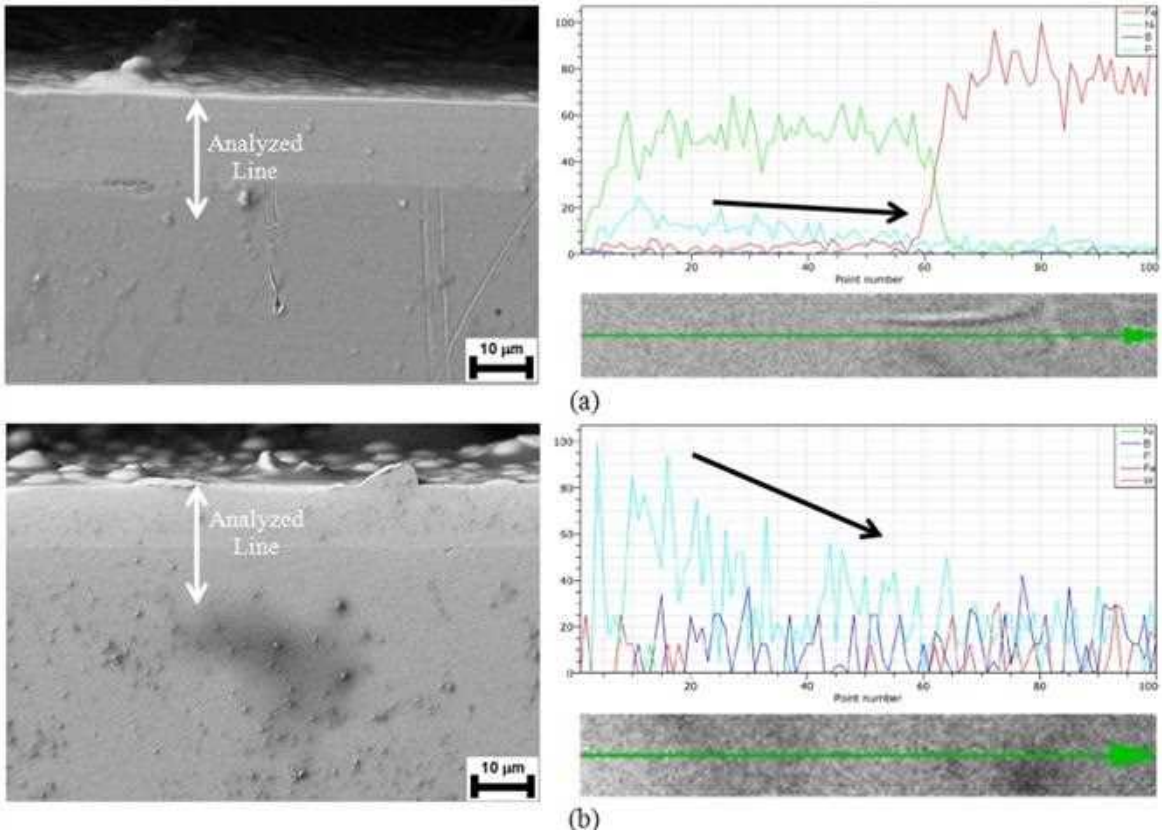


Figure 3. FEG-SEM cross-sectional views and corresponding line EDS elemental distributions of (a) ENPB and (b) ENPBW coatings

The ENPB coating exhibited a significantly smoother surface compared to the ENPBW coating (Figs. 1 and 2). Although both ENPB and ENPBW coatings exhibited a typical nodular surface, the size of the globules was below 2-3 µm on the ENPB coating surface, while their diameters ranged between 6-8 µm on the electroless ENPBW coating surface, implying that the ENPB coating was more compact and uniform. The average surface roughness (R_a) of the ENPB coating was about 0.11 µm, which was much smaller than that of the ENPBW coating (~0.36 µm), indicating that W could make the coating rougher. The coating surface became rougher as a result of the preferential deposition of Ni ions and B elements on and around the W particles [32]. The protrusions formed on the surface due to the excess particle concentration, which can be attributed to an increase in surface roughness, are consistent with observations reported in Ni-B alloys by Tan et al. [33]. In addition, the FEG-SEM images (Fig. 4) reveal that the electroless ENPBW coating consisted of small and large nodular clusters along with uniformly distributed nanovoids, whose formation is intrinsically associated with the reaction mechanism of electroless plating. According to the widely accepted hydrogen radical theory [34], the evolution of H_2 gas during the deposition process leads to the development of gas channels on the coating surface. The thickness of the nodular protrusion over the surface of ENPBW coating was about in the range of 2-3 µm (inset in Fig. 4 a). No cracks, voids and pores were detected across the cross section of ENPB and ENPBW coatings and the coatings applied to the mild steel substrate were highly uniform and strongly adhered to the surface (Figs. 1 b and 2 b). It was observed that the elements making up the coating were nearly evenly distributed across the surface (Figs. 1 c and 2 c). Additionally, the detection of W in the ENPBW coating's composition shows that the electroless plating process successfully deposited a ENPBW coating.

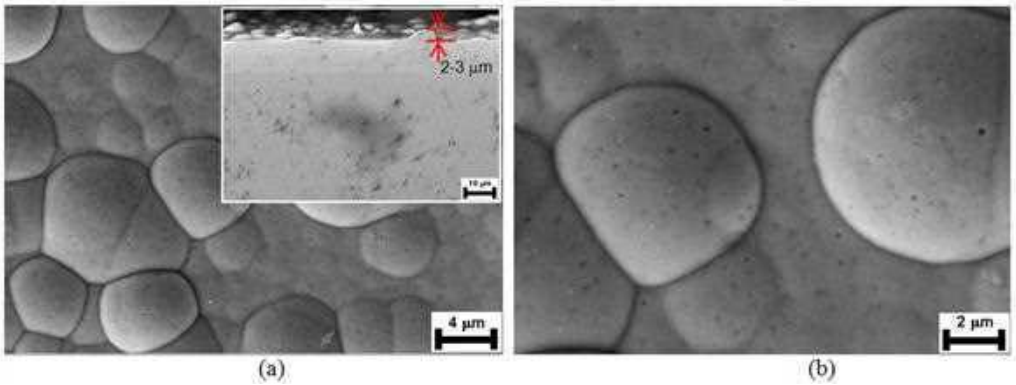


Figure 4. (a) Low (5000X) and (b) high (10000X) magnification top-view FEG-SEM views of the ENPBW coating (Inset: the side-view FEG-SEM image of the ENPBW coating)

Figure 5 displays the XRD patterns of the ENPB and ENPBW coatings. The patterns reveal the coexistence of amorphous and crystalline phases: a broad hump at lower angles reflects the presence of amorphous domains, while distinct diffraction peaks at approximately $2\theta = 45°$ and 52°, corresponding to the (111) and (200) planes of Ni, indicate a preferential crystalline orientation. The pronounced peak broadening accompanied by a low height suggests that the as-deposited coatings possess an amorphous structural nature [26]. According to the literature, although the as-deposited ENPB coating generally exhibits a fully amorphous structure [6], a crystalline phase was formed at the initial stage of deposition. This phenomenon may be attributed to the increased deposition rate. Specifically, during the early stage of the process, the crystalline structure tends to develop rapidly due to the high deposition rate, leading to the preferential formation of a crystalline phase rather than an amorphous one. Despite the limited incorporation of P and B into the Ni matrix, a crystalline structure was obtained in the ENPB ternary system. The formation of this crystalline structure, despite the low P and B content, is likely associated with the simultaneous dissolution of P and B at the grain boundaries [6]. As seen in Fig. 5, the incorporation of W into the ENPB matrix reduced peak broadening, resulting in sharper diffraction peaks. Notably, the absence of W-specific peaks in the XRD patterns indicates the formation of a solid solution within the Ni matrix [17], as the measured W content of 19.6% is well below the reported solubility limit of 39% for Ni [26]. The incorporation of W thus sharpens the (111) and (200) reflections by disrupting the Ni-P structures, thereby enhancing the crystalline nature of the coating. It can thus be inferred that the formation of a Ni-W solid solution not only promotes increased crystallinity but also diminishes the amorphous fraction of the Ni grains. A similar observation was reported by Balaraju et al. [30] for electrolessly deposited Ni-W-P coatings, where an increase in W content was found to enhance the crystalline character of the film, as evidenced by the intensified Ni (111) diffraction peak. This effect appears to have occurred in the ENPBW coating deposited in the present study. At the same time, the incorporation of larger size W (r=2.02 Å) than Ni (r=1,62 Å), P (r=1,23 Å) and B (r=1,17 Å) resulted in an increase in the intensity of the (111) plane and caused shifting 2θ angle to the right. The formation of distinct crystalline phases in the ENPBW coating can be attributed to the increased volume fraction of these phases in the deposit, which arises from the co-deposition of W [10]. High-resolution micrographs of this coating show a disordered atomic arrangement within it (Fig. 4). This behavior can be attributed to incorporating larger W atoms into the Ni crystal structure, resulting in significant distortion in the lattice structure due to the high concentration of W atoms.

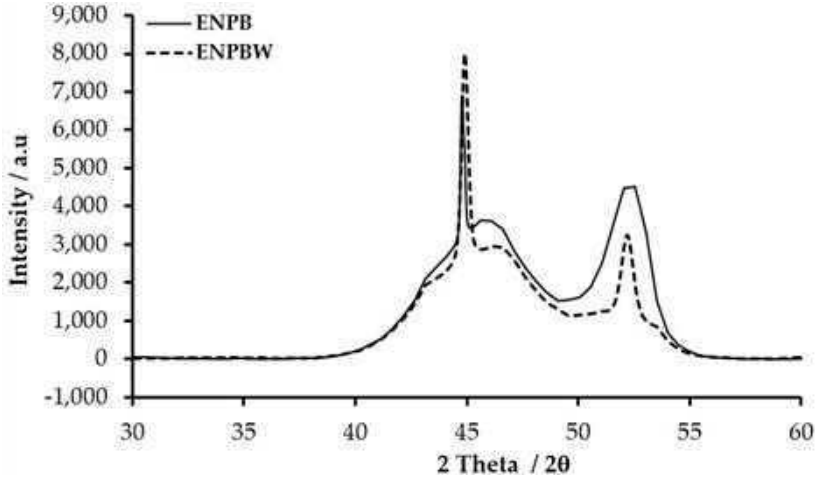


Figure 5. XRD pattern of ENPB and ENPBW coatings

Table 2 presents the roughness and hardness values of the coatings. Based on the surface roughness measurements, the ENPBW coating exhibited the highest surface roughness. The surface roughness values of the current electroless ENPB coating are quite close to the substrate roughness. The results of the surface roughness and hardness measurements reveal significant insights into the performance of various coatings on mil steel substrates. Among the coatings analyzed, the ENPBW coating exhibited the highest surface roughness, indicating its potential impact on friction and wear characteristics. When measuring microhardness, untreated steel had a base hardness of 158±3.8 $HV_{0.025}$. Applying an ENPB coating greatly improved this property, increasing the hardness to 655±10 $HV_{0.025}$, which is considerably higher than that of bulk Ni (100-150 HV) and electrodeposited Ni (250-350 HV) [30], and is comparable to the values reported in the literature for similar electroless deposits [24]. In the case of the as-deposited ENPB coating, the incorporation of third elements into the Ni-P and/or Ni-B matrix enhances the mechanical properties of the coating by promoting a column-free microstructure and improving the densification of the deposited layer [6]. Although the ENPBW coating also improved hardness to 571±35 $HV_{0.025}$, it did not reach the levels achieved by its ENPB counterpart. As reported elsewhere [27], the hardness of the Ni-P coating increased to about 591 HV with the incorporation of W, consistent with the strengthening effect attributed to W addition. The gradual changes in P content within the coating are responsible for this variation in microhardness, demonstrating the significant influence of compositional differences on coating properties. These findings collectively highlight the crucial role surface treatments play in improving mechanical performance, laying the groundwork for future research that aims to optimize coating formulations for enhanced durability and functionality across diverse applications.

Table 2. Surface roughness (R_a, R_y, R_z, R_q, R_t) and hardness values of the coatings

Surface	Surface Roughness Values (μm)					Hardness
	R_a	R_y	R_z	R_q	R_t	$HV_{0.025}$
Untreated Steel	0.06	1.00	0.70	0.09	1.00	158±3.8
ENPB Coating	0.11	1.90	1.10	0.19	1.90	655±10
ENPBW Coating	0.36	6.40	3.90	0.55	6.40	571±35

3.2. Tribology Characterization

Figure 6 illustrates the wear rate of electroless ENPB and ENPBW coatings under dry sliding conditions. It is interesting to point out that the ENPBW coating exhibited better wear resistance compared to the ENPB coating. The ENPBW coating exhibited a 90.7% improvement in wear resistance compared to

the ENPB coating. As a result, the ENPBW coating exhibited a lower wear rate compared to the ENPB coating. Numerous researchers have reported correlations between various mechanical properties, such as elastic modulus, hardness, and fracture toughness, and tribological parameters, including wear rate and coefficient of friction, for different coating systems. Collectively, these studies demonstrate that the effective formation of a graded coating contributes substantially to improved tribological behavior [7]. In accordance with these findings, the present study also demonstrated similar improvements for the ENPBW coating. Examining the morphological features of the ENPB and ENPBW coatings (Figs. 1a and 2a) revealed that the nodules grew larger as the amount of Na_2WO_4 in the plating bath increased. This type of morphology allows the electroless ENPBW coating to achieve improved wear resistance and more stable friction coefficient fluctuations curve by reducing the contact area, similar to Ni-B coatings [2], [20].

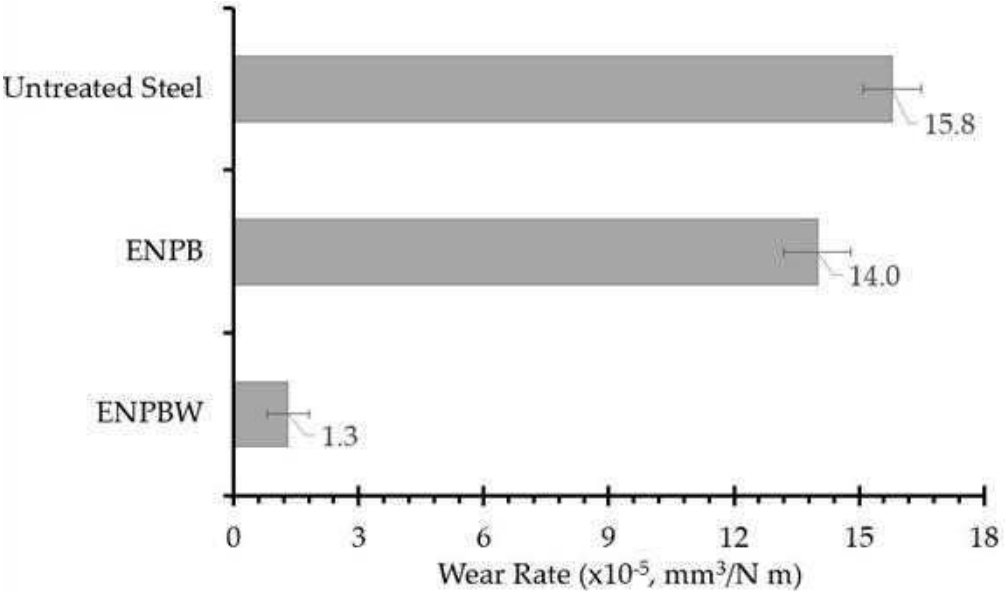


Figure 6. Wear rates of untreated steel, ENPB and ENPBW coatings

Distinct SEM morphologies of the worn surfaces were observed for the electroless ENPB and ENPBW coatings. The worn surface of untreated steel (Fig. 7a) displayed deep scratches along the sliding direction, indicative of abrasive wear caused by the hard Al_2O_3 ball (R_a = 0.20 μm) interacting with the softer steel substrate. As shown in Fig. 7b, the worn surface of the ENPB coating appeared relatively smooth and free of cracks, yet exhibited pronounced plastic deformation associated with delamination, consistent with its higher wear rate compared to the ENPBW coating. In contrast, as depicted in Fig. 7c, the ENPBW coating displayed wear tracks with shallow grooves oriented parallel to the sliding direction. In certain regions, micro-cracking and micro-fatigue perpendicular to the sliding direction were also detected, attributed to localized oxidation within the coating. Compared with the ENPB coating, the ENPBW coating demonstrated superior resistance to delamination and plastic deformation under load. This improvement can be ascribed to the incorporation of W into the ENPB matrix, which effectively suppressed delamination [14]. Short cracks were observed both along and adjacent to the wear track of the ENPBW coating, acting as stress-relief sites that prevented catastrophic failure under the 5 N load. A comparable phenomenon was previously reported for graded Ni-P deposits [7], [35]. According to Wang's theory, a gradual variation in P concentration across the coating thickness can inhibit crack propagation and enhance fracture toughness [36]. Consequently, the ENPBW coating, characterized by a significant gradient in cross-sectional hardness, exhibited improved wear resistance relative to the ENPB coating. Examination of the Al_2O_3 counter-body wear surfaces (Fig. 7) revealed that the wear scar radius on the ball corresponding to the ENPB coating was notably smaller than that of the ENPBW coating, suggesting that the relatively lower initial surface roughness of the ENPB coating contributed to reduced abrasive interactions during sliding.

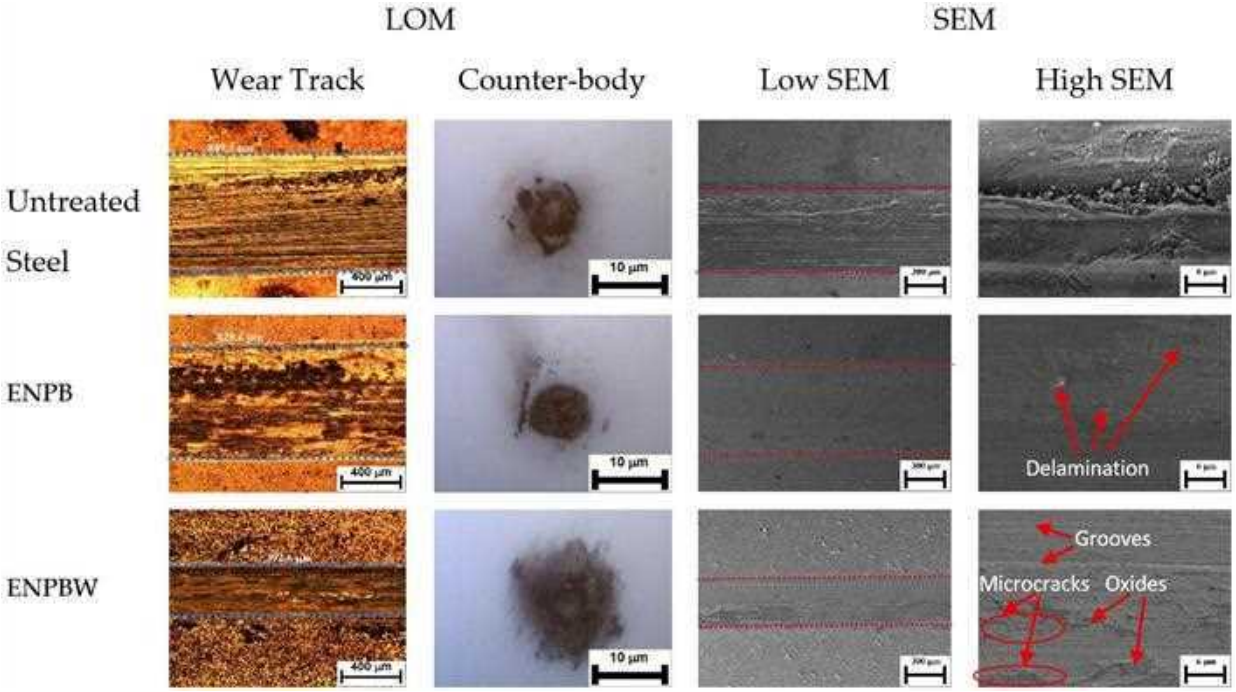


Figure 7. LOM and FEG-SEM images of the wear tracks formed on the surfaces of the untreated steel, ENPB and ENPBW coatings, and LOM images of their corresponding testing balls after the wear test

During reciprocating motion, the contact area continuously evolves, leading to variations in the coefficient of friction (CoF). The CoF curves of the selected contact pairs over a sliding distance of 57.5 m are presented in Fig. 8. For the untreated steel, the CoF initially increased within the first meter and subsequently stabilized at approximately 0.68. The reciprocating wear tests of the coatings revealed a distinct run-in period at the initial stage, attributed to the cutting of surface asperities and the consequent increase in shear resistance. During this stage, the ENPB coating exhibited lower CoF values than the ENPBW coating due to its lower initial surface roughness (Table 2). This behavior can be further explained by the self-lubricating nature of B, which minimizes direct contact between abrasive particles and the Ni-P matrix and facilitates smoother relative sliding between the coating surfaces, thereby reducing wear of the coatings [19], [34], [37]. For the ENPB coating, the CoF rapidly increased from 0.45 to 0.9 after the initial 24 m run-in period and remained near this level with pronounced fluctuations until the end of the test. This abrupt increase in the CoF can be attributed to the brittle fracture of the ENPB coating, which exhibits the highest hardness; under the applied load of 5 N, the coating layer fractured after 24 m of sliding. The resulting debris from the coating degradation subsequently adhered to the sliding track, causing the CoF curve to fluctuate with alternating rises and drops. Consequently, the high specific wear rate and the significant fluctuations in CoF observed during the steady state are closely related to the detachment of ENPB surface nodules at the interface between the Al_2O_3 ball and the ENPB coating, as also reported in [37].

In contrast, the incorporation of W into the ENPB matrix led to a superior tribological performance. The ENPBW coating reached a steady state at an earlier stage and maintained a relatively lower CoF throughout the test. The formation of a stable oxide film within the wear track (Fig. 7) served as a protective barrier, limiting direct interaction between the Al_2O_3 ball and the coating and thereby reducing friction. The EDS spectrum of the worn surface of the ENPBW coating (Fig. 9) indicates the formation of an oxide film during dry sliding. The presence of this oxide layer on the worn surface can hinder direct contact between the coating and the Al_2O_3 ball, thereby contributing to reduced wear, as also noted by Algul et al. [6]. The presence of W markedly enhanced the tribological performance by suppressing abrupt fluctuations in friction, indicating that the quaternary coating offers a favorable combination of hardness,

small and large nodular surface morphology, and improved wear resistance, ultimately contributing to reduced friction under the applied 5 N load.

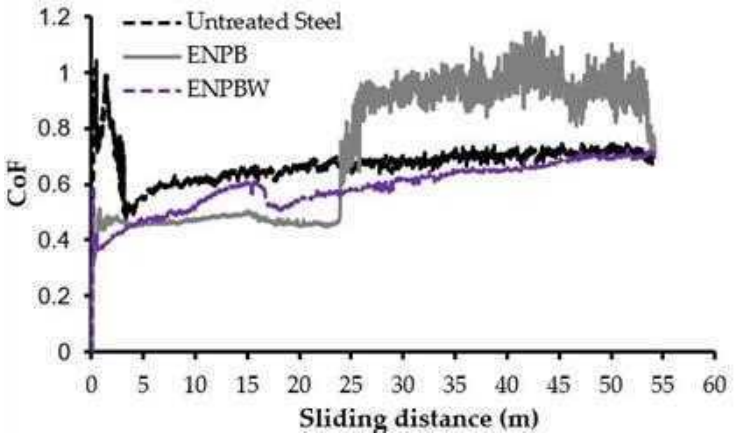


Figure 8. Friction coefficient curves of the untreated steel, ENPB and ENPBW coatings

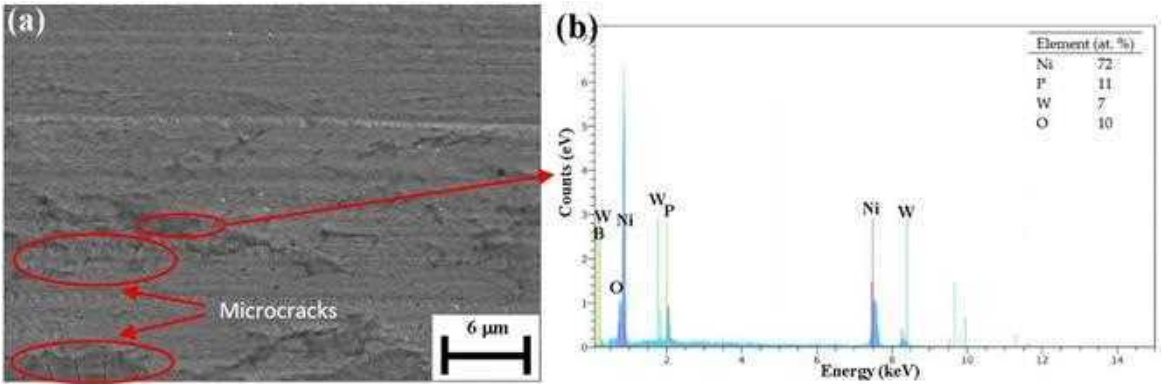


Figure 9. (a) FEG-SEM image and (b) EDS result of the wear track formed on the ENPBW coating

4. CONCLUSIONS

This study systematically examined the microstructural evolution, mechanical response, and dry sliding tribological behavior of electroless ENPB and ENPBW coatings deposited under identical bath conditions. The findings provide insights not only into coating performance but also into the broader tribological mechanisms governing electroless polyalloy systems.

First, the incorporation of W significantly modified the evolution of surface and cross-sectional microstructure. The ENPBW coating exhibited larger nodular clusters, higher roughness, and a graded P distribution, features known in tribology to influence asperity interactions, oxide formation, and microfracture resistance. The formation of a Ni-W solid solution evidenced by sharper (111) and (200) XRD peaks also reflects an increase in lattice distortion, which is associated with improved load-bearing capability in metal matrix coatings.

Although the ENPB coating achieved the highest hardness (655 ± 10 HV), hardness alone did not predict tribological performance. Instead, the ENPBW coating displayed a markedly superior wear resistance (1.3×10^{-5} $mm^3/N{\cdot}m$) and a more stable friction response. This behavior aligns with established tribological principles, which attribute enhanced wear resistance not only to hardness but also to factors such as oxide film stability, crack arrest mechanisms, and heterogeneity in composition and morphology.

In this context, the graded P distribution observed in the ENPBW coating likely contributes to improved fracture toughness and crack deflection mechanisms widely reported for graded Ni-P systems. The formation of a protective tribo-oxide layer during sliding further reduced direct metal-ceramic

contact, stabilizing the friction coefficient and suppressing the severe fluctuations observed in the ENPB coating.

Overall, the results demonstrate that controlled W incorporation enables a property balance combining moderate hardness with enhanced wear resistance, stable friction behavior, and robust mechanical integrity. These characteristics position ENPBW coatings as promising candidates for components subjected to high-cycle sliding, abrasive contacts, and environments where consistent tribological performance is essential, such as gears, bearing interfaces, and abrasive fluid-handling systems.

Future research should explore (i) the effect of varying W concentration, (ii) heat treatment–induced microstructural evolution, and (iii) long-term performance under corrosive or lubricated environments, to fully optimize and validate the coating system for engineering applications.

Declaration of Ethical Standards

The author declares to comply with ethical guidelines, including original research publication, data reporting, citation and authorship.

Credit Authorship Contribution Statement

The author contributed to all phases of the study including conceptualization, methodology, analysis of the findings, investigation process, writing and reviewing the manuscript.

Declaration of Competing Interest

The author declares no conflicts of interest regarding this manuscript.

Funding / Acknowledgements

This work has been supported by Bilecik Şeyh Edebali University Scientific Research Projects Coordination Unit under grant number: 2020-02.BŞEÜ.03-01.

Data Availability

Data is available from the corresponding author upon reasonable request.

Use of Artificial Intelligence

The author confirms that no generative AI or AI-assisted technologies were used in the writing of this manuscript or in the production of the data/images presented.

5. REFERENCES

[1] S. S. Rouzmeh, R. Naderi, and M. Mahdavian, "A sulfuric acid surface treatment of mild steel for enhancing the protective properties of an organosilane coating," *Progress in Organic Coatings*, vol. 103, pp. 156-164, 2017, doi: 10.1016/j.porgcoat.2016.10.033.

[2] S. Arias, J. G. Castaño, E. Correa, F. Echeverría, and M. Gómez, "Effect of heat treatment on tribological properties of Ni-B coatings on low carbon steel: wear maps and wear mechanisms," Journal of Tribology, vol. 141, no. 9, pp. 1-9, 2019, doi: 10.1115/1.4043906.

[3] A. S. Hamdy, M. A. Shoeib, H. Hady, and O. F. Abdel Salam, "Electroless deposition of ternary Ni–P alloy coatings containing tungsten or nano-scattered alumina composite on steel," Journal of Applied Electrochemistry, vol. 38, pp. 385-394, 2008, doi: 10.1007/s10800-007-9451-9.

[4] P. Sahoo and S. K. Das, "Tribology of electroless nickel coatings–a review," Materials and Design, vol. 32, no. 4, pp. 1760-1775, 2011, doi: 10.1016/j.matdes.2010.11.013.

[5] V. B. Chintada, R. Koona, and M. V. A. R. Bahubalendruni, "State of art review on nickel-based electroless coatings and materials," Journal of Bio- and Tribo-Corrosion, vol. 7, no. 134, pp. 1-14, 2021, doi: 10.1007/s40735-021-00568-7.

[6] H. Algul, M. Uysal, and A. Alp, "A comparative study on morphological, mechanical and tribological properties of electroless NiP, NiB and NiBP coatings," Applied Surface Science Advances, vol. 4, pp. 1-10, 2021, doi: 10.1016/j.apsadv.2021.100089.

[7] A. Hadipour, S. M. Monirvaghefi, and M. E. Bahrololoom, "Electroless deposition of graded Ni–P coatings," Surface Engineering, vol. 31, no. 6, pp. 399-405, 2015, doi: 10.1179/1743294414Y.0000000430.

[8] V. B. Chintada, T. R. Gurugubelli, M. R. Tamtam, and R. Koutavarapu, "Advancements in nickel-phosphate/boron based electroless composite coatings: a comprehensive review of mechanical properties and recent developments," Materials, vol. 16, no. 6116, pp. 1-26, 2023, doi: 10.3390/ma16186116.

[9] Q. Barati and S. M. M. Hadavi, "Electroless Ni-B and composite coatings: A critical review on formation mechanism, properties, applications and future trends," Surfaces and Interfaces, vol. 21, pp. 1-13, 2020, doi: 10.1016/j.surfin.2020.100702.

[10] Z. A. Hamid, H. B. Hassan, and A. M. Attyia, "Influence of deposition temperature and heat treatment on the performance of electroless Ni-B films," Surface and Coatings Technology, vol. 205, no. 7, pp. 2348-2354, 2010, doi: 10.1016/j.surfcoat.2010.09.025.

[11] J. N. Balaraju, A. Priyadarshi, V. Kumar, N. T. Manikandanath, P. P. Kumar, and B. Ravisankar, "Hardness and wear behaviour of electroless Ni-B coatings," Materials Science and Technology, vol. 32, no. 16, pp. 1654-1665, 2016, doi:10.1080/02670836.2015.1137683.

[12] E. Duru, F. Doğan, M. Uysal, H. Akbulut, and S. Aslan, "Optimization of Ni-B coating bath and effect of DMAB concentration on hardness and wear," Surfaces and Interfaces, vol. 22, pp. 1-9, 2021, doi:10.1016/j.surfin.2020.100880.

[13] F. Madah, C. Dehghanian, and A. A. Amadeh, "Investigations on the wear mechanisms of electroless Ni-B coating during dry sliding and endurance life of the worn surfaces," Surface and Coatings Technology, vol. 282, pp. 6-15, 2015, doi:10.1016/j.surfcoat.2015.09.003

[14] S. Kundu, S. K. Das, and P. Sahoo, "Friction and wear behavior of electroless Ni-P-W coating exposed to elevated temperature," Surfaces and Interfaces, vol. 14, pp. 192-207, 2019, doi: 10.1016/j.surfin.2018.12.007.

[15] R. Agrawal, O. Prakash, L. S. Brar, and A. Mukhopadhyay, "A systematic investigation of lead-free electroless Ni-B-W coating properties using Taguchi's methodology," Coatings, vol. 13, no. 1585, pp. 1-21, 2023, doi: 10.3390/coatings13091585.

[16] A. I. Aydeniz, A. Göksenli, G. Dil, F. Muhaffel, C. Calli, and B. Yüksel, "Electroless Ni-B-W coatings for improving hardness, wear and corrosion resistance," Materiali in Tehnologije, vol. 47, no. 6, pp. 803-806, 2013.

[17] M. C. L. D. Oliveira, O. V. Corrêa, B. Ett, I. J. Sayeg, N. B. D. Lima, and R. A. Antunes, "Influence of the tungsten content on surface properties of electroless Ni-W-P coatings," Materials Research, vol. 21, no. 1, pp. 1-13, 2018, doi: 10.1590/1980-5373-MR-2017-0567.

[18] F. Mindivan and H. Mindivan, "The study of electroless Ni-P/Ni-B duplex coating on HVOF-sprayed martensitic stainless steel coating," Acta Physica Polonica A, vol. 131, no. 1, pp. 64-67, 2017, doi: 10.12693/APhysPolA.131.64.

[19] F. Mindivan, H. Mindivan, and A. Bayram, "The electroless monolayer and duplex Ni-B and Ni-P coatings for 316L stainless steel in synergistic combination of mechanical (wear) and chemical (corrosion) processes," Advanced Engineering Materials, vol. 25, pp.1-17, 2023, doi: 10.1002/adem.202201501.

[20] P. Biswas, S. K. Das, and P. Sahoo, "Mechanical, tribological and corrosion performances of autocatalytic duplex Ni–P/Ni–Mo–P coating," Arabian Journal for Science and Engineering, vol. 49, no. 2, pp. 2443-2462, 2024, doi: 10.1007/s13369-023-08246-1.

[21] ASTM, ASTM E92: Test methods for Vickers hardness and Knoop hardness of metallic materials. West Conshohocken, PA: ASTM International, 2017.

[22] ISO, ISO 4287: Geometrical product specifications (GPS)-surface texture: profile method-terms, definitions and surface texture parameters. Geneva, Switzerland: ISO, 2002.

[23] ASTM, ASTM G133: Test method for linearly reciprocating ball-on-flat sliding wear. West Conshohocken, PA: ASTM International, 2005, doi: 10.1520/G0133-05R16.

[24] H. Gul, H. Algul, A. Akyol, M. Uysal, and A. Alp, "Evaluation of wear and corrosion behavior of electroless Ni-BP/CNT composite coatings on aluminum surfaces," Diamond and Related Materials, vol. 137, pp. 1-13, doi: 10.1016/j.diamond.2023.110075.

[25] S. Roy and P. Sahoo, "Corrosion study of electroless Ni-P-W coatings using electrochemical impedance spectroscopy," Portugaliae Electrochimica Acta, vol. 30, no. 3, pp. 203-220, 2012. doi:10.4152/pea.201203203

[26] T. X. Jiang and H. H. Wu, "Deposition and characterization of electroless nickel-phosphorus-boron coatings from acidic bath," Journal of Electrochemistry, vol. 6, no. 1, pp. 1-8, 2000.

[27] S. M. A. Shibli and K. S. Chinchu, "Development and electrochemical characterization of Ni-P coated tungsten incorporated electroless nickel coatings," Materials Chemistry and Physics, vol. 178, pp. 21-30, 2016, doi: 10.1016/j.matchemphys.2016.04.034

[28] F. Zhao, H. Hu, J. Yu, J. Lai, H. He, Y. Zhang, H, Qi, D. Wang, "Mechanical and tribological properties of Ni-B and Ni-BW coatings prepared by electroless plating," Lubricants, vol. 11, no. 2, pp. 1-13, 2023, doi: 10.3390/lubricants11020042.

[29] M. Barman, T. K. Barman, and P. Sahoo, "Effects of W and Mo concentrations on mechanical behaviour of Ni-B based coatings-a comparative study," Journal of The Institution of Engineers (India): Series D, pp. 1-18, 2024, doi: 10.1007/s40033-024-00696-7.

[30] J.N. Balaraju, Kalavati, K.S. Rajam, "Surface morphology and structure of electroless ternary Ni-W-P deposits with various W and P contents," Journal of Alloys and Compounds, vol. 486, no. 1-2, pp. 468-473, 2009, doi: 10.1016/j.jallcom.2009.06.173.

[31] I. M. Fedorchenko, Y. A. Guslienko, T. N. Dvernikova, and A. F. Khrienko, "Composite electrolytic nickel-phosphorus-boron coatings," Soviet Powder Metallurgy and Metal Ceramics, vol. 20, pp. 726-728, 1981.

[32] A. Ren and M. Kang, "Tribological behavior and wear mechanism of Ni-B composite coatings strengthened with doping WC@MoS2 powders," Surfaces and Interfaces, vol. 56, p. 105688, 2025, doi: 10.1016/j.surfin.2024.105688.

[33] S. Tan, H. Algül, E. Kiliçaslan, A. Alp, H. Akbulut, M. Uysal, "The effect of ultrasonic power on high temperature wear and corrosion resistance for Ni based alloy composite coatings," Colloids and Surfaces A: Physicochemical and Engineering Aspects, vol. 656, pp. 1-16, 2023, doi: 10.1016/j.colsurfa.2022.130345.

[34] C. Huang, Z. Zhang, J, Yan, L. Sun, J. Wang, "Enhancing wear and corrosion resistance of electroless Ni-P coatings in CO2-saturated NaCl solution through polytetrafluoroethylene incorporation," Corrosion Science, vol. 226, pp.1-17, 2024, doi: 10.1016/j.corsci.2023.111620.

[35] L. Wang, Y. Gao, Q. Xue, H. Liua, and T. Xu, "A novel electrodeposited Ni-P gradient deposit for replacement of conventional hard chromium," Surface and Coatings Technology, vol. 200, no. 12-13, pp. 3719-3726, 2006, doi: 10.1016/j.surfcoat.2004.10.016.

[36] S. Touri and S. M. Monirvaghefi, "Fabrication and characterization of functionally graded Ni-P electroless coating with variable properties along the surface of the coating," Mater. Today Commun., vol. 24, pp. 1-7, 2020, doi: 10.1016/j.mtcomm.2020.101203.

[37] G. Di Egidio, C. Martini, E. Ghassemali, and A. Morri, "Electroless Ni-P + diamond-like carbon multilayer: Influence on tribological behaviour of AlSi10Mg produced by powder bed fusion-laser beam," Wear, vols. 566-567, pp. 1-19, 2025, doi: 10.1016/j.wear.2025.205803.

Konya Mühendislik Bilimleri Dergisi., c.14, s.2, 775-802, 2026
Konya Journal of Engineering Sciences v.14, n.2, 775-802, 2026
ISSN: 2667-8055 (Electronic)
DOI: 10.36306/konjes.1605354

PERFORMANCE ASSESSMENT OF A RURAL PHOTOVOLTAIC–LITHIUM ION BATTERY ENERGY SYSTEM: EFFECTS OF TILT ANGLES, SOILING FACTOR, AND BATTERY TEMPERATURE

[1] Furkan DINCER, [2,*]Emre OZER

[1]*Department of Electrical and Electronics Engineering, Faculty of Engineering and Architecture, Kahramanmaras Sutcu Imam University, Kahramanmaras, Türkiye*
[2]*Gaziantep Islam Science and Technology University, Gaziantep, Türkiye*
[1] furkandincer@ksu.edu.tr, [2]emre.ozer@gibtu.edu.tr

Highlights

- A proposed off-grid energy storage system tailored for rural areas.
- A self-sufficient, sustainable solution designed for Nigerian climatic conditions.
- An innovative approach to addressing Nigeria's energy crisis.
- In-depth analysis of the system with 27 different scenarios.
- Evaluation of 3 critical performance factors: tilt angle, temperature, and soiling.

Graphical Abstract

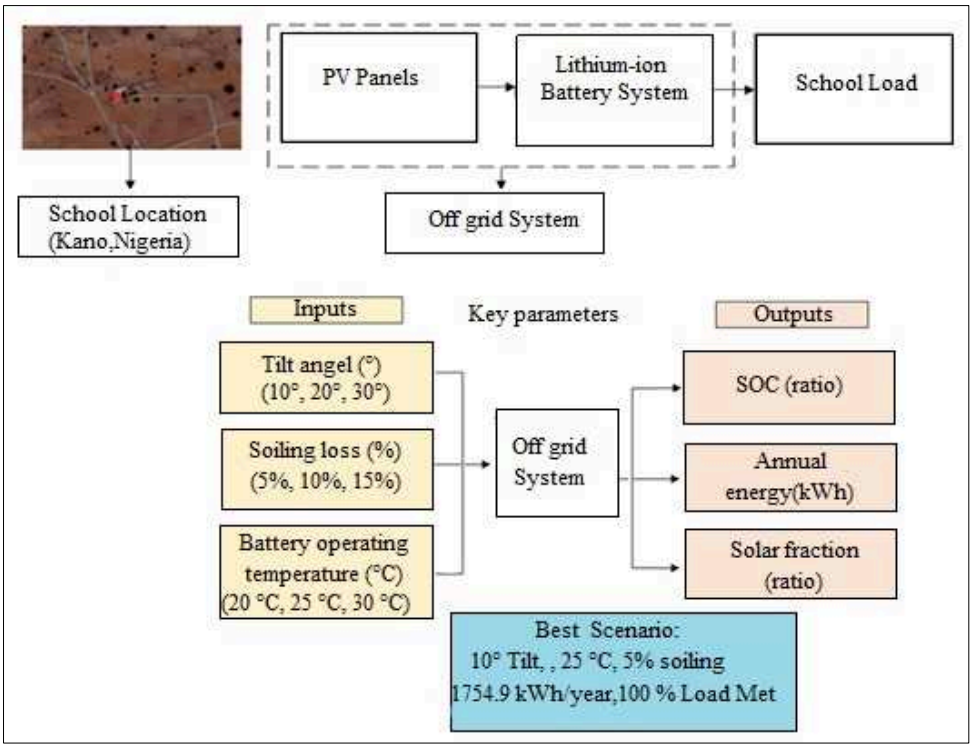


Figure General flow chart of the PV–lithium-ion battery system for off grid system

***Corresponding Author:** Emre OZER, emre.ozer@gibtu.edu.tr

Konya Mühendislik Bilimleri Dergisi., c.14, s.2, 775-802, 2026
Konya Journal of Engineering Sciences v.14, n.2, 775-802, 2026
ISSN: 2667-8055 (Electronic)
DOI: 10.36306/konjes.1605354

PERFORMANCE ASSESSMENT OF A RURAL PHOTOVOLTAIC–LITHIUM ION BATTERY ENERGY SYSTEM: EFFECTS OF TILT ANGLES, SOILING FACTOR AND BATTERY TEMPERATURE

[1]Furkan DINCER, **[2,*]Emre OZER**

[1]*Department of Electrical and Electronics Engineering, Faculty of Engineering and Architecture, Kahramanmaras Sutcu Imam University, Kahramanmaras, TÜRKİYE*
[2]*Gaziantep Islam Science and Technology University, Gaziantep, TÜRKİYE*
[1]furkandincer@ksu.edu.tr, [2]emre.ozer@gibtu.edu.tr

(Received: 22.12.2024; Accepted in Revised Form: 02.12.2025)

ABSTRACT: This paper discusses the case of an off-grid school in Kano, Nigeria. A self-sufficient and environmentally friendly green energy system was designed for the school. The system has been designed to meet the electricity needs of an isolated school with 45 students. The system consists of solar panels and lithium-ion batteries. The average daily energy consumption of the school was calculated to be 4.8 kWh, based on the specific devices used and their operating durations. The study also examined the impact of three critical parameters on energy generation and battery performance: (i) soiling loss, (ii) panel tilt angle, and (iii) battery operating temperature. A total of 27 different scenarios were analyzed using the PVsyst 8 simulation program, with the panel tilt angles varying (10°, 20°, 30°), the battery operating temperatures varying (20°, 25°, 30°), and soiling loss varying (5%, 10%, 15%). A 5% soiling loss, 10° panel tilt and 25° battery temperature achieved the highest energy generation, 1,754.92 kWh. Consequently, the proposed system effectively met the school's annual energy needs without any energy loss.

Keywords: *Lithium-ion Battery Storage, Off Grid System, Operating Battery Temperature, Photovoltaic, SOC, Soiling Loss.*

1. INTRODUCTION

The depletion of fossil fuel resources, and policies aimed at reducing CO2 emissions, are increasing the focus on renewable energy sources [1-3]. The Renewable Capacity Statistics Report, published by the International Renewable Energy Agency (IRENA) in March 2024, shows 43% of global capacity was renewable energy by end of 2023.The global renewable energy generation capacity reached 3,869 gigawatts at the end of 2023. With a capacity of 1,418 gigawatts, solar energy constitutes approximately 37% of the overall capacity. Thus, solar energy ranks first among other energy sources (wind, hydroelectricity, bioenergy, etc.), having increased by 345 GW in 2023, accounting for three quarters of the total increase [4, 5].

In Nigeria, renewable sources accounted for only 25% of total generation in 2021 [6]. Despite its considerable potential, the utilization of solar energy remains relatively low, with only 102 MW (approximately 0.3%) currently in operation. In Nigeria, where over 80 million rural residents lack access to electricity, and where rural areas constitute 60% of the country's population, it is crucial to ensure the generation of electricity from photovoltaic (PV) sources [7]. In rural areas where grid electricity is unavailable, PV systems provide an effective solution for meeting energy demands [8, 9].

Studies have been conducted on the provision of electricity from renewable energy sources in off-grid areas in Nigeria. In a study conducted in Jos, Nigeria, Akinsipe et al. [10] evaluated the technical and economic feasibility of a PV and battery system for supplying electricity to a residential building in an off-grid area. Similarly, Babatunde et al. [11] proposed a hybrid system to meet the energy needs of a rural health center. The study selected six rural communities from six geopolitical regions of Nigeria for analysis. Another study focused on the design and optimization of a hybrid power system for a small off-

***Corresponding Author:** Emre OZER, emre.ozer@gibtu.edu.tr

grid village in Itapaji City [12]. Oladeji et al. [13] designed a system that meets the daily energy needs of a building in North-Western Nigeria with a system of photovoltaics and batteries using the Homer program. Another study by Adesina et al. [14] designed, implemented, and analyzed the performance of a 3.5 kVA off-grid solar PV system for a household in Ilorin City. It can be concluded that off-grid PV systems in Nigeria offer a sustainable solution by providing access to electricity, especially in rural and remote areas.

The design and optimization of renewable energy systems under various climatic and geographical conditions is a prominent area of research in the current literature. For instance, methodologies have been devised to enhance energy efficiency in electronic systems [15]. The utilization of statistical modeling and optimization techniques has been employed to assess the performance of energy systems [16]. A body of research has emerged on the subject of site selection and sizing in hybrid energy systems [17], with optimal energy solutions being proposed for the coordinated regulation of hydroelectric and solar power generation [18]. Furthermore, management strategies that prioritize the equilibrium between energy demand and supply have been developed [19].

Several studies on off-grid renewable energy systems are comparatively presented with the results of this study in Table 1. Previous studies have focused on techno-economic analyses [10-11] and particular technical parameters (e.g., panel tilt angle, azimuth, and battery) [37]. In contrast, this paper presents the optimal scenario for achieving 100% load coverage at the school level by considering multiple parameters (panel tilt angle, battery temperature, and dust accumulation rate) together. In this way, the paper provides practical contributions to the design and optimization of off-grid PV-battery systems for educational buildings.

Table 1. Comparative summary of related studies on off-grid systems

Study	System components	Location and Application Area	Method	Key Parameters	Main Findings
Akinsipe et al. (2021)[10]	Off-grid PV–battery hybrid system	Residential building in Nigeria	HOMER	Techno-economic assessment	For a daily load of 8.58 kWh, an optimum system was designed with 10 PV modules (275 Wp each) and 5 batteries (100 Ah each)
Babatunde et al. (2019)[11]	Off-grid hybrid system (PV, wind, diesel generator, battery)	Six rural health centers in Nigeria	HOMER	Techno-economic assessment	PV/diesel/battery system was found to be the most optimal with an energy cost (COE) of 0.507–0.542 $/kWh
Ebhota & Tabakov (2022) [37]	Off-grid PV–battery hybrid system	Household in South Africa	PVSyst	Panel tilt, azimuth, battery temperature	For a daily load of ≈3.9 kWh, optimum conditions were: 40° tilt, 0° azimuth, and ≤20 °C battery temperature
This study	Off-grid PV–battery hybrid system	School building in Nigeria	PVSyst	Panel tilt angle, battery temperature, soiling ratio	For a daily load of ≈4.8 kWh, the most suitable scenario was: 10° tilt, 25 °C battery temperature, 5% soiling

In recent years, studies on PV–battery hybrid systems have increased rapidly; however, off-grid applications at the school scale remain limited in the literature. In particular, environmental and technical parameters, such as tilt angle, soiling rate, and battery operating temperature, which have significant impacts on system performance, have not been examined in detail. Optimizing such systems under realistic conditions is a crucial issue, especially in regions without grid access. The aim of this study is to address this gap by analyzing indicators such as energy production, battery state of charge (SOC), solar fraction, and annual energy output under different scenarios using PVSyst simulation. Through multi-scenario analyses, the most suitable configuration was identified (10° tilt angle, 25°C battery temperature, and 5% soiling), yielding an annual production of 1754.9 kWh with 100% load coverage. Therefore, this study comprehensively examines the energy and battery performance of school-scale PV-battery hybrid systems. This perspective contributes to the existing literature on the subject.

The main contributions of this research include:

- Analysis of the PV-battery hybrid power system at a school.
- Assessment of various operating scenarios based on different tilt angles, battery temperatures, and soiling to determine the best operating parameters.
- Key performance indicators, such as annual energy generation, load coverage ratio, battery state of charge (SOC), and solar fraction were examined in detail.
- The study provides practical insights into the design and optimization of renewable energy applications for school-scale systems.

However, a substantial proportion of the extant literature is often oriented towards individual parameters or particular scenarios. This study comprehensively analyzes the three critical parameters: (i) tilt, (ii) temperature, and (iii) soiling, and thoroughly examines their effects on performance. The study was introduced as follows: The first section outlines the location, rationale for its selection, and meteorological characteristics. The second section discusses the placement (orientation) of the PV panels and provides a detailed analysis of the load profile. The third section provides an overview of the system components, including the PV panels and batteries, along with their respective specifications. The fourth section presents the results of the study and analyzes the impact of various parameters, such as soiling loss, panel tilt angle, and battery process temperature, on the system's performance. The paper concludes by discussing the findings.

2. METHODOLOGY

This study focuses on the design and optimization of a PV system with energy storage to meet the energy needs of a school using the PVsyst 8 simulation program. The methodology is comprised of several key stages. Initially, the geographic location and meteorological characteristics were determined. Then, photovoltaic panels and battery systems were incorporated. Lastly, different parameters were studied using PVsyst 8 software, including orientation, tilt, soiling loss, and battery temperature. The next section presents the process involved in designing the system for maximum energy efficiency.

Figure 1 presents the fundamental ideas and variables. In Figure 1, a general flow chart of the PV-Li-ion battery system is provided, along with the parameters that were considered. The top section of the figure shows the school's position in the Kano region of Nigeria. As illustrated, the system's primary components comprise panels, lithium-ion batteries, and the load of the educational institution. The parameters of inputs for the system under consideration include the tilt angle of the panels (10°, 20°, 30°), the yearly soiling loss (5%, 10%, 15%), and the operating temperature of the batteries (20 °C, 25 °C, 30 °C). The system's outputs include state of charge (SOC), annual energy production (kWh), and solar fraction. The results of the scenario analyses indicated that the optimal performance was achieved with a combination of a 10° tilt, a battery temperature of 25 °C, and 5% dust loss. In this scenario, the system generated 1,754.9 kWh of energy per year and exhibited 100% load coverage.

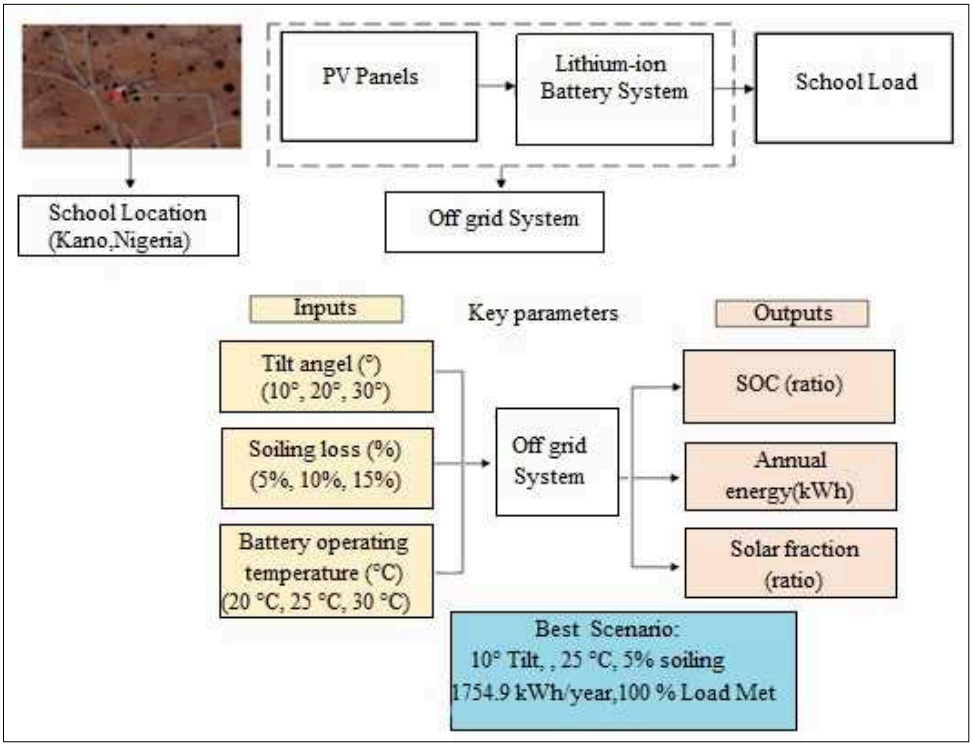


Figure 1. General flow chart of the PV–lithium-ion battery system for off grid system

A detailed system modelling and validation process was conducted within the PVsyst 8 simulation. The PV-lithium battery system was modeled by accurately defining the load profile, component specifications, panel orientation, shading parameters, and storage configuration. The load profile was constructed with hourly resolution to reflect the school's daily consumption behavior. All panel and battery specifications were input manually based on real manufacturer datasheets to ensure accuracy. In order to validate the performance of the system, 27 different scenarios were produced by varying the tilt angle (10°, 20°, 30°), temperature (20°C, 25°C, 30°C), and soiling loss (5%, 10%, 15%). These revealed how each of these affected energy generation and battery performance. The model's reliability was confirmed by observing zero unmet load energy in certain scenarios and full battery utilization under varying conditions, ensuring that the proposed system design is both feasible and optimized for the selected location.

Figure 2 presents the flow diagram of the proposed methodology, including the main steps of the simulation and evaluation process. In the first step, the required input data (selection of location and climatic data, PV panel capacity, load profile, and battery specifications) were defined. In the second step, simulation scenarios (tilt angle, battery operating temperature, and soiling rate) were established. In the third step, the PVSyst simulation was performed, and the panel generation, battery state of charge (SOC), solar fraction, and energy flows were calculated. In the fourth step, the main outputs (available solar energy, energy provided to the user, unused energy, and annual energy production) were obtained. Finally, in the last step, all scenarios were compared, and the performance evaluation was conducted to identify the most suitable system configuration.

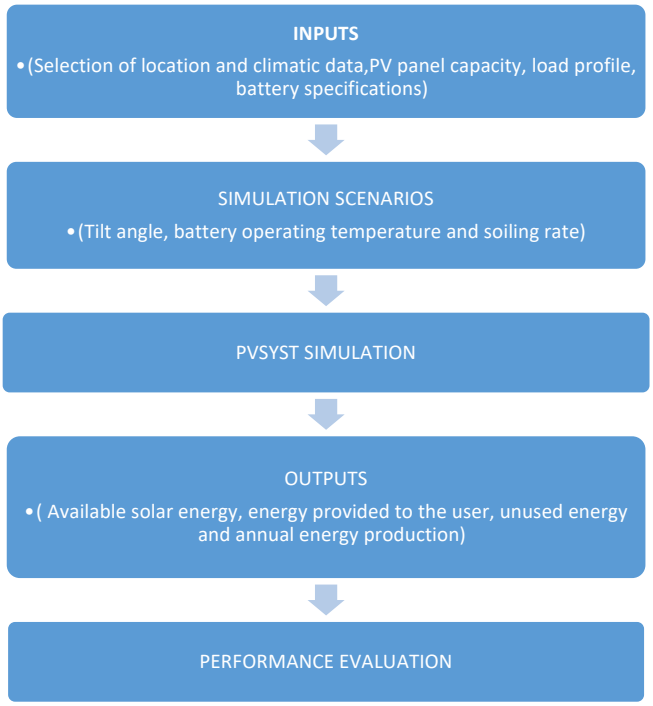


Figure 2. Flowchart of the proposed system simulation steps

2.1. Selection of Location

The study was conducted in a rural area of Nigeria. Nigeria is distinguished as one of the African countries with a considerable energy deficit [7, 20, 21]. A significant proportion of the country's population resides in rural areas, where the energy crisis is particularly acute. Therefore, energy needs are largely met from traditional sources, such as fossil fuels. However, the use of renewable energy sources offers a promising solution to bridge this energy gap in Nigeria. The country's annual solar radiation is estimated to be between 1400 and 2500 kWh/m², which makes the use of PV systems a highly viable option [22]. Figure 3 illustrates the solar energy potential map of Nigeria.

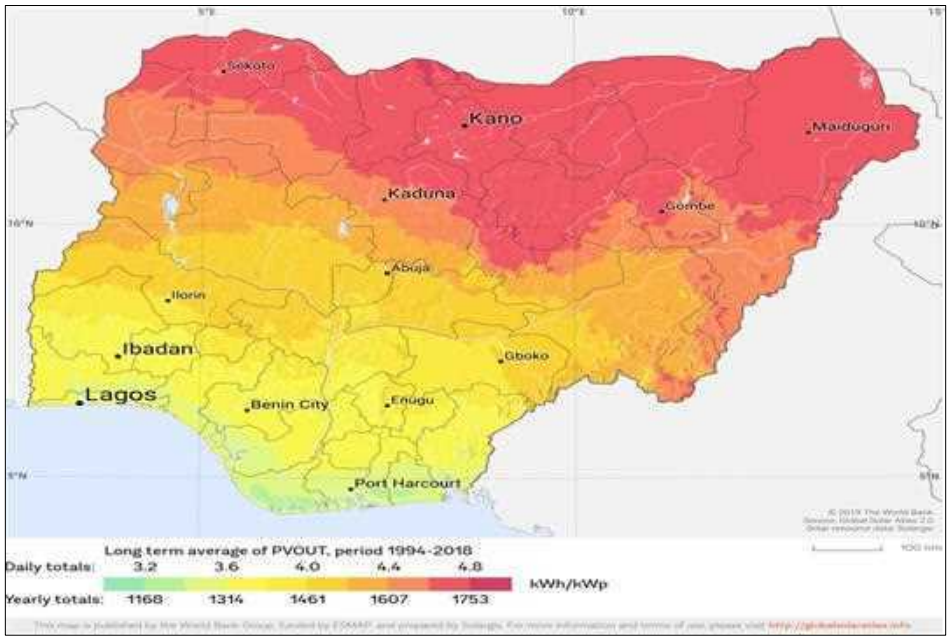
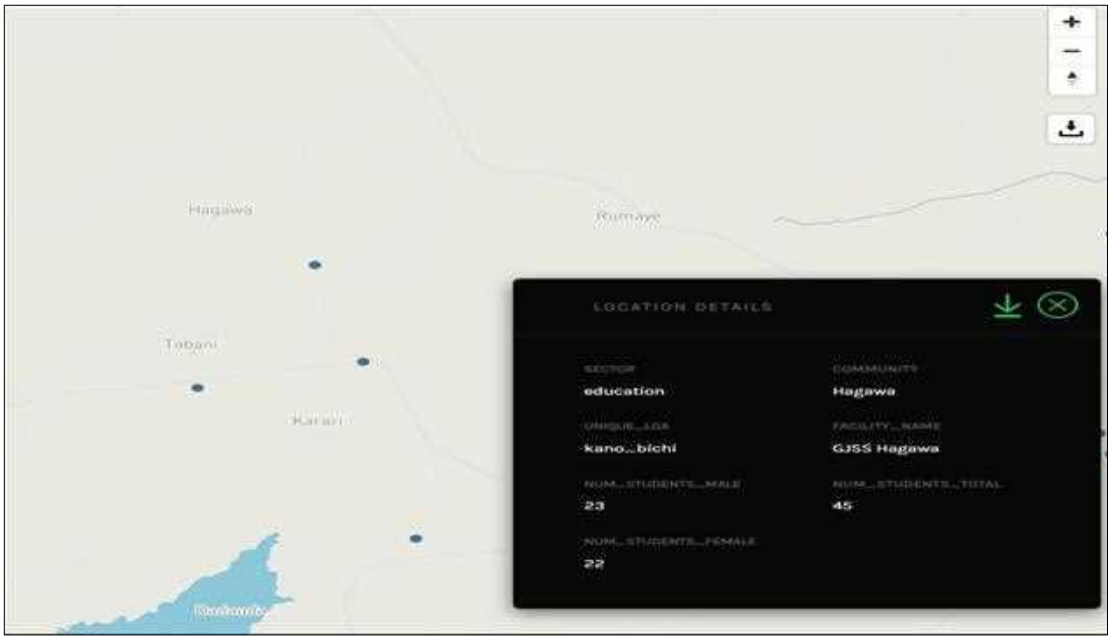


Figure 3. Solar energy potential map of Nigeria [23]

Kano City, situated in the northern part of the country, was selected for this study because of its considerable potential for harnessing solar energy. The Rural Electrification Agency database was utilized to identify an appropriate educational facility in the Kano region [24]. Areas with up to 100 people living off-grid in Kano were selected from the database. A school that met these criteria was selected from the resulting list. The selected school and its satellite image are shown in Figures 4 (a) and 4 (b), respectively.



(a)



(b)

Figure 4. A view of school location from (a) rural electrification agency database [24] and (b) satellite image

A detailed summary of the information relating to the identified school can be found in Table 2 [24]. As can be seen from the table, the school has two classes, three teachers, and a total of 45 students.

Table 2. Key information about the identified school

Data	Value
State	Kano
Facility name	GJSS Hagawa
Facility type	Junior Secondary school only
Education type	Formal only
School locations	12°15'29.8"N 8°10'08.1"E
Latitude, Longitude (using PVsyst 8)	12,25°,8,17°
Number of male students	23
Number of female students	22
Number of total students	45
Number of total classrooms	2
Number of total teachers	3

Climatic variables, including solar radiation, wind, and temperature, play a significant role in determining the efficiency and performance of PV power plants. Consequently, the precision of these parameters has a direct impact on the performance of solar power systems. Meteonorm is a database comprising weather data collected from meteorological stations around the world over many years. In this study, data were generated synthetically from the Meteonorm 8.1 database between 2010 and 2021. As illustrated in Table 3, the 12-month average values of these data are as follows. The mean global horizontal irradiation of the study area was 2176.5 kWh/m², with the highest value observed in April and the lowest in December. The monthly average horizontal diffuse irradiation is 950.8 kWh/m², with the maximum value observed in May and the minimum value observed in November. The monthly average temperature was 26.5 °C, with the highest temperature recorded in May and the lowest recorded in January. Additionally, the mean monthly wind speed and relative humidity are 2.5 m/s and 46.4 %, respectively.

Table 3. Meteorological data of the selected location

Month	Global horizontal irradiation (kWh/m²)	Temperature (°C)	Wind Velocity (m/s)	Relative humidity (%)
January	158.4	21.0	2.79	27.4
February	155.4	24.3	2.70	22.5
March	197.3	28.5	2.61	19.9
April	203.7	31.0	2.39	26.6
May	203.0	31.5	2.60	45.3
June	194.4	28.8	2.80	65.0
July	197.6	27.0	2.60	74.6
August	176.1	25.9	2.20	79.8
September	182.9	26.5	2.00	78.5
October	183.5	27.6	2.01	53.2
November	169.8	24.6	2.40	33.0
December	154.4	21.3	2.69	30.7
Year	2176.5	26.5	2.5	46.4

The sun exposure and shading analysis for the selected location is illustrated in Figure 5. The graph demonstrates the annual availability of sunlight, based on the position of the sun. According to the figure, the sun's rays begin to hit the panels at approximately 7:30–8:00 a.m., ending at around 4:30–5:00 p.m.

Consequently, the panels receive an average of 8–9 hours of direct sunlight per day. While the duration of solar radiation approaches 10 hours during the summer months, it rarely falls below 7 hours during the winter, resulting in a notably high solar radiation duration. This finding suggests that the specified location exhibits a favorable daily profile for solar energy generation.

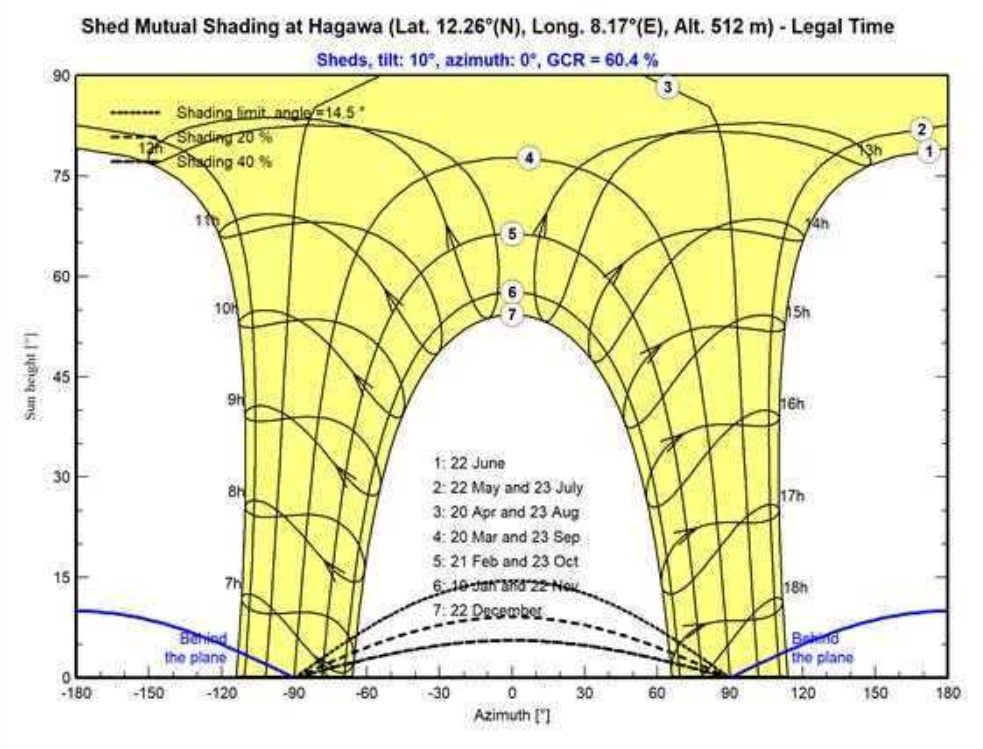


Figure 5. Sun paths diagram for the selected location

2.2. Load Profile

The load profile has been prepared using an example of a school that works between the hours of 7 a.m. to 3 p.m. from Monday to Friday. The school has two classrooms, each with a computer and 12 lamps. Additionally, there is a rest room for teachers and an office for school administration, which is equipped with one refrigerator, one television, and one printer. For security purposes, two lamps remain on from 7 p.m. to 7 a.m. The school also uses five ceiling fans, with two in each classroom and one in the teacher's room. The total daily energy consumption is 4,808 Wh/day, and the monthly energy consumption is 144.2 kWh/month. Table 4 presents the consumption data in detail. The hourly energy consumption profile of all equipment within the system, which varies throughout the day, is detailed in Figure 6.

Table 4. Energy requirements for the school

Description of Item	Quantity	Load (Watts per unit)	Daily Hour of Utilization	Daily Energy (Wh)
Lamps	12	14	4	672
Computer	2	100	5	1000
Printer	1	100	2	200
Refrigerator	1	600	24	600
Ceiling fan	5	60	6	1800
Lamps for security	2	14	12	336
TV	1	100	2	200
Total				4808 Wh/day

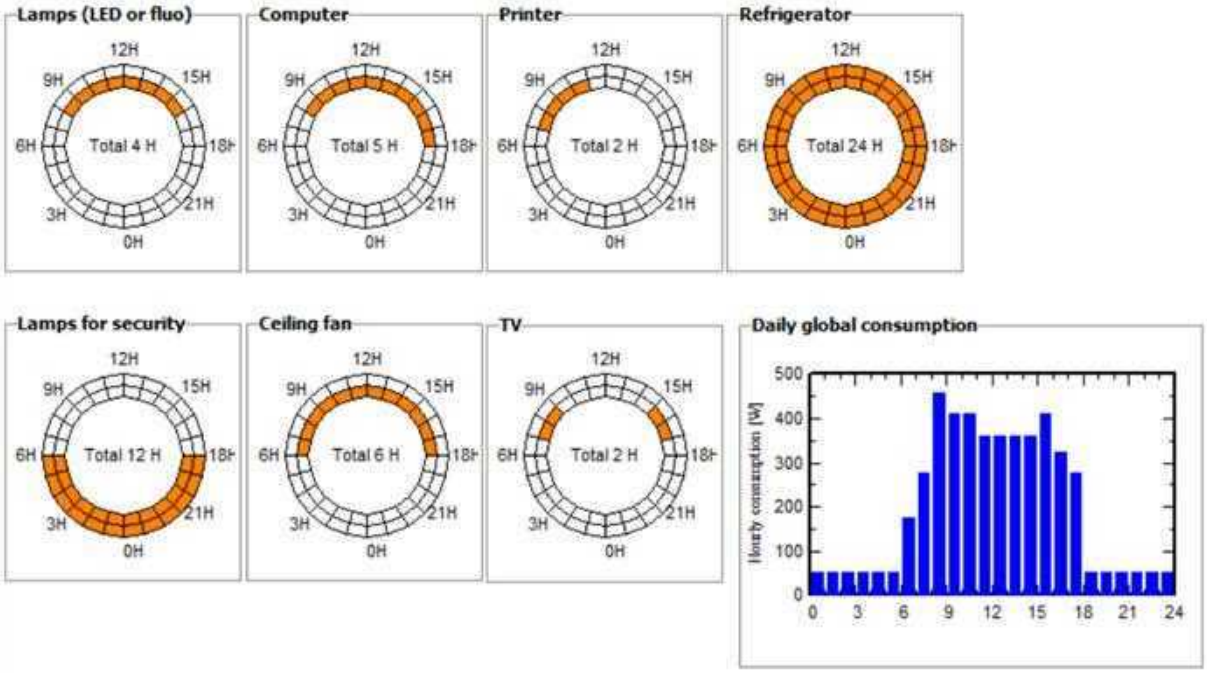


Figure 6. Hourly load profile

2.3. System Design

The system design involves the arrangement and placement of PV panels to optimize energy generation while considering space constraints. In this design, the panels are arranged in a ground-mounted array with no limitations on the number of rows or columns, allowing for flexibility in the installation. Figure 7 shows the panels are tilted at 10° to maximize sunlight based on latitude and season. Each panel is spaced 5 meters apart to minimize shading effects and to ensure adequate airflow for cooling, which enhances system efficiency. The panels' orientation and spacing ensure consistent and reliable energy output for the school throughout the year.

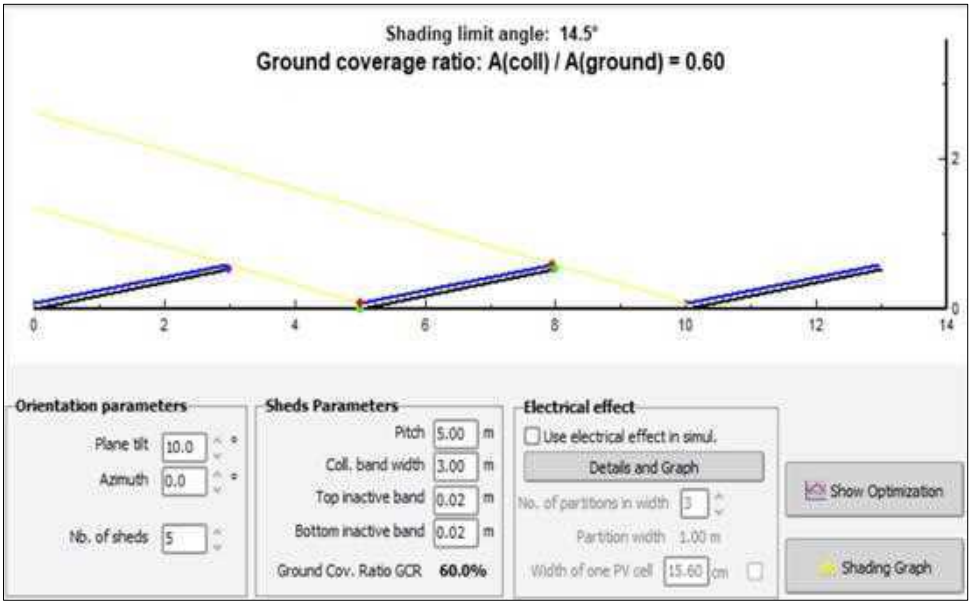


Figure 7. Orientation parameters of the system

Other essential components of the system design include batteries, PV panels, and inverters. Figure 8 illustrates a diagram of a typical off-grid system with energy storage. As can be seen, the user's load demand is satisfied through the use of PV arrays and batteries. The batteries are charged by the PV arrays and provide electricity for the load when required. There is no generator system for external support. Our proposed system is designed in accordance with this principle.

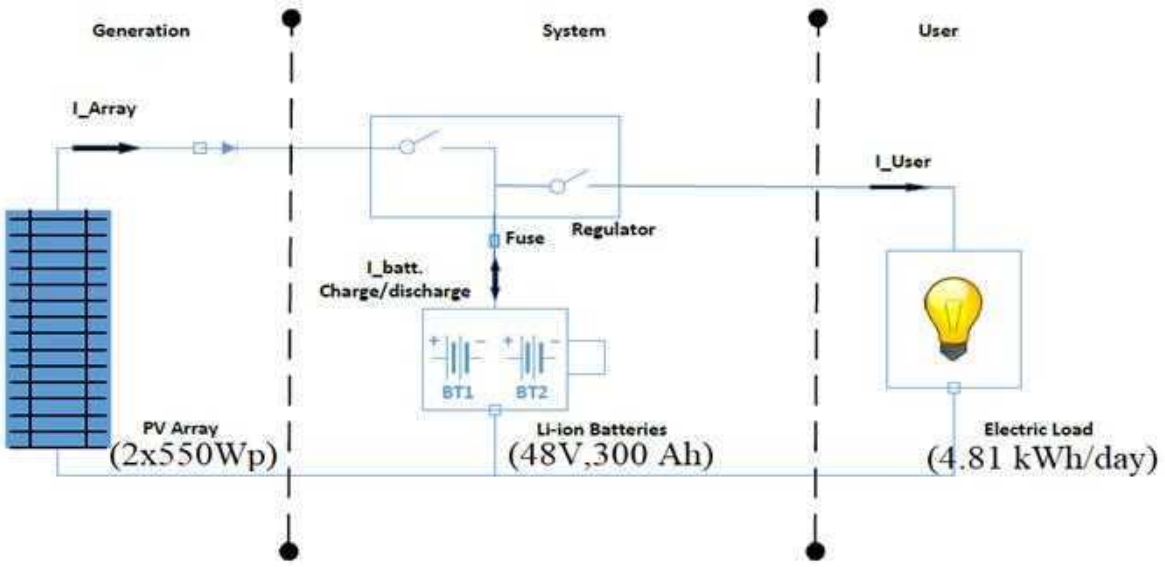


Figure 8. Block diagram of the proposed system

As it is known, the process of converting solar energy into electrical energy is based on the principle of PV and photocurrent generated by solar irradiation in PV cells [25]. The excitation of electrons in the PV cell by a photon is the initial step in the process that results in the flow of an electrical current. The current in this circuit is completed by a forward-biased diode. The conversion process is modeled using the equivalent circuit of the PV cell shown in Figure 9. The equivalent circuit model of a solar cell basically

consists of a current source, diodes, and resistors [26,27]. The current-voltage (I–V) characteristics of the PV cell are calculated based on the following equations [25,28].

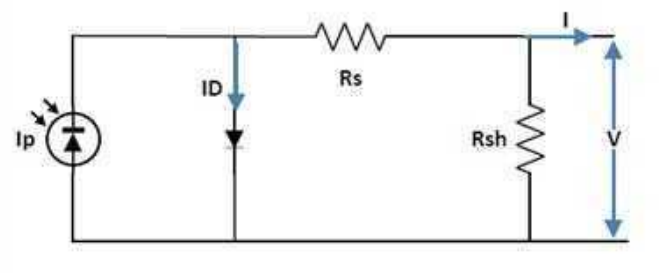


Figure 9. The equivalent circuit of a PV cell

In applying Kirchhoff's current law to the circuit diagram illustrated in Figure 9, eq. (1) [25,28] is derived;

$$I = I_p - I_D - I_r \tag{1}$$

Here, I represents the current of the PV cell, I_p represents the photocurrent, I_D represents the diode current, and I_r represents the current generated in the resistor connected in parallel in the circuit [25,28].

$$I_D = I_s \left[exp\left(\frac{q(V+R_s I)}{Ak_B T}\right) - 1 \right] \tag{2}$$

Equation 2 allows for the calculation of the diode current. I_s represents the saturation current, R_s represents the series resistance, q represents the electronic charge, A represents the ideality factor, k_B represents the Boltzmann constant, and T represents the absolute junction temperature.

Parallel current (I_r) can be calculated with ease by dividing the voltage (V) between the terminals by the resistance (R_{sh}) using Eq. 3.

$$I_r = \frac{V}{R_{sh}} \tag{3}$$

The interrelation between current and voltage can be determined by utilizing the three previously mentioned equations, as illustrated in equation 4. Here, I_0 refers to the reverse saturation current of the diode [25,28].

$$I = I_p - I_0 \left[exp\left(\frac{q(V+R_s I)}{Ak_B T}\right) - 1 \right] - \frac{V+IR_s}{R_{sh}} \tag{4}$$

The selection of PV panels is facilitated within the PVsyst software interface, as illustrated in Figure 10. In this section, the manufacturer, module power, cell technology, and model information can be defined. Furthermore, the approximate number of modules necessary to meet system requirements, along with the operating voltages (Vmpp and Voc) applicable under different temperature conditions, are calculated and presented to the user.

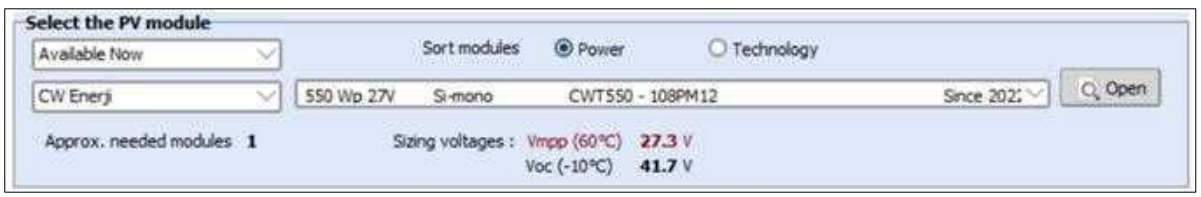
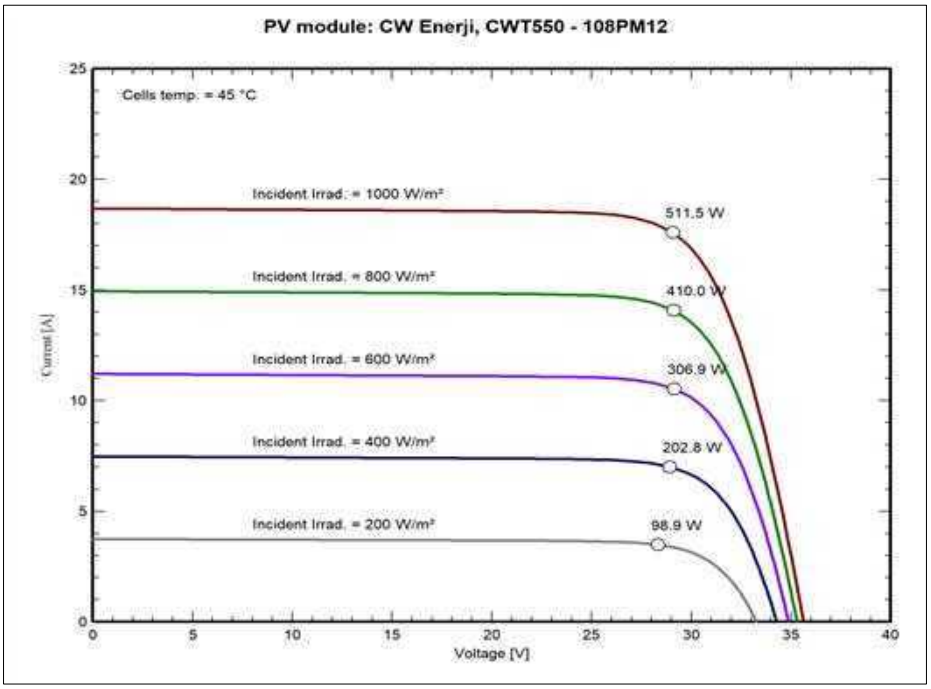
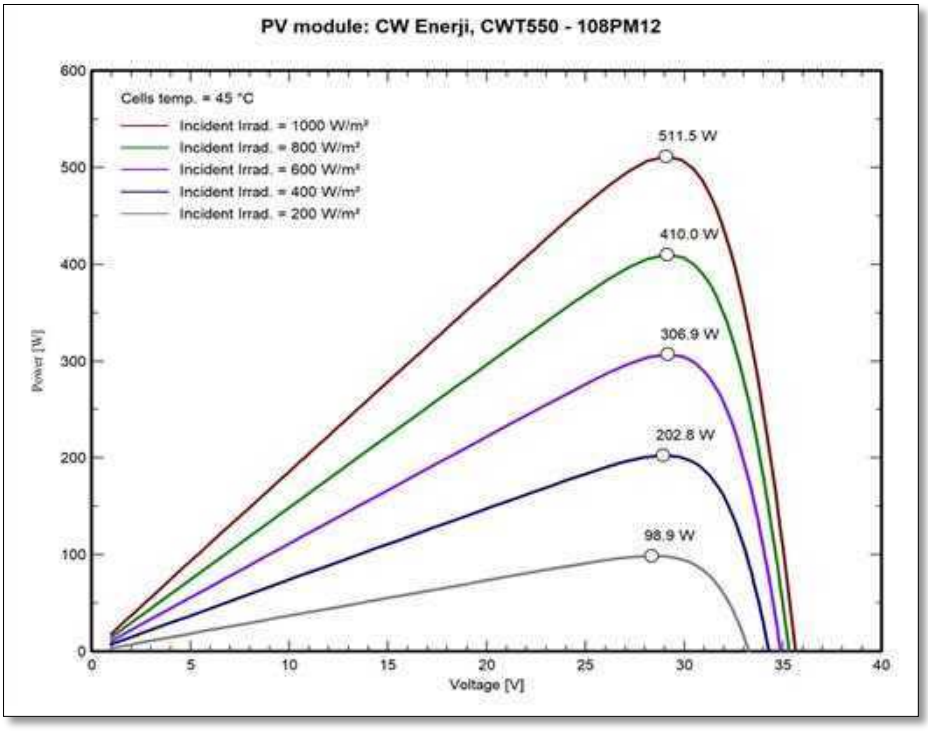


Figure 10. PV panel selection in PVsyst simulation program

The PV panels used in the system are manufactured by CW Energy, with a nominal power rating of 550 Watt-peak (Wp). The current-voltage characteristics of these modules are shown in Figure 11 (a) while the power–voltage characteristics are presented in Figure 11 (b). Table 5 provides detailed specifications of the selected PV panels presented by PVsyst software [29]. With a total of 54 cells in series and 2 cells in parallel, these two panels are designed to provide an optimal combination of voltage and current for energy generation.



(a)



(b)

Figure 11. (a) The current-voltage and (b) the power-voltage characteristics of the PV panel

Table 5. Specifications of selected PV panel

Specification	Value
Type	Monofacial
Manufacturer	CW Energy
Model	CWT550-108PM12
Technology	Si-mono (Twin half cells)
Nominal power	550 Wp
Module Length	1965 mm
Module width	1303 mm
Module weight	28.50 kg
Module area	2560 m^2
Cells in series	54
Cell in parallel	2
Short-circuit current (I_{sc})	18.49 A
Open circuit voltage (V_{oc})	37.90 V
Max. Power point current (Impp)	17.46 A
Max. Power point voltage (Vmpp)	31.50 V
Rshunt (Rsh)	180 ohm

A second crucial component of the system is the batteries. When the energy obtained from PV system is insufficient to meet the load demand, the batteries will be activated to fulfill the remaining energy requirements. The Huawei manufacturer was selected for the batteries due to its extensive product range. The Luna2000-15-SO, with an inverter 5 kW model battery and has been in production since 2023, employs Li-ion (LFP) technology with a nominal voltage of 48 V and a capacity of 300 Ah (at C10) [30]. At 95 % depth of discharge (DOD), the stored usable energy in the battery is 13.9 kWh. DOD is a parameter that indicates how much of the battery's current capacity is being used and is typically expressed as a percentage (%) [30]. The long-term performance of lithium-ion batteries decreases due to physical and chemical degradation over time, leading to capacity losses. These degradations are represented by different models and are directly related to the DOD and state of charge (SOC) parameters, which are important parameters [32]. Table 6 provides a detailed account of the specifications of the battery presented by PVsyst software.

Table 6. Specifications of selected battery

Specification	Value
Nb. of cells in Series/in parallel	15/3 (total 45 cells)
Charge cut-off voltage	54 V
Discharge cut-off voltage	40.5V
Maximum charging current	100 A
Internal resistance (at 20 °C)	8 m ohm
Open circuit voltage at SOC (50 %)	49.05 V
Stored energy at DOD (95 %)	13.9 kWh
Specific energy	85 Wh/kg
Total stored energy during the battery life	58 MWh
Width/depth/height	670/150/1320 mm
Weight	164 kg

Accurate determination of battery capacity is essential for ensuring energy continuity. In this study, the battery capacity was calculated based on one of the commonly used methods in the literature, which considers the total DC load power and the system's autonomy period. The capacity calculation was performed using Equation 5 [33,34]:

$$C = \frac{P_{load} x\, A_{bat}\, x\, t}{V_b x K_b x DoD} \quad (5)$$

Where C is the battery capacity (Ah), A_{bat} is the autonomy period (2 days), DoD is the depth of discharge (80%), K_b is the coefficient of the battery (1.14), P_{load} is the capacity of the total DC power load (4.81 kWh/day = 200.4 W), t is the working time per day of the load (24 h), and V_b is the battery voltage (48 V). In order to ensure uninterrupted energy supply under low solar radiation conditions, the autonomy period was assumed to be 2 days. Based on the calculations performed using equation 5, the theoretical capacity was found to be approximately 220 Ah. However, since the selected battery model did not include a 220 Ah option, the closest available option of 300 Ah was chosen. This selection provides a safety margin to extend the battery's lifespan and to account for potential uncertainties.

Figure 12 illustrates the voltage-SOC relationship for the battery. The battery's charge cut-off voltage is 54 V, while its discharge cut-off voltage is 40.5 V. At a temperature of 20 °C, the battery takes 105 hours to charge with a 3 A current and 105 hours to discharge with the same current. The system utilized a single battery.

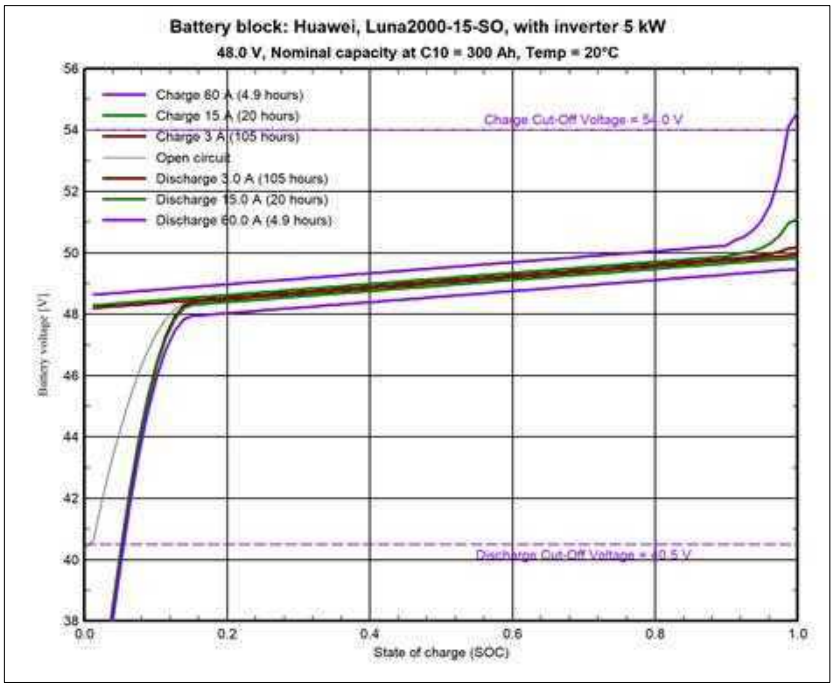


Figure 12. Battery voltage vs SOC characteristics of the selected battery

Soiling is defined as the process by which particulate matter, including but not limited to dust, sand, and pollen, adheres to the surface of a photovoltaic (PV) panel. This accumulation, or soiling, impedes the effective absorption of radiation by the module, thereby reducing its overall efficiency [35]. This results in energy production losses, which can have a particularly deleterious impact in arid, dusty regions [35,36]. According to the findings of several case studies, the annual loss of soil typically ranges from 3% to 6% [35]. Consequently, a 5% value is frequently accepted as a standard assumption [37]. However, under conditions where monthly cleaning is not performed and rainfall is limited, soiling-related losses can reach up to 20% [36,38]. In order to enable a meaningful comparison, a 5% value was adopted as the reference for evaluating soiling losses. Nevertheless, in scenarios where no cleaning is carried out or precipitation is inadequate, soiling-related losses were considered up to 15%.

Given the proximity of the system to the desert, it is anticipated that soiling losses may occur. Consequently, only the soiling loss section was modified, with the annual soiling loss factor set at 5%, and no alterations were made to the other losses defined in the detailed losses section of the program. In light of these considerations, the summary of the proposed system is presented in Table 7.

Table 7. Summary of the proposed system

Specification	Value
Number of PV panels	2
Panel area	5 m^2
Nominal PV power	1100kWh
Number of batteries	1
Battery nominal Voltage	48V
Daily energy needs	4.81kWh
Plate Tilt	10°
Operating battery temperature	25 °C
Yearly soiling loss	5 %

The values for two parameters, i.e., soiling loss and working battery temperature, are defined by the relevant interfaces of the program. These parameters have been determined in the sections shown in Figs. 13 and 14, respectively. Soiling is determined by entering percentage values in the system losses section. The operating battery temperature can be accessed from the system definition section of the program.

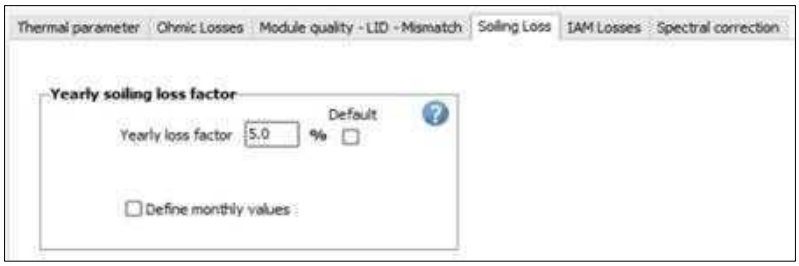


Figure 13. Determination of Soiling Loss parameter in the program

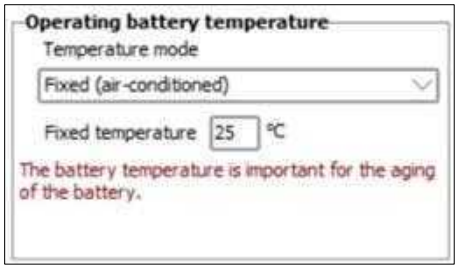


Figure 14. Determination of operating battery temperature in the program

3. RESULTS AND DISCUSSION

Based on the defined parameters, the system was simulated, and the obtained results are presented in this section. Furthermore, the system was analyzed through the creation of scenarios encompassing diverse panel orientations (tilt values), battery temperatures and system soiling losses. A total of 27 scenarios were defined for each of the three features, with 20, 25, and 30 Celsius degrees of battery temperature, 10, 20, and 30 degrees for tilt angle, and 5, 10, and 15 % for annual soiling loss factor. The

proposed system (i.e. 10° plate tilt, 25 °C battery temperature, 5 % yearly soiling loss) is representative of the fourth scenario outlined in Table 10.

Table 8 provides a summary of the numerical main results for the proposed system. For an annual global horizontal irradiance of 2176.5 kWh/m², the system generated 1754.9 kWh of energy. The total energy generated was sufficient to meet the load requirement. Each month, the system load was fully met without any energy loss, indicating that the solar fraction value was 1.

Table 8. Numerical main results

Months	Glob Hor (kWh/m²)	GlobEff (kWh/m²)	E_ Avail (kWh)	E_Unused (kWh)	E_ User (kWh)	E_ Load (kWh)
January	158.4	161.5	151.8	0.00	149.0	149.0
February	155.4	153.0	141.0	0.00	134.6	134.6
March	197.3	188.8	170.5	16.03	149.0	149.0
April	203.7	188.5	168.7	20.18	144.2	144.2
May	203.0	182.1	163.5	10.92	149.0	149.0
June	194.4	171.7	156.7	8.50	144.2	144.2
July	197.6	175.5	161.4	8.87	149.0	149.0
August	176.1	159.8	147.9	6.11	149.0	149.0
September	182.9	172.0	157.5	4.80	144.2	144.2
October	183.5	179.9	163.8	5.75	149.0	149.0
November	169.8	173.3	159.8	11.57	144.2	144.2
December	154.4	158.8	149.2	1.22	149.0	149.0
Year	2176.5	2065.0	1891.9	93.95	1754.9	1754.9

In this context, "GlobHor" represents global horizontal irradiance, "GlobEff" represents effective correlation for global, IAM, and shading, "E_Avail" represents available solar energy, "E_Unused" represents unused energy (battery full), "E_Miss" represents missing energy, "E_User" represents energy provided to the user, and "E_Load" represents the energy requirement of the user (load). Additionally, "SolFrac" represents the solar fraction (EUsed/Load).

Table 9 presents the detailed loss analysis of the proposed system. The abbreviations in the Table 9 represent the loss parameters of the system. ModQual (kWh) refers to the module quality loss, indicating the energy reduction caused by the inherent quality characteristics of the PV modules. MisLoss (kWh) denotes the module array mismatch loss, which occurs due to variations between modules within the same array. OhmLoss (kWh) represents the ohmic wiring loss, caused by electrical resistance in the system's wiring. EArrMPP (kWh) is the array's virtual energy at the maximum power point (MPP), while EArrUfix (kWh) indicates the array's virtual energy when operating at a fixed voltage. EUnused (kWh) refers to unused energy, which occurs when the battery is fully charged and cannot store additional energy. Finally, EArray (kWh) represents the effective energy available at the output of the array after accounting for these losses.

In Table 9, Module quality loss (ModQual) is 20.278 kWh, while array mismatch loss (MisLoss) is very low at 0.984 kWh. Ohmic losses (OhmLoss) are significant at 59.432 kWh, reflecting cabling efficiency. Maximum power point energy (EArrMPP) peaks in spring, but in April, 14.67 kWh of unused energy (EUnused) occurred due to full battery capacity. The annual net output energy (EArray) is calculated as 1,857.8 kWh. Overall, the system performs well, but reducing ohmic losses and unused energy could further improve efficiency.

Table 9. Losses in the proposed system

Month	ModQual (kWh)	MisLoss (kWh)	OhmLoss (kWh)	EArrMPP (kWh)	EArrUfix (kWh)	EUnused (kWh)	EArray (kWh)
January	1.627	0.079	4.551	153.2	153.2	0.00	153.2
February	1.514	0.073	4.412	142.4	142.4	0.00	142.4
March	1.826	0.089	5.584	171.5	171.5	3.85	167.4
April	1.805	0.088	5.581	169.5	169.5	14.67	154.0
May	1.753	0.085	5.232	164.8	164.8	6.68	157.7
June	1.681	0.082	4.981	158.4	158.4	2.48	155.9
July	1.730	0.084	4.991	162.8	162.8	4.01	158.5
August	1.587	0.077	4.485	149.0	149.0	3.74	145.2
September	1.690	0.082	4.978	158.9	158.9	3.66	155.2
October	1.757	0.083	5.089	167.1	167.1	6.53	160.5
November	1.709	0.081	5.063	161.7	161.7	8.65	153.0
December	1.599	0.078	4.463	150.6	150.6	0.00	150.6
Year	20.278	0.984	59.432	1907.0	1907.0	45.94	1857.8

The results of all evaluated scenarios are presented in Table 10 as detailed. The initial three columns of the table represent the variables that are to be observed with regard to their impact when introduced as input to the system. The remaining columns present the resulting data based on the specified parameters. In the displayed table, the term "Generation " refers to the energy generated by the PV panels. The term "loss energy" is used to describe the difference between the energy required for the system and the energy that is actually supplied. The term "solar fraction" is used to describe the rate at which the energy required for the system is met by solar sources. If the solar fraction is equal to 1 or if the loss of energy is 0, it can be concluded that the system is capable of providing the requisite energy for the load.

Table 10. Energy generation of the system under all simulation scenarios, presented separately

Scenario	Tilt (°)	Operating battery temperature (°C)	Yearly soiling loss factor (%)	Generation (kWh/year)	Loss energy (kWh/year)	Solar Fraction
1	10	20	5	1750.37	4.55	0.997
2	10	20	10	1741.25	13.67	0.992
3	10	20	15	1673.65	81.27	0.953
4	10	25	5	1754.92	0	1
5	10	25	10	1742.09	12.83	0.992
6	10	25	15	1671.84	83.08	0.952
7	10	30	5	1754.92	0	1
8	10	30	10	1743.02	11.9	0.993
9	10	30	15	1671.82	83.1	0.952
10	20	20	5	1740.43	14.49	0.991
11	20	20	10	1713.51	41.41	0.976
12	20	20	15	1653.32	101.6	0.942
13	20	25	5	1740.43	14.49	0.991
14	20	25	10	1713.18	41.74	0.976
15	20	25	15	1651.33	103.59	0.941
16	20	30	5	1740.75	14.17	0.991

17	20	30	10	1713.23	41.69	0.976
18	20	30	15	1651.73	103.19	0.941
19	30	20	5	1679.33	75.59	0.956
20	30	20	10	1646.07	108.85	0.938
21	30	20	15	1582.64	172.28	0.901
22	30	25	5	1679.92	75	0.957
23	30	25	10	1645.07	109.85	0.937
24	30	25	15	1581.28	173.64	0.901
25	30	30	5	1680.32	74.6	0.957
26	30	30	10	1643.52	111.4	0.936
27	30	30	15	1581.31	173.61	0.901

Table 10 illustrates that the highest energy generation occurs at a tilt of 10° and the lowest energy generation occurs at a tilt of 30°. A 30° tilt results in an approximate 10% reduction in energy generation compared to a 10° tilt. In scenarios where the tilt and battery temperature are equivalent, an increase in panel dusting from 5% to 15% results in an average reduction of 5% in energy generation.

A comprehensive analysis of all potential scenarios reveals that only two (scenarios 4 and 7) result without any loss of energy. The highest energy generation is 1745.92 kWh/year in scenario 4, whereas the amount of lost energy is 0 kWh/year. In scenario 27, energy generation is 1581.31 kWh/year and loss of energy is 173.61 kWh/year. The two scenarios with the worst performance are scenarios 24 and 27. The ranking of all scenarios from best to worst is presented in Figure 15.

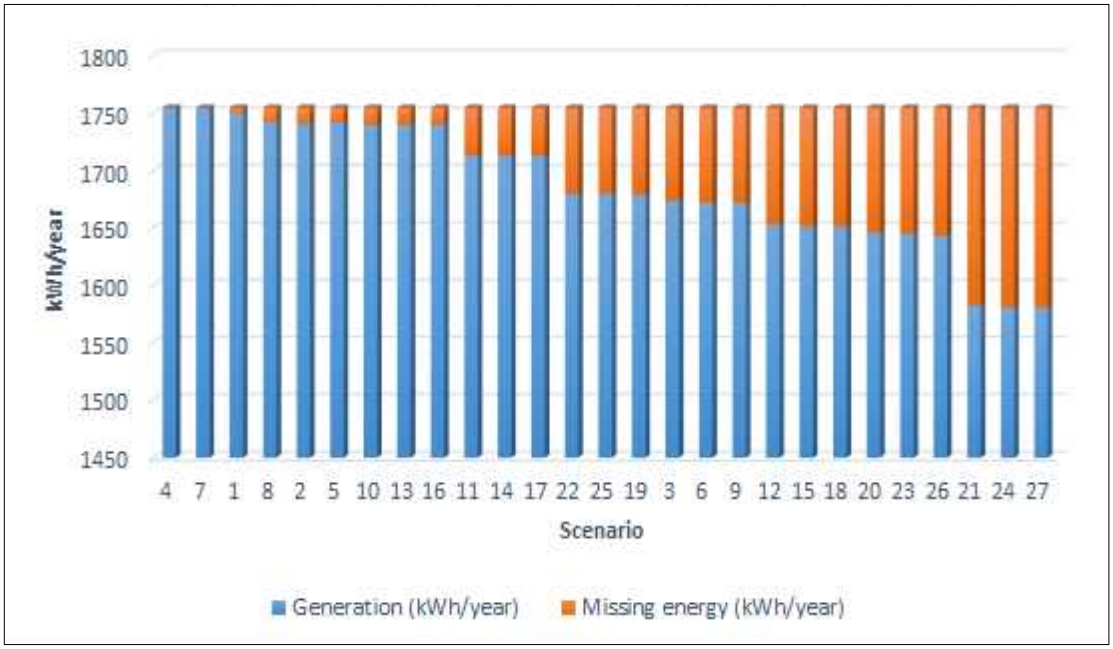


Figure 15. Energy performance evaluation of the proposed system from best to worst case scenarios

The simulation program facilitates the acquisition of comprehensive data regarding the operational status and performance of the battery. Table 11 illustrates the mean of SOC, charge time, discharge time, and battery current charge/discharge efficiency (EffBatI) values for all scenarios. Depending on the operating conditions, batteries show wear and tear over time. In this context, temperature represents a significant factor influencing battery performance and lifetime. The objective of this study was to investigate the impact of temperature on the results of the SOC and battery charge/discharge efficiency measurements.

Table 11. Battery operation and performance of the system under all simulation scenarios

Scenario	Tilt (°)	Operating battery temperature (°C)	Yearly soiling loss factor (%)	SOCmean (ratio)	Charge duration (Hour)	Discharge duration (Hour)	EffBatI (%)
1	10	20	5	0.778	2409	6351	91.3
2	10	20	10	0.641	2431	6303	92.1
3	10	20	15	0.384	2418	6237	91.7
4	10	25	5	0.774	2406	6354	90.9
5	10	25	10	0.664	2438	6309	91.6
6	10	25	15	0.37	2435	6167	91.2
7	10	30	5	0.774	2407	6353	90.8
8	10	30	10	0.647	2441	6306	91.5
9	10	30	15	0.351	2433	6202	91.2
10	20	20	5	0.731	2408	6314	90.7
11	20	20	10	0.627	2436	6243	90.8
12	20	20	15	0.34	2418	6182	91.6
13	20	25	5	0.73	2404	6321	90.4
14	20	25	10	0.618	2441	6236	90.4
15	20	25	15	0.331	2434	6158	91.1
16	20	30	5	0.729	2406	6328	90.2
17	20	30	10	0.615	2437	6246	90.3
18	20	30	15	0.335	2437	6138	91.1
19	30	20	5	0.643	2392	6241	90.6
20	30	20	10	0.533	2381	6190	90.6
21	30	20	15	0.345	2382	6118	91.3
22	30	25	5	0.628	2385	6284	90.3
23	30	25	10	0.529	2399	6139	90.3
24	30	25	15	0.346	2385	6024	90.9
25	30	30	5	0.629	2382	6290	90.3
26	30	30	10	0.547	2385	6151	90.2
27	30	30	15	0.335	2392	6051	91

As illustrated in Table 11, the shortest charging time was observed in Scenario 20, where the battery temperature was 20 °C, the tilt angle was 30°, and the annual fouling (soiling) loss was 10%. The longest charging time was observed in Scenario 14, where the battery temperature was 25 °C, the inclination angle was 20°, and the annual fouling loss was 10%. The lowest value in terms of discharge time was 6024 hours in Scenario 24, where the battery temperature was 25 °C, the inclination angle was 30°, and the annual fouling loss was 15%. The highest discharge time of 6,354 hours was observed in Scenario 4, where the battery temperature was 25 °C, the inclination angle was 10°, and the annual fouling loss was 5%. Consequently, it was evident that all three parameters, namely, the inclination angle, battery temperature, and fouling factor, exerted a significant influence on the charging and discharging times of the battery.

Figures 16 and 17 illustrate the impact of varying soiling factors and temperatures on the battery's charge/discharge current efficiency and mean of SOC values, respectively.

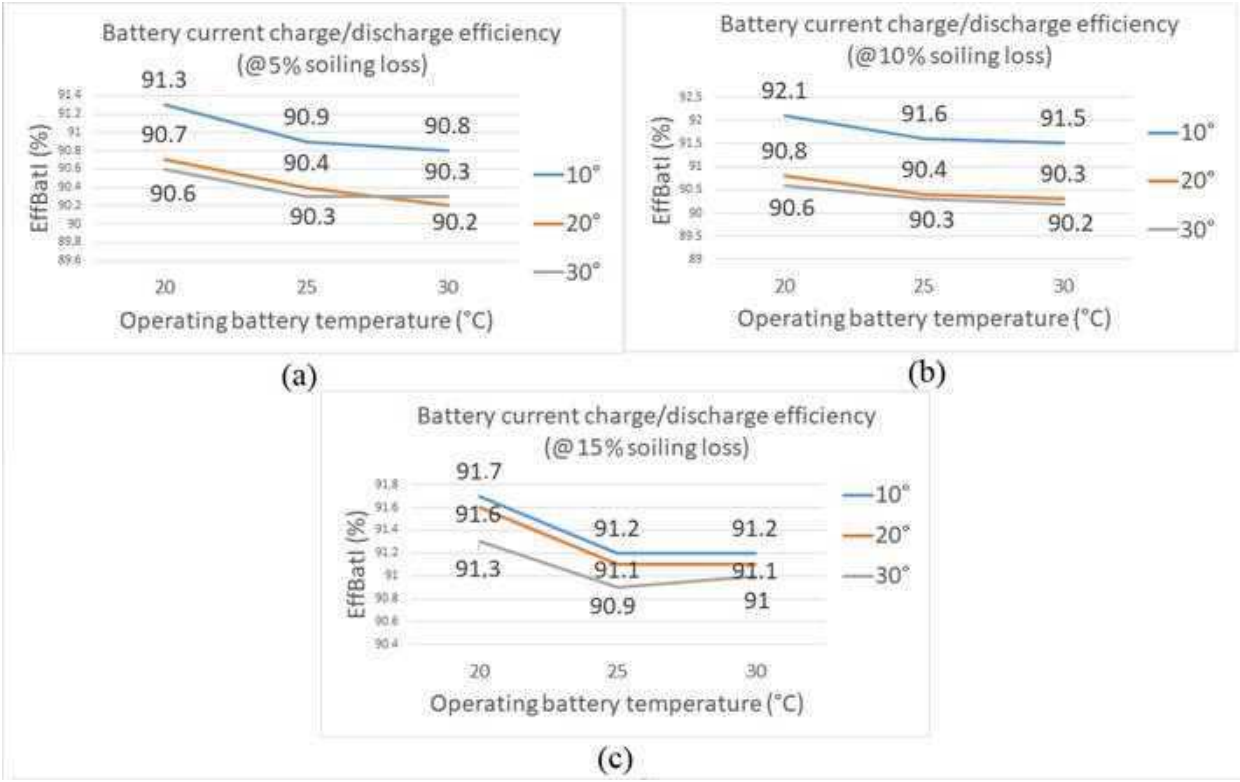


Figure 16. Battery current charge/discharge efficiency (a) 5%, (b) 10% and (c) 15 % soiling loss

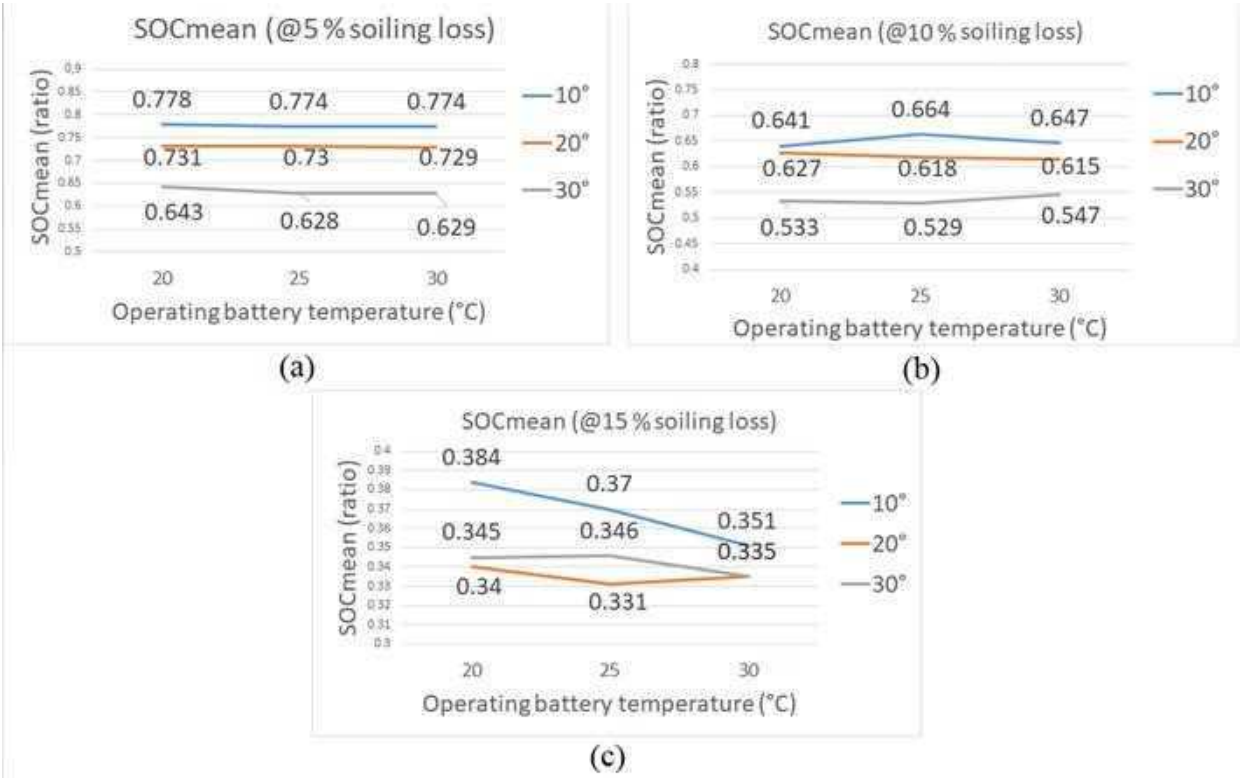


Figure 17. Battery mean of SOC (a) 5%, (b) 10% and (c) 15% soiling loss

Figure 16 illustrates that, while panel tilt and soiling remain constant, an increase in temperature typically results in a reduction in the battery's charging and discharging efficiency. For example, with a soiling rate of 5% and a panel tilt of 10°, the efficiency of the battery is 91.3% when the temperature is 20 °C, while this efficiency decreases to 90.8% when the temperature increases to 30 °C. This shows that the increase in temperature negatively affects the efficiency of the battery in the charging and discharging processes.

As illustrated in Figure 16 (c), when the panel tilt is set to 30° and the soiling rate is 15%, it is noted that an increase in temperature enhances the efficiency of the battery charge/discharge current. In this case, the efficiency increased from 90.9% to 91% when the temperature increased from 25 °C to 30 °C. The data indicate that an increase in temperature does not invariably have a deleterious effect; rather, it can result in enhanced efficiency under a range of specific conditions. However, in all the other graphs of Figure 16, it is evident that the rise in temperature reduces the overall efficiency of the battery charge/discharge current.

As can be seen in Figure 17, when the panel tilt and soiling are held constant, the mean value of the state of charge (SOC) generally decreases as the temperature increases. The highest SOC mean value is 0.778 in Figure 17 (a), but it decreases to 0.331 in Figure 17 (c). As the tilt angle increases (to 20° and 30°), the mean SOC values decrease, and this decrease is observed to become more pronounced with rising battery temperature. As the rate of soiling loss increases, the mean value of the SOC generally decreases.

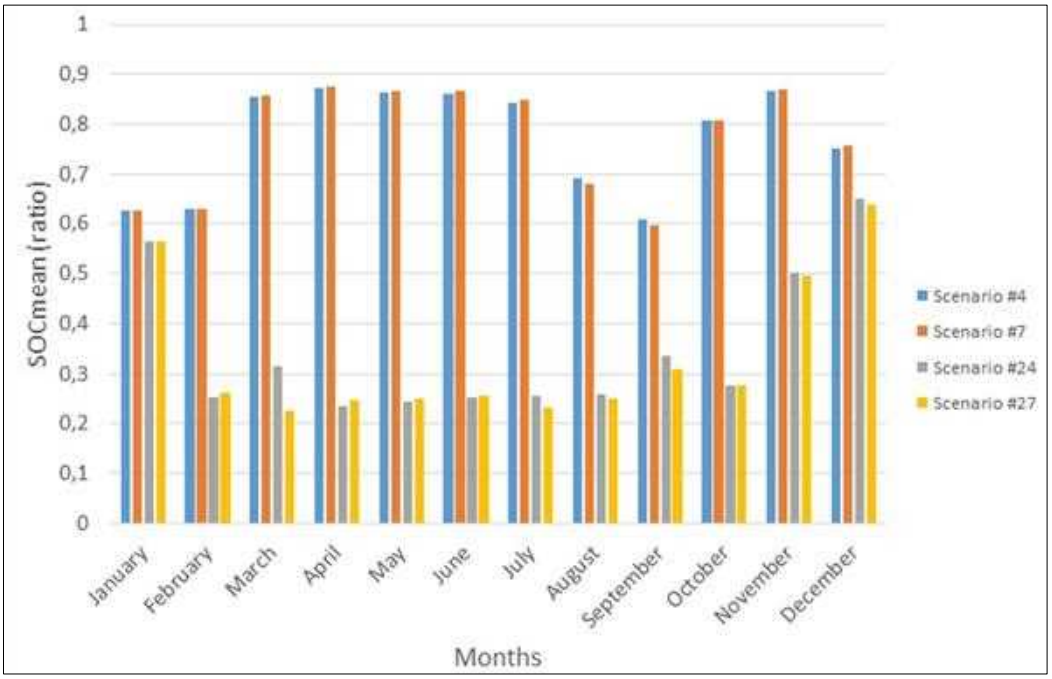


Figure 18. Monthly distribution of SOC, including two best- and two worst-case scenarios

It should be noted that the values displayed in Figure 17 represent annual averages. In order to gain further insight, the monthly average SOC distribution for the two most and least effective scenarios is presented in Figure 18. It can be observed that Scenarios 4 and 7 demonstrate the most favorable performance throughout the year. In these scenarios, SOC ratios exceed 0.8 in March, May, June, July, and October, indicating that the batteries are optimally charged during these periods and that the energy storage capacity is at its highest. In contrast, scenarios 24 and 27 display comparatively reduced performance. In these scenarios, the SOC ratios fall below 0.5, particularly in February, July, August, and September. This result indicates that the batteries are less charged and that the energy storage capacity is lower during these periods. Overall, Scenarios 4 and 7 demonstrate more stable and higher SOC values, while Scenarios 24 and 27 demonstrate more volatile and underperforming SOC values throughout the year.

The main conclusions derived from the study are as follows:

- The performance of the school-scale PV-battery hybrid system was evaluated on an annual basis, and it was found that the total annual production of 1754.9 kWh was sufficient to meet 100% of the load demand.
- Through a multi-factor analysis, the optimal combination consists of the 10° tilt angle, 25 °C battery temperature, and 5% soiling rate. During the winter months, production was sufficient to meet consumption without excess energy, whereas during the summer months, a small surplus occurred, limited by battery capacity.
- Unlike previous studies, this research takes a more integrated perspective by taking into account such factors as tilt, temperature, and soiling at the same time.
- As a result, the paper provides a more comprehensive optimization compared to existing solutions. It's a practical school-level design and implementation guide.

3.1. Impact of Tilt, Battery Temperature, and Soiling on System Performance

Soiling reduces the efficiency of PV systems. This section analyzes the effect of soiling on system performance using the values obtained in Table 10. Figure 19, created using values in Table 10, indicates the impact of the soiling loss factor on system performance. In particular, Figure 19 shows the yearly generation of electricity based on the three different soiling loss factors of 5%, 10%, and 15%. A significant decrease in energy production is observed when the annual soiling loss factor is increased from 5% to 15%. For instance, under conditions of a 10° panel tilt and a 25 °C battery temperature, annual production was 1754.92 kWh for a 5% soiling loss, whereas it decreased to 1671.84 kWh for a 15% soiling loss. This decline corresponds to a 4.7% decrease in production. Similar trends are seen in other cases as well. It becomes necessary to clean the panels or experience enough rainfall to keep the systems working effectively.

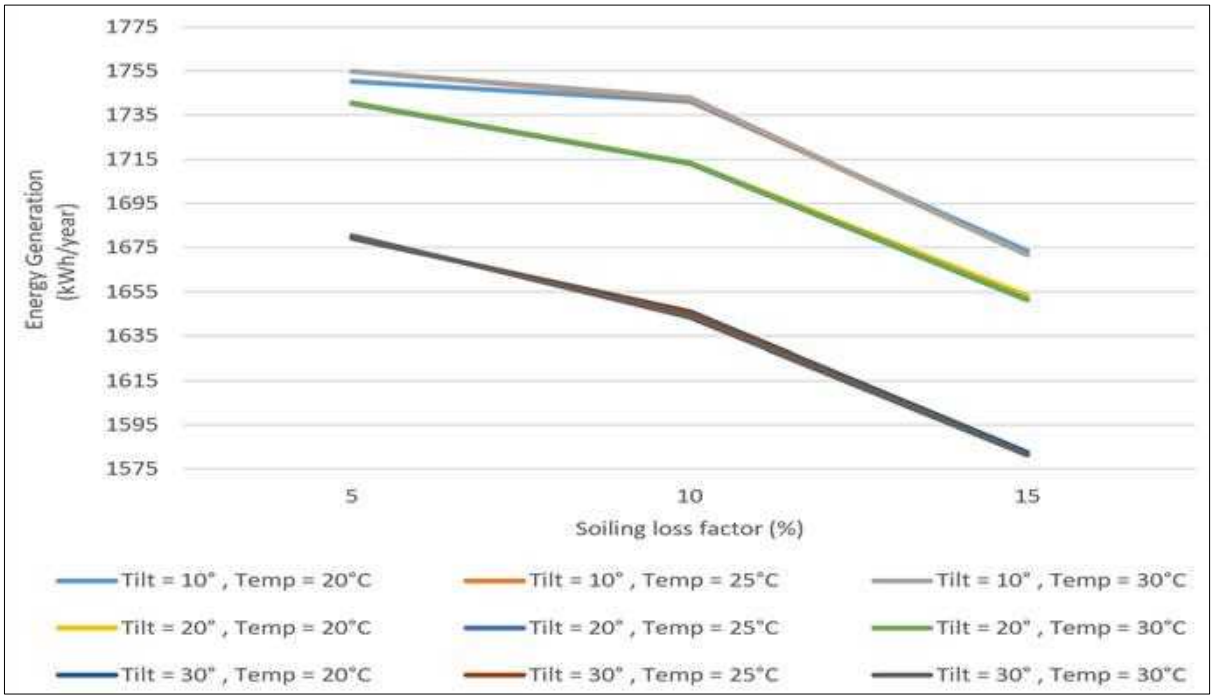


Figure 19. Effect of soiling loss on energy generation

The battery operating temperature is a critical parameter that directly affects energy storage performance and battery life in off-grid systems. The effect of battery operating temperature (20–30 °C)

on annual energy generation under different tilt angles (10°, 20°, 30°) and soiling rates (5%, 10%, 15%) is demonstrated in Fig. 20, utilizing the findings presented in Table 10. The findings reveal that changes in battery temperature have a negligible impact on annual energy production. For instance, at a tilt of 10° and soiling rate of 10%, the production values were 1741.25 kWh/year (20 °C), 1742.09 kWh/year (25 °C), and 1743.02 kWh/year (30 °C). As evidenced by the graph, changes in battery temperature result in only minor changes in energy generation. Conversely, an increase in soiling rate leads to substantial decreases in energy generation.

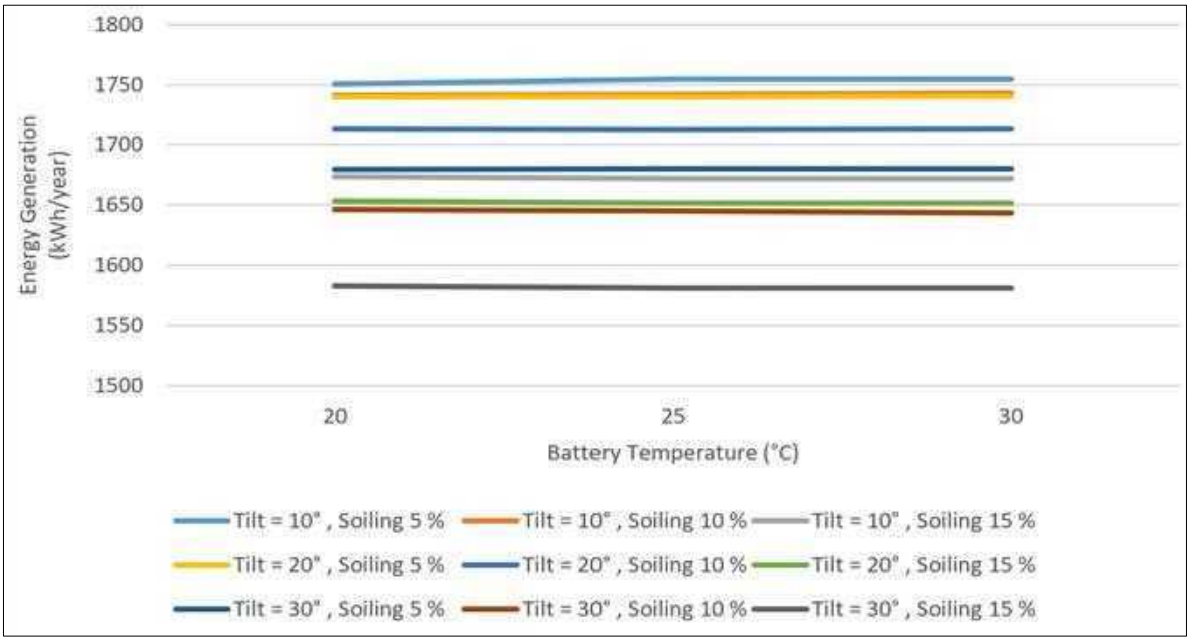


Figure 20. Effect of battery operating temperature on energy generation

The effect of the tilt angle is illustrated in Fig. 21. As can be seen from the figure, increasing the tilt angle leads to a decrease in annual energy generation. For instance, under a soiling rate of 5%, the yearly generation decreases from approximately 1750 kWh/year at 10° tilt to about 1680 kWh/year at 30° tilt.

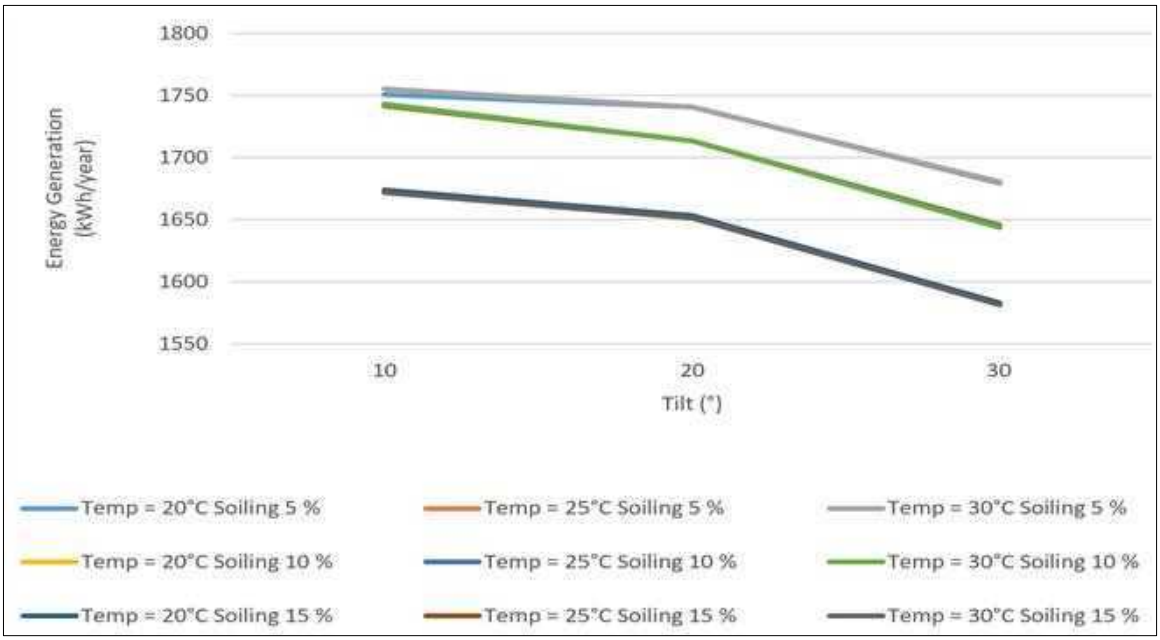


Figure 21. Effect of tilt angle on energy generation

3.2. Discussion of System Performance

This section discusses the findings of the proposed PV-battery hybrid system. This study is different from previous research as it provides a full performance analysis of a PV–lithium-ion battery system for off-grid schools. It does this by using multi-parameter modelling. This investigates how the tilt of solar panels, operating temperature and soiling affect energy output and battery performance. In total, 27 different configurations were simulated and compared, making it one of the most extensive PV-battery performance assessments under realistic environmental constraints. The study also includes battery metrics like SOC, charge/discharge duration, and efficiency, offering deeper insights into system behavior.

The proposed system differs significantly from existing studies in terms of scope and technical detail. For instance, a comparable residential PV system study performed in Durban, South Africa, utilized 2.1 kWp panels and 24 V lead-acid batteries. It has been reported that the system generated 2,662 kWh annually under conditions of 0° azimuth, 40° tilt, and 20 °C battery temperature, with a solar fraction value of 96.31% [39]. The study in Nigeria has developed a system to meet all energy demand (solar fraction = 100%) at 1,750 annual kWh. This system utilizes 1.1 kWp panels and 48 V lithium-ion batteries. In the context of the study, the following variables were examined: panel tilt angle (10°–30°), battery temperature (20 °C–30 °C), and soiling factor (5%–15%). The analysis revealed that optimal production levels were attained at a 10° tilt and 25 °C battery temperature. Soiling caused a 5% reduction in generation, whereas both studies emphasize the pivotal role of panel orientation and battery temperature on performance. Due to variations in geographical location, a low tilt angle is advantageous in Nigerian conditions, whereas a higher tilt angle increases efficiency in South African conditions.

From the analysis of the 27 cases of the proposed system, the impact of the panel angle, battery temperature, and soil on energy generation can be explained. More tilt angle means less energy because less solar radiation reaches the panels.

The panel tilt angle is a critical parameter in the system's energy generation. An additional scenario was created to observe the effect of the tilt angle. All other parameters were kept constant and the panel tilt was set to 0°. The tilted system (10°) exhibited higher performance in terms of annual available energy (1,891.82 kWh) and usable energy (1,754.92 kWh), with no energy shortage and achieving a 100% solar fraction. In contrast, the non-tilted system (0°) generated 1,853.6 kWh of annual available energy and 1,731.1 kWh of usable energy, resulting in a shortage of 23.9 kWh and a solar fraction of 98.64%.

The study also examined the effect of battery technology on system performance. In addition, the research evaluated the impact of battery type on system performance. For the purpose of comparison, a battery was utilized in an alternative scenario, with the other components remaining unchanged. A lithium-ion (LFP) battery offers approximately 13 kWh of storage capacity, whereas a gel-based lead-acid battery with equivalent capacity requires 24 units. A Li-ion (LFP) battery provides approximately 13 kWh of storage capacity. A lead-acid (gel) battery with similar capacity requires 24 units. Both generate the same energy (1,750 kWh a year), but they perform differently. For instance, the Li-ion system had 2.3 kWh/year of missing energy and 91.9 kWh/year of excess energy, whereas the lead-acid system had no missing energy and a lower excess energy of 72.3 kWh/year. In terms of efficiency, Li-ion batteries demonstrate higher internal battery efficiency (91.0%) and capacity retention (SOC: 0.696), whereas lead-acid batteries perform slightly better in terms of energy efficiency (90.3%). Regarding the cycle life of the batteries, research findings indicated that lithium-ion batteries demonstrated an operational lifespan of approximately 10 years, whereas lead-acid batteries exhibited a lifespan ranging from 3 to 5 years. Lead-acid batteries are cheaper and use less energy in the short term. Li-ion batteries are more sustainable due to their long-term efficiency, low maintenance and longer lifespan.

The study examined 27 scenarios to analyse all three critical parameters. Additional values can be tested by increasing scenarios, but this only increases sensitivity. It won't change the current analysis' trends and results. Soiling is another significant factor influencing system performance. Regular cleaning of the panels is crucial to ensure optimal energy output, as dirt and debris can substantially reduce efficiency.

Moreover, increasing the battery temperature results in reduced effectiveness of the charging-discharging cycle. In order to maintain optimal performance and extend battery life, it would be advisable to prevent high temperatures. Optimal temperature levels must be maintained to achieve charging efficiency and longevity.

Among all 27 scenarios, Scenario 15 showed the lowest mean state of charge (SOCmean = 0.331). In this case, the panel tilt was set at 20°, the battery operating temperature was 25 °C, and the annual soiling loss factor reached 15%. The main reason for the low SOC is the reduction in solar input due to soiling, which limited the PV energy for charging the battery. Although both the tilt and battery temperature were moderate, the cumulative effect of soiling caused insufficient energy generation to maintain a stable state of charge.

PVsyst uses MPPT (Maximum Power Point Tracking) based on the selected location's climatic data and the components' technical specs. The operating voltage of the MPPT system depends on the selected equipment. Furthermore, MPPT performance is influenced by environmental conditions. In the simulation, PV generation occurs at or near the maximum power point. Therefore, the drops in SOC across different scenarios are not due to MPPT inefficiency, but to environment and system-level losses.

4. CONCLUSIONS

This study presents the design of a self-sufficient off-grid system to meet the year-round energy needs of a school in Nigeria. Given the importance of reliable access to electricity in the country, the proposed renewable energy system can be applied in similar regions facing energy access challenges.

The study findings show that the proposed system is sufficient to fully meet the school's demand throughout the year with an annual usable energy production of 1,754.9 kWh. Furthermore, among the 27 scenarios analyzed, the most efficient operating condition was determined to be when the panel tilt is 10°, the battery temperature is 25 °C, and the soiling factor is 5%. Lithium-ion batteries are a feasible option for applications due to their high efficiency and long life. When seasonal conditions are examined, energy production is sufficient to meet the load during winter months, but a small amount of excess energy is generated during summer months. This additional energy can be used for needs such as additional lighting or cooling during the summer months. Compared to existing studies, this research provides more information about PV-battery hybrid systems by analyzing multiple parameters together, thus providing valuable contributions to the literature on the optimization of these systems.

Future studies should explore integrating technologies like automated cleaning systems and thermal management solutions. Additionally, further research into different battery chemistries and their performance under various environmental conditions could provide insights into enhancing the overall efficiency and sustainability of off-grid renewable energy systems.

Declaration of Ethical Standards

The authors declare that they comply with the ethics guidelines.

Credit Authorship Contribution Statement

Both authors contributed equally to this study. Author2 was responsible for data organization, research, methodology, software development, validation, visualization, and writing. Author1 provided conceptualization and supervision of Author2. Therefore, this article reflects the equal contribution of both authors.

Declaration of Competing Interest

There are no competing interests with any person or institution in the article prepared.

Funding / Acknowledgements

No funding was received to assist with the preparation of this manuscript. Authors would like to thank editors and anonymous reviewers for their suggestions to improve the paper.

Data Availability

The data supporting the findings of this study are available from the corresponding author upon request.

Use of Artificial Intelligence

No artificial intelligence tools were used in this article.

5. REFERENCES

[1] Alami et al., "Management of potential challenges of PV technology proliferation," Sustainable Energy Technologies and Assessments, vol. 51, p. 101942, 2022. A. H. Alami *et al.*, "Management of potential challenges of PV technology proliferation," *Sustainable Energy Technologies and Assessments,* vol. 51, p. 101942, 2022. https://doi.org/10.1016/j.seta.2021.101942.

[2] F. Dincer and E. Ozer, "Assessing the potential of a rooftop grid-connected photovoltaic system for Gaziantep Islamic Science and Technology University/Turkey," *Jordan Journal of Electrical Engineering*, vol. 9, no. 2, pp. 149-165, 2023. http://doi.org/10.5455/jjee.204-1670146602.

[3] S. Yilmaz and F. Dincer, "Optimal design of hybrid PV-Diesel-Battery systems for isolated lands: A case study for Kilis, Turkey," *Renewable and Sustainable Energy Reviews*, vol. 77, pp. 344-352, 2017. https://doi.org/10.1016/j.rser.2017.04.037.

[4] IRENA-International Renewable Energy Agency, "Renewable Capacity Statistics 2024". [Online]. Available:https://www.irena.org/Publications/2024/Mar/Renewable-capacity-statistics-2024. [Accessed: Sep.15,2024].

[5] F. Dincer and E. Ozer, "Numerical Analysis of Bifacial Photovoltaic Systems Under Different Snow Climatic Conditions," *Sustainability*, vol. 17, no. 14, p. 6350, 2025. https://doi.org/10.3390/su17146350.

[6] IRENA- International Renewable Energy Agency, "Energy Profile". [Online]. Available: https://www.irena.org/Data/Energy-Profiles (Select country: Nigeria) [Accessed: Sep.15,2024].

[7] A. O. Amole, S. Oladipo, O. E. Olabode, K. A. Makinde, and P. Gbadega, "Analysis of grid/solar photovoltaic power generation for improved village energy supply: A case of Ikose in Oyo State Nigeria," *Renewable Energy Focus,* vol. 44, pp. 186-211, 2023. https://doi.org/10.1016/j.ref.2023.01.002.

[8] B. A. Akgül, F. Alisinanoğlu, S. Ozyazıcı, M. F. Hasoğlu, and B. Haznedar, "Analysis of transportable off-grid solar power generation for rural electricity supply: an application study of Sanliurfa, Turkey," *Pamukkale Üniversitesi Mühendislik Bilimleri Dergisi,* vol. 29, no. 5, pp. 458-467, 2023. doi: 10.5505/pajes.2022.87894.

[9] M. Çubukçu and M. Çolak, "Gökçeada'da Şebekeden Bağımsız Bir Fotovoltaik Güç Sistemi Benzetimi ve Karşılaştırmalı Gerçek Performans İncelemesi," *Pamukkale Üniversitesi Mühendislik Bilimleri Dergisi,* vol. 19, no. 5, pp. 201-208, 2013. doi: 10.5505/pajes.2013.08108.

[10] O. C. Akinsipe, D. Moya, and P. Kaparaju, "Design and economic analysis of off-grid solar PV system in Jos-Nigeria," *Journal of Cleaner Production,* vol. 287, p. 125055, 2021. https://doi.org/10.1016/j.jclepro.2020.125055.

[11] O. M. Babatunde, O. S. Adedoja, D. E. Babatunde, and I. H. Denwigwe, "Off-grid hybrid renewable energy system for rural healthcare centers: A case study in Nigeria," *Energy Science & Engineering,* vol. 7, no. 3, pp. 676-693, 2019. DOI: 10.1002/ese3.314.

[12] BB. Adebanji, G. A. Adepoju, P. Olulope, T. Fasina, and O. Adetan, "Feasibility and optimal design of a hybrid power system for rural electrification for a small village," *International Journal of Electrical and Computer Engineering (IJECE),* vol. 10, no. 6, pp. 6214-6224, 2020. http://doi.org/10.11591/ijece.v10i6.pp6214-6224.

[13] A. Oladeji, O. Balogun, and S. Aliyu, "Use of standalone photovoltaic system for office building: the case study of national centre for hydropower research and development, Nigeria," *Nigerian Journal of Technology,* vol. 36, no. 4, pp. 1208-1217, 2017. https://doi.org/10.4314/njt.364.1494.

[14] L. M. Adesina, O. Ogunbiyi, and K. Makinde, "Design, implementation and performance analysis of an off-grid solar powered system for a Nigerian household," *MethodsX,* vol. 10, p. 102247, 2023. https://doi.org/10.1016/j.mex.2023.102247.

[15] M. E. Şahin and F. Blaabjerg, "A hybrid PV-battery/supercapacitor system and a basic active power control proposal in MATLAB/simulink," *Electronics,* vol. 9, no. 1, p. 129, 2020.https://doi.org/10.3390/electronics9010129.

[16] M. Zaibi, G. Champenois, X. Roboam, J. Belhadj, and B. Sareni, "Smart power management of a hybrid photovoltaic/wind stand-alone system coupling battery storage and hydraulic network," *Mathematics and Computers in Simulation,* vol. 146, pp. 210-228, 2018.https://doi.org/10.1016/j.matcom.2016.08.009.

[17] C. D. Rodríguez-Gallegos *et al.*, "A siting and sizing optimization approach for PV–battery–diesel hybrid systems," *IEEE Transactions on Industry Applications,* vol. 54, no. 3, pp. 2637-2645, 2017. doi: 10.1109/TIA.2017.2787680.

[18] C. Yıldız, Ö. F. Keçecioğlu, İ. Karadöl, and M. Şekkeli, "Kararsız hes ve ges üretimlerinin düzenlenmesi için optimal enerji karışımı tespiti: Malatya ili örneği," *Gazi Journal of Engineering Sciences,* vol. 4, no. 2, pp. 84-90, 2018. https://dx.doi.org/10.30855/GJES.2018.04.02.002.

[19] M. E. Şahin and F. Blaabjerg, "PV powered hybrid energy storage system control using bidirectional and boost converters," *Electric Power Components and Systems,* vol. 49, no. 15, pp. 1260-1277, 2022. https://doi.org/10.1080/15325008.2022.2055675.

[20] A. Tansu, A. T. Ogungbemi, and F. T. Hocanın, "The challenges and serviceability of solar power: suggestion on solving the Nigeria energy crisis," *International Journal of Energy Studies,* vol. 7, no. 2, pp. 127-141, 2022. DOI: 10.58559/ijes.1177950.

[21] C. Ozoegwu, C. Mgbemene, and P. A. Ozor, "The status of solar energy integration and policy in Nigeria," *Renewable and sustainable energy reviews,* vol. 70, pp. 457-471, 2017. https://doi.org/10.1016/j.rser.2016.11.224.

[22] R. O. Yakubu, L. D. Mensah, D. A. Quansah, M. S. Adaramola, and Y. Hammed, "Performance evaluation of bifacial solar PV modules under different climatic regions in Nigeria," in *E3S Web of Conferences*, 2022, vol. 354: EDP Sciences, p. 02006.https://doi.org/10.1051/e3sconf/202235402006.

[23] Global Solar Atlas, "Nigeria photovoltaic power potential". Available: https://globalsolaratlas.info/download/Nigeria. [Accessed: Sep.15,2024].

[24] REA-Rural Electrification Agency, "Off-grid infrastructure" Available: https://database.rea.gov.ng/ [Accessed: Sep.15,2024].

[25] İ. Karadöl, Ö. F. Keçecioğlu, H. Açıkgöz, and M. Şekkeli, "Kahramanmaraş Bölgesi İçin Güneş ve Rüzgâr Enerjisi Hibrit Sisteminin İncelenmesi," *Kahramanmaraş Sütçü İmam Üniversitesi Mühendislik Bilimleri Dergisi,* vol. 20, no. 2, pp. 89-96, 2017. https://doi.org/10.17780/ksujes.321514.

[26] S. Adak, H. Cangi, and A. S. Yılmaz, "Fotovoltaik Sistemin Çıkış Gücünün Sıcaklık ve Işımaya Bağlı Matematiksel Modellemesi ve Simülasyonu," *International Journal of Engineering Research and Development,* vol. 11, no. 1, pp. 316-327, 2019. https://doi.org/10.29137/umagd.456988.

[27] R. Bayindir, I. Colak, O. Kaplan, and C. Can, "MATLAB/GUI based simulation for photovoltaic systems," in *2011 international conference on power engineering, energy and electrical drives*, 2011: IEEE, pp. 1-4. doi: 10.1109/PowerEng.2011.6036532.

[28] M. Şahin and H. Okumuş, "Güneş Pili Modülünün Matlab/Simulink ile Modellenmesi ve Simülasyonu (Modeling and Simulation of Solar Cell Module in Matlab/Simulink)," *EMO Bilimsel Dergi,* vol. 3, no. 5, pp. 17-25, 2013. https://izlik.org/JA54YR64RF.

[29] CW Energy- "Technical Document". [Online]. Available: https://cw-enerji.com/tr/urun/cw-enerji-550wp-108pm-m12-hc-mb-gunes-paneli-831.html [Accessed: Sep.15,2024].

[30] Huawei- LUNA2000-5/10/15-S0 ," Smart String Energy Storage System" [Online]. Available: https://solar.huawei.com/download?p=%2F-%2Fmedia%2FSolar%2Fattachment%2Fpdf%2Feu%2Fdatasheet%2FLUNA2000-5_10_15-S0.pdf [Accessed: Sep.15,2024].

[31] G. Yüksek and A. Alkaya, "Effect of the depth of discharge and C-rate on battery degradation and cycle life," in *2023 14th International Conference on Electrical and Electronics Engineering (ELECO)*, 2023: IEEE, pp. 1-5. doi: 10.1109/ELECO60389.2023.10415967.

[32] F. Dincer and E. Ozer, "Numerical and Experimental Analysis of Photovoltaic-Integrated Energy Storage for Electric Vehicle Fast Charging," *IEEE Access,* 2025. doi: 10.1109/ACCESS.2025.3590468.

[33] B. A. Aderemi, S. D. Chowdhury, T. O. Olwal, and A. M. Abu-Mahfouz, "Techno-economic feasibility of hybrid solar photovoltaic and battery energy storage power system for a mobile cellular base station in Soshanguve, South Africa," *Energies,* vol. 11, no. 6, p. 1572, 2018.https://doi.org/10.3390/en11061572.

[34] P. O. Oviroh and T.-C. Jen, "The energy cost analysis of hybrid systems and diesel generators in powering selected base transceiver station locations in Nigeria," *Energies,* vol. 11, no. 3, p. 687, 2018. https://doi.org/10.3390/en11030687.

[35] IRENA-International Renewable Energy Agency, "Soiling Losses–Impact on the Performance of Photovoltaic Power Plants 2022". [Online]. Available:https://iea-pvps.org/wp-content/uploads/2023/01/IEA-PVPS-T13-21-2022-REPORT-Soiling-Losses-PV-Plants.pdf [Accessed: Aug.13,2025].

[36] B. Guo, W. Javed, B. Figgis, and T. Mirza, "Effect of dust and weather conditions on photovoltaic performance in Doha, Qatar," in *2015 First Workshop on Smart Grid and Renewable Energy (SGRE)*, 2015: IEEE, pp. 1-6 doi: 10.1109/SGRE.2015.7208718.

[37] A. Kimber, L. Mitchell, S. Nogradi, and H. Wenger, "The effect of soiling on large grid-connected photovoltaic systems in California and the southwest region of the United States," in *2006 IEEE 4th World Conference on Photovoltaic Energy Conference*, 2006, vol. 2: IEEE, pp. 2391-2395. https://doi.org/10.1109/WCPEC.2006.279690..

[38] M. Yang, J. Ji, and B. Guo, "Image-based PV soiling loss quantification under laboratory conditions," in *2021 IEEE 48th Photovoltaic Specialists Conference (PVSC)*, 2021: IEEE, pp. 2264-2269. doi: 10.1109/PVSC43889.2021.9518980.

[39] W. S. Ebhota and P. Y. Tabakov, "Impact of Photovoltaic Panel Orientation and Elevation Operating Temperature on Solar Photovoltaic System Performance," *International Journal of Renewable Energy Development,* vol. 11, no. 2, 2022. https://doi.org/10.14710/ijred.2022.43676.

Konya Mühendislik Bilimleri Dergisi., c.14, s.2, 803-829, 2026
Konya Journal of Engineering Sciences v.14, n.2, 803-829, 2026
ISSN: 2667-8055 (Electronic)
DOI: 10.36306/konjes.1689665

INVESTIGATION OF THE EFFECT OF HEIGHT AND DIAMETER ON THERMODYNAMIC PERFORMANCE IN SOLAR CHIMNEY POWER PLANT DESIGN: A CFD ANALYSIS

[1]Mustafa ÖNAL, [2,]*Ali KOÇ, [3]Özkan KÖSE, [4]Yıldız KOÇ, [5]Hüseyin YAĞLI

[1,2,3,4] *Department of Mechanical Engineering, Faculty of Engineering and Natural Sciences, İskenderun Technical University, Iskenderun, Hatay, TÜRKİYE*
[5] *Mechanical Engineering Department, Engineering Faculty, Gaziantep University, Gaziantep, TÜRKİYE*
[1]mustafa.onal@iste.edu.tr, [2]ali.koc@iste.edu.tr, [3]ozkan.kose@iste.edu.tr, [4]yildiz.koc@iste.edu.tr, [5]yagli@gantep.edu.tr

Highlights

- The effects of different solar chimney geometric parameters are evaluated by CFD.
- The optimum solar chimney geometry is determined.
- The power generation and thermal efficiency changes are observed.

Graphical Abstract

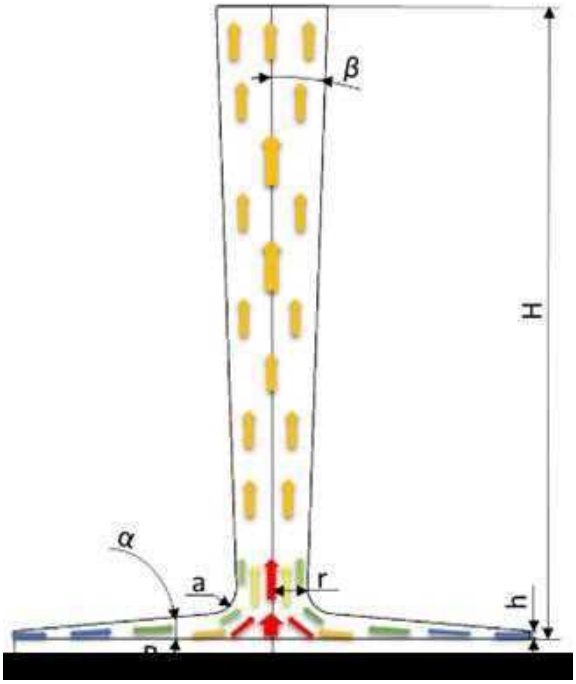


Figure Design of the Solar Chimney Power Plants

***Corresponding Author:** Ali KOÇ, ali.koc@iste.edu.tr

Konya Mühendislik Bilimleri Dergisi., c.14, s.2, 803-829, 2026
Konya Journal of Engineering Sciences v.14, n.2, 803-829, 2026
ISSN: 2667-8055 (Electronic)
DOI: 10.36306/konjes.1689665

INVESTIGATION OF THE EFFECT OF CHIMNEY DIAMETER ON THERMODYNAMIC PERFORMANCE IN SOLAR CHIMNEY POWER PLANT DESIGN: A CFD ANALYSIS

[1]Mustafa ÖNAL, [2,*]Ali KOÇ, [3]Özkan KÖSE, [4]Yıldız KOÇ, [5]Hüseyin YAĞLI

[1,2,3,4] *Department of Mechanical Engineering, Faculty of Engineering and Natural Sciences, İskenderun Technical University, Iskenderun, Hatay, TÜRKİYE*
[5] *Mechanical Engineering Department, Engineering Faculty, Gaziantep University, Gaziantep, TÜRKİYE*
[1]mustafa.onal@iste.edu.tr, [2]ali.koc@iste.edu.tr, [3]ozkan.kose@iste.edu.tr, [4]yildiz.koc@iste.edu.tr, [5]yagli@gantep.edu.tr

(Received: 02.05.2025; Accepted in Revised Form: 03.12.2025)

ABSTRACT: With technological advancements, living standards and energy demand have risen significantly. However, dependence on fossil fuels has led to environmental issues like climate change and resource depletion. Renewable sources, such as solar power, offer a sustainable alternative. This study examines the solar chimney power plant (SCPP), which harnesses solar energy. Solar radiation is captured by the glass collector, which heats the air within the system. As the air warms, its density decreases, so it rises up the chimney. The air speed reaches its peak at the narrowest part of the chimney. A wind turbine and a generator are placed at this point to obtain power from the system. In this investigation, the performance of the SCPP designs, resulting from 440 distinct combinations of 4 chimney heights, 22 chimney radii, and 5 collector radii, was analyzed using numerical simulations. An ideal gas was selected as the fluid for the simulations. A 3D design was chosen to examine the area in the chimney's shadow. Instead of defining a heat flux from the ground, the sun was defined using coordinates and a date. Furthermore, the pressure drop due to the height of the chimney outlet was calculated and defined for the system under boundary conditions. The design with the highest power output consisted of a chimney radius of 4.25 meters, a collector radius of 100 meters, and a chimney height of 200 meters. The corresponding values for velocity, mass flow rate, power, and efficiency for this optimal design were 33.40 m/s, 2213.17 kg/s, 731.33 kW, and 3.33%, respectively.

Keywords: *CFD, Diameter, Height, Renewable energy, Solar Chimney, Solar Energy.*

1. INTRODUCTION

In the current era, the global emphasis on sustainable energy has reached unprecedented levels, driven by a combination of environmental concerns, economic considerations, and the pursuit of technological innovation. As societies worldwide navigate complex challenges, including climate change and the finite nature of conventional energy resources, the quest for alternative, renewable energy solutions has gained paramount importance [1-4]. Among the various options being explored, solar energy emerges as a beacon of promise, offering an environmentally friendly and practically boundless source of power. This pursuit is not merely an aspiration for a greener future but a strategic imperative as nations strive for energy security, technological advancement, and a resilient response to the evolving dynamics of our world.

Many studies have been conducted in this field with the aim of solar chimney power generation providing a carbon-free method of electricity generation that supports sustainable development and advances the transition to a green economy and a safer environment [5-9]. This technology finds

***Corresponding Author:** Ali KOÇ, ali.koc@iste.edu.tr

application in various fields such as ventilation, desalination, electricity generation and agro-food processing [10-11]. The idea of solar chimney systems was first introduced by Hanns Günther. The theoretical framework was further developed, and the first operational facility was constructed in 1981 in Manzanares, Spain. This project, led by German structural engineer J. Schlaich, was followed by refinements to the theoretical foundation by Haaf et al. [12] in 1983. Nasraoui et al. [13] aimed to improve the efficiency of solar chimneys by exploring different configurations of solar collectors, including conventional, parallel, and counter-flow designs. Their CFD analysis utilized a maximum of 300746 meshes, with assumed inlet and outlet pressures of the solar chimney being zero. They also considered solar radiation at 880 W/m^2. Their efforts resulted in a claimed increase in system efficiency of up to 28%. The system is comprised of three key components: a solar chimney, a solar collector, and an absorbing ground layer. A wind turbine, coupled with a generator, is utilized to convert the kinetic energy of the ascending air into electrical energy [10]. Schlaich et al. [14] expanded on this concept by investigating the commercial and economic feasibility of large-scale solar chimney plants, with capacities of up to 200 MW. Furthermore, a variety of other studies have been conducted to refine and optimize solar chimney technology. Singh et al. [15] conducted a Computational Fluid Dynamics (CFD) analysis of hybrid PV and solar chimney systems, assuming inlet and outlet pressures to be zero and considering 850 W/m^2 solar radiation. Using a collector radius of 1.5 meters and a solar chimney height of 3 meters, they applied four different mesh refinement techniques, reaching a total of 225,820 mesh elements. This approach led to a maximum solar chimney power output of 2,258 W. Kebabsa et al. [16] conducted a two-dimensional analysis of the solar chimney, obtaining a power output of 0.34 W from a system with a radius of 12.5 meters and a height of 12.3 meters. They recommended an optimal collector entrance angle of 9.1 degrees for improved performance. In their theoretical investigation, Nouar and colleagues [17] estimated the operational performance of the Manzanares prototype when adapted to the Algerian context. The study reported that a 100-m chimney could produce approximately 49.34 kW at noon in June, while a 200-m chimney would increase the output to about 99 kW. These findings underline the significant role of chimney height in enhancing system performance. Ikhlef and Larbi [18] reported that an SCPP system of Manzanares scale in Algeria would produce 52.5 kW at 200 m and 111.66 kW at 300 m, emphasizing the performance gains associated with taller chimneys. Larbi et al. [19] reported that an SCPP in Adrar with a 200-m chimney and 500-m collector could generate 140–200 kW annually. Under 30 °C and 800 W/m² irradiance conditions, the output rose from 142 kW with a 444-m collector to 342 kW with a 690-m collector, highlighting the effect of collector size on performance. Koonsrisuk et al. [20] showed that the Manzanares prototype produces 67–80 kW, while reducing the H/R² ratio from 0.013 to 0.005 by enlarging the collector radius raises the output to 165 kW and increases mass flow by 30% (765–996 kg/s). Toghraie et al. [21] reported that chimney diameter has an optimal value for SCPPs, with pressure, mass flow, efficiency and power output decreasing when the diameter exceeds this point. In their analytical study, Choi et al. [22] modeled a solar chimney with a collector radius of 3000 m, a chimney diameter of 100 m and a chimney height of 1000 m reporting a maximum output of 85 MW. They showed that while increasing the chimney diameter initially boosts power output exponentially, the effect diminishes beyond a certain point. For instance, a diameter of 200 m was estimated to double the output to roughly 170 MW. Cuce et al. [23] provided a comprehensive review showing that increases in both collector radius and stack height yield higher power outputs. However, when considering changes in stack diameter, the power initially increases but then decreases beyond a certain threshold, suggesting an optimum diameter for maximum performance. In their study, Pradhan et al. [24] analyzed the geometric design parameters of small- and large-scale SCPPs. For small-scale models, they found that a collector inclination of 0° was ideal, while for large-scale systems with an 800 m chimney height and 100 m diameter, the optimal inclination was limited to 5°. Hassan et al. [25] reported that a 1° split stack outlet for the Manzanares plant doubled the output from 34 kW to 68 kW, while angles of 2° and 3° reduced it to 65 kW and 59 kW. They also emphasized that the flow rate increases with the collector inclination, but inclinations greater than 6° create density-driven circulation below the collector, reducing airflow and turbine performance. In laboratory experiments, Motoyama et

al. [26] observed that a divergent chimney produced 50% higher airflow velocity and 44.4% higher rotational speed than a cylindrical chimney under the same conditions. Similarly, Ohya et al. [27] demonstrated that the power output of divergent chimneys was 4–5 times greater. Their comparison of chimney divergence angles showed that the 4° design achieved the highest power output and airflow velocity. According to Ahirwar and Sharma [28], the optimal power output for a system modeled on the Manzanares plant occurs with a 190-m chimney and an inclined collector. They reported that the non-inclined case yields 37.08 kW, while a 6° inclination increases output by 95% to 72.33 kW. Ghorbani et al. [29] showed that a 1.5° divergent flue in a 200-m hybrid cooling tower raised radiator airflow velocity by 6.2%, from 5.65 to 6 m/s. Das and Candramohan [30] found that a 2° divergent chimney design maximized power and airflow in small-scale SCPPs, while larger angles diminished performance. Gitan et al. [31] showed that in Malaysian conditions, a 10° collector inclination increased power output by 3.5 kW compared to a horizontal design, with collector efficiency at 51% and system efficiency at 0.165%. Karimi-Pour-Fard and Beheshti [32] examined the influence of collector inclination on the performance of the Manzanares pilot plant. Their findings demonstrated that adjusting the collector slope to 2° led to a substantial enhancement in energy generation, with the power output rising by approximately 55%, from 44 kW to 70 kW. This result underscores the significant role of geometric optimization in improving the efficiency of solar chimney systems.

When the above studies are examined, there are very few studies in which the sun is clearly defined as a source in CFD analyses. In many studies, the sun's effect is defined by providing heat flux from the collector area. Moreover, there are a limited number of studies in which the density of air is considered variable (compressible fluid). It has been observed that the pressure difference resulting from the height change between the chimney inlet and outlet is almost not taken into account in any study.

In this study, the effects of different solar chimney geometric parameters on thermodynamic performance were investigated using CFD analysis and the optimum solar chimney geometry was obtained. First, solar chimney models with heights ranging from 50 m to 200 m were created at fixed radii (between 20-100 m). Then, pressure distribution, velocity vectors, fluid outlet temperatures, air mass flow rate, power generation and thermal efficiency changes were observed within the solar chimney. Secondly, different models were created by changing the radius at fixed solar chimney height (between 50-200 m). Then, inside the solar chimney, pressure distribution, velocity vectors, fluid outlet temperatures as well as air mass flow rate, power generation and thermal efficiency changes were observed. Finally, the designed models were compared with each other and the optimum radius and height were obtained.

2. MATERIAL AND METHODS

2.1. System Introduction

When designing the SCPPs, many parameters should be taken into consideration. In this research, the values presented in Table 1 were considered fixed.

Table 1. Constant parameters regarding solar chimney power plants [25]

h (m)	α (°)	β (°)	a (m)	I (W/m²)
0.6	5	2	2	700

The parameters influencing the geometric configuration of a SCPP include the collector inlet angle (α), collector inlet height (h), chimney leaving angle (β), curvature radius at the collector-chimney junction (a), collector radius (R), chimney height (H), chimney radius (r), and solar radiation intensity (I). Designs were made for various chimney height, chimney radius, and collector radius values, while considering the parameters in Table 1 as constants. Figure 1 illustrates the design parameters associated with the SCPP. Considering the parameters in Table 1 as constant, designs were made for different chimney height, chimney radius and collector radius values. Figure 1 shows the design parameters of the SCPP.

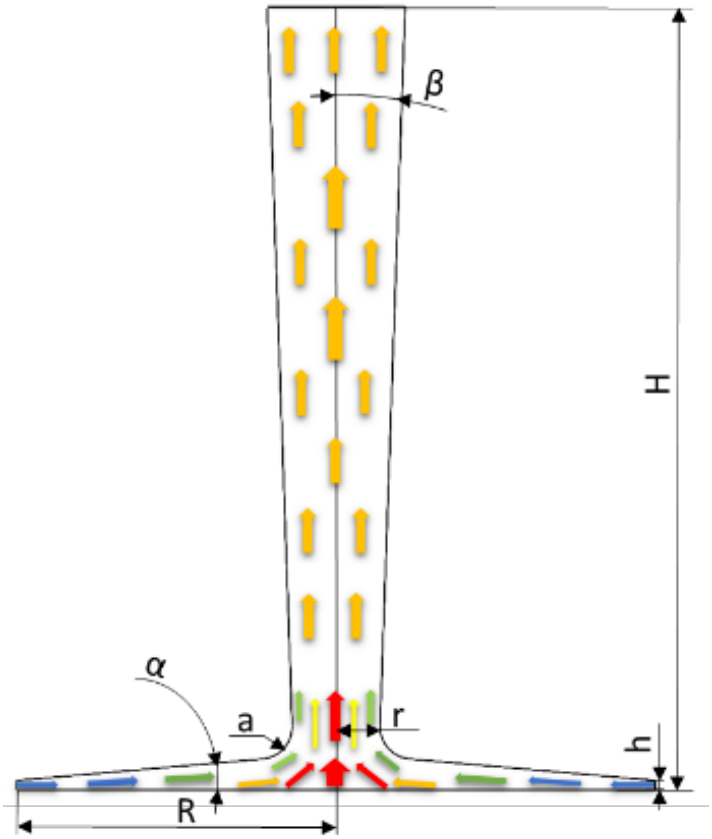


Figure 1. Design of the SCPP

The design must be divided into many small parts before being introduced to the numerical analysis program. These pieces are called mesh. Mesh sizes are reduced in critical areas of the system. This increases the accuracy of numerical analysis. Figure 2 shows the mesh structure of the design.

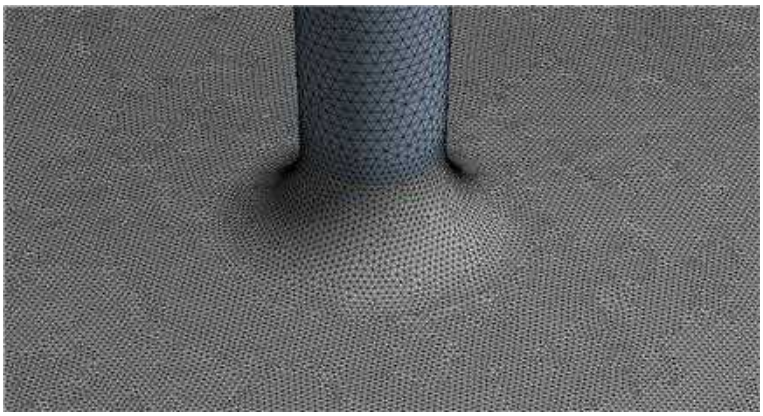


Figure 2. Mesh structure of the design

The areas where the mesh is dense are as important as the size of the mesh elements. Quantities such as speed or temperature show rapid changes near the surface. For this reason, the mesh element number should be increased in areas close to the surface. Figure 3 shows that the mesh is concentrated close to the surface of the chimney.

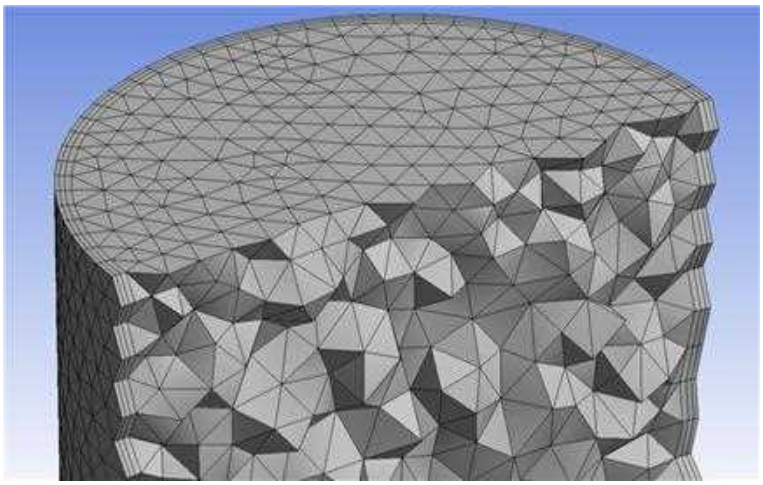


Figure 3. Mesh structure on the chimney surface

A dense network structure consisting of 3 elements can be seen on the chimney surface. This dense mesh structure continues along the collector surface. On the other hand, a denser mesh structure is needed due to high temperature differences in areas close to the collector area. For this reason, a dense mesh structure consisting of 4 layers was used on the collector area. Figure 4 shows the mesh structure on the collector area.

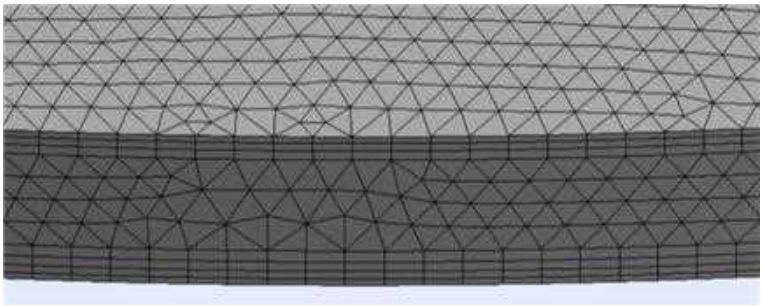


Figure 4. Mesh structure on the collector area

Considering the mesh properties mentioned above, the number of mesh elements for a SCPP with a chimney height of 50 m, a collector radius of 20 m and a chimney radius of 1.5 m was determined as 1,384,905 and the number of nodes as 400,394. The mesh independence test for the relevant dimensions is shown in Table 2. The mesh structure designed for these dimensions has also been applied to other designs in a way that maintains mesh quality.

Table 2. Mesh independence testing for CFD solution reliability

Number of elements	V (m/s)	P (kW)	% change in V	% change in P
119,124	9.81	2.311	1.62	4.79
570,317	9.93	2.392	0.49	1.45
950,937	9.96	2.415	0.16	0.49
1,384,905	9.97	2.427	-	-

Upon completion of the mesh structure, the numerical analysis program was configured with the defined problem. Several methods, distinct from those found in the literature, were employed during these configurations. The first notable difference lies in the choice of fluid. While many studies assume the fluid to be an incompressible fluid, this work treats the fluid as an ideal gas. Another distinction lies in the approach used to determine the heat sources. In numerous publications, an average heat flux is assigned and applied from the collector area or a constant temperature is set for the collector area. In contrast, this study eschews such assumptions and defines the solar input to the program based on the location, date, and time of the Iskenderun region. Another unique perspective lies in the boundary conditions of the system. In other studies, the inlet and outlet pressures of the system were assumed to be equal to atmospheric pressure. In contrast, in this study, the pressure difference that will occur due to the height difference between the regions where the air enters and exits the system was calculated and the boundary conditions were defined.

Table 3. Conditions at the boundaries

Boundary Conditions	Model Specifications
Environmental Temperature	$T_0 = 300$ K
Outlet Pressure	$P_o = P_i - \rho g H$
Inlet Pressure	$P_i = 101.325$ kPa
Chimney	Non-transparent and insulated
Collector	Transparent

2.2. Mathematical Model

The selection of energy equations must account for the boundary conditions. The flow in all three directions of the three-dimensional system is modeled using the continuity equation and the Navier-Stokes equation [33].

The momentum in the x-direction:

$$\rho\left(\frac{\partial u}{\partial t}+u\frac{\partial u}{\partial x}+v\frac{\partial u}{\partial y}+w\frac{\partial u}{\partial z}\right)=-\frac{\partial P}{\partial x}+\mu\left(\frac{\partial^2 u}{\partial x^2}+\frac{\partial^2 u}{\partial y^2}+\frac{\partial^2 u}{\partial z^2}\right) \quad (1)$$

The momentum in the y-direction:

$$\rho\left(\frac{\partial v}{\partial t}+u\frac{\partial v}{\partial x}+v\frac{\partial v}{\partial y}+w\frac{\partial v}{\partial z}\right)=-\frac{\partial P}{\partial y}+\mu\left(\frac{\partial^2 v}{\partial x^2}+\frac{\partial^2 v}{\partial y^2}+\frac{\partial^2 v}{\partial z^2}\right) \quad (2)$$

The momentum in the z-direction:

$$\rho\left(\frac{\partial w}{\partial t}+u\frac{\partial w}{\partial x}+v\frac{\partial w}{\partial y}+w\frac{\partial w}{\partial z}\right)=-\frac{\partial P}{\partial z}+\mu\left(\frac{\partial^2 w}{\partial x^2}+\frac{\partial^2 w}{\partial y^2}+\frac{\partial^2 w}{\partial z^2}\right) \quad (3)$$

Steady flow equation:

$$\rho\left(\frac{\partial u}{\partial x}+\frac{\partial v}{\partial y}+\frac{\partial w}{\partial z}\right)=0 \quad (4)$$

Turbulance model is selected as realizable k-ε model. Turbulence kinetic energy equation:

$$\frac{\partial}{\partial t}(\rho k)+\frac{\partial}{\partial x_j}(\rho k u_j)=\frac{\partial}{\partial x_j}\left[\left(\mu+\frac{\mu_t}{\sigma_\varepsilon}\right)\frac{\partial k}{\partial x_j}\right]+G_k+G_b-\rho\varepsilon-Y_m \quad (5)$$

$$\frac{\partial}{\partial t}(\rho\varepsilon)+\frac{\partial}{\partial x_j}(\rho k\varepsilon_j)=\frac{\partial}{\partial x_j}\left[\left(\mu+\frac{\mu_t}{\sigma_\varepsilon}\right)\frac{\partial \varepsilon}{\partial x_j}\right]+\rho C_1 S\varepsilon-\rho C_2\frac{\varepsilon^2}{k+\sqrt{v\varepsilon}}+C_{1\varepsilon}\frac{\varepsilon}{k}C_{3\varepsilon}G_b \quad (6)$$

Turbulence viscosity is calculated from Equation 7:

$$\mu_t=\rho C_\mu\frac{k^2}{\varepsilon} \quad (7)$$

C_μ is calculated from Equation 8:

$$C_\mu=\frac{1}{A_0+A_s\frac{kU^*}{\varepsilon}} \quad (8)$$

$$U^*=\sqrt{S_{ij}S_{ij}+\widetilde{\Omega}_{ij}\widetilde{\Omega}_{ij}} \quad (9)$$

$$\widetilde{\Omega}_{ij}=\overline{\Omega}_{ij}-\varepsilon_{ijk}\omega_k-2\varepsilon_{ijk}\omega_k \quad (10)$$

In Equation 10, the average rotational velocity tensor around a rotating reference with angular velocity ω_k is expressed by $\overline{\Omega}_{ij}$. The constants A_s and A_0 are defined as follows, respectively:

$$A_s=\sqrt{6}\,\cos\varphi\,,\qquad A_0=4.04 \quad (11)$$

$$\varphi=\left(\cos^{-1}\left(\sqrt{6}\frac{S_{ij}S_{jk}S_{ki}}{\tilde{S}^3}\right)\right)/3\,,\quad \tilde{S}=\sqrt{S_{ij}S_{ij}}\,,\quad S_{ij}=\frac{1}{2}\left(\frac{\partial u_j}{\partial x_i}+\frac{\partial u_i}{\partial x_j}\right) \quad (12)$$

C_μ has been shown to depend on the angular velocity of the rotating system, the mean strain and rotation rates, the turbulent kinetic energy, and its dissipation rate.

$$C_1=max\left(\frac{\eta}{5+\eta},(0.43)\right) \quad (13)$$

$$\eta = S\left(\frac{k}{\varepsilon}\right) \tag{14}$$

The value of G_b for ideal gases is calculated as:

$$G_b = -\frac{\mu_t}{\rho Pr_t}\frac{\partial \rho}{\partial x_j} g_i \tag{15}$$

$$C_{3\varepsilon} = \tanh\left|\frac{v}{u}\right| \tag{16}$$

In this context, ε and k represent the dissipation rate and turbulent kinetic energy, respectively. Ym accounts for the contribution of fluctuating expansion in compressible turbulence to the overall dissipation rate, G_b indicates the production of turbulence kinetic energy due to buoyancy, G_k corresponds to the production of turbulence kinetic energy caused by mean velocity gradients and μ_t denotes the eddy viscosity.

$$\rho = \rho_0\big(1 - \beta(T - T_0)\big) \tag{17}$$

Here, β and ϱ denote the thermal expansion coefficient and density, respectively. To compute the solar radiation entering the system, a DO (discrete ordinate) model was employed for solar tracking The model utilizes the following equations:

$$(\vec{r}, \vec{s})\mathrm{I}_\lambda(\alpha_\lambda, \sigma_s) + \nabla \cdot (\mathrm{I}_\lambda(\vec{r}, \vec{s})\,\vec{s}) = \frac{\sigma_s}{4\pi}\int_0^{4\pi} \mathrm{I}_\lambda(\vec{r}, \vec{s}')\,\Phi(\vec{r}, \vec{s}')\,d\Omega' + \mathrm{I}_{b\lambda}n^2\alpha_\lambda \tag{18}$$

Here, $\alpha\lambda$ represents the absorption coefficient, σs denotes the reflection coefficient, n is the refractive index, and λ corresponds to the wavelength. The total radiation intensity in the $\vec{s}$ direction is defined as the summation of spectral light intensity across wavelength bands and is given by:

$$\mathrm{I}(\vec{r}, \vec{s}) = \sum_k \mathrm{I}_\lambda(\vec{r}, \vec{s})\,\Delta\lambda_k \tag{19}$$

In the SCPP, the Grashof number is defined by the following expression:

$$Gr = H^3 \Delta T \frac{g\beta}{\vartheta^2} \tag{20}$$

$$\Delta T = T_ç - T_0 \tag{21}$$

The gravitational acceleration is represented by g, while the *kinematic viscosity* is denoted by ϑ. The Richardson number is defined as a function of the Reynolds number and the Grashof number. When the Richardson number exceeds 10, forced convection becomes negligible. Conversely, if the Richardson number falls below 0.1, natural convection can be disregarded. In cases where the Richardson number lies between 0.1 and 10, the flow is classified as mixed convection, where both forced and natural convection play significant roles.

$$Ri = \frac{Gr}{Re^2} \tag{22}$$

In solar chimney power plant (SCPP) systems, where no external mechanism is employed to drive airflow, heat transfer is governed by natural convection. The governing parameter for such convective processes is the Rayleigh number, which is defined as

$$Ra = \frac{g\beta\Delta T {H_c}^3}{\alpha\vartheta} \tag{23}$$

Here, Hc denotes the collector height, and α is the thermal diffusion coefficient. The preliminary evaluations indicate that the Rayleigh number significantly exceeds the critical threshold of 109, suggesting that the flow regime within the system can be characterized as turbulent [34].

$$P = \frac{1}{2} Bmv^2 \tag{24}$$

Betz's law expresses the theoretical maximum power extractable from wind and is denoted by B. According to this principle, wind turbines are unable to capture more than 59.25% of the kinetic energy in the air. The value 0.5925 is referred to as the Betz coefficient.

$$A = \pi R^2 \tag{25}$$

$$\eta = \frac{P}{IA} \tag{26}$$

Where A represents the surface area of the SCPP's base, I represents solar radiation intensity and η denotes its efficiency.

3. RESULTS AND DISCUSSION

Numerical analyses were conducted for SCPPs with four different chimney heights, five different collector radii, and 22 different chimney radii. In Figure 5, velocity vectors are presented in a cross-section of a SCPP with a chimney height of 50 meters, collector radius of 20 meters, and chimney radius of 1 meter. The velocity vectors are thoroughly analyzed, especially in the constricted region of the chimney.

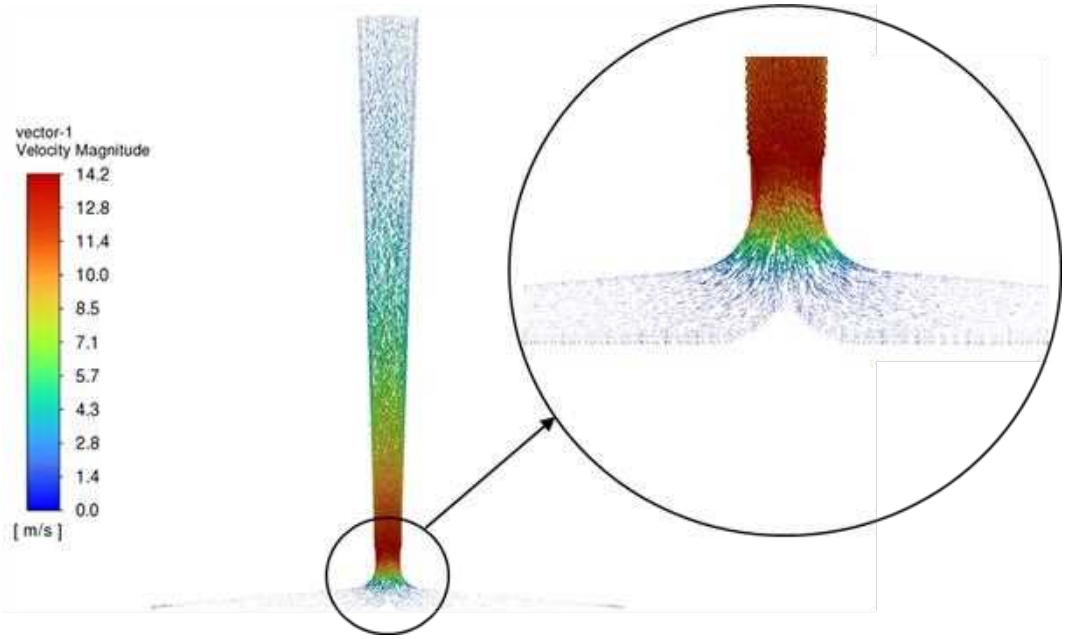


Figure 5. Velocity vectors

Figure 5 illustrates the velocity vectors within the solar chimney power system, with particular emphasis on the narrow section of the chimney. The air slowly enters the system from the collector inlet but its velocity increases until the narrow section of the chimney. Upon nearing this section, the air changes direction and flows upward. At the junctions of the collector and chimney, where this change of direction occurs, vortices will form, leading to energy losses since the air cannot make a sudden change of direction. To mitigate these energy losses during the design process, a curve with a radius of 2 meters is created at the junction between the chimney and the collector. This ensures that all velocity vectors at the chimney inlet are directed upwards. As the chimney widens at a 2-degree angle towards the outlet, the air velocity gradually decreases towards the chimney exit. The pressure gradients in a SCPP with the above-mentioned geometric parameters are depicted in Figure 6.

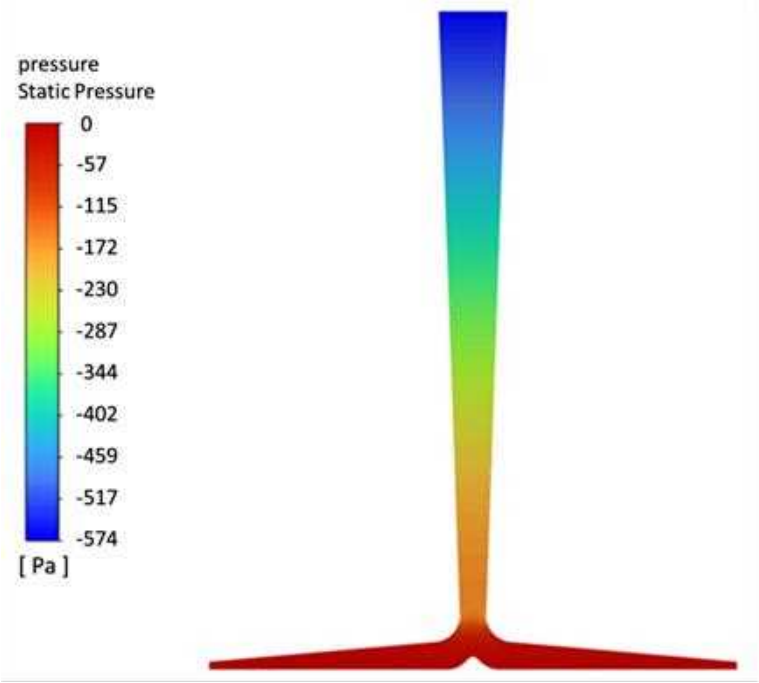


Figure 6. Pressure gradient

In numerous investigations, it is common to assume that the inlet and outlet pressures equate to atmospheric pressure, resulting in pressure differentials being gauged as atmospheric pressure at the collector inlet and chimney outlet. Nevertheless, a distinct negative pressure is noted in the narrow segment of the chimney. However, in this research, there exists a pressure variance between the air inlet and outlet points. Figure 6 shows a gradual decrease in pressure from the collector inlet level to the chimney outlet. The pressure values presented in Figure 6 represent relative pressure measurements. Figure 7 illustrates the temperature distribution across the cross-section of the SCPP.

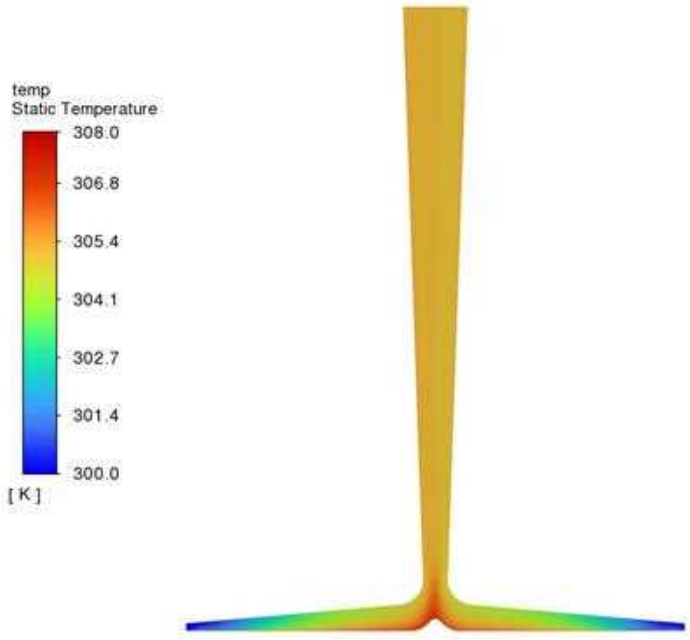


Figure 7. Temperature gradient

As solar radiation penetrates the collector inlet, it causes a temperature increase on the surface. As the air moves towards the center of the collector, it gradually warms up due to the hot ground. After the heated air is directed towards the chimney, the temperature becomes homogeneous. The geometric parameters used for the numerical analysis are shown in Table 4.

Table 4. Geometric parameters

Variable	Range	Increment
H	50 - 200 m	50 m
R	20 – 100 m	20 m
r	0.75 – 6 m	0.25 m

The region with the smallest diameter of the chimney is where the air velocity reaches its maximum across the entire system, which is why the wind turbine is positioned there. Two key factors contribute to this acceleration of velocity. The first factor is the radius of the collector. When the radius of the collector is increased, more solar radiation is captured by the system. This additional radiation heats up the collector area surface, which in turn raises the temperature of the air near the ground. As the air warms, it becomes lighter and rises faster, which results in an increase in velocity as the air moves upwards toward the chimney. The second factor is the height of the chimney. As the heated air near the ground becomes less dense, it creates a density gradient that generates a buoyant force, causing the air to move towards the chimney outlet. A taller chimney allows the air to be exposed to this force for a longer distance, resulting in a higher velocity as it ascends through the chimney. Thus, both a larger collector radius and greater chimney height lead to an increase in air velocity within the system. Figure 8 illustrates the change in velocity for a fixed collector radius based on the chimney radius and height.

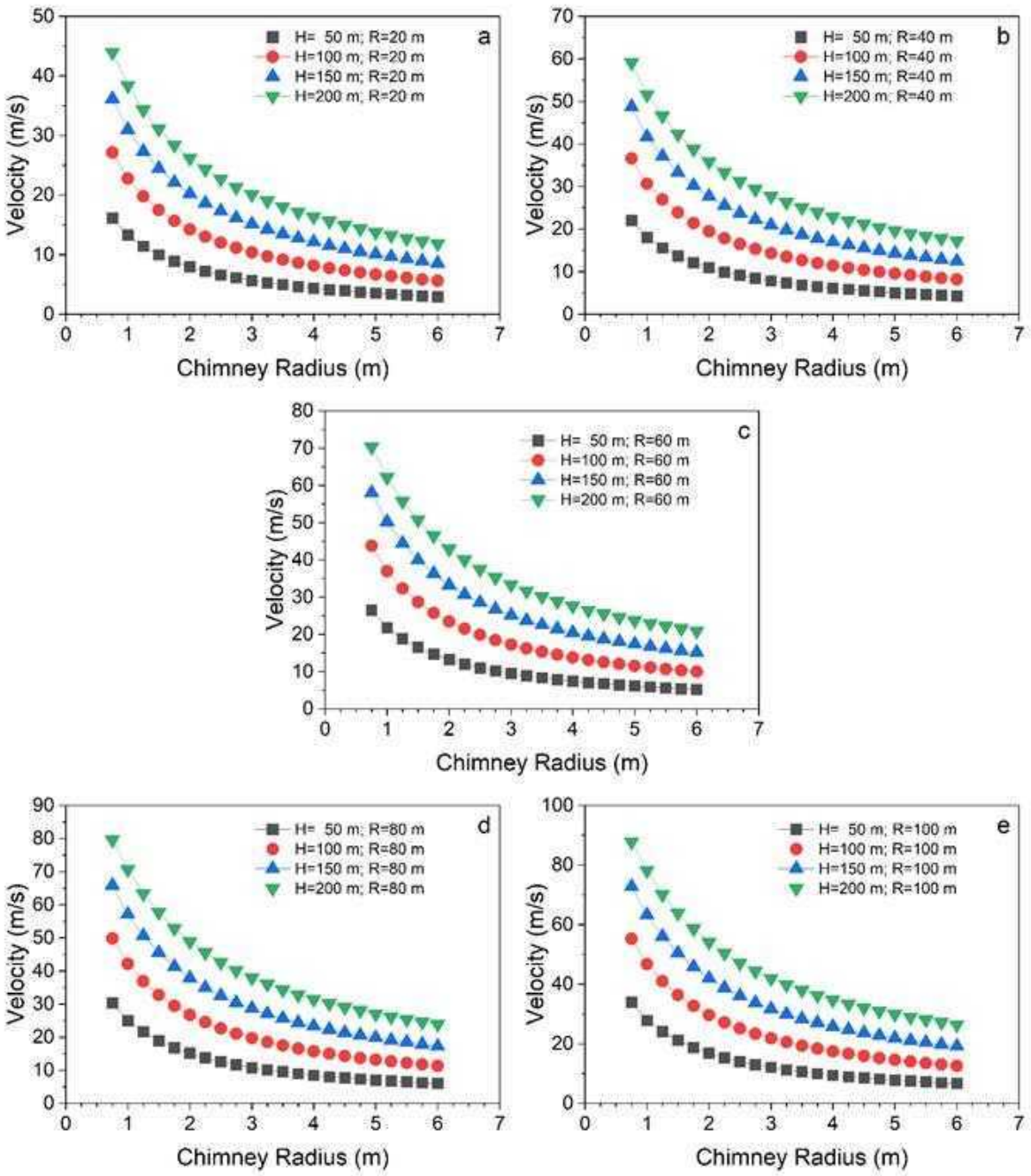


Figure 8. Velocity value depending on chimney radius and chimney height

As the chimney height increases, the pressure at the outlet of the system decreases, thus increasing the air velocity with the effect of the pressure difference. On the other hand, an increase in chimney radius results in an enlargement of the cross-sectional area and a decrease in velocity. In Figure 8e, it is seen that the highest speed is 87.79 m/s at 0.75 m chimney radius, 100 m collector radius and 200 m chimney height. The high speed achieved is due to the wide range of operating parameters. In a system using a high chimney and a wide collector, the narrow chimney radius of 0.75 m creates a combination that combines all the parameters needed to increase speed. As an example, illustrating this situation, Ghorbani et al. [29] obtained a velocity of 16.343 m/s in a design with a 200 m chimney height, 100 m collector radius, and 25 m chimney radius, with some hot gas addition. With the same stack height and collector radius, the resulting velocity was 63.92, 41.99, and 26.45 m/s for 1.5, 3, and 6 m stack radii, respectively. Examining this data range, increasing the chimney radius to 25 m would result in a velocity of around 11 m/s, which is lower than the velocity obtained by Ghorbani et al. [29] in their hot gas addition system. On the other hand, in Figure 8a, it is seen that the lowest speed is 2.94 m/s at 50 m chimney height, 20 m collector radius and 6 m chimney radius. Figure 9 illustrates the change in mass flow rate for a fixed collector radius based on chimney height and radius.

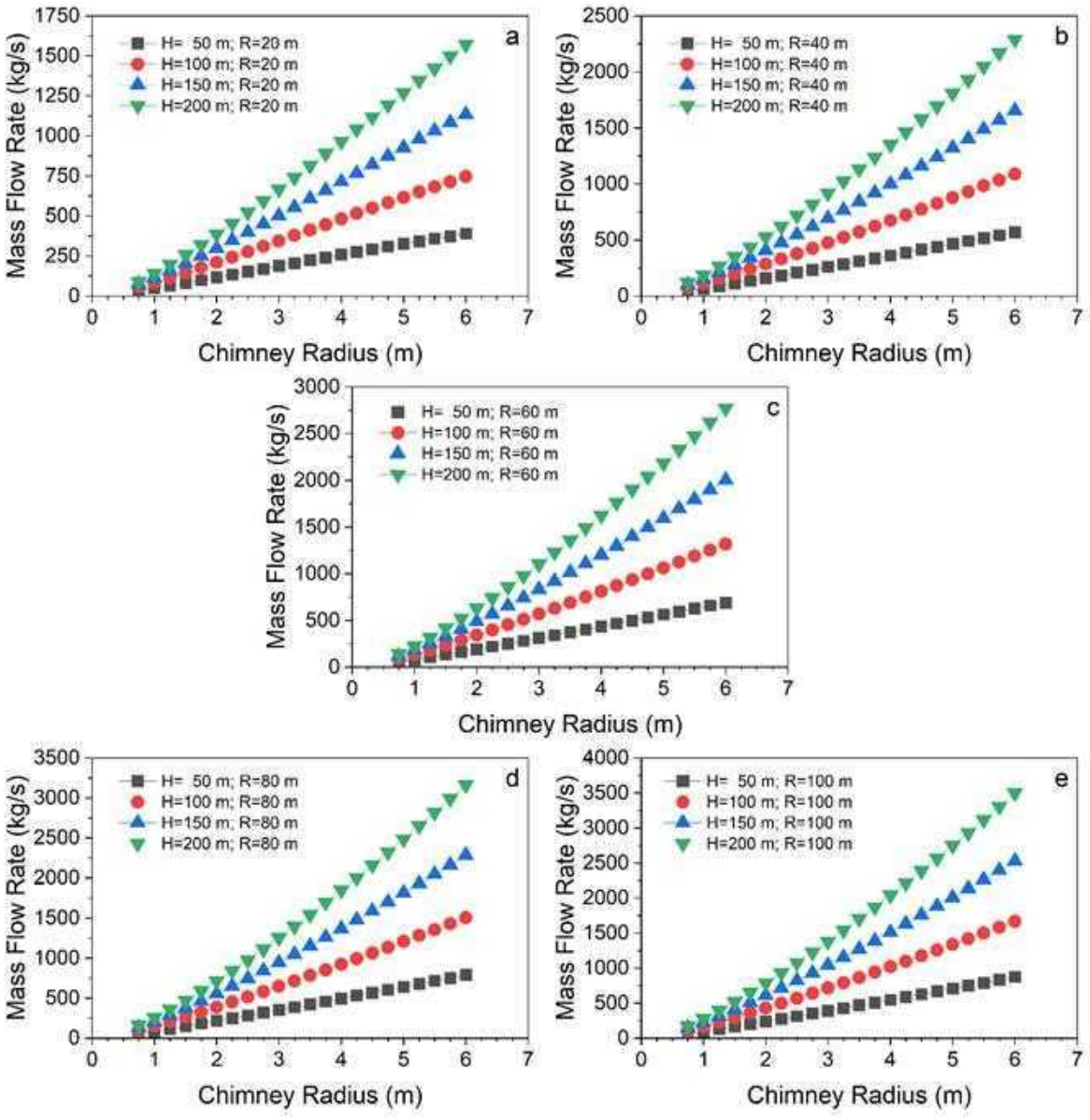


Figure 9. Mass flow rate depending on chimney radius and chimney height

As the chimney height increases, the pressure difference between the system's inlet and outlet grows, leading to a higher mass flow rate. An increase in chimney radius enables a larger volume of air to flow through the system, thereby enhancing the mass flow rate. As shown in Figure 9e, the maximum mass flow rate of 34.98 kg/s is achieved with a chimney radius of 6 m, a collector radius of 100 m and a chimney height of 200 m. Conversely, Figure 9a reveals the minimum mass flow rate of 33.21 kg/s, observed with a chimney height of 50 m, a collector radius of 20 m, and a chimney radius of 0.75 m. Figure 10 illustrates the change in temperature for a fixed collector radius based on chimney height and radius.

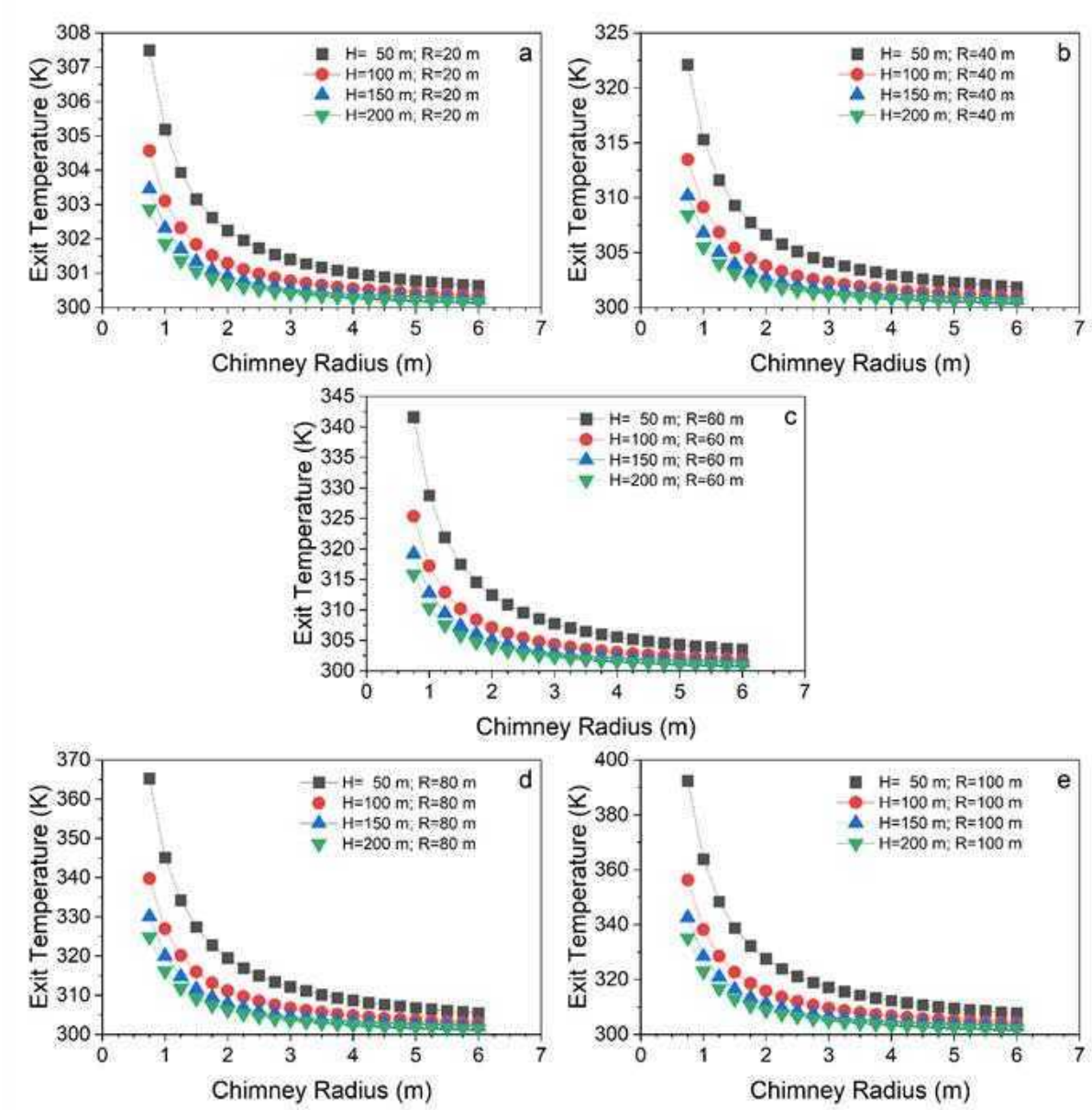


Figure 10. Outlet temperature value depending on chimney radius and chimney height

As the chimney height increases, the pressure difference increases and this causes an increase in the mass flow rate. Although the amount of heat entering the collector is constant, the increase in the mass flow rate causes the amount of heat transferred per unit of air to decrease. Therefore, as chimney height increases, the chimney exit temperature decreases. Increasing the chimney radius allows more air to enter the system, resulting in an increase in mass flow rate and a decrease in temperature. Increasing the chimney radius allows more air to enter the system, which results in a higher mass flow rate. However, this also causes a decrease in temperature, as the heat is distributed over the greater airflow. In Figure 10e, it is seen that the highest chimney outlet temperature is 392.43 K at 0.75 m chimney radius, 100 m collector radius and 50 m chimney height. In Figure 10a, it is seen that the lowest chimney outlet temperature is 300.16 K at 200 m chimney height, 20 m collector radius and 6 m chimney radius. Figure 11 shows the changes in power for a fixed collector radius depending on the chimney height and radius.

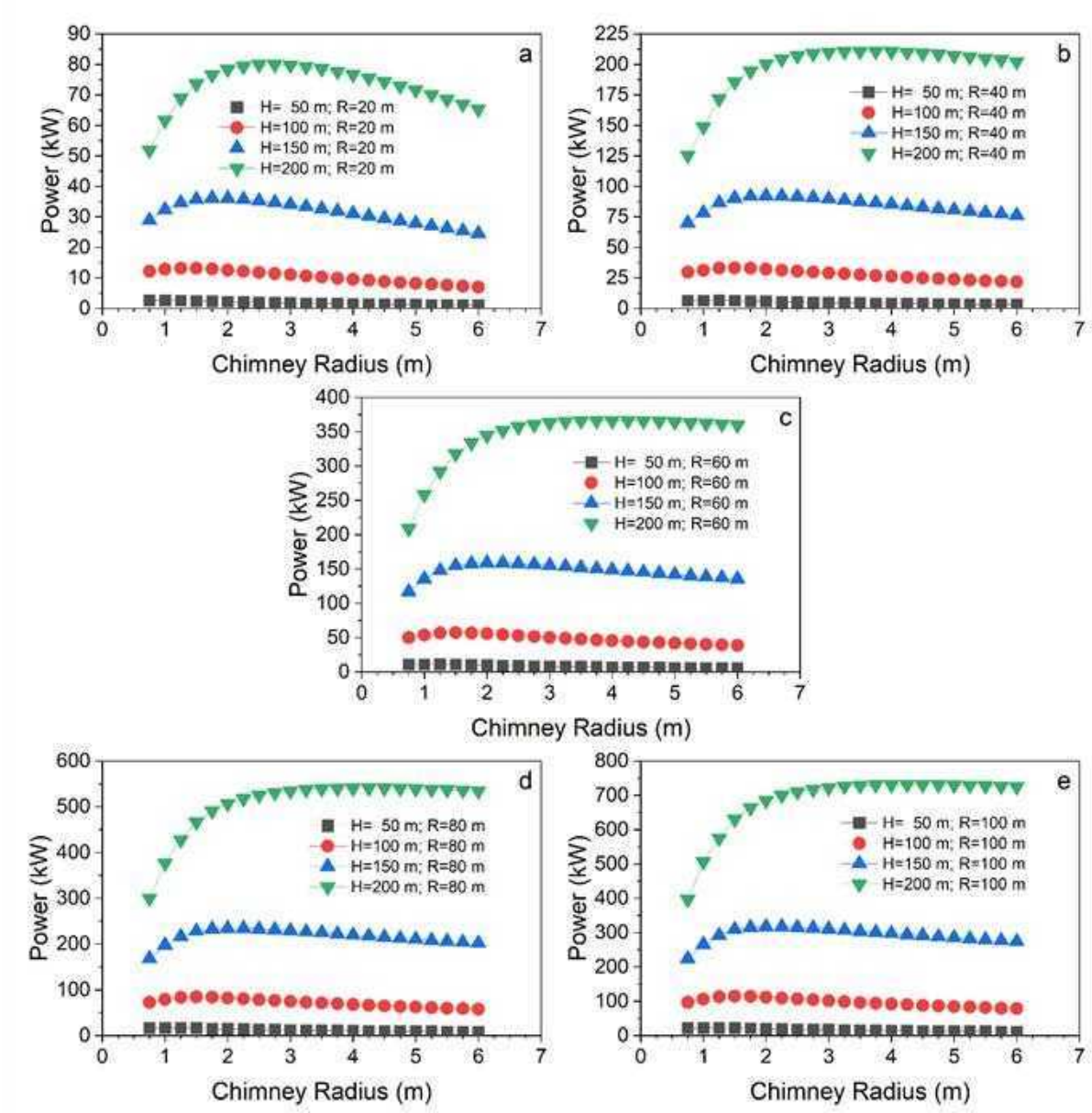


Figure 11. Power change depending on chimney height and chimney radius

The increasing pressure difference caused by greater chimney height leads to higher air velocity and mass flow rate, which in turn enhances the power output of the system. However, with an increase in chimney radius, the velocity within the chimney decreases, while the mass flow rate increases due to the expanded cross-sectional area allowing greater airflow. Taking into account the reduction in velocity and the rise in mass flow rate, it is concluded that there exists an optimal chimney radius that maximizes the power output of the system. Power values were calculated using Equation 24. In line with the calculated power values, it can be said that the optimum chimney radius value increases with the chimney height. Figure 11 shows an increase in power values along with chimney height. Additionally, optimum value for chimney radius is observed for the highest power value. In Figure 11e, it is seen that the highest power is 731.33 kW at 4.25 m chimney radius, 100 m collector radius and 200 m chimney height. In Figure 11a, it is seen that the lowest power is 1 kW at 50 m chimney height, 20 m collector radius and 6 m chimney radius. Figure 12 shows the changes in efficieny for a fixed collector radius depending on the chimney height and radius.

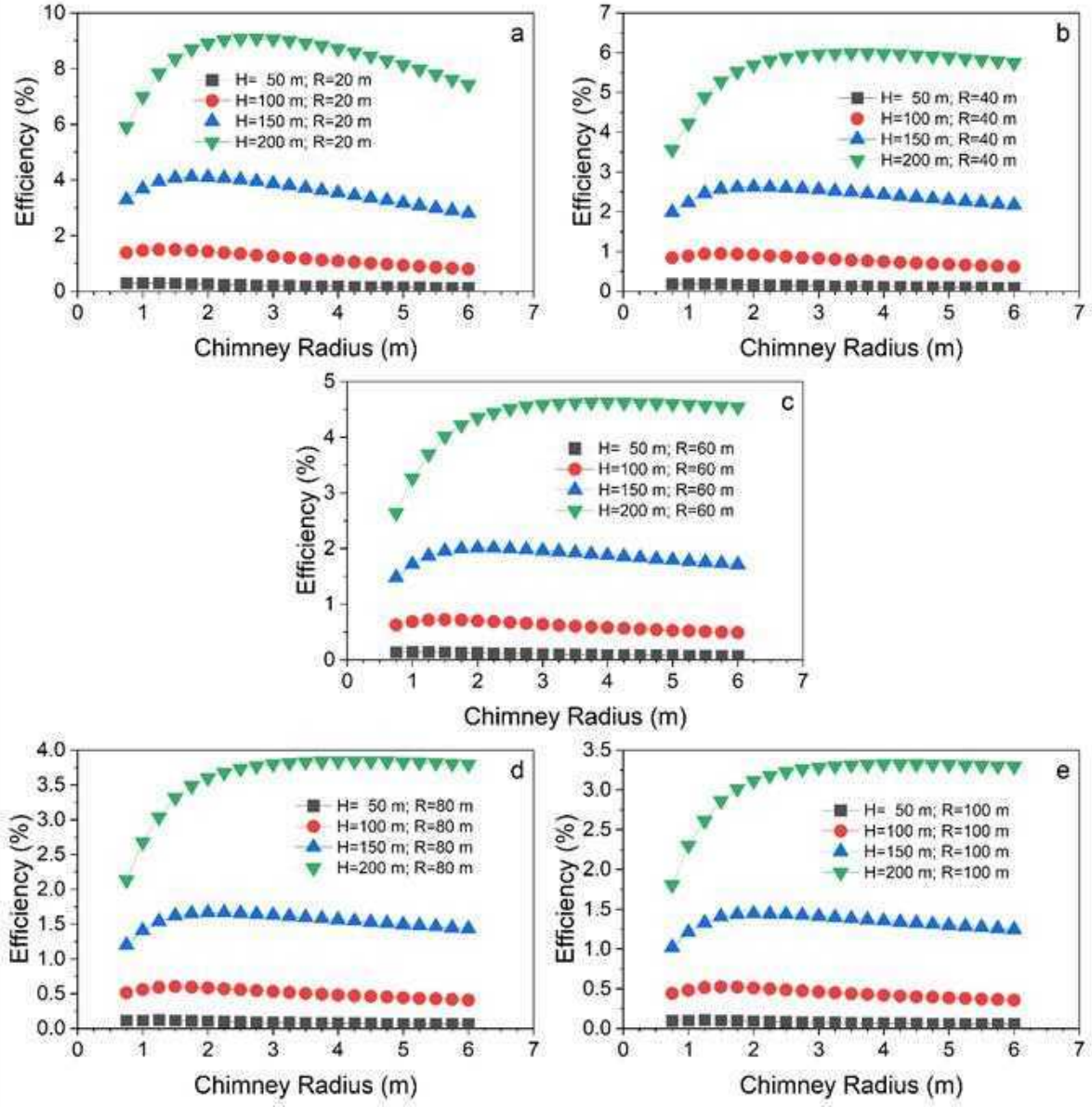


Figure 12. Efficiency change depending on chimney height and chimney radius

Efficiency values were calculated using Equation 26. Since the collector radius is constant, the amount of heat entering the system does not change. Therefore, the power and efficiency values exhibit parallelism with each other. In Figure 12a, it is seen that the highest efficiency is 9.09% at 200 m chimney height, 20 m collector radius and 2.75 m chimney radius. In Figure 12e, it is seen that the lowest efficiency is 0.05% at 6 m chimney radius, 100 m collector radius and 50 m chimney height. Figure 13 shows the change in speed for fixed chimney height depending on the collector and chimney radius.

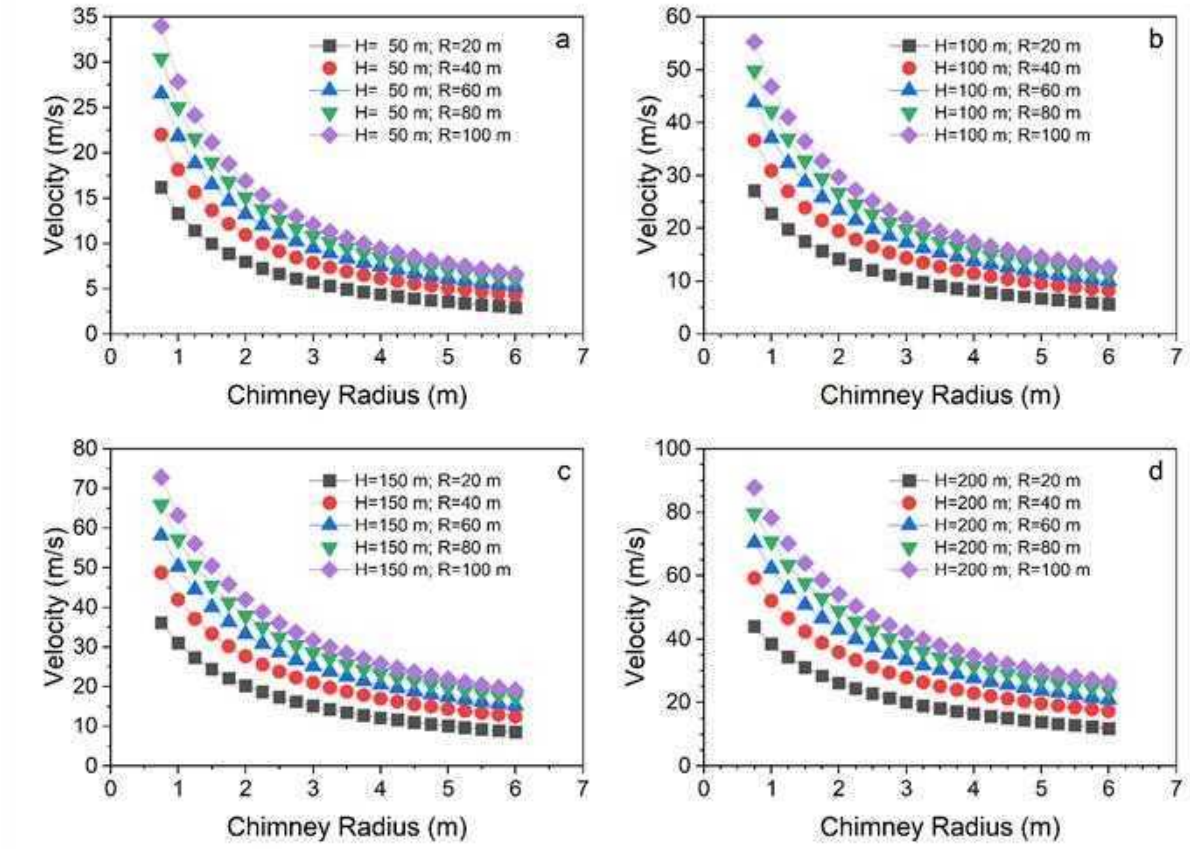


Figure 13. Speed change depending on collector and chimney radius

With increase in collector radius, the amount of heat entering the system increases, and increase in velocity is observed. Expanding the chimney radius enlarges the cross-sectional area, leading to a decrease in velocity. Figure 13 illustrates the change in velocity based on chimney and collector radius. In Figure 13d, it is seen that the highest speed is 87.79 m/s at 0.75 m chimney radius, 100 m collector radius and 200 m chimney height. In Figure 13a, it is seen that the lowest speed is 2.94 m/s at 50 m chimney height, 20 m collector radius and 6 m chimney radius. Figure 14 shows the change in mass flow rate for fixed chimney height based on chimney and collector radius.

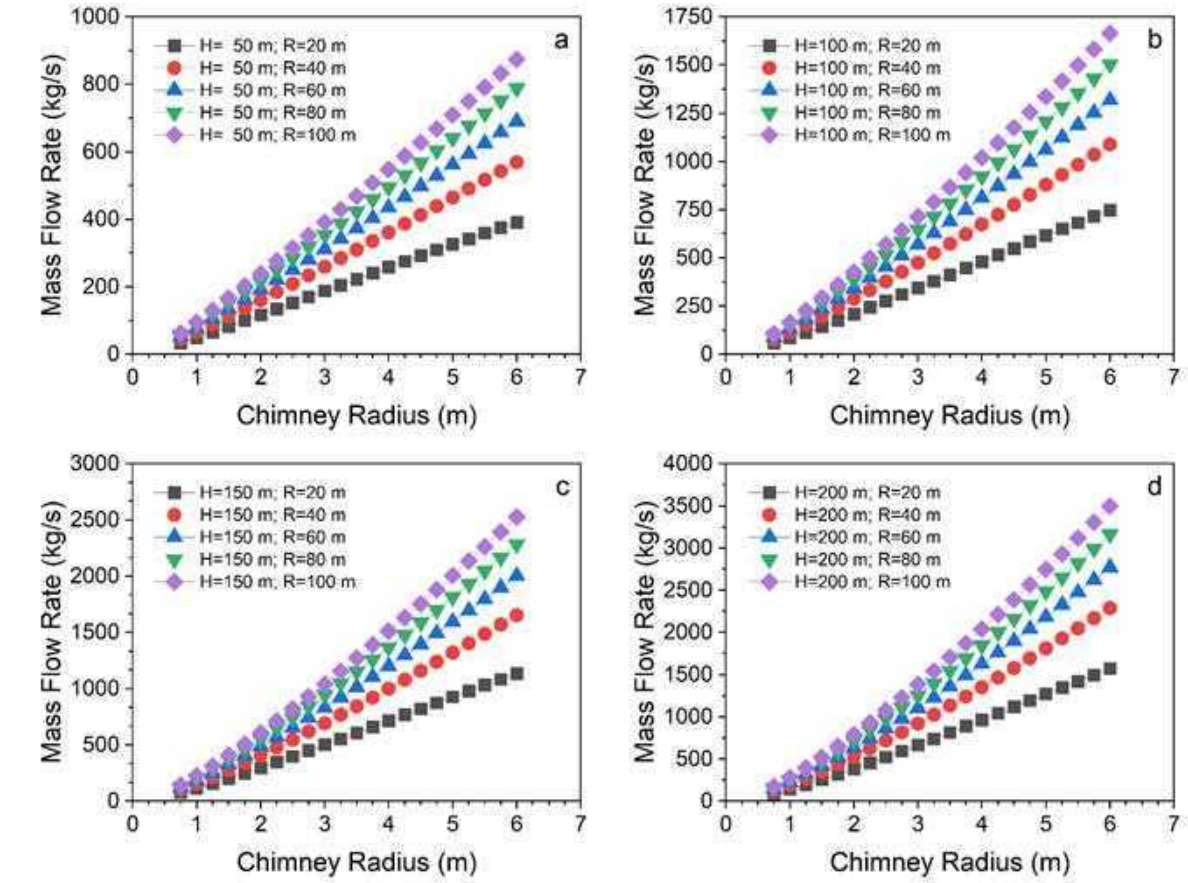


Figure 14. Mass flow rate change depending on collector and chimney radius

Increasing the collector radius leads to a higher amount of heat absorbed by the collector, which results in an increase in the mass flow rate. Similarly, expanding the chimney radius allows more air to pass through the collector, further increasing the mass flow rate. Figure 14d shows the highest mass flow rate of 34.98 kg/s at a chimney height of 200 m, collector radius of 100 m, and chimney radius of 6 m. Figure 14a shows the lowest mass flow rate of 33.21 kg/s at a chimney height of 50 m, collector radius of 20 m, and chimney radius of 0.75 m. Figure 15 illustrates how exit temperature varies with collector and chimney radius. Figure 15 depicts the variation in exit temperature for fixed chimney height depending on the collector and chimney radius.

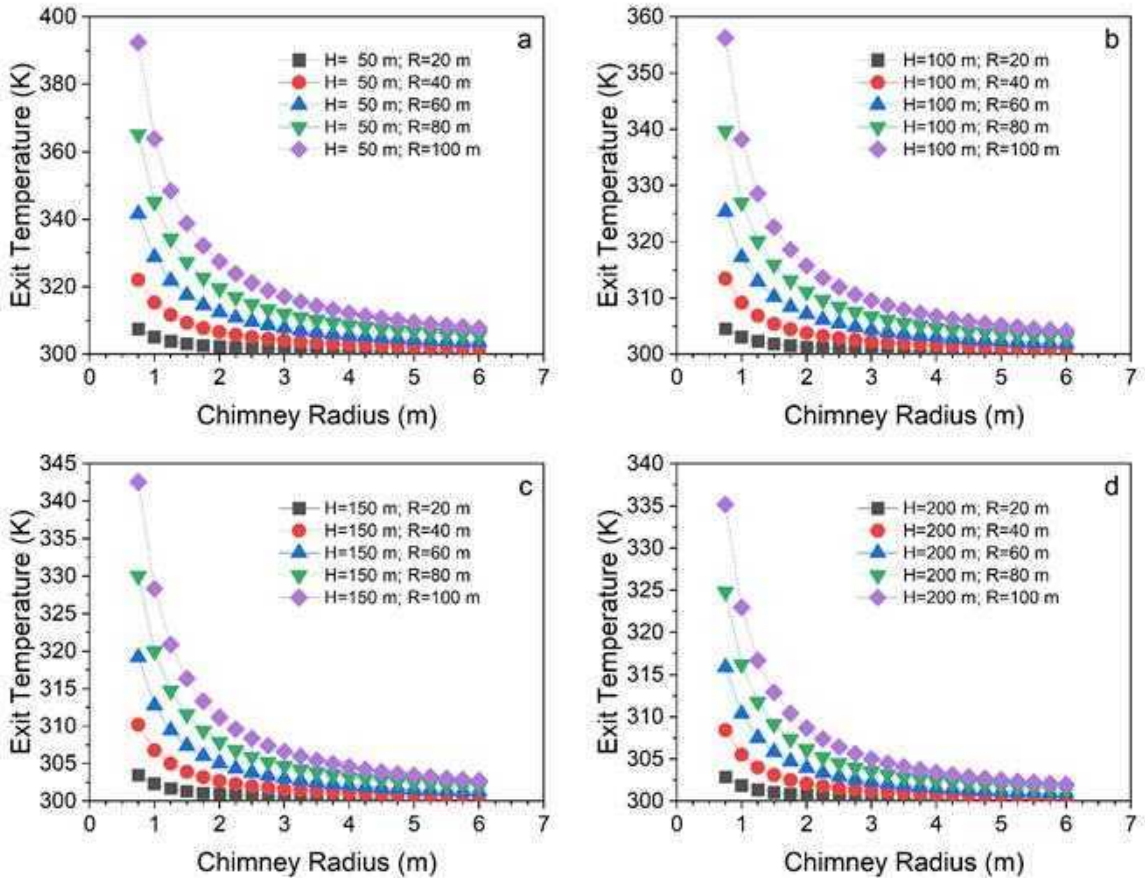


Figure 15. Temperature change depending on collector and chimney radius

As the collector radius increases, the amount of heat absorbed by the system rises, leading to an increase in temperature. Increasing the chimney radius leads to a higher mass flow rate, causing a decrease in the heat transferred per unit air, and therefore, the chimney exit temperature decreases. In Figure 15a, it is seen that the highest chimney outlet temperature is 392.43 K at 0.75 m chimney radius, 100 m collector radius and 50 m chimney height. In Figure 15d, it is seen that the lowest chimney outlet temperature is 300.16 K at 200 m chimney height, 20 m collector radius and 6 m chimney radius. Figure 16 illustrates the change in power for fixed chimney height based on chimney and collector radius.

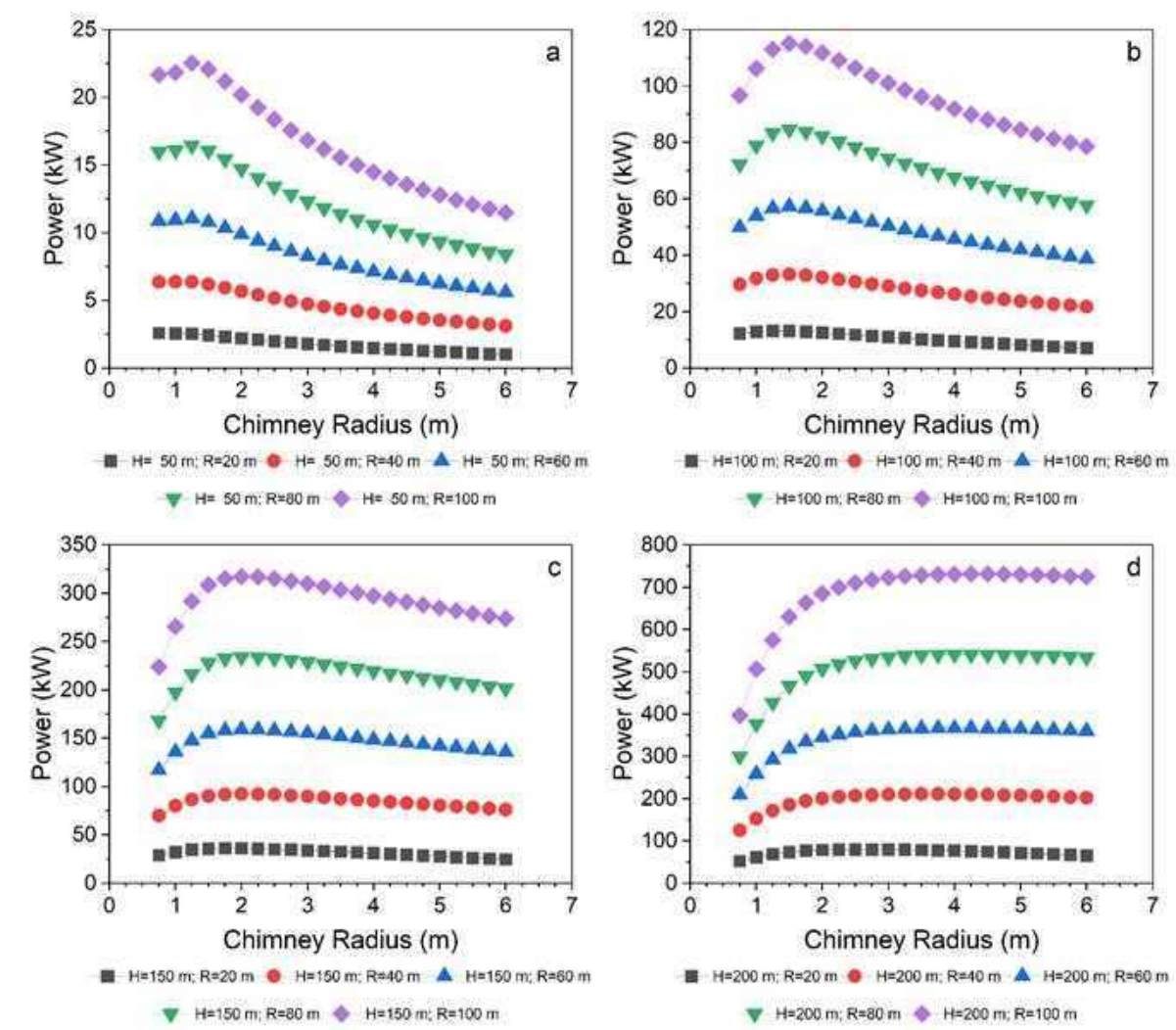


Figure 16. Power change depending on collector and chimney radius

As the collector radius increases, more heat is absorbed by the collector, leading to higher speed, mass flow rate, temperature and power values. As for the increase in the chimney radius, the speed decreases and the mass flow rate increases. For this reason, it has been determined that the chimney radius has an optimum value to reach the highest power value for each geometric parameter. It has been determined that this optimum chimney radius value increases depending on the chimney height. In Figure 16d, it is seen that the highest power is 731.33 kW at 4.25 m chimney radius, 100 m collector radius and 200 m chimney height. In Figure 16a, it is seen that the lowest power is 1 kW at 50 m chimney height, 20 m collector radius and 6 m chimney radius. Figure 17 illustrates the change in efficiency for fixed chimney height based on chimney and collector radius.

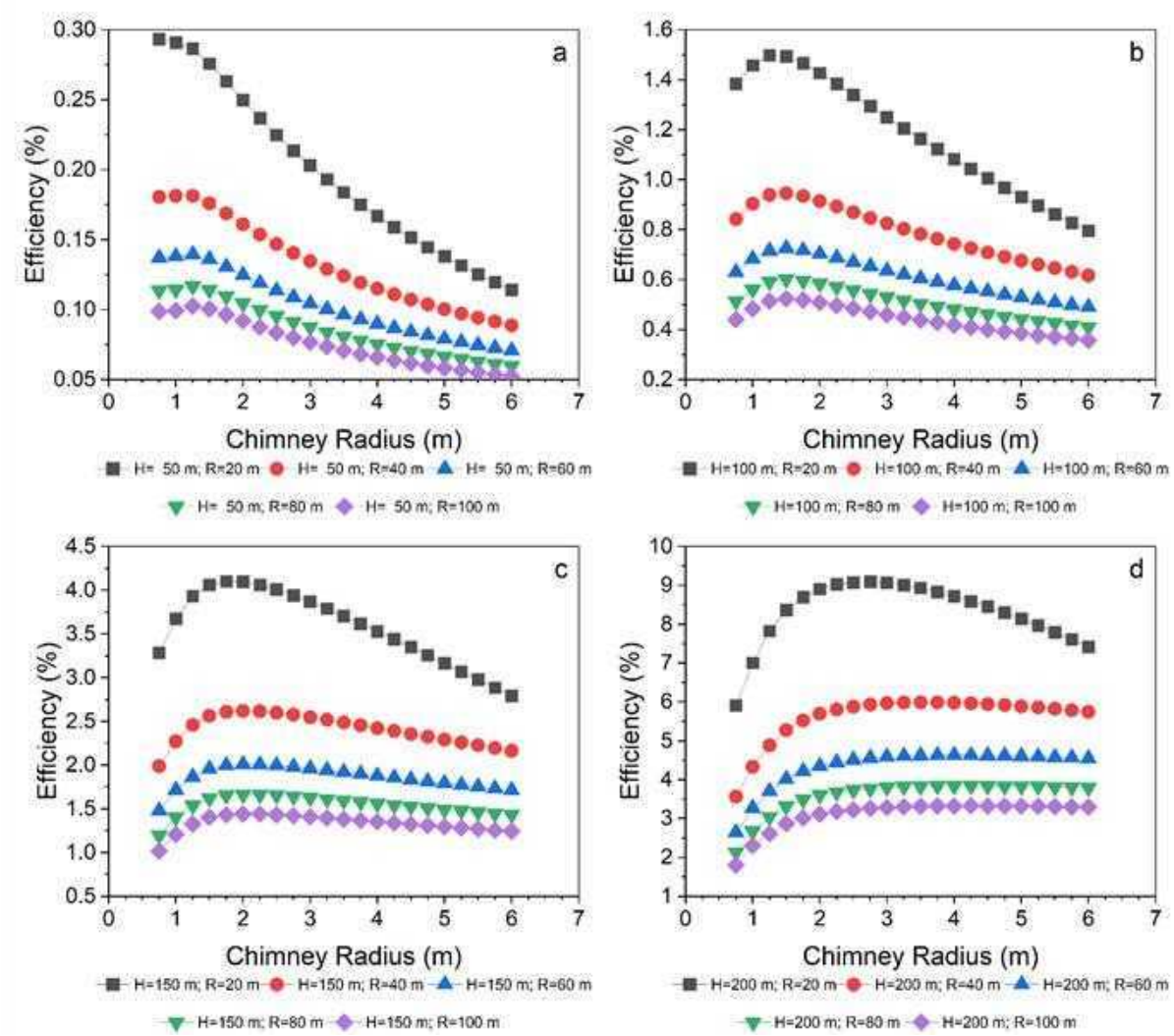


Figure 17. Efficiency change depending on collector and chimney radius

In Figure 17d, it is seen that the highest efficiency is 9.09% at 200 m chimney height, 20 m collector radius and 2.75 m chimney radius. In Figure 17a, it is seen that the lowest efficiency is 0.05% at 6 m chimney radius, 100 m collector radius and 50 m chimney height. As the collector radius expands, more heat is absorbed by the collector, and the efficiency value does not increase in parallel with the power. The highest power values are achieved with a collector radius of 100 m, while the highest efficiency values are reached with a collector radius of 20 m. Figure 18 shows the three-dimensional visual of the optimum chimney radius depending on the chimney height and collector radius.

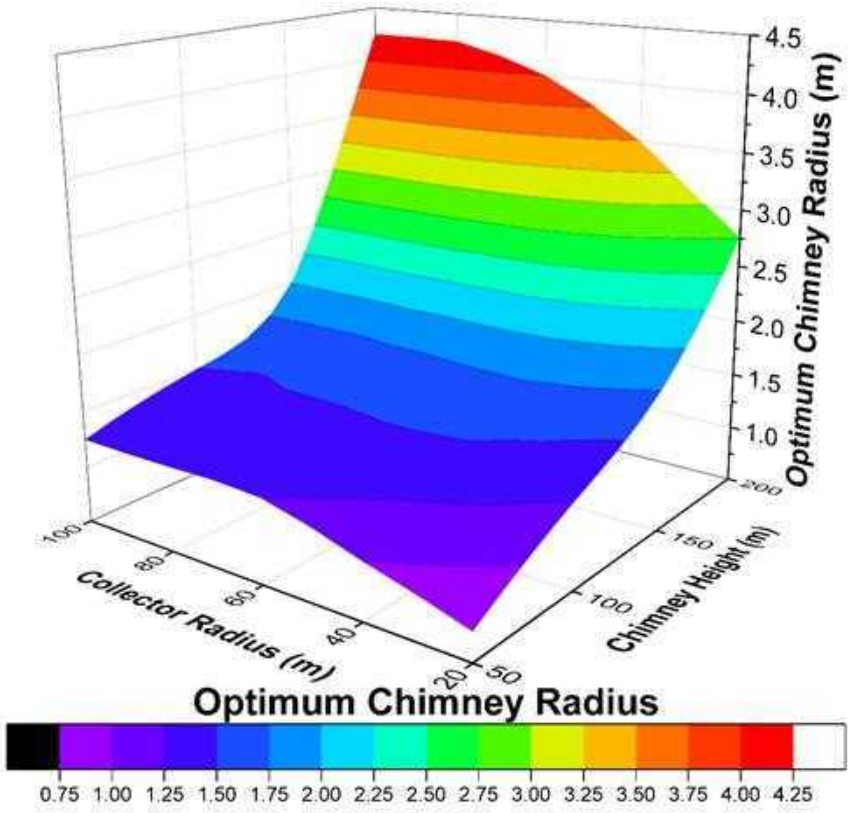


Figure 18. Optimum chimney radius depending on chimney height and collector radius

The optimum chimney radius is the chimney radius value that produces the highest power when the collector radius and chimney height are constant. A total of 20 different combinations were created with five different collector radii and four different chimney heights. Each combination has an optimum chimney radius value. Figure 18 shows that the optimal chimney radius increases with both the chimney height and collector radius. For SCPP designs with a 50 m chimney height, the optimal chimney radius values for collector radii of 20, 40, 60, 80, and 100 m are 0.75, 1, 1.25, 1.25, and 1.25 m, respectively. For a 200 m chimney height, the optimum chimney radius values obtained for collector radius values of 20, 40, 60, 80, 100 m are calculated as 2.75, 3.50, 4.00, 4.25, 4.25 m, respectively. It is clear that the optimal chimney radius increases with the collector radius, although the rate of increase gradually diminishes. However, the impact of an increase in chimney height on power is more significant than that of the collector radius.

To verify the accuracy of the obtained results, a comparison was made with the study conducted by Toghraie et al. [35] presented in Figure 19. In that study, the researchers investigated the optimum chimney radius for a solar chimney power plant model with a collector radius of 100 m and a chimney height of 100 m. This comparison enabled the evaluation of the consistency and reliability of the present findings with the results available in the literature.

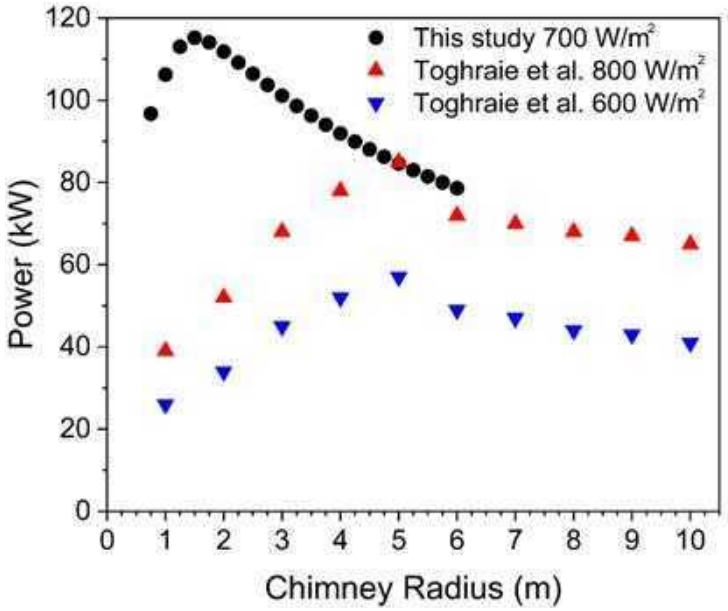


Figure 19. Consistency test of the results with the literature [35]

When the results obtained from this study are compared with those reported by Toghraie et al., it is observed that similar outcomes are achieved at relatively large chimney radius values, whereas the optimum chimney radius differs between the two studies. This variation can primarily be attributed to differences in the collector inlet angle and the chimney leaving angle, both of which significantly influence the flow behavior and overall system performance.

4. CONCLUSIONS

- The SCPP operates by converting solar radiation into electricity, making it a prominent renewable energy solution. The effectiveness and output of the system are inherently linked to its design parameters.
- This research evaluates the performance of the SCPP based on 440 unique configurations, which include varying chimney heights, chimney radii, and collector radii, analyzed through numerical simulations.
- For each design, the mesh was generated with a maximum skewness value maintained below 0.7, employing between 1.1 million and 15 million elements to ensure adequate resolution for capturing flow characteristics and enhancing the reliability of the numerical results.
- The results revealed that increasing chimney height enhanced velocity, mass flow rate, power output, and overall efficiency, though it led to a reduction in the temperature difference.
- Furthermore, expanding the collector radius resulted in higher values for temperature, power, mass flow rate, and velocity but decreased efficiency.
- The study also indicated the necessity for optimization in chimney radius, as a larger radius increased mass flow rates while reducing temperature and velocity.
- However, an optimal chimney radius was found to be critical for maximizing both power and efficiency.
- The design yielding the lowest power output featured a chimney radius of 6.00 meters, a collector radius of 20 meters, and a chimney height of 100 meters. The corresponding velocity, mass flow rate, power, and efficiency values for this design were 2.94 m/s, 390.20 kg/s, 1.00 kW, and 0.11%, respectively.
- The lowest efficiency obtained in the designs was obtained in SCPP with 0.05% efficiency value, 50 m chimney height, 100 m collector radius and 6.00 m chimney radius.

- The design yielding the highest power output featured a chimney radius of 4.25 meters, a collector radius of 100 meters, and a chimney height of 200 meters. The corresponding velocity, mass flow rate, power, and efficiency values for this design were 33.40 m/s, 2213.17 kg/s, 731.33 kW, and 3.33%, respectively.
- The highest efficiency obtained in the designs was obtained in SCPP with 9.09% efficiency value, 200 m chimney height, 20 m collector radius and 2.75 m chimney radius.

Declaration of Ethical Standards

The paper is performed in accordance with ethical standards.

Credit Authorship Contribution Statement

Mustafa ÖNAL: Determination of materials and methods, conducting numerical analyses, writing the sudy.

Ali KOÇ: Supervision; Review and editing of the study.

Özkan KÖSE: Visualization of results.

Yıldız KOÇ: Increasing the originality of the study and contributing to the mathematical model.

Hüseyin YAĞLI: Literature review and determination of the study's focus.

Declaration of Competing Interest

The author declares that they have no financial interests or personal relationships.

Funding / Acknowledgements

There is no funding for this research.

Data Availability

The findings of this study can be obtained from the corresponding author.

Use of Artificial Intelligence

No artificial intelligence tools were used in this article.

5. REFERENCES

[1] Karami, S., Roghabadi, F. A., Maleki, M., Ahmadi, V., & Sadrameli, S. M. "Materials and structures engineering of sun-light absorbers for efficient direct solar steam generation," *Solar Energy*, 225, 747-772, 2021.

[2] Tan, J. D., Chang, C. C. W., Bhuiyan, M. A. S., Nisa'Minhad, K., & Ali, K. "Advancements of wind energy conversion systems for low-wind urban environments: A review," *Energy Reports*, 8, 3406-3414, 2022.

[3] Nassar, Y. F., Abdunnabi, M. J., Sbeta, M. N., Hafez, A. A., Amer, K. A., Ahmed, A. Y., & Belgasim, B. "Dynamic analysis and sizing optimization of a pumped hydroelectric storage-integrated hybrid PV/Wind system: A case study," *Energy Conversion and Management*, 229, 113744, 2021.

[4] Roy, D., & Samanta, S. "Development and multiobjective optimization of a novel trigeneration system based on biomass energy," *Energy Conversion and Management*, 240, 114248, 2021.

[5] Setia, G. A., Zaen, Z. Z., Haz, F., Iskandar, H. R., Winanti, N., & Hidayat, M. R. "Optimization of

the Hybrid Power Plant Design (PV-Wind) for Residential Load," *In 2021 3rd International Conference on High Voltage Engineering and Power Systems*, 227-231, 2021.

[6] Das, P., & Chandramohan, V. P. "Computational study on the effect of collector cover inclination angle, absorber plate diameter and chimney height on flow and performance parameters of solar updraft tower (SUT) plant," *Energy*, 172, 366-379, 2019.

[7] Al-Kayiem, H. H., Aurybi, M. A., Gilani, S. I., Ismaeel, A. A., & Mohammad, S. T. "Performance evaluation of hybrid solar chimney for uninterrupted power generation," Energy, 166, 490-505, 2019.

[8] Xu, Y., & Zhou, X. "Performance of divergent-chimney solar power plants," Solar Energy, 170, 379-387, 2018.

[9] Zuo, L., Liu, Z., Ding, L., Qu, N., Dai, P., Xu, B., & Yuan, Y. "Performance analysis of a wind supercharging solar chimney power plant combined with thermal plant for power and freshwater generation," Energy Conversion and Management, 204, 112282, 2020.

[10] Das, P., & Chandramohan, V. P. "3D numerical study on estimating flow and performance parameters of solar updraft tower (SUT) plant: Impact of divergent angle of chimney, ambient temperature, solar flux and turbine efficiency," Journal of Cleaner Production, 256, 120353, 2020.

[11] Sivaram, P. M., Mande, A. B., Premalatha, M., & Arunagiri, A. "Investigation on a building-integrated passive solar energy technology for air ventilation, clean water and power," Energy Conversion and Management, 211, 112739, 2020.

[12] Haaf, W., Friedrich, K., Mayr, G., & Schlaich, J. "Solar chimneys part I: principle and construction of the pilot plant in Manzanares," International Journal of Solar Energy, 2(1), 3-20, 1983.

[13] Nasraoui, H., Driss, Z., & Kchaou, H. "Novel collector design for enhancing the performance of solar chimney power plant," Renewable Energy, 145, 1658-1671, 2020.

[14] Schlaich, J. R., Bergermann, R., Schiel, W., & Weinrebe, G. "Design of commercial solar updraft tower systems—utilization of solar induced convective flows for power generation," J. Sol. Energy Eng., 127(1), 117-124, 2005.

[15] Singh, A. P., Kumar, A., & Singh, O. P. "Performance enhancement strategies of a hybrid solar chimney power plant integrated with photovoltaic panel," Energy Conversion and Management, 218, 113020, 2020.

[16] Kebabsa, H., Lounici, M. S., Lebbi, M., & Daimallah, A. "Thermo-hydrodynamic behavior of an innovative solar chimney," Renewable Energy, 145, 2074-2090, 2020.

[17] Nouar, H.; Tahri, T.; Chiba, Y. Study on the Performance of a solar chimney power plant Chlef, Algeria region. In Proceedings of the 2018 International Conference on Applied Smart Systems, Medea, Algeria, 24–25 November 2018; pp. 1–5.

[18] Ikhlef, K.; Larbi, S. Energy Performance Analysis of a Solar Chimney Power Plant with and without Thermal Storage System. In Proceedings of the 6th International Conference on Automation, Control, Engineering and Computer Science, Istanbul, Turkey, 21–23 October 2019; Volume 11, pp. 1–7.

[19] Larbi, S.; Bouhdjar, A.; Chergui, T. Performance analysis of a solar chimney power plant in the southwestern region of Algeria. Renew. Sustain. Energy Rev. 2010, 14, 470–477.

[20] Koonsrisuk, A.; Lorente, S.; Bejan, A. Constructal solar chimney configuration. Int. J. Heat Mass Transf. 2010, 53, 327–333.

[21] Toghraie, D.; Karami, A.; Afrand, M.; Karimi-Pour-Fard, A. Effects of geometric parameters on the performance of solar chimney power plants. Energy 2018, 162, 1052–1061.

[22] Choi, Y.J.; Kam, D.H.; Park, Y.W.; Jeong, Y.H. Development of analytical model for solar chimney power plant with and without water storage system. Energy 2016, 112, 200–207.

[23] Cuce, E., Cuce, P. M., Carlucci, S., Sen, H., Sudhakar, K., Hasanuzzaman, M., & Daneshazarian, R. (2022). Solar Chimney Power Plants: A Review of the Concepts, Designs and Performances. Sustainability, 14(3), 1450.

[24] Pradhan, S., Chakraborty, R., Mandal, D. K., Barman, A., & Bose, P. (2021). Design and

performance analysis of solar chimney power plant (SCPP): A review. Sustainable Energy Technologies and Assessments, 47, 101411.

[25] Hassan, A., Ali, M., & Waqas, A. (2018). Numerical investigation on performance of solar chimney power plant by varying collector slope and chimney diverging angle. Energy, 142, 411-425.

[26] Motoyama, M.; Sugitani, K.; Ohya, Y.; Karasudani, T.; Nagai, T.; Okada, S. Improving the power generation performance of a solar tower using thermal updraft wind. Energy Power Eng. 2014, 6, 362.

[27] Ohya, Y., Wataka, M., Watanabe, K., & Uchida, T. (2016). Laboratory experiment and numerical analysis of a new type of solar tower efficiently generating a thermal updraft. Energies, 9(12), 1077.

[28] Ahirwar, M.J.; Sharma, P. Analyzing the Effect of Solar Chimney Power Plant by Varying Chimney Height, Collector Slope and Chimney Diverging Angle. Int. J. Innov. Res. Technol. 2019, 6, 213–219.

[29] Ghorbani, B.; Ghashami, M.; Ashjaee, M.; Hosseinzadegan, H. Electricity production with low grade heat in thermal power plants by design improvement of a hybrid dry cooling tower and a solar chimney concept. Energy Convers. Manag. 2015, 94, 1–11.

[30] Das, P.; Candramohan, V.P. Performance characteristics of divergent chimney solar updraft tower plant. Int. J. Energy Res. 2020, 45, 17159–17174.

[31] Gitan, A.A.; Abdulmalek, S.H.; Dihrab, S.S. Tracking collector consideration of tilted collector solar updraft tower power plant under Malaysia climate conditions. Energy 2015, 93, 1467–1477.

[32] Karimi-Pour-Fard, P.; Beheshti, H. Performance enhancement and environmental impact analysis of a solar chimney power plant: Twenty-four-hour simulation in climate condition of isfahan province, iran. Int. J. Eng. 2017, 30, 1260–1269.

[33] Cable, M. "An evaluation of turbulence models for the numerical study of forced and natural convective flow in Atria," Doctoral dissertation, 25-38, 2009.

[34] Cuce, E., Cuce, P. M., Sen, H., Sudhakar, K., Berardi, U., & Serencam, U. (2021). Impacts of ground slope on main performance figures of solar chimney power plants: a comprehensive CFD research with experimental validation. International Journal of Photoenergy, 2021(1), 6612222.

[35] Toghraie, D., Karami, A., Afrand, M., & Karimipour, A. (2018). Effects of geometric parameters on the performance of solar chimney power plants. Energy, 162, 1052-1061.

Konya Mühendislik Bilimleri Dergisi, c.14, s.2, 830-842, 2026
Konya Journal of Engineering Sciences, v.14, n.2, 830-842, 2026
ISSN: 2667-8055 (Electronic)
DOI: 10.36306/konjes.1591993

IMPROVING EOG-BASED CLASSIFICATION PERFORMANCE: A COMPARATIVE ANALYSIS WITH VARIOUS MACHINE LEARNING ALGORITHMS

[1,*]Khalid Hani ABUSHAHLA, [2]Ayse Nur AY GUL

[1,2]*Biomedical Technologies Application and Research Center (BIYOTAM), Sakarya University of Applied Sciences, 54050, Sakarya, TÜRKİYE*
[1]22500305002@subu.edu.tr, [2]ay@subu.edu.tr

Highlights

- Nine ML models were compared on the UNIOVI-EOG multiclass dataset.
- Random Forest achieved the best accuracy of 99.997%.
- TabNetClassifier offered accurate and interpretable EOG classification.
- The Roza index confirmed the ranking of standard evaluation metrics.
- K-fold validation and ROC analysis supported robust model evaluation.

Graphical Abstract

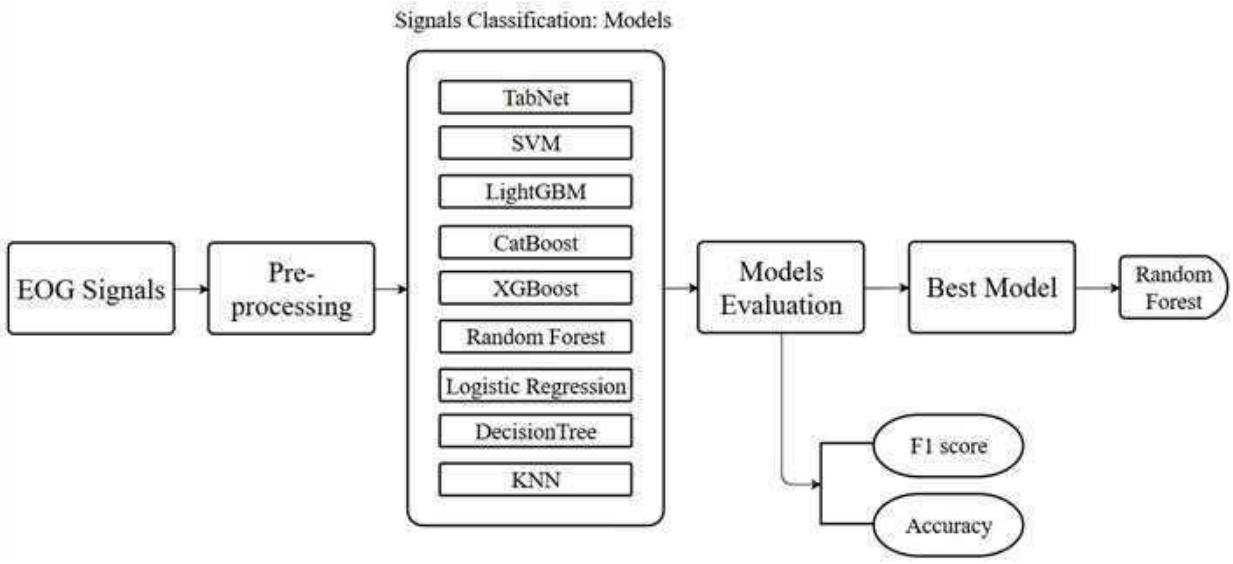


Figure Workflow of the proposed machine learning-based EOG signal classification framework.

***Corresponding Author:** Khalid Hani ABUSHAHLA, 22500305002@subu.edu.tr

Konya Mühendislik Bilimleri Dergisi, c.14, s.2, 830-842, 2026
Konya Journal of Engineering Sciences, v.14, n.2, 830-842, 2026
ISSN: 2667-8055 (Electronic)
DOI: 10.36306/konjes.1591993

IMPROVING EOG-BASED CLASSIFICATION PERFORMANCE: A COMPARATIVE ANALYSIS WITH VARIOUS MACHINE LEARNING ALGORITHMS

[1,*]Khalid Hani ABUSHAHLA, [2]Ayse Nur AY GUL

[1,2]*Biomedical Technologies Application and Research Center (BIYOTAM), Sakarya University of Applied Sciences, 54050, Sakarya, TÜRKİYE*
[1]22500305002@subu.edu.tr, [2]ay@subu.edu.tr

(Received: 27.11.2024; Accepted in Revised Form: 03.12.2025)

ABSTRACT: This study aims to evaluate and compare various models for the classification of Electrooculogram (EOG) signals, which play a significant role in fields such as human-computer interaction and medical diagnostics due to their ability to non-invasively monitor eye movements. Accurate EOG signal classification enables precise detection and interpretation of eye movement patterns, which are crucial for various clinical and assistive applications. A wide range of models was investigated, including traditional machine learning techniques, ensemble methods, and interpretable deep learning approaches. Each model was assessed using accuracy, precision, recall, F1 score, and specificity metrics. The Random Forest model achieved the highest accuracy of 99.997%, while models such as CatBoost, XGBoost, LightGBM, and TabNet also demonstrated strong performance. Additionally, we computed the Roza composite index to jointly capture both the balance and overall strength of metrics across models. Roza values confirmed the ranking observed with standard metrics. The findings provide valuable insights into the effectiveness of different algorithms for EOG signal classification and contribute to the development of more accurate and practical EOG-based systems.

Keywords: *Ensemble models, EOG, Machine learning, Signal classification, UNIOVI-EOG***.**

1. INTRODUCTION

Using superficial electrodes, the Electrooculographic (EOG) signals are produced by the potential difference between the eye's cornea and retina, which allows for the detection of both vertical (up-down) and horizontal (left-right) eye movements and all sub gazes and eye movements. Also, EOG measures the electrical activity of the extraocular muscles [1]. EOG has recently been used in HMI applications because it is a less invasive method of acquisition than electroencephalography (EEG) [2], [3], [4].

Electrooculography (EOG) records physiological eye signal by measuring the corneo-retinal potential, reflecting both voluntary and involuntary ocular activity [5]. Electroencephalography (EEG), in contrast, captures the brain's electrical signals through scalp electrodes, providing detailed information on neural activity and cognitive functions [6]. While EEG offers richer data for comprehensive brain monitoring, EOG is simpler, more patient-friendly, and particularly effective for tracking eye movements in various clinical and interface applications [7].

An equilibrium sense test called the Hallpike caloric test uses ocular activity as a diagnostic tool for disorders affecting the oculomotor system, such as sleep disorders and neurodegenerative diseases [8], [9]. EOG has been applied to many different tasks, including evaluating neurological and cognitive performance, assessing sleep and wakefulness, and examining eye movements in a range of illnesses. EOG is a valuable tool for many clinical and scientific applications since it is a noninvasive, reasonably priced way to measure eye movements [10].

Since the advent of artificial intelligence, machine learning prediction models have been widely applied for risk assessment and supporting medical diagnostics [11]. In recent years, EOG signals have been used to assess physiological and behavioral states using machine learning techniques, revealing

***Corresponding Author:** Khalid Hani ABUSHAHLA, 22500305002@subu.edu.tr

patterns, and associations that are not immediately obvious to humans and due to their wide range of applications in different fields, it has attracted a lot of attention in scientific initiatives [12].

In the literature, substantial research has used machine learning approaches to exploit EOG signals for various applications, such as safety precautions, healthcare diagnostics, and human–computer interaction [2].

One of the early works discussing brain-computer interfaces (BCIs) is Liu et al. which addresses the challenge of adapting to changing brain states, particularly in scenarios where the subject's intent is unknown. This paper introduces a method for initializing parameters in Gaussian mixture models (GMMs) for unsupervised BCI classifier adaptation, showing superior adaptability and class discovery compared to existing methods. Application to real EEG and EOG data confirms its effectiveness with significantly lower error rates [13].

R. Doniec et al. introduced a recognition algorithm utilizing physiological signals from EOG to classify common road types during driving scenarios. Their study achieved remarkable accuracy rates in detecting driver hypovigilance, showcasing the potential for enhancing road safety [14].

Also R. Ileri et al. proposed a novel approach for dyslexia detection using EOG signals and a 1D Convolutional Neural Network (CNN), demonstrating high accuracy for diagnosing dyslexia without complex feature extraction techniques. The accuracy achieved for horizontal and vertical EOG signals was 98.70% and 80.94%, respectively [15].

On other topics, the researchers developed an Artificial Neural Network (ANN)-based method for differentiating among nine classes of EOG signals, achieving exceptional accuracy, precision, recall, and F1 scores, highlighting the potential for precise eye tracking in smart technology applications. The model achieved an accuracy, precision, recall, and F1 score of 99% [16].

Furthermore, a group of scientists investigated using machine learning models such as K-Nearest Neighbor (KNN), Long-Short Term Memory (LSTM), Support Vector Machine (SVM), and Decision Tree (DT) to classify EOG signals from the UNIOVI-EOG dataset. Their main goal was to control a robotic arm based on classified signals. Notably, the KNN model achieved an outstanding F1 score of 0.9996 [17].

In addition to all previous studies Kemalasari et al. focused on electrooculogram-based sleepiness detection using an Artificial Neural Network (ANN) technique, achieving significant accuracy rates and showcasing the potential of EOG signals in monitoring sleep-related disorders [18].

Also, Piaseczna et al. evaluated the intoxication level with EOG analysis and machine learning, achieving substantial accuracy and performance metrics, underscoring the potential of EOG-based systems in healthcare diagnostics and safety measures [19].

In the field of RNN, Saga, Watanabe, and Naruse proposed a recurrent neural network to predict saccade offset time points from EOG signals, enhancing the measurement of eye-fixation-related potential, showcasing advancements in automated measurement techniques for cognitive workload estimation [20].

While the research of Wang and Matsushita is closely related to studies on sleep, a group of researchers explored non-contact determination of sleep/wake state in residential environments using neural network learning of microwave radar and EEG-EOG measurements, demonstrating promising accuracy rates for continuous sleep monitoring in real-world settings [21].

One of the significant works in the EOG HCI is done by López et al. which was a detailed comparison of classification techniques for the control of EOG-based Human-Computer Interfaces (HCIs), showcasing the robustness and effectiveness of machine learning algorithms in HCI applications also it created a very important dataset which is discussed in this work [22].

Although numerous studies have successfully applied machine learning to EOG signals for diverse applications—such as dyslexia detection [15], driver vigilance monitoring [14], and robotic arm control [17]—most of these works focus on specific use-cases or limited algorithmic comparisons. There remains a gap in comprehensive comparative analyses that evaluate a wide range of machine learning algorithms on standardized EOG datasets, such as UNIOVI-EOG, to identify optimal models and inform

future research directions.

All of which contributed to the significance of studying EOG, human interaction techniques, and the ways in which emerging technology can be utilized to benefit from EOG. Furthermore, a substantial initiative of research has been established concerning the interaction between EOG and HCIs. Numerous studies have been undertaken, shedding light on the reasons behind the escalating interest in this domain [12].

In summary, this study addresses a comparative evaluation of machine learning algorithms on EOG signals by systematically analyzing nine models using the UNIOVI-EOG dataset. Through performance assessment with key metrics, it aims to identify optimal algorithms and support the development of more effective EOG-based applications in clinical, diagnostic, and human-computer interface fields.

2. MATERIAL AND METHODS

In this study, a comprehensive methodology was presented for testing and evaluating multiple machine learning models using the UNIOVI-EOG dataset [22]. This dataset was prepared by the University of Oviedo for experimental purposes, utilizing the BlueGain EOG device. The dataset consists of electrooculography signals recorded from 9 healthy participants, comprising 7 males and 2 females, with a mean age of 28.3 , and standard deviation of ±5.4 [22]. The complete block diagram of the study is given in Figure 1.

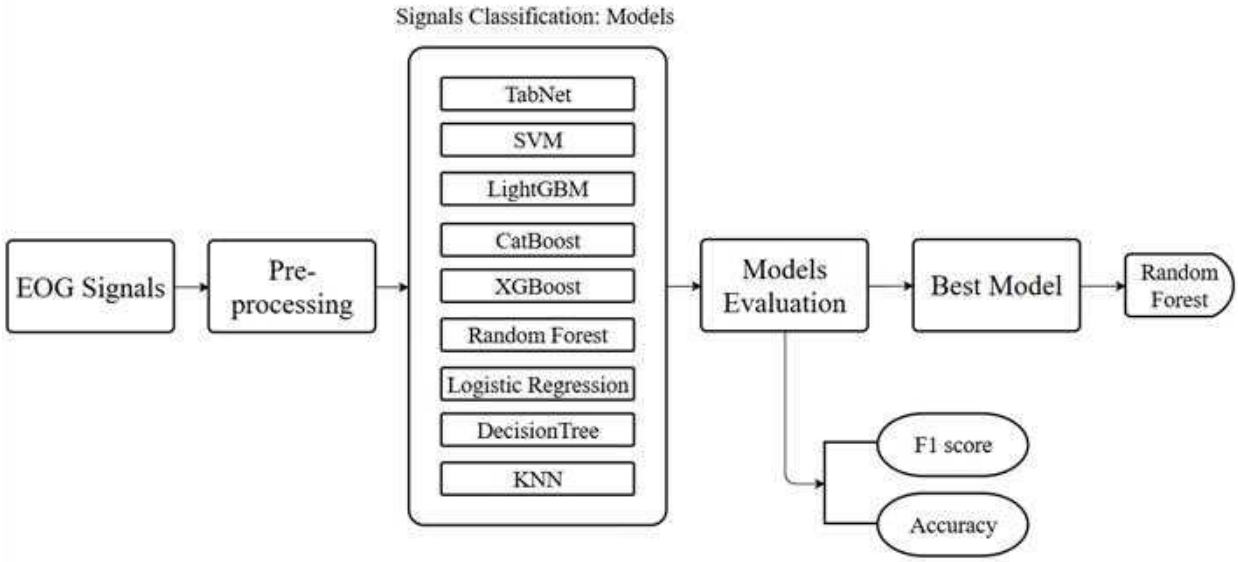


Figure 1. The complete block diagram of the study.

2.1. Data Preprocessing

The initial step involves loading the UNIOVI-EOG dataset and conducting essential preprocessing steps. This includes the separation of features and labels, standardization of features, and encoding of categorical variables if applicable. Additionally, the dataset was divided into two main splits, training 80% and testing 20% to facilitate subsequent model training and evaluation. In this process, the horizontal and vertical channels were combined to form nine gaze direction classes, consistent with the labeling approach applied in the original dataset preparation [22].

2.2. Dataset exploration

The dataset used in this study is UNIOVI-EOG, which has about 12 million rows and four columns. The EOG channel signal is shown in the first column, and each first-stage classifier's C value is shown in the second. The horizontal and vertical channels are represented by the third and fourth columns, respectively. The gaze direction is determined by the label values in these columns [22]. Both horizontal and vertical channels were simultaneously recorded at a sampling frequency of 1 kHz as reported in the original dataset description [22]. The preceding graphs in Fig 2 depict the distribution of data within each column.

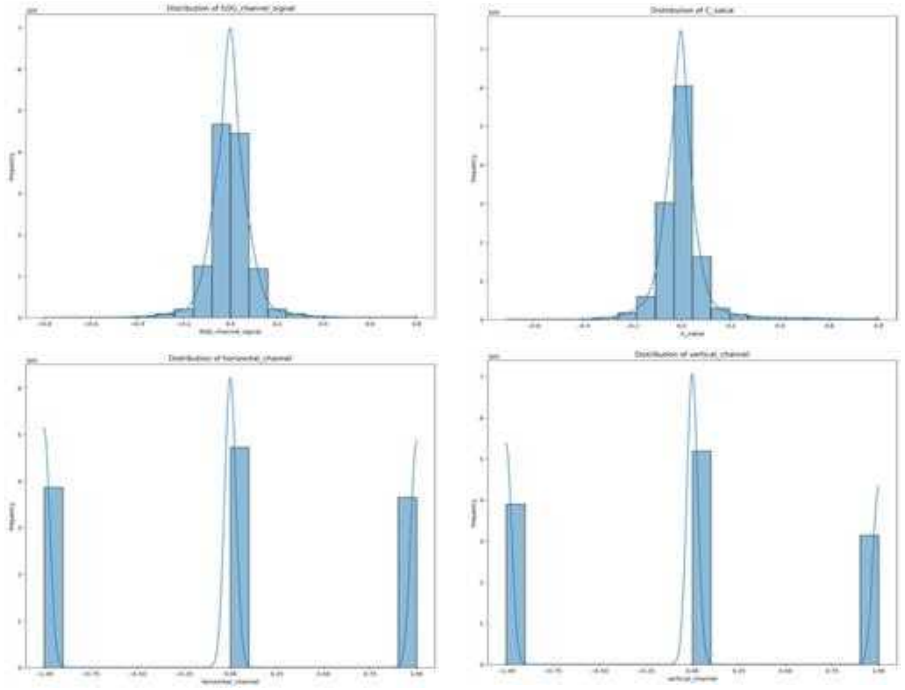


Figure 2. Distribution of data columns
A: Distribution of EOG signals channel (first column) which ranges between -1 and 1.
B: Distribution of C value (second column) which ranges between -1 and 1.
C: Distribution of horizontal channel labels which contain 3 values (-1, 0, 1).
D: Distribution of Vertical channel labels which contain 3 values (-1, 0, 1).
Columns C and D together form the label for classification and provide 9 different classes (Figure 5).

2.3. Models Training and Evaluation

In this study, a wide range of machine learning models was selected for evaluation, including Support Vector Machine (SVM), TabNetClassifier [23], LightGBM [24], CatBoost [25], XGBoost [26], Random Forest (RF), Logistic Regression (LR), Decision Tree (DT) and K-Nearest Neighbors (KNN). Those models composed of deep learning models, conventional machine learning models, and ensemble models aid in combining the diversity of several models to get more accurate predictions [27]. Each model undergoes training on the training set and subsequent evaluation using established evaluation metrics.

All model training and evaluation procedures were performed in Google Colab Pro using Python 3.12.12 and widely used machine-learning libraries, including TensorFlow, NumPy, Pandas, scikit-learn, CatBoost, PyTorch-TabNet, LightGBM, and XGBoost. To support reproducibility, all experiments were executed within a fixed software environment. The Python runtime (version 3.12.12) and all library installations were kept constant throughout the analysis, and a consistent random seed (seed = 42) was applied during model training. Although individual library version numbers are not listed, all computations were performed in an isolated Colab Pro environment, ensuring that the results can be reliably replicated.

One of the main tools used in the evaluation was a confusion matrix which is a tabular representation, arranged by class, that shows the numbers of correctly and incorrectly predicted values (e.g., pixels or picture objects) in relation to the observed or expected values (training samples). It is a classification tool that offers important performance metrics for the algorithm. The confusion matrix provides information that is the basis for many other measurements [28]. And out of this main tool, Several other metrics were extracted and calculated, including accuracy, which measures the ratio of correct predictions to the total number of instances evaluated and F-Measure (FM) or F1 score which represents the harmonic mean between recall and precision values [29]. Recall represents the percentage of correctly identified positive patterns, while precision measures the proportion of correctly predicted positive patterns out of all patterns classified as positive [30]. Another evaluation tool is the ROC curve (Receiver Operating Characteristic curve), a graphical representation that illustrates the performance of a classification model across all threshold levels [31]. Roza values were computed using the MATLAB code provided in Melek & Melek [32], applied to our evaluation metrics.

2.4. Model Comparison

Finally, comparative analysis of the models was conducted based on evaluation metrics, cross-validation results, and visualizations. When choosing the best-performing model(s) for a specific job, factors such model interpretability, computational efficiency, and scalability were considered. The methodology presented ensures a rigorous and systematic approach to model testing and evaluation, facilitating decision-making in real-world applications.

Through the execution of this methodology, The research aimed to provide insights into the performance of machine learning models including Support Vector Machine (SVM), TabNetClassifier, LightGBM, CatBoost, XGBoost, Random Forest, Logistic Regression, Decision Tree and KNN, and their applicability to realm of EOG signal classification and gazes movements.

Through the training and analysis, the Random Forest demonstrated exceptional predictive performance, while Logistic Regression showed the weakest performance, though still acceptable in certain contexts. Other models provided very good results as well, which will be discussed in the next results section with all models trained using default parameters.

3. RESULTS AND DISCUSSION

After training, the evaluation metrics for each model were measured to assess their performance. These metrics are presented in Table 1.

Table 1. Evaluation metrics of nine machine learning models for EOG classification. Columns include Accuracy, F1 score, Precision, Recall, and Specificity, along with composite measures: av_NAoGP (average normalized polygon area), G_C (centroid distance), Roza (composite index of balance and magnitude), and Roza_T (reciprocal of Roza for stability).

Model	Accuracy	F1 score	Precision	Recall	Specificity	av_NAoGP	G_C	Roza	Roza_T
SVM	0.9264	0.9251	0.9336	0.9264	0.9892	0.8837	0.0190	46.75	0.0213
TabNetClassifier	0.9843	0.9843	0.9845	0.9843	0.9969	0.9739	0.0038	250.93	0.0039
LightGBM	0.9943	0.9943	0.9943	0.9943	0.9994	0.9907	0.0015	628.71	0.0015
CatBoost	0.9957	0.9957	0.9957	0.9957	0.9994	0.9929	0.0011	873.97	0.0011
XGBoost	0.9959	0.9959	0.9959	0.9959	0.9994	0.9933	0.0010	935.14	0.0010
Random Forest	0.9999	0.9999	0.9999	0.9999	0.9999	0.9999	~0.0000	2.87×10^{16}	~0.0000
Logistic Regression	0.8781	0.8765	0.8987	0.8781	0.9999	0.8208	0.0365	22.74	0.0439
DecisionTree	0.9999	0.9999	0.9999	0.9999	0.9999	0.9998	~0.0000	6.42×10^{16}	~0.0000
KNN	0.9993	0.9993	0.9993	0.9993	0.9999	0.9989	0.0002	5069.81	0.0002

In Figure 3, the classification performance of the models is compared based on Accuracy and F1 score, where most models demonstrate high and consistent results, particularly the ensemble methods which achieve superior performance.

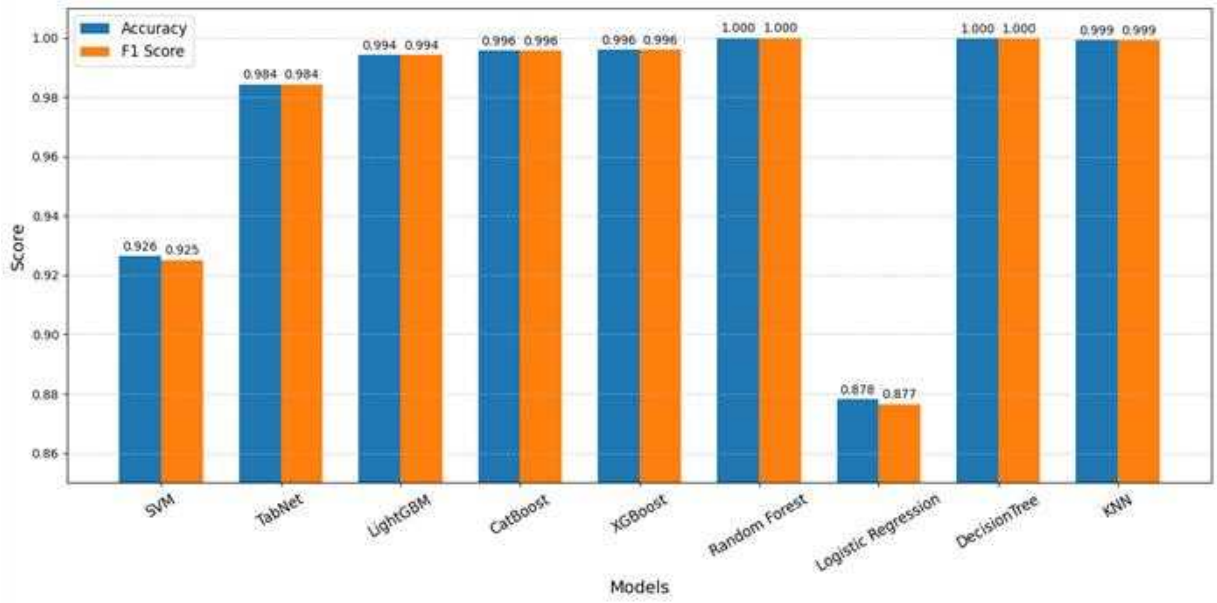


Figure 3. Comparison of classification performance based on Accuracy and F1 score for all evaluated models. Ensemble methods achieved the highest and most consistent performance.

To ensure a thorough evaluation process, ROC curves were computed for each model. The corresponding figures are presented in Figure 4.

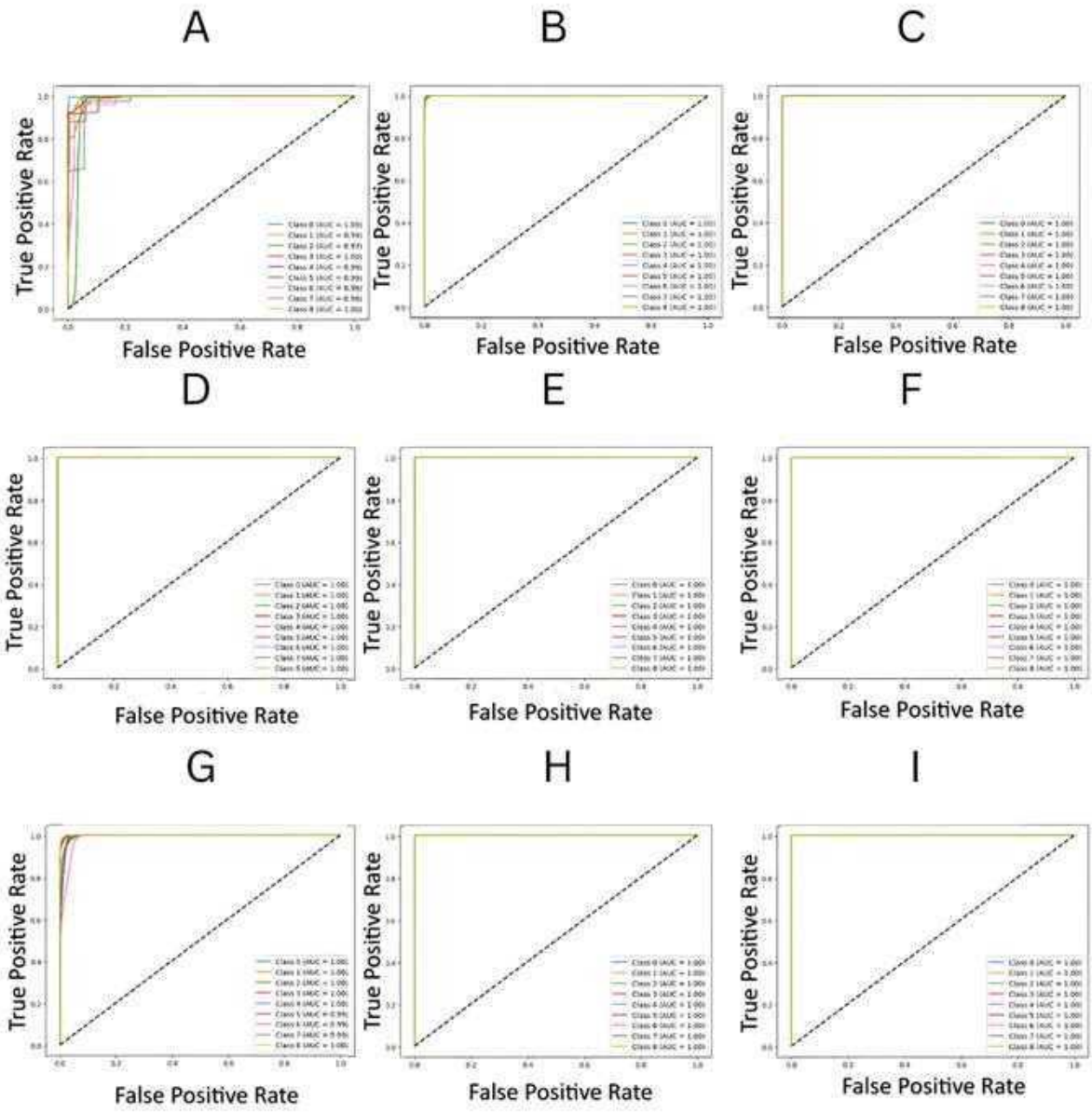


Figure 4. ROC curves for multi-class classification models applied to EOG signal classification. (A) SVM, (B) TabNetClassifier, (C) LightGBM, (D) CatBoost, (E) XGBoost, (F) Random Forest, (G) Logistic Regression, (H) Decision Tree, and (I) KNN. Each subplot presents the ROC curve and corresponding AUC values for the nine target classes.

The ROC curve analysis confirmed the stable and high classification performance for models such as Random Forest, LightGBM, CatBoost, XGBoost, TabNet, Decision Tree, and KNN, while minor variations were observed for SVM and Logistic Regression in certain classes. The dataset UNIOVI-EOG utilized in this primary study is relatively new. Literature discussing this dataset itself is scarce, limited mainly to one reference. However, several other researchers have employed various EOG signals datasets to address the classification problem of EOG signals. A list of previous results attempting to solve the same problem with different datasets is provided in the following table.

In addition to the standard metrics, we computed the Roza composite index using the MATLAB code provided in the work of Mesut Melek and Negin Melek [32] (Table 1), which jointly summarizes the magnitude and balance of Accuracy, F1 score, Precision, Recall, and Specificity. The Roza values mirrored the ranking observed with conventional metrics—Logistic Regression showed the lowest composite performance (Roza ≈ 22.7), SVM was moderate (≈ 46.8), and boosted/ensemble models increased substantially (TabNet ≈ 250.9, LightGBM ≈ 628.7, CatBoost ≈ 874.0, XGBoost ≈ 935.1). For models with near-perfect metrics (Random Forest, Decision Tree), Roza inflated to extreme values ($\sim 10^{16}$) due to a vanishing centroid term; this reflects a limitation of the index in saturated systems rather than a practical superiority gap. This artifact arises because extremely small centroid distances produce disproportionately large Roza values. Therefore, Roza_T (the reciprocal) is reported for stability, which remains small and stable and preserves the same ordering. Overall, Roza/ Roza_T corroborate our primary findings while offering a concise, holistic summary of model performance.

Furthermore, the high accuracies observed for ensemble models such as Random Forest, CatBoost, XGBoost, LightGBM, and KNN (≥99%) can be attributed to several factors. First, the UNIOVI-EOG dataset is large, well-balanced, and contains clearly separable gaze classes with minimal label noise, which enhances learning. Second, ensemble and boosting algorithms are capable of capturing accurate, nonlinear relationships, allowing them to achieve near-perfect classification. Importantly, we employed 5-fold cross-validation and held-out test splits, which reduces the risk of overfitting and confirms that the results are robust and reliable. While such high accuracy is encouraging, future validation on external datasets will further strengthen confidence in the generalizability of the findings.

Table 2. Previous work and literature evaluation metrics and used model summaries.

Authors	Methods	Accuracy
Ay Gul, A. N. et al. [17]	KNN, LSTM, SVM, DT	99.96% [F1 score]
Kemalasari et al. [18]	ANN	87.00%
Piaseczna, N. et al. [19]	"Boosted DT	94.00%
Wang, X. et al.[21]	KNN	95.27%
López, A. et al. [22]	KNN, ANN, SVM and Ensemble Classifier	99.99%
Murugan, S. et al. [33]	SVM, KNN, and Ensemble Classifier	98.70%
Ileri, R. et al. [15]	1D CNN	98.70% H - 80.94% V
Doniec, R. et al. [14]	RF Classifier	87.08%
Latïfoglu, F. et al. [34]	KNN, SVM, DT	89.13% and 80.47%
Alam, Md. M. et al. [16]	ANN	99.00% [F1 score]
Thakur, B. et al. [35]	SVM	99.20%
Pal, M. et al. [36]	SVM	95.83%
O'Bard, B. et al. [37]	SVM, KNN, DT	96.90%
Hernández Pérez, S. N. et al. [38]	KNN, SVM, and DT	79.90%
Current study	SVM, TabNetClassifier, LightGBM, CatBoost, XGBoost, RF, LR, DT, KNN	99.997%

The performance metrics reveal a diverse array of models employed in the analysis, each exhibiting varying degrees of accuracy, precision, recall, and F1 score. Among the methodologies explored, conventional machine learning techniques such as SVM, Logistic Regression, Decision Trees, and KNN have been contrasted against more advanced ensemble methods and deep learning architectures like TabNetClassifier, gradient boosting frameworks as LightGBM, CatBoost, XGBoost, and ensemble learning like Random Forest. Starting with the traditional model, Logistic Regression stands out with a decent accuracy of 87.82%, which, while not the highest, demonstrates its simplicity. Its performance, though respectable, is surpassed by the ensemble methods and gradient boosting algorithms. SVM, another classical model, exhibits strong performance with an accuracy of 92.64%, reflecting its capability to handle both linear and non-linear classification tasks effectively. However, the true innovation lies in the utilization of ensemble methods and boosting algorithms. CatBoost, XGBoost, and LightGBM showcase remarkable and unique accuracy rates exceeding 99.5%, suggesting their robustness in handling complex datasets and potential to uncover intricate patterns. Moreover, the introduction of TabNetClassifier signifies a move towards more interpretable deep learning architectures. TabNetClassifier combines the power of deep learning with explainability, making it suitable for applications where model interpretability is crucial [20], [23] . Moreover, since it's a deep network, it usually performs better on bigger datasets [35], [39]. Its accuracy of 98.43% places it among the top-performing models, presenting the promising explainable deep learning in classification tasks.

Notably, Random Forest and Decision Tree models obtained near-perfect accuracy scores. While Decision Tree classifiers are known for their simplicity and interpretability, Random Forest enhances this concept by aggregating multiple decision trees, thereby reducing variance, and improving predictive performance [40]. Referring to table 2 and the listed previous works, it was discussing EOG signals have utilized a variety of models for EOG signal classification and creating adaptable systems applicable in the field. However, most of these works have been confined to a limited range of models such as SVM, KNN, and occasionally NNs, resulting in a cluster of repetitive studies. In contrast, our work stands out for its comprehensiveness and depth. By exploring nine different models with a big dataset and 5 folds of K-fold Validation, this study achieved more robust and validated results, thereby enhancing the reliability and applicability of our findings in practical settings. Nine labels of EOG data are displayed in Figure 5.

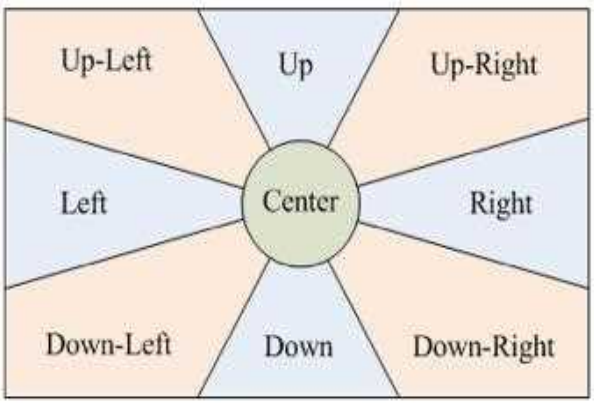


Figure 5. Nine Labels of EOG data.

During training, K-fold cross-validation was employed with a value of 5 for k [41], ensuring the robustness and reliability of our results. Interestingly, this level of detail was not commonly mentioned in most literature works, highlighting a unique aspect of our approach. In this research training process,

employing early stopping notably facilitated the training of very large datasets like UNIOVI-EOG. This feature, however, is not available in many other models. Early stopping enabled the system to monitor and stop the training of TabNetClassifier model effectively, preventing overfitting and improving generalization even on giant datasets. Computational resources and time were saved by ending the training phase when the model's performance on the validation set stabilized. However, it's important to note that the effectiveness of early stopping can vary depending on the complexity of the dataset and the architecture of the model [23]. In this work, a special system that detects and predicts the nine labels within the dataset using various models was developed. While similar studies that utilized the same dataset tended to predict data separately, our work provided more detailed results. For instance, while other studies like López, A. et al. [22] focused on predicting labels in one direction first, then in the vertical and horizontal directions separately, our system predicted labels across all directions as depicted in the image. The paper investigates a wide variety of models for EOG signal classification, ranging from sophisticated ensemble approaches and deep learning architectures to conventional machine learning techniques. Conventional models such as SVM and Logistic Regression have reasonable accuracy, however boosting algorithms and ensemble techniques such as CatBoost, XGBoost, and LightGBM have astonishing accuracy rates that surpass 99.5%. With its promising accuracy findings, TabNetClassifier is a step towards interpretable deep learning architectures.

Comparing this research to earlier studies, which primarily concentrated on restricted models, reveals its depth and comprehensiveness. Robustness is ensured by using K-fold cross-validation, and training efficiency is facilitated by early stopping, particularly on big datasets such as UNIOVI-EOG. The study offers a comprehensive examination of numerous models and techniques, offering insightful information about the EOG signal classification. Additionally, recent works such as Melek & Melek (2022) introduced the Roza metric, which may serve as a complementary evaluation approach for future studies on classification systems [32].

These results, while exceptionally high, are consistent with the structured and balanced nature of the UNIOVI-EOG dataset and the strong generalization capabilities of ensemble methods. Nonetheless, external dataset testing remains necessary to confirm the robustness and real-world transferability of the models.

4. CONCLUSIONS

Finally, our analysis of EOG signal classification, supported by K-fold cross-validation, reveals a broad spectrum of model performances. Random Forest emerges as the standout performer with an accuracy of 99.997%, while Logistic Regression and SVM, at 87.818% and 92.643% respectively, indicate relatively weaker performance in this context. Ensemble methods like XGBoost, LightGBM, and CatBoost showcase superior accuracy rates exceeding 99.5%, demonstrating their strong capability in handling complex datasets. Additionally, the introduction of TabNetClassifier marks a promising step in interpreting deep learning architectures for EOG signal classification. Through comprehensive evaluation using techniques such as confusion matrices, ROC curves, and AUC scores, we ensure robustness and reliability in our model assessment, enabling a thorough examination of strengths and weaknesses. However, even though Random Forest showed very high performance, it may still have some limitations such as being slower to train and harder to interpret compared to simpler models. This work significantly advances the field by offering a deep analysis of diverse models and methodologies.

Declaration of Ethical Standards

The authors declare that they comply with all ethical standards.

Credit Authorship Contribution Statement

Khalid Hani ABUSHAHLA: Conceptualization, Methodology, Software, data processing, Visualization, Investigation, Writing-Reviewing and Editing.
Ayse Nur AY GUL: Conceptualization, Data curation, Writing - Reviewing and Editing

Declaration of Competing Interest

The authors have no competing interests to declare that are relevant to the content of this article.

Funding / Acknowledgements
No funding was received for conducting this study.

Data Availability

The data that support the findings of this study are available in the public dataset described in [22], at https://doi.org/10.1016/j.bspc.2022.104263.

These data were derived from the following resource available in the public domain:

https://www.sciencedirect.com/science/article/pii/S1746809422007170?via%3Dihub.

Use of Artificial Intelligence

AI tools were used only to improve language and readability. The authors remain fully responsible for the manuscript.

REFERENCES

[1] C.-S. Hsieh and C.-C. Tai, "An Improved and Portable Eye-Blink Duration Detect," *Instrumentation Science & Technology*, vol. 41, no. 5, pp. 429–444, Sep. 2013, doi: 10.1080/10739149.2013.796560.
[2] F. D. Pérez-Reynoso, L. Rodríguez-Guerrero, J. C. Salgado-Ramírez, and R. Ortega-Palacios, "Human–Machine Interface: Multiclass Classification by Machine Learning on 1D EOG Signals for the Control of an Omnidirectional Robot," *Sensors*, vol. 21, no. 17, p. 5882, Aug. 2021, doi: 10.3390/s21175882.
[3] G. Gautam and G. Sumanth, "Eye Movement Based Electronic Wheel Chair For Physically Challenged Persons," *IJSTR*, vol. 3, no. 2, pp. 206–212, 2014.
[4] Q. Huang *et al.*, "An EOG-Based Human–Machine Interface for Wheelchair Control," *IEEE Trans. Biomed. Eng.*, vol. 65, no. 9, pp. 2023–2032, Sep. 2018, doi: 10.1109/TBME.2017.2732479.
[5] N. Melek, "Comparison of EEG and EOG signals in classification of sleep stages," *Pamukkale J Eng Sci*, vol. 29, no. 6, pp. 607–616, 2023, doi: 10.5505/pajes.2022.88122.
[6] N. Manshouri, M. Maleki, and T. Kayikcioglu, "An EEG-based stereoscopic research of the PSD differences in pre and post 2D&3D movies watching," *Biomedical Signal Processing and Control*, vol. 55, p. 101642, Jan. 2020, doi: 10.1016/j.bspc.2019.101642.
[7] M. Melek, N. Manshouri, and T. Kayikcioglu, "An automatic EEG-based sleep staging system with introducing NAoSP and NAoGP as new metrics for sleep staging systems," *Cogn Neurodyn*, vol. 15, no. 3, pp. 405–423, Jun. 2021, doi: 10.1007/s11571-020-09641-2.
[8] R. Garcia-Bermudez *et al.*, "Evaluation of electro-oculography data for ataxia SCA-2 classification: A blind source separation approach," in *2010 10th International Conference on Intelligent Systems Design and Applications*, Cairo, Egypt: IEEE, Nov. 2010, pp. 237–241. doi: 10.1109/ISDA.2010.5687258.

[9] M. Djeha, F. Sbargoud, M. Guiatni, K. Fellah, and N. Ababou, "A combined EEG and EOG signals based wheelchair control in virtual environment," in *2017 5th International Conference on Electrical Engineering - Boumerdes (ICEE-B)*, Boumerdes: IEEE, Oct. 2017, pp. 1–6. doi: 10.1109/ICEE-B.2017.8192087.

[10] L. Tao, H. Huang, C. Chen, L. Feijs, J. Hu, and W. Chen, "Review of electrooculography-based human-computer interaction: recent technologies, challenges and future trends," *Conn Health Telemed*, vol. 2, no. 3, p. 2000010, 2023, doi: 10.20517/chatmed.2023.05.

[11] J. Dong *et al.*, "Machine learning-based intradialytic hypotension prediction of patients undergoing hemodialysis: A multicenter retrospective study," *Computer Methods and Programs in Biomedicine*, vol. 240, p. 107698, Oct. 2023, doi: 10.1016/j.cmpb.2023.107698.

[12] C. Belkhiria, A. Boudir, C. Hurter, and V. Peysakhovich, "EOG-Based Human–Computer Interface: 2000–2020 Review," *Sensors*, vol. 22, no. 13, p. 4914, Jun. 2022, doi: 10.3390/s22134914.

[13] G. Liu, G. Huang, J. Meng, D. Zhang, and X. Zhu, "Improved GMM with parameter initialization for unsupervised adaptation of Brain–Computer interface," *Numer Methods Biomed Eng*, vol. 26, no. 6, pp. 681–691, Jun. 2010, doi: 10.1002/cnm.1362.

[14] R. Doniec *et al.*, "Classification of Roads and Types of Public Roads Using EOG Smart Glasses and an Algorithm Based on Machine Learning While Driving a Car," *Electronics*, vol. 11, no. 18, p. 2960, Sep. 2022, doi: 10.3390/electronics11182960.

[15] R. Ileri, F. Latifoğlu, and E. Demirci, "A novel approach for detection of dyslexia using convolutional neural network with EOG signals," *Med Biol Eng Comput*, vol. 60, no. 11, pp. 3041–3055, Nov. 2022, doi: 10.1007/s11517-022-02656-3.

[16] Md. M. Alam, Md. M. S. Raihan, M. R. Chowdhury, and A. B. Shams, "High Precision Eye Tracking Based on Electrooculography (EOG) Signal Using Artificial Neural Network (ANN) for Smart Technology Application," in *2021 24th International Conference on Computer and Information Technology (ICCIT)*, Dhaka, Bangladesh: IEEE, Dec. 2021, pp. 1–6. doi: 10.1109/ICCIT54785.2021.9689821.

[17] A. N. A. Gul, M. Sahin, T. Kandis, K. Kavrak, and Z. Oner, "Robotic Arm Control Using Machine Learning-Based EOG Signal Classifier," in *2023 Medical Technologies Congress (TIPTEKNO)*, Nov. 2023, pp. 1–4. doi: 10.1109/TIPTEKNO59875.2023.10359205.

[18] Kemalasari, F. F. Zakiyyah, and Moch. Rochmad, "Electrooculogram-Based Sleepiness Detection Using Artificial Neural Network (ANN) Technique," in *2023 Sixth International Conference on Vocational Education and Electrical Engineering (ICVEE)*, Surabaya, Indonesia: IEEE, Oct. 2023, pp. 297–303. doi: 10.1109/ICVEE59738.2023.10348384.

[19] N. Piaseczna, K. Duraj, R. Doniec, and E. Tkacz, "Evaluation of Intoxication Level with EOG Analysis and Machine Learning: A Study on Driving Simulator *," in *2023 45th Annual International Conference of the IEEE Engineering in Medicine & Biology Society (EMBC)*, Sydney, Australia: IEEE, Jul. 2023, pp. 1–4. doi: 10.1109/EMBC40787.2023.10340736.

[20] T. Saga, H. Watanabe, and Y. Naruse, "Recurrent Neural Network to Predict Saccade Offset Time Points from Electrooculogram Signals for Automatic Measurement of Eye-Fixation-Related Potential," *Applied Sciences*, vol. 13, no. 10, p. 6230, May 2023, doi: 10.3390/app13106230.

[21] X. Wang and D. Matsushita, "Non-contact determination of sleep/wake state in residential environments by neural network learning of microwave radar and electroencephalogram–electrooculogram measurements," *Building and Environment*, vol. 233, p. 110095, Apr. 2023, doi: 10.1016/j.buildenv.2023.110095.

[22] A. López, J. R. Villar, M. Fernández, and F. J. Ferrero, "Comparison of classification techniques for the control of EOG-based HCIs," *Biomedical Signal Processing and Control*, vol. 80, p. 104263, Feb. 2023, doi: 10.1016/j.bspc.2022.104263.

[23] S. O. Arik and T. Pfister, "TabNet: Attentive Interpretable Tabular Learning," Dec. 09, 2020, arXiv:1908.07442. Accessed: Feb. 27, 2024. [Online]. Available: http://arxiv.org/abs/1908.07442

[24] G. Ke *et al.*, "LightGBM: A Highly Efficient Gradient Boosting Decision Tree," in *Advances in Neural Information Processing Systems*, Long Beach, CA, USA: Curran Associates, Inc., 2017, pp. 3146–3154.

[25] L. Prokhorenkova, G. Gusev, A. Vorobev, A. V. Dorogush, and A. Gulin, "CatBoost: unbiased boosting with categorical features," Jan. 20, 2019, arXiv:1706.09516. Accessed: Feb. 27, 2024. [Online]. Available: http://arxiv.org/abs/1706.09516

[26] T. Chen and C. Guestrin, "XGBoost: A Scalable Tree Boosting System," in *Proceedings of the 22nd ACM SIGKDD International Conference on Knowledge Discovery and Data Mining*, Aug. 2016, pp. 785–794. doi: 10.1145/2939672.2939785.

[27] A. Sharma and R. Rani, "Ensembled machine learning framework for drug sensitivity prediction," *IET Systems Biology*, vol. 14, no. 1, pp. 39–46, 2020, doi: 10.1049/iet-syb.2018.5094.

[28] I. Düntsch and G. Gediga, "Confusion Matrices and Rough Set Data Analysis," *J. Phys.: Conf. Ser.*, vol. 1229, no. 1, p. 012055, May 2019, doi: 10.1088/1742-6596/1229/1/012055.

[29] Ž. Đ. Vujovic, "Classification Model Evaluation Metrics," *IJACSA*, vol. 12, no. 6, 2021, doi: 10.14569/IJACSA.2021.0120670.

[30] H. M and S. M.N, "A Review on Evaluation Metrics for Data Classification Evaluations," *IJDKP*, vol. 5, no. 2, pp. 01–11, Mar. 2015, doi: 10.5121/ijdkp.2015.5201.

[31] Google for Developers, "Classification: ROC Curve and AUC | Machine Learning." Accessed: Feb. 27, 2024. [Online]. Available: https://developers.google.com/machine-learning/crash-course/classification/roc-and-auc

[32] M. Melek and N. Melek, "Roza: a new and comprehensive metric for evaluating classification systems," *Computer Methods in Biomechanics and Biomedical Engineering*, vol. 25, no. 9, pp. 1015–1027, Jul. 2022, doi: 10.1080/10255842.2021.1995721.

[33] S. Murugan, P. K. Sivakumar, C. Kavitha, A. Harichandran, and W.-C. Lai, "An Electro-Oculogram (EOG) Sensor's Ability to Detect Driver Hypovigilance Using Machine Learning," *Sensors*, vol. 23, no. 6, 2023, doi: 10.3390/s23062944.

[34] F. LatiFoğlu, M. Y. Esas, R. İLerï, S. Özmen, and E. DemïRcï, "Using electrooculography with visual stimulus tracking test in diagnosing of ADHD: findings from machine learning algorithms," *Turkish Journal of Medical Sciences*, vol. 52, no. 5, pp. 1616–1626, Jan. 2022, doi: 10.55730/1300-0144.5502.

[35] B. Thakur, P. Syal, and P. Kumari, "An Electrooculogram Signal Based Control System in Offline Environment," in *Proceedings of the 2017 4th International Conference on Biomedical and Bioinformatics Engineering*, Seoul Republic of Korea: ACM, Nov. 2017, pp. 68–73. doi: 10.1145/3168776.3168794.

[36] M. Pal, A. Banerjee, S. Datta, A. Konar, D. N. Tibarewala, and R. Janarthanan, "Electrooculography based blink detection to prevent Computer Vision Syndrome," in *2014 IEEE International Conference on Electronics, Computing and Communication Technologies (CONECCT)*, Bangalore, India: IEEE, Jan. 2014, pp. 1–6. doi: 10.1109/CONECCT.2014.6740337.

[37] B. O'Bard and K. George, "Classification of eye gestures using machine learning for use in embedded switch controller," in *2018 IEEE International Instrumentation and Measurement Technology Conference (I2MTC)*, Houston, TX, USA: IEEE, May 2018, pp. 1–6. doi: 10.1109/I2MTC.2018.8409769.

[38] S. N. Hernández Pérez, F. D. Pérez Reynoso, C. A. G. Gutiérrez, M. D. L. Á. Cosío León, and R. Ortega Palacios, "EOG Signal Classification with Wavelet and Supervised Learning Algorithms KNN, SVM and DT," *Sensors*, vol. 23, no. 9, p. 4553, May 2023, doi: 10.3390/s23094553.

[39] J. Lu *et al.*, "Deep learning model to predict exercise stress test results: Optimizing the diagnostic test selection strategy and reduce wastage in suspected coronary artery disease patients," *Computer Methods and Programs in Biomedicine*, vol. 240, p. 107717, Oct. 2023, doi: 10.1016/j.cmpb.2023.107717.

[40] D. Petkovic, R. Altman, M. Wong, and A. Vigil, "Improving the explainability of Random Forest classifier – user centered approach," in *Biocomputing 2018*, Kohala Coast, Hawaii, USA: WORLD SCIENTIFIC, Jan. 2018, pp. 204–215. doi: 10.1142/9789813235533_0019.

[41] F. Sohil, M. U. Sohali, and J. Shabbir, "An introduction to statistical learning with applications in R," Stat. Theory Relat. Fields, vol. 6, no. 1, p. 87, 2022, doi: 10.1080/24754269.2021.1980261.

Konya Mühendislik Bilimleri Dergisi, c.14, s.2, 843-868, 2026
Konya Journal of Engineering Sciences, v.14, n.2, 843-868, 2026
ISSN: 2667-8055 (Electronic)
DOI: 10.36306/konjes.1775942

PREDICTION OF CRITICAL SUBMERGENCE FOR HORIZONTAL INTAKES UNDER ASYMMETRICAL APPROACH FLOW CONDITIONS

[1,*]Serkan GÖKMENER, [2]Dalal Abdulkareem Hussein AL-OBAIDI

[1]*Hydraulics Laboratory, Department of Civil Engineering, Middle East Technical University, 06800, Ankara, Türkiye*
[2]*Department of Civil Engineering, Çankaya University, 06790, Ankara, Türkiye*
[1]gokmener@metu.edu.tr, [2]dalaliqdam@gmail.com

Highlights

- Critical submergence was investigated for asymmetric flows at horizontal intakes.
- A wide range of data was used to derive generalized empirical equations.
- The effect of the approach Froude number on critical submergence was studied.
- Intake Froude number and intake geometry dominated the critical submergence.

***Corresponding Author:** Serkan GÖKMENER, gokmener@metu.edu.tr

Konya Mühendislik Bilimleri Dergisi, c.14, s.2, 843-868, 2026
Konya Journal of Engineering Sciences, v.14, n.2, 843-868, 2026
ISSN: 2667-8055 (Electronic)
DOI: 10.36306/konjes.1775942

PREDICTION OF CRITICAL SUBMERGENCE FOR HORIZONTAL INTAKES UNDER ASYMMETRICAL APPROACH FLOW CONDITIONS

[1,*]Serkan GÖKMENER, [2]Dalal Abdulkareem Hussein AL-OBAIDI

[1]*Hydraulics Laboratory, Department of Civil Engineering, Middle East Technical University, 06800, Ankara, Türkiye*
[2]*Department of Civil Engineering, Çankaya University, 06790, Ankara, Türkiye*
[1]gokmener@metu.edu.tr, [2]dalaliqdam@gmail.com

(Received: 05.09.2025; Accepted in Revised Form: 08.12.2025)

ABSTRACT: Air-entraining vortices at intake structures present serious challenges to the functionality of water intake systems, resulting in reduced efficiency and possible damage to hydraulic equipment. The present study aims to predict the critical submergence, S_c, which is the minimum vertical distance between the free surface and intake pipe to avoid air-entraining vortices, for horizontal intakes under asymmetrical approach flow conditions. Dimensional analysis was utilized to investigate the influences of intake geometry, approach Froude number, intake Froude number, Reynolds number, and Weber number. Two hundred and twenty-five experimental data for asymmetrical approach flow conditions were evaluated to derive more general and accurate empirical equations predicting the dimensionless critical submergence, S_c/D_i. The results indicate that the intake Froude number $(Fr)_i$, and the geometric parameter are the most important parameters that affect S_c/D_i. Accordingly, the most accurate empirical equations were obtained while considering all the flow and geometric parameters to predict S_c/D_i. On the contrary, the accuracy of the empirical equations considering only $(Fr)_i$ gives moderate results in predicting S_c/D_i.

Keywords: *Air-entraining vortices, Approach Froude number, Critical submergence, Horizontal intakes, Intake Froude number.*

1. INTRODUCTION

Air-entraining vortices generated by swirling flows are a common problem in the operation of water intake structures. Their formation can cause serious economic and operational issues, such as pipeline vibrations, cavitation damage, reduced intake efficiency, diminished hydraulic machinery performance, higher head losses, and lower discharge capacity [1]. Therefore, designing and operating intake structures to minimize vortex formation is essential. A key factor in preventing vortex development is maintaining adequate water depth above the intake. The vertical distance between the free surface and the intake opening, known as submergence, plays a decisive role. When submergence falls below a certain threshold, surface vortices that entrain air into the intake begin to form. The limiting condition at which air first reaches the intake is referred to as the critical submergence. To ensure reliable intake performance, the operating water level must remain above this critical depth, thereby preventing the formation of air-entraining vortices that extend from the free surface to the intake entrance. In the literature, there are several empirical equations proposed by researchers to predict the critical submergence for horizontal intake structures. Analytical approaches were used to predict critical submergence at intakes and used experimental data to validate their findings [2], [3], [4], [5], [6], [7], [8], [9]. In addition, other researchers experimentally explained the occurrence of air-entraining vortex as a function of the intake Froude number due to the turbulent nature of the phenomenon [10], [11], [12], [13], [14]. They introduced empirical equations and charts for predicting the dimensionless critical submergence as a function of the intake Froude number. Moreover, the effect of intake geometry and approach Froude number on the development of air-entraining vortices has been investigated in only a few studies. Researchers such as

***Corresponding Author:** Serkan GÖKMENER, gokmener@metu.edu.tr

[15], [16] focused on the effect of intake orientation, while [1], [17], [18], [19] focused on the effect of sidewall clearance on predicting the dimensionless critical submergence. Furthermore, the effect of the approach Froude number on critical submergence was considered by [20], [21] for lateral intakes.

Although numerous studies have provided valuable insights into intake design for preventing air-entraining vortices, to the authors' best knowledge, no research has specifically investigated the influence of the approach Froude number on vortex formation at horizontal intakes. In addition, [1], [17], [18], [19] were the only researchers to introduce a geometry parameter, defined in terms of sidewall clearances and intake size, as a function of dimensionless critical submergence. Nevertheless, these studies did not take into account the influence of the approach Froude number and were constrained by certain limitations related to flow conditions and geometric characteristics. For example, [17], [18], [19] carried out experiments considering a wide range of Froude, Reynolds and Weber numbers with varying pipe diameters; however, the experimental setup that was used in those studies was a small-scale model. On the other hand, [1] conducted their experiments on a large-scale model, but the pipe diameter was kept constant and accordingly, the ranges of Froude, Reynolds and Weber numbers were narrower when compared to [17], [18], [19]. Consequently, the main objective of this study is to merge and reanalyze the datasets of [1], [18] in order to overcome the limitations of previous works and to develop new, more generalized dimensionless equations for predicting critical submergence under asymmetrical approach flow as a function of both flow and geometric parameters. In addition, this study is the first to address the influence of the approach Froude number on vortex formation at horizontal intakes under asymmetrical approach flow conditions.

The remainder of this study is structured as follows: Section 2 presents the theoretical background and methodology adopted in this research. The findings and their discussion are outlined in Section 3. Finally, Section 4 concludes the study by summarizing the key results and implications of the study.

2. MATERIAL AND METHODS

2.1. Modeling Air-Entraining Vortices

Critical submergence, S_c, is defined as the vertical distance between the free surface at which air-entraining vortices first appear and the summit point of the intake pipe [10], [11], [13], [22]. Accurate prediction of S_c is therefore essential for the control and prevention of air-entraining vortices at intake structures. The parameters influencing S_c can be categorized into flow, fluid, and geometric parameters. Flow parameters include the mean circulation imposed on the flow (Γ), the mean velocity within the intake pipe (V_i), the mean velocity in the approach channel (V_{app}), and gravitational acceleration (g). Fluid parameters consist of dynamic viscosity (μ), fluid density (ϱ), and surface tension (σ). Geometric parameters are represented by the distances between the left and right channel sidewalls (b_1 and b_2), the intake pipe diameter (D_i), and the vertical clearance between the pipe invert and the reservoir bed (a). Figure 1 illustrates a schematic of a horizontal intake structure with these geometric parameters. Accordingly, the independent flow, fluid, and geometric variables governing critical submergence, S_c, can be expressed as follows:

$$S_c = f_1(\rho, \mu, \sigma, g, V_i, V_{app}\ \Gamma, D_i, a, b_1, b_2\ ) \tag{1}$$

The variables that are given in Equation (1) were converted into dimensionless terms by applying Buckingham's Π theorem;

$$S_c = f_2(\frac{b_1}{D_i}, \frac{b_2}{D_i}, \frac{a}{D_i}, (Fr)_{app}, (Fr)_i, Re, We, K_o) \tag{2}$$

where $\frac{b_1}{D_i}$ and $\frac{b_2}{D_i}$ represents intake sidewall clearances with respect to the center of intake pipe diameter, $^{a}/_{D_i}$ is the aspect ratio of bottom clearance to intake diameter, $(Fr)_{app} = {}^{V_{app}}\Big/\sqrt{g(D_i + S_c)}$ is the approach

Froude number, $(Fr)_i = {V_i}/{\sqrt{gD_i}}$ is the intake Froude number, $Re = {V_i D_i \rho}/{\mu}$ is the intake Reynolds number, $We = {\rho V_i^2 D_i}/{\sigma}$ is the intake Weber number and $K_o = {\Gamma}/{D_i V_i}$ is the intake Kolf number.

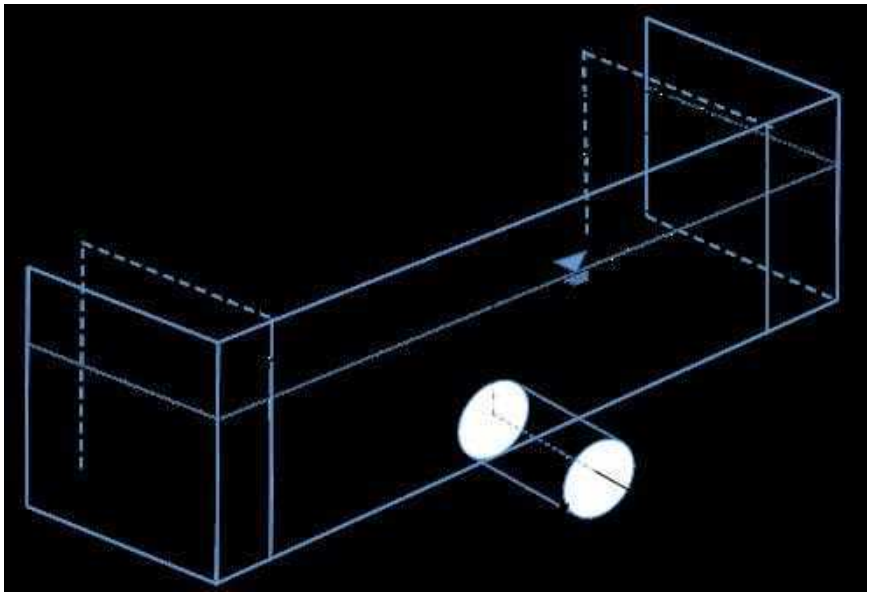


Figure 1. A sketch of the horizontal intake structure

For asymmetrical approach flow conditions, $\frac{b_1}{D_i}$ and $\frac{b_2}{D_i}$ are represented as $\frac{(b_1+b_2)}{D_i}\left(\frac{b_1}{b_2}\right)$, which becomes the dimensionless term of the asymmetry of the approach flow and Equation (2) can be written for asymmetrical approach flow conditions as:

$$S_c = f_3\left(\frac{(b_1+b_2)}{D_i}\left(\frac{b_1}{b_2}\right), \frac{a}{D_i}, (Fr)_{app}, (Fr)_i, Re, We, K_o\right) \quad (3)$$

In this study, the vertical distance between the intake pipe and the bottom of the reservoir, a, is zero. Therefore, ${a}/{D_i}$ parameter which is related to intake geometry, can be eliminated from Equation (3). In addition, the Kolf number, K_o, which is associated with the circulation parameter, can be eliminated, since there is no imposed or induced circulation on the approach flow [1], [4], [6], [18]. Finally, the geometrical parameter, $\frac{(b_1+b_2)}{D_i}\left(\frac{b_1}{b_2}\right)$ is symbolized as ψ. Accordingly, Equation (3) can be simplified as shown below for asymmetrical approach flow conditions:

$$S_c = f_3(\psi, (Fr)_{app}, (Fr)_i, Re, We) \quad (4)$$

2.2. Experimental Procedure

Gogus and Gokmener [1] conducted experiments in a 1:30 scaled model of Beyhan 1 Dam's intake structure in the Hydraulics Laboratory of Middle East Technical University. The reservoir itself had dimensions of 6.35 m, 6.7 m, and 2.05 m, in width, length, and height, respectively. To regulate the kinetic energy of inflowing water, an energy dissipation device was installed at the reservoir's upstream section. Three identical intake structures, each connected to pipes with a uniform pipe diameter of D_i=26.5 cm, that conveyed flow toward the tailwater of the channel.

Haspolat and Gogus [18] carried out experiments using a small-scale experimental setup constructed in the Hydraulics Laboratory of Middle East Technical University. The experimental setup consists of three primary components: the reservoir, the horizontal intake pipe, and the rectangular open channel. The reservoir dimensions were 3.10 m in both length and width, and 2.20 m in depth. Four intake diameters were tested: 30 cm, 25 cm, 10 cm, and 5 cm.

In the previous research, the procedures implemented were as follows: To begin the experiment, the reservoir was filled above the critical submergence level. A constant water surface level was obtained in the system by adjusting the inflow and the outflow rates. Observation of the flow conditions for 10 to 20 minutes was essential to ensure that no formation of vortices occurs at this stage. Then the level was decreased gradually, slowly and carefully, by opening a drainage pipe valve until an air-entraining vortex on the free surface is observed. After the formation of the vortex, the water level, location of the vortex and discharge values were measured and recorded. Depending on the experiment, this procedure took 30 minutes to 7 hours. Repeatability tests were carried out to enhance the critical submergence measurements. The water level in the reservoir was adjusted and measured on two further occasions to reproduce the conditions at which vortex formation occurred, after recording the initial critical submergence. The average of these three measurements was then taken to represent the final critical submergence value, lower than 5% variation of the critical submergence from the mean for a certain intake discharge was found in this study [1].

Since the only experimental data from those studies are considered in this study, the experimental setup and procedure are only summarized in this study. If the readers want to have more information about the experimental studies of Haspolat and Gogus [18] and Gogus and Gokmener [1] in detail, they can look at the related studies in the literature [1], [18], [19], [23]. Nonetheless, the experimental setups belonging to those studies, along with the measurement points, are provided in Figures 2 and 3.

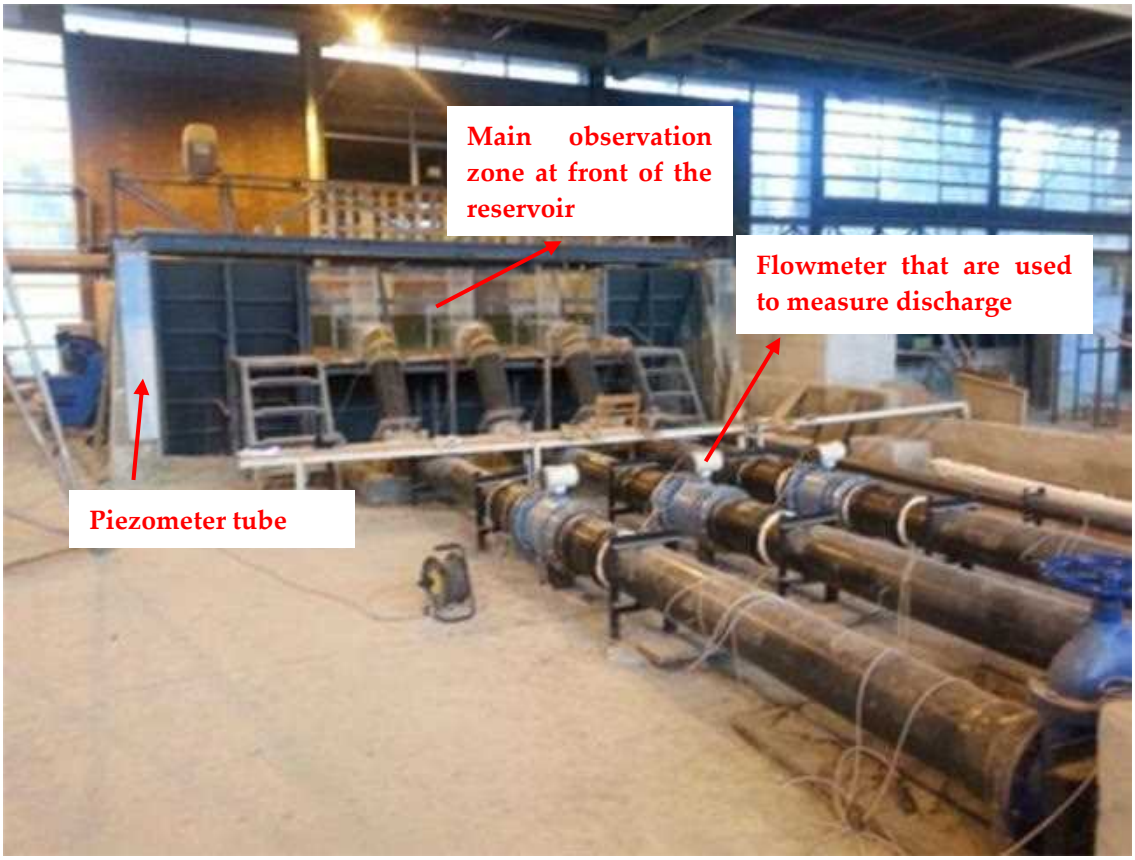


Figure 2. The downstream view of the experimental setup used by Gogus and Gokmener [1]

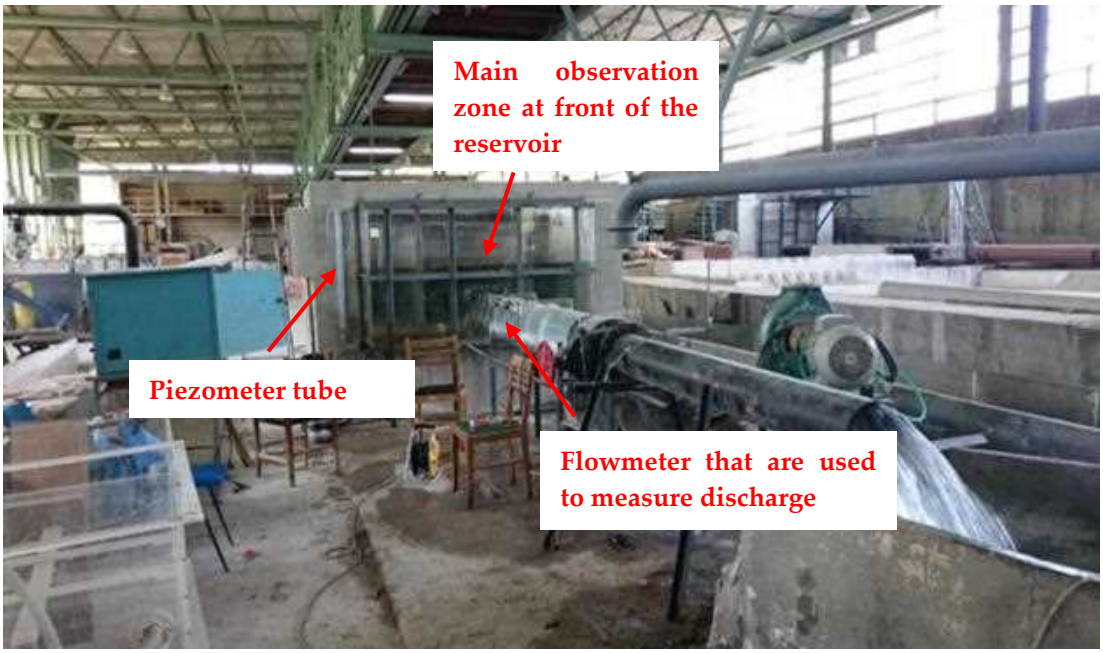


Figure 3. The downstream view of the experimental setup used by Haspolat and Gogus [18]

2.3. Statistical Performance Indicators

In order to assess the accuracy and reliability of empirical equations, several statistical performance indicators were employed. These indicators provide a comprehensive assessment of the equation's predictive performance [24].

2.3.1 Coefficient of Correlation (R^2)

The coefficient of determination (R^2) measures the proportion of the variance in the observed data that the model explains. An R^2 value closer to 1 indicates a better fit between the observed and predicted values [25].

$$R^2 = 1 - \frac{\sum_{i=1}^{n}\left(\left(\frac{S_c}{D_i}\right)_{obs,i} - \left(\frac{S_c}{D_i}\right)_{pred,i}\right)^2}{\sum_{i=1}^{n}\left(\left(\frac{S_c}{D_i}\right)_{obs,i} - \overline{\left(\frac{S_c}{D_i}\right)_{obs}}\right)^2} \quad (5)$$

where $\left(\frac{S_c}{D_i}\right)_{obs,i}$ is the observed (measured) value, $\left(\frac{S_c}{D_i}\right)_{pred,i}$ is the predicted (calculated) value, $\overline{\left(\frac{S_c}{D_i}\right)_{obs}}$ is the average of observed values and n is the number of data (observations).

2.3.2 Standard Error of Regression (SER)

The standard error of regression (SER) represents the standard deviation of the residuals (errors) and indicates the typical size of prediction errors made by the model. Lower SER values reflect better model performance.

$$SER = \sqrt{\frac{\sum_{i=1}^{n}\left(\left(\frac{S_c}{D_i}\right)_{obs,i} - \left(\frac{S_c}{D_i}\right)_{pred,i}\right)^2}{n-2}} \tag{6}$$

2.3.3 Mean Absolute Percentage Error (MAPE)

The mean absolute percentage error (MAPE) demonstrates the prediction error as a percentage and provides a normalized measure of prediction accuracy. A lower MAPE value indicates higher prediction accuracy.

$$MAPE = \frac{100}{n}\sum_{i=1}^{n}\left|\frac{\left(\frac{S_c}{D_i}\right)_{obs,i} - \left(\frac{S_c}{D_i}\right)_{pred,i}}{\left(\frac{S_c}{D_i}\right)_{obs,i}}\right| \tag{7}$$

2.3.4 Average Absolute Deviation (AAD)

The average absolute deviation (AAD) measures the average magnitude of errors in a set of predictions, without considering their direction. Smaller AAD values imply that the model predictions are close to the observed data.

$$AAD = \frac{1}{n}\sum_{i=1}^{n}\left|\left(\frac{S_c}{D_i}\right)_{obs,i} - \left(\frac{S_c}{D_i}\right)_{pred,i}\right| \tag{8}$$

2.3.5 Root Mean Square Error (RMSE)

The root mean square error (RMSE) is another measure of the differences between observed and predicted values. It penalizes larger errors more severely than AAD. A lower RMSE indicates a better predictive capability of the model.

$$RMSE = \sqrt{\frac{1}{n}\sum_{i=1}^{n}\left(\left(\frac{S_c}{D_i}\right)_{obs,i} - \left(\frac{S_c}{D_i}\right)_{pred,i}\right)^2} \tag{9}$$

3. RESULTS AND DISCUSSION

225 experimental data from Haspolat and Gogus [18] and Gogus and Gokmener [1] were evaluated to investigate the effect of approach Froude number, intake Froude number, Reynolds number, Weber number and geometrical parameter on dimensionless critical submergence at single horizontal intakes under asymmetrical approach flow conditions. Moreover, various empirical equations were generated to predict dimensionless critical submergence, S_c/D_i. The ranges of significant flow and geometric parameters are listed in Table 1.

Table 1. Ranges of significant hydraulic and geometric parameters analyzed in the study under asymmetrical approach flow conditions

	Range							
D_i (cm)	Q_i (lt/s)	S_c/Di	$(Fr)_{app}$	$(Fr)_i$	Re	We	ψ	No. of Observations
30	66.31 ~ 24.95	1.81 ~ 0.41	0.070 ~ 0.029	0.55 ~ 0.21	281439 ~ 105895	3620 ~ 513	3.06 ~ 1.50	32
26.5	126.81 ~ 68.67	2.47 ~ 1.08	0.052 ~ 0.016	1.43 ~ 0.77	609260 ~ 329921	19206 ~ 5632	7.92 ~ 2.01	34
25	52.98 ~ 24.27	1.08 ~ 0.35	0.114 ~ 0.031	0.69 ~ 0.32	268875 ~ 123169	3997 ~ 839	4.46 ~ 1.03	88
10	45.03 ~ 11.63	3.21 ~ 1.29	0.130 ~ 0.032	5.79 ~ 1.50	573617 ~ 148120	45116 ~ 3008	9.17 ~ 2.80	43
5	14.33 ~ 4.07	4.40 ~ 1.32	0.081 ~ 0.034	10.43 ~ 2.96	365146 ~ 103697	36564 ~ 2949	14.40 ~ 5.60	28

Moreover, geometrical and hydraulic data from 20 experiments conducted under asymmetrical approach flow conditions are randomly presented in Table 2.

Table 2. Example data from the experiments conducted under asymmetrical approach flow conditions

b_1 (cm)	b_2 (cm)	D_i (cm)	ψ	Q (lt/s)	V_i (m/s)	V_{app} (m/s)	$(Fr)_{app}$	$(Fr)_i$	R_e	W_e	$(S_c/D_i)_{measured}$
40	120	26.5	2.010	124.44	2.26	0.104	0.038	1.40	597915	18498	1.77
40	120	26.5	2.010	110.00	1.99	0.105	0.041	1.24	528515	14453	1.48
40	120	26.5	2.010	100.56	1.82	0.100	0.040	1.13	483137	12078	1.38
40	120	26.5	2.010	87.19	1.58	0.092	0.038	0.98	418941	9081	1.23
40	120	26.5	2.010	78.81	1.43	0.086	0.036	0.89	378635	7418	1.17
60	70	25	4.457	35.22	0.72	0.068	0.034	0.46	178727	1766	0.60
60	70	25	4.457	37.58	0.77	0.069	0.034	0.49	190743	2011	0.68
60	70	25	4.457	41.66	0.85	0.073	0.035	0.54	211418	2471	0.75
60	70	25	4.457	45.89	0.94	0.077	0.036	0.60	232890	2999	0.83
60	70	25	4.457	49.38	1.01	0.082	0.038	0.64	250634	3473	0.86
20	30	10	3.333	42.49	5.41	0.202	0.099	5.47	541278	40172	3.21
20	30	10	3.333	36.79	4.69	0.191	0.098	4.73	468629	30112	2.86
20	30	10	3.333	32.15	4.10	0.220	0.130	4.14	409549	22998	1.92
20	30	10	3.333	27.04	3.45	0.192	0.116	3.48	344450	16268	1.81
20	30	10	3.333	22.92	2.92	0.172	0.107	2.95	292036	11694	1.66
20	30	10	3.333	16.64	2.12	0.133	0.084	2.14	211944	6159	1.51
20	40	10	3.000	45.03	5.74	0.208	0.110	5.79	573617	45116	2.61
20	40	10	3.000	37.58	4.79	0.176	0.094	4.83	478765	31429	2.56
20	40	10	3.000	32.91	4.19	0.163	0.090	4.23	419188	24094	2.36
20	40	10	3.000	27.04	3.45	0.140	0.078	3.48	344450	16268	2.23

3.1. Variation of S_c/D_i with Dimensionless Flow and Geometric Parameters

Variations of dimensionless critical submergence, S_c/D_i, with approach Froude number $(Fr)_{app}$, intake Froude number $(Fr)_i$, Reynolds numbers, Re, and Weber number, We, are illustrated in Figures 4-7, respectively. Figure 4 presents the relationship between S_c/D_i and $(Fr)_{app}$. For S_c/D_i values lower than 1, S_c/D_i values are almost identical regardless of an increment on the $(Fr)_{app}$. On the other hand, when S_c/D_i values are greater than 1, the relationship between S_c/D_i and $(Fr)_{app}$ becomes complex under asymmetrical approach flow conditions. The data points display a relatively stable trend, with S_c/D_i values greater than 1 while $(Fr)_{app}<0.07$, where S_c/D_i values generally tend to increase with increasing $(Fr)_{app}$. However, when $(Fr)_{app}$ values are greater than 0.05, the variability in critical submergence becomes more pronounced, indicating a potential influence of additional governing parameters, such as intake geometry or asymmetric flow conditions. The absence of a clear monotonic trend suggests that the relationship between these parameters under asymmetrical approach flow conditions is non-trivial, likely governed by complex hydrodynamic interactions rather than a simple functional dependence.

The correlations between S_c/D_i and intake Froude number $(Fr)_i$, Reynolds number, Re, and Weber number, We, are illustrated in Figures 5-7, respectively. In Figure 5, S_c/D_i generally increases with $(Fr)_i$, showing a scattered but upward trend, particularly for $(Fr)_i$ values above 2. Conversely, according to Figure 6, it is possible to mention that S_c/D_i values generally increase with the increment of Re, especially when S_c/D_i values are lower than 1 or Re values are greater than 300000. However, for the Re values greater than 200000 and S_c/D_i values greater than 1, a transition zone is observed, and the spread of data shows an irregular distribution. Obtaining smaller S_c/D_i values where the Re values are smaller than 200000 can be explained by relatively low turbulence and high stability of the approach flow caused by larger sidewall clearances or large intake pipe diameters, where the intake velocity is small. However, when Reynolds number exceeds 200000, the turbulence becomes more significant along with the geometrical considerations such as sidewall clearance, intake pipe diameter and asymmetry degree on critical submergence. Thus, strong increments are obtained for S_c/D_i values with increasing Re.

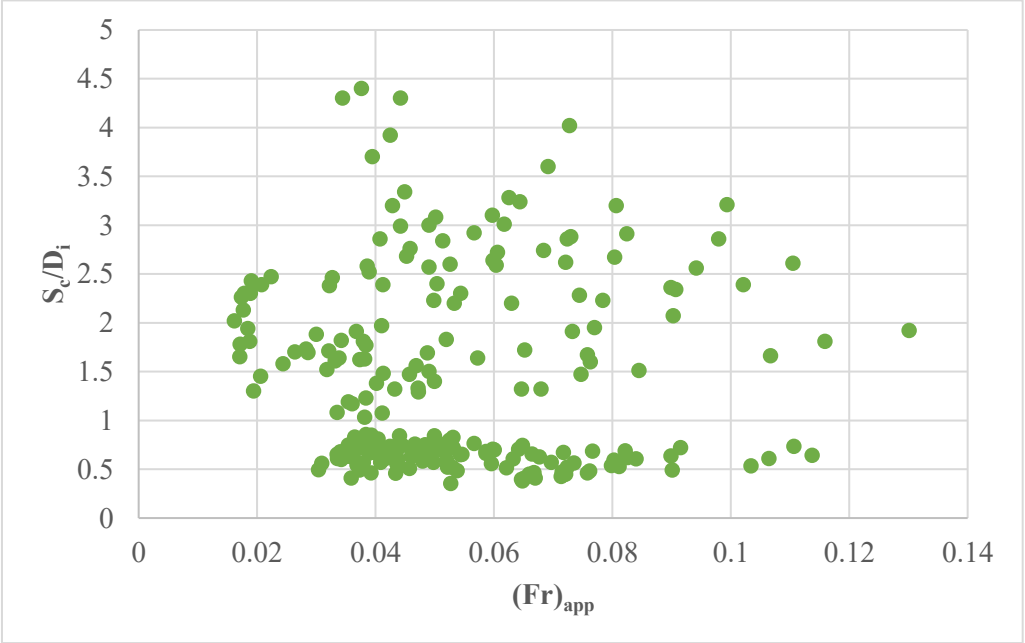


Figure 4. Variation of dimensionless critical submergence, S_c/D_i vs. $(Fr)_{app}$ under asymmetrical approach flow conditions

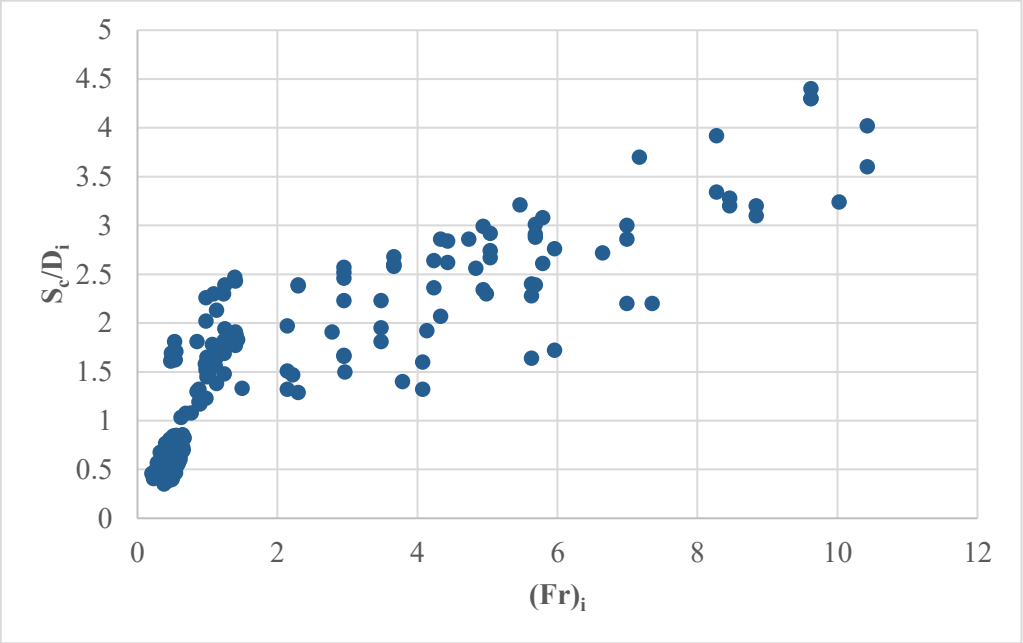


Figure 5. Variation of dimensionless critical submergence, S_c/D_i vs. $(Fr)_i$ under asymmetrical approach flow conditions

Finally, Figure 7, which presents the relationship between S_c/D_i and We demonstrates a similar trend to Figure 5, where higher We values correspond to greater S_c/D_i values. Across Figures 5-7, a lower S_c/D_i value indicates small flow parameter values, suggesting a regime where submergence remains relatively low before increasing with flow intensity. The variability of S_c/D_i values for given $(Fr)_i$, Re and We, particularly at intermediate values, indicates the influence of additional governing factors such as turbulence, surface tension effects, or asymmetric intake conditions.

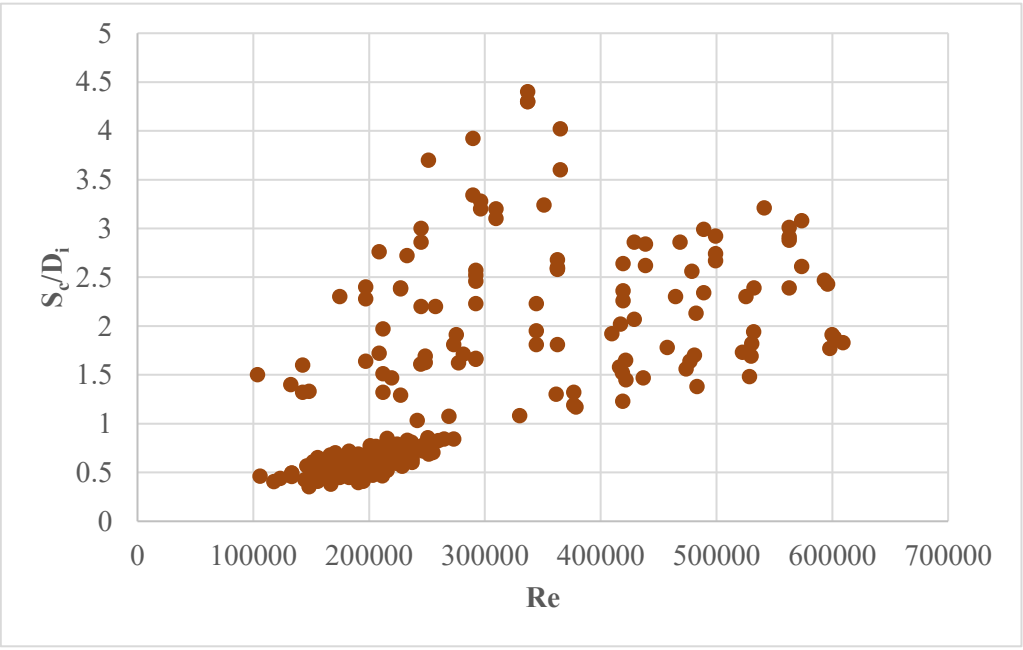


Figure 6. Variation of dimensionless critical submergence, S_c/D_i vs. Re under asymmetrical approach flow conditions

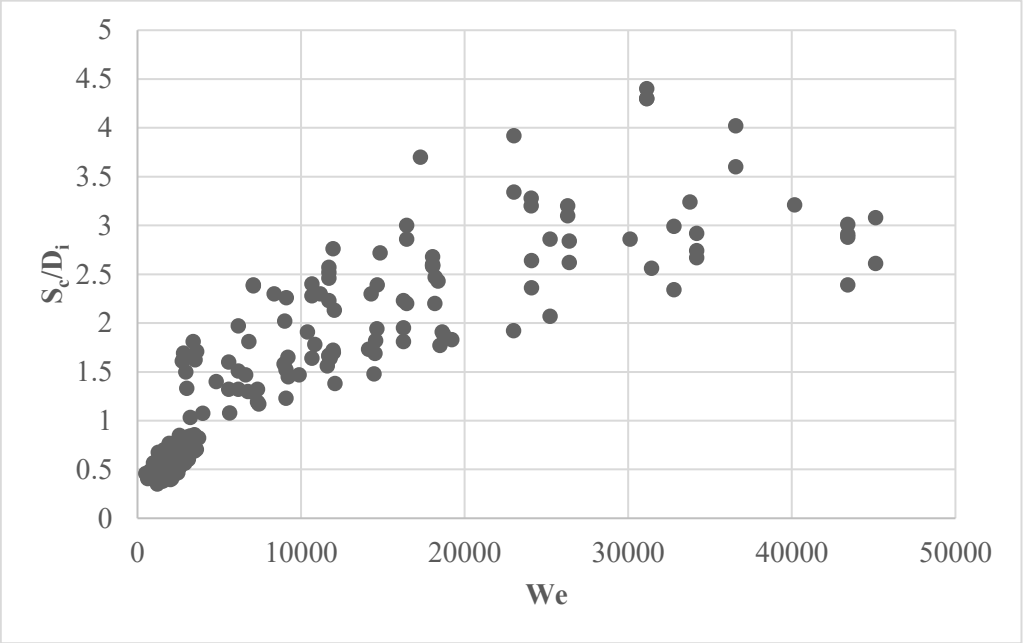


Figure 7. Variation of dimensionless critical submergence, S_c/D_i vs. We under asymmetrical approach flow conditions

Figure 8 illustrates the variation of Sc/Di as a function of the (Fr)i for varying dimensionless geometric parameter, ψ, values while Di≤ 10 cm. From the figure, it can be clearly seen that as the (Fr)i increases, Sc/Di also increases under asymmetrical approach flow conditions. This indicates that higher-energy flow conditions require greater submergence to avoid any air-entraining vortices from forming at the intake. In other words, greater (Fr)i values correspond to stronger inertial forces, increasing the tendency for vortex formation. Consequently, a greater submergence is required to suppress vortex formation, thereby ensuring stable flow conditions at the intake. The geometric parameter ψ, defined as ψ = (b1 + b2) (b1/b2)/Di, accounts for the sidewall clearance and the asymmetric degree of the intake structure. Greater ψ values indicate wider or lower asymmetric intake structures, influencing flow convergence and vortex development. A detailed analysis of the data reveals that for small ψ values ($2 < \psi < 5$), the corresponding Sc/Di values are relatively low, and these points are predominantly observed at lower (Fr)i values than 6. This suggests that narrower intake structures require lower submergence in low-energy flow conditions. On the other hand, greater ψ values ($\psi > 5$) are observed within the range of all tested (Fr)i values ($1.5 < (Fr)i < 10.5$) This scattered trend may be explained because of the reduced asymmetry, leading to relatively weaker vortices on the approach flow conditions, which leads formation of air-entraining vortices even at relatively lower (Fr)i values. While (Fr)i values are smaller than 6, Sc/Di values generally increase with increasing ψ value within the range of $2 < \psi < 5$. However, for ψ values exceeding 5, Sc/Di values are independent of intake geometry because of the aforementioned situation. On the contrary, for (Fr)i values greater than 6, the development of air-entraining vortices is observed for only ψ values greater than 5. In this range, the general trend shows that as ψ values are increased Sc/Di values are increasing for a given (Fr)i value.

Variation of S_c/D_i with $(Fr)_i$ for varying ψ while $D_i > 10$ cm under asymmetrical approach flow conditions is demonstrated in Figure 9. While $(Fr)_i$ values are smaller than 0.8, the formation of air-entraining vortices is observed for the narrower sidewall clearances ($1 < \psi < 5$). On the other hand, for the ψ values greater than 5, air-entraining vortices occur for the $(Fr)_i$ values greater than 0.8. For the cases of $(Fr)_i < 0.5$ and $\psi < 5$, S_c/D_i values are close to each other for a given $(Fr)_i$. Therefore, this situation indicates that the effect of intake geometry is low compared to the intake Froude number for smaller $(Fr)_i$ values. However, when $(Fr)_i$ values exceed 0.8, S_c/D_i values increase with increasing ψ for a given $(Fr)_i$. As the only exception, the obtained S_c/D_i values for $\psi > 6$ fall at similar points with the obtained S_c/D_i values for $2 < \psi < 4$ and lower points with the S_c/D_i values for $4 < \psi < 6$ for a given $(Fr)_i$. This situation can be explained

by the decreased effect of sidewall clearances as the sidewall clearance increases. As the distance between the intake and the sidewalls increases, the flow separations occurring along the sidewalls dissipate before reaching the intake entrance, thereby reducing the likelihood of vortex formation. Moreover, as the sidewall clearance increases, the approach flow area becomes wider, which weakens the rotational characteristics of the flow. Thus, the air-entraining vortices occur at lower submergence for wider sidewall clearances after a limit for a given $(Fr)_i$.

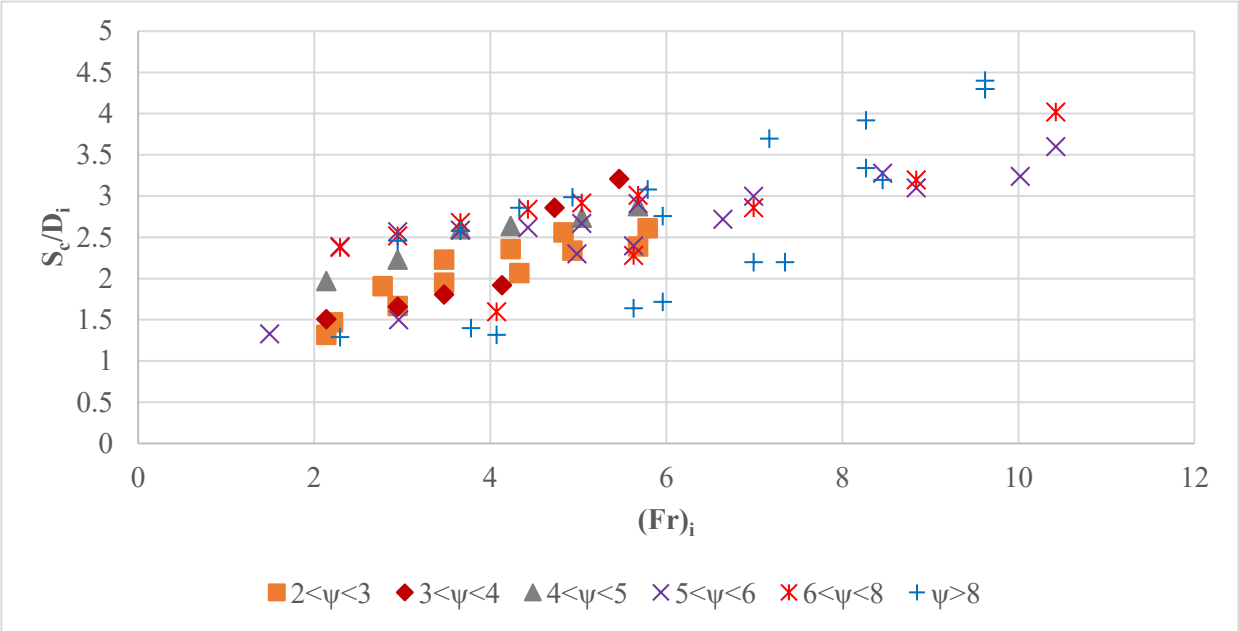


Figure 8. Variation of S_c/D_i with $(Fr)_i$ for varying ψ while $D_i \leq 10$ cm under asymmetrical approach flow conditions

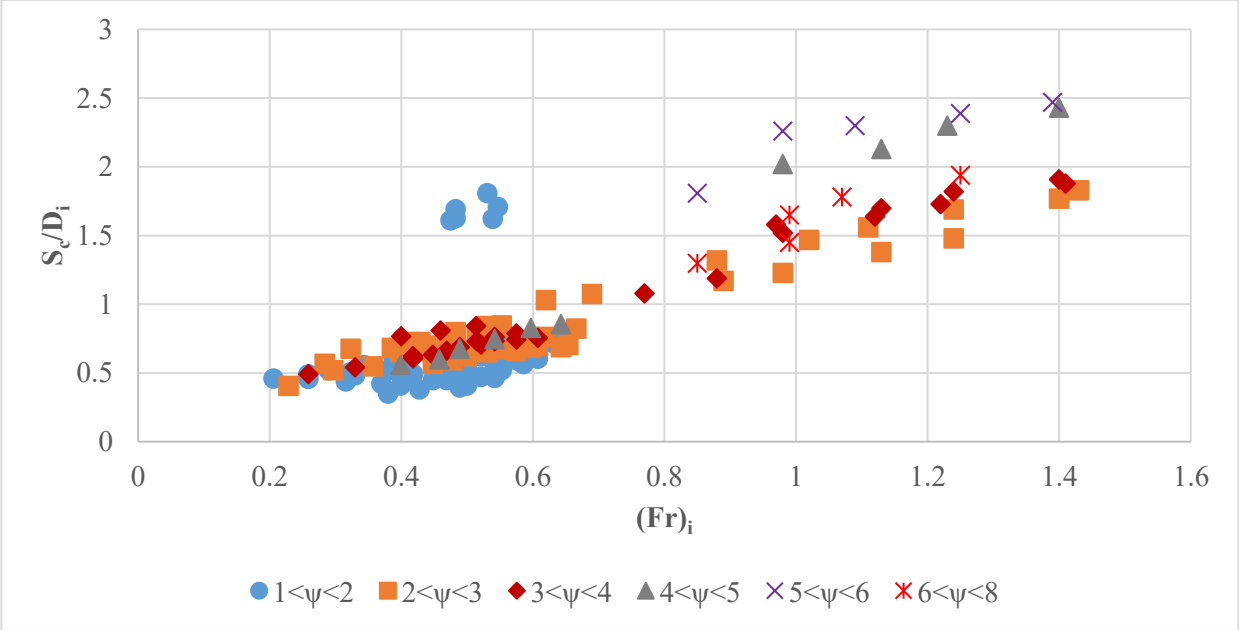


Figure 9. Variation of S_c/D_i with $(Fr)_i$ for varying ψ while $D_i > 10$ cm under asymmetrical approach flow conditions

The relationship between S_c/D_i and $(Fr)_i$ for varying ψ values for all tested intake pipe diameters is demonstrated in Figure 10. The graph reveals a generally positive correlation between the S_c/D_i and $(Fr)_i$. As $(Fr)_i$ increases, so does S_c/D_i, indicating that higher flow energy necessitates greater submergence depths to avoid the formation of air-entraining vortices. This trend is physically consistent, as higher intake Froude numbers imply stronger inertial forces, which intensify surface disturbances and increase the potential for vortex formation. Consequently, higher submergence is required to maintain intake efficiency and suppress vortex development. The influence of geometry is clearly illustrated through the classification of data by the dimensionless geometric parameter ψ. At low ψ values (i.e., $1< \psi <2$), which correspond to narrower sidewall clearances, the data show relatively high S_c/D_i values even at low and $(Fr)_i$ values. This suggests that narrower geometries promote stronger vortex activity due to more pronounced sidewall effects, resulting in the earlier onset of air entrainment. Under such conditions, a higher submergence depth is necessary to mitigate vortex formation. In the intermediate range of ψ (approximately $2 < \psi < 6$), both hydraulic and geometric influences appear to interact more dynamically. Data in this range show greater dispersion, indicating that in addition to $(Fr)_i$ and ψ, other flow parameters such as the Reynolds and Weber numbers may also play a role in determining critical submergence. This variability suggests that moderate geometries are more sensitive to changes in secondary hydraulic factors. For greater values of ψ (i.e., $\psi > 8$), which represent wider sidewall clearances, the observed (S_c/D_i) values tend to be lower, even at greater $(Fr)_i$ values. This trend reflects improved flow stability associated with broader approach flow zones. In such configurations, the distance between the intake and the sidewalls reduces the impact of boundary layer separation near the walls. As a result, separation vortices dissipate before reaching the intake entrance, minimizing their contribution to vortex formation. Additionally, a greater sidewall spacing provides a wider approach flow area, which weakens the rotational component of the flow and suppresses vortex strength. Physically, narrow geometries cause the flow to closely interact with sidewalls, where boundary layer separation is more likely to generate coherent rotational structures near the intake. These vortices can evolve into air-entraining vortices if the submergence is insufficient. However, when the distance between the intake and the sidewalls increases, these flow separations dissipate before affecting the intake. Moreover, wider geometries allow the approach flow to develop more uniformly and symmetrically, thereby reducing the intensity and likelihood of vortex formation. Consequently, lower submergence depths are sufficient to maintain stable operation under these conditions. In summary, the graph provides a comprehensive depiction of how both hydraulic conditions and structural geometry influence critical submergence. These findings prove the importance of considering sidewall clearance in the design of horizontal intake structures. Wider geometries not only reduce the risk of vortex formation but also enable more efficient and stable hydraulic performance by lowering the submergence requirement under asymmetrical approach flow conditions.

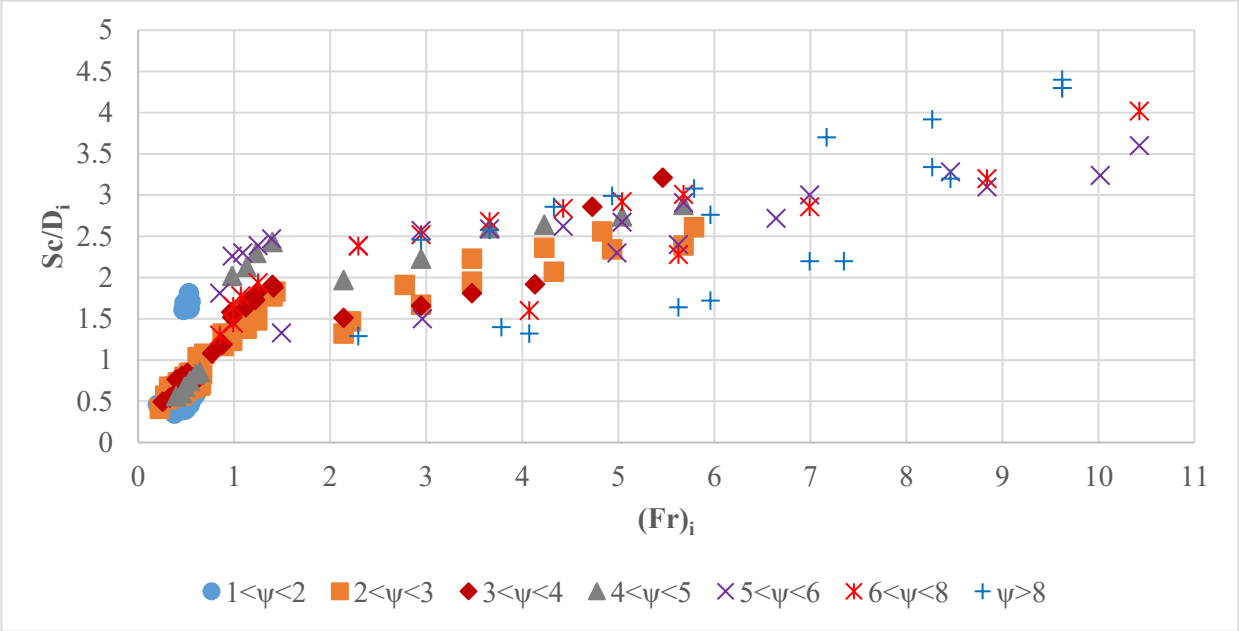


Figure 10. Variation of S_c/D_i with $(Fr)_i$ for varying ψ under asymmetrical approach flow conditions

3.2. Derivation of Empirical Formulas to Predict Dimensionless Critical Submergence, S_c/D_i

In order to predict S_c/D_i for single horizontal intake structures under asymmetrical approach flow conditions, ten empirical equations are derived as a function of $(Fr)_{app}$, $(Fr)_i$, Re, We and ψ with varying combinations by applying non-linear regression in MATLAB. The raw empirical equations that are obtained from Equation (4) are provided below:

$$\frac{S_C}{D_i} = \left(Fr_{app}\right)^a (Fr)_i{}^b (Re)^c (We)^d (\psi)^e \quad (10)$$

where a, b, c, d and e are the regression coefficients.

Then, the combinations are generated by excluding We, Re, ψ and $(Fr)_i$, respectively. Afterwards, the same procedure is repeated without considering $(Fr)_{app}$. In this case, the empirical equations are generated by excluding We, Re and ψ and $(Fr)_i$, respectively:

$$\frac{S_C}{D_i} = (Fr)_i{}^a (Re)^b (We)^c (\psi)^d \quad (11)$$

where a, b, c and d are the regression coefficients.

Table 3 presents a comparative assessment of various empirical equations developed to predict the dimensionless critical submergence, S_c/D_i, for horizontal intake structures under asymmetrical approach flow conditions. Each equation incorporates different combinations of hydraulic and geometric parameters such as the $(Fr)_{app}$, $(Fr)_i$, Re, We and ψ. Their predictive performances are evaluated using several statistical indicators, including the correlation coefficient (R^2), standard error of regression (SER), mean absolute percentage error (MAPE), average absolute deviation (AAD), and root mean square error (RMSE).

Table 3. Derived empirical equations with their performance indicators

No	Equation	R^2	SER	MAPE	AAD	RMSE
(12)	$\frac{S_C}{D_i} = \left(Fr_{app}\right)^{-0.488} (Fr)_i^{0.214} (Re)^{-0.488} (We)^{0.576} (\psi)^{-0.158}$	0.949	0.220	11.98%	0.149	0.218
(13)	$\frac{S_C}{D_i} = \left(Fr_{app}\right)^{-0.589} (Fr)_i^{0.696} (Re)^{-0.102} (\psi)^{-0.313}$	0.895	0.316	22.04%	0.243	0.314
(14)	$\frac{S_C}{D_i} = \left(Fr_{app}\right)^{-0.093} (Fr)_i^{0.508} (\psi)^{-0.061}$	0.847	0.381	29.74%	0.310	0.378
(15)	$\frac{S_C}{D_i} = \left(Fr_{app}\right)^{-0.067} (Fr)_i^{0.479}$	0.846	0.382	29.47%	0.308	0.380
(16)	$\frac{S_C}{D_i} = \left(Fr_{app}\right)^{-0.118}$	0.002	0.969	83.55%	0.820	0.967
(17)	$\frac{S_C}{D_i} = (Fr)_i^{-0.089} (Re)^{-0.459} (We)^{0.665} (\psi)^{0.201}$	0.904	0.303	16.28%	0.209	0.300
(18)	$\frac{S_C}{D_i} = (Fr)_i^{0.457} (Re)^{0.009} (\psi)^{0.062}$	0.833	0.398	27.85%	0.308	0.395
(19)	$\frac{S_C}{D_i} = (Fr)_i^{0.443} (\psi)^{0.133}$	0.829	0.402	25.00%	0.297	0.401
(20)	$\frac{S_C}{D_i} = (Fr)_i^{0.576}$	0.801	0.433	19.31%	0.291	0.432
(21)	$\frac{S_C}{D_i} = 1.182\ (Fr)_i^{0.493}$	0.827	0.405	27.53%	0.313	0.403

Among all equations, Equation (12) exhibits the highest predictive accuracy with an R^2 value of 0.949 and minimal error metrics (SER = 0.220, MAPE = 11.98%, RMSE = 0.218). This equation includes a comprehensive set of parameters: $(Fr)_{app}$, $(Fr)_i$, Re, We and ψ, indicating that a full representation of both flow dynamics and geometrical configuration enhances the equation's reliability. Similarly, Equation (17) also shows robust performance (R^2=0.904), and includes $(Fr)_i$, Re, We and ψ, making it a practical yet accurate alternative. These models reinforce the notion that the inclusion of multiple flow and geometry-related variables significantly improves the prediction of critical submergence. In contrast, Equation (16), which relies solely on the approach Froude number, $(Fr)_{app}$, yields an extremely low R^2 value of 0.002, indicating that $(Fr)_{app}$ alone has negligible explanatory power for predicting S_c/D_i. Even Equation (15), which involves $(Fr)_{app}$ and $(Fr)_i$ achieves only moderate accuracy (R^2=0.846) and relatively high MAPE and RMSE values. These results suggest that while the approach Froude number may have a minor supplementary role, it is not sufficient on its own to model vortex-induced submergence behavior accurately.

Equations (20) and (21), which include only $(Fr)_i$, yield R^2 values of 0.801 and 0.827, respectively. These moderate but acceptable performance metrics suggest that the intake Froude number is the single most important parameter when predicting critical submergence, likely due to its direct relationship with the inertial forces at the intake entrance. Nevertheless, these simpler models, while useful in practice, may not be adequate in scenarios involving complex flow or geometrical interactions. As a summary, the analysis clearly highlights that incorporating a comprehensive set of parameters, particularly $(Fr)_i$, Re, We and ψ, significantly enhances the accuracy of empirical formulations for predicting dimensionless critical submergence. While simpler models may be easier to implement, their reduced predictive power limits their applicability in high-precision engineering contexts. Equation (12), by capturing the key physical mechanisms governing vortex formation, stands out as the most reliable and generalizable model for design and analysis purposes. The comparison of measured and predicted S_c/D_i values, along with error lines, are plotted in Figures 11-17.

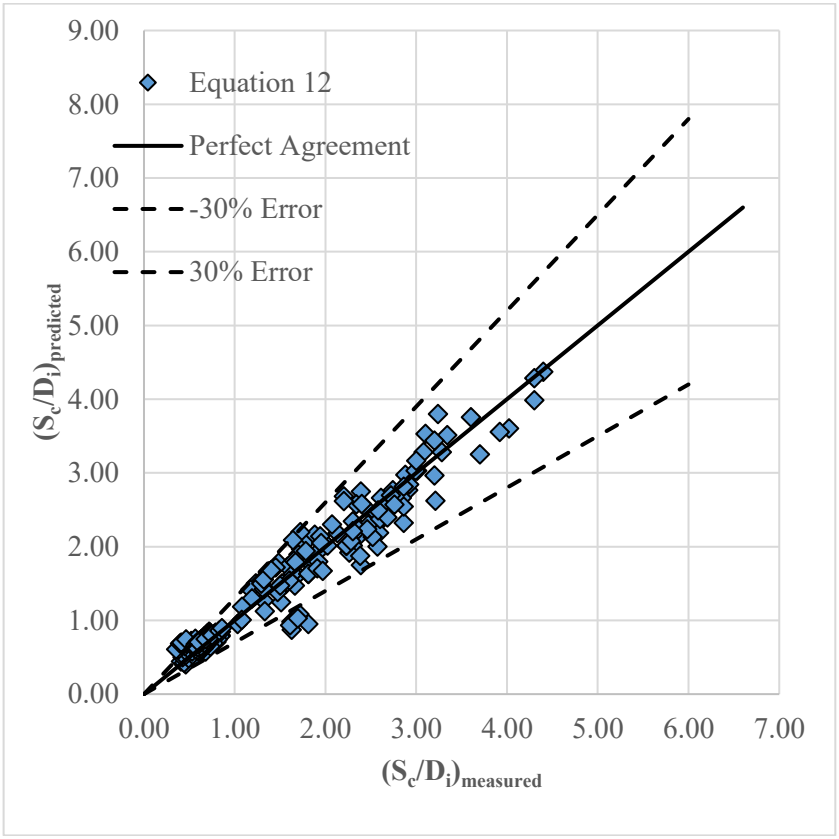


Figure 11. Comparison of $(S_c/D_i)_{measured}$ data with $(S_c/D_i)_{predicted}$ data obtained from Equation (12)

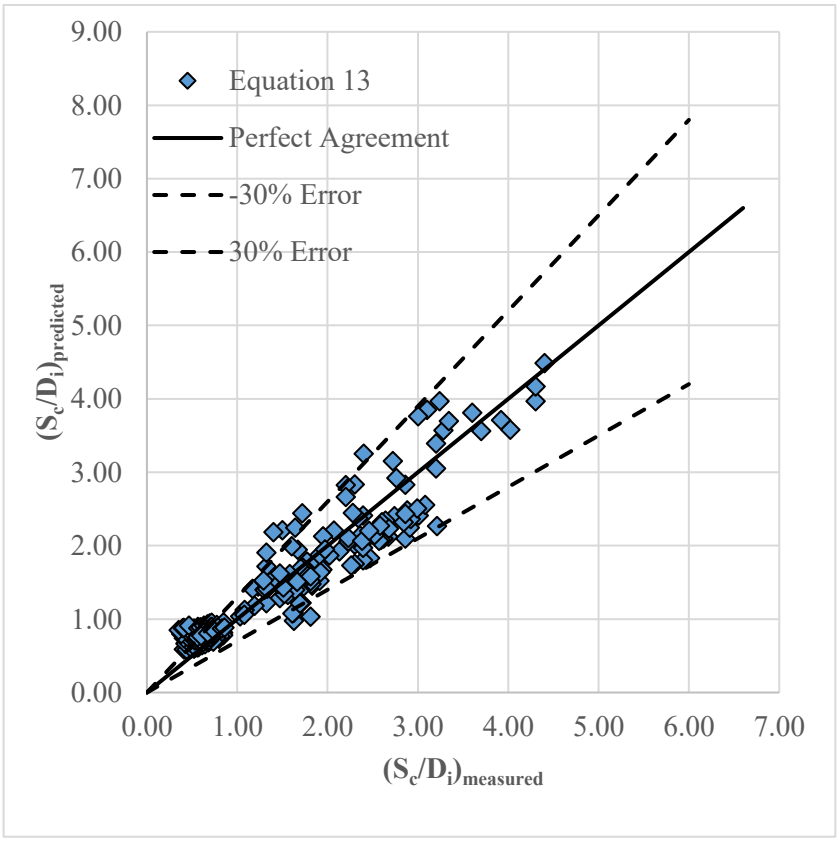


Figure 12. Comparison of $(S_c/D_i)_{measured}$ data with $(S_c/D_i)_{predicted}$ data obtained from Equation (13)

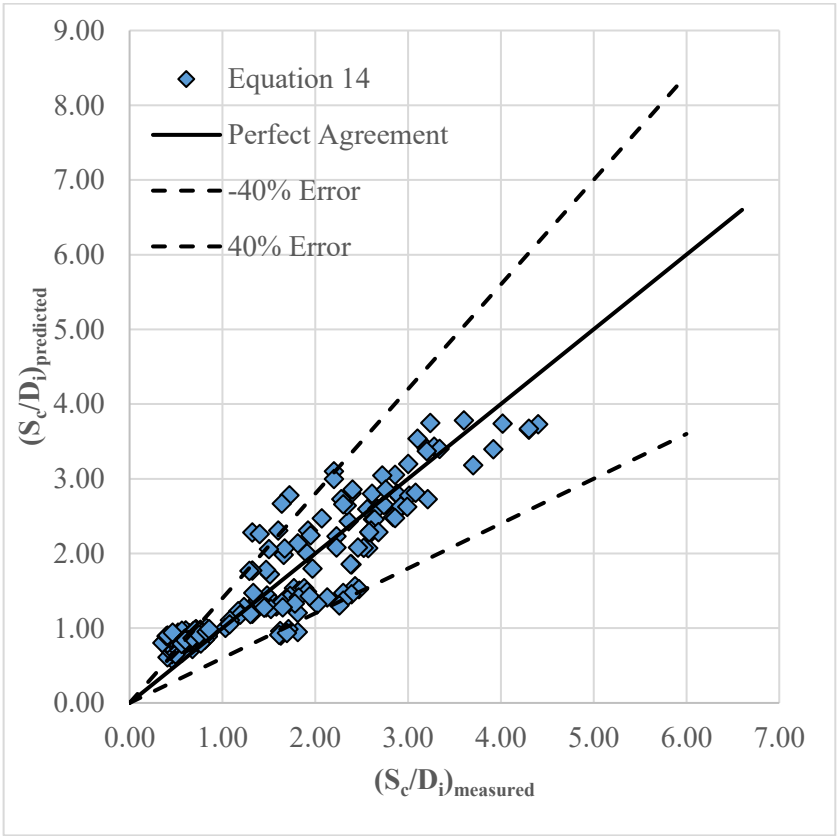


Figure 13. Comparison of $(S_c/D_i)_{measured}$ data with $(S_c/D_i)_{predicted}$ data obtained from Equation (14)

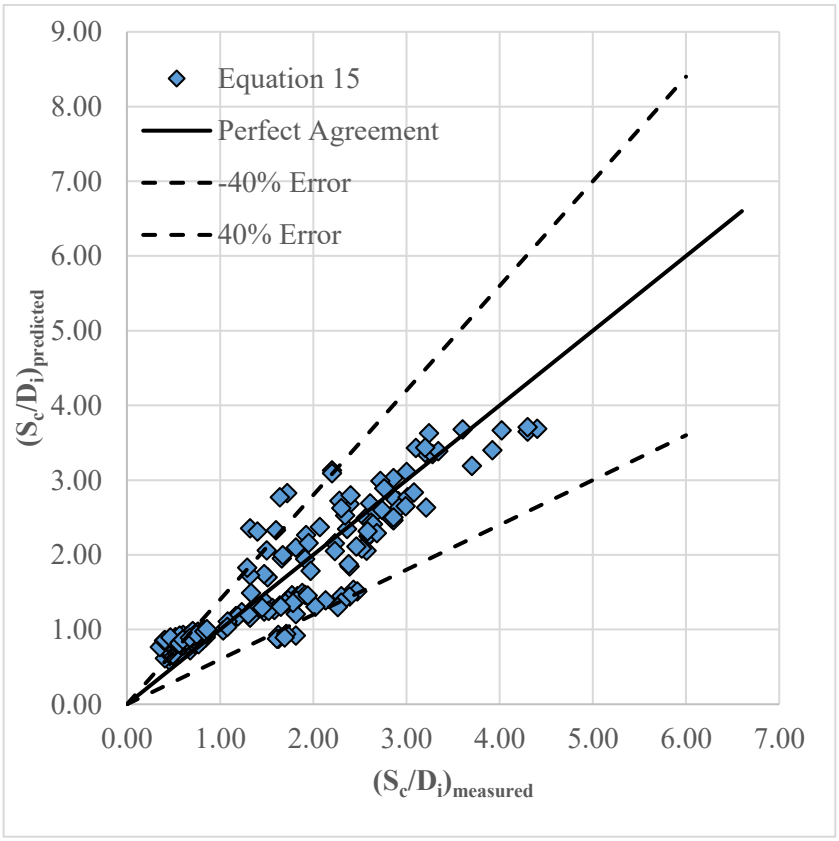


Figure 14. Comparison of $(S_c/D_i)_{measured}$ data with $(S_c/D_i)_{predicted}$ data obtained from Equation (15)

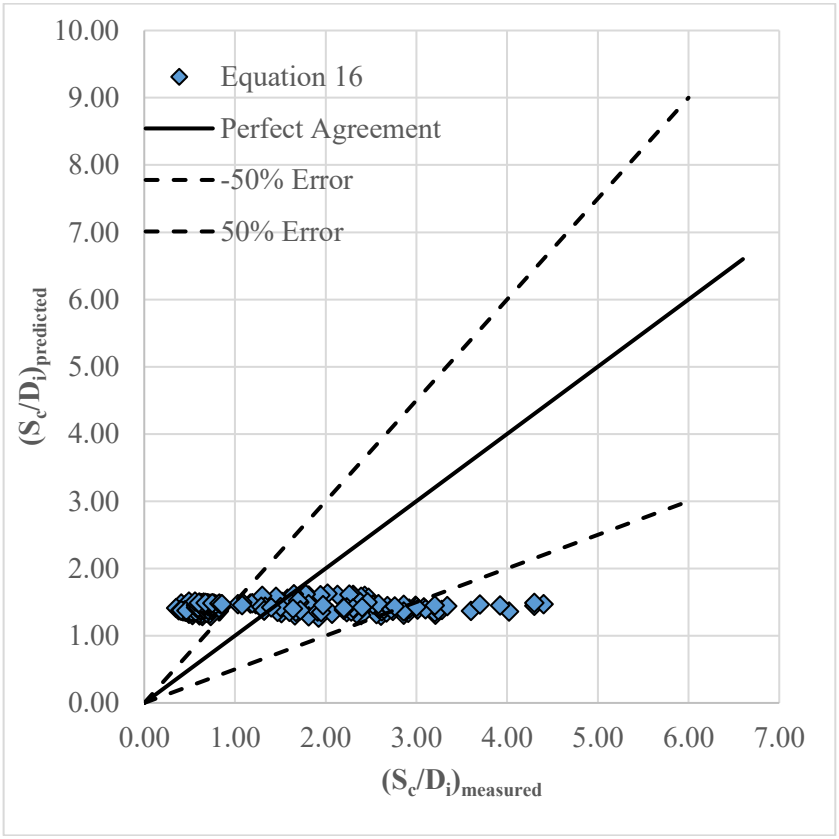


Figure 15. Comparison of $(S_c/D_i)_{measured}$ data with $(S_c/D_i)_{predicted}$ data obtained from Equation (16)

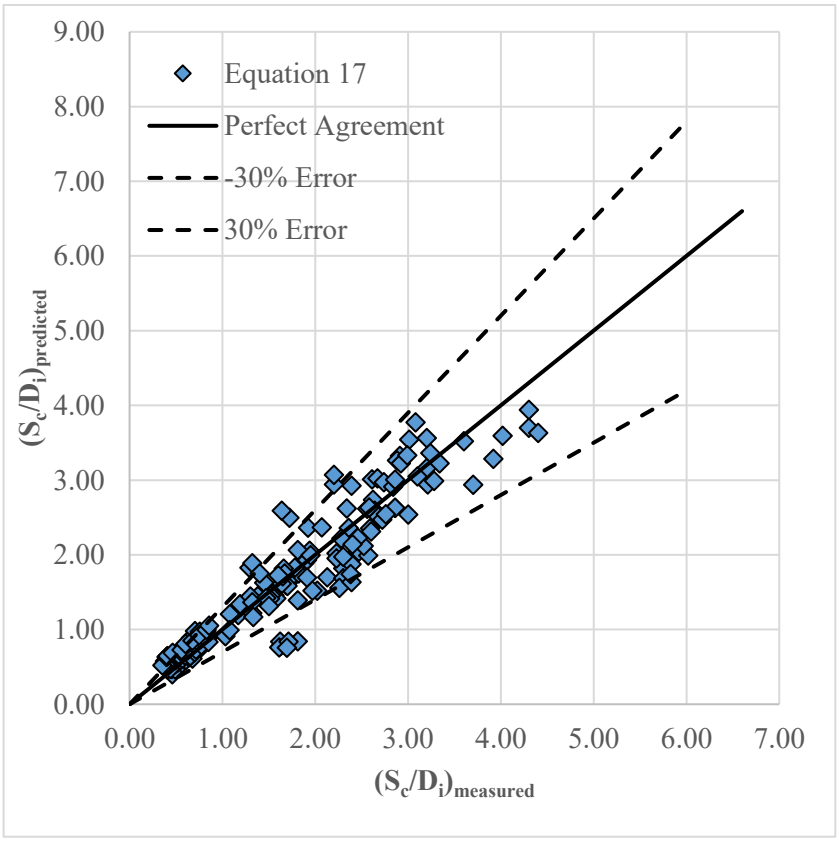


Figure 16. Comparison of $(S_c/D_i)_{measured}$ data with $(S_c/D_i)_{predicted}$ data obtained from Equation (17)

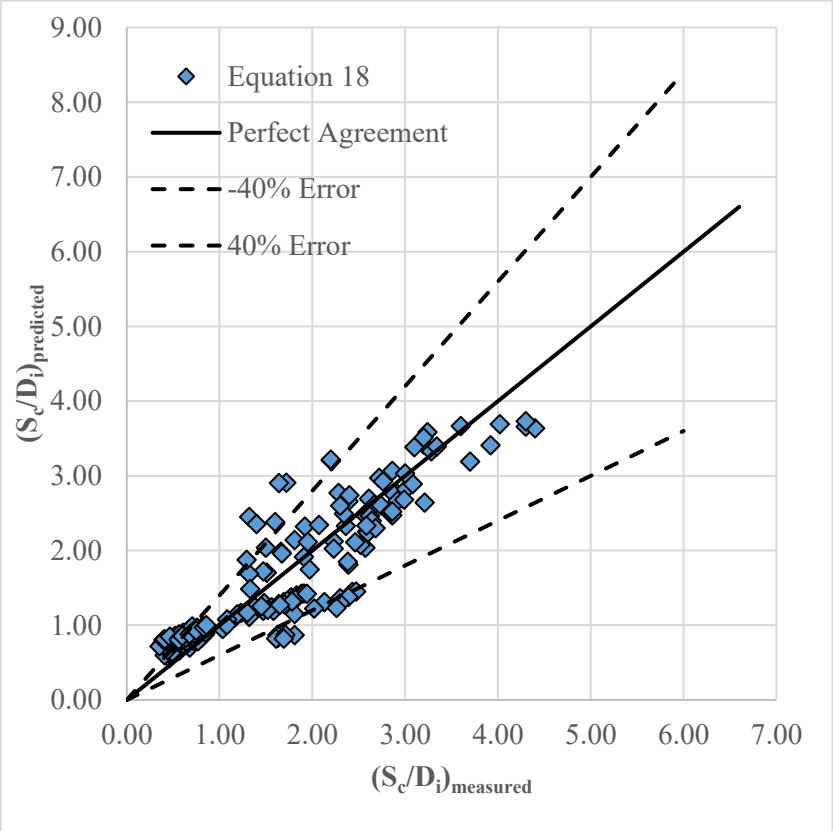


Figure 17. Comparison of $(S_c/D_i)_{measured}$ data with $(S_c/D_i)_{predicted}$ data obtained from Equation (18)

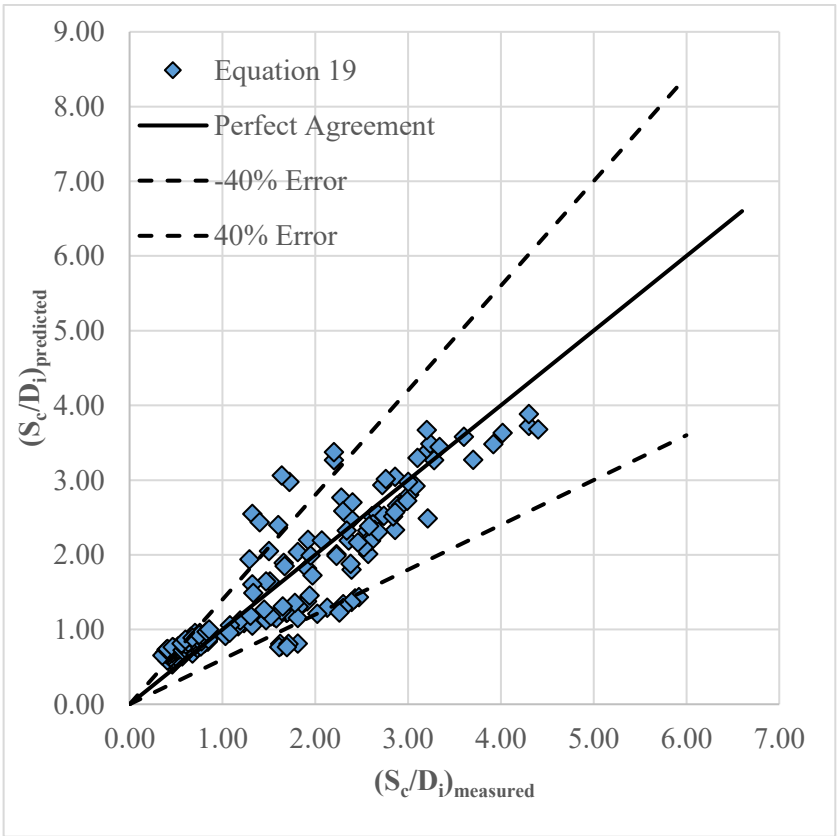


Figure 18. Comparison of $(S_c/D_i)_{measured}$ data with $(S_c/D_i)_{predicted}$ data obtained from Equation (19)

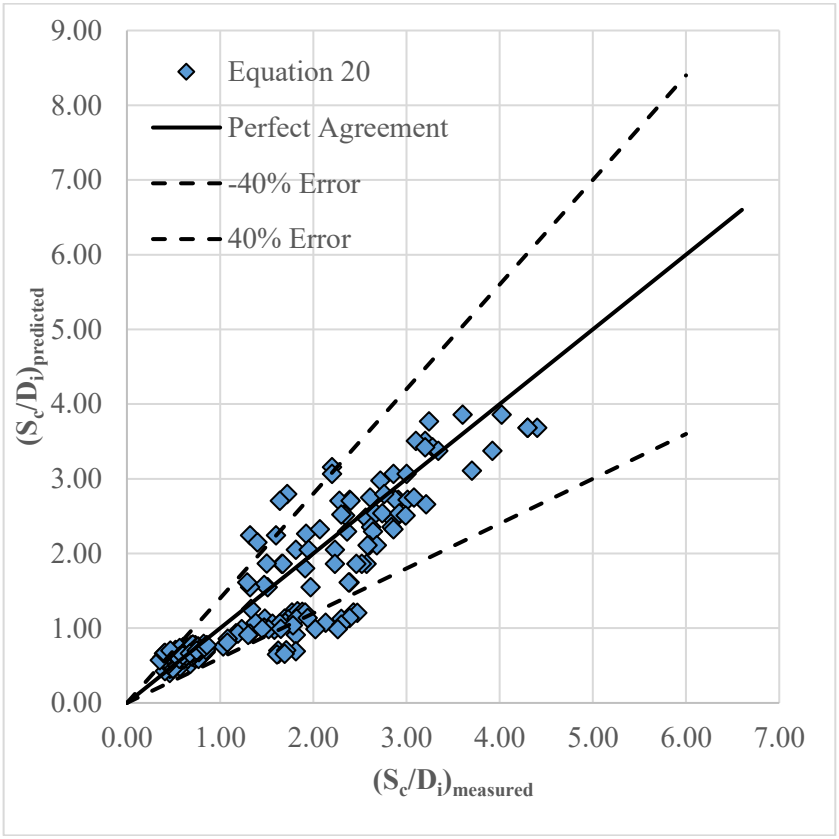


Figure 19. Comparison of $(S_c/D_i)_{measured}$ data with $(S_c/D_i)_{predicted}$ data obtained from Equation (20)

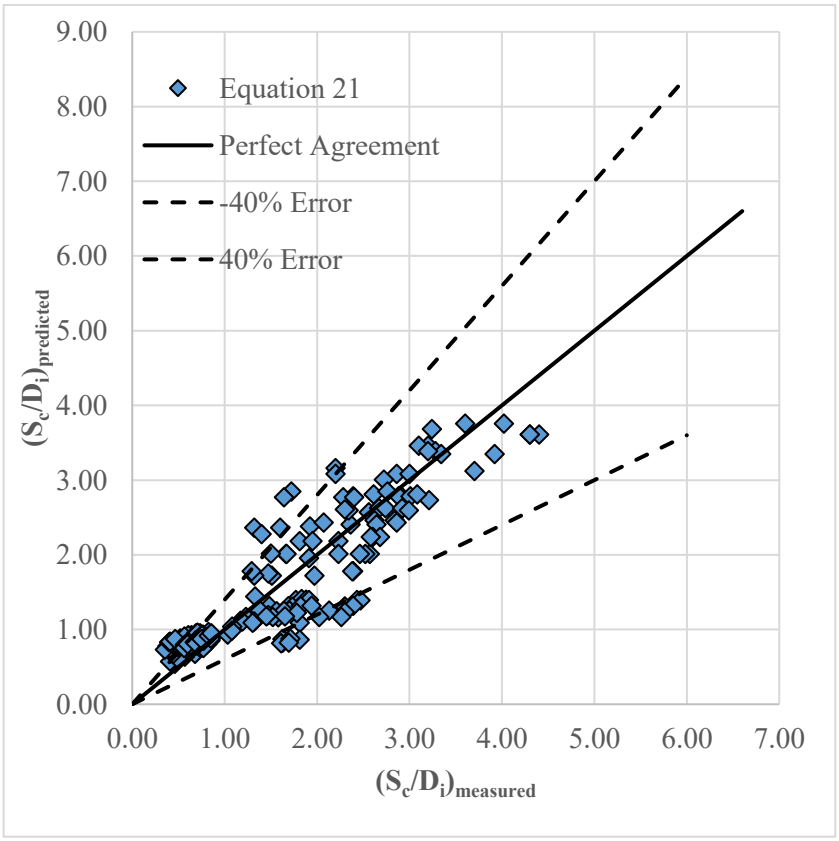


Figure 20. Comparison of $(S_c/D_i)_{measured}$ data with $(S_c/D_i)_{predicted}$ data obtained from Equation (21)

3.3 Comparison of the Present Study with the Previous Studies in the Literature

Figure 21 presents a comparative evaluation of predicted versus measured values of the dimensionless critical submergence, S_c/D_i, under asymmetrical approach flow conditions, to present the performance of Equation (17), Haspolat and Gogus [18] and Gogus and Gokmener [1] equations. Importantly, these predictions are generated by applying each study's empirical equation to the same combined dataset used for Equation (17). As seen in Figure 21, most of the data points associated with Equation (17) cluster closely around the 1:1 line and fall within the ±30% error bounds, indicating high predictive accuracy and consistency. This performance demonstrates the robustness of Equation (17), which was derived by integrating the datasets of both Haspolat and Gogus [18] and Gogus and Gokmener [1], and includes key flow and geometric parameters such as the intake Froude number, Reynolds number, and the dimensionless geometric parameter ψ. As a result, Equation (17) offers a more comprehensive and physically meaningful representation of the critical submergence phenomenon. In contrast, the predictions obtained using the original equations from both Haspolat and Gogus [18] and Gogus and Gokmener [1] display more noticeable deviations from the 1:1 line, with several points falling outside the ±30% error margins. These discrepancies suggest that while the original equations may perform well within the specific experimental conditions under which they were developed, their predictive power diminishes when applied to a broader dataset that spans varying geometries and flow regimes. This observation highlights the limitations of single-study models in terms of generalizability. Furthermore, Gogus and Gokmener's [1] equation predicts S_c/D_i values up to more than 100 times compared to the measured Sc/Di values while the intake Froude number $(Fr)_i$, is greater than 1.5. Since Gogus and Gokmener's [1] equation was derived by using the measured $(Fr)_i$ values within the range of 0.5 and 1.5, Gogus and Gokmener's [1] equation is not proper to predict the S_c/D_i values under flow conditions having greater $(Fr)_i$ values. Consequently, the data collected from Haspolat and Gogus's [18] study, which have $(Fr)_i$ greater than 1.5, are not tabulated in Figure 21.

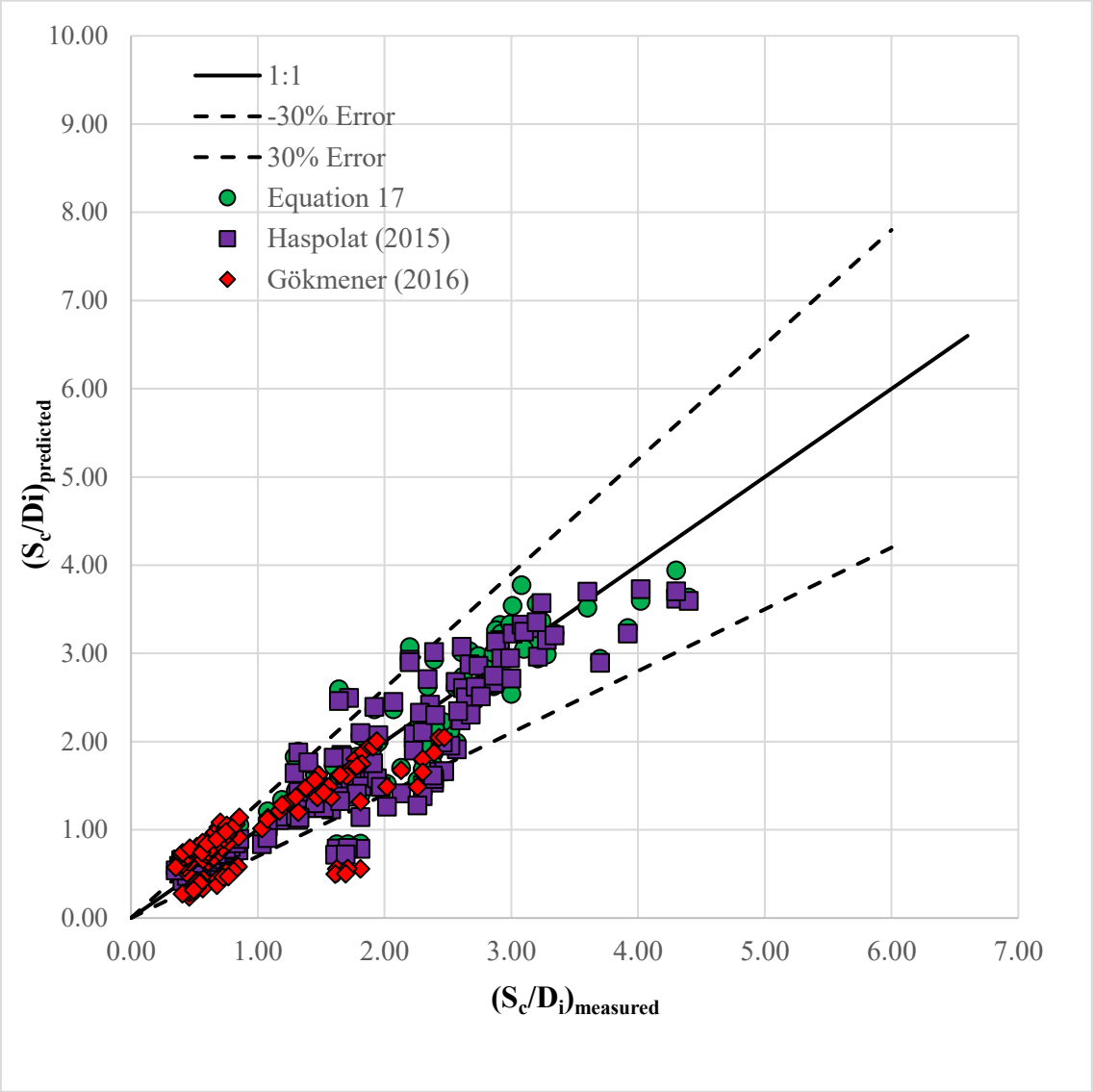


Figure 21. Comparison of $(S_c/D_i)_{measured}$ and $(S_c/D_i)_{predicted}$ from Equation (17), Haspolat and Gogus [18] and Gogus and Gokmener [1] , under asymmetrical approach flow conditions

As seen in Figure 22, the empirical equations given by Haspolat and Gogus [18] converge with the empirical equations presented in the literature up to $(Fr)_i$ values of 0.5. However, Haspolat's equations tend to underestimate the dimensionless critical submergence Sc/Di for a given intake Froude number (Fr)i when compared to the other empirical equations when (Fr)i is increased greater than 0.5. In contrast, the predictions obtained from the equations developed by Gordon and Gogus and Gokmener [1] yield notably higher values of Sc/Di for a given $(Fr)_i$ values and their results are found to be similar. The primary reason behind this discrepancy lies in the scale of the experimental setups Haspolat and Gogus [18] conducted experiments using a relatively small-scale model, whereas Gordon derived their dimensionless formulations from prototype data. Similarly, Gogus and Gokmener [1] employed large-scale physical models, approximately at a scale of 1:30. As a result, the lower submergence values predicted by equation are likely influenced by scale effects, such as the dominance of viscous and surface tension forces that are more prominent in small-scale models but tend to diminish in prototype conditions due to the increased Reynolds and Weber numbers. In accordance with these considerations, the applicability of Haspolat and Gogus [18] equation to real-life engineering practice may require a scale coefficient factor to account for these physical inconsistencies. Moreover, Equations 10 and 20, which are developed in the present study

by integrating insights from three independent research efforts, are located between the trends of Haspolat and Gogus [18] and Gogus and Gokmener [1]. This suggests that the proposed equations represent a balanced interpolation between small- and large-scale data and may offer improved generalizability across a wide range of hydraulic conditions.

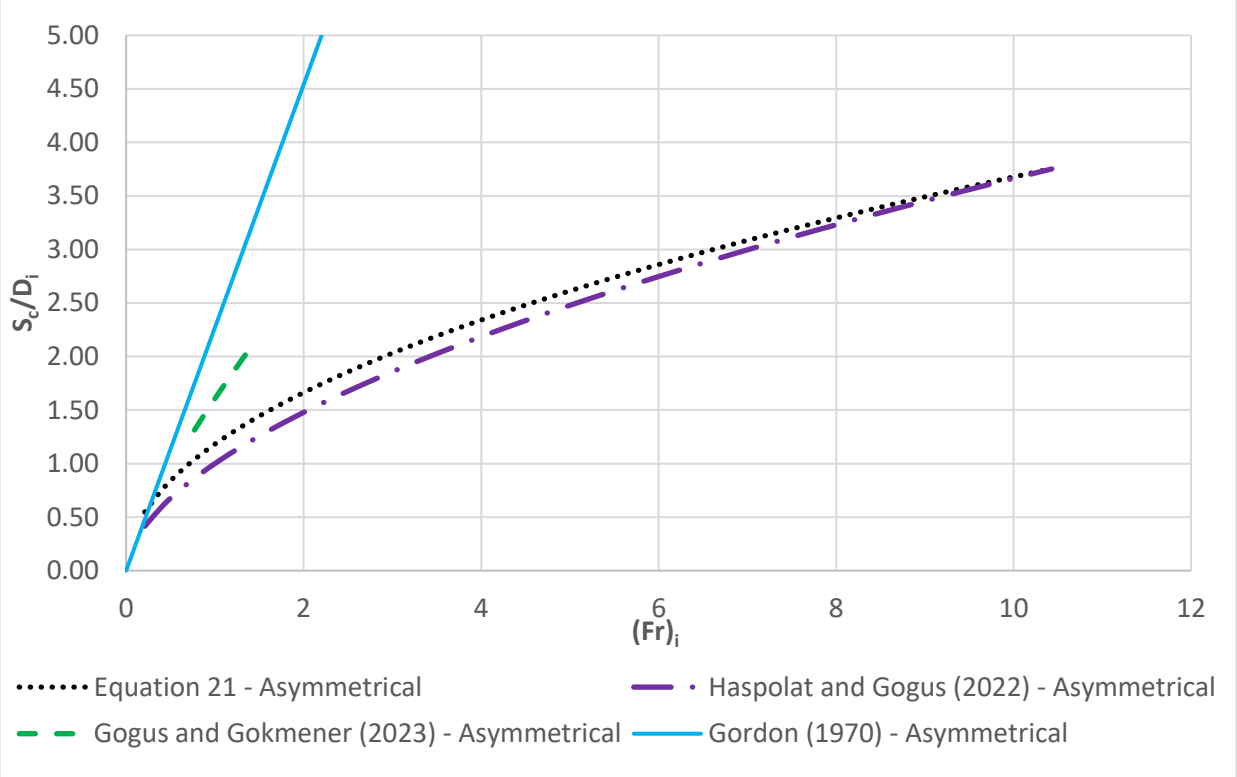


Figure 22. Comparison of Equation 21 obtained in this study with the other predictors presented in the literature

3.4 Limitations and Applicability of the Present Study

The empirical equations proposed in this study are valid within the hydraulic and geometric ranges reported in Table 1 for single horizontal intake structures under asymmetrical approach flow conditions. The database covers intake pipe diameters between 5 and 30 cm with a bottom clearance, $a/D_i=0$, a wide range of the dimensionless geometric parameter ψ, and steady, subcritical approach flow in a rectangular reservoir with fully turbulent conditions, $Re \gtrsim 10^5$. Within these boundaries, Equations (12)–(21) provide reliable estimates of S_c/D_i. The experiments were conducted without imposed circulation, pipe blockage, wind, or wave action; therefore, the equations are not intended for vertical intakes, multiple interacting intakes, sloping approach channels, or strongly circulating approach flows. In addition, the comparison in Figure 22 shows that small-scale models may underestimate critical submergence due to scale effects, whereas large-scale and prototype-based datasets yield higher submergence values. Accordingly, the present equations, which are derived by combining both small- and large-scale data, are recommended primarily for prototype-like, turbulent flow conditions, and their extrapolation beyond the tested parameter ranges should be treated with caution.

4. CONCLUSIONS

This study has provided a detailed and data-driven investigation into the determination of dimensionless critical submergence, S_c/D_i, at single horizontal intake structures under asymmetrical approach flow conditions. Utilizing a robust dataset compiled from 225 experimental measurements derived from three studies conducted by Haspolat and Gogus [18] and Gogus and Gokmener [1], how flow dynamics and structural geometry affect the formation of air-entraining vortices, which are critical to the safe and efficient design of water intake systems. The findings demonstrate that the intake Froude number $(Fr)_i$ is the most important hydraulic parameter influencing critical submergence. The results consistently show that as $(Fr)_i$ increases, the required submergence to suppress vortex formation also increases. However, this relationship is modulated by geometric effects, particularly the dimensionless geometrical parameter the ψ. In narrower geometries (i.e., small ψ), more confined approach flow conditions lead to stronger rotational flow components, resulting in greater critical submergence requirements. Conversely, in wider geometries (i.e., ψ), flow separation effects are diminished and vortex intensity is reduced, allowing stable intake operation at lower submergence. From a modeling perspective, ten empirical equations were developed to predict S_c/D_i, each incorporating different combinations of flow and geometric parameters. Among these, Equation (12) demonstrated the highest statistical accuracy ($R^2 = 0.949$), suggesting that multi-variable models that integrate both hydraulic and geometric characteristics offer superior predictive capability. Notably, the intake Froude number $(Fr)_i$ and geometric parameters emerged as the most influential predictors, whereas Reynolds and Weber numbers exhibited comparatively weaker effects. Furthermore, equations relying solely on the approach Froude number $(Fr)_{app}$, proved inadequate, confirming its negligible role in capturing the physical mechanisms of vortex formation at horizontal intakes. The integration of datasets across multiple studies allowed for the development of generalized models, specifically Equation (17), that outperform individual equations from the literature in terms of accuracy and applicability to varied conditions. These equations offer robust tools for engineering practice, particularly when assessing intake behavior under complex or site-specific configurations. In summary, this study advances the understanding of vortex-induced air entrainment at intakes by bridging experimental evidence with empirical modeling. The results emphasize that critical submergence is a function of not only flow intensity but also intake geometry and structural configuration. The comprehensive analysis presented here provides a solid foundation for developing intake designs that minimize vortex-related risks while maintaining hydraulic efficiency.

The following recommendations are proposed to guide future research endeavors:

1. It is recommended that future intake designs consider both the intake Froude number and geometric parameter, ψ, as primary design criteria when evaluating the risk of vortex-induced air entrainment. Simplified design approaches relying solely on the intake Froude number may underestimate critical submergence requirements, especially in narrow geometries or high-flow conditions.

2. While simplified models may be useful for preliminary evaluations, more comprehensive models should be employed during the detailed design phase to ensure higher precision and operational reliability.

3. The relationship between critical submergence and different types of intake shapes, along with varying approach channel sidewall angles, should be tested in detail.

Declaration of Ethical Standards

The authors declare to comply with all ethical guidelines, including authorship, citation, data reporting, and original research publication.

Credit Authorship Contribution Statement

Conceptualization: Serkan Gökmener; Methodology: Serkan Gökmener; Formal analysis and investigation: Serkan Gökmener, Dalal Al-Obaidi; Writing- original draft preparation: Serkan Gökmener, Dalal Al-Obaidi; Writing- review and editing: Serkan Gökmener, Dalal Al-Obaidi, Supervision: Serkan Gökmener.

Declaration of Competing Interest

The authors declare no conflicts of interest.

Funding / Acknowledgements

No funding or research grant was received during the review, research or compilation of the article. The authors thank Prof. Dr. Mustafa Göğüş for his contribution and suggestions during the study.

Data Availability

The data analyzed in this study are available in the literature.

Use of Artificial Intelligence

The authors used ChatGPT 4.1 for language editing and improvement of readability during manuscript preparation. The authors reviewed and verified all outputs and take full responsibility for the final content.

5. REFERENCES

[1] M. Gogus and S. Gokmener, "Critical Submergence for Single and Multiple Horizontal Intake Structures," *Arab J Sci Eng*, vol. 48, no. 10, pp. 13091–13115, Oct. 2023, doi: 10.1007/s13369-023-07651-w.

[2] K. Taştan, "Critical submergence for a horizontal pipe intake," *Ain Shams Engineering Journal*, vol. 11, no. 4, pp. 933–938, Dec. 2020, doi: 10.1016/j.asej.2020.02.010.

[3] N. Eroğlu and T. Bahadırlı, "Prediction of critical submergence for a rectangular intake," *Journal of Energy Engineering*, vol. 133, no. 2, pp. 91–103, 2007, doi: 10.1061/ASCE0733-94022007133:291.

[4] N. Yildirim and F. Kocabaş, "Critical Submergence for Intakes in Still-Water Reservoir," *Journal of Hydraulic Engineering*, vol. 124, no. 1, pp. 103–104, 1998, doi: 10.1061/(ASCE)0733-9429(1998)124:1(103).

[5] N. Yildirim, K. Taştan, and M. M. Arslan, "Critical submergence for dual pipe intakes," *Journal of Hydraulic Research*, vol. 47, no. 2, pp. 242–249, 2009, doi: 10.3826/jhr.2009.3352.

[6] N. Yildirim, H. Akay, and K. Taştan, "Critical submergence for multiple pipe intakes by the potential flow solution," *Journal of Hydraulic Research*, vol. 49, no. 1, pp. 117–121, Feb. 2011, doi: 10.1080/00221686.2010.535651.

[7] N. Yıldırım, A. S. Eyüpoğlu, and K. Taştan, "Critical Submergence for Dual Rectangular Intakes," *Journal of Energy Engineering*, vol. 138, no. 4, pp. 237–245, Dec. 2012, doi: 10.1061/(asce)ey.1943-7897.0000073.

[8] K. Taştan, "Critical submergence for isolated and dual rectangular intakes," *Sadhana - Academy Proceedings in Engineering Sciences*, vol. 41, no. 4, pp. 425–433, Apr. 2016, doi: 10.1007/s12046-016-0474-y.

[9] M. Hashid, A. Hussain, and Z. Ahmad, "Critical submergence for side circular intake in an open channel flow," *Journal of Hydraulic Research*, vol. 59, no. 1, pp. 136–147, 2021, doi: 10.1080/00221686.2020.1744749.

[10] J. L. Gordon, "Vortices at intakes," *Water Power*, vol. 4, pp. 137–138, 1970.

[11] J. R. Reddy and J. A. Pickford, "Vortices at intakes in conventional sumps," *Water Power*, vol. 3, pp. 108–109, 1972.

[12] A. J. Rindelsand and J. S. Gulliver, "An experimental study of critical submergence to avoid free-surface vortices at vertical intakes," 1983.

[13] M. Jiming, L. Yuanbo, and H. Jitang, "Minimum Submergence before Double-Entrance Pressure Intakes," *Journal of Hydraulic Engineering*, vol. 126, no. 8, pp. 628–631, 2000, doi: 10.1061/(ASCE)0733-9429(2000)126:8(628).

[14] G. Möller, M. Detert, and R. M. Boes, "Vortex-Induced Air Entrainment Rates at Intakes," *Journal of Hydraulic Engineering*, vol. 141, no. 11, p. 04015026, Nov. 2015, doi: 10.1061/(asce)hy.1943-7900.0001036.

[15] H. Sarkardeh, A. R. Zarrati, and R. Roshan, "Effect of intake head wall and trash rack on vortices," *Journal of Hydraulic Research*, vol. 48, no. 1 EXTRA ISSUE, pp. 108–112, 2010, doi: 10.1080/00221680903565952.

[16] M. Khanarmuei, H. Rahimzadeh, and H. Sarkardeh, "Effect of dual intake direction on critical submergence and vortex strength," Mar. 04, 2019, *Taylor and Francis Ltd.* doi: 10.1080/00221686.2018.1459896.

[17] M. Gogus, M. Koken, and A. Baykara, "Formation of air-entraining vortices at horizontal intakes without approach flow induced circulation," *Journal of Hydrodynamics*, vol. 28, no. 1, pp. 102–113, 2016, doi: 10.1016/S1001-6058(16)60612-1.

[18] E. Haspolat and M. Gogus, "Estimation of Critical Submergence at Single Horizontal Intakes Under Asymmetric Flow Conditions," *Arab J Sci Eng*, 2022, doi: 10.1007/s13369-021-06507-5.

[19] E. Haspolat, "Determination of Critical Submergence Depth at Horizontal Intakes," Master Thesis, Middle East Technical University, Ankara, 2015.

[20] B. Das, Z. Ahmad, and P. K. Sharma, "Critical Submergence for Single Lateral Rectangular Hydraulic Intakes under Uniform Approach Flow," *Journal of Hydraulic Engineering*, vol. 150, no. 6, Nov. 2024, doi: 10.1061/jhend8.hyeng-13867.

[21] M. Hashid and T. I. Eldho, "Effect of intake pipe blockage on the critical submergence for lateral dual intakes," 2023, *Taylor and Francis Ltd.* doi: 10.1080/00221686.2023.2232763.

[22] J. E. Hite and W. C. Mih, "Velocity of Air-Core Vortices at Hydraulic Intakes," *Journal of Hydraulic Engineering*, vol. 120, no. 3, pp. 284–297, 1994, doi: 10.1061/(ASCE)0733-9429(1994)120:3(284).

[23] S. Gökmener, "Investigation of Critical Submergence at Single and Multiple-Horizontal Intake Structures Having Air-Entraining Vortices," Master Thesis, Middle East Technical University, Ankara, 2016.

[24] C. J. Willmott and K. Matsuura, "Advantages of the mean absolute error (MAE) over the root mean square error (RMSE) in assessing average model performance," *Clim Res*, vol. 30, no. 1, pp. 79–82, 2005.

[25] M. Fuladipanah, M. A. Hazi, and O. Kisi, "An in-depth comparative analysis of data-driven and classic regression models for scour depth prediction around cylindrical bridge piers," *Appl Water Sci*, vol. 13, no. 12, p. 231, 2023.

Konya Mühendislik Bilimleri Dergisi, c.14, s.2, 869-900, 2026
Konya Journal of Engineering Sciences, v.14, n.2, 869-900, 2026
ISSN: 2667-8055 (Electronic)
DOI: 10.36306/konjes.1709436

DETERMINING THE LOCATION OF ELECTRIC VEHICLE CHARGING STATIONS IN ANTALYA PROVINCE USING GIS-BASED FUZZY MULTI-CRITERIA DECISION MAKING TECHNIQUES

[1]Aleyna KENAR, [2]Eray BAYSAL, [3,*]Eren KAMBER, [4]Ufuk AYDOĞMUŞ, [5]Hacer YUMURTACI AYDOĞMUŞ

[1,2,3,4,5] *Alanya Alaaddin Keykubat Üniversitesi, Rafet Kayış Mühendislik Fakültesi, Endüstri Mühendisliği Bölümü, Antalya*
[1]aleynakeenar@gmail.com, [2]eraybaysal27@gmail.com, [3]eren.kamber@alanya.edu.tr, [4]ufuk.aydogmus@alanya.edu.tr, [5]hacer.aydogmus@alanya.edu.tr

Highlights

- This study provides insight into EVCS planning, balancing needs and sustainability.
- An integrated MCDM approach is used with BWM, crisp EDAS and fuzzy-EDAS methods.
- Trapezoidal fuzzy numbers is employed to improve decision-making.
- Seeking a holistic solution by integrating triple sustainability and techniques.
- The study adds new insight to literature by integrating MCDM techniques and GIS.

Graphical Abstract

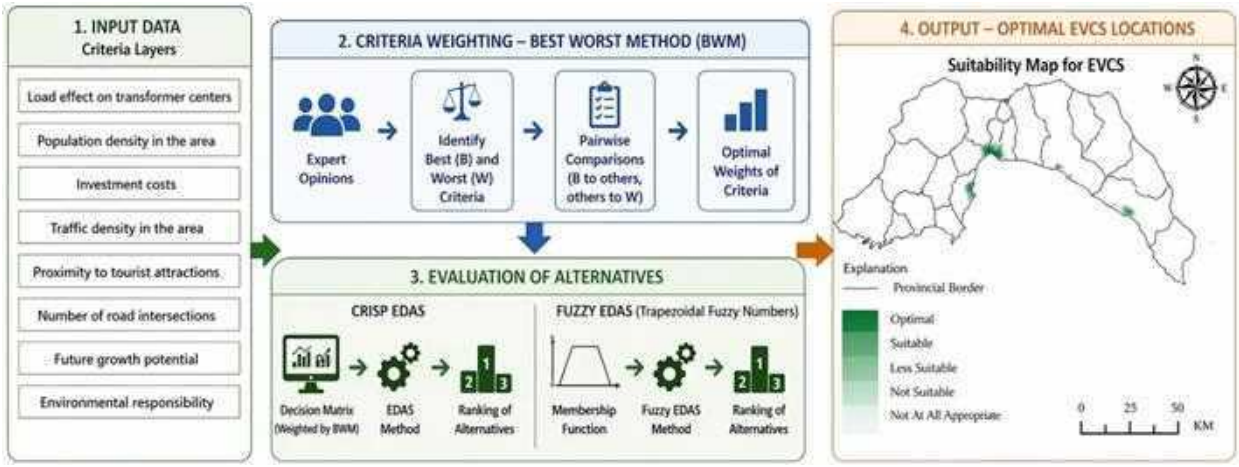


Figure Suitability mapping for alternatives

***Corresponding Author:** Eren KAMBER, eren.kamber@alanya.edu.tr

Konya Mühendislik Bilimleri Dergisi, c.14, s.2, 869-900, 2026
Konya Journal of Engineering Sciences, v.14, n.2, 869-900, 2026
ISSN: 2667-8055 (Electronic)
DOI: 10.36306/konjes.1709436

DETERMINING THE LOCATION OF ELECTRIC VEHICLE CHARGING STATIONS IN ANTALYA PROVINCE USING GIS-BASED FUZZY MULTI-CRITERIA DECISION MAKING TECHNIQUES

[1]Aleyna KENAR, [2]Eray BAYSAL, [3,*]Eren KAMBER, [4]Ufuk AYDOĞMUŞ, [5] Hacer YUMURTACI AYDOĞMUŞ

[1,2,3,4,5] Alanya Alaaddin Keykubat University, Rafet Kayış Faculty of Engineering, Industrial Engineering Departmant, Antalya, TÜRKİYE

[1]aleynakeenar@gmail.com, [2]eraybaysal27@gmail.com, [3]eren.kamber@alanya.edu.tr, [4]ufuk.aydogmus@alanya.edu.tr, [5]hacer.aydogmus@alanya.edu.tr

(Received: 30.05.2025; Accepted in Revised Form: 09.12.2025)

ABSTRACT: The purpose of this study is to use combination of Geographic Information Systems (GIS) and Multi-Criteria Decision Making (MCDM) techniques to identify electric vehicle charging station (EVCS) locations in Antalya province. Nowadays, sustainable transportation infrastructure has gained great importance. Correct positioning of EVCS plays an important role in terms of efficient use of energy resources, increasing user satisfaction and balancing the social, environmental and economic dimensions of sustainability. In this study, the current status of electric vehicles (EV) in Turkey and the world, the rate of diffusion of EV technologies and sustainable transportation policies are presented within the scope of the literature. Spatial data obtained with the help of QGIS program, which is GIS software, provided guidance in determining potential station locations. The Best-Worst Method (BWM) was employed to calculate the criteria weights. Proposed model was solved by EDAS and fuzzy EDAS methods designed with the expert opinions at different uncertainty levels. The results contributed to determine Antalya province's best possible EVCS locations. In addition to offering useful insight on topics like urban and transportation planning, the study advances the sustainable growth of EV infrastructure in Antalya province and contributes literature by utilizing the fuzzy structure of the MCDM approach. Finally, the validity of the study is presented through sensitivity analysis.

Keywords: *Best-Worst Method, Electric Vehicle Charging Station, Geographic Information Systems, Multi-Criteria Decision Making, Sustainability, Trapezoidal Fuzzy EDAS.*

1. INTRODUCTION

The importance of environmental issues such as global warming, the increase in carbon footprints, climate change, and the rapid depletion of natural resources is increasing day by day. With the increase in environmental problems, humanity's thoughts on protecting the environment have also developed, and the understanding of environmental sensitivity has evolved. This concept influences people's behaviors towards environmental pollution while supporting the adoption of a sustainable lifestyle [1]. Today, the understanding of sustainability encompasses not only trends in economic growth but also a social and philosophical perspective. This concept offers a multidimensional structure, providing a broad perspective in ecological, economic, social, psychological, demographic, spatial, and temporal aspects [2]. In this context, businesses also undertake their responsibilities to protect natural resources and reduce their negative impacts on the environment. Especially in the field of logistics, it has become increasingly clear that important steps need to be taken to protect the environmental balance [3].

In this context, the idea of "green logistics," which includes several approaches aimed at reducing the adverse effects that logistics operations have on the environment, has gained popularity. This concept, developed to minimize environmental impacts and seen as an important part of sustainable development, has been embraced [4]. One of the reasons for the emergence of environmental problems is the high

***Corresponding Author:** Eren KAMBER, eren.kamber@alanya.edu.tr

greenhouse gas emissions caused by traditional transporttan systems that use fossil fuels. Countries and international organizations are developing various strategies to reduce these emissions and create transportation infrastructure that is more compatible with the environment, and they are trying to transform production and consumption models with innovative technologies to reduce the carbon footprint [5], [6]. Reducing the use of fossil fuels, minimizing the risks of energy dependency, and building a sustainable future are at the core of many countries' strategic plans in recently [7].

EVs have emerged as an important technology shaping the future of eco-friendly transportation [8]. EVs offer advantages such as lower carbon emissions, the potential to reduce noise pollution, and high energy efficiency compared to internal combustion engine vehicles. However, one of the most important stages in the widespread adoption of EVs is the proper planning and implementation of the charging infrastructure required by the vehicles. When establishing EV charging infrastructure, various factors such as environmental sustainability, efficient use of energy resources, economic feasibility, and user-friendly design need to be evaluated simultaneously [9].

In this context, the focus of the study is to identify potential locations for EVCS in Antalya province based on specific criteria. At the same time, it involves identifying potential locations with the help of GIS and selecting the optimal one using crisp EDAS and fuzzy EDAS method. The aim is to place charging stations by adopting a sustainability and user-centered approach in this study. With the rise in EV usage, the environmental impacts of the infrastructure and its capacity to meet user requirements have also been evaluated. Meeting the expectations of EV users and maintaining environmental sustainability is severely constrained by the unplanned location of EV charging stations. Users find it challenging to access charging stations since the current infrastructure is unable to keep up with the quickly growing demand for EV charging [10], [11]. The existing stations have been randomly positioned without considering important issues such as economic and environmental sustainability and social needs. This issue leads to the inefficient use of energy resources and a decrease in the satisfaction of EV owners.

This research aims to create a more holistic and balanced solution by evaluating the concepts of economic, environmental, and social sustainability together and using various techniques. In the literature review, it was observed that some of the MCDM studies conducted for electric vehicles did not include fuzzy numbers at all, and limited number of studies where fuzzy numbers were used, trapezoidal fuzzy numbers were not included. In this direction, the integration of trapezoidal fuzzy numbers into MCDM methods within the scope of the problem of determining the charging station location of electric vehicles shows the originality of the study. Furthermore, the study's novel viewpoint on literature is demonstrated by the integration of fuzzy numbers, MCDM techniques, and GIS. With these aims, the study will positively contribute to the energy efficiency of the region where it will be implemented. At the same time, it will also contribute positively to the widespread use of EVs, enabling the advancement of sustainable transportation. By providing a multidisciplinary perspective on the placement of charging stations, it aims to fill a significant gap in areas such as urban planning and make positive contributions to literature.

1.1 Literature Review

The interconnection of humans and the environment has influenced the attitudes and actions of societies toward nature throughout history [7]. According to Şen, et al. [2], the concept of sustainability now includes social and philosophical viewpoints in addition to economic growth patterns. The concept of sustainability is a holistic approach consisting of three fundamental components. These components are the environmental, social, and economic dimensions. These elements interact with each other, and in the absence of any one of them, sustainability cannot be fully achieved [12]. The environmental dimension emphasizes the importance of securing natural resources and producing without causing environmental damage. The social dimension aims to elevate phenomena such as human health, education quality, and social justice to adequate levels for societies. The economic dimension focuses on the effective management of financial resources and the implementation of efforts aimed at increasing societal welfare [13].

With the increase of environmental pollution in the 1960s, the concept of environmental sensitivity emerged in industrialized countries [14]. The adoption and implementation of more environmental laws among countries worldwide is shown to be an effect of the widespread environmental sensitivity. Studies conducted in Indonesia and the Philippines show that public awareness about environmental pollution significantly reduces gas emissions [15]. When the number of green consumers reaches a significant level, environmentally conscious consumers cause dirty firms to lose market share and competitive advantage, positively impacting environmental effects [16].

The carbon footprint is used to measure the impact of societal behaviors on the world and emerged from the term ecological footprint in the 1990s [17]. The concept of the carbon footprint measures the impact of human behavior on the environment in terms of carbon dioxide equivalents [5]. The calculation of the carbon footprint amount contributes to the effective management of greenhouse gas emissions and the development and support of low-carbon production techniques [6]. The concept of carbon footprint is defined as the total of gases such as carbon dioxide and methane that result from the actions of individuals or institutions [18]. Since the 21st century, the increase in carbon dioxide emissions worldwide has been exacerbating the environmental impacts of greenhouse gas emissions and accelerating global warming [19]. Therefore, governments have resorted to numerous legal regulations to draw attention to environmental and energy issues such as increasing pollution and resource scarcity. Within the framework of these regulations, more than 120 countries have announced their "carbon neutral" targets. Especially in the transportation sector, significant steps have been taken towards transitioning from traditional fuel-powered vehicles to electric vehicles [20]. To reduce the carbon footprint, steps such as opting for renewable energy sources, using public transportation, and conserving energy can be taken [21], [22].

Green logistics is a strategy developed to minimize environmental impacts and is considered an important part of sustainable development [4]. Global transportation systems account for 25% of carbon emissions and 23% of total energy consumption, leading to significant environmental and economic issues [23]. Green logistics aims to enhance the overall performance of firms by integrating environmental goals into supply chain processes [24]. Recycling and waste management are also considered one of the fundamental components of green logistics [25]. Green logistics practices are important not only in waste management, transportation, and storage processes but also for reducing companies' environmental footprints [26]. Reducing fossil fuel consumption and transitioning to a more environmentally friendly lifestyle due to climate change is now inevitable [27].

EV technologies, have not received sufficient attention due to the widespread use of traditional internal combustion engines and the limited battery capacities of electric vehicles. The concern over the depletion of fossil fuels and their ecological impacts has led to a renewed interest in EV technologies [28]. The history of EVs dates to the 1800s; the first electric vehicle and motor were invented by Thomas Davenport in 1835. The traditional fuel-powered Model T, which Henry Ford began mass production of in 1908, negatively impacted the market share of electric vehicles. In the 1970s, it began to regain interest due to the emergence of air pollution and oil crises. In 1997, Toyota's hybrid vehicle, the Prius, entered the market, and in 2006, Tesla's Roadster model pioneered electric vehicles with long battery capacity and range [29].

The energy consumption of EVs places a significant burden on electrical grids. The integration of renewable energy sources with EVs will contribute to reducing environmental impacts as it decreases the use of traditional fuels [30]. The use of electricity generated from renewable energy sources such as solar energy is an important alternative for the sustainability of EVs [31]. One of the biggest issues with EVs is range anxiety, or concerns about battery capacity [32]. The use of commercial EVs in daily operations has introduced new challenges; particularly, charging times, limited battery capacities, and the need for charging stations are among the factors that must be considered in route planning [33].

EVs are categorized into various types based on their different technologies and features. Among these are hybrid electric vehicles (HEV), fully electric vehicles (FEV), plug-in hybrid electric vehicles (PHEV), and fuel cell electric vehicles (FCEV). HEV are vehicles that integrate both electric and internal

combustion engine technologies, combining the advantages of both [34]. The biggest advantage of HEV is its ability to recover kinetic energy generated during situations like braking and charge the batteries [35]. The fully electric FEV has been developed as a solution to increasing environmental pollution [36]. FEV, which can be charged seamlessly at both stations and home-type outlets, is seen as a user-friendly alternative [37]. The lower energy cost per kilometer for electricity compared to traditional fuels makes FEV economically advantageous as well 38]. Distance issues due to battery capacity and high initial prices have caused FEV to remain in the background until now [39]. PHEV, where electric and traditional motors work in an integrated manner, offers the possibility of using traditional and electric fuel together [40]. The long driving range, energy efficiency, and low exhaust emissions are among the advantages of PHEV [41]. FCEV is an ecological alternative that uses hydrogen gas as an energy source and releases water vapor as a byproduct into the environment [42]. The main fuel source of FCEV, hydrogen gas, is considered an environmentally friendly fuel source due to its ability to be stored and transported in liquid and gas forms, its support for green energy, and its zero exhaust emissions [43]. However, the difficulties in supplying hydrogen gas and the lack of the necessary infrastructure are seen as the biggest obstacles in front of these vehicles [44].

The primary advantages of electric vehicles (EVs) are the absence of exhaust emissions and their contribution to enhancing air quality in metropolitan environments, hence promoting public health [45]. Compared to traditional vehicles, the fact that EVs have fewer moving parts significantly reduces maintenance costs [44]. The noise-free operation of EVs reduces noise pollution in urban environments, thereby improving living standards [46]. EVs convert 60-70% of the energy they use into kinetic energy, offering greater energy efficiency. By 2025, the widespread adoption of EVs has the potential to reduce 1.5 billion metric tons of CO2 emissions globally each year [47]. As for their disadvantages, the biggest drawback of EVs is their limited driving range due to battery capacities [48]. One of the issues hindering the widespread adoption of EVs is the uneven distribution of charging stations [49]. The high purchase costs and charging times of EVs are seen as another disadvantage [50]. Lithium-ion batteries; battery performance, charge/discharge times, weights, and sizes negatively affect the costs of EVs [47].

The country with the largest EV fleet in the world is China. European countries, on the other hand, have reached the highest number by achieving annual sales of 3.2 million EVs [51]. Global EV sales in 2023 grew by 35% compared to the previous year, approaching 14 million. Turkey launched its first domestic and national car under the TOGG brand in 2018 [52]. The number of registered EV vehicles in Turkey for the first time reached 14,552 in 2022. The most significant growth occurred in 2023, with the number of EVs rising to 80,043. Turkey aims to increase the number of EVs to 2.5 million by 2030 [53]. Agrawal and Rajapatel [54], stated that the use of electric vehicles is expected to reach 28 million by 2030 and 56 million by 2050.

EVCSs are stations that provide the energy infrastructure needed to supply fuel to EVs [55]. To eliminate the obstacles in front of EVs and to enhance charging efficiency, the design and planning of EVCS are very important [56]. EV charging stations can be categorized into three main types: grid-based, renewable energy-based, and hybrid charging stations [57]. The energy required for EVCS must be provided, and this infrastructure needs to be built without negatively impacting the grid [58]. It is extremely important to have connection equipment compatible with various types of vehicles in the EVCS [59]. Ensuring safety measures is primarily important for users to receive a secure service and for the electrical infrastructure to operate smoothly [60], [61]. At charging stations, there should be simple interfaces, screens, and mobile device-supported payment platforms that allow users to easily carry out their transactions [62].

China, which has established over 1.15 million public charging stations by the end of 2023, has become one of the leading countries in this regard [63]. According to the International Council on Clean Transportation, the United States Federal Government plans to deploy an additional 500,000 electric vehicle charging stations over the next decade with a $15 billion fund investment. In Europe, various organizations such as the International Electrotechnical Commission have prepared various drafts to establish the criteria for EVSE [64]. Turkey has announced its "2053 Net Zero Emissions" goals [65]. The

number of charging stations in Turkey, which was 15 in 2011, reached 582 by 2019 [66]. The number of charging sockets has increased from 3,081 at the beginning of 2023 to 17,233 by April 2024 [67]. The lack of a sufficient number of charging stations to meet user needs is seen as the main reason why EVs are not adopted by vehicle users in Turkey 68].

MCDM is an approach that helps rank options and make the best decision under specific criteria [69]. Turan [70], described MCDM problems as "problems where the best option is selected from a possible solution set by improving multiple criteria." MCDM is defined as a method where the most suitable alternative is determined by scoring certain characteristics of the options [71]. The MCDM methods, which allow for clear and straightforward decision-making, manage the decision phase by considering both qualitative and quantitative data [72]. Which MCDM technique to use varies according to the problem's objective and the characteristics of the process steps [73].

One of the MCDM methods, EDAS (Evaluation based on Distance from Average Solution), was developed by Keshavarz Ghorabaee, et al. [74], in 2015.This method is based on the distances of the alternatives from the average solution. In this respect, the EDAS method does not require the calculation of suitable and rare solutions, unlike other MCDM techniques [75]. When reviewing the literature, it has been observed that the EDAS method has been applied in various studies. For example, it has been applied such as the optimization of energy processes [76], evaluation of logistics company websites [77], evaluation of wireless network environments [78], risk assessment in metro constructions [79], and machine selection in textile workshops [80].

GIS is defined as a system that helps in the acquisition, storage, and analysis of data related to an event or object and its corresponding location according to different structured data sets [81]. GIS made progress in the early 1960s and its use became even more widespread in the 1980s [82]. GIS presents analyzed information to the user in visual forms (maps, graphs, etc.), helping to simplify the understanding of complex information [83]. The way GIS manages complex information represents a significant transformation in this sector [84]. GIS is particularly used in the fields of urban and regional planning, real estate, agriculture, forestry, landscape architecture, geology, military, security, tourism, archaeology, local governments, demography, education, environment, and health [85]. GIS, by analyzing spatial data, has become an indispensable tool for strategic planning in many sectors and plays a vital role in decision-making processes [86]. Articles on EVCS site selection using MCDM are summarized in Table 1.

Table 1. Literature Review Table

Author(s)	Details of the Study	Solution Methodology	Country / Application Type
Morocho-Chicaiza et al. [87]	Existing gas stations were considered for the location of EVCS. The importance levels of a total of twelve sub-criteria under four main criteria were evaluated under three different scenarios. In the scenarios, the criteria were weighted as follows: equally for all criteria, using the AHP method, and using the fuzzy analytic hierarchy process (FAHP) method.	MCDM (VIKOR, TOPSIS and PROMETHEE)	Ecuador / Cuenca
Mhana and Awad [88]	Twelve criteria were identified and weighted using the AHP and FAHP methods to evaluate the suitability of candidate locations for station installation.	MCDM and GIS	Iraq and Saudi Arabia / Baghdad and Riyadh
Gokler [83]	For the positioning of EVCS, a model integrating the FUCOM and GIS methods was proposed, and spatial analyses were performed considering thirteen criteria. The accuracy of the technique was discussed by comparing the current locations with the proposed locations.	FUCOM, GIS, BWM-GIS, AHP-GIS	Turkey / Istanbul
Zhao and Hao [9]	The aim was to determine the most suitable locations for EVCS by evaluating them under four main criteria with a total of nineteen sub-criteria.	MCDM (DEMATEL, EWM, GRA-TOPSIS)	China / Qingdao
Razeghi et al. [89]	Four main criteria were evaluated in an integrated manner with more than sixteen data points. Factors such as public parking lots, gas stations, and shopping centers were taken into account when determining the locations of candidate sites.	ArcGIS, MCDM, photovoltaic energy potential analysis	Iran / Khuzestan

Algafri et al. [90]	The aim was to maintain charging costs, battery wear, and drivers' energy demands at optimal levels.	AHP, goal programming, SUMO and GAMS with BARON solver	Smart city charging station optimization
Krishankumar and Ecer [91]	Using the CRITIC method, the importance levels of a total of eight sub-criteria under three main criteria were determined, and a correlation analysis was performed. Using the CRADIS method, the options were ranked according to the appropriate solution.	MCDM	India / Tamil Nadu
Gonul et al. [92]	Six criteria were identified, and expert opinions were sought to evaluate these criteria. The weighted sum technique was used to determine the most suitable locations for EVCS.	Weighted sum method	Turkey / Edirne-Ankara highway
Erbas et al. [93]	Fifteen criteria were determined and evaluated using the FAHP and TOPSIS techniques.	GIS, MCDM (FAHP, TOPSIS)	Turkey / Ankara
Zhao et al. [94]	The aim was to determine the most suitable locations for photovoltaic EVCS. With the help of expert opinions, ten sub-criteria were determined under four main criteria, fuzzy DEMATEL was used for their weighting, and fuzzy MULTIMOORA techniques were used to determine the locations.	GIS, FAHP, Fuzzy DEMATEL, Fuzzy MULTIMOORA	China / Qingdao
Kaya et al. [95]	A three-stage model was proposed to determine the best locations for EVCS. First, twenty sub-criteria were identified under four main criteria and rated using the FAHP method. Second, a suitability map was created using GIS. Third, performance evaluation was conducted using the ELECTRE technique.	GIS, FAHP, ELECTRE	Turkey / Istanbul
Elomiya et al. [96]	A model was proposed and evaluated using GIS, machine learning, and SWARA techniques for the positioning of EVCS. Twenty sub-criteria were determined under five main criteria and rated using AHP, FAHP, and SWARA techniques.	GIS, RF, MCDM (SWARA)	Czech Republic / Prague
Kazempour et al. [97]	The aim was to determine the best locations for residential street-level EVCS for a transition to a sustainable green perspective. Five exclusion criteria were used for pre-analysis filtering, while eight suitability criteria were used for weighting using the AHP method.	GIS, AHP	United Kingdom / Birmingham
Kaya et al. [98]	A total of nineteen, sub-criteria, including five main criteria, were identified that affect the locations of EVCS. The most suitable locations for EVCS were determined based on these criteria.	GIS, MCDM (AHP, PROMETHEE, VIKOR)	Turkey / Istanbul
Carra et al. [99]	The AHP method was used to determine the degrees and results of the eight identified criteria. A global survey was conducted to analyze the identified results, and the responses were evaluated using Monte Carlo simulation.	MCDM (AHP), Monte Carlo Simulation	
Rane et al. [100]	The ratings of the thirteen criteria identified for the application of the weighted overlay technique were transferred to GIS, and a solution was reached using the TOPSIS technique.	Multiple Influence Factor (MIF), GIS, AHP (TOPSIS)	India / Mumbai
Guler and Yomralıoglu [101]	In the model aimed at determining the best locations for EVCS, ten criteria were identified and rated using the AHP and FAHP techniques, and the TOPSIS technique was used in the selection of candidate locations.	GIS, MCDM (FAHP, AHP, TOPSIS)	Turkey / Istanbul
Hisoglu and Comert [102]	A GIS-based MCDM technique was applied to six different criteria for the location selection of solar-powered electric vehicle charging stations.	GIS, MCDM	Turkey / Ankara - Istanbul highway
Janchomphu et al. [103]	Nine different criteria were weighted using the AHP method, and the GIS technique was also used to determine the best location for EVCS.	GIS, MCDM (AHP)	Thailand / Chonburi
Kumar and Channi [104]	The AHP method was applied with five different criteria to find the optimal locations for EVCS site selection.	MCDM (TOPSIS)	

Comparing this study with the studies in Table 1, this study departs significantly from the single-stage or solely GIS-based decision processes commonly seen in the electric vehicle charging station (EVCS)

location literature, especially in Asian-based applications. In the context of India, for instance, the determination of EVCS locations commonly employs a GIS–MIF–TOPSIS integration; however, such analyses tend to be restricted to spatial suitability considerations, thereby concluding the decision process within a single evaluative tier [100]. Similarly, although the multi-criteria planning research conducted in Ecuador incorporates existing fossil fuel stations as potential alternatives and introduces scenario-based weighting, the methodological design does not articulate a multi-layer integration between spatial analysis and the final decision optimization stage [87]. Moreover, within the Chinese literature, studies focused on the implementation of photovoltaic-supported charging infrastructures emphasize environmental sustainability and energy efficiency metrics, frequently utilizing hybridized models such as fuzzy DEMATEL–MULTIMOORA or entropy–GRA–TOPSIS [9], [89], [94]. Nevertheless, a common limitation in these approaches is the consolidation of spatial suitability evaluation and final alternative prioritization into a single, undifferentiated criterion set, which constrains the capacity to systematically integrate operational, infrastructural, and urban-scale planning realities within the site selection process. In contrast, the present study explicitly addresses these methodological constraints by adopting a two-stage, hierarchically structured, and integrative decision framework. Specifically, a total of 16 criteria were operationalized, with 8 criteria dedicated to GIS-based spatial suitability assessment and the remaining 8 criteria employed in the subsequent MCDM stage for the final ranking of candidate locations. This approach transcends the conventional "generate suitability surface → select the highest-scoring site" paradigm by re-evaluating each candidate location through operational, economic, environmental, and urban accessibility dimensions. Consequently, the proposed framework is substantively more comprehensive than the single-stage EVCS siting models prevalent in India [100], and more holistically configured than the PV-centric siting models commonly reported in China, since it explicitly integrates local mobility networks, land-use structure, infrastructural accessibility, and urban planning considerations [9], [94]. Overall, the study establishes a clear methodological demarcation between the determination of spatial suitability and the optimization of candidate alternatives through multi-criteria analysis, thereby delivering a robust, transferable, and context-adaptive decision support model for EVCS infrastructure planning.

Arayıcı and Poyrazoğlu, [105], developed optimal solutions using the routing method by considering geographical criteria in their charging station location studies. Demirtaş, et al. [106], on the other hand, took into account both geographical criteria and the distances along the route in their studies. Studies like these in literature are generally limited to a single method or focus solely on geographic analyses. While there are a number of studies that integrate GIS and MCDM in the literature, these kinds of studies are limited. Using a variety of methodologies, this study attempts to develop a more comprehensive and well-rounded answer by assessing the ideas of social, environmental, and economic sustainability together. In literature, although there are researches that integrate GIS and MCDM, their quantity is quite scarce. By combining the concepts of social, environmental, and economic sustainability and applying a variety of methodologies, this study seeks to develop a more comprehensive and well-rounded answer. In this study, instead of installing sockets at existing gas stations, etc., a new station has been positioned. The uniqueness of this study is increased by the fact that no prior research has been done on the placement of EVCS in Antalya province. The study's significance includes its support for sustainability, carbon footprint reduction, and green logistics, its environmentally friendly approach, the lack of similar research in Antalya province, the integration of GIS and MCDM techniques, and the development of a model that accounts for local electricity grid overloads and user requirements.

2. MATERIAL AND METHODS

In this study, the aim is to determine the locations of EV charging stations in the province of Antalya. In determining suitable locations for the placement of charging stations, the EDAS, Fuzzy EDAS, and BWM methods from GIS and MCDM are used in an integrated manner. In this section, information about trapezoidal fuzzy numbers, crisp EDAS, Fuzzy EDAS, and BWM methods have been provided.

2.1 Fuzzy Numbers

Trapezoidal fuzzy numbers are preferred to describe uncertainty flexibly and over a wide range in the study. The single peak of triangular fuzzy numbers can be insufficient in cases where expert opinions are gathered at various levels of uncertainty. Gaussian fuzzy numbers, on the other hand, can cause difficulties in the application stage due to their more complex parameter calculations. However, by using the four parameters of trapezoidal fuzzy numbers, it is possible to control both the suitability range and the gradual transition parts. In this study, the use of trapezoidal fuzzy numbers has enabled the collection of different expert opinions within a common framework, resulting in more realistic outcomes [107], [108], [109].

Definition 1: Let's assume that $\widetilde{A}=(a_1, a_2, a_3, a_4)$ is a trapezoidal fuzzy number. The fuzzy value of $\widetilde{A}$ is obtained using Equation (1).

$$\kappa(\widetilde{A}) = \frac{1}{3}\left(a_1 + a_2 + a_3 + a_4 - \frac{a_3 a_4 - a_1 a_2}{a_3 + a_4 - a_1 - a_2}\right) \quad (1)$$

Definition 2: Let $\widetilde{A} = (a_1, a_2, a_3, a_4)$ be a fuzzy number in trapezoidal form. The Ψ nction, which represents the maximum value between $\widetilde{A}$ and zero, is obtained by Equation (2).

$$\Psi(\widetilde{A}) = \begin{cases} \widetilde{A}, if\ \kappa(\widetilde{A}) > 0 \\ 0, if\ \kappa(\widetilde{A}) \leq 0 \end{cases} \quad (2)$$

Let's assume that the fuzzy decision matrix $\widetilde{X}$ is as in Equation (3):

$$\widetilde{X} = [\widetilde{X}_{kz}]_{n\times m} = \begin{bmatrix} \widetilde{x}_{11} & \widetilde{x}_{12} & \cdots & \widetilde{x}_{1m} \\ \widetilde{x}_{21} & \widetilde{x}_{22} & \cdots & \widetilde{x}_{2m} \\ \vdots & \vdots & & \vdots \\ \widetilde{x}_{m1} & \widetilde{x}_{m1} & \cdots & \widetilde{x}_{mn} \end{bmatrix} \quad (3)$$

According to the z-th criterion, let the k-th alternative be $A_1, A_2, A_3, A_4, \ldots, A_n, (k = 1, 2, \ldots, n)$ therefore each member of the decision matrix is represented by the triangular fuzzy number $\widetilde{x}_{kz} = (\widetilde{x}_{kz1}, \widetilde{x}_{kz2}, \widetilde{x}_{kz3})$. For each criterion, the weights are expressed as $\widetilde{w} = (w_1, w_2, w_3)$ [110].

2.2 EDAS Method

Developed by Keshavarz Ghorabaee, et al. [74], in 2015, the EDAS method has been compared with MCDM methods such as VIKOR and TOPSIS, and its consistency has been proven. This method, unlike other MCDM techniques, ranks alternatives based on their distances from the average solution without requiring the calculation of suitable and rare solutions. The EDAS method is widely used in problems where a large number of alternatives need to be evaluated simultaneously [75], [80], [111]. The EDAS method takes into account the average response values instead of the extreme points of the response. This way, it ensures that the alternatives are evaluated more accurately against fluctuations in the solutions. This method selects the sample value farthest from the average of a criterion based on the benefit-cost trend, thereby optimizing the criterion's response to the most suitable level. Additionally, it can model risk in environments with uncertainty and multiple criteria through simple calculations [76], [79]. Below, the solution steps of the EDAS method are explained in accordance with the method steps developed by Keshavarz Ghorabaee, et al., [74].

Step 1: Creation of the Decision Matrix

In the solution phase of the method, the decision matrix is first created. Equation (4) contains the X decision matrix of size m*n. Rows represent alternatives (k=1,2,…,m), while columns represent criteria (z=1,2,…,n).

$$X = \begin{bmatrix} x_{11} & x_{12} & \cdots & x_{1n} \\ x_{21} & x_{22} & \cdots & x_{2n} \\ \vdots & & \vdots & \vdots \\ x_{m1} & x_{m2} & \cdots & x_{mn} \end{bmatrix} \quad (4)$$

Step 2: Determining the Average Solution

In the second step of the method, the average solution of the criteria involved in the problem is determined. The average solution (AV), is calculated using Equations (5) and (6).

$$AV = [AV_k]_{1\times n} \quad (5)$$

$$AV_j = \frac{\sum_{k=1}^{m} X_{kz}}{m} \quad (6)$$

Step 3: Calculation of Positive and Negative Distance Matrices from the Mean

Using AV values, the positive distance matrix from the average (PDA) and the negative distance matrix from the average (NDA) are calculated. The calculations vary depending on whether the criteria are benefit-oriented or cost-oriented.

$$PDA = [PDA_{kz}]_{k\times z} \quad (7)$$

$$NDA = [NDA_{kz}]_{k\times z} \quad (8)$$

If the criteria are benefit-oriented, distance matrices are calculated using Equations (9) and (10).

$$PDA_{kz} = \frac{\max(0,(X_{kz}-AV_z))}{AV_z} \quad (9)$$

$$NDA_{kz} = \frac{\max(0,(AV_z - X_{kz}))}{AV_z} \quad (10)$$

If the criteria are cost-oriented, distance matrices are calculated using Equations (11) and (12).

$$PDA_{kz} = \frac{\max(0,(AV_z - X_{kz}))}{AV_z} \quad (11)$$

$$NDA_{kz} = \frac{\max(0,(X_{kz} - AV_z))}{AV_z} \quad (12)$$

Step 4: Calculation of Weighted Total Distance Matrices

Weighted distance matrices are calculated for the alternatives. For the positive distance matrix (SP_k), Equation (13) is used, and for the negative distance matrix (SN_k) for which Equation (14) is used.

$$SP_k = \sum_{z=1}^{n} w_z PDA_{kz} \quad (13)$$

$$SN_k = \sum_{z=1}^{n} w_z NDA_{kz} \quad (14)$$

Step 5: Normalization of SP_k and SN_k Values

At this step of the method, the SP_k and SN_k values are normalized using Equations (15) and (16). The NSP_k and NSN_k values are calculated.

$$NSP_k = \frac{SP_k}{max_k(SP_k)} \quad (15)$$

$$NSN_k = 1 - \frac{SN_k}{max_k(SN_k)} \quad (16)$$

Step 6: Calculation of Evaluation Scores (AS_k).

Evaluation scores (AS_k) for each alternative are calculated using the values of NSP_k and NSN_k with Equation (17) in the final step of the EDAS method. The calculated AS_k values must fall between 0 and 1.

$$AS_k = \frac{1}{2}(NSP_k + NSN_k) \tag{17}$$

$$0 \leq AS_k \leq 1 \tag{18}$$

The calculated AS_k values of the alternatives are ranked from highest to lowest. The alternative with the highest AS_k value is determined to be the best option according to the EDAS method.

2.3 Fuzzy EDAS Method

With the emergence of fuzzy decision-making models, the development of fuzzy MCDM techniques has also increased. Fuzzy MCDM methods are techniques applied to solve uncertainties in real life. Various MCDM techniques such as fuzzy TOPSIS, fuzzy VIKOR, etc., have been converted into fuzzy models [110], [112]. The fuzzy EDAS method is an extended MCDM method of the EDAS method using fuzzy set theory. In this method, the weighting of criteria and the rating of alternatives for each criterion are expressed using linguistic terms. These linguistic terms are mostly modeled with positive trapezoidal fuzzy numbers [113], [114], [115].

Below, the application steps of the fuzzy EDAS method are explained in accordance with the method steps developed by Keshavarz Ghorabaee, et al., [116].

Step 1: In the first step of the fuzzy EDAS method, the fuzzy average decision matrix ($\widetilde{AV}_z$) is determined for all criteria.

$$\widetilde{AV}_z = \frac{\sum_{k=1}^{n} \tilde{x}_{kz}}{n} \tag{19}$$

Step 2: The optimal solution should have the maximum distance from the negatively applicable solutions. At the same time, it should have the minimum distance compared to the best and ideal solutions. Therefore, in the second step of the fuzzy EDAS method, the fuzzy positive distance matrix (PDA) and the fuzzy negative distance matrix (NDA) from the mean are defined by Equations (22) and (23). B indicates that the criterion is benefit-oriented, while C indicates that it is cost-oriented.

$$PDA = [\widetilde{pda}_{kz}]_{n\times m} \tag{20}$$

$$NDA = [\widetilde{nda}_{kz}]_{n\times m} \tag{21}$$

$$\widetilde{pda} = \begin{cases} \dfrac{\Psi(\tilde{x}_{kz} \ominus \widetilde{av}_z)}{\kappa(\widetilde{av}_z)}, if\ z \in B \\ \dfrac{\Psi(\widetilde{av}_z - \tilde{x}_{kz})}{\kappa(\widetilde{av}_z)}, if\ z \in C \end{cases} \tag{22}$$

$$\widetilde{nda} = \begin{cases} \dfrac{\Psi(\widetilde{av}_z - \tilde{x}_{kz})}{\kappa(\widetilde{av}_z)}, if\ z \in B \\ \dfrac{\Psi(\tilde{x}_{kz} \ominus \widetilde{av}_z)}{\kappa(\widetilde{av}_z)}, if\ z \in C \end{cases} \tag{23}$$

Step 3: The fuzzy weighted sums of positive distances ($\widetilde{sp}_k$) and the fuzzy weighted sums of negative distances ($\widetilde{sn}_k$) from the average matrix are calculated. The values of $\widetilde{sp}_k$ and $\widetilde{sn}_k$ are calculated using Equations (24) and (25).

$$\widetilde{sp}_k = \oplus_{z=1}^{m} (\tilde{w}_z \oplus \widetilde{pda}_{kz}) \tag{24}$$

$$\widetilde{sn}_k = \bigoplus_{z=1}^{m} (\widetilde{w}_z \oplus \widetilde{nda}_{kz}) \quad (25)$$

Step 4: The fuzzy normalized values of $\widetilde{SN}_k$ and $\widetilde{SP}_k$ are calculated using Equations (26) and (27).

$$\widetilde{nsp}_k = \frac{\widetilde{sp}_k}{max_k(\kappa(\widetilde{sp}_k)} \quad (26)$$

$$\widetilde{nsn}_k = 1 - \frac{\widetilde{sn}_k}{max_k(\kappa(\widetilde{sn}_k)} \quad (27)$$

Step 5: Using Equation (28), fuzzy evaluation scores are calculated for all alternatives, and the calculated evaluation scores are defuzzied.

$$\widetilde{as}_k = \frac{\widetilde{nsp}_k \oplus \widetilde{nsn}_k}{2} \quad (28)$$

Step 6: The alternatives are ranked in descending order based on their fuzzy evaluation scores in the final step. Among the ranked alternatives, the one with the highest evaluation score is the best alternative.

2.4 Best Worst Method

The Best-Worst Method is a MCDM method developed by Rezaei, [117], to determine the weights of criteria [118]. This method is based on identifying the best and worst criteria and comparing these criteria with other criteria. This way, it allows for more consistent decisions with less decision-maker burden and computational requirements compared to traditional pairwise comparison methods like AHP [119], [120].

The BWM can achieve more effective and consistent results compared to traditional pairwise comparison methods like AHP. In AHP, criteria are compared pairwise with each other, while in the Best-Worst Method, the best criterion is compared with other criteria and the worst criterion is compared with other criteria. These pairwise comparisons are not random; they are systematic comparisons. With n being the number of criteria, (2n-3) pairwise comparisons are made. Thanks to this method, the decision-maker is able to make consistent decisions and thus obtain more reliable weights [118], [119], [121]. One of the most significant advantages of the Best-Worst Method is that it requires fewer comparisons compared to traditional pairwise comparison methods. In other words, it is a method that allows decision-makers to obtain more consistent results with less effort. However, in large sets of criteria, it can be difficult for the decision-maker to identify the best and worst criteria. In such cases, additional procedures need to be applied to determine the best and worst criteria. It is thought that the BWM can compensate for the shortcomings of traditional pairwise comparison methods [119], [120], [121]. Below, the solution steps of the BWM are explained in accordance with the method steps developed by Rezaei (2015) [117].

Step 1: Determining the Criteria Set

In the first step of the BWM method, the n criteria $\{C_1, C_2, \dots, C_n\}$ to be used in the evaluation of alternatives are determined.

Step 2: Determination of Strong and Weak Criteria in the Criterion Set

In the second phase of the method, the most important-strong (B) and the least important-weak (W) criteria are determined.

Step 3: Determining the Dominance Level of the Strong Criterion Over Other Criteria

In the third step, the degree of importance of the criterion identified as strong is determined in relation to the other criteria. The degree of importance is determined using a number between 1 and 9. According to the criterion being compared; a value of 1 indicates that the importance levels are equal, while a value of 9 indicates the highest level of importance. As a result, the A_B vector, which consists of n criteria, is obtained, as stated in Equation (29). This vector is the pairwise comparison of the strong criterion with other criteria in a decision problem.

$$A_B = (a_{B1}, a_{B2}, \dots, a_{Bn}) \quad (29)$$

In the A_B vector, a_{BB}= 1, and this indicates that it will be compared with the strong criterion itself

Step 4: Weakness of the Criteria Determining the Dominance Level of the Criterion

In the fourth step, the degree of importance of the criterion identified as weak is determined in relation to the other criteria. The degree of importance is determined using a number between 1 and 9. According to the criterion being compared; a value of 1 indicates that the importance levels are equal, while a value of 9 indicates the highest level of importance. As a result, the A_W vector, consisting of n criteria, is obtained, which is included in Equation (30). This vector is the pairwise comparison of the weak criterion with the other criteria in a decision problem.

$$A_W = (a_{1W}, a_{2W}, \dots, a_{nW}) \tag{30}$$

In the A_W vector, a_{WW}= 1, and this indicates that the weak criterion will be compared with itself.

Step 5: Calculation of Optimal Weights

At this step, the aim is to determine the most suitable weights for the criteria in such a way that the maximum absolute difference is achieved. The z values that minimize the maximum absolute differences should be found using the following min-max model:

$$\min \max \{|w_B - a_{Bz}\, w_z|, |w_z - a_{zw}\, w_w|\} \tag{31}$$

s.t.

$$\sum_{z=1}^{n} w_z = 1 \tag{32}$$

$$w_z \geq 1, \forall z \tag{33}$$

The above min-max model is being transferred to the following linear programming model:

$$min\ \xi$$

s.t.

$$|w_B - a_{Bz}\, w_z| \leq \xi w_z\ , \forall z \tag{34}$$

$$|w_z - a_{zw}\, w_w| \leq \xi w_w\ , \forall z \tag{35}$$

$$\sum_{z=1}^{n} w_z = 1 \tag{36}$$

Step 6: Determination of the Consistency Ratio

The consistency ratio (CR) is calculated using the consistency index values (CI) in Table 2 to determine the reliability of the calculated optimal weights (ξ) in the final step of the method [117]. CR values are calculated using Equation (37). An increase in the CR value indicates weak consistency, while a decrease indicates high consistency.

$$CR = \frac{\xi}{CI} \tag{37}$$

Table 2. Consistency index values

ξ^*	1	2	3	4
CI	0.00	0.44	1.00	1.63

3. RESULTS AND DISCUSSION

The purpose of this study is to choose an EVCS location in the Turkish Mediterranean province of Antalya. Figure 1 shows the study area. By examining the studies in the literature, the criteria to be used in site selection have been determined. The determined criteria were weighted by obtaining opinions from three different experts. One of the experts is an academician with a doctoral degree, while the other two

are mid-level and senior managers with at least 10 years of experience in the energy sector. Using the QGIS program, a software of GIS, suitability maps for each criterion for the province of Antalya were created by considering the criterion weights. As a result of the analyses conducted using the QGIS program, alternative locations to be considered for site selection have been identified. As a result, the EDAS and fuzzy EDAS methods were utilized for the evaluation of alternative locations.

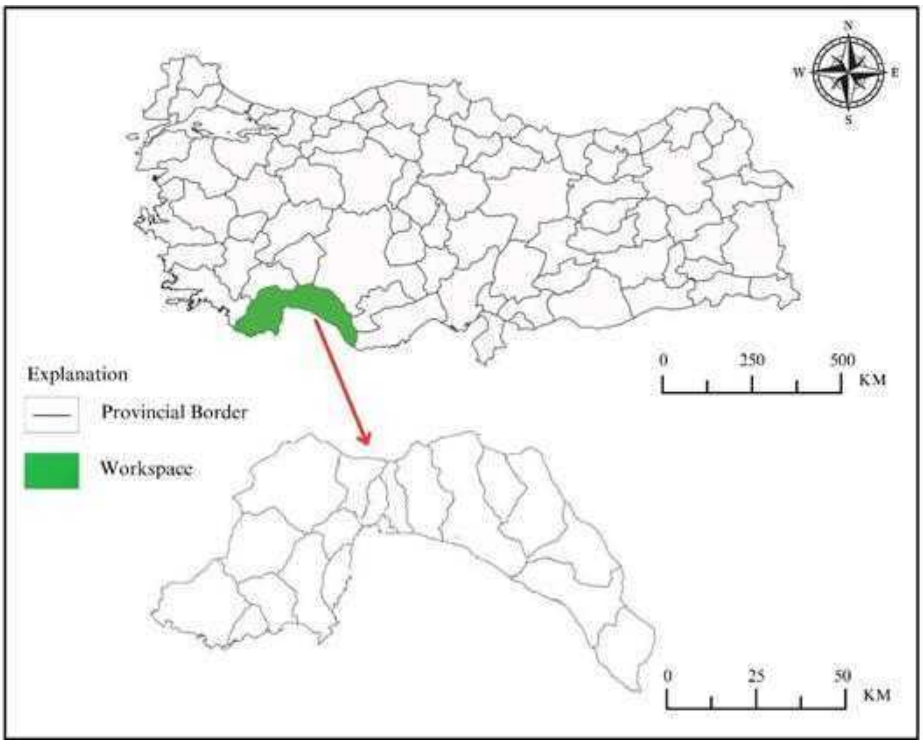


Figure 1. Workspace Map

3.1 Determination of Criteria to be Used in Identifying Alternative Locations

The studies in literature have been examined, and the criteria used in these studies have been listed. As a result of the literature review conducted, eight different criteria to be used in determining alternative locations have been identified. Table 3 includes these criteria and their explanations.

3.2 Reclassification of Criteria

The determined criteria were reclassified based on the opinions of three different experts. Values between 1 and 5 have been assigned to the determined ranges. Table 4 includes the criteria and their reclassifications.

Table 3. Descriptions of criteria

Criterion	Description	Author(s)/Year
Distance to Main Roads (K1)	Charging stations should be located close to main roads, as these routes are heavily used and easy access is important for users.	[96], [103], [122], [123]
Distance to Gas sStations (K2)	Locating EV charging stations near fuel stations reduces costs and benefits hybrid vehicle users, making them suitable sites for EVSE	[9], [88], [89], [95]
Distance to the Current EVCS (K3)	For balanced distribution and accessibility, new EVCS should be placed away from existing ones, with 0–1000 meters considered ideal	[93], [100], [124]
Distance to Shopping Malls (K4)	Shopping centers, due to their high foot traffic and amenities, offer users a place to spend time while charging. Therefore, EVCS should be located near them.	[83], [89], [91], [101]

Distance to Parking Lots (K5)	Parking areas ease long EV charging times, so stations should be nearby. Experts see 0–1000 meters as ideal; over 1001 meters is a	[96], [122]
Slope (K6)	High slopes increase station costs, so low-slope areas are preferred for placement.	[88], [102], [122], [124]
Distance to the Transformer (K7)	To reduce energy loss and ensure quality, EVCS should be located close to transformers.	[87], [93], [125]
Distance from Official Institutions (K8)	Due to 11high population and mobility, EVCS should be placed close to official institutions.	[122], [124]

Table 4. Criteria and reclassification table

Criteria	Classification	Value	Description
K1 (meters)	0-1000	5	Most Suitable
	1001-2000	4	Suitable
	2001-3000	3	Somewhat Suitable
	3001+	1	Not at all appropriate
K2 (meters)	0-1000	5	Most Suitable
	1001-2000	4	Suitable
	2001-3000	3	Somewhat Suitable
	3001+	1	Not at all appropriate
K3 (meters)	0-1000	5	Most Suitable
	1001-2000	1	Not at all appropriate
	2001-3000	2	Not Suitable
	3001-4000	3	Somewhat Suitable
	4001+	4	Suitable
K4 (meters)	0-1000	5	Most Suitable
	1001-2000	4	Suitable
	2001-3000	3	Somewhat Suitable
	3001-4000	2	Not Suitable
	4001+	1	Not at all appropriate
K5 (meters)	0-1000	5	Most Suitable
	1001+	1	Not at all appropriate
K6 (degree)	0-2	5	Most Suitable
	3-5	4	Suitable
	6-8	3	Somewhat Suitable
	10-12	2	Not Suitable
	13+	1	Not at all appropriate
K7 (meters)	0-1000	5	Most Suitable
	1001-2000	4	Suitable
	2001-3000	3	Somewhat Suitable
	3001-4000	2	Not Suitable
	4001+	1	Not at all appropriate
K8 (meters)	0-1000	5	Most Suitable
	1001-2000	4	Suitable
	2001-3000	3	Somewhat Suitable
	3001-4000	2	Not Suitable
	4001+	1	Not at all appropriate

3.3 Creation of Suitability Maps

The data for the criteria were obtained through the Overpass Turbo application. The following processing steps were applied to the data obtained from the Overpass Turbo application using the QGIS application.

The data was converted to Shapefile (shp) format, and the project coordinate reference system (CRS) EPSG:32637 – WGS 84 / UTM zone 37N was used as a reference to ensure all data is in the same format and coordinates.

Except for the slope criterion, all criteria were processed with the multi-ring buffer tool, applying five "buffer" operations of 1000 meters each.

To obtain the slope data, the 30 M DEM image of the region was first downloaded. Subsequently, a slope analysis was performed on the DEM data to obtain the slope data.

The "raster" process was applied to convert the data subjected to the buffer operation and the slope data from vector to Raster.

The "reclassification" process was applied to the data converted to raster to obtain suitability maps. With the opinions received from experts, values between 1 and 5 were assigned to appropriate ranges and the necessary definitions were made through the application. In this way, the data was reclassified and suitability maps were obtained.

Figure 2 shows the suitability maps of the reclassified data using the QGIS application, which is a software for geographic information systems.

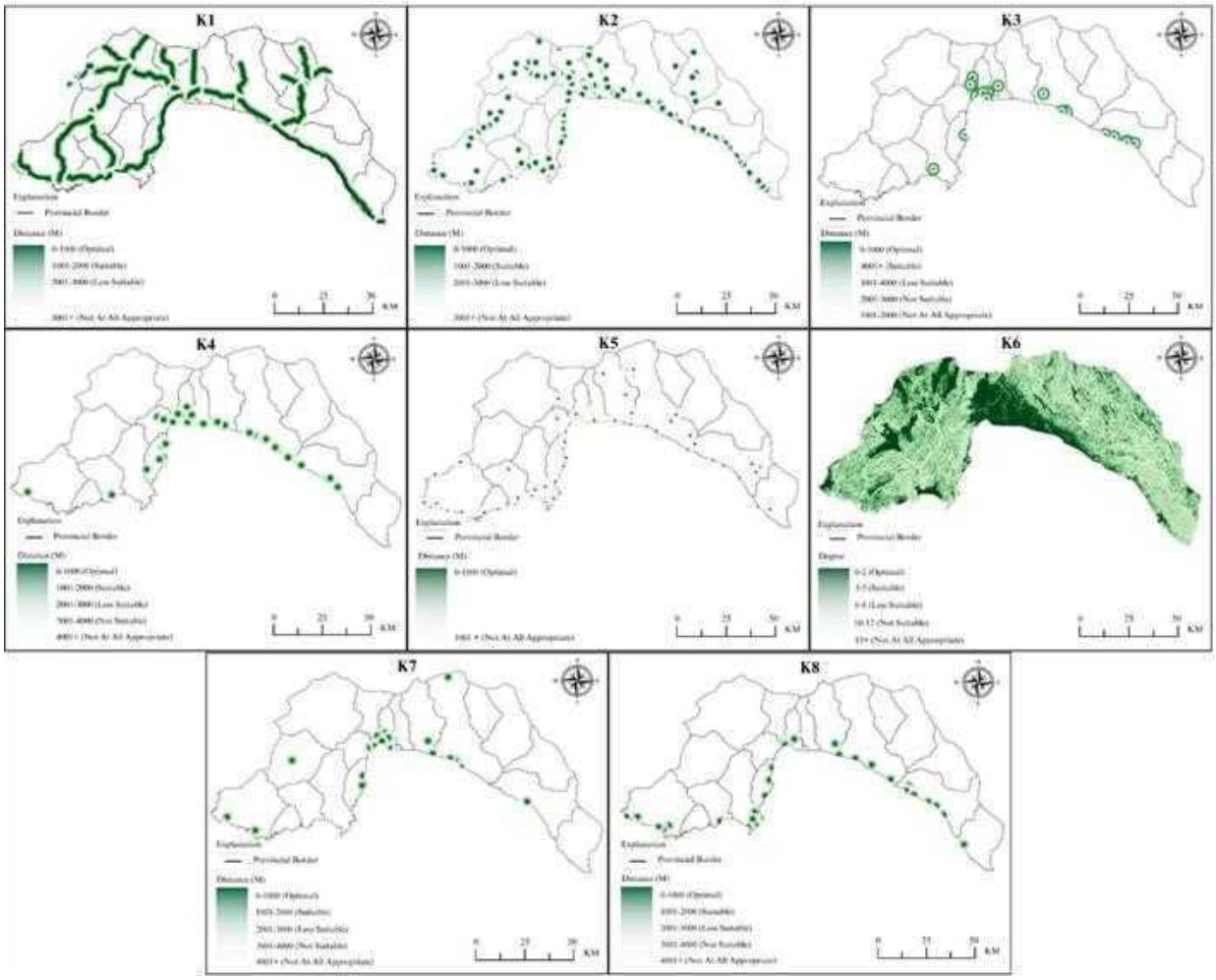


Figure 2. Suitability maps of the criteria

Based on expert judgment, ratings ranging from 0 to 100 were assigned in order to generate a suitability map for the station to be established. The scored criteria were subjected to the normalizing process. The criteria, scores, and weights are listed in Table 5. Using normalized weight values, the "Raster Calculator" operation available in the QGIS application was applied. Figure 3 shows the suitability map of alternative locations for the electric vehicle charging station to be established in Antalya province.

Table 5. Weights of criteria for GIS suitability map

Criteria	Scores	Weights
Distance to main roads (meters)	85	0.1465
Distance to fuel stations (meters)	70	0.1206
Distance to the existing EVCS	60	0.1034
Distance to shopping centers	75	0.1293
Distance to parking lots (meters)	50	0.0862
Slope (degrees)	65	0.1120
Distance to the transformer (meters)	90	0.1551
Distance to official institutions	85	0.1465

As a result of the analyses conducted in accordance with the determined criteria and weightings, the most suitable alternative locations for establishing an electric vehicle charging station, as shown in Figure 3, have been identified as the districts of Kemer, Konyaaltı, Muratpaşa, Manavgat, and Alanya.

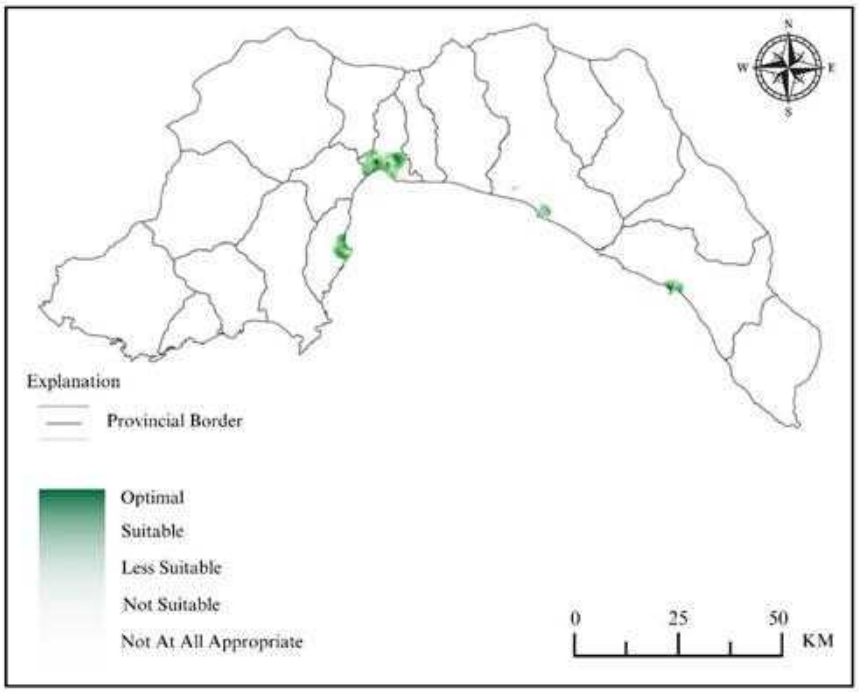


Figure 3. Suitability map of alternative locations for the electric vehicle charging station to be established in Antalya province

Studies in the literature have been examined, and the criteria used in the studies have been listed. As a result of the literature review, eight different criteria to be used in the comparison between alternatives have been identified. Table 6 includes the criteria and their explanations.

Among the determined criteria, those evaluated as cost criteria are: the load effect on transformer centers, investment costs, and environmental responsibility criteria. Other criteria are considered as beneficial criteria. In Table 7, a table has been prepared indicating the abbreviations and directions of the criteria.

Table 6. Criteria and explanations

Criterion	Description	Author(s)/Year
Load Effect on Transformer Stations	Due to high power consumption, EVCS should be placed in areas with low transformer load. Thus, transformer capacity and load level are key criteria.	[9], [87]
Traffic Density in the Area	High-traffic areas indicate high charging demand from both local and outside users. Therefore, traffic density should be considered when locating EVCS.	[92], [102], [126]
Population Density in the Area	Densely populated areas have higher transport needs, leading to increased EV use and charging demand.	[95], [96], [122]
Number of Road Intersections in the Area	A high number of intersections indicate a dense transport network and more vehicles. EVCS in such areas can serve more users effectively.	[9], [93]
Investment Costs	Lower land, installation, and maintenance costs make a location more suitable for EVCS, so areas with lower investment costs are preferred.	[9], [87], [127]
Proximity to Tourist Attractions	Tourism and attractions boost seasonal population and traffic, increasing demand from visitors.	[83], [95], [96]
Future Growth Potential	As EV use grows, the area's expansion potential and ability to meet future demand are key. Thus, regions with growth potential are preferred for long-term EVCS success.	[92], [99]
Environmental Responsibility	Noise, air, and environmental pollution are key concerns in EVCS placement, so environmental responsibility should guide station positioning.	[83], [96], [99]

Table 7. Criteria abbreviations and direction table

Abbreviation	Criteria Names	Criteria Direction
C1	Load effect on transformer centers	Cost
C2	Population density in the area	Benefit
C3	Investment costs	Cost
C4	Traffic density in the area	Benefit
C5	Proximity to tourist attractions	Benefit
C6	Number of road intersections	Benefit
C7	Future growth potential	Benefit
C8	Environmental responsibility (air pollution, distance from water sources, etc.)	Cost

3.4 Determination of Criterion Weights

The Best-Worst method was used to determine the criterion weights. A total of three experts evaluated criteira as shown in Table 7. Each expert has determined the best and worst criteria and scored according to the Best-Worst method. The Best-Worst ratings of each expert are presented in Table 8.

Table 8. Experts' best-worst scoring table

	Expert-1			Best: C1			Worst: C8	
	C1	C2	C3	C4	C5	C6	C7	C8
C1	1	2	7	3	5	6	4	8
C8	9	8	3	7	5	4	6	1
	Expert-2			Best: C5			Worst: C1	
	C1	C2	C3	C4	C5	C6	C7	C8
C5	8	3	7	3	1	4	5	6
C1	1	7	3	7	9	6	5	4
	Expert-3			Best: C3			Worst: C8	
	C1	C2	C3	C4	C5	C6	C7	C8
C3	2	3	1	3	5	5	7	8
C8	8	7	9	7	5	5	3	1

In the implementation phase of the Best-Worst method, the weights of the criteria were determined according to each expert's evaluations by following the steps from Equation (29) to (37). Finally, the average weights were considered by taking the averages. Table 9 contains the overall results table of the criteria weights determined using the Best-Worst method.

Table 9. Best-worst overall results table

Experts / Criteria	**C1**	**C2**	**C3**	**C4**	**C5**	**C6**	**C7**	**C8**	**ξ**
Expert -1	0.324	0.202	0.057	0.135	0.081	0.067	0.101	0.030	0.081
Expert -2	0.032	0.144	0.062	0.144	0.347	0.108	0.086	0.072	0.086
Expert -3	0.193	0.128	0.310	0.128	0.077	0.077	0.055	0.029	0.076
Average	0.183	0.158	0.143	0.136	0.168	0.084	0.081	0.044	0.081

3.5 Application of EDAS Method

EDAS and Fuzzy In the application phase of the EDAS method, the linguistic expressions found in Table 10 have been used. In Table 11, the EDAS and Fuzzy scale equivalents of the expressions are specified.

Table 10. Scale and evaluation table [92]

Abbreviation	**Evaluation**	**Scale**	**Fuzzy Scale**
VH	Very High	100	(0.80, 0.90, 1, 1)
H	High	85	(0.70, 0.80, 0.80, 1)
MH	Medium High	70	(0.50, 0.60, 0.70, 0.80)
M	Medium	50	(0.40, 0.50, 0.50, 0.60)
ML	Medium Low	30	(0.20, 0.30, 0.40, 0.50)
L	Low	20	(0.10, 0.20, 0.20, 0.30)
VL	Very Low	10	(0, 0, 0.10, 0.20)

The evaluation of each alternative by experts in terms of specific criteria is presented in Table 11.

Table 11. Scaling of alternatives according to criteria

		Criteria							
Expert-1		C1	C2	C3	C4	C5	C6	C7	C8
	Kemer	ML	M	H	ML	VH	MH	ML	H
	Muratpaşa	H	VH	M	VH	M	MH	VH	M
Alternatives	Konyaaltı	MH	H	MH	H	M	H	H	M
	Manavgat	M	MH	MH	M	H	M	MH	MH
	Alanya	ML	M	MH	M	VH	M	MH	H
		Criteria							
Expert-2		C1	C2	C3	C4	C5	C6	C7	C8
	Kemer	ML	ML	MH	L	VH	MH	VH	VH
	Muratpaşa	VH	VH	H	VH	M	VH	L	MH
Alternatives	Konyaaltı	M	H	VH	H	VH	H	ML	VH
	Manavgat	H	MH	M	M	ML	M	H	MH
	Alanya	ML	H	H	MH	VH	VH	MH	VH
		Criteria							
Expert-3		C1	C2	C3	C4	C5	C6	C7	C8
	Kemer	ML	MH	H	M	VH	M	M	MH
	Muratpaşa	VH	VH	M	VH	M	H	MH	VH
Alternatives	Konyaaltı	H	H	VH	MH	M	M	H	MH
	Manavgat	MH	H	MH	H	H	VH	MH	H
	Alanya	MH	MH	MH	MH	H	MH	VH	MH

Step 1: Creation of the Decision Matrix

In the first step of the EDAS method, the average decision matrix is created by taking the arithmetic mean of the data obtained from three experts. Table 12 contains the average decision matrix.

Table 12. Average decision matrix table

	Criteria	**C1**	**C2**	**C3**	**C4**	**C5**	**C6**	**C7**	**C8**
	Criterion	Cost	Benefit	Cost	Benefit	Benefit	Benefit	Benefit	Cost
	Weights	0.183	0.158	0.143	0.136	0.168	0.084	0.081	0.044
Alternatives	**Kemer**	30	50	80	33.333	100	46.666	60	85
	Muratpaşa	95	100	61.667	100	50	85	63.333	73.333
	Konyaaltı	68.333	85	90	80	66.666	73.333	66.666	73.333
	Manavgat	68.333	75	63.333	61.666	66.666	66.666	75	75
	Alanya	43.333	68.333	75	63.333	95	73.333	80	85

Step 2: Determination of Average Solutions

The average solution (AV_z) is determined by using Equation (6). The average solutions are presented in Table 13.

Table 13. Determination of average solutions ($\boldsymbol{AV_z}$)

Criteria	**C1**	**C2**	**C3**	**C4**	**C5**	**C6**	**C7**	**C8**
Kemer	30	50	80	33.333	100	46.666	60	85
Muratpaşa	95	100	61.666	100	50	85	63.333	73.333
Konyaaltı	68.333	85	90	80	66.666	73.333	66.666	73.333
Manavgat	68.333	75	63.333	61.666	66.666	66.666	75	75
Alanya	43.333	68.333	75	63.333	95	73.333	80	85
$\boldsymbol{AV_z}$	61	75.666	74	67.666	75.666	69	69	78.333

Step 3: Determination of Average Positive and Negative Distance Matrices

The average positive distance matrix (PDA) and the average negative distance matrix (NDA) are calculated using average solutions. In the calculations, Equations (9) and (10) are used for benefit-oriented criteria, and Equations (11) and (12) are used for cost-oriented criteria. Tables 14 and 15 contain the average positive distance and average negative distance matrices.

Table 14. Average positive distance matrix (***PDA***)

Criteria	C1	C2	C3	C4	C5	C6	C7	C8
Kemer	0.508	0	0	0	0.321	0	0	0
Muratpaşa	0	0.321	0.166	0.477	0	0.231	0	0.063
Konyaaltı	0	0.123	0	0.182	0	0.062	0	0.063
Manavgat	0	0	0.144	0	0	0	0.086	0.042
Alanya	0.289	0	0	0	0.255	0.062	0.159	0

Table 15. Average negative distance matrix (***NDA***)

Criteria	C1	C2	C3	C4	C5	C6	C7	C8
Kemer	0	0.339	0.081	0.507	0	0.323	0.130	0.085
Muratpaşa	0.557	0	0	0	0.339	0	0.082	0
Konyaaltı	0.120	0	0.216	0	0.118	0	0.033	0
Manavgat	0.120	0.008	0	0.088	0.118	0.033	0	0
Alanya	0	0.096	0.013	0.064	0	0	0	0.085

Step 4: Calculation of Weighted Total Distance Matrices

The weighted total distance matrices SP_k and SN_k values are calculated for each alternative. In the calculations, the values of SP_k and SN_k are obtained using Equations (13) and (14), respectively. The values of SP_k and SN_k calculated in Table 16 are presented.

Table 16. Calculation of positive (SP_k) and negative distance (SN_k) values

	SP_k	SN_k
Kemer	0.147	0.176
Muratpaşa	0.162	0.166
Konyaaltı	0.052	0.075
Manavgat	0.029	0.058
Alanya	0.114	0.029

Step 5: Normalization of SP_k and SN_k Values

The SP_k and SN_k values are normalized. Using the normalized SP_k and SN_k values, alternative evaluation scores (AS_k) are calculated for each alternative. The calculated AS_k scores are sorted from highest to lowest to determine the location where the station will be established. In the calculations, Equations (15) and (16) are used for the values of NSP_k and NSN_k respectively, and Equation (17) is used for the value of AS_k. The values of NSP_k, NSN_k and AS_k calculated in Table 17 are included.

Table 17. Calculation of normalized negative distance, positive distance and alternative evaluation score values

	NSP_k	NSN_k	AS_k	Ranking
Kemer	0.907	0	0.453	3
Muratpaşa	1	0.057	0.528	2
Konyaaltı	0.323	0.569	0.446	4
Manavgat	0.182	0.668	0.425	5
Alanya	0.704	0.830	0.767	1

In the evaluation conducted using the EDAS method, Alanya was chosen as the best alternative. Subsequently, the alternatives of Muratpaşa, Kemer, Konyaaltı, and Manavgat were ranked in order.

3.6 Application of Fuzzy EDAS Method

Step 1: Creation of the Fuzzy Average Decision Matrix

In the first step of the fuzzy EDAS method, a fuzzy average decision matrix is created for each criterion, and the average solution ($\widetilde{AV}_z$) is calculated using Equation (19). Table 18 contains the fuzzy average decision matrix.

Table 18. Fuzzy average decision matrix

	C1	C2	C3	C4
Kemer	(.2, .3, .4, .5)	(.366, .466, .533, .633)	(.633, .733, .766, .933)	(.233, .333, .366, .466)
Muratpaşa	(.766, .866, .933, 1.0)	(.8, .9, 1.0, 1.0)	(.5, .6, .6, .733)	(.8, .9, 1.0, 1.0)
Konyaaltı	(.533, .633, .666, .8)	(.7, .8, .8, 1.0)	(.7, .8, .9, .933)	(.633, .733, .766, .933)
Manavgat	(.533, .633, .666, .8)	(.566, .666, .733, .866)	(.466, .566, .633, .733)	(.5, .6, .6, .733)
Alanya	(.3, .399, .5, .6)	(.533, .633, .666, .8)	(.566, .666, .733, .866)	(.466, .566, .633, .733)
$\widetilde{AV}_z$	(.466, .566, .633, .74)	(.593, .693, .746, .86)	(.573, .673, .726, .84)	(.526, .626, .673, .773)
	C5	**C6**	**C7**	**C8**
Kemer	(.8, .9, 1.0, 1.0)	(.333, .433, .466, .566)	(.466, .566, .633, .7)	(.666, .766, .833, .933)
Muratpaşa	(.4, .5, .5, .6)	(.666, .766, .833, .933)	(.466, .566, .633, .7)	(.566, .666, .733, .8)
Konyaaltı	(.533, .633, .666, .733)	(.6, .7, .7, .866)	(.533, .633, .666, .833)	(.566, .666, .733, .8)
Manavgat	(.533, .633, .666, .833)	(.533, .633, .666, .733)	(.566, .666, .733, .866)	(.566, .666, .733, .866)
Alanya	(.766, .866, .933, 1.0)	(.566, .6666, .733, .8)	(.6, .7, .799, .866)	(.666, .766, .833, .933)
$\widetilde{AV}_z$	(.606, .706, .753, .833)	(.54, .64, .68, .78)	(.526, .626, .693, .793)	(.606, .706, .773, .866)

Step 2: Calculation of Fuzzy Positive and Negative Distance Matrices from the Mean

The fuzzy positive distance from the average (PDA) and the fuzzy negative distance from the average (NDA) are calculated. The calculations performed using Equations (22) and (23) are presented in Table 19 and Table 20.

Table 19. Fuzzy positive distance matrix from the mean ($\boldsymbol{PDA}$)

	C1	C2	C3	C4
Kemer	(.266,.266,.333,.540)	(.000,.000,.000,.000)	(.000,.000,.000,.000)	(.000,.000,.000,.000)
Muratpaşa	(.000,.000,.000,.000)	(.207,.207,.254,.140)	(.073,.073,.146,.107)	(.274,.274,.327,.227)
Konyaaltı	(.000,.000,.000,.000)	(.107,.107,.054,.140)	(.000,.000,.000,.000)	(.107,.107,.093,.160)
Manavgat	(.000,.000,.000,.000)	(.027,.027,.013,.006)	(.107,.107,.093,.107)	(.000,.000,.000,.000)
Alanya	(.166,.166,.133,.140)	(.000,.000,.000,.000)	(.007,.007,.000,.000)	(.000,.000,.000,.000)
	C5	**C6**	**C7**	**C8**
Kemer	(.194,.194,.247,.167)	(.000,.000,.000,.000)	(.000,.000,.000,.000)	(.000,.000,.000,.000)
Muratpaşa	(.000,.000,.000,.000)	(.126,.126,.153,.153)	(.000,.000,.000,.000)	(.040,.040,.040,.107)
Konyaaltı	(.000,.000,.000,.000)	(.060,.060,.020,.086)	(.007,.007,.000,.040)	(.000,.000,.000,.000)
Manavgat	(.000,.000,.000,.000)	(.000,.000,.000,.000)	(.040,.040,.040,.073)	(.000,.000,.000,.000)
Alanya	(.160,.160,.180,.167)	(.026,.026,.053,.020)	(.074,.074,.106,.073)	(.000,.000,.000,.000)

Table 20. Fuzzy negative distance matrix from the mean ($\boldsymbol{NDA}$)

	C1	C2	C3	C4
Kemer	(.000,.000,.000,.034)	(.227,.227,.213,.027)	(.060,.060,.020,.193)	(.293,.293,.307,.307)
Muratpaşa	(.300,.300,.300,.534)	(.000,.000,.000,.000)	(.000,.000,.000,.000)	(.000,.000,.000,.000)
Konyaaltı	(.060,.067,.033,.060)	(.000,.000,.000,.000)	(.127,.127,.174,.093)	(.000,.000,.000,.000)
Manavgat	(.060,.067,.033,.060)	(.000,.000,.000,.000)	(.000,.000,.000,.000)	(.027,.027,.073,.040)
Alanya	(.000,.000,.000,.000)	(.060,.060,.000,.000)	(.000,.000,.000,.000)	(.060,.060,.040,.040)
	C5	**C6**	**C7**	**C8**
Kemer	(.000,.000,.000,.000)	(.207,.207,.214,.214)	(.060,.060,.060,.093)	(.060,.060,.060,.067)
Muratpaşa	(.207,.207,.253,.233)	(.000,.000,.000,.000)	(.060,.060,.060,.093)	(.000,.000,.000,.000)
Konyaaltı	(.000,.000,.000,.000)	(.060,.060,.086,.000)	(.000,.000,.000,.000)	(.000,.000,.000,.000)
Manavgat	(.000,.000,.000,.000)	(.000,.000,.000,.000)	(.000,.000,.000,.000)	(.000,.000,.000,.000)
Alanya	(.000,.000,.000,.000)	(.000,.000,.000,.000)	(.000,.000,.000,.000)	(.060,.060,.060,.067)

Step 3: Calculation of the Fuzzy Weighted Sums of Positive and Negative Distances

The fuzzy weighted sums of positive ($\widetilde{SP}_k$) and negative distances ($\widetilde{SN}_k$) are calculated from the average matrix. The $\widetilde{SP}_k$ and $\widetilde{SN}_k$ values are calculated using Equations (24) and (25), respectively. The calculated $\widetilde{SP}_k$ and $\widetilde{SN}_k$ values are presented in Table 21.

Table 21. Calculation of fuzzy weighted sums of positive ($\boldsymbol{\widetilde{SP}_k}$) and negative distances ($\boldsymbol{\widetilde{SN}_k}$) values

	$\boldsymbol{\widetilde{SP}_k}$	$\boldsymbol{\widetilde{SN}_k}$
Kemer	(.000,.039,.080,.198)	(.320,.152,.075,.007)
Muratpaşa	(.003,.068,.139,.261)	(.228,.097,.055,.004)
Konyaaltı	(.000,.017,.057,.278)	(.241,.067,.014,.000)
Manavgat	(.000,.005,.055,.265)	(.262,.059,.008,.000)
Alanya	(.000,.023,.100,.290)	(.233,.053,.003,.000)

Step 4: Calculation of Fuzzy Normalized Values of $\widetilde{SN}_k$ and $\widetilde{SP}_k$

The fuzzy normalized values of $\widetilde{SN}_k$ and $\widetilde{SP}_k$ are calculated. Fuzzy evaluation scores ($\widetilde{AS}_k$) are also calculated for all alternatives. The alternatives are ranked from highest to lowest by applying the defuzzification process ($Def\ (AS_k)$) to the fuzzy evaluation scores. The values of $\widetilde{NSP}_k$ and $\widetilde{NSN}_k$ are calculated using Equations (26) and (27), respectively, while the value of $\widetilde{AS}_k$ is calculated using Equation (28). The $Def\ (AS_k)$ values are calculated using Equation (16). The values of $\widetilde{NSP}_k$,$\widetilde{NSN}_k$, $\widetilde{AS}_k$ and $Def\ (AS_k)$ calculated in Table 22 are presented.

Table 22. Calculation of normalized negative distance, positive distance, alternative evaluation score and defuzzification process values

	$\boldsymbol{\widetilde{NSP}_k}$	$\boldsymbol{\widetilde{NSN}_k}$	$\boldsymbol{\widetilde{AS}_k}$	$\boldsymbol{Def\ (AS_k)}$
Kemer	(.000,.346,.709,1.749)	(-1.459,-.165,.423,.942)	(-.729,.091,.566,1.346)	.322
Muratpaşa	(.030,.597,1.233,2.310)	(-.749,.257,.579,.969)	(-.359,.427,.906,1.640)	.658
Konyaaltı	(.000,.148,.502,2.457)	(-.850,.488,.891,1.000)	(-.425,.318,.696,1.729)	.555
Manavgat	(.000,.044,.487,2.347)	(-1.011,.545,.937,1.000)	(-.505,.295,.712,1.673)	.530
Alanya	(.000,.206,.886,2.569)	(-.787,.597,.974,1.000)	(-.393,.401,.930,1.785)	.676

In the evaluation conducted using the Fuzzy EDAS method, the ranking obtained was as follows: Alanya in first place, Muratpaşa in second place, Konyaaltı in third place, Manavgat in fourth place, and Kemer in fifth place. While Alanya and Muratpaşa maintained their current rankings in both methods, the other districts varied.

In the classical EDAS framework, the evaluation process is conducted on the basis of precise (crisp) numerical inputs, whereby each criterion score reflects a single fixed value without considering the variability inherent in expert judgment. In contrast, the Fuzzy EDAS approach models decision-makers' assessments through trapezoidal membership functions, allowing the representation of vagueness, hesitation, and gradational preference structures. This formulation broadens the dispersion range of expert evaluations, particularly for the criteria C1 (transformer load), C5 (touristic attractiveness), and C7 (future growth potential), thereby rendering the relative performance differentials among alternatives more explicit.

This study addresses the electric vehicle charging station (EVCS) siting process through a two-stage decision framework, structurally separating geographic information system (GIS)-based spatial suitability analysis from the multi-criteria alternative evaluation stage. The use of 16 criteria in total (8 spatial and 8 decision-support related) enables the site selection process to move beyond mere geographic suitability and incorporate a comprehensive assessment that includes accessibility, sustainability, and operational feasibility. In this respect, the study provides a structure that is more transparent, adaptable, and open to decision-maker intervention compared to approaches that handle spatial analysis and final decision-making within a single evaluation layer [89, 90]. Furthermore, international studies conducted in different geographical contexts indicate that indicators such as accessibility, population density, and mobility patterns vary across regional conditions [97, 103]. By incorporating expert judgments in a manner aligned with local context, this study directly integrates these contextual differences into the model. The proposed framework therefore offers a re-applicable, scenario-based, and policy-integrable decision support model that can be effectively adapted to different urban scales, demographic structures, and infrastructure conditions.

3.7 Sensitivity Analysis

Sensitivity analysis is included in this section to examine the effects of possible changes in criteria weights on the EVCS location selection problem as seen in Figure 4.

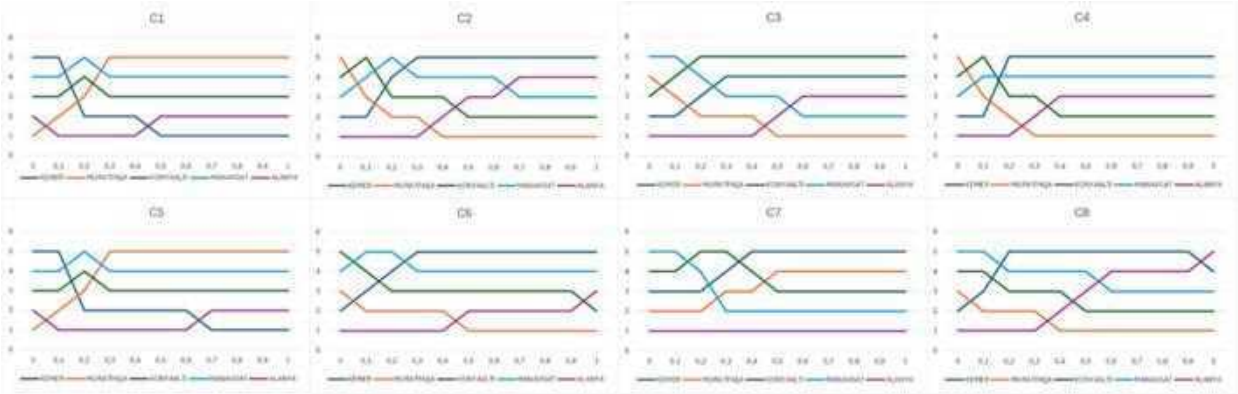


Figure 4. Results of sensitivity analysis

Sensitivity analysis was conducted for all criteria between C1-C8 used within the EVCS location selection decision problem, with criterion weights ranging from 0 to 1 (increasing by 0.1). Changes in criterion weights affect the ranking of alternatives, and Figure 4 demonstrates sensitivity.

According to the sensitivity analysis results, the variations in criterion weights have a limited effect on the overall ranking of the alternatives. In particular, the rankings remain highly stable under changes in the weights of C1, C2, C5, and C6, indicating a high level of decision robustness in the model. In contrast, for C3, C4, C7, and C8, weight adjustments lead to minor shifts in secondary and tertiary rankings at specific intervals. These shifts suggest that the sensitivity is more pronounced among alternatives with closely aligned performance scores.

Overall, no single criterion demonstrates a dominant influence capable of fundamentally altering the ranking, indicating that the model is not overly dependent on any individual criterion and that the multi-criteria structure functions in a balanced manner. Additionally, the fact that ranking variations occur only in selected criteria and only among alternatives with marginal performance differences confirms that the proposed decision model possesses a strong and stable structural reliability.

4. CONCLUSIONS

In this study, the EVCS site selection research conducted within the scope of Antalya province has been thoroughly addressed using both GIS-based location analyses and EDAS methods. The literature review began with the concept of sustainability; under this main heading, the subtopics of environmental sensitivity, carbon footprint, and green logistics were examined. In the relevant section, the importance of sustainable vehicles and the concept of green logistics were discussed, followed by a review of EV and EVCS in the literature. In the study, the literature review was conducted to develop a model for investigating the EVCS site selection problem in the province of Antalya. However, the necessary conditions and requirements for EVCS have been defined, and similar studies related to EVCS site selection problems have been listed.

Fuzzy numbers can be used due to the decision maker's ability to express themselves better using linguistic expressions and the inadequacy of classical decision-making methods in the face of uncertainty [129]. In the literature, some of the MCDM studies for electric vehicles [83, 128] did not include fuzzy numbers at all, and in the limited number of studies [93, 96, 122] where fuzzy numbers were used, trapezoidal fuzzy numbers were not included. According to Kaya and Kahraman, trapezoidal fuzzy numbers are suitable for representing exact ranges [130]. In this context, the integration of trapezoidal fuzzy numbers into MCDM methods for the problem of locating charging stations for electric vehicles shows the originality of the study. In addition, by integrating fuzzy numbers, MCDM techniques and GIS, the study shows a new perspective on literature. For these purposes, the study will contribute positively to the energy efficiency of the region where it will be implemented. It will also contribute positively to the widespread use of EVs by advancing sustainable transportation. By providing a multidisciplinary perspective on the placement of charging stations, it aims to fill an important gap in fields such as urban planning and to make positive contributions to literature.

This research conducted in the province of Antalya aims to evaluate many elements together, such as sustainability, economic feasibility, and social benefit. Eight different criteria were determined for use in GIS-based analyses, and these criteria were evaluated using the GIS software QGIS, taking into account geographical data layers. The determined criteria were integrated with provincial-level maps to identify physical and locational advantages for potential charging station installations. In the literature, similar criteria have been considered in studies such as Alkan et al. [124], Bilgilioğlu [122], Hişoğlu and Cömert [102], Elomiya et al. [96]. Scores were assigned to the criteria based on expert evaluations, and then these scores were used to calculate the criteria weights. The most important criteria were determined to be the distance to the transformer, the distance to the main roads, and the distance to official institutions, while the least important criterion, according to the experts, was the distance to parking lots. Considering the determined weights, the suitability maps of the criteria were combined, and a suitability map was obtained.

It has been determined that the most suitable alternative locations for the installation of EVCS are the districts of Kemer, Konyaaltı, Muratpaşa, Manavgat, and Alanya. In the next phase, the MCDM application step was taken, considering eight additional criteria, resulting in a comprehensive evaluation with a total of sixteen criteria. The load impact on transformer centers, investment costs, and environmental responsibility were evaluated as cost-oriented criteria, while the other criteria were assessed as benefit-oriented. The EDAS and fuzzy EDAS methods were applied, taking into account the potential uncertainty in expert opinions. According to the EDAS method, Alanya has been selected as the most suitable district with a higher weight than the other alternative locations. Following Alanya, in order, are the districts of Muratpaşa, Kemer, Konyaaltı, and Manavgat.

The results obtained by applying the fuzzy EDAS method also largely support the results obtained by the EDAS method. The fact that the Kemer district ranks 3rd when the EDAS method is applied and 5th when the fuzzy EDAS method is applied indicates differing prioritizations among expert opinions. In addition, the fact that two methods yield largely similar results suggests that Alanya is a strong candidate region for station installation. All these findings and recommendations are guiding in a broad framework, from policymakers at the provincial level to private sector investors. As emphasized in the literature, such as the studies by Morocho-Chicaiza et al. [87] and Zhao and Hao [9], it is anticipated that the use of EV will become even more widespread in the future. In conclusion, this research conducted in the province of Antalya is significant both for providing concrete data for practical applications and for serving as a guide in various academic fields (logistics, urban planning, sustainable energy, etc.).

This study stands out in the literature by addressing the EVCS siting process through a two-stage decision framework, structurally separating the spatial suitability analysis from the multi-criteria alternative evaluation stage. The use of a total of 16 criteria, designed separately for GIS-based spatial analysis and MCDM-based alternative ranking, enables the site selection process to be assessed not only in terms of geographical suitability but also in relation to operational, economic, and urban accessibility considerations. This approach provides an enhanced contribution to decision quality, particularly when compared with single-stage models or those relying solely on suitability maps. Moreover, the incorporation of expert evaluations supports the alignment of theoretical-prioritized criteria with local contextual priorities during the weighting process. As expert-based weighting is a widely accepted and commonly employed approach in MCDM studies, the selection of experts with substantial domain knowledge in this study serves to mitigate potential subjectivity within the evaluation process.

Nevertheless, the proposed method entails certain limitations. The spatial analyses conducted are constrained by the currency and resolution of available datasets, and because urban infrastructure, land use patterns, and traffic conditions may evolve over time, the model should be periodically updated to maintain relevance. Additionally, the approach does not explicitly model dynamic operational variables such as station operating costs, demand distribution patterns, or grid load management. Integrating these factors into future iterations of the model would support the optimization of proposed station locations not only at the planning level but also in terms of operational efficiency. However, these limitations are inherent to the scope of the study and do not diminish the applicability or validity of the proposed framework. On the contrary, the adaptability of the model across different datasets, varying city scales, and distinct policy environments demonstrates the flexibility and scalability of the proposed decision support structure.

Declaration of Ethical Standards

The authors declare that all ethical guidelines including authorship, citation, data reporting, and publishing original research.

Credit Authorship Contribution Statement

Aleyna Kenar: Investigation, Methodology, Software, Data curation, Analysis, Visualization, Writing - original draft preparation. **Eray Baysal:** Investigation, Methodology, Software, Data curation, Analysis, Visualization, Writing -original draft preparation. **Eren Kamber:** Conceptualization, Investigation, Methodology, Data curation, Analysis, Project Administration, Writing- review and editing. **Ufuk Aydoğmuş:** Conceptualization, Investigation, Methodology, Data curation, Analysis, Visualization, Writing- review and editing. **Hacer Yumurtacı Aydoğmuş:** Conceptualization, Methodology, Supervision, Project Administration, Writing- review and editing.

Declaration of Competing Interest

The author declares that there is no conflict of interest.

Funding / Acknowledgements

The authors have not disclosed any funding.

Data Availability

All data generated or analyzed during this study are included in this published article.

Use of Artificial Intelligence

The authors state that artificial intelligence tools are only used for language editing and improving readability.

5. REFERENCES

[1] M. M. Geng and L. Y. He, "Environmental regulation, environmental awareness and environmental governance satisfaction," *Sustainability*, vol. 13, no. 7, pp. 3960, 2021.

[2] H. Şen, A. Kaya, and B. Alpaslan, "Sürdürülebilirlik üzerine tarihsel ve güncel bir perspektif," *Ekonomik Yaklaşım Derneği*, vol. 29, no. 107, pp. 1–47, 2018.

[3] M. H. Mücevher, "Sürdürülebilir lojistik için üç öncelikli strateji: Yeşil lojistik, tersine lojistik ve yalın lojistik," *Enderun Dergisi*, vol. 5, no. 1, 2021.

[4] M. Vienažindienė, V. Tamulienė, and J. Zaleckienė, "Green logistics practices seeking development of sustainability: Evidence from Lithuanian transportation and logistics companies," *Energies*, vol. 14, no. 22, pp. 7500, 2021.

[5] T. Wiedmann and J. C. Minx, "A definition of 'carbon footprint'," in Ecological Economics Research Trends, C. C. Pertsova, Ed., vol. 1, Hauppauge, NY, USA: Nova Science Publishers, pp. 1–11, 2008.

[6] Q. Zhao, F. Han, Y. Huang, X. She, Z. You, and B. Zhang, "Research of the carbon footprint calculation and evaluation method based on the pattern microalgae for biodiesel production," *Renew. Energy*, vol. 231, pp. 120912, 2024.

[7] K. S. Uralovich, T. U. Toshmamatovich, K. F. Kubayevich, I. B. Sapaev, S. S. Saylaubaevna, Z. F. Beknazarova, and A. Khurramov, "A primary factor in sustainable development and environmental sustainability is environmental education," *Caspian J. Environ. Sci.*, vol. 21, no. 4, pp. 965–975, 2023.

[8] R. Çakmak and A. Turan, "Türkiye'de iller bazında elektrikli araç şarj istasyonu altyapısı: Ölçevler aracılığıyla analizi," *Karadeniz Fen Bilimleri Dergisi*, vol. 12, no. 1, pp. 246–268, 2022.

[9] H. Zhao and X. Hao, "Location decision of electric vehicle charging station based on a novel grey correlation comprehensive evaluation multi-criteria decision method," *Energy*, vol. 299, pp. 131356, 2024.

[10] A. Ç. Aydınoğlu, T. Çetin, A. U. Topal, and S. Şişman, "Elektrikli araç şarj istasyonlarının optimum yerleşimine yönelik coğrafi analiz araçlarının geliştirilmesi," *Akıllı Ulaşım Sistemleri ve Uygulamaları Dergisi*, vol. 8, no. 1, pp. 39–52, 2025.

[11] F. S. Durmuş and H. Kaymaz, "Elektrikli araç şarj yöntemleri," *Akıllı Ulaşım Sistemleri ve Uygulamaları Dergisi*, vol. 3, no. 2, pp. 123–139, 2020.

[12] O. Bozoğlu and E. Ciğerim, "Sürdürülebilirlik, sürdürülebilir kalkınma ve sürdürülebilir üniversiteler," *Socrates J. Interdiscip. Soc. Stud.*, vol. 8, no. 18, pp. 146–158, 2022.

[13] Y. Gazibey, A. Keser, and Y. Gökmen, "Türkiye'de illerin sürdürülebilirlik boyutları açısından değerlendirilmesi," *Ankara Univ. SBF Dergisi*, vol. 69, no. 3, pp. 511–544, 2014.

[14] M. Yeşil and Y. Turan, "Çevresel duyarlılık üzerine bir ölçek geliştirme çalışması," *ODÜ Sos. Bilim. Araşt. Dergisi*, vol. 10, no. 2, pp. 418–435, 2020.

[15] X. Chen, B. Huang, and C. T. Lin, "Environmental awareness and environmental Kuznets curve," *Econ. Model.*, vol. 77, pp. 2–11, 2019.

[16] R. Rodríguez-Ibeas, "Environmental product differentiation and environmental awareness," *Environ. Resour. Econ.*, vol. 36, pp. 237–254, 2007.

[17] M. Wang, X. Zhong, H. Yuan, D. Zhang, L. Cheng, and J. Zhang, "Integrating carbon and water footprint into nature-based solution (NBS) for urban planning in a highly built-up area in Guangzhou, China," *Sci. Total Environ.*, vol. 951, pp. 175505, 2024.

[18] R. Ramli, K. R. Purba, and I. Baydarova, "Preliminary study on the carbon footprint awareness & the analysis among university students in Malaysia," *in Proc. 2024 20th IEEE Int. Colloq. Signal Process. Appl. (CSPA)*, pp. 202–206, 2024.

[19] B. A. Bingül, "CO_2 emisyonu ve beşerî sermaye ilişkisi üzerine literatür araştırması," *Kırklareli Univ. İİBF Dergisi*, vol. 9, no. 1, pp. 81–91, 2020.

[20] G. Qing, Y. Xiang, Y. Shang, X. Liu, H. Zhou, and Y. Huang, "Carbon footprint evaluation for electric vehicles considering green electricity trading," *Renew. Energy*, pp. 121510, 2024.

[21] I. G. Romero, H. B. Rai, Á. O. Bas, and J. C. P. Prado, "Can reusable packaging revolutionise e-commerce? Unveiling the environmental impact through a comparative carbon footprint analysis," *J. Clean. Prod.*, pp. 143738, 2024.

[22] J. Dai, Z. Ahmed, A. Sinha, U. K. Pata, and R. Alvarado, "Sustainable green electricity, technological innovation, and ecological footprint: Does democratic accountability moderate the nexus?," *Utilities Policy*, vol. 82, pp. 101541, 2023.

[23] I. V. Larina, A. N. Larin, O. Kiriliuk, and M. Ingaldi, "Green logistics-modern transportation process technology," *Prod. Eng. Arch.*, vol. 27, no. 3, pp. 184–190, 2021.

[24] E. Kamber and M. Baskak, "Green logistics park location selection with circular intuitionistic fuzzy CODAS method: The case of Istanbul," *J. Intell. Fuzzy Syst.*, vol. 46, no. 2, pp. 4173–4189, 2024.

[25] S. İncaz, "Lojistik ve sürdürülebilirlik bağlamında yeni yaklaşımlar," *Nişantaşı Univ. Sos. Bil. Dergisi*, vol. 3, no. 1, pp. 149–162, 2015.

[26] G. Akandere, "Dijitalleşme düzeyi ve yeşil lojistik uygulamaların lojistik performansa etkisi," *Nevşehir Hacı Bektaş Veli Univ. SBE Dergisi*, vol. 11, no. 4, pp. 1979–2000, 2021.

[27] S. Verma, A. Sharma, B. Tran, and D. Alahakoon, "A systematic review of digital twins for electric vehicles," *J. Traffic Transp. Eng. (Engl. Ed.)*, 2024.

[28] M. Mazman, D. Uzun, C. Kaypmaz, and E. Biçer, "Elektrikli araçlar için enerji depolama çözümleri," *Mühendis ve Makina*, vol. 53, no. 628, pp. 21–25, 2012.

[29] S. Kocabey, "Elektrikli otomobillerin dünü, bugünü ve geleceği," *Akıllı Ulaşım Sistemleri ve Uygulamaları Dergisi*, vol. 1, no. 1, pp. 16–23, 2018.

[30] J. A. P. Lopes, F. J. Soares, and P. M. R. Almeida, "Integration of electric vehicles in the electric power system," *Proc. IEEE*, vol. 99, no. 1, pp. 168–183, 2010.

[31] R. Rotas, P. Iliadis, N. Nikolopoulos, and A. Tomboulides, "Evaluating synergies between electric vehicles and photovoltaics: A comparative study of urban environments," *World Elect. Veh. J.*, vol. 15, no. 9, pp. 397, 2024.

[32] M. Nilsson, "Electric vehicles: An interview study investigating the phenomenon of range anxiety," *Lindholmen Science Park (Sweden)*, Task 5000, Elvire, 2011.

[33] J. Lin, W. Zhou, and O. Wolfson, "Electric vehicle routing problem," *Transp. Res. Procedia*, vol. 12, pp. 508–521, 2016.

[34] M. A. Hannan, F. A. Azidin, and A. Mohamed, "Hybrid electric vehicles and their challenges: A review," *Renew. Sustain. Energy Rev.*, vol. 29, pp. 135–150, 2014.

[35] M. Ehsani, K. V. Singh, H. O. Bansal, and R. T. Mehrjardi, "State of the art and trends in electric and hybrid electric vehicles," *Proc. IEEE*, vol. 109, no. 6, pp. 967–984, 2021.

[36] U. Lee, S. Jeon, and I. Lee, "Design for shared autonomous vehicle (SAV) system employing electrified vehicles: Comparison of battery electric vehicles (BEVs) and fuel cell electric vehicles (FCEVs)," *Clean. Eng. Technol.*, vol. 8, pp. 100505, 2022.

[37] E. Yalçınsoy, "Hibrit ve elektrikli araç bataryalarının soğutulmasının hesaplamalı olarak araştırılması," *M.S. thesis*, Bursa Uludağ Univ., Bursa, Turkey, 2023.

[38] J. A. Sanguesa, V. Torres-Sanz, P. Garrido, F. J. Martinez, and J. M. Marquez-Barja, "A review on electric vehicles: Technologies and challenges," *Smart Cities*, vol. 4, no. 1, pp. 372–404, 2021.

[39] M. Safari, "Battery electric vehicles: Looking behind to move forward," *Energy Policy*, vol. 115, pp. 54–65, 2018.

[40] J. Zhao, X. I. Xi, Q. I. Na, S. Wang, S. N. Kadry, and P. M. Kumar, "The technological innovation of hybrid and plug-in electric vehicles for environment carbon pollution control," *Environ. Impact Assess. Rev.*, vol. 86, pp. 106506, 2021.

[41] J. García-Villalobos, I. Zamora, J. I. San Martín, F. J. Asensio, and V. Aperribay, "Plug-in electric vehicles in electric distribution networks: A review of smart charging approaches," *Renew. Sustain. Energy Rev.*, vol. 38, pp. 717–731, 2014.

[42] S. Vengatesan, A. Jayakumar, and K. K. Sadasivuni, "FCEV vs. BEV—A short overview on identifying the key contributors to affordable & clean energy (SDG-7)," *Energy Strategy Rev.*, vol. 53, pp. 101380, 2024.

[43] U. Asif and K. Schmidt, "Fuel cell electric vehicles (FCEV): Policy advances to enhance commercial success," *Sustainability*, vol. 13, no. 9, pp. 5149, 2021.

[44] H. Özbay, C. Közkurt, A. Dalcalı, and M. Tektaş, "Geleceğin ulaşım tercihi: Elektrikli araçlar," *Akıllı Ulaşım Sistemleri ve Uygulamaları Dergisi*, vol. 3, no. 1, 2020. [Online]. Available: https://dergipark.org.tr/en/download/article-file/1069158

[45] H. Shahrier and M. A. Habib, "Electric vehicle (EV) type choice model: Latent class modelling (LCM) approach," *Int. J. Transp. Sci. Technol.*, 2024.

[46] D. Kazak, "Elektrikli araçların avantajları, dezavantajları ve yangın riskleri: Batarya güvenliği ve yangın söndürme çözümleri üzerine bir inceleme," *Uluslararası Sos. Beşeri Bil. Araşt. Dergisi*, vol. 11, no. 110, pp. 1492–1503, 2024.

[47] M. VikramGoud, P. K. Biswas, C. Sain, T. S. Babu, and P. K. Balachandran, "Advancement of electric vehicle technologies, classification of charging methodologies, and optimization strategies for sustainable development: A comprehensive review," *Heliyon*, pp. e39299, 2024.

[48] M. E. Vilberger, N. S. Popov, E. A. Domakhin, V. I. Anibroev, and M. E. Mosin, "Increasing the energy efficiency of an electric vehicle powered by hydrogen fuel cells," *Int. J. Hydrogen Energy*, vol. 85, pp. 406–415, 2024.

[49] J. Wu, Q. Li, Y. Bie, and W. Zhou, "Location-routing optimization problem for electric vehicle charging stations in an uncertain transportation network: An adaptive co-evolutionary clustering algorithm," *Energy*, pp. 132142, 2024.

[50] J. Suvvala, C. Dhananjayulu, H. Kotb, and A. ELrashidi, "Integration of renewable energy sources using multiport converters for ultra-fast charging stations for electric vehicles: An overview," *Heliyon*, 2024.

[51] P. K. Das and M. Y. Bhat, "Global electric vehicle adoption: Implementation and policy implications for India," *Environ. Sci. Pollut. Res.*, vol. 29, no. 27, pp. 40612–40622, 2022.

[52] H. N. D. Şenyapar and M. R. Tür, "Turkey's domestic car TOGG in the framework of new trends in electric vehicles and consumer ethnocentrism," *Balkan J. Electr. Comput. Eng.*, vol. 11, no. 2, pp. 115–128, 2023.

[53] N. Tunçel, "Intention to purchase electric vehicles: Evidence from an emerging market," *Res. Transp. Bus. Manag.*, vol. 43, pp. 100764, 2022.

[54] M. Agrawal and M. S. Rajapatel, "Global perspective on electric vehicle 2020," *Int. J. Eng. Res. Technol.*, vol. 9, no. 1, pp. 8–11, 2020.

[55] M. Zhang, S. Lou, Y. Wu, Y. Wang, and R. Chen, "Research on charging station planning method considering electric vehicle charging queuing," *in Proc. 2022 IEEE 3rd China Int. Youth Conf. Electr. Eng. (CIYCEE)*, pp. 1–5, 2022.

[56] L. Luo, W. Gu, S. Zhou, H. Huang, S. Gao, J. Han, ..., and X. Dou,"Optimal planning of electric vehicle charging stations comprising multi-types of charging facilities," *Appl. Energy*, vol. 226, pp. 1087–1099, 2018.

[57] V. H. U. Eze, M. C. Eze, C. C. Ogbonna, S. A. Ugwu, K. Emeka, and C. A. Onyeke, "Comprehensive review of recent electric vehicle charging stations," *Glob. J. Sci. Res. Publ.*, vol. 1, no. 12, pp. 16–23, 2021.

[58] G. H. Fox, "Electric vehicle charging stations: Are we prepared?," *IEEE Ind. Appl. Mag.*, vol. 19, no. 4, pp. 32–38, 2013.

[59] S. Cheikh-Mohamad, M. Sechilariu, F. Locment, and Y. Krim, "PV-powered electric vehicle charging stations: Preliminary requirements and feasibility conditions," *Appl. Sci.*, vol. 11, no. 4, pp. 1770, 2021.

[60] A. J. Alrubaie, M. Salem, K. Yahya, M. Mohamed, and M. Kamarol, "A comprehensive review of electric vehicle charging stations with solar photovoltaic system considering market, technical requirements, network implications, and future challenges," *Sustainability*, vol. 15, no. 10, pp. 8122, 2023.

[61] B. Bommana, J. S. Kumar, R.S. Nuvvula, P. P. Kumar, B. Khan, S. Muthusamy, and R. Inapakurthi, "A comprehensive examination of the protocols, technologies, and safety requirements for electric vehicle charging infrastructure," *J. Adv. Transp.*, vol. 2023, no. 1, pp. 7500151, 2023.

[62] C. Li, S. Zhang, W. Ling, L. Zhao, and Y. Pan, "Enhancing user experience in electric vehicle charging applications (EVCA): A comprehensive analysis in the Chinese context," *J. Knowl. Econ.*, pp. 1–36, 2024.

[63] F. Alanazi, "Electric vehicles: Benefits, challenges, and potential solutions for widespread adaptation," *Appl. Sci.*, vol. 13, no. 10, pp. 6016, 2023.

[64] A. Kerem and H. Gürbak, "Elektrikli araçlar için hızlı şarj istasyonu teknolojileri," *Gazi Univ. J. Sci. Part C: Des. Technol.*, vol. 8, no. 3, pp. 644–661, 2020.

[65] Türkiye Cumhuriyeti Ulaştırma ve Altyapı Bakanlığı, "Elektrikli araç şarj istasyonlarının yer seçiminin belirlenmesi projesi," 2023. [Online]. Available: https://www.uab.gov.tr/uploads/pages/bakanlik-yayinlari/elektrikli-arac-sarj-istasyonlarinin-yer-seciminin-belirlenmesiprojesi.pdf. [Accessed Feb. 20, 2025].

[66] E. Çetin, "Elektrikli araç şarj istasyonu entegre edilen mevcut bir elektrik tesisatındaki revizyon ihtiyacının Simaris ortamında incelenmesi," *Pamukkale Univ. Müh. Bilim. Derg.*, vol. 28, no. 2, pp. 222–233, 2022.

[67] M. Bildirici and O. Kaplan, "Electric vehicle projection and incentive recommendations in Türkiye," in *Proc. 2024 12th Int. Conf. Smart Grid (icSmartGrid)*, pp. 835–839, 2024.

[68] M. Şen, M. S. Yiğiter, and M. Özcan, "Why are consumers switching to electric vehicles? Analyzing consumers preferences for electric vehicles," *Case Stud. Transp. Policy*, vol. 14, pp. 101108, 2023.

[69] A. T. Özyalçın and H. Bircan, "Çok kriterli karar verme problemlerinin çözümüne yönelik otomasyon geliştirme," *Int. J. Manag. Inf. Syst. Comput. Sci.*, vol. 7, no. 1, pp. 1–32, 2023.

[70] G. Turan, "Çok kriterli karar verme," in *Çok Kriterli Karar Verme Yöntemleri*, B. F. Yıldırım and E. Önder, Eds. Bursa: Dora Basım Yayınları, 2018, pp. 15–20.

[71] E. Dalbudak and Ö. F. Rençber, "Çok kriterli karar verme yöntemleri üzerine literatür incelemesi," *Gaziantep Univ. İİBF Dergisi*, vol. 4, no. 1, pp. 1–17, 2022.

[72] G. Yannis, A. Kopsacheili, A. Dragomanovits, and V. Petraki, "State-of-the-art review on multi-criteria decision-making in the transport sector," *J. Traffic Transp. Eng. (Engl. Ed.)*, vol. 7, no. 4, pp. 413–431, 2020.

[73] G. O. Odu, "Weighting methods for multi-criteria decision making technique," *J. Appl. Sci. Environ. Manag.*, vol. 23, no. 8, pp. 1449–1457, 2019.

[74] M. Keshavarz Ghorabaee, E. K. Zavadskas, L. Olfat, and Z. Turskis, "Multi-criteria inventory classification using a new method of evaluation based on distance from average solution (EDAS)," *Informatica*, vol. 26, no. 3, pp. 435–451, 2015.

[75] M. Özmen, "OECD ülkelerinin telekomünikasyon sektörü açısından SMAA-EDAS yöntemi ile değerlendirilmesi," *Niğde Ömer Halisdemir Univ. Müh. Bilim. Dergisi*, vol. 9, no. 1, pp. 224–237, 2020.

[76] D. Tiwari and V. Soni, "Multi-response optimization in the ORC-VCR system using the EDAS method," *Energy Build.*, vol. 313, pp. 114281, 2024.

[77] A. Özbek and M. Engür, "EDAS yöntemi ile lojistik firma web sitelerinin değerlendirilmesi," *Selçuk Univ. Sos. Bil. MYO Dergisi*, vol. 21, no. 2, pp. 417–429, 2018.

[78] S. Rathor and S. C. Agrawal, "Wireless network environment evaluation using EDAS method," *in Proc. 2023 1st Int. Conf. Cogn. Comput. Eng. Educ. (ICCCEE)*, pp. 1–5, 2023.

[79] W. H. Hou, X. K. Wang, H. Y. Zhang, J. Q. Wang, and L. Li, "Safety risk assessment of metro construction under epistemic uncertainty: An integrated framework using credal networks and the EDAS method," *Appl. Soft Comput.*, vol. 108, pp. 107436, 2021.

[80] A. Ulutaş, "EDAS yöntemi kullanılarak bir tekstil atölyesi için dikiş makinesi seçimi," *İşletme Araşt. Dergisi*, vol. 9, no. 2, pp. 169–183, 2017.

[81] D. Uçar and A. Ö. Doğru, "CBS projelerinin stratejik planlaması ve SWOT analizinin yeri," *TMMOB Harita ve Kadastro Müh. Odası*, no. 10, 2005.

[82] F. Aladağ, "Dijital beşerî bilimler ve Türkiye araştırmaları: Bir literatür değerlendirmesi," *Türkiye Araştırmaları Literatür Dergisi*, vol. 18, no. 36, pp. 773–796, 2020.

[83] S. H. Gökler, "Optimal site selection for electric vehicle charging stations: Analysis with hybrid FUCOM and geographic information systems," *Energy*, vol. 307, pp. 132659, 2024.

[84] N. A. Alzahrani, S. N. H. S. Abdullah, N. Adnan, K. A. Z. Ariffin, M. Mukred, I. Mohamed, and S. Wahab, "Geographic information systems adoption model: A partial least square-structural equation modeling analysis approach," *Heliyon*, vol. 10, no. 15, 2024.

[85] R. Nişancı, V. Yıldırım, and H. E. Çolak, "Coğrafi bilgi sistem uygulamaları," *Bilim ve Teknik*, no. 514, pp. 58–63, 2010.

[86] H. Fidan, "Pazarlama bilgi sistemi (PBS) ve coğrafi bilgi sistemi (CBS)'nin pazarlamada kullanımı," *Yaşar Univ. E-Dergisi*, vol. 4, no. 14, pp. 2151–2171, 2009.

[87] W. Morocho-Chicaiza, A. Barragán-Escandón, E. Zalamea-León, D. Ochoa-Correa, J. Terrados-Cepeda, and X. Serrano-Guerrero, "Identifying locations for electric vehicle charging stations in urban areas through the application of multicriteria techniques," *Energy Reports*, 12, 1794-1809, 2024.

[88] K. H. Mhana and H. A. Awad, "An ideal location selection of electric vehicle charging stations: Employment of integrated analytical hierarchy process with geographical information system," *Sustainable Cities and Society*, 107, 105456, 2024.

[89] M. Razeghi, A. R. Araghi, A. Naseri, and H. Yousefi, "Strategic deployment of GIS-optimized solar charging stations for electric vehicles: A multi-criteria decision-making approach," *Energy Conversion and Management: X*, 24, 100712, 2024.

[90] M. Algafri, A. Alghazi, Y. Almoghathawi, H. Saleh, and K. Al-Shareef, "Smart City Charging Station allocation for electric vehicles using analytic hierarchy process and multiobjective goal-programming," *Applied Energy*, 372, 123775, 2024.

[91] R. Krishankumar and F. Ecer, "A multi-criteria framework for electric vehicle charging location selection using double hierarchy preferences and unknown weights," *Engineering Applications of Artificial Intelligence*, 133, 108251, 2024.

[92] Ö. Gönül, A. C. Duman, and Ö. Güler, "A comprehensive framework for electric vehicle charging station siting along highways using weighted sum method," *Renewable and Sustainable Energy Reviews*, 199, 114455, 2024.

[93] M. Erbaş, M. Kabak, E. Özceylan, and C. Çetinkaya, "Optimal siting of electric vehicle charging stations: A GIS-based fuzzy Multi-Criteria Decision Analysis," *Energy*, 163, 1017-1031, 2018.

[94] H. Zhao, J. Gao, and X. Cheng, "Electric vehicle solar charging station siting study based on GIS and multi-criteria decision-making: a case study of China," *Sustainability*, 15(14), 10967, 2023.

[95] Ö. Kaya, K. D. Alemdar, A. Atalay, M. Y. Çodur, and A. Tortum, "Electric car sharing stations site selection from the perspective of sustainability: A GIS-based multi-criteria decision making approach," *Sustainable Energy Technologies and Assessments*, 52, 102026, 2022.

[96] A. Elomiya, J. Křupka, S. Jovčić, V. Simic, L. Švadlenka, and D. Pamucar, "A hybrid suitability mapping model integrating GIS, machine learning, and multi-criteria decision analytics for optimizing service quality of electric vehicle charging stations," *Sustainable Cities and Society*, 106, 105397, 2024.

[97] M. Kazempour, H. Sabboubeh, K. P. Moftakhari, R. Najafi, and G. Fusco, "GIS-Based Geospatial Analysis for Identifying Optimal Locations of Residential On-Street Electric Vehicle Charging Points in Birmingham, UK," *Sustainable Cities and Society*, 105988, 2024.

[98] Ö. Kaya, A. Tortum, K. D. Alemdar, and M. Y. Çodur, "Site selection for EVCS in Istanbul by GIS and multi-criteria decision-making," *Transportation Research Part D: Transport and Environment*, 80, 102271, 2020.

[99] M. Carra, G. Maternini, and B. Barabino, "On sustainable positioning of electric vehicle charging stations in cities: An integrated approach for the selection of indicators," *Sustainable cities and society*, 85, 104067, 2022.

[100] N. L. Rane, A. Achari, A. Saha, I. Poddar, J. Rane, C. B. Pande, and R. Roy, "An integrated GIS, MIF, and TOPSIS approach for appraising electric vehicle charging station suitability zones in Mumbai, India," *Sustainable Cities and Society*, 97, 104717, 2023.

[101] D. Guler and T. Yomralioglu, "Suitable location selection for the electric vehicle fast charging station with AHP and fuzzy AHP methods using GIS," *Annals of GIS*, 26(2), 169-189, 2020.

[102] S. Hisoglu and R. Comert, "Gis-Based Optimum Site Selection for Solar Electric Vehicle Charging Station: Ankara-Istanbul Highway Case," *The International Archives of the Photogrammetry*, Remote Sensing and Spatial Information Sciences, 46, 267-272, 2021.

[103] W. Janchomphu, N. Pannucharoenwong, S. Hemathulin, S. Echaroj, and P. Iamtrakul, "Suitability factors for electric vehicle charging stations using analytic hierarchy process: a case study in Chonburi Thailand," *Engineered Science*, 29, 1110, 2024.

[104] P. Kumar and H. K. Channi, "Optimal Electric Vehicle Charging Station Placement: A Multi-Criteria Decision-Making Approach for Site Selection," *In 2024 International Conference on Integrated Circuits and Communication Systems (ICICACS)*, pp. 1-6, IEEE, 2024.

[105] K. C. Arayıcı and G. Poyrazoğlu, "Elektrikli araç şarj istasyonu doğru konumlandırılması [Optimal placement of electric vehicle charging stations]," unpublished, 2018.

[106] M. Demirtaş, E. Yılmaz, Ü. N. A. L. Ceren, T. Küçükpehlivan, B. Ağaçsapan, and T. Aksoy, "Elektrikli araçlar ve şarj istasyonlarının konumlandırılması," *GSI J. Ser. C: Adv. Inf. Sci. Technol.*, vol. 4, no. 1, pp. 11–32, 2021.

[107] B. Öztürk, "Çok kriterli karar verme tekniklerinden bulanık TOPSIS ve bulanık analitik hiyerarşi süreci," *Ph.D. dissertation*, Bursa Uludağ Univ., Bursa, Turkey, 2011.

[108] S. Zhang and T. Chen, "A new approach for fuzzy multiple attribute decision-making problems based on trapezoidal fuzzy numbers," *Expert Syst. Appl.*, vol. 36, no. 3, pp. 5200–5205, 2009.

[109] F. Ecer, "Üyelik fonksiyonu olarak üçgen bulanık sayılar mı yamuk bulanık sayılar mı?," *Gazi Univ. İİBF Dergisi*, vol. 9, no. 2, pp. 161–180, 2007.

[110] C. Kahraman, M. Keshavarz Ghorabaee, E. K. Zavadskas, S. Cevik Onar, M. Yazdani, and B. Oztaysi, "Intuitionistic fuzzy EDAS method: An application to solid waste disposal site selection," *J. Environ. Eng. Landsc. Manag.*, vol. 25, no. 1, pp. 1–12, 2017.

[111] A. Jaleel and T. Mahmood, "The integrating of environmental sustainability assessment by using bipolar complex fuzzy soft Aczel-Alsina aggregation operators with EDAS approach," *J. Environ. Manag.*, vol. 375, pp. 123642, 2025.

[112] M. A. Kara, "Bulanık EDAS yöntemi ile Doğu Karadeniz bölgesi illerinin yaşanabilirlik düzeylerinin değerlendirilmesi," *Afyon Kocatepe Univ. İİBF Derg.*, vol. 26, no. 2, pp. 250–263, 2024.

[113] F. Ezer, "Performance evaluation of different types of banks in Turkey using fuzzy EDAS method," *J. Optim. Decis. Mak.*, vol. 1, no. 1, pp. 42–62, 2022.

[114] E. Küçük, E. Dinç, and T. Öztürk, "Bulanık EDAS yöntemi ile tıbbi aromatik bitki işleme tesisi yer seçimi: Artvin örneği," *Artvin Çoruh Univ. Orman Fak. Dergisi*, vol. 25, no. 1, pp. 136–150, 2024.

[115] F. K. Bayrakdaroğlu and N. Kundakcı, "Bulanık EDAS yöntemi ile AR-GE projesi seçimi," *Uluslararası İktisadi ve İdari İncelemeler Dergisi*, no. 24, pp. 151–170, 2019.

[116] M. Keshavarz Ghorabaee, E. K. Zavadskas, M. Amiri, and Z. Turskis, "Extended EDAS method for fuzzy multi-criteria decision-making: An application to supplier selection," *Int. J. Comput. Commun. Control*, vol. 11, no. 3, pp. 358–371, 2016.

[117] J. Rezaei, "Best-worst multi-criteria decision-making method," *Omega*, vol. 53, pp. 49–57, 2015.

[118] G. Demir and H. Bircan, "Kriter ağırlıklandırma yöntemlerinden BWM ve FUCOM yöntemlerinin karşılaştırılması ve bir uygulama," *Cumhuriyet Univ. İİBF Dergisi*, vol. 21, no. 2, pp. 170–185, 2020.

[119] E. Çakır and M. Can, "Best-worst yöntemine dayalı ARAS yöntemi ile dış kaynak kullanım tercihinin belirlenmesi: Turizm sektöründe bir uygulama," *Atatürk Univ. Sos. Bil. Ens. Derg.*, vol. 23, no. 3, pp. 1273–1300, 2019.

[120] S. H. H. Petrudi, H. Ghomi, and M. Mazaheriasad, "An integrated fuzzy Delphi and Best Worst Method (BWM) for performance measurement in higher education," *Decis. Anal. J.*, vol. 4, pp. 100121, 2022.

[121] B. F. Yıldırım, "Güçlü zayıf yöntemi ile proje değerlendirme için alternatif bir ölçek önerisi: KOSGEB örneği," *Yönetim Bilim. Dergisi*, vol. 18, no. 38, pp. 747–765, 2020.

[122] S. S. Bilgilioğlu, "Coğrafi bilgi sistemleri ve bulanık analitik hiyerarşi süreci ile elektrikli araç şarj istasyonu yer seçimi," *Afyon Kocatepe Univ. Fen ve Müh. Bilim. Derg.*, vol. 22, no. 1, pp. 165–174, 2022.

[123] C. Calvo-Jurado, J. M. Ceballos-Martínez, J. C. García-Merino, M. Muñoz-Solano, and F. J. Sánchez-Herrera, "Optimal location of electric vehicle charging stations using proximity diagrams," *Sustain. Cities Soc.*, vol. 113, pp. 105719, 2024.

[124] T. Alkan, Ö. F. Atiz, and S. S. Durduran, "Elektrikli araç şarj istasyonları için AHP yöntemi ile uygun yer seçimi: Konya örneği," *Niğde Ömer Halisdemir Univ. Müh. Bilim. Derg.*, vol. 12, no. 1, pp. 1–1, 2023.

[125] M. S. K. Asnaz and B. Özdemir, "Elektrikli araç şarj istasyonlarının çok kriterli karar verme yöntemleri ile optimal konumlandırması," *Akıllı Ulaşım Sistemleri ve Uygulamaları Dergisi*, vol. 4, no. 2, pp. 175–187, 2021.

[126] O. Yenigün, T. Boyar, and K. Yıldız, "Genetik algoritma ve coğrafi sistemlerle İstanbul'daki elektrikli araç şarj istasyonlarının optimal konumunun belirlenmesi," *Bilişim Teknol. Dergisi*, vol. 17, no. 1, pp. 1–9, 2024.

[127] W. Meng and L. Kai, "Optimization of electric vehicle charging station location based on game theory," *in Proc. 2011 Int. Conf. Transp., Mech. Electr. Eng. (TMEE)*, Dec. 2011, pp. 809–812.

[128] A., Tansu, Ö.F. Atiz, and S.S. Durduran. "Suitable site selection for electric vehicle charging stations with AHP method: The case of Konya." *Niğde Ömer Halisdemir University Journal of Engineering Sciences*, 12(1), 193–199, 2023.

[129] U. Aydoğmuş, H. Yumurtacı Aydoğmuş, D. Karaman, A. Yildiz, M. Can, "Application of interval type 2 fuzzy AHP method in bank selection process of an SME". *Mehmet Akif Ersoy University Journal of Economics and Administrative Sciences Faculty*, 10(2), 1042-1070, 2023.

[130] M. U. Aslam, S. Xu, Z. Rasheed, M. Noor-ul-Amin, S. Hussain, and M. Waqas, "Improved fuzzy control charts for monitoring defined health ranges using trapezoidal fuzzy numbers", *Expert Systems with Applications*, 278, 127310, 2025.

Konya Mühendislik Bilimleri Dergisi, c.14, s.2, 901-916, 2026
Konya Journal of Engineering Sciences, v.14, n.2, 901-916, 2026
ISSN: 2667-8055 (Electronic)
DOI: 10.36306/konjes.1812754

COMPARATIVE ANALYSIS OF TARGET LOCALIZATION ACCURACY IN RADAR PPI IMAGES USING GEOMETRIC ENCLOSURES

[1,*]Sercan KÜLCÜ

[1]*Computer Engineering Department, Giresun University, Türkiye*
[1]sercan.kulcu@giresun.edu.tr

Highlights

- Concave hull method achieves 58–70 m avg. localization error in radar-AIS fusion.
- The proposed method improves accuracy by up to 12.7% over the bounding box method.
- The proposed method improves accuracy by up to 2.1% over the convex hull method.
- The proposed method preserves echo concavities from clutter, noise and structure.
- The proposed method offers a lightweight and robust solution for ASVs.

Graphical Abstract

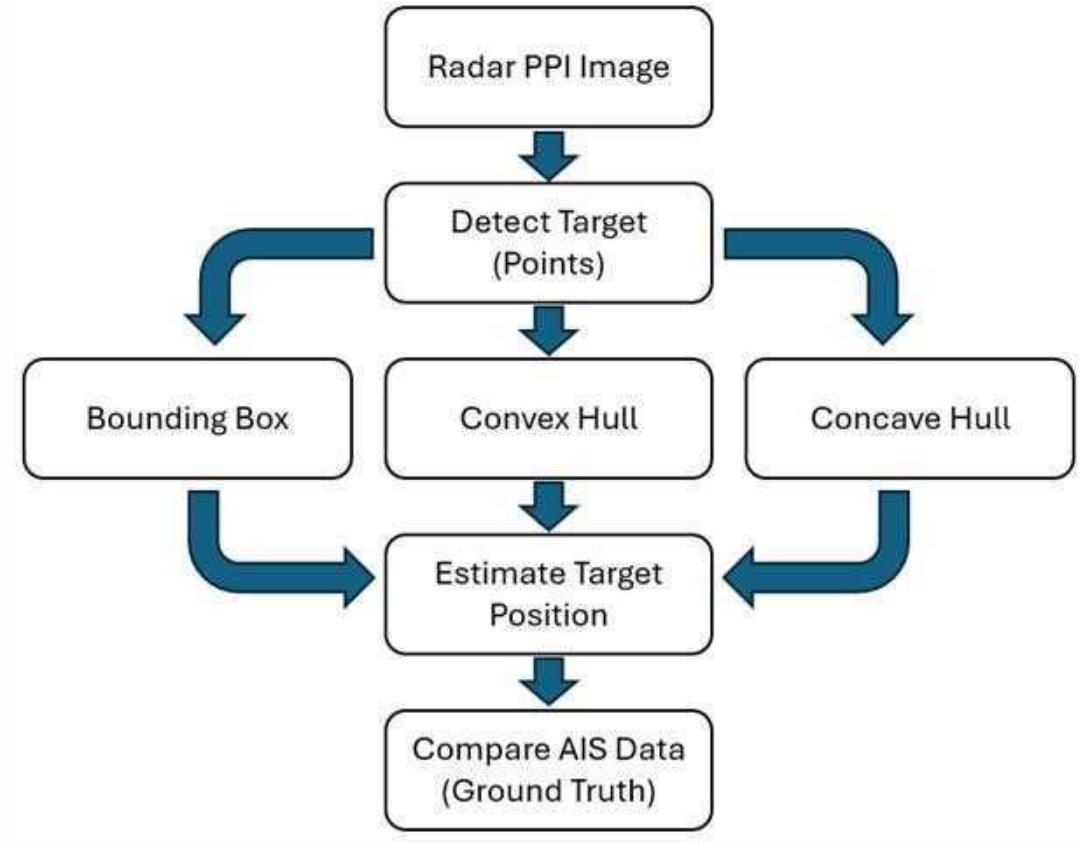


Figure Flowchart of the proposed framework.

***Corresponding Author:** Sercan KÜLCÜ, sercan.kulcu@giresun.edu.tr

Konya Mühendislik Bilimleri Dergisi, c.14, s.2, 901-916, 2026
Konya Journal of Engineering Sciences, v.14, n.2, 901-916, 2026
ISSN: 2667-8055 (Electronic)
DOI: 10.36306/konjes.1812754

COMPARATIVE ANALYSIS OF TARGET LOCALIZATION ACCURACY IN RADAR PPI IMAGES USING GEOMETRIC ENCLOSURES

[1,*]Sercan KÜLCÜ

[1]*Computer Engineering Department, Giresun University, Türkiye*
[1]sercan.kulcu@giresun.edu.tr

(Received: 29.10.2025; Accepted in Revised Form: 10.12.2025)

ABSTRACT: Maritime surveillance systems require sensor fusion of radar Plan Position Indicator (PPI) imagery with Automatic Identification System (AIS) data. However, systematic azimuth errors (0°–5°) and irregular echo shapes reduce ship localization accuracy significantly. This study compares three geometric enclosure methods (bounding boxes, convex hulls, and concave hulls) using the publicly available DLR Baltic Sea dataset (X-band, ~10 m resolution, 781 synchronized scans of 4 ships). A 4.5° azimuth offset compensation is applied to minimize target position deviation. Target positions are estimated from calculated bounding box centers and hull centroids from radar images. Validation against AIS ground truth data achieved the lowest average localization errors (58–70 m) for concave hull centroids in the tested scenarios. It demonstrates up to 12.7% improvement over bounding boxes solution and a 2.1% improvement over convex hulls solution. The results show the accuracy of the concave hulls method in target detection and preservation of echo concavities caused by sea clutter, and noise etc. Within the tested X-band radar configuration and traffic scenarios, the concave hull method offers a lightweight and robust solution for real-time Vessel Traffic Services (VTS) and autonomous surface vehicles (ASVs).

Keywords: *AIS fusion, Autonomous surface vehicles, Computer vision, Geometric enclosures, Radar PPI, Target localization.*

1. INTRODUCTION

Maritime surveillance systems, such as Vessel Traffic Services (VTS) and autonomous surface vehicles (ASVs), rely on radar Plan Position Indicator (PPI) images for real-time target detection and tracking. Challenges arise from irregular echo shapes and uneven target distributions caused by sea clutter. Thus, azimuth errors (0°–5°) often reduce localization accuracy when sensor fusing radar data with AIS ground truth data. Geometric hulls, such as bounding boxes, convex hulls, and concave hulls, offer intuitive ways to enclose echo points and estimate target center points. Recent developments emphasize hull-based methods to better adapt to complex geometries [1,2].

Early work by Nemirko and Dulá proposed a nearest-convex-hull (NCH) classifier. It represents classes as convex hulls of training points in multidimensional space. It classifies test points via linear programming to measure closeness. It achieved 0.23% error on the UCI Breast Cancer Wisconsin dataset by outperforming SVM (3.05%) and k-NN (2.70%) methods. It reduces computation by using only extreme vertices and handling overlaps without adjustment [3]. Extending hull concepts to radar, Külcü presented a framework for ASVs that uses HSV segmentation, Gaussian smoothing, and morphological operations to detect yellow targets and own-ship markings on PPI images. It performed Euclidean distance tracking with velocity recovery and produced 98.7% true positives and 59% fewer false positives over 7,200 frames [2].

For VTS collision risk assessment, Xu et al. outlined a three-step pipeline. It consists of background subtraction for ship centers of gravity, Kalman-Hungarian tracking for trajectories, and fuzzy fusion of radar-AIS speed/heading. It reduces variances (speed: 1.30; heading: 26.53) in Yangtze River dataset [4].

***Corresponding Author:** Sercan KÜLCÜ, sercan.kulcu@giresun.edu.tr

Similarly, Xu et al. advanced multi-sensor fusion with low-rank decomposition. It used Kalman inter-frame tracking with evidence-based reasoning for object detection. They reduce the speed variance from 2.55 to 0.38 and the heading from 28.35 to 23.48 [5]. Xu et al. also integrated these methods for risk visualization. They extracted potential targets through subtraction, reconstructed trajectories, and mapped safe/forbidden speeds with DCPA/TCPA metrics in Yangtze River frames dataset [6].

In oriented object detection, Guo et al. developed convex hull feature adaptation (CFA) methodology. They modeled layouts as dynamic hull clusters with convex IoU to minimize background and segmented aliased features. It enabled efficient convex polygon estimation in MS COCO dataset and set the state-of-the-art in DOTA and SKU110K-R datasets [7]. Liang et al. proposed deep learning integrations such as DeepHullNet combining Pointer Networks and Transformers for convex/concave hulls. The proposed solution improved the accuracy by 5-8% and accelerated its speed by 100x compared to Jarvis March or alpha shapes for GeoAI tasks [8].

Concave hulls have proven to be effective for non-convex clutters. Guan et al. optimized 3D concave hull learning for small sea targets by selecting interior points near ridge midpoints. They also added external complements to surround the sea clutter in areas. Their model outperformed multi-feature CFAR detectors on CSIR and X-band data [9]. Shi and Hu selected low-correlation 3D features from 8D space via mRMR. Then, they proposed the mRMR-Tri-Concave Hull detector, which generates controllable concave boundaries to narrow decision regions. They increase the detection probability compared to convex hulls in radar data. They emphasized adaptive concave hull modeling in non-convex environments [10]. Shi et al. improved this solution with FB-ICHC, extracting new features (RPZR, RCV, WPHR) from Doppler spectra. They used a two-stage concave hull and achieved 20% higher detection rate and 49% faster running time in benchmarks [11].

Underwater and SAR applications also benefit from geometric hulls. Gao et al. converted the YOLOv5 model to GCT-YOLOv5 by using Ghost modules. This approach reduced parameters by 48% and improved mAP@0.5 by 3.1% for real-time maritime operations [12]. Yang et al. used rotated bounding boxes, pair-alignment modules, and adaptive IoU to outperform eight rotated detectors and leading networks. They constructed SRNet for SAR ship segmentation [13]. Xu et al. treated the plots as probabilistic clouds for trajectory merging. They accelerated AIS-radar matching in ports by applying AIS-guided transformations and clustering for robust tracks among false alarms [14].

Li et al. used concave hull relations and shape contexts for point cloud registration. They reduced errors due to occlusions via SAC-IA [15]. Korban et al. used radar polarization and energy matrices to detect ASVs as shiny dots in clutter [16]. Fowdur et al. generated three DLR marine radar datasets with AIS truth for benchmarking. They developed an extended center tracker that reduces fragmentation [1].

Despite significant progress in radar–AIS sensor fusion for maritime surveillance, accurate target localization remains challenging. Two primary systematic errors persist: (i) radar echoes are irregular due to sea clutter, multipath reflections and limited radar resolution, causing large centroid deviations (ii) azimuth biases arise from antenna misalignment, time-delay mismatches, or uncompensated motion, producing consistent rotational offsets between radar and AIS positions. Bounding boxes and convex hulls are widely used in oriented object detection, ship segmentation, and point-cloud registration. Concave (alpha) hulls have shown promise for clutter-robust small-target detection. However, no study has systematically compared bounding-box centers, convex-hull, and concave-hull centroids for ship localization in real X-band radar PPI images with synchronized AIS ground truth.

This work fills that gap. It presents the first controlled quantitative comparison of the three geometric enclosure methods under optimal 4.5° azimuth-bias compensation. Results reveal consistent accuracy improvements, with concave-hull centroids performing best on a publicly available real-world dataset. It also contains synchronized AIS ground truth data. Unlike previous studies that focused on detection probability or tracking continuity, we demonstrate an average error reduction of up to 12.7% for irregular echoes with concave hulls centroids in the evaluated dataset. These findings present concave hulls as a lightweight, calibration-robust alternative to deep learning methods. It offers immediate operational value for VTS and ASV systems in dynamic maritime environments.

This article consists of four main sections. The introduction section reviews previous research and identifies key shortcomings. The materials and methods section describes the DLR Baltic Sea dataset, AIS location information, radar PPI imagery, and 4.5° azimuth offset correction. This section explains three localization methods: bounding box, convex hull, and concave hull. The results and discussion section compares localization errors for Target 2 and Target 4 using time-series plots and statistical tables. The conclusions section highlights the accuracy of concave hulls and outlines future research directions.

2. MATERIALS AND METHODS

2.1 Dataset

DLR's real-world marine radar repository (Baltic Sea campaigns) provides PPI images (X-band, ~10m resolution) and synchronized AIS data for four vessels [1].

2.1.1 AIS data

The dataset includes AIS data synchronized with radar PPI images. The AIS data provides precise positional information for 4 vessels. The data is structured in a CSV format. It provides navigational parameters for vessels over a sequence of time steps. The AIS data provides ground truth for validating radar-based target localization.

The AIS dataset includes the following key attributes for each vessel:

- Step: Represents the time step, ranging from 0 to 780 in the provided data. It indicates the temporal progression of the vessel tracks.
- East and North: These fields denote the vessel's position in a local Cartesian coordinate system in meters. These coordinates describe the spatial movement of each vessel.
- Course Over Ground (COG): Measured in degrees (0–360°), this indicates the direction of the vessel's movement relative to the ground.
- Speed Over Ground (SOG): Represents the vessel's speed relative to the ground in knots.
- True Heading: Indicates the direction the vessel, measured in degrees, aligning closely with COG unless influenced by external factors such as currents or wind.
- Vessel Number: A unique identifier for each vessel.

Figure 1 shows the real AIS paths of four vessels in East-North coordinates. Figure 2 shows the same paths relative to Vessel 1. Each line has a different color and an arrow. The arrow shows the direction of the movement. These figures help to check radar position accuracy against AIS truth.

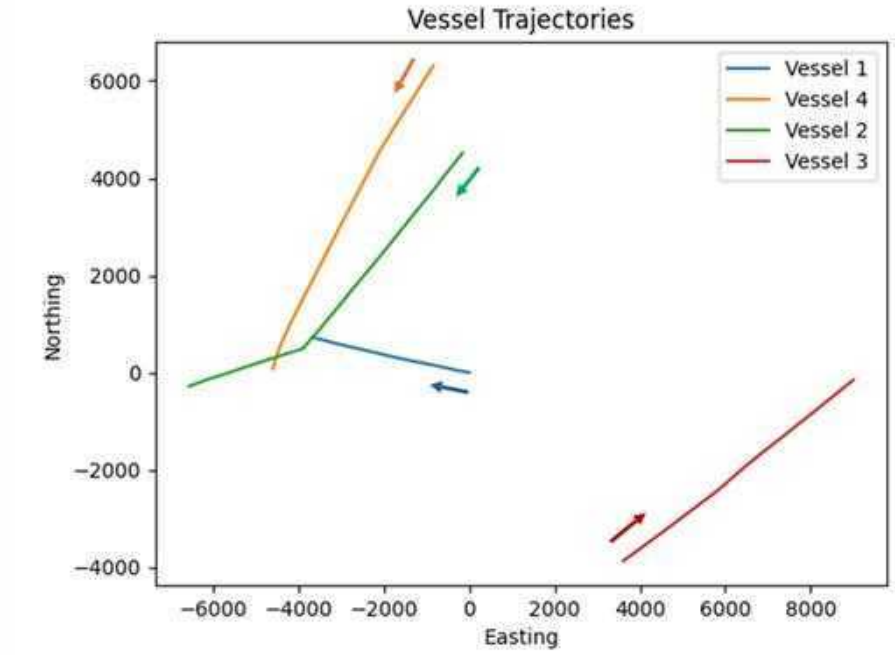


Figure 1. AIS absolute positions.

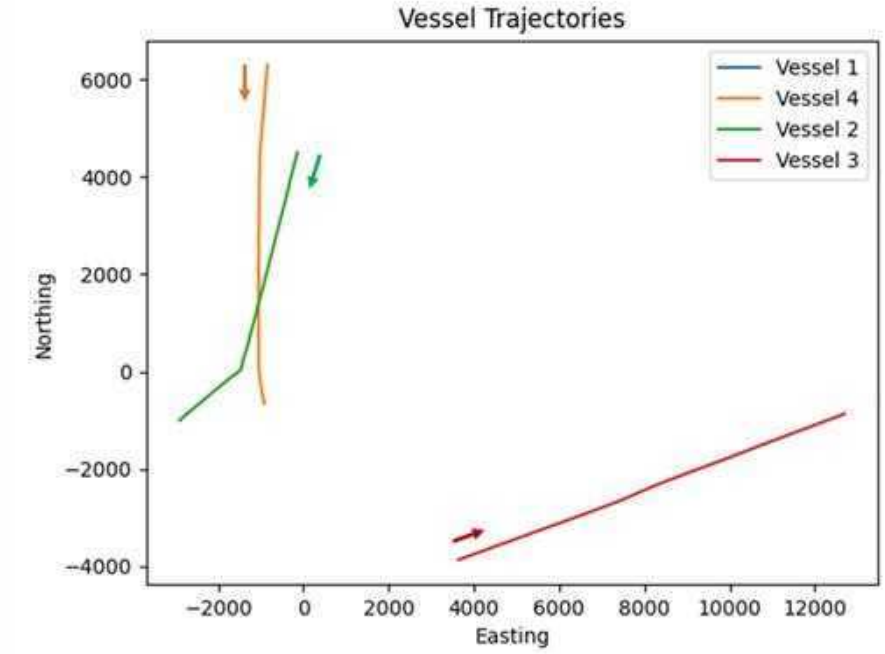


Figure 2. AIS positions relative to Vessel 1.

The dataset contains tracks belonging to four vessels, each have distinct movement patterns:

- Vessel 1: Maintains a consistent northwest trajectory with a COG of 280–285° and a SOG ranging from 9.2 to 9.5 knots. True Heading (283–287°) closely aligns with COG, showing minimal external influences.
- Vessel 2: Follows a southwest trajectory, with COG from 221–223° to 251–254° over time. Its SOG is higher, ranging from 20.6 to 21.1 knots. The vessel's position reflects significant westward and southward movement.
- Vessel 3: Moves northeast with a COG of 54–57° and a SOG of 16.5–16.7 knots. True

Heading (~58°) aligns closely with COG, indicating consistent movement. Vessel 3 was excluded from all quantitative comparisons because it leaves the radar's 3 NM range after step 80. Radar detections exist for Vessel 3 only in 10% of the total frames.

- Vessel 4: Moving on a southwest trajectory with a COG of 209–216° and an SOG ranging from 17.2 to 18.6 knots. The True Heading (198–208°) is closely aligned with COG.

2.1.2 Radar PPI Images

The radar PPI images were captured using an X-band marine radar system with approximately 10-meter resolution. Each PPI scan corresponds to a single step in the AIS dataset. It provides polar-coordinate representations of maritime targets under all-weather conditions. The images depict a circular field of view centered on the radar platform. Radar is assumed to be co-located with Vessel 1 for relative positioning. It has 3 nautical miles (NM) range and azimuthal bearings from 0° (North) to 360° clockwise. The dataset comprises 781 sequential frames (Steps 0–780), each showing 3–4 cooperative targets. Vessel 2, Vessel 3, and Vessel 4 relative to Vessel 1, which appears stationary at the display center in stabilized mode. The PPI dataset provides raw polar echoes for computational processing, with detections converted to Cartesian coordinates for sensor fusion with AIS. Not all scans detect every vessel due to temporary occlusion or low RCS, but temporal interpolation ensures robust tracking across 780 steps. A sample radar PPI image is given in Figure 3.

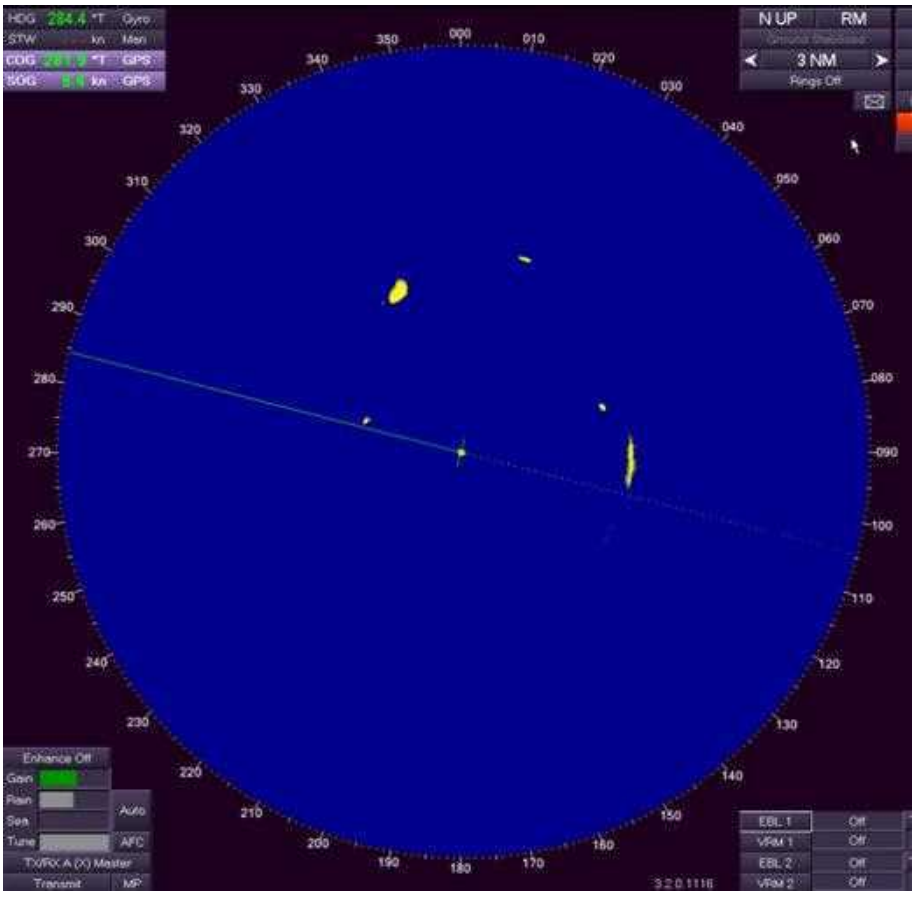


Figure 3. A sample PPI image.

Radar PPI images show a 3 NM range. The central blue zone is 940 pixels wide. So, one pixel is equivalent to (3 NM = 5556 m / 470 pixels) 11.82 m. This value is used for all conversions to calculate errors for AIS comparison.

2.2 Azimuth Offset Compensation

A systematic azimuth bias exists between the radar PPI display and the AIS reference positions. To determine the optimal global correction, a constant rotation θ is exhaustively searched in 0.5° steps from 0.0° to 5.0°. For each candidate θ, every detected echo pixel is first converted from image coordinates (x_img, y_img) to a polar form (r, φ) relative to the known PPI center (528, 516), then rotated by θ to obtain φ′ = φ + θ, and finally transformed to local East-North meters using the calibrated scale of m/pixel. The centroids (bounding-box center, convex hull, or concave hull) of all clusters are computed in meters, matched to the nearest AIS position of Targets 2 and 4 in the same frame, and the mean absolute error across both targets and all valid frames is recorded. The value θ = 4.5° yields the clear global minimum (combined mean error = 11.81 pixels equivalent) and is therefore uniformly applied to all subsequent analyses (see Table 1). Vessel 3 has not been considered because it is not visible on the radar screen in most frames.

Table 1. Mean localization error (in pixels) for different azimuth offset (θ).

Vessel / θ	**0.0°**	**0.5°**	**1.0°**	**1.5°**	**2.0°**	**2.5°**	**3.0°**	**3.5°**	**4.0°**	**4.5°**	**5.0°**
Vessel 2 (px)	12.54	11.60	10.56	9.53	8.31	7.14	6.28	**5.86**	5.99	6.63	7.65
Vessel 4 (px)	15.71	15.45	14.74	14.22	13.34	11.42	9.48	7.66	6.10	**5.18**	5.27
Total (px)	28.25	27.05	25.30	23.75	21.65	18.56	15.76	13.52	12.09	**11.81**	12.92

Error decreases steadily up to 4.5°, where the total error reaches a minimum of 11.81 pixels. Beyond this, the error rises again, indicating over-correction. Vessel 4 benefits more from compensation than Vessel 2, likely due to its larger radar cross-section and stable trajectory. We select θ = 4.5° as the optimal offset for all the following analyses. This value reduces aggregate bias and aligns radar-derived positions closely with AIS references. This fixed offset is assumed to be constant over the entire sequence; time-varying or target-specific biases are not considered in the current study.

2.3 Radar Echo Segmentation and Target-Specific Point Cloud Generation

The hull-based localization methods evaluated in this study require, as input, separate sets of echo pixels $\mathcal{P}_i$ belonging to each maritime target i. These point sets are produced by a lightweight, fully automatic, and reproducible image-processing pipeline that has been used in [2].

The pipeline proceeds as follows. The original RGB PPI image is converted from RGB to HSV colour space. Yellow target echoes (the standard colour used in marine X-band radar displays for detected returns) are isolated by a wide but robust HSV threshold (lower_yellow = [10, 50, 50], upper_yellow = [50, 255, 255]). A binary mask is generated and cleaned with a single iteration of morphological closing (3×3 kernel) followed by one dilation iteration to close small gaps inside echoes while preserving the overall shape. External contours are extracted using OpenCV's RETR_EXTERNAL mode with CHAIN_APPROX_NONE. Contours smaller than 16 pixels are discarded to remove speckle noise and residual sea-clutter fragments.

Each remaining contour is treated as one independent target echo cluster $\mathcal{P}_i$. When multiple vessels are present in the same frame, spatial separation is naturally achieved because the yellow echoes of different ships rarely merge at the given resolution and sea state of the DLR Baltic Sea dataset. In the rare frames where minor overlap occurs (most notably around step 180, where a clear increase in localization error is observed in Figures 4, 5, and 6), the contour-based separation may assign some shared pixels to one of the targets. However, the hull centroid still yields lower average error than the bounding-box approach.

The resulting point sets $\mathcal{P}_i$ (all foreground pixels inside each filtered contour) are then converted from image coordinates to local Cartesian coordinates (using the known image center and the pixel-to-meter scaling factor derived from the 3 NM display range) and subjected to the fixed 4.5° azimuth offset compensation described in Section 2.2 before bounding-box, convex-hull, and concave-hull centroids are

computed. This simple colour-threshold and morphological approach avoid complex CFAR detectors or learning-based segmentation to keep the method lightweight and executable in real time on embedded VTS/ASV hardware.

2.4 Target Detection with Minimum Bounding Rectangle

The Minimum Bounding Rectangle (MBR) is also known as the axis-aligned bounding box (AABB). It is a simple and computationally efficient method for enclosing radar echo clusters. This technique encapsulates all echo pixels of the target within the smallest rectangle aligned with the coordinate axes. It has (0(n)) time complexity, where (n) represents the number of echo points [17]. It is suitable for real-time applications on resource-constrained embedded systems.

A set of echo pixels ($\mathcal{P}_i = \{(\mathrm{x_j}, \mathrm{y_j}) \mid \mathrm{j} = 1, \ldots, \mathrm{n}\}$) for target i, are obtained after polar-to-Cartesian transformation and azimuth offset correction. AABB is defined as given in (1).

$$\mathrm{AABB}_i = \left(\min_j x_j,\ \min_j y_j,\ \max_j x_j,\ \max_j y_j\right) \tag{1}$$

The estimated target position is computed as the geometric center of this rectangle as given in (2).

$$\widehat{c_i} = \left(\frac{\min_j x_j + \max_j x_j}{2},\ \frac{\min_j y_j + \max_j y_j}{2}\right) \tag{2}$$

This centroid ($\widehat{\mathrm{c_i}}$) serves as the target position for sensor fusion with AIS ground truth data. This method requires no parameter tuning or iterative optimization. This makes it robust to isolated outliers that merely expand the rectangle without disrupting the internal structure. However, the axis-aligned constraint shifts the estimated centroid of empty corner regions from the target real centroid. It causes deviation in the case of long, diagonal, or irregular echoes.

Algorithm 1 provides a lightweight, deterministic, and robust baseline for real-time target localization, ideal for initial deployment in VTS and ASVs. It has (0(n)) time complexity, where (n) is the number of echo pixels.

Algorithm 1: Bounding Box Detection and Center Estimation

Input: Set of radar pixels Pi = {(xj, yj) ⁞ j = 1, ..., n}
Output: Axis-aligned bounding box (AABB) and centroid ci

```
Initialize xmin, ymin → +∞; xmax, ymax → −∞
for each (xj, yj) in Pi do
    xmin ← min(xmin, xj); xmax ← max(xmax, xj)
    ymin ← min(ymin, yj); ymax ← max(ymax, yj)
end for
width = xmax − xmin; height = ymax − ymin
ci.x = (xmin + xmax) / 2; ci.y = (ymin + ymax) / 2
return AABB = (xmin, ymin, xmax, ymax), ci = (ci.x, ci.y)
```

2.5 Target Detection with Convex Hull

The convex hull method computes the smallest convex polygon that fully encloses all radar echo points. Unlike the axis-aligned bounding box, the convex hull adapts to the actual spatial extent and orientation of the echo cluster. This significantly reduces bias caused by empty corner regions in diagonal or irregular shapes [18]. This approach provides a tighter geometric fit, particularly for large maritime targets with extended radar cross-sections (RCS).

Given a set of echo pixels ($\mathcal{P}_i = \{(\mathrm{x_j}, \mathrm{y_j}) \mid \mathrm{j} = 1, \ldots, \mathrm{n}\}$) in Cartesian coordinates, the convex hull ($\mathcal{CH}_i$) is defined as the minimal convex set containing all points, as given in (3).

$$\mathcal{CH}_i = \{\textstyle\sum_{k=1}^{m} \lambda_k p_k \mid \leq n,\ p_k \in \mathcal{P}_i,\ \lambda_k \geq 0,\ \sum_{k=1}^{m} \lambda_k = 1\} \tag{3}$$

where (m) is the number of vertices on the hull boundary. The target position is estimated using the centroid of the final convex polygon. It is the center of mass assuming uniform density, calculated as given in (4).

$$\widehat{c_i} = \frac{1}{6A} \sum_{k=0}^{m-1} (x_k y_{k+1} - x_{k+1} y_k) \left(\frac{x_k + x_{k+1}}{2}, \frac{y_k + y_{k+1}}{2} \right), \quad (x_m, y_m) = (x_0, y_0) \tag{4}$$

where (A) is the polygon area is computed via the shoelace formula. It is given in (5).

$$A = \frac{1}{2} \left| \sum_{k=0}^{m-1} (x_k y_{k+1} - x_{k+1} y_k) \right| \tag{5}$$

This centroid ($\widehat{\mathrm{c}_\mathrm{i}}$) serves as the detected target position for AIS fusion. The convex hull eliminates displacement errors inherent in axis-aligned bounding boxes. It conforms to the outer boundary of the echo. It is effective with compact or convex-like echo patterns. However, it may overestimate the true center in cases of significant concavities caused by sea clutter, or fragmented returns.

Algorithm 2 offers a robust and geometrically meaningful improvement over bounding boxes, providing more accurate localization. It maintains computational feasibility for real-time VTS and ASV applications. It has ($O(n \log n)$) time complexity due to convex hull computation. It has (O(m)) space complexity, where ($\mathrm{m} \leq \mathrm{n}$) is the number of hull vertices.

Algorithm 2: Convex Hull Centroid Estimation

Input: Pi = {(xj, yj) | j = 1, ..., n}
Output: Convex hull vertices Vi and centroid ci

```
Vi ← ConvexHull(Pi)  // e.g., Graham Scan, O(n log n)
let Vi = {v0, v1, ..., vm−1}, vm = v0
A = 0; cx = 0; cy = 0
for k = 0 to m−1 do
    cross = vk.x * v(k+1).y − v(k+1).x * vk.y
    A += cross; cx += (vk.x + v(k+1).x) * cross
    cy += (vk.y + v(k+1).y) * cross
end for; A = |A| / 2
ci.x = cx / (6 * A); ci.y = cy / (6 * A)
return Vi, ci = (ci.x, ci.y)
```

2.6 Target Detection with Concave Hull

The concave hull is also known as an alpha shape. It generates a non-convex polygon that tightly conforms to the natural boundary of radar echo points. Unlike the convex hull, it preserves concavities [19]. Concavities are generally caused by sea clutter, echo fragmentation, or environmental interference. It has the ability to model complex, irregular geometries. This makes it effective for accurate target localization. Echo shapes are often far from convex in maritime radar PPI images.

Given a set of echo pixels ($\mathcal{P}_i = \{(x_j, y_j) \mid j = 1, \ldots, n\}$) in Cartesian coordinates, the concave hull ($\mathcal{H}_\alpha(\mathcal{P}_i)$) is defined as the boundary of the α-complex as given in (6).

$$\mathcal{H}_\alpha(\mathcal{P}_i) = \partial\left(\bigcup_{p\in\mathcal{P}_i} B(p,\alpha)\right) \setminus \text{interior edges} \quad (6)$$

where $(B(p,\alpha))$ is a disk of radius (α) centered at point (p), and interior edges are removed to form the outer boundary. The parameter (α) controls the level of concavity. Smaller values produce tighter, more detailed hulls; larger values approach the convex hull.

The target position is estimated using the centroid of the concave polygon. It is computed by using shoelace formula over its boundary vertices $(\{v_k\}_{k=0}^{m-1})$ as given in (7) with polygon area given in (5).

$$\widehat{c_i} = \left(\frac{1}{6A}\sum_{k=0}^{m-1}(x_k + x_{k+1})(x_k y_{k+1} - x_{k+1}y_k),\ \frac{1}{6A}\sum_{k=0}^{m-1}(y_k + y_{k+1})(x_k y_{k+1} - x_{k+1}y_k)\right) \quad (7)$$

In this study, (α) is empirically set to 0.1, ensuring robust capture of echo concavities without overfitting to noise. The concave hull minimizes the displacement of the estimated centroid from the true vessel center. It excludes clutter-filled or empty regions within convex bounds.

Algorithm 3 provides the best localization accuracy among the three methods. Its lightweight computation and robustness make it ideal. It has $(O(n \log n))$ time complexity due to Delaunay triangulation. It has $(O(n))$ space complexity for triangulation and boundary storage.

Algorithm 3: Concave Hull Centroid Estimation

Input: Pi = {(xj, yj) | j = 1, ..., n}, radius α
Output: Concave hull Vi and centroid ci

```
DT ← Delaunay(Pi); Eα ← ∅
for each triangle t in DT and edge e = (p, q) in t do
  if |e| ≤ 2α and e not shared by two triangles
    on same side of α-disk then add e to Eα
  end if
end for; Vi ← ordered outer α-shape from Eα
Compute A, cx, cy as in Algorithm 2
ci.x = cx / (6 * A); ci.y = cy / (6 * A)
return Vi, ci = (ci.x, ci.y)
```

3. RESULTS AND DISCUSSION

3.1 Experiments Using Bounding Box Centers

Figure 4 shows the localization error (in meters) per time step for Target 2 (blue dots, 697 valid measurements) and Target 4 (orange dots, 665 valid measurements). It uses the bounding box center as the estimated location. Both targets show significant temporal variation in error, with values ranging from 5 m to 175 m. Target 2 exhibits higher fluctuation, particularly during the early (steps 0–150) and late (steps 600–700) phases. Target 4 shows a more stable error behavior between steps 200 and 500. A clear U-shaped trend is observed, with minimum errors around steps 300–400. Deviations increase toward the sequence endpoints, likely due to changes in relative geometry, and radar cross-section (RCS) modulation.

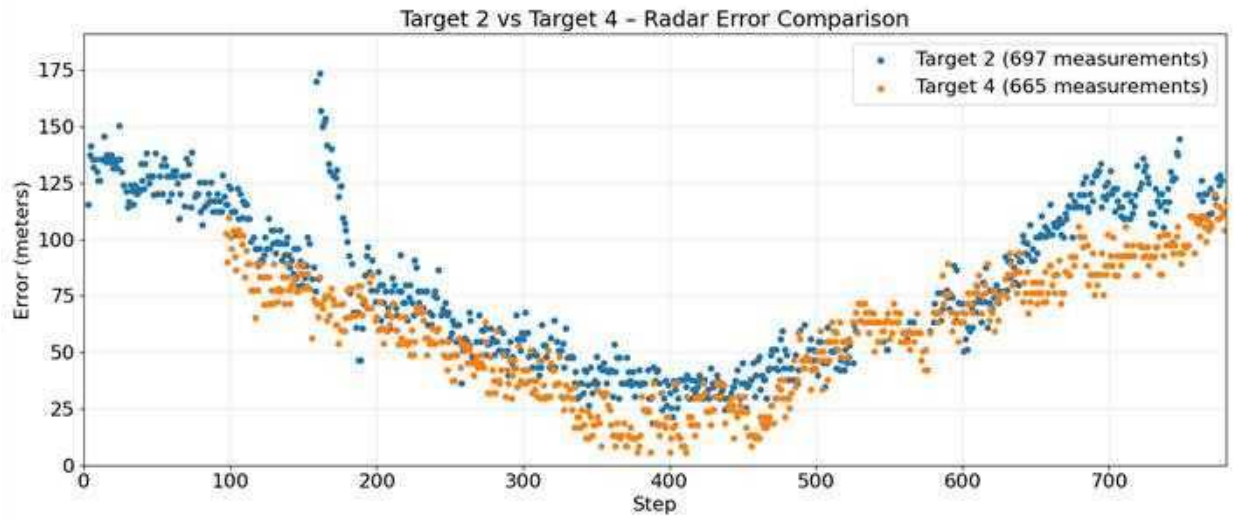


Figure 4. Localization errors using bounding box

Table 2 summarizes the performance of the bounding box method. Target 2 records a mean error of 80.51 m (median: 76.18 m), with a standard deviation of 35.39 m, reflecting significant variability. The maximum error reached 173.74 m, indicating large deviations under unfavorable observation conditions. In contrast, Target 4 achieves a lower mean error of 59.37 m (median: 60.66 m), with reduced variability (std. dev. 27.40 m) and a maximum error of 120.45 m. The minimum errors are 18.81 m (Target 2) and 5.95 m (Target 4). It demonstrates that high-accuracy localization is possible under optimal conditions.

Table 2. Localization errors using bounding box center

Target / Metric	Number of measurements	Mean (m)	Median (m)	Min (m)	Max (m)	Std. Dev. (m)
Target 2	697	80.51	76.18	18.81	173.74	35.39
Target 4	665	59.37	60.66	5.95	120.45	27.40

These results show the limitations of the bounding box method. Empty corner regions within the AABB systematically displace the estimated center from the true vessel position. It leads to persistent positive bias in error. This effect is particularly valid for Target 2, which likely exhibits greater echo irregularity due to its higher speed and maneuvering behavior. The observed performance gap motivates the exploration of more adaptive geometric enclosures.

3.2 Experiments Using Convex Hull Centroids

Figure 5 shows the localization error (in meters) over time steps for Target 2 (blue dots, 696 valid measurements) and Target 4 (orange dots, 649 valid measurements). A significant improvement is observed compared to the bounding box method. The error values range between 10 m and 160 m. There is a significant reduction in high error outliers (>140 m). Both targets show a well-defined U-shaped error profile. Minimum errors are concentrated around steps 300-450, where the relative geometry and radar appearance appear favorable. Target 4 shows stable performance in the mid-to-late phases (Step 200-700), with most errors clustered between 40-80 m. Target 2, although still exhibiting higher variability, benefits from a downward shift in the overall error density, particularly in the central region of the sequence.

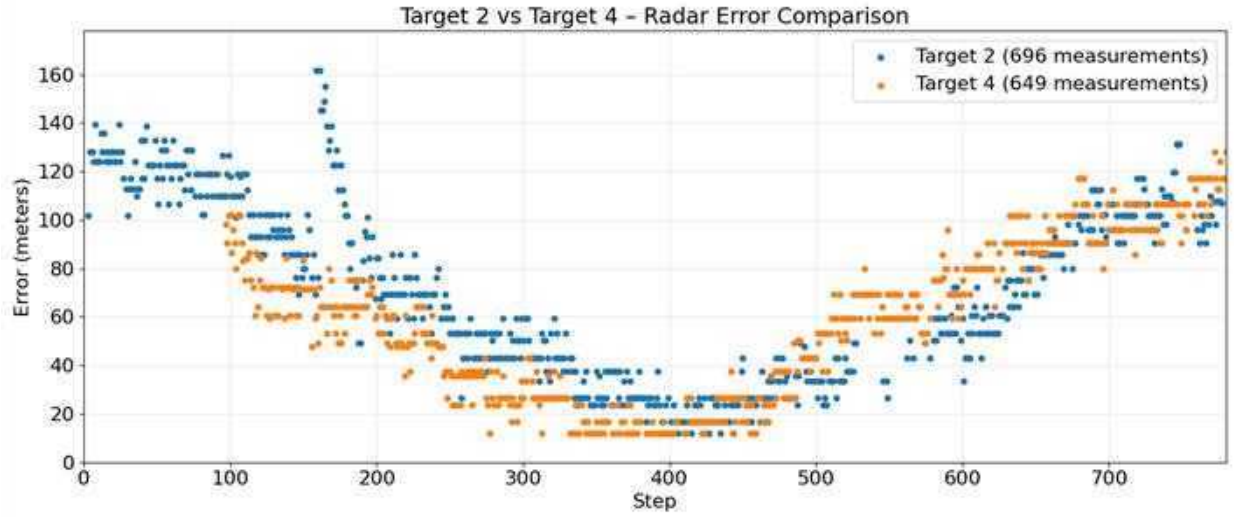


Figure 5. Localization errors using convex hull centroid

Table 3 shows the statistical performance of the convex hull method. Target 2 achieves a mean error of 71.85 m (median: 70.37 m), reflecting a 10.8% reduction compared to the bounding box mean (80.51 m). Variability remains high (standard deviation: 36.26 m), and the maximum error is 164.82 m. In contrast, Target 4 records a mean error of 59.18 m (median: 60.66 m), almost equal to the bounding box median, but with a slight improvement in the mean and a reduced standard deviation of 30.96 m. The minimum errors were 11.90 m (Target 2) and 10.57 m (Target 4), indicating better localization under optimal conditions.

Table 3. Localization errors using convex hull centroid

Target / Metric	Number of measurements	Mean (m)	Median (m)	Min (m)	Max (m)	Std. Dev. (m)
Target 2	696	71.85	70.37	11.90	164.82	36.26
Target 4	649	59.18	60.66	10.57	128.14	30.96

These results confirm that the convex hull method provides measurable gains in localization accuracy. It allows better fit to the true extent of radar echoes. The reduction in systematic bias, particularly evident in the tighter error clustering for Target 4, confirms its superiority over bounding boxes. However, because the convex hull enforces convexity, it may still contain internal gaps or may not capture concavities caused by shadowing, sea clutter, or echo fragmentation. This limitation motivates the adoption of concave hulls, which are designed to conform to the irregular patterns.

3.3 Experiments Using Concave Hull Centroids

Figure 6 shows the localization error (in meters) for Target 2 (blue dots, 696 valid measurements) and Target 4 (orange dots, 653 valid measurements). A significant improvement in the distribution error is seen compared to previous results. The error values are now tightly clustered, with most errors ranging between 10 m and 130 m. There has been a significant reduction in outliers with high errors (>150 m). Both targets exhibit a U-shaped error trend, with minimum errors between Steps 300 and 450, where the radar geometry and target orientation are optimal. Target 4 demonstrates stability throughout the sequence, with errors below 80 m after Step 200. Target 2, despite higher maneuverability and echo variability, shows improved performance in the mid and late phases (Step 200-700), showing dense clustering around 60-90 m.

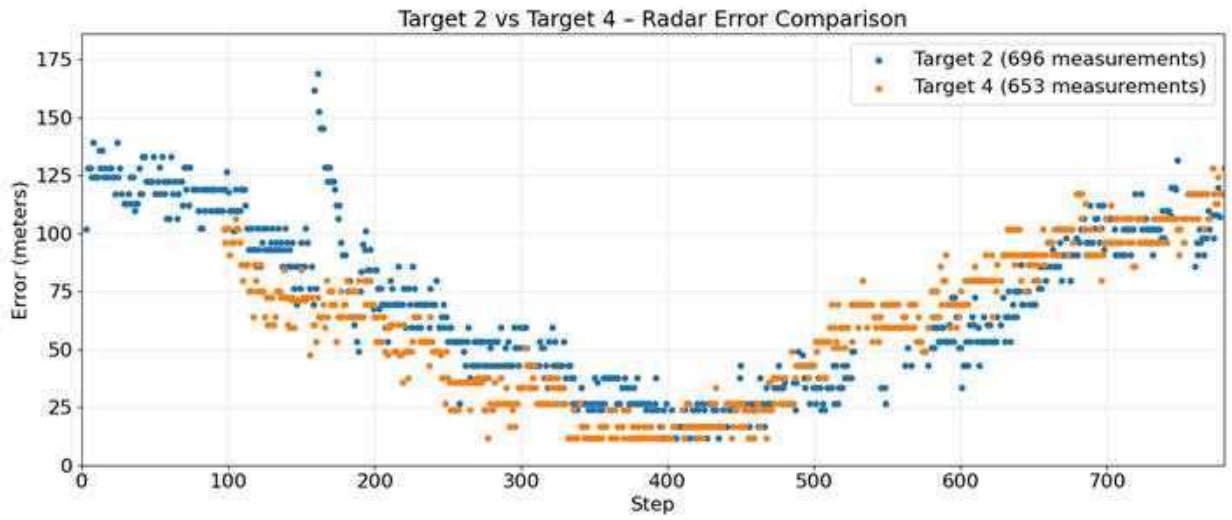


Figure 6. Localization errors using concave hull

Table 4 shows the performance of the concave hull method. Target 2 achieves a mean error of 70.32 m (median: 69.17 m), representing a 12.7% improvement over the bounding box (80.51 m) and a 2.1% reduction compared to the convex hull (71.85 m). The deviation is comparable, with a maximum error of 161.09 m (standard deviation: 35.89 m). Target 4 records the best performance with a mean error of 58.44 m (median: 59.46 m), representing a 1.6% improvement over the bounding box and a 1.3% improvement over the convex hull. Furthermore, the standard deviation is 29.16 m and the maximum error is 127.17 m. Minimum errors reached 11.59 m (Target 2) and 11.23 m (Target 4), confirming better localization.

Table 4. Localization errors using concave hull centroid

Target / Metric	Number of measurements	Mean (m)	Median (m)	Min (m)	Max (m)	Std. Dev. (m)
Target 2	696	70.32	69.17	11.59	161.09	35.89
Target 4	653	58.44	59.46	11.23	127.17	29.16

These results demonstrate that using concave hulls centroid is a better method for localization in maritime PPI imagery. They preserve the true concave structure of radar echoes, including gaps caused by clutter or environmental interference. The method minimizes external forces. It provides positional estimates closest to the AIS ground truth data. The error reduction, particularly for Target 4, with its stable trajectory and larger radar cross-section, validates the concave hull approach for operational use in VTSs and ASVs.

3.4 Sensitivity Analysis of the Concave Hull Parameter α

To address concerns about the robustness of the chosen α value, an additional sensitivity study was performed using α = 0.02, 0.05, 0.1 (original), and 0.2 on the complete set of valid detections for Target 2 and Target 4. The results are summarized in Table 5.

Table 5. Localization errors for different concave hull α values

α value	Target 2 mean ± std (m)	Target 4 mean ± std (m)
0.02	71.81 ± 36.12	59.33 ± 29.45
0.05	70.58 ± 36.01	58.31 ± 29.34
0.1	70.32 ± 35.89	58.44 ± 29.16
0.2	72.19 ± 37.44	59.87 ± 30.28

Table 5 presents the sensitivity of concave hull localization accuracy to the α parameter. The lowest mean errors are achieved at $\alpha = 0.1$ (Target 2: 70.32 m; Target 4: 58.44 m). A very small $\alpha = 0.02$ increases the mean error by 2.1 % for Target 2 and 1.5 % for Target 4 due to overfitting to noise, while also raising the standard deviation. At $\alpha = 0.05$, the performance is virtually identical to $\alpha = 0.1$. A larger $\alpha = 0.2$ degrades accuracy by 2.7 % and 2.4 % respectively, as the hull begins approximating the convex hull and loses concavity preservation. Consequently, the interval $\alpha \in [0.05, 0.1]$ yields stable results, confirming that the superiority of the concave hull approach.

Figure 7 presents a side-by-side comparison of three geometric enclosure techniques applied to the same radar echo set. The bounding box (a) encloses all points in the smallest axis-aligned rectangle, using the geometric center as the estimate. This is simple and fast but is susceptible to systematic bias caused by empty corners in irregular echoes. The convex hull (b) reduces corner biases and better adapts to the extent of the echo. It fills in internal concavities (e.g., superstructure shadowing or clutter) while creating the smallest convex polygon. The concave hull (c) conforms tightly to the natural boundary of the echo, preserving the concavities and creating the centroid closest to the true center.

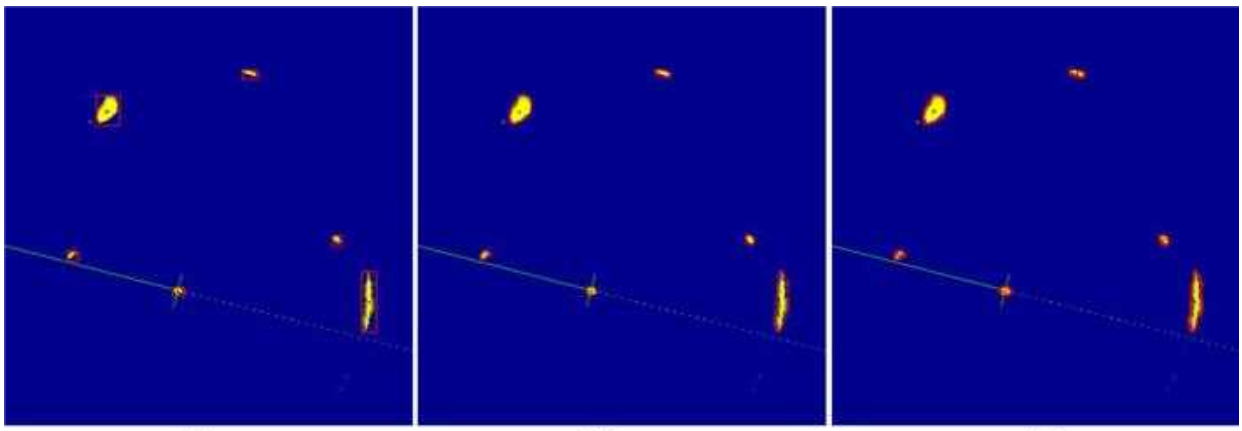


Figure 7. Visual comparison of geometric enclosure methods applied to radar echo clusters in PPI images: (a) Bounding Box (BB), (b) Convex Hull, (c) Concave Hull (alpha-shape).

The superiority of concave hull centroids method arises from the fundamental geometric properties of real radar echo clusters in PPI images. Maritime targets generate highly non-convex point clouds due to sea-clutter masking, superstructure shadowing, multipath gaps, and radar resolution effects.

Axis-aligned bounding boxes include large empty corner regions, producing systematic centroid bias. Convex hulls eliminate corner bias but enforce convexity, thereby filling internal concavities and displacing the centroid toward the geometric center of the filled region rather than the true mass center of the observed echo pixels. Concave hulls (α-shapes) are the only method among the three that explicitly preserve natural concavities while remaining tight to the observed data points. Their centroid therefore approximates the true center of mass of the visible echo pixels. A detailed view of the target in Figure 7 is given in Figure 8.

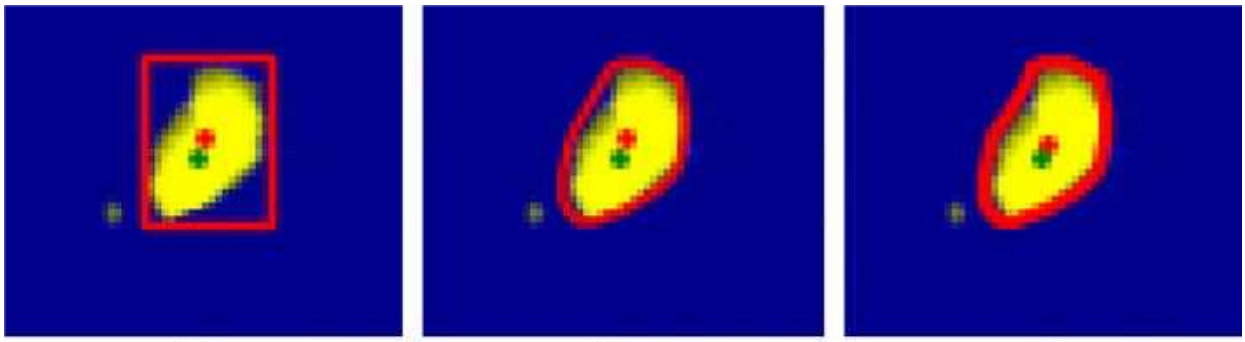


Figure 8. Detailed view of a single radar echo cluster: (a) Bounding Box (BB), (b) Convex Hull, (c) Concave Hull (alpha-shape).

4. CONCLUSIONS

This study compares three methods for locating target positions in radar imagery: bounding boxes, convex hulls, and concave hulls. DLR Baltic Sea dataset used and matched with real AIS data. Results on the DLR Baltic Sea dataset show that using concave hulls is the most accurate method. It achieves average error of only 70.32 meters for Target 2 and 58.44 meters for Target 4. This is improvement up to 12.7% according to bounding boxes method and enhancement up to 2.1% with respect to convex hulls method. Concave hulls perform well because they follow the true shape of radar echoes, including waves, and signal reflections from vessel superstructures. Bounding boxes contain empty corners that cause large errors. Convex hulls accommodate but still miss internal gaps.

These findings improve safety for real-time vessel traffic monitoring and autonomous vehicles. The concave hull method is fast, reliable, and operates under various sea conditions. The 4.5° azimuth correction provides optimal radar-AIS matching. This will help build more robust collision avoidance systems. Future work could automatically adjust concave hull settings, combine them with machine learning algorithms, and track multiple vessels in dense traffic scenarios.

Declaration of Ethical Standards

The author declares that he complies with all ethical standards.

Credit Authorship Contribution Statement

Author 1: Designing, conception, data analysis and interpretation, visualization, implementation of methods, and writing the manuscript.

Declaration of Competing Interest

The author has no competing interests to declare that are relevant to the content of this article.

Funding / Acknowledgements

The author declares that no funding was used in the study.

Data Availability

The data that support the findings of this study are available at https://doi.org/10.26090/rwmr (accessed on 23 October 2025) under DLR's export control principles.

Use of Artificial Intelligence

The author acknowledges that the use of AI tools is limited to language editing and readability improvements. The author remains fully responsible for the accuracy, originality, and integrity of the manuscript, in compliance with ethical and legal standards.

5. REFERENCES

[1] J. S. Fowdur, M. Baum, and F. Heymann, "Real-world marine radar datasets for evaluating target tracking methods," Sensors, vol. 21, no. 14, p. 4641, Jul. 2021, doi: 10.3390/s21144641.

[2] S. Külcü, "Radar image-based object detection and tracking for autonomous surface vehicles," Turk. J. Marit. Mar. Sci., vol. 12, no. 1, pp. 35–47, 2026, doi: 10.52998/trjmms.1743670.

[3] A. P. Nemirko and J. H. Dulá, "Machine learning algorithm based on convex hull analysis," Proc. Comput. Sci., vol. 186, pp. 381–386, 2021, doi: 10.1016/j.procs.2021.04.160.

[4] X. Xu, B. Wu, L. Xie, Â. P. Teixeira, and X. Yan, "A novel ship speed and heading estimation approach using radar sequential images," IEEE Trans. Intell. Transp. Syst., vol. 24, no. 10, pp. 11107–11120, Oct. 2023, doi: 10.1109/TITS.2023.3281547.

[5] X. Xu, B. Wu, Â. P. Teixeira, X. Yan, and C. Guedes Soares, "Integration of radar sequential images and AIS for ship speed and heading estimation under uncertainty," IEEE Trans. Intell. Transp. Syst., vol. 25, no. 6, pp. 5688–5702, Jun. 2024, doi: 10.1109/TITS.2023.3338293.

[6] X. Xu, B. Wu, Â. P. Teixeira, and C. Guedes Soares, "Ship collision risk assessment and visualization using radar sequential images for intelligent maritime supervision," IEEE Trans. Intell. Transp. Syst., vol. 26, no. 6, pp. 9004–9017, Jun. 2025, doi: 10.1109/TITS.2025.3539011.

[7] Z. Guo, X. Zhang, C. Liu, X. Ji, J. Jiao, and Q. Ye, "Convex-hull feature adaptation for oriented and densely packed object detection," IEEE Trans. Circuits Syst. Video Technol., vol. 32, no. 8, pp. 5252–5266, Aug. 2022, doi: 10.1109/TCSVT.2022.3140248.

[8] H. Liang, S. Wang, S. Gao, H. Li, C. Su, H. Lu, X. Zhang, X. Chen and Y. Chen, "Deephullnet: A deep learning approach for solving the convex hull and concave hull problems with transformer," Int. J. Digit. Earth, vol. 17, no. 1, p. 2358843, 2024, doi: 10.1080/17538947.2024.2358843.

[9] J. Guan, Wu, X., Ding, H., Liu, N., Huang, Y., Cao, Z., & Wei, J., "Detection of small targets on sea surface based on 3-D concave hull learning algorithm," J. Electron. Inf. Technol., vol. 45, no. 5, pp. 1602–1610, May. 2023, doi: 10.11999/JEIT220448.

[10] Y. Shi and Y. Hu, "mRMR-Tri-ConcaveHull detector for floating small targets in sea clutter," IEEE J. Sel. Topics Appl. Earth Observ. Remote Sens., vol. 16, pp. 6799–6811, 2023, doi: 10.1109/JSTARS.2023.3297278.

[11] S. Shi, J. Wang, J. Wang, and T. Li, "False-alarm-controllable detection of marine small targets via improved concave hull classifier," Remote Sens., vol. 17, no. 11, p. 1808, May. 2025, doi: 10.3390/rs17111808.

[12] X. Gao, L. Zhang, X. Chen, C. Lin, R. Hao, and J. Zheng, "GCT-YOLOv5: A lightweight and efficient object detection model of real-time side-scan sonar image," Signal, Image Video Process., vol. 18, no. Suppl 1, pp. S565–S574, Apr. 2024, doi: 10.1007/s11760-024-03174-5.

[13] X. Yang, Q. Zhang, Q. Dong, Z. Han, X. Luo, and D. Wei, "Ship instance segmentation based on rotated bounding boxes for SAR images," Remote Sens., vol. 15, no. 5, p. 1324, Feb. 2023, doi: 10.3390/rs15051324.

[14] J. Xu, Y. Suo, Y. Jiang, and Q. Yang, "A fast algorithm for matching AIS trajectories with radar point data in complex environments," Remote Sens., vol. 16, no. 23, p. 4360, Nov. 2024, doi: 10.3390/rs16234360.

[15] M. Li, Q. Liu, and S. Peng, "Point cloud registration based on concave hull association," Remote Sens. Lett., vol. 14, no. 3, pp. 313–322, Mar. 2023, doi: 10.1080/2150704X.2023.2195569.

[16] D. Korban, O. Melnyk, O. Onishchenko, S. Kurdiuk, V. Shevchenko, and T. Obniavko, "Radar-based detection and recognition methodology of autonomous surface vehicles in challenging

marine environment," Sci. J. Silesian Univ. Technol. Ser. Transp., vol. 122, pp. 111–127, 2024, doi: 10.20858/sjsutst.2024.122.7.

[17] M. Feng, T. Zhang, S. Li, G. Jin, and Y. Xia, "An improved minimum bounding rectangle algorithm for regularized building boundary extraction from aerial LiDAR point clouds with partial occlusions," Int. J. Remote Sens., vol. 41, no. 1, pp. 300–319, Jan. 2020, doi: 10.1080/01431161.2019.1641245.

[18] X. Zhang, Z. Tang, J. Yu, M. Guo, and L. Jiang, "Convex hull properties and algorithms," Appl. Math. Comput., vol. 216, no. 11, pp. 3209–3218, Aug. 2010, doi: 10.1016/j.amc.2010.04.044.

[19] S. Asaeedi, F. Didehvar, and A. Mohades, "α-Concave hull, a generalization of convex hull," Theor. Comput. Sci., vol. 702, pp. 48–59, Nov. 2017, doi: 10.1016/j.tcs.2017.08.014.

Konya Mühendislik Bilimleri Dergisi, c.14, s.2, 917-950, 2026
Konya Journal of Engineering Sciences, v.14, n.2, 917-950, 2026
ISSN: 2667-8055 (Electronic)
DOI: 10.36306/konjes.1716813

AN OVERVIEW OF MULTIMODAL LEARNING: CONCEPTS, CHALLENGES, APPLICATIONS AND DATASETS

[1,*]Ali Hüsameddin ATEŞ, [2]Ulaş YURTSEVER

[1,2]*Sakarya University, Faculty of Computer and Information Sciences, Department of Computer Engineering, 54050, Sakarya, Türkiye*
[1,2]*Sakarya University, Research, Development and Application Center (SARGEM), Interdisciplinary Artificial Intelligence Lab., 54050, Sakarya, Türkiye*
[1]aliates@sakarya.edu.tr, [2]ulas@sakarya.edu.tr

Highlights

- Key concepts and challenges in multimodal learning are systematically reviewed.
- Core challenges, including representation learning, alignment, translation, fusion, missing modality, and co-learning, are analyzed.
- Domain-specific applications and datasets for multimodal learning are presented.

Graphical Abstract

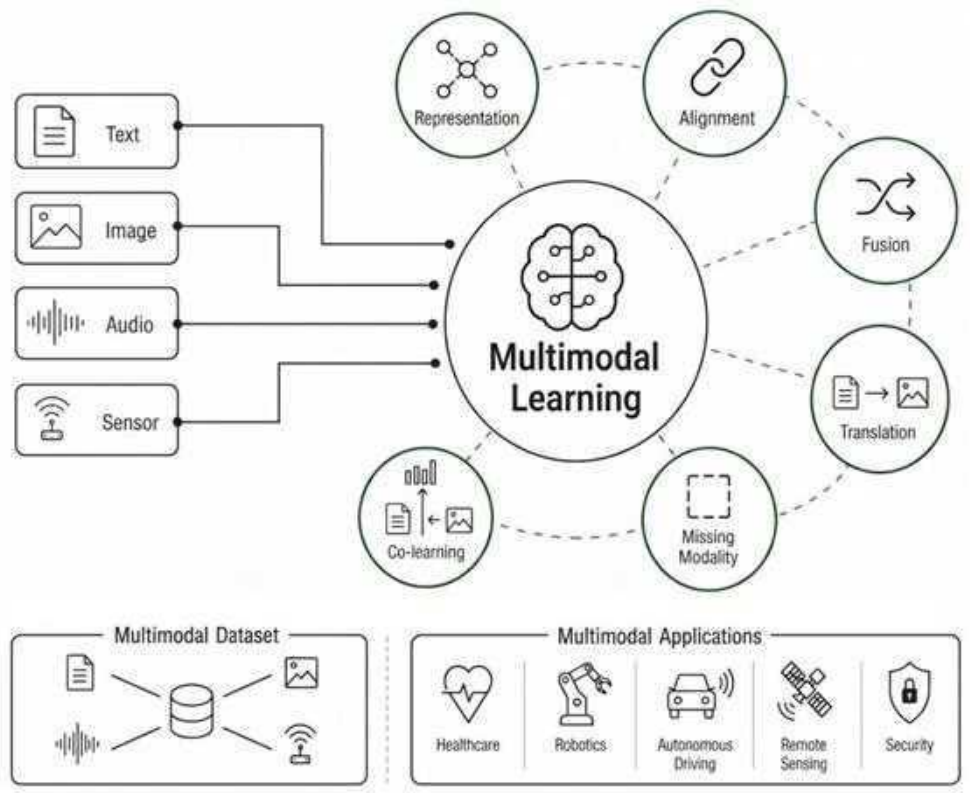


Figure Conceptual overview of multimodal learning

***Corresponding Author:** Ali Hüsameddin ATEŞ, aliates@sakarya.edu.tr

Konya Mühendislik Bilimleri Dergisi, c.14, s.2, 917-950, 2026
Konya Journal of Engineering Sciences, v.14, n.2, 917-950, 2026
ISSN: 2667-8055 (Electronic)
DOI: 10.36306/konjes.1716813

AN OVERVIEW OF MULTIMODAL LEARNING: CONCEPTS, CHALLENGES, APPLICATIONS AND DATASETS

[1,*]Ali Hüsameddin ATEŞ, [2]Ulaş YURTSEVER

[1,2]Sakarya University, Faculty of Computer and Information Sciences, Department of Computer Engineering, 54050, Sakarya, Türkiye
[1,2]Sakarya University, Research, Development and Application Center (SARGEM), Interdisciplinary Artificial Intelligence Lab., 54050, Sakarya, Türkiye
[1]aliates@sakarya.edu.tr , [2]ulas@sakarya.edu.tr

(Received: 10.06.2025; Accepted in Revised Form: 10.12.2025)

ABSTRACT: Given the multifaceted nature of reality, phenomena can be interpreted not only through singular perspectives but also by bringing together various dimensions. Meaning often emerges from the convergence of diverse perspectives, contexts, and forms of representation. The construction of systems capable of analyzing this multilayered structure requires integrating heterogeneous types of information within a holistic, interactive framework. For this multilayered structure to be processable by artificial intelligence systems, the synthesis of heterogeneous information types from various sources in a holistic structure is mandated. In response to this requirement, multimodal learning is an approach that aims to develop more contextual and generalizable artificial intelligence systems by combining heterogeneous data from different modalities (e.g., text, images, audio, sensor data) within an integrated structure. Based on recent literature, this review examines the conceptual foundations of multimodal learning and its key technical challenges, including representation learning, alignment, fusion, translation, missing modality, and co-learning. This study systematically compares and classifies more than 50 of the most prominent review articles published between 2010 and 2025 in a comprehensive table, summarizing the challenges they address, their application areas, and practical contributions. Attention has been drawn to areas often neglected in the literature, such as co-learning and missing modality, as well as to other critical gaps persisting in the field. Furthermore, the paper presents multimodal applications in healthcare, robotics, autonomous driving, remote sensing, and security, along with common multimodal datasets. By bridging theoretical foundations and real-world applications, this study provides a comprehensive reference for the field of multimodal learning.

Keywords: *Artificial Intelligence, Multimodal Applications, Multimodal Challenges, Multimodal Datasets, Multimodal Learning.*

1. INTRODUCTION

In recent years, the adoption of artificial intelligence (AI) applications has become increasingly widespread across various domains. The historical process that began with the use of traditional machine learning algorithms for fundamental problems has accelerated further with the advent of big data and the emergence of deep learning architectures, resulting in a sustained surge of research in AI. Advancements in deep learning have paved the way for the integration of artificial intelligence across domains, such as healthcare, education, media, manufacturing, and planning, and have spearheaded its widespread adoption across numerous sectors. Developed deep learning-based applications beyond sectoral automation hold significant promise for advancing the widespread use of AI to address the problems encountered [1]–[3].

The efficient utilization and success of deep learning applications depend on the employed architecture and the input dataset [4]. Conventional deep learning architectures are typically designed to

***Corresponding Author:** Ali Hüsameddin ATEŞ, aliates@sakarya.edu.tr

operate on a single data type, such as images, text, audio, or signals, whereas most real-world problems require the integration of meaningful information from diverse data sources to produce richer and more informative outputs [5]. With the proliferation of Internet of Things (IoT) systems, it has become possible to simultaneously collect multiple data types (e.g., image, audio, sensor, and signal data) from various devices [6]. Thus, there has been a growing emphasis on training deep learning architectures that go beyond a single data source, employing more complex, integrated approaches that leverage data from multiple sources. The process of training these architectures, which involves integrating semantically similar data obtained from diverse sources and utilizing it synchronously during model training, is referred to as multimodal learning [5]. This paradigm represents a critical evolution in AI, enabling systems to move beyond isolated data processing toward a holistic synthesis akin to human perception. By integrating distinct sensory modalities, models can achieve a level of contextual awareness and robustness unattainable with unimodal approaches alone, thereby paving the way for more intelligent and adaptive autonomous systems.

Multimodal learning is a learning approach that aims to achieve superior results by integrating diverse data types (modalities) from various sources that semantically indicate the same concept within model training [7]. This approach, surpassing the limitations of traditional models based on a single data modality, enables the development of architectures more attuned to real-world problems by integrating multiple data types. Accordingly, architectures based on multiple modalities offer innovative solutions in applications developed across numerous fields, such as autonomous driving, robotic systems, healthcare, environmental science, media, and security systems [8]. For example, in media analysis, models trained by concurrently utilizing text and image data can generate textual descriptions from images and synthesize unique visuals from textual prompts [9]–[11]. In sentiment analysis, the concurrent use of an individual's image, audio, and speech text enables more consistent inferences and the contextual analysis of their movements and behaviors [12]–[14]. In healthcare, more accurate diagnoses and treatment recommendations can be obtained by jointly evaluating medical imaging (e.g., MRI, CT scans) and electronic health records; additionally, patients' health status can be monitored through the real-time collection and assessment of various personal data via wearable sensors [15]–[19]. In autonomous driving, significant improvements in safer navigation can be achieved by synchronously combining camera, LiDAR, and radar sensors with map information. [20]–[22]. In the environmental domain, air pollution can be detected more accurately by combining sensor data from ground stations [23], traffic density information, and satellite data. More precise weather forecasts can also be made using temperature, humidity, and wind data [24].

While multimodal learning offers innovative solutions in many fields, the successful deployment of such systems in real-world scenarios extends beyond mere data combination; it requires robust architectural frameworks capable of handling the inherent heterogeneity of multiple data types and the asynchronous nature of multimodal data streams [25]. The challenges encountered in multimodal learning are generally examined under the headings of accurate modality representation [26], alignment [27], fusion of different representations [28], inter-modality translation when necessary [29], completion of missing modality data [30], and modeling co-learning strategies during training [31].

This study addresses the fundamental principles of multimodal learning, its challenges and associated solution approaches, and various application areas and datasets. By presenting both theoretical foundations and practical applications, this study provides a comprehensive perspective on multimodal learning. Unlike existing reviews, this study focuses not only on specific modality types but also on the fundamental building blocks of the field, namely representation, alignment, fusion, translation, missing modality, and co-learning, systematically associating them with solution approaches from the current literature. More than 50 review studies published between 2010 and 2025 are classified in a comprehensive table, and a structured synthesis of the existing literature is provided. Accordingly, the study offers a holistic framework that analyzes challenges in depth at the theoretical level and establishes connections with application areas, thereby distinguishing itself from similar studies in the literature.

The remainder of this paper is organized as follows. Section 2 introduces the concept and historical development of multimodal learning and explains its role in enabling AI systems to process heterogeneous data sources within a unified learning framework. Section 3 discusses the main technical challenges of multimodal learning, including representation learning, alignment, fusion, translation, missing modality, and co-learning, together with solution strategies proposed in the literature. Section 4 presents major application domains in which multimodal learning has been widely adopted, such as autonomous driving, robotics, healthcare, remote sensing, and security systems. Section 5 presents commonly used multimodal datasets and evaluation metrics, covering different modality types, learning tasks, and application domains. Section 6 summarizes the key technical challenges addressed throughout the review and outlines possible research directions for each challenge in a comparative table. Finally, Section 7 concludes the study by highlighting the overall findings and contributions of the review.

1.1. Scope and Literature Selection Methodology

To construct a comprehensive overview of multimodal learning, a broad literature search was conducted across major academic databases, primarily the Web of Science, extending to Scopus, ScienceDirect, IEEE Xplore, ACM Digital Library, arXiv, and Google Scholar, covering the 2010-2025 period. The search strategy focused on title-based queries incorporating variations of keywords such as "multimodal", "multi-modal", "multi-source", "multi-task", "multi-learning", and "multi-purpose" combined with "deep learning" or "machine learning" and "survey" or "review".

The selection criteria were designed to identify studies that make a significant contribution to the theoretical or practical understanding of the multimodal learning domain. Rather than adhering to a rigid systematic review protocol, the inclusion process was relevance-based, specifically targeting articles that address at least one of the following critical components identified in our taxonomy: Representation learning, Alignment, Translation, Fusion, Missing modality, and Co-learning. Furthermore, studies providing details on multimodal learning applications and datasets, or those offering unique contributions to the field, were also included. Conversely, unimodal studies that lacked a clear contribution to the multimodal domain or did not address the aforementioned core challenges or practical aspects were excluded from the analysis. This methodology ensured that the selected literature provided a coherent basis for the multimodal learning taxonomy, and the final research comprises nearly 50 review and survey articles, which are summarized in Table 1.

2. MULTIMODAL LEARNING

Artificial intelligence models, whose foundations were laid in machine learning and later became widespread with the advent of deep learning architectures, typically use a single data source. The proliferation of IoT devices diversified data sources and led to the emergence of big data; subsequently, as data processing capabilities increased, the data sources used in AI models also diversified, leading to the emergence of multimodal architectures. Multimodal learning is a training approach that integrates different data types, such as text, images, video, and signal data, into a single model, enabling the model to learn complex intermodal relationships and achieve more comprehensive and generalizable representations without relying on a single data modality. [7].

The complexity of real-world problems necessitates integrating and concurrently using information from diverse data sources when designing AI architectures. For example, models trained in medical diagnosis and various healthcare fields need to evaluate multiple data types simultaneously, such as various imaging modalities like MRI and CT scans, clinical data, and laboratory results, to provide more accurate diagnoses and treatment recommendations [32]–[34]. In autonomous vehicle systems, various sensor data, such as camera images, LiDAR and radar outputs, and GPS location data, must be evaluated concurrently for the vehicle to perceive its environment more comprehensively [35]–[39]. In AI-integrated security and surveillance systems, effective performance requires the joint processing of diverse data sources, including camera and infrared sensor data, motion data, and audio signals. [40], [41]. For emotion

and behavior analysis, more accurate inferences can be obtained by collectively evaluating facial expressions, audio signals, and various physiological signals. [42]–[44]. For robotic systems to exhibit more natural and contextual behaviors, they need to use a system that integrates audio, visual, and various sensor data [45]–[47].

Multimodal architectures, which are not constrained by a single modality, can achieve more accurate and reliable results by leveraging complementary information from different data types. Knowledge learned across modalities improves generalization in scenarios that the model has not previously encountered. It plays a significant role in capturing complex inter-modality relationships and in extracting more comprehensive, multidimensional representations of real-world objects and concepts [48], [49]. For example, when difficulties arise in perceiving audio signals in a noisy environment, an architecture that is fed both the speaker's lip movements and audio signals can overcome this challenge [50], [51]. However, when data from one source is missing or ambiguous, information from other modalities can fill these gaps during training, thereby preventing a decline in model performance [30].

Multimodal learning is a rapidly developing research area with great potential in the field of artificial intelligence. Advancements in this area play a critical role in developing more context-aware and generalizable artificial intelligence (AI) systems for solving complex problems across many sectors; furthermore, it is emerging as a crucial field poised to help make future AI applications more effective and efficient.

3. MULTIMODAL LEARNING CHALLENGES

The theoretical foundations of multimodal architectures are predicated on learning feature representations in vector spaces from different data sources and subsequently fusing these representations appropriately to create a unified, general representation, thereby yielding a multimodal model. During the model training process, various challenges are encountered at each stage [7].

In the initial stage of the training process in multimodal learning, a significant challenge emerges in constructing effective representations for each modality. This process is referred to as representation learning. [52], [53]. Since images consist of pixels, text of words, and audio signals of waveforms, modality-specific encoders are required to transform these heterogeneous data types into meaningful and comparable feature vectors [54]. These encoders must be designed to preserve modality-specific information while transforming raw data into high-dimensional feature vectors. For example, features such as color, texture, and shape related to objects are extracted from an image, whereas features such as tone, speed, and rhythm are extracted from an audio recording. The fact that different modalities possess distinct attributes and characteristics, including their varying scales, dimensions, formats, and distributions, complicates the representation learning process [26], [55].

After representations for the modalities are obtained, it is necessary to align them within a common semantic space. For this purpose, data representations from each modality are mapped into a common representation space by associating semantically matching parts of the data across modalities. Thus, meaningful relationships can be established across different data types, and information from the modalities can be used in a more interactive and complementary manner. For example, in a model that takes both images and their descriptive texts as input, each word must be associated with the image's objects in a common semantic space to align the modalities. In another task, such as video transcription, aligning image-text inputs requires matching the speaker's lip movements to the speech text and creating a mapping between each text token and its corresponding lip visuals.

After the modality-specific representations are learned and aligned, it is critical to fuse these heterogeneous features and effectively integrate them into the constructed architecture. Early, late, and hybrid fusion techniques are commonly used in this regard. In early fusion, data from different modalities are fused immediately after feature representations are extracted from each modality. Although early fusion provides a rich data representation by combining different data types, the extracted features may lack homogeneity and standard dimensionality, which can lead to errors during model evaluation. In late fusion, each modality first performs its own specific feature extraction, and the extracted features are then

sent to the model, where the incoming feature representations are fused at the final stage. However, in this case, capturing inter-modal relationships early on becomes more difficult. Conversely, when some modalities are more decisive than others for certain tasks, the assignment of appropriate weights to each modality also becomes highly significant. In hybrid or intermediate fusion, which is used to address this issue, the aim is to exhibit a modality-specific hybrid approach by combining the advantages of both early and late fusion [56].

At certain stages of training, it may be necessary to transform or translate features obtained from one modality into the form of another modality. The primary objective of the translation is to convert the source modality into the target modality while preserving its semantic information. Basic translation tasks include converting a textual input into an image, describing an image with explanatory text, or transcribing a speech signal into textual form. However, due to the representation of different modalities in their own distinct data spaces, a direct translation between them is generally not feasible. In such cases, it is necessary to develop architectures capable of performing translation by learning specialized inter-modality translation functions.

Another common challenge in real-world datasets is missing modality. In multimodal datasets used for training, data samples across modalities must be aligned and synchronized. This synchronization requires semantically aligned modality data to be simultaneously available during the training phase in multimodal learning scenarios combining multiple data sources. If even a single sample is missing in any modality, this synchronized structure is disrupted, and the question arises of how to continue training the model. For instance, when training an emotion analysis model with image, audio, and text inputs, if the transcript for some video frames is missing, it is necessary to develop complementary strategies to compensate for the missing modality data through various methods (e.g., using feature vectors from lip movements).

In multimodal learning, designs in which each modality is processed through a separate training stream may be preferred to capture modality-specific features more effectively, as in late-fusion or modality-specific branch architectures. In such cases, insufficient interaction between modalities during training may limit inter-modality learning and mutual knowledge transfer. Therefore, multimodal co-learning strategies are needed to foster information exchange between modalities, enabling each modality to leverage the strengths of others and compensate for missing or noisy data through complementary inputs. Thus, instead of merely combining modalities through fusion techniques, the aim is to develop architectures that can correct each other's errors, learn collaboratively, and compensate for missing data.

Alongside all these technical challenges, multimodal learning also presents systematic challenges. Creating labeled datasets with multiple modalities is more time-consuming and labor-intensive than creating unimodal datasets. Moreover, the parallel processing of multiple data streams increases the computational load during training, thereby extending training times, requiring more powerful hardware, and making scalability to practical applications more challenging. However, intra- and inter-modality biases can arise during training, and the transparency and interpretability of models may be overlooked.

Multimodal learning has the potential to achieve superior learning performance with richer representations than single-modal learning, provided that these technical and systematic challenges are effectively addressed during training. Accordingly, this review focuses on technical rather than systematic challenges, namely representation learning, alignment, translation, fusion, missing modality, and co-learning, and discusses the methodologies generally proposed for each. In this regard, Table 1 summarizes the most prominent review articles on multimodal learning published between 2010 and 2025 according to specific aspects. For each review article, details are provided regarding its primary focus area, the multimodal challenges it addresses, its inclusion of applications, tasks, and datasets, and any additional multimodal concepts mentioned in the study. To facilitate a structured exploration, the table uses a multifaceted taxonomy that maps each contribution to primary technical challenges and practical deliverables. The chronological arrangement enables systematic tracking of the multimodal learning literature, while the aspect-based classification facilitates comparison across review scopes and guides researchers toward studies relevant to theoretical foundations, applications, and datasets.

Table 1. A comparative analysis of the most prominent review studies in the field of multimodal learning.

Year	Review	Area/Scope	R	A	T	F	M	C	A	D	Others
2010	Atrey et al. [57]	Fusion				✓				✓	Methods for multimodal fusion and evaluation metrics.
2015	Lahat et al. [58]	General/Theoretical				✓			✓		Other multimodal challenges at the data and model design level.
2017	Ramachandram et al. [5]	General/Theoretical				✓			✓	✓	Multimodal regularization.
2019	Baltrusaitis et al. [7]	General/Theoretical	✓	✓	✓	✓		✓	✓		Taxonomy of multimodal learning challenges.
	Guo et al. [52]	General/Theoretical	✓						✓		Multimodal representation learning frameworks and typical models.
	Y. Li et al. [59]	Representation Learning	✓	✓		✓			✓		Multiview representation learning taxonomy.
2020	Gao et al. [60]	General/Theoretical				✓					Representative multimodal deep learning models.
	C. Zhang et al. [53]	Vision & Language	✓			✓			✓	✓	Methods for general multimodal tasks.
2021	Y. Zhang et al. [61]	Computer Vision				✓				✓	Multimodal evaluation metrics.
	Joshi et al. [62]	Explainable AI (XAI)				✓			✓	✓	Multimodal explanation, generation, and evaluation approaches.
	Mogadala et al. [63]	Vision & Language							✓	✓	Various vision and language integration methods.
	Bayoudh et al. [56]	Computer Vision	✓			✓			✓	✓	Multitask learning, multimodal transfer learning.
2022	Rahate et al. [31]	Co-learning						✓	✓	✓	Multimodal co-learning taxonomy.
	Sleeman et al. [64]	Classification				✓					Multimodal classification methods.
	J. Li et al. [65]	Remote Sensing				✓				✓	Open-source codes in DL-based multimodal RS data fusion.
	Liang et al. [29]	General/Theoretical	✓	✓		✓		✓			Foundational principles in multimodal research.
	Ma et al. [66]	Meta-learning							✓	✓	Multimodal meta-learning methods.
	Chai et al. [67]	Computer Vision				✓	✓		✓	✓	Multimodal loss functions and learning methods.
	Uppal et al. [68]	Vision & Language							✓	✓	Models for vision and language tasks and evaluation metrics.
	Zhu et al. [69]	General/Theoretical	✓						✓	✓	Data modalities and their characteristics and evaluation metrics.
	Erdem et al. [70]	NLP							✓	✓	Neural natural language generation tasks and learning strategies.
	Dimitri [25]	General/Theoretical				✓			✓	✓	General principles of multimodality.
	Ektefaie et al. [71]	Graph Neural Networks							✓		Multimodal graphs.
2023	Wang et al. [72]	General/Theoretical							✓	✓	Multimodal pre-trained models.
	Tang et al. [73]	Fusion				✓			✓	✓	Architectures and evaluation metrics for multimodal sensor-based image fusion.
	Cao et al. [48]	Zero-shot Learning							✓	✓	Multimodal zero-shot learning algorithms and evaluation metrics.
	Manzoor et al. [26]	General/Theoretical							✓	✓	Multimodal pretraining approaches.
	Peng et al. [74]	Knowledge Graphs									Multimodal knowledge graph architecture.
	Barua et al. [75]	General/Theoretical	✓	✓	✓	✓		✓	✓		General tendency of multimodal learning.
	Lin et al. [76]	Federated Learning							✓	✓	Multimodal federated learning taxonomy.
	Tabakhi et al. [77]	Biomedical & Healthcare				✓			✓	✓	Multi-omics data challenges.
	P. Xu et al. [78]	NLP									Multimodal transformers.
	Akkus et al. [79]	General/Theoretical	✓		✓	✓			✓	✓	General multimodal architectures, training paradigms, and multipurpose models.
	Zhou et al. [80]	Cross-Modal Retrieval								✓	Cross-modal retrieval, subspace learning methods, and pre-trained models.

Table 1. (Continued)

Year	Review	Area/Scope	R	A	T	F	M	C	A	D	Others
2023	Jabeen et al. [8]	General/Theoretical							✓	✓	Models for multimodal tasks and evaluation metrics
2024	Rodis et al. [81]	Explainable AI (XAI)							✓	✓	Multimodal explainable AI methods and evaluation metrics.
	Chen et al. [82]	NLP							✓	✓	Large multimodal models and attention mechanisms.
	Wu et al. [30]	Missing Modality					✓		✓	✓	Multimodal missing modality methodologies.
	Raya et al. [83]	Clustering								✓	Multimodal clustering methods and evaluation metrics.
	Jiao et al. [28]	Fusion	✓	✓	✓	✓			✓	✓	Multimodal fusion techniques.
	Yu et al. [84]	Continual Learning								✓	Multimodal continual learning approaches and evaluation metrics.
	Warner et al. [27]	Biomedical & Healthcare	✓	✓	✓	✓		✓			Multimodal models for clinical predictions.
	Bayoudh [85]	Computer Vision							✓	✓	Multimodal hybrid deep learning architectures.
	M. Xu et al. [86]	Vision & Language									Multimodal foundation models and resource-efficient strategies.
	Waqas et al. [87]	Biomedical & Healthcare				✓				✓	Multimodal graph neural networks and transformers.
	S. Li et al. [88]	Alignment and Fusion		✓		✓				✓	Multimodal models with diverse modalities
2025	T. Li et al. [89]	Biomedical & Healthcare				✓				✓	Comparative performance of multimodal fusion strategies.
	Zhan et al. [90]	Missing Modality					✓				Summary of literature on missing modality.
	Nguyen et al. [91]	Fusion	✓		✓					✓	Summary of fusion methods used for Speech Emotion Recognition (SER).
	An et al. [92]	Fusion	✓			✓					LLM-centric multimodal fusion.
	Liu et al. [93]	NLP									Task taxonomy, benchmarks, evaluation metrics, and key challenges for multimodal LLMs.
	Zong et al. [94]	Self-Supervised Learning	✓	✓		✓			✓		Specific challenges and solutions for self-supervised multimodal learning.
	This Work	General/Theoretical	✓	✓	✓	✓	✓	✓	✓	✓	Holistic taxonomy, gap analysis, and future research directions.

Abbreviations for multimodal learning aspects: R: Representation learning, **A:** Alignment, **T:** Translation, **F:** Fusion, **M:** Missing modality, **C:** Co-learning, **A:** Applications or tasks, **D:** Datasets (All aspects refer to the multimodal domain). ✓: Deeply examined the aspect.

The evaluation presented in Table 1 illustrates the specific criteria addressed by the reviewed articles. The "✓" symbol indicates that the respective study comprehensively examines the multimodal dimension of the corresponding criterion, such as addressing a specific technical challenge, presenting an application or task-specific domain, or providing dataset details, explicitly confirming that the study is conducted exclusively within the multimodal domain. Conversely, blank entries denote that the criterion is not covered or falls outside the scope of the study.

An analysis of the table reveals a distinct trend. While foundational topics such as fusion and representation learning are extensively covered across most reviews, critical challenges, including alignment, translation, missing modality, and co-learning, are frequently omitted. This disparity highlights that while certain aspects of multimodal learning are mature, significant gaps persist in achieving deep semantic alignment between heterogeneous data sources, enabling flexible cross-modal translation for generative tasks, and ensuring system robustness against real-world data imperfections. Consequently, Table 1 provides a visual and analytical summary of the prevailing strengths and deficiencies in the literature.

A quantitative analysis of the reviewed literature reveals distinct trends in both publication volume and methodological focus. As illustrated by the temporal distribution of the selected studies, research interest in multimodal learning has followed an exponential trajectory, particularly surging after 2017. This inflection point correlates strongly with the introduction of the Transformer architecture, which shifted the dominant paradigm from traditional CNN-RNN fusion approaches toward unified, attention-based frameworks.

Regarding the distribution of challenges, early studies (2010–2015) predominantly focused on fusion strategies for classification tasks. However, recent literature (2020–2025) exhibits a marked shift toward alignment and representation learning, driven by the rise of large-scale vision-language models (e.g., CLIP) and generative tasks. Furthermore, when the studies are grouped by the multimodal challenges highlighted in this paper, representation learning and fusion emerge as the most frequently covered topics. In contrast, critical aspects such as handling missing modalities, co-learning strategies, and robust evaluation are examined in depth only in a comparatively small subset of reviews.

In addition to these quantitative insights, a detailed examination of the more than 50 review articles summarized in Table 1 reveals specific structural and thematic gaps in the existing literature. Firstly, consistent with the quantitative findings, it has been observed that challenges frequently encountered in real-world scenarios, such as co-learning and missing modality, are either not addressed at all or only superficially covered in a majority of the reviews. There are few studies that systematically and in-depth focus on these topics. This situation indicates that these significant challenges, which are vital for system robustness, need to be addressed more comprehensively. Secondly, a significant portion of existing reviews have focused on fundamental theoretical approaches or specific modality pairs (e.g., image-text). Although in-depth analyses exist for some complex application areas such as biomedical imaging and remote sensing, the challenges faced by multimodal learning in other fields, including robotics and environmental science, have received limited attention. Thirdly, while many review articles include multimodal datasets on a modality-by-modality basis, studies that systematically and comparatively analyze these datasets across application areas and task types are limited. This limitation reveals a significant gap in guiding researchers to select datasets for specific application areas, underscoring the need for more comprehensive investigations in this field. Additionally, the majority of reviews in Table 1 have inadequately covered practical aspects essential for researchers, such as loss functions, evaluation metrics, and open-source code sharing. This highlights the necessity for a more comprehensive consideration of practical aspects in the field of multimodal learning.

Consequently, these quantitative imbalances and qualitative gaps demonstrate the importance of reviews in the field that are not only conceptual but also application-oriented. This study highlights these deficiencies and offers a more holistic perspective by concurrently evaluating challenges, application areas, and practical implementation details.

3.1. Representation Learning

For machines to analyze data, the data must first be encoded into a numerical representation (e.g., a vector) that machines can process. Data identifiability is enabled by extracting its distinctive features. These distinguishing attributes make the data semantically separable, forming the basis of the learning process. In this context, the primary objective of machine learning is to automatically learn meaningful and discriminative representations of data and, through these representations, perform tasks such as decision-making, classification, or prediction more successfully. The more effectively the data is represented, the greater the success achieved in the subsequent stages of learning and decision-making. Consequently, the quality of data representation directly impacts the overall model performance [95].

Representation learning is the process of extracting features that transform raw data into meaningful vector spaces compatible with the relevant task. This process is crucial for the model to handle data properly. Raw data (e.g., pixels, audio waveforms, or character sequences) is often not directly usable by learning models. Therefore, data is transformed into low-dimensional, dense, and semantically rich representations in the network's intermediate layers, making it processable by the model [52]. For instance,

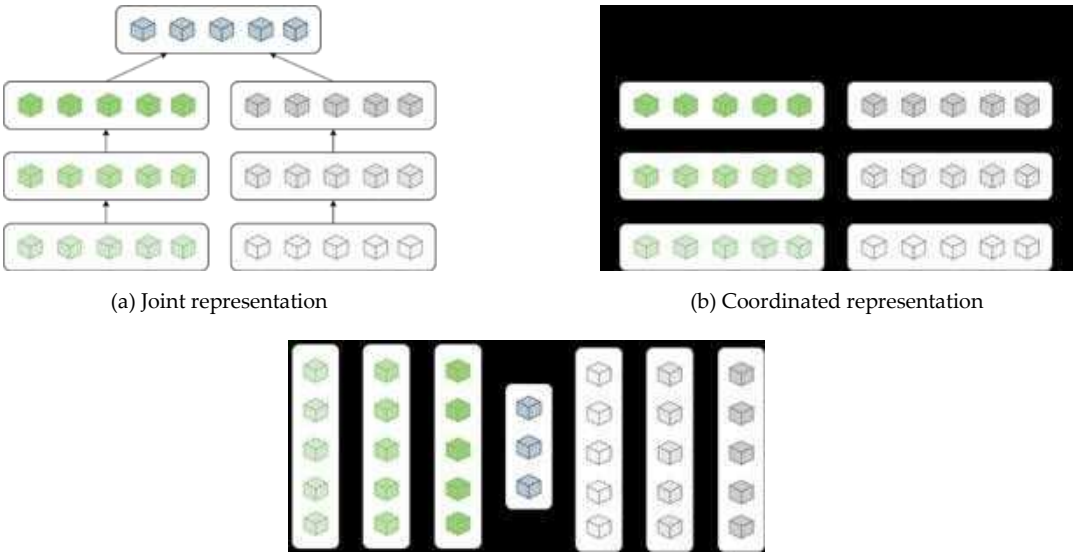
to obtain meaningful representations of data, various techniques extract features such as shapes, edges, and textures from an image; tone, rhythm, and pitch information from an audio recording; or semantic context from a text.

The inherent nature of each modality, including differences in distributions, scales, and structural characteristics, necessitates that representation learning methods be designed modality-specifically. For instance, while image data is transformed into edge, texture, and object-based features, text is typically vectorized using word embedding methods, and audio signals are represented via spectral analysis. These obtained representations are generally in tensor format and are referred to as feature maps in image-based structures and embedding matrices in text-based structures [69].

While traditional learning architectures are limited to unimodal structures focusing on a single modality, multimodal systems require the representation of multiple data types within a single architecture [95]. This situation entails more complex architectural requirements, involving not only representation learning but also the alignment, fusion, and inference of these representations as a meaningful whole [28].

In multimodal systems, although the modalities convey the same semantic information, their unique forms and distributions make the data inherently heterogeneous. For example, although a speaker's face image, speech audio, and textual transcript semantically convey the same content, they possess distinct structural characteristics and representations. Therefore, modality-specific representation learning is required, followed by the coherent integration of these representations, preserving semantic relationships. Furthermore, to enable translation between modalities, when necessary, cross-modal relationships must be established between these representations.

Consequently, a robust representation learning framework not only improves model accuracy but also enhances the model's explainability, generalizability, and resilience to missing modality. In line with all these objectives, establishing a homogeneous representation learning structure is of great importance for an efficient training process [52].



(a) Joint representation

(b) Coordinated representation

(c) Encoder-decoder representation

Figure 1. Three types of multimodal representation. (a) Joint representation seeks to project multiple modalities into a shared semantic space, enabling unified processing. (b) Coordinated representation keeps the modalities in separate spaces while aligning them through constraints to ensure semantic consistency. (c) Encoder-decoder models perform cross-modal translation by converting one modality into another while preserving the original meaning across modalities [52].

In recent years, self-supervised representation learning approaches [96] have emerged as a powerful paradigm, particularly in multimodal systems. In these approaches, representations are learned without

requiring labels by leveraging the inherent structure of the data. For example, contrastive learning-based methods perform learning more effectively by mapping similar samples to nearby representations and dissimilar samples to distant ones in the representation space. Thus, it has become possible to learn effective representations from large-scale unlabeled data.

Baltrusaitis et al. [7] classified multimodal representation learning into two categories: joint representation and coordinated representation. Subsequent studies have adopted a similar classification with minor modifications. In the joint representation approach, representations extracted from different modalities are combined in a common vector space to form a single unified representation. Conversely, in the coordinated representation approach, each modality is represented in its own space, but the relationship between them is coordinated through a similarity or structure constraint.

Guo et al. [52] regard the encoder-decoder as a third structure for representation learning, as it performs cross-modal mapping by encoding the input modality into a latent space and decoding it with respect to the target modality. As illustrated in Figure 1, the encoder component transforms the input modality into a modality-independent latent representation, and the decoder converts this representation into the target modality, enabling the learning of semantic relationships between modalities.

Similarly, Li et al. [59] divided multimodal representation learning into two main categories: representation alignment and representation fusion, and Liang et al. [29] classified it into: fusion, coordination, and fission. Representation fusion and coordination are fundamentally based on the joint and coordinated representation approaches, respectively. However, representation fission typically creates a larger set of disjoint representations from the input modalities, enabling a more detailed evaluation of the multimodal structure and providing insight into its internal characteristics.

3.2. Alignment

While human perception can effectively address real-world problems by seamlessly integrating multiple modalities, for machines, this integration poses a significant challenge. To overcome this challenge, multimodal alignment attempts to identify the mutual relationships and semantic connections between different modalities. Uncovering the relationships among modalities is vital for acquiring more comprehensive and semantically rich representations.

The integration of complementary information across modalities enables more robust, generalizable representations, providing a more comprehensive understanding that enhances the model's ability to generalize to novel, unprecedented situations. For instance, a facial expression may have different meanings across cultures, but when evaluated in context with the tone and content of speech, its true meaning can be inferred more accurately. On the other hand, cross-modal information transfer can be achieved through mutual connections between aligned modalities, and missing or noisy data in one modality can be compensated for by the other. For example, while speech recognition performance degrades in a noisy environment, considering the speaker's lip movements can significantly improve recognition accuracy. In addition, alignment enables information associated with one modality to be retrieved using another modality. For tasks such as identifying the counterpart of an image region in its caption, finding the appropriate video segment for a given text query, or detecting frames in a video where searched objects are located, alignment maps between sub-components of modalities are learned, discovering their interconnections [28].

Baltrusaitis et al. [7] divided multimodal alignment into two categories: explicit alignment and implicit alignment. In explicit alignment, as in retrieving a video segment via a textual query, there is a direct mapping; whereas in implicit alignment, alignment is achieved through latent representations during model training and is typically used as an intermediate step for another task. As illustrated in Figure 2, Jiao et al. [28] classified multimodal alignment into discrete alignment and continuous alignment. While discrete alignment is employed for data with discrete structures across different modalities, such as in cross-modality retrieval, where relationships between samples can be easily determined, continuous alignment is used for aligning data that cannot be easily segmented, as in continuous signals. Li et al. [59] categorized multimodal alignment into three categories: distance-based, similarity-based, and correlation-

based. Distance-based alignment focuses on minimizing the Euclidean distance between modality representations, whereas similarity-based alignment aims to maximize the similarity, such as dot-product similarity, between representations. On the other hand, correlation-based alignment attempts to align by maximizing the statistical correlation between representations, as in Canonical Correlation Analysis (CCA).



(a) Discrete alignment (b) Continuous alignment

Figure 2. Illustration of alignment strategies between modalities. (a) Discrete alignment establishes direct correspondences between distinct units or segments across different modalities, making it suitable for data with well-defined structures. (b) Continuous alignment handles data streams without clear segment boundaries, enabling flexible mapping between continuous signals over time or across sequences [28].

3.3. Fusion

Fusion, one of the most extensively studied topics in the field of multimodal learning, is most simply defined as the integration of feature matrices obtained from different modalities into a unified representation. This fusion process seeks to preserve the salient information from each modality, effectively leverage the complementary strengths across modalities, and ultimately establish a more robust decision-making mechanism by integrating data from diverse sources [53]. The unique information carried by each modality and the inter-modality integration, allowing different modalities to offer varied perspectives on the same event, enhance the overall perceptual capacity of the system. For instance, in a system analyzing a human face, emotions may not be correctly classified when only visual information is used; however, when speech tone, textual content, and facial expressions are combined, emotion recognition accuracy increases significantly. In real-world applications, data sources may suffer from missing data, noise, or distortions. In such situations, multimodal fusion enables the system to make decisions without depending on a single modality. For instance, in autonomous driving, when camera-based perception becomes insufficient in dark environments, LiDAR or radar data can be used to maintain environmental perception. Thus, performance degradation due to data loss can be prevented.

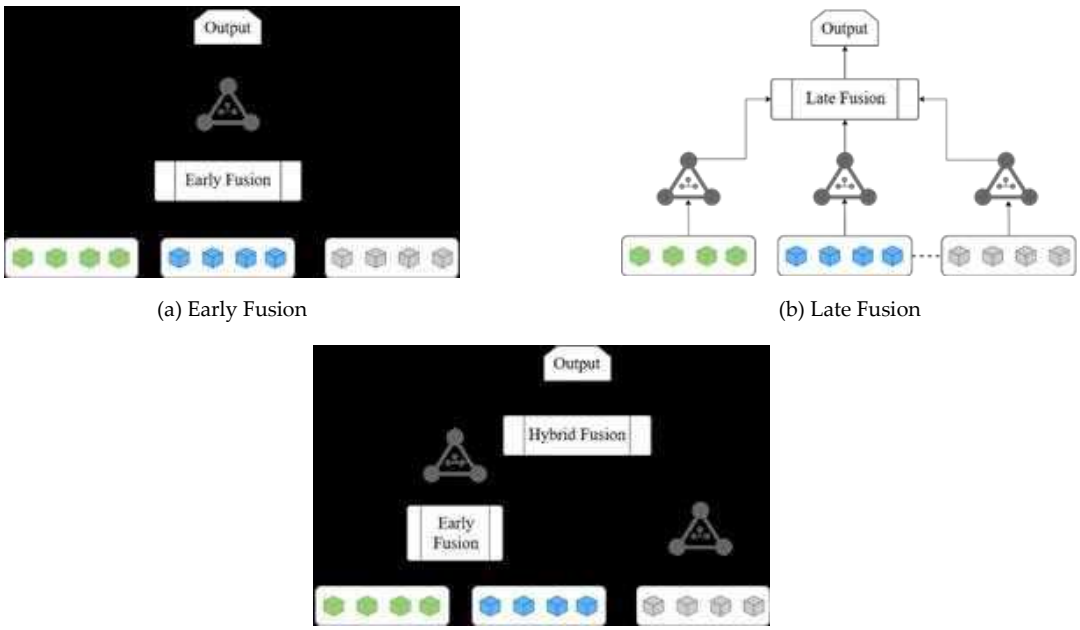
Fusion is typically a preparatory stage preceding the model's decision-making mechanism, and the employed methods are classified according to the stage at which the information is integrated: Early (feature-level), Late (decision-level), and Hybrid (Intermediate) fusion, as illustrated in Figure 3 [7]. In early fusion, integration is performed by concatenating modality-specific feature representations. The fused representations are then passed through a model assumed to be suitable for all modalities, and the model is trained to learn the relationships between low-level feature representations [97]. Early fusion at the initial stages allows better capture of relationships among feature vectors, which positively impacts model performance [57]. In contrast, while the fusion of diverse modalities enables enriched data representations in the initial stages, the resulting features may suffer from inconsistencies in scale and structure owing to the absence of homogeneity and standard dimensionality, potentially causing data-induced errors during inference [56].

In late fusion, features extracted from modalities are sent to modality-specific models and processed separately. Subsequently, the model outputs are combined using methods such as max-fusion [98], average fusion [99], low-rank fusion [100], and majority vote [101]. When input modalities are uncorrelated and exhibit significant differences in sampling rates or dimensionality, late fusion becomes more feasible, as it allows for independent feature extraction and avoids the complexity of joint optimization across unrelated modalities, including the integration of error losses [5]. Despite the use of certain fusion techniques to optimize results, the independent model outputs from each modality can

negatively affect the overall performance of the multimodal structure [56]. Therefore, various machine learning and deep learning methods are employed to optimize the fusion process [61].

The simple concatenation of modality representations, whether in early or late fusion, is sometimes insufficient to achieve high accuracy. To leverage the strengths of both early and late fusion, hybrid (intermediate) fusion combines them concurrently. Hybrid fusion offers structural flexibility when modalities have very different structures and when pre-processing is needed before combination, thereby utilizing the advantages of both early and late fusion [28].

Structurally, each of these three fusion methods has its distinct strengths and weaknesses. While early fusion captures inter-modality correlations and feature relationships more effectively, late fusion can better address overfitting; however, its contextual adequacy is relatively limited due to the absence of simultaneous training across modalities. Late fusion is also a suitable option when modalities differ significantly in dimensionality and sampling rate. However, it is more sensitive to missing modality problems than early fusion. Hybrid fusion offers a structurally more flexible solution between early and late fusion; however, it often comes with considerably higher computational costs and increased learning complexity compared to other approaches [73].



(a) Early Fusion (b) Late Fusion

(c) Hybrid Fusion

Figure 3. Fig. Three types of multimodal fusion strategies. (a) Early fusion integrates features from different modalities at the input level, creating a combined representation for the model. (b) Late fusion processes modalities independently, combining the model outputs at the decision level. (c) Hybrid fusion combines early and late fusion techniques, integrating information at multiple levels within the architecture [73].

3.4. Translation

Multimodal translation is the conversion of data from a source modality to a target modality while preserving the underlying semantic meaning. Unlike traditional translation, which is limited to interlingual conversion, multimodal translation involves translation between disparate data types, such as text, images, audio signals, or motion data. The aim is to represent the content of the source modality within the target modality without loss of semantic meaning.

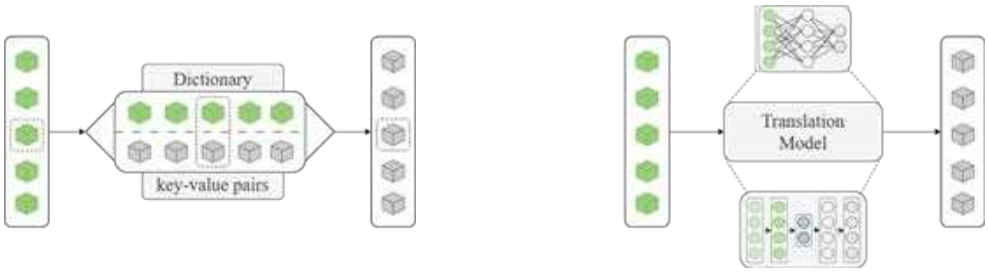
Multimodal translation is employed in a variety of tasks across different modality pairs. Translation between visual and textual modalities is fundamental to image captioning, visual question answering, and image synthesis. Similarly, speech-related tasks such as text-to-speech and speech-to-text rely on translation between textual and auditory modalities, while audiovisual speech recognition involves

mapping between visual and auditory inputs. Moreover, inter-modality translation can be leveraged during multimodal training to address missing modality, enabling the model to compensate for missing or noisy data.

In the translation, cross-modal mapping is required to establish semantic relationships correctly between modalities. The mapping approaches proposed are generally categorized into example-based and generative approaches, as illustrated in Figure 4 [7]. Example-based methods rely on dictionary lookups and translate inputs by retrieving their closest counterparts from a predefined dictionary. Although this search is constrained by the modality data available during training, the resulting translation is deterministic and has no inherent randomness. However, in the generative approach, instead of directly retrieving the output, a model learns to map from the source modality space to the target modality space, producing the translated output [64].

Generative models have a structure that produces random samples from the source modality to the target modality. In these models, both the form of the generated target modality and the evaluation criteria tend to exhibit considerable variability and uncertainty. Therefore, building a model that thoroughly understands both source and target modalities to perform accurate translation is considerably more challenging than example-based methods. However, despite these challenges, recent large-scale generative translation models have been widely adopted and demonstrate strong performance, producing high-quality outputs across various tasks [29].

Generative models are categorized into grammar-based, encoder-decoder, and continuous generation models [7]. Grammar-based models use predefined grammar rules and templates to impose constraints on the target data, enabling simpler and more consistent outputs. In encoder-decoder models, the source modality is encoded into a latent vector, which is then decoded to generate the target modality. Continuous generation models are used for translating sequential data that cannot be translated in a single step. These models generate outputs at each time step and are particularly well-suited for sequence-to-sequence translation tasks, such as text-to-speech synthesis [64].



(a) Example-based translation (b) Generative translation

Figure 4. Two types of multimodal translation methodologies. (a) Example-based translation directly retrieves a corresponding target from a predefined dictionary of source-target pairs when given a source instance. (b) Generative translation employs a two-stage process: first, a translation model is trained using a dictionary of paired examples, and subsequently, this trained model synthesizes the target modality from a given source input [7].

3.5. Missing Modality

Multimodal learning has emerged as a powerful paradigm that enables the integration of information from diverse data sources to enhance learning performance and generalization. Although these systems offer the potential to construct rich and unified representations, one of the most persistent challenges in practice is the missing modality problem. Contrary to the ideal conditions assumed in theoretical models, real-world multimodal datasets frequently suffer from missing or corrupted modality data due to technical limitations in data collection, sensor malfunctions, privacy concerns, or institutional restrictions. Accordingly, the presence of missing or corrupted modalities during training necessitates the development of robust strategies to sustain effective model learning, minimize adverse effects on model performance, and bridge the gap between theoretical advances and real-world applications in multimodal learning.

In real-world multimodal systems, data completeness cannot always be guaranteed, and different missing-modality scenarios may arise, each posing unique challenges for model design and performance. As seen in Figure 5, these scenarios can be categorized into full-modality, noisy-modality, and missing-modality. The full-modality case represents the ideal condition where all data streams from different modalities are available and intact. In the noisy-modality setting, although modality data is available, it is often corrupted or degraded, which may impair the learning process. In the most severe case, the missing-modality setting, data from one or more modalities is entirely absent. Both missing and noisy modality scenarios necessitate the development of robust strategies in multimodal learning to ensure reliable model performance in the presence of such imperfections or data loss [30].

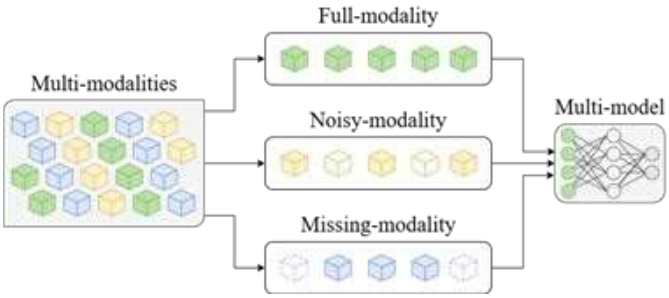


Figure 5. Missing modality scenarios. Full-modality, representing the ideal case where all data streams are complete and intact. Noisy-modality, depicting a situation where data from one or more modalities are present but corrupted or contain imperfections. Missing-modality, where specific data instances are entirely absent [30].

To address the missing modality, several models have adopted strategies based on generative approaches and transfer learning. In generative approaches, the missing modality is reconstructed during training by leveraging representations derived from the existing modalities. Conversely, transfer learning utilizes an auxiliary dataset that does not suffer from missing modality. This dataset enables the learning of inter-modality knowledge, which is then used to estimate the missing target modality in the primary dataset [67].

Wu et al. [30] proposed a taxonomy that categorizes methods for addressing missing modalities into modality-level, representation-level, architecture-level, and decision-level methods, as illustrated in Figure 6. In this taxonomy, methods at the modality level address missing modality by applying various imputation strategies directly at the data level. These methods include imputing zeros or random values for missing values, inserting statistical estimates such as class-wise means, randomly selecting a sample, using samples retrieved via nearest-neighbor algorithms, or synthesizing the missing modality using generative deep learning models that exploit inter-modality correlations.

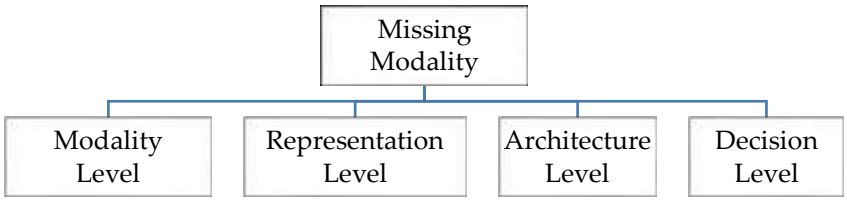


Figure 6. Addressing the missing modality at four stages within multimodal learning. (a) Data-level approaches aim to directly address missing modality at the input stage by reconstructing or providing imputations. (b) Representation-level approaches aim to address missing modality by manipulating modality representations, leveraging their mutual relationships and complementary aspects. (c) Architecture-level approaches address missing modality by leveraging adaptive architectural designs and strategies during model development. (d) Decision-level aims to reduce the effects of missing modality by strategically planning and integrating the contributions of different models or components, particularly at the decision-making stage [30].

Representation-level methods handle missing modality at the representation learning phase. These methods involve imposing certain constraints between modality representations using coordinated representation to make learned representations semantically consistent, creating a unified representation

by combining existing representations through various arithmetic operations, using the average of existing representations in place of the missing data representation, generating missing modality data from an existing modality representation through cross-modal mapping via a generative model, or reconstructing the missing modality by decoding the feature representations extracted by modality-specific encoders.

Architecture-level methods address the missing modality in the model's architectural design. These methods encompass fusing all representations after separately computing attention for existing modalities, masking missing modalities after capturing inter-modality dependencies using masked-attention, replacing the missing modality with special masked tokens in Transformer architecture, employing knowledge distillation models that reconstruct missing modality in the student model using a teacher model with complete modality access, predicting missing modality by propagating modalities through a graph neural network, and adapting the missing modality from other modalities leveraging the rich contextual understanding and generalization capabilities of multimodal large language models.

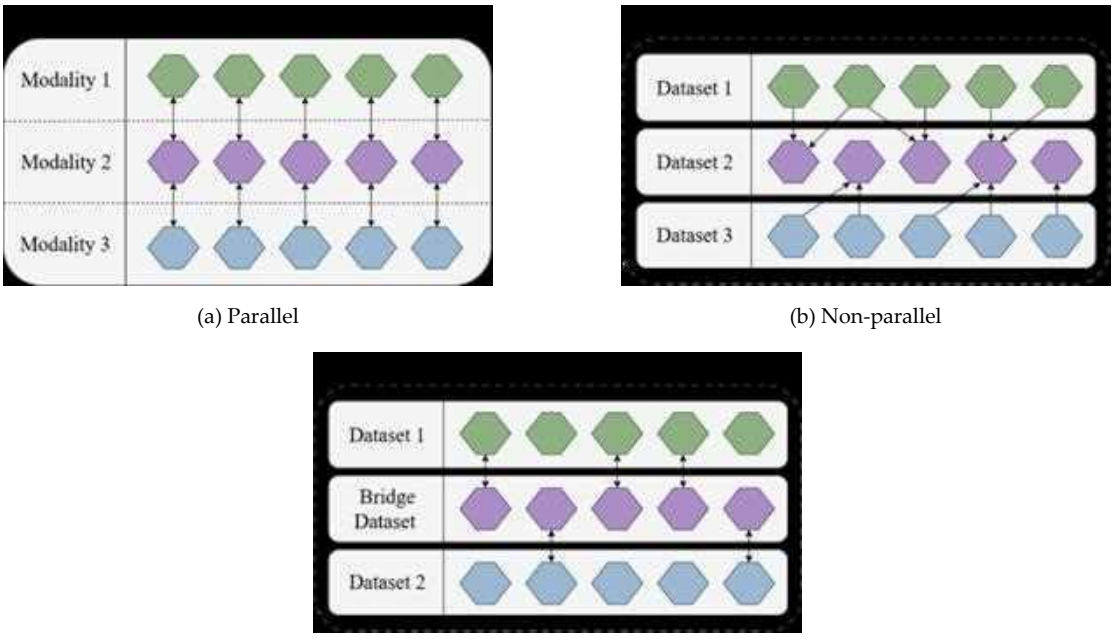
Decision-level methods aim to resolve the missing modality problem at the model's prediction stage. These methods comprise aggregating predictions from multiple models via ensemble learning using various arithmetic operations, compensating for missing modality via task-specific models built from suitable combinations of available modalities, mitigating missing modality by selectively utilizing specific modalities, and a system that routes instructions to relevant sub-modules via a multitasking LLM architecture.

3.6. Co-learning

Multimodal learning is an approach designed to achieve richer and more meaningful representation learning by processing multiple modalities. In such systems, integrating diverse modalities aims to enhance the model's performance at the decision-making or task-prediction level, thereby improving accuracy and generalizability. Although the fusion of different modalities significantly increases the model's learning capacity, ensuring a consistent and reliable data flow in real-world applications remains a major challenge. Various factors, such as missing or noisy data, weak signals, or mislabeled training samples, can negatively impact the performance of multimodal models, thereby limiting their capacity to acquire comprehensive, contextually reliable knowledge representations, which are essential for effective multimodal learning. To address these issues, co-learning extends beyond the conventional fusion of modalities by promoting interactive learning and enabling the transfer of knowledge or representational capacity across modalities. Specifically, co-learning facilitates the knowledge transfer from a modality with rich data and well-structured representations to another that suffers from data scarcity or degradation. Thus, modalities with limited knowledge can leverage the complementary strengths of other, more informative modalities, leading to improved accuracy and generalization through cross-modal knowledge transfer and enabling an integrative learning process that combines intra- and inter-modality knowledge.

Co-learning enables each modality to preserve its modality-specific features while enriching its semantic representations through complementary interactions across modalities. Accordingly, the primary objective of co-learning is to optimize knowledge transfer between different modalities and enhance the model's robustness and efficiency, particularly under adverse real-world conditions. Co-learning becomes especially valuable in scenarios involving missing, noisy, or limited modalities, as it enables the model to compensate for deficiencies by leveraging richer information from complementary modalities. For instance, in low-light environments where RGB camera data becomes unreliable for object detection, integrating complementary modalities, such as thermal or LiDAR sensors, can significantly enhance detection accuracy. Similarly, in acoustically noisy settings, visual cues like the speaker’s lip movements can be incorporated to improve the robustness of speech transcription. These scenarios illustrate inter-modality co-learning, where information from more reliable modalities compensates for the limitations of others, thereby enhancing overall model performance.

Baltrusaitis et al. [7] classified co-learning methods based on data parallelism into parallel, non-parallel, and hybrid co-learning, as illustrated in Figure 7. Parallel co-learning involves modalities that are directly aligned, such as speech audio and the corresponding speaker's video, or an image and its caption, all originating from the same source. Non-parallel co-learning refers to modalities that lack direct alignment but overlap at a more general level. For example, textual descriptions of video scenes may only loosely correspond to visual content in certain segments, without a strict one-to-one mapping. Hybrid co-learning connects two non-parallel modalities through a shared intermediary modality. A typical example is machine translation, where different languages are aligned using a shared pivot language to bridge the modalities.



(a) Parallel (b) Non-parallel

(c) Hybrid

Figure 7. Co-learning approaches based on data parallelism. (a) The parallel approach refers to the situation where modalities from the same dataset are in a direct mutual relationship; in this approach, there is a one-to-one correspondence between different modalities for each data instance. (b) Non-parallel approach defines the situation where modalities from different datasets are used; there is no direct instance-based correspondence between these modalities, but an overlap is ensured in terms of general categories or concepts. (c) The hybrid approach refers to the situation where the connection between the samples is established through a third modality or dataset, which serves as a bridging data source [7].

Rahate et al. [31] addressed multimodal co-learning methods from multiple methodological perspectives and specific scenarios, and proposed a comprehensive taxonomy categorizing co-learning approaches based on factors such as the presence of missing or noisy modality, data parallelism, modality annotation, domain adaptation, and concerns related to interpretability and fairness. Under the presence of the modality category, challenges arising from fully or partly missing modalities during training or inference are addressed. These challenges are typically mitigated through knowledge transfer mechanisms across modalities using methods such as co-training, knowledge distillation, autoencoders, multimodal embeddings, and GANs. Data parallelism, where co-learning is classified as parallel, non-parallel, or hybrid depending on the alignment of modalities, as typically proposed in the literature. Representative co-learning techniques include encoder–decoder architectures with attention, contrastive learning, and teacher–student frameworks based on data parallelism. Noisy modality, which covers challenges posed by label noise or data noise within modalities.

Co-learning strategies to alleviate the effects of noisy modality comprise methods such as co-teaching, graph-based models, GANs, adversarial learning, and meta-learning. Modality annotation encompasses co-learning approaches at different levels of supervision, ranging from fully supervised to unsupervised,

depending on the availability of annotations. Techniques such as multi-view learning, alignment frameworks, and multiple instance learning are employed to mitigate the adverse effects of limited data annotation. Domain adaptation, which considers both domain adaptation and domain generalization under homogeneous or heterogeneous settings. To support learning across different domains, co-learning utilizes methods such as transfer learning, multimodal embeddings, and disentanglement strategies. Finally, interpretability and fairness emphasize the need for models to be explainable and unbiased. To improve model transparency and fairness, co-learning approaches include multimodal factorization, counterfactual analysis, and bias detection tools. In conclusion, the proposed taxonomy, grounded in the principle of knowledge transfer between modalities, provides a structured bridge between the various challenges in multimodal settings and corresponding co-learning methods.

4. MULTIMODAL APPLICATIONS

In recent years, advancements in artificial intelligence and the increasing capability to process large-scale data have facilitated the development of multimodal systems that can simultaneously integrate and analyze diverse data sources. By mirroring human perception in interpreting and interacting with the external world, multimodal applications aim to construct more comprehensive and generalizable models by jointly processing heterogeneous modalities such as images, audio, text, and sensor data. By leveraging the complementary and reinforcing characteristics of information provided by each modality, these systems effectively reduce the ambiguities and limitations inherent in unimodal approaches, thereby enabling more robust, accurate, and context-aware inferences.

While multimodal applications have been developed for a wide range of tasks across various domains, they have become prominent in areas such as autonomous driving, robotics, healthcare, remote sensing, and security systems. For instance, in autonomous driving, environmental perception is significantly enhanced by simultaneously using RGB cameras, LiDAR, radar, map data, and various sensors, enabling the development of more stable systems for diverse autonomous driving tasks, such as lane tracking, object detection, and motion planning. In robotics, advanced models designed for complex physical tasks leverage the integration of linguistic and sensory data to enhance system autonomy and adaptability, thereby improving perception, decision-making, and task execution. In healthcare, integrating MRI, EEG, PET, and clinical data enables the development of systems that accelerate diagnostics and improve clinical decision-making. In remote sensing, the fusion of hyperspectral imagery, thermal data, and a range of sensor outputs facilitates satellite-based semantic mapping and the monitoring of environmental changes over time. In security systems, integrating network traffic data with visual, auditory, and sensor inputs enables the construction of intelligent surveillance systems that significantly improve threat and anomaly detection capabilities.

In the following sections, various proposed multimodal applications across key domains, including autonomous driving, robotic systems, healthcare, remote sensing, and security systems, are presented, along with corresponding multimodal datasets and the modality types specific to each domain.

4.1. Autonomous Driving

With the rapid advancement of autonomous vehicle technologies, multimodal perception systems have emerged as essential components for enabling vehicles to accurately interpret their surroundings and make safe driving decisions. To navigate safely in complex and dynamic traffic environments, autonomous vehicles must precisely detect and understand objects, pedestrians, other vehicles, and road conditions. Addressing these challenges requires integrating diverse sensors with complementary characteristics, effectively overcoming the limitations of single-sensor modalities.

Among the most commonly used modalities in autonomous vehicles are RGB or thermal camera images, LiDAR scans, radar data, GPS, IMU, and various ultrasonic sensor inputs. While cameras provide high-resolution visual information by capturing color, texture, and semantic features of objects, LiDAR sensors determine the precise locations and dimensions of objects by generating 3D depth information

and point clouds. Radar sensors, on the other hand, can operate effectively under adverse weather conditions and directly measure the velocity of moving objects.

The fusion of these diverse modalities creates a more robust and reliable perception system by leveraging the complementary strengths of each sensor while compensating for their individual limitations. Vora et al. [102] proposed an approach called PointPainting, which overlays LiDAR-generated point clouds with image-based semantic segmentation outputs to enhance 3D object detection, achieving successful results on the KITTI [103] and nuScenes [104] datasets.

Similarly, using a CNN-based method, Schlosser et al. [105] combined LiDAR and camera data for pedestrian detection creating a 6-channel integration that combines RGB image features with depth data from LiDAR sensors. The proposed model significantly improved pedestrian detection performance in complex urban environments, particularly on the KITTI dataset.

Hwang et al. [106] introduced a novel approach based on multimodal large language models (MLLMs) for autonomous driving, built upon Google's Gemini. By jointly processing camera images and linguistic data, their model demonstrated effective capabilities in driving planning, scene understanding, and spatial reasoning. RadarNet [107] fused LiDAR and radar sensor data using early fusion and attention-based late fusion mechanisms to improve the detection of dynamic and long-range objects. The proposed model achieved successful results in detecting distant objects and perceiving dynamic objects on nuScenes [104] and other datasets.

Cho et al. [108] proposed a real-time multi-sensor fusion framework named EMMA, which integrates LiDAR, radar, and camera data to enhance the detection and tracking of moving objects in urban driving scenarios. Evaluations on the nuScenes [104] and WOMD [109] datasets validated the model's effectiveness in dynamic object detection and tracking.

4.2. Robotic Systems

Robotic systems are evolving from operating in controlled industrial environments, where machines merely execute pre-programmed tasks, toward more advanced systems capable of interacting with dynamic and uncertain real-world settings and making autonomous decisions. At the heart of this transformation lies the ability of robots to perceive their surroundings comprehensively, interpret these perceptions, and act accordingly. Achieving human-like perception and enabling robots to interact effectively with their environments and perform complex tasks requires the concurrent processing of visual, auditory, textual, and physical data. By integrating these multimodal inputs, robotic systems are increasingly able to analyze visual scenes for object recognition, comprehend spoken instructions, and synthesize this information to execute more sophisticated behaviors.

In recent years, advancements in large language models have accelerated the development of general-purpose multimodal robotic systems based on LLMs. These models facilitate the integrated processing of visual, linguistic, and action-related information, significantly enhancing robots' embodied reasoning, complex task planning, and environmental interaction capabilities. Google's PaLM-E [110], RT-2 [111], and Gemini Robotics [112] are pioneering examples of general-purpose multimodal robotic models designed for embodied reasoning and tasks that combine vision and language. PaLM-E, built upon the PaLM [113] language model, integrates visual, textual, and perceived physical data from the scene to construct multimodal sentences, thereby enhancing the robot's environmental perception and achieving successful results in textual and visual mobile manipulation tasks. PaLM-E demonstrated strong performance on the OK-VQA [114] dataset that evaluates the ability to answer visual questions that require cultural knowledge and reasoning. Unlike PaLM-E, the RT-2 model represented actions as text tokens, allowing both natural language responses and robotic actions to be expressed in the same format. Gemini Robotics, based on Gemini 2.0, is a general-purpose Vision-Language-Action (VLA) model that enables training and controlling robots through visual, linguistic, and action-related information, representing a significant step towards the development of multi-purpose robots in real-world settings.

4.3. Healthcare

In recent years, as AI research in healthcare has advanced rapidly, multimodal applications have become increasingly significant in medical diagnosis and treatment. Especially, with the widespread use of deep learning models and the advancement of medical imaging technologies, more comprehensive and consistent multimodal systems have been designed by integrating visual, physiological, and clinical data to enable early detection and treatment of diseases. Traditional medical models often focus on a single modality; however, the complex nature of diseases and variations among individuals often require integrating multiple data sources.

Since each modality captures different aspects of a disease, multimodal approaches allow for more comprehensive and in-depth analysis by jointly evaluating heterogeneous data sources such as various imaging techniques (e.g., MRI, CT, PET, EEG, X-ray, and ultrasound), clinical data, electronic health records, patient symptoms, genomic information, and diverse physiological signals. This integrated and multimodal perspective helps build a holistic patient profile and enhances diagnostic accuracy.

Dai et al. [16] proposed a hybrid 3D medical image classification model that integrates 2D and 3D convolutional neural networks (CNNs) through a reciprocal attention mechanism, leveraging multiple MRI modalities to construct richer representations for medical diagnosis. The developed model achieved high classification performance on the MRNet [115] and PROSTATEx [116] datasets.

Kumar et al. [117] introduced a Transformer-based multimodal framework for tuberculosis detection. This model, trained on a dataset comprising X-ray images and clinical data such as patient demographics, laboratory tests, and clinical symptoms, used a cross-modal Transformer fusion architecture and achieved high accuracy in tuberculosis diagnosis, yielding faster, more effective results on heterogeneous multimodal data compared to traditional methods.

In the context of Parkinson's disease diagnosis, Alrawis et al. [118] proposed a model that integrates EEG signals and MRI images, where feature matrices extracted via wavelet transforms and fMRI were combined using principal component analysis (PCA), followed by classification with LightGBM [119]. The results, which achieved higher accuracy than those of single-modality models, revealed that the multimodal approach holds strong potential for diagnosing Parkinson's disease. Abdelaziz et al. [15] proposed a CNN and convolutional autoencoder-based model that fuses MRI and PET scans to identify pathological regions associated with Alzheimer's disease. The model achieved strong diagnostic performance using the ADNI [120] dataset, supporting its effectiveness in brain disease detection.

4.4. Remote Sensing

Remote sensing is a crucial field of observation that enables the monitoring and analysis of large geographical areas by collecting physical data of the Earth's surface from space or at high altitudes. Remote sensing systems are employed in a wide range of critical applications, including environmental monitoring, natural disaster forecasting, agricultural analysis, urban planning, and climate change studies. To address the limitations of traditional systems that rely on single-modality data and often provide restricted information, multimodal systems have gained increasing prominence by integrating data from multiple sources to enable more comprehensive and accurate inferences.

With the recent advances in deep learning, multimodal remote sensing systems that incorporate optical and hyperspectral imagery, LiDAR and SAR scans, and other sensor data offer more detailed and accurate Earth observations, as each sensor captures different physical properties. The integration of these sensor modalities plays a pivotal role in diverse applications, including land analysis and classification, forest monitoring, agricultural yield prediction, settlement mapping, urban planning, natural disaster assessment, and climate change monitoring.

Cui et al. [121] proposed the CMIM-Net architecture, which can match between infrared and RGB images. To ensure consistent and reliable matching across modalities, the model jointly learns modality-specific and modality-invariant feature representations, achieving strong performance in both near-field and remote sensing tasks. Dong et al. [122] introduced the ChangeCLIP network, a CLIP-based model for

detecting regional changes in remote sensing imagery. By leveraging region-specific image pairs and textual prompts generated from them using the CLIP model, the proposed model achieved high scores across several change-detection datasets.

Bandara et al. [123] introduced HyperTransformer, a Transformer-based architecture for pansharpening, which aims to reconstruct high-resolution hyperspectral images (HR-HSI) by integrating low-resolution hyperspectral (LR-HSI) data with high-resolution panchromatic (PAN) images. By leveraging attention mechanisms to capture inter-modality dependencies between PAN and HSI modalities, the model achieved promising results on widely used benchmark datasets. Huang et al. [124] presented GRRNet, an encoder-decoder architecture for building segmentation in urban areas that integrates high-resolution aerial imagery with LiDAR data. By jointly processing both visual and elevation data, the model achieved more precise building boundary detection compared to traditional approaches.

4.5. Security Systems

Security and surveillance systems are increasingly adopting multimodal approaches to ensure accurate detection of threats and anomalies. Traditional systems, which typically rely on a single data source, often fall short in identifying complex events or predicting potential threats. In contrast, multimodal security applications aim to overcome these limitations by integrating heterogeneous information sources such as video streams, audio signals, system logs, biometric data, and various sensor inputs. This integration enables a more contextual understanding of events, leading to enhanced detection accuracy and more reliable outcomes in complex scenarios.

Wang et al. [125] addressed network security and real-time threat detection in distributed systems by employing a multimodal large language model (LLM) that combines heterogeneous sources, such as network traffic, system logs, visual data, and sensor inputs, using weighted summation, while preserving data privacy via federated learning. Their approach achieved an accuracy of 96.4% on a distributed dataset derived from 10 TB of network traffic, significantly outperforming traditional models. In conventional surveillance systems, which often rely on visual modality, detecting complex behaviors, such as aggression, remains challenging. As a solution,

Jaafar et al. [126] proposed a multimodal deep learning architecture that effectively detects aggression in surveillance systems by combining audio, video, and textual data. In the study, comparative analysis of different fusion strategies demonstrated that integrating multiple modalities led to more accurate and reliable detection.

In the context of malware detection, Ismail et al. [127] introduced the MIDALF architecture, which converts binary files into both grayscale images and audio signals. The model employs contrastive learning to extract malware-specific features from images, while a CNN learns malware waveforms from audio spectrograms. On the BODMA dataset, the proposed model achieved a classification accuracy of 99.7% between malicious and benign samples, outperforming several baseline methods.

5. MULTIMODAL DATASETS AND EVALUATION METRICS

5.1. Multimodal Datasets

Comprehensive datasets are essential for developing and evaluating multimodal applications, particularly for training, testing, and comparing architectures that integrate multiple data modalities. A wide range of multimodal datasets is available in the literature, each associated with specific application domains.

In autonomous driving, datasets such as KITTI [103], nuScenes [104], and WOD [128] provide synchronized data from multiple sources, including camera images, LiDAR scans, and GPS signals. This enables the development of more accurate and reliable systems for tasks such as object detection, route tracking, and motion planning. In robotics, datasets such as OK-VQA [114], MCube Lab [129], and Vision&Touch [130] offer diverse sensory inputs specific to robotic platforms. By integrating visual,

haptic, and linguistic data, these datasets support advancements in perception, physical interaction, and natural language communication for intelligent robotic systems. In healthcare, datasets such as MRNet [115], PROSTATEx [116], and ADNI [120] integrate various imaging modalities, including MRI, PET, and EEG, along with clinical data, holding significant potential for medical data analysis and improved diagnostic accuracy. In remote sensing, datasets such as SEN12MS [131], AIRS [132], and M4-SAR [133] combine SAR, optical, and multispectral imagery, enabling applications such as land classification, mapping, and remote object detection. In the field of security, datasets such as Kinetics [134], CASIA-SURF [135], and CUBRE [136] contribute to the development of more effective systems for anomaly detection, identity verification, and threat analysis. By concurrently using video, audio, text, and sensor data, these datasets enable more robust multimodal threat assessment frameworks.

The following table presents notable multimodal datasets across the fields of autonomous driving, robotic systems, healthcare, remote sensing, and security, emphasizing the modalities involved and their corresponding application areas.

Table 2. Multimodal datasets along with the integrated modalities and their respective application domains.

Dataset	Modalities	Application	Area
KITTI [103]	Camera, 3D-LiDAR, GPS, IMU data	Detection, tracking, prediction, segmentation, panoptic, and planning for autonomous driving.	Autonomous Driving
nuScenes [104]	Camera, LiDAR, radar, GPS, IMU data		
WOD [128], WOMD [137]	Camera, LiDAR, Map, and Object data	Self-driving, interactive motion forecasting.	
Argoverse [138], [139]	Camera, LiDAR, 6-DOF pose, HD map	Self-driving, scenarios, motion forecasting, and map change.	
ONCE [140]	Camera, LiDAR	Self-driving in diverse environments and millions of samples.	
OK-VQA [114]	Image, Text	Visual question answering (VQA) requires external world knowledge.	Robotic Systems
MCube Lab [129]	RGB-D, Mechanical sensors data	Planar robotic manipulation.	
Vision&Touch [130]	RGB, Mechanical sensors data	Real-world robot manipulation.	
S3E [141]	Camera, LiDAR, IMU, UWB, RTK, Motion data	Collaborative robotic systems.	
HARMONIC [142]	Camera, EMG, Eye Gaze, and Mechanical sensors data	Human-robot interaction.	
MHHRI [143]	Camera, Microphone, Depth, EDA, Temperature, 3-axis wrist acceleration	Human-robot interaction.	
EEG-ImageNet [144]	EEG, Image	Inferring visual perception from brain activity.	Healthcare
MRNet [115]	MRI (T1, T2)	Detection of general abnormalities and specific diagnoses on knee MRI exams.	
PROSTATEx [116]	MRI (T1, T2)	Classification of prostate lesions.	
ADNI [120]	MRI, PET, Clinical data	Alzheimer's disease detection.	
CLIPdb [145]	Multi-resource data (sequence, structure, metadata, etc.)	Mining RNA–protein binding motifs and interactions.	
MHEALTH [146]	EEG, Motion (Accelerometer, Magnetometer, Gyroscopes)	Health monitoring, human activity recognition.	
SEN12MS [131]	SAR, Multi-spectral image, MODIS land cover maps	Land cover mapping.	Remote Sensing
AIRS [132]	Infrared, Microwave, Other sensors data	Earth atmosphere observation.	
M4-SAR [133]	SAR and Optical data	Optical-SAR fusion in remote object detection.	
M3LEO [147]	SAR and Optical data	Earth terrain observation.	
GRACO [148]	Camera, LiDAR, IMU, GPS	Simultaneous localization and mapping (SLAM).	

Table 2. (Continued)

Dataset	Modalities	Application	Area
Kinetics [134]	Video, Optical flow	Human action recognition.	Security Systems
CASIA-SURF [135]	RGB, Depth, Infrared (IR)	Face anti-spoofing.	
CUBRE [136]	Activities of daily living (ADLs), User behavior, Network traffic, Energy consumption, Environmental sensors	Cyber–physical anomaly detection in smart homes.	
UCA [149]	Video, Text	Surveillance anomaly detection.	
SWaT [150]	Network traffic, Physical data (i.e., sensors and actuators)	Cyber-physical systems (CPS).	

5.2. Evaluation Metrics

Evaluating multimodal learning systems presents unique challenges compared to unimodal tasks, because models must be assessed not only by their final task performance but also by how effectively they integrate and align diverse modalities. Since multimodal systems are applied to a wide spectrum of tasks, ranging from classification and detection to retrieval, captioning, and generative modeling, no single metric can adequately capture overall performance. Instead, the choice of evaluation metrics is closely tied to the specific multimodal task and the characteristics of the data involved [8].

The main task families in multimodal learning include classification, detection, segmentation, retrieval, sequence generation, generative modeling, and clustering [68]. Classification tasks typically report accuracy, precision, recall, F1-score, and area under the ROC curve (AUROC) [68], [151]. Object detection and segmentation both rely on IoU-based overlap criteria but use them differently. In object detection, IoU is primarily used for matching predicted and ground-truth bounding boxes and for computing AP/mAP across predefined thresholds [20]. In segmentation, overlap is commonly evaluated at the pixel or region level using mean IoU (mIoU) and the Dice coefficient [61], [152]. Retrieval tasks commonly use ranking metrics like Recall@K and normalized discounted cumulative gain (nDCG) [63]. For vision-language generation, text-based metrics such as BLEU, ROUGE, METEOR, CIDEr, and SPICE are standard [68], increasingly complemented by learned similarity scores like CLIP-Score [79]. Generative multimodal models that synthesize media are assessed with distributional measures such as Fréchet Inception Distance (FID) and Inception Score (IS) [153]. Furthermore, specific domains employ specialized metrics, such as temporal consistency measures for video generation and mean opinion score (MOS) for audio synthesis [154].

In addition to these conventional task-level metrics, multimodal evaluation should also examine whether models effectively exploit complementary information across modalities rather than relying on a dominant single modality. Since integration quality is difficult to capture through a single task metric alone, ablation-based modality removal, missing-modality robustness tests, cross-modal consistency analyses, and alignment-oriented retrieval metrics are often used to provide more direct evidence of how well modalities are integrated [61], [73].

Beyond these task-specific scores, evaluating multimodal systems requires a broader perspective, including robustness to missing or corrupted modalities, probability calibration under distribution shifts, and fairness across demographic or domain-specific subgroups [84]. For many open-ended generation and reasoning tasks, automatic metrics also correlate imperfectly with human judgments, which motivates the inclusion of human evaluation protocols that assess fluency, consistency, and cross-modal faithfulness [62]. However, standardized benchmarks and shared evaluation suites that jointly assess these dimensions remain scarce, and many studies still focus on a single primary metric, which limits comparability across different approaches. Therefore, developing more holistic, multi-objective evaluation protocols and widely adopted benchmark collections represents an important direction for future multimodal research.

6. SUMMARY OF CHALLENGES AND FUTURE RESEARCH DIRECTIONS

This section summarizes the main challenges in multimodal learning and outlines possible future research directions. These challenges encompass several critical stages of the multimodal learning pipeline, ranging from developing effective representations for heterogeneous data modalities to aligning them in a unified learning space. The following table presents a structured overview of these key challenges, the corresponding solution approaches currently employed in the literature, and potential future directions.

Table 3. Multimodal learning: technical challenges and feature research directions.

Challenge	Description	Research Directions
Representation	Effectively representing modality-specific information.	Self-supervised learning, contrastive learning, modality-aware encoder architectures, task-specific representation learning.
Alignment	Semantic matching between modalities.	Latent space alignment, semantic-preserving alignment, cross-modal attention, and joint embedding methods.
Fusion	Combining different modalities to make joint decisions.	Adaptive fusion, transformer-based multi-head attention, graph fusion, and dynamic weighting.
Translation	Translating from one modality to another without loss of meaning.	Encoder-decoder structures, modality-to-modality GANs, VAE-based translation systems, quality-aware translation models.
Missing Modality	Preventing missing modality data from degrading model performance.	Masked attention, modality hallucination, knowledge distillation, teacher-student models, cross-modal imputation.
Co-Learning	Inter-modality information transfer and joint learning.	Parallel-nonparallel co-learning architectures, curriculum-based co-training, unsupervised co-learning, and shared-private frameworks.

Beyond the specific technical solutions for individual challenges outlined in Table 3, several broader, cross-cutting research avenues require further investigation to advance the field beyond its current limitations. A primary direction involves the evolution of unified and efficient architectures. Current systems predominantly employ modality-specific encoders with either late fusion or cross-modal attention mechanisms, both of which can limit scalability and parameter sharing across modalities. Future research is expected to gravitate toward "one-for-all" foundation models capable of processing arbitrary modalities within a single, shared parameter space. However, the escalating computational cost of such models necessitates a focus on parameter-efficient fine-tuning (PEFT) strategies, in which most pre-trained parameters are kept frozen and only small task-specific modules are updated, and sparse architectures like Mixture-of-Experts (MoE), enabling massive pre-trained models to adapt to downstream multimodal tasks with minimal resource overhead.

Another critical avenue lies in enhancing the cognitive capabilities of multimodal systems through reasoning, causality, and interpretability. Most existing models rely on statistical correlations, making them susceptible to learning spurious biases and hallucinations—such as ignoring visual context in favor of language priors. Future studies should aim to integrate causal inference and compositional reasoning mechanisms into multimodal fusion, allowing models to distinguish true cause-and-effect relationships from mere associations, although this remains a challenging and exploratory frontier.

Finally, reducing the reliance on large-scale annotated datasets remains a persistent goal. Consequently, advanced self-supervised and unsupervised learning paradigms will play a pivotal role. Developing objectives that effectively leverage the vast amounts of unlabeled multimodal data—moving beyond simple contrastive pairs to dense alignment, masked signal modeling, and generative pre-training—will be key to building robust systems. Furthermore, as these models scale, addressing safety,

alignment, and robustness against adversarial attacks and bias becomes an indispensable requirement for trustworthy multimodal AI.

7. CONCLUSION

This review has provided a comprehensive overview of the increasingly prominent field of multimodal learning by exploring its conceptual foundations, key challenges, proposed solution strategies, practical application domains, and multimodal datasets. In particular, it has addressed fundamental aspects of multimodal learning, including the representation of heterogeneous modalities, semantic alignment, information fusion, cross-modal translation, handling missing modalities, and collaborative learning across different sources, along with core solution strategies to address these challenges. Furthermore, the study has outlined real-world application domains, including autonomous driving, robotics, healthcare, remote sensing, and security, and has presented commonly used multimodal datasets that support research and development in these areas.

Despite considerable progress, multimodal learning continues to confront unresolved technical and systemic challenges. From a technical perspective, future research is anticipated to prioritize the development of more expressive and modality-aware representations, the enhancement of semantic coherence in modality alignment, the design of flexible and adaptive fusion mechanisms, the construction of reliable cross-modal translation frameworks, and the development of robust models capable of handling missing modality scenarios. In addition, advanced co-learning strategies are expected to support further improvements in the field by enabling more effective cross-modal collaboration.

From a practical perspective, several critical systematic challenges in multimodal learning remain unresolved. Chief among these is the limited availability of well-annotated multimodal datasets, biases introduced during training, and the lack of transparency and interpretability in current models. Given that data plays a central role in multimodal systems, the difficulty of collecting high-quality labeled datasets, coupled with the need for continual learning after model deployment, necessitates the adoption of alternative training paradigms, such as few-shot, zero-shot, self-supervised, and unsupervised learning, alongside advanced co-learning strategies that enhance synergy across modalities. Addressing modality-specific biases and ensuring fairness and ethical integrity in model development are essential for building trustworthy systems. Additionally, beyond achieving high accuracy, it is also critical to enhance the transparency and interpretability of models, particularly in sensitive domains such as healthcare and law, thereby improving their explainability and clarifying their decision-making mechanisms. Lastly, the high computational cost and parameter complexity inherent in multimodal architectures continue to pose major scalability challenges in real-world applications. Consequently, future work should also prioritize the design of more efficient and scalable models to facilitate broader adoption of multimodal learning systems.

In conclusion, recent advances in multimodal learning represent a pivotal step toward the development of intelligent systems capable of perceiving and interacting with the world in a more human-like manner. The integration of heterogeneous data modalities has shown considerable promise in addressing complex tasks across a wide range of domains. This review aims to provide a foundation for future research by presenting a systematic and comprehensive overview of the core concept, key challenges, solution strategies, application domains, multimodal datasets, and future research directions in multimodal learning.

Declaration of Ethical Standards

The authors declare that they have carried out this completely original study by adhering to all ethical rules, including authorship, citation, and data reporting.

Credit Authorship Contribution Statement

The authors declare that their contributions to the work are equal.

Declaration of Competing Interest

The authors declare no conflicts of interest.

Declaration of Generative AI

The authors assert that they employed DeepL, Gemini, ChatGPT, and Grammarly for the purpose of English translation and refinement. Following the use of these tools, the authors meticulously examined and amended the work as deemed necessary, thereby assuming complete accountability for the content of the publication.

Funding / Acknowledgements

No funding is available for this research.

Data Availability

No data were generated or analyzed in this study.

REFERENCES

[1] P. P. Shinde and S. Shah, "A Review of Machine Learning and Deep Learning Applications," *Proceedings - 2018 4th International Conference on Computing, Communication Control and Automation, ICCUBEA 2018*, Jul. 2018, doi: 10.1109/ICCUBEA.2018.8697857.

[2] S. Dong, P. Wang, and K. Abbas, "A survey on deep learning and its applications," *Comput. Sci. Rev.*, vol. 40, p. 100379, May 2021, doi: 10.1016/J.COSREV.2021.100379.

[3] S. Sengupta *et al.*, "A review of deep learning with special emphasis on architectures, applications and recent trends," *Knowl. Based. Syst.*, vol. 194, p. 105596, Apr. 2020, doi: 10.1016/J.KNOSYS.2020.105596.

[4] J. Hestness *et al.*, "Deep Learning Scaling is Predictable, Empirically," Dec. 2017, Accessed: Mar. 06, 2025. [Online]. Available: https://arxiv.org/abs/1712.00409v1

[5] D. Ramachandram and G. W. Taylor, "Deep multimodal learning: A survey on recent advances and trends," *IEEE Signal Process. Mag.*, vol. 34, no. 6, pp. 96–108, Nov. 2017, doi: 10.1109/MSP.2017.2738401.

[6] X. Wang, Y. Han, V. C. M. Leung, D. Niyato, X. Yan, and X. Chen, "Convergence of Edge Computing and Deep Learning: A Comprehensive Survey," *IEEE Communications Surveys and Tutorials*, vol. 22, no. 2, pp. 869–904, Apr. 2020, doi: 10.1109/COMST.2020.2970550.

[7] T. Baltrusaitis, C. Ahuja, and L. P. Morency, "Multimodal Machine Learning: A Survey and Taxonomy," *IEEE Trans. Pattern Anal. Mach. Intell.*, vol. 41, no. 2, pp. 423–443, Feb. 2019, doi: 10.1109/TPAMI.2018.2798607.

[8] S. Jabeen, X. Li, M. S. Amin, O. Bourahla, S. Li, and A. Jabbar, "A Review on Methods and Applications in Multimodal Deep Learning," *ACM Transactions on Multimedia Computing, Communications, and Applications*, vol. 19, no. 2s, pp. 1–41, Jun. 2023, doi: 10.1145/3545572.

[9] A. Radford *et al.*, "Learning Transferable Visual Models From Natural Language Supervision," *Proc. Mach. Learn. Res.*, vol. 139, pp. 8748–8763, Feb. 2021, Accessed: Mar. 06, 2025. [Online]. Available: https://arxiv.org/abs/2103.00020v1

[10] A. Singh *et al.*, "FLAVA: A Foundational Language and Vision Alignment Model," *CVPR 2022*. doi: 10.1109/CVPR52688.2022.01519.

[11] R. Rombach, A. Blattmann, D. Lorenz, P. Esser, and B. Ommer, "High-Resolution Image Synthesis With Latent Diffusion Models," 2022. doi: 10.48550/ARXIV.2204.11824.

[12] H. D. Le, G. S. Lee, S. H. Kim, S. Kim, and H. J. Yang, "Multi-Label Multimodal Emotion Recognition With Transformer-Based Fusion and Emotion-Level Representation Learning," *IEEE Access*, vol. 11, pp. 14742–14751, 2023, doi: 10.1109/ACCESS.2023.3244390.

[13] P. Tzirakis, J. Chen, S. Zafeiriou, and B. Schuller, "End-to-end multimodal affect recognition in real-world environments," *Information Fusion*, vol. 68, pp. 46–53, Apr. 2021, doi: 10.1016/J.INFFUS.2020.10.011.

[14] S. Poria, E. Cambria, R. Bajpai, and A. Hussain, "A review of affective computing: From unimodal analysis to multimodal fusion," *Information Fusion*, vol. 37, pp. 98–125, Sep. 2017, doi: 10.1016/J.INFFUS.2017.02.003.

[15] M. Abdelaziz, T. Wang, and A. Elazab, "Fusing Multimodal and Anatomical Volumes of Interest Features Using Convolutional Auto-Encoder and Convolutional Neural Networks for Alzheimer's Disease Diagnosis," *Front. Aging Neurosci.*, vol. 14, p. 812870, Apr. 2022, doi: 10.3389/FNAGI.2022.812870.

[16] Y. Dai, Y. Gao, F. Liu, and J. Fu, "Mutual Attention-based Hybrid Dimensional Network for Multimodal Imaging Computer-aided Diagnosis," Jan. 2022, Accessed: Mar. 06, 2025. [Online]. Available: https://arxiv.org/abs/2201.09421v1

[17] Q. Zhou, S. Ye, M. Wen, Z. Huang, M. Ding, and X. Zhang, "Multi-modal medical image fusion based on densely-connected high-resolution CNN and hybrid transformer," *Neural Comput. Appl.*, vol. 34, no. 24, pp. 21741–21761, Dec. 2022, doi: 10.1007/S00521-022-07635-1.

[18] J. Zhou *et al.*, "Cohesive Multi-Modality Feature Learning and Fusion for COVID-19 Patient Severity Prediction," *IEEE Transactions on Circuits and Systems for Video Technology*, vol. 32, no. 5, pp. 2535–2549, May 2022, doi: 10.1109/TCSVT.2021.3063952.

[19] K. Mahato, T. Saha, S. Ding, S. S. Sandhu, A. Y. Chang, and J. Wang, "Hybrid multimodal wearable sensors for comprehensive health monitoring," *Nature Electronics 2024 7:9*, vol. 7, no. 9, pp. 735–750, Sep. 2024, doi: 10.1038/s41928-024-01247-4.

[20] D. Feng *et al.*, "Deep Multi-Modal Object Detection and Semantic Segmentation for Autonomous Driving: Datasets, Methods, and Challenges," *IEEE Transactions on Intelligent Transportation Systems*, vol. 22, no. 3, pp. 1341–1360, Mar. 2021, doi: 10.1109/TITS.2020.2972974.

[21] M. Person, M. Jensen, A. O. Smith, and H. Gutierrez, "Multimodal Fusion Object Detection System for Autonomous Vehicles," *Journal of Dynamic Systems, Measurement and Control, Transactions of the ASME*, vol. 141, no. 7, Jul. 2019, doi: 10.1115/1.4043222/726548.

[22] P. Zhang, X. Li, X. Lin, and L. He, "A New Literature Review of 3D Object Detection on Autonomous Driving," *Journal of Artificial Intelligence Research*, vol. 82, pp. 973–1015, Feb. 2025, doi: 10.1613/JAIR.1.15961.

[23] Y. Zheng, F. Liu, and H. P. Hsieh, "U-Air: When urban air quality inference meets big data," *Proceedings of the ACM SIGKDD International Conference on Knowledge Discovery and Data Mining*, vol. Part F128815, pp. 1436–1444, Aug. 2013, doi: 10.1145/2487575.2488188.

[24] X. Zhang *et al.*, "Multi-modal spatio-temporal meteorological forecasting with deep neural network," *ISPRS Journal of Photogrammetry and Remote Sensing*, vol. 188, pp. 380–393, Jun. 2022, doi: 10.1016/J.ISPRSJPRS.2022.03.007.

[25] G. M. Dimitri, "A Short Survey on Deep Learning for Multimodal Integration: Applications, Future Perspectives and Challenges," *Computers 2022, Vol. 11, Page 163*, vol. 11, no. 11, p. 163, Nov. 2022, doi: 10.3390/COMPUTERS11110163.

[26] M. A. Manzoor, S. Albarri, Z. Xian, Z. Meng, P. Nakov, and S. Liang, "Multimodality Representation Learning: A Survey on Evolution, Pretraining and Its Applications," *ACM Transactions on Multimedia Computing, Communications and Applications*, vol. 20, no. 3, Feb. 2023, doi: 10.1145/3617833.

[27] E. Warner *et al.*, "Multimodal Machine Learning in Image-Based and Clinical Biomedicine: Survey and Prospects," *Int. J. Comput. Vis.*, vol. 132, no. 9, pp. 3753–3769, Sep. 2024, doi: 10.1007/S11263-024-02032-8.

[28] T. Jiao, C. Guo, X. Feng, Y. Chen, and J. Song, "A Comprehensive Survey on Deep Learning Multi-Modal Fusion: Methods, Technologies and Applications," *Computers, Materials & Continua*, vol. 80, no. 1, pp. 1–35, Jul. 2024, doi: 10.32604/CMC.2024.053204.

[29] P. P. Liang, A. Zadeh, and L. P. Morency, "Foundations and Trends in Multimodal Machine Learning: Principles, Challenges, and Open Questions," *ACM Comput. Surv.*, vol. 56, no. 10, Sep. 2022, doi: 10.1145/3656580.

[30] R. Wu, H. Wang, H.-T. Chen, and G. Carneiro, "Deep Multimodal Learning with Missing Modality: A Survey," Sep. 2024, Accessed: Mar. 07, 2025. [Online]. Available: https://arxiv.org/abs/2409.07825v3

[31] A. Rahate, R. Walambe, S. Ramanna, and K. Kotecha, "Multimodal Co-learning: Challenges, applications with datasets, recent advances and future directions," *Information Fusion*, vol. 81, pp. 203–239, May 2022, doi: 10.1016/J.INFFUS.2021.12.003.

[32] A. Waqas *et al.*, "SELF-NORMALIZING FOUNDATION MODEL FOR ENHANCED MULTI-OMICS DATA ANALYSIS IN ONCOLOGY," 2024.

[33] A. Waqas, A. Tripathi, A. Mukund, P. Stewart, M. Naeini, and G. Rasool, "BIO24-031: Hierarchical Multimodal Learning on Pan-Squamous Cell Carcinomas for Improved Survival Outcomes," *Journal of the National Comprehensive Cancer Network*, vol. 22, no. 2.5, Apr. 2024, doi: 10.6004/JNCCN.2023.7137.

[34] Z. J. Cao and G. Gao, "Multi-omics single-cell data integration and regulatory inference with graph-linked embedding," *Nature Biotechnology 2022 40:10*, vol. 40, no. 10, pp. 1458–1466, May 2022, doi: 10.1038/s41587-022-01284-4.

[35] B. Salehi *et al.*, "Deep Learning on Multimodal Sensor Data at the Wireless Edge for Vehicular Network," *IEEE Trans. Veh. Technol.*, vol. 71, no. 7, pp. 7639–7655, Jul. 2022, doi: 10.1109/TVT.2022.3170733.

[36] M. Bijelic *et al.*, "Seeing through fog without seeing fog: Deep multimodal sensor fusion in unseen adverse weather," *Proceedings of the IEEE Computer Society Conference on Computer Vision and Pattern Recognition*, pp. 11679–11689, 2020, doi: 10.1109/CVPR42600.2020.01170.

[37] P. Hu *et al.*, "T-READi: Transformer-Powered Robust and Efficient Multimodal Inference for Autonomous Driving," *IEEE Trans. Mob. Comput.*, 2024, doi: 10.1109/TMC.2024.3462437.

[38] L. Zheng *et al.*, "RCFusion: Fusing 4-D Radar and Camera with Bird's-Eye View Features for 3-D Object Detection," *IEEE Trans. Instrum. Meas.*, vol. 72, 2023, doi: 10.1109/TIM.2023.3280525.

[39] D. Khan, M. Baek, M. Y. Kim, and D. Seog Han, "Multimodal Object Detection and Ranging Based on Camera and Lidar Sensor Fusion for Autonomous Driving," *APCC 2022 - 27th Asia-Pacific Conference on Communications: Creating Innovative Communication Technologies for Post-Pandemic Era*, pp. 342–343, 2022, doi: 10.1109/APCC55198.2022.9943618.

[40] X. Yun, Y. Sun, X. Yang, and N. Lu, "Discriminative Fusion Correlation Learning for Visible and Infrared Tracking," *Math. Probl. Eng.*, vol. 2019, no. 1, p. 2437521, Jan. 2019, doi: 10.1155/2019/2437521.

[41] S. Meng and Y. Liu, "Multimodal Feature Fusion YOLOv5 for RGB-T Object Detection," *Proceedings - 2022 Chinese Automation Congress, CAC 2022*, vol. 2022-January, pp. 2333–2338, 2022, doi: 10.1109/CAC57257.2022.10055263.

[42] M. Ehatisham-Ul-Haq *et al.*, "Robust Human Activity Recognition Using Multimodal Feature-Level Fusion," *IEEE Access*, vol. 7, pp. 60736–60751, 2019, doi: 10.1109/ACCESS.2019.2913393.

[43] J. Li, J. Li, X. Wang, X. Zhan, and Z. Zeng, "A Domain Generalization and Residual Network Based Emotion Recognition from Physiological Signals," *Cyborg and Bionic Systems*, Feb. 2023, doi: 10.34133/CBSYSTEMS.0074.

[44] Q. Li, Y. Liu, F. Yan, Q. Zhang, and C. Liu, "Emotion recognition based on multiple physiological signals," *Biomed. Signal Process. Control*, vol. 85, p. 104989, Aug. 2023, doi: 10.1016/J.BSPC.2023.104989.

[45] H. Liu, T. Fang, T. Zhou, and L. Wang, "Towards Robust Human-Robot Collaborative Manufacturing: Multimodal Fusion," *IEEE Access*, vol. 6, pp. 74762–74771, 2018, doi: 10.1109/ACCESS.2018.2884793.

[46] W. Wang, R. Li, Y. Chen, Y. Sun, and Y. Jia, "Predicting Human Intentions in Human-Robot Hand-Over Tasks Through Multimodal Learning," *IEEE Transactions on Automation Science and Engineering*, vol. 19, no. 3, pp. 2339–2353, Jul. 2022, doi: 10.1109/TASE.2021.3074873.

[47] C. E. Lee, J. Baek, J. Son, and Y. G. Ha, "Deep AI military staff: cooperative battlefield situation awareness for commander's decision making," *Journal of Supercomputing*, vol. 79, no. 6, pp. 6040–6069, Apr. 2023, doi: 10.1007/S11227-022-04882-W.

[48] W. Cao *et al.*, "A review on multimodal zero-shot learning," *Wiley Interdiscip. Rev. Data Min. Knowl. Discov.*, vol. 13, no. 2, p. e1488, Mar. 2023, doi: 10.1002/WIDM.1488.

[49] Z. Lin, S. Yu, Z. Kuang, D. Pathak, and D. Ramanan, "Multimodality Helps Unimodality: Cross-Modal Few-Shot Learning with Multimodal Models," pp. 19325–19337, Aug. 2023, doi: 10.1109/CVPR52729.2023.01852.

[50] L. A. Kumar, D. K. Renuka, S. L. Rose, and M. C. Shunmugapriya, "Attention based Multi Modal Learning for Audio Visual Speech Recognition," *AIST 2022 - 4th International Conference on Artificial Intelligence and Speech Technology*, 2022, doi: 10.1109/AIST55798.2022.10065019.

[51] Q. Song, B. Sun, and S. Li, "Multimodal Sparse Transformer Network for Audio-Visual Speech Recognition," *IEEE Trans. Neural Netw. Learn. Syst.*, vol. 34, no. 12, pp. 10028–10038, Dec. 2023, doi: 10.1109/TNNLS.2022.3163771.

[52] W. Guo, J. Wang, and S. Wang, "Deep Multimodal Representation Learning: A Survey," *IEEE Access*, vol. 7, pp. 63373–63394, 2019, doi: 10.1109/ACCESS.2019.2916887.

[53] C. Zhang, Z. Yang, X. He, and L. Deng, "Multimodal Intelligence: Representation Learning, Information Fusion, and Applications," *IEEE Journal on Selected Topics in Signal Processing*, vol. 14, no. 3, pp. 478–493, Mar. 2020, doi: 10.1109/JSTSP.2020.2987728.

[54] S. F. Zhang, J. H. Zhai, B. J. Xie, Y. Zhan, and X. Wang, "Multimodal Representation Learning: Advances, Trends and Challenges," *Proc. Int. Conf. Mach. Learn. Cybern.*, vol. 2019-July, Jul. 2019, doi: 10.1109/ICMLC48188.2019.8949228.

[55] A. Gaonkar, Y. Chukkapalli, P. J. Raman, S. Srikanth, and S. Gurugopinath, "A Comprehensive Survey on Multimodal Data Representation and Information Fusion Algorithms," *2021 International Conference on Intelligent Technologies, CONIT 2021*, Jun. 2021, doi: 10.1109/CONIT51480.2021.9498415.

[56] K. Bayoudh, R. Knani, F. Hamdaoui, and A. Mtibaa, "A survey on deep multimodal learning for computer vision: advances, trends, applications, and datasets," *The Visual Computer 2021 38:8*, vol. 38, no. 8, pp. 2939–2970, Jun. 2021, doi: 10.1007/S00371-021-02166-7.

[57] P. K. Atrey, M. A. Hossain, A. El Saddik, and M. S. Kankanhalli, "Multimodal fusion for multimedia analysis: A survey," *Multimed. Syst.*, vol. 16, no. 6, pp. 345–379, Nov. 2010, doi: 10.1007/S00530-010-0182-0.

[58] D. Lahat, T. Adali, and C. Jutten, "Multimodal Data Fusion: An Overview of Methods, Challenges, and Prospects," *Proceedings of the IEEE*, vol. 103, no. 9, pp. 1449–1477, Sep. 2015, doi: 10.1109/JPROC.2015.2460697.

[59] Y. Li, M. Yang, and Z. Zhang, "A Survey of Multi-View Representation Learning," *IEEE Trans. Knowl. Data Eng.*, vol. 31, no. 10, pp. 1863–1883, Oct. 2019, doi: 10.1109/TKDE.2018.2872063.

[60] J. Gao *et al.*, "A Survey on Deep Learning for Multimodal Data Fusion," *Neural Comput.*, vol. 32, no. 5, pp. 829–864, May 2020, doi: 10.1162/NECO_A_01273.

[61] Y. Zhang, D. Sidibé, O. Morel, and F. Mériaudeau, "Deep multimodal fusion for semantic image segmentation: A survey," *Image Vis. Comput.*, vol. 105, p. 104042, Jan. 2021, doi: 10.1016/J.IMAVIS.2020.104042.

[62] G. Joshi, R. Walambe, and K. Kotecha, "A Review on Explainability in Multimodal Deep Neural Nets," *IEEE Access*, vol. 9, pp. 59800–59821, 2021, doi: 10.1109/ACCESS.2021.3070212.

[63] A. Mogadala, M. Kalimuthu, and D. Klakow, "Trends in Integration of Vision and Language Research: A Survey of Tasks, Datasets, and Methods," *Journal of Artificial Intelligence Research*, vol. 71, pp. 1183–1317, Aug. 2021, doi: 10.1613/JAIR.1.11688.

[64] W. C. Sleeman, R. Kapoor, and P. Ghosh, "Multimodal Classification: Current Landscape, Taxonomy and Future Directions," *ACM Comput. Surv.*, vol. 55, no. 7, Jul. 2022, doi: 10.1145/3543848.

[65] J. Li *et al.*, "Deep learning in multimodal remote sensing data fusion: A comprehensive review," *International Journal of Applied Earth Observation and Geoinformation*, vol. 112, p. 102926, Aug. 2022, doi: 10.1016/J.JAG.2022.102926.

[66] Y. Ma, S. Zhao, W. Wang, Y. Li, and I. King, "Multimodality in meta-learning: A comprehensive survey," *Knowl. Based. Syst.*, vol. 250, p. 108976, Aug. 2022, doi: 10.1016/J.KNOSYS.2022.108976.

[67] W. Chai and G. Wang, "Deep Vision Multimodal Learning: Methodology, Benchmark, and Trend," *Applied Sciences 2022, Vol. 12, Page 6588*, vol. 12, no. 13, p. 6588, Jun. 2022, doi: 10.3390/APP12136588.

[68] S. Uppal *et al.*, "Multimodal research in vision and language: A review of current and emerging trends," *Information Fusion*, vol. 77, pp. 149–171, Jan. 2022, doi: 10.1016/J.INFFUS.2021.07.009.

[69] Y. Zhu, Y. Wu, N. Sebe, and Y. Yan, "Vision+X: A Survey on Multimodal Learning in the Light of Data," *IEEE Trans. Pattern Anal. Mach. Intell.*, Oct. 2022, doi: 10.1109/TPAMI.2024.3420239.

[70] E. Erdem *et al.*, "Neural Natural Language Generation: A Survey on Multilinguality, Multimodality, Controllability and Learning," *Journal of Artificial Intelligence Research*, vol. 73, pp. 1131–1207, Apr. 2022, doi: 10.1613/JAIR.1.12918.

[71] Y. Ektefaie, G. Dasoulas, A. Noori, M. Farhat, and M. Zitnik, "Multimodal learning with graphs," *Nat. Mach. Intell.*, vol. 5, no. 4, pp. 340–350, Sep. 2022, doi: 10.1038/s42256-023-00624-6.

[72] X. Wang *et al.*, "Large-scale Multi-modal Pre-trained Models: A Comprehensive Survey," *Machine Intelligence Research*, vol. 20, no. 4, pp. 447–482, Aug. 2023, doi: 10.1007/S11633-022-1410-8.

[73] Q. Tang, J. Liang, and F. Zhu, "A comparative review on multi-modal sensors fusion based on deep learning," *Signal Processing*, vol. 213, p. 109165, Dec. 2023, doi: 10.1016/J.SIGPRO.2023.109165.

[74] J. Peng, X. Hu, W. Huang, and J. Yang, "What Is a Multi-Modal Knowledge Graph: A Survey," *Big Data Research*, vol. 32, p. 100380, May 2023, doi: 10.1016/J.BDR.2023.100380.

[75] A. Barua, M. U. Ahmed, and S. Begum, "A Systematic Literature Review on Multimodal Machine Learning: Applications, Challenges, Gaps and Future Directions," *IEEE Access*, vol. 11, pp. 14804–14831, 2023, doi: 10.1109/ACCESS.2023.3243854.

[76] Y. M. Lin, Y. Gao, M. G. Gong, S. J. Zhang, Y. Q. Zhang, and Z. Y. Li, "Federated Learning on Multimodal Data: A Comprehensive Survey," *Machine Intelligence Research*, vol. 20, no. 4, pp. 539–553, Aug. 2023, doi: 10.1007/S11633-022-1398-0.

[77] S. Tabakhi, M. Naimul, I. Suvon, P. Ahadian, and H. Lu, "Multimodal Learning for Multi-omics: A Survey," vol. 01, Feb. 2023, doi: 10.1142/S2811032322500047.

[78] P. Xu, X. Zhu, and D. A. Clifton, "Multimodal Learning With Transformers: A Survey," *IEEE Trans. Pattern Anal. Mach. Intell.*, vol. 45, no. 10, pp. 12113–12132, Oct. 2023, doi: 10.1109/TPAMI.2023.3275156.

[79] C. Akkus *et al.*, "Multimodal Deep Learning," Jan. 2023, Accessed: Mar. 17, 2025. [Online]. Available: https://arxiv.org/abs/2301.04856v1

[80] K. Zhou, F. H. Hassan, and G. K. Hoon, "The State of the Art for Cross-Modal Retrieval: A Survey," *IEEE Access*, vol. 11, pp. 138568–138589, 2023, doi: 10.1109/ACCESS.2023.3338548.

[81] N. Rodis, C. Sardianos, G. Th. Papadopoulos, P. Radoglou-Grammatikis, P. Sarigiannidis, and I. Varlamis, "Multimodal Explainable Artificial Intelligence: A Comprehensive Review of

Methodological Advances and Future Research Directions," Sep. 2024, doi: 10.1109/ACCESS.2024.3467062.

[82] Z. Chen *et al.*, "Evolution and Prospects of Foundation Models: From Large Language Models to Large Multimodal Models," *Computers, Materials & Continua*, vol. 80, no. 2, pp. 1753–1808, Aug. 2024, doi: 10.32604/CMC.2024.052618.

[83] S. Raya, M. Orabi, I. Afyouni, and Z. Al Aghbari, "Multi-modal data clustering using deep learning: A systematic review," *Neurocomputing*, vol. 607, p. 128348, Nov. 2024, doi: 10.1016/J.NEUCOM.2024.128348.

[84] D. Yu *et al.*, "Recent Advances of Multimodal Continual Learning: A Comprehensive Survey," Oct. 2024, Accessed: Apr. 14, 2025. [Online]. Available: https://arxiv.org/abs/2410.05352v2

[85] K. Bayoudh, "A survey of multimodal hybrid deep learning for computer vision: Architectures, applications, trends, and challenges," *Information Fusion*, vol. 105, p. 102217, May 2024, doi: 10.1016/J.INFFUS.2023.102217.

[86] M. Xu *et al.*, "A Survey of Resource-efficient LLM and Multimodal Foundation Models," Jan. 2024, Accessed: Apr. 14, 2025. [Online]. Available: https://arxiv.org/abs/2401.08092v2

[87] A. Waqas, A. Tripathi, R. P. Ramachandran, P. A. Stewart, and G. Rasool, "Multimodal data integration for oncology in the era of deep neural networks: a review," *Front. Artif. Intell.*, vol. 7, p. 1408843, Jul. 2024, doi: 10.3389/FRAI.2024.1408843.

[88] S. Li and H. Tang, "Multimodal Alignment and Fusion: A Survey," Nov. 2024, Accessed: Nov. 21, 2025. [Online]. Available: https://arxiv.org/pdf/2411.17040

[89] T. Li *et al.*, "Deep learning in multi-modal breast cancer data fusion: a literature review," *Quant. Imaging Med. Surg.*, vol. 15, no. 11, pp. 11578–11610, Nov. 2025, doi: 10.21037/QIMS-2024-2903.

[90] Y. Zhan, R. Yang, J. You, M. Huang, W. Liu, and X. Liu, "A systematic literature review on incomplete multimodal learning: techniques and challenges," *Systems Science and Control Engineering*, vol. 13, no. 1, p. 2467083, Dec. 2025, doi: 10.1080/21642583.2025.2467083.

[91] N. M. Nguyen, T. T. Nguyen, P.-N. Tran, C. P. Lim, N. T. Pham, and D. N. M. Dang, "Multimodal fusion in speech emotion recognition: A comprehensive review of methods and technologies," *Eng. Appl. Artif. Intell.*, vol. 163, p. 112624, Jan. 2026, doi: 10.1016/J.ENGAPPAI.2025.112624.

[92] J. An, J. Lee, J. Lee, and Y. Son, "Towards LLM-Centric Multimodal Fusion: A Survey on Integration Strategies and Techniques," Jun. 2025, Accessed: Nov. 21, 2025. [Online]. Available: https://arxiv.org/pdf/2506.04788

[93] X. Liu, H. Liu, X. Liu, and H. Liu, "Symmetry-Aware Advances in Multimodal Large Language Models: Architectures, Training, and Evaluation," *Symmetry 2025, Vol. 17*, vol. 17, no. 9, p. 1400, Aug. 2025, doi: 10.3390/SYM17091400.

[94] Y. Zong, O. Mac Aodha, and T. M. Hospedales, "Self-Supervised Multimodal Learning: A Survey," *IEEE Trans. Pattern Anal. Mach. Intell.*, vol. 47, no. 7, pp. 5299–5318, 2025, doi: 10.1109/TPAMI.2024.3429301.

[95] Y. Bengio, A. Courville, and P. Vincent, "Representation learning: A review and new perspectives," *IEEE Trans. Pattern Anal. Mach. Intell.*, vol. 35, no. 8, pp. 1798–1828, 2013, doi: 10.1109/TPAMI.2013.50.

[96] L. Ericsson, H. Gouk, C. C. Loy, and T. M. Hospedales, "Self-Supervised Representation Learning: Introduction, advances, and challenges," *IEEE Signal Process. Mag.*, vol. 39, no. 3, pp. 42–62, May 2022, doi: 10.1109/MSP.2021.3134634.

[97] K. Liu, Y. Li, N. Xu, and P. Natarajan, "Learn to Combine Modalities in Multimodal Deep Learning," May 2018, Accessed: May 04, 2025. [Online]. Available: https://arxiv.org/pdf/1805.11730

[98] A. Jain, K. Nandakumar, and A. Ross, "Score normalization in multimodal biometric systems," *Pattern Recognit.*, vol. 38, no. 12, pp. 2270–2285, Dec. 2005, doi: 10.1016/J.PATCOG.2005.01.012.

[99] G. K. Verma and U. S. Tiwary, "Multimodal fusion framework: A multiresolution approach for emotion classification and recognition from physiological signals," *Neuroimage*, vol. 102, no. P1, pp. 162–172, Nov. 2014, doi: 10.1016/J.NEUROIMAGE.2013.11.007.

[100] Z. Liu, Y. Shen, V. B. Lakshminarasimhan, P. P. Liang, A. Zadeh, and L. P. Morency, "Efficient Low-rank Multimodal Fusion with Modality-Specific Factors," *ACL 2018 - 56th Annual Meeting of the Association for Computational Linguistics, Proceedings of the Conference (Long Papers)*, vol. 1, pp. 2247–2256, May 2018, doi: 10.18653/v1/p18-1209.

[101] E. Morvant, A. Habrard, and S. Ayache, "Majority Vote of Diverse Classifiers for Late Fusion," *Lecture Notes in Computer Science (including subseries Lecture Notes in Artificial Intelligence and Lecture Notes in Bioinformatics)*, vol. 8621 LNCS, pp. 153–162, 2014, doi: 10.1007/978-3-662-44415-3_16.

[102] S. Vora, A. H. Lang, B. Helou, and O. Beijbom, "PointPainting: Sequential Fusion for 3D Object Detection," *CVPR 2020*.

[103] A. Geiger, P. Lenz, C. Stiller, and R. Urtasun, "Vision meets robotics: The KITTI dataset," *International Journal of Robotics Research*, vol. 32, no. 11, pp. 1231–1237, Sep. 2013, doi: 10.1177/0278364913491297.

[104] H. Caesar *et al.*, "nuScenes: A Multimodal Dataset for Autonomous Driving," *CVPR 2020*.

[105] J. Schlosser, C. K. Chow, and Z. Kira, "Fusing LIDAR and images for pedestrian detection using convolutional neural networks," *Proc. IEEE Int. Conf. Robot. Autom.*, vol. 2016-June, pp. 2198–2205, Jun. 2016, doi: 10.1109/ICRA.2016.7487370.

[106] J.-J. Hwang *et al.*, "EMMA: End-to-End Multimodal Model for Autonomous Driving," Oct. 2024, Accessed: May 16, 2025. [Online]. Available: https://arxiv.org/pdf/2410.23262

[107] B. Yang, R. Guo, M. Liang, S. Casas, and R. Urtasun, "RadarNet: Exploiting Radar for Robust Perception of Dynamic Objects," *Lecture Notes in Computer Science (including subseries Lecture Notes in Artificial Intelligence and Lecture Notes in Bioinformatics)*, vol. 12363 LNCS, pp. 496–512, 2020, doi: 10.1007/978-3-030-58523-5_29.

[108] H. Cho, Y. W. Seo, B. V. K. V. Kumar, and R. R. Rajkumar, "A multi-sensor fusion system for moving object detection and tracking in urban driving environments," *Proc. IEEE Int. Conf. Robot. Autom.*, pp. 1836–1843, Sep. 2014, doi: 10.1109/ICRA.2014.6907100.

[109] K. Chen *et al.*, "WOMD-LiDAR: Raw Sensor Dataset Benchmark for Motion Forecasting," *Proc. IEEE Int. Conf. Robot. Autom.*, pp. 4766–4773, 2024, doi: 10.1109/ICRA57147.2024.10610651.

[110] D. Driess *et al.*, "PaLM-E: An Embodied Multimodal Language Model," *Proc. Mach. Learn. Res.*, vol. 202, pp. 8469–8488, Mar. 2023, Accessed: May 17, 2025. [Online]. Available: https://arxiv.org/pdf/2303.03378

[111] A. Brohan *et al.*, "RT-2: Vision-Language-Action Models Transfer Web Knowledge to Robotic Control," *Proc. Mach. Learn. Res.*, vol. 229, Jul. 2023, Accessed: May 17, 2025. [Online]. Available: https://arxiv.org/pdf/2307.15818

[112] G. R. Team *et al.*, "Gemini Robotics: Bringing AI into the Physical World," Mar. 2025, Accessed: May 17, 2025. [Online]. Available: https://arxiv.org/pdf/2503.20020

[113] A. Chowdhery *et al.*, "PaLM: Scaling Language Modeling with Pathways," Apr. 2022, Accessed: May 17, 2025. [Online]. Available: https://arxiv.org/pdf/2204.02311

[114] K. Marino, M. Rastegari, A. Farhadi, and R. Mottaghi, "OK-VQA: A Visual Question Answering Benchmark Requiring External Knowledge," *Proceedings of the IEEE Computer Society Conference on Computer Vision and Pattern Recognition*, vol. 2019-June, pp. 3190–3199, May 2019, doi: 10.1109/CVPR.2019.00331.

[115] N. Bien *et al.*, "Deep-learning-assisted diagnosis for knee magnetic resonance imaging: Development and retrospective validation of MRNet," *PLoS Med.*, vol. 15, no. 11, p. e1002699, Nov. 2018, doi: 10.1371/JOURNAL.PMED.1002699.

[116] S. G. Armato *et al.*, "PROSTATEx Challenges for computerized classification of prostate lesions from multiparametric magnetic resonance images," vol. 5, no. 4, p. 044501, Nov. 2018, doi: 10.1117/1.JMI.5.4.044501.

[117] S. Kumar, S. Sharma, and K. T. Megra, "Transformer enabled multi-modal medical diagnosis for tuberculosis classification," *J. Big Data*, vol. 12, no. 1, pp. 1–21, Dec. 2025, doi: 10.1186/S40537-024-01054-W.

[118] M. Alrawis, S. Al-Ahmadi, and F. Mohammad, "Bridging Modalities: A Multimodal Machine Learning Approach for Parkinson's Disease Diagnosis Using EEG and MRI Data," *Applied Sciences 2024, Vol. 14, Page 3883*, vol. 14, no. 9, p. 3883, May 2024, doi: 10.3390/APP14093883.

[119] G. Ke *et al.*, "LightGBM: A Highly Efficient Gradient Boosting Decision Tree," *Adv. Neural Inf. Process. Syst.*, vol. 30, 2017, Accessed: May 18, 2025. [Online]. Available: https://github.com/Microsoft/LightGBM.

[120] "ADNI | Alzheimer's Disease Neuroimaging Initiative." Accessed: May 18, 2025. [Online]. Available: https://adni.loni.usc.edu/

[121] S. Cui, A. Ma, Y. Wan, Y. Zhong, B. Luo, and M. Xu, "Cross-Modality Image Matching Network with Modality-Invariant Feature Representation for Airborne-Ground Thermal Infrared and Visible Datasets," *IEEE Transactions on Geoscience and Remote Sensing*, vol. 60, 2022, doi: 10.1109/TGRS.2021.3099506.

[122] S. Dong, L. Wang, B. Du, and X. Meng, "ChangeCLIP: Remote sensing change detection with multimodal vision-language representation learning," *ISPRS Journal of Photogrammetry and Remote Sensing*, vol. 208, pp. 53–69, Feb. 2024, doi: 10.1016/J.ISPRSJPRS.2024.01.004.

[123] W. G. C. Bandara and V. M. Patel, "HyperTransformer: A Textural and Spectral Feature Fusion Transformer for Pansharpening," *Proceedings of the IEEE Computer Society Conference on Computer Vision and Pattern Recognition*, vol. 2022-June, pp. 1757–1767, Mar. 2022, doi: 10.1109/CVPR52688.2022.00181.

[124] J. Huang, X. Zhang, Q. Xin, Y. Sun, and P. Zhang, "Automatic building extraction from high-resolution aerial images and LiDAR data using gated residual refinement network," *ISPRS Journal of Photogrammetry and Remote Sensing*, vol. 151, pp. 91–105, May 2019, doi: 10.1016/J.ISPRSJPRS.2019.02.019.

[125] Y. Wang and X. Yang, "Design and implementation of a distributed security threat detection system integrating federated learning and multimodal LLM," Feb. 2025, Accessed: May 17, 2025. [Online]. Available: https://arxiv.org/pdf/2502.17763

[126] N. Jaafar and Z. Lachiri, "Multimodal fusion methods with deep neural networks and meta-information for aggression detection in surveillance," *Expert Syst. Appl.*, vol. 211, p. 118523, Jan. 2023, doi: 10.1016/J.ESWA.2022.118523.

[127] S. J. I. Ismail, Hendrawan, B. Rahardjo, T. Juhana, and Y. Musashi, "MIDALF—multimodal image and audio late fusion for malware detection," *EURASIP J. Inf. Secur.*, vol. 2025, no. 1, pp. 1–20, Dec. 2025, doi: 10.1186/S13635-025-00188-5.

[128] P. Sun *et al.*, "Scalability in Perception for Autonomous Driving: Waymo Open Dataset," *Proceedings of the IEEE Computer Society Conference on Computer Vision and Pattern Recognition*, pp. 2443–2451, Dec. 2019, doi: 10.1109/CVPR42600.2020.00252.

[129] K. T. Yu, M. Bauza, N. Fazeli, and A. Rodriguez, "More than a Million Ways to Be Pushed: A High-Fidelity Experimental Dataset of Planar Pushing," *IEEE International Conference on Intelligent Robots and Systems*, vol. 2016-November, pp. 30–37, Apr. 2016, doi: 10.1109/IROS.2016.7758091.

[130] M. A. Lee *et al.*, "Making Sense of Vision and Touch: Self-Supervised Learning of Multimodal Representations for Contact-Rich Tasks," *Proc. IEEE Int. Conf. Robot. Autom.*, vol. 2019-May, pp. 8943–8950, Oct. 2018, doi: 10.1109/ICRA.2019.8793485.

[131] M. Schmitt, L. H. Hughes, C. Qiu, and X. X. Zhu, "SEN12MS -- A CURATED DATASET of GEOREFERENCED MULTI-SPECTRAL SENTINEL-1/2 IMAGERY for DEEP LEARNING and DATA FUSION," *ISPRS Annals of the Photogrammetry, Remote Sensing and Spatial Information Sciences*, vol. 4, no. 2/W7, pp. 153–160, Sep. 2019, doi: 10.5194/ISPRS-ANNALS-IV-2-W7-153-2019.

[132] H. H. Aumann *et al.*, "AIRS/AMSU/HSB on the aqua mission: Design, science objectives, data products, and processing systems," *IEEE Transactions on Geoscience and Remote Sensing*, vol. 41, no. 2 PART 1, pp. 253–263, Jul. 2003, doi: 10.1109/TGRS.2002.808356.

[133] C. Wang, W. Lu, X. Li, J. Yang, and L. Luo, "M4-SAR: A Multi-Resolution, Multi-Polarization, Multi-Scene, Multi-Source Dataset and Benchmark for Optical-SAR Fusion Object Detection," May 2025, Accessed: May 19, 2025. [Online]. Available: https://arxiv.org/pdf/2505.10931

[134] J. Carreira, E. Noland, C. Hillier, and A. Zisserman, "A Short Note on the Kinetics-700 Human Action Dataset," Jul. 2019, Accessed: May 18, 2025. [Online]. Available: https://arxiv.org/pdf/1907.06987

[135] S. Zhang *et al.*, "CASIA-SURF: A Large-Scale Multi-Modal Benchmark for Face Anti-Spoofing," *IEEE Trans. Biom. Behav. Identity Sci.*, vol. 2, no. 2, pp. 182–193, Apr. 2020, doi: 10.1109/TBIOM.2020.2973001.

[136] Y. Majib, M. Alosaimi, A. Asaturyan, and C. Perera, "Dataset for cyber–physical anomaly detection in smart homes," *Frontiers in the Internet of Things*, vol. Volume 2-2023, 2023, doi: 10.3389/friot.2023.1275080.

[137] S. Ettinger *et al.*, "Large Scale Interactive Motion Forecasting for Autonomous Driving : The Waymo Open Motion Dataset," *Proceedings of the IEEE International Conference on Computer Vision*, pp. 9690–9699, Apr. 2021, doi: 10.1109/ICCV48922.2021.00957.

[138] B. Wilson *et al.*, "Argoverse 2: Next Generation Datasets for Self-Driving Perception and Forecasting," Jan. 2023, Accessed: May 19, 2025. [Online]. Available: https://arxiv.org/pdf/2301.00493

[139] J. Lambert and J. Hays, "Trust, but Verify: Cross-Modality Fusion for HD Map Change Detection," Dec. 2022, Accessed: May 19, 2025. [Online]. Available: https://arxiv.org/pdf/2212.07312

[140] J. Mao *et al.*, "One Million Scenes for Autonomous Driving: ONCE Dataset," Jun. 2021, Accessed: May 19, 2025. [Online]. Available: https://arxiv.org/pdf/2106.11037

[141] D. Feng *et al.*, "S3E: A Multi-Robot Multimodal Dataset for Collaborative SLAM," Nov. 2024, doi: 10.1109/LRA.2024.3490402.

[142] B. A. Newman, R. M. Aronson, S. S. Srinivasa, K. Kitani, and H. Admoni, "HARMONIC: A Multimodal Dataset of Assistive Human-Robot Collaboration," *International Journal of Robotics Research*, vol. 41, no. 1, pp. 3–11, Jul. 2018, doi: 10.1177/02783649211050677.

[143] O. Celiktutan, E. Skordos, and H. Gunes, "Multimodal Human-Human-Robot Interactions (MHHRI) Dataset for Studying Personality and Engagement," *IEEE Trans. Affect. Comput.*, vol. 10, no. 4, pp. 484–497, Oct. 2019, doi: 10.1109/TAFFC.2017.2737019.

[144] S. Zhu, Z. Ye, Q. Ai, and Y. Liu, "EEG-ImageNet: An Electroencephalogram Dataset and Benchmarks with Image Visual Stimuli of Multi-Granularity Labels," Jun. 2024, Accessed: May 18, 2025. [Online]. Available: https://arxiv.org/pdf/2406.07151

[145] Y. C. T. Yang *et al.*, "CLIPdb: A CLIP-seq database for protein-RNA interactions," *BMC Genomics*, vol. 16, no. 1, pp. 1–8, Feb. 2015, doi: 10.1186/S12864-015-1273-2.

[146] O. Banos, R. Garcia, and A. Saez., "MHEALTH - UCI Machine Learning Repository." Accessed: May 16, 2025. [Online]. Available: https://archive.ics.uci.edu/dataset/319/mhealth+dataset

[147] M. J. Allen *et al.*, "M3LEO: A Multi-Modal, Multi-Label Earth Observation Dataset Integrating Interferometric SAR and Multispectral Data," Jun. 2024, Accessed: May 19, 2025. [Online]. Available: https://arxiv.org/abs/2406.04230v2

[148] Y. Zhu, Y. Kong, Y. Jie, S. Xu, and H. Cheng, "GRACO: A Multimodal Dataset for Ground and Aerial Cooperative Localization and Mapping," *IEEE Robot. Autom. Lett.*, vol. 8, no. 2, pp. 966–973, Feb. 2023, doi: 10.1109/LRA.2023.3234802.

[149] T. Yuan *et al.*, "Towards Surveillance Video-and-Language Understanding: New Dataset, Baselines, and Challenges," *CVPR 2024*, doi: 10.1109/CVPR52733.2024.02082.

[150] J. Goh, S. Adepu, K. N. Junejo, and A. Mathur, "A Dataset to Support Research in the Design of Secure Water Treatment Systems," *Lecture Notes in Computer Science (including subseries Lecture Notes in Artificial Intelligence and Lecture Notes in Bioinformatics)*, vol. 10242 LNCS, pp. 88–99, 2017, doi: 10.1007/978-3-319-71368-7_8.

[151] X. Xu *et al.*, "A Comprehensive Review on Synergy of Multi-Modal Data and AI Technologies in Medical Diagnosis," *Bioengineering 2024, Vol. 11*, vol. 11, no. 3, Feb. 2024, doi: 10.3390/BIOENGINEERING11030219.

[152] K. H. Zou *et al.*, "Statistical Validation of Image Segmentation Quality Based on a Spatial Overlap Index: Scientific Reports," *Acad. Radiol.*, vol. 11, no. 2, p. 178, 2004, doi: 10.1016/S1076-6332(03)00671-8.

[153] Z. Zhang, Z. Li, K. Wei, S. Pan, and C. Deng, "A survey on multimodal-guided visual content synthesis," *Neurocomputing*, vol. 497, pp. 110–128, Aug. 2022, doi: 10.1016/J.NEUCOM.2022.04.126.

[154] X. Tan *et al.*, "NaturalSpeech: End-to-End Text to Speech Synthesis with Human-Level Quality," *IEEE Trans. Pattern Anal. Mach. Intell.*, vol. 46, no. 6, pp. 4234–4245, Jun. 2024, doi: 10.1109/TPAMI.2024.3356232.

Konya Mühendislik Bilimleri Dergisi, c.14, s.2, 951-965, 2026
Konya Journal of Engineering Sciences, v.14, n.2, 951-965, 2026
ISSN: 2667-8055 (Electronic)
DOI: 10.36306/konjes.1726530

SEISMIC SOIL MICROZONATION IN TURKEY: BRIDGING GAPS BETWEEN INTERNATIONAL STANDARDS AND LOCAL IMPLEMENTATION

[1,*]Kaveh DEHGHANIAN

[1]*Department of Civil Engineering, Istanbul Aydin University, Istanbul, Turkey*
[1]kavehdehghanian@aydin.edu.tr

Highlights

- Critical evaluation of soil microzonation under Turkish Earthquake Code (TBEC 2018)
- Comparative analysis with Eurocode, NEHRP/ASCE, Japanese, and Chinese standards
- Identification of implementation gaps in municipal-level applications in Turkey
- Emphasis on Vs-based classification and site-specific seismic response analysis
- Integrating microzonation into urban planning for seismic resilience

***Corresponding Author:** Kaveh DEHGHANIAN, kavehdehghanian@aydin.edu.tr

Konya Mühendislik Bilimleri Dergisi, c.14, s.2, 951-965, 2026
Konya Journal of Engineering Sciences, v.14, n.2, 951-965, 2026
ISSN: 2667-8055 (Electronic)
DOI: 10.36306/konjes.1726530

SEISMIC SOIL MICROZONATION IN TURKEY: BRIDGING GAPS BETWEEN INTERNATIONAL STANDARDS AND LOCAL IMPLEMENTATION

[1,*]Kaveh DEHGHANIAN

[1]*Department of Civil Engineering, Istanbul Aydin University, Istanbul, Turkey*
[1]kavehdehghanian@aydin.edu.tr

(Received: 25.06.2025; Accepted in Revised Form: 14.12.2025)

ABSTRACT: Seismicity and geological settings of Turkey are very active and complex, where advanced techniques have to be implemented to mitigate seismic risks through techniques such as soil microzonation. The present study critically reviews the soil microzonation practice under the provisions of the Turkish earthquake code (TEC) and the implementation problems, such as inconsistent geotechnical data, insufficient local capacity, and enforcement gaps in regulations. The study highlights 951ort similarities and differences in the classification of soils, site-specific ground motion analyses, and geotechnical hazards assessments (e.g., liquefaction, landslides) by comparing Turkey against international practices such as Eurocode (EU), Japanese, American (NEHRP/ASCE/IBC), and Chinese (GB). The methodology puts important emphasis on detailed investigations of the site, including drilling boreholes, conducting in situ tests (SPT, CPT), and geophysical survey (MASW) to derive seismic microzonation maps as a reliable means. These maps provide assessments of shear wave velocity, amplification potential, and liquefaction susceptibility—information essential for seismic design and urban planning. Comparative results show that while site-specific assessments and Vs-based soil classification are common to all standards, they differ in their regulatory frameworks and treatment of hazards and in the rigor applied to their implementation. Findings support the 951ort h of embracing the best practices of the global standards in order to enhance the Turkish soil microzonation, which will lead to safer construction practices and urban development resilient to earthquakes.

Keywords: *Soil Microzonation; Turkish Earthquake Code (TEC); Site Effects; Seismic Risk Assessment; Geotechnical Investigation.*

***Corresponding Author:** Kaveh DEHGHANIAN, kavehdehghanian@aydin.edu.tr

1. INTRODUCTION

Extremely vulnerable to earthquakes, Turkey considers seismic security of utmost importance. The Turkish Seismic Code (TEC), also known as the Regulation on Buildings to be Constructed in Seismic Zones (2018), is the primary law governing construction and reinforcement against seismic activities. In tandem with other supporting legal instruments, such as Law No.1976 on the Transformation of Areas under Disaster Risk, this code aims to enhance seismic resilience through strict safety standards and urban transformation projects. The TEC defines seismic zones in detail across Turkey and requires site-specific geotechnical surveys and investigations to be conducted before construction. Compliance with these rules is subsequently checked and enforced under Law No. 4708, which pertains to Building Inspection. In addition to the main TEC, the Regulation on the Principles of Building Design and Construction (2019) provides supplementary requirements for both structural and non-structural elements, which may also include base isolation systems and energy dissipation devices. Law No. 2634 on Urban Development further emphasizes urban planning that integrates seismic risk assessment to minimize potential hazards [1]. Understanding these seismic regulations is crucial for property investments in Turkey, as they significantly impact the viability and cost of such investments. New buildings must undergo the rigorous process of seismic risk assessments, whereas existing constructions require retrofitting to meet the stated structural integrity requirements. Properties that meet such standards are to be marketed at a higher price due to their greater safety and lower long-term risks. On the contrary, properties that fail to meet the standards risk losing value and legal liability. The importance of soil microzonation in relation to Turkish earthquake standards will be emphasized, with a focus on its contribution to seismic risk assessment and mitigation. This study synthesizes a variety of academic materials and official documents into a cogent narrative, which will then propose an overview of how microzonation facilitates safe construction practices and urban planning in earthquake-prone regions of Turkey. Turkey is highly vulnerable to earthquakes, given its special tectonic position at the junction of several active fault systems. The country straddles the North Anatolian Fault Zone (NAFZ), one of the most active strike-slip faults in the world, the East Anatolian Fault Zone (EAFZ), and the Aegean Extension Zone. This complex geodynamic setting has generated powerful earthquakes throughout history, with devastating consequences. Notable examples include the 1999 İzmit earthquake (M7.4), which claimed more than 17,000 lives, the 2023 Kahramanmaraş earthquakes (7.7 and 7.6), which affected 11 provinces, and the 1939 Erzincan earthquake (M7.8). These events have demonstrated the significant impact of local soil conditions on damage patterns. For instance, during the 1999 İzmit earthquake, soft soil amplification caused extreme damage in the Avcılar district, and in the 2023 earthquakes, vast liquefaction was recorded in Hatay's alluvial plains. This makes soil microzonation critical, given that 75% of Turkey's population resides in urban areas with high seismic risk. Current TEC implementation usually relies upon generalized soil classifications. Municipal development plans rarely include site-specific information on ground response. Some of the discrepancies between regulatory requirements and practice can be seen in the variable quality of geotechnical data among different municipalities, and a few municipalities possess the technical capacity to conduct rigorous microzonation studies—the demands involved in enforcing TEC requirements for existing buildings. The study aims to determine how microzonation initiatives in Turkey can help bridge these gaps by conducting systematic comparisons with international standards, identifying transferable best practices, and proposing practical improvements for the effective implementation of TEC. The research focuses on urban areas in which rapid construction frequently outpaces site investigations, and soil amplification effects are most pronounced. The economic impact of earthquakes would be most significant.

Turkey is considered one of the most seismically active countries in the world, situated between the colliding North Anatolian Fault Zone (NAFZ) and the East Anatolian Fault Zone (EAFZ), as well as the Aegean Extension Zone. Throughout history, devastating earthquakes have occurred, highlighting the importance of local soil conditions in distributing damage. Notable examples include the Erzincan earthquake in 1939 (Mw 7.8), the İzmit earthquake in 1999 (Mw 7.4), and the Kahramanmaraş earthquake in 2023 (Mw 7.7, 7.6). For instance, site amplification caused extensive destruction in Avcılar during the 1999 İzmit earthquake, while widespread liquefaction was observed in the alluvial plains of Hatay in 2023 [2]. Meanwhile, soil microzonation is emerging as a crucial tool for urban planning and seismic design, aimed at minimizing risks. Unlike extensive seismic hazard maps, microzonation offers data at a localized level about soil amplification, liquefaction susceptibility, and landslide hazards [3,4]. All this information is necessary for incorporating seismic safety into municipal planning, land-use management, and infrastructure development. In Turkey, the importance of microzonation is recognized by the Ministry of Public Works and AFAD, which issued manuals and pilot studies for municipalities [5]. However, implementation is uneven across regions, and geotechnical capacity and enforcement vary.

At the international level, soil microzonation has been advanced through several studies in Europe (Eurocode 8), the U.S. (NEHRP/ASCE/IBC), Japan, and China [6-12]. These frameworks emphasize Vs-based soil classification, liquefaction evaluation, and site-specific response analysis. Foundational works by Darendeli [13] and Menq [14] have shaped the global practice by providing soil dynamic property models that have gained wide acceptance. Microzonation has been extensively studied in Turkey by Ansal et al. [3], Çetin et al. [22], and Özcep et al. [15], highlighting the importance of site effects in the Marmara and western Anatolia regions. Recent advances in using MASW, HVSR, and GIS-based approaches [15, 16, 19] demonstrate that local-scale studies are improving; however, this is still an evolving process with further integration into the Turkish Earthquake Code (TBEC 2018).

This research paper aims to provide an exhaustive comparison of the importance and applications of soil microzonation as outlined in standards for major regions, including Europe (Eurocode), Japan, the United States (NEHRP, ASCE/SEI, IBC), and China (GB). By evaluating the similarities, differences, strengths, and weaknesses of the aforementioned international standards, this research advocates for best practices, potential harmonization, and a global commitment to enhancing seismic safety through the application of advanced microzonation techniques. The analysis will also focus on how each of these standards defines soil classification, site-specific ground motion analysis, and other critical geotechnical hazards, such as liquefaction, thereby providing a holistic view of the international landscape of seismic microzonation.

1.1 Turkish Earthquake Codes and Site Effects

The Turkish Earthquake Code (TEC), particularly the version in effect since 2007 (TEC 2007), is the primary code governing seismic safety in Turkey. It provides a compendium of regulations for the design and construction of earthquake-resistant buildings. An essential aspect of the TEC is its incorporation of provisions that acknowledge and account for local site effects, which are greatly influenced by soil conditions. This highlights the fact that the Turkish regulatory framework acknowledges the significant impact of a site's geological and geotechnical characteristics on the propagation of seismic waves and, consequently, on the response of structures during an earthquake. Numerous devastating earthquakes have struck Turkey throughout its long history, many of which have highlighted the critical role of local soil conditions in amplifying ground motion and causing structural damage. Studies have shown that deep alluvial basins are prevalent in many urban settings in Turkey and significantly amplify seismic waves originating from even distant earthquakes, resulting in severe shaking. [2]. This phenomenon is known as site amplification and is a matter of great concern, addressed by the TEC through its stipulations for site-specific seismic design parameters.

The classification of soil types based on dynamic properties to influence the design spectral acceleration values is the primary purpose of the TEC. Such classification, therefore, is vital for selecting site seismic design parameters. While the details concerning soil classification have changed in the different iterations of TEC (e.g. TEC 1998, TEC 2007, TEC 2018), the basic reasoning behind soil classification has remained the same: to differentiate soils depending on their anticipated performance when subjected to seismic loading. These classifications typically consider factors such as shear wave velocity, soil stiffness, and the presence of liquefaction layers. For example, some soil types, particularly those with low shear wave velocity and high water content, are recognized as being more prone to liquefaction and severe ground deformation during an earthquake. Geotechnical Investigations, Site-Specific Studies. The TEC requires a detailed geotechnical investigation to characterize subsurface conditions. They typically comprise boreholes, in-situ tests (such as Standard Penetration Tests (SPT) and Cone Penetration Tests (CPT)), and laboratory testing of soil samples. The information obtained from these investigations is necessary for assessing possible geotechnical hazards, such as liquefaction, settlement, and landslides. If general vulnerability indices were relied upon, such as those that do not fully represent local soil behavior, the damage assessment would be severely compromised, thereby strengthening the need for site-specific studies [3]. It is from the above that knowledge of subsurface geology and geotechnical properties becomes vital for the application of TEC and the seismic safety of structures. The Turkish Earthquake Codes (TEC/TBEC) have undergone many changes during the last 30 years: 1)1998 TEC: Soil classification was based more on empirical indices such as SPT N-values and soil type. Seismic design spectra were generally inclusive, with only slight consideration for site effects [3]

2) 2007 TEC: The introduction of Vs30-based soil classification made the codes aligned with NEHRP and Eurocodes. This paradigm shift from using empirical parameters toward shear wave velocity as the main parameter for soil classification was advocated by both geotechnical and geophysical investigations [6,9]. The 2007 code also mandated liquefaction evaluation in critical areas. Similar to the heightened changes made by the 2018 TBEC, their other main achievements include the adoption of probabilistic seismic hazard maps developed by AFAD, the revision of design spectra incorporating period-dependent amplification factors, and the implementation of mandatory site-specific response analyses for critical structures [19]. Liquefaction and landslide susceptibility analyses were made compulsory, and microzonation results were now effectively linked to urban transformation policies under Law no. 6306. Table 1 illustrates the evolution of soil classification methodologies in Turkish codes in comparison to Eurocode 8 and NEHRP. This evolution suggests that Turkey is striving to adopt international practices; however, challenges persist in ensuring consistency, data quality, and technical capacity at the municipal level.

Table 1. Evolution of Turkish Earthquake Codes Compared with Eurocode 8 and NEHRP/ASCE

Aspect	TEC 1998	TEC 2007	TBEC 2018	Eurocode 8 (2004)	NEHRP/ASCE (2010–2023)
Soil Classification Basis	Mainly SPT N-values and soil type (empirical)	Introduced Vs30 (average shear wave velocity of top 30 m) in addition to SPT/CPT	Refined Vs30-based classification with more categories; aligned with NEHRP	Primarily Vs30 (Types A–E) with optional NSPT and Cu when Vs unavailable	Primarily Vs30 (Classes A–F), supplemented by NSPT and Cu
Design Spectra	Generalized; limited site-specific detail	Site-dependent spectral shapes introduced	Adopted AFAD 2018 probabilistic hazard maps with site factors	Elastic response spectra vary by soil type (A–E)	Period-dependent response spectra with soil amplification factors
Geotechnical Hazards	Limited; liquefaction rarely considered explicitly	Liquefaction evaluation required in critical regions	Liquefaction, landslides, settlements explicitly required	Geohazards addressed indirectly through geotechnical provisions	Detailed liquefaction, landslide, and fault 955ort he evaluation guidelines
Site-Specific Response Analysis	Rarely required	Allowed for special structures	Mandatory for important/critical structures (bridges, hospitals, etc.)	Required for important structures and complex sites	Required for Site Class F and critical facilities
Hazard Maps	Deterministic zonation maps	Updated probabilistic zonation (2007 AFAD)	Full probabilistic hazard maps (AFAD 2018) integrated	Probabilistic Seismic Hazard Analysis (PSHA) recommended	National hazard maps are periodically updated (FEMA, USGS)
Integration into Planning	Weak municipal implementation	Some municipal-level guidance (pilot studies)	Linked to Law No. 6306 (Urban Transformation) and AFAD guidelines	Left to national annexes of EU states	Enforced through IBC adoption at the state/local level

1.2. The Importance of Soil Microzonation

Of all mechanisms to reduce seismic risk, soil microzonation is perhaps the most promising method in seismically active countries, such as Turkey. This procedure involves subdividing an urban area into small zones based on their geology, geotechnics, and seismic characteristics, to anticipate different responses to ground motions during and after an earthquake. Unlike regional seismic hazard maps, which provide an assessment of broad front ranges, microzonation studies provide highly detailed local-scale data on how different soil conditions will affect ground shaking intensity, potential liquefaction, and susceptibility to landslides [4]. Hence, it establishes integrated approaches for effective urban planning, land-use management, and the application of appropriate building codes.

The seismic microzonation study generally involves several phases. In the first stage, the region's seismicity and seismic hazard are evaluated to delineate the earthquake potential of the area. This is then followed by thorough geological and geotechnical investigations, comprising boreholes and geophysical surveys (such as Multi-Channel Analysis of Surface Waves – MASW), as well as laboratory tests, to characterize the subsurface soil layers and their dynamic properties. The information collected will be used to model the site response, predict ground motion amplification, and assess geotechnical hazards, such as liquefaction and settlement [2, 4]. The final output of a microzonation study typically comprises a set of maps that delineate zones with similar seismic responses. Such maps can include Ground Motion Amplification Maps, which show areas where seismic waves are likely to be amplified due to local soil conditions. Liquefaction Potential Maps: identifying areas where liquefaction may occur, a phenomenon in which granular soils that are saturated lose strength and stiffness during the shaking of an earthquake. Landslide Susceptibility Maps: Showing the areas prone to earthquake-induced landslides. Shear Wave Velocity Maps: mapping the distribution of shear wave velocities, which is an essential parameter in site classification and seismic response analyses.

1.3. Microzonation in the Turkish context

Soil microzonation is extremely important for Turkey, since the country is highly earthquake-prone and past earthquakes have revealed considerable local site effects leading to damage. Recognizing the importance of microzonation, Turkish authorities, particularly the Ministry of Public Works and Settlement and the General Directorate of Disaster Affairs (AFAD), have prepared manuals and conducted pilot studies to implement microzonation methodologies at the municipal level [5]. Microzonation data need to be integrated into the Turkish Building Earthquake Code (TBEC). While TBEC absorbs period-dependent spectral acceleration values and design spectra with ground effects, microzonation studies contribute inputs for accurate site-specific design. For instance, general vulnerability indices by themselves (as Kg index) have been shown to lead to underestimation of damage potentials, especially in situations where site conditions are complex or introduce a geotechnical hazard, e.g., liquefaction [2]. Hence, microzonation provides detailed information, enabling the TBEC to tailor its approach to the local seismic hazards that buildings are designed and constructed to withstand. Microzonation studies in Turkey began in the 1990s, with particular attention given to early projects in Istanbul and Izmir, which focused on basin effects and liquefaction [3,18]. Ansal et al. [3] provided microzonation projects at a municipal scale, while Çetin et al. [18] highlighted the significant role that microzonation played in Bornova, İzmir. More recent studies by Özcep et al. [15] and Alimoradi et al. [16] have highlighted the importance of integrating Vs-based soil classification with GIS tools in urban planning.

Institutional efforts are aided by AFAD, which prepared the 2007 Microzonation Manual [4] and updated the 2023 AFAD Microzonation Guide [19]. Detailed liquefaction risk maps were produced by Istanbul Metropolitan Municipality (İBB) [20]. Municipalities like Bursa and Hatay have also implemented microzonation, as they were affected by previous earthquake damage [2].

The 2023 Kahramanmaraş earthquakes dramatically ushered in the realization of microzonation; their severe liquefaction in the Amik Basin of Hatay, as well as the amplification in urban centers, revealed the gulf between code and what was done within the locality. These developments also underscored the need for microzonation information to comply with TBEC, as they primarily relate to the retrofitting of existing structures and guiding urban transformation. In short, Turkey has made considerable progress in adopting microzonation concepts, although these concepts still lack full integration into national building practice. Closing that gap will require the systematic application of AFAD guidelines, the creation of enhanced municipal technical capacity, and alignment with international best practices.

2. METHODOLOGY

2.1. European Standards: Eurocode (EN)

Eurocode formal name EN: Design for buildings and civil engineering works in the European context concerning earthquakes. It includes comprehensive European standards and guidelines for earthquake-resistant design in buildings and civil engineering works, part of a set of Eurocode harmonizations intended to standardize construction practices across Europe. Eurocode accounts for the significant effects of geotechnical conditions on seismic response, thereby including detailed provisions for seismicrozonation and site-specific analysis [6]. The basis of the Eurocode concept in soil microzonation lies in its system of soil classification, which primarily classifies types of ground based on the average shear wave velocity in the top meters (Vs). It is relevant because it significantly influences the shape of the elastic response spectrum used in seismic design. Eurocode defines several soil types in a range from Type A (rock or other rock-like geological formation, with at most 3 m of softer material at the surface) to Type E (a surface layer of alluvium ranging in thickness from 3 m to 20 m, with Vs values below 180 m/s, under a stiffer material) [7]. V's thresholds for each of the ground types are specified, enabling a standard assessment across different European countries.

Besides Vs, the Eurocode also considers other geological and geotechnical parameters, such as the number of blows in a Standard Penetration Test (SPT) and undrained shear strength (Cu), especially when Vs data are lacking or considered unreliable. Such a multi-parameter system provides a measure of flexibility without compromising an adequate site characterization framework. The standard also encompasses how to determine the topographic amplification factors that consider the influence of irregular ground surfaces, like slopes and valleys, on seismic ground motion. Eurocode further emphasizes seismic hazard zoning, which involves dividing a region into zones with varying levels of seismic hazard. This is typically carried out following a probabilistic seismic hazard assessment (PSHA), allowing the design ground acceleration to be assessed for a given site. For sites with complex geological conditions or significant structures, site-specific ground motion analyses must be carried out in accordance with Eurocode. This could involve advanced techniques for the site responses to seismic shaking, considering the non-linear behavior of soils under strong ground motion. One remarkable aspect of the Eurocode is its flexibility, which permits each member state to define its own National Annexes, allowing it to utilize these avenues to adjust specific parameters or add guidance based on local geological conditions and seismic activity. This way, even though the principles are unified for seismic design, some room remains for regional differences. The time when Eurocode became operational marked a new dawn in seismic engineering practice in Europe, subjecting it to a more uniform and scientifically rigorous procedure in soil microzonation and earthquake-resistant design.

2.2. Japanese Standard

Japan's long struggle with seismic loads over time has been visually depicted in the evolution of earthquake engineering and seismic design. These extensive experiences are reflected in highly sophisticated and stringent standards for soil microzonation, which are embedded within their building codes and comprehensive disaster prevention strategies. The microzonation scheme in Japan is unique in its emphasis on extreme detail during investigations, the use of the most advanced analytical techniques, and a focus on mitigating peculiarly interesting geotechnical hazards, such as liquefaction [8]. Japanese Building Codes consider soil conditions on a composite basis, taking into account the geological, topographical, and mechanical properties of soils. Although similar to shear wave velocity, Japanese codes differ from Eurocode and American codes in their standards for site investigation, which appear to increase the requirements for the number of borehole data, in situ tests, and geophysical surveys needed to characterize the subsurface condition across a site accurately. The emphasis on detailed investigation stems from Japan's historical experience with complex soil profiles and the need for a precise understanding of ground behavior during earthquakes.

S-wave velocity (Vs) is fundamental to Japanese microzonation practices in understanding and classifying soils, as well as performing seismic response analysis. Methods for determining the dynamic parameters of soils, including Vs, and using these parameters in numerical simulations to predict site-specific ground motion are provided by existing Japanese standards. In such simulations, essential aspects such as the non-linear behavior of soils under strong shaking are incorporated, as these are crucial for predicting ground motions in areas with soft soil deposits. One of the most notable aspects of the Japanese microzonation standard is its significant emphasis on assessing liquefaction potential and its mitigation. Japan has experienced numerous catastrophic earthquakes, where liquefaction has been responsible for severe damage to buildings, infrastructure, and lifelines. As a result, its codes provide very detailed procedures for evaluating liquefaction susceptibility, frequently based on empirical methods gleaned from numerous case studies and extensive laboratory testing. If liquefaction potential is identified, mitigatory measures, such as ground improvement techniques or alternative foundation design solutions, must be implemented as stipulated by the standards. Japan has a multi-tiered approach to microzonation, recognizing that the level of detail available in a study changes the importance of the area, hazard potential, and development type. This ranges from generic zonation for regional planning to detailed, site-specific microzonation for critical facilities and high-density urban areas. This tiered approach thus allows the efficient allocation of resources while ensuring the maintenance of seismic safety at appropriate levels across various contexts [9]. Continuous updating and refinement of Japanese microzonation practices signify a commitment to learning from past earthquakes and improving the resilience of the built environment.

2.3. American Standards: NEHRP, ASCE/SEI, IBC

The United States has a seismic design provision and soil microzonation model, mostly through collaborative efforts between the National Earthquake Hazards Reduction Program (NEHRP), the American Society of Civil Engineers (ASCE), and the International Building Code (IBC) in the ASCE/SEI standard of minimum design loads and associated criteria for the buildings and other structures. NEHRP lays the foundation for research and recommendations, ASCE/SEI incorporates it through consensus, and references it in the IBC, which is enacted by state and local jurisdictions [10]. This layered approach ensures a uniform yet flexible seismic design framework nationwide.

However, seismic design provisions and soil microzonation practices in the United States mainly involve a collaborative framework among the National Earthquake Hazards Reduction Program (NEHRP), the ASCE standard ASCE/SEI (Minimum Design Loads and Associated Criteria for Buildings and Other Structures), and the International Building Code (IBC). NEHRP lays the groundwork for basic research and recommendations, which are then interpreted into the ASCE/SEI standard through a consensus process. Finally, these recommendations are incorporated into the IBC, which is enacted by state and local

jurisdictions [11]. This layered approach ensures a uniform yet flexible framework for seismic design nationwide.

There is, however, a collaborative approach among the National Earthquake Hazards Reduction Program (NEHRP), the ASCE standard ASCE/SEI (Minimum Design Loads and Associated Criteria for Buildings and Other Structures), and the International Building Code (IBC) in seismic design provisions and soil microzonation in America. NEHRP lays the foundation for research and recommendations, while ASCE/SEI incorporates it through consensus and references it in the IBC, which is then enacted by state and local jurisdictions [11]. Thus, the layered approach provides a uniform yet flexible framework for seismic design nationwide.

Sites that fall under Site Class F or are places of importance in a country with tall buildings are required to have site-specific ground motion procedures as mandated by the American standards. These are detailed geotechnical investigations, followed by site response analysis, to accurately define the seismic forces and displacements the structure would experience. The equivalent linear D and subsequent non-linear D or D simulations aim to capture the unique characteristics of site response to the shaking caused by the earthquake and the possible presence of non-linear soil behavior at high ground motions. Another aspect covered in the American standards is the provision of comprehensive guidelines and procedures for evaluating and mitigating other geohazards related to microzonation. Among the aspects of liquefaction analysis are methods for assessing the liquefaction susceptibility of granular soils and mitigation methods, such as ground improvement methods. Furthermore, geohazards such as seismic-induced landslides, fault rupture, and differential settlements are also addressed in this effort to enhance seismic assessments at more minor scales. These standards are constantly evolving as new scientific research and lessons learned from earthquakes are applied, reinforcing the idea that will make the built environment in the USA even more seismic-resilient.

2.4. Chinese standards: GB50011

China has unique conditions with a large territory and significant seismic activities. The old institution has established a comprehensive seismic design code for the country, known as GB (Code for Seismic Design of Buildings). This national standard is of great importance in framing the earthquake-resistant construction code, and its special mention includes soil microzonation, which realizes the profound impact of local site conditions upon seismic ground motion. The Chinese concept of microzonation, as mentioned in GB-no., is more oriented towards site characterization, seismic fortification intensity, and the ground motion parameters to be selected for design. GB site classification is based on a combination of factors, including soil type classification, shear wave velocity, and the presence of adverse geological conditions. While Vs is an important criterion, it parallels Euro-American standards in that the Chinese code is equally considerate of other soil parameters and geological formations in its classification. This multi-dimensional style aims to capture the multicultural geology of China. The classifications thus appointed have a bearing on the selection of design response spectra and seismic force calculations for the structure, taking into account the possible amplification or de-amplification effects of local soil that need to be considered in the design. A characteristic of the Chinese seismic code is the designation of "seismic fortification intensity area." These zones, based on historical seismicity and probabilistic seismic hazard assessment, characterize the required seismic resistance of buildings and structures. The seismic fortification intensity will, in turn, affect the level of the design earthquake and hence the extent and detail of the microzonation study required at any given site. It follows, therefore, that the higher the fortification intensity, the more site investigations and seismic response analysis will be carried out. GB specifies particular ground motion parameters and design response spectra depending on soil conditions and seismic intensities. It also prescribes that adjustments should be made to these parameters, considering the site classification, so that the design ground motion truly reflects the expected shaking at the building foundation. The Chinese standards further address other geotechnical hazards in conjunction with liquefaction, but the specific methodologies and criteria may not easily align with those from international

codes. These ongoing adjustments and upgrades to GB are part of a series of activities by China aimed at achieving a more earthquake-resistant construction for the preservation of its rapidly urbanizing regions from earthquake-induced destruction [12].

3. RESULTS AND DISCUSSION

3.1. Comparative Analysis of International Standards

The earlier sections have outlined the soil microzonation approaches as laid down by European, Japanese, American, and Chinese standards. Each of these frameworks has developed in its own right, shaped by regional seismic realities and the philosophical underpinnings of engineering; nevertheless, a comparative analysis reveals significant similarities in some basic principles and notable divergences in their particular methodologies and implementations. Understanding these converging and diverging characteristics is essential for appreciating the world's current state-of-the-art in seismic microzonation and discerning avenues for future harmonization.

3.1.1. Similarities in approach

Local site conditions can significantly modify seismic ground motion through amplification and attenuation. All the seismic design codes studied recognize this fact; therefore, a site-specific characterization of soil is mandatory if a given site needs to be seismically designed. Thus, all these codes incorporate a soil classification system to account for the effects of site conditions. The other parametric requirement that they all share in common is the Vs. Vs is here defined as the average shear wave velocity in the upper meters, being a metric that Eurocode, ASCE, and possibly Japanese and Chinese standards might refer to for classifying soil profiles. The sheer popularity of Vs enjoys has proven it to be a simple yet robust method for characterizing soil stiffness, which is correlated with the ground motion amplification potential. Such an analogical classification by Vs is likely to be quantitative and relatively objective across different nations. Beyond that, all standards emphasize the assessment of site-specific ground motion for critical structures in areas with complex geological conditions or high seismic hazard. Although actual analysis methods may vary (e.g., equivalent linear, nonlinear analyses), the principle remains the same: to obtain site-specific performance from seismic shaking associated with an earthquake, given a generalized design spectrum. Such site-specific investigations would involve extensive geotechnical studies, including but not limited to boreholes and geophysical surveys, to provide the necessary input parameters for the analysis. Geotechnical hazards, other than ground amplification, such as liquefaction, are another common observation. Japan, having gained vast experience in liquefaction, has elaborated provisions for its assessment and mitigation. Nonetheless, American and Chinese standards contain recommendations regarding the evaluation of liquefaction potential, while Eurocode implicitly accounts for it through its general geotechnical design principles. Thus, given that microzonation considers all seismic-induced hazards, its inclusion in these standards demonstrates a mature understanding of earthquake engineering.

3.1.2. Differences in Soil Classification Details and Thresholds

Vs values in standards differ in threshold, and also the number of soil classes. For example, Eurocode specifies ground types from A to E with specific Vs ranges, whereas ASCE/SEI uses six site classes from A to F, having slightly variant Vs boundaries. The Chinese GB has a classification of sites according to Vs and soil type, but its categories and criteria are probably more influenced by regional geological features peculiar to China. Such differences may lead to disagreements in the classification of a site from one code to another, which could result in different design parameters and seismic forces for that site. This thereby accentuates the difficulty in achieving full interoperability of international codes in the absence of a globally recognized standard system for soil classification.

3.1.3. Variations in Treatment of Liquefaction and Other Hazards

There is no doubt that liquefaction has been discussed in every standard. Cumulatively, standards investigate liquefaction, and some delve deeper than others, while others are more general. Perhaps the

Japanese standards have more stringent liquefaction assessment and mitigation requirements than those of any other country. The American standards have also defined detailed procedures for liquefaction. On the other hand, Chinese standards have some provisions, but the methodology applied is specific to them. Eurocode recognizes geotechnical hazards, but is more general and leaves national annexes or specific geotechnical design codes for detailed procedures. A similar level of detail is present for other hazards, such as seismic-induced landslides or fault rupture, reflecting regional priorities and the incidence of these hazards.

3.1.4. Differences in Regulatory Frameworks and Implementation

By these necessary frameworks, the differences appear to be much greater when they are considered within the regulatory and implementation framework. Eurocode is a common approach for European countries, while it is possible to customize its application through National Annexes to accommodate some regional features. The U.S. adopts NEHRP recommendations into ASCE/SEI and subsequently into the IBC, resulting in a multi-step process for a specific application. Japan has made its standards so much interwoven with the national building code, a centralized approach to seismic safety. China's GB is such a national obligatory standard: the seismic fortification intensity areas have been determining design requirements. These created different regulatory scenarios that affected the pace of adoption of new research, the enforceability mechanism, and the overall effectiveness of microzonation practices.
Strengths and Weaknesses of Every Standard: Eurocode: Strengths: Harmonized throughout Europe, clear Vs-based classification, adaptable through National Annexes. Promotes harmony across the seismic design agenda. Weaknesses: Some inconsistencies may arise between countries due to reliance on National Annexes. It may be less prescriptive in some aspects of geotechnical hazard assessments compared to other codes. Japanese Standards: Strengths: Very detailed site investigation requirements, advanced analytical techniques, heavy emphasis on liquefaction assessment and mitigation. Based on a very significant real-life earthquake experience. Weaknesses: May be too prescriptive, resulting in higher investigation and design costs. May not enjoy flexibility in countries that do not have sufficient historical seismic data. American Standards (NEHRP, ASCE/SEI, IBC): Strengths: Comprehensive site classification system, well-thought-out framework for site-specific analysis, and further detailed guidelines for liquefaction and other geohazards. Keeping up to date based on research outcomes and operating knowledge. Weaknesses: The multi-layered nature of the adoption scenario could be somewhat slow. The inconsistent adoption process of various portions of the IBC causes issues among different states and cities. Chinese Standards (GB): Strengths: Clearly defined seismic fortification intensity areas, comprehensive site classification, and a mandatory national standard guaranteeing its wide application. Deals with various geological conditions. Weaknesses: For certain geotechnical hazards, specific methods may be less detailed than those found in Japanese or American codes. Language barriers may hinder international collaboration and understanding. However, the legitimacy of soil microzonation within a global framework is yet to be viewed differently by most nations worldwide. While Vs-based classification and the need for site-specific analysis are standard, they converge only at fundamental principles. Some of the identified areas include thresholds for classification, the depth of treatment for defined hazards, and the boundaries of regulatory frameworks set by divided interests on some of the latter issues. Future international collaborations may involve establishing standards for site characterization and hazard assessment as common references, leveraging the existing strengths of individual standards to ultimately enhance global seismic resilience.
Recent research has refined seismic microzonation methodologies, especially for high-risk countries such as Turkey. Important international references that can be consulted are [13-15], which contain updated frameworks for liquefaction assessment and site classification of hazards. In particular, while the NEHRP 2023 guidelines [13] introduced updated procedures for soil characterization based on Vs, Japan's 2022 standards [21] offered enhanced protocols, particularly in urban microzonation. These advancements underscore the need for Turkey to align its practices more closely with those observed elsewhere in the

world, particularly in light of recent earthquakes. Local Turkish sources now complement this international perspective through critical institutional reports [16, 17]. The AFAD 2023 Microzonation Guide [19] establishes updated technical criteria for municipal implementations, and İBB's liquefaction maps [17] demonstrate applied methodologies for Istanbul. Academic works analyze Turkey-specific ground response patterns, with Çetin et al. [22] providing the Bornova district as a benchmark for local microzonation. These Turkish-language resources bridge the gap between international theory and regional practice, offering actionable insights for TEC compliance.

4. CONCLUSION

Soil microzonation is a valuable tool in modern earthquake engineering and urban planning, as it bridges the gap between regional seismic hazard assessment and site-specific design. A comparative study of the European (Eurocode), Japanese, American (NEHRP, ASCE/SEI, IBC), and Chinese (GB) standards revealed a globally shared perspective regarding the basic necessity of understanding and considering how local site effects can modify seismic ground motion. All these documents recognize that ground shaking characteristics are distinctly influenced by the condition of the underlying soil, thus requiring an elaborate site investigation to assess the safety and resilience of the built environment using advanced analytical methodologies. Probably, the most general feature of alignment between these various international standards is the use of shear wave velocity, chiefly Vs, as the vital indicator for soil classification. This standard metric has provided a quantitative basis for determining soil profile stiffness, enabling the variation of site-specific design response spectra and seismic forces. Additionally, a shared principle is the use of site-dependent ground motion analysis for the most significant facilities or those in challenging geological conditions; this approach involves moving beyond generalizing assumptions and considers each site for seismic design purposes. Despite these generalities, there are still some striking differences among the aforementioned standards in terms of their respective approaches and criteria for classification, as well as the extent to which individual geotechnical hazards have been addressed. Liquefaction is a relatively common practice among all standards. Still, more detailed and complicated procedures are found in the Japanese codes, which align with a rich historical background concerning the destruction caused by this phenomenon. There are also differences in the schemes of the regulations and the implementation process, which can have a significant impact on flexibility and the rate of uptake and enforcement of microzonation guidelines across different regions.

The following section summarizes the strengths of all four standards: the Eurocode establishes a harmonized, although flexible, framework for Europe; Japanese standards provide the most in-depth investigation of the site and liquefaction assessment; and American standards offer a strong and continuously evolving framework by the NEHRP and ASCE/SEI. An aforementioned mandatory national code, focusing on seismic fortification intensities, ensures China's broad application of seismic standards. Those differences also underscore that there will still be more hurdles to achieving complete harmony in the world, especially when defining the exact words for various soil classes and demonstrating the precise method of assessing complex geotechnical hazards, in short. A global commitment to soil microzonation underscores its crucial role in earthquake risk mitigation. Future developments in this area will likely focus on refining techniques for site characterization, enhancing numerical modeling of soil response during high-intensity shaking, and improving the correlation of findings from microzoning with urban planning and land policy. It would also ensure stronger global seismic resilience by fostering better international collaboration and establishing more unified guidelines for site classification and hazard assessment. Ultimately, such protections will safeguard life and property from all unpredictable forces generated by earthquakes. In summary, services microzonation works with ever-greater precision and effectiveness. Soil microzonation stands at the nexus of earthquake risk mitigation as it integrates regional seismic hazard maps and local soil response characteristics. Aside from Turkey, the other examples show the uniformity of their approach on the following three critical principles around the world: 1) Soil

classification, based on Vs30, is the key parameter to assess site effects, 2) Probabilistic seismic-hazard assessments fed back into building codes, and 3) Site-specific response and liquefaction studies performed for particular structures needing attention.
The Turkish regulatory system followed a similar approach: TEC 1998 was based on empirical soil indices; TEC 2007 introduced Vs30 and site-specific analyses; and TBEC 2018 aligned with international best practices by introducing probabilistic hazard maps, liquefaction and landslide requirements, and integrating them with urban transformation policies. This stepwise evolution, as represented in Table X, demonstrates a clear progression of the Turkish code system toward the global standard. Nevertheless, some barriers to practicality exist. Case studies in Istanbul, İzmir, Bursa, and Hatay demonstrated how local site effects and liquefaction significantly impact the patterns of earthquake damage. During the 2023 Kahramanmaraş earthquakes, it was shown that while TBEC 2018 requires microzonation-compatible parameters, municipal supervision and technical capacity remain lacking. Such a gap gravely confines the effectiveness of what should otherwise be advanced provisions.

In the future, Turkey's priorities should revolve around:
1) Deepening the municipal-level microzonation studies via MASW, HVSR, and GIS-based methods;

2) Standardizing data quality and reporting requirements on a region-wide basis;

3) Capability building within municipalities for enforcement and implementation, and

4) Integrating more robustly the AFAD guidelines into planning and retrofitting projects with TBEC provisions.

In this way, Turkey will find its way to level off regulatory ambition with practical application. This will not only position Turkish practice at par with Eurocode and NEHRP but could also serve as a model for other earthquake-risk countries seeking to match international standards with local realities. Ultimately, implementing a soil microzonation system that is securely integrated with the Turkish Earthquake Code will lead to safer construction practices, more resilient cities, and reduced seismic risks for future generations.

Declaration of Ethical Standards

The authors affirm that the present study was conducted under all relevant ethical guidelines and standards. This includes the proper attribution of authorship, accurate citation of sources, transparent reporting of research data, and the commitment to publishing original and non-plagiarized work. All data presented are authentic and derived from original investigations conducted by the authors.

Authorship Contribution Statement

Kaveh Dehghanian: Conceptualization, Methodology, Formal Analysis, Writing – Original Draft, Visualization, Supervision, Data Curation, Software, Investigation, Validation, Writing – Review & Editing, Project Administration, Resources

Declaration of Competing Interest

The author declare that there are no known competing financial or non-financial interests or personal relationships that could have appeared to influence the work reported in this paper.

Funding / Acknowledgements

This research received no specific grant from any funding agency in the public, commercial, or not-for-profit sectors.

Data Availability

The datasets generated and analyzed during the current study are available from the corresponding author upon reasonable request.

Use of Artificial Intelligence

Artificial Intelligence (AI) tools has not been used in this study. All technical content, analysis, interpretations, and conclusions were developed solely by the author. The author takes full responsibility for the integrity and originality of the work.

5. REFERENCES

[1] Karanfiloglu Law Office, “Understanding Turkish seismic safety regulations,” 2025. [Online]. Available:https://www.karanfiloglu.av.tr/en/understanding-turkish-seismic-safety-regulations/ [Accessed: June 23, 2025].

[2] G. Boyraz Bıçakcı, F. Özçep, S. Karabulut, and M. Cengiz, "The importance of seismic microzonation under the threat of an earthquake of the North Anatolian Fault in Nilüfer, Bursa, Türkiye," Journal of Applied Geophysics, vol. 229, p. 105489, 2024, doi: 10.1016/j.jappgeo.2024.105489.

[3] Ansal, A., Ergun, Z., Guler, E.: Seismic microzonation for earthquake risk mitigation in Turkey. In: Proc. 13th World Conf. Earthquake Eng. (13WCEE), Vancouver, Canada (2004). Available at: https://www.iitk.ac.in/nicee/wcee/article/13_1428.pdf [Accessed: June 23, 2025].

[4] Republic of Turkey Ministry of Public Works and Settlement: Seismic microzonation for municipalities manual. General Directorate of Disaster Affairs, Ankara (2007). Available at: https://en.afad.gov.tr/kurumlar/en.afad/40106/xfiles/seismic_microzonation_manual_eng.pdf

[5] Republic of Turkey Ministry of Public Works and Settlement: Seismic microzonation pilot studies for municipalities. General Directorate of Disaster Affairs, Ankara (2007). Available at: https://en.afad.gov.tr/kurumlar/en.afad/40108/xfiles/seismic_microzonation_pilot_studies_eng.pdf

[6] CEN (European Committee for Standardization): EN 1998-1:2004. Eurocode 8: Design of structures for earthquake resistance. Brussels (2004). Available at: https://www.phd.eng.br/wp-content/uploads/2015/02/en.1998.1.2004.pdf

[7] Ivanov, A.: Prospects of transition to European standards: Features of Eurocode 8. Res. Gate (2021). https://www.researchgate.net/publication/390997056

[8] Iwasaki, T.: Soil liquefaction studies in Japan: State-of-the-art. Soil Dyn. Earthq. Eng. 5(1), 2–68 (1986). https://doi.org/10.1016/0267-7261(86)90024-2

[9] FEMA: FEMA P-2082-1. NEHRP recommended seismic provisions for new buildings and other structures. Federal Emergency Management Agency, Washington, DC (2020). Available at: https://www.fema.gov/sites/default/files/2020-10/fema_2020-nehrp-provisions_part-1-and-part-2.pdf

[10] International Code Council (ICC): The future of hazard resilience: Building codes and best practices. Washington, DC (2021). Available at: https://www.iccsafe.org/wp-content/uploads/The-Future-of-Hazard-Resilience-Building-Codes-and-Best-Practices.pdf

[11] China Architecture Press: GB 50011-2010 (2016 English version). Code for seismic design of buildings. Beijing (2016). Available at: https://www.codeofchina.com/standard/GB50011-2010(2016).html

[12] Boulanger, R.W., Ziotopoulou, K.: Liquefaction evaluation methods: Updates from NEHRP 2023 guidelines. Earthq. Spectra 39(2), 45–67 (2023). https://doi.org/10.1193/1.1620526

[13] Darendeli, M.B.: Development of a new family of normalized modulus reduction and material damping curves. Ph.D. dissertation, University of Texas, Austin (2001)

[14] Menq, F.Y.: Dynamic properties of sandy and gravelly soils. Ph.D. dissertation, University of Texas, Austin (2003)

[15] Özcep, F., Yıldırım, E., et al.: Seismic site classification and microzonation in Marmara region. Soil Dyn. Earthq. Eng. 114, 1–12 (2018). https://doi.org/10.1016/j.soildyn.2018.05.021

[16] Alimoradi, A., Gokceoglu, C., et al.: GIS-based microzonation for seismic site effects and amplification. Eng. Geol. 272, 105630 (2020). https://doi.org/10.1016/j.enggeo.2020.105630

[17] Japanese Geotechnical Society (JGS): Revised standards for seismic microzonation in urban areas. JGS Press, Tokyo (2022)

[18] China Architecture Press: GB 50011-2021. Chinese code for seismic design of buildings. Beijing (2021)

[19] AFAD (Disaster and Emergency Management Authority): Türkiye sismik mikrobölgeleme rehberi (güncellenmiş versiyon). AFAD Yayın No. 2023/8, Ankara (2023). Available at: https://www.afad.gov.tr/kurumlar/afad.tr/2023/mikrobolgeleme-rehber.pdf

[20] İstanbul Büyükşehir Belediyesi (İBB): İstanbul ili sıvılaşma riski haritaları. İBB Deprem Risk Yönetimi Dairesi, İstanbul (2022)

[21] Ansal, A.: Türkiye'de deprem tehlike analizinde güncel yaklaşımlar. Türkiye Deprem Mühendisliği Derg. 5(2), 45–62 (2021)

[22] Çetin, K.Ö., et al.: İzmir'de sismik mikrobölgeleme çalışmaları: Bornova örneği. In: Proc. Zemin Dinamiği ve Deprem Mühendisliği Sempozyumu, İzmir, pp. 112–125 (2020)

Konya Mühendislik Bilimleri Dergisi, c.14, s.2, 966-978, 2026
Konya Journal of Engineering Sciences, v.14, n.2, 966-978, 2026
ISSN: 2667-8055 (Electronic)
DOI: 10.36306/konjes.1739978

AN INVESTIGATION OF THE EFFECT OF GEOPOLYMER COATED GEOTEXTILES ON THE BEHAVIOR OF WEAK SOILS UNDER LOADS

[1,*]Talha SARICI, [2]Mustafa ÖZCAN, [3]Aybüke MUTLU

[1,2,3] *Inonu University, Civil Engineering Department, Malatya, Türkiye*
[1]talha.sarici@inonu.edu.tr, [2]mustafa.ozcan@inonu.edu.tr, [3]mutluaybuke4444@gmail.com

Highlights

- Weak cohesive and cohesionless soil were reinforced with geotextile
- The improvement rate increased by coating geotextile with geopolymer
- Different mixture ratios were investigated to analyze mixture effect on coating

Graphical Abstract

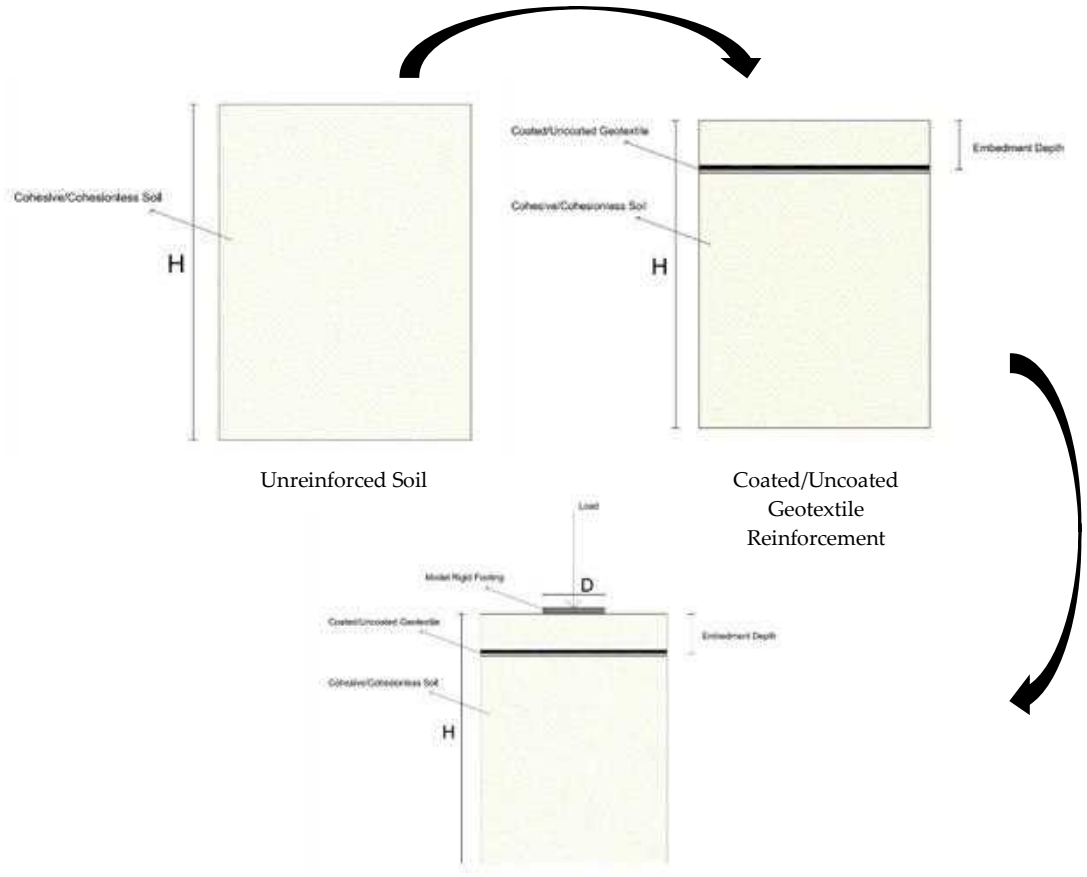


Figure Schematic representation of small-scale model loading tests

***Corresponding Author:** Talha SARICI, talha.sarici@inonu.edu.tr

Konya Mühendislik Bilimleri Dergisi, c.14, s.2, 966-978, 2026
Konya Journal of Engineering Sciences, v.14, n.2, 966-978, 2026
ISSN: 2667-8055 (Electronic)
DOI: 10.36306/konjes.1739978

AN INVESTIGATION OF THE EFFECT OF GEOPOLYMER COATED GEOTEXTILES ON THE BEHAVIOR OF WEAK SOILS UNDER LOADS

[1,*]Talha SARICI, [2]Mustafa ÖZCAN, [3]Aybüke MUTLU

[1,2,3] *Inonu University, Civil Engineering Department, Malatya, Türkiye*
[1]talha.sarici@inonu.edu.tr, [2]mustafa.ozcan@inonu.edu.tr, [3]mutluaybuke4444@gmail.com

(Received: 11.07.2025; Accepted in Revised Form: 14.12.2025)

ABSTRACT: Developing technology diversifies and improves the applications of geotechnical engineering as well as all other engineering fields. In the context of this study, an experimental program was conducted to investigate the effect of geotextile, which has been used in remediation works for a long time, and the recently increasingly popular geopolymer coated geotextile elements on the behavior of cohesionless and cohesive soil underloads. Firstly, the optimum geotextile embedment depth for cohesionless and cohesive soil was investigated. Then, geotextile elements coated with geopolymers with different mixture ratios were placed at the optimum depth and were subjected to load with vertical loading tests. Load-displacement curves of the experiments were generated; failure load values were obtained and compared. When the results of experimental studies were evaluated, it was observed that uncoated geotextile and coated geotextile components improved the behavior of both cohesive and non-cohesive weak soil underloads. The obtained increases reached up to 279% compared to the weak soils, however, amounts of increase were variable for both soils. It was predicted that the results obtained from the study can provide inspiration and guidance for the further usage of geopolymer coating applications in field and literature studies.

Keywords: *Coated geotextile, Cohesionless soil, Cohesive soil, Geotextile, Soil stabilization.*

1. INTRODUCTION

Before construction, a series of investigations are required to determine whether the foundation soil is geotechnically adequate. These investigations include observational and experimental studies and are required by directives/regulations in many regions [1]. As a result of geotechnical investigations, it is vital for the pre-construction process to take the necessary measures when it is determined that the foundation soil is inadequate against the loads from the structure. The foundation soil may be inadequate in terms of bearing capacity, have different settlement amounts and/or liquefaction potentials. At this point, soil improvement studies are conducted to eliminate these inadequacies [2-4]. While different improvement projects can respond to different problems, some methods can provide answers to more than one problem at the same time [5]. In this context, geotextiles can be placed in the ground to both increase the strength of the soil against incoming loads and reduce the amount of settlement by concentrating the loads on it [6-8]. Geotextile applications can be made as a single layer or placed in the soil in several layers [9]. It has a woven structure and is mostly powered by the friction force formed with soil layers between which it remains. Thus, while its axial capacity resists, the soil layers restrict its movement [6,7]. Although it can be subjected to abrasion/degradation due to in-ground effects, its service life in the soil can be increased with different methods [10,11]. At this point, geotextiles can be coated with chemical mixtures, but while geotextiles on their own do not cause damage to the environment, the presence of these chemicals can eliminate this advantage [10].

Previous studies [11-13] have shown that cement coated geotextiles can both withstand environmental impacts for longer periods of time and increase the load capacity of the geotextile. However, cement threatens the ecosystem due to the components it contains. In addition, the impact of the cement industry

***Corresponding Author:** Talha SARICI, talha.sarici@inonu.edu.tr

on the environment is often destructive and steps are being taken to reduce activities [14]. On the other hand, the formation of a rigid coating layer on the geotextile element, unlike the geotextile, can significantly increase the resistance to the loads transferred to the soil [11]. At this point, it is seen that geopolymer mixtures have been used as coating mixtures in recent studies [5,10,15]. Geopolymers, which can be formed with the use of alkaline activator and different binders, are considered to be more environmentally friendly than cement. In addition, the use of blast furnace slag and fly ash, which are waste materials as binders, contributes to waste recycling. The usage of these mixtures in different structural elements has been stated that the strength values obtained can be quite high [16]. In this context, it has been seen that the performance of the geotextile can be increased by coating with geopolymer. The geopolymer mixture also fills the pores of the geotextile, forming a rigid plate and increasing the resistance of the soil against loads [5]. Different binders, mixing ratios and layer thicknesses directly affect the efficiency of the coated geotextile. Geotextile coated with geopolymer resists the loads transferred to the soil and takes the loads on itself. Thus, the geotechnical properties of the soil can be improved [5,10].

When studies in the literature were evaluated, it was seen that there were studies on coated and uncoated geotextiles, but there were not enough studies on geopolymer coating and the effect of geopolymer coating on the behavior of weak soils underloads. In this context, within the scope of this study, to investigate geopolymer coating effect on this behavior, experimental studies were conducted by applying vertical loads with coated and uncoated geotextiles placed in cohesive and cohesionless weak soil. In order to obtain maximum performance from the reinforcement elements, the optimum depth was investigated, and recommendations were made for both soils. In addition, the deformations of the coated geotextile elements under load were also observed and interpreted. It is thought that, with coating process, geotextile elements will become preferable not only in slope applications but also in subbase projects such as geogrids in soil improvement solutions.

2. MATERIALS AND METHODS

In the experimental studies, the cohesive soil, placed in a test tank to create a weak soil, was obtained from an un-constructed area in the Kiltepe region of Malatya, Türkiye. The cohesionless soil was obtained from a sand quarry operating in Malatya. The soils were oven dried by heating at 110 (±5) degrees in the laboratory. The cohesive soil was crushed to reduce the grain size and sieved for classification and ease of processing. The engineering properties of the soil were determined by traditional laboratory tests. Based on the laboratory studies, the properties of the cohesive and cohesionless soils are presented in Table 1 and 2, respectively.

Within the scope of the study, the cohesionless soil was used as in its loose state. For the cohesive soil, the water content was chosen as 40 percent to create a weak soil environment [17]. The tank was divided into equal parts of 5 cm, and the soils were placed in the test tank as layers by calculating the required soil mass for each 5 cm height. The properties of the geotextile used in the study are as shown in Table 3 and the diameter of the geotextile element (15cm) selected for the experimental study was chosen according to the surface area of the application. The geotextiles used in the experimental studies were placed at 5 different depths (0.17, 0.33, 0.67, 1 and 1.33 times the diameter (D) of the model rigid foundation) [18-20]. After the geotextile placement, the soil remaining above the geotextile was again weighed and placed in layers. The optimum embedment depth and maximum bearing strength values were experimentally determined by vertical loading tests conducted at different depths (Figure 1).

In the first stage, a 5 cm diameter model rigid foundation was placed on the unreinforced soil and subjected to loading. In the following experiments at different embedment depths, the cohesionless soil mass was kept constant and geotextile reinforcements were placed at the determined depths, and the results were obtained by performing vertical loading experiments with a loading rate of 1.0 mm/min [28].

Table 1. Properties of cohesive soil [20]

Parameters	Units	Values	Standards
Natural unit volume weight (γ_n)	kN/m^3	16.80	[21]
Specific gravity (G_s)	-	2.65	[21]
Classification	-	ML	[22]
Maximum unit volume weight (γ_{dmax})	kN/m^3	15.30	[23]
Optimum water content (ω_{opt})	%	25.5	[23]
Plastic limit (L_P)	%	29.83	[24]
Liquid limit (L_L)	%	45.16	[24]

Table 2. Properties of cohesionless soil [5]

Parameters	Units	Values	Standards
Specific gravity (G_s)	-	2.74	[21]
Classification	-	SP	[22]
Minimum dry unit volume weight (γ_{dmin})	kN/m^3	14.50	[25]
Maximum dry unit volume weight (γ_{dmax})	kN/m^3	16.50	[25]
Coefficient of curvature (C_c)	-	0.926	[26]
Coefficient of uniformity (C_u)	-	2.375	[26]
Angle of internal friction (φ)	Degree (°)	40	[27]



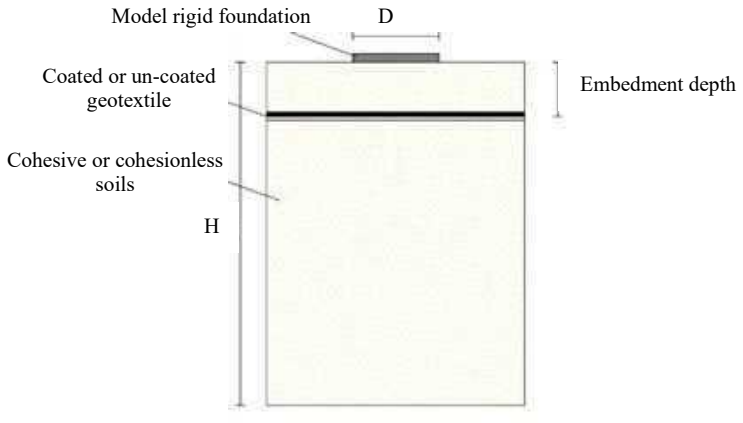


Figure 1. Weak soil deposits, vertical loading test set-up and schematic illustration (D= diameter of footing, H= depth of the experimental tank)

The same procedures were repeated for cohesive weak soil environments. Based on these studies, the optimum geotextile embedment depth was determined separately for both cohesionless and cohesive soils. At all depths beyond these depths, it was observed that the bearing capacity obtained in weak soil environments decreased and the geotextile reinforcement did not perform sufficiently. Based on these experiments, after determining the optimum depths, the behavior of geotextile reinforcement coated with

geopolymers prepared at different w/s ratios at these depths was investigated in weak soil environments.

Table 3. Properties of geotextile [28]

Parameters	Units	Values
Raw material	-	Polypropylene
Type	-	Unwoven
Tensile strength	kN/m	13/15
Unit weight	g/cm^2	500
Pore opening	μ	120
Thickness	μ	1500
Elongation at break	%	50
Dynamic puncture strength	μ	20000
Static puncture strength	kN	2.5
UV resistance	%	70
Liquid permeability	m/s	0.06

The geopolymers prepared at optimum mixing ratios of (0.35-0.40-0.45) w/s (alkali solution/binder material) as recommended by Gupta et al. [10] for the experimental studies were placed in the cohesionless and cohesive weak soils at the optimum depth determined and loading experiments were conducted. The mixture ratios used to form geopolymer elements are shown in Table 4. Before starting the experiment, solutions were prepared by mixing the determined amounts of sodium hydroxide, sodium silicate and water and the solution was kept for 24 hours since the reaction was exothermic and then blast furnace slag (BFS) was added to obtain the geopolymer mixture. It was mixed until the agglomeration disappeared and applied to the pre-cut geotextile surface with a brush at a rate of approximately 0.5 g/cm2. Then, the surface was cured in air for 7 days and the experimental results obtained at the end of the curing period were analyzed to determine the optimum w/s content. The properties of components of alkaline activated solution (AAS) were shown in Table 5. The experimental program for the experimental studies conducted with different soils and variables shown in Table 6.

Table 4. Geopolymer mixture ratios [10]

w/s ratio	Mixture amount (kg/m^2)	Binder (kg/m^2)	Sodium Hydroxide (kg/m^2)	Sodium Silicate (kg/m^2)	Water (kg/m^2)
0.35	0.2497	0.1583	0.058	0.706	0.498
0.40	0.2229	0.1358	0.00356	0.0439	0.0389
0.45	0.1997	0.1176	0.00312	0.0382	0.0407

Table 5. Properties of AAS [29]

Parameter	Sodium Hydroxide	Sodium Silicate
Density (g/cm^3)	-	1.381
BOME (Be) (20℃)	-	40
Na_2O (%)	-	10.11
SiO_2 (%)	-	28.45
Module	-	3.11
Molecular formula	NaOH	-
Molecular mass (g/mol)	40	-
Color	White	-
Ph	13-14	-
Relative density (g/cm^3)	2.13	-

Table 6. Experimental study program

Soil type	Embedment depth	w/s ratio
Cohesionless	0.17/0.33/0.67/1/1.33D	-
Cohesionless	0.33D	0.35/0.40/0.45
Cohesive	0.17/0.33/0.67/1/1.33D	-
Cohesive	0.67D	0.35/0.40/0.45

3. RESULTS AND DISCUSSION

3.1. Cohesionless soil

In the first stage, geotextiles were placed at various depths in weak soils and analyses were conducted with a model loading setup to determine an optimum embedment depth. The load value corresponding to 5% and 10% of the foundation diameter was selected as the failure load [5]. The load and displacement curves of the experimental studies with cohesionless soil are shown in Figure 2 and the failure load values are shown in Figure 3.

In Figures 2 and 3, SGT-U is the unreinforced cohesionless soil, SGT-017 is 0.17D deep geotextile placement, SGT-033 is 0.33D deep geotextile placement, SGT-067 is 0.67D deep geotextile placement, SGT-100 is 1D deep geotextile placement, SGT-133 is 1.33D deep geotextile placement.

When Figure 2 is evaluated, it was observed that the inclination of the load-displacement curve was constant up to a deformation of approximately 4 mm and then changes were observed in the following displacements. While the load-displacement behavior was the same for SGT-U, SGT-017, SGT-033 up to 4 mm displacement, a significant increase was obtained in the use of SGT-067 with increasing displacement. When the failure loads given in Figure 3 were also evaluated, it can be clearly seen that the best performance was obtained using SGT-033 placement. It was thought that a deformation of 4 mm was required for the cohesionless soil placed in its loosest state to compress underload and then transfer the load to the geotextile.

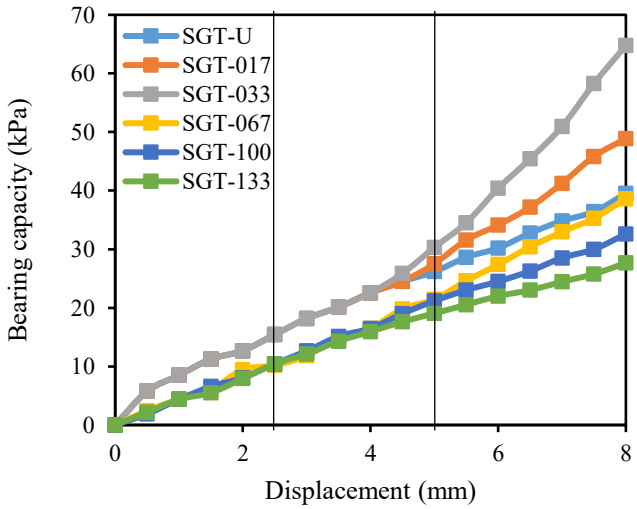


Figure 2. Load-displacement curves of unreinforced and reinforced cohesionless weak soil deposit at different embedment depths

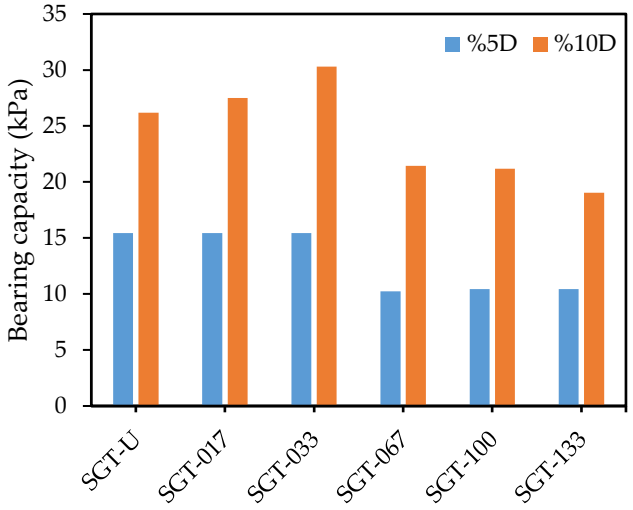


Figure 3. Failure load values for different geotextile embedment depths in cohesionless weak soil

However, in the layout after SGT-033, it was observed that stress areas were formed in the cohesionless soil before the stresses were transferred to the geotextile. At this point, the geotextile separates the soil layers from each other and since the stresses do not reach the geotextile, the soil responds to the loads through an area as much as the layer above the geotextile. This leads to smaller failure load values even in the unreinforced condition of the cohesionless soil. Therefore, 0.33D was chosen as the optimum depth at which the soil stresses were transferred to the geotextile and the efficiency of the geotextile was the highest among all applications.

After determining the optimum embedment depth, the geotextile surface was coated with geopolymers prepared at w/s ratios of 0.35 (SGP-030), 0.40 (SGP-040) and 0.45 (SGP-045). The coated geotextiles were placed at optimum depth between the soil layers and model loading tests were conducted. Results of the vertical loading tests are given in Figure 4 and bearing capacities are presented in Table 7.

When Figure 4 and Table 7 are evaluated, the maximum performance was obtained with the specimens prepared at a w/s ratio of 0.45 (SGP-045) among the different geopolymer coated geotextiles placed at a depth of 0.33D. When the distance between the geotextile and the soil surface was very small, the incoming stresses forced the cohesionless soil to heave and created a soil deposit at a lower depth because the geotextile with coating behaved as a stiffer volume in the middle of the cohesionless soil [5]. However, it can be clearly seen that much higher load values can be achieved with coated geotextile applications compared to uncoated geotextile. Therefore, coating the geotextile element significantly improves the performance of the geotextile in cohesionless soil. In fact, this improvement was doubled with the use of SGP3 compared to SGT-033. It was also seen that the amount of improvement varies when different mixture ratios were evaluated. Therefore, it was clearly seen that the binder ratio in geopolymer blends directly affected the behavior under loads. Images of the coated geotextiles after the experiments performed are given in Figure 5.

When Figure 5 was evaluated, it was observed that the amount of deformation decreased significantly as the w/s ratio increased. The reason for this is thought to be the formation of a more rigid plate due to the enhancement of the geopolymerization reaction. The longer it takes for the plate to fail, the longer the load transfers to the geotextile element. In addition, considering that the loads transferred to the soil first come on the coating element, the effect of this layer on the behavior underload is quite high [5]. In addition, the fact that the stresses in the cohesionless soil under load are concentrated from the bottom of the foundation towards the center of the coated geotextile can be understood by the concentration of cracks in the center of the coated geotextile. According to Figure 5, it is predicted that more rigid coating leads to better bearing performance.

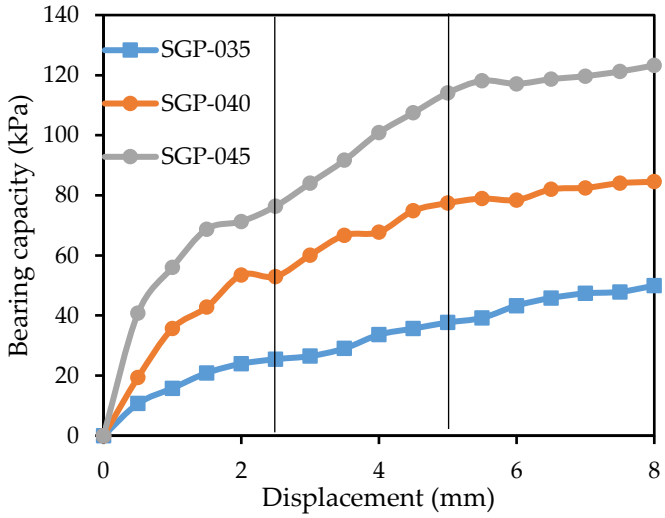


Figure 4. Load-displacement curves of reinforcement application using geopolymer coated geotextile

Table 7. Bearing capacities of coated geotextile applications

Name	Soil type	Embedment depth	w/s ratio	Bearing capacity (kPa)	
				%5D	%10D
SGP-035	Cohesionless	0.33D	0.35	53.17	77.20
SGP-040	Cohesionless	0.33D	0.40	25.61	37.74
SGP-045	Cohesionless	0.33D	0.45	17.42	51.79



Figure 5. Post-experiment images of geopolymer-coated geotextiles with different w/s ratios, 0.35, 0.40 and 0.45, respectively

3.2. Cohesive soil

Experimental studies were conducted to investigate how uncoated and coated geotextiles change the behavior of cohesive weak soil underloads. Figure 6 shows the load-displacement curves of the geotextile usage, and the failure load values are given in Figure 7. Figure 6 shows that the best performance was obtained with CGT-067. Considering the failure load values given in Figure 7, 1.72 times more failure load could be obtained with CGT-067 usage compared to the unreinforced cohesive weak soil. Since the maximum performance was obtained with CGT-067, 0.67D was selected as the optimum embedment depth. It was observed that at depths higher than this depth, the behavior of the cohesive weak soil under load changed and only after very long deformations, CGT-100 and CGT-133 reached the load values of the cohesive unreinforced soil. Cohesive soil, which has a very low resistance potential due to its high-

water content, had less soil volume interacted due to the interruption between the layers and therefore could not create sufficient resistance [10].

In the Figures 6 and 7, CGT-U is the unreinforced weak soil, CGT-017 is the geotextile application at 0.17D depth, CGT-033 is the geotextile application at 0.33D depth, CGT-067 is the geotextile application at 0.67D depth, CGT-100 is the geotextile application at 1D depth, CGT-133 is the geotextile application at 1.33D depth.

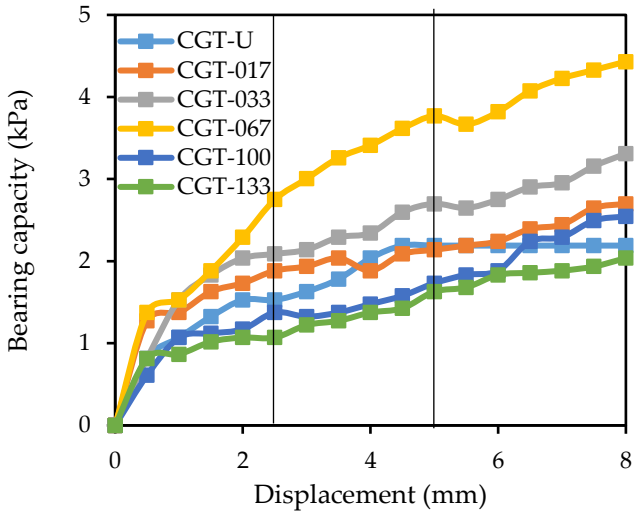


Figure 6. Load-displacement curves of unreinforced and geotextile reinforced cohesive weak soil at different embedment depths

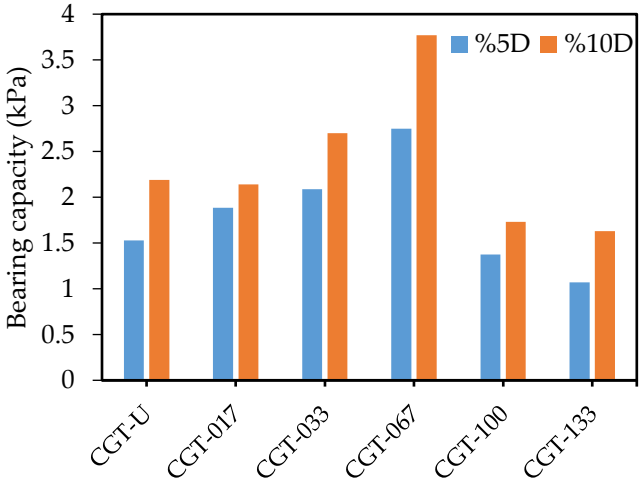


Figure 7. Load-displacement curves of unreinforced and geotextile reinforced clayey weak soil at different embedment depths

Then, the effect of the coated geotextile on the behavior of cohesive soil under loads were investigated. In this context, geotextiles were coated with geopolymers prepared at w/s ratios of 0.35 (CGP-035)-0.40 (CGP-040)-0.45 (CGP-045). The coated geotextiles were placed at an embedment depth of 0.67D and subjected to vertical loading. The load-displacement curves are presented in Figure 8 and bearing capacities are presented in Table 8.

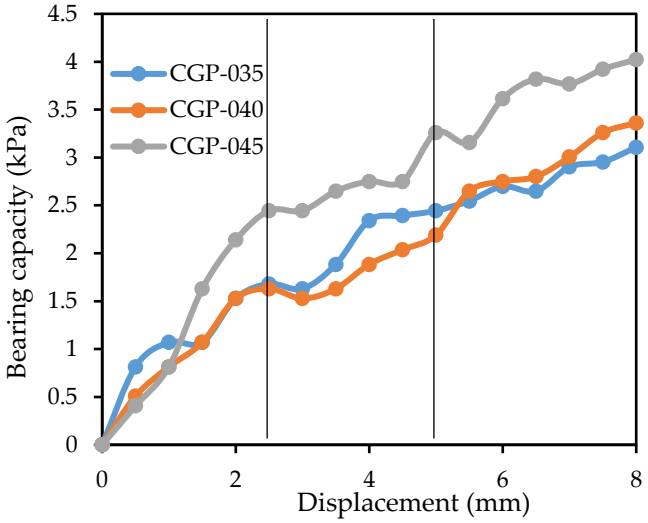


Figure 8. Load-displacement curves of geopolymer coated geotextile application on cohesive soil

Table 8. Bearing capacities of coated geotextile applications

Name	Soil type	Embedment depth	w/s ratio	Bearing capacity (kPa)	
				%5D	%10D
CGP-035	Cohesive	0.67D	0.35	1.68	2.44
CGP-040	Cohesive	0.67D	0.40	1.63	2.19
CGP-045	Cohesive	0.67D	0.45	2.44	3.26

Figure 8 and Table 8 show that the highest improvement is achieved with CGP-045 at a w/s ratio of 0.45. The improvement in value obtained was lower than using CGT-067. At this point, it was thought that the high-water content of the cohesive soil was an important factor. Even if the geotextile divides the soil layer, it interacts more with the soil layers due to its woven structure and its lower stiffness. However, obtaining a very rigid layer in the geopolymer coating process can cause the loads to be met in the layer above the coated geotextile. In fact, the soil, which is quite weak, fails in this upper layer and therefore less soil volume is trying to resist the load. As the rigid foundation penetrates into the soil, the cohesive soil tries to form a denser form, but due to the high-water content, the soil around the foundation projection can take the load to be transferred downwards. At this point, it is predicted that the distribution of the vertical resistance areas to be collected against the vertical load reduces the bearing capacity to be obtained. Figure 9 shows the post-experiment images of the coated geotextiles.



Figure 9. Post-experiment image of geotextiles coated with geopolymer at different w/s ratios, 0.35, 0.40 and 0.45, respectively

When Figure 9 is evaluated, similar to the cohesionless soil, more rigid plates were obtained, and less deformation was observed as the geopolymerization enhancement increased. Distribution of the vertical

resistance areas to be collected against the vertical load reduces the bearing capacity to be obtained. Therefore, increased stiffness resulted in higher bearing capacities and less damage to the coating.

3.3. Literature comparison

In the last stage, the experiments performed on cohesionless soil in this study and the and study performed by Öztürk et al. [11] were compared in terms of improvement ratios. Öztürk et al. [11] performed loading experiments by placing geotextile and cement coated geotextile on cohesionless soil with 70% relative density. In both studies, coated and un-coated geotextiles were placed at determined optimum embedment depth. In this context, the failure load values obtained with coated and uncoated geotextile were ratioed to the failure load of the unreinforced soil and the improvement ratio values were obtained for both studies [20]. Figure 10 shows the improvement ratios obtained for both this study and Öztürk et al. [11].

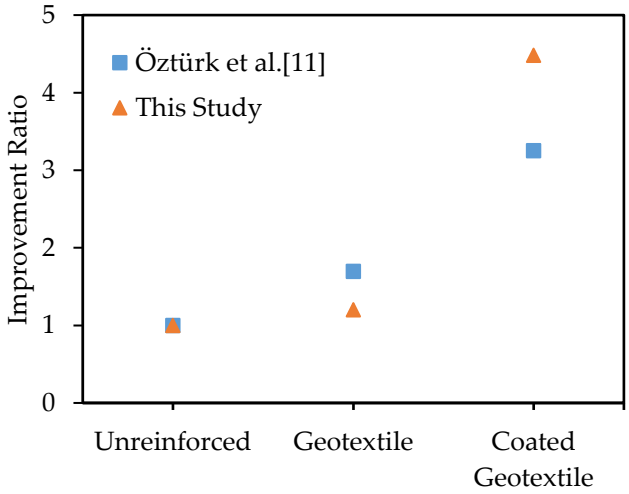


Figure 10. Comparison of improvement ratios

When Figure 10 is evaluated, it is seen that significant increases in bearing capacity can be obtained by using both geotextile and coated geotextile in cohesionless soil. The improvement ratio values were calculated as 1.2 and 1.69 for the usage of un-coated geotextile, 4.48 and 3.25 for coated geotextile for this study and Mitat et al. [11], respectively. Even though the density values for the cohesionless soil and the coating element were different, the improvement trend is similar for both types of coatings. However, a higher rate of improvement was achieved with the geopolymer coating process compared to the cement coating.

Considering the production waste (blast furnace slag) usage in geopolymer structure, coating process contributes to recycling and provides economic benefits. Also, geopolymer structures are more eco-friendly than cement-based elements. In addition, using geotextile elements reduces the thickness of embankment layers, with contribution of coating process, more gain can be achieved. In this context, more contributions can be made in terms of sustainability. For field applications, considering a road embankment, after geotextile placement on the desired layer, geopolymer mixture can be transported to project area and be applied similar to concrete applications. Since geopolymerization process is faster than hydration, possible time gains should also be considered. In this context, coating geotextiles with geopolymers has a high usability as an alternative to cement.

4. CONCLUSIONS

In order to investigate how uncoated and geopolymer-coated geotextile with different mixture ratios placed in cohesive and cohesionless soil change the behavior of weak soil under load, vertical loading tests were conducted. In the first stage of the experimental studies, the model rigid foundation was placed on the unreinforced soil, and the load was applied with the model loading test setup, and the results were recorded. Then, the optimum embedment depth was investigated by placing geotextile at different depths (0.17D, 0.33D, 0.67D, 1D and 1.33D). After determining the optimum geotextile embedment depth, geopolymer mixture was prepared and geotextile surface was coated with geopolymer prepared at different mixture ratios (0.35, 0.40 and 0.45 w/s). The coated geotextiles were placed at the optimum embedment depth in both cohesive and cohesionless soil and model loading tests were performed. Results obtained from the experimental studies revealed that:

- Usage of geotextile improves the behavior underloads for both cohesive and cohesionless soils. In the cohesionless soil, an increase of 16% in the failure load value was observed with the geotextile usage. However, this difference increased with increasing deformation due to the working principle of the geotextile. Such that, when a deformation of 8 mm was reached, an increase of 64% was achieved with the geotextile. In cohesive soil, while the failure load value increased by 72%, this value was 102% with increasing deformation.

- The use of coated geotextiles significantly improved the performance of weak soils within the scope of experimental studies. In cohesionless soil, an increase of 279% in failure load was obtained with coated geotextiles placed at optimum depth (0.33D). In cohesive soil, a 52% increase in the failure load was obtained with the coated geotextile placed at the optimum depth (0.67D). The difference in the reinforcement ratio was predicted to be due to the difference in the interlocking between the geopolymer coated geotextile and the soil.

- It was observed that the different mixture ratios used to form the geopolymer had a direct effect on the performance obtained. It was observed that the best performance was obtained with 0.45 w/s in coated geotextiles placed at the optimum depth for both soils. It is thought that this gain was achieved due to the increased mixture ratio increasing the stiffness of the coating. It was also observed that the deformation was less in coated geotextiles with 0.45 w/s ratio compared to 0.35 and 0.40 w/s ratios in both soils.

- This study aims to improve capacity gain where geotextile is suitable or chosen for application. In addition, the proposed method can be used in civil engineering projects where underground leakages are considered as dangerous considering separation capabilities of coating process. In addition, excessive pore pressures should be considered for soils with water presence to prevent possible failures. Pervious coating elements (e.g.: pervious concrete) may be investigated in future studies to eliminate pore pressure effects.

- Findings of this study are valid for cohesive/non-cohesive soils, geotextiles and geopolymers whose properties are described in the previous sections and cannot be used alone in design.

Declaration of Ethical Standards

The author(s) of this article declare that the materials and methods used in this study do not require ethical committee permission and/or legal-special permission.

Credit Authorship Contribution Statement

Talha Sarici: Writing - review and editing, Writing - original draft, Verification, Supervision, Software, Resources, Project management, Methodology, Research**. Mustafa Özcan:** Writing- revising and

editing, Methodology, Formal analysis. **Aybüke Mutlu:** Validation, Methodology, Research.

Declaration of Competing Interest

The author(s) of this article declare that there is no conflict of interest in this study.

Funding / Acknowledgements

There is no funding / acknowledgements

Data Availability

Researchers can contact the correspondent author for the data required.

Use of Artificial Intelligence

No artificial intelligence tools were used in this article.

5. REFERENCES

[1] F. Statescu, D. Cotiusca-Zauca, V. L. Pavel, P. Cojocaru, and M. Pastia, "Modern techniques for investigation of some of the soil physical properties," *Scientific Papers*, vol. 41, 2015.

[2] T. Sarici and M. Ozcan, "Evaluation of the behavior of screw pile groups in clay soils under compressive and uplift forces," *Geomechanics and Engineering*, vol. 41, no. 5, p. 543, 2025.

[3] T. Geçkil, T. Sarıcı, and B. Karabaş, "Siyah karbon stabilizasyonlu zeminin rijit kaplama kalınlığı ve maliyetine etkileri," *El-Cezeri*, vol. 8, no. 3, pp. 1372–1384, 2021.

[4] M. Orhan, N. S. Işık, and M. Özer, "Zeminlerin ince tane büyüklüğünün doğru belirlenmesinin önemi," *Politeknik Dergisi*, vol. 6, no. 4, pp. 671–675, 2003.

[5] T. Sarici and M. Ozcan, "Using geopolymer coated and uncoated geotextile as a hybrid method to improve uplift capacity of screw piles in cohesionless soil," *Alexandria Engineering Journal*, vol. 105, pp. 666–681, 2024.

[6] X. Man, H. Zhou, X. Liu, Y. Chen, and H. Qu, "Permeability test of geotextile-soil system under different sand filling heights," *Journal of Measurements in Engineering*, vol. 13, no. 1, pp. 168–184, 2025.

[7] A. Z. Abdulkrem, A. S. A. Rashid, T. Amhadi, K. N. Mat Said, A. H. Abdul Rashid, A. Ismail, and A. Dehghanbanadaki, "The effectiveness of nonwoven kenaf geotextile in improving load bearing of soft soil," *Transportation Infrastructure Geotechnology*, vol. 12, no. 1, pp. 1–18, 2025.

[8] M. G. Eltarabily, T. Selim, M. K. Elshaarawy, and M. H. Mourad, "Numerical and experimental modeling of geotextile soil reinforcement for optimizing settlement and stability of loaded slopes of irrigation canals," *Environmental Earth Sciences*, vol. 83, no. 8, p. 246, 2024.

[9] J. N. Thuo, K. H. Yang, and C. C. Huang, "Infiltration into unsaturated reinforced slopes with nonwoven geotextile drains sandwiched in sand layers," *Geosynthetics International*, vol. 22, no. 6, pp. 457–474, 2015.

[10] S. Gupta, A. GuhaRay, A. Kar, and V. P. Komaravolu, "Performance of alkali-activated binder-treated jute geotextile as reinforcement for subgrade stabilization," *International Journal of Geotechnical Engineering*, 2021.

[11] M. Öztürk, C. Kayadelen, G. Altay, and Y. Önal, "Investigation of load-displacement behavior of cement-coated geotextile reinforced sandy soils," *Niğde Ömer Halisdemir Üniversitesi Mühendislik Bilimleri Dergisi*, vol. 12, no. 4, pp. 1232–1238, 2023.

[12] M. Öztürk, G. Altay, and C. Kayadelen, "Assessment of the utilization of cement-treated geotextile as a reinforcement element for highway base layer under cyclic loading," *Transportation Geotechnics*, vol. 48, p. 101333, 2024.

[13] A. Fakhrabadi, M. Ghadakpour, A. J. Choobbasti, and S. S. Kutanaei, "Influence of the non-woven geotextile (NWG) on the engineering properties of clayey-sand treated with copper slag-based geopolymer," *Construction and Building Materials*, vol. 306, p. 124830, 2021.
[14] N. Mohamad, K. Muthusamy, R. Embong, A. Kusbiantoro, and M. H. Hashim, "Environmental impact of cement production and solutions: A review," *Materials Today: Proceedings*, vol. 48, pp. 741–746, 2022.
[15] V. S. Jayawardane, V. Anggraini, A. T. Li-Shen, S. C. Paul, and S. Nimbalkar, "Strength enhancement of geotextile-reinforced fly-ash-based geopolymer stabilized residual soil," *International Journal of Geosynthetics and Ground Engineering*, vol. 6, no. 4, p. 50, 2020.
[16] E. Ekinci, İ. Türkmen, F. Kantarci, and M. B. Karakoç, "The improvement of mechanical, physical and durability characteristics of volcanic tuff based geopolymer concrete by using nano silica, micro silica and Styrene-Butadiene Latex additives at different ratios," *Construction and Building Materials*, vol. 201, pp. 257–267, 2019.
[17] T. Sarici and M. Ozcan, "Investigation of screw pile behavior in cohesive soil under uplift and compressive forces by experimental studies and numerical analyses," *Arab Journal for Science and Engineering*, 2024.
[18] S. Aria, S. K. Shukla, and A. Mohyeddin, "Optimum burial depth of geosynthetic reinforcement within sand bed based on numerical investigation," *International Journal of Geotechnical Engineering*, 2020.
[19] S. M. Yousuf, M. A. Khan, S. M. Ibrahim, F. Ahmad, P. Samui, and A. K. Sharma, "An evaluation of square footing response on lime-treated geotextile-reinforced silty sand: Contrasting experimental and computational approaches," *Frontiers in Built Environment*, vol. 10, 2024.
[20] B. Ok, T. Sarici, A. Demir, T. Talaslioglu, and A. Yildiz, "Investigation of construction and demolition materials reinforced by geosynthetics," *Proceedings of the Institution of Civil Engineers - Engineering Sustainability*, vol. 176, no. 5, pp. 285–298, 2023.
[21] ASTM International, "Standard test methods for specific gravity of soil solids by water pycnometer," ASTM D854, 2014.
[22] ASTM International, "Standard practice for classification of soils for engineering purposes (Unified Soil Classification System)," ASTM D2487, 2017.
[23] ASTM International, "Standard test method for determination of water content of soil by direct heating," ASTM D4959, 2016.
[24] ASTM International, "Standard test methods for liquid limit, plastic limit, and plasticity index of soils," ASTM D4318, 2017.
[25] ASTM International, "Standard test methods for minimum index density and unit weight of soils and calculation of relative density," ASTM D4254, 2016.
[26] ASTM International, "Standard test method for particle-size analysis of soils," ASTM D422, 2007.
[27] ASTM International, "Standard test method for direct shear test of soils under consolidated drained conditions," ASTM D3080, 2011.
[28] T. Sarici, T. Geckil, B. Ok, and H. S. Aksoy, "An investigation of the usability of alkali-activated blast furnace slag-additive construction demolition waste as filling material," *Materials*, vol. 18, no. 2, p. 398, 2025.
[29] T. Geckil, T. Sarici, and H. S. Aksoy, "The usability of construction and demolition wastes stabilized using alkali activated fly ash as filler material," *Revista de la Construcción*, vol. 24, no. 2, pp. 428–448, 2025.

Konya Mühendislik Bilimleri Dergisi, c.14, s.2, 979-997, 2026
Konya Journal of Engineering Sciences, v.14, n.2, 979-997, 2026
ISSN: 2667-8055 (Electronic)
DOI: 10.36306/konjes.1768025

A NOVEL APPROACH FOR ANALYTICAL MODEL OF METAL-METAL FUNCTIONALLY GRADED CIRCULAR BEAM

[1,*]Ali ÖZTÜRK

[1]*Necmettin Erbakan University, Faculty of Engineering, Department of Mechanical Engineering, Meram, 42090, Konya, TÜRKİYE*
[1]aliozturk@erbakan.edu.tr

Highlights

- A novel approach to define metal-metal functionally graded circular beam
- Mathematical formulation based on higher-order shear deformation theory
- Kinematic relations derived of functionally graded circular beam after modelling
- Very flexible approach to be used for any type of loading
- A practical approach simplifying to calculate stress analysis and deflections

***Corresponding Author:** Ali ÖZTÜRK, aliozturk@erbakan.edu.tr

Konya Mühendislik Bilimleri Dergisi, c.14, s.2, 979-997, 2026
Konya Journal of Engineering Sciences, v.14, n.2, 979-997, 2026
ISSN: 2667-8055 (Electronic)
DOI: 10.36306/konjes.1768025

A NOVEL APPROACH FOR ANALYTICAL MODEL OF *METAL-METAL FUNCTIONALLY* GRADED CIRCULAR BEAM

[1,*]Ali ÖZTÜRK

[1]*Necmettin Erbakan University, Faculty of Engineering, Department of Mechanical Engineering, Meram, 42090, Konya, TÜRKİYE*
[1]aliozturk@erbakan.edu.tr

(Received: 18.08.2025; Accepted in Revised Form: 15.12.2025)

ABSTRACT: Functionally graded materials are advanced inhomogeneous materials in which element gradation changes continuously and smoothly from one phase to the other. The purpose of this study is to derive a novel and flexible model for metal-metal functionally graded circular beams. By means of this novel model, it is possible to determine the displacements numerically under all kinds of loading as well as to perform both elastic and plastic stress analysis. The mathematical formulation is derived through higher-order shear deformation theory. For this purpose, macro-mechanical model of functionally graded circular beam is constructed initially. Then, kinematic relations of functionally graded circular beam are derived. Based on Hamilton's principle, a system of differential equations governing the static behavior of a functionally graded circular beam is derived. Numerical results are presented after exact solutions are obtained. The advantage of this novel model is that it is possible to define not only linear gradation but also parabolic gradation from center to the surface of the beam.

Keywords: *Analytical Model, Circular Beam, Flexure, Functionally Graded Material (FGM), Higher-Order Shear Deformation Theory*

1. INTRODUCTION

Today, with developing technology, the need for more functional materials is continuously increasing. Since both high strength and high thermal resistance are required, especially in space technology, composite materials, which are called functionally graded materials (FGMs) in the international literature and mostly consisting of metal-ceramic couple, have been developed in order to combine these two properties in one material [1]. The composition is varied from a ceramic-rich surface to a metal-rich surface with a desired variation of the volume fractions of the two materials in between the two surfaces [2]. FGMs are anisotropic materials since the material properties change from one surface to the other. In classical composite materials, sharp changes that occur at the junction of different materials can cause stress concentrations and crack formations. In FGMs, this problem is eliminated by means of the gradual transition from one material to the other.

Various applications related to beams, cylinders, disks, plates and shells made of FGMs have been seen in both experimental and theoretical studies in the literature [3]-[11]. Various equivalent single-layer theories with enough approaches have been developed to correctly foresee the behaviors of functionally graded beams, plates and shells [12]-[16]. Since the advent of FGMs, the structural behavior of functionally graded components under multiple loading has been the subject of many theoretical and experimental studies, including bending, stability, free and forced vibration analyses. To mention some of the studies on; Reddy [17] has reported the theory of nonlinear beams attached to a microstructure using a modified dual stress theory and the corresponding nonlinear static problem of functionally graded beams is investigated using the finite element method [18]. Madenci and Gülcü [19] proposed artificial neural networks-based model was performed well for maximum displacement of functionally graded beams

***Corresponding author:** Ali ÖZTÜRK, aliozturk@erbakan.edu.tr

such as Young's modulus ratio, length to thickness ratio, effect of shear correction factor, effect of power-low exponent. An alternative solution procedure presented by Madenci [20] using variational methods for static analysis of functionally graded beams with parabolic shear deformation beam theory and mixed formulation. Since the functionally graded structures are mostly used in high temperature environments, significant changes in the mechanical properties of the component materials are expected. Consideration of this temperature dependence is essential for an accurate estimation of the mechanical response. Thus, the effective material properties (such as Young's modulus) are assumed to be temperature dependent and can be expressed as a nonlinear function of temperature. Several micro-mechanical models of FGMs have been developed and studied by researchers [21]-[32]. Akbarzadeh, Abedini [33] examined the influence of alternative micromechanical models on the macroscopic behavior of a functionally graded plate based on classical and shear-deformation plate theories.

The effects of radial non-uniformity of material on the mechanical response in cylinders under different loading conditions have been studied by many researchers [34]-[36]. Nedin, Nesterov [37] analyzed thermal conductivity problem of functionally graded cylinders by using two semi-analytic methods. Wang and Mai [38] obtained one-dimensional and time-dependent temperature distribution in a functionally graded cylinder with finite element method and performed stress analysis accordingly. Shao [39] considered a cylinder made of functionally graded material as a multi-layer cylinder and performed stress analysis by taking each layer as homogeneous but the material properties vary radially from one layer to the other and independent of the temperature. As can be seen, in some of the studies carried out so far, the functionally graded cylinder was considered as very thin layers, and these layers were considered homogeneous within themselves. Also, the material properties were taken to vary from layer to layer accordingly. In some, the material properties are taken to vary with the exponential function in the radial direction.

There are still some uncertainties about the most reasonable homogenization schemes for the estimation of stresses in each spherical structure, as there are very few experimental results that can provide suitable test databases for metal-ceramic functionally graded devices. While this is applied to metal-ceramic FGMs, it is applied to even more metal-metal FGMs. Indeed, metal-metal FGMs are also gaining more attention in engineering.

In the literature, there is not enough test data for the distribution of volume fractions or associated Young's modulus in cylindrical metal-metal functionally graded structures. Elaborating tools for micro and macro structure design in FGMs is a challenge for modern industry. Mathematical modelling and numerical simulation are indeed extremely useful tools for the design and investigation of FGMs. The objective of this study is to provide a flexible model for metal-metal functionally graded circular beams such that it is possible to perform both elastic and plastic stress analysis in addition to determining the deflections numerically under any type of loading.

2. MATERIAL AND METHODS

2.1. Macro-Mechanical Model of Functionally Graded Circular Beam

In most of the construction and aviation industries, the primary structural element is the beam to carry the force acting perpendicular to the longitudinal axis. Functionally graded beams are widely used in applications such as thermal and electrical structural components. Various studies have been carried out on functionally graded beams related to material gradation along with the thickness direction. Sorting of the beams is based on the ratio of length and thickness. If the ratio of length/thickness is less than 4 the beam is called a short beam while if this ratio is greater than 10 it is called a long beam. Various elastic theories are developed to investigate the deformation of beams. Classical beam theory is used for the long beams which are based upon Euler Bernoulli assumptions. Classical beam theory is also widely used in the mechanical analysis of long functionally graded beams, whereas most of the authors develop the power-law model to express gradation in the functionally graded beam.

In the present study, a cylindrical rod is used as a functionally graded beam with the variation of material properties along the radial direction. The novelty of this study is that a parabolic form [40], is used instead of the power-law model, which is more flexible to define the material distribution along the radial direction. This approach is more convenient to express miscellaneous types of distributions such as concave, convex and linear variations with the appropriate selection of material parameters. According to this parabolic form, yield strength and modulus of elasticity of the functionally graded beam are defined as:

$$\sigma_{(r)} = \sigma_0 \left[1 - n_S \left(r/R \right)^{k_S} \right] \tag{1}$$

$$E_{(r)} = E_0 \left[1 - n_E \left(r/R \right)^{k_E} \right] \tag{2}$$

respectively, where r is the radial coordinate of the rod (variable), R is the radius of the rod (constant), $\sigma_{(r)}$ is the yield strength along the radius (variable), σ_0 is the yield strength at the center (constant), n_S is the material parameter related with the yield strength such that $0 \le n_S < 1.0$, k_S is the material parameter related with the yield strength such that $k_s > 1.0$, $E_{(r)}$ is the modulus of elasticity along the radius (variable), E_0 is the modulus of elasticity at the center (constant), n_E is the material parameter related with the modulus of elasticity such that $0 \le n_E < 1.0$ and k_E is the material parameter related with the yield strength such that $k_E > 1.0$.

2.2. Kinematic Relations of Functionally Graded Circular Beam

In this study, it is assumed that the material properties of the functionally graded circular beam vary arbitrarily in the radial direction. For such a structure, a Cartesian coordinate system is chosen such that x-axis is at the neutral axis of the circular beam whereas the positive z-axis is directed upward and perpendicular to the x-axis. u, v, and w are the corresponding elastic displacement components at x, y and z respectively (Figure 1).

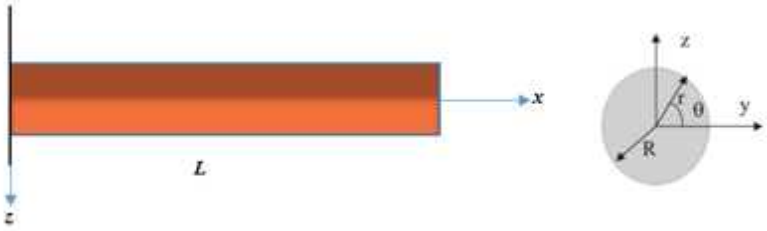


Figure 1. Geometry of the functionally graded circular beam

The volume fraction of material changes gradually along the z-axis. The equivalent single layer theories are developed by assuming the form of the displacement field as a linear combination of unknown functions [41]

$$\varphi_i(x,y,z,t) = \sum_{j=0}^{N} (z)^j \varphi_i^j (x,y,t) \tag{3}$$

where φ_i is the i[th] component of displacement, (x, y) in-plane coordinates, z radial coordinate, t time and φ_i^j are functions to be determined. For one dimensional problems such as beams, based on the kinematic assumption of third-order shear deformation beam theory as Reddy [42], consider the displacement field

$$u(x,z,t) = u_0(x,t) + r\phi_x(x,t) - \frac{4}{3R^2} r^3 (\phi_x + \frac{\partial w_0}{\partial x})$$
$$v(x,z,t) = 0$$
$$w(x,z,t) = w_0(x,t) \tag{4}$$

where u_0 is the axial displacement, w_0 the transverse displacement and ϕ_x is the rotation of the cross section at the centroidal axis. The corresponding displacements are assumed $z = r\sin\theta$. The linear strains associated with displacement field are:

$$\varepsilon_{xx} = \varepsilon_{xx}^{(0)} + r\varepsilon_{xx}^{(1)} + r^3\varepsilon_{xx}^{(3)} \tag{5a}$$
$$\gamma_{xz} = \gamma_{xz}^{(0)} + r^2\gamma_{xz}^{(2)} \tag{5b}$$

where

$$\begin{Bmatrix} \varepsilon_{xx}^{(0)} \\ \varepsilon_{xx}^{(1)} \\ \varepsilon_{xx}^{(3)} \end{Bmatrix} = \begin{Bmatrix} \dfrac{\partial u_0}{\partial x} \\ \dfrac{\partial \phi_x}{\partial x} \\ -\dfrac{4}{3R^2}(\dfrac{\partial \phi_x}{\partial x} + \dfrac{\partial^2 w_0}{\partial x^2} \end{Bmatrix} \tag{6a}$$

$$\begin{Bmatrix} \gamma_{xz}^{(0)} \\ \gamma_{xz}^{(2)} \end{Bmatrix} = \begin{Bmatrix} \phi_x + \dfrac{\partial w_0}{\partial x} \\ -\dfrac{4}{R^2}(\phi_x + \dfrac{\partial w_0}{\partial x}) \end{Bmatrix} \tag{6b}$$

Assuming that the material components of the functionally graded circular beam obey the generalized Hooke's law, the stress state can be expressed as [43]

$$\sigma_{xx} = Q_{11}\varepsilon_{xx} \tag{7a}$$
$$\tau_{xz} = Q_{55}\gamma_{xz} \tag{7b}$$

in which elastic constants Q_{11} and Q_{55} by using equivalent macro-mechanical Young's modulus $E_{(r)}$ of the functionally graded circular beam:

$$\{Q_{11}; Q_{55}\} = \left\{ E_{(r)}; \frac{E_{(r)}}{2(1+\upsilon)} \right\} \tag{8}$$

2.3. Euler-Lagrange Equations of Functionally Graded Circular Beam

According to Hamilton's principle, the equation of motion of functionally graded beams can be derived in terms of the force resultants as [44]

$$\begin{aligned}&\int_0^T\int_0^L\int_A\left[\sigma_{xx}\left(\delta\varepsilon_{xx}^{(0)}+r\delta\varepsilon_{xx}^{(1)}+r^3\delta\varepsilon_{xx}^{(3)}\right)+\tau_{xz}\left(\delta\gamma_{xz}^{(0)}+r^2\delta\gamma_{xz}^{(2)}\right)\right]dx\,dt\,dA-\int_0^T\int_0^L\left(f\,\delta u_0+q\delta w_0\right)dt\,dx\\&-\int_0^T\int_0^L\int_A\rho\left\{\left[\dot{u}_0+r\dot{\phi}_x-\frac{4}{3R^2}r^3(\dot{\phi}_x+\frac{\partial\dot{w}_0}{\partial x})\right]\left[\delta\dot{u}_0+r\delta\dot{\phi}_x-\frac{4}{3R^2}r^3(\delta\dot{\phi}_x+\frac{\partial\delta\dot{w}_0}{\partial x})\right]+\dot{w}_0\delta\dot{w}_0\right\}dx\,dt\,dA=0\end{aligned}\tag{9}$$

The stress resultants terms, N_{xx} is axial, M_{xx} and P_{xx} are the bending moment resultants, Q_x and R_x are shear force resultants which are expressed as

$$\begin{Bmatrix}N_{xx}\\M_{xx}\\P_{xx}\end{Bmatrix}=\int_{-R/2}^{R/2}\begin{Bmatrix}1\\r\\r^3\end{Bmatrix}\sigma_{xx}dz\tag{10a}$$

$$\begin{Bmatrix}Q_x\\R_x\end{Bmatrix}=\int_{-R/2}^{R/2}\begin{Bmatrix}1\\r^2\end{Bmatrix}\tau_{xz}dz\tag{10b}$$

By inserting Equations 10a and 10b into Equation 9, the new form is obtained as

$$\begin{aligned}&\int_0^T\int_0^L\left(N_{xx}\delta\varepsilon_{xx}^{(0)}+M_{xx}\delta\varepsilon_{xx}^{(1)}+P_{xx}\delta\varepsilon_{xx}^{(3)}+Q_x\delta\gamma_{xz}^{(0)}+R_x\delta\gamma_{xz}^{(2)}\right)dt\,dx\\&-\int_0^T\int_0^L\left\{I_0\dot{u}_0\delta\dot{u}_0+\left[I_2\dot{\phi}_x-\frac{4}{3R^2}I_4\left(\dot{\phi}_x+\frac{\partial\dot{w}_0}{\partial x}\right)\right]\delta\dot{\phi}_x+f\,\delta u_0+q\delta w_0\right\}dt\,dx\\&-\int_0^T\int_0^L\left\{-\frac{4}{3R^2}\left[I_4\dot{\phi}_x-\frac{4}{3R^2}I_6\left(\dot{\phi}_x+\frac{\partial\dot{w}_0}{\partial x}\right)\right]\left(\delta\dot{\phi}_x+\frac{\partial\delta\dot{w}_0}{\partial x}\right)+I_0\dot{w}_0\delta\dot{w}_0\right\}dt\,dx=0\end{aligned}\tag{11}$$

By revising Equation 11, one can write that

$$\int_0^T\int_0^L \left\{ \begin{array}{l} \left(-\frac{\partial N_{xx}}{\partial x} - f + I_0 \frac{\partial^2 u_0}{\partial t^2} \right) \delta u_0 + \left(-\frac{\partial \bar{M}_{xx}}{\partial x} + \bar{Q}_x + (I_2 - 2\frac{4}{3R^2} I_4 + (\frac{4}{3R^2})^2 I_6) \frac{\partial^2 \phi_x}{\partial t^2} - \frac{4}{3R^2}(I_4 - \frac{4}{3R^2} I_6) \frac{\partial^3 w_0}{\partial x \partial t^2} \right) \delta \phi_x \\ + \left[-\frac{4}{3R^2} \frac{\partial^2 P_{xx}}{\partial x^2} - \frac{\partial \bar{Q}_x}{\partial x} - q + \frac{4}{3R^2}((I_4 - \frac{4}{3R^2} I_6) \frac{\partial^3 \phi_x}{\partial x \partial t^2} - \frac{4}{3R^2} I_6 \frac{\partial^4 w_0}{\partial^2 x \partial t^2}) + I_0 \frac{\partial^2 w_0}{\partial t^2} \right] \delta w_0 \end{array} \right\} dt\,dx$$
$$+ \int_0^T\int_0^L \left\{ N_{xx} \delta u_0 + \bar{M}_{xx} \delta \phi_x - \frac{4}{3R^2} P_{xx} \frac{\partial \delta w_0}{\partial x} + \left[\bar{Q}_x + \frac{4}{3R^2} \left(\frac{\partial P_{xx}}{\partial x} - (I_4 - \frac{4}{3R^2} I_6) \frac{\partial^2 \phi_x}{\partial t^2} + \frac{4}{3R^2} I_6 \frac{\partial^3 w_0}{\partial x \partial t^2} \right) \right] \delta w_0 \right\} dt\,dx = 0 \tag{12}$$

where the new variables, introduced in arriving at the last expression, are derived as

$$\bar{M}_{xx} = M_{xx} - \frac{4}{3R^2} P_{xx} \tag{13a}$$

$$\bar{Q}_x = Q_x - \frac{4}{R^2} R_x \tag{13b}$$

$$I_i = \int_{-R/2}^{R/2} \rho(z)^i \, dz \tag{13c}$$

Thus, Euler-Lagrange equations are obtained as

$$\delta u_0 : \quad \frac{\partial N_{xx}}{\partial x} + f = I_0 \frac{\partial^2 u_0}{\partial t^2} \tag{14a}$$

$$\delta w_0 : \quad \frac{\partial \bar{Q}_x}{\partial x} + \frac{4}{3R^2} \frac{\partial^2 P_{xx}}{\partial x^2} + q = I_0 \frac{\partial^2 w_0}{\partial t^2} + \frac{4}{3R^2} \left((I_4 - \frac{4}{3R^2} I_6) \frac{\partial^3 \phi_x}{\partial x \partial t^2} - \frac{4}{3R^2} I_6 \frac{\partial^4 w_0}{\partial x^2 \partial t^2} \right) \tag{14b}$$

$$\delta \phi_x : \quad \frac{\partial \bar{M}_{xx}}{\partial x} - \bar{Q}_x = (I_2 - 2\frac{4}{3R^2} I_4 + (\frac{4}{3R^2})^2 I_6) \frac{\partial^2 \phi_x}{\partial t^2} - \frac{4}{3R^2}(I_4 - \frac{4}{3R^2} I_6) \frac{\partial^3 w_0}{\partial x \partial t^2} \tag{14c}$$

The primary variables of the theory are:

$$\left\{ u_0,\ w_0,\ \phi_x,\ \frac{\partial w_0}{\partial x} \right\} \tag{15}$$

The corresponding secondary variables are:

$$\left\{ N_{xx},\ \bar{Q}_x + \frac{4}{3R^2}(\frac{\partial P_{xx}}{\partial x} - (I_4 - \frac{4}{3R^2} I_6) \frac{\partial^2 \phi_x}{\partial t^2} + \frac{4}{3R^2} I_6 \frac{\partial^3 w_0}{\partial x \partial t^2}),\ \bar{M}_{xx},\ -\frac{4}{3R^2} P_{xx} \right\} \tag{16}$$

2.4. Constitutive Equations of Functionally Graded Circular Beam

By substituting Equations 7a and 7b into Equations 10a and 10b respectively the constitutive equations can be expressed as follows:

$$\begin{Bmatrix} N_{xx} \\ M_{xx} \\ P_{xx} \end{Bmatrix} = \begin{bmatrix} A_{xx} & B_{xx} & E_{xx} \\ B_{xx} & D_{xx} & F_{xx} \\ E_{xx} & F_{xx} & H_{xx} \end{bmatrix} \begin{Bmatrix} \varepsilon_{xx}^{(0)} \\ \varepsilon_{xx}^{(1)} \\ \varepsilon_{xx}^{(3)} \end{Bmatrix} \tag{17a}$$

$$\begin{Bmatrix} Q_x \\ R_x \end{Bmatrix} = \begin{bmatrix} A_{xz} & D_{xz} \\ D_{xz} & F_{xz} \end{bmatrix} \begin{Bmatrix} \gamma_{xz}^{(0)} \\ \gamma_{xz}^{(2)} \end{Bmatrix} \tag{17b}$$

where the rigidities D_{xx} denotes the bending stiffness, B_{xx} denotes the bending-extensional coupling stiffnesses, E_{xx}, F_{xx} and H_{xx} denote the higher-order stiffnesses, D_{xz} and A_{xz} denote the extensional stiffnesses as follows

$$\left\{A_{ij},\, B_{ij},\, D_{ij},\, E_{ij},\, F_{ij},\, H_{ij}\right\} = \int_{-R/2}^{R/2} Q_{ij} \left\{1,\, r,\, r^2,\, r^3,\, r^4,\, r^6\right\} dz \tag{18}$$

2.5. Exact Solutions

The equations of equilibrium and stress resultant displacement relations of the third-order shear deformation beam theory is summarized below for constant material and geometric properties as [45]

$$\frac{\partial M_{xx}}{\partial x} = Q_x + \frac{4}{3R^2}\frac{\partial P_{xx}}{\partial x} - \frac{4}{R^2}R_x \tag{19a}$$

$$\frac{\partial Q_x}{\partial x} = -q_x + \frac{4}{R^2}\frac{\partial R_x}{\partial x} - \frac{4}{3R^2}\frac{\partial^2 P_{xx}}{\partial x^2} \tag{19b}$$

$$M_{xx} = D_{xx}\frac{\partial \phi_x}{\partial x} - \frac{4}{3R^2}F_{xx}\left(\frac{\partial \phi_x}{\partial x} + \frac{\partial^2 w_0}{\partial x^2}\right) \tag{19c}$$

$$Q_x = \bar{A}_{xz}\left(\phi_x + \frac{\partial w_0}{\partial x}\right) \tag{19d}$$

$$P_{xx} = F_{xx}\frac{\partial \phi_x}{\partial x} - \frac{4}{3R^2}H_{xx}\left(\frac{\partial \phi_x}{\partial x} + \frac{\partial^2 w_0}{\partial x^2}\right) \tag{19e}$$

$$R_x = \bar{D}_{xz}\left(\phi_x + \frac{\partial w_0}{\partial x}\right) \tag{19f}$$

where stiffnesses are

$$\bar{A}_{xz} = A_{xz} - \frac{4}{R^2}D_{xz}, \quad \bar{D}_{xz} = D_{xz} - \frac{4}{R^2}F_{xz} \tag{20}$$

The stress resultant displacement relationships can be expressed as

$$M_{xx} = \frac{\bar{D}_{xx}}{\bar{A}_{xz}}\frac{\partial Q_x}{\partial x} - D_{xx}\frac{\partial^2 w_0}{\partial x^2} \tag{21a}$$

$$R_x = \frac{\bar{D}_{xz}}{\bar{A}_{xz}}Q_x \tag{21b}$$

$$P_{xx} = \frac{\bar{F}_{xx}}{\bar{A}_{xz}}\frac{\partial Q_x}{\partial x} - F_{xx}\frac{\partial^2 w_0}{\partial x^2} \tag{21c}$$

where stiffnesses are

$$\bar{D}_{xx} = D_{xx} - \frac{4}{3R^2}F_{xx}, \quad \bar{F}_{xx} = F_{xx} - \frac{4}{3R^2}H_{xx} \tag{22}$$

Replacing Pxx and Rxx in Equation 19a with the expressions in Equations 21b and 21c one can obtain

$$\left(\frac{\bar{D}_{xx}}{D_{xx}}\right)\frac{\partial M_{xx}}{\partial x} = \left(\frac{\hat{A}_{xz}}{\bar{A}_{xz}}\right)Q_x - \frac{4}{3R^2}\left(\frac{F_{xx}\bar{D}_{xx}}{D_{xx}\bar{A}_{xz}} - \frac{\bar{F}_{xx}}{\bar{A}_{xz}}\right)\frac{\partial^2 Q_x}{\partial x^2} \tag{23}$$

Then simplifying the coefficients yields

$$0 = -\frac{4}{3R^2}\left(\frac{F_{xx}\bar{D}_{xx}}{D_{xx}\bar{A}_{xz}} - \frac{\bar{F}_{xx}}{\bar{A}_{xz}}\right)\frac{\partial^2 Q_x}{\partial x^2} - \left(\frac{\hat{A}_{xz}}{\bar{A}_{xz}}\right)Q_x + \left(\frac{\bar{D}_{xx}}{D_{xx}}\right)\frac{\partial M_{xx}}{\partial x} + C_1 \tag{24}$$

To determine ϕ_x it is written that

$$D_{xx}\phi_x = -D_{xx}\frac{\partial w_0}{\partial x} + \frac{4}{3R}\frac{F_{xx}}{\hat{A}_{xz}}Q_x + C_1\frac{x^2}{2} + C_2 x + C_3 \tag{25}$$

Finally, one can derive the relation

$$D_{xx}w_0 = -D_{xx}\phi_x + \frac{D_{xx}}{\hat{A}_{xz}}Q_x \tag{26}$$

For a cantilever beam under uniform distributed load, the boundary conditions are

$$w_0(0) = \frac{\partial w_0}{\partial x}(0) = \frac{\partial M_{xx}}{\partial x}(L) = M_{xx}(L) = P_{xx}(L) = 0 \tag{27}$$

Thus, the solutions for the functionally graded circular beam are

$$Q_x(x) = \left(\frac{q_0\mu}{\lambda^3\cosh\lambda \mathrm{L}}\right)[\sinh\lambda x - \lambda L\cosh\lambda(L-x)] + \frac{q_0\mu}{\lambda^2}(L-x) \tag{28}$$

$$M_{xx}(x) = q_0\left(Lx - \frac{x^2}{2} - \frac{L^2}{2}\right) \tag{29}$$

$$\begin{aligned} w_0(x) &= \frac{q_0L^4}{24D_{xx}}\left(\frac{6x^2}{L^2} - \frac{4x^3}{L^3} + \frac{x^4}{L^4}\right) + \left(\frac{q_0\mu}{2\lambda^2}\right)\left(\frac{\hat{D}_{xx}}{\hat{A}_{xz}D_{xx}}\right)(2Lx - x^2) \\ &+ \left(\frac{q_0\mu}{\lambda^4\cosh\lambda xL}\right)\left(\frac{\hat{D}_{xx}}{\hat{A}_{xz}D_{xx}}\right)[\cosh\lambda x + \lambda L\sinh\lambda(L-x)] - \left(\frac{q_0\mu}{\lambda^4}\right)\left(\frac{\hat{D}_{xx}}{\hat{A}_{xz}D_{xx}}\right)\left(\frac{1+\lambda L\sinh\lambda L}{\cosh\lambda L}\right) \end{aligned} \tag{30}$$

where

$$\lambda^2 = \frac{\bar{A}_{xz}D_{xx}}{\frac{4}{3R}(F_{xx}\hat{D}_{xx} - \hat{F}_{xx}D_{xx})}, \quad \mu = \frac{\hat{A}_{xz}\hat{D}_{xz}}{\frac{4}{3R}(F_{xx}\hat{D}_{xx} - \hat{F}_{xx}D_{xx})} \tag{31}$$

3. RESULTS AND DISCUSSION

This section presents numerical calculation for the functionally graded circular beam. Material properties are considered in a new approximation of the parabolic form proposed in Equations 1 and 2 to demonstrate the effect of non-homogeneity on deflections and stress distributions. For the case study, material of the cylindrical functionally graded beam is assumed to be Aluminum (Al) of which the properties are given in Table 1 for the numerical applications of the new mechanical model. These properties are E (modulus of elasticity), G (modulus of rigidity), ρ (density) and ν (Poisson's ratio).

Table 1. Material properties

Material	E (GPa)	G (GPa)	ρ (kg/m3)	ν
Aluminum	70	27	2702	0.3

It is also assumed that its center is rich in aluminum. The variation of dimensionless deflection and normal stress is obtained by using following forms

$$\bar{w}(x) = \frac{w(x)E_0}{q}, \quad \bar{\sigma}_{xx} = \frac{\sigma_{xx}R^2}{qL^2} \tag{32}$$

3.1. Effects of Gradient Material Parameters on Material Properties

The changes of the modulus of elasticity depending on the dimensionless radius of the cylindrical section cantilever beam depending on the material parameter n_E are shown in Figures 2-5. When the graphs are examined, with the increase of the k_E parameter, the area showing the isotropic property towards the cross-section center of the functionally graded circular beam increases and the change in the modulus of elasticity starts to become parabolic. With the increase of the n_E parameter, the modulus of elasticity decreases towards the rod surface. As shown in Figures 2-5, the more increase of n_E parameter, the more decrease of elastic modulus at the surface. k_E value does not affect the modulus of elasticity values at the center and at the surface, however it affects the variation along the radius. In other words, it affects only the concavity of the distribution. The greater the k_E value, the more concavity the distribution is. If a material is selected such that sudden change occurs near the surface, this situation can be represented by means of greater k_E values.

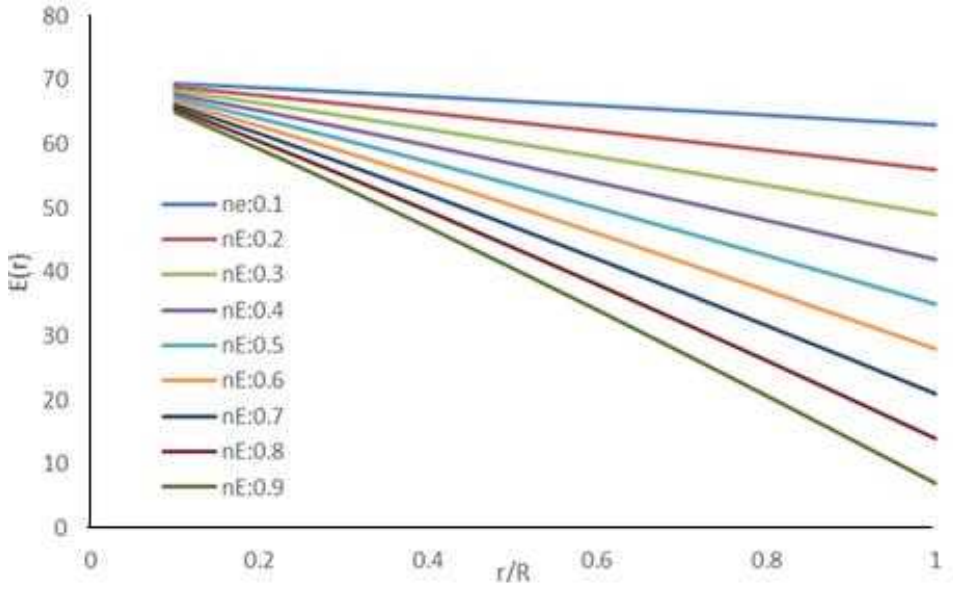


Figure 2. Distribution of Young's modulus according to n_E for $k_E = 1.1$

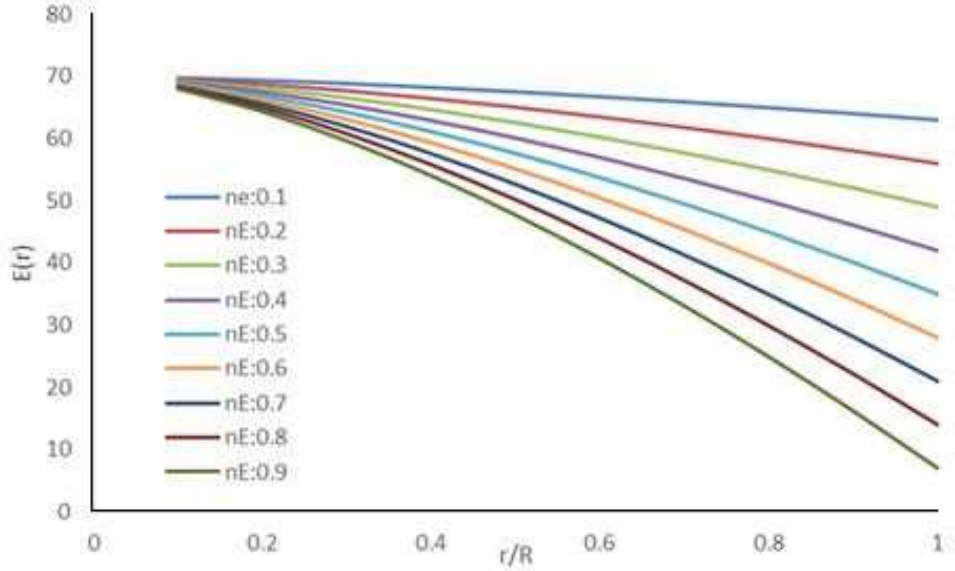


Figure 3. Distribution of Young's modulus according to n_E for $k_E = 1.5$

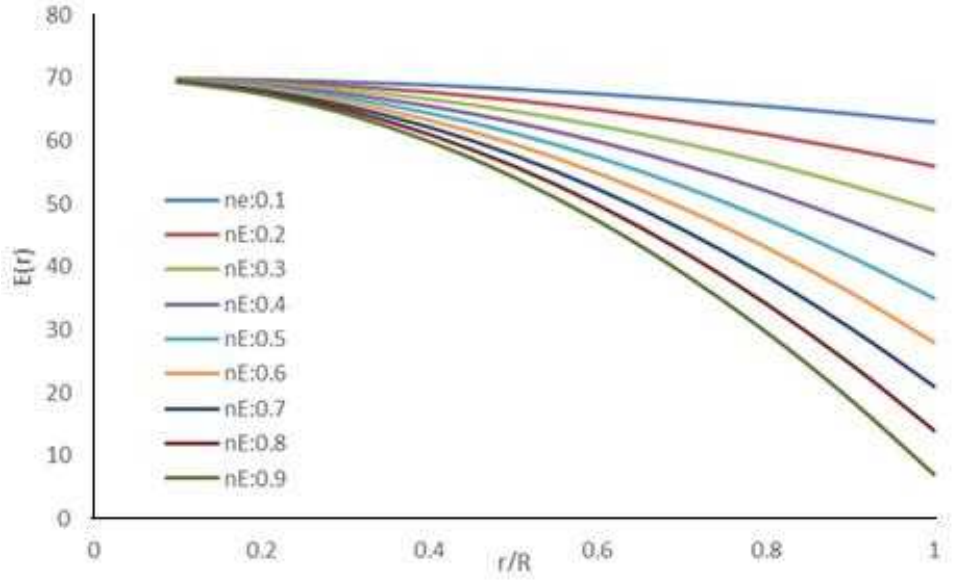


Figure 4. Distribution of Young's modulus according to n_E for $k_E = 2.0$

3.2. Effects of Gradient Material Parameters on Flexure

Consider a cantilever functionally graded circular beam to which a uniformly distributed force q is applied in the longitudinal axis. The variation of the dimensionless deflection with respect to the dimensionless coordinate is plotted in Figures 6 to 9 based on different n_E values and k_E values 1.1, 1.5, 2, 5. When the effect of the material parameter n_E on the displacement is examined in general, the displacement value increases with the increase of the n_E parameter. The reason for this can be interpreted that increasing of the k_E parameter yields to decrease the modulus of elasticity. However, increasing of the k_E value, which is another parameter, causes decrease of the displacement value. Because the increase

in the k_E parameter increases the isotropic property of the material. The maximum dimensionless displacement value is 0.2091 for $n_E = 0.9$ and $k_E = 1.1$ while the minimum dimensionless displacement value is 0.2002 for $n_E = 0.9$ and $k_E = 5.0$.

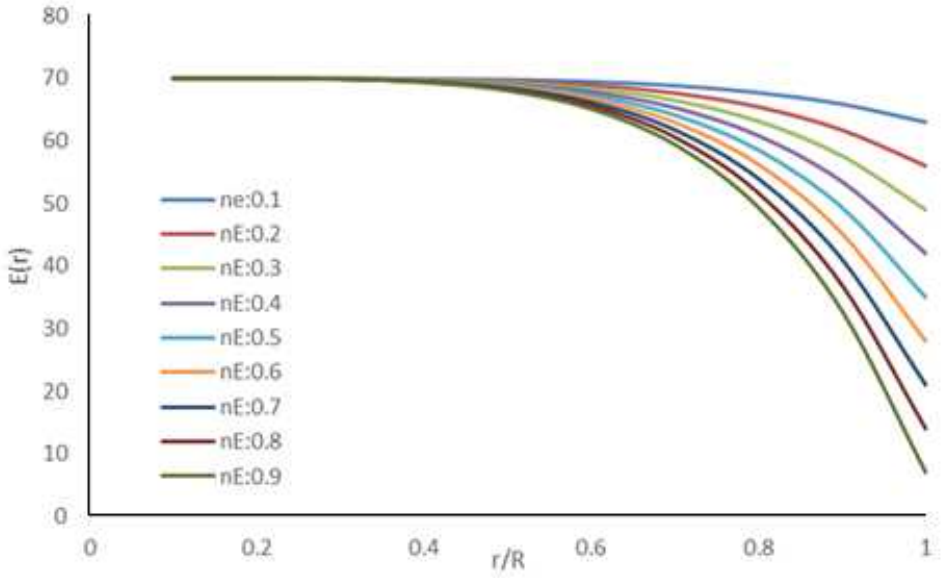


Figure 5. Distribution of Young's modulus according to n_E for $k_E = 5.0$

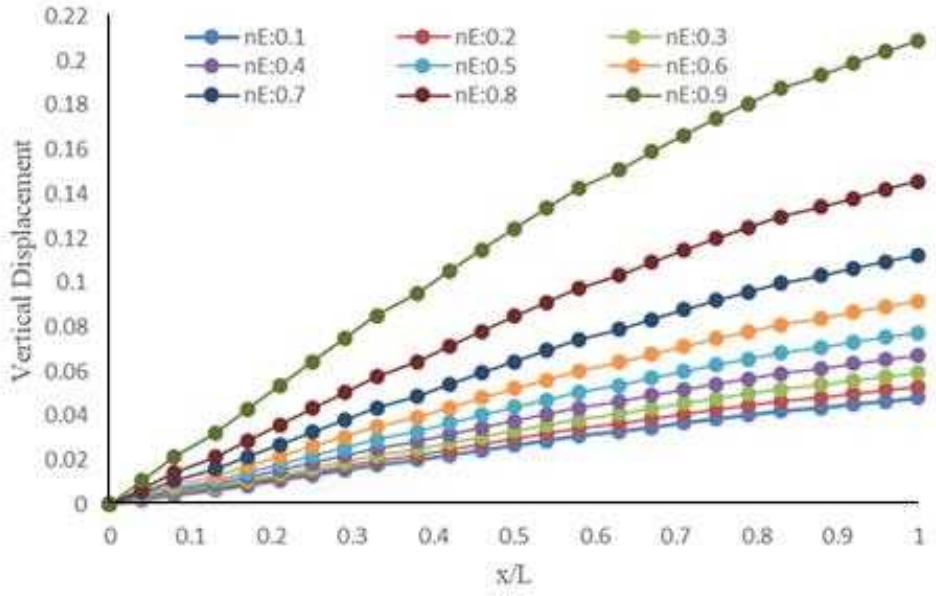


Figure 6. Vertical displacement distribution according to n_E for $k_E = 1.1$

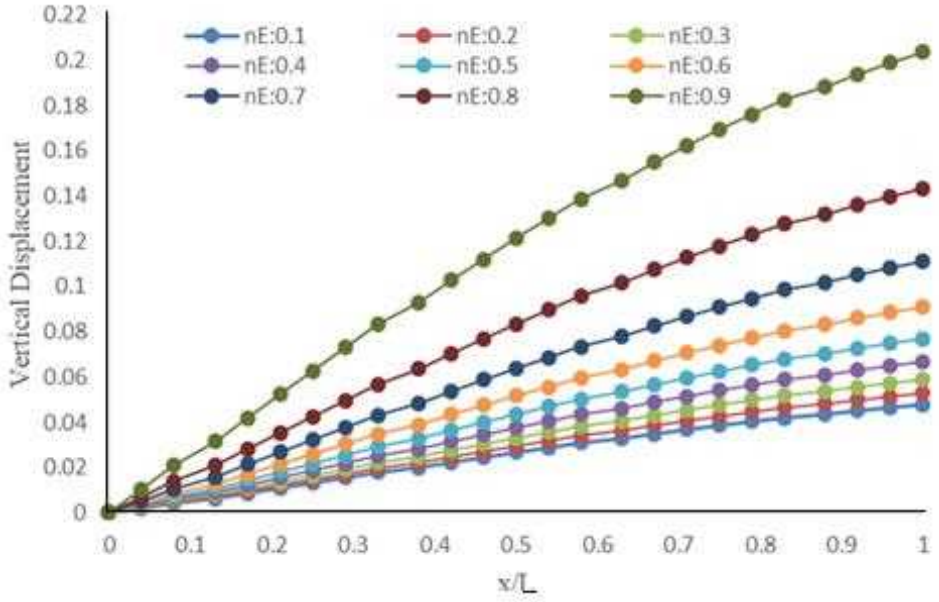


Figure 7. Vertical displacement distribution according to n_E for $k_E = 1.5$

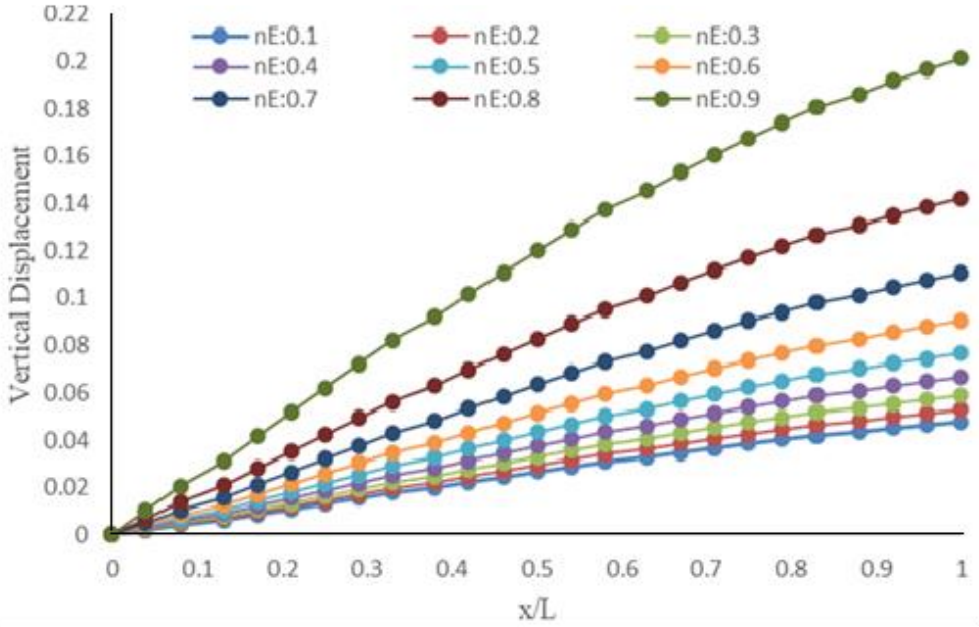


Figure 8. Vertical displacement distribution according to n_E for $k_E = 2$

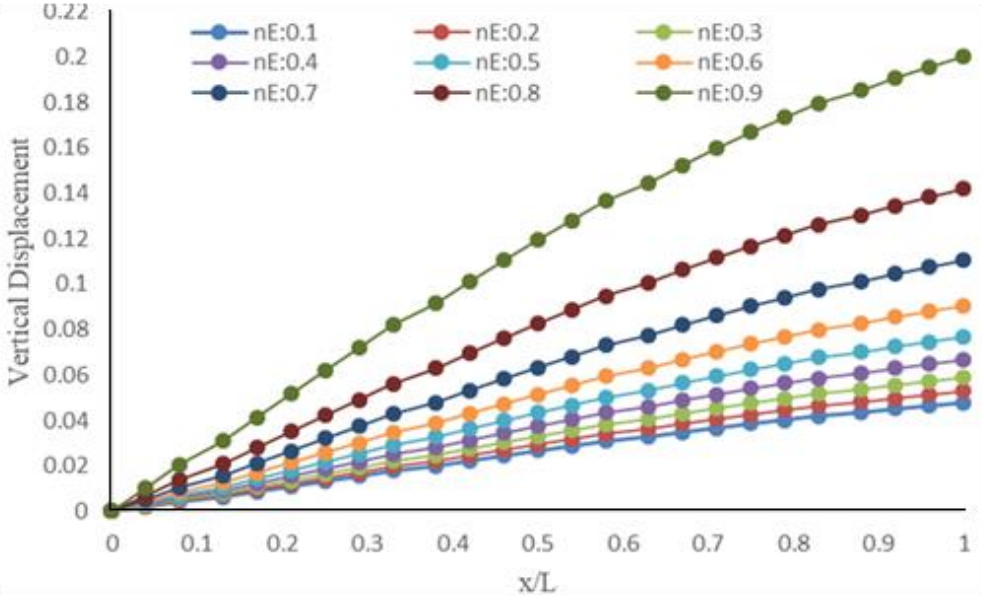


Figure 9. Vertical displacement distribution according to n_E for $k_E = 5$

The dimensionless normal stress value changes, obtained depending on the material parameter related to the yield strength n_S value, are given in Figures 10-13 depending on the parameter related to the yield strength k_S value. The dimensionless normal stress, which initially shows a linear change along the beam radial coordinate, starts to change parabolic with the increase of the n_S parameter. What is more interesting here is that with the increase of the k_S parameter, the dimensionless normal stress variation along the beam radial coordinate becomes more parabolic and the peak points of the curves increase. In addition, with the increase of k_S value, the peak points of the stress curves occur in coordinates close to the beam surface.

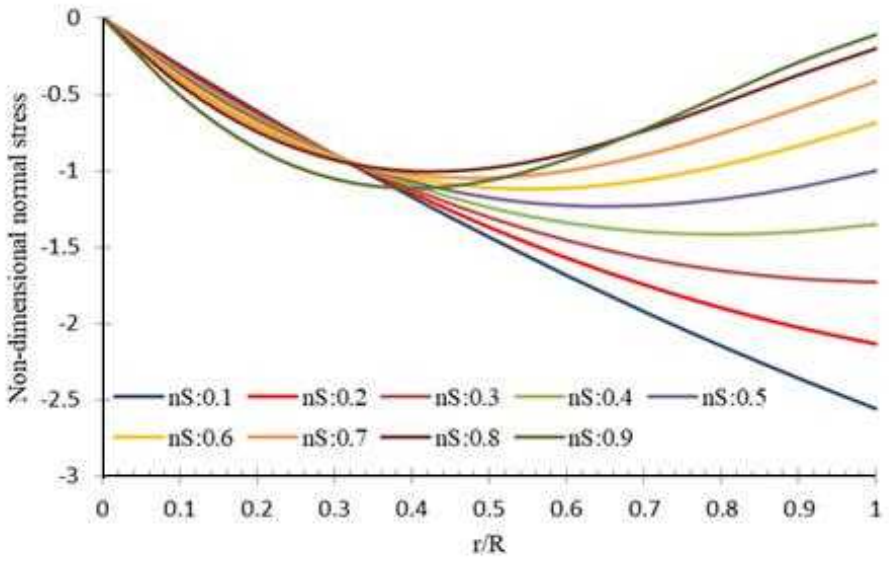


Figure 10. Distribution of dimensionless normal stress according to n_S for $k_S = 1.1$

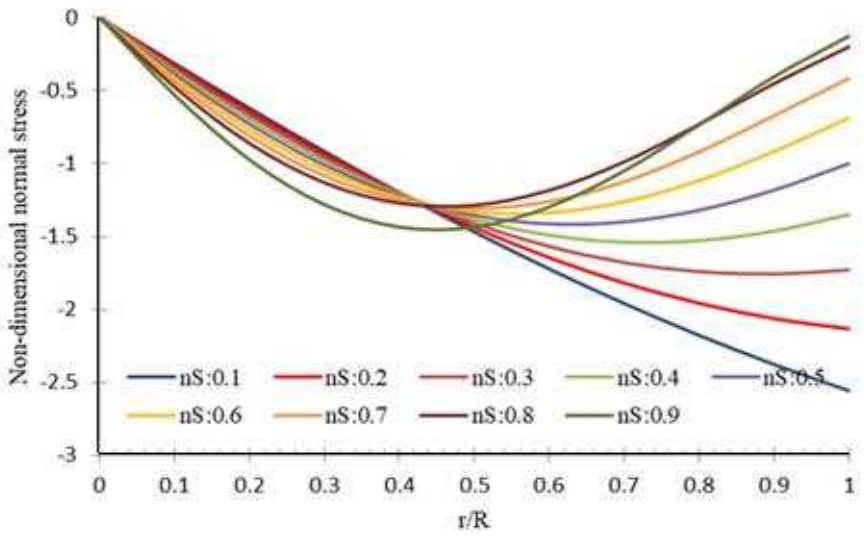


Figure 11. Distribution of dimensionless normal stress according to n_S for $k_S = 1.5$

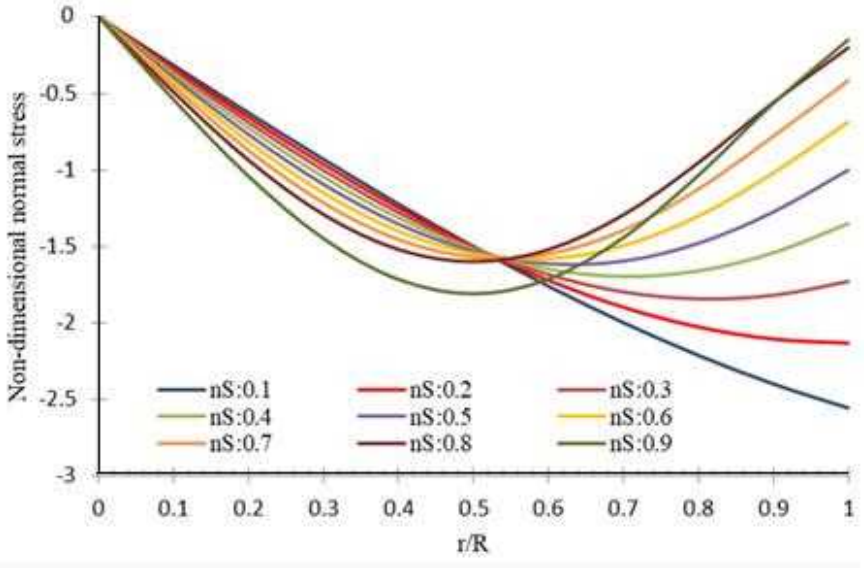


Figure 12. Distribution of dimensionless normal stress according to n_S for $k_S = 2$

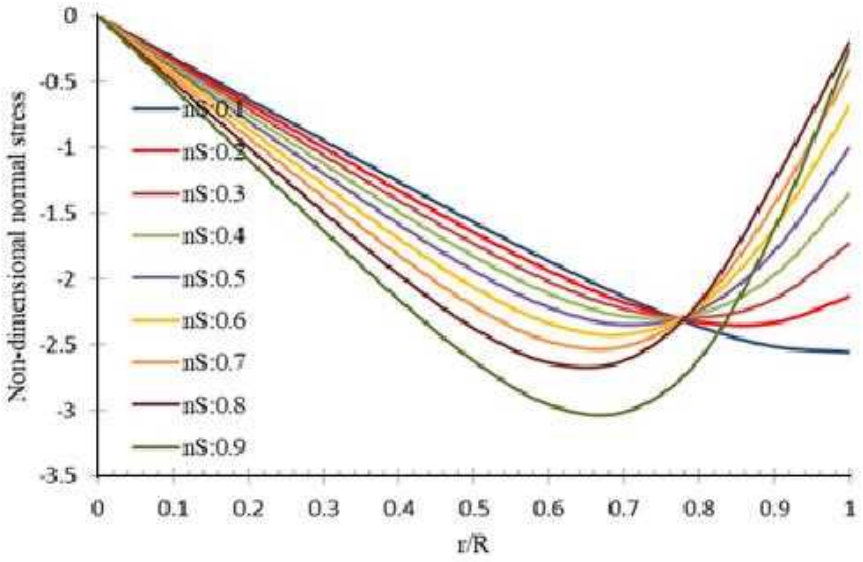


Figure 13. Distribution of dimensionless normal stress according to n_S for $k_S = 5$

4. CONCLUSIONS

In this paper, a novel approach is introduced for modeling of a functionally graded circular beam which consists of two different metals. This novel approach gives flexibility to define the type of the functionally graded circular beam. It is observed that it is possible to define any type of gradation by means of this approach such as linear or parabolic from center to the surface of the beam. In other words, this approach is valid for not only functionally graded beams but also homogeneous beams by inserting zero into n_S and n_E values. In addition, gradation type from center to surface can easily be presented by changing k_S and k_E values. For instance, the greater the k_E value, the more concavity the distribution is. If a material is selected such that sudden change occurs near the surface, this situation can be represented by means of greater k_E values. The dimensionless normal stress, which initially shows a linear change along the radial coordinate, starts to change parabolic with the increase of the n_S parameter. Besides, the dimensionless normal stress variation along the radial coordinate becomes more parabolic with the increase of the k_S parameter and the peak points of the curves increase. Moreover, in this paper, it is also shown that inhomogeneity and gradation type have a great effect on both stresses and deflections.

Declaration of Ethical Standards

The author declares to comply with all ethical guidelines, including authorship, citation, data reporting and publishing original research.

Credit Authorship Contribution Statement

The author has written and reviewed the paper himself.

Declaration of Competing Interest

The author declares no conflicts of interest.

Funding / Acknowledgements

The author has received no financial support for this paper.

Data Availability

No data to be shared.

Use of Artificial Intelligence

The author confirms that no generative AI or AI-assisted technologies were used in the writing of this manuscript or in the derivations of the equations.

REFERENCES

[1] A. Tounsi et al., "A four variable trigonometric integral plate theory for hygro-thermo-mechanical bending analysis of AFG ceramic-metal plates resting on a two-parameter elastic foundation," *Steel and Composite Structures,* vol. 34, no. 4, pp. 511-524, 2020.

[2] H. Yin, L. Sun and G.H. Paulino, "Micromechanics-based elastic model for functionally graded materials with particle interactions," *Acta Materialia,* vol. 52, no. 12, pp. 3535-3543, 2004.

[3] Ö. Özdemir, "Vibration analysis of rotating Timoshenko beams with different material distribution properties", *sujest*, c. 7, sy. 2, ss. 272–286, 2019.

[4] M. H. Saraçoğlu et al., "Deflection analysis of functionally graded equal strength beams", *European Mechanical Science*, 6(2), 119-128, 2022.

[5] A. Bouamoud, B. Boucham, F. Bourada, M.S.A. Houari and A. Tounsi, "Thermomechanical bending investigation of FGM sandwich plates using four shear deformation plate theory," *Steel and Composite Structures*. vol. 32, no. 5, pp. 611-632, 2019.

[6] B. Bouderba and H. M. Berrabah, "Bending response of porous advanced composite plates under thermomechanical loads," *Mechanics Based Design of Structures and Machines*. vol. 50, no. 9, pp. 3262-3282, 2022.

[7] A. Ozturk and M. Gulgec, "Analytical solution of thermal stresses in a functionally graded solid cylinder within parabolic continuous grading," *Applied Mechanics and Materials*, vol. 307, pp. 364-367, 2013.

[8] F. Bourada et al., "Dynamic investigation of porous functionally graded beam using a sinusoidal shear deformation theory," *Wind and Structures*. vol. 28, no. 1, pp. 19-30, 2019.

[9] F. Allahkarami, H. Tohidi, R. Dimitri and F. Tornabene, "Dynamic stability of bi-directional functionally graded porous cylindrical shells embedded in an elastic foundation," *Applied Sciences*, vol. 10, no. 4, p. 1345, 2020.

[10] O. Allam et al., "A generalized 4-unknown refined theory for bending and free vibration analysis of laminated composite and sandwich plates and shells," *Computers and Concrete,* vol. 26, no. 2, pp. 185-201, 2020.

[11] A. Ozturk, "Overall heat transfer coefficient of functionally graded hollow cylinder," *Solid State Phenomena*, vol. 267, pp. 177-181, 2017.

[12] R. Benferhat, T.H. Daouadji and B. Adim, "A novel higher order shear deformation theory based on the neutral surface concept of FGM plate under transverse load," *Advances in materials Research*. vol. 5, no. 2, p. 107, 2016.

[13] A. Chikh et al., "Thermo-mechanical postbuckling of symmetric S-FGM plates resting on Pasternak elastic foundations using hyperbolic shear deformation theory," *Structural Engineering and Mechanics.* vol. 57, no. 4, pp. 617-639, 2016.

[14] A. Chikh et al., "Thermal buckling analysis of cross-ply laminated plates using a simplified

HSDT," *Smart Structures and Systems.* vol. 19, no. 3, 289-297, 2017.
[15] A. Attia et al., "A refined four variable plate theory for thermoelastic analysis of FGM plates resting on variable elastic foundations," *Structural Engineering and Mechanics*. vol. 65, no. 4, pp. 453-464, 2018.
[16] M. Yousfi et al., "Free vibration of FGM plates with porosity by a shear deformation theory with four variables," *Structural Engineering and Mechanics*, vol. 66, no. 3, pp. 353-368, 2018.
[17] J. N. Reddy, "Microstructure-dependent couple stress theories of functionally graded beams," *Journal of the Mechanics and Physics of Solids*, vol. 59, no. 11, pp. 2382-2399, 2011.
[18] A. Arbind and J.N. Reddy, "Nonlinear analysis of functionally graded microstructure-dependent beams," *Composite Structures,* vol. 98, pp. 272-281, 2013.
[19] E. Madenci and Ş. Gülcü, "Optimization of flexure stiffness of FGM beams via artificial neural networks by mixed FEM," *Structural Engineering and Mechanics*, vol. 75, no. 5, pp. 633-642, 2020.
[20] E. Madenci, "A refined functional and mixed formulation to static analysis of FGM beams," *Structural Engineering and Mechanics*, vol. 69, no. 4, pp. 427-433, 2019.
[21] M.M. Gasik, "Micromechanical modelling of functionally graded materials," *Computational Materials Science,* vol. 13, no. 1, pp. 42-55, 1998.
[22] J.R. Zuiker, "Functionally graded materials: choice of micromechanics model and limitations in property variation," *Composites Engineering*, vol. 5, no. 7, pp. 807-819, 1995.
[23] H-S. Shen and Z-X. Wang, "Assessment of Voigt and Mori–Tanaka models for vibration analysis of functionally graded plates," *Composite Structures*, vol. 94, no. 7, pp. 2197-2208, 2012.
[24] E. Madenci, Y.O. Özkılıç and L. Gemi, "Buckling and free vibration analyses of pultruded GFRP laminated composites: Experimental, numerical and analytical investigations," *Composite Structures*, vol. 254, article 112806, 2020.
[25] T.H. Daouadj and B. Adim B, "Mechanical behaviour of FGM sandwich plates using a quasi-3D higher order shear and normal deformation theory," *Structural engineering and mechanics: An international journal*, vol. 61, no. 1, pp. 49-63, 2017.
[26] E. Moshkelgosha et al., "Fluid-structure coupling of concentric double FGM shells with different lengths," *arXiv preprint arXiv*:190500879, 2019.
[27] M. Lee, I. Park and U. Lee, "An approximate spectral element model for the dynamic analysis of an FGM bar in axial vibration," *Structural engineering and mechanics: An international journal*, vol.61, no. 4, pp. 551-561, 2017.
[28] A. Heydari and M. Shariati, "Buckling analysis of tapered BDFGM nano-beam under variable axial compression resting on elastic medium," *Structural engineering and mechanics: An nternational journal*, vol. 66, no. 6, pp. 737-748, 2018.
[29] G-L. She et al., "Study on thermal buckling and post-buckling behaviors of FGM tubes resting on elastic foundations," *Structural engineering and mechanics: An international journal,* vol. 66, no.6, pp. 729-736, 2018.
[30] B. Hadj, B. Rabia, T.H. Daouadji, "Influence of the distribution shape of porosity on the bending FGM new plate model resting on elastic foundations," *Structural Engineering and Mechanics*, vol. 72, no. 1, pp. 61-70, 2019.
[31] Y. Tlidji, R. Benferhat and H.D. Tahar, "Study and analysis of the free vibration for FGM microbeam containing various distribution shape of porosity," *Structural Engineering and Mechanics*, vol. 77, no. 2, 217-229, 2021.
[32] M.A. Attia and R.M. Abo-Bakr, "A semi-analytical study on the nonlinear pull-in instability of FGM nanoactuators," *Structural Engineering and Mechanics,* vol. 76, no. 4, 451-463, 2020.
[33] A.H. Akbarzadeh, A. Abedini and Z.T. Chen, "Effect of micromechanical models on structural responses of functionally graded plates," *Composite Structures*, vol. 119, pp. 598-609, 2015.
[34] M. Ghannad and H. Gharooni, "Displacements and stresses in pressurized thick FGM cylinders with exponentially varying properties based on FSDT," *Structural engineering and mechanics: An international journal,* vol. 51, no. 6, pp. 939-953, 2014.

[35] Y. Chen, "Transfer matrix method for solution of FGMs thick-walled cylinder with arbitrary inhomogeneous elastic response," *Smart structures and systems*, vol. 21, no. 4, pp. 469-477, 2018.

[36] C. Sachdeva and S.S. Padhee, "Functionally graded cylinders: Asymptotically exact analytical formulations," *Applied Mathematical Modelling*, vol. 54, pp. 782-802, 2018.

[37] R. Nedin, S. Nesterov and A. Vatulyan, "On reconstruction of thermalphysic characteristics of functionally graded hollow cylinder," *Applied Mathematical Modelling*, vol. 40, no. 4, 2711- 2719, 2016.

[38] B-L. Wang and Y-W. Mai, "Transient one-dimensional heat conduction problems solved by finite element," *International Journal of Mechanical Sciences*, vol. 47, no. 2, 303-317, 2005.

[39] Z.S. Shao, "Mechanical and thermal stresses of a functionally graded circular hollow cylinder with finite length," *International Journal of Pressure Vessels and Piping*, vol. 82, no. 3, pp. 155-163, 2005.

[40] A. Ozturk and M. Gulgec, "Elastic–plastic stress analysis in a long functionally graded solid cylinder with fixed ends subjected to uniform heat generation," *International Journal of Engineering Science*, vol. 49, no. 10, pp. 1047-1061, 2011.

[41] E. Reissner, "Reflections on the theory of elastic plates," *Applied mechanics reviews*, vol. 38, no. 11, pp. 1453-1464, 1985.

[42] J.N. Reddy, "A simple higher-order theory for laminated composite plates," *Journal of applied mechanics*, vol. 51, no. 4, pp. 745-752, 1984.

[43] K. Pradhan and S. Chakraverty, "Effects of different shear deformation theories on free vibration of functionally graded beams," *International Journal of Mechanical Sciences*, vol. 82, pp. 149-160, 2014.

[44] J.N. Reddy, *Energy Principles and Variational Methods in Applied Mechanics*, 3rd Edition, John Wiley & Sons, 2017.

[45] J. Reddy, C. Wang and K. Lee, "Relationships between bending solutions of classical and shear deformation beam theories," *International Journal of Solids and Structures*, vol. 34, no. 26, pp. 3373-3384, 1997.

Konya Mühendislik Bilimleri Dergisi, c.14, s.2, 998-1015, 2026
Konya Journal of Engineering Sciences, v.14, n.2, 998-1015, 2026
ISSN: 2667-8055 (Electronic)
DOI: 10.36306/konjes.1722297

THE COMPARISON OF FUZZY INFERENCE SYSTEM AND THE BEES ALGORITHM FOR OPTIMAL DESIGN OF BALANCING HOLE OF CENTRIFUGAL PUMP IMPELLER

[1,*]Selahattin SEFACI, [2]Osman ACAR, [3]Mete KALYONCU, [4]Saim KOÇAK

[1]*Sempa Pompa Makina A.Ş., Konya*
[2]*Selçuk Üniversitesi Teknoloji Fakültesi, Konya*
[3,4]*Konya Teknik Üniversitesi Mühendislik ve Doğa Bilimleri Fakültesi, Konya*
[1]s.sefaci@sempapompa.com, [2]osmanacar@selcuk.edu.tr, [3]mkalyoncu@ktun.edu.tr, [4]skocak@ktun.edu.tr

Highlights

- Mamdani-type inference mechanism with 54 expert-derived linguistic rules
- BA consistently yields superior optimization accuracy
- Increasing hole diameter beyond optimal thresholds disrupts fluid flow stability

Graphical Abstract

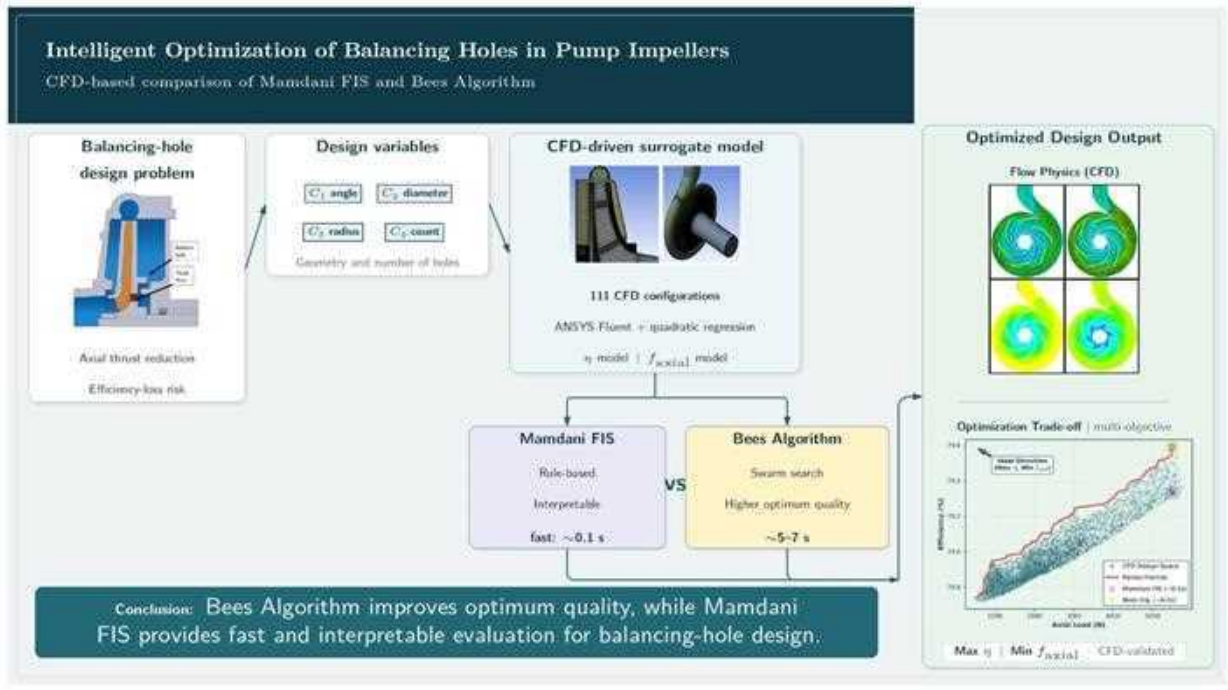


Figure CFD-Based Optimization of Balancing Holes in Centrifugal Pump Impellers Using Mamdani FIS and The Bees Algorithm

***Corresponding Author:** Selahattin SEFACI, s.sefaci@sempapompa.com

Konya Mühendislik Bilimleri Dergisi, c.14, s.2, 998-1015, 2026
Konya Journal of Engineering Sciences, v.14, n.2, 998-1015, 2026
ISSN: 2667-8055 (Electronic)
DOI: 10.36306/konjes.1722297

THE COMPARISON OF FUZZY INFERENCE SYSTEM AND THE BEES ALGORITHM FOR OPTIMAL DESIGN OF BALANCING HOLE OF CENTRIFUGAL PUMP IMPELLER

[1,*]Selahattin SEFACI, [2]Osman ACAR, [3]Mete KALYONCU, [4]Saim KOÇAK

[1]Sempa Pompa Makina A.Ş., Konya
[2]Selçuk Üniversitesi Teknoloji Fakültesi, Konya
[3,4]Konya Teknik Üniversitesi Mühendislik ve Doğa Bilimleri Fakültesi, Konya
[1]s.sefaci@sempapompa.com, [2]osmanacar@selcuk.edu.tr, [3]mkalyoncu@ktun.edu.tr, [4]skocak@ktun.edu.tr

(Received: 18.06.2025; Accepted in Revised Form: 15.12.2025)

ABSTRACT: This study presents a comprehensive comparison of two distinct computational approaches, Fuzzy Inference System (FIS) and The Bees Algorithm (BA) for optimizing the design of balancing holes in centrifugal pump impellers. These holes are essential for reducing axial thrust without compromising hydraulic efficiency. The optimization parameters include hole center angle, hole diameter, radial placement, and the number of holes. By employing computational fluid dynamics (CFD) simulations, a data-driven regression model was derived from 111 configurations of a TKF 125-400 pump model. The Mamdani-type FIS uses triangular and trapezoidal membership functions and linguistic rules, while the BA, inspired by the foraging behavior of honeybees, utilizes a swarm intelligence approach for multi-objective optimization. Comparative performance is evaluated based on axial thrust minimization and efficiency retention. The findings suggest that while BA provides superior optimization accuracy, the FIS offers greater speed, interpretability, and adaptability for real-time applications in pump design.

Keywords: *Axial load of impellers, Balancing holes, Centrifugal pump, CFD, Fuzzy inference system, The bees algorithm.*

1. INTRODUCTION

Centrifugal pumps remain one of the most widely used fluid machinery types in industrial applications, where design optimization plays a crucial role in enhancing both hydraulic and mechanical performance. A persistent challenge in centrifugal pump design is the management of axial thrust, which if not properly controlled, results in bearing wear, increased maintenance costs, and decreased pump lifespan. Balancing holes have been widely utilized to mitigate axial forces, but their incorporation often leads to complex trade-offs with hydraulic performance, efficiency, cavitation behavior, and flow stability.

A persistent operational challenge is the generation of axial force caused by the pressure difference between the suction and pressure sides of the impeller. If this force is not properly managed during design, it can lead to bearing wear, efficiency losses, and reduced pump lifespan[1]. Balancing holes are commonly employed to alleviate this issue by equalizing pressure between the front and rear cavities of the impeller[2, 3]. While effective in reducing axial force, these holes also induce recirculation from the pressure side to the suction side, often compromising hydraulic performance[4]. Therefore, identifying an optimal balancing hole configuration that minimizes axial force without degrading efficiency remains a key design objective. Recent advances in multi-objective optimization, particularly those using computational fluid dynamics (CFD) with Bayesian and Pareto-based methods, have enabled more accurate evaluation of design trade-offs[5]. Such methods can reduce axial force by over 40% while maintaining hydraulic efficiency near its baseline values, offering a robust approach for balancing mechanical stability and performance in centrifugal pump design.

***Corresponding Author:** Selahattin SEFACI, s.sefaci@sempapompa.com

1.1. Balancing Hole Design in Centrifugal Pump

The geometric characteristics of balancing holes, particularly their diameter, radial position, and circumferential location, directly influence pump internal flow structures, disk friction losses, cavitation behavior, and axial load distribution. Xun et al. [6] systematically studied the effect of circumferential balance hole placement on cavitation suppression using a low specific speed pump model with ANSYS CFX and Shear Stress Transport (SST) k-ω turbulence model. Their findings demonstrated that positioning balance holes at $\varphi = 20°$ significantly lowered NPSHa from 5.67 m to 2.7 m while suppressing cavitation erosion intensity. Cheng et al. [7] extended these investigations on semi-open impeller pump, revealing that positioning the balance hole at $\theta = 15°$ yielded superior cavitation performance with critical NPSHa reduced to 0.66 m and axial forces reduced by up to 60%.

In addition to circumferential position, balance hole diameter has been identified as a key parameter influencing rear chamber dynamics. Dong et al. [8, 9] demonstrated through comprehensive CFD analysis that increasing the hole diameter up to 8 mm reduced disk friction losses and stabilized leakage flows at approximately 2% of total flow rate. Beyond this threshold, further diameter increases showed diminishing benefits. Xie et al.[10] further evaluated balance hole optimization in gas-liquid multiphase pump, confirming that optimal designs suppressed gas accumulation, enhanced head by 8%, and improved efficiency by 2% under high gas volume conditions. Fathi et al.[11] also emphasized the role of balancing holes in reverse operation (pump-as-turbine), where holes with 6.5 mm diameter reduced axial force by up to 90%, contributing to mechanical endurance improvements without severely compromising head and power output.

Recently the effect of balancing-hole diameter on cavitation performance and axial force in a low specific-speed centrifugal pump has been explored[12], demonstrating that increased hole diameters can reduce the cavitation number and alter both the magnitude and direction of axial force under cavitating conditions. While this study makes a valuable contribution by linking balancing-hole geometry to cavitation and axial loads, its scope remains constrained to a single low specific-speed pump configuration and focuses mainly on cavitation phenomena rather than a broader predictive framework. In contrast, the present research advances this field by developing validated regression models for both efficiency and axial load across a wider range of balancing-hole geometries and operating conditions, and by integrating these models with optimization algorithms to deliver a more generalizable design framework for pump performance enhancement.

1.2. Optimization Techniques for Centrifugal Pump Design

Beyond empirical studies, computational optimization approaches have been extensively employed to enhance pump performance. Traditional optimization methods, such as Response Surface Methodology (RSM) and experimental design, have laid the foundation for more advanced multi-objective frameworks. Wang et al.[13] utilized RSM and CFD simulations to optimize high specific speed centrifugal pump, demonstrating that blade number (Z=3), outlet blade angle (β_2=30°), and inlet velocity coefficient (k_0=3.9) produced maximum hydraulic efficiency of 89.5%. Similarly, Bashiri et al. [14] applied a hybrid Particle Swarm Optimization (PSO) and Artificial Neural Network (ANN) framework to optimize impeller geometry, achieving a 6.59% increase in pump efficiency and a 9.95% increase in pump head.

Multi-objective evolutionary algorithms have also shown remarkable success in balancing conflicting design objectives. Chang et al.[15] applied Non-Dominated Sorting Genetic Algorithm-II (NSGA-II) to optimize energy storage pump impellers, incorporating advanced sampling, neural network modeling, and CFD analyses. This approach yielded a 2.75% efficiency improvement while carefully managing head losses. Safikhani et al. [16] combined CFD, GMDH neural networks, and Genetic Algorithms within a Pareto-based framework, achieving a wide range of optimal trade-offs

between pump efficiency (68.4%–94.6%) and NPSHr (1.5 m–3.9 m). Qi et al. [17] integrated entropy generation theory with PSO optimization to reduce turbulent dissipation and wall friction losses, improving pump efficiency from 73% to 75.5%.

In parallel, machine learning and artificial intelligence (AI) techniques have been increasingly incorporated into centrifugal pump optimization, maintenance, and fault detection. Dave et al. [18] developed predictive maintenance frameworks utilizing large high-resolution datasets and multiple classification algorithms including ANN, Random Forest, SVM, and Naive Bayes, with ANN achieving perfect classification accuracy. Wang et al. [19] further demonstrated the benefits of adaptive PID control systems integrated with real-time parameter estimation, improving transient responses and reducing flow regulation errors.

A parametric optimization study aimed at reducing the axial thrust caused by pressure imbalance behind the impeller in centrifugal pump, the optimization focused on the diameter, number, and location of balance holes [8]. Design samples were generated using the Sobol sequence, and CFD-based analyses were performed on these samples. A multi-objective cost function was formulated by normalizing head and power consumption and optimized alongside axial thrust. As a result of Bayesian optimization and Pareto analysis, axial thrust was reduced by 40.59%, while head and power consumption were preserved at rates of 99.98% and 99.87%, respectively.

1.3. Fuzzy Logic Applications in Pump Systems

Given the inherent uncertainties in complex turbomachinery systems, fuzzy logic has been recognized as a powerful tool to handle vague, imprecise, or incomplete data for both design and operational optimization. Gupta et al.[20] proposed an advanced fuzzy rule-based Failure Mode and Effects Analysis (FMEA), integrating Dempster-Shafer theory for risk prioritization in centrifugal pump components. This approach improved the reliability of risk assessments over traditional RPN-based methods.

In fault diagnosis, fuzzy logic has been effectively combined with statistical feature extraction and rule-based classifiers. Sakthivel et al.[21] developed decision tree-fuzzy and rough set-fuzzy hybrid models, achieving 99.3% fault classification accuracy in centrifugal pump condition monitoring. Ergur [22] employed a Fuzzy Wavelet Neural Network (FWNN) to extend limited experimental datasets, enabling multi-objective optimization of impeller blade number, and yielding optimal performance at seven blades.

The integration of fuzzy logic with heuristic algorithms has further broadened its application scope. Zhang et al. [23] combined Genetic Algorithms (GA) with fuzzy logic to optimize semi-open impeller designs, improving efficiency from 50.19% to 55.41% while reducing near-wall entropy losses. Kleinmann et al. [24] designed a fuzzy-based health monitoring system that successfully quantified degradation severity across multiple failure modes, enhancing predictive maintenance capabilities.

In advanced biomedical and energy applications, fuzzy logic has been coupled with metaheuristic algorithms such as the Bees Algorithm. Incebay et al. [25] proposed a Modified and Constrained Bees Algorithm (MCBA) integrated with fuzzy logic for centrifugal blood pump optimization, achieving optimal wall shear stress and efficiency values at varying operating points. El-koliel et al. [26] demonstrated superior speed regulation performance for electrical submersible pump using fuzzy controllers, outperforming conventional PI control schemes. Wang and Binglei [27] introduced B-Spline Neural Networks (BSNN) to automate fuzzy rule extraction, providing effective fault detection despite incomplete expert knowledge.

A previous study has explored centrifugal pump optimization using CFD and geometric modifications to enhance hydraulic efficiency and flow characteristics[28]. While these efforts improved overall performance, they did not examine the effects of balancing hole geometry on axial thrust and mechanical stability—key factors influencing pump reliability. The present study builds on this foundation by integrating validated regression modeling with intelligent optimization techniques, such as the Bees Algorithm and Fuzzy Inference System, to analyze and optimize balancing hole configurations for improved efficiency and reduced axial load.

1.4. Gap in Current Research

While significant research has been conducted on both balancing hole optimization and the application of computational intelligence techniques to centrifugal pump, limited studies exist that directly compare fuzzy inference systems and bio-inspired algorithms such as the Bees Algorithm specifically for balancing hole design optimization. Most prior work has focused on either the hydraulic effects of balancing holes or the application of optimization techniques to global pump design parameters, with few investigations targeting the delicate balance between axial thrust minimization and efficiency preservation for balancing hole geometry.

Therefore, this study aims to fill this research gap by developing and comparing two distinct optimization frameworks: (i) a Fuzzy Inference System utilizing linguistic rule bases and membership functions, and (ii) the Bees Algorithm inspired by natural swarm intelligence. By evaluating both approaches on a common design problem using regression models trained on extensive CFD data, this work offers a systematic and comprehensive assessment of their relative strengths, computational efficiency, and applicability for centrifugal pump balancing hole design.

2. MATERIAL AND METHODS

In centrifugal pump, axial thrust generated by the pressure difference between the front and rear faces of the impeller is a critical issue that leads to reduced bearing life and overheating, ultimately compromising pump reliability and efficiency. One of the widely used and cost-effective methods to counter this axial thrust is drilling balancing holes on the impeller. However, this technique, while mitigating axial loads, introduces internal fluid recirculation as shown in Figure 1, which can negatively affect hydraulic performance and overall pump efficiency. Therefore, a crucial engineering challenge arises: how to design and position balancing holes in a way that effectively reduces axial thrust while minimizing the detrimental impact on pump efficiency.

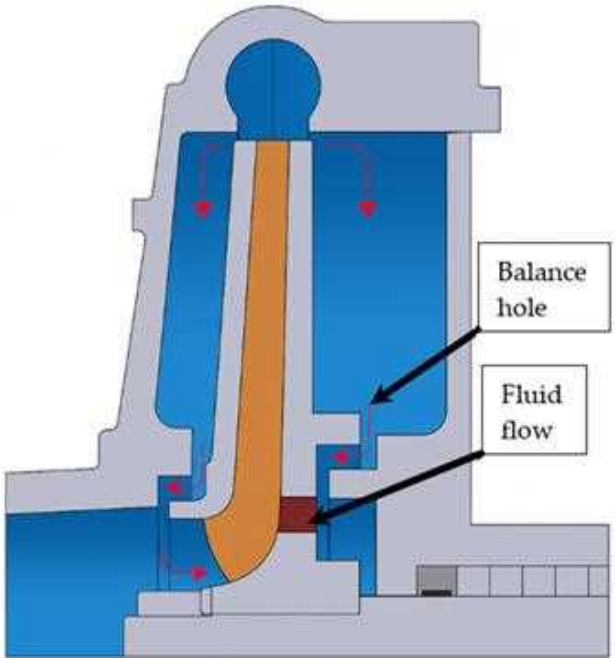


Figure 1. Flow Direction Inside the Impeller Through the Balancing Hole [29].

2.1. Design Variables and Objective Functions

In the optimization of centrifugal pump impellers with balancing holes, the goal is to minimize axial loads while preserving or improving pump efficiency. To achieve this, four critical geometric parameters were selected as design variables due to their direct influence on fluid dynamics and mechanical performance. These are:

Hole Central Angle (C_1, in degrees)

Hole Diameter (C_2, in mm)

Hole Central Diameter (C_3, in mm)

Number of Holes (C_4, discrete values: 3 or 6)

These variables were chosen within practical manufacturing constraints and to ensure rotor balance. The values of each design variable were bounded as shown in Table 1 to avoid structural interference and to comply with the configuration of the reference TKF 125-400 pump, which contains six impeller blades, 350 m^3/h flow rate, 50 m head, 1500 rpm speed.

Table 1. Design Variable Ranges for Optimization

Parameter	Symbol	Min Value	Max Value
Hole Central Angle (°)	C_1	0	22.5
Hole Diameter (mm)	C_2	6	12
Hole Central Diameter (mm)	C_3	100	130
Number of Holes	C_4	3	6

To formulate the optimization problem, two objective functions were modeled using a full quadratic regression approach based on 111 CFD simulations conducted in ANSYS Fluent. The validity and predictive reliability of the regression models developed for pump efficiency and axial load were

comprehensively assessed using statistical analyses performed in Minitab at a 95% confidence level. The efficiency regression model achieved an R^2 of 90.99%, with adjusted and predicted R^2 values of 89.79% and 80.35%, respectively, demonstrating strong explanatory power and excellent predictive performance with minimal overfitting. Similarly, the axial load regression model exhibited outstanding accuracy, with R^2 = 99.75%, R^2(adj) = 99.71%, and R^2(pred) = 99.58%, confirming its exceptional fit and generalization capability. Analysis of variance (ANOVA) indicated that all main effects (C_1, C_2, C_3, and C_4) were highly significant ($p < 0.001$), while several interaction terms—particularly C_2C_2, C_1C_3, and C_3*C_4—also contributed meaningfully to the overall model response. All variance inflation factors (VIF < 2) verified the absence of multicollinearity among predictors, ensuring model stability and interpretability. Diagnostic evaluations confirmed that residuals were randomly and normally distributed, satisfying regression assumptions, with only a few boundary CFD cases exhibiting large, standardized residuals due to extreme geometric configurations rather than model deficiencies. Moreover, the physical trends of the coefficients were consistent with hydraulic principles: larger hole angles improved efficiency, while excessive hole diameters and smaller central diameters increased axial thrust. Collectively, these results validate the robustness, statistical soundness, and physical consistency of the proposed regression models, confirming their suitability for accurately predicting centrifugal pump performance across varying balancing-hole geometries. These functions relate the design variables to two main performance outputs: pump hydraulic efficiency (η) and axial load (f_{axial}).

Pump Efficiency (η):

$$\eta = 84.63 - 0.0103C_1 - 0.4501C_2 - 0.0397C_3 - 0.2512C_4 + 0.000108C_1^2 + 0.01417C_2^2 + 0.000117C_3^2 + 0.000404C_1C_2 + 0.000034C_1C_3 + 0.000755C_1C_4 + 0.000501C_3C_2 + 0.01397C_4C_2 + 0.000486C_3C_4 \quad (1)$$

Axial Load (f_{axial} in Newton):

$$f_{axial} = 14501 - 98.4C_1 - 1901.7C_2 + 70.9C_3 - 1601C_4 - 0.239C_1^2 + 61.23C_2^2 - 0.345C_3^2 + 1.750C_1C_2 + 0.831C_1C_3 + 1.335C_1C_4 - 1.247C_3C_2 + 88.25C_4C_2 + 2.203C_3C_4 \quad (2)$$

Three separate objective functions were considered to analyze trade-offs between mechanical and hydraulic performance:

Multi-objective function (f_{obj1}) combines efficiency loss and normalized axial load relative to a baseline impeller without holes.

$$f_{obj1} = 80.866 - \eta + f_{axial}/8858.76 \quad (3)$$

Efficiency-focused function (f_{obj2}) represents the efficiency loss alone.

$$f_{obj2} = 80.866 - \eta \quad (4)$$

Axial load-focused function (f_{obj3}) reflects the normalized axial load only.

$$f_{obj3} = 8858.76/f_{axial} \quad (5)$$

The complete optimization problem is formally defined as:

$x = (C_1, C_2, C_3, C_4)$

subject to $g_{min} \leq x \leq g_{max}$

min $(f_{obj1}, f_{obj2}, f_{obj3})$

These formulations enable evaluating how balancing hole configurations affect centrifugal pump performance, guiding designs that extend bearing life while maintaining hydraulic efficiency.

2.2. The Bees Algorithm Implementation

The Bees Algorithm (BA) is a bio-inspired optimization technique modeled after the foraging

behavior of honeybees [30]. In the context of centrifugal pump impeller optimization, it provides a robust method for solving complex multi-objective problems involving both discrete and continuous design variables. The algorithm balances exploration and exploitation of the solution space, making it well-suited to identify optimal configurations for balancing holes that minimize axial thrust while preserving hydraulic efficiency.

The implementation of the Bees Algorithm in this study involved several key steps. First, a population of 20 scout bees (n) was initialized randomly within the defined boundaries of the four design variables: hole central angle (C_1), hole diameter (C_2), hole central diameter (C_3), and number of holes (C_4). Each bee represents a potential design solution. The fitness of each solution was evaluated using the multi-objective regression models developed in Section 2.1. The fitness functions included combinations of pump efficiency loss and normalized axial load, depending on the optimization scenario (multi-objective, efficiency-only, or axial-load-only).

A subset of the most promising solutions (m = 10) was selected for neighborhood search. Among them, the top elite sites (e = 4) received a larger number of recruited bees (n_ep = 20) to conduct intensive local search, while the remaining selected sites received fewer recruits (n_sp = 10). The local search was performed by exploring the vicinity of each selected site within a predefined patch size (ngh = 0.5), which controls the local search radius. The search continues iteratively, refining the population by selecting the best individuals from each generation and repeating the neighborhood exploration. A maximum of 11 iterations (i_{max}) was used to ensure convergence within a reasonable computational time.

Table 2. The Bees Algorithm Parameters

Parameter	Symbol	Value
Population size	n	20
Number of selected sites	m	10
Number of elite sites	e	4
Recruited bees for elite sites	n_{ep}	20
Recruited bees for other selected sites	n_{sp}	10
Neighborhood patch size	ngh	0.5
Maximum number of iterations	i_{max}	11

The number of balancing holes (C_4), being a discrete variable with only two valid options (3 or 6), was manually fixed during some runs to enhance result precision. This prevented the algorithm from selecting infeasible fractional values that would violate design constraints or cause dynamic imbalance.

The Bees Algorithm was executed on a personal computer with an Intel® Core™ i7 processor @ 2.6 GHz and 16 GB RAM, under a Windows 10 (64-bit) environment. The optimized results for each objective function demonstrated the algorithm's capability to effectively explore the design space and converge towards configurations that reduce axial force while maintaining or improving efficiency. This implementation confirmed the algorithm's suitability for high-dimensional, nonlinear optimization problems in pump design.

2.3. Fuzzy Inference System Design

To complement the optimization-based Bees Algorithm, a Fuzzy Inference System (FIS) was developed to provide a fast, explainable, and robust method for evaluating the impact of balancing hole design parameters on the axial load and pump efficiency. The primary objective of the FIS is to minimize axial thrust while reducing the efficiency loss caused by the addition of balancing holes. This system is particularly useful in scenarios where numerical simulations are computationally expensive or where interpretability of the decision-making process is essential.

The FIS uses four key design parameters as inputs:

C_1: Hole central angle (0°–22.5°)

C_2: Hole diameter (6–12 mm)

C_3: Hole central diameter (100–130 mm)

C_4: Number of holes (3 or 6)

Each variable is fuzzified using triangular membership functions, with linguistic terms assigned as in Table 3.

Table 3. Fuzzification of the design variables

Variable	Linguistic Terms	Membership Function Range
Hole Central Angle	Small, Medium, Large	[0–7.5], [5–17.5], [15–22.5]
Hole Diameter	Narrow, Medium, Wide	[6–8], [7–11], [10–12]
Hole Central Diameter	Inner, Middle, Outer	[100–110], [105–125], [120–130]
Number of Holes	Few, Many	Discrete: 3 (Few), 6 (Many)

Two normalized output variables were defined to standardize performance evaluation across different pump designs. Axial Load (f_{axial}) is normalized between 0 and 1. Efficiency Loss ($\Delta\eta$) is calculated as the difference between the maximum achievable efficiency (80.866%) and the actual efficiency, normalized to a 0–1 scale.

The output membership functions are also defined using triangular distributions with linguistic terms such as Very Low, Low, Medium, High, and Very High for axial load, and None, Low, Medium, and High for efficiency loss.

The rule base was formulated by analyzing CFD and regression outputs. A total of 54 expert-derived fuzzy rules were created, incorporating combinations of all input variable states.

Table 4. Fuzzy rules for selection of optimal design parameters

Rule	Hole Central Angle(C_1)	Hole Diameter (C_2)	Hole Central Diameter(C_3)	Number of Hole(C_4)	THEN Efficiency	AND Axial Load
1	Medium	Medium	Medium	Medium	Medium	Medium
10	Low	Low	Medium	High	Medium-High	Medium
20	Medium	High	Medium	Medium	Low	Low
30	High	High	Low	Low	High	Medium
40	High	Medium	High	High	Low	Low
50	Very High	Very High	High	High	Very Low	Very Low
54	Very High	Very High	Very High	Very High	Very Low	Very Low

These rules enable the system to infer performance metrics even in regions of the design space where simulation data is sparse.

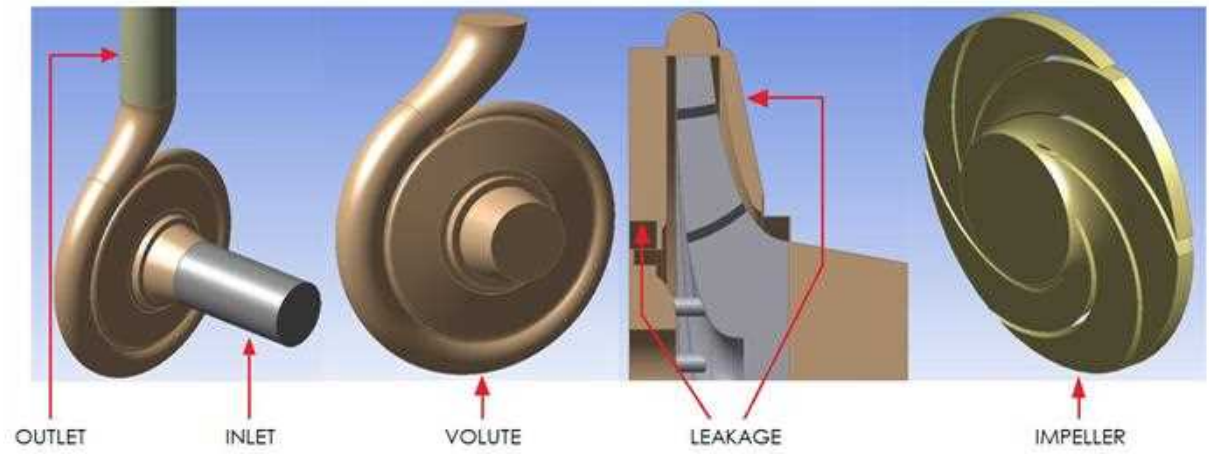
The FIS follows a Mamdani-type inference mechanism consist of fuzzification to convert crisp input values into fuzzy sets using defined membership functions, and consist of rule evaluation to apply fuzzy rules using min–max logic based on the Mamdani approach, and consist of aggregation to combine the results of all applicable rules, and consist of defuzzification to use the centroid method to convert the

fuzzy output back to crisp numerical values. This approach supports real-time decision-making in the design phase and provides insight into how each input contributes to overall performance.

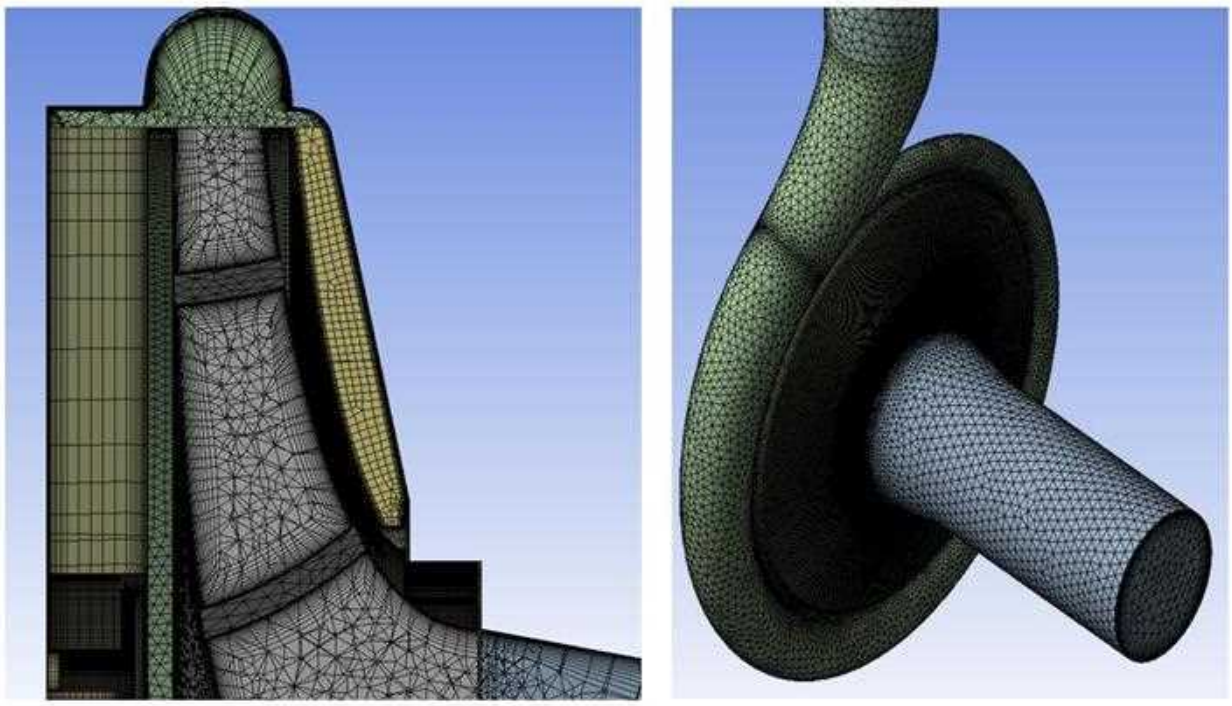
The Computational Fluid Dynamics (CFD) analysis was carried out using the Finite Volume Method (FVM) under the assumption of steady flow. Boundary conditions were specified by applying static pressure at the inlet and mass flow rate at the outlet, in line with the pump's operating conditions. To improve solution accuracy, mesh refinement was performed near the wall regions, ensuring that the non-dimensional wall distance (y^+) values stayed within the acceptable range, with suitable wall functions applied. For turbulence modeling, the SST k–ω turbulence model was employed, while maintaining y^+ values below 300. The computational mesh was generated using Ansys Meshing software and the CAD model was generated using SolidWorks as shown in Figure 2-b-a, with hexahedral elements applied in regions prone to leakage and energy loss, and tetrahedral elements used elsewhere in the domain. To verify grid independence, the final mesh was constructed with approximately 5.5 million elements and a skewness value of 0.94. The pump boundary conditions are presented in Table 5.

Table 5. Pump Boundary Conditions

Location	Boundary Condition
Inlet	Pressure Inlet
Outlet	Mass Flow Outlet
Impeller	Rotating Reference Frame



a)



b)

Figure 2. Illustration of **a)** CAD design and **b)** Ansys meshing.

3. RESULTS AND DISCUSSION

The Bees Algorithm was executed on a computer equipped with an Intel® Core™ i7 @ 2.6 GHz processor, 16 GB RAM, and running Windows 10 64-bit. The results are presented in Table 6. The algorithm was executed for three different objectives. The first objective function is f_{obj1}, abbreviated as MOO (Multi-Objective Optimization) in Table 6. The second objective function is f_{obj2}, abbreviated as OE (Efficiency Optimization) in Table 6, which only considers the differences between efficiencies as the objective. The third objective function is f_{obj3}, abbreviated as OAL (Axial Load Optimization) in Table 6, which only considers the ratio of axial loads as the objective. Additionally, in order to obtain more precise results, the number of balancing holes (C_4) was manually adjusted. Otherwise, the algorithm would have generated values ranging between 3 and 6 during the optimization process. The convergence graph of the optimization is shown in Figure 2.

Table 6. Results of optimization by using The Bees Algorithm.

		Angle (Degree) (C_1)	Hole Diameter (C_2)	Center Diameter (C_3)	Fitness Value
MOO	**C_4=3**	22.5	6	100	1.8975
	C_4=6	22.5	6	100	1.9248
OE	**C_4=3**	22.5	6	100	1.2773
	C_4=6	22.5	6	100	1.5827
OAL	**C_4=3**	15	12	126	0.1909
	C_4=6	15	12	100	0.0974

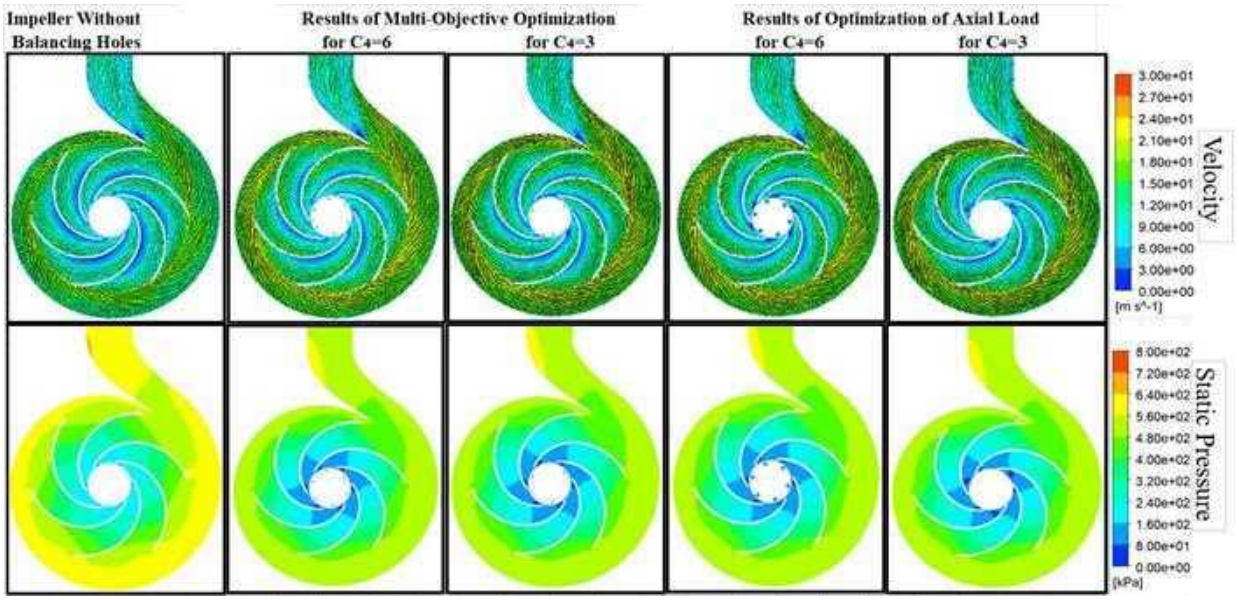


Figure 3. CFD analysis for result of Bee algorithm

Figure 3 presents a comparative analysis of different centrifugal pump impeller designs, focusing on velocity distribution and static pressure under various optimization conditions. The columns represent five design scenarios: an impeller without balancing holes, and impellers optimized either through multi-objective optimization or axial load optimization, each under two parameter settings (C_4=6 and C_4=3). The top row illustrates the velocity vector fields, while the bottom row shows the corresponding static pressure distributions.

The unoptimized impeller (first column) exhibits irregular and chaotic flow patterns, indicating inefficiencies such as flow recirculation and potential performance losses. In contrast, the optimized designs, particularly under the multi-objective and axial load optimization with C_4=6, display smoother and more organized velocity fields. This suggests better hydraulic performance and reduced energy losses. Designs with C_4=3 show slightly more turbulence and less favorable flow alignment, implying that a higher C_4 value may be more effective for performance enhancement.

In terms of static pressure distribution, the unoptimized impeller again shows non-uniform pressure zones, which could contribute to higher axial loads and mechanical stress. Optimized designs, especially with C_4=6, reveal a more balanced and consistent pressure field, indicating improved pressure recovery and potentially lower axial thrust. Overall, the figure demonstrates that incorporating balancing holes and employing optimization techniques, especially with a higher C_4 value, significantly enhances both the velocity and pressure characteristics of the impeller, leading to better pump efficiency and durability.

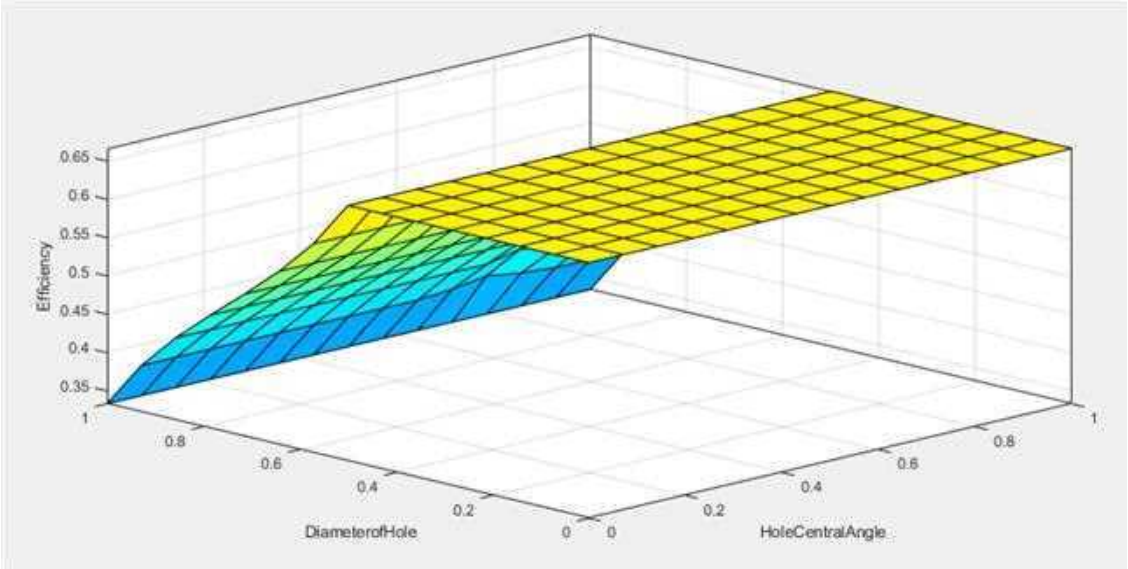


Figure 4. The 3D surface plot illustrates the relationship between efficiency, hole central angle, and hole diameter

The graph in Figure 4 shows that efficiency improves as the hole central angle increases, reaching a plateau when the angle exceeds approximately 0.3, indicating an optimal alignment for fluid flow. Conversely, increasing the hole diameter leads to a noticeable drop in efficiency, especially when the diameter exceeds 0.4. This suggests that while a larger central angle enhances flow characteristics and system performance, an oversized hole disrupts flow stability and causes energy loss. Overall, the highest efficiency is achieved with a moderate-to-large central angle and a small hole diameter, highlighting the importance of geometrical optimization in design.

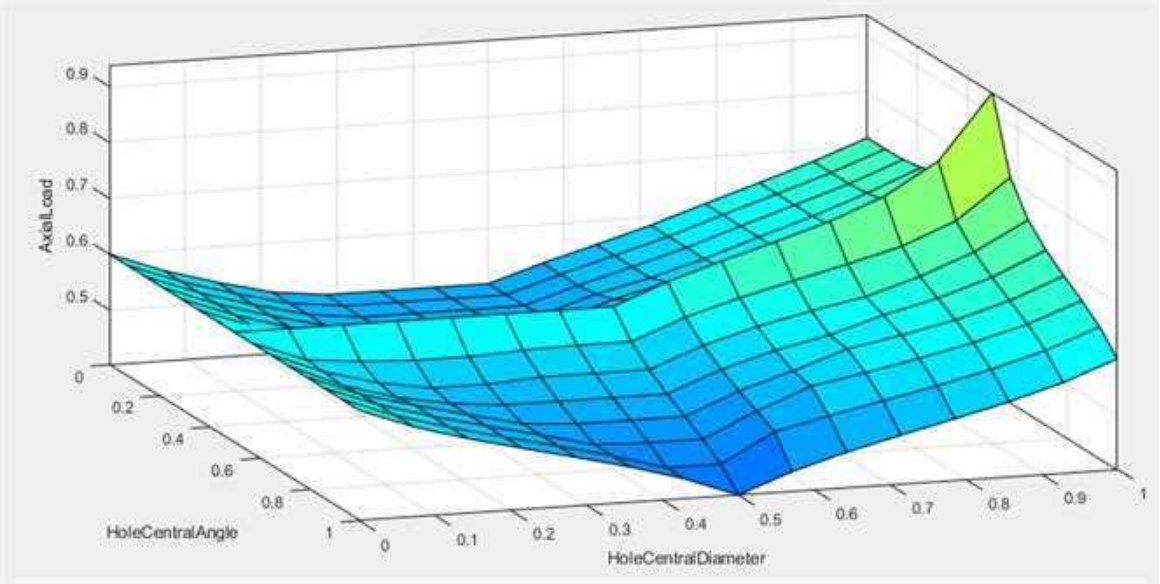


Figure 5. The 3D surface plot illustrates the relationship between axial load, hole central angle, and hole central diameter.

The 3D surface plot in Figure 5 illustrates how axial load varies with respect to hole central angle and hole central diameter in a mechanical or fluid system, likely involving a balancing or pressure-relief mechanism. The graph shows that axial load reaches its minimum when the hole central angle is around 1.0 and the hole diameter is approximately 0.4, suggesting an optimal configuration for reducing axial forces. As the hole diameter increases beyond 0.6, the axial load rises significantly, especially at lower

angles, indicating that large holes can compromise structural balance and increase force on axial components. Similarly, at low hole central angles, axial load tends to remain higher, implying insufficient pressure balancing. This analysis highlights that an ideal design should feature a large hole central angle and a moderately sized hole diameter to minimize axial load and enhance system stability.

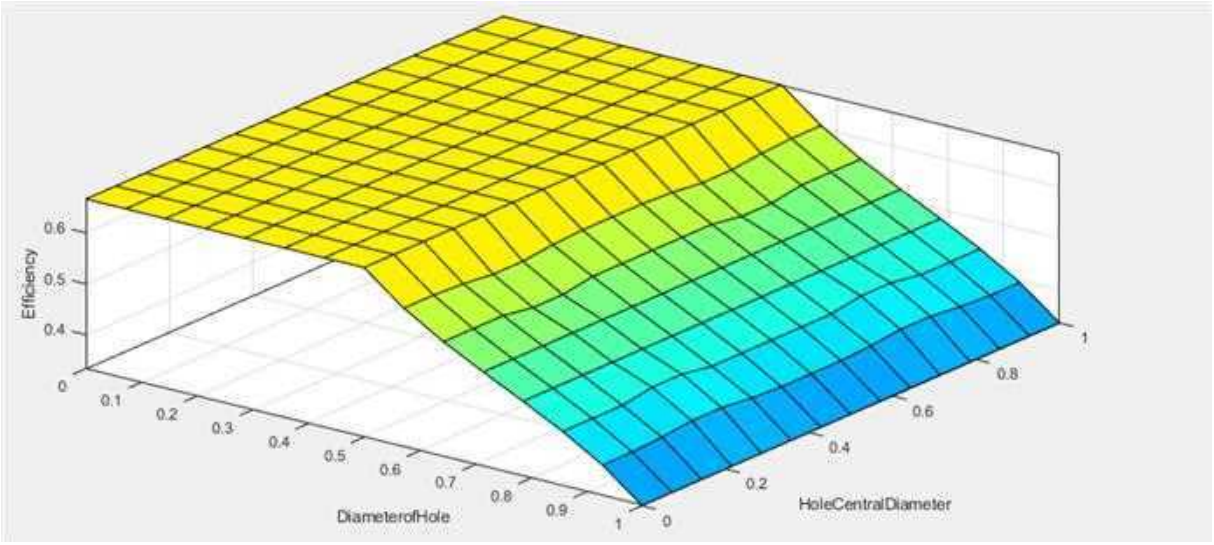


Figure 6. The 3D surface plot illustrates the relationship between efficiency, diameter of hole, and hole central diameter.

The surface graph in Figure 6 illustrates the relationship between Efficiency and two geometric parameters: Diameter of Hole and Hole Central Diameter. As shown, Efficiency is highest when both the Diameter of Hole and the Hole Central Diameter are small, with values peaking around 0.65. As either parameter increases, Efficiency declines steadily, reaching a minimum of approximately 0.3 when both parameters approach their maximum values. This trend suggests that smaller hole dimensions are more favorable for maintaining higher Efficiency, possibly due to reduced losses or better structural performance. The surface also shows a relatively flat region at lower parameter values, indicating that Efficiency is less sensitive to small changes in dimensions in that range. Overall, the graph highlights the importance of optimizing hole sizes to achieve better Efficiency outcomes.

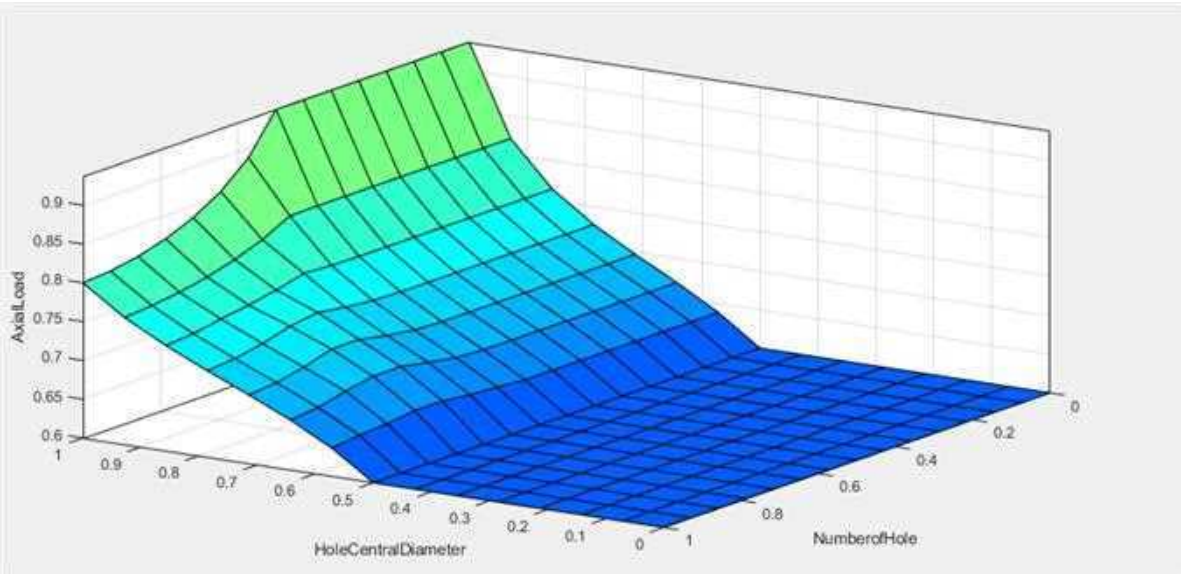


Figure 7. The 3D surface plot illustrates the relationship between axial load, number of hole, and hole central

diameter.

The surface graph in Figure 7 illustrates the variation of Axial Load with respect to two parameters: Hole Central Diameter and Number of Holes. From the plot, it is evident that Axial Load increases with an increase in the Hole Central Diameter, especially when the Number of Holes is low. The highest Axial Load values are observed when the Hole Central Diameter approaches 1 and the Number of Holes is close to 0. Conversely, as the Number of Holes increases and the Hole Central Diameter decreases, the Axial Load significantly drops, stabilizing around a lower value of approximately 0.6. This indicates that both increasing the number of holes and reducing their central diameter tend to weaken the axial load-bearing capacity of the structure. The surface trend emphasizes the critical impact of these geometrical features on structural integrity, suggesting that minimizing the number and size of central holes can help maintain higher axial strength.

Table 7. The optimal design variables obtained from Fuzzy inference system

Hole Central Angle (C_1, degrees)	**Hole Diameter** (C_2, mm)	**Hole Central Diameter** (C_3, mm)	**Number of Holes** (C_4)
7.5°	6	130	3

Table 8. Results of CFD analysis for the optimal design parameter in Table 7.

Torque (Nm)	**P_{water}**	**P_{shaft}**	**Efficiency (%)**	**Hole flow rate (m^3/h)**	**Axial Load(N)**	**Radial load(N)**
395,25	48,39	61,23	79,03	4,55	5894,41	152,96

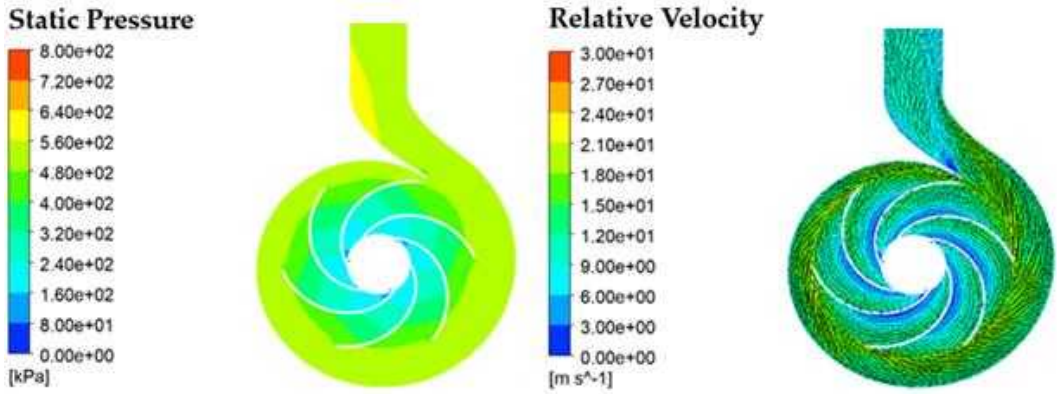


Figure 8. CFD analysis for result of Mamdani-type FIS.

Figure 8 illustrates the static pressure and relative velocity distribution within a centrifugal pump impeller and volute. The first image presents the static pressure distribution in kilopascals (kPa), with values ranging from 0 to 800 kPa. The color contour shows a gradual increase in pressure from the impeller eye toward the volute outlet. The pressure is lowest in the central region (inlet), indicated by blue and cyan colors, and progressively increases outward, shifting to green and yellow. This pattern reflects the expected pressure buildup due to the centrifugal action of the impeller, confirming that energy is being effectively transferred from the rotating blades to the fluid. However, slight asymmetry in the pressure distribution might suggest non-uniform loading or minor flow separation, particularly near the tongue of the volute.

The second image in Figure 8 displays the relative velocity field within the same impeller, measured

in meters per second (m/s), ranging up to 30 m/s. The velocity vectors are superimposed over a color map, with high velocities (red and yellow) concentrated near the blade tips and lower velocities (blue) toward the hub and suction side. The smooth curvature and alignment of the velocity vectors indicate stable and efficient flow within the impeller channels. However, areas of elevated velocity near the volute tongue and sharp gradients in velocity magnitude could indicate potential zones of flow acceleration or minor turbulence. Overall, both figures together demonstrate that the impeller operates with generally favorable pressure recovery and relatively uniform velocity distribution, suggesting a well-performing design with localized areas that may benefit from further optimization to minimize losses or mechanical loading.

4. CONCLUSIONS

In this work, an integrated optimization framework was developed to investigate the effect of balancing hole configurations on the hydraulic and mechanical performance of centrifugal pump impellers. Utilizing regression models derived from CFD data, multi-objective formulations were established and solved through the Bees Algorithm, while a parallel Fuzzy Inference System was implemented for rapid evaluation based on expert rules.

The Bees Algorithm consistently yielded superior optimization outcomes across all objective functions by effectively navigating the nonlinear and mixed-variable design space. The convergence characteristics confirmed the robustness of the proposed framework for complex pump design problems despite of negligible longer process duration of solutions as 5-7 seconds. Meanwhile, the FIS demonstrated its value in providing fast in 0.1 seconds, explainable predictions with minimal computational cost, particularly when extensive CFD evaluations are impractical.

The complementary strengths of both methods suggest that a hybrid or sequential deployment of these algorithms may offer significant advantages for centrifugal pump design, balancing computational efficiency with optimization precision. Future studies may further explore adaptive hybridization schemes and broader application to other turbomachinery components.

Declaration of Ethical Standards

The authors confirm that the manuscript is an original work, has not been published previously, and is not under consideration for publication elsewhere. All listed authors have made significant contributions to the conception, design, and execution of the research

Credit Authorship Contribution Statement

Conceptualization, Selahattin SEFACI. and Osman ACAR ,Methodology, Selahattin SEFACI, Osman ACAR ,and Mete KALYONCU ;Software and CFD simulations, Selahattin SEFACI; Validation, Selahattin SEFACI and Mete KALYONCU.; Formal analysis, Selahattin SEFACI, Osman ACAR.; Investigation, Selahattin SEFACI and Mete KALYONCU; Data curation, Selahattin SEFACI and Osman ACAR.; Writing—original draft preparation, Selahattin SEFACI; Writing—review and editing, Osman ACAR and Mete KALYONCU ;Visualization, Selahattin SEFACI and Osman ACAR ;Supervision, Saim KOÇAK All authors have read and agreed to the published version of the manuscript.

All authors have read and approved the final version of the manuscript.

Declaration of Competing Interest

The authors declare that they have no known competing financial interests or personal relationships

that could have appeared to influence the work reported in this paper.

Funding / Acknowledgements

No funding was received for this study. However, Sempa Pompa A.Ş. supported the study in terms of software. Thus, we would like to express our sincere gratitude for the outstanding support and cooperation you have provided.

Data Availability

Data can be provided upon request.

Declaration of Generative AI Use

The authors confirm that no generative artificial intelligence tools were used in the preparation of this manuscript, including for the generation of scientific content, research data, interpretations, analyses, or language editing and readability improvements. All content presented is the original work of the authors, who maintain full responsibility for the accuracy, integrity, and originality of the study in compliance with ethical and legal standards.

Nomenclature

a) Design Variables
- C_1 — Hole central angle (°)
- C_2 — Hole diameter (mm)
- C_3 — Hole central diameter (mm)
- C_4 — Number of holes

b) Performance Metrics
- η — Hydraulic efficiency
- f_{axial} — Axial load (N)
- $\Delta\eta$ — Efficiency loss
- f_{obj1}, f_{obj2}, f_{obj3} — Optimization objective functions

c) CFD and Mathematical Symbols
- y^+ — Non-dimensional wall distance
- SST — Shear Stress Transport
- R^2 — Coefficient of determination
- VIF — Variance Inflation Factor

d) Physical Parameters
- Pwater — Water power
- Pshaft — Shaft power
- Q — Flow rate
- ω — Angular velocity

5. REFERENCES

[1] W.-d. Cao, X. Dai, and Q.-x. Hu, "Effect of impeller reflux balance holes on pressure and axial force of centrifugal pump," *Journal of Central South University,* vol. 22, no. 5, pp. 1695-1706, 2015.

[2] X. Luo, H. Xie, J. Feng, Z. Ge, and G. Zhu, "Influence of the balance hole on the performance of a gas–liquid two–phase centrifugal pump," *Ocean Engineering,* vol. 244, p. 110316, 2022.

[3] Z. Liu, X. Chen, D. Wang, and Y. Hou, "Experiment and analysis of balance hole liquid leakage in centrifugal pump," *Transactions of the Chinese Society of Agricultural Engineering,* vol. 33, no. 7, pp. 67-74, 2017.

[4] C. W. Dong Wei, "Influence of balance hole diameter on performance and balance chamber pressure of centrifugal pump," *Nongye Jixie Xuebao/Transactions of the Chinese Society of Agricultural Machinery,* vol. 46, no. 6, 2015.

[5] B. K. Thileep Kumar, "Design Optimization of Balancing Holes in a Centrifugal Pump," 2025.

[6] D. Xun *et al.*, "Effect of the circumferential position of balance holes on the cavitation performance and cavitation erosion of centrifugal pump," *Journal of Applied Fluid Mechanics,* vol. 18, no. 1, pp. 131-144, 2024.

[7] X. Cheng, J. Luo, B. Xiong, and Y. Jiang, "Influence of the balance hole circumferential position on the cavitation performance of the semiopen impeller centrifugal pump," *Mathematical Problems in Engineering,* vol. 2021, no. 1, p. 4472433, 2021.

[8] W. Dong, Z. Liu, H. Zhang, G. Zhang, H. Jiang, and P. Li, "Effects of the balance hole diameter on the flow characteristics of the rear chamber and the disk friction loss in the centrifugal pump," *Processes,* vol. 10, no. 3, p. 613, 2022.

[9] W. Dong, D. Chen, J. Sun, Y. Dong, Z. Yang, and J. Yan, "Influence of balance hole diameter on leakage flow of the balance chamber in a centrifugal pump," *Shock and Vibration,* vol. 2021, no. 1, p. 8860493, 2021.

[10] H. Xie, X. Luo, C. Li, S. Yan, and G. Zhu, "Research on the Influence of Balance Hole on the Performance of Ocean energy gas-liquid multiphase pump," in *IOP Conference Series: Earth and Environmental Science*, 2021, vol. 766, no. 1: IOP Publishing, p. 012024.

[11] M. Fathi, H. Alemi, M. Raisee, and A. Nourbakhsh, "The effects of balancing holes on the axial force of a centrifugal pump in the reverse mode," in *Journal of Physics: Conference Series*, 2024, vol. 2707, no. 1: IOP Publishing, p. 012048.

[12] W. Cao, X. Yang, and Z. Jia, "Numerical simulation of cavitation flow in a low specific-speed centrifugal pump with different diameters of balance holes," *Journal of Marine Science and Engineering,* vol. 10, no. 5, p. 619, 2022.

[13] C. Wang *et al.*, "Automatic optimization of centrifugal pump for energy conservation and efficiency enhancement based on response surface methodology and computational fluid dynamics," *Engineering Applications of Computational Fluid Mechanics,* vol. 17, no. 1, p. 2227686, 2023.

[14] M. Bashiri, S. Derakhshan, and J. Shahrabi, "Design optimization of a centrifugal pump using particle swarm optimization algorithm," *International Journal of Fluid Machinery and Systems,* vol. 12, no. 4, pp. 322-331, 2019.

[15] H. Chang *et al.*, "Efficiency optimization of energy storage centrifugal pump by using energy balance equation and non-dominated sorting genetic algorithms-II," *Journal of Energy Storage,* vol. 114, p. 115817, 2025.

[16] H. Safikhani, A. Khalkhali, and M. Farajpoor, "Pareto based multi-objective optimization of centrifugal pumps using CFD, neural networks and genetic algorithms," *Engineering Applications of Computational Fluid Mechanics,* vol. 5, no. 1, pp. 37-48, 2011.

[17] H. Qi *et al.*, "Performance optimization of centrifugal pump based on particle swarm optimization and entropy generation theory," *Frontiers in Energy Research,* vol. 10, p. 1094717, 2023.

[18] G. S. Dave, A. P. Pandhare, A. P. Kulkarni, and D. V. Khankal, "Innovative data techniques for centrifugal pump optimization with machine learning and AI model," *PloS one,* vol. 20, no. 6, p. e0325952, 2025.

[19] Y. Wang, H. Zhang, Z. Han, and X. Ni, "Optimization design of centrifugal pump flow control system based on adaptive control," *Processes,* vol. 9, no. 9, p. 1538, 2021.
[20] G. Gupta, H. Ghasemian, and A. A. Janvekar, "A novel failure mode effect and criticality analysis (FMECA) using fuzzy rule-based method: A case study of industrial centrifugal pump," *Engineering Failure Analysis,* vol. 123, p. 105305, 2021.
[21] N. Sakthivel, V. Sugumaran, and B. B. Nair, "Comparison of decision tree-fuzzy and rough set-fuzzy methods for fault categorization of mono-block centrifugal pump," *Mechanical systems and signal processing,* vol. 24, no. 6, pp. 1887-1906, 2010.
[22] H. ERGÜR, "Multiple performance optimization of a single stage centrifugal pump using an intelligent system approach," *Journal of Applied Fluid Mechanics,* vol. 15, no. 4, 2022.
[23] F. Zhang *et al.*, "Optimization design of a semi-open centrifugal impeller using GA-fuzzy logic combination strategy," *Journal of Applied Fluid Mechanics,* vol. 16, no. 7, pp. 1427-1441, 2023.
[24] S. Kleinmann, R. Stetter, and P. K. K. Prasad, "Optimization of a pump health monitoring system using fuzzy logic," in *2013 Conference on Control and Fault-Tolerant Systems (SysTol)*, 2013: IEEE, pp. 251-256.
[25] O. Incebay, A. Onder, M. A. Sen, R. Yapici, and M. Kalyoncu, "Fuzzy-based modeling and speed optimization of a centrifugal blood pump using a modified and constrained Bees algorithm," *Computer Methods and Programs in Biomedicine,* vol. 221, p. 106867, 2022.
[26] S. M. El-Koliel, H. Eleissawi, and A. S. Nada, "Speed control of electrical submersible pumps using fuzzy logic control," *International Journal of Power Electronics and Drive Systems (IJPEDS),* vol. 13, no. 4, pp. 2515-2528, 2022.
[27] K. Wang and B. Lei, "Using B-spline neural network to extract fuzzy rules for a centrifugal pump monitoring," *Journal of Intelligent Manufacturing,* vol. 12, no. 1, pp. 5-11, 2001.
[28] B. K. T. KUMAR, "Design Optimization of Balancing Holes in a Centrifugal Pump."
[29] S. Sefacı, "Tek Kademeli Santrifüj Pompalarda Dengeleme Deliklerinin Pompa Performansına Etkisinin Sayısal ve Deneysel Araştırılması," Konya Teknik Üniversitesi, 2022.
[30] D. T. Pham, A. Ghanbarzadeh, E. Koç, S. Otri, S. Rahim, and M. Zaidi, "The bees algorithm—a novel tool for complex optimisation problems," in *Intelligent production machines and systems*: Elsevier, 2006, pp. 454-459.

Konya Mühendislik Bilimleri Dergisi, c.14, s.2, 1016-1032, 2026
Konya Journal of Engineering Sciences, v.14, n.2, 1016-1032, 2026
ISSN: 2667-8055 (Electronic)
DOI: 10.36306/konjes.1747032

DESIGN AND IMPLEMENTATION OF AN OFFLINE AUTOCLAVE WEB SIMULATOR

[1,*]Ali Özhan AKYÜZ, [2]Mustafa AYAN, [3]Kazım KUMAŞ, [4]Durmuş TEMİZ

[1]*Bucak Computer and Informatics Faculty, Burdur Mehmet Akif Ersoy University, Burdur, Türkiye*
[1,2,3,4]*Bucak Emin Gulmez Vocational School of Technical Sciences, Burdur Mehmet Akif Ersoy University, Burdur, Türkiye*
[1]aakyuz@mehmetakif.edu.tr, [2]mayan@mehmetakif.edu.tr, [3]kkumas@mehmetakif.edu.tr, [4]dtemiz@mehmetakif.edu.tr

Highlights

- Web-based, single-file simulator requires no installation or internet access.
- Real-time phase simulation and interactive alerts enhance autoclave training.
- Users test how temperature and load types affect sterilization outcomes.

Graphical Abstract



Figure Flowchart of the proposed method

***Corresponding Author:** Ali Özhan AKYÜZ, aakyuz@mehmetakif.edu.tr

Konya Mühendislik Bilimleri Dergisi, c.14, s.2, 1016-1032, 2026
Konya Journal of Engineering Sciences, v.14, n.2, 1016-1032, 2026
ISSN: 2667-8055 (Electronic)
DOI: 10.36306/konjes.1747032

DESIGN AND IMPLEMENTATION OF AN OFFLINE AUTOCLAVE WEB SIMULATOR

[1,*]Ali Özhan AKYÜZ, [2]Mustafa AYAN, [3]Kazım KUMAŞ, [4]Durmuş TEMİZ

[1]Bucak Computer and Informatics Faculty, Burdur Mehmet Akif Ersoy University, Burdur, Türkiye
[1,2,3,4]Bucak Emin Gulmez Vocational School of Technical Sciences, Burdur Mehmet Akif Ersoy University, Burdur, Türkiye
[1]aakyuz@mehmetakif.edu.tr, [2]mayan@mehmetakif.edu.tr, [3]kkumaş@mehmetakif.edu.tr, [4]dtemiz@mehmetakif.edu.tr

(Received: 20.07.2025; Accepted in Revised Form: 18.12.2025)

ABSTRACT: This study presents a fully web-based, interactive simulator designed to facilitate understanding and training in autoclave sterilization processes, which are critical in healthcare and laboratory environments. Given the complexity of traditional theoretical training methods and the high costs and safety risks of using real equipment, digital simulation tools offer a crucial educational alternative. The simulator is a single-file application built with modern web technologies — HTML5, CSS3, and JavaScript — and requires no external installation or an internet connection. The core features of the simulator include real-time phase simulation, parameter adjustment with dynamic graphics, and interactive safety warnings for critical safety conditions. Users can experience all stages of the sterilization cycle (pre-vacuum, heating, sterilization, drying) and instantly observe how parameters such as temperature, time, and load type affect the process. In a pilot usability study conducted with 20 undergraduate students, more than 90% reported that the simulator improved their understanding of autoclave phases and safety protocols, highlighting its pedagogical effectiveness. Preliminary data and pilot feedback indicate that the interface is intuitive, understandable, and educationally beneficial. This digital tool demonstrates significant potential to reinforce theoretical knowledge and to prepare learners for practical applications, thereby addressing a critical gap in education.

Keywords: *Autoclave, Digital Education, Interactive Learning, Sterilization, Web-Based Simulator.*

1. INTRODUCTION

Sterilization is one of the cornerstones of modern healthcare and biological research. Sterilization of medical devices, glassware, textiles, and culture media used in hospitals, laboratories, and production facilities is essential to minimize the risk of infection and ensure safe working conditions. Inadequate sterilization can lead to increased nosocomial infections, experimental errors, and serious health problems [1,2].

Since their invention by Charles Chamberland in the late 19th century, autoclaves have become one of the most important tools of sterilization technology. The basic principle is to destroy microorganisms, spores, and pathogens by using saturated water vapor under high temperature (usually 121-134°C) and pressure (1-3 bar). Autoclaves are now widely used in both healthcare and industrial production facilities. They are considered the gold standard for sterilizing a wide variety of materials, including surgical instruments, laboratory glassware, textiles, and liquid culture media [3,4].

Autoclaves are produced in different types as technological developments advance. Basically, they fall into three main categories: gravity displacement, pre-vacuum, and pulsed vacuum autoclaves. Gravity autoclaves expel air from above by introducing steam at the bottom of the chamber; this method is simple and economical but may be less effective with complex or porous loads. Pre-vacuum autoclaves, on the other hand, remove air from the sterilization chamber using a vacuum pump, allowing steam to reach all

***Corresponding Author:** Ali Özhan AKYÜZ, aakyuz@mehmetakif.edu.tr

surfaces more efficiently, and are especially preferred for textiles, porous materials, and complex instruments. Pulse-vacuum systems offer the highest sterilization efficiency with multiple vacuum and steam cycles [5]. The autoclave cycle usually consists of four main phases: pre-vacuum (deaeration), heating, sterilization, and drying. Proper management of each phase is critical to the success of sterilization. For example, incomplete removal of air in the pre-vacuum phase can prevent steam from reaching all surfaces, resulting in inadequate sterilization. Failure to achieve the targeted temperature and pressure values during heating and sterilization can allow particularly heat-resistant bacterial spores to survive. The drying phase is important for removing moisture, especially in textiles and porous materials; otherwise, humid environments can create conditions favorable to microbial growth [6].

Typical errors encountered in autoclave use include insufficient water level, starting cycles before the lid is fully closed, incorrect load placement, overloading, inappropriate temperature and time settings, and neglecting regular maintenance. Such errors can lead to both sterilization failure and instrument malfunction. Furthermore, safe use of autoclaves requires ensuring that safety measures such as safety valves, pressure gauges, and automatic lockout systems are functioning correctly. In practice, critical failures, such as autoclave explosions and thermal injuries, are often caused by user errors or technical deficiencies [7].

In recent years, significant innovations in autoclave technology have emerged. Digital control panels, automatic data logging, remote monitoring, RFID-based load tracking, and advanced security systems have increased both ease of use and safety. In addition, energy efficiency and environmentally friendly designs have also come to the fore. However, to use these technological developments effectively and safely, users need to be well trained [8].

With the increasing prevalence of digitalization and distance education, there is a growing need for interactive educational tools that facilitate the understanding of complex technical processes. Especially during the pandemic, digital simulations have provided an important solution for quickly and safely training healthcare workers and laboratory personnel. Digital autoclave simulators allow users to learn basic principles in a safe, repeatable, and cost-effective way before they encounter real devices. Such simulators play an important role in both reinforcing theoretical knowledge and preparing for practical application [9, 10].

Previous research has examined digital and computer-based autoclave simulations from various technical perspectives; however, these studies have generally focused on process modeling and optimization rather than interactive learning. Existing approaches include virtual autoclave concepts for composite laminates, simulations of curing processes, and finite-element-based thermal analyses; however, most lack web-based accessibility, real-time parameter manipulation, and educational design. Therefore, there remains a clear need for browser-based, user-centered autoclave simulators that support experiential learning and allow safe exploration of sterilization parameters.

This analysis highlights a gap in literature for browser-based, interactive, user-centered, education-focused autoclave simulators. Our approach addresses this gap by providing a fully web-based tool that simulates the four-stage sterilization cycle (pre-vacuum, heating, sterilization, and drying) in real time, enabling dynamic parameter adjustments and delivering critical safety warnings. Consequently, users can safely reinforce theoretical knowledge while encountering potential errors on real devices.

In this study, a fully browser-based interactive autoclave simulator was developed and introduced using modern web technologies (HTML5, CSS3, JavaScript). The simulator enables users to experience a real autoclave cycle step by step, adjusting parameters (temperature, time, water level, and load type), observing phase transitions, and monitoring results in real time. Furthermore, thanks to the simulator's interactive interface, users can learn about the autoclave's components, experience safety warnings, and observe typical user errors in a safe environment. For example, when the water level is insufficient, the simulator warns and does not start the cycle, highlighting a critical real-life safety precaution. This approach offers a more participatory, hands-on learning environment than traditional training methods, enabling users to understand sterilization processes better and avoid potential errors. Furthermore, the simulator's flexibility allows testing different scenarios and error conditions in a safe environment. As a

result, such digital training tools significantly enhance knowledge and skills in areas where sterilization is critical.

2. LITERATURE REVIEW

Although a range of digital and computer-based autoclave simulations has been reported in the literature, most efforts have focused on technical modeling and process optimization rather than interactive learning. Research on user-centered, web-based educational tools remains scarce, and only a limited number of studies provide real-time simulation, dynamic parameter manipulation, or feedback on operational errors. Accordingly, this section reviews the primary contributions and limitations of existing work, thereby contextualizing the need for browser-based autoclave simulators that support experiential learning, which are summarized in Table 1. Previous research on digital or computer-based autoclave simulations can be broadly categorized into technical, simulation-focused studies, and works that offer only limited support for educational and interactive learning.

Table 1. Summary of Previous Studies on Autoclave Simulation and Their Educational Limitations

Year	Authors	Study Focus	Main Contribution	Limitation
2020	Kaychenov et al. [15]	Autoclave thermal model for canned food	Simulator model based on operator and control system actions	Lacks user experience and web-based interaction
2021	He et al.[16]	Finite element simulation of aerospace composite curing	Temperature and stress-strain analysis during curing	Focused on technical accuracy, with no real-time parameter adjustment
2021	Boehler et al. [22]	IoT-based steam sterilization counters	Sensor modeling for sterilization validation	Physical device focus; not an interactive simulator
2023	Kou et al.[17]	Multi-phase flow in autoclaves (CFD-DPM)	Analysis of mixing and suspension behavior	Purely technical modeling, no educational interactivity
2023	Hoelle et al. [18]	3D thermal runaway simulation in batteries	Empirical CFD modeling of heat release	Technical simulation only; lacks an educational user interface
2025	Radchuk et al.[19]	PLC-controlled electric autoclave automation	Remote access and automation for training	Dependent on physical hardware; not web-based
2025	Garcia-Martinez et al. [20]	Thermal effects in autoclave cooling for composites	CFD modeling of thermal dynamics	The education-focused simulation was not addressed

In the first group, Johnston et al. introduced a virtual autoclave concept for composite laminates, although it did not provide a user-friendly web interface [11]. In contrast, Blest et al. simulated curing processes for composite materials, but did not address interactive or pedagogical use [12]. Altinsu et al. modeled the production phases using MATLAB/Simulink but did not present a browser-based learning environment [13]. Similarly, He et al. and Kou et al. concentrated on finite-element analysis and multiphase flow modeling, prioritizing technical accuracy over user interaction [16, 17].

The second group includes studies that offer only limited educational or interactive learning perspectives, such as Angel et al., who applied logistic regression to estimate sterilization stages without a real-time simulation environment [14], and Kaychenov et al., who modeled canned-food sterilization with no educational design focus [15]. Hoelle et al. examined thermal runaway processes [18], whereas Radchuk et al. explored PLC-controlled electric autoclaves that enable remote access for training;

however, their simulations remained hardware-dependent [19]. Garcia-Martinez et al. investigated the thermal effects of autoclave cooling, yet their work did not target pedagogical use [20]. Caliani et al. developed a non-isothermal dynamic model of a high-pressure autoclave reactor for polyethylene production, using PID control to stabilize operation near an unstable steady state. The validated model successfully predicts temperature and concentration gradients as well as polymer properties in industrial ethylene homopolymerization [21].

Collectively, these studies demonstrate that, despite valuable advances in modeling and simulation, a clear gap remains in web-based, interactive autoclave simulators that support experiential learning and real-time parameter exploration.

3. MATERIAL AND METHODS

3.1. Technical Infrastructure of the Simulator

The developed autoclave simulator is a digital training tool designed with modern web technologies that run entirely on the client side. The application is built on an HTML5 structure, with a CSS3-enhanced user interface and dynamic functionality provided by JavaScript. The graphical interface uses a scalable, interactive SVG (Scalable Vector Graphics) diagram that represents the structural and functional components of the autoclave. This diagram allows the user to visually perceive the autoclave's internal structure and main parts, and to open information windows via clickable hotspot regions. The simulation's phase indicators and animations are managed in real time with JavaScript. The state of the autoclave in each phase is visualized with color changes, moving steam effects, and heater animations. The time-dependent changes in parameters such as temperature and pressure are presented to the user through live graphics generated with the Chart.js library. All these functions are integrated into a single HTML file and can run in any modern web browser, without the need for an external server or internet connection. This structure gives the simulator the advantage of both offline use and easy deployment. The code structure is designed to be modular and readable. JavaScript functions perform basic tasks such as starting the simulation, managing phase transitions, updating parameters, triggering animations, and conducting safety checks. The user interface has been developed in accordance with responsive design principles and can be used on different screen sizes. Additionally, all components and visual effects of the simulator are labeled in accordance with accessibility standards, and their color contrasts are optimized for optimal visibility. In this way, an accessible experience is also provided for users who are visually impaired or colorblind.

The web-based autoclave simulator developed within the scope of this study adheres to modern educational technology standards for user interaction, safety, and educational features. For instance, the hotspot-based interactions and parameter sliders (temperature, time, water level) in the simulator allow users to experience every step and receive instant feedback (<input type="range" id="temp">, <rect class="hotspot" ...>). This supports experiential learning and enables users to reinforce theoretical knowledge within a practical context. The simulator is compatible with xAPI/SCORM-compliant frameworks that can track the educational process by recording user actions. To illustrate, every user movement and simulation event is stored as a detailed log entry using the addLogEntry() function, providing educators with an infrastructure for evaluating student performance and transferring data to learning management systems [23, 24]. Furthermore, a design approach aligned with WCAG (Web Content Accessibility Guidelines) principles has been adopted for accessibility. Measures such as role="button", aria-label, and keyboard accessibility (using the keydown event) have been implemented for all SVG hotspots. This ensures that users with special needs, such as visual impairment or color blindness, can also effectively use the simulator [25].

Consequently, the simulator supports not only the transfer of technical and theoretical knowledge but also an educational experience that is academically compliant and traceable. Additionally, it offers a learning environment that is both accessible and pedagogically effective.

3.2. Functional Features and User Scenario

The simulator includes several functional features that model the basic functions and safety mechanisms of a real autoclave device, and a typical usage scenario of the simulator consists of the following steps:

3.2.1. Parameter Settings: Users can set basic sterilization parameters such as temperature (between 100-140°C), sterilization time (between 5-60 minutes), water level (between 0-100%), and load type (solid, liquid, porous) before simulation. These parameters directly affect the simulation's dynamics and results. The parameters can be easily changed via sliders and drop-down menus in the interface. In addition, the recommended sterilization time is automatically updated according to the selected load type and temperature. This feature provides users with realistic, practical experience.

After the simulator is started, the user sets the sterilization parameters such as temperature, time, water level, and load type through the sliders and drop-down menus presented on the interface. The system can automatically update the recommended sterilization time according to the selected parameters. Furthermore, the user can create various scenarios by experimenting with temperature and time combinations suitable for different load types.

3.2.2. Phase Display and Animations and Starting Simulation: The simulator animatedly shows the autoclave cycle in four main phases (pre-vacuum, heating, sterilization, drying). The visual effects and color changes associated with each phase allow the user to follow the process step by step. Phase transitions are clearly indicated in both the phase display on the screen and the process log. For instance, during the heating phase, the heater animation and room color changes, while during the sterilization phase, the steam animation and constant temperature/pressure values are highlighted.

The autoclave cycle is started by clicking on the “Start Use Cycle” button. The simulation begins with the pre-vacuum phase and proceeds to the heating, sterilization, and drying phases. In each phase, relevant animations and phase indicators become active. The user can follow phase transitions using both the phase indicator on the screen and the process log.

3.2.3. Real-Time Graphics and Monitoring the Process: The temporal variations of temperature and pressure values are visualized using Chart.js-based real-time charts. These graphs allow the user to monitor the dynamics of the sterilization process in real time. Temperature (°C) and pressure (bar) values are displayed in different colors and on separate axes. The user can observe the change of these values at every moment of the simulation and evaluate the efficiency of the process.

During the simulation, temperature and pressure values can be monitored in real time on the graph. At the same time, water level and safety warnings are displayed on the screen. The user can open information windows by clicking on different components of the autoclave. This interaction supports the learning of both theoretical knowledge and the device's structural features.

3.2.4. Interactive SVG and Information Windows: The main components of the autoclave (sterilization chamber, lid, pressure gauge, whistle, heater, vacuum generator, wastewater cooler, safety valve) are designed as clickable on the SVG. When the user clicks on these components, description windows pop up with information about the function and technical specifications of the relevant part. This feature is particularly effective for learning the structural and functional components of the autoclave.

3.2.5. Safety Warnings and Automatic Stop: When the water level drops below a critical threshold (e.g., 20%) during the simulation, the system automatically stops the cycle and warns the user both visually and textually. When the water level drops below 50%, preventive warnings are displayed, allowing the user to intervene early. This feature helps users understand the safety risks encountered in real autoclave use.

When the water level drops below the critical level, the simulation automatically stops, and the user is warned. The user can also manually terminate the simulation using the “Emergency Stop” button. These

features ensure that emergencies encountered in real autoclave use can be safely simulated in a digital environment.

3.2.6. Transaction Log: All important events, phase transitions, warnings, and user actions are recorded in a time-stamped transaction log. This log makes it easy for the user to follow the simulation process step by step and perform retrospective reviews. The log details critical events such as phase starts, parameter changes, safety warnings, and cycle ends.

When the simulation is complete, the system displays a notification of successful cycle completion and records the event in the process log. The user can review the entire process and important events in the log. In addition, the effectiveness of sterilization can be evaluated from the temperature and pressure graphs obtained at the end of the simulation.

3.2.7. Emergency Stop Function: During the simulation, the user can manually terminate the cycle using the "Emergency Stop" button. This feature allows users to experience the emergency procedures in real autoclaves in a digital environment and develop crisis management skills.

Thanks to this detailed technical and functional structure, the simulator can be used as an effective digital tool for both training and preparation before practical application. The simulator is designed to be flexible and customizable to meet the needs of different user profiles (students, instructors, laboratory staff).

3.3. Software Architecture and Technical Details

The autoclave simulator is designed with a modular and extensible software architecture to ensure maintainability, traceability, and flexibility for future extensions. Figure 1 illustrates the modular architecture of the simulator system. Users interact with the interface to select load types (Textile, Liquids, Metal) and adjust parameters such as temperature, duration, and water level. These inputs are sent through the UI Manager to the Simulation Controller, which serves as the core control unit managing load profiles, operating the state machine (Vacuum → Heating → Sterilization → Drying), and generating simulation data. The Load Manager determines default parameters based on the selected load type and forwards them to the Visualization & Feedback Components. This module presents real-time temperature and pressure graphs, indicators, and warning messages to the user. All events occurring during the simulation are recorded by the Logger and passed to the Data Output Layer, where summary reports, safety checks, and validation logs are generated. This architecture ensures a modular, traceable, and extensible system where each module has a defined responsibility and interactions between layers are structured through clear data flows.

The interface layer is developed using HTML5 and CSS3, following responsive design principles to guarantee smooth operation across desktop, tablet, and mobile devices. The autoclave components are represented as interactive SVG graphics, with "hotspot" regions that enable users to access detailed information about each part. The core simulation engine, implemented in JavaScript, manages phase transitions, parameter updates, animations, and safety checks, with separate functions for each phase to improve clarity and maintainability. Real-time visualization of temperature and pressure is achieved using Chart.js, allowing learners to observe dynamic changes and evaluate the efficiency of the sterilization process. All events, including phase transitions, safety warnings, and user interactions, are logged with time stamps, facilitating both learning assessment and process tracking.

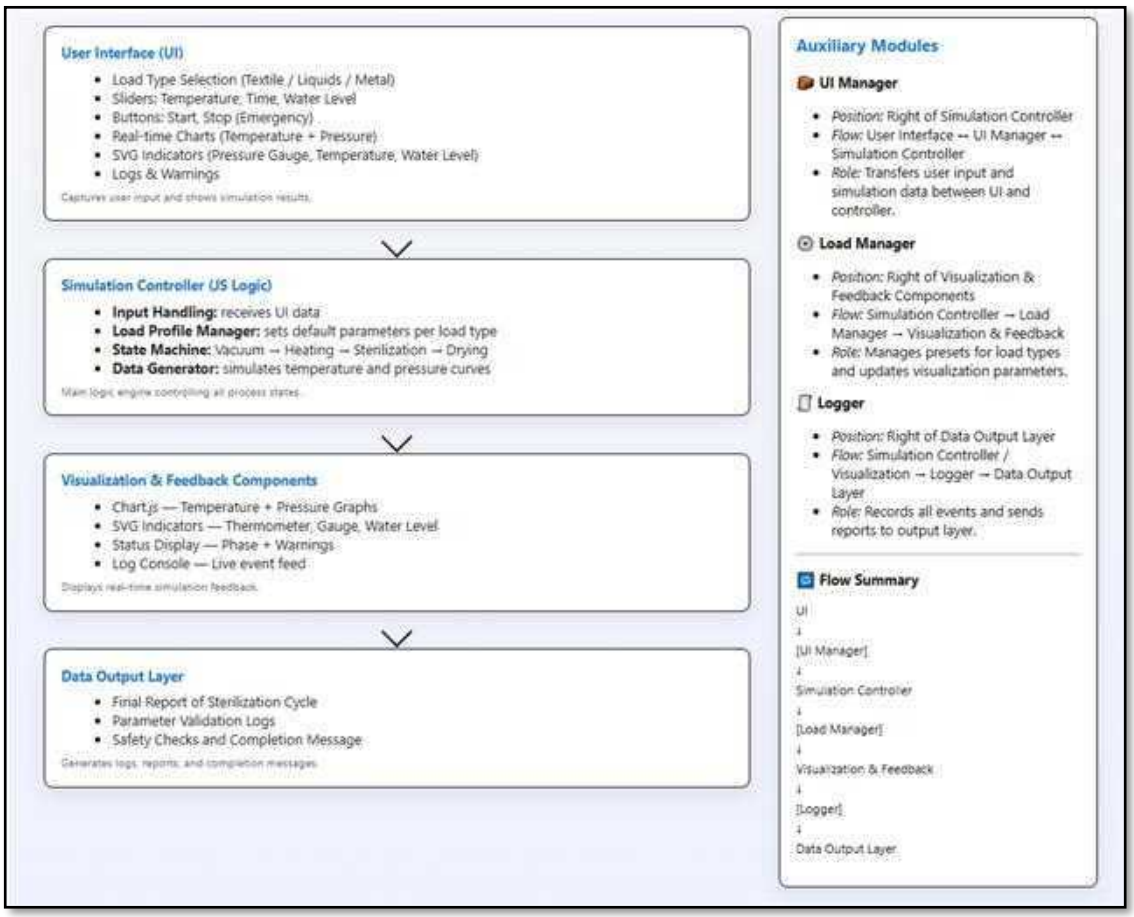


Figure 1. Modular Software Architecture and Data Flow of the Autoclave Simulator

3.4. Accessibility Strategies

The simulator is designed in accordance with accessibility standards to ensure usability for diverse learners. All interface colors comply with WCAG guidelines and are optimized for contrast, including options suitable for color-blind users. Interactive elements, such as buttons, sliders, and SVG hotspots, are properly labeled with "aria-label" and "title" attributes, making the simulator fully operable via keyboard. Explanation windows are compatible with screen readers, and audio alerts can be implemented for critical warnings or end-of-cycle notifications. The simulator's responsive design ensures a consistent and accessible experience across different screen sizes and device types.

3.5. Educational Assessment and Integration

The simulator incorporates pedagogical strategies to enhance experiential learning and knowledge retention. Scenario-based training allows instructors to configure different load types, parameter combinations, and error conditions, enabling learners to explore real-world situations in a safe digital environment. Automatic feedback provides users with immediate information on sterilization success, mistakes made, and recommended corrective actions. Trainers can evaluate learner performance using the log and graphical process, supporting monitoring and assessment of learning progress. Additionally, the simulator is compatible with learning management systems via SCORM and xAPI standards, allowing integration into online education platforms. This integration, combined with real-time visualization, safety mechanisms, and interactive structural information, aligns with constructivist and active learning principles, offering a pedagogically informed and flexible educational tool.

3.6. Calculation Schemes Used

3.6.1. Vapor Pressure and Temperature Relationship

The effectiveness of autoclave sterilization depends on the relationship between temperature and pressure. In the simulator, the approximate relationship between the saturated vapor pressure of water and temperature is modeled as follows:

$$P = P_0 . e^{\frac{L}{R}(\frac{1}{T_0} - \frac{1}{T})} \quad (1)$$

In Equation (1), P_0 and T_0 represent the reference temperature and pressure, T the absolute temperature, L the heat of vaporization, and R the gas constant in the SI unit system. This equation is a simplified version of the Clausius-Clapeyron equation that describes the relationship between water vapor pressure and temperature [26].

3.6.2. Simplified Pressure Calculation Used in the Simulator

In the simulator, pressure values corresponding to temperature are assigned intermittently to enable fast, user-friendly calculations. This approach mirrors the temperature-pressure couplings commonly used in autoclave sterilization. This method directly reflects the widely accepted temperature-pressure pairs in autoclave sterilization (e.g., 121°C ≈ 2 bar, 134°C ≈ 3 bar) and provides the user with a realistic experience. It also reduces the computational burden, allowing the simulation to run quickly and smoothly.

3.6.3. Graphical Representation of Temperature and Time

In the simulator, temperature and pressure values are modeled as follows, depending on time [27-30]:

Heating Phase: Temperature, (T(t)), increases linearly [27-30].

$$T(t) = T_{initial} + (T_{target} - T_{initial}) . \frac{t}{t_{heating}} \quad (2)$$

, where t is the elapsed time; heating refers to the total time of the heating phase.

Sterilization Phase: The temperature is kept constant: $T(t)=T_{target}$ (3)

Drying Phase: The temperature (T(t)) decreases linearly from the target value (T_{target}) to the final value (T_{final}) (e.g. room temperature) [27-30].

$$T(t) = T_{final} - (T_{target} - T_{final}) . \frac{t}{t_{drying}} \quad (4)$$

$$P = \begin{cases} 3.0 \text{ bar if } T \geq 134^0 C \\ 2.0 \text{ bar if } 121^0 C \leq T \leq 134^0 C \\ 1.5 \text{ bar if } 115^0 C \leq T \leq 121^0 C \\ 1.0 \text{ bar if } 100^0 C \leq T \leq 115^0 C \\ 0.1 \text{ bar if } T < 100^0 C \end{cases} \quad (5)$$

In each phase, the pressure corresponding to the temperature value is also updated according to equation (5) described above. This modeling not only reflects the basic dynamics of the actual autoclave

cycle, but also allows the user to monitor temperature and pressure changes in real time throughout the process. These equations enable realistic and educational modeling of temperature and pressure changes in the background of the simulator. In particular, the Clausius-Clapeyron equation captures the fundamental relationship between water's vapor pressure and temperature. In contrast, the simplified pressure table was chosen to provide the user with a quick and understandable experience [27-30].

4. RESULTS

The advanced autoclave simulator aims to provide users with both theoretical and practical knowledge by modeling the physical and operational processes of an autoclave in a detailed, interactive manner. At the beginning of the simulation, the user is asked for four basic parameters: sterilization temperature (e.g. 121 ^{0}C, 134 ^{0}C), sterilization time (e.g. 15, 20, 30 minutes), water level (in percentage, e.g. 100%, 50%, 10%) and load type (solid material, liquid material, or porous material). Once the user selects the temperature and load type, the simulator automatically sets the recommended sterilization time based on scientific sources. For instance, for solid surgical instruments, 15 minutes at 121 ^{0}C and only 3 minutes at 134 ^{0}C are sufficient, whereas for liquid materials, 20 minutes at 121 ^{0}C and 5 minutes at 134 ^{0}C are required. For porous textile loads, longer times are recommended, such as 30 minutes at 121 ^{0}C and 10 minutes at 134 ^{0}C. This relationship is summarized in Table 2.

Table 2. Recommended Sterilization Time and Temperature Based on Load Type

Load Type	Temperature (°C)	Recommended Time (min)
Solid (Surgical Instruments)	134	3
	121	15
	115	30
Liquid (Culture Media)	134	5
	121	20
	115	45
Porous (Textiles)	134	10
	121	30
	115	60

When the water level drops below 20%, the simulator either does not start the cycle or automatically stops the ongoing cycle for safety reasons, similar to a real autoclave.

Once the simulation starts, the process proceeds through four main phases. In the first phase, “Pre-Vacuum”, the air in the autoclave chamber is exhausted by the vacuum pump. This phase lasts about 45 seconds, and the pressure in the chamber drops from 1 atmosphere (about 1 bar) to 0.1 bar. This is necessary so that the steam can reach every part of the load, as air reduces the sterilization effectiveness. In the second phase, “Heating”, electric heaters or a steam generator are activated, and the temperature and pressure in the room are gradually increased. For example, at room temperature (25 °C), the selected target temperature is reached in approximately 75 seconds. As the temperature rises, the vapor pressure of the water also increases: 1 bar at 100 ^{0}C, 1.5 bar at 115 ^{0}C, 2 bar at 121 ^{0}C, and 3 bar at 134 ^{0}C. This physical relationship is dynamically modeled in the simulator, and the pressure gauge needle moves accordingly.

The corresponding pressure values across different temperature ranges, which ensure the physical consistency of the simulation, are presented in Table 3 below.

Table 3. Temperature and Pressure Values

Temperature (°C)	Pressure (bar)
≥ 134	3.0
121 - 133	2.0
115 - 120	1.5
100 - 114	1.0
< 100	0.1

When the heating phase is completed, the third phase, "Sterilization," begins. In this phase, the selected temperature and pressure are kept constant for a period determined by the type of load (e.g., 15 minutes). During this time, the water level slowly decreases; for example, a 0.25% loss is simulated every minute. If the water level drops below 10%, the simulator automatically terminates the cycle for safety reasons and warns the user, as in a real device.

When the sterilization phase is completed, the "Drying" phase begins. In this phase, the chamber temperature is reduced to 40 ^{0}C in a controlled manner, and the moisture within is removed by vacuum, ensuring the load is completely dry and sterile. The standard duration of each operational phase is outlined in Table 4 below.

Table 4. Phase Transition Durations in the Sterilization Cycle

Phase	Duration (seconds)	Description
Pre-Vacuum	45	Air removal process.
Heating	75	Temperature rises to target value.
Sterilization	Time × 60	Holding at target temperature.
Drying	90	Removing moisture.

The drying phase lasts approximately 90 seconds. During this entire process, the color of the inner chamber of the autoclave on the simulator interface changes from blue to red depending on the temperature: light blue at 25 ^{0}C, orange at 121 ^{0}C, and red at 134 ^{0}C. The needle of the pressure gauge turns upwards at 0.1 bar and to the right at 3 bar. The water level indicator visually reflects the current water level. In addition, the temperature and pressure values are plotted on a graph in real time; for example, the temperature axis is scaled from 20 ^{0}C to 150 ^{0}C and the pressure axis is scaled from 0 to 4 bar.

The simulator provides the user with time-stamped notifications and logs for every important event (e.g., phase transitions, low-water-level warnings, loop start or stop). If the user sets the water level too low, a notification will be sent to "⚠ Warning: Water level too low! Sterilization may fail." will appear on the screen, and the cycle will not start. If the "Emergency Stop" button is pressed at any time during the cycle, the simulator immediately terminates the process and records this in the log. Furthermore, by clicking different parts of the autoclave (e.g., lid, heater, vacuum generator, safety valve), the user can view detailed descriptions of each part's function and technical specifications on the screen. This also supports learner self-assessment and reflection, as users can experiment and immediately observe the consequences of errors or parameter changes. It strengthens understanding of safety protocols and the rationale behind operational limits. Due to these features, the simulator teaches users the physical principles, operational steps, safety protocols, and error conditions of a real autoclave, integrating numerical data and visual animations. Thus, by experimenting with different parameters, the user can experience and learn about the factors that affect sterilization success.

Figure 2 shows the main interface and interactive SVG diagram of the autoclave simulator. By clicking on components of the autoclave, the user can open information windows and visually examine the device's structural operation. Interactive SVG components allow students to explore the autoclave design in detail, linking visual learning with procedural understanding.



Figure 2. Simulator Main Interface and Interactive Components

Figure 3 illustrates the temporal variations of temperature and pressure during the simulation. On the graph, heating, sterilization, and drying phases are separated by different colors or background tones. With this graph, the user can instantly monitor the phase transitions and the effect of parameter changes. The process log is recorded during the simulation and on the event tracking screen. The user can follow phase transitions, warnings, and their interventions step by step through this log. This visual differentiation reinforces cognitive understanding of phase-specific dynamics and real-time response to parameter changes.

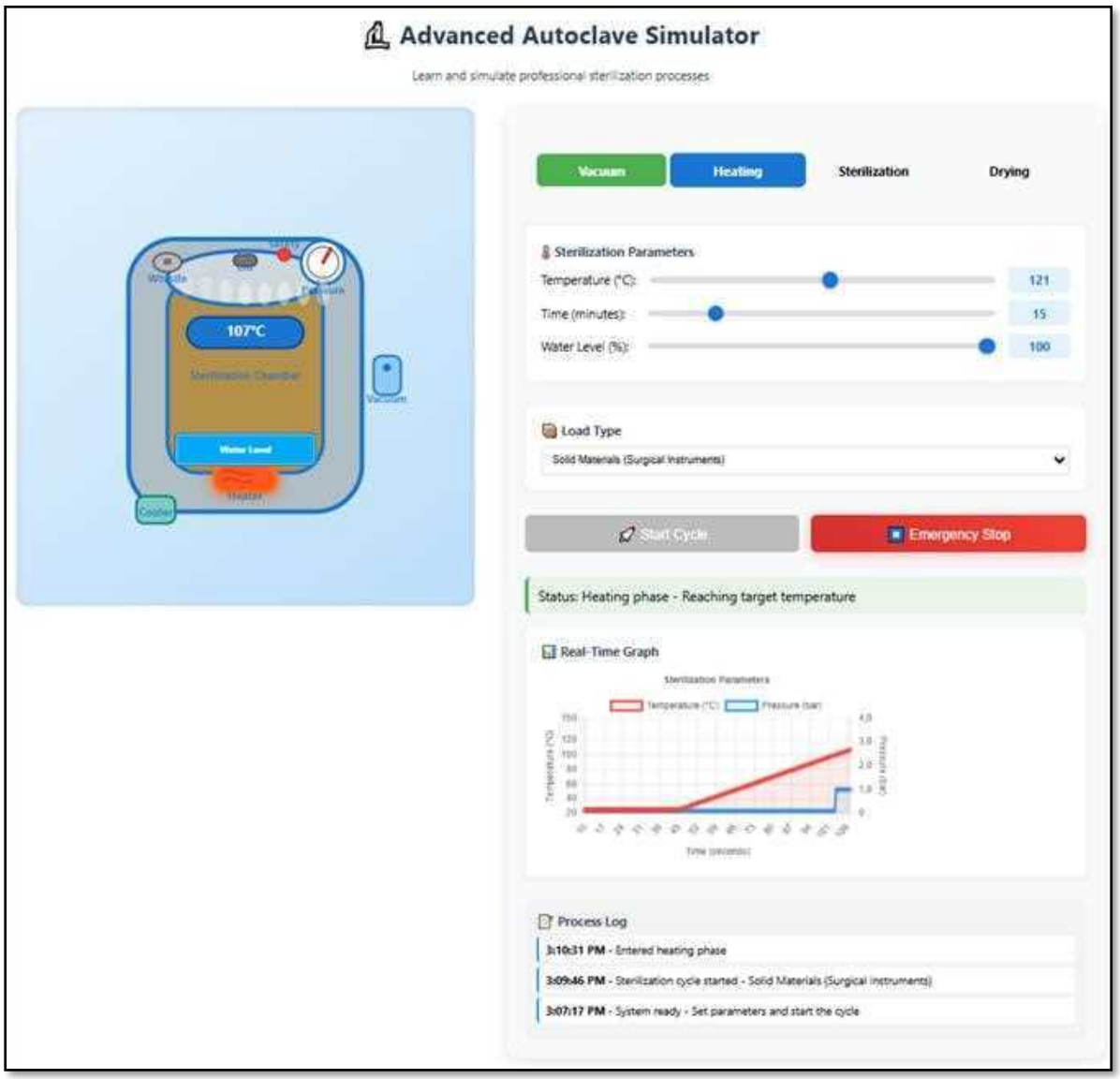


Figure 3. Time-dependent variation of temperature (°C) and pressure (bar) values during simulation.

To provide a clearer quantitative representation of the simulator's performance and enhance the scientific rigor of the results, four supporting tables have been incorporated. Table 2 summarizes the recommended sterilization time–temperature relationships for different load types, based on standard autoclave operation guidelines. Table 5 presents three example simulation scenarios that illustrate how variations in load type, temperature, and sterilization duration influence total process time and the corresponding pressure–temperature transitions.

Table 5. Example Simulation Scenarios

Scenario	Load Type	Temperature (°C)	Recommended Time (min)	Phase Transition Times	Total Time	Temperature and Pressure
Scenario 1	Solid (Surgical Instruments)	121	15	Pre-Vacuum: 45 sec Heating: 75 sec Sterilization: 15 min (900 sec) Drying: 90 sec	~17 min (~1010 sec)	Heating: 25°C → 121°C (2.0 bar) Sterilization: 121°C (2.0 bar) Drying: 121°C → 40°C (0.1 bar)
Scenario 2	Liquid (Culture Media)	134	5	Pre-Vacuum: 45 sec Heating: 75 sec Sterilization: 5 min (300 sec) Drying: 90 sec	~7 min (~410 sec)	Heating: 25°C → 134°C (3.0 bar) Sterilization: 134°C (3.0 bar) Drying: 134°C → 40°C (0.1 bar)
Scenario 3	Porous (Textiles)	121	30	Pre-Vacuum: 45 sec Heating: 75 sec Sterilization: 30 min (1800 sec) Drying: 90 sec	~32 min (~1920 sec)	Heating: 25°C → 121°C (2.0 bar) Sterilization: 121°C (2.0 bar) Drying: 121°C → 40°C (0.1 bar)

5. DISCUSSION

The increasing integration of web-based simulation tools into educational settings has significantly expanded opportunities for practical training in fields where equipment cost, safety considerations, and accessibility pose longstanding challenges. Autoclave devices, widely used in hospital sterilization units and laboratory environments, require both procedural knowledge and situational awareness—skills that traditionally depend on access to physical devices. By providing a controlled, interactive, and risk-free learning environment, the developed autoclave simulator addresses several logistical and safety-related

limitations, supporting the broader adoption of digital training approaches consistent with recent trends in educational technologies [9], [10].

Compared to conventional instruction or static digital resources, the simulator offers several pedagogical advantages. First, the real-time visualization of temperature–pressure dynamics enables learners to form meaningful conceptual associations between physical principles and operational outcomes, reinforcing core aspects of moist-heat sterilization processes described in clinical sterilization literature [1], [4], [27]. The graphical separation of heating, sterilization, and drying phases (Figure 3) mirrors the temporal structure of real autoclave cycles. It supports better cognitive mapping of phase transitions, which can otherwise be abstract or counterintuitive for novice learners. Additionally, the interactive SVG interface (Figure 2) allows users to inspect components such as the chamber, heater, vacuum pump, and safety valve, promoting structural understanding—an element emphasized in hospital sterilization guidelines and training practices [2].

The quantitative data presented in Tables 2–5 reinforce the simulation's physical validity. Recommended time–temperature pairs (Table 2) are consistent with standard autoclave operation recommendations drawn from established sterilization protocols [1], [6], while the pressure–temperature relationships (Table 3) reflect thermodynamic principles documented in moist-heat sterilization and vapor-pressure modeling studies [26], [27]. Likewise, the modeled durations of operational phases (Table 4) align with typical autoclave cycle profiles used in industrial and medical environments [8], [15]. Collectively, these structured data tables enhance the simulator's scientific grounding and expand its potential use in analytical or comparative instructional activities.

Pedagogically, the simulator supports experiential and constructivist learning by allowing users to manipulate cycle parameters and observe their immediate consequences. This dynamic interaction encourages iterative experimentation, facilitating deeper conceptual engagement compared to passive instructional formats. Evaluated through established educational frameworks, the simulator demonstrates strong alignment with Levels 1 and 2 of Kirkpatrick's Training Evaluation Model, as it promotes positive learner engagement and measurable improvements in conceptual understanding [31]. Furthermore, interface accessibility, ease of use, and real-time feedback correspond to constructs emphasized in the Technology Acceptance Model (TAM), suggesting high potential for user adoption and sustained educational impact [32].

Performance tests indicate that the simulator functions reliably across major browsers and mobile devices, although some older browsers exhibit minor inconsistencies in animation rendering and visual transitions. These issues point to the need for further optimization—particularly in responsive layout, graphics scaling, and accessibility adjustments—to support broader institutional deployment. Adoption in resource-constrained settings may also benefit from expanded offline compatibility modes or lightweight rendering options.

In addition to its pedagogical strengths, the simulator's open-source architecture offers educators, instructional designers, and healthcare institutions opportunities for further customization. Previous digital training studies have shown that interoperability with learning management systems (LMS) and support for data standards such as SCORM and xAPI can significantly enhance monitoring, evaluation, and integration into structured curricula [23], [24]. Thus, incorporating such interoperability features may improve the simulator's applicability within formal training programs.

Despite its educational utility, the current simulator version has several limitations. Advanced failure scenarios—such as sensor malfunction, power outage, steam leakage, or mechanical obstruction—are not yet modeled, even though such conditions are clinically significant in real autoclave operation. Including these scenarios in future versions would enable more comprehensive simulation-based training, especially in risk mitigation and emergency response contexts. Moreover, the simulator currently lacks built-in user assessment tools, automated feedback mechanisms, and performance analytics. Integrating these features could strengthen alignment with higher levels of Kirkpatrick's model (behavior and results) and facilitate the implementation of competency-based evaluation frameworks.

Further enhancement could include multilingual interface support, enriched accessibility features aligned with WCAG 2.0 standards [25], improved browser compatibility, and integration with digital credentialing or microlearning platforms. Future research may also compare the simulator's learning impact against traditional hands-on autoclave training or hybrid instructional methods, contributing to the growing literature on simulation-based education in healthcare and laboratory sciences.

5. CONCLUSIONS

The developed web-based autoclave simulator offers an innovative and pedagogically grounded approach to sterilization training by connecting theoretical knowledge with safe, interactive, and real-time practice. Its parameters control safety alerts and activity logging mechanisms, enhancing experiential learning and providing a modern alternative to traditional laboratory environments. With these capabilities, the simulator not only contributes a functional tool for sterilization education but also establishes one of the first browser-based, interactive, and log-driven autoclave training platforms, filling a distinct gap in the literature and offering a reproducible foundation for future research and instructional innovation.

Future improvements will focus on strengthening its instructional adaptability and implementation in broader learning contexts. Planned features include realistic error scenarios (e.g., sensor or power failures), automated performance analytics with personalized feedback, and scenario-based training modules designed to improve decision-making skills. Additionally, compliance with SCORM/xAPI standards, multilingual and accessibility enhancements, and expanded reporting and data export capabilities will support seamless integration into learning management systems and distance education settings.

Declaration of Ethical Standards

Authors declare to comply with all ethical guidelines including authorship, citation, data reporting, and publishing original research.

Credit Authorship Contribution Statement

A.Ö.A: Conceptualization, Resources, Coding, Writing -review & editing, Supervision. M.A: Investigation, Methodology. K.K: Investigation, Methodology. D.T: Investigation, Methodology.

Declaration of Competing Interest

The authors declare that they have no known competing financial interests or personal relationships that could have appeared to influence the work reported in this paper.

Funding / Acknowledgements

No funding is available for this research

Data Availability

The source code for the simulations is available on GitHub (https://aliakyuz12.github.io/autoclave-/) and can be used for educational purposes.

Use of Artificial Intelligence

Generative artificial intelligence (AI) tools were not used to generate scientific content, research data, interpretations, or analyses. The authors acknowledge that the use of AI tools is limited to language editing and readability improvements. The authors remain fully responsible for the accuracy, originality, and integrity of the manuscript, in compliance with ethical and legal standards.

5. REFERENCES

[1] W. A. Rutala and D. J. Weber, "Disinfection and sterilization in health care facilities: An overview and current issues," *Infect. Dis. Clin*., vol. 35, no. 3, pp. 575–607, 2021, doi:10.1016/j.idc.2021.04.004

[2] B. Bal and A. Balaraju, "Overview of the central sterilization supply department, an integral part of the hospital," *J. Infect. Dev. Ctries*., vol. 19, no. 03, pp. 325–334, 2025, doi:10.3855/jidc.18646

[3] M. Davies, "Unwrapping the history of sterilisation," *ACORN: J. Perioper. Nurs. Aust*., vol. 30, no. 4, pp. 41–46, 2017.

[4] A. R. Talekar and A. G. Pise, "Systematic approach of autoclave qualification: A review," *Int. J. Med. Pharm. Sci*., vol. 13, no. 9, pp. 1–6, 2023, doi:10.31782/IJMPS.2023.13901

[5] T. Centea, L. K. Grunenfelder, and S. R. Nutt, "A review of out-of-autoclave prepregs–Material properties, process phenomena, and manufacturing considerations," *Compos. Part A: Appl. Sci. Manuf*., vol. 70, pp. 132–154, 2015, doi: 10.1016/j.compositesa.2014.09.029

[6] P. DeSantis, "Steam sterilization in autoclaves," in Handbook of Validation in Pharmaceutical Processes, 4th ed. Boca Raton, FL, USA: CRC Press, 2021, pp. 217–230.

[7] M. Kumaran, N. Fredrick, G. Dudeja, R. Sukumaran, and C. Dorairaj, "Steam sterilization: Review of autoclaves, validation, instrument packing, and sterility failures," *Indian Journal of Ophthalmology*, vol. 74, no. 2, pp. 173–182, 2026, doi: 10.4103/ijo.ijo_2023_25.

[8] V. Antonucci et al., "Analysis of heat transfer in autoclave technology," *Polym. Compos*., vol. 22, no. 5, pp. 613–620, 2001, doi:10.1002/pc.10564

[9] N. V. Ronzhina, I. M. Kondyurina, A. A. Воронина, K. A. Игишев, and N. A. Loginova, "Digitalization of Modern Education: Problems and Solutions," *International Journal of Emerging Technologies in Learning (iJET)*, vol. 16, no. 4, pp. 122-135, 2021, doi: 10.3991/ijet.v16i04.18203.

[10] A. T. Bates, Technology, E-Learning and Distance Education. New York, NY, USA: Routledge, 2005.

[11] A. Johnston, P. Hubert, G. Fernlund, R. Vaziri, and A. Poursartip, "Process modeling of composite structures employing a virtual autoclave concept," *Science and Engineering of Composite Materials*, vol. 5, no. 3–4, pp. 235–252, 1996, doi: 10.1515/SECM.1996.5.3-4.235

[12] D. C. Blest, S. McKee, A. K. Zulkifle, and P. Marshall, "Curing simulation by autoclave resin infusion," *Composites Science and Technology*, vol. 59, no. 16, pp. 2297–2313, 1999,doi: 10.1016/S0266-3538(99)00084-6.

[13] B. Altinsu, O. Koçak, and A. Akpek, "Design and analysis of an autoclave simulation using MATLAB/Simulink,"*2016 Medical Technologies National Congress (TIPTEKNO)*, 2016, pp. 1–4. doi: 10.1109/TIPTEKNO.2016.7863081.

[14] L. Angel, J. Viola, M. Vega, and R. Restrepo, "Sterilization process stages estimation for an autoclave using logistic regression models," *2016 XXI Symposium on Signal Processing, Images and Artificial Vision (STSIVA)*, 2016, pp. 1–5, doi: 10.1109/STSIVA.2016.7743337

[15] A. Kaychenov, A. Vlasov, A. Maslov, I. Selyakov, and Y. Glukhikh, "Development of an autoclave thermal processes model for the simulator of canned food sterilization process," *KnE Life Sciences*, pp. 437–449, 2020, doi: 10.18502/kls.v5i1.6103

[16] J. He, F. Cong, M. Cao, X. Li, and S. Wang, "Finite element simulation of the autoclave curing process of aerospace resin-based composite material," *IOP Conf. Ser.: Earth Environ. Sci*., vol. 693, no. 1, p. 012123, 2021, doi: 10.1088/1755-1315/693/1/012123

[17] B. Kou, Y. Hou, W. Fu, N. Yang, J. Liu, and G. Xie, "Simulation of multi-phase flow in autoclaves using a coupled CFD-DPM approach," *Processes*, vol. 11, no. 3, p. 890, 2023, doi:10.3390/pr11030890

[18] S. Hoelle, F. Dengler, S. Zimmermann, and O. Hinrichsen, "3d thermal simulation of lithium-ion battery thermal runaway in autoclave calorimetry: Development and comparison of modeling approaches," *Journal of The Electrochemical Society*, vol. 170, no. 1, p. 010509, 2023, doi: 10.1149/1945-7111/acac06

[19] O. V. Radchuk, M. Y. Savchenko, S. V. Sokolov, and O. S. Sokolov, "Automation of a laboratory electric autoclave using a programmable logic controller," *J. Chem. Technol*., vol. 33, no. 1, pp. 239–248, 2025, doi:10.15421/jchemtech.v33i1.310425

[20] A. Garcia-Martinez, A. Fernandez-Jimenez, J. M. G. C. Sanchez, and A. J. Gutierrez-Trashorras, "Thermal effects of cooling dynamics in autoclave processing on composite materials," *Int. J. Adv. Manuf. Technol.*, vol. 137, no. 5, pp. 2979–2989, 2025, doi:10.1007/s00170-025-15346-9

[21] E. Caliani, M. Cavalcanti, L. M. F. Lona, and F. A. N. Fernandes, "Modeling and simulation of high-pressure industrial autoclave polyethylene reactor," *Express Polym. Lett*., vol. 2, no. 1, pp. 57–64, 2008, doi:10.1016/S1570-7946(06)80117-3

[22] L. Boehler, M. Daniol, R. Sroka, D. Osinski, and A. Keller, "Sensors in the autoclave-modelling and implementation of the IoT steam sterilization procedure counter," *Sensors*, vol. 21, no. 2, p. 510, 2021, doi:10.3390/s21020510

[23] A. Bakharia, K. Kitto, A. Pardo, D. Gašević, and S. Dawson, "Recipe for success: lessons learnt from using xAPI within the connected learning analytics toolkit," *in Proc. 6th Int. Conf. Learn. Anal. Knowl*., 2016, pp. 378–382, doi: 10.1145/2883851.2883882

[24] F. B. García and A. H. Jorge, "Evaluating e-learning platforms through SCORM specifications," *in IADIS Virtual Multi Conference on Computer Science and Information Systems*, 2006, pp. 53–58.

[25] B. Caldwell et al., "Web content accessibility guidelines (WCAG) 2.0," WWW Consortium (W3C), vol. 290, no. 1–34, pp. 5–12, 2008.

[26] J. Huang, "A simple accurate formula for calculating saturation vapor pressure of water and ice," *J. Appl. Meteorol. Climatol*., vol. 57, no. 6, pp. 1265–1272, 2018, doi: 10.1175/JAMC-D-17-0334.1

[27] B. M. Boca, E. Pretorius, R. Gochin, R. Chapoullie, and Z. Apostolides, "An overview of the validation approach for moist heat sterilization, part II," *Pharmaceutical technology*, vol. 26, no. 10, pp. 96–113, 2002.

[28] C. V. Fiorello, C. A. Harms, S. K. Chinnadurai, and D. Strahl-Heldreth, "Best-practice guidelines for field-based surgery and anesthesia on free-ranging wildlife. II. Surgery," *J. Wildl. Dis*., vol. 52, no. 2s, pp. S28–S39, 2016, doi: 10.7589/52.2S.S28

[29] N. Han, L. An, L. Fan, L. Hua, and G. Gao, "Research on temperature field distribution in a frame mold during autoclave process," *Materials*, vol. 13, no. 18, p. 4020, 2020, doi: 10.3390/ma13184020

[30] M. Fernández-Gracía, J. F. Sánchez-Pérez, F. del Cerro, and M. Conesa, "Mathematical Model to Calculate Heat Transfer in Cylindrical Vessels with Temperature-Dependent Materials," *Axioms*, vol. 12, no. 4, p. 335, 2023, doi:10.3390/axioms12040335

[31] Y. Kaya, R. Günay, and F. K. Damgacı, "Kirkpatrick dört düzey program değerlendirme modeli," *Uluslararası Eğitim Bilimleri Dergisi*, no. 5, pp. 89–97, 2015.

[32] R. Ibrahim et al., "E-learning acceptance based on technology acceptance model (TAM)," *J. Fundam. Appl. Sci*., vol. 9, no. 4S, pp. 871–889, 2017,doi:10.4314/jfas.v9i4s.50